



MINISTERUL CERCETĂRII ȘI INOVĂRII

Aerospace Europe CEAS 2017 Conference European Aerospace "Quo Vadis?" (6th CEAS Air & Space Conference)



Palace of the Parliament - Bucharest, ROMANIA
16th-20th October 2017

Organized by:



COMOTI
ROMANIAN RESEARCH &
DEVELOPMENT INSTITUTE FOR
GAS TURBINES



Asociația Aerospațială și Astronautică a României

Romanian Research and Development Institute for Gas Turbines COMOTI

Coordinator: Ionuț PORUMBEL

PROCEEDINGS
of the 6th CEAS Air and Space Conference
Aerospace Europe 2017

Peer reviewed technical papers presented at the conference

Bucharest, 2017

Editor: George Bogdan GHERMAN

ISBN: 978-973-0-25597-3

Selected papers were published in:

CEAS Aircraft Journal

CEAS Space Journal

Transportation Research Procedia

INCAS Bulletin

For these papers, only the abstract is included in these Proceedings

Validation of the SmartBasing Aircraft Rotation and Retirement Strategy

*Jeffrey M. Newcamp
Delft University of Technology
PhD Candidate
Kluyverweg 1, 2629 HS Delft, Netherlands
j.m.newcamp@tudelft.nl*

*W.J.C. Verhagen
Delft University of Technology
Assistant Professor*

*Richard Curran
Delft University of Technology
Professor*

ABSTRACT

SmartBasing provides fleet managers tools with which to manage their end-of-life aircraft fleets. The principles of SmartBasing include reassigning aircraft to different bases and assigning aircraft to a new mix of mission types to actively manage the remaining useful lifetime of each aircraft in a fleet. This paper employs a single case study aircraft to validate the SmartBasing approach for a dynamic strategy for aircraft retirement. The United States Air Force's A-10 Thunderbolt II was used for validation because it is an ageing fleet that experienced a partial fleet retirement in 2013. The efficacy of the SmartBasing principles was tested using the aircraft retired in 2013 by altering usage patterns and basing locations in the years leading to the 2013 retirement. It was shown that SmartBasing would have been a valid technique for managing the A-10 fleet prior to its partial retirement. Better aircraft utilisation planning could have expended more residual aircraft lifetime prior to retirement, resulting in savings of more than 1.88 full aircraft lifetimes or over 83 million USD.

KEYWORDS: *military aircraft, aircraft rotations, military retirements, SmartBasing*

Towards Automation of Aerial Refuelling Manoeuvres with the Probe-and-Drogue System: Modelling and Simulation

Nicolas Fezans

DLR (German Aerospace Center)

Research Scientist

DLR-FT-FDS, Lilienthalplatz 7, 38108 Braunschweig

nicolas.fezans@dlr.de

Thomas Jann

DLR (German Aerospace Center)

Research Scientist

thomas.jann@dlr.de

ABSTRACT

DLR is presently investigating the use of automation techniques to support pilots during aerial refuelling manoeuvres with the so-called probe-and-drogue system. During aerial refuelling manoeuvres the tanker and receiver aircraft need to fly very close to each other and this close proximity induces a very significant aerodynamic interaction between them. In order to develop new assistance / automation function for aerial refuelling and to test them in piloted simulations, real-time simulation models including all the relevant effects must be developed. Unlike in many other works with similar modelling needs, Reynolds-Averaged Navier Stokes (RANS) CFD computations were preferred to more simple techniques for the modelling of the aerodynamic interaction between tanker, receiver, hose, and drogue. The real-time simulation environment developed contains two complete aircraft models, which can both be controlled by the pilots either manually or through the auto flight functions. With other words, the tanker is no point mass model with prescribed trajectory, but dynamically reacts to external disturbances and the external disturbances affect both aircraft in a representative way. The dedicated aerial refuelling systems are also modelled and the whole infrastructure was ported to the DLR AVES simulator, such that complete refuelling manoeuvres can be flown by the pilots in a realistic environment, in order for the pilots to assess novel automation/assistance functions. This paper gives both a general overview on the modelling work performed and some specifics on selected parts of the model and the developed simulation infrastructure.

KEYWORDS: AAR, aerial refuelling, formation flight, flight control, probe-and-drogue



Composite Wind Turbine Blade using Prepreg Technology

VINTILĂ Ionuț Sebastian

*National Research & Development Institute for Gas Turbines COMOTI
Scientific researcher*

*Address: 220 D Iuliu Maniu Ave., 061126, sector 6, Bucharest, Romania
E-mail: sebastian.vintila@comoti.ro*

CONDRUZ Mihaela Raluca

*National Research & Development Institute for Gas Turbines COMOTI
Scientific researcher assistant*

FUIOREA Ion

*National Research & Development Institute for Gas Turbines COMOTI
Scientific Researcher*

MĂLĂEL Ion

*National Research & Development Institute for Gas Turbines COMOTI
Scientific Researcher*

SIMA Mihail

*National Research & Development Institute for Gas Turbines COMOTI
Scientific researcher*

ABSTRACT

This paper describes the design and manufacturing process of a 4500 mm long composite vertical axis Darrieus wind turbine blade (VAWT) and 0.6 m chord with NACA 0021 blade profile, using the autoclave technology. By using the autoclave technology as the manufacturing process, a higher fiber content was achieved which implies a higher specific stiffness and strength, thus leading to lighter blades, compared to a wet hand layup processes. Due to autoclave constraints, four composite blade segments were manufactured to assemble one 4500 mm blade. The composite structure has 3 mm thickness and two composite spar beams, cured at room temperature, are reinforcing the blade inside all along its length. CFD showed a maximum value of 25.4 MPa in the 8 ply configuration of the airfoil and a 2.5 MPa on the leading edge, also a maximum displacement of 4.27 mm localized around the trailing edge end was observed. A maximum Von Mises stress value was 280 MPa and it was located at the airfoil – collar interface, Having a tensile strength of 955 MPa, Hexply M79/42%/200T2X2/CHS-3K prepreg was considered appropriate for the manufacturing of this type of structure in the 8 ply configuration.

KEYWORDS: Wind energy, composite structures, autoclave technology, prepreg, structural analysis

1. INTRODUCTION

The international wind energy market showed a new record in 2003 with a growth rate of 15%, reaching an increase of 26% in the last 5 years. Globally, a total power of 8.3 GW was installed. The total installed wind energy power has now reached more than 40 GW, and the average growth in the market during the past five years has been of 26% per year. This illustrates the world's concern regarding the energy supply and consumption in a modern and civilized society and how the use of wind turbines for electricity generation was increased during the past 25 – 30 years [1]. In order to ensure the required shape stability, strength and damage resistance of the VAWT, its blades are produced from long fiber reinforced polymeric composites [2]. In these composites, long fibers ensure longitudinal stiffness and strength, while the resin



matrix is responsible for fracture toughness, delamination strength and out-of-plane strength and stiffness of the composite [3]. Wind turbine blades are long structures that require light, stiff and cheap materials; hence, the choice of materials has usually been strictly limited to composites. Nowadays, blades are still mainly made of glass fibers, carbon fibers slowly becoming a feasible opportunity due to cost reducing from the last years and superior mechanical properties which lead to the possibility of obtaining even larger blades with an increase in energy power; among resins, epoxy is now preferred thanks to its better strength, chemical resistance, adhesion to the fibers, lower thermal shrinkage and easier workability compared to the other low-cost resins [4]. Nevertheless, other materials can be used like aramid, polyethylene and cellulose but they provide lower mechanical properties and lower density. The polymeric composites with the above-mentioned fibers have polymeric matrices, typically thermosets or thermoplastics. Wind turbines blades, during their normal operating cycle (around 20 years), pass through severe environmental conditions e.g. wide range of temperatures, hail, ultraviolet and bird collisions etc. They bear static and dynamic lift, drag and inertial loads so it is important to select the best-suited materials that can withstand these challenges, otherwise they can suffer structural damages and fatigue related issues due to cyclic loading. These problems of fatigue could be resolved by improving the materials characteristics for the blade manufacturing, manufacturing process parameters and blade design and configuration modifications. It is of utmost importance that the blades should be highly rigid, having low weight and must possess rotational inertia, and above all they can resist wear and fatigue. The flapwise and edgewise bending loads cause high longitudinal, tensile and compressive stresses in the material that can lead to fatigue damage. The upwind side of the blades is subjected to tensile stresses while the downwind side is subjected to compression stresses [5]. The blade's shape stability should corresponds to the minimum deflection area under wind loads. This can be achieved by increasing the moment of inertia of the blade, using a corresponding blade design, and by increasing the flexural stiffness of the blade material. The flapwise bending is countered by the use of spars, internal webs or spar caps inside the blade, while the edges of the profile carry the edgewise bending. There are two primary blade designs that are used for VAWT that operate on different principles: Savonius type and Darrieus type [6]. Savonius type uses aerodynamic drag from wind to rotate the blades and to produce power. This type of blade is however rugged and simplistic thus reducing the costs due to their ease of manufacture, less maintenance and can resist longer in harsh environments. On the other hand, Darrieus type designs, uses wind lift forces to rotate the blades. These blades have an airfoil shape which ensure the air traveling along the leading edge with greater speed than the air on the trailing edge, creating an area of lower pressure on the outside of the blade, thus it can spin faster than the speed provided by the wind resulting in higher efficiency. However, this higher efficiency is attenuated through a higher production cost [7].

During blade designing phase some aerodynamic factors must be taken into account: the airfoils shape which define the cross sectional areas which are defined by suction and pressure sides, the flatwise direction which denotes the lines that are perpendicular to the chord line, edgewise the parallel ones; and also denotes the lines that are perpendicular to the rotor plane, lead-lag the in-plane lines. Nevertheless, the design strategy for the composite blades considers aerodynamic loading, assessed via computational fluid dynamics and variable structural properties including prepreg material, thickness and layup sequence of the blade airfoil and design and of the two "I" shaped reinforcing spars.

2. RESEARCH GOAL AND METHODOLOGY OF WORK

The goal of the present paper was to design and manufacture a vertical axis wind turbine, made out of three 4500 mm identical thermoset composite blades. The final 2 kW VAWT will be assembled and mounted in COMOTI's Sf. Gheorghe site. All CAD models were developed with SolidEdge ST4 and SolidWorks 2010. The technology chosen to manufacture the wind turbine blades was the autoclave technology due to its higher process performances including overall cured material properties.

In the proposed blade design, the airfoil profile has a constant chord (600 mm) along the length of the blade (4500 mm). Four individual sectors, having the following dimensions 1125 x 600 mm will be manufactured and join using three collars (as marked blue in Fig. 1), to form one of the three VAWT blades. Two 4500 mm long composite reinforcing spars will be positioned inside each blade, offering stability to entire blade during operation. Each "I" shaped composite reinforcing spar will be bonded to the blade with



Araldite adhesive. Furthermore, each composite blade has two connection points (metallic inserts in two of the composite collar, as indicating in Fig. 1) on one of its broadsides for assembly to the rotor through metallic supporting struts (Fig. 10a). A 1:9 scale model was manufactured using two layers of glass fibers and one of carbon fiber on a foam core and assembled on a vertical axis to emphasize the overall aspect of the larger model (Fig. 10b).

3. RESULTS AND DISCUSSIONS

3.1. Numerical simulations (static and modal analysis)

Due to the low ratio between the blades dimensions, 4500 x. 600 mm and the thickness of composite layers, around 3 mm, the composite structure was modeled with SHELL elements. The investigated solution is characterized by the use of a single metallic insert on the composite collar, presented in Fig. 1. The load is composed of dynamic pressure caused by wind of 40 m/s, 1 MPa.

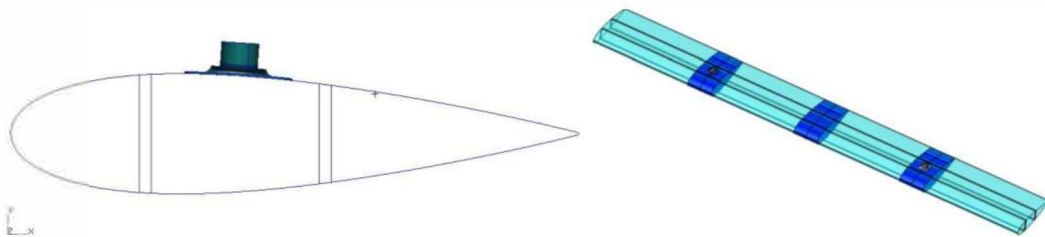


Figure 1. Composite wind turbine blade assembly

The use of composite materials has involved new approaches in terms of material's strength, mainly due to their mechanical properties. Evaluation of tensile strength was made based on empirical consideration criteria, and these can be considered a generalization of classical failure theory, in case of laminar materials defining a yielding surface in the stress space in a similar way defining the flow area in the case of elastoplastic materials.

Strength Analysis

The main tension distribution and the displacements for the first collar is shown in Fig. 2.

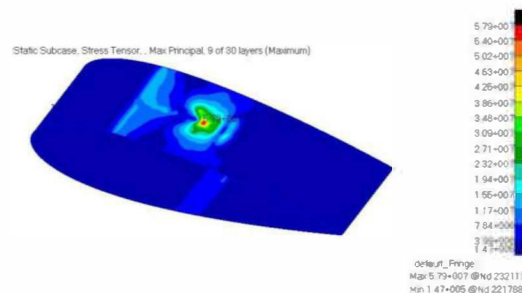
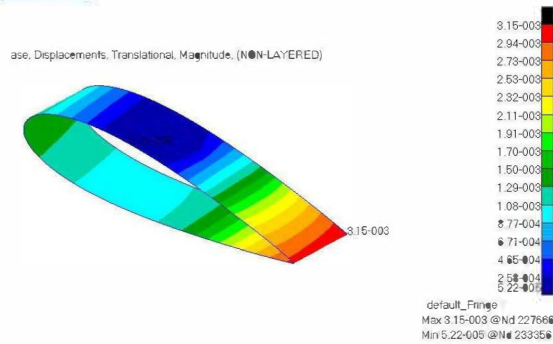
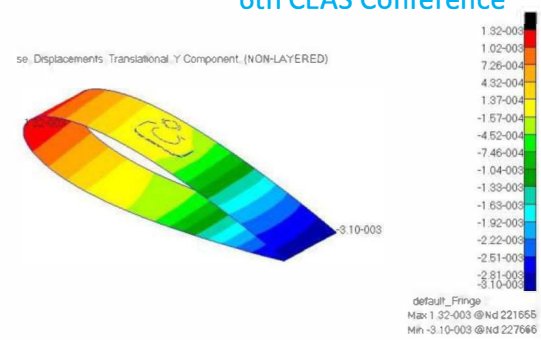
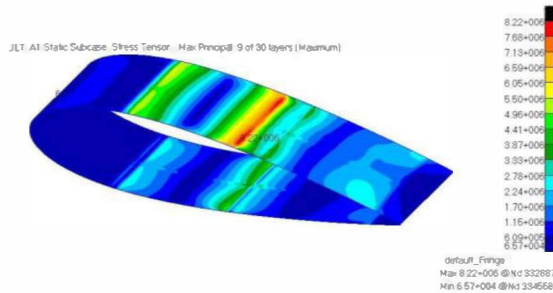
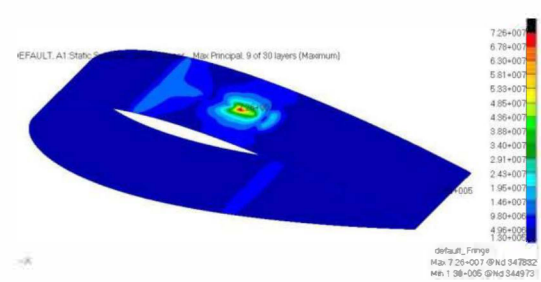
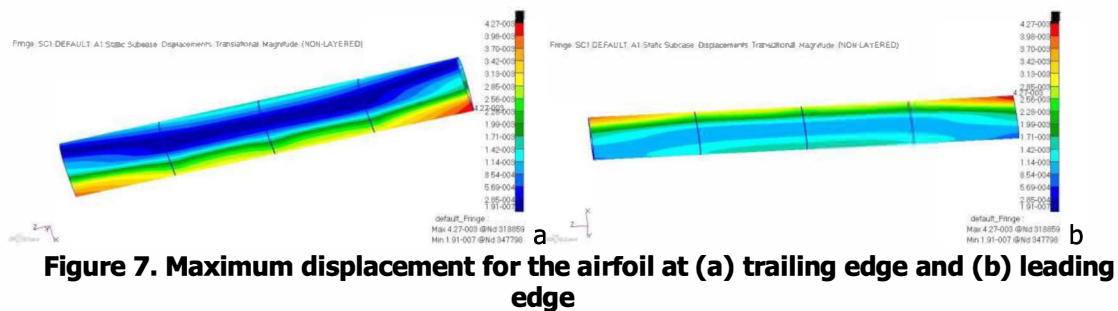
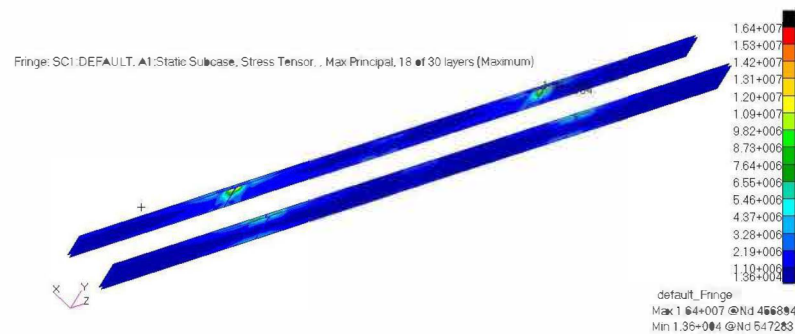


Figure 2. Main strain distribution [Pa] –first collar (maximum on all 8 layers)

The maximum main strain value is 58 MPa and is located in the contact region between the collar and the metallic insert (Fig. 2). The maximum strain value for the spars and collar exterior surface is 82 MPa (Fig. 5) and for the contact region between the insert and the collar is 73 MPa (Fig. 6).


Figure 3. Total displacement [mm]

Figure 4. Displacement on OY [mm]

Figure 5. Main strain distribution [Pa] – second collar (maximum on all 8 layers)

Figure 6. Main strain distribution [Pa] – third collar (maximum on all 8 layers)

As for the airfoil, the maximum displacement is 4.27 mm and is localized near the trailing edge end (Fig. 7).


Figure 7. Maximum displacement for the airfoil at (a) trailing edge and (b) leading edge

Figure 8. Maximum stress on the 4500 mm length spars

Von Mises stresses for the metallic inserts are shown in Fig. 9.

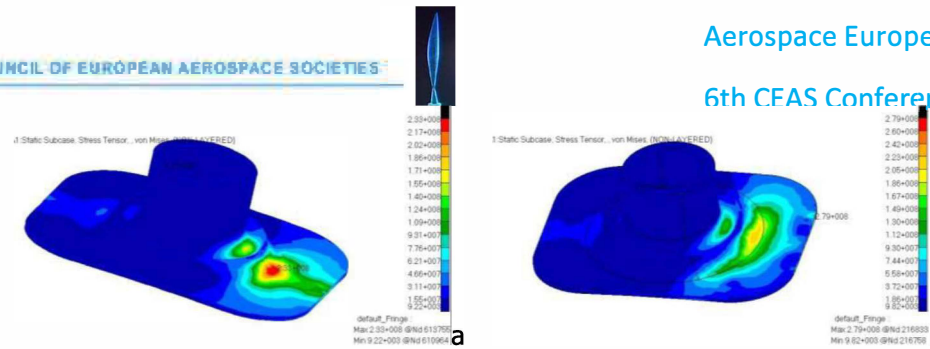


Figure 9. Von Mises maximum stresses for (a) metallic insert locked in XOY plane – 233 MPa and for (b) metallic insert locked on all three directions – 279 MPa

It was proposed a material with a yield limit of at least 500 MPa, and a minimum safety factor of 1.82. We will use the Al7075 alloy with a yielding stress 503 MPa and a safety factor of 1.82 which is an adequate value, maximum Von Mises stress being located only on a reduce area fig.9 b). According the IEC 61400-1[xx] the maximum safety factor for unfavorable load is 1.35 which is smaller than safety factor of proposed solution, 1.82. . Since the tensile / compression strength of the material used is 955 MPa for carbon fiber Hexply M79/42%/200T2X2/CHS-3K, it appears that there are no problems with the failure of the composite material for the configuration used. The overall maximum failure indice value calculated based on the Tsai-Wu criterion is 0.113, indicating that the probability of failure is very small (failure occurs for a failure indice value greater than 1). The actual frequency of the first vibration mode is 23 Hz, 10 times the nominal frequency, and there are no problems with overlapping the working mode with its own frequencies.

3.2. Mold design and manufacturing process

The manufacturing of a vertical Darrieus wind turbine with three identical blades (Fig. 10), symmetrically placed at an angle of 120° , is the main purpose of this paper. The three blades are NACA 0021 type, with a length of 4500 mm and a 600 mm chord. For their fabrication, an 8 ply configuration was proposed. Prior to one step autoclave manufacturing protocol and process, mould (1125 x 700mm mm, weight 66 Kg) was designed using SolidEdge ST4 in order to obtain airfoil blade final acceptance tolerances (figure 11). The parameters of the VAWT are presented in Table 1.

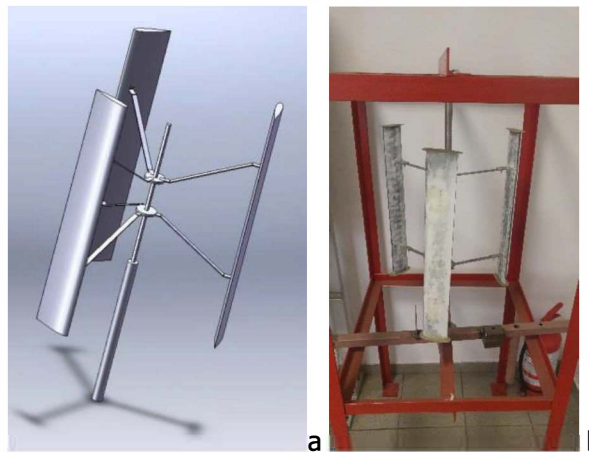


Figure 10. (a) The CAD model of the VAWT with 4500 mm long blades; (b) Scaled (1:9) VAWT mounted on a metallic support

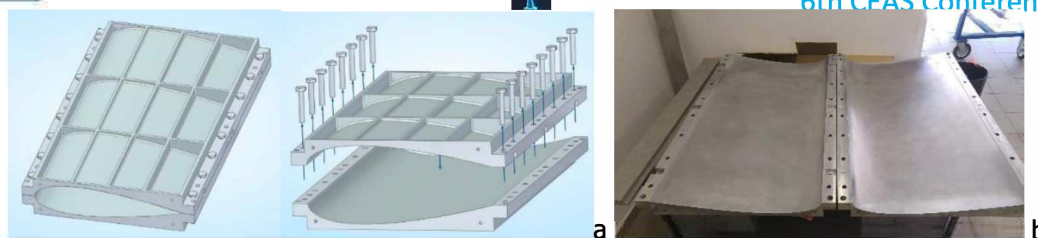


Figure 11. (a) CAD model of the mould (b) manufactured two piece aluminium mould



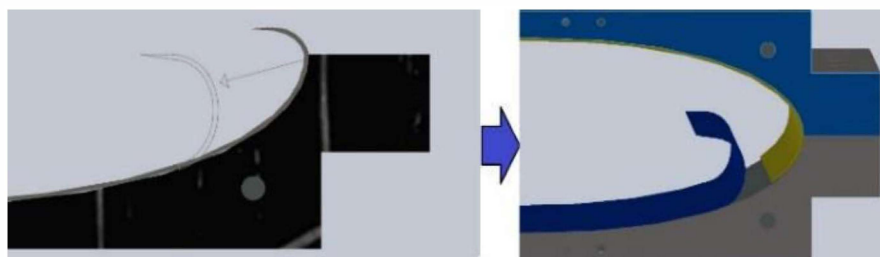
Figure 12. COMOTI's autoclave

Usable diameter [mm]	1500
Usable length [mm]	2500
Maximum pressure [bar]	20
Maximum temperature [°C]	400
Loading agent	Aer
Maximum load	20 kg composite 100 kg aluminium 350 kg steel

Table 1. VAWT parameters

Rotor diameter [m]	3.6
Rotor height [m]	4.4
Number of blades	3
Chord [m]	0.6
Turbine area [m ²]	16
Wind velocity [m/s]	8

A number of 16 plies were cut (a set of each plies for each half-mould) from the M79 prepreg having the following dimensions: 8 plies with 1125 mm in length and width between from 630 to 770 mm, and 8 plies with 1125 in length and width between 630 to 490 mm. Each set of 8 plies were previously bond together before laying on each of the half-moulds. Prior to closing the mold, the plies folded at the edges of the first half-mould were pulled 100mm inward to allow for longer plies of the second half-mould to fold on the first half-mould (Fig. 13). After closing the mold, the plies were stretched, forming both the leading and trailing edges. An inner vacuum bag was build-up and wrapped around a layer of release film, then placed inside the mould. The entire mould was then covered in a breather cloth and the assembly was inserted into an external vacuum bag. The inner vacuum bag and external vacuum bag were bond together, connected to autoclave's vacuum lines and cured (Fig. 14).



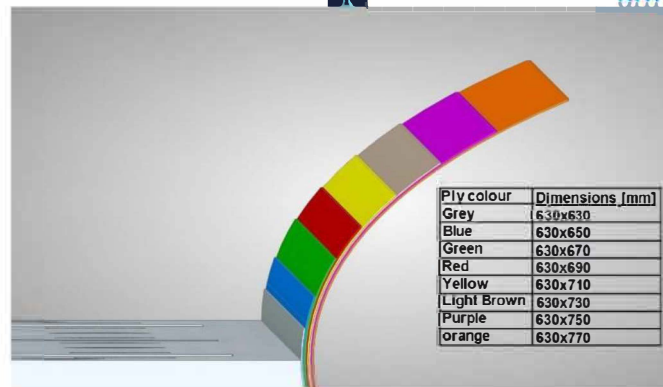


Figure 13. Each set of 8 prepreg plies placed on each half-mould prior to closing the mould and vacuum bag assembly



Figure 14. Vacuum bag assembly

The curing cycle was selected considering prepreg technical sheet and the properties of the mold (90°C temperature, XXX HOUR , 2 bar pressure, vacuum), and it is showed in Fig. 15. After the curing cycle, the components were allowed to cool over night until ambient temperature to avoid the internal tensions in the structures when they are released from the molds.

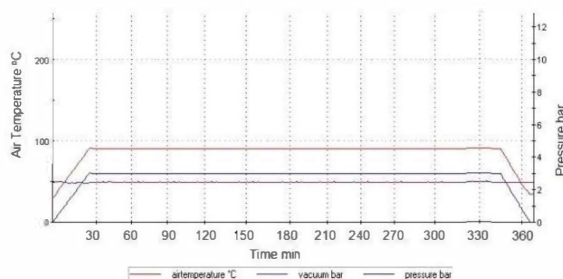


Figure 15. Graphic representation of the curing cycle

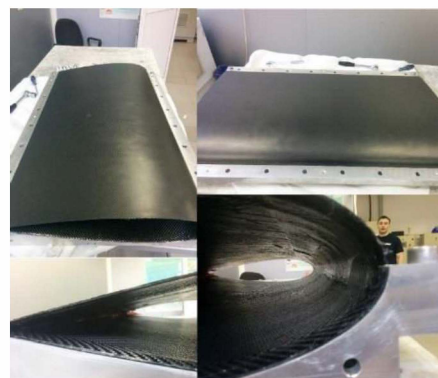


Figure 16. A composite blade sector

A manufacturing protocol was established for a section of a composite spars (300 mm in length). Namely, in order to manufacture the spar from the leading edge, glass fiber, epoxy resin, a Ø18 mm x 120 mm (3 mm thick) pipe and two welded metal plates were required (Fig. 16). The spar consists in a three part ensemble: two soles (which will attached to the airfoil) and a central piece, connected to the two soles, as presented in Fig. 17 a.

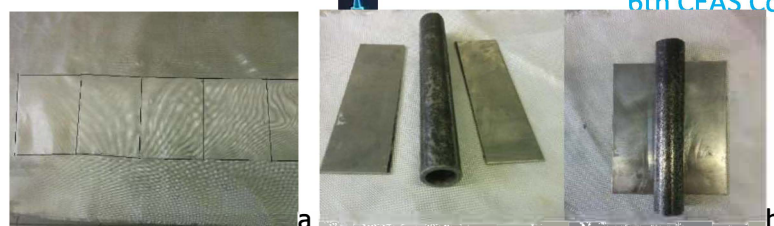


Figure 17. The glass fiber cloth (a) and metallic parts (b)

After curing the two soles and the central piece, an $\varnothing 18$ mm hole was made on one of the soles to allow the spar to be attached to the turbine's shaft. After the hole was performed, the central piece was mounted on the sole and an adhesive layer (Araldite) was applied and allowed to cure for 24 hours, after which, the second soul was bonded. After the spar was assembled, it was inserted into the blade at a distance of 142 mm from the leading edge (as shown in Fig. 18 b). The placement of the two spars within the composite blade, were realized according to Fig. 19. Each blade sector will be firstly bonded to the spars, one by one, after which they will be secured with a collar made out of 5 layers of carbon fiber and epoxy resin, cured at room temperature. Fraza cu gaura de prinderea pe



Figure 18. (a) The three components that assemblies the spar and (b) inserting the spar within the blade, near the leading edge

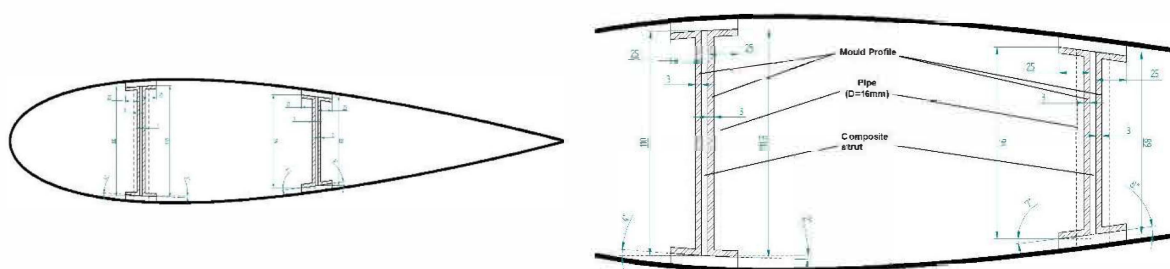


Figure 19. Spar dimensions and positioning

The four composite sectors manufactured with autoclave technology are presented within Fig. 18. The two spars will be manufactured out of carbon fiber according to the manufacturing trial previously presented.



Figure 19. Vertical axis wind turbine composite blades

4. CONCLUSIONS

The autoclave technology involves substantially higher costs than room temperature curing, due to the need of precursor materials (prepregs) whose cost sometimes exceeds the room temperature curing process, and due to the storage conditions of the prepregs. On the other hand, using autoclave technology, components with high structural properties are obtained. The stress analysis results showed that there are no problems with the failure of the composite material for the configuration used. The overall maximum value of the yield value calculated based on the Tsai-Wu criterion is 0.113, indicating that the probability of failure is very small (the yield is for a yield value greater than 1). The actual frequency of the first vibration mode is 23 Hz, 10 times the nominal frequency, and there are no problems with overlapping the working mode with its own frequencies. Using M79 prepreg material, a 1,82 safety factor was obtained. According to the stress analyses, 2 mm thickness is enough for the composite blades to withstand the loads while having the two spars bonded inside the structure. Four composite sectors were manufactured via autoclave technology for the assembly of one wind turbine composite blade. The two spars are under development and will be bonded to the structure.

ACKNOWLEDGEMENT

The work is conducted under the project "Research in the field of small and medium wind turbines adapted to the conditions in Romania", PN 16.26.02.01.

REFERENCES

- [1] P. Brøndsted, H. Lilholt, A. Lystrup; 2005; "Composite Materials for Wind Power Turbine Blades"; *Annu. Rev. Mater. Res.*; **35**, pp. 505–38,
- [2] L. Mishnaevsky Jr.; "Composite Materials in Wind Energy Technology, Thermal to Mechanical Energy Conversion, Engines and Requirements", Thermal to Mechanical Energy Conversion: Engines and Requirements, <https://www.eolss.net/sample-chapters/C08/E3-11-42.pdf>
- [3] H. Ahmad, Materials and Manufacturing Techniques for Wind Turbine Blades, Wind Turbine Concepts and Applications, Wind Power Project Management 2012, <https://www.scribd.com/doc/97296344/Materials-and-Manufacturing-Techniques-for-Wind-Turbine-Blades>
- [4] P. Bortolotti; "Carbon Glass Hybrid Materials for Wind Turbine Rotor Blades"; *Master Thesis*; University of Technology; Delft, 2012
- [5] O. T. Thomsen; 2009; "Sandwich Materials for Wind Turbine Blades — Present and Future"; *Journal of Sandwich Structures & Materials*; **11**(1); pp. 7-26
- [6] O. Hammond; "Design of an Alternative Hybrid Vertical Axis Wind Turbine"; Polytechnic Institute; Worcester, Degree of Bachelor of Sciences, March 28, 2014, WORCESTER POLYTECHNIC INSTITUTE, <https://web.wpi.edu/Pubs/E-project/Available/E-project-032814->



094103/unrestricted/MQP Final Report 2013-2014.pdf

[7] M. Ragheb; "Vertical Axis Wind Turbines"; 2013

<http://mragheb.com/NPRE%20475%20Wind%20Power%20Systems/Vertical%20Axis%20Wind%20Turbines.pdf>

[8] T. Burton, D. Sharpe, N. Jenkins, E. Bossanyi - Wind Energy Handbook, 2001, John Wiley & Sons, Ltd, pg.212, ISBN 0 471 48997 2;

Composite material designs for lightweight space packaging structures

CONDRUZ Mihaela Raluca

National Research & Development Institute for Gas Turbines COMOTI

Scientific researcher assistant

Address: 220 D Iuliu Maniu Ave., 061126, sector 6, Bucharest, Romania

E-mail: raluca.condruz@comoti.ro

VOICU Lucia Raluca

National Research & Development Institute for Gas Turbines COMOTI

Scientific researcher

PUȘCAȘU Cristian

National Research & Development Institute for Gas Turbines COMOTI

Technical development engineer

VINTILĂ Ionuț Sebastian

National Research & Development Institute for Gas Turbines COMOTI

Scientific researcher

SIMA Mihail

National Research & Development Institute for Gas Turbines COMOTI

Scientific researcher

DEACONU Marius

National Research & Development Institute for Gas Turbines COMOTI

Scientific researcher

DRĂGĂȘANU Luminița

National Research & Development Institute for Gas Turbines COMOTI

Scientific researcher

ABSTRACT

This paper presents a study on advanced material designs suitable for lightweight space packaging structures. During this study, several material designs were proposed, evaluated and in the end three packaging structures were designed, manufactured and validated through a test campaign. The material designs proposed consisted in hybrid laminates composed of a composite substrate and integrating metallic foils with high atomic number (Low Z - High Z - Low Z concept) and metallic coatings to increase the structure's protection against harsh space conditions. The packaging structure design selected was a 2U CubeSat. A FEM analysis was performed on two different designs which showed good mechanical resistance under static loads, and regarding the modal analysis, the natural vibration frequencies of the CubeSat were in the imposed limits (outside of the critical range of 1-125 Hz). To reproduce the dynamic environment encountered during launching stage, vibration tests were performed. The structures were validated through a test campaign (vibration tests) and their first vibration mode overcomes 100 Hz, results predicted by the FEM analysis.

KEYWORDS: *polymeric composites, space structures, metallic coating, CubeSat, FEA*

RESPONSE SURFACE ANALYSIS and DESIRABILITY FUNCTION OPTIMIZATION TO OBTAIN AERODYNAMICALLY OPTIMIZED STORE with LOW ASPECT RATIO WINGS

Umut Can KÜÇÜK

*Senior Research Engineer, Aerodynamic Division, TUBITAK SAGE
TUBITAK SAGE, Mamak Ankara, 06261, Turkey
umut.kucuk@tubitak.gov.tr*

ABSTRACT

In the current work multi objective response surface analysis and desirability function optimization are performed to determine optimum size and shape of the lifting surfaces on a store with strake-fin configuration. In order to cover various flow conditions, CFD simulations are conducted at Mach numbers of 0.8, 1.5 and 2.5 and for angle of attack values 4° , 7° , 12° . Through the results of CFD analysis surrogate models are constructed with least squares estimation and desirability function optimization is performed to find geometry which satisfy externally defined requirements.

KEYWORDS: *Response Surface, CFD, Optimization, Strake*

NOMENCLATURE

CFD – Computational Fluid Dynamics
CPU – Central Processing Unit
D – Distance
k – Ratio of Strake Span to Fin Span
FRC – Fin Root Chord
FS – Fin Span
SRC – Strake Root Chord
SS – Strake Sweep Angle
TR – Taper Ratio

1 INTRODUCTION

Traditionally, the amount of time which is separated for the preliminary design stages are limited such that it is not practically possible to investigate all design options with great detail. However, it is generally expected from the results of the preliminary design studies to cover all possible ways that design can develop through the dynamically changing mission requirements. Therefore, fast aero-prediction methods play crucial role especially in the preliminary design stages. Unfortunately, these fast aero-prediction methods which are generally rely on linear theories and/or experimental correlations may not be so accurate depending on the investigated flow scenarios.

Aerodynamic investigation of stores with very low aspect ratio wings (i.e strakes) are one of the most challenging case for fast-aero prediction codes. In such a case, CFD analyses provide more accurate results compared to the semi-empirical methods. Recent work conducted by Christopher et al [1] compares prediction capabilities of semi empirical aero prediction codes and CFD methods in capturing aerodynamic behaviors of the missile configurations with strakes. Their study shows that for most of the investigated flight conditions and missile geometries, CFD analyses provide more accurate results compared to the semi-empirical methods. However, CFD computations are time consuming and therefore costly such that investigating large number of aerodynamic shapes via CFD analyses is not practical in the early stages of the design process. To reduce number of geometries that are investigated and to decrease the amount of CPU time spend in CFD analyses, response surface methodology can be used as a very efficient tool. Response surface analysis can provide an analysis environment which can answer all possible mission requirements even in the early stages of the design stages.

In this study response surface analysis and desirability function optimization is performed to obtain aerodynamically optimized lifting surfaces on a cylindrical store geometry. For the investigations, effect of 7 different design parameters are examined. Experimental points are determined with Face Centered Composit Design and each of the geometry obtained with design of experiment are computationally analysed at various flow conditions. Results of the computational analyses are used to obtain surrogate models which basically explain effect of each parameter on static stability, lift to drag ratio and normal force of the store.

2 COMPUTATIONAL APPROACH

Steady RANS solutions are carried out with the commercially available flow solver ANSYS Fluent 14.0.7 by using one equation turbulence model Spalart Allmaras. Computations are obtained with pressure-based coupled algorithm and gradients are calculated with Green Gauss Node Based Method with 2nd order accuracy. In order to capture flow near the wall 12 layers of boundary layer elements are employed and first layer thickness is determined such that y^+ value kept below 1 for each investigated flow condition.

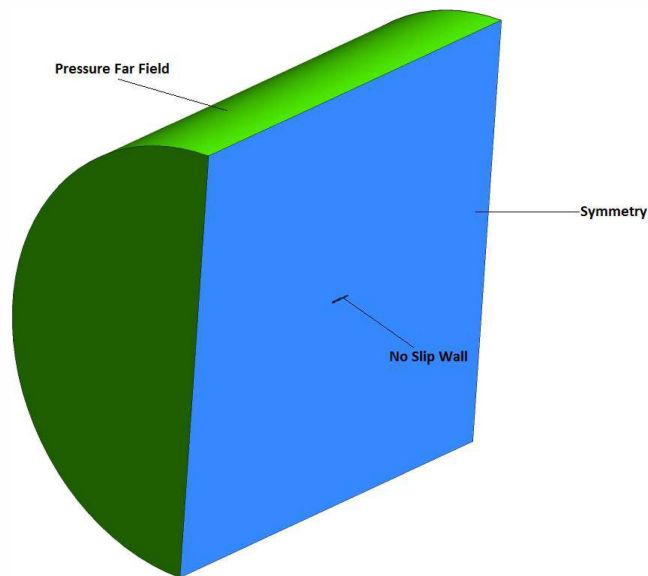


Figure 1. Computational Domain and Boundary Conditions

Computational domain and defined boundary conditions for flow solver is shown in Figure 1. External boundaries except symmetry plane are defined as pressure far field and no slip wall boundary condition is applied to the store surface. Symmetry boundary condition is also used to reduce computational cost. Although total number of mesh changes with the change in geometrical parameters, it is kept on the order of 2.5 million for each case. Surface mesh on the store and symmetry plane is shown in the Figure 2 for one of the geometric alternatives.

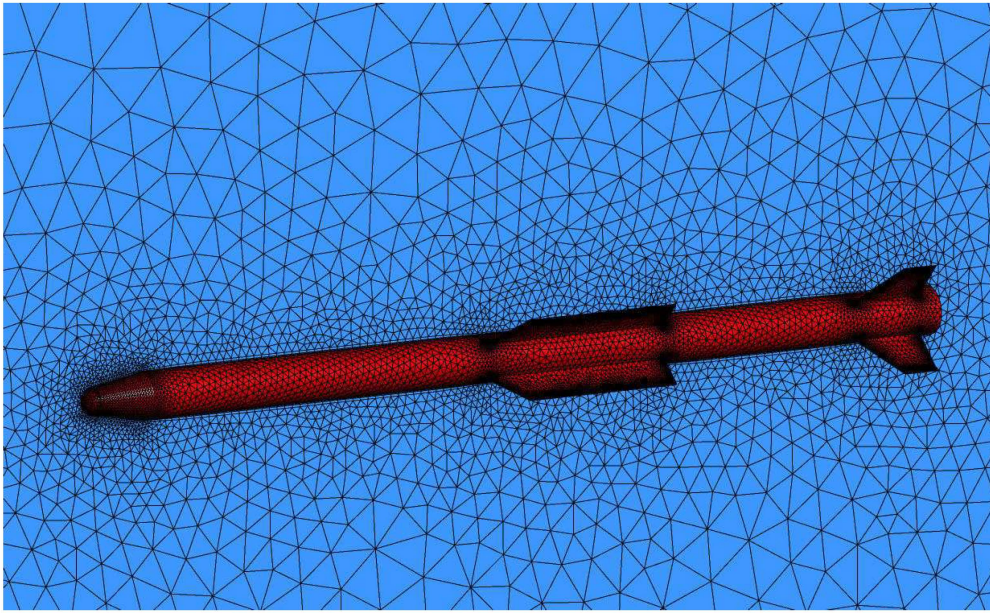


Figure 2. Surface Mesh on Store and Symmetry Plane

3 PERFORMANCE MEASURES

To construct aerodynamic design environment, lift to drag ratio, stability margin and normal force coefficient are taken as primary performance parameters. Lift to drag ratio is directly related to aerodynamic efficiency of the air vehicle. For agile store, higher lift to drag ratios leads to less energy lost during the maneuver. Furthermore, maximum range of the air vehicle heavily depends on the lift to drag ratios. At the same time, stability margin determines the response of the air vehicle to the disturbances and its tendency to restore its position. For the purposes of the study, only static stability is taken into account. Static stability of any air vehicle can be explained with the stability margin which is the distance between the aerodynamic center, where resultant aerodynamic forces are acting, and center of gravity. At the same time, Normal force is a measure of maneuvering capability of the air vehicle. Depending on the requirements it is applicable to limit the normal force or maximize it.

Each performance parameters are obtained for 3 different Mach numbers (0.8, 1.5, 2.5) and for 3 angle of attacks (4°, 7°, 12°). Performance parameters obtained at each flight condition contributes equally to the overall performance of the air vehicle. In other words, overall performance is calculated as the average of the performance measures obtained at each flight condition. Similar approach is also used in earlier study [2] such that overall performance calculated with 1 where λ and n represent performance parameter and the number of flight conditions respectively.

$$\lambda_{overall} = \frac{1}{n} \sum_{k=1}^n \lambda_k \quad \text{Equation 1}$$

4 GEOMETRICAL VARIABLES

In order to construct relevant response surfaces to capture the aerodynamic problem, it is first mandatory to define geometrical design variables that may affect the aerodynamic behaviour of the store. In this study, fin span, fin root chord, fin taper ratio which is defined as ratio of fin tip chord to the fin root chord, strake root chord, strake sweep angle, distance between strake trailing edge and fin leading edge are taken as design variables with ratio of strake span to the fin span. For the purposes of this study, trailing edges for both strakes and tail fins are kept perpendicular to the store surface. General view of store with variable geometric parameters is shown in Figure 3.

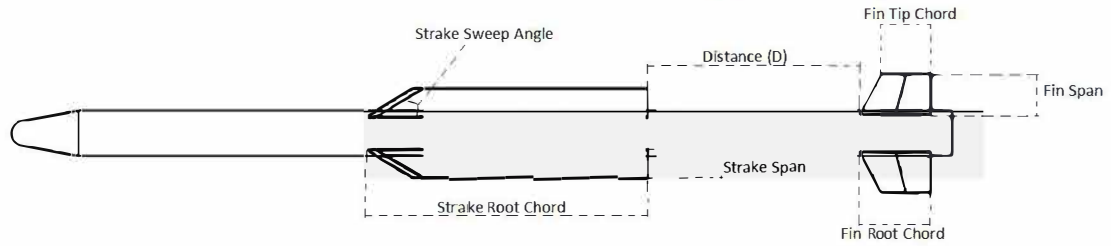


Figure 3. General View of Strake-Fin Configuration Store with Variable Geometric Parameters.

5 RESPONSE SURFACE METHODOLOGY

Response surface methodology is used to construct empirical models, which represent dependency of the responses on input variables. In order to construct response surfaces experimental runs are carried out with systematically selected input variables. Determining experimental data points plays crucial role in accuracy and validity of the response surface model. Experimental points must be properly placed in the design space such that maximum amount of information can be gained from limited number of experimental runs. It is possible to find many methods for constructing experimental designs in the literature. BOX-Behnken, Space Filling and Central Composite Designs are only few of the most widely used experimental design methods in the industry. In this study, Face Centered Composite Design (FCCD) with seven variables is employed to get maximum amount of information with limited number of experimental points. Originally central composite design is a first order experimental design which is enriched by additional points such that it allows second order estimations [3] with high efficiency. FCCD introduces $2(k-f) + 2k + C_p$ number of experimental points where k is the number of geometrical variables, C_p is the central point and f is the factorial number. Factorial number is used to limit the number of design points by excluding some diagonal points. In this work, by taking factorial number equal to 1, number for design points is reduced to 79.

After collection of experimental data, responses of these experimental runs are used to develop empirical formulations. The degree of the response surface equations may change depending on the complexity of the process and required accuracy. Generally, first order or second order models produce sufficiently good results. Since, it was expected to have some non-linear behaviour of the responses in the current study, second order models are constructed with standard least squares method [4]. Second order models have following form;

$$y = \beta_0 + \sum_{i=1}^k \beta_i x_i + \sum_{i=1}^k \beta_{ii} x_i^2 + \sum_{1 \leq i < j}^k \beta_{ij} x_i x_j + \varepsilon \quad \text{Equation 2}$$

Where y is response, x is regressor, β is regression coefficient and ε is the residual. For least square regression modelling it is automatically assumed that residuals are randomly and independently distributed. To check whether any of these assumptions are violated or not it is customary to investigate normal probability plot and plot of residuals versus predicted response values [5].

In this study, normal probability plots and plots of residuals versus predicted response values are constructed for lift to drag ratio, dimensionless static margin and normal force coefficient. Straight line in the normal probability plot indicates normal distribution of the residuals, whereas S-shape curve indicates normality assumption is violated. Expected tendency in the plot of residuals versus predicted values is random distribution of the residuals which represents homogeneity of the residuals.

Normal probability plots are shared in Figure 4, Figure 5 and Figure 6. As can be seen from these figures residuals are placed around straight line such that normality satisfied with 95% confidence interval. Furthermore, plots of residuals versus predicted values are shown in Figure 7, Figure 8 and Figure 9. From these figures it is seen that residuals have sufficiently homogeneous distribution through the investigated design space. Therefore, constructed regression models for lift to drag ratio, dimensionless static margin and normal force coefficient do not violate normality and independent distribution assumption.

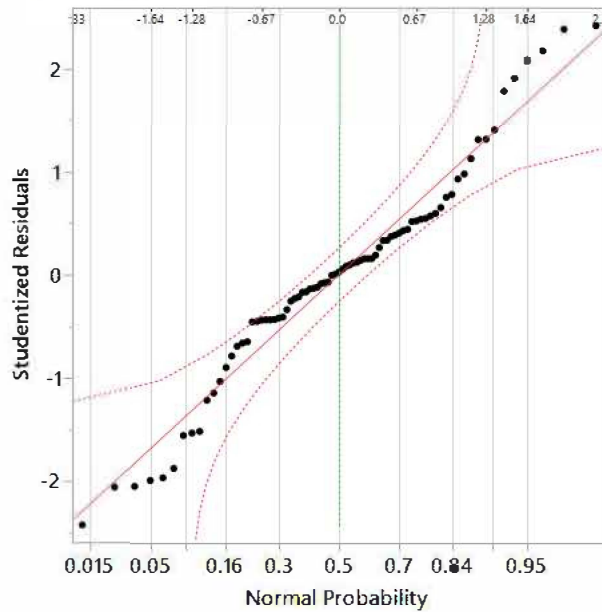


Figure 4. Normal Probability Plot with 95% Confidence Interval for Lift to Drag Ratio (L/D)

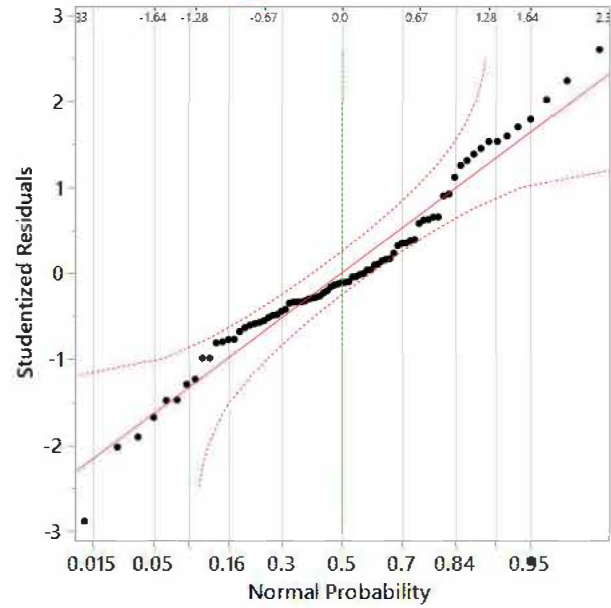


Figure 5. Normal Probability Plot with 95% Confidence Interval for Dimensionless Static Margin (SM)

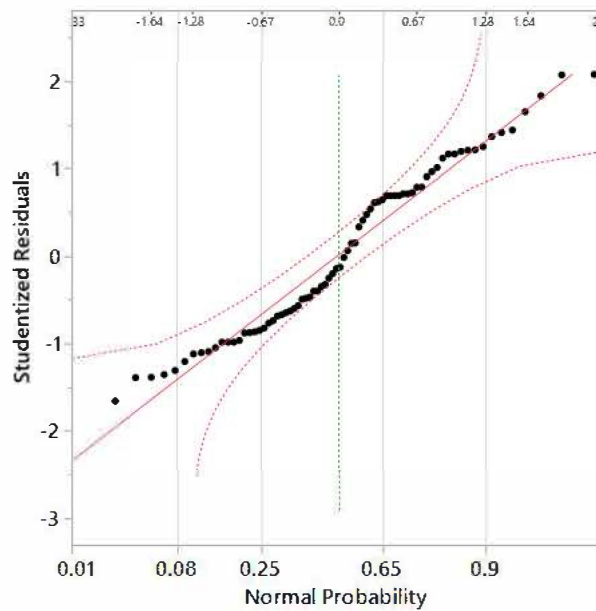


Figure 6. Normal Probability Plot with 95% Confidence Interval for Normal Force Coefficient (CN)

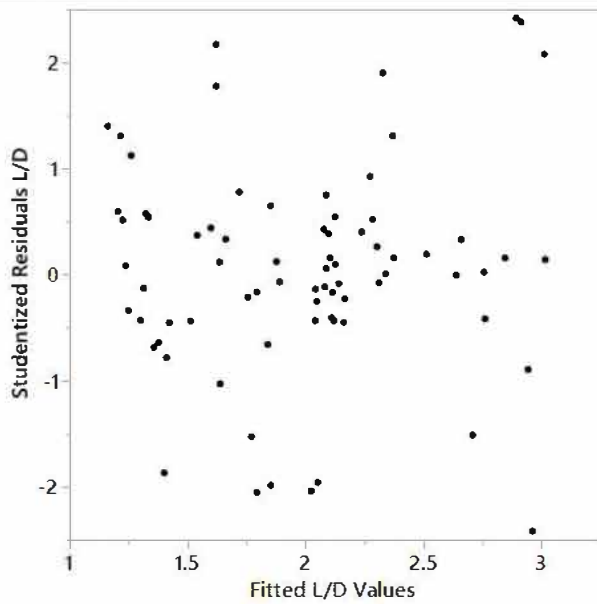


Figure 7. Plot of Residuals vs Fitted Values for Lift to Drag Ratio (L/D)

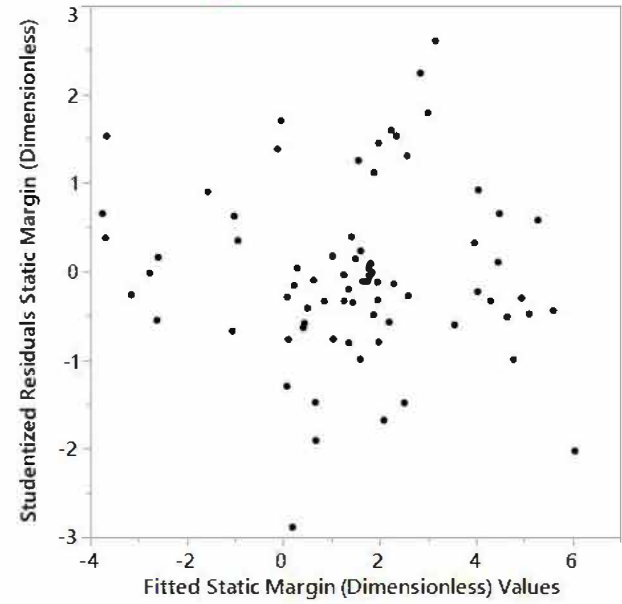


Figure 8. Plot of Residuals vs Fitted Values for Dimensionless Static Margin (SM)

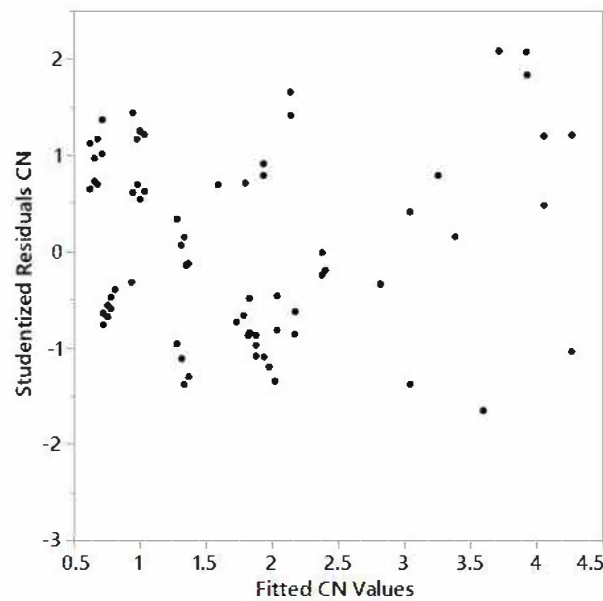


Figure 9. Plot of Residuals vs Fitted Values for Normal Force Coefficient

After obtaining statistically valid response surface models it is beneficial to check prediction capabilities of the regression models. In order to analyse performance of these constructed response surface equations for each of the responses, coefficient of determination (R^2), adjusted coefficient of determination (R_a^2) and percentage root mean square error (RMSE%) values are investigated. These values are presented in Table 1. As can be seen from this table all regression models have high performance values with acceptable RMSE values.

Table 1. Performance Parameters of the Constructed Regression Models

Parameter	Lift to Drag Ratio(L/D)	Dimensionless Static Margin (SM)	Normal Force Coefficient (CN)
R^2	0.9973	0.9963	0.9928
R_a^2	0.9972	0.9963	0.9927
RMSE%	1.3731	7.0090	4.8000

From the constructed regression models, it is possible to obtain important information about the impact levels of each factor to the regression model via p value approach [4]. Generally high p values indicate low impact of the corresponding variable on the regression model, whereas low p values indicate significant effects. Results of the p value approach for each of the regression model are given in Table 2, Table 3 and Table 4 for lift to drag ratio, normal force coefficient and dimensionless static margin respectively. From these tables it can be seen that interactions between geometrical variables have significant effect on the aerodynamic performance. Furthermore, information which is obtained from p value approach can be used for future aerodynamic design studies.

Table 2. Significance Levels of the Regressor Variables on Regression Model Constructed for Lift to Drag Ratio

Source	P Value
FS	0
k (SS/FS)	0
FRC	0
SRC	0
FS*k (SS/FS)	0
SRC*k (SS/FS)	0
FS*FS	0
FRC*k (SS/FS)	0
SSA	0
FRC*FS	0
D	0.00002
TR*k (SS/FS)	0.00134
FS*D	0.00171
TR*FS	0.00277
SSA*k (SS/FS)	0.02966

Table 3. Significance Levels of the Regressor Variables on Regression Model Constructed for Normal Force Coefficient

Source	PValue
FS	0
k (SS/FS)	0
FS*k (SS/FS)	0
SRC	0
SRC*k (SS/FS)	0
FRC	0
FS*SRC	0
FRC*FS	0
TR	0
TR*FS	0.00049

Table 4. Significance Levels of the Regressor Variables on Regression Model Constructed for Dimensionless Static Margin

Source	PValue
D	0
k (SS/FS)	0
FS	0
SRC	0
k (SS/FS)*D	0
SRC*k (SS/FS)	0
FS*k (SS/FS)	0
FS*D	0
FRC	0
FS*SRC	0
SRC*D	0
TR	0
FS*FS	0
k (SS/FS)*k (SS/FS)	0.00001
SSA	0.00004
SSA*k (SS/FS)	0.00009
FRC*k (SS/FS)	0.00018
FS*SSA	0.00305

6 DESIRABILITY FUNCTION APPROACH AND OPTIMIZATION

To perform multi objective aerodynamic optimization for a store with strake-fin configuration desirability function approach [6] is performed. In this approach it is possible to search and obtain optimal values for each of the responses depending on the optimization criterions and priorities. Basically, method of desirability function optimization involves creating desirability functions for each responses and a single composite response function. The composite response function represents global desirability and it is created by the geometric mean of the individual desirability values which takes values between 0 and 1 such that they indicate least and most desirable responses respectively.

It is also possible to arrange priorities of the responses with weighting factors such that high weighting factors indicate higher priority.

Different functions are employed depending on the optimization criteria. If certain response is to be maximized and U is the upper acceptable value for the response where L is the lower, desirability function (d) is defined by following equation;

$$d = \begin{cases} 0 & y < L \\ \left(\frac{y-L}{U-L}\right)^r & L \leq y \leq U \\ 1 & y > U \end{cases} \quad \text{Equation 3}$$

Similarly, if response is desired to be minimized desirability function is defined with Equation 4;

$$d = \begin{cases} 1 & y < L \\ \left(\frac{U-y}{U-L}\right)^r & L \leq y \leq U \\ 0 & y > U \end{cases} \quad \text{Equation 4}$$

In Equation 3 and Equation 4, r represents weighting factor which is basically measure of how important to be close to the target. High values of r should be employed when it is highly important to be close to the target value.

It is also possible to optimize response function when specific target value is the most desirable response. In this case if T is the target value, desirability function is given by;

$$d = \begin{cases} 0 & y < L \\ \left(\frac{y-L}{U-L}\right)^{r_1} & L < y < T \\ 1 & y = T \\ \left(\frac{U-y}{U-T}\right)^{r_2} & T < y < U \\ 0 & y > U \end{cases} \quad \text{Equation 5}$$

After obtaining desirability values for each of the responses a single composite desirability function which indicates overall desirability value can be constructed by taking geometric mean of the desirability values as shown in the Equation 6.

$$D = (d_1 d_2 \dots d_n)^{1/n} \quad \text{Equation 6}$$

7 RESULTS OF THE DESIRABILITY OPTIMIZATION

Optimized store geometries, which are obtained with the desirability function optimization, are shown in this section. Although it is possible to increase number of design examples, for the purposes of the present work only two different optimization studies are carried out. For each case computed and predicted values are compared with each other to understand prediction capabilities of the desirability function approach.

7.1 Case 1 – Maximum Lift to Drag Ratio, Maximum Normal Force Coefficient and Target Static Margin

Case 1 is to reach a design which has high aerodynamic efficiency, high normal force coefficient and zero static margin over the investigated flow conditions. According to these goals, constructed optimization setup and its results are given in Table 5.

Table 5. Optimization Summary for Case 1

Case 1: Total Desirability= 0.935							
Response	Lower Limit	Upper Limit	Goal	Relative Importance	Predicted Value	Computed Value	% Prediction Error
CN	0.5	4.5	Maximize	1	4.27	4.24	0.70
L/D	1	3.25	Maximize	1	3.02	2.98	1.32
S. Margin	-4	7	Target = 0	1	0.00	0.00	0.00

For the Case 1, total desirability value is 0.935 which indicates that all goals are highly satisfied. Furthermore, as can be seen from Table 5, predicted and computed values of three aerodynamic parameters have excellent agreement with each other.

Obtained geometry from the desirability optimization is shown in Figure 10 for the Case 1. As expected, total area of lifting surfaces is maximized in order to reach highest possible normal force coefficient. Moreover, distance between strake and fins are adjusted such that static margin meets the target value.


Figure 10. Desirable Geometry for Case 1

7.2 Case 2 – Maximum Lift to Drag Ratio, Target Normal Force Coefficient and Target Static Margin

Case 2 is designed to reach store geometry which has target normal force coefficient and target static margin with highest possible lift to drag ratio. This case represents a situation in which normal force and therefore maneuvering capability is limited possibly due to structural considerations. Furthermore, in this case predetermined static margin is to be obtained for ensuring level of static stability over the investigated flow conditions. Summary of the desirability function optimization for the case 2 is given in Table 6.

Table 6. Optimization Summary for Case 2

Case 2: Total Desirability= 0.906							
Response	Lower Limit	Upper Limit	Goal	Relative Importance	Predicted Value	Computed Value	% Prediction Error
CN	0.5	4.5	Target= 3	1	3.05	2.98	2.30
L/D	1	3.25	Maximize	1	2.71	2.63	2.95
S. Margin	-4	7	Target= 3	1	2.99	3.15	5.35

For the case 2, total desirability value is 0.906 which indicates that goals are again highly satisfied. Although, discrepancies between the predicted and computed values are more significant compared to the case 1 prediction errors are still in the acceptable range.

Desirable geometry, which is obtained from optimization to meet the goals of the case 2, is shown in Figure 11. For this case total area of the lifting surfaces are limited to meet the target value of normal force coefficient. Furthermore, it is seen that strakes are placed further downstream compared to the geometry obtained in Case 1 to get high level of static margin.



Figure 11. Desirable Geometry for Case 2

8 CONCLUSION

In this study, desirability function optimization is carried out to determine aerodynamic shape of a store with strake-fin configuration. Through the results of the study, it is clear that desirability function optimization is capable of determining aerodynamically optimized configurations. It is also shown that response surface methodology is very efficient way of obtaining and characterizing the effect of the design variables on the overall performance. To reduce computational cost and time spend in the process of analyzing effect of each design variables, response surface methodology can be used especially for the cases in which fast aero prediction methods are not sufficient. This study can be extended by adding more flight conditions and more specified considerations of flight mechanics. It can be also beneficial to perform optimization with more sophisticated methods, such as genetic algorithms, to compare relative advantageous of the different ways of optimization.

REFERENCES

1. Rosema, C., Abney, E., Westmoreland, S., Moore, H. "A Comparison of Predictive Methodologies for Missile Configurations with Strakes." 33rd AIAA Applied Aerodynamics Conference. 2015.
2. Anderson, M. B., Burkhalter, J. E., Jenkins, R. M. "Missile aerodynamic shape optimization using genetic algorithms." *Journal of Spacecraft and Rockets* 37.5 (2000): 663-669.
3. Englund, W. C., Stanley, D. O., Lepsch, R. A., McMillin, M. M., Unal, R. "Aerodynamic configuration design using response surface methodology analysis." NASA STI/Recon Technical Report A 94 (1993): 10718.
4. Myers, R. H., Montgomery, D. C., Anderson-Cook, C. M. "Response Surface Methodology: Process and Product Optimization Using Designed Experiments."
5. Candiotti, L. V., De Zan, M. M., Cámara, M. S., & Goicoechea, H. C. "Experimental design and multiple response optimization, using the desirability function in analytical methods development." *Talanta* 124 (2014): 123-138.
6. Derringer, G. and Suich, R. (1980), "Simultaneous Optimization of Several Response Variables." *Journal of Quality Technology* 12, 214–219

More Electrical Non-propulsive Architectures Integration

Nawal JALJAL, Jean-Philippe SALANNE, René MEUNIER, Bruno THORAVALL, Clélia LEVEL
Safran S.A.,
Magny-Les-Hameaux, 78772, France
Email: nawal.jaljal@safrangroup.com

ABSTRACT

This paper discusses some thoughts about aircraft integration associated with more electrical non-propulsive architectures in the context of future hybrid propulsive concepts. In order to optimize the aircraft integration outcome, the coupling between propulsive and non-propulsive power sources must be considered. Despite a general tendency to increase non propulsive energy onboard, the related energy and power consumption remains minor against propulsive need. However, the design of thermal engines is strongly affected by the non-propulsive energy off-takes altering the overall behavior of the engine due to operability considerations. In a new context of hybridization, integration strategies show synergies between a thermal engine's operability requirement, efficiency and more electrical non-propulsive architectures. This leads to new opportunities to design electrical architectures and associated power management.

KEYWORDS: *Hybrid, Architecture, Electrical, Aircraft, Non-propulsive.*

Testing of Experimental and Numerical Methods for Investigation of the Unsteady Flow Induced by Rotor Influence on Heliport

Wit Stryczniewicz

Paweł Ruchała

Grzegorz Krysztofiak

Wiesław Zalewski

Adam Dziubiński

Małgorzata Wojtas

Kazimierz Szumański

Institute of Aviation, Aerodynamics Department

Krakowska 110/114, 02-256 Warsaw, Poland

[*wit.stryczniewicz@ilot.edu.pl*](mailto:wit.stryczniewicz@ilot.edu.pl)

The paper presents results of experimental and numerical investigations of the rotor wake in ground effect. Vibrations caused by unsteady pressure fluctuation in the rotor wake are believed to be dangerous for construction of the heliports and services performed in the buildings, eg. in hospital operating room. The purpose of the research was to develop methodology for investigation of rotor influence on helipads and buildings. In the proposed approach the full scale and model test were combined. The numerical simulations and full scale tests were performed on two blade full scale rotor. The unsteady flow field in the rotor wake was investigated in model scale with use of Particle Image Velocimetry and pressure measurements. The results of both full and model scale investigations were consistent. The unsteady flow structures, hypothesized to be responsible for the vibrations propagations, were visualized in the model scale. The pressure fluctuations were measured both in model and full scale. The performed research proved the feasibility of proposed approach and has paved the way for detailed investigations leading to development of a general model of the phenomenon.

Keywords: rotor wake in ground, heliport, moving mesh, unsteady pressure measurements, wake flow visualisation



Graph-Based Algorithms And Data-Driven Documents For Formulation And Visualization Of Large MDO Systems

Benedikt Aigner

Institute of Aerospace Systems, RWTH Aachen University

Ph.D. Student

Wüllnerstr. 7, 56062 Aachen, Germany

benedikt.aigner@ilr.rwth-aachen.de

Imco van Gent

Faculty of Aerospace Engineering, Delft University of Technology

Ph.D. Student

Kluyverweg 1, 2629HS, Delft, The Netherlands

Gianfranco La Rocca

Faculty of Aerospace Engineering, Delft University of Technology

Assistant Professor

Eike Stumpf

Institute of Aerospace Systems, RWTH Aachen University

Full Professor

Leo L.M. Veldhuis

Faculty of Aerospace Engineering, Delft University of Technology

Full Professor

ABSTRACT

A new system is presented that enables the visualization of large multidisciplinary design optimization (MDO) problems and their solution strategy. This visualization system is the result of a cooperation between RWTH Aachen University and Delft University of Technology (DUT) within the EU project AGILE. In AGILE, collaborative MDO is performed in large, heterogeneous teams of experts by solving MDO problems using a collection of design and analysis tools. The two main phases of such a collaborative MDO project are the formulation and the execution phase. This paper focuses on the visualizations required to support the formulation phase of the MDO problem. In this phase three main steps have been identified: the set-up of the repository of interconnected tools, the definition of the MDO problem at hand, and the determination of the solution strategy to solve that MDO problem. KADMOS, an open-source MDO support system developed by DUT, uses graph-based analysis to formulate an MDO problem and its solution strategy, based on the disciplinary analyses available in a repository. The results of KADMOS are stored in a standardized format called CMDOWS, which is eventually used to trigger the execution phase by means of a simulation workflow platform of choice. Although based on XML, the readability of the CMDOWS file is quite poor also for MDO experts, especially for large MDO systems involving thousands of variables, thus preventing visual inspection of the formalized MDO problem. Providing visualization capabilities to thoroughly inspect the outcome of the three aforementioned formulation steps becomes a key factor to enable the specification of large MDO systems in a heterogeneous team. Therefore, one of the main hurdles for using MDO as a development process can be removed. Conventional visualization methods (such as N2-charts, functional dependency tables, and design structure matrices) have major scalability limitations. Therefore VISTOMS, a dynamic visualization package based on the open-source visualization library D3.js, was developed by RWTH Aachen to enable the visualization and inspection of the different MDO system specification steps. The developed visualization capabilities are demonstrated by means of a wing design optimization problem performed at DUT. As shown in this use case, VISTOMS enables the visualization and inspection of a large MDO system containing more than ten different aircraft design tools, interlinking thousands of variables.

KEYWORDS: MDO, visualization, KADMOS, CMDOWS, VISTOMS

Application of a visualization environment for the mission performance evaluation of civilian UAS

E. Fokina

*Institute of Aircraft Design, Technical University of Munich
Research Associate and Ph.D. Candidate
Boltzmannstraße 15, 85748 Garching bei München, Germany
ekaterina.fokina@tum.de*

J. Feger

*Institute of Aircraft Design, Technical University of Munich
Research Associate and Ph.D. Candidate*

M. Hornung

*Institute of Aircraft Design, Technical University of Munich
Professor, Head Institute of Aircraft Design*

ABSTRACT

Future unmanned aerial vehicle applications require the development of new advanced design environments. In order to get an effective Unmanned Aerial System, UAS, solution it is necessary to take into account all elements of the system, e.g. to bring together aircraft design, payload, communication and other elements into one multidisciplinary design process. Compared to manned aircrafts, an Unmanned Aerial Vehicle, UAV, interacts with the environment through the onboard sensors. Therefore the sensor and communication performances as well as their implementation in the whole system play an important role for a mission fulfillment. An UAV design is then strongly driven by the mission, sensors and communication systems requirements. In the classic aircraft design approaches the sensor and communication performances are not part of the primary requirements and are taken into account on the operational analysis stage only, when the aircraft concept is already quite detailed. In order to take into account the sensor and communication requirements early enough an operational environment has to be simulated and implemented into the design loop.

KEYWORDS: *UAV, visualization, operational analysis, aircraft design, mission performance analysis*



Automated handling and positioning of large dry carbon fibre cut-pieces with cooperating robots in rear pressure bulkhead production

Lars Brandt

*German Aerospace Centre
Scientist*

*Am Technologiezentrum 4, 86150 Augsburg
Lars.Brandt@dlr.de*

Mona Eckardt

*German Aerospace Centre
Scientist*

ABSTRACT

For new generation long-haul aircrafts the rear pressure bulkhead is made of carbon fibre reinforced plastics. The production process is usually realised by a manually performed dry fibre preforming process followed by a vacuum assisted resin infusion. The preforming process is laborious, complex and for the workers non-ergonomic due to the handling of large cut-pieces with high positioning accuracy requirements. In order to fulfil the increasing production rates, this process has to be enhanced. For this reason the German Aerospace Centre in Augsburg develops an automated preforming process using a female tooling of the pressure bulkhead. This paper presents first investigations to handle large cut-pieces of the rear pressure bulkhead plybook by cooperating robots. The grippers used in this process are passive adjustable. They consist of five elements which are connected by ball-joints. Due to these ball-joints the geometry can be adapted to different shapes. The main objective is an investigation of suitable gripper movements in order to pick-up the cut-pieces from a table by draping it, transport and place it with high lay-up accuracy in the pressure bulkhead tooling. In total four different pick-up strategies are investigated to figure out which one is suitable to handle the cut-pieces without wrinkles, folds and bridging. The best strategy is optimised and used for lay-up tests where the same requirements obtain as for the pick-up movement. In conclusion the used gripper system can ensure a material handling without damage. Consequently it is possible to realise the preforming process with the passive and less complex gripper system. This may result in a more reliable and cost-effective process.

KEYWORDS Aircraft, Automated production process, Carbon fibre reinforced plastics, Cooperating robots, Rear pressure bulkhead production

1 INTRODUCTION

The increasing amount of civil air traffic results in a higher demand of aircrafts. In addition the demand for fuel efficiency and cost-effectiveness is increasing. This leads to the requirement to decrease the weight of aircrafts. An approach to reduce the weight is the use of carbon fibre reinforced plastics (CFRP) for structural components. More than half the structural mass of the Boeing 787 and Aircraft A350 is made of CFRP. Up to now the production of CFRP parts consists of a high proportion of manually performed process steps.

The German Aerospace Centre (DLR) in Augsburg addresses this problem by working on process automation for these parts. A special part of this work is the realisation of automated production processes of large structural components, for example fuselage panels and pressure bulkheads. The DLR focuses on thermoset processes for these parts. Therefore a preform with dry carbon fibre textiles has to be prepared before it is infused by a vacuum-assisted process..

In this paper an automated preforming process for the rear pressure bulkhead of a next generation long-haul aircraft is shown. More precisely the handling properties for the large cut-pieces covering the whole diameter of the double curved tooling are investigated. The process is realised by

cooperating robots which handle the cut-pieces with passive adjustable grippers. The large cut-pieces are used to form the shape of the part. In present production lines they are handled manually by two workers. They pick-up the cut-piece by hand from a table and transport it to the tooling. Due to the high positioning requirements and the size of the cut-piece, the exact positioning of it is a difficult requirement. This results in non-ergonomic handling positions for the workers and high process times.

In a previous automation approach the overall handling qualities of these cut-pieces with cooperating robots were investigated. The cut-piece was placed by hand at the tooling surface. From this position the cut-piece was picked-up and placed again at the same position by cooperating robots. Fig. 1 shows the test set-up. As material a non-crimp fabric was used. This material has a higher shear strength compared to the material which is used for the production of the component. The result of these first investigations showed that a general handling of large cut-pieces in a double curved tooling by cooperating robots is possible [1].



Figure 1: First handling test of large cut-pieces with cooperating robots [1]

This paper is based on this approach and attempts to achieve a complete automated handling process of the cut-pieces. The paper starts with the definition of the use case where the target structure and the test set-up are explained. The next chapter gives a clarification about general characteristics of draping and states the draping properties based on the use-case investigated. After that the procedure used to adapt the grippers to the lay-up surface is explained. Subsequently the robot offline programming is detailed. This is followed by a description of the performing tests, consisting of the strategies for material pick-up, the optimisation of this movement, the handling and the lay-up. Finally a summary of the results, a discussion and a conclusion is given. For the automated processing of smaller cut-pieces in the preform refer to [2] and [3].

2 TARGET STRUCTURE

As a target structure the rear pressure bulkhead of the Airbus A350 is used. The tooling is double curved and its cross section is about 3600mm in length and 650mm in height. For the tests a tooling half of the original scaled rear pressure bulkhead tooling is used.

The plybook of the rear pressure bulkhead consists of two different categories of cut-pieces. On the one hand it includes cut-pieces for reinforcement. These cut-pieces have small dimensions and exist in different shapes. Due to their dimensions they are not appropriate for a handling with cooperating robots. Handling procedures for these cut-pieces can be found in [2] and [3].

On the other hand large cut-pieces are part of the plybook. These are up to four meters in length and cover the total length of the tooling. Four of them cover the complete surface and therefore form the shape of the rear pressure bulkhead. For the investigations in this paper one of the large cut-pieces is used to perform the tests. This cut-piece is modified in its position to fit the tooling half. The cut-piece is around 4100mm in length and 1150mm in width. As material a 1270mm wide satin fabric made of 6k carbon fibres is used. The mass per unit-area is 370gsm. Fig. 2 shows a schematic view of the tool half and the cut-piece used for the investigations.

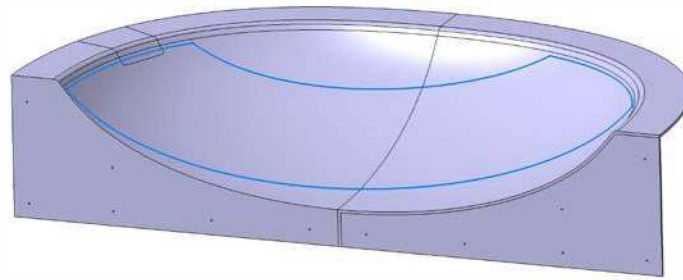


Figure 2: Tool shape and sample cut-piece

3 EXPERIMENTAL SET-UP

For the investigations a test bench of the DLR Augsburg is used. In this test bench two industrial robots are assembled on one linear axis. For the test with cooperating robots two identical grippers are attached. These grippers were developed to handle non-crimp fabrics to build a preform of a cylindrical half shell with local reinforcements [4]. The original grippers consist of nine elements which are connected by ball-joints. Due to the low width of the cut-pieces used in these tests compared to the cut-pieces used for the cylindrical half shell, the number of elements is reduced to five. This reduction results in a higher stiffness of the gripper which leads to better handling properties of the material. The element in the middle is fixed and the other ones can be rotated in x, y and z direction. Due to this characteristic the gripper can be adjusted to different surface geometries. At the bottom of each module eleven vacuum cups are placed. In [5] and [6] tests were made which show that these cups are appropriate to handle dry textiles.

On one side of the linear axis the tooling half is placed and on the other side a flat table is positioned to pick-up the cut-piece. Fig. 3 shows the test set-up.

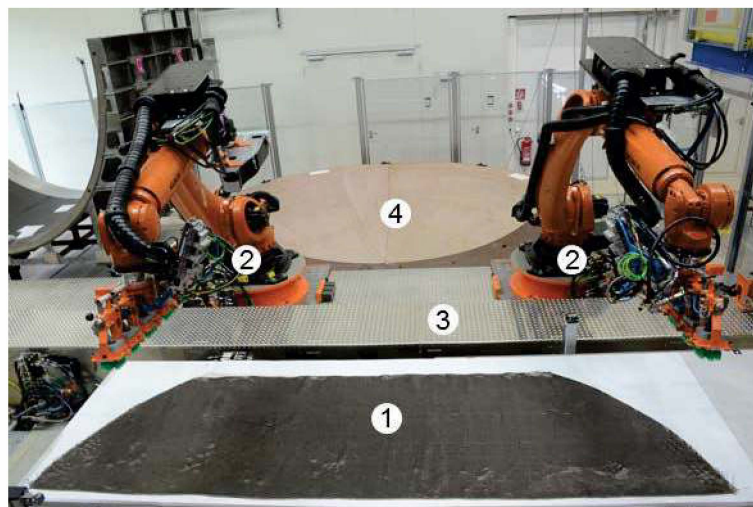


Figure 3: Test setup with pick-up table (1), robots and end-effectors (2), linear-axis (3) and mold (4)

4 CHARACTERISTICS OF DRAPING

For the investigations the material is picked-up from the table and placed in a double curved female tooling. Due to their passive adjustability the grippers have to drape the cut-piece during pick-up.

As mentioned in [4] there are different possibilities to drape dry fiber cut-pieces. A seed point or seed curve is chosen which is defined as the start point of the draping process. From this fixed point or curve the cut-piece is draped in all directions until it is lying at the surface of the tooling. For manually processes draping is almost unreproducible and often fiber deformations occur. Fig. 4 shows different fixations for the draping process.

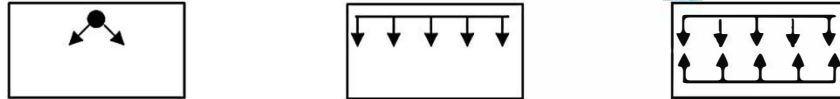


Figure 4: Point fixation (a), line fixation (b), double-line fixation (c) [4]

For automated processes the type of draping depends on the gripper, the tooling and the material properties. In the majority of the draping processes for dry textiles, the cut-piece is provided at a flat table. From this table the cut-piece is picked up by one or more robots. The amount of robots which are used to pick up the cut-piece depends on its size. Cut-pieces with a small size and/or complex shapes are often handled by one robot. In this case commonly kinematic grippers are used. These drape the cut-piece when it is completely picked-up from the table. One disadvantage of this type of grippers is the high complexity of the construction and the need of a control system. Fig. 5 shows an example for draping by a kinematic gripper. A test scenario with this gripper can be found in [7].



Figure 5: Draping by a kinematic gripper

In contrast, cut-pieces with almost rectangular shapes and a length of more than 2m are often handled by two robots. Both robots have to do synchronized movements to handle the cut-piece. The grippers which are used here are only passive adjustable. This means that the orientation of the grippers must be adapted to the surface geometry before the pick-up process starts. The final gripper orientation is equal to the curvature of the tooling where the cut-piece is placed. It follows that draping takes place during the pick-up process. When this process part is finished the cut-piece is already draped in the orientation of the tooling surface. Then the cut-piece can be placed at this surface without further deformations.

The surface geometry has an influence how complex draping is. When a cut-piece is placed at a single curved tooling, draping is less complex because only one orientation has to be adapted. This kind of draping can be performed with mostly all type of material with a low thickness. For draping in a double curved tooling the orientation of the draped material has to be adapted at least in two directions. A draping simulation is used to figure out if the material can perform the desired draping. Here woven fabrics are mostly suitable for draping at a double curved surface.

For the investigations in this paper the pick-up process is described in more detail. It starts with the first element of the gripper moving to the cut-piece surface. After placing this element, the vacuum flow is activated. Due to this the cut-piece is fixed at the first element. From this point the gripper is moving until the second element of the gripper is placed at the cut-piece surface. During this movement the material between the first and the second element is draped. Draping ends when the second element reaches its pick-up position. Compared to Fig. 4 there are in total five line fixations which are generated by the five elements of the gripper. The material of the cut-piece, each located between two line fixations, is draped. Fig. 6 shows this type of draping schematically.

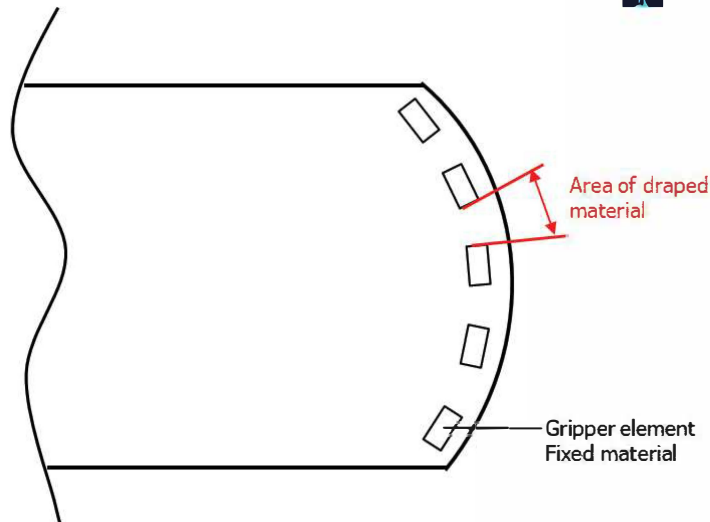


Figure 6: Draping area between the gripper elements

5 ROBOT OFFLINE PROGRAMMING

The robot programming is done via Dassault Delmia V5 in combination with CATIA V5. The cut-piece mentioned in chapter 3 is constructed on the mold surface and with the composite design workbench a flattening (2D-geometry of the cut-piece) is generated. This gives a possible geometry for the cut-piece as well as an indication for the robot movement design. Starting by defining the robot positions for the lay-up, the movements are reverse engineered to the pick-up.

First a tool center point (TCP) is determined for each end-effector element. Afterwards coordinate systems are generated on the three dimensional model of the cut-piece for each lay-up position of every gripper element. As a result five coordinate systems on each side of the cut-piece are needed. Therefore a visual basic program has been written to resemble the kinematic structure of the two grippers to create these coordinate systems. For each short side of the cut-piece a parallel curve is generated and the centre point of the curve is determined. This point together with a straight line perpendicular to the outer edge of the cut-piece defines the first coordinate system and the position of the centre element of the gripper. It is used to construct spheres to each side to resemble the ball-joints to the next elements. The outer intersection between the parallel curve and the two spheres provides the TCPs for the next two elements. Together with additional perpendicular lines they determine the corresponding coordinate systems. This step is performed for all ten gripping points.

In order to determine the coordinate systems for the pick-up, the TCPs have to be transferred to the flattening of the cut-piece. The composite design workbench provides the functionality to transfer additional geometries according to the internally calculated cut-piece transformation. This function is used to transfer the TCPs on the flattening and create coordinate systems together with perpendicular lines to the cut-pieces outer edge on its short sides.

With the coordinate systems in the mold the adjustments of the individual elements can be calculated. Therefore the four transformation matrices ${}_{0-0}T_{0-1}$, ${}_{0-1}T_{0-2}$, ${}_{0-0}T_{1-0}$, and ${}_{1-1}T_{1-2}$ between the elements are calculated and the Euler angles between the elements are determined.

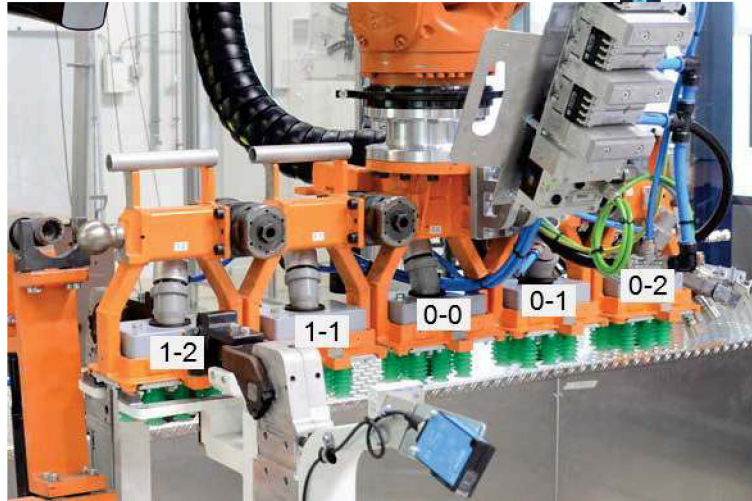


Figure 7: End-effector in the automatic adjustment station

Fig. 7 shows the end-effector in the automatic adjustment station with the designation of the elements. This adjustment station can be used to adapt the gripper elements to fit its position in the mold. Although the system is designed to do these adjustments automatically it is done manually for this paper. In [8] the automated adjustment station is described in more detail.

6 STRATEGIES FOR MATERIAL PICK-UP

In total four different pick-up strategies are investigated:

1. a rolling movement, short to long side,
2. a contrary rolling movement
3. a seesaw movement
4. a rolling movement, long to short side

The best strategy is used for optimisation and further tests. For all described strategies the grippers are adapted to the surface geometry where the cut-piece is placed. The movements of both grippers occur at the same time.

For the first strategy the cut-piece is picked-up by both grippers from the short side to the long side of the cut-piece. The first element of the gripper is placed closed to the short side. Then a rolling movement is performed until the fifth element is placed close to the long side. From this point the cut-piece is lifted (Fig. 8, R01 and R02: EDCBA).

During the material pick-up from element 1 to 5 the distance between the grippers increases. This generates tension in the material. At one point the tension is too high to be compensated by the vacuum cups which hold the cut-piece and as a result the cut-piece peels off.

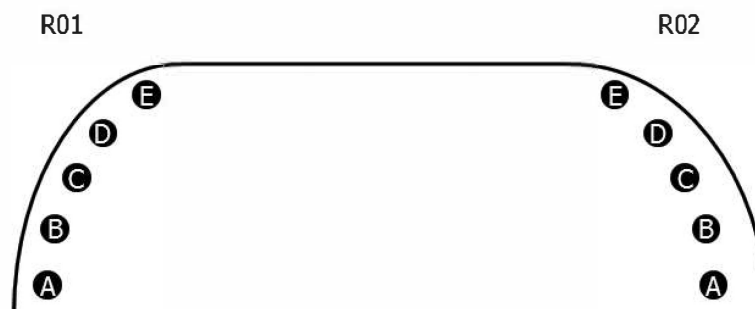


Figure 8: Material pick-up strategies for robots R01 and R02

The contrary rolling movement is performed with the grippers picking up the material in the opposite direction. One gripper (R02) picks the material from the long side to the short side and the other one (R01) from the short side to the long side (Fig. 8, R02: ABCDE, R01: EDCBA).

Both grippers start with the material pick-up at opposite sides of the cut-piece. During the material pick-up by the first element of each gripper the material which should be picked-up by the fifth element is not fixed at this time. During the pick-up by the first element a material displacement occurs at the other edge which results in a deviation of the grip points generated in CATIA.

For the third strategy the grippers start the pick-up movement in the middle between both cut-piece edges. From there a rolling movement is performed to pick-up the material with the next two elements in the direction of the long side. After that a rolling movement is done from the long side to the short side, to pick-up the material with the last two elements. This is resembled by the combination of CBADE in Fig. 8 for both robots.

The problem of this strategy consists in the second rolling movement from the long side to the short side. During this movement the cut-piece is already fixed at the elements A, B and C. As a result the material is dragged over the table, the vacuum cups bend and finally the material peels off. Due to this and the result of the contrary rolling movement the pick-up strategy of the seesaw with contrary moving grippers was not investigated further.

Strategy four picks up the cut-piece with both grippers from the long side to the short side (Fig. 8, R01 and R02: ABCDE). The first element of the gripper is placed close to the long side. Then a rolling movement is performed until the fifth element is placed at the cut-piece close to the short side. From this point the cut-piece is lifted.

During this movement the material is draped between the elements. The distance between the grippers decreases within the whole material pick-up. A generated tension in the material can be compensated by the flexible vacuum cups. The cups prevent a material deviation of the picked material and therefore a displacement of the grip points.

This last pick-up strategy shows the best properties and is used for further investigations.

7 OPTIMISED PICK-UP MOVEMENT

Although the first approach for generating the pick-up coordinate systems is a good approximation it became evident that further requirements have to be fulfilled. Especially for cut-pieces with a strong curvature on the short sides the end-effector orientations in the last gripping points are crucial (Fig. 8, element E).

It can be observed that the material detaches on the first gripping element (Fig. 8, element A) due to great rotations around the z-axis between the first and the last element. Thereby the z-axis is defined as surface normal of the pick-up table oriented in the table plane. This can be explained by the increasing distance between the first two elements (Fig. 8, E-E) of each end-effector. The satin weaved material contains carbon fibres running through the material preventing it to stretch. As a consequence no end-effector element pair (A-A, B-B, C-C, D-D, E-E) may increase their distance after they picked up the cut-piece. To ensure the pick-up movement is compliant two key factors have to be considered: the adjustments on the end-effector and the orientation of the coordinate systems for pick-up. Since the end-effector adjustments are crucial for the lay-up, only the coordinate systems orientation can be modified. In case of the cut-piece used in this paper an adjustment of 5° for position E of robot 1 (compare Fig. 8) from 43° to 38° was sufficient.

8 LAY-UP

The transportation to the mold has to be done with a fixed distance between the robots and tilted end-effectors to resemble an average catenary between the cut-piece and the robots. When the position above the mold is reached the final lay-up movement starts. By lowering the end-effectors in the direction of the mold the material touches the mold first in the middle of the cut-piece and spreads to both sides. Sliding of the material on its short side can be countered by the robot movement. Therefore the material on the short side has to touch the mold first. Here is the maximum

slope of the mold. Then the robots perform a rolling and lowering movement. Thus material in the critical part of mold is placed first and then dragged to its ideal position.

9 RESULTS

The used satin weaved material shows a high drapability and associated a good permeability to air. Both characteristics are a challenge for the robotic handling of this material with vacuum cups and especially for large cut-pieces. Its drapability is necessary for a wrinkle free lay-up in the highly spherical bulkhead mold though. The required draping of the cut-piece has to be done by the robot movement strategy due to the fact that the end-effectors are only passive adjustable. Even though this reduces weight on the robot it adds complexity to the process.

The investigations show a proof of concept, the pick-up and transport as well as the lay-up of the test cut-piece was successful.



Figure 9: Transportation of the cut-piece (left), lay-up result (right)

Fig. 9 shows the transportation and lay-up result of the cut-piece. While picking up the cut-piece folds are introduced. They are built because the grip points and the drop points are located in different positions on the cut-piece. This allows the described draping process. On the right the lay-up result is presented. The positioning of the cut-piece is ambivalent: on the right side it is in the tolerance of the laser projected contour. On the left hand side the cut-piece is out of tolerance. Two main folds are visible on the cut-piece, one on the left of the long side and the other one on the right hand side. In addition several wrinkles cover the cut-piece and the traces of the suction cups are visible.

10 DISCUSSION AND CONCLUSION

As seen in the results cooperative handling of large, air-permeable carbon fiber fabrics on the principle of volume flow is possible. Although the error tolerance for robot movements regarding jerks, translation and rotation differences between the robots and work angles for the end-effectors is low. The higher stiffness of the grippers due to reduction to five elements reduces vibrations and therefore increases reliable handling of the material. It is conceivable that the two significant folds could be prevented with a slight end-effector rotation or a single movement of one robot with one element correcting the placement position. Regarding the areal wrinkles the authors suggest that previous handling trials affected the cut-piece.

This suggests that a passive draping is possible although the quality of the process should be enhanced. Further work has to be done to adjust the grippers with the automatic adjustment station to minimize the positioning errors. In addition the quality of the lay-up has to be examined and compared to a hand laid cut-piece. Assessing the robot programming, a more automated tool for all cut-pieces in the part is preferable, i.e. a software tool that implements cooperating robots. This would reduce the programming efforts significantly. [9] and [10] show a possible approach for an automated path planning.



11 ACKNOWLEDGEMENT

The authors like to thank Dr. Marcin Malecha and Christoph Frommel for their enduring support. Special thanks go out to our colleagues at the ZLP in Augsburg that helped on this research.

REFERENCES

1. G. Braun, A. Buchheim, F. Fischer, T. Gerngross; 2013; "Handgeführter Endeffektor für die automatisierte Handhabung von textilen Zuschnitten" (Hand guided endeffector for an automated handling of textile cut-pieces); DLRK; Stuttgart; 10.-12. September 2013
2. M. Körber, P. Gänswürger, T. Gerngroß; 2013; "Endeffektor zur schonenden Drapierung von textilen Zuschnitten für Faserverbundbauteile (Endeffector for the draping process of dry carbon fibre fabrics used to build components of carbon fibre reinforced plastics)"; DLRK; Stuttgart; 10.-12. September 2013
3. T. Gerngroß, D. Nieberl; 2016; "Automated manufacturing of large, three-dimensional CFRP parts from dry textiles": CEAS Aeronautical Journal; Volume 7 (Issue 2); pp. 241-257
4. M. Eckardt, A. Buchheim, T. Gerngroß; 2016; "Investigation of an automated dry fibre preforming process for an aircraft fuselage demonstrator using collaborating robots"; CEAS Aeronautical Journal; Volume 7 (Issue 3); pp. 429-440
5. D. Sener; 2011; "Handling von Faserhalbzeugen in der automatisierten CFK-Produktion (Handling of fibre textiles within the automated production of CFRP)"; Deutsches Zentrum für Luft- und Raumfahrt e.V., Institut für Bauweisen und Strukturtechnologie, Augsburg
6. L. Larsen; G. Braun; 2011; "Entwurf und Test eines Saugsystems für das automatisierte Handling von Kohlefaserlegen (Design and test of a suction system for an automated handling of dry carbon fibre fabrics)"; Deutsches Zentrum für Luft- und Raumfahrt e.V., Institut für Bauweisen und Strukturtechnologie, Augsburg
7. C. Frommel; M. Körber; M. Kießig; M. Mayer; 2017; "Comparison of fibre angles between mechanical draped carbon fibres and draping simulation"; SAMPE Europe; Stuttgart; 14.-16. November 2017
8. D. Deden; 2015; "Entwicklung einer mobile Plattform für die Justage eines rekonfigurierbaren Roboterendeffektors zur Handhabung textiler Halbzeuge (Developement of an automated adjustment station for an passive adjustable gripper used for handling of dry carbon fibre textiles)"; Deutsches Zentrum für Luft- und Raumfahrt e.V., Institut für Bauweisen und Strukturtechnologie, Augsburg
9. L. Larsen; J. Kim; M. Kupke; A. Schuster; 2017; "Automatic Path Planning of Industrial Robots Comparing Sampling-Based and Computational Intelligence Methods"; FAIM; Modena; 27.-30. Juni 2017
10. L. Larsen; M. Kaspar; A. Schuster; M. Vistein; J. Kim; M. Kupke; 2017; "Towards Full Automatic Path Planning of Cooperating Robots in Industrial Applications"; CASE; Xi'an; 20.-23. August 2017

A THERMAL-SOLAR SYSTEM FOR DE-ORBITING OF SPACE DEBRIS

Constantin Sandu^{1}, Dan Brasoveanu², Valentin Silivestru¹, Georgel Vizitiu¹, Bogdan Filipescu³, Radu Constantin Sandu⁴*

¹*COMOTI, Bucharest, Romania*

²*Systems Engineering Group Inc. (SEG), MD, USA*

³*Teletrans. Craiova, Romania*

⁴*S.C. Structural Management Solutions S.R.L., Bucharest, Romania*

**Corresponding author: E-mail : constantin.sandu@comoti.ro*

ABSTRACT

This paper presents a system for removal of space debris, which can be placed on geocentric, heliocentric or Sun-synchronous orbit. The system is composed of two parabolic mirrors, a large one and a small one. The concave face of the large parabolic mirror is oriented toward the concave face of the small parabolic mirror. Sunlight is focused by the large parabolic mirror in its focal point. Then, the light rays are reflected by the small parabolic mirror (which has the same focal point as the large parabolic mirror) and form parallel rays directed along the axis. A guide-tube having a honeycomb structure plated with gold is attached to the convex side of the large parabolic mirror within a spherical articulation. Elastic lens filled with liquid are placed at the end of this guide tube. The guide-tube is normally closed by a gold plated shutter. When the shutter is opened, the light coming from Sun is focused by lens in one focal point onto target debris. The high power of focused light locally vaporizes/ionizes the debris material. The thrust created in this way de-orbits the space debris pushing it toward the Earth surface.

KEYWORDS: space debris de-orbiting, removal

SOLAR-GRAVITATIONAL SPACECRAFT USED FOR TRAVELING IN THE SOLAR SYSTEM

Constantin Sandu^{1}, Dan Brasoveanu², Valentin Silvestru¹, Bogdan Filipescu³, Radu Constantin Sandu⁴*

¹*COMOTI, Bucharest, Romania*

²*Systems Engineering Group Inc. (SEG), MD, USA*

³*Teletrans. Craiova, Romania*

⁴*S.C. Structural Management Solutions S.R.L., Bucharest, Romania*

**Corresponding author: E-mail : constantin.sandu@comoti.ro*

ABSTRACT

In some previous papers, the authors presented the theory and design of the Electromagnetic Gravitational Spacecraft. According to this theory, the Electromagnetic Gravitational Spacecraft no longer uses the Theorem of Momentum Conservation for propulsion like rockets or other space vehicles. The gravitational spacecraft is propelled by an artificial flux of gravitational radiation produced on the board of spacecraft, which permeates and attracts the spacecraft body. This flux of gravitational radiation is produced through multiple reflections of electromagnetic waves between multiple reflective layers embedded within the spacecraft hull. The generation of gravitational radiation in this way is a consequence of Einstein's General Theory of Relativity. This discovery was published as a theorem in a modern physics journal.

In the case of Solar Gravitational Spacecraft the solar light is used for generating gravitational waves through multiple reflections between two or multiple reflective layers which are important components of the spacecraft. The solar light is inserted in the direction perpendicular to the reflective layers by a double parabolic mirror system which strongly concentrates the solar light.

The paper presents only the main design and working principle of this type of spacecraft. While the absence of propellant is a great advantage, this type of spacecraft will not be soon preferred for future travels within the solar system because much research work is necessary for improving the reflection coefficient of mirrors, the cooling of reflective layers, and the design of a system which continuously feeds the spacecraft with concentrated solar light when it navigates at great distance from the Sun.

KEYWORDS: solar, gravitational spacecraft, space travel

NOMENCLATURE

a, acceleration, [m/s²]
 c, speed of light, [m/s]
 d, distance, [m]
 E, energy of a packet of photons, [J]
 E, electric field, [dyne/SC in CGS]
 E_e, irradiance in proximity of Earth, [W/m²]
 F, force, [N]
 g_{ik}, metric (or fundamental) tensor
 G, universal constant of gravitation [Nm²/kg²]
 h, Planck's constant, [J·s]
 H, magnetic field intensity, [Oe in CGS]
 M, mass, [kg]
 P, power, [W]
 r, radius, [m]
 R, reflectivity, dimensionless
 R, Ricci's scalar curvature
 R, Riemann's curvature tensor
 s, length in the 4-dimensional space [m]

t , time, [s]
 T , the invariant of the energy-impulse tensor
 T_{ik} , energy-impulse tensor
 δ , Kroneker symbol
 λ , wave length, [m]
 Φ , gravitational potential, [N·m/kg]

1. INTRODUCTION

It is very clear that the propulsion systems which rely on the Theorem of Momentum Conservation cannot represent the future for space propulsion because the amount of propellant which can be carried on board is limited.

The authors demonstrated in previous AIAA papers [1...10] that our civilization should replace the current present propulsion systems with a new type of propulsion system which no longer uses the Theorem of Momentum Conservation and relies on a Gravitational Principle instead. According to the Gravitational Principle, a spacecraft can move in space without propellant being attracted by its hull which generates artificial gravitational waves spanning the spacecraft body. Such a spacecraft uses no propellant. The Gravitational Principle is based on the 'Theorem of Conversion of Electromagnetic Energy into Gravitational Energy published by authors in the Journal of Advances in Physics [11]. This theorem shows that in some circumstances the electromagnetic waves (radiation) are converted into gravitational waves (radiation). The present paper demonstrates the transformation of solar light into gravitational radiation usable for propulsion of solar-gravitational spacecraft.

2. DESCRIPTION OF ELECTROMAGNETIC GRAVITATIONAL PROPULSION PRINCIPLES

For a clear understanding of the Solar-Gravitational Spacecraft, a short presentation of the principles of Electromagnetic Gravitational Spacecraft is necessary.

The Electromagnetic Gravitational Spacecraft relies on 4 design principles [1]:

- 1)-Usage of energy in wave form only. This means that both power and propulsion are generated and transferred in wave form (excluding chemical energy and ion acceleration by magnetic and electric fields);
- 2)-The principle of radiant hull – the ship hull is integrated into the propulsion system and emits an attractive radiation that permeates the entire body of ship. This means that the spacecraft moves in space due to attraction not due to pushing as in the case of present spacecraft;
- 3)-The use of artificial gravitation generated onboard the spacecraft, according to the Theorem indicated at point 4.
- 4)-The Theorem of Conversion of Electromagnetic Waves (radiation) into Gravitational Waves (radiation) for generation of gravitational radiation onboard the spacecraft. This theorem mainly affirms that electromagnetic waves (radiation) which are reflecting between two or more parallel and highly reflective surfaces is transformed into gravitational waves (radiation), which are directed the line perpendicular to the reflective surfaces. The power of gravitational waves radiated in this way is proportional with the square of the reflecting electromagnetic energy, E^2 , and the square of frequency of this energy, ν^2 . This theorem was demonstrated in previous papers by the authors [2, 5 and 11].

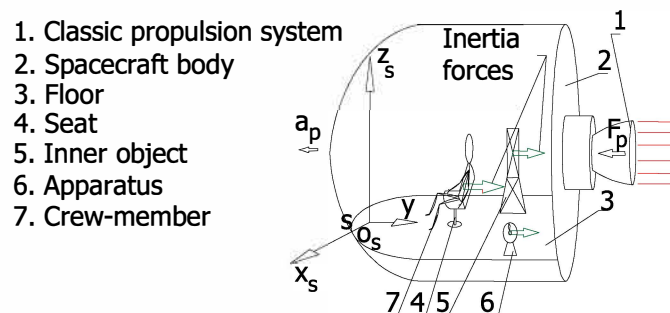


Figure 1: Spacecraft using the Theorem of Momentum Conservation for propulsion

For understanding the main differences between the two propulsion principles, the classic principle of propulsion is presented in fig.1 and the Gravitational Principle of propulsion is presented in fig. 2 for the case of a cubical gravitational spacecraft. [1]

In the classic spacecraft shown in fig.1, the crew-member 7, apparatus 6 and an inner object 5 are subject to inertia forces.

In the cubical gravitational spacecraft shown in fig.2, electromagnetic energy 8 injected among the reflective multilayer surfaces of hull area ABCD generates artificial gravitational radiation according to the Theorem of Conversion of Electromagnetic Radiation (Waves) into Gravitational Radiation (Waves).

1. Crew-member
2. Seat
3. Spacecraft's hull
4. Inner object
5. Apparatus
6. Floor
7. Uniform gravitational radiation emitted by the ABCD section of hull
8. Electromagnetic energy E in form of waves(radiation) injected between the reflective layers of hull section ABCD for generating gravitational waves (radiation)

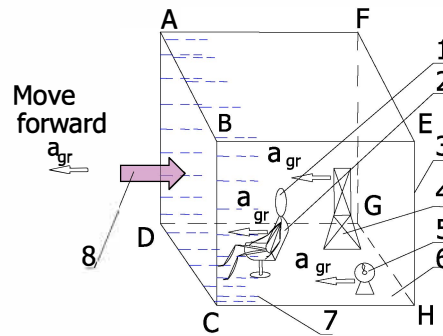


Figure 2: Cubic spacecraft using the Gravitational Principle of propulsion

This gravitational radiation is directed along the line normal to the face ABCD toward the spacecraft body. This radiation simultaneously attracts forward the spacecraft body and all the onboard crew-members, apparatus, inner objects etc with acceleration a_{gr} . In other words, the crew-member, its seat, the whole spacecraft are attracted by the same gravitational force in the same direction and for this reason the crew-member feels no inertia forces during spacecraft acceleration. In a gravitational spacecraft, the crew does not sense a difference between the gravitational radiation emitted by a far star (planet) and the artificial gravitational radiation emitted by a part of spacecraft hull (in fig.2 the emitting part of spacecraft is face ABCD).

If face ADGF is activated through injection of electromagnetic energy in its center, it also begins to radiate gravitational waves toward the spacecraft body. If the face ABCD is inactivated, the spacecraft begins to move suddenly in the direction normal to the ADGF surface. If the face ADGF is activated and face ABCD is not inactivated then the spacecraft moves in the direction EA (HD). The main components of gravitational spacecraft are presented in fig.3 showing gravitational spacecraft with a tetrahedron shape]

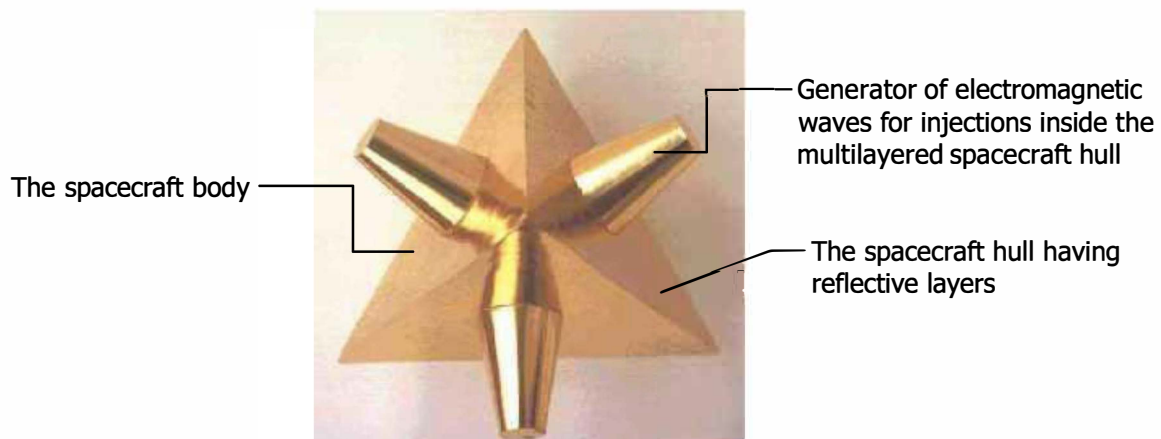


Figure 3: The components of a gravitational spacecraft having a tetrahedron shape

While precedent papers [1...10] defined and detailed all the design principles of gravitational spacecraft, a solution for a designing a generator of powerful electromagnetic waves was not found yet. The following sections of this paper show that this kind of spacecraft can be fed with concentrated solar light.

3. A BRIEF PRESENTATION OF THE THEOREM OF CONVERSION OF ELECTROMAGNETIC RADIATION (WAVES) INTO GRAVITATIONAL RADIATION (WAVES)

This theorem is important for understanding the operation of Electromagnetic Gravitational Spacecraft and Solar-Gravitational Spacecraft.

For this reason, although previously demonstrated in [11] the main steps of this demonstration are repeated below.

Einstein field equations are:

$$R_{ik} - \frac{1}{2} \cdot g_{ik} \cdot R = -\frac{8\pi G}{c^4} \cdot T_{ik} \quad (1)$$

In the above equations i and k take values from 0 to 3. The values 1, 2 and 3 indicate space coordinates (for example $x_1=x$, $x_2=y$, $x_3=z$ when Cartesian coordinates are used and $x_1=r$, i.e., radius, $x_2=\theta$, $x_3=\varphi$ when spherical coordinates are used). The value 0 of index is reserved for the temporal coordinate, which is $x_0 = c \cdot t$, where 'c' is the speed of light in vacuum and 't' is time.

R_{ik} , g_{ik} and T_{ik} are tensors. R_{ik} is the curvature tensor of second order (or Riemann's tensor); g_{ik} is the tensor that defines the space metric; R is Ricci's scalar curvature of space and G is the universal constant from Newton's Law of gravitation. T_{ik} is the energy-momentum tensor of matter (also known as the stress-energy tensor).

For electromagnetic waves, which propagate freely through space, the components of the energy-momentum tensor are given below.

$$\begin{aligned} T_{00} &= \frac{1}{8\pi} (E^2 + H^2), \quad T_{0i} = -\frac{1}{4\pi} (\vec{E} \times \vec{H})_i \\ T_{ik} &= -\frac{1}{4\pi} (E_i E_k + H_i H_k) + \frac{1}{8\pi} \delta_{ik} (E^2 + H^2) \end{aligned} \quad (2)$$

where $i, k=1, 2, 3$, $\delta_{ik} = 1$ for $i=k$ and $\delta_{ik} = 0$ for $i \neq k$.

It is known that 'contraction', (i.e., the multiplication of covariant field Eq. (1) with the metric tensor expressed in counter-variant form, which is labelled g^{ik} , followed by a summation), provides a new form of Einstein's field equations which is given below.

$$R = \frac{8\pi G}{c^4} T \quad (3)$$

where R is the invariant of curvature R_{ik} (also known as Ricci's scalar curvature).

Notes: Equation (4) was derived taking into account that:

1) The definition of the counter-variant metric tensor g^{ik} is based on the covariant metric tensor:

$$\sum_{k=0}^3 g_{jk} \cdot g^{ik} = \delta_j^i, \quad \delta_j^i = 1 \text{ when } i=j \text{ and } \delta_j^i = 0 \text{ when } i \neq j.$$

$$2) \quad g^{ik} \cdot R_{ik} = R.$$

$$3) \quad g^{ik} \cdot T_{ik} = T.$$

In the case of note 3), due to the fact that $g^{ik} = -1$ when $i=k=1, 2, 3$, $g^{ik} = 1$ when $i=k=0$ and $g^{ik} = 0$ when $i \neq k$ and taking into account the values of electromagnetic stress-energy tensor given by expressions (2), the result is:

$$T = \sum_{i=0}^3 g^{ii} T_{ii} = (-1) \cdot T_{11} + (-1) \cdot T_{22} + (-1) \cdot T_{33} + 1 \cdot T_{00} = 0$$

(4)

Eq. (4) shows that the invariant T of the energy-momentum tensor T_{ik} is null for a free electromagnetic field. Based on Eq. (4), the scalar curvature R is null.

This result is of a tremendous importance because it shows that **electromagnetic waves propagating freely through space do not generate gravitational fields.**

The situation is similar for the case when electromagnetic waves are confined inside a sphere, where the scalar curvature R is null (fig.4).

However, outside the sphere, the gravitational field must exist because, if the total energy of electromagnetic waves confined inside the sphere is E , then according to Einstein's formula, the relativistic mass of photons is:

$$M = \frac{E}{c^2} \quad (5)$$

and according to Newton, such a mass must produce a gravitational field with potential:

$$\Phi = -\frac{G \cdot M}{r} \quad (6)$$

where G is Newton's gravitational constant and r is the distance from sphere's center ($r > r_0$, r_0 =sphere's radius).

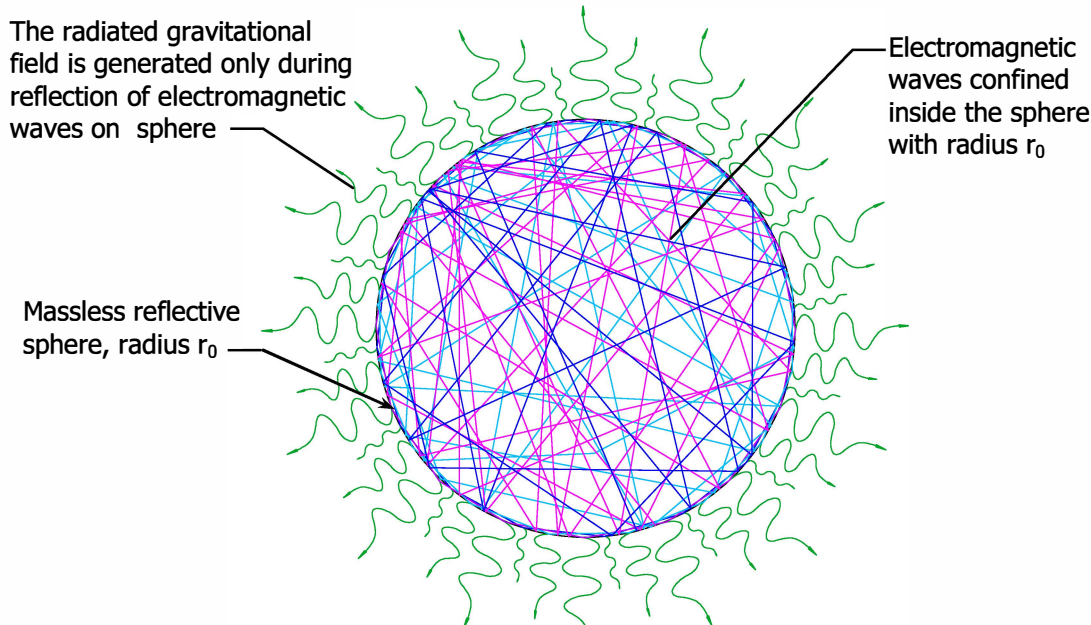


Fig.4: The scalar curvature R of an electromagnetic field confined within a massless sphere (radius r_0) is zero while outside the sphere the gravitational field should exist

In Einstein's view, the mass M of electromagnetic waves confined inside sphere modifies the continuum space-time curvature, this being characterized by Schwarzschild's metric given below.

$$ds^2 = \frac{r - \alpha}{r + \alpha} c^2 dt^2 - \frac{r + \alpha}{r - \alpha} dr^2 - (r + \alpha)^2 \cdot d\theta^2 - [(r + \alpha) \cdot \sin \theta]^2 \cdot d\phi^2 \quad (7)$$

where r, θ, ϕ are spherical coordinates, t is time, $\alpha = GMc^{-2}$.

Thus, we arrive to an implausible situation:

On one hand, according to equation (4) the gravitational field **should not exist** inside the sphere because the invariant T of stress-momentum tensor T_{ik} is null and on the other hand, the gravitational field **should exist** outside the sphere both in Newton's and Einstein's interpretation

because the potential Φ is not zero according to equation (6) and the space element ds is not zero, too, according to Schwarzschild's metric (7).

This contradiction can be solved only by admitting that gravitons are generated during reflection of electromagnetic waves on sphere's wall.

Thus, a previous paper [11] finally demonstrated the 'Theorem of Conversion of Electromagnetic Radiation (Waves) into Gravitational Radiation (Waves):

'During normal reflection of an electromagnetic wave on a reflective surface, electromagnetic energy is partially converted into gravitational energy. The frequency of the emitted gravitational wave is equal to the frequency of incident wave. The energy of emitted gravitational wave is proportional to the cube of frequency of electromagnetic wave. The direction of gravitational wave is opposite to that of the incident electromagnetic wave'.

4. USE OF 'THEOREM OF CONVERSION OF ELECTROMAGNETIC RADIATION (WAVES) INTO GRAVITATIONAL RADIATION (WAVES)' FOR PROPULSION OF GRAVITATIONAL SPACECRAFT

Assume two packs of electromagnetic waves 1, 2 having the same energy E and the same frequency are continuously reflected between two parallel reflective surfaces A, B. The two surfaces are separated by a gap, $d = \lambda$ (λ is the wave length supposed constant and equal in value for the two packets of electromagnetic energy, E) (fig. 5). During normal reflection of the two packs of electromagnetic energy E by surfaces A, B, a continuous flux of gravitational power is generated.

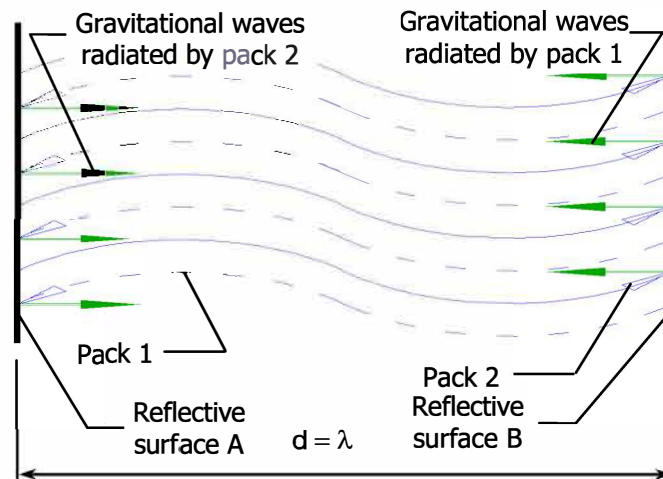


Figure 5: Two packs of electromagnetic energy which continuously radiate gravitational waves through multiple reflections

The radiated flux of gravitational power P_g is: [11]

$$P_g = \frac{512 \cdot G}{5 \cdot c^5} \cdot E^2 \cdot \nu^2 \quad (8)$$

where ν is the frequency of the two packs of electromagnetic energy, E , c is the speed of light and G is Newton's gravitational constant.

In formula (8) one can see that although G/c^5 is very small, $E^2 \cdot \nu^2$ can have great values if the reflecting electromagnetic energy E is sufficiently large and frequency of electromagnetic energy is high enough.

Two or more reflective surfaces as presented in fig. 5 compose the hull of gravitational spacecraft. For example, in fig.2 the hull of spacecraft has cubic faces. Any face is composed of two or more reflective surfaces. When electromagnetic energy E is injected between the reflective surfaces of hull

(for example ABCD), it generates through multiple reflections gravitational radiations which pulls (attracts) the spacecraft body to the left. When the electromagnetic energy E is injected in face ABEF of hull, the spacecraft is pulled (attracted) upwards etc.

5. DESIGN OF THE SOLAR-GRAVITATIONAL SPACECRAFT

Unfortunately at present there is no current technology for generating packets of electromagnetic energy having high energy and frequency. In addition, reflective surfaces able to efficiently reflect electromagnetic energy have not been created yet. These are the main reasons for which the gravitational spacecraft has not been developed yet.

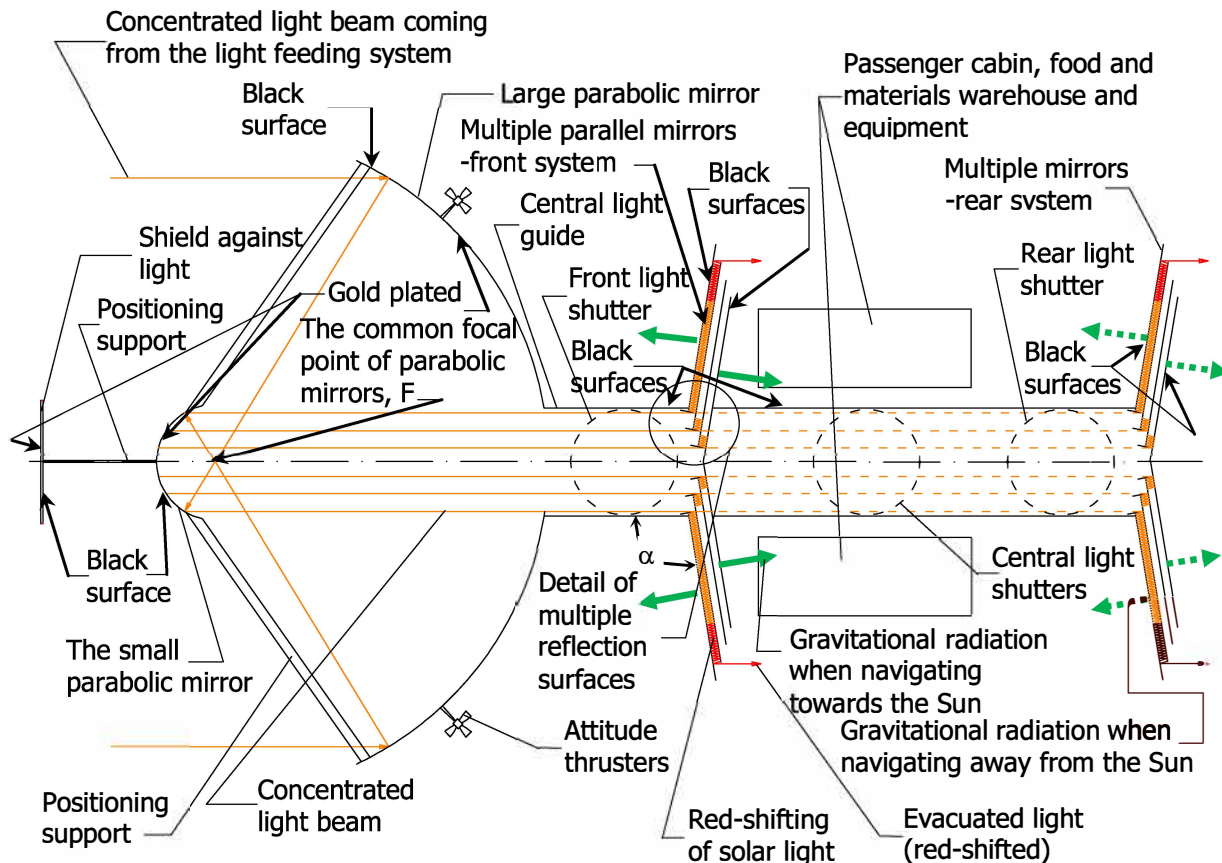


Figure 6: The simplified scheme of solar-gravitational spacecraft

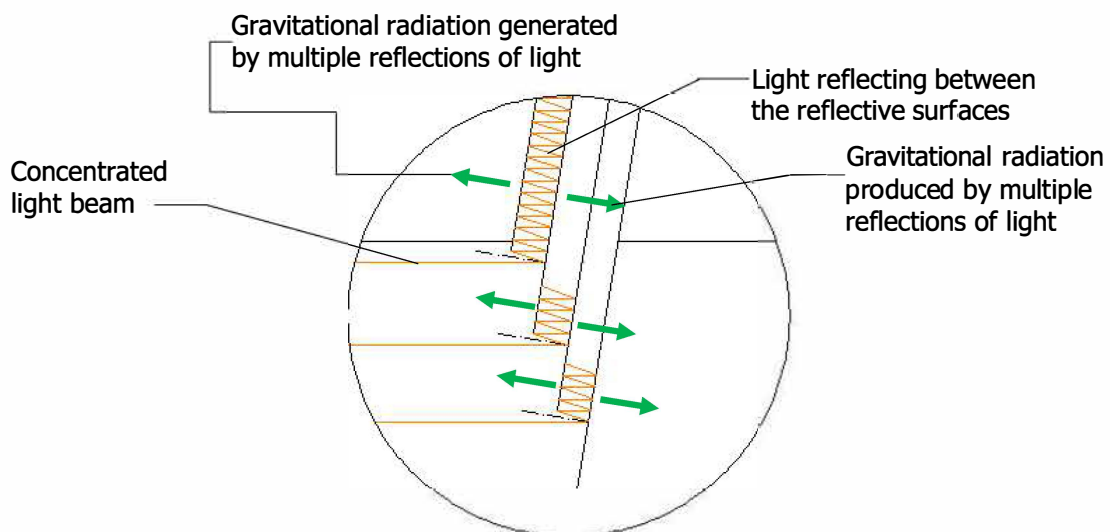


Figure 7: Detail of multiple reflection of light between the reflective surfaces

In the case of solar-gravitational spacecraft which is schematically presented in figs.6, 7, the problem of high electromagnetic energy is solved using concentrated solar light.

The solar light rays are collected by the large parabolic mirror and reflected to the focal point of mirror F. The focal point F is the same for the small parabolic mirror which is placed face to face with the large parabolic mirror. After leaving the focal point F, the light rays are reflected by the small parabolic mirror in parallel light rays (concentrated light beam) through the central light guide. When the front light shutter is opened, the concentrated light beam enters the multiple parallel mirrors. The mirrors are placed at an angle $\alpha = 90^\circ + \delta$, where δ is a very small angle. When the light rays reflect between mirrors gravitational waves are generated while the frequency of light decreases (all the components of the white light coming from Sun are red-shifted). [11]

At the end of process the light is evacuated in space as a brilliant red light. In this situation, the spacecraft is accelerated to the direction of Sun because the gravitational radiation generated by the front system of multiple parallel mirrors is spanning the passenger cabin which has the most of mass of spacecraft (the parabolic mirrors have a negligible mass).

The shutter is a thin disc plated with gold on the both faces. If the front light shutter is closed, the light is sent back to the small parabolic mirror, to the large parabolic mirror and then to the Sun and gravitational radiation is not generated.

The front system of parallel mirrors is composed of two halves which move aside letting the concentrated light beam to reach the rear system of multiple parallel mirrors (the central and rear shutters are opened). The concentrated light beam begins to reflect between the rear system of mirrors generating gravitational radiation. In this situation the spacecraft is moving in opposite direction relatively to the Sun. When the central shutter is placed at 45° the concentrated beam is directed to the left, right, upper or lower systems of parallel mirrors (these systems are not represented). The gravitational radiation spans the cabin attracting the spacecraft to the left, right, upwards or downwards. The left, right, upper or lower systems of parallel mirrors have a smaller surface area than the front and rear systems of parallel mirrors. Their role is only to correct the trajectory of spacecraft while the front and rear systems of parallel mirrors is for accelerating or decelerating of spacecraft. In addition to the mentioned systems, the spacecraft has attitude classic thrusters for contingency situations when solar light is not available.

The large and small parabolic mirrors, plane mirrors and light guide are made of composite materials (graphite fibre or graphene base) and are gold plated on the reflective surfaces. The heat is radiated in space through radiation of black surfaces of the above mentioned components. The passenger cabin is plated with gold foil or Mylar for reflection of light.

For a better understanding of design, a mock-up of spacecraft is presented in figs 8a, 8b and 8c.

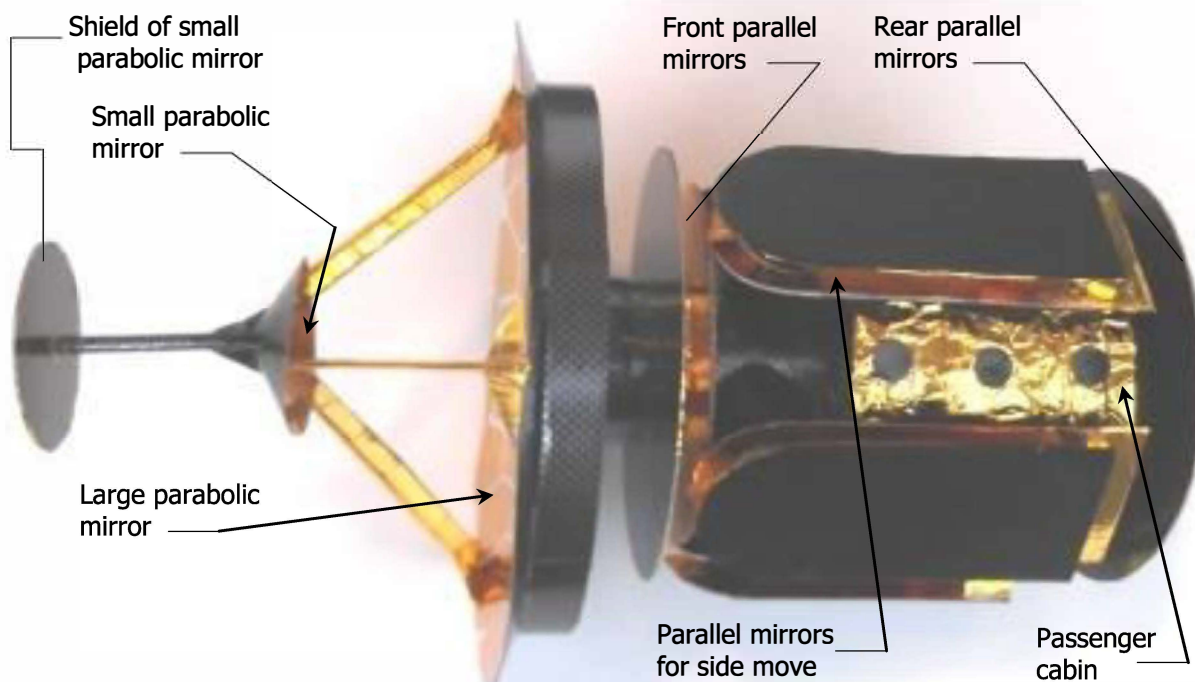
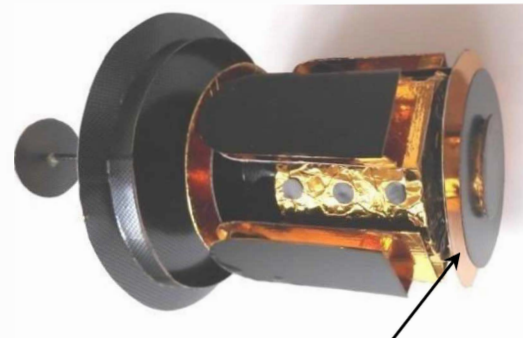


Fig.8a-Side view of a spacecraft (mock-up)


Fig.8b-View of small and large parabolic mirrors (mock-up)


Rear parallel mirrors

Fig.8c- Side view of spacecraft (mock-up)

6. CALCULATION OF GRAVITATIONAL RADIATED POWER

In ideal conditions (reflectivity coefficient of surfaces $R=1$), the gravitational power radiated by two parallel mirrors due to multiple reflection of two packets of photons having energy E each, is given in the table 1 for infrared, visible and ultraviolet light.

Table 1: Power of gravitational radiation produced through reflection of infrared to ultraviolet light





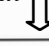
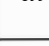
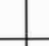
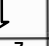
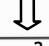

E, kJ  ν, Hz 	1	10^3	10^5	10^7	10^9	10^{11}	10^{13}
$\frac{dE}{dt}, kW$ 	$\frac{dE}{dt}, kW$ 	$\frac{dE}{dt}, kW$ 	$\frac{dE}{dt}, kW$ 	$\frac{dE}{dt}, kW$ 	$\frac{dE}{dt}, kW$ 	$\frac{dE}{dt}, kW$ 	$\frac{dE}{dt}, kW$ 
3×10^{11} (infrared)	2.5×10^{-25}	2.5×10^{-19}	2.5×10^{-15}	2.5×10^{-11}	2.5×10^{-7}	2.5×10^{-3}	2.5×10^1
3×10^{14} (infra red)	2.5×10^{-19}	2.5×10^{-13}	2.5×10^{-9}	2.5×10^{-5}	2.5×10^{-1}	2.5×10^3	2.5×10^7
3.75×10^{14} (red)	4×10^{-19}	4×10^{-13}	4×10^{-9}	2×10^{-5}	4×10^{-1}	4×10^3	4×10^7
5×10^{14} (yellow)	0.7×10^{-18}	0.7×10^{-12}	0.7×10^{-8}	0.7×10^{-4}	0.7×10^0	0.7×10^4	0.7×10^8
5.75×10^{14} (light green)	0.9×10^{-18}	0.9×10^{-12}	0.9×10^{-8}	0.9×10^{-4}	0.9×10^0	0.9×10^4	0.9×10^8
6×10^{14} (dark green)	1×10^{-18}	1×10^{-12}	1×10^{-8}	1×10^{-4}	1×10^0	1×10^4	1×10^8
6.25×10^{14} (light blue)	1.1×10^{-18}	1.1×10^{-12}	1.1×10^{-8}	1.1×10^{-4}	1.1×10^0	1.1×10^4	1.1×10^8
6.5×10^{14} (dark blue)	1.2×10^{-18}	1.2×10^{-12}	1.2×10^{-8}	1.2×10^{-4}	1.2×10^0	1.2×10^4	1.2×10^8
7×10^{14} (light violet)	1.4×10^{-18}	1.4×10^{-12}	1.4×10^{-8}	1.4×10^{-4}	1.4×10^0	1.4×10^4	1.4×10^8
7.5×10^{14} (dark violet)	1.6×10^{-18}	1.6×10^{-12}	1.6×10^{-8}	1.6×10^{-4}	1.6×10^0	1.6×10^4	1.6×10^8
3×10^{15} (ultra violet)	1.6×10^{-17}	1.6×10^{-11}	1.6×10^{-7}	1.6×10^{-3}	1.6×10^1	1.6×10^5	1.6×10^9
3×10^{16} (ultra violet)	2.5×10^{-15}	2.5×10^{-9}	2.5×10^{-5}	2.5×10^{-1}	2.5×10^3	2.5×10^8	2.5×10^{11}

Table 1 shows that the radiated gravitational power can have high values if the energy E of the reflecting light packets is sufficiently high.

Only half of this power is used for propulsion because the rest of power is lost in space.

7. NAVIGATION OF SOLAR GRAVITATIONAL SPACECRAFT INSIDE THE SOLAR SYSTEM AT GREAT DISTANCE FROM EARTH

The irradiance decreases with the square of distance from Sun. As a result, propulsion of such spacecraft becomes difficult at great distance from Sun. However, solar gravitational spacecraft can navigate even in this case if a feeding system with concentrated light is used (fig.9). [12]

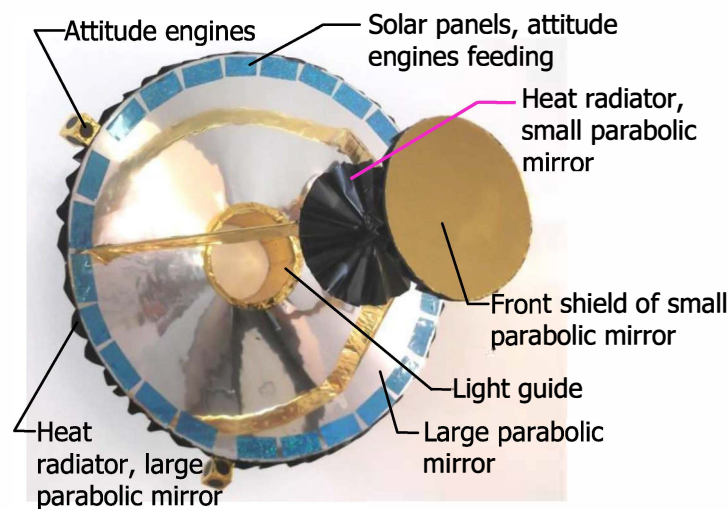


Figure 9-Feeding system with concentrated light for solar gravitational spacecraft (mock-up)

The feeding system is a large construction composed of a large parabolic mirror and a small parabolic mirror which have the same focal point. The system is built on an orbit around Earth and lifted to Earth's orbit around Sun. The large parabolic mirror which is directed toward the sun collects the sun-light which is transformed into a concentrated light beam by the small parabolic mirror. In this case the spacecraft navigates in the concentrated light beam emitted by the feeding system (fig.10).

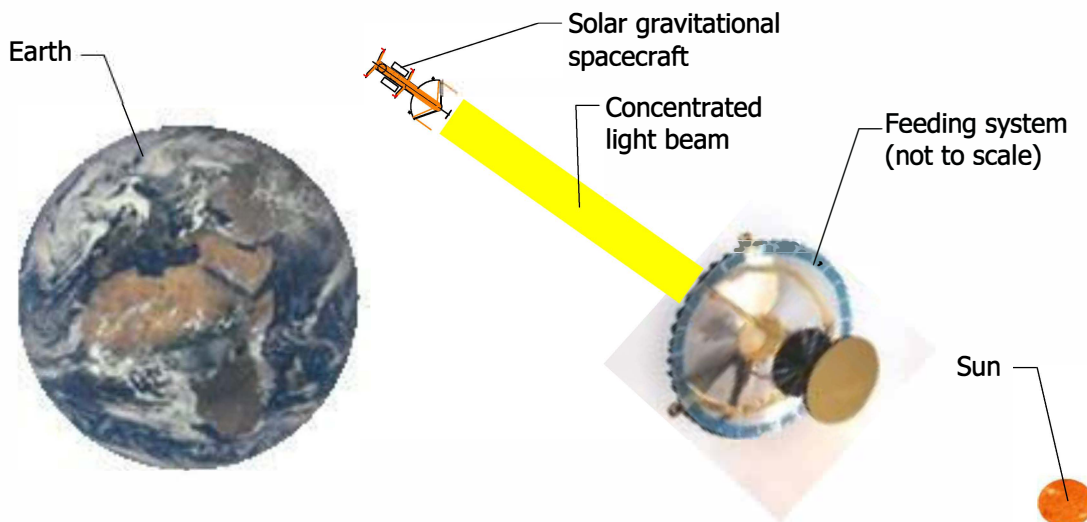


Figure 10: Navigation of solar gravitational spacecraft along the concentrated light beam emitted by the feeding system

The concentrated light beam is a spiral with approximately zero curvature i.e., it is almost a straight line. However, for continuous navigation in the concentrated light beam the solar gravitational

spacecraft must make continuous corrections opening the central light shutters (fig.7) (the front and rear shutters are used only for acceleration and deceleration of spacecraft).

8. THE PROBLEM OF MIRROR REFLECTIVITY

While in space there is plenty of light to be collected and reflected for creating gravitational radiation, the low reflectivity of materials is a great problem which must be solved. Until this problem is solved, the packets of light having energy E cannot be maintained due to absorption of light during reflection. Today, the best reflective materials can reach a reflectivity $R=0.98...0.99$ while for creating pulses of high energy E , reflectivity must be very virtually 1.

New artificial materials or charging of reflective layers with electrons at high potential could offer the necessary reflectivity. This is a very difficult problem of solid physics and much research work is needed for finding a solution.

9. THE FUTURE OF SOLAR GRAVITATIONAL SPACECRAFT

The solar gravitational spacecraft is an intermediate step towards building the electromagnetic-gravitational spacecraft. Looking at equation (8) one can see that if electromagnetic energy with high frequency is employed, the working electromagnetic energy E can be greatly reduced.

In ideal conditions (reflectivity coefficient of surfaces $R=1$), the gravitational power radiated by two parallel mirrors due to multiple reflection of two packets of electromagnetic waves having energy E each, when frequencies in the X, gamma rays or higher are used, is given in the table 2.

Table 2: Power of gravitational radiation produced through reflection of X and gamma rays

$E, \text{ kJ}$ $\nu, \text{ Hz}$	1 $\frac{dE}{dt}, \text{ kW}$	10^3 $\frac{dE}{dt}, \text{ kW}$	10^5 $\frac{dE}{dt}, \text{ kW}$	10^7 $\frac{dE}{dt}, \text{ kW}$	10^9 $\frac{dE}{dt}, \text{ kW}$	10^{11} $\frac{dE}{dt}, \text{ kW}$	10^{13} $\frac{dE}{dt}, \text{ kW}$
3×10^{15} (ultraviolet)	1.6×10^{-17}	1.6×10^{-11}	1.6×10^{-7}	1.6×10^{-3}	1.6×10^1	1.6×10^5	1.6×10^9
3×10^{16} (ultraviolet)	2.5×10^{-15}	2.5×10^{-9}	2.5×10^{-5}	2.5×10^{-1}	2.5×10^3	2.5×10^8	2.5×10^{11}
3×10^{17} (X-Ray)	2.5×10^{-13}	2.5×10^{-7}	2.5×10^{-3}	2.5×10^1	2.5×10^5	2.5×10^9	2.5×10^{13}
3×10^{18} (X-Ray)	2.5×10^{-11}	2.5×10^{-5}	2.5×10^{-1}	2.5×10^3	2.5×10^7	2.5×10^{11}	2.5×10^{15}
3×10^{20} (gamma ray)	2.5×10^{-7}	2.5×10^{-1}	2.5×10^3	2.5×10^7	2.5×10^{11}	2.5×10^{15}	2.5×10^{19}
3×10^{22} (gamma ray)	2.5×10^{-3}	2.5×10^3	2.5×10^7	2.5×10^{11}	2.5×10^{15}	2.5×10^{19}	2.5×10^{23}
3×10^{24} (very high ν)	2.5×10^1	2.5×10^7	2.5×10^9	2.5×10^{15}	2.5×10^{19}	2.5×10^{23}	2.5×10^{27}
3×10^{26} (very high ν)	2.5×10^5	2.5×10^{11}	2.5×10^{13}	2.5×10^{19}	2.5×10^{23}	2.5×10^{27}	2.5×10^{31}
3×10^{28} (very high ν)	1.25×10^9	1.25×10^{15}	1.25×10^{17}	1.25×10^{23}	1.25×10^{27}	1.25×10^{31}	1.25×10^{35}

Table 2 shows that the radiated gravitational power can have very high values if the frequency of electromagnetic waves is high even if E has smaller magnitude.

Only half of this power is used for propulsion because the rest is lost in space.

Again, the main problem is the reflectivity of mirrors.

Metallic mirrors can reflect only ultraviolet light but not X-rays, gamma rays and higher frequencies. Another problem is that a technology yielding X, gamma or higher frequency rays using solar light is imperative.

10. CONCLUSIONS

- The solar gravitational spacecraft uses gravitational attraction for propulsion instead of theorem of momentum conservation. For this reason, the solar gravitational spacecraft no longer uses propellant.
- The gravitational radiation is produced on board the solar gravitational spacecraft through multiple reflections of concentrated sun-light between two or more mirrors. This process is endorsed today by advanced physics journals.
- The main problem which must be solved for building solar gravitational spacecraft is increasing the reflectivity of mirrors up to virtually 1. For achieving this goal, much research work is necessary in the field of solid physics. The reflectivity of metallic mirrors can be increased developing special materials or by charging the mirror metal with electrons of at very high electric potentials.
- In the future, developing technology for producing of X, gamma or higher frequency rays using solar light must be accompanied with correspondent advancements for manufacturing high reflectivity mirrors for the respective rays.

REFERENCES

1. Sandu, C., Brasoveanu, D.; 2007; Sonic-Electromagnetic-Gravitational-Spacecraft, Part 1 – Principles, Proceedings of the AIAA SPACE 2007 Conference & Exposition, Long Beach, California, September 18-20, 2007, paper AIAA-2007-6203.
2. Sandu C., Brasoveanu D.; 2007; Sonic-Electromagnetic-Gravitational-Spacecraft, Part 2 – Law of Conversion of Electromagnetic Radiation into Gravitational Radiation, Proceedings of the AIAA SPACE 2007 Conference & Exposition, Long Beach, California, September 18-20, 2007, paper AIAA- 2007-6203.
3. Sandu C., Brasoveanu D.; 2007; Sonic-Electromagnetic-Gravitational-Spacecraft, Part 3 – Other Aspects of Energy Conversion and Natural Gravitational Fields, Proceedings of the AIAA SPACE 2007 Conference & Exposition, Long Beach, California, September 18-20, 2007, paper AIAA- 2007-6203.
4. Sandu C., Brasoveanu D.; 2007; Sonic-Electromagnetic-Gravitational-Spacecraft, Part 4 – Doppler Effects, Inertia and Mass Increase, Proceedings of the AIAA SPACE 2007 Conference & Exposition, Long Beach, California, September 18-20, 2007, paper AIAA-2007-6203.
5. Sandu C., Brasoveanu D.; 2007; Sonic-Electromagnetic-Gravitational-Spacecraft, Part 5 – Energy Conversion and Thrust Force, Proceedings of the AIAA SPACE 2007 Conference & Exposition, Long Beach, California, September 18-20, 2007, paper AIAA-2007-6203.
6. Sandu C., Brasoveanu D.; 2007; Sonic-Electromagnetic-Gravitational-Spacecraft, Part 6 – Land-Based Generators of Artificial Gravitation and SEGs Propelled by Counter-Gravitational Radiation, Proceedings of the AIAA SPACE 2007 Conference & Exposition, Long Beach, California, September 18-20, 2007, paper AIAA-2007-6203.
7. Sandu C., Brasoveanu D.; 2007; Sonic-Electromagnetic-Gravitational-Spacecraft, Part 7 – SEGs Design, Proceedings of the AIAA SPACE 2007 Conference & Exposition, Long Beach, California, September 18-20, 2007, paper AIAA-2007-6203.
8. Sandu C., Brasoveanu D.; 2007; Sonic-Electromagnetic-Gravitational-Spacecraft, Part 8 – Planetary and Interplanetary Ships, Gravitational Bulbs and Cannons, Proceedings of the AIAA SPACE 2007 Conference & Exposition, Long Beach, California, September 18-20, 2007, paper AIAA-2007-6203.
9. Sandu C., Brasoveanu D.; 2007; Sonic-Electromagnetic-Gravitational-Spacecraft, Part 9 – Technology of SEGs, Proceedings of the AIAA SPACE 2007 Conference & Exposition, Long Beach, California, September 18-20, 2007, paper AIAA-2007-6203.
10. Sandu C., Brasoveanu D.; 2007; Sonic-Electromagnetic-Gravitational-Spacecraft, Part 10 – Space Propulsion, Proceedings of the AIAA SPACE 2007 Conference & Exposition, Long Beach, California, September 18-20, 2007, paper AIAA-2007-6203.
11. Sandu, C., Brasoveanu, D.; 2017; On the Theoretical Possibility to Generate Gravitational Waves Using Electromagnetic Waves, Journal of Advances in Physics, , Volume 13 Number 2, page 4692, March 2017, ISSN2347-3487.
12. Sandu, C., Brasoveanu, D., Anghel, O., Voicu, R., Zavodnic, F.; 2015; Special Equipment Which Uses Concentrated Solar Light for Earth Protection against Asteroids-Advanced Design and Technology, CEAS 2015, 8–11 September, 2015, Delft, The Netherlands.

Aircraft Ground Operations: Steps Towards Automation

Diego Alonso Tabares

Airbus SAS

Senior Engineer

1 Rond-Point Maurice Bellonte, 31707, Blagnac, France

diego.alonso-tabares@airbus.com

Felix Mora-Camino

Laboratoire ENAC-Optim, ENAC

Professor

7 Avenue Edouard Belin, 31055, Toulouse, France

ABSTRACT

This paper introduces and analyses the state of the art of aircraft ground handling at airports. The main opportunities for automation of these activities are pointed out. This leads to identify different challenges to be overcome to build safe and efficient automated ground handling operations. Greatest opportunity for automation lies with automated docking of ground support equipment to aircraft in the short term, with further autonomous vehicles moving around the aircraft and automated systems within the aircraft later on. An autonomous fleet management formulation for automated vehicles is also presented.

KEYWORDS: *turnaround time, ground operations, ground handling, automation*

External Wireless System for Ultimate Flight Control in Contingency Situations

Filip NICULESCU,

*National Research and Development Institute for Gas Turbines COMOTI
Engineer*

*220 D Iuliu Maniu Bd., sector 6, cod 061126, OP 76, CP174, Bucharest, Romania
filip.niculescu@comoti.ro*

Andrei MITRU

*National Research and Development Institute for Gas Turbines COMOTI
Research engineer*

Constantin SANDU

*National Research and Development Institute for Gas Turbines COMOTI
PhD. engineer*

Constantin VÎLCU

*Research Phd. engineer
National Research and Development Institute for Gas Turbines COMOTI*

ABSTRACT

This paper presents an External Wireless System (EWS) which is completely independent from any other system of the aircraft including the power supply. The EWS is used when the electrical, mechanical and hydraulic control systems of the aircraft fail concomitantly and the pilots lose control of the aircraft completely or partially. A EWS unit consists of a solar cell, independent control surface, battery, electrical wires, and stepper geared motor with planetary gears. The battery is charged continuously by solar cells, and the stepper drives the control surface through the planetary gear. The control surfaces have a very slow motion due to the low available power. The role of EWS is only to stabilize the aircraft flight and to direct it to the closest tarmac or acceptable landing place. The EWS units are placed on aircraft wings and tail. All the EWS units are controlled by an independent control unit with the dimension of a mobile phone. Both the pilots dispose of such independent control units. In case of ultimate contingency situations, when the electrical power system, the mechanical, electrical and hydraulic control systems and engines of aircraft fail, the pilot activates the independent control unit (ICU) of the EWSs and directs the aircraft to the closest airport or to an appropriate field for emergency landing.

KEYWORDS: *Wireless System for Aircraft, Flight Control, Flight in Contingency Situations*

SPACE TECHNOLOGY FOR REDUCTION OF DESERT AREAS ON EARTH AND WEATHER CONTROL

Constantin Sandu^{1*}, Dan Brasoveanu², Valentin Silivestru¹, Bogdan Filipescu³, Radu Constantin Sandu⁴

¹COMOTI, Bucharest, Romania

²Systems Engineering Group Inc. (SEG), MD, USA

³Teletrans. Craiova, Romania

⁴S.C. Structural Management Solutions S.R.L., Bucharest, Romania

*Corresponding author: E-mail : constantin.sandu@comoti.ro

ABSTRACT

In precedent papers the authors presented the idea of a space system composed of two opposite parabolic mirrors (large and small) having the same focal point. This system is able to concentrate solar power in a strong light beam having irradiance of hundreds or thousands of times stronger than the solar irradiance on Earth's orbit. The system can be placed on a Sun synchronous orbit around the Earth or on the Earth's orbit around the Sun at a distance of several hundred km from ground.

When the concentrated light beam is directed toward the Earth surface it can locally melt, vaporize or decomposes tones of ground in its elements. This is happening because when the ground is hit by the light beam, ground temperature can reach thousands of degrees Celsius. At such temperatures the matter is decomposed into constitutive elements. For example, the silicate oxides which are frequently found in the composition of desert ground are decomposed into oxygen and silicon. Similarly, other oxides release oxygen and other type of oxides or constitutive elements.

A network of deep and large channels can be dug in this way in hot deserts as Sahara. When these channels are connected with the seas & oceans, a network of water channels is created in those deserts. In this way, the local climate of deserts will change because channel water is vaporized during daytime when air temperature reaches 50°C and condenses during nighttime when air temperature is around 0°C. Presence of clouds over the hot deserts can lead to a reduction of ground temperature and rain follows. The channel water can be desalinized for producing drinking water and for irrigation using simple equipment.

In addition to these advantages, channel deserts can be a solution for melting of polar ice calottes and flooding of seaside areas that are inhabited areas

On the other hand, the system composed of two opposite mirrors can be used for strength decreasing or deviation of hurricanes and tornados. The power of these meteorological phenomena increased in the last time due to global warming producing disasters of tens of billions of dollars. The hurricane is a thermal engine working in Carnot cycle. Due to this fact, although the difference between the cold source temperature (temperature of high atmosphere) and hot source temperature (temperature of ocean surface) is of only 100 °C, the thermal efficiency is $\eta_t=0.333$ leading to increasing of hurricane's total energy at extremely high levels. The cold source can be heated through vaporizing the system of clouds of hurricane formed in the high atmosphere by the concentrated light beam directed from space. In this way the energy of hurricane or tornado no longer increases and damages produced at ground level are limited. Another possibility is to vaporize locally the hurricane's eye-wall for its deviation far away of dense populated areas.

KEYWORDS: weather control, desert climate change, hurricanes' and tornados' deviation

An Object-Oriented Approach to a Scenario-Based System Dynamics Fleet Model

Gilbert Tay

*Technical University of Munich
Research Associate, Institute of Aircraft Design
85748 Garching, Germany
Gilbert.Tay@tum.de*

Raoul L. Rothfeld

*Bauhaus Luftfahrt e.V.
Research Associate, Economics and Transportation
82024 Taufkirchen, Germany*

ABSTRACT

Expanding the current capabilities of a scenario-based system dynamics fleet model is paramount in order to incorporate wider ranging boundary conditions for the assessment of the impact of future aircraft technologies at a global aircraft fleet level. These expanded capabilities are necessary in order to better assess the impact of novel aircraft technologies and ambitious environmental policies in order to mitigate the environmental impact of the civil air transport industry. However, this further expansion of capabilities would not be possible without a paradigm shift in the way the current fleet model is implemented, as the increased complexity would make the fleet modeling an extremely inefficient and daunting task. An object-oriented approach to address the current limitations of the current system dynamics fleet model as well as the incorporation of future expanded capabilities of the new fleet model are presented.

KEYWORDS: *system dynamics, global fleet, aircraft fleet modeling, object-oriented*

Considerations of direct solar thermal power generation systems for space propulsion

Alexandru Onea

*Karlsruhe Institute of Technology, Hermann-von-Helmholtz-Platz-1, Eggenstein-Leopodshafen,
Germany, alexandru.onea@kit.edu*

Nerea Diez de los Rios Ramos

Karlsruhe Institute of Technology

Wolfgang Hering

Karlsruhe Institute of Technology

Robert Stieglitz

Karlsruhe Institute of Technology

ABSTRACT

Recently, a concentrating solar power system coupled to AMTEC (Alkali Metal Thermal-to-Energy Converter) units [1] has been proposed as alternative to the NASA solar electric propulsion (SEP) system, which is based on PV (photovoltaic) technology. The main advantages are related to the significant lower mass, size at launch, and robust construction. Such aspects recommend this concept as a viable solution to the PV based power systems for missions in low Earth orbit (LEO) and low medium Earth orbits (MEO), such as the proposed space tug. The present paper discusses the adaptation to space environment and the possibilities for the reduction of the radiation heat losses in the unit.

KEYWORDS: *AMTEC, space propulsion, CSP, heat losses, radiation*

ANALYSIS OF AIRCRAFT ROLLING OVER POTHoles AND RUTS

Jose E. Gómez Viñas

*Airbus Defence & Space / TEAYY Landing Gear Domain
John Lennon s/n, 28906 Getafe (Madrid) Spain
jose-esteban.gomez-vinas@airbus.com*

Jose M. Chorro Martínez

Airbus Defence & Space / TEAYY Landing Gear and Ground Loads Domain

Angel Martínez Pérez

Airbus Defence & Space / TEAYY Landing Gear and Ground Loads Domain

Silvia Parra Adan

Airbus Defence & Space / TAECD Aeroelasticity and Structural dynamics Domain

Alvaro Ros Contreras

ALTRAN engineering / Landing Gear and Ground Loads Domain

KEYWORDS: Dynamic Loads, Rut, Pothole, Landing Gear, Flight Test, A400M.

NOMENCLATURE:

CBR California Bearing ratio
EBH Equivalent Bump Height
FWD Forward
MID Middle
AFT Rear
SC Servicing Class

A/C Aircraft
MLG Main landing Gear
NLG Nose Landing Gear
MTW Maximum Take Off Weight
MLW Maximum Landing Weight

ABSTRACT

The aircraft A400M has the capability to operate on unpaved runways. As part of the demonstration of this feature, it is necessary to make analysis of the aircraft rolling over runway profiles that could contain potholes and ruts. The A400M aircraft has a non-conventional landing gear in which the main landing gear (LH and RH) consists of three independent articulated-type struts positioned along the aircraft longitudinal axis. As the legs are positioned along the aircraft in the longitudinal axis, during the rolling over potholes and ruts the vertical load distribution between the three legs is changing during the rolling over the potholes and ruts. The complexity of the landing gear is increased as all the struts have a twin wheel arrangement, fitted to the main fitting by a trailing arm assembly.

The analysis of these features is required by two reasons: aircraft safety and operator costs. Aircraft safety is affected because in the case that the ultimate loads of the landing gears are exceeded a collapsing of the landing gears will occur with the consequent loss of the aircraft controllability on ground. In this case a runaway could occur at aircraft high speeds with hazardous or catastrophic consequences. If this operation is only permitted at low speeds without safety impact, damages incurred on the aircraft imply maintenance and repair costs for the operator.

Regulations of civil aircrafts include discrete load conditions (CS25.491 and FAR25.491) that cover the analysis of potholes and ruts. In the case of civil runways exists an inspector that should know the dimensions of the runway and taxiway safety areas at the airport. At airports certificated under Part 139, the dimensions of the safety areas should be documented in the airport certification manual. During the safety area inspection, the inspector should determine if there are any hazardous ruts or a pothole. The airport is responsible for establishing a schedule for regular and routine pavement inspections to ensure all areas are thoroughly inspected.



In the case of military aircrafts operating in unpaved runways, two options could be followed: to define the limitations of the aircraft in terms of pothole and rut size or to comply with the requirements defined in a specific aerodrome regulation. In the first option is needed to define which are the maximum size of the ruts and potholes the airplane can transverse. In the second option, the airplane is designed for crossing the potholes and ruts defined in the aerodrome manual. In both cases, the inspection of the runways has the capability to decide whether the pothole or the rut should be repaired after the measurements of the dimensions.

For the A400M aircraft, it has been followed the first option, i.e. definition of the potholes and rut sizes that the aircraft can cross. This information is included in aircraft characteristics for airport planning manual (ACAP) so the aerodrome director can use it to introduce the runway repairs when needed. It is interesting the methodology followed in the A400M because allows defining in a simple manner the aircraft operation over potholes and ruts. First at all, an aircraft model has been built capable to calculate the landing gear loads during the potholes and ruts crossing. Taking into account the results of the model, it has been generated a list of flight test cases necessary for the model validation. Once the model has been validated with a set of flight test cases, it is possible to define the aircraft limitations for any of the aircraft operating conditions.

The flight tests were performed with different aircraft configuration in order to capture the effects of different aircraft parameters: aircraft weight, centre of gravity position, aircraft longitudinal speed, braking and thrust.

TECHNOLOGY FOR TERRAFORMATION OF MARS, OTHER PLANETS AND NATURAL SATELLITES

Constantin Sandu^{1*}, Dan Brasoveanu², Valentin Silivestru¹, Bogdan Filipescu³, Radu Constantin Sandu⁴

¹COMOTI, Bucharest, Romania

²Systems Engineering Group Inc. (SEG), MD, USA

³Teletrans. Craiova, Romania

⁴S.C. Structural Management Solutions S.R.L., Bucharest, Romania

*Corresponding author: E-mail : constantin.sandu@comoti.ro

ABSTRACT

This paper presents principles and technologies for terraformation of Mars, other planets and natural satellites. It is certain that our civilization must expand within the solar system. Mars is the closest planet to Earth. However, in the future our civilization will probably colonize other planets and also natural satellites of other planets.

In the case of Mars, a lot of energy and labor will be required because this planet lacks a sufficiently dense atmosphere and is much colder than Earth. The new technology presented in this paper makes easier the terra-formation of this planet, by creating an Earth-like atmosphere and heating inhabited areas of planet with additional solar light.

A space system composed of two opposite parabolic mirrors (large and small) having a common focal point can be used for creating a respirable atmosphere on planet. The concentrated light beam generated by this system can be thousands of times more intense than sun light.

The system can be placed either on a Sun synchronous orbit around Mars (being oriented continuously with the large parabolic mirror to the Sun) or on Mars's orbit around the Sun (in this case the system follows the planet at a small distance). When the concentrated light beam is directed to the Martian ground, the local soil temperature reaches thousands of degrees Celsius and the matter melts vaporizes or separates in constitutive elements.

KEY WORDS: Mars terraformation, natural satellites terraformation

NOMENCLATURE

E_{Es} , average irradiance at earth's surface, [W/m²]

E_M , irradiance in proximity of Mars, [W/m²]

P, power, [W]

r, radius, [m]

R, reflectivity, dimensionless

1. INTRODUCTION

In our days, our civilization has begun the expansion into the solar system. The first target is Mars. After Mars, expansion will continue to other planets and natural satellites.

The first Martian colonies will be housed in shelters with controlled atmosphere and protection against radiations and green houses for plant cultivation.

The second stage is terraformation, i.e. transformation of Mars into an Earth like planet. This option requires the creation of a dense Martian atmosphere, generation of an artificial magnetic field for protection against radiations and heating of large areas of planet's surface.

The next chapters of this paper present an affordable technology which can be applied at planetary scale for terraformation of planet Mars and other planets and natural satellites from our solar system.

2. DESIGN OF SPACE SYSTEM-INSTRUMENT OF TERFORMATION

In a precedent paper, the authors presented the idea of a space system used for protecting Earth against asteroids. [1] That space system can be used as an instrument for terraformation of Mars, other planets and natural satellites, too.

For a better understanding of this terraformation method, the main components of space system are presented in fig. 1. The system is composed of two parabolic mirrors (large and small) placed face to face, having a common focal point, F and coincident axis.

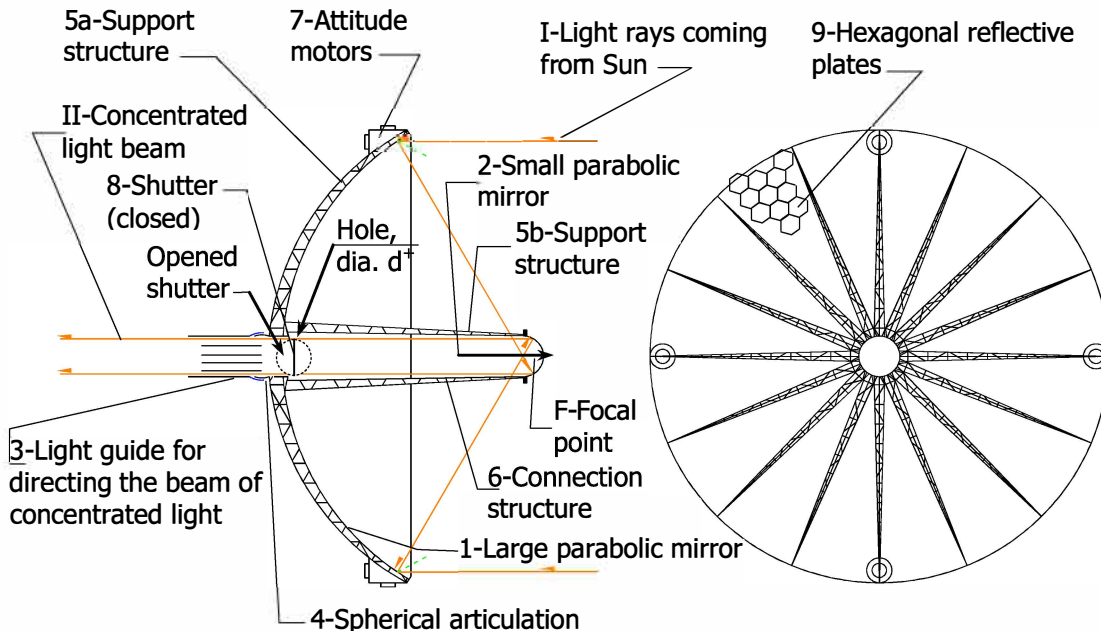


Figure 1: Design features of space system

The components of system and their roles are:

- 1-the large parabolic mirror-collects solar light
- 2-the small parabolic mirror concentrates the light rays in a beam passing through the hole having dia. d^+ placed in the large parabolic mirror
- 3- Light guide - directs the beam of concentrated light-it has a honeycomb reflective structure being articulated onto the large parabolic mirror with spherical articulation 4
- 4- Spherical articulation-permits targeting the light guide and concentrated light beam toward a point on Mars's surface
- 5a-Support structure-it is the support structure of the large parabolic mirror
- 5b-Support structure-it is the support structure of the small parabolic mirror
- 6-Connection structure-connects the two parabolic mirrors
- 7-Attitude motors-control the system attitude
- 8-Shutter-opens or closes the concentrated light beam access to the light guide
- 9-Hexagonal reflective plates-form the large parabolic mirror being placed on support structure 5a and 5b

The large and small parabolic mirrors are made of thin reflective plates which are manufactured from composite material (graphite fiber or graphene basis) and covered with a 5 microns gold film. The gold film confers a good reflectivity of solar light and graphite fiber allows quick transmission of heat through conductivity and cooling of mirrors through radiation. The reflective plates 9 are placed on support structure 5a and 5b. When the diameter of small parabolic mirror is under 5m, this mirror can be made as a single piece.

The system works as follows:

The large parabolic mirror is oriented with the concave surface to the Sun. The light rays I (kept parallel to each other with high accuracy) coming from Sun (visible, infrared and ultraviolet light) are captured and concentrated by the large parabolic mirror in its focal point, F . The light rays are then reflected by the small parabolic mirror as parallel rays directed along the common axis of both mirrors (this is possible because the parabolic mirrors have the same focal point, F , and coincident axis). If the shutter is opened, the concentrated light beam passes through the hole ' d^+ ' placed in the center

of large parabolic mirror. If the shutter is closed, the concentrated light beam is reflected back to the small parabolic mirror, then to the large parabolic mirror and finally to the Sun. In this situation the system is shut off.

When the shutter is opened, the concentrated light beam enters the light guide tube made of fine reflective honeycomb cells. Being articulated by the large parabolic mirror with a spherical articulation, the light guide can direct the concentrated light beam to the planet's surface. When the light guide and reflective honeycomb have a pyramidal shape, the light beam can be concentrated onto a very small area on planet's surface where temperature can reach very high values, theoretically infinite when the area of impact on surface is reduced to a point.

The system can be built on an orbit around Earth. Transportation of system's components in space can be assured by rockets as presented in fig.2. Robots can assemble the system on orbit (like NASA's Spiderfab) - fig.3. Building such a large structure in space is possible because the gravitational force of Earth is balanced by the inertia force generated by rotation on geocentric orbit. After building the system on geocentric orbit, it can be accelerated by busters for placement on the Mars's orbit around Sun.

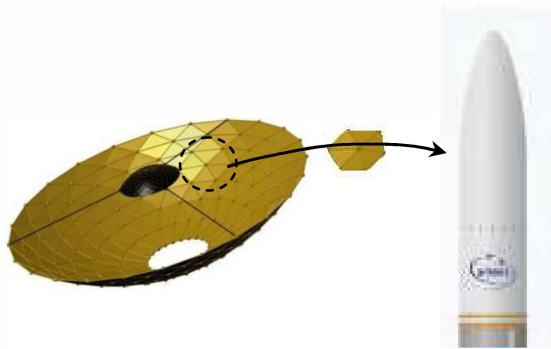


Figure 2: Transportation of system in space

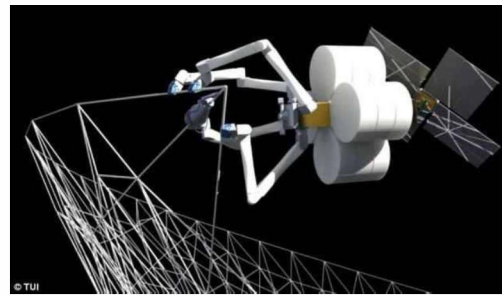


Figure 3: NASA's Spiderfab robot

3. THE POWER OF SPACE SYSTEM

The maximum power of such a system depends on solar power collected by the large parabolic mirror. Table 1 presents the total collected solar power, P_{lpm} , and the total available power, P_e as a function of the radius of large parabolic mirror, r_{lpm} .

[Notes: The average solar irradiance on orbit of Mars was considered $E_M = 590 \text{ Wm}^{-2}$ (which is about 44% of irradiance on an orbit around Earth); the average reflectivity coefficient of gold plated mirrors was considered $R=0.98$]

Table 1-Power of system function of radius of large parabolic mirror

Case no.	Radius of large parabolic mirror, r_{lpm} [m]	Collected solar power, P_{lpm} [MW] (irradiance was taken $E_M=590 \text{ W/m}^2$)	Available power P_e [MW] (Reflectivity coefficient was taken $R=0.98$ for gold)
1	50	4.6	4.5
2	60	6.7	6.5
3	70	9.1	8.9
4	80	11.8	11.6
5	90	15.01	14.7
6	100	18.5	18.2
7	200	74.1	72.7
8	400	296.6	290.6
9	500	1068.14	1025.8

4. The chemical composition of Mars

Mars's color is red because Martian surface is a thick layer of oxidized iron dust and rocks of the same color. [2] Practically most of Mars's surface is covered by this dusty layer. Elementary sodium, potassium, chloride and magnesium can also be soil components.

Under the layer of dust, there is a crust (about 50 km thick) composed of volcanic basalt rock. Composition of basalt is 45...55% SiO₂, 17...22% MgO, approx 14% Al₂O₃, 5–14 % FeO, approx. 10% CaO, other oxides and elements.

This crust is a single piece, i.e. not formed from tectonic plates like Earth's crust.

Under the crust there is an inactive mantle having consistency of a hot paste and probably made mainly of silicon, oxygen, iron, and magnesium. The thickness of this mantle is probably of 5,400 to 7,200 km.

Under the mantle, Mars probably has a solid core with an estimated diameter of 3000...4000km made of sulfur, iron and nickel.

Due to the fact that the core is not moving, Mars has no magnetic field. For this reason, Mars surface is not protected from radiations as Earth surface.

On Mars, water exists as ice inside soil and at poles because Mars is colder than Earth. The average temperature ranges between minus 125 °C near poles during winter up to 20 °C near the equator.

4. CREATING A THICKER ATMOSPHERE ON MARS

The present Mars atmosphere is very thin and has the following composition: [3]

Carbon dioxide (CO₂) - 95.32%

Nitrogen (N₂) - 2.7%

Argon (Ar) - 1.6%

Oxygen (O₂) - 0.13%

Carbon Monoxide (CO) - 0.08% and other minor components (Ne, NO, H₂O, Xe).

The goal is to make Martian atmosphere thicker and enriched in oxygen and nitrogen.

When the concentrated light beam is targeted on Mars surface (fig.4), very high temperatures are reached. If the honeycomb cells of light guide have a pyramidal shape, the whole energy can be focused onto a very small area or even point-like in which case the local temperature can be theoretically infinite.

At very high temperature, the FeO which forms the dusty layer of Mars surface and the other oxides which are found in basaltic crust composition (SiO₂, MgO, Al₂O₃, CaO) can be separated into elements or in other oxides. Finally, all the oxides are decomposed into oxygen and other elements.

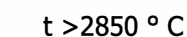
When the concentrated light beam targets the layer of dust, first the FeO is decomposed at temperature $t=575\text{ }^{\circ}\text{C}$ according to equation (1):



The oxide Fe₃O₄ is called 'magnetite'. It was demonstrated that at the temperature of melting point (1597 °C) + 300 °C, the magnetite is decomposed in Fe and oxygen. [4,5] Iron atoms, being heavier than atoms of oxygen remain on the planet surface. The oxygen atoms recombine in O₂ molecules enriching Martian atmosphere with oxygen.

After the decomposition of FeO from the dust layer, the concentrated light beam begins to decompose the crust magnetite located under the dust layer.

Most of oxides composing magnetite are extremely heat resistant and decompose at very high temperatures:





These temperatures are easily obtained in the point where the concentrated light beam impacts the crust. This is the simplest technology for generating oxygen for Martian atmosphere. For developing Earth-like atmosphere nitrogen is necessary because the current concentration of this gas in Mars atmosphere is only 2.7%. This element is essential for life. Evidence of indigenous nitrogen was found in sediments and Aeolian deposits on Mars. [6] It is possible to release nitrogen captured in those sediments and Aeolian deposits heating them with the presented space system.

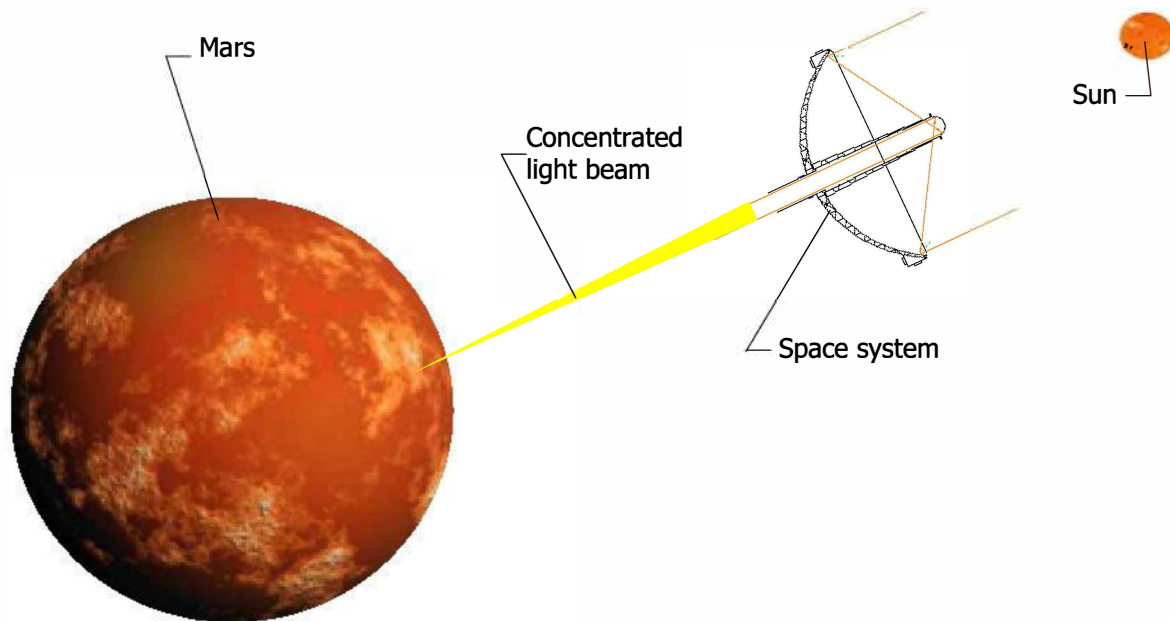


Figure 4: Generating of Mars's atmosphere

5. LOCAL HEATING OF MARS SURFACE

Mars is a cold planet. Using more space systems placed on the orbit of Mars around Sun, heated zones can be created in the equatorial area of planet (fig.5). This time the honeycomb cells of light guide are slightly divergent conditioning the local irradiance on Mars's surface to be equal to the average irradiance on Earth's surface ($E_{Es}=1000 \text{ W/m}^2$). In this way, local temperature in zones where intense human activities occur can be increased to an appropriate value which is close to the average temperature of Earth's surface.

6. CREATING AN ARTIFICIAL MAGNETIC FIELD ON MARS FOR PROTECTION AGAINST RADIATIONS

Mars does not have a magnetic field like Earth because its core is solid and does not rotate. For this reason the planet's surface is not protected against radiations like terrestrial surface. In the case of Earth, radiations like solar wind-high speed particles generated by Sun are kept away by the magnetic field of Earth. [7]

The magnitude of magnetic field of Earth created by the rotating iron core of Earth has the intensity of 25 to 65 microteslas (0.25 to 0.65 Gauss). [8]

The magnetic field of Earth is equivalent with an inverted magnetic dipole as shown presented in fig.7.

It is impossible to manufacture a single and strong dipole penetrating the entire planet Mars. However, as it was shown in equation (1), magnetite (Fe_3O_4) can be easily created through decomposition at low temperature (575°C) of FeO which is present in the dust layer existent on Mars's surface.

The magnetite can be easily magnetized in a strong magnetic field created by an electromagnet being transformed into a 'Lodestone' like magnet.

Such natural magnets can be created and incorporated in high quantities in Mars's ground for creating magnetic fields over populated areas. The south poles of magnets must be placed normal to the rotation axis of planet in equatorial area and oriented to the exterior (fig.8).

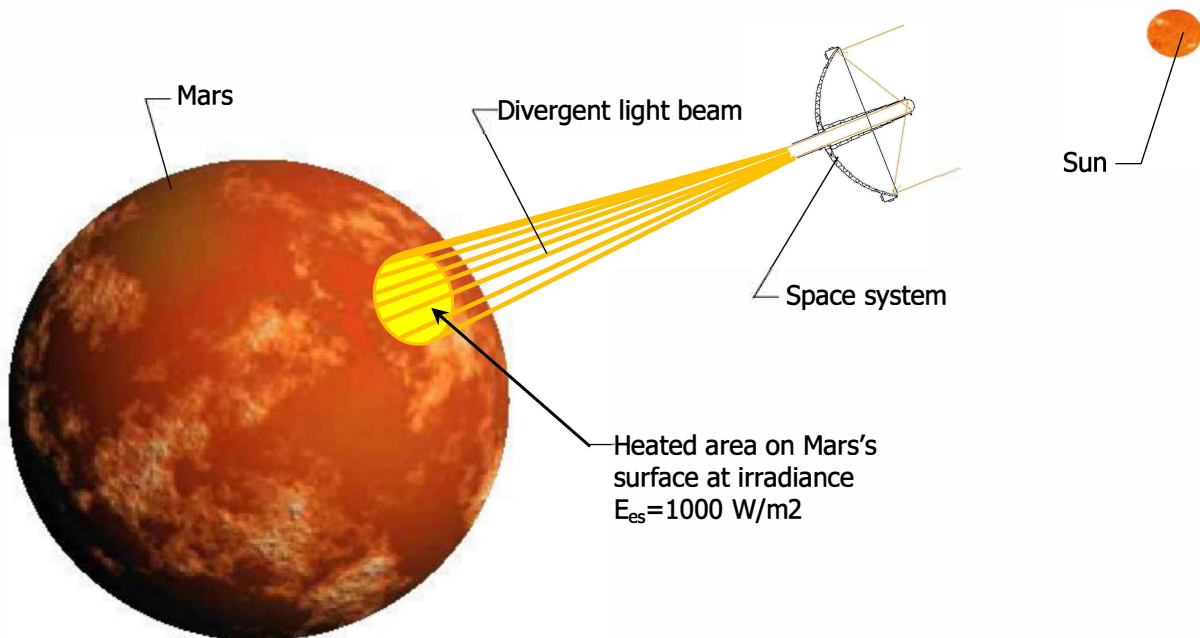


Figure 5: Additional heating of surface areas on Mars

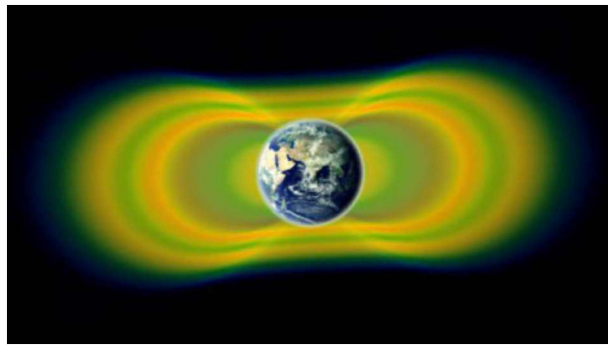


Figure 6: Van Allen Belts

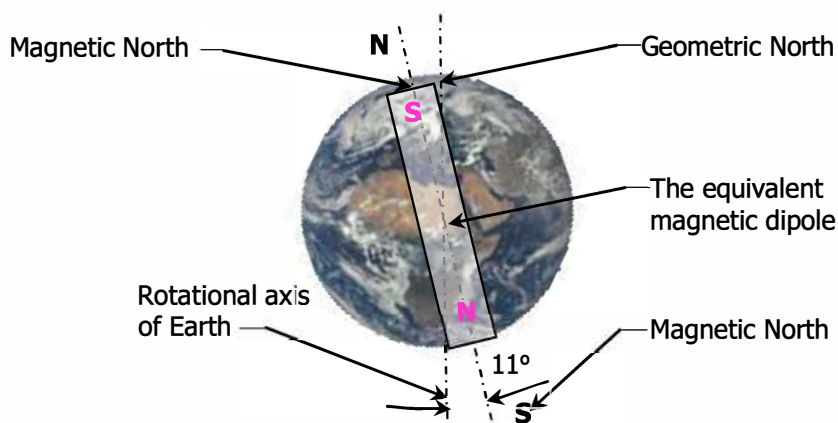


Figure 7: Positioning of equivalent magnetic dipole for Earth

In order to create a strong magnetic field, the individual magnets must be stacked in large pillars which are buried in the ground. This is necessary because the permanent 'Lodestone' like magnets create a magnetic field spanning a smaller region than the magnetic field of Earth and the most populated areas should be placed in the equatorial region of Mars.

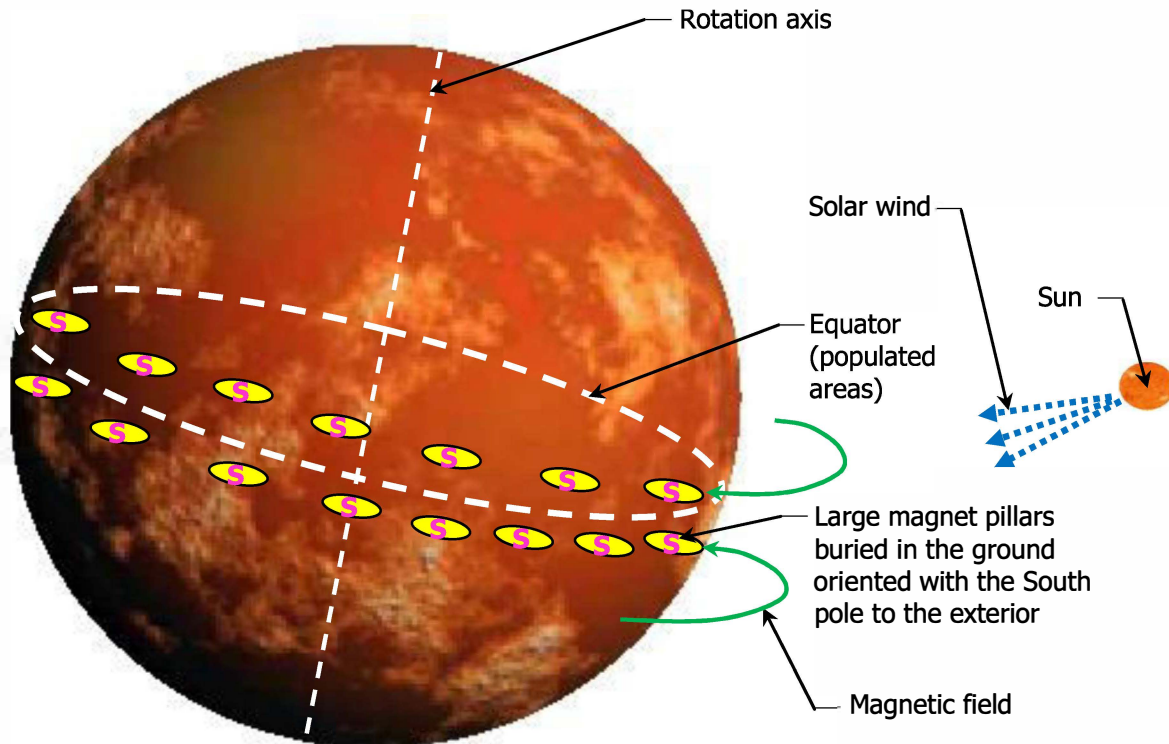


Figure 8: Generating of magnetic field of Mars

7. Terraformation of Venus. Mercury and other natural satellites found in the solar system

Environmental conditions on Venus are extremely hostile. Venus's atmosphere is composed mostly of carbon dioxide with floating clouds of sulphuric acid and sulphur dioxide.

Surface conditions on Venus's surface are difficult: temperature is around 450 °C at equator and atmospheric pressure is about 90 bars at ground level. Water in any form is absent.

In addition, unexpectedly, the magnetic field of Venus is just 0.000015 times Earth's field. [9]

For this reason, terraformation of Venus must be a long term goal which could take hundreds of years.

The first hope is given by carbon dioxide, sulphuric acid and sulphur dioxide eating bacteria. These bacteria must be artificially grown to resist conditions on Venus surface. Consumption of carbon dioxide atmosphere will lead to decreasing pressure at planet surface and to the reduction of temperature due to the dampening of a green house effect. Only after that a suitable atmosphere could be created using the space system presented in this paper.

Terraformation of Mercury is a difficult process, too, due to the vicinity of Sun. For this planet and some natural satellites including the moon, Europa of Jupiter and Enceladus of Saturn terraformation of underground space should be considered. This location must be considered for protection against radiations, heat or cold. In these cases, large spaces should be created underground using controlled atomic explosions. The spaces should be illuminated by artificial light. Circuits of water and air should also be created.

6. CONCLUSIONS

- The space system composed of two parabolic mirrors placed face to face and having a common focal point can be used for generating atmosphere on Mars and local heating its surface.
- Oxygen can be produced through the decomposition of oxides from the dust layer and crust. Nitrogen can be produced through separation of this gas from existing sediments and Aeolian deposits.
- Large quantities of magnetite (Fe_3O_4) obtained through heating of FeO at 575 °C melted in regular pieces which can be magnetized for creating permanent magnets. Large pillars buried under ground composed of multiple magnets oriented with the South poles to the exterior of planet along the equator create an equatorial protection against radiation (solar wind particles).
- The first stage of Venus terraformation is the use of artificial bacteria which can tolerate up to 90 bar and 450 °C (conditions at planet's surface) and consume CO_2 , sulphuric acid and sulphur dioxide and reduce pressure and temperature by dampening the green house effect.
- Terraformation of Mercury and other natural satellites as Moon, Europa and Enceladus must be limited to the creation of large underground spaces using atomic explosions.

REFERENCES

1. Sandu, C., Brasoveanu, D., Anghel, O., Voicu, R., Zavodnic, F.; 2015; Special Equipment Which Uses Concentrated Solar Light for Earth Protection against Asteroids-Advanced Design and Technology, CEAS 2015, paper no. 132, Delft, The Netherlands
2. Sharp, T., Space.Com., <https://www.space.com/16895-what-is-mars-made-of.html>
3. <https://nssdc.gsfc.nasa.gov/planetary/factsheet/marsfact.html>
4. Darkhn, L.S.; 1949; Melting Point of Magnetite-Silica Mixtures in Air, J. Am. Chem. Soc., 1949, 71 (3), pp 1114–1114, March 1949
5. Sibieude, F, Ducarroir, M., Tofighi, Ambriz, J.; 1982; High temperature experiments with a solar furnace: The decomposition of Fe_3O_4 , Mn_3O_4 , CdO , International Journal of Hydrogen Energy, December 1982
6. Stern, J.C., et.al.; 2015; Evidence for indigenous nitrogen in sedimentary and aeolian deposits from the Curiosity Rover Investigations at Gale Crater, Mars, Proceedings of the National Academy of Sciences, 2015
7. https://www.nasa.gov/mission_pages/sunearth/news/gallery/ScienceCover.html
8. Finlay, C. C. and al.; 2010; International Geomagnetic Reference Field: the eleventh generation, Geophysical Journal International, the 1-st of December 2010, 183 (3):1216–1230
9. <https://image.gsfc.nasa.gov/poetry/venus/V3.html>

PASSENGER SPACEPLANES AND AIRPLANES THAT HAVE VARIABLE CONFIGURATION FOR SONIC BOOM REDUCTION

Constantin Sandu^{1}, Dan Brasoveanu², Valentin Silivestru¹, Bogdan Filipescu³, Radu Constantin Sandu⁴*

¹*COMOTI, Bucharest, Romania*

²*Systems Engineering Group Inc. (SEG), MD, USA*

³*Teletrans. Craiova, Romania*

⁴*S.C. Structural Management Solutions S.R.L., Bucharest, Romania*

^{*}*Corresponding author: E-mail : constantin.sandu@comoti.ro*

ABSTRACT

In the last time, the interest for passenger space plane, supersonic passenger aircraft and supersonic business jets is increasing. For reducing sonic boom effects at ground level, some companies proposed airplanes having fuselage with small traversal section or having curved fuselage.

This paper presents a new practical method for exciting vibrations in the leading edge of wing, tail and airplane's nose surfaces in order to scatter the shock wave and to reduce the sonic boom impact at ground level.

The leading edges of wing, tail and airplane nose are covered with thin elastic fairings made of carbon fibre composite material which are separated through small gaps by the adjacent surfaces of wing, tail and nose. When the aircraft flies over populated areas, compressed air bleed from the engine compressors excites the vibration of carbon fibre fairings. The air is released through calibrated nozzles and directly impinges on the fairing surface generating their vibration. Thus, the shock waves are scattered and the impact of sonic boom on ground is much reduced.

KEYWORDS: sonic boom mitigation, shock wave scattering, boomless aircraft

A NEW DESIGN OF SPACE EQUIPMENT FOR RAPID DISINTEGRATION IN ATMOSPHERE AFTER REENTRY

Constantin Sandu^{1}, Dan Brasoveanu², Valentin Silvestru¹, Bogdan Filipescu³, Radu Constantin Sandu⁴*

¹*COMOTI, Bucharest, Romania*

²*Systems Engineering Group Inc. (SEG), MD, USA*

³*Teletrans. Craiova, Romania*

⁴*S.C. Structural Management Solutions S.R.L., Bucharest, Romania*

**Corresponding author: E-mail : constantin.sandu@comoti.ro*

ABSTRACT

The present intensification of space activities generated an important problem: Disintegration of space debris after re-entry into Earth's atmosphere. After the end of operational life, satellites re-enter the Earth atmosphere and are disintegrated by the high temperature produced by friction with air. Final rocket stages become space debris after exhausting the propellant and are also disintegrated into air. On average, one piece of space debris enters the Earth atmosphere every day. In many cases, some solid pieces of space debris having a considerable mass were found on the ground. Complete disintegration of space debris into the atmosphere is absolutely necessary in order to prevent accidents caused by impacts on populated areas.

This paper proposes a new design for a rapid disintegration of space equipment after re-entry. During re-entry the configuration of space equipment is changing through opening of some articulated doors for reaching of high stagnation temperature of air captured inside followed by a rapid disintegration in air.

KEYWORDS: fast space debris disintegration, debris re-entry, increasing of disintegration speed of space debris

1. INTRODUCTION

Today, the growth of space activities is exponential. This growth generated an important problem: The need for rapid disintegration of space debris after re-entry in Earth's atmosphere. Space debris is non functional manmade objects or fragments of such objects. Only 6% of catalogued objects are functional, the rest of them are space debris. [1] At the end of operational life, satellites re-enter the Earth's atmosphere being disintegrated through burning initiated by the friction with air. This is happening for final rocket stages which become space debris after consuming of propellant. In many cases the space debris fallen on ground had large dimensions (helium tank, thrust chamber, propellant tank, pressure sphere). [2]

It is known that the lifetime on orbit of a manmade object can be very long. For example, satellites of the SPOT family which are placed on a Sun-synchronous orbit can orbit about 200 years at 822 km altitude representing a high risk for other satellites. [3] Although regulations were issued for direct deorbiting of satellites after finishing of operational life these regulations do not solve the need of rapid burning of satellite in atmosphere being possible as fragments to fall on ground. [4]. A proposal for solving this problem was issued by ESA through the so called 'design for demise' [5]. According to this concept, design of a space system must take into account the on-ground safety requirements. The design for demise proposes separation of satellite in components due to the centrifugal forces produced during re-entry. This concept does not respond to the need of rapid burning of satellite in atmosphere for reduction of possibility as large fragments to reach the ground.

In this paper, the authors propose a new design for rapid disintegration of space debris after re-entry. This new design is inspired by the cause leading to the disintegration of Space Shuttle Columbia, which occurred on the 1st of February, 2003 [6]. Columbia disintegrated over Texas and Louisiana when it re-entered the Earth atmosphere. During launch, a piece of foam insulation struck the left wing of the orbiter deteriorating its ablative protection. [6]. When the space shuttle re-entered the Earth atmosphere, this damage allowed hot air to penetrate into the wing creating an irregular hole. In this way, air entered the left wing with high speed, became very hot when stagnating and destroyed the internal structure of wing.

2. THE DISASTER OF SPACE SHUTTLE COLUMBIA AND LESSONS LEARNT

During re-entry, shock waves produced by hypersonic velocities and the frictional effect of the atmosphere began to heat the surface of Columbia space shuttle [7]. The temperatures varied depending on location: The orbiter's nose and leading edges of the wings experiencing temperatures greater than 1,538°C [7].

At this phase, the breach created during launching in the ablative protection of the left wing allowed to hot gases to penetrate the wing and to advance in same direction inside the wing and to the mid of fuselage (Fig.1). [7] This caused significant damages. This phase can be named 'phase I' from 'Initialization'.

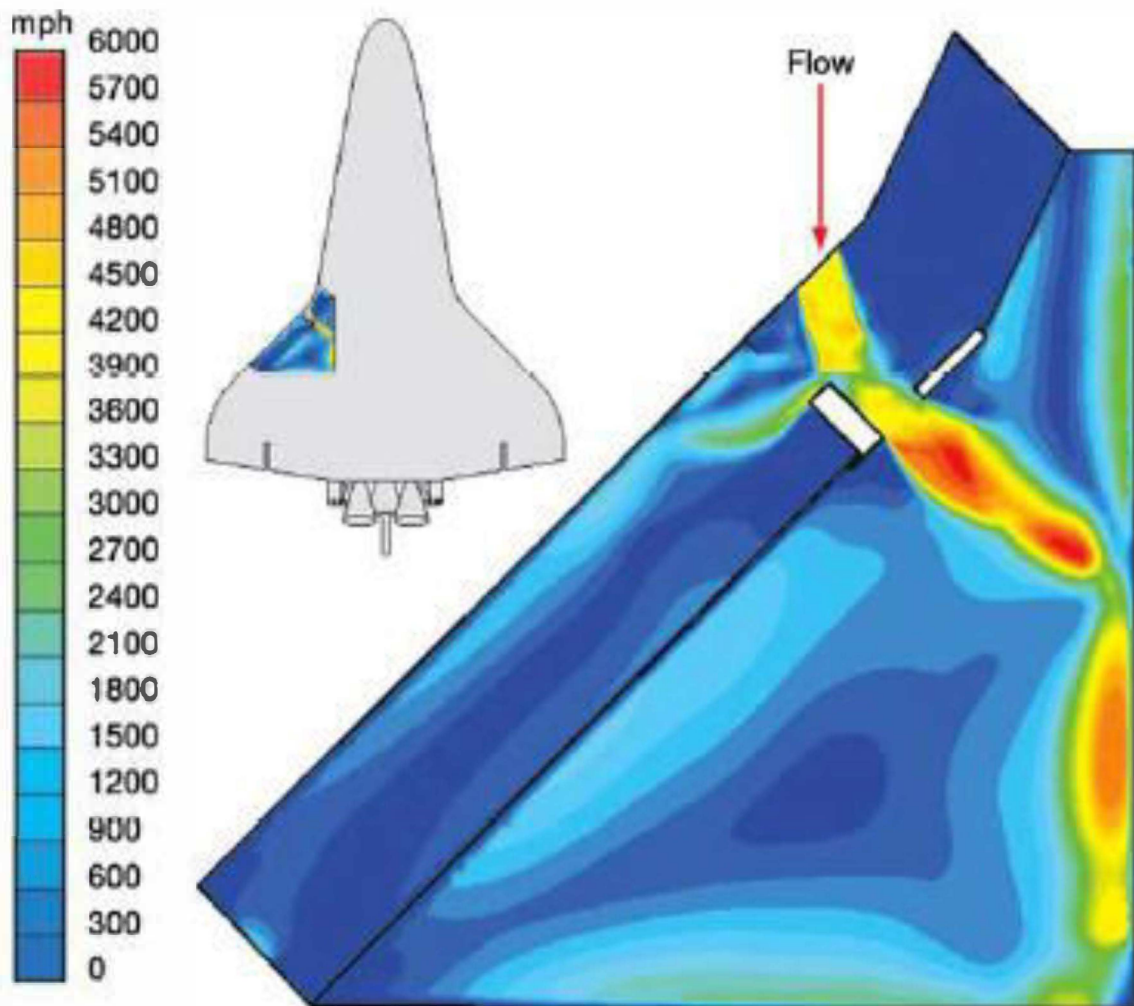


Figure 1: Temperature of left wing at the beginning of disaster (phase I) [7]

During this phase the wing lost its aerodynamic characteristics and the initiation of destruction process was extremely short, lasting from 13:59:37.5 GMT to 13:59:39.7 GMT (2.2 s)-Fig.2 [7].

After phase I, the process was accelerated as it is shown in Fig.3. [7] This phase can be named 'phase A' from 'Acceleration'. In the case of Columbia this phase lasted 0.07 s.

The destruction process continued with total dispersal of space vehicle and burning in atmosphere (Fig.4). This phase can be named 'phase D' from 'Dispersal'. In the case of Columbia this process lasted 55 s.

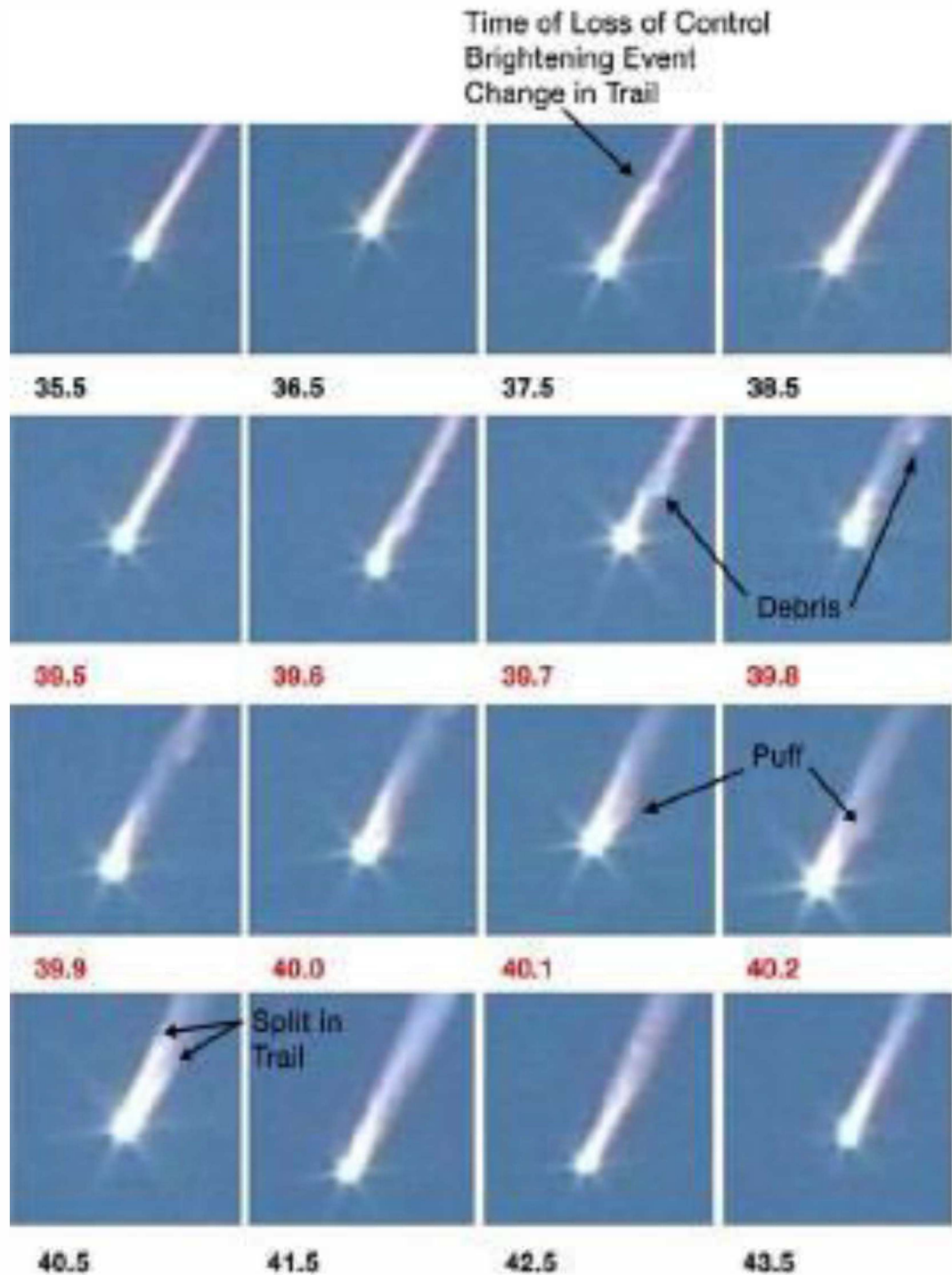


Figure 2: Sequences of initiation of destruction process (phase I) [7]

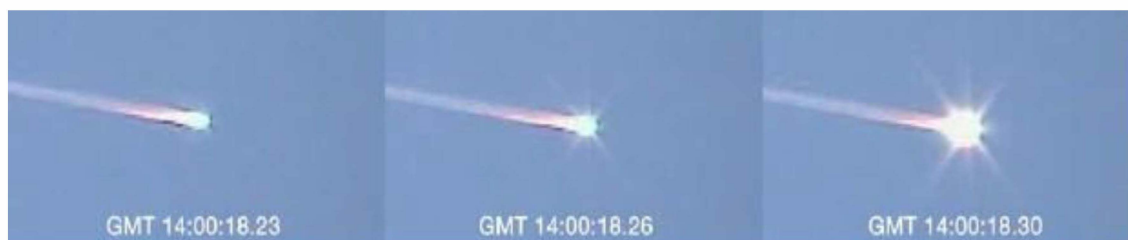


Figure 3: Acceleration of destruction process (phase A) [7]



Figure 4: Total dispersal phase (phase D) [7]

3. PRESENTATION OF NEW DESIGN FOR SPACE EQUIPMENT

The difficulties of space removal led to 'Design for dismissal' concept. The present paper presents a new vision of this concept.

Taking as example a satellite, it is known that its equipments are covered by a protection box which shields them against environmental factors: cosmic radiation, solar wind, light (ultraviolet, visible, infrared), dust and rarefied atmosphere.

Usually this box is a prism which has a pretty low dynamic drag. As a result, the reaching of high temperatures on satellite surface is delayed, therefore satellite disintegration is delayed. The situation is even more critical in the case of the last stages of launching rockets which have a good aerodynamic shape for a low aerodynamic drag during ascending phase of rocket.

According to the space equipment design presented in this paper, special doors must be incorporated in the external fairing of space equipment. The holes in fairings can have any shape (rectangular, triangular, hexagonal, circular and other) depending on the position of the fairing of space equipment. Doors fitted on every hole must be articulated by the fairing of space equipment. The articulation must be cylindrical, i.e., to permit rotating of door around an axis. The articulation must permit opening the door to the interior of box when pressure on external face of fairing increases and closing the door when the pressure inside the fairing is higher than the external pressure.

The door has a special shape being fixed by fairing through brazing with low fusible metals or strong resins (Araldite, Loctite) which are decomposed at low temperatures (150...200°C to maximum 700°C in some special cases). Both the resins and metallic alloys must be extremely resistant at low temperatures but must lose their strength when temperature reaches several hundred of Celsius degrees. In the early stages of re-entry, the epoxy resins decompose at temperatures between 150...200 °C and the braze alloys are melting when the local temperature reaches 200...700 °C. As a result, the covers are pushed inside the fairing of space equipment and the external air enters inside where stagnates reaching extremely high temperatures. The new external geometry of space equipment leads to increasing of aerodynamic drag and converts kinetic energy into heat, which enhances burning of equipment in atmosphere.

There are more doors placed on the fairing of space equipment. Thus, no matter how space equipment might rotate during re-entry, when one door is opened by the dynamic pressure, the rest of doors are closed by the same dynamic pressure. Thus, the inside heating due to air stagnation is maximum, leading to the rapid disintegration of space equipment.

In the case when covers are not articulated, they are pushed inside the equipment by the pressure of ambient air. In this way, the air begins to flow through the interior around the components of space equipment. In such a situation the air does not stagnate inside the space equipment and dynamic drag is low. For this reason the heating rate will be lower than when articulated covers are used.

Disintegration of space equipment will be even faster if the components of satellites are wrapped in 0.05 mm thick foil made of aluminium or magnesium. These light-weight foils will be burned firstly leading to a fast disintegration and burning of the component of space debris. This new technology clearly can be clearly understood from Figs. 5...9. Applying of this design will determine space debris to be disintegrated according to phases I, A, D which were observed in the case of Columbia.

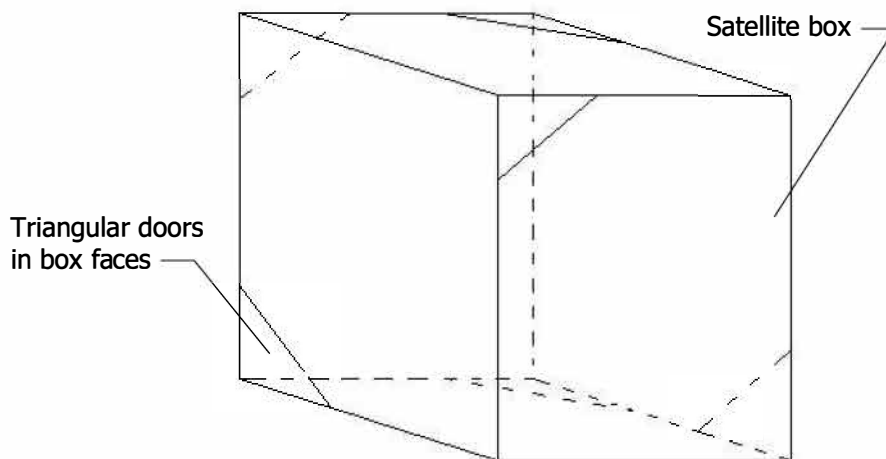


Figure 5: Example of satellite box with doors

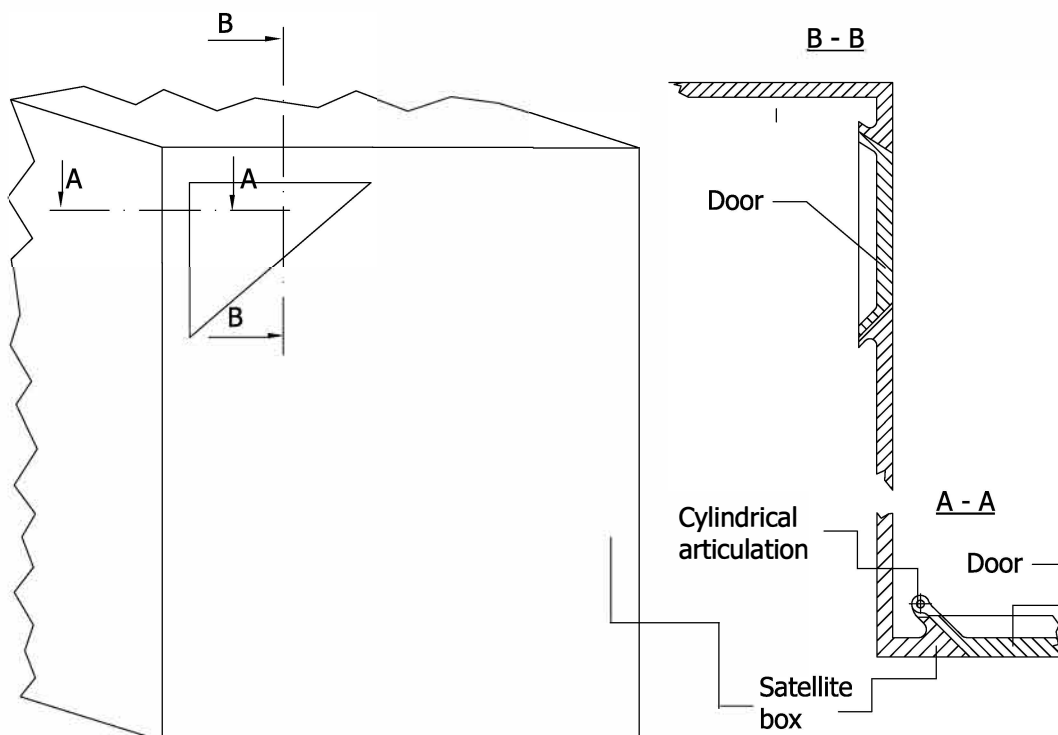


Figure 6: Design of doors

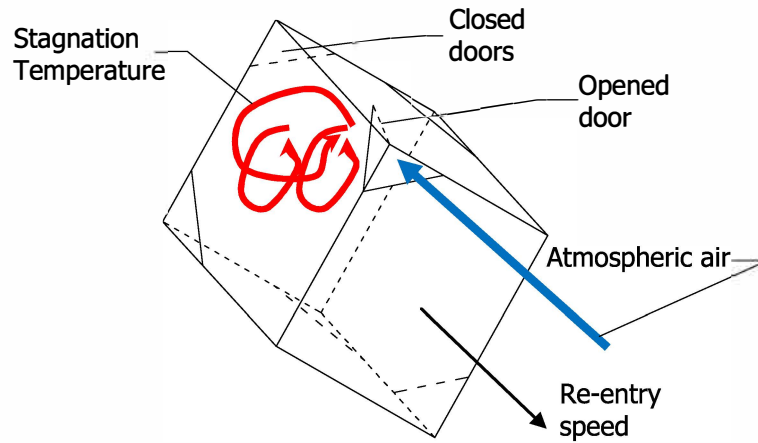


Figure 7: Reaching of stagnation temperatures inside a satellite box

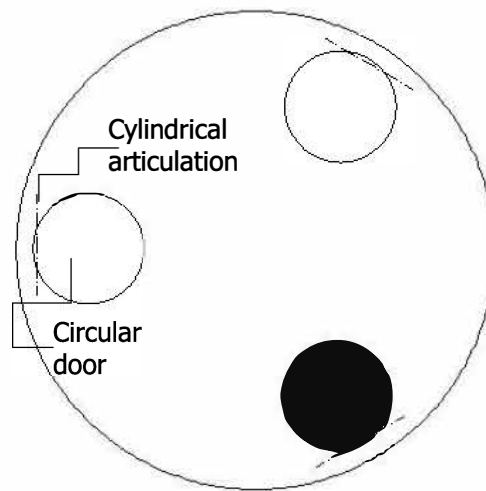


Figure 8: Example of fuel tank with circular doors

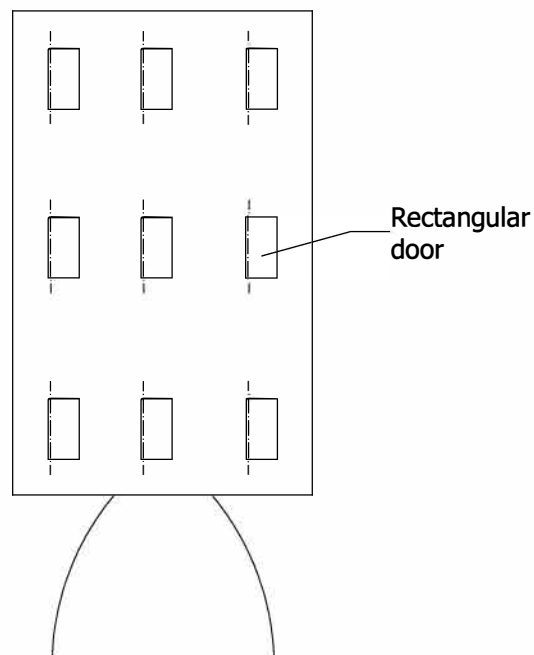


Figure 9: Example of last stage of rocket with rectangular doors

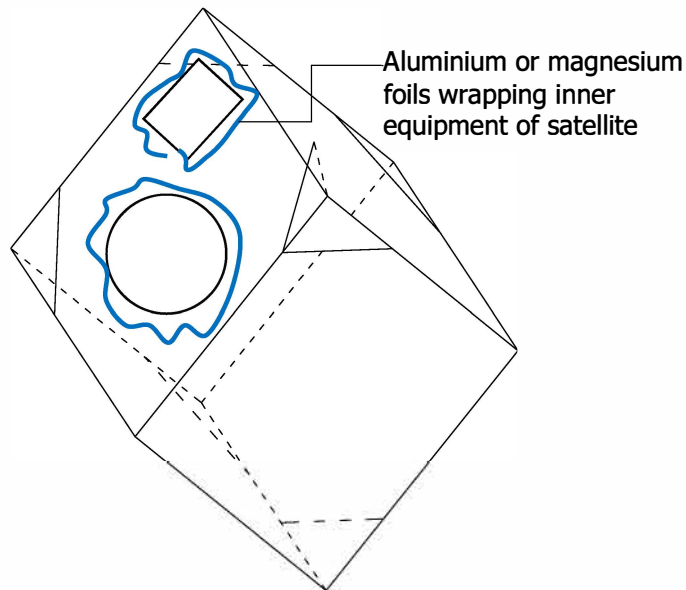


Figure 10: Example of satellite equipment wrapped by aluminium or magnesium foil

5. CONCLUSIONS

- For rapid disintegration of dismissed space equipment, multiple doors must be placed on the external surface of equipment.
- All the doors must open to the interior of equipment. In this way stagnation temperature are reached inside disregard the position of equipment during re-entry.
- The doors are glued with strong epoxy materials or are brazed with low melting temperature metallic alloys. During re-entry these materials are decomposed or are melted due heating freeing the doors.
- For a faster burning, internal assemblies of space equipment can be wrapped in aluminium or magnesium foil.

REFERENCES

1. IAA Position Paper – Space Debris Final Issue Approved for Publication; 2005; <http://iaaweb.org/iaa/Studies/spacedebrismitigation.pdf>
2. <http://www.aerospace.org/cords/all-about-debris-and-reentry/spacecraft-reentry/>
3. Alby, F.; 2005; Spot 1 end of life disposition maneuvers, Advances in Space Research 35 (2005) 1335–1342
4. Position Paper on Space Debris Mitigation - Implementing Zero Debris Creation Zones; 2005; International Academy of Astronautics-Final issue approved for publication
5. http://www.esa.int/Our_Activities/Operations/Space_Debris/Mitigating_space_debris_generation
6. <http://www.spacesafetymagazine.com/space-disasters/columbia-disaster/columbia-tragedy-repeated/>
7. Crew Survival Investigation Report, National Aeronautics and Space Administration, NASA/SP-2008-565

Resistance of Composite Laminates to the Initiation and Propagation of Delamination under Low Velocity Impact

Yigeng Xu

*Cranfield University - School of Aerospace, Transport and Manufacturing
 Cranfield, Bedfordshire MK43 0AL, UK
Yigeng.Xu@cranfield.ac.uk*

Zeng Shen

*University of Hertfordshire – School of Engineering and Technology
 College Lane Campus, Hatfield AL10 9AB, UK
zeng.shen@herts.ac.uk*

William Tiu

*BAE SYSTEMS, Rochester, Kent, ME1 2XX, UK
william.tiu@baesystems.com*

Yizhong Xu

*UiT, The Arctic University of Norway – Faculty of Engineering Science & Technology
 Narvik 8505, Norway
Yizhong.xu@uit.no*

Amit Ramji

*Cranfield University - School of Aerospace, Transport and Manufacturing
Amit.Ramji@cranfield.ac.uk*

Marzio Grasso

*University of Hertfordshire – School of Engineering and Technology
m.grasso@herts.ac.uk*

ABSTRACT

A key factor affecting the use of carbon fibre reinforced composite laminates is the low velocity impact (LVI) damage which may be introduced accidentally during manufacture, operation or maintenance of the component. Among the various failure mechanisms involved in the damage process, delamination is the dominant failure mode and may reduce the post-impact compressive strength of the component significantly. The resistances to delamination initiation and propagation of the material are key material properties for damage tolerance design of aerospace structures. This paper presents an experimental study of the resistance of composite laminates to delamination initiation and propagation under low velocity impact. The impact force history obtained from the instrumented drop-weight impact test is used to detect the delamination threshold load (DTL) which is a parameter representing the material resistance to the

initiation of delamination. Repeated impact test is carried out to characterise the resistance to delamination propagation under LVI. Good damage tolerance capacity of the composite laminates is demonstrated by the observation that the peak impact force under the repeated impact is higher than the one under the first impact when the impact energy is kept the same. The multiple delamination initiated under the first impact may act as subsequent impact energy absorbers and help to stop the propagation of the delamination. The effect of delamination initiation on the damage tolerance capacity of the composite laminates should be investigated further for the design and application of composite materials in aerospace industry.

KEYWORDS: *low velocity impact, composite laminates, delamination threshold load*

Onboard Functional Requirements for Specific Category UAS and Safe Operation Monitoring

Christoph Torens

*German Aerospace Center (DLR), Institute of Flight Systems
Research Scientist
38108 Braunschweig, Germany
christoph.torens@dlr.de*

Florian Nikodem

*German Aerospace Center (DLR), Institute of Flight Systems
Research Scientist*

Johann C. Dauer

*German Aerospace Center (DLR), Institute of Flight Systems
Research Scientist*

Joerg S. Dittrich

*German Aerospace Center (DLR), Institute of Flight Systems
Head of Department Unmanned Aircraft*

ABSTRACT

The new concept for operation of drones, published by EASA in 2015 enables new ways to influence and possibly reduce the necessary safety targets of certain software components without reducing the overall safety of the unmanned aircraft system (UAS). Based on a safety assessment, the so called *specific category* enables new aircraft system architectures and mission designs. In this context, this paper proposes runtime monitoring as a mitigation strategy for the operation getting out of control to formally assure predefined properties in flight and thus assure the safety of the operation in progress. One particular aspect of this safe operation monitoring is geofencing, the capability to assure containment of the UAS in a previously restricted area. In the regulatory framework of a *specific operation* risk assessment, such a geofence can be interpreted as a harm barrier. The functional requirements for this geofencing use case are discussed regarding their impact on the underlying *specific operation* risk assessment. To achieve this, we develop a taxonomy of geofencing characteristics. Consequently, the geofencing requirements are assessed regarding their robustness and applicability for certification purposes. As a result, by monitoring the integrity of the system at runtime, exemplified in this paper with the use case of geofencing, it is investigated if the requirements and thus costs of development and certification process for the remaining components can be reduced.

KEYWORDS: UAS, Safety Requirements, Specific Operation Risk Assessment (SORA), Runtime Monitoring, Geofencing

Wind tunnel testing of the control system for a new morphing wing application with a full-scaled portion of a real wing

M.J. Tchatchueng Kammegne

*École de Technologie Supérieure, Montréal, Québec H3C 1K3, Canada
 PhD Student
 1100 Notre Dame West, H3C 1K3, Montreal, Quebec, Canada
 mjtchatchueng@yahoo.ca*

R.M. Botez

*École de Technologie Supérieure, Montréal, Québec H3C 1K3, Canada
 Full Professor
 1100 Notre Dame West, H3C 1K3, Montreal, Quebec, Canada
 ruxandra.botez@etsmtl.ca*

L.T. Grigorie

*École de Technologie Supérieure, Montréal, Québec H3C 1K3, Canada
 Associate Professor
 1100 Notre Dame West, H3C 1K3, Montreal, Quebec, Canada
 ltgrigorie@yahoo.com*

M. Mamou

*Aerodynamics Laboratory, National Research Council Canada
 Senior Research Officer
 1200 Montréal Road, K1A 0R6, Ottawa, Ontario, Canada*

Y. Mebarki

*Aerodynamics Laboratory, National Research Council Canada
 Research Officer
 1200 Montréal Road, K1A 0R6, Ottawa, Ontario, Canada*

ABSTRACT

The paper presents the implementation and the experimental testing of a control system for a morphing wing model developed with a full-scaled portion of a real aircraft wing. The morphing wing experimental model was designed, manufactured and tested during an international research project involving industrial partners, research entities and academia from Canada and Italy. Based on the dimensions of a full scale wing tip structure, the model contained two morphable parts: the wing and the attached aileron. The wing has been equipped with a flexible upper surface made from composite materials and morphed by using four miniature electrical actuators. To evaluate the aerodynamic performance of the morphing system during the wind tunnel tests, the air flow behavior over the upper surface has been analyzed based on the information provided by an array of 32 Kulite pressure sensors. Also, in the wind tunnel tests an infrared camera has been used to provide a second opinion related to the aerodynamic performance of the system.

KEYWORDS: *Morphing wing, Control system, Experimental model, Wind tunnel testing, Infra-red analysis*

SOLAR-GRAVITATIONAL SYSTEM FOR DEORBITING SPACE DEBRIS AND REENTRY IN EARTH'S ATMOSPHERE AND ACCELERATING ACTIVE SATELITES FOR ORBIT REESTABLISHMENT

Constantin Sandu^{1}, Dan Brasoveanu², Valentin Silivestru¹, Bogdan Filipescu³, Radu Constantin Sandu⁴*

¹*COMOTI, Bucharest, Romania*

²*Systems Engineering Group Inc. (SEG), MD, USA*

³*Teletrans. Craiova, Romania*

⁴*S.C. Structural Management Solutions S.R.L., Bucharest, Romania*

**Corresponding author: E-mail : constantin.sandu@comoti.ro*

ABSTRACT

This paper presents a technology for de-orbiting of space debris or accelerating of active satellites using gravitational interaction. Paper published in a physical review presented the possibility to generate a flux of gravitational radiation through multiple reflections of electromagnetic radiation between two or more parallel mirrors. When the gravitational radiation generated in this way interacts with a body, that body will be attracted in a direction which is perpendicular to the mirrors' surface. Generation of gravitational radiation in this way occurs when electromagnetic energy (as solar light) is continuously fed into the gap between mirrors. When the total energy of light reflecting continuously between the reflective surfaces is sufficiently high, the radiated gravitational power becomes significant. Deceleration and atmosphere re-entry are triggered when this radiation impacts the rear end of space debris. Acceleration and orbit re-establishment occurs when this radiation is directed to the front of operational satellites.

The paper presents only the main design principles of this concept related by collection and reflection of solar light between reflective surfaces.

Conclusions are that this new technology could be currently applied in future but much research work is necessary in the field of solid physics for increasing materials reflectivity to extremely high values.

KEYWORDS: space debris removal, gravitational radiation

NOMENCLATURE

a, acceleration, [m/s²]
 c, speed of light, [m/s]
 d, distance, [m]
 E*, energy, [J]
 E, electric field, [dyne/SC in CGS]
 G, universal constant of gravitation [Nm²/kg²]
 h, Planck's constant, [J·s]
 m, mass, [kg]
 P, power, [W]
 r, radius, [m]
 R, reflectivity, dimensionless

Greek

λ , wave length, [m]

1. INTRODUCTION

The presence of space debris around Earth constitutes a difficult problem. Practically, 85% of orbiting objects are space debris. Space debris is distributed in all regions of near Earth space, particularly in the GEO and LEO regions, as shown in fig.1 and fig.2. [1]

The presence of space debris is already a great danger becoming the main threat to safety of space exploration and exploitation.

The space debris are composed of used boost stages of rockets, spent rocket upper stages, paint exfoliations, pieces of solid rocket motors, remnants of old scientific experiments, non-functional satellites, various fragments which are the result of collisions, materials detached from International Space Station, components of satellites destroyed by missiles etc. [2]

The number of objects in orbit will grow, even if no further objects are launched into space because the collisions cannot be kept under control. Unconstrained collisions can lead to a cascade effect with no further possibility of human intervention and leading to an increased level of hazard for space operations.



Figure 1: Space debris in GEO region [ESA] Figure 2: Space debris in LEO region [ESA]

There are three categories of space debris: [3]

Category I (<1cm) - this causes significant damage to vulnerable parts of a satellite

Category II (1-10 cm) – causes serious damages or destruction of a satellite after a collision

Category III (>10cm)-destroys a satellite in a collision and it can be tracked

This paper presents a so called solar-gravitational system for removal of space debris through a new technology: deceleration of space debris using gravitational attraction. The system can be launched in space as any satellite on a geocentric, heliocentric or Sun-synchronous orbit.

2. GENERATING OF ARTIFICIAL GRAVITATIONAL FIELD

Generating of artificial gravitation is a new challenge for our civilization in the field of propulsion. An article published in the Journal of Advances in Physics demonstrates the 'Theorem of Conversion of Electromagnetic Radiation (Waves) into Gravitational Radiation (Waves)' [4, 5]. This theorem shows that electromagnetic energy in the form of electromagnetic radiation (waves) can be converted into gravitational energy, i.e., gravitational radiation (waves). Generation of gravitational radiation in this way is a direct consequence of Einstein's General Theory of Relativity.

According to the mentioned theorem, a flux of gravitational radiation must be produced through multiple reflections of electromagnetic waves between two or more parallel mirrors (reflective layers). When the gravitational radiation generated in this way interacts with a body, that body will be attracted in a direction which is perpendicular to the mirrors' surface.

If a large amount of electromagnetic radiation (solar light) is injected into the gap existing between two mirrors and begins to reflect between them, the radiated gravitational power becomes significant. Maximum radiated power is emitted when the light direction is normal to the mirrors surfaces and when the distance between mirrors is equal to a half of wave length of the continuously reflecting light. The gravitational radiation generated in this way can be called 'artificial' because it is generated by equipment which normally does not exist in nature.

It must be mentioned that the radiation of a gravitational wave during reflection of a light ray by a reflective surface is a natural effect which must occur frequently in nature. However, the gravitational wave generated by a single reflection of a light ray is too weak. An extreme large number of reflections is necessary for generating gravitational radiation with a significant power which is usable for interaction with space debris.

The next sub-sections discuss the production of this radiation as a result of multiple reflections of concentrated solar light and how to direct this radiation to the rear of space debris for inducing deceleration or to the front side of satellites that need to be accelerated and boosted back onto desired orbits.

2.1 The physical basis of gravitational emissions

For understanding this important phenomenon, the main steps of the demonstration of 'Theorem of Conversion of Electromagnetic Radiation (Waves) into Gravitational Radiation (Waves)' are presented below:[4]

The reflection of a photon on a reflective surface can be considered the most violent process in Universe even more violent than the head-on collision of neutron stars because the acceleration of matter during this normal reflection has a huge value due to the high speed of light:

$$a = \frac{\Delta V}{\Delta t} = \frac{-c - (+c)}{T} = \frac{-2c}{T} = -2cv \quad (1)$$

where,

- ΔV is speed variation,
- Δt is the duration of photon-surface interaction
- c is the speed of light in vacuum
- T is the oscillation period of light
- v is the frequency of light

During reflection, the matter of photon oscillates as a quadrupole (fig. 1) and for this reason it must generate gravitational waves. The direction of the electric field E and magnetic field, H , are perpendicular to the photon's travel direction. During reflection, the matter of photon oscillates in radial direction simultaneously with electric field, E , and magnetic field, H . When the associated photonic wave is reflected the sense of the electric field, E , and magnetic field, H , are reversed. On the other hand, during reflection the photon's matter oscillates longitudinally due to direction reversal.

Note: It was demonstrated in advanced physics that only a quadrupole and not a dipole can generate gravitational waves.

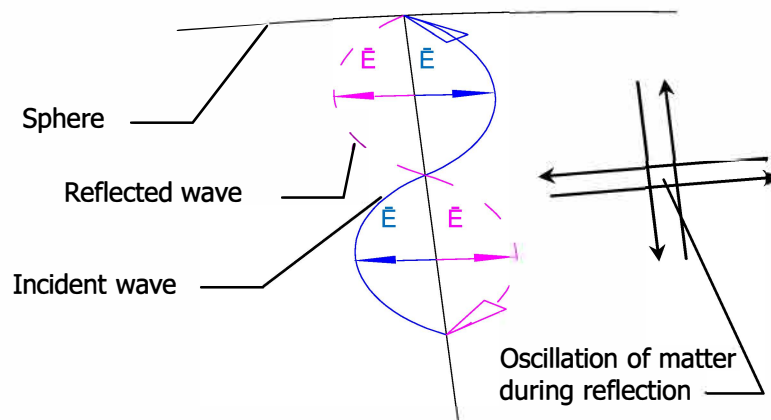


Figure 1: During reflection, the matter of a photon oscillates like a

Unexpectedly, the direction of graviton emitted during normal reflection of a photon is opposite to the direction of the incident photon. While intuition indicates that the graviton is emitted in the direction of the incident wave, actually the momentum conservation law shows that the opposite is true (fig.2).

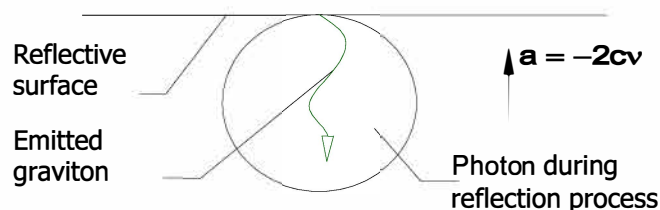


Figure 2: Inertia determines the direction of graviton emission along the path of reflected wave

The physical explanation is as follows:

Reflection of photon by a mirror is equivalent to a strong braking. Because the photon is not electrically charged, the single force which opposing this braking is gravitation. Thus, the graviton-

CEAS 2017 paper no. 211

Page | 3

SOLAR-GRAVITATIONAL SYSTEM FOR DEORBITING SPACE DEBRIS AND REENTRY IN EARTH'S ATMOSPHERE AND
ACCELERATING ACTIVE SATELLITES FOR ORBIT REESTABLISHMENT

Copyright © 2017 by authors

photon interaction would tend to counter the deceleration process produced by reflection i.e., the graviton 'attempts to accelerate' the photon along the initial direction.

The laws of energy and momentum conservation support this conclusion. Assume the mass of the emitted graviton is m_g , E_{if}^* - the energy of incident photon, E_{rf}^* - the energy of reflected photon and E_g^* = the energy of graviton, then the energy balance during the reflection process is given by:

$$E_{if}^* = E_{rf}^* + E_g^* \quad (2)$$

Based on Eq. (2), reflection causes a red shift i.e., the frequency of the reflected wave is smaller than the frequency of incident wave, $\nu_{rf} < \nu_{if}$. This red shift is obviously extremely low and cannot be observed visually. On the other hand, according to the law of momentum conservation:

$$h \cdot \nu_{if} / c + h \cdot \nu_{rf} / (-c) + m_g \cdot (-c) = 0 \quad (3)$$

where ν_{if} is the frequency of incident photon, ν_{rf} is the frequency of reflected photon and m_g is the mass of graviton. Equation (3) shows that the direction of radiated gravitational wave is opposite to the incident electromagnetic wave i.e. the same as the reflected wave in the case of normal reflection and that the propagation speed of gravitational wave is c (this fact, was already demonstrated for weak gravitational fields).

The energy of a graviton emitted during reflection can be easily evaluated using dimensional analysis. The graviton energy should depend on Planck's constant, h , frequencies of incident and reflected electromagnetic wave, $\nu_{if} > \nu_{rf} \approx \nu_g$ (ν_g - frequency of gravitational wave), c - speed of light and G - gravitational constant:

$$E_g^* = \frac{\chi^* \cdot G \cdot h^2}{c^5} \cdot \nu_g^3 \quad (4)$$

where χ^* is a constant composed of universal constants, i.e. it itself is a universal constant.

The constant χ^* shows that during normal reflection of photons, the gravitons are emitted as energy quanta. The energy of emitted graviton is proportional to the cube of light frequency.

The equation (4) can be written in a new form (5),

$$E_g^* = \frac{\chi^* \cdot G}{c^5 \cdot h} \cdot h^3 \cdot \nu^3 = \frac{\chi^* \cdot G}{c^5 \cdot h} \cdot E_e^{*3} = h_{ge} \cdot E_e^{*3} \quad (5)$$

Eq. (5) reveals a connection between radiated gravitational energy, E_g^* , and reflecting electromagnetic energy, E_e^* : The radiated gravitational energy is proportional with the cube of electromagnetic energy, and the proportionality constant is $h_{ge} = \frac{\chi^* \cdot G}{c^5 \cdot h}$ which is composed of gravitational constants and can also be considered a universal constant.

2.2 Theorem of Conversion of Electromagnetic Radiation (Waves) into Gravitational Radiation (Waves)

This theorem states: [4]

'During normal reflection of an electromagnetic wave on a reflective surface, electromagnetic energy is partially converted into gravitational energy. The frequency of the emitted gravitational wave is equal to the frequency of incident wave. The energy of emitted gravitational wave is proportional with the cube of frequency of electromagnetic wave. The direction of gravitational wave is opposite to that of the incident electromagnetic wave.'

If two packs of electromagnetic waves 1, 2 each having energy E^* , frequency, ν , and implicitly the same number of photons n , reflect continuously between two mirrors A, B separated by a gap $d = \lambda$ (fig.3), the radiated gravitational power according to equation (6):

$$P_g = 2 \cdot n \cdot \frac{1}{T} \cdot \frac{\chi^* \cdot G \cdot h^2}{c^5} \cdot v^3 = \frac{2n\chi^* G h^2 v^2}{c^5} \cdot v^2 = \frac{\chi^* G}{c^5} \cdot E^{*2} \cdot v^2 \quad (6)$$

Eq. (6) shows that the radiated gravitational power generated by electromagnetic waves reflecting between two parallel mirrors separated by a gap λ is proportional to the square of energy E^* of each incident pack of electromagnetic waves, and their frequency, v .

In the above equation, the incidence angle was taken equally to zero.

The equipment presented in fig. 3 can continuously generate a uniform flux of gravitational power because reflection of pack 2 on mirror A and of pack 1 on mirror B is instantaneously followed by reflection of pack 1 on mirror A and of pack 2 on mirror B.

Each gravitational flux (created by mirrors A and B), penetrate mirrors B and A respectively, leaving the space between mirrors. This vectored flux of gravitational radiation can be obviously used to create gravitation forces exerted on bodies (particularly braking space debris for de-orbiting and accelerating satellites for re-establishing orbit).

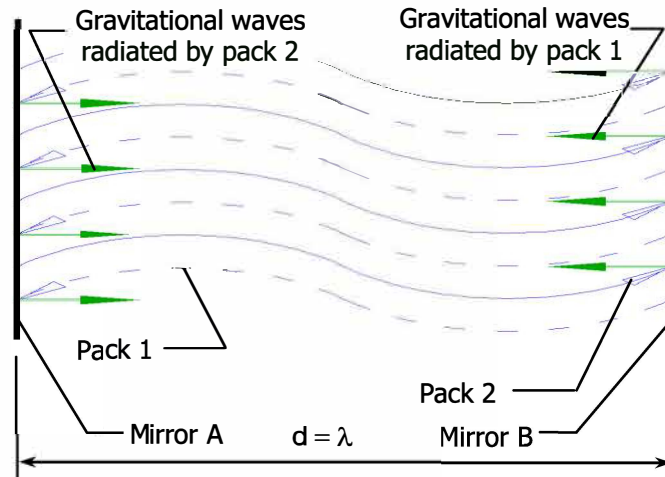


Figure 3: Two packs of electromagnetic energy which continuously radiate gravitational waves through multiple reflections

[Note: The maximum radiated gravitational power can be four times higher than that given in equation (6). This phenomenon can take place because stationary waves can exist between the two mirrors even when the distance d is equal to a half of the wavelength $\lambda/2$ ($d = \lambda/2$)].

In fig. 4 a system composed of $q+1$ mirrors is able to multiply by q the radiated gravitational power. Two adjacent mirrors are separated by distances $d = \lambda$ (fig.4). Between any pair of adjacent mirrors, two packs of electromagnetic waves with energy E are injected. The total gravitational power radiated by system, P_{gq} is given by equation 7.

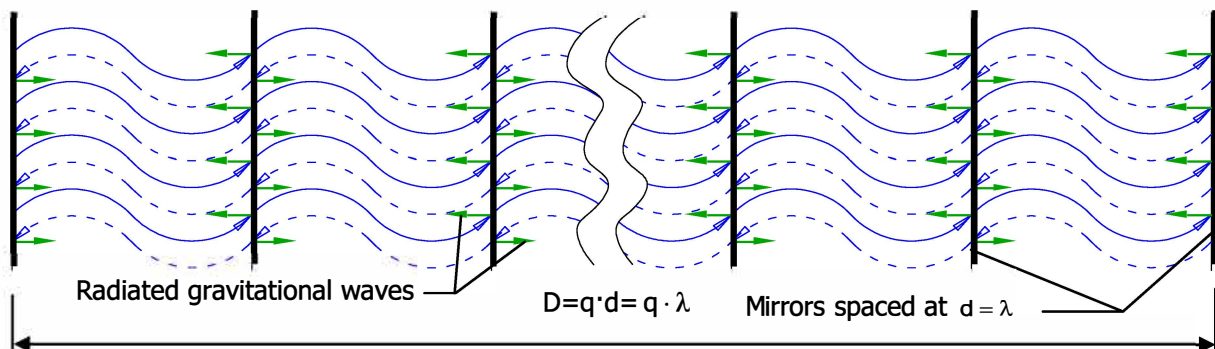


Figure 4: Equipment with multiple reflecting surfaces for increasing the power of gravitational radiation

To greatly boost the power of gravitational radiation a large number of pairs of mirrors must be used. When $(q+1)$ mirrors (thin reflective layers) are used, the radiated power becomes:

$$P_{gq} = q \cdot P_g = \frac{q \cdot \chi^* \cdot G}{c^5} E^{*2} \cdot v^2 \quad (7)$$

The constant χ^* must be finally determined by experiments. Initial evaluations, based on another consequence of Einstein's General relativity yielded the value:

$$\chi^* \approx 512 / 5 = 102.4 \quad (8)$$

Equation (7) is useful for calculation of gravitational action on bodies (space debris, satellites etc.).

2.3 Design of solar-gravitational system for de-orbiting of space debris

The operating principle of a gravitational system for de-orbiting of space debris is presented in fig.5, 6. The large parabolic mirror is permanently oriented towards the Sun, collects light rays and directs them to the focal point, F. The small parabolic mirror has the same focal point, F, and is positioned face to face with the large parabolic mirror. The light rays focused into focal point F by the large parabolic mirror are reflected then by the small parabolic mirror in parallel light rays (concentrated light beam) which enters the central light guide when the light shutter is opened. After that, the concentrated light beam enters the cellular wave guide which directs it to the multiple parallel mirrors. The mirrors are placed at an angle $\alpha = 90^\circ + \delta$, where δ is a very small angle. When the light rays reflect between mirrors, gravitational waves are generated while the frequency of light decreases (all the components of the white light coming from Sun are red-shifted). [4]

At the end of this process, light is evacuated in space as brilliant red light. The gravitational radiation (I) is convergent (fig.5) and it is used for decelerating space debris forcing re-entry and burning in atmosphere. The gravitational radiation (II) is divergent and it is lost into space. The shutter is a thin disc plated with gold on both faces. If the front light shutter is closed, the light is sent back to the small parabolic mirror, to the large parabolic mirror and then to the Sun. In this situation gravitational radiation is not generated.

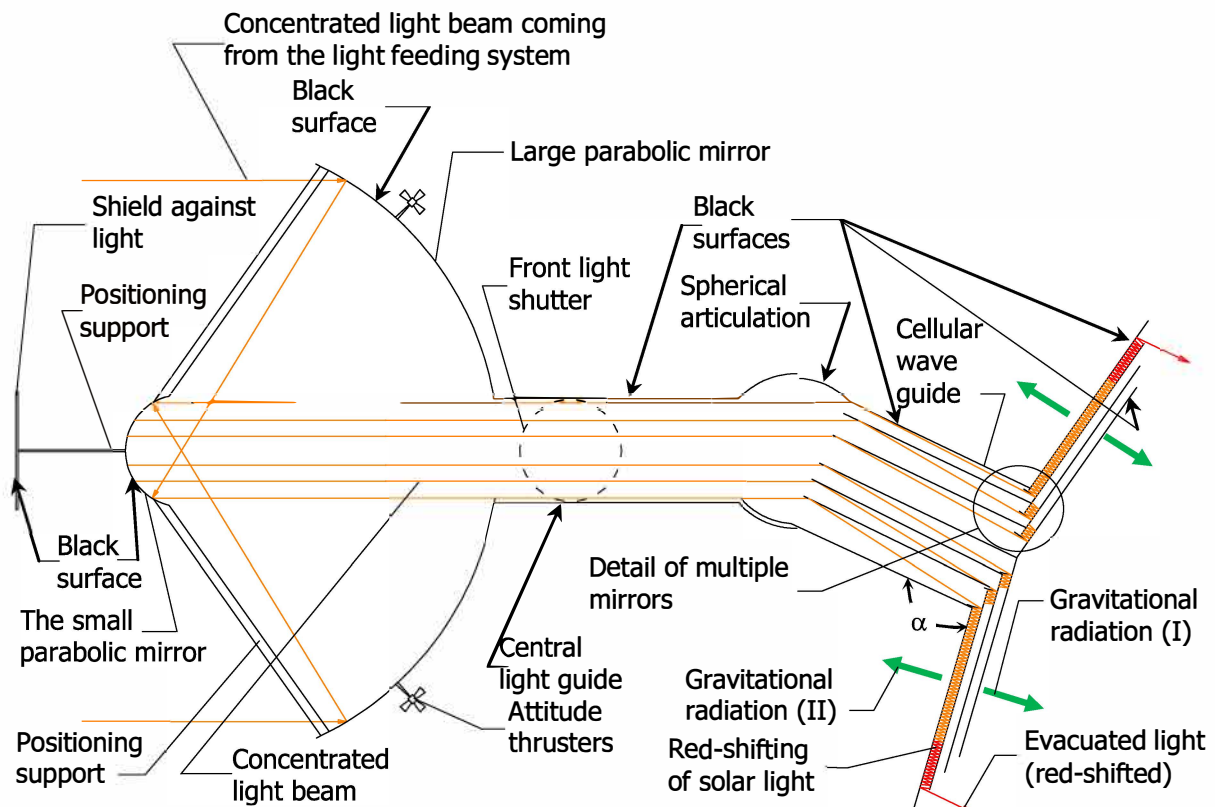


Figure 5: The scheme of a solar-gravitational de-orbiting for space debris

The large and small parabolic mirrors, plane mirrors and light guides are made of composite materials (graphite fibre or grapheme base) and are gold plated on the reflective surfaces. The heat is radiated in space through radiation of black surfaces of the above mentioned components.

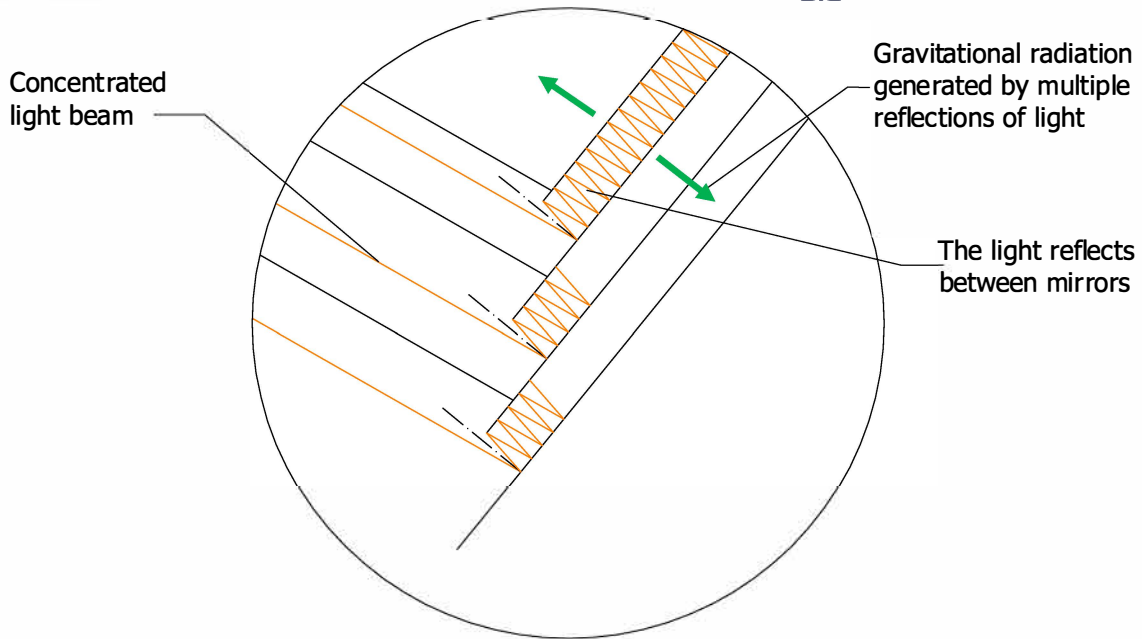


Figure 6: Detail of multiple reflection of light between mirrors

3. CALCULATION OF RADIATED GRAVITATIONAL POWER

In ideal conditions (reflectivity coefficient of surfaces $R=1$), the gravitational power radiated by two parallel mirrors due to multiple reflection of two packets of light (i.e., $q=1$) having energy E^* each, for infrared, visible and ultraviolet light is given in the Table 1.

Table 1: Power of gravitational radiation produced through reflection of infrared to ultraviolet light

$E^*, \text{ kJ}$ $\nu, \text{ Hz}$	1	10^3	10^5	10^7	10^9	10^{11}	10^{13}
$\frac{dE^*}{dt}, \text{ kW}$ $\frac{dE^*}{dt}, \text{ kW}$ $\frac{dE^*}{dt}, \text{ kW}$ $\frac{dE^*}{dt}, \text{ kW}$ $\frac{dE^*}{dt}, \text{ kW}$ $\frac{dE^*}{dt}, \text{ kW}$ $\frac{dE^*}{dt}, \text{ kW}$	$\frac{dE^*}{dt}, \text{ kW}$	$\frac{dE^*}{dt}, \text{ kW}$	$\frac{dE^*}{dt}, \text{ kW}$	$\frac{dE^*}{dt}, \text{ kW}$	$\frac{dE^*}{dt}, \text{ kW}$	$\frac{dE^*}{dt}, \text{ kW}$	$\frac{dE^*}{dt}, \text{ kW}$
3×10^{11} (infrared)	2.5×10^{-25}	2.5×10^{-19}	2.5×10^{-15}	2.5×10^{-11}	2.5×10^{-7}	2.5×10^{-3}	2.5×10^1
3×10^{14} (infra red)	2.5×10^{-19}	2.5×10^{-13}	2.5×10^{-9}	2.5×10^{-5}	2.5×10^{-1}	2.5×10^3	2.5×10^7
3.75×10^{14} (red)	4×10^{-19}	4×10^{-13}	4×10^{-9}	2×10^{-5}	4×10^{-1}	4×10^3	4×10^7
5×10^{14} (yellow)	0.7×10^{-18}	0.7×10^{-12}	0.7×10^{-8}	0.7×10^{-4}	0.7×10^0	0.7×10^4	0.7×10^8
5.75×10^{14} (light green)	0.9×10^{-18}	0.9×10^{-12}	0.9×10^{-8}	0.9×10^{-4}	0.9×10^0	0.9×10^4	0.9×10^8
6×10^{14} (dark green)	1×10^{-18}	1×10^{-12}	1×10^{-8}	1×10^{-4}	1×10^0	1×10^4	1×10^8
6.25×10^{14} (light blue)	1.1×10^{-18}	1.1×10^{-12}	1.1×10^{-8}	1.1×10^{-4}	1.1×10^0	1.1×10^4	1.1×10^8
6.5×10^{14} (dark blue)	1.2×10^{-18}	1.2×10^{-12}	1.2×10^{-8}	1.2×10^{-4}	1.2×10^0	1.2×10^4	1.2×10^8
7×10^{14} (light violet)	1.4×10^{-18}	1.4×10^{-12}	1.4×10^{-8}	1.4×10^{-4}	1.4×10^0	1.4×10^4	1.4×10^8
7.5×10^{14} (dark violet)	1.6×10^{-18}	1.6×10^{-12}	1.6×10^{-8}	1.6×10^{-4}	1.6×10^0	1.6×10^4	1.6×10^8
3×10^{15} (ultra violet)	1.6×10^{-17}	1.6×10^{-11}	1.6×10^{-7}	1.6×10^{-3}	1.6×10^1	1.6×10^5	1.6×10^9

3×10^{16} (ultra violet)	2.5×10^{-15}	2.5×10^{-9}	2.5×10^{-5}	2.5×10^{-1}	2.5×10^3	2.5×10^8	2.5×10^{11}
--------------------------------------	-----------------------	----------------------	----------------------	----------------------	-------------------	-------------------	----------------------

Table 1 shows that the radiated gravitational power can have high values if the energy E of the reflecting light packets is sufficiently high. The distance between reflective layers is of the order of wave length of light. For increasing radiated gravitational power, a high number q of reflective layers can be used. Only half of this power is used for actuating space debris because the rest is lost in space (fig.8).

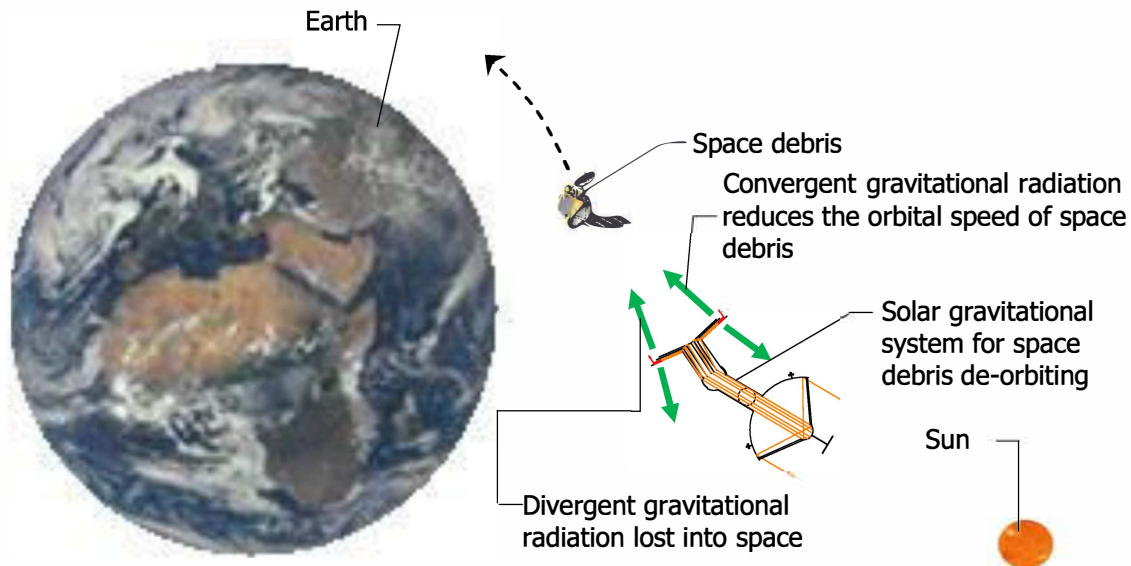


Figure 8: Action of solar-gravitational system for space removal

4. THE PROBLEM OF MIRRORS' REFLECTIVITY

There is plenty of light in space to be collected for generation gravitational radiation through multiple reflections. However, the low reflectivity of present materials is a great problem which must be solved. Until this problem will be solved, the solar-gravitational system for space debris de-orbiting cannot be built. , In reality, packets of light having energy E cannot be maintained a long period of time in a continuous reflecting process due to absorption of light during reflection. The best reflective materials (gold, silver, aluminum) can reach a reflectivity of only $R=0.98...0.99$ while for creating large packets of energy E, reflectivity must be very close by 1.

New artificial materials or charging of reflective layers with electrons at a very high potential could offer the necessary reflectivity. This is a very difficult problem of solid physics and much research work is necessary for solving it.

5. CONCLUSIONS

- The solar-gravitational system for space debris de-orbiting uses gravitational attraction for reduction of orbital speed of space debris. In this way the space debris enters the dense atmosphere and burns. This system could be currently used in future both for space debris de-orbiting and orbit reestablishing of satellites.

- The gravitational radiation is produced through multiple reflections of concentrated sun-light between two or more parallel mirrors. This possibility is recognized today by advanced physics.

- The main problem which must be solved for building of a gravitational system for space debris de-orbiting is increasing mirrors' reflectivity. This must be very high, close to 1. Much research work is necessary in the field of solid physics for obtaining mirrors with very high reflectivity. This can be

achieved if new materials are developed or by charging the mirror metal with electrons at very high electric potentials.

REFERENCES

1. <https://www.universetoday.com/13587/space-debris-illustrated-the-problem-in-pictures/>
2. Andrenucci, M., Pergola, P, Ruggiero, A.; 2011; Active Removal of Space Debris Expanding-Expanding foam application for active debris removal, Final Report, Contract Number: 4000101449/10/NL/CBi
3. Ze, Z.; 2011; SPACE DEBRIS AND PRESENT ACTIVE DEBRIS REMOVAL TECHNIQUES, 2011 Beijing Space Sustainability Conference October 13-14, 2011, Beijing
4. Sandu, C., Brasoveanu, D.; 2017; On the Theoretical Possibility to Generate Gravitational Waves Using Electromagnetic Waves, Journal of Advances in Physic, , Volume 13 Number 2, page 4692, March 2017, ISSN2347-3487.
5. Sandu C. and Brasoveanu D.; 2007; Sonic-Electromagnetic-Gravitational–Spacecraft, Part 2 – Law of Conversion of Electromagnetic Radiation into Gravitational Radiation’, Proceedings of the AIAA SPACE 2007 Conference & Exposition, Long Beach, California, September 18-20, 2007, paper AIAA-2007-620

A Java Toolchain of Programs for Aircraft Design

*Agostino De Marco,
Assistant professor*

Department of Industrial Engineering (DII) – University of Naples "Federico II"
Via Claudio 21, 80125 Napoli - ITALY

E-mail: agodemar@unina.it

*Vincenzo Cusati,
PhD Student*

Department of Industrial Engineering (DII) – University of Naples "Federico II"
E-mail: vincenzo.cusati@gmail.com

*Vittorio Trifari,
PhD Student*

Department of Industrial Engineering (DII) – University of Naples "Federico II"

*Manuela Ruocco,
PhD Student*

Department of Industrial Engineering (DII) – University of Naples "Federico II"

*Fabrizio Nicolosi,
Associate professor*

Department of Industrial Engineering (DII) – University of Naples "Federico II"

*Pierluigi Della Vecchia
Assistant professor*

Department of Industrial Engineering (DII) – University of Naples "Federico II"

ABSTRACT

The purpose of this work is to provide a comprehensive overview of JPAD (Java toolchain of Programs for Aircraft Design), a java-based framework conceived as a fast and efficient tool useful as support in the preliminary design phases of an aircraft, and during its optimization process. The software platform is made to perform fast multi-disciplinary analysis of an established aircraft configuration and to search for an optimized configuration in a domain, whose boundaries are defined by the user. The following sections will focus on the description of the software structure and on the results obtained from a case study carried out assuming as baseline a regional turboprop aircraft model similar to ATR-72.

KEYWORDS: AIRCRAFT DESIGN, SOFTWARE ENGINEERING, JAVA

NOMENCLATURE

Latin

ADP – Aircraft delivery Price
 AEA – Association of European Airlines
 AEO – All Engines Operative
 ATA – Air Transportation Association of America
 BFL – Balanced Field Length
 C_a – Cost of complete airplane less engine
 C_e – Cost of the engine
 C_{noise} – Unit noise rate
 DAF – Design of Aircraft and Flight technologies research group
 DP – Depreciation period
 ECAC – European Civil Aviation Conference
 C_L – Lifting coefficient
 DOC – Direct Operating Costs
 FAR – Federal Aviation Regulations

GUI – Graphical user interface
 ICAO – International Civil Aviation Organization
 JPAD – Java toolchain of Programs for Aircraft Design
 K_{ldg} – Landing charges constant
 K_{nav} – Navigation charges constant
 K_{grd} – Ground charges constant
 $L_{approach}$ – Certified noise level, approach measure point
 $L_{flyover}$ – Certified noise level, flyover measure point
 $L_{lateral}$ – Certified noise level, lateral measure point
 LR – Labour rate
 $m_{block\ fuel}$ – fuel mass
 M – Mach number



MTOW – Maximum Take-Off Weight
 n_e – number of engines
 n_{cm} – number of crew members
 OEI – One Engine Inoperative
 OEW – Operating Empty Weight
 P_{fuel} – Fuel price
 R – Range
 R_a – Interest annual rate
 R_i – Insurance annual rate
 Re – Reynolds number
 RV – Residual value
 T/W – Thrust ratio
 t_b – Block time
 t_f – Flight time
 T_d – Departure airport threshold noise
 T_a – arrival airport threshold noise
 TI – Total investment
 TNAC – Transport Aircraft Noise Classification Group
 V – Aircraft speed

V_b – Block speed
 W/S – Wing loading
 W_a – Empty Weight of the Airplane less Engines
 XML – eXtensible Markup Language
 XLS – Excel file format

Greek

α_b – angle of attack in body reference frame
 α_w – angle of attack of the wing in local reference frame

Subscripts

C_{Lmax} – Maximum lifting coefficient
 $C_{M_{cg}}$ – Pitching moment coefficient referred to the aircraft center of gravity
 V_{sTO} – Aircraft stall speed in take-off configuration
 Z_{cg} – vertical position of the center of gravity in body reference frame

1 INTRODUCTION

Nowadays the preliminary design phase of an aircraft is becoming very challenging due to the need for more demanding requirements which deals with different fields of applications. In this perspective, there is a certain need for simple design tools both in aircraft industries and academic research groups which can perform fast and reliable multi-disciplinary analyses and optimizations.

This paper provides a comprehensive overview of JPAD (Java toolchain of Programs for Aircraft Design), a Java-based open-source library conceived as a fast and efficient tool useful as support in the preliminary design phases of an aircraft, and during its optimization process. The library has been completely realized at the Department of Industrial Engineering of the University of Naples "Federico II" where is still in development.

The main goal of this library is to perform fast multi-disciplinary analyses of a parametrically defined aircraft model and to search for an optimized configuration. All the basic principles and approaches to aircraft preliminary design and analysis, followed during the development of the tool, are well described in some Aircraft Design textbooks. [1] [2] [3] [4] [5] [6] [7].

One of the main features of JPAD lies in the smart management of both the aircraft parametric model, which is conceived as a set of interconnected and parameterized components, and the available analyses. The library has been developed with the purpose of simplify the composition of the input file for the user and doing fast analysis with a satisfying grade of accuracy [8] [9]. Section 2 will show the library architecture and its main advantages. Another key point is the possibility to easily interface JPAD with other external tools in order to achieve a higher level of accuracy.

As stated in [10], the JPAD library is an alternative to a plethora of similar software tools, both freeware and commercial. Most of these tools have an important history, and many of them have been in use for decades. Some of them were conceived with poor software design criteria, have a rigid textual input and come with no visualization features.

This is the main reason why JPAD has been developed paying a lot of attention to simplicity and flexibility. Moreover, it has been conceived as an open-source tool differently from the most popular aircraft design programs available, such as Advance Aircraft Analysis [11], RDS [12] or Piano [13].

JPAD is a general computational library that includes several modules, among which is important to highlight the aerodynamic and stability ones. These are based on several prediction methodologies, developed by the DAF research group of the University of Naples "Federico II", like the ones used for the fuselage [14] [15] or the vertical tail [16] [17] analyses. The capability to develop such methodologies derives from the experience gained by the group, both through numerical analyses and wind tunnel tests, during several years of activity in the field of application of regional turboprop and general aviation aircraft, as explained in [18] [19] [20].

Since JPAD must perform also multi-disciplinary optimizations, the DAF group has growth also in this field of application as described in [21] [22] [23] [24].

2 SOFTWARE STRUCTURE

To achieve a clear input file organization a considerable study has been done. The result is an input structure composed by different XML files with the purpose to allow users to easily manage all data needed to execute the desired analyses. In Fig. 1 the entire structure of the software is schematized. It is possible to clearly note that there are two main blocks: input and core.

The input block is defined by two main parts: aircraft and analyses definitions. The first one defines the aircraft model in parametric way using a main file (Aircraft.xml, see Fig. 3) which collects all the components, linking them to their related xml file (i.e. fuselage.xml, vtail.xml, and so on) which contains all geometrical data.

The second one defines all necessary data for each analysis presents into core module (see Fig. 2). Since the aircraft model contains only geometrical data, it is necessary to define several further data referred to each analysis.

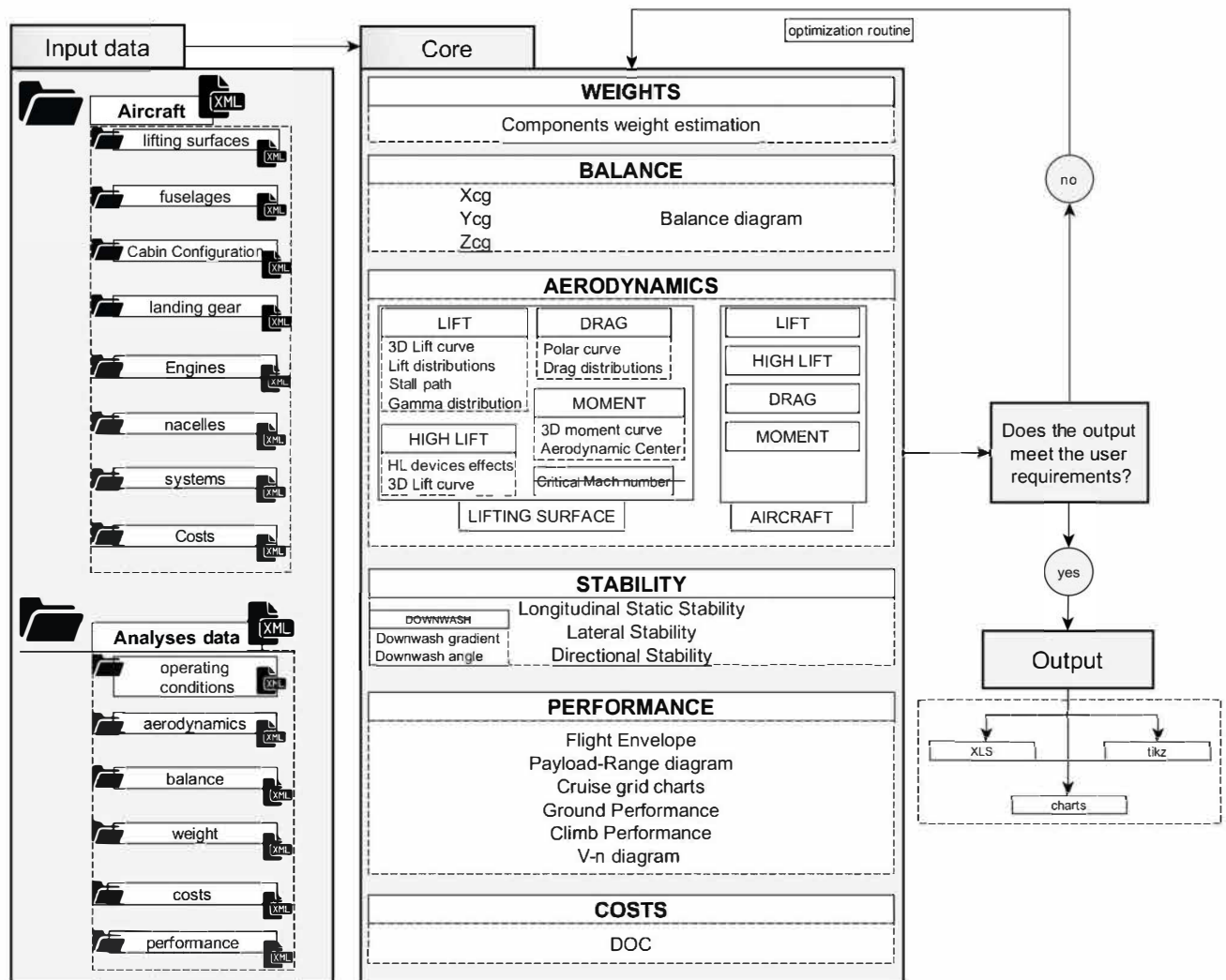



Figure 1: JPAD schematic flow-chart.

```

1 <?xml version="1.0" encoding="utf-8"?>
2 <jpad_config>
3   <!-- Input data, shared across analysis tasks -->
4   <global_data>
5     <n_limit>2.5</n_limit>
6     <cruise_lift_coefficient>0.45</cruise_lift_coefficient>
7     <reference_range unit="mm">825</reference_range>
8     <maximum_altitude_at_maximum_speed unit="ft">16000</
9     <maximum_cruise_mach_number>0.43</
10    <maximum_cruise_mach_number>
11    <optimum_cruise_altitude unit="ft">16000</
12    <optimum_cruise_altitude>
13    <optimum_cruise_mach_number>0.45</
14    <optimum_cruise_mach_number>
15    <block_time unit="h">1.5</block_time>
16    <flight_time unit="h">1.35</flight_time>
17  </global_data>
18  <!-- Required analysis tasks -->
19  <analyses id="JPAD Test analysis">
20    <weights
21      file="analysis_weights.xml"
22      method_fuselage="JENKINSON"
23      method_wing="ROSKAM"
24      method_htail="JENKINSON"
25      method_vtail="JENKINSON"
26      method_canard=""
27      method_macell="TORENBECK_1976"
28      method_landing_gears="ROSKAM"
29      method_systems="TORENBECK_2013"
30    /> <!-- method_XXX="AVERAGED" if not present -->
31    <balance
32      file="analysis_balance.xml"
33      method_fuselage=""
34      method_wing=""
35      method_htail=""
36      method_vtail=""
37      method_canard=""
38    /> <!-- method_XXX="AVERAGED" if not present -->
39    <aerodynamics file="analysis_aerodynamics.xml"/>
40    <performance file="analysis_performance.xml"/>
41    <costs file="analysis_costs.xml"/>
42  </analyses>
43 </jpad_config>

```

Figure 2: An example of the analysis.xml file.


Aircraft.xml

```

1 <?xml version="1.0" encoding="utf-8"?>
2 <jpad_config>
3   <aircraft id="JPAD Test Aircraft DAF-2016" type="JET" regulations="FAR_25">
4     <global_data>
5       <cabin_configuration file="cabin_configuration.xml">
6         </cabin_configuration>
7       </global_data>
8       <lifting_surfaces>
9         <wing file="wing.xml">
10           <position>
11             <x unit="m">12.0</x>
12             <y unit="m">0.0</y>
13             <z unit="m">-0.6</z>
14           </position>
15           <rigging_angle unit="deg">2.0</rigging_angle>
16         </wing>
17         <horizontal_tail file="htail.xml">
18           <vertical_tail file="vtail.xml">
19             </vertical_tail>
20           </horizontal_tail>
21         </lifting_surfaces>
22         <fuselages>
23           <fuselage file="fuselage.xml">
24             </fuselage>
25           </fuselages>
26           <power_plant>
27             <engine file="engineTurboprop.xml">
28               <engine file="engineTurboprop.xml">
29                 </engine>
30             </power_plant>
31             <macelle file="macelle.xml">
32               <macelle file="macelle.xml">
33                 </macelle>
34             </macelle>
35             <landing_gears file="landing_gear.xml">
36               </landing_gears>
37             <systems file="systems.xml">
38               </systems>
39             </aircraft>
40           </jpad_config>

```

Wing.xml

```

1 <?xml version="1.0" encoding="utf-8"?>
2 <jpad_config>
3   <aircraft id="JPAD Test Aircraft DAF-2016" type="JET" regulations="FAR_25">
4     <global_data>
5       <main_spar_non_dimensional_position type="PERCENT_CHORD">
6         ref_to="LOCAL_CHORD">0.25</
7         main_spar_non_dimensional_position>
8       <secondary_spar_non_dimensional_position type="
9         PERCENT_CHORD" ref_to="LOCAL_CHORD">0.55</
10        secondary_spar_non_dimensional_position>
11       <composite_correction_factor>0.1</
12       composite_correction_factor>
13       <roughness unit="m">0.405e-5</roughness>
14     </global_data>
15     <equivalent_wing>
16       <surface unit="m">36.9</surface>
17       <aspect_ratio>13.09</aspect_ratio>
18       <non_dimensional_spar_station_kink>0.363</
19       non_dimensional_spar_station_kink>
20       <sweep_quarter_chord unit="deg">12.56</sweep_quarter_chord>
21       <twist_at_tip unit="deg">2.5</twist_at_tip>
22       <dihedral unit="deg">2.5</dihedral>
23       <taper_ratio>0.55</taper_ratio>
24       <x_offset_root_chord_leading_edge unit="m">0.477</
25       x_offset_root_chord_leading_edge>
26       <x_offset_root_chord_trailing_edge unit="m">0.367</
27       x_offset_root_chord_trailing_edge>
28       <airfoil>
29         <airfoil_root file="nac63209.xml">
30           <airfoil_kink file="nac63209.xml">
31             <airfoil_tip file="nac63209.xml">
32               </airfoil>
33             </airfoil_kink>
34           </airfoil_root>
35         </airfoil>
36       </equivalent_wing>
37       <panels>
38         <panel id="Inner panel">
39           </panel>
40         <panel id="Outer panel" linked_to="Inner panel">
41           </panel>
42       </panels>
43       <asymmetric_flaps>
44       </asymmetric_flaps>
45       <slats>
46       </slats>
47       <asymmetric_flaps>
48       </asymmetric_flaps>
49       <spoilers>
50       </spoilers>
51     </aircraft>
52   </jpad_config>

```

Figure 3: An extract from a general aircraft.xml input file.

The structure described above allows to generate different aircrafts, or different configurations of the same model, combining different components. Table 1 shows how to generate several aircrafts starting from a given reference model, by changing the wing and the power plant.

Table 1: Creation of different aircraft models from the same reference

REFERENCE	NEW MODEL 1	NEW MODEL 2	NEW MODEL 3
FUSELAGE	FUSELAGE	FUSELAGE	FUSELAGE
WING	WING 1	WING 2	WING 3
HORIZONTAL TAIL	HORIZONTAL TAIL	HORIZONTAL TAIL	HORIZONTAL TAIL
VERTICAL TAIL	VERTICAL TAIL	VERTICAL TAIL	VERTICAL TAIL
POWER PLANT	POWER PLANT 1	POWER PLANT 2	POWER PLANT 3
LANDING GEAR	LANDING GEAR	LANDING GEAR	LANDING GEAR

The possibility to generate a series of different aircrafts in a simple and fast way, allows to easily perform comparisons between these latter. For example, assuming different wings and engines as shown in Table 1, it is possible to estimate the effects that some design parameters have on a specific output. Fig. 4 shows how the FAR-25 take-off field length behaves with different values of the wing surface and the engine static thrust at fixed aircraft maximum take-off weight. This feature plays also a key role in the optimization process described in Fig. 1.

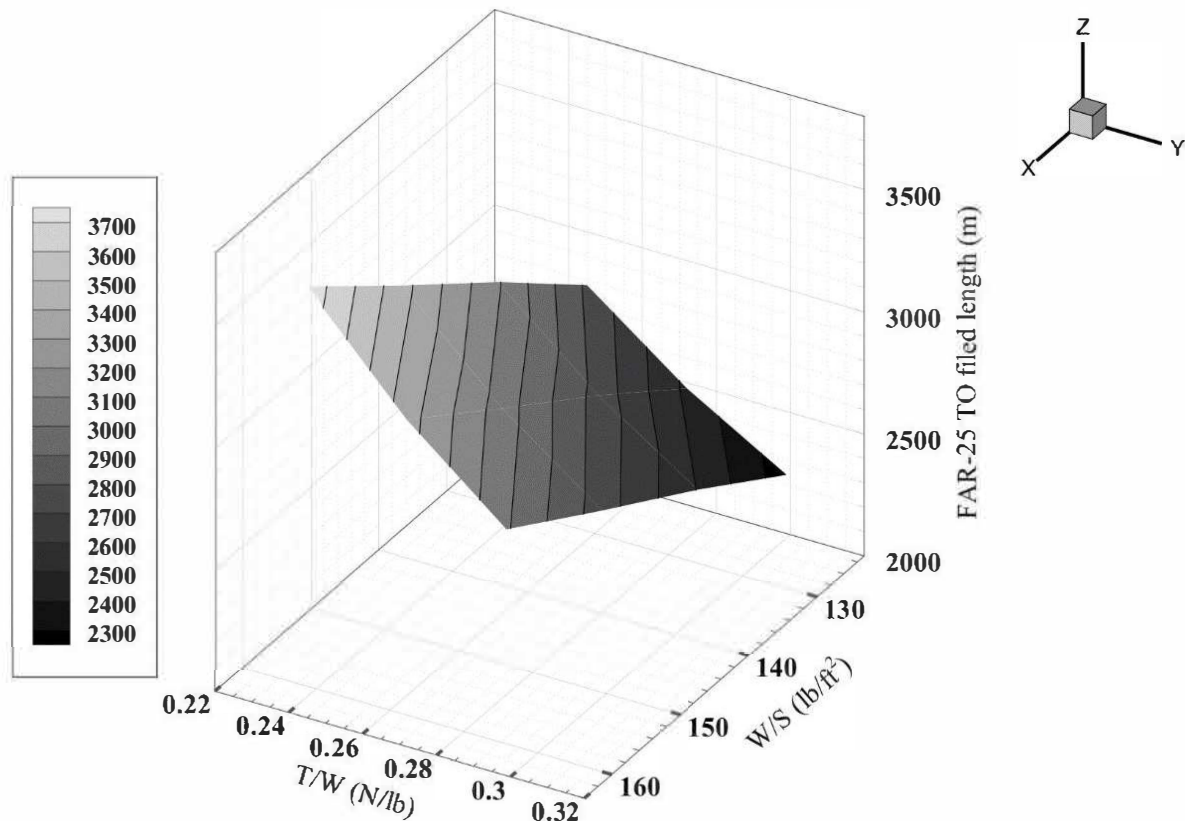


Figure 4: FAR-25 take-off field length at different wing loadings W/S and thrust-weight ratios T/W .

In the same way, it is possible to perform a complete analysis (those present into core block in Fig. 1), or a specific one, combining different analyses files (see Fig. 2). This allows an easier evaluation of generic cost function during optimization tasks resulting in reduced amount of computational costs required for this kind of operations.

Besides the input, the second main block is the core which manages all the available analyses. This contains several independent modules, as shown in the Fig. 1, that deals with following application fields.

- **Weights:** estimates the aircraft weight breakdown starting from a first guess maximum take-off weight and some mission requirements. In particular, it evaluates each aircraft component mass using well-known semi-empirical equations [1] [5] [6] [7]
- **Balance:** estimates the center of gravity position related to each weight condition and draws the balance diagram.
- **Aerodynamics and Stability:** the aerodynamics module estimates all the aerodynamic characteristics concerning lift, drag and moments coefficients at different operating conditions for each aircraft component (wing, tails, fuselage and nacelles). Whereas the stability module gives useful data about static stability of the whole aircraft considering non-linearity effects as well.
- **Performance:** evaluates most important aircraft performance such as Payload-Range diagram, mission profile, cruise flight envelope, ground performance, climb performance and the cruise grid chart.
- **Costs:** estimates the DOC breakdown.

JPAD allows to obtain different kind of output: charts and data in XLS format (as shown in Fig. 5). In this way, the comparison between two or more aircraft (or simply between slightly different configurations of the same aircraft) is easier and more efficient.

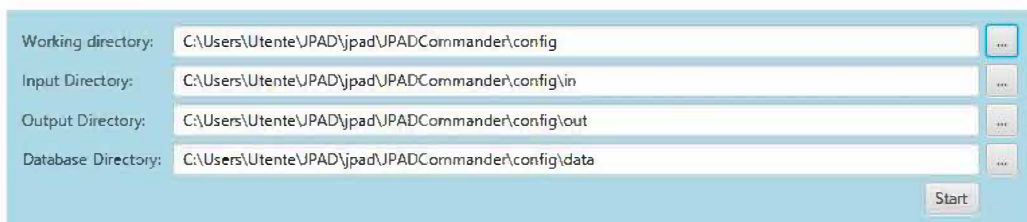
Description	Unit	Value
Ground roll distance	m	763.4976659
Rotation distance	m	165.4983558
Airborne distance	m	231.5465274
AEO take-off distance	m	1160.542549
FAR-25 take-off field length	m	1334.623931
Balanced field length	m	1225.663607
Ground roll distance	ft	2504.913602
Rotation distance	ft	542.9736083
Airborne distance	ft	759.6670847
AEO take-off distance	ft	3807.554295
FAR-25 take-off field length	ft	4378.687439
Balanced field length	ft	4021.20606
Stall speed take-off {VsTO}	m/s	53.67149021
Decision speed {V1}	m/s	55.82318509
Rotation speed {V_Rot}	m/s	56.35506473
Minimum control speed {VMC}	m/s	46.98027511
Lift-off speed {V_LO}	m/s	60.77409554
Take-off safety speed {V2}	m/s	63.95159767
Stall speed take-off {VsTO}	kn	104.3290307
Decision speed {V1}	kn	108.5115909
Rotation speed {V_Rot}	kn	109.5454822
Minimum control speed {VMC}	kn	91.32234902
Lift-off speed {V_LO}	kn	118.1353909
Take-off safety speed {V2}	kn	124.3119609
V1/VsTO		1.04
V_Rot/VsTO		1.05
VMC/VsTO		0.88
V_LO/VsTO		1.13
V2/VsTO		1.20
Take-off duration	s	31.51824683

Figure 5: A detail of the output XLS file for the performance analysis.

An important element of JPAD is the graphical user interface (GUI). The GUI of JPAD is completely designed using the JavaFX library [25] and the related development tool JavaFX Scene Builder [26]. Building the GUI means to find a perfect compromise between functionalities and simplicity. In fact, JPAD must handle the management of an entire aircraft as well as complex multi-disciplinary analyses and optimizations. To make as easier as possible the use of this tool, a sort of wizard paradigm has been used to guide the user from the definition of the aircraft model to the output visualization, passing through the analyses manager.

At first, as shown in Fig. 6, the user must define all the folders in which the software expects to find the following resources:

- the input files;
- the external resources, such as engine decks and databases containing data about methodologies formulation;
- the folder in which all the output files and charts must be stored.



Working directory:	C:\Users\Utente\JPAD\jpad\JPADCommander\config	...
Input Directory:	C:\Users\Utente\JPAD\jpad\JPADCommander\config\in	...
Output Directory:	C:\Users\Utente\JPAD\jpad\JPADCommander\config\out	...
Database Directory:	C:\Users\Utente\JPAD\jpad\JPADCommander\config\data	...

Start

Figure 6: Definition of the required folders.

After that the user must follow the guideline of the main three buttons shown in Fig. 7. Focusing on the input manager, the user can simply define an aircraft model by loading it from an external XML file, or by choosing it among a list of possible default aircrafts.

The structure of this manager has been designed using different tabs; this with the aim of giving a complete overview of the aircraft, and its component, without having to manage too many data all in one time.

As shown in Fig. 8, each tab is provided with an input area with all the text fields related to every single data, a text area with a detailed overview of the object in exam, and the graphic representation of the component with its three views.

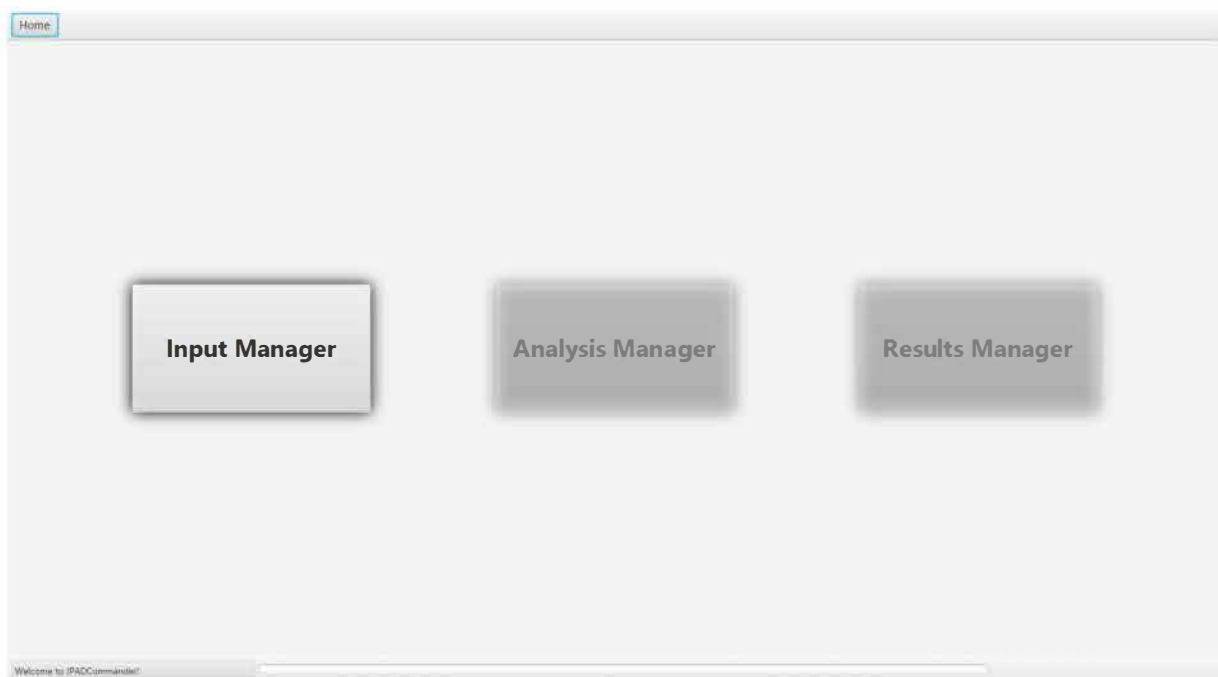


Figure 7: JPAD GUI main view.

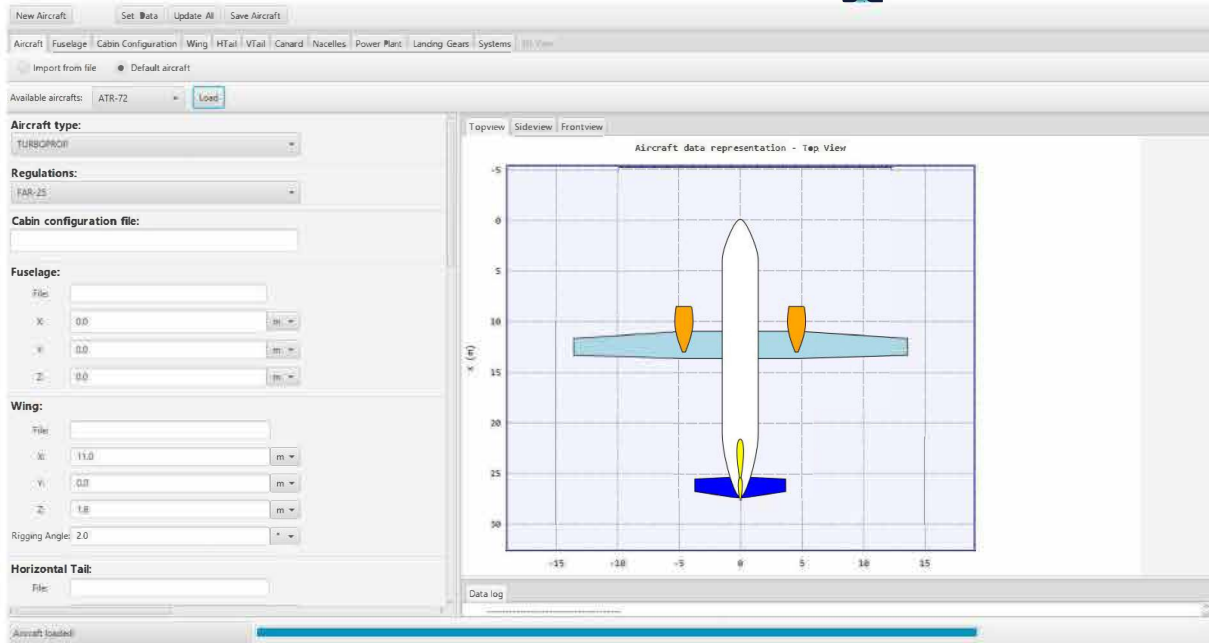


Figure 8: JPAD GUI input manager view.

3 CASE STUDY: ATR-72

To show the potentiality of the JPAD library, a multi-disciplinary analysis has been performed assuming a parametric aircraft model similar to the ATR-72. The analysis results that will be reported concerns lift and longitudinal static stability analysis (including the non-linear effects) as well as some of the main performance and the DOC. These latter will also be compared to public domain data from online brochures and flight manuals.

3.1 Aerodynamics and Longitudinal Stability

Using JPAD, is possible to evaluate the lift coefficient curve both of an airfoil, by means of the internal aerodynamic database based on [27], and of a 3D lifting surface as shown in the Fig. 9 using data in Table 2.

Table 2: ATR-72 model airfoil data

Station	Airfoil	Re	$C_{L\max}$
Root	NACA 23018	$6.28 \cdot 10^6$	1.65
Kink	NACA 23018	$6.28 \cdot 10^6$	1.65
Tip	NACA 23015	$4.41 \cdot 10^6$	1.70

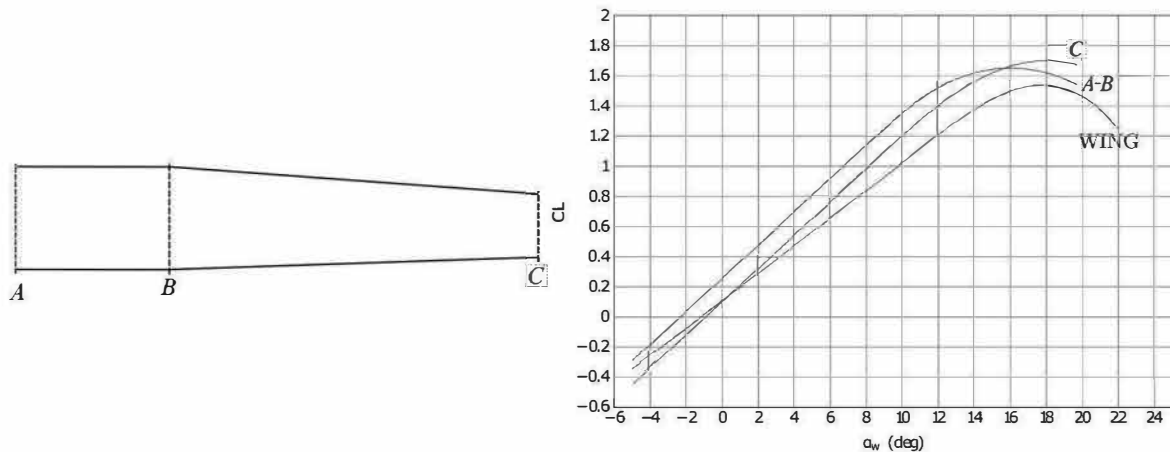


Figure 9: 2D and 3D lift results for regional turboprop. $M=0.2$. [28]

All aerodynamic results are then incorporated in the module in charge of the longitudinal static stability analysis, which can be executed for a given aircraft at a fixed flight condition.

An important JPAD innovation is that the downwash gradient and the related angle have been evaluated considering a variable distance between the horizontal tail and the wing, improving the formulations proposed in [29]. In this way, the downwash calculation turns out to be more accurate.

The distances in the downwash angle formula are not considered between the aerodynamic center of wing and the aerodynamic center of horizontal tail as usual, but variable and they are measured from the vortex shed plane behind the wing to the horizontal tail. In order to perform this improved method an iterative process is necessary.

First, referring to Fig. 10, it is necessary to evaluate the geometrical distances m_0 and x_0 described below.

- x_0 : distance between the aerodynamic centre of the wing and the aerodynamic centre of the horizontal tail calculated along the x axis.
- m_0 : distance between the aerodynamic centre of the horizontal tail and the horizontal line passing through the trailing edge of the airfoil root of the wing.

Then, starting from a value of $\alpha_a = 0^\circ$ (and $\varepsilon = 0^\circ$) and proceeding with an increase of angle of attack equal to $\Delta\alpha$, it is possible to evaluate the distances m and r geometrically for each angle of attack using Eq.1 and Eq. 2. These two distances allow to calculate the downwash angle using the formula proposed in [29], but they depend, in turn, on the downwash angle, so an iterative process is necessary.

$$m|_i = d \sin(\psi + i_w - \alpha_{0L} - i\Delta\alpha + \varepsilon) \quad (1)$$

$$x|_i = d \cos(\psi + i_w - \alpha_{0L} - i\Delta\alpha + \varepsilon) + \frac{3}{4}c_r \cos(-\alpha_{0L} - i\Delta\alpha + \varepsilon) \quad (2)$$

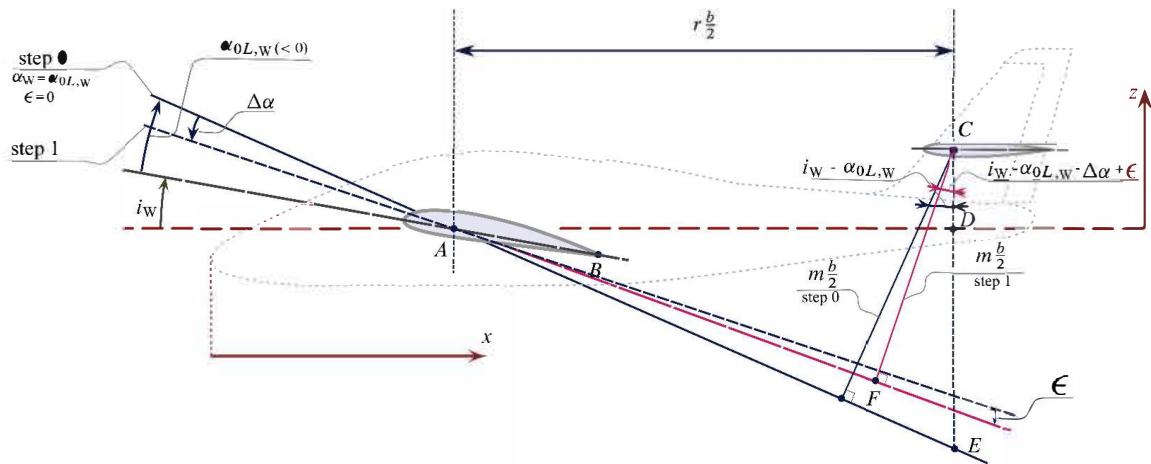


Figure 10: Arm definitions for downwash evaluation.

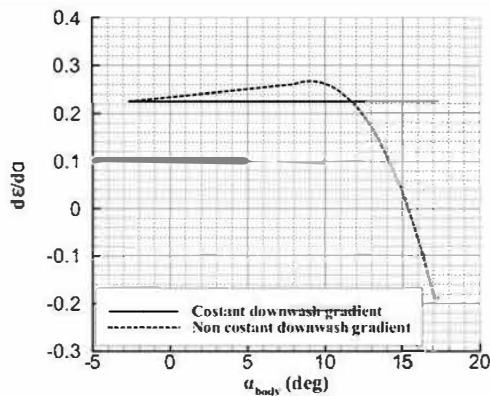


Figure 11: Variability of downwash gradient at M=0.4. [28]

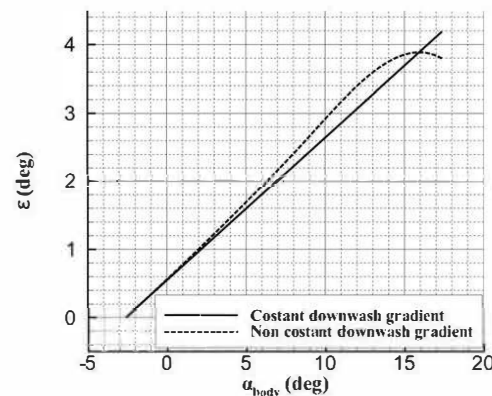


Figure 12: Variability of downwash angle at M=0.4. [28]

The stability calculation considers also the propulsion effects, the fuselage pitching moment effect [14], and the pendular stability due to the axial component of the aerodynamic force.

The charts from Fig. 11 to Fig. 15 show the results obtained for the regional turboprop under examination.

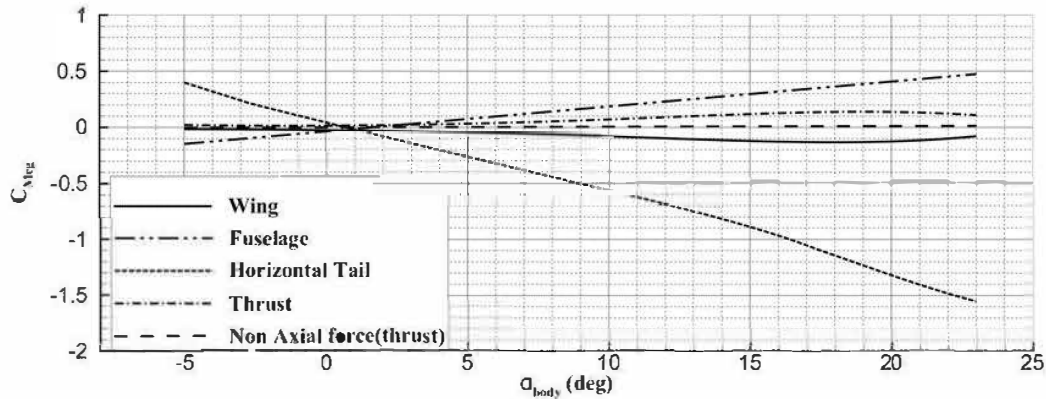


Figure 13: $C_{M_{cg}}$ vs. α_b of aircraft components – Cruise condition. [28]

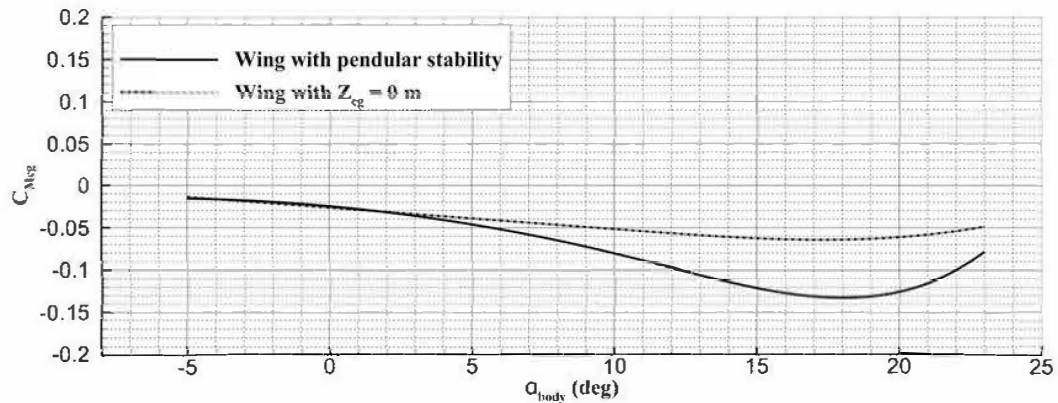


Figure 14: $C_{M_{cg}}$ vs. α_b for the wing with and without pendular stability – Cruise condition. [28]

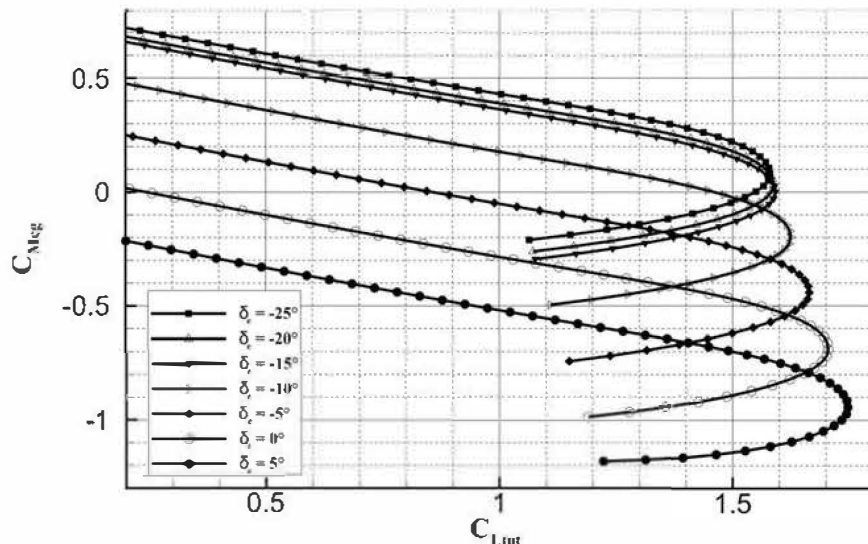


Figure 15: $C_{M_{cg}}$ vs. $C_{L_{tot}}$ with elevator deflections – Cruise condition. [28]

3.2 Performance

Most of the performance analyses carried out by JPAD are simulation-based to achieve a higher fidelity level with respect to classical semi-empirical formulations. One remarkable example can be found in [10] concerning the ground performance evaluation.

JPAD can perform in less than 30 seconds the following performance calculations using the results of the aerodynamics and stability module.

- Take-off
- Climb (AEO and OEI)
- Cruise
- Descent
- Landing
- Mission profile analysis
- Payload-Range
- Flight maneuvering and gust envelope

To show the level of accuracy achieved by JPAD, some relevant performance will be compared with the data from the brochure of the ATR-72 [30]. Fig. 16 to Fig. 18 show respectively the Payload-Range chart, the balanced field length evaluation and the cruise flight envelope; while Table 3 provides the above-mentioned numerical comparisons. To perform these analyses a turboprop engine deck has been modeled starting from the ones proposed in literature.

Table 3: Numerical comparisons between JPAD performance and public domain data

PERFORMANCE	JPAD	ATR-72 brochure [30]	Difference (%)
Design Range (with 68 passengers at 95kg)	890 Nm	890 Nm	<1.0%
Balanced Field Length	1225 m	1223 m	<1.0%
FAR-25 Landing Field Length	1162 m	1048 m	10.9%
Max cruise Mach number at 17kft	0.440	0.444	<1.0%
Service ceiling AEO	26709 ft	25000 ft	6.8%
Service ceiling OEI	14712 ft	14200 ft	3.6%

As can be seen from Table 3, the maximum difference between the JPAD output and the brochure data is never bigger than 11% proving the reliability of the library. The biggest difference can be found in the FAR-25 landing field length and this may be due to the use of a simplified semi-empirical evaluation of the airborne phase, or to the uncertainty of some simulation parameters of the ground roll phase.

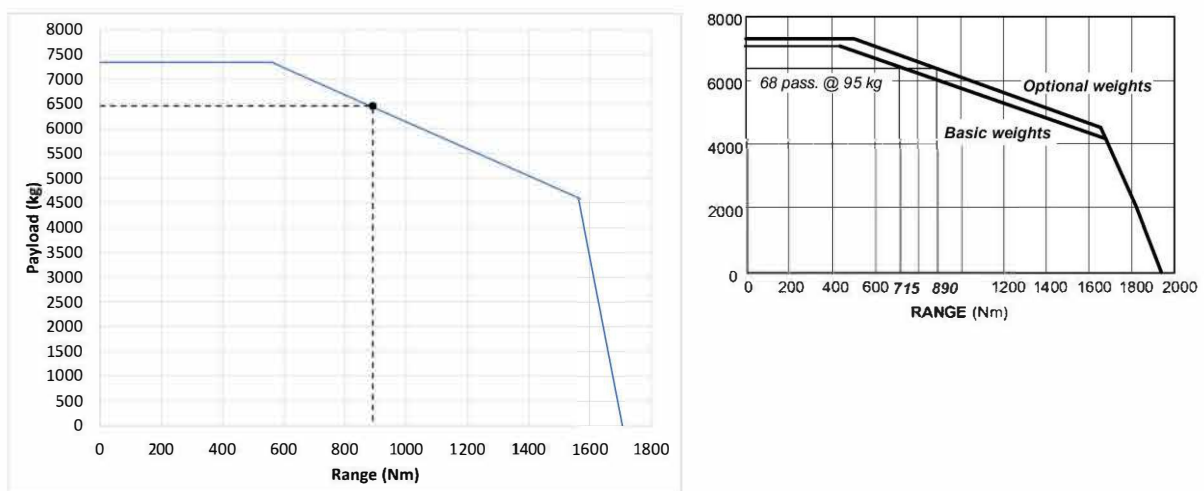


Figure 16: Payload-Range comparison between JPAD (left) and the ATR-72 brochure [30] (right) for the optional weights condition.

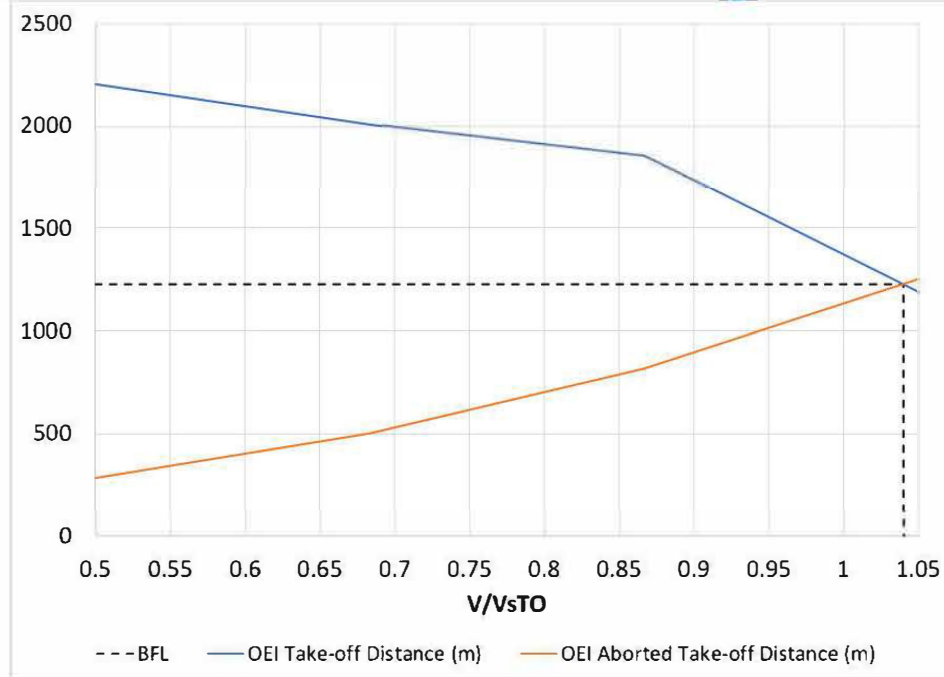


Figure 17: Balanced Field Length evaluation in JPAD

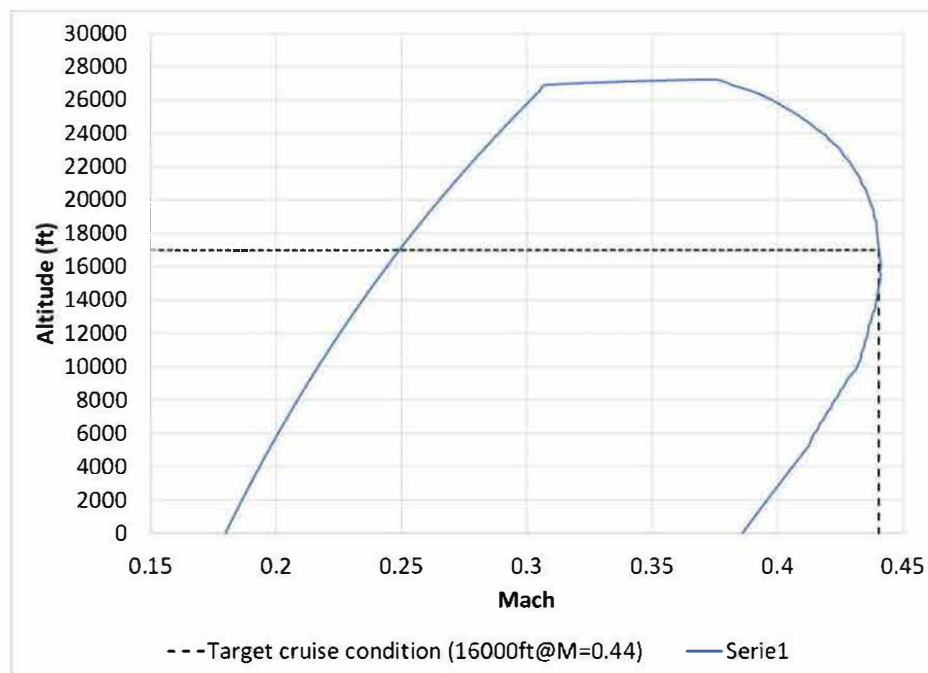


Figure 18: Cruise flight envelope evaluation in JPAD

3.3 Costs

An import feature of JPAD is the capability of the estimation of the Direct Operating Costs (DOC). This concerns flight operations and consider different items:

- **Capital costs:** depreciation, interest, and insurance.
- **Fuel cost.**
- **Charges:** landing, navigation, ground handling, noise, emissions.
- **Crew costs:** flight and cabin.
- **Direct maintenance:** airframe and engine

To estimate these cost items, the methodologies defined by AEA [31] for capital, fuel, a part of charges (landing, navigation and ground-handling) and crew costs has been implemented while the ATA [32] method has been used for direct maintenance costs. Noise charges are calculated by using the formulation recommended by the Transport Aircraft Noise Classification Group (TNAC) within the European Civil Aviation Conference (ECAC) [33] [34]. The emissions charges are estimated using formulation prescribed by ICAO in annex 16 volume 2 [35]. The equations implemented into the costs module of the code are reported in the Table 4 (from Eq. (3) to Eq. (19)).

Table 4 DOC equations

Capital costs	Depreciation	$DOC_{DEP} = \frac{TI}{DP} (1 - RV)$	(3)
	Interest	$DOC_{INS} = R_a \cdot ADP$	(4)
	Insurance	$DOC_{INT} = R_i \cdot TI$	(5)
Fuel cost		$DOC_{FUEL} = P_{fuel} \cdot m_{block\ fuel}$	(6)
Charges	Landing	$DOC_{ldg} = K_{ldg} \cdot MTOM$	(7)
	Navigation	$DOC_{nav} = K_{nav} \cdot R \cdot \sqrt{\frac{MTOM}{50}}$	(8)
	Ground-Handling	$DOC_{grd} = K_{grd} \cdot PL$	(9)
	Noise	$DOC_{noise} = C_{noise} \times \left(\frac{10^{(L_{approach} - Ta)/10} + 10^{((L_{flyover} + L_{lateral})/2 - Ta)/10}}{10^{((L_{flyover} + L_{lateral})/2 - Ta)/10}} \right)$	(10)
	Emissions: NOx	$DOC_{NOx} = C_{NOx} \cdot m_{NOx, LTO} \cdot a$ (11) $DOC_{CO} = C_{CO} \cdot m_{CO, LTO} \cdot a$ (12) $DOC_{HC} = C_{HC} \cdot m_{HC, LTO} \cdot a$ (13)	
Crew costs	Flight	$DOC_{COCKPIT\ CREW} = LR_{COCKPIT} \cdot n_{cm}$	(14)
	Cabin	$DOC_{CABIN\ CREW} = LR_{CABIN} \cdot n_{cm}$	(15)
Direct maintenance costs	Airframe: Material	$DOC_{AF\ MAT} = \frac{(C_{FHa} \cdot t_f + C_{FCa})}{V_B \cdot t_B}$ (16) $C_{FHa} = 3.08 \cdot \frac{C_a}{10^6}$ $C_{FCa} = 6.24 \cdot \frac{C_a}{10^6}$	
	Labour	$DOC_{AF\ LAB} = \frac{(K_{FHa} \cdot t_f + K_{FCa}) \cdot LR \cdot \sqrt{M}}{V_B \cdot t_B}$ (17) $K_{FCa} = 0.05 \cdot \frac{W_a}{1000} + 6 - \frac{630}{(W_a/1000 + 120)}$ $K_{FHa} = 0.59 \cdot K_{FCa}$	
	Engine: Material	$DOC_{E\ MAT} = \frac{(C_{FHe} \cdot t_f + C_{FCe})}{V_B \cdot t_B}$ (18) $C_{FCe} = 2.0 \cdot n_e \cdot \frac{C_e}{10^5}$ $C_{FHe} = 2.5 \cdot n_e \cdot \frac{C_e}{10^5}$	



	Labour	$DOC_{E LAB} = \frac{(K_{FHe} \cdot t_f + K_{FCe}) \cdot LR}{V_B \cdot t_B} \quad (19)$ $K_{FCe} = \left(0.3 + 0.03 \cdot \frac{T}{1000} \right) \cdot n_e$ $K_{FHe} = \left(0.6 + 0.027 \cdot \frac{T}{1000} \right) \cdot n_e$
--	--------	--

Table 5 Economic assumptions for DOC

Economic Assumptions	
Life span	12 years
Residual value	0.2
No. seats	68
Aircraft price	14.4 Mil.\$
Engine price (each)	1.0 Mil.\$
Spares	1.84 Mil.\$
Interest	5.0% per year
Insurance	1.0% per year
No. of flights	2700 flights
Utilisation	2484 hr/year
Block Time	0.92 hr
Block Fuel (mission)	611 kg
Fuel Price	0.8 \$/gal

Table 6 Data for DOC estimation

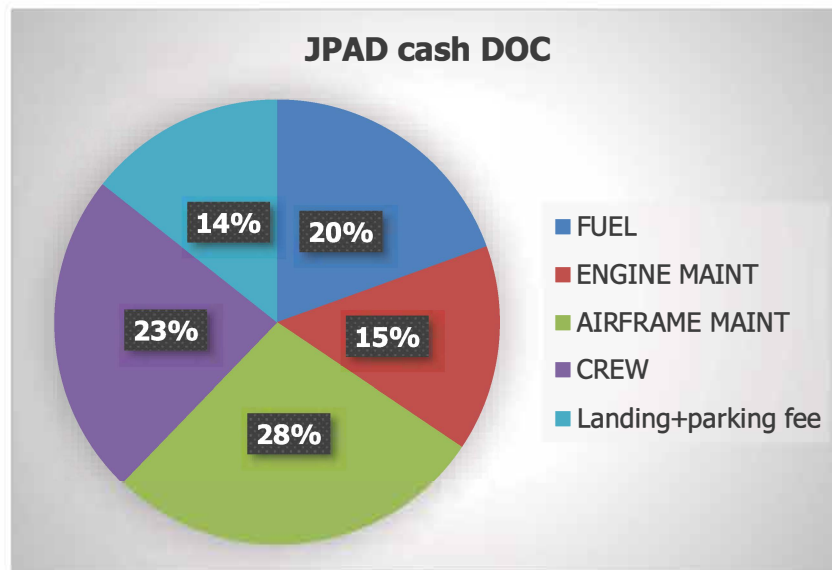
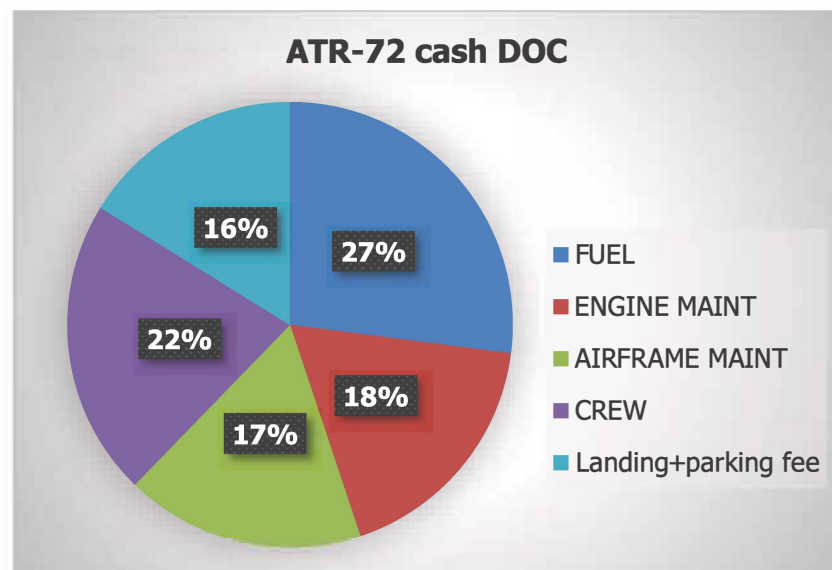
Performance	
Range (Mission)	200 nm
Mach cruise	0.44
Power	2750 shp
SFC	0.45 lbm/lbs*hr
TO Thrust	7700 lbs
No. Engines	2
Weights	
MTOW	22000 Kg
OEW	12950 Kg
PAYLOAD	7050 Kg
FUEL max	5000 Kg
Engine Weight	480 Kg
Airframe Weight	11990 Kg

In this section, to compare the JPAD results with respect to data present in a ATR-72 brochure [30], only the cash DOC composed by fuel, crew, maintenance and charges has been considered. In Table 5 and Table 6 the economic assumptions and weights and performance data used for the comparison are respectively resumed.

The results are shown in Table 7 in terms of cash DOC per trip and pie charts in Fig. 19 and Fig. 20. It is possible to see a good agreement except for the airframe maintenance. This is due to lack of public domain data, both for engine and airframe, which can be useful to conceive a more accurate methodology. The difference in landing charges may be due to the different data environment. In fact, ATR-72 brochure refers to US environment while JPAD uses the formulation suggested by European airlines.

Table 7 JPAD costs results comparison

	BROCHURE (\$/trip) [30]	JPAD (\$/trip)
Fuel	182	183
Engine maintenance	120	148
Airframe maintenance	117	261
Crew	145	147
Landing fee	109	135
Total cash DOC	673	868

**Figure 19 JPAD estimation of cash DOC for ATR-72****Figure 20 Cash DOC ATR-72 [30]**

CONCLUSION

The purpose of this work was to provide a comprehensive overview of JPAD (Java toolchain of Programs for Aircraft Design). The software structure and the results obtained from a case study has been showed in order to verify the code effectiveness to perform fast multidisciplinary analyses. The first step is to define the geometry by composing different xlm files (fuselage.xml, wing.xml, and so on). In this way is possible to generate different aircrafts in a simple and fast way and it allows to easily perform comparisons between several aircrafts. This feature plays a key role in the optimization process. In similar manner, user defines the analyses which the code have to perform by filling out the appropriate xml file (Analysis_Weights.xml, Analysis_Performance.xml, and so on). Results are clearly collected into excel files. The entire process lasts only a few seconds (less than a minute). The research group is currently working on the communication of JPAD with external tools such as AVL and USAF Digital Datcom.

ACKNOWLEDGMENT

The research presented in this paper has been performed in the framework of the project CERVIA PON03PE_00124_1 (Metodi di CERTificazione e Verifica Innovativi ed Avanzati) proposed by DAC (Campania Aerospace District) and financed by the Italian MIUR (Italian Ministry for Research and Education).

REFERENCES

- [1] L. Jenkinson, P. Simpkin e D. Rhodes, *Civil Jet Aircraft Design*, London: Arnold Publishers, 1999.
- [2] L. Nicolai e G. Charichner, *Fundamentals of Aircraft and Airship Design*, Reston, Virginia: AIAA Education Series, 2010.
- [3] E. Obert, *Aerodynamic Design of Transport Aircraft*, Delft, The Netherlands: IOS Press, 2009.
- [4] C. Perkins e R. Hage, *Airplane Performance Stability and Control*, New York, Washington: Wiley, 1949.
- [5] D. Raymer, *Aircraft Design: A Conceptual Approach*, Washington DC: AIAA Education Series, 1992.
- [6] J. Roskam, *Airplane Design Part I-VI*, Lawrence, KS: DAR Corporation, 2000.
- [7] E. Torenbeek, *Advanced Aircraft Design*, Delft, The Netherlands: Wiley, 2013.
- [8] F. Nicolosi, A. De Marco, L. Attanasio e P. Della Vecchia, «Development of a Java-Based Framework for Aircraft Preliminary Design and Optimization,» *Journal of Aerospace Information Systems*, 13(6), pp. 234-242, 2016.
- [9] F. Nicolosi, A. De Marco, L. Attanasio e D. Gambardella, «Development of a Java-based framework for aircraft preliminary design and optimization,» *16th AIAA/ISSMO Multidisciplinary Analysis and Optimization Conference*, 2015.
- [10] V. Trifari, M. Ruocco, V. Cusati, F. Nicolosi e A. De Marco, «Java framework for parametric aircraft design – ground performance,» *Aircraft Engineering and Aerospace Technology*, 89(4), 2017.
- [11] D. Corporation, "Advanced Aircraft Analysis," DAR Corporation, [Online]. Available: <http://www.darcorp.com/Software/AAA/>. [Accessed 31 07 2017].
- [12] D. Raymer, "RDS," [Online]. Available: <http://www.aircraftdesign.com/rds.shtml>. [Accessed 31 07 2017].
- [13] Lissys, "Piano 5 for Windows," Lissys Ltd, [Online]. Available: <http://www.piano.aero/>. [Accessed 31 07 2017].
- [14] F. Nicolosi, P. Della Vecchia, D. Ciliberti e V. Cusati, «Fuselage Aerodynamic Prediction Methods,» *Aerospace Science and Technology, AESCTE*, vol. 55, pp. 332-343, 2016.
- [15] F. Nicolosi, P. Della Vecchia, D. Ciliberti e V. Cusati, «Development of a new Preliminary Design Metodologies for Regional Turboprop by CFD Analysis,» *20th ICAS Conference, St. Petersburg (Russia)*, 2014.

- [16] F. Nicolosi, P. Della Vecchia e D. Ciliberti, «Aerodynamic interference issues in aircraft directional control,» *ASCE's Journal of Aerospace Engineering*, vol. 28, n. 1, 2015.
- [17] F. Nicolosi, P. Della Vecchia e D. Ciliberti, «An investigation on vertical tailplane contribution to aircraft side force,» *Aerospace Science and Technology (Elsevier)*, vol. 1, n. 28, pp. 401-416, 2013.
- [18] L. Pascale e F. Nicolosi, «Design and aerodynamic analysis of a light twin-engine propeller aircraft,» *26th ICAS Conference, Anchorage, US*, vol. 1, 2008.
- [19] F. Nicolosi, S. Corcione e P. Della Vecchia, «Commuter Aircraft Aerodynamic Characteristics through Wind Tunnel Tests,» *Aircraft Engineering and Aerospace Technology (Emerald)*, vol. 88, n. 4, pp. 523-534, 2016.
- [20] F. Nicolosi, P. Della Vecchia e S. Corcione, «Design and Aerodynamic Analysis of a Twin-engine Commuter Aircraft,» *Aerospace Science and Technology (Elsevier)*, vol. 40, pp. 1-16, 2015.
- [21] P. Della Vecchia, «Aerodynamic guidelines in the design and optimization of new regional turboprop aircraft,» *Aerospace Science and Technology*, vol. 38, pp. 88-104, 2014.
- [22] P. Della Vecchia, E. Daniele e E. D'Amato, «An airfoil shape optimization technique coupling parsec parameterization and evolutionary algorithm,» *Aerospace Science and Technology*, vol. 32, n. 1, pp. 103-110, 2014.
- [23] P. Della Vecchia, L. Stingo, S. Corcione, D. Ciliberti, F. Nicolosi e A. De Marco, «Game theory and evolutionary algorithms applied to MDO in the AGILE European project,» *18th AIAA/ISSMO Multidisciplinary Analysis and Optimization Conference, Denver, Colorado*, 2017.
- [24] T. Lefebvre, N. Bartoli, S. Dubreuil, M. Panzeri, R. Lombardi, P. Della Vecchia, F. Nicolosi, P. Ciampa, K. Anisimov e A. Savelyev, «Methodological enhancements in MDO process investigated in the AGILE European project,» *18th AIAA/ISSMO Multidisciplinary Analysis and Optimization Conference, Denver, Colorado*, 2017.
- [25] Oracle, "JavaFX: Getting Started with JavaFX," Oracle, [Online]. Available: <http://docs.oracle.com/javase/8/javafx/get-started-tutorial/jfx-overview.htm#JFXST784>. [Accessed 31 07 2017].
- [26] Gluon, "Scene Builder," Gluon, [Online]. Available: <http://gluonhq.com/products/scene-builder/>. [Accessed 31 07 2017].
- [27] I. Abbott e A. Von Doenhoff, *Theory of wing sections*, New York: Dover, 1959.
- [28] M. Ruocco, V. Trifari e V. Cusati, «A Java-based framework for aircraft preliminary design - Wing aerodynamic analysis module, Longitudinal static stability and control module,» *12th READ Conference, Warsaw (Poland)*, 2016.
- [29] R. Slingerland, *Prediction of Tail Downwash, Ground Effect and Minimum Unstick Speed of Jet Transport Aircraft*, Delft, The Netherlands : University of Delft, 2005.
- [30] ATR, "ATR 72-500 The Ultra Efficient Standard," [Online]. Available: http://www.aviation-broker.com/uploads/media/specs_atr_72-500.pdf. [Accessed 31 07 2017].
- [31] Association of European Airlines, «AEA Requirements,» Bruxelles, 1989.
- [32] Air Transportation Association of America, «Standard method of estimating comparative direct operating costs of turbine powered transport airplanes,» 1967.
- [33] ERLIG, *Recommendation ECAC/27-4, NOx Emission Classification Scheme*, Paris, France: European Civil Aviation Conference (ECAC), 2003.
- [34] European Union, *Amended Proposal COM 2002/683 of the European Parliament and the Council for a Directive on the Establishment of a Community Framework for Noise Classification for Civil Subsonic Aircraft of 29.11.2002*, Bruxelles, Belgium, 2002.
- [35] I. International Civil Aviation Organization, *ICAO's Policies on Charges for Airports and Air Navigation Services, Annex 16, volume 2*, 2004.

Effects of MR Damper on Flutter of a Wing/Store Configuration

A. Mazidi

Assistant Professor

School of Mechanical Engineering, Yazd University, Yazd, Iran

amazidi@yazd.ac.ir

H. Pourshamsi

Msc Student

School of Mechanical Engineering, Yazd University, Yazd, Iran

S. A. Fazelzadeh

Professor

School of Mechanical Engineering, Shiraz University, Shiraz, Iran

Fazelzad@shirazu.ac.ir

ABSTRACT

In this paper, the flutter analysis of an aircraft wing carrying an external store by means of a Magneto Rheological (MR) damper is studied. The wing performs as a thin beam with the structural model, incorporating bending-torsion flexibility and transverse shear deformation; rotary inertia and warping restraint are neglected. Thus, the wing structural model is strictly along the lines of classical beam theory and valid for long, straight, homogeneous, isotropic wings. Modified Bouk-Wen model is used to simulate the MR damper. The aeroelastic partial governing equations are determined via Hamilton's variational principle. Also, modified Peter's finite-state aerodynamic model is employed. The resulting partial differential equations are transformed into a set of ordinary differential equations through the assumed mode method. The numerical results for a wing are compared with published results and good agreement is observed. Then, simulation results for the wing with an elastically attached external store via MR damper are presented to show the effects of MR damper voltage and wing design parameters on the wing/store flutter. Results show that increasing the MR damper voltage increases the wing flutter speed and also decreases the flutter frequency.

KEYWORDS: *wing/store, flutter, MR damper*

A Study on the Micro Gravity Sloshing Modeling of Propellant Quantity Variation

Dong-yeon Lee

*Korea Advanced Institute of Science and Technology
291, Daehak-ro, Yuseong-gu, Daejeon, Republic of Korea
rpsxkfhtm@kaist.ac.kr*

Min-hyun Cho

*Korea Advanced Institute of Science and Technology
Mhcho01994@kaist.ac.kr*

Han-lim Choi

*Korea Advanced Institute of Science and Technology
hanlimc@kaist.com*

Min-jea Tahk

*Korea Advanced Institute of Science and Technology
Mjtahk317@gmail.com*

ABSTRACT

In this study, the sloshing phenomenon is analyzed for the internal fluid mass change. And the change of the sloshing modeling design variables according to the fluid mass change is also analyzed. First, the sloshing phenomenon for each case is analyzed by CFD when the internal fluid mass is fixed. An appropriate sloshing modeling structure is proposed based on the analyzed results. The PSO method, which is one of the parameter optimization methods, is used as a method for appropriately selecting design variables of proposed sloshing modeling. In the same way, assuming a situation where the internal fluid mass changes in several levels, the sloshing modeling design variables for each internal fluid mass are calculated. The internal fluid varies from 10% to 90% in 10% increments so it is divided into 9 levels. By understanding the relationship between the optimized modeling design variables and the internal fluid mass, a sloshing model can be proposed to respond to the internal fluid mass change.

KEYWORDS : Sloshing Modeling, second-order system, Parameter Optimization, Parametric Study



Numerical analysis of propeller effects on wing aerodynamic: tip mounted and distributed propulsion

*P. Della Vecchia**

**University of Naples Federico II
Phd, Assistant Professor
Via Claudio, 21 80125, Naples
pierluigi.dellavecchia@unina.it*

*D. Malgieri**

Master of Engineering

*F. Nicolosi**

Associate Professor

*A. De Marco**

Phd, Assistant Professor

ABSTRACT

The purpose of this investigation is determinate the effects of propeller on wing aerodynamic, both for a propeller mounted in the middle of the wing, and for tip mounted propeller. Especially, it is investigated how a tip-mounted propeller can decrease wing induced drag, and how distributed propulsion can increase the high-lift aerodynamic. Analyses are carried out using a Virtual Disk Model on CFD software, showing a good agreement comparing numerical results with experimental data obtained by previous works. Wing tip engine with propeller, has been employed on a general aviation aircraft wing with an installed thrust to accomplish with cruise performance, reducing the induced drag. Distributed propeller engines on the wing allows improving of low speed performance, increasing the aircraft lift coefficient. Induced drag can be reduced of about 2-3% a low cruise lift coefficient, until 8-10% at relative high cruise lift coefficient. Maximum achievable lift coefficient could be increased of about 20-30% in clean configuration, and more than 50% in flapped configuration.

KEYWORDS: *aircraft propeller simulation, tip propeller effects, distributed propulsion*

Valveless Pulsed Detonation Chamber Controlled by Hartmann Oscillators

Tudor Cuciuc
Institute for Applied Physics
Scientific researcher
5, Academiei St., Chisinau, Republic of Moldova
cuciuctud@yahoo.com

Constantin E. Hritcu
Romanian Research and Development Institute for Gas Turbines COMOTI, Iasi Branch
Head of Branch
61.bis, Dumitru Mangeron Blvd., Iasi, Jud. Iasi., 700050, Romania.

Gabriel G. Ursescu
Romanian Research and Development Institute for Gas Turbines COMOTI, Iasi Branch
Scientific researcher

Ionut Porumbel
Romanian Research and Development Institute for Gas Turbines COMOTI
Scientific researcher
220D, Iuliu Maniu Blvd., Bucharest, sector 6, 061126, Romania

Cleopatra F. Cuciumita
Romanian Research and Development Institute for Gas Turbines COMOTI
Scientific researcher

ABSTRACT

The paper presents the design of a valveless, high operation frequency pulsed detonation chamber, controlled by means of a system of shock waves generated by two supersonic jets impinging on a Hartmann oscillator. An extended review of the earlier research efforts in the field is included. Theoretical considerations regarding the operation of the pulsed detonation chamber are presented. A diagram of the proposed solution and the CAD model of the design of the experimental model that materializes the concept are also included.

KEYWORDS: *Detonation, valveless, Hartmann oscillator, supersonic propulsion*

NOMENCLATURE

C_i - Sound - fluid model constant
 β_i - Non-linear damping
 μ_i - Energy supply by velocity
 ω_{0i} - Individual initial angular frequency
 ξ_i - Linear coordinate

Subscripts:
 1,2 - Individual pipes
 Dot - first time derivative (velocity)
 Double dot - second time derivative (acceleration)

1 INTRODUCTION

The paper presents the design of a valveless, high operation frequency pulsed detonation chamber (PDC), controlled by means of a system of shock waves generated by two supersonic jets impinging on a Hartmann type resonator [1, 2]. The Hartmann resonator is an acoustic wave generator driven by shock wave oscillations in an over-expanded air jet [3]. The Mach disk occurring in the supersonic jet downstream of the nozzle is forced to oscillate in the jet axial direction in the presence of a cavity aligned with the jet flow direction and placed in a bluff body placed downstream of the supersonic jet nozzle. Usually, the bluff body is placed near the end of the first cell of the supersonic jet pattern.

Experimental investigations of such systems date back from the mid XX century [3, 4] and numerous studies and review papers have been published to the date.

The early efforts have been focused on understanding the basics of the physical mechanism behind the observed oscillations, and on the effect of various geometrical parameters of the experimental setup on the system acoustics. Morch [3] presented a series of experimental measurements of pressure oscillations and Schlieren visualizations in planar Hartmann resonators investigating the effect of the resonator geometry on the shock wave position and on the acoustic parameters, in an effort to understand the underlying physical mechanism of the observed flow instabilities.

Smith and Powell [4] investigated, by means of optical and acoustic measurements, the amplification of the aero-acoustic oscillations induced by coupling the Hartmann oscillator with a Helmholtz type oscillator, proposing a theoretical mechanism of operation based on the position of the Mach disk with respect to the supersonic jet nozzle and the Hartmann cavity. It was found that the oscillations are driven over a wide range of upstream pressures, jet-to-cavity distances and cavity dimensions, while the maximum amplitude of the shock oscillation is limited by the size of the shock cell.

The frequency and amplitude of the oscillations were determined to be a function of the location of the resonating cavity with respect to the jet nozzle [4], and of resonance cavity geometry (both length [5] and diameter [6]), influencing the emitted sound tone and intensity.

Theoretical and experimental investigations of the acoustic waves generation mechanism in a Hartmann generator were reported by Gravitt [7], highlighting the critical role of the pressure instabilities occurring in the supersonic jet exiting the nozzle which force the oscillations in the resonator channel. A theory of the source of the pulsations registered in a Hartmann - Sprenger resonator tube triggered by the jet issuing from a convergent nozzle and supported by experimental observations, was also advanced by Kawahashi and Suzuki [8].

Experimental data correlating the distance between the jet nozzle and the Hartmann resonator with the frequency of the oscillations is presented in a more recent study by Glaznev and Korobeinikov [9]. In the light of the insights into the structure of a supersonic under-expanded jet [10, 11], a novel oscillation generation mechanism, based on the data, is proposed, showing that the frequency of the oscillations is driven by the resonator length and volume. Davies [12] presented a series of Schlieren flow visualizations in a supersonic axisymmetric turbulent jet, focusing on the effect of preheating the impinging supersonic jet on the density fluctuations in the jet potential core. The interaction between a uniform, supersonic axisymmetric jet impinging on a flat plate has been investigated experimentally and theoretically by Carling and Hunt [13]. The results indicated that jet behaviour in the near wall region jet is controlled by the expansion of the jet boundary and the reflections on the boundaries.

Tam and Block [14] carried out frequency measurements in the subsonic flow over rectangular cavities, proposing a mathematical model correlating the measured tones and the pressure oscillations, based on the coupling between shear layer instabilities and acoustic feedback.

The impingement of a shear layer upon a cavity edge was examined by Rockwell and Knisely [15]. A significant change in the flow structure is observed, extending along the entire length of the shear layer. Vortical structures visualizations indicated that an impinging structure may alternatively undergo either an entire or partial sweeping inside the cavity, or an escape, involving vortex deformation and convection downstream, past the edge.

Savory [16] presented a series of experimental studies aimed at improving the acoustic power output of the oscillator by surrounding the jet with rings of various size and materials. He, along with Hartmann and Trudso [17], also proposed the addition of a stem along the jet axis in order to stabilize the flow and allow the operation of the oscillator even at large subsonic Mach numbers. Cavities of various sizes and shapes were added around the main Hartmann resonator to increase the amplitude of the oscillations and to select the propagation direction of the sound waves [6, 18]. Variable cross - section area resonator cavities were also studied [19].

A review of the self - induced flow oscillations occurring in supersonic flows, and of the underlying physical mechanisms, was published by Jungowski [20], including the case of free jets impinging obstacles. Recordings of the development of the oscillations in this case have been presented by Ostapenko et al. [21] and Petroff and Shipulin [22]. It was observed that, starting from its farthest upstream position, the Mach disk moves towards the bluff body obstacle, generating a compression wave that intensifies and transforms into a shock wave travelling towards the Mach disk. The interference of these two shocks generates a third shock wave travelling upstream, towards the nozzle, affecting the geometrical properties of the jet expansion at the nozzle and its reflection at the

jet boundary, causing a decrease in the diameter of the Mach disk, and displacing it upstream, back to the initial position, creating a closed loop feedback mechanism [23].

The experimental work of Finley and his team was concerned with the dynamics of supersonic jets impinging on flat plates [24] or bluff bodies [25, 26]. The effect of the distance between the jet nozzle and the obstacle on the jet structure was investigated in detail. It was concluded that the flow oscillation occurs when the terminal shock of the jet is influenced by the transport of pressure fluctuations in the stagnation bubble caused by the jet shocks on the obstacle [27]. If the terminal shock occurs downstream of the first jet cell, a change in pressure will reflect on the shock wave position. Depending upon the distance between nozzle and obstacle, the jet structure variations may occur abruptly or in a fluctuating manner. The mechanism for producing the stagnation bubbles via shock waves was described by Ginzburg [28]. Significant pressure fluctuations accompanied by screech have been also recorded for large distances (over 3 - 8 shock cell lengths) between the supersonic jet nozzle and the obstacle [29]. The coupling, in this case, is achieved through the free shear layer at the jet boundary, which was shown to be very sensitive to periodic disturbances.

Demin [30] expanded the scope of the previous studies by adding small cavities on the flat plate on which the supersonic jet impinges. Oscillations of the jet flowing away from the axis were observed, generating noise frequencies in the range 1 - 50 Hz. Experimental measurements on supersonic jets impinging proper Hartmann resonators were reported by Brocher et al. [31], resulting into a significantly increased oscillations amplitude. The acoustic coupling effect of a secondary resonator has been investigated by Kawahashi et al. [32], while the influence of the resonator tube angle on the temperature was presented by Iwamoto et al. [33]. A cylindrical geometry of a supersonic jet impinging a Hartmann resonator was studied by Wu et al. [34], showing strong pressure oscillations caused by circular shock waves oscillating radially and permitting either inflow, or outflow.

The role of coherent vortices in the generation of self - sustained oscillations in a system containing a supersonic jet impinging on a bluff obstacle, including measurements of the fluctuating force on the bluff body, has been studied by Ziada and Rockwell [35] and Kaykayoglu and Rockwell [36]. Sarohia and Back [37] presented experimental investigations of resonance in a Hartmann resonator and identified several resonance modes (jet instability, jet regurgitant and screech), occurring as a function of the resonator geometry and the dynamic pressure in the device. Sobeiraj and Szumowsky [38] extended the scope of previous studies and, while confirming the significant impact of the cavity shape on the resonator acoustics, determined that the shape of the supersonic nozzle does not affect the switching between the resonance modes.

More recently, the focus of the research efforts in the field of self - sustained oscillations induced by Hartmann resonators shifted more to the application of the effect in various flow control solutions. A fluidic actuator based on the Hartmann effect was developed by Kastner and Samimy [39, 40]. The actuator used the region between the jet nozzle and the resonator for flow control. The critical control parameter for the device was found to be the distance from the jet nozzle to the resonator. Noise sources were identified and located in the actuator flow using a three-dimensional microphone array [41]. Raman et al. [42] measured the resonance frequencies in a similar flow control device and provided detailed unsteady pressure measurements in the flow control region. The shape of the jet wave pattern produced by Hartmann oscillators as a function of their internal geometry was studied by Raghu and Raman [43]. Gregory [44, 45] studied the application of Hartman oscillators as high frequency flow control devices used to improve the performance of an aircraft (enhanced lift, reduced drag, decreased noise levels, delayed stall), proposing a piezo - fluidic actuator solution that allows the oscillation frequency to be specified independent of the upstream pressure.

Savin [46] tackled the design of sound generators for applications in metallurgy and chemistry by proposing a simplified closed model of the self oscillating process triggered by a planar supersonic jet in a resonator, based on Schlieren flow visualizations and pointwise pressure fluctuation measurements. The model is able to predict both the amplitude and the frequency of the oscillations as a function of the jet velocity and on the resonator geometry, and is also useful in aircraft design, as it enables the designer to avoid unwanted resonance regimes on critical aerodynamic surfaces.

A parametric experimental study of cylindrical Hartmann resonators was carried out by Sreejith et al. [47] in order to develop active flow control applications for aerodynamic noise reduction and separation control. Tapered channels were observed to result in higher resonance frequencies than straight channels, while the high frequency oscillations are found to be independent of the resonator geometry. Another parametric study by Sarpotdar et al. [48] focused on the correlations between the nozzle - to - cavity distance and the resonance frequency, finding a reduced influence.

Murugappan and Gutmark [49] examined the effect of reduced nozzle - to - resonator distances and reporting the existence of a minimal distance under which the resonance mode switches back from screech to jet regurgitant. The value of this distance is strongly influenced by the diameter ratio between the resonating channel and the nozzle. Resonance parameters of the flow in tapered resonator channel were experimentally analyzed by McAlevy and Pavlak [50]. The channel geometry was not found to have a significant impact upon the initiation and propagation of the oscillations. Conical cavities were also investigated by Neemeh et al. [51] and Rakowsky et al. [52].

The sound generation of jets impinging on flat plates, used in coating control and heat transfer processes, was investigated by Arthurs and Ziada [53, 54, 55]. The reported measurements of pressure fluctuation indicate the generation of intense sound waves for a significant range of jet exit velocities and distances from the nozzle to the obstacle. The influence of the impingement angle and of the jet thickness are also quantified. The studies identify that different physical mechanisms are controlling the flow dynamics, depending on the distance between the nozzle and the obstacle. For small distances, the jet oscillation is controlled by the hydrodynamic flow instability. At large distances, acoustic coupling of this instability and a resonant acoustic modes occurs. In this regime, the impingement distance controls the frequency of the phenomenon. Phase - locked Particle Image Velocimetry measurements are used to measure convection velocity near the plate and a new feedback model to predict the oscillation frequency as a function of flow velocity, impingement distance and nozzle thickness is proposed. Verma and Manisankar [56] presented experimental measurements aimed at analyzing the source of the flow asymmetries occurring in over-expanded planar nozzles, highlighting the critical role played by the jet boundary layer.

More recent applications of the Hartmann effect relate to the intensification of the shock waves travelling through the resonator such as to increase the flow temperature to large enough values to allow fluidic fuel ignition in combustors. Brocher and Ardisson [57] studied the acoustics of a needle Hartmann-Sprenger generator, assessing the influence of the upstream pressure, the incoming stream chemical composition, the geometry of the resonating cavity, and the material properties of the device on the tube's end wall temperature. Kawahashi et al. [58] investigated the effect of conical and stepped resonators on the intensity of the generated shock waves to increase the temperature jump through the shock waves. The influence of the resonator geometry and flow Mach numbers has been determined, and a single step geometry of the resonating cavity has been identified as optimal. An overview of the current research work carried out in this field is presented by Bogdanov [59].

As show by the previously cited work, most of the research efforts carried out in the field have focused on singular, round or planar supersonic jets. Investigations on the coupled effects of supersonic jet systems impinging on Hartmann type resonators are yet scarce [60, 61, 62], even though the interaction effects of closely spaced supersonic jets have been studied both experimentally, for planar [63], round [64, 65], conical [66], or rectangular [67] supersonic jets, and theoretically [68]. Numerical and experimental studies of the vortical structures occurring in the case of two jets impinging at an angle on a flat plate were also reported by Chammem et al. [69].

2 PROPOSED CONCEPT DESCRIPTION

The paper presents an application of coupled supersonic jets impinging on a Hartmann type resonator used for the development of an aerodynamic system capable to function as an aerodynamic valve for a PDC. To ensure the correct air flow through the combustor, the classical pulsed detonation combustor design proposes a set of valves that open and close the admission of the air, or air-fuel mixture, in the combustor. The typical detonation frequency in such devices is low. Higher operating frequencies can be expected to increase the specific impulse of the engine, allowing for a more compact combustor, and, due to inertial effects, to smooth out the mechanical vibrations in the combustor. The main problem in using mechanical valves is the high wear they experience, even more so at high frequencies. Also, the valves are subject to very high operating temperatures, and will induce pressure losses in the flow. Therefore, high frequency valveless designs are an obvious goal for the future pulsed detonation combustor development. Furthermore, the use of a Hartmann shock wave generation system to control the flow into the PDC may also serve as a very efficient, reliable and simple ignition system, naturally correlated with the fresh mixture inflow, if the strength of the shock waves is sufficient.

The proposed concept is based on taking advantage of the phenomenon of synchronizing the oscillation of a non-linear self-oscillating system with the frequency of forced oscillations, or with the

frequency of another self-oscillating system when they are coupled [70]. The lock-in and synchronization phenomena can be observed, and successfully used in applications, in hydrodynamic and thermo- gas-dynamic processes for flow control over bodies [71, 72, 73], or for intensification or damping of transfer processes in thermo-acoustic systems [74].

To intensify the processes occurring in shock wave generators (increasing pressure pulsation amplitude and resonator temperature), and to stabilize the self-oscillating operating regime, the concept proposes placing two nearly identical shock wave generators in front of the central detonator chamber. From a practical standpoint, the best suited solution is to use a bi-dimensional, rectangular section, shock wave generator with its exit directed towards the detonation chamber. Conceptually, the system of resonators in the detonation chamber may be regarded as the interaction of two non-linear, self-oscillating systems of type Van der Pol [75, 76]:

$$\ddot{\xi}_1 - \mu_1(1 - \beta_1 \xi_1^2)\dot{\xi}_1 + \omega_{01}^2 \xi_1 = C_1 \xi_2 \quad (1)$$

$$\ddot{\xi}_2 - \mu_2(1 - \beta_2 \xi_2^2)\dot{\xi}_2 + \omega_{02}^2 \xi_2 = C_2 \xi_1 \quad (2)$$

To adapt the equation system (1) - (2) for the quantitative analysis of the hydrodynamic interaction of two shock wave generators, the value of the coefficients need to be experimentally determined. This is out of the scope of the present work.

The synchronization effect of the shock wave generators placed face to face may be observed in the analysis in Fig. 1. For the case of two interacting generators (Fig. 1 - left), the amplitude of the pressure oscillations at the closed end of the generators, as well as the stability of the self-oscillating regime increases compared to the case of a single resonator (Fig. 1 - right).

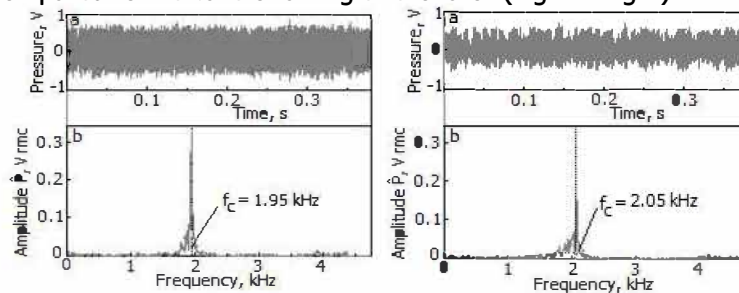


Figure 1: Pressure variation (a) and pulsation spectrum (b) near the closed end of the lateral resonators. Left - 2 resonators in opposition of phase. Right - 1 resonator.

The proposed combustor is of rectangular construction, and includes a shockwave generator with coupled resonators. It consists of the following (notations apply to Fig. 2):

1. Combustor casing;
2. High pressure air chambers;
3. Supersonic nozzle;
4. Lateral resonators;
5. Outer side walls of the lateral resonators;
6. Central detonation chamber;
7. End walls of the lateral resonators;
8. End wall of the central resonator;
9. Separation walls.

More details on the geometry and on the flow can be found in [77] - [80].

The combustor (1) is fed by the high pressure air chambers (2), where the air is delivered by the engine compressors (1 - Fig. 3 [81]) and which feed the air into the supersonic nozzles (3). Two lateral resonators (4), delimited by walls (5), (7) and (9) are placed with their open endings towards the supersonic nozzles (3). Between the lateral resonators (4), the central detonation chamber (6) is placed, delimited by walls (8) and (9). The central detonation chamber (6) and the two lateral resonators (4) are separated by sharp angled walls (9), with the sharp angle edge placed at the open end of the central detonation chamber (6). The supersonic jets are formed by the diverging end supersonic nozzles (3) and provide an increase in temperature at the closed ends of the resonators (4) and of the central detonation chamber (6).

As the supersonic jets impact the sharp edged walls (9) placed at the open ends of the lateral resonators (4), shock waves are formed and travel towards the closed end of the resonators (7). The air entrained by the supersonic jets shear layers is directed into the lateral resonator chambers (4). A

numerical simulation of the flow can be found in [79, 80]. The air stream detaches in the central region of the combustor from the side walls (5) and enters the lateral resonators (5) at a variable angle with respect to the combustor centreline. The travelling shock waves impact the end walls of the resonators (7) and are reflected backwards, towards the lateral resonators (4) open ends, causing an increase in the wall pressure. An earlier model of the proposed resonator tubes and their operation can be found in [82, 83, 84]. When the backwards travelling shockwaves reach the open ends of the lateral resonators (4), they are converted into expansion waves. This moment in time separates the two operation phases of the resonator: the filling phase, before the previously mentioned point in time, and the exhaust phase, which follows.

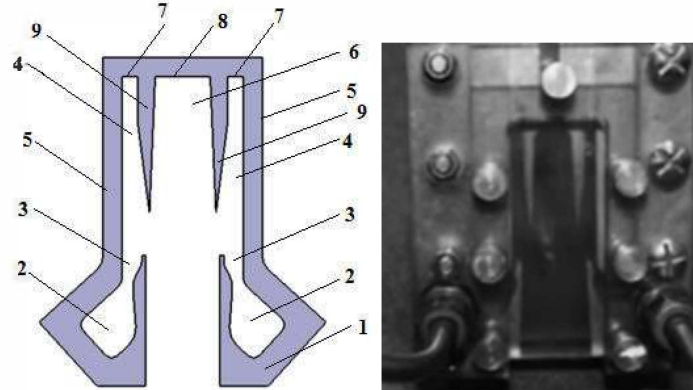


Figure 2: Diagram (left) and experimental model (right) of the PDC

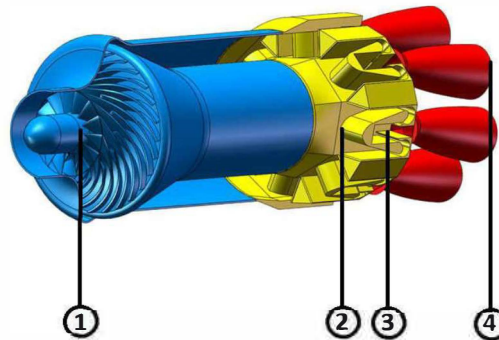


Figure 3: Diagram of the TIDE engine using the proposed PDC

During the filling phase, the air stream velocity in the lateral resonators (4) decreases to zero, and the air mass flow rate deflected around the lateral resonators (4) into the central detonation chamber (6) continuously increases up to the maximum value, which is the inlet mass flow rate. During this process, the velocity of the supersonic jets is basically constant.

The filling phase can be further divided into two sub-phases. In the first, the air mass flow rate entering the central detonation chamber (6) increases slowly, as the velocity of the air stream entering the lateral resonators (4) decreases from the maximum value to zero. In the second sub-phase, both the air mass flow rate entering the central detonation chamber, and its velocity suffer a jump increase due to the sudden opening of the transversal cross-section between the supersonic jets and the side walls (5), allowing the evacuation of the air from the lateral resonators (4). The second sub-phase is significantly shorter than the first sub-phase, creating the conditions for a shock wave to appear in the central detonation region (6), travelling towards its closed end (8). If the proper conditions for creating such a shock wave are not met, then a sonic pressure wave with a $\frac{1}{4}$ wavelength is formed inside the central detonation chamber (6). In this case, a supplementary increase in the pressure at the central detonation chamber end wall (8) can be achieved through proper profiling of the central detonation chamber [85].

During the exhaust phase, the air from the lateral resonators (4) is exhausted initially due to the pressure difference between the lateral resonators (4) and the central detonation chamber (6), and through supersonic jet entrainment afterwards. This process is very fast and it ends up by creating a maximum pressure deficit inside the lateral resonators (4). At the end of the exhaust phase, the

supersonic jets outside the lateral resonators (4) is directed towards the combustor exit, forming two planar high speed jets.

As a new filling phase starts, the supersonic jet is suddenly deviated towards the lateral resonator wall (5). In the same time, part of the fluid in the central detonation chamber (6) is injected into the lateral resonators (4), under the initial action of the pressure difference, and by jet entrainment afterwards. The deviation of the supersonic jet towards the lateral wall opens up the way for the evacuation of the fluid in the central detonation chamber (6) through the combustor outlet.

The cycle of successively generating shock waves through the impact of the supersonic jet with the lateral resonators (4) and the central combustion chamber (6) has a frequency, f , that is a function of the local speed of sound and of the length of the lateral resonators (4) and central detonation chamber (6), chosen to be of equal length.

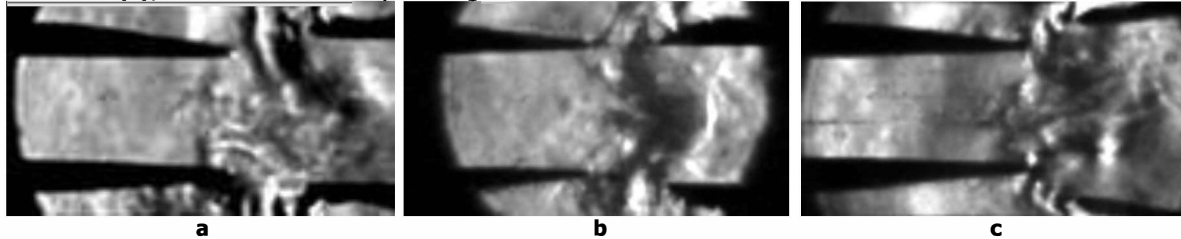


Figure 4: Interaction between shock wave generators

The synchronization of the lateral shock wave generators may occur in different manners, as observed during the concept validation experimentation (Fig. 4). At large distances between the supersonic nozzle and the open ends of the resonators, the synchronization occurs in opposition of phase (Fig. 4a). At smaller distances, a switching - phase opposition regime occurs (Fig. 4b), as the opposition of phase is preserved, but the jets that are partially, or completely, evacuated from the resonators remain coupled throughout the entire oscillation cycle. This jet couple, directed toward the central detonation chamber (6), oscillates both in the transversal direction, from one wall to the other, and longitudinally, maintaining the propagation direction. Finally, in the third self-oscillating regime (Fig. 4c), occurring at even smaller distances, the lateral resonators operate in phase. In this case, horse shoe vortices detach from the region the two jets meet. The results in Fig. 1 refer to this latter regime, which can be predicted from the theoretical analysis of the equation system (1) - (2).

The results presented above were obtained on an reduced height experimental model (Fig. 2 - right), including the central detonation chamber, the nozzles, and the lateral resonators. This may have caused three-dimensional disturbances, such as, for instance, the twisting of the jets in the region where the incoming supersonic jet meets the resonator exhaust jet.

The advantage of the selected constructive solution resides in converting a larger fraction of the supersonic jets kinetic energy to shock wave energy by using the exhaust phase supersonic jet kinetic energy as well. In conventional Hartman generators, this supersonic jet kinetic energy is not used, and is exhausted by the resonator fluid in the ambient air.

The sharp edges of the walls (9) are used in order to reduce the aerodynamic drag imposed on the exhaust jet. Also, an increase in the shock wave amplitude is expected due to the superposition of the oblique shockwave reflected backwards by the central detonation chamber end wall (8), over the normal shock wave. The shape of the diverging channel of the supersonic nozzles (3) was designed to ensure a faster deviation of the supersonic jet towards the lateral wall during the shock wave formation phase. The numerical simulation of the process is available in [80].

3 PDC OPERATION

For ignition, the fuel is injected into the high pressure air chambers (2) placed upstream of the supersonic nozzles (3). Due to the effect of the shock waves and to the Hartman-Sprenger effect they create, the combustible mixture close to the end wall of the lateral resonators (7) is heated up to a temperature that creates ignition. After a short while, the flame front reaches from behind the reflected shock wave and combines with it forming a planar detonation wave. At the open end of the lateral resonators (4), the detonation wave ignites the combustible mixture existing in the central detonation chamber (6), creating there a new detonation wave travelling towards the end wall of the central detonation chamber (8). The admission of the combustible mixture inside the central detonation chamber (6) occurs during the first sub-phase of the filling phase, described in the

previous section, while the detonation wave travels inside the central detonation chamber occurs during the second sub-phase of the filling phase. When reaching the end wall of the central detonation chamber (8), the combustion process stops, and the detonation wave becomes a reflected shock wave that travels, together with the burned gas, towards the combustor outlet.

The detonation waves in the lateral resonators (4) may block the entry of the supersonic jets both in the lateral resonators (4) and in the central detonation chamber. After the exhaust of the burned gas from the lateral resonators (4), the detonation wave may dissipates or transforms into a shock wave, and the supersonic jet may initiate a new lateral resonator shock wave generation cycle, hence a new detonation cycle both in the lateral resonators (4) and in the central detonation chamber (6).

4 CONCLUSION

The PDC constructive solution presented in Fig. 2 was subjected to experimental [77, 78] and numerical studies [79, 80] which resulted in the significant optimization of its operation. The geometry of this initial concept has also been altered, and the final PDC has been proven to operate at frequencies in the range of 350 Hz, under premixed conditions. The results related to the optimized PDC based on the proposed concept are under review for publication.

The proposed PDC design has the advantage of providing a valid solution for the valveless control of the inlet by means of the shockwave system created by the impingement of the supersonic jets onto the Hartmann resonators. The fuel self-ignition, predicted by the numerical simulations, has not been, however, experimentally demonstrated yet, possibly due to heat losses unaccounted for in the simulations. Further experimental and numerical research is planned in two on-going national research programs (MILADEE and ASHCAP).

ACKNOWLEDGEMENT

This work was funded by the European Commission, through the Framework Programme 7 European research project no. 335091 – TIDE

REFERENCES

1. J. Hartmann, 1919, "About a New Method for Generating Sound Vibrations", *Letters of the Royal Danish Academy of Mathematics and Physical Sciences*, **1** (13)
2. J. Hartmann, 1939, "Construction, Performance, and Design of Acoustic Air - Jet Generator", *Journal of Scientific Instrumentation*, **16**, pp. 140 - 149
3. K.A. Morch, 1964, "A Theory for the Mode of Operation of the Hartmann Air Jet Generator", *Journal of Fluid Mechanics*, **20** (1), pp. 141 - 159
4. T.J.B. Smith, A. Powell, 1964, "Experiments Concerning the Hartmann Whistle", *Report 64-42*, Department of Engineering, University of California, Los Angeles, USA
5. P.A. Thompson, 1964, "Jet Driven Resonance Tube", *AIAA Journal*, **2** (7), pp. 1230-1233
6. E. Brun, R.M.G. Boucher, 1957, "Research on Acoustic Air-Jet Generator: New Development", *Journal of Acoustical Society of America*, **29** (5), pp. 573 - 583
7. J.C. Gravitt, 1959, "Frequency Response of Acoustic Air - Jet Generator", *Journal of the Acoustic Society of America*, **31** (11), pp. 1516-1518
8. M. Kawahashi, M. Suzuki, 1979, "Generative Mechanism of Air Column Oscillations in a Hartmann - Sprenger Tube Excited by an Air Jet Issuing from a Convergent Nozzle", *Journal of Applied Mathematics and Physics*, **30** (5), pp. 797 - 810
9. V.N. Glaznev, Y.G. Korobeinikov, 2001, "Hartmann Effect. Region of Existence and Oscillation Frequencies", *Journal of Applied Mechanics and Technical Physics*, **42** (4), pp. 616 - 620
10. C.H. Lewis Jr., D.J. Carlson, 1964, "Normal Shock Location in Underexpanded Gas and Gas Particle Jets", *AIAA Journal*, **2** (4)
11. C.S. Tsein, 1967, "Axisymmetric Supersonic Turbulent Air Jets Issuing from a Nozzle with Underexpansion", Editor N. Abramovich, Mashinostroenie in *Investigation of Turbulent Air Jets, Plasma and Real Gas*, Moscow, USSR
12. M.R. Davies, 1972, "Quantitative Schlieren Measurements in a Supersonic Turbulent Jet", *Journal of Fluid Mechanics*, **51** (3), pp. 435 - 447

13. J.C. Carling, B.L. Hunt, 1974, "The Near Wall Jet of a Normally Impinging, Uniform, Axisymmetric, Supersonic Jet", *Journal of Fluid Mechanics*, **66** (1), pp. 159 - 176
14. C.K.W. Tam, P.J.W. Block, 1978, "On the Tones and Pressure Oscillations Induced by Flow over Rectangular Cavities", *Journal of Fluid Mechanics*, **89** (2), 373-399
15. D. Rockwell, C. Knisely, 1979, "The Organised Nature of Flow Impingement upon a Corner", *Journal of Fluid Mechanics*, **93**, pp. 413
16. L.E. Savory, 1950, "Experiments with Hartmann Acoustic Generator", *Engineering*, **170** (4411), pp. 136 - 138
17. J. Hartmann, E. Trudso, 1951, "Synchronization of Air-Jet Generators with an Appendix on the Stem Generator", *Letters of the Royal Danish Academy of Mathematics and Physical Sciences*, **26** (10), 1951
18. V.P. Kurkin, 1962, "Sound Generated by a Gas Jet Siren", *Soviet Physics - Acoustics*, **7** (4), pp. 357-359
19. H. Sprenger, 1954, "On Thermal Effects in Rough Resonators", *Letters of the Aerodynamics Institute, Federal Institute for Technology, Zurich, Switzerland*, **21**, pp. 18-35
20. W.M. Jungowski, 1975, "Some Self Induced Supersonic Flow Oscillations", *Progress in Aerospace Science*, **18**, pp. 151 - 175
21. W.A. Ostapenko, W.N. Glazneff, A.P. Petroff, W.N. Shevtchenko, A.P., Burdinski, E.M. Shipulin, 1973, "Experimental Investigation of Strong Pulsation in Supersonic Jets", *A Selection in Aero-hydrodynamics*, Novosibirsk, pp. 175-181
22. A.P. Petroff, E.M. Shipulin, 1973, "Visualization by Shadow Method of Unsteady Processes in Jets", *A Selection in Aerohydrodynamics*, Novosibirsk, pp. 169-174, 1973
23. A. Powell, 1962, "Nature of the Feedback Mechanism in Some Fluid Flows Producing Sound", *Fourth International Congress on Acoustics*, Copenhagen, Denmark, art. 022
24. P.J. Finley, 1963, "Experiments on Jets Directed from Blunt Bodies Against A Supersonic Air Stream", *Ph.D. Thesis*, Cambridge University, UK
25. E.P. Sutton, P.J. Finley, 1964, "The Flow of a Jet from the Nose of an Axisymmetric Body in a Supersonic Airstream", *Archiwum Mechaniki Stosowanej*, **3** (16), pp. 782-803
26. P.J. Finley, 1966, "The Flow of a Jet from a Body Opposing a Supersonic Free Stream", *Journal of Fluid Mechanics*, **26**, pp. 337-368
27. G.T. Kalghatgi, B.L. Hunt, 1976, "The Occurrence of Stagnation Bubbles in Supersonic Jet Impingement Flows", *Aerospace Quarterly*, **XXVII**, pp. 169--186
28. I. P. Ginzburg, B.G. Semiletchenko, W.S. Terpigorieff, W.N. Uskoff, 1970, "Some Peculiarities Resulting from the Interaction of a Supersonic, Under-expanded Jet with a Flat Plate", *Journal of Engineering Physics*, **19** (3), pp. 412-417
29. G. Neuwerth, 1972, "Acoustic Feedback of a Subsonic and Supersonic Free Jet which Impinges on an Obstacle", *5th DGLR-Meeting*, Berlin, Germany
30. W.S. Demin, 1974, "Peculiarities Resulting from the Interaction of a Supersonic Jet with a Flat Plate Having a Cavity", *Gas-dynamics and physical kinetics*, Annual Progress Report, Novosibirsk, Russia, pp. 142
31. E. Brocher, C. Maresca, M.-H. Bournay, 1970, "Fluid Dynamics of the Resonance Tube", *Journal of Fluid Mechanics*, **43**, pp. 369-384
32. M. Kawahashi, T. Shimzu, M. Suzuki, 1973, "Transient Thermal Phenomena and the Attainable Limit of Thermal Effects in Hartman-Sprenger Tube", *Euromech 73. Oscillatory Flows in Ducts*, Aix-en-Provence, France
33. J. Iwamoto, M. Kobashi, I., Ariga, I. Watanabe, 1973, "On Thermal Effects of Hartmann-Sprenger Tubes with Various Internal Geometries", *Euromech 73. Oscillatory Flows in Ducts*, Aix-en-Provence, France
34. J.H.T. Wu, P.O. Ostrowski, R.A. Neemeh, P. Lee, 1973, "Cylindrical Aerodynamic Resonator", McGill Mechanical Engineering Report No. 73-6
35. S. Ziada, D. Rockwell, 1982, "Vortex-Leading-Edge Interaction", *Journal of Fluid Mechanics*, **118**, pp. 79-107
36. R. Kaykayoglu, D. Rockwell, 1985, "Vortices Incident upon a Leading Edge: Instantaneous Pressure Fields", *Journal Fluid Mechanics*, **156**, pp. 439-461
37. V. Sarohia, H.L. Back, 1979, "Experimental Investigation of Flow and Heating in a Resonance Tube" *Journal of Fluid Mechanics*, **94** (4), pp. 649 - 672, 1979

38. G.B. Sobeiraj, A.P. Szumowsky, 1991, "Experimental Investigations of an Underexpanded Jet from a Convergent Nozzle Impinging on a Cavity", *Journal of Sound and Vibrations*, **149**, pp. 375 - 396
39. J. Kastner, M. Samimy, 2002, "Development and Characterization of Hartman Tube Fluidic Actuators for High - Speed Flow Control", *AIAA Journal*, **40** (10), pp. 1926 - 1934
40. M. Samimy, J. Kastner, M. Debiassi, 2002, "Control of a High-Speed Impinging Jet using a Hartmann - Tube based Fluidic Actuator", AIAA-2002-2822, *1st AIAA Flow Control Conference, American Institute for Aeronautics and Astronautics*, Saint Louis, MO, USA, 2002
41. J. Hileman, B. Thurow, M. Samimy, 2002, "Acoustic Source Localization Using a 3-D Microphone Array in a Mach 1.3 Jet", AIAA-2002-0366, *40th Aerospace Sciences Meeting & Exhibit*, Reno, NV, USA
42. G. Raman, S. Khanafseh, A.B. Cain, E. Kerschen, 2004, "Development of High Bandwidth Powered Resonance Tube Actuators with Feedback Control", *Journal of Sound and Vibration*, **269** (3-5), pp. 1031-1062
43. S. Raghu, G. Raman, 1999, "Miniature Fluidic Devices for Flow Control", FEDSM 99-7526, *Proceedings of the ASME Fluids Engineering Division Summer Meeting*, 1999
44. J.W. Gregory, 2005, "Development of Fluidic Oscillators as Flow Control Actuators", *Ph. D. Thesis*, Purdue University, West Lafayette, IN, USA
45. J.W. Gregory, J.P. Sullivan, 2003, "Characterization of Hartmann Tube Flow with Porous Pressure - Sensitive Paint", AIAA 2003-3713, *33rd Fluid Dynamics Conference, American Institute for Aeronautics and Astronautics*, Orlando, FL, USA
46. A. V. Savin, 1996, "On Mechanism of Self - Oscillatory Interaction of Plane Supersonic Jet with Acoustic Resonator", *Experimental, Thermal and Fluid Science*, **12**, pp. 388 - 398, 1996
47. G.J. Sreejith, S. Narayanan, T.J.S. Jothi, K. Srinivasan, 2008, "Studies on conical and cylindrical resonators", *Applied Acoustics*, **69** (12), pp. 1161-1175
48. S. Sarpotdar, G. Raman, A.B. Cain, 2005, "Powered Resonance Tubes: Resonance Characteristics and Actuation Signal Directivity", *Experiments in Fluids*, **39**, pp. 1084-1095
49. S. Murugappan, E. Gutmark, 2005, "Parametric Study of the Hartmann- Sprenger Tube", *Experiments in Fluids*, **38**, pp. 813-823
50. R.F. McAlevy, A. Pavlak, 1970, "Tapered Resonance Tubes: Some Experiments", *AIAA Journal*, **8**, pp. 571-572
51. R.A. Neemeh, P.P. Ostrowski, J.H.T. Wu, 1984, "Thermal Performance of a Logarithmic-Spiral Resonance Tube", *AIAA Journal*, **22**, pp. 1823-1825
52. E.L. Rakowsky, A.P. Corrado, V.P. Marchese, 1974, "Fluidic Explosive Initiator", *Fluidics Quarterly*, **6**, pp. 13-32
53. D. Arthurs, S. Ziada, 2011, "The Planar Jet - Plate Oscillator", *Journal of Fluids and Structures*, **27**, pp. 105 - 120
54. D. Arthurs, S. Ziada, 2014, "Effect of Nozzle Thickness on the Self - Excited Impinging Planar Jet", *Journal of Fluids and Structures*, **44**, pp. 1 - 16
55. D. Arthurs, S. Ziada, 2014, "Development of a Feedback Model for the High-Speed Impinging Planar Jet", *Experiments in Fluids*, **55** (5), pp. 1 - 16
56. S.B. Verma C. Manisankar, 2014, "Origin of Flow Asymmetry in Planar Nozzles with Separation", *Shock Waves*, **24**, pp. 191-209
57. E. Brocher, J.-P. Aridssone, 1983, "Heating Characteristics of a New Type of Hartmann - Sprenger Tube", *International Journal of Heat and Fluid Flow*, **4** (2), pp. 97-102
58. M. Kawahashi, R. Bobone, E. Brocher, 1984, "Oscillations Modes in Single-Step Hartmann - Sprenger Tubes", *Journal of the Acoustic Society of America*, **75** (3), pp. 780-784
59. V.V. Bogdanov, 2015, "Contemporary Achievements in the Field of Acoustic Ignition Systems", *International Conference on Industrial Engineering, Procedia Engineering*, **129**, pp. 702 - 707
60. J. Hartmann, E. Trudso, 1951, "Synchronisation of air-jet generators with an appendix on the stem generator", *Matematisk-fysiskemeddelelser*, Denmark, **26** (10), pp. 1-39
61. M. Kawahashi, M. Suzuki, 1974, "Studies on resonance tube with a secondary resonator", *Bulletin JSME*, **17** (107), pp. 595-602.
62. I.A. Leyva, V., Tangirala, A.J. Dean, 2003, "Investigation of Unsteady Flow Field in a 2-Stage PDE Resonator", AIAA-2003-0715, Reno
63. S.C Johnston, 1977, Gasdynamic Measurements for the LASL Intense Neutron Source", *Sandia Energy Report*, SAND77-8294, Sandia Laboratories, Livermore, CA, USA

64. J.M. Seiner, J.C. Manning, M.K. Ponton, 1988, "Dynamic Pressure Loads Associated with Twin Supersonic Plume Resonance", *AIAA Journal*, **26**, pp. 954-960
65. R.W. Wlezien, 1989, "Nozzle Geometry Effects on Supersonic Jet Interaction", *AIAA Journal*, **27** (10)
66. G. Raman, R. Taghavy, 1998, "Coupling of Twin Rectangular Supersonic Jets", *Journal of Fluid Mechanics*, **354**, pp. 123 - 146
67. R. Joshi, P. Panickar, K. Srinivasan, G. Raman, 2006, "Nozzle-Orientation Effects and Nonlinear Interactions Between Twin Jets of Complex Geometry", *Journal of Aircraft*, **43** (2)
68. P.J. Morris, 1990, "Instability Waves in Twin Supersonic Jets", *Journal of Fluid Mechanics*, **220**, pp. 293 - 307
69. T. Chammem, H. Mhiri, O. Vauquelin, 2013, "Dominant Flow Features of Two Inclined Impinging Jets Confined in Large Enclosure", *World Academy of Science, Engineering and Technology*, **7** (4), pp. 27-35
70. A. Pikovsky, M. Rosenblum, J. Kurths, 2001, "Synchronization - A Universal Concept in Nonlinear Sciences", Cambridge University Press, **12**, Cambridge, UK
71. T. Cuciuc, M. Bologa, 2000, "Dynamic control of flow around of the cylinder by periodic perturbation of a boundary layer", *Scientific works of Iasi Polytechnic Institute*, **XLVI (L)**, pp. 15-19
72. L.H. Feng, J.J. Wang, 2014, "Modification of a circular cylinder wake with synthetic jet: Vortex shedding modes and mechanism", *European Journal of Mechanics B/Fluids*, **43**, pp. 14-32
73. T.V. Kuchuk, 2007, "Cross flow around a cylinder at periodic disturbances in the boundary layer by electrolysis bubbles", *Surface Engineering and Applied Electrochemistry*, **43** (2), pp. 100-106
74. S. Balusamy, L.K.B. Li, Z. Han, M.P. Juniper, S. Hochgreb, 2015, "Nonlinear dynamics of a self-excited thermoacoustic system subjected to acoustic forcing", *Proceedings of the Combustion Institute*, **35** (3), pp. 3229-323
75. J. Fischer, S. Bergweiler, M., Abel, 2013, "The Arnold-Tongue of Coupled Acoustic Oscillators", *ArXiv e-prints*, 1311.5797
76. J.L. Fischer, 2014, "Nichtlineare Kopplungsmechanismen akustischer Oszillatoren am Beispiel der Synchronisation von Orgelpfeifen", *Ph.D. thesis*, University of Potsdam, Germany
77. I. Porumbel, C.F. Cuciumita, C. Nechifor, R. Kuncser, T. Cuciuc, 2017, "Experimental Measurements in Hartmann Oscillators", *CEAS 2017 - Aerospace Europe*, 16 - 20 October, Bucharest, Romania
78. T. Cuciuc, I. Porumbel, 2016, "Detonating Combustion in a Hartmann Resonator Pulsed Detonation Combustor", *8th International Conference Materials Science and Condensed Matter Physics*, September 12 - 16, Chisinau, Moldova
79. I. Porumbel, T. Cuciuc, C.F. Cuciumita, C.E. Hritcu, F.G. Florean, 2014, "Large Eddy Simulation of Non-Reactive Flow in a Pulse Detonation Chamber", *Advances in Applied and Pure Mathematics. Proceedings of the 7th International Conference on Finite Differences, Finite Elements, Finite Volumes, Boundary Elements (F-and-B '14)*, Gdansk, Poland
80. I. Porumbel, B.G. Gherman, I. Malael, V. Dragan, 2017, "Numerical Simulation of Detonation in a Valveless Pulsed Detonation Chamber", *CEAS 2017 - Aerospace Europe*, 16 - 20 October, Bucharest, Romania
81. C.F. Cuciumita, B.G. Gherman, I. Porumbel, 2013, "Novel Pulse Detonation Engine Concept", *CEAS 2013 Air and Space Conference - Innovative Europe*, Linköping, Sweden
82. R.A. Neemeh, J.H.T. Wu, M.N. Elabdin, 1981, "Cylindrical Resonators", *Proceedings of the thirteenth International Symposium on Shock Tubes and Waves*, State University of New York Press, Albany, New York, U.S.A., pp. 385-381
83. R.A. Neemeh, P.P. Ostrowski, J.H.T. Wu, 1984, "Thermal performance of a logarithmic-spiral resonance tube", *AIAA Journal*, **22** (12), pp. 1823-1825
84. M.A. Goldfeld, N.N. Fedorova, I.A. Fedorchenko, G.A. Pozdnyakov, K.Yu. Timofeev, Yu.V. Zhakharaova, 2015, "Experimental and numerical study of pulsating transversal jets", *Progress in Flight Physics*, **7**, pp. 297-310
85. K.V. Kessaev, 1990, "Theoretical Model of Resonance Tube", *Aviatsionnaja Technika*, pp. 49-52

Numerical Simulation of Detonation in a Valveless Pulsed Detonation Chamber

Ionut Porumbel

*Romanian Research and Development Institute for Gas Turbines COMOTI
Scientific researcher
220D, Iuliu Maniu Blvd., Bucharest, sector 6, 061126, Romania
ionut.porumbel@comoti.ro*

Bogdan G. Gherman

*Romanian Research and Development Institute for Gas Turbines COMOTI
Head of Computational Fluid Dynamics Department*

Ion Malael

*Romanian Research and Development Institute for Gas Turbines COMOTI
Scientific researcher*

Valeriu Dragan

*Royal Institute of Technology
Post doctoral researcher
Brinellvägen 8, 114 28, Stockholm, Sweden*

ABSTRACT

The paper presents Reynolds Averaged Navier Stokes numerical simulation of the premixed, detonation flow inside a valveless pulsed detonation chamber. The control of the admission of the fresh mixture is achieved through a shock wave system generated by the interaction of two supersonic jets impinging on a Hartmann oscillator. Several phases in the operation of the detonation chamber can be observed in the numerical simulation. The numerical simulation shows that self – ignition of the fuel – air mixture occurs at 0.150 ms after the flow starts to flow into the PDC, in two symmetrical positions inside the lateral resonators, in the straight channel at the middle of their vertical dimension and around the middle of the straight channels of the resonators, in the axial direction. After this, during the propagation phase, the temperature inside the supersonic nozzle remains high enough to continue to ignite the fresh mixture whenever the pressure in the divergent section of the nozzle is low enough to allow it to enter the computational domain. Once the inlets close, the temperature starts decreasing throughout the combustor, with high temperature regions being maintained towards the outlet, where the influence of the hot central jet core is still present, and near the PDC walls. The lateral resonators cool much faster, since their temperature was much lower at the beginning of the cycle. The numerical data is analyzed, and the shortcomings of the numerical simulation are discussed. Future solution for improving detonation modeling are proposed.

KEYWORDS: *RANS, detonation, supersonic combustion*

1 INTRODUCTION

Pulsed detonation chambers (PDC) are not a novel research issue. The detonation and deflagration processes have been studied intensely in the last century. The detonation process was observed for the first time in gaseous fuels by Bertolet in 1881. Later on, Chapman [1] and Jouguet [2] discovered that the products resulted from the detonation propagate at sonic speed relative to the detonation wave. The studies showed a fast energy convergence rate that occurs during detonation, corroborated to much higher thermodynamic efficiencies compared to the deflagration process.

While remaining an exotic phenomenon, of strictly academic interest, for quite a while, the study of detonation took an important step forward in the interest of combustion researchers in the mid-XX century, as supersonic flight appeared as an achievable possibility. A first approach was the definition

of various thermodynamic cycles aiming at modelling the detonation powered engine, improving on the Chapman - Jouguet theory. A first attempt was the development of the Humphrey cycle [3], based on constant volume heat addition with an isentropic expansion and an isobaric heat rejection. Another cycle used for shocks and detonation wave engines is the ZND (Zeldovich-von Neumann-Doring) cycle [4]. The theory defines an intermediate state, the ZND point, defining the chemical reaction start point. Another cycle worth mentioning is the Fickett-Jacobs cycle [5].

Over the last decade, the application of the above mentioned cycles was studied in several analyses (e.g. [6] performed with various degrees of success. A detailed review of the work carried out in the field of PDC design, including theoretical and experimental approaches, can be found in [7].

The application of detonation waves in propulsion system dates back to the 1940s [8], but the complexity of the problem delayed the first successful demonstrator flight to as late as 2008 (DARPA's Blackswift [9]). The demonstration flight was, however, at low speed, and the project was soon cancelled. During this time, a significant number of PDC constructive solutions has been proposed, none completely successful: pure (e.g. [10] combined-cycle (e.g. [11]) and hybrid (e.g. [12]). The pure PDC is comprised of one or more detonation tubes an inlet and a nozzle. The main problem of the solution is the low inlet pressure at high altitudes. The combined-cycle PDC is typically used for ramjets or scram jets. However this type of engine only works efficiently until Mach 5 [13]. The hybrid PDC replaces the classical deflagration combustor with a PDC to enhance the engine performance, reduce flight time and, possibly, decrease pollutant emission.

The optimal PDC operating frequency has been an important research objective. To approach the performances of a classical gas turbine engine, the PDC must operate at least at 75 Hz for a near stoichiometric fuel air mixture [14]. Increasing the frequency allows for a reduction in the combustor size, and engine weight and drag. One solution [15] for high frequencies proposes a series of out-of-phase initiation chambers connected to a main PDC. Another frequency increasing solution, applicable for mechanical valves, is to reduce the deflagration phase time by enhancing the fuel-air mixing, either through increasing the turbulence [16], or through controlling the geometry [17].

Aerodynamic valve solutions have also been used in some PDC applications. The most important requirement related to this approach is to prevent the flashback. Proposed solutions were to place a detonation initiator equipped with an aerodynamic isolator at the chamber inlet [18], or to accelerate the flow to the supersonic regime upstream of the combustor inlet [19]. Other valveless high frequency solutions (e.g. [20]) propose the generation of high frequency oscillations at the combustor inlet, though the interaction of supersonic jets, or by using stationary or moving walls. A wedge-shaped object detonation wave stabilization concept [21] initiates the detonation wave through the coupling of the reaction waves with the leading shock waves. The solutions present several important advantages related to better mixing, ease of initiation, flashback prevention, detonation control, reduced size, low emissions and stability [22]. Rotating, tangential exhaust PDCs has also been recently proposed (e.g. [23]), based on a quite old pioneering idea [24], but operating at low frequency and inlet pressure. An extensive review of the current state-of the art can be found in [25]. The paper presents Reynolds Averaged Navier Stokes (RANS) numerical simulation of the premixed, detonation flow inside a valveless PDC, which is part of a novel detonation engine [26]. The control of the admission of the fresh mixture is achieved through a shock wave system generated by the interaction of two supersonic jets impinging on a Hartmann oscillator [27].

2 SIMULATION SETUP

The geometry of the PDC used for the numerical simulation is presented in Fig. 1. To diminish the computational load, the computational domain presented in Fig. 2 was simplified by removing the subsonic part upstream of the critical section of the Laval nozzles and was discretized by a three dimensional computational grid, to a total of 2,180,546 computational cells, on a structured, Cartesian grid, shown in Fig. 1. The cell size varied between 0.1 mm and 0.52 mm, with the smaller values near the walls. The estimated Kolmogorov scale is of 1.6 μm , placing the resolution within RANS scope.

The boundary conditions imposed on the computational domain were of the following types:

- Solid, no-slip, adiabatic wall boundary conditions;
- Sonic inflow boundary conditions ($p^* = 6 \text{ bar}$, $T^* = 500 \text{ K}$; $M = 1$, Gas composition: Hydrogen / air stoichiometric mixture);
- Extrapolation supersonic outflow.

The numerical simulation used the ANSYS CFX commercial solver, using the pressure based with the SIMPLE (semi-implicit methods for pressure linked equations) numerical method. The turbulence model was the $k - \epsilon$ model [28], widely used in combustion research, with reasonable results for high Reynolds number cases [29]. Finite rate chemistry described by a one – step simplified reaction mechanism [30] and the EDM combustion model [31], was used to describe the chemistry. The model was selected as the best CFX available compromise between computational load and accuracy.

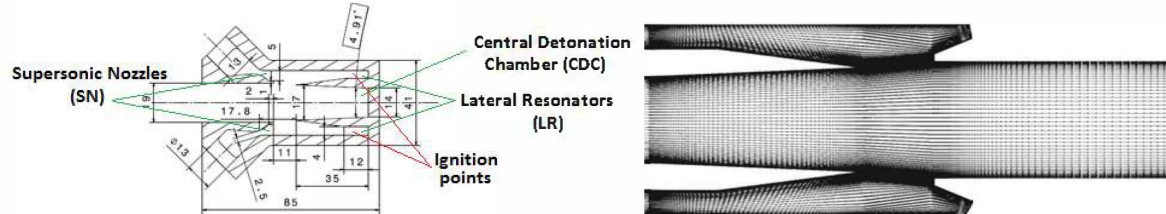


Figure 1 – Computational domain (left) and discretization grid (right)

3 RESULTS AND DISCUSSION

The numerical simulation allowed the observation of four phases in the operation of the studied PDC: the ignition phase, the propagation phase, and cooling phase, and the readmission phase.

3.1 The ignition phase: 0.000 - 0.250 ms

The first important aspect that was verified through the reactive flow numerical simulation was the self ignition of the fuel / air mixture and the initiation of the detonation wave inside the PDC. Fig. 2 presents the temporal evolution of the flow temperature between 0 ms and 0.25 ms.

The numerical simulation shows that self – ignition of the stoichiometric fuel – air mixture occurs at 0.150 ms after the flow starts into the PDC, in two symmetrical positions in the LR, shown in Fig. 1.

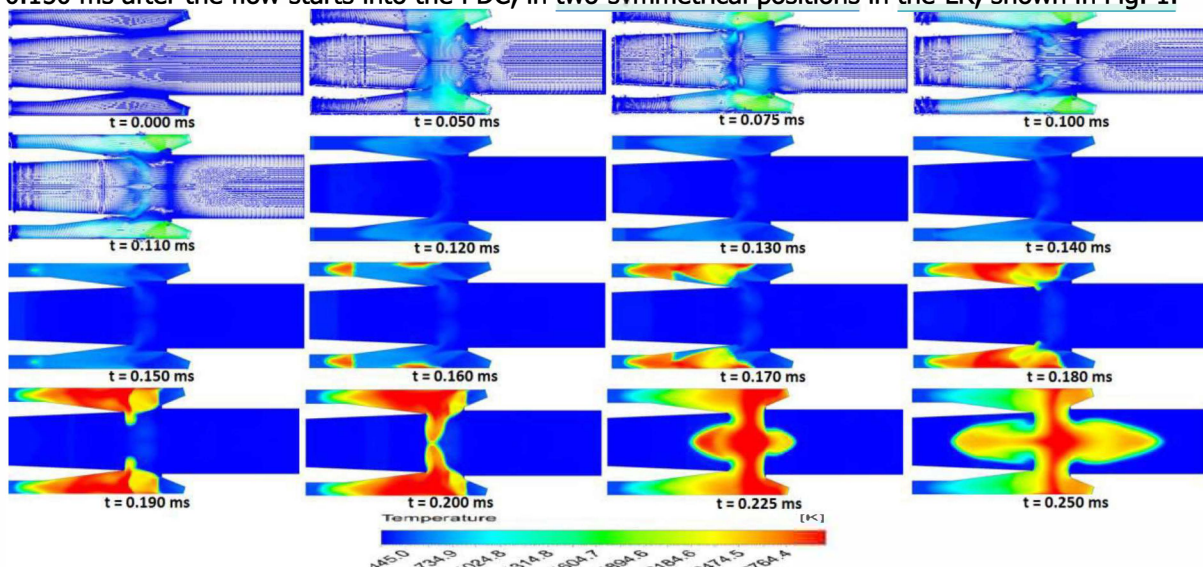


Figure 2 – Temperature scalar field evolution during the ignition phase

To better understand the flow through the PDC, the temporal evolution of the velocity vector field, and the scalar fields of pressure, and Hydrogen and water mass fractions are presented in Figs. 3 - 6. The flow enters the PDC with a slightly higher temperature (500 K) than the atmospheric air, visible in light blue in Fig. 2. A bow expansion wave appears at the SN exit. The air streams issuing from the two SN first enter the two LR (Fig. 3), where they create pressure waves propagating axially along the flow direction both in the LR, and into the CDC (Fig. 4). As the Supersonic Jets (SJ) flow into the LR, the flow is entrained from the stagnant CDC into the LR (Fig. 3), increasing the pressure levels there, and the intensity of the pressure waves propagating inside the LR. The entrained air interferes with the incoming jets composed of premixed Hydrogen and air and creates, around $t = 0.050$ ms, vortices that pushed the combustible mixture into the CDC (Fig. 5).

The mixture in this region is then slowly convected in both axial and transversal directions by the low velocity flow existing here, and will play a critical role in the transition from deflagration to

detonation. The pressure waves mentioned earlier reach the back wall of the LR between $t = 0.110 - 120$ ms (Fig. 4), and the pressure near the closed ends of the LR starts raising sharply. The pressure waves are reflected back by the back wall of the LR and start moving towards the incoming SJ (Fig. 4), which are still flowing towards the LR closed ends (Fig. 3). The flow behind the pressure waves reverses direction entrained by the pressure gradient. When the pressure waves returning from the back wall meet the incoming jets, the local pressure increases even higher and forces the flow in the SJ to break suddenly, triggering the formation of a shock wave around the middle of the LR.

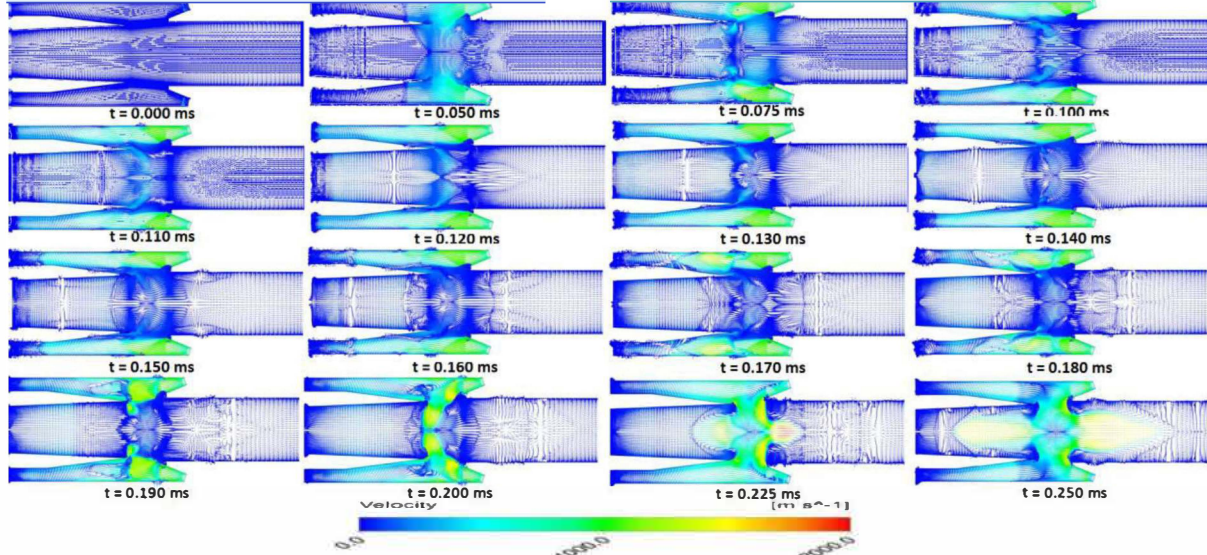


Figure 3 – Velocity vector field evolution during the ignition phase

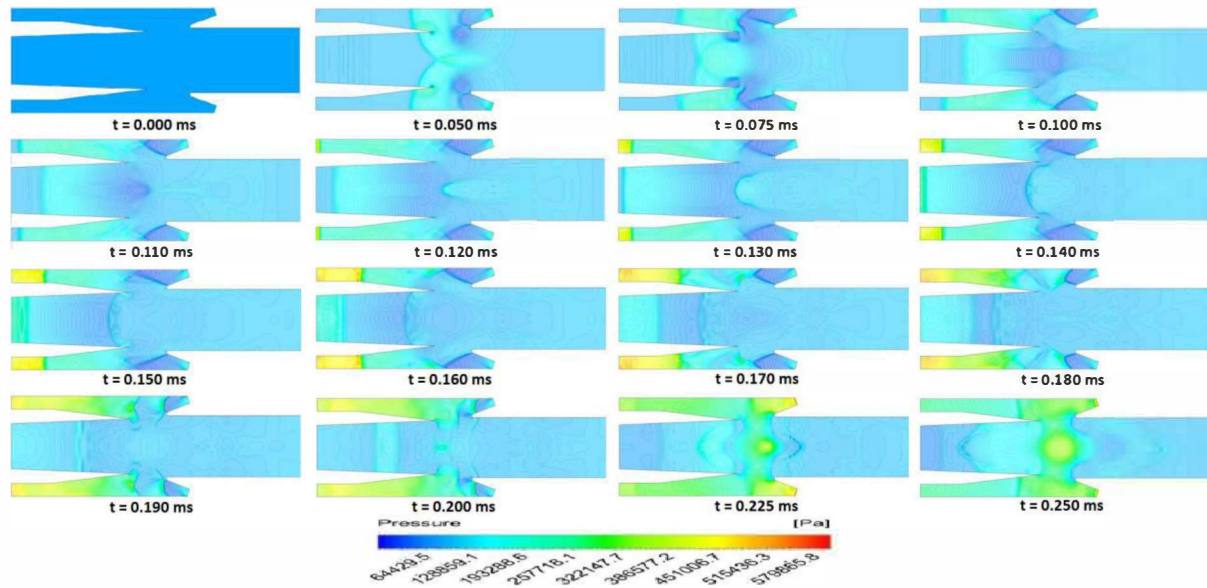


Figure 4 – Pressure scalar field evolution during the ignition phase

At this point, the temperature rises sharply through the shock wave (Fig. 2) due to the meeting of the two suddenly breaking air streams, and the fuel – air mixture starts propagating upstream, as a deflagration wave, through the fresh mixture in the SJ. A secondary couple of ignition points appears on the LR walls at $t = 160$ ms, possibly due to wall friction (Figs. 2 and 6), helping to propagate the combustion wave into the fresh mixture. However, these secondary ignition points may be an artifact of the numerical simulation, due to an insufficient resolution of the computational grid. The limited available computational power prevented the use of a higher resolution grid to further test the issue. In any case, the two combustion region merge at $t = 0.170$ ms, reducing the importance of the secondary ignition points, since they are enveloped in the burned region in any case.

The combustion process spreads through the LR, which are almost completely filled with combustion products at $t = 0.180$ ms. It is important to note that regions near the LR closed ends remain

untouched by the combustion process, as the combustible mixture was never convected by the incoming SJ jets this region in the initial stages of the process. This may be one of the optimization issues to be solved in the future, but the complete elimination of this region may prove impossible, since a volume of increasingly higher pressure must exist at the LR closed ends.

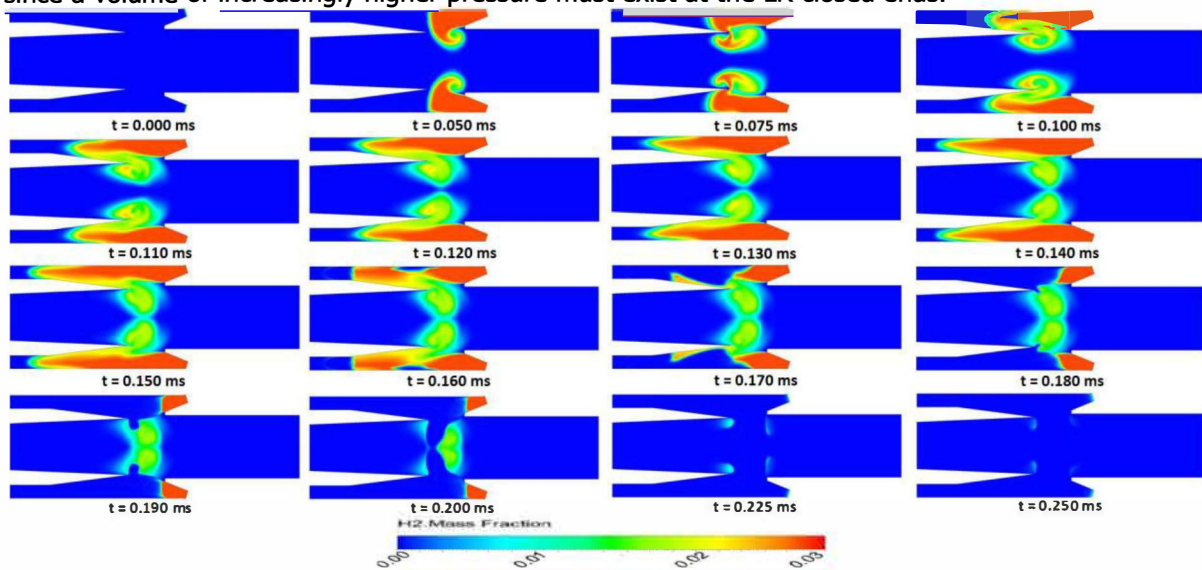


Figure 5 – Hydrogen mass fraction scalar field evolution during the ignition phase

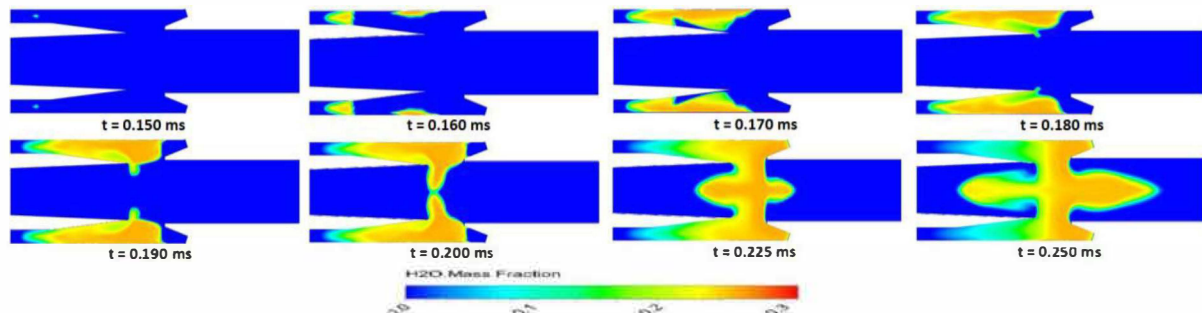


Figure 6 – Water mass fraction scalar field evolution during the ignition phase

Meanwhile, this shock wave propagates upstream through the LR increasing the local pressure. Typical shock cell structures can be observed in Fig. 4 at $t = 0.180$ ms. While the SN flow is still under-expanded, it tends to further expand downstream of the SN through an expansion fan [32]. These expansion waves reflect on both the fluid boundary of the jet, and on the solid surface of the wall, but the effect of the reflection is different in the two cases. On the fluid surface, constant pressure at the boundary must be preserved, therefore the reflection on the fluid boundary creates shock waves returning into the jet. On the contrary, to ensure the no-slip wall condition, the waves reflected back into the jet remain expansion waves. Thus, these alternating expansion and compression regions create a stationary structure of so-called shock cells [33]. Similar behavior of SJ in the close neighborhood of solid walls is frequently reported in the literature (e.g. [33]).

The increasing pressure starts flattening the bow expansion wave formed at the exhaust of the two SN, while also pushing it back, inside the SN, starting at $t = 0.190$ ms (Fig. 4).

The local pressure in the LR regions close to the outer walls increases, and the direction of the incoming SJ is deflected towards the central region of the PDC (Fig. 3). The flow in the LR reverses direction and is directed now towards the SN. At this time ($t = 0.190$ ms), the flame reaches the central region of the PDC (Figs. 2 and 6), and starts propagating mainly transversally through the combustible mixture brought here by the entrainment vortices mentioned earlier, at $t = 0.200$ ms (Fig. 5). The sudden increase in temperature in the CDC inlet triggers a sudden increase in pressure in the central region of the PDC at $t = 225$ ms (Fig. 4). The pressure gradient occurring between this region and the neighbouring zones, both upstream and downstream, creates a strong axial acceleration, up to supersonic values (Fig. 3). The incoming SJ suffer a sharp turn immediately after exiting the SN, and the flow pattern at $t = 0.250$ ms becomes similar to the non – reactive case flow

[34] (Fig. 3). A central SJ jet oriented towards the PDC outlet is formed, delimited by a strong shock wave also propagating outwards (Fig. 4). The combustion front is coupled and rides right behind this travelling shock wave, in a typical detonation front pattern (Figs. 2 and 6). The pressure in the SN is higher now than the inlet pressure (Fig. 4), and the flow of fresh mixture into the PDC is blocked. In the CDC, pressure waves are propagating from the central region towards the closed end starting with the inception of the flow, driven tangentially by the incoming SJ. These waves travel slower in the CDC than in the LR, due to the larger volume available in the central region. The initial pressure wave reaches the back wall of the CDC only at $t = 0.140$ ms, and the pressure in the pocket created between the reflected pressure wave and the back wall is much lower than in the similar pockets created in the LR. The combustible mixture does not have sufficient time to reach the CDC (Fig. 5), so no ignition occurs here. Once the detonation wave is created in the central PDC region, the strong pressure gradient it creates also propagates into the CDC and overcomes the reflected pressure wave, driving a high speed flow towards the back wall. The CDC plays no active role in this phase.

3.2 The detonation propagation phase: 0.250 - 0.600 ms

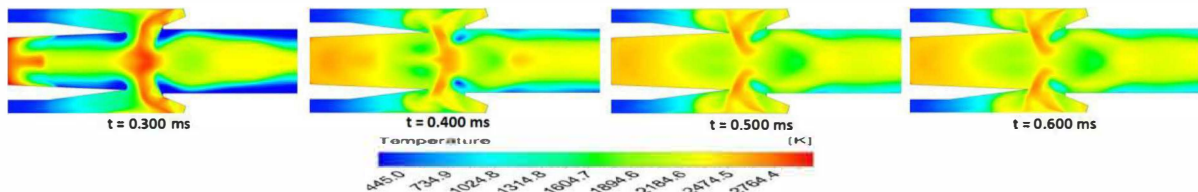


Figure 7 – Temperature scalar field evolution during the detonation propagation phase

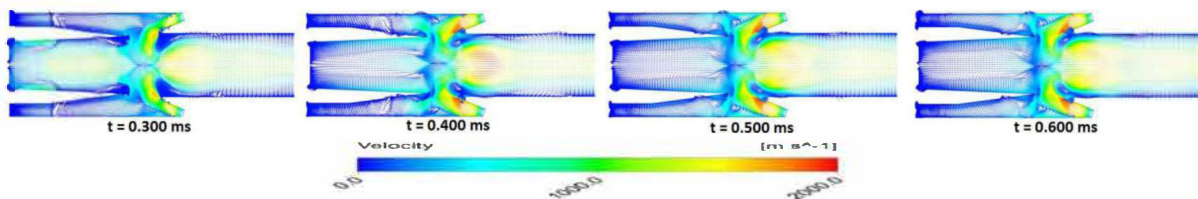


Figure 8 – Velocity vector field evolution during the detonation propagation phase

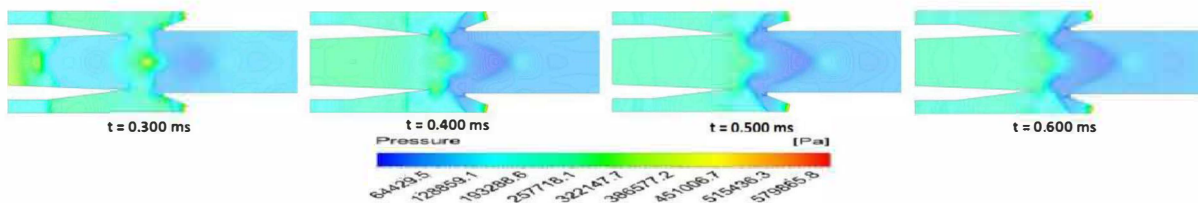


Figure 9 – Pressure scalar field evolution during the detonation propagation phase

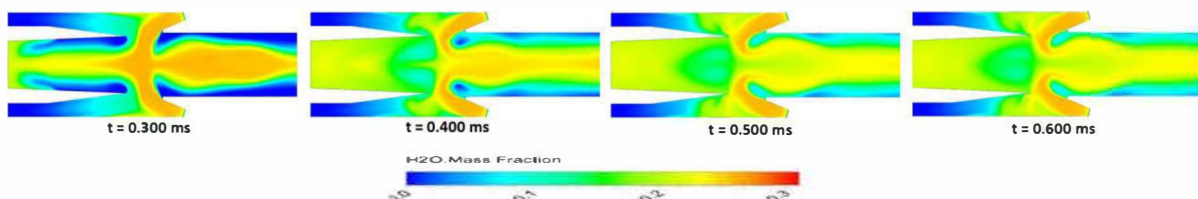


Figure 10 – Water mass fraction scalar field evolution during the detonation propagation phase

Once the detonation is initiated in the central region around $t = 0.225$, the detonation wave starts propagating towards the PDC exit. Figs. 7 – 10 present the evolution of, respectively, temperature, velocity vector, pressure, and water mass fraction between 0.300 ms and 0.600 ms. The Hydrogen mass fraction field is omitted, as the Hydrogen amounts in the PDC in this phase are negligible.

The velocity in the central jet core increases up to $t = 0.400$ ms (Fig. 8), as long as it is supported by combustion (Figs. 7 and 10). The acceleration is mainly axial (Fig. 8). The direction of the SJ remains largely unchanged (Fig. 8), with a sharp turning of the jets immediately downstream of the SN exits, due to the large pressure in the region between the SN exits and the entrance in the LR (Fig. 9).

In the central jet region, the pressure gradually decreases as the combustion process stops due to fuel depletion. The pressure wave propagating towards the CDC back wall reaches it between $t = 0.300$ ms and $t = 0.400$ ms and is reflected back, while the pressure behind decreases due to the

increasing available volume. Due to the combined effect of disappearing combustion and expansion behind the reflected wave, the pressure in the CDC tends towards a uniform value at $t = 0.500$ ms. No significant amounts of Hydrogen were observed in the computational domain in this phase. In the LR and at the exit of the two SN, the pressure levels remain high enough to stop the admission of the fresh mixture into the PDC. However, the temperature inside the SN remains high enough (Fig. 7) to continue to ignite the fresh mixture whenever the pressure in the divergent section of the SN decreases enough to allow it to enter the computational domain. This situation can be observed at $t = 0.600$ ms, when the pressure in the SN tends to drop (Fig. 9), due to the entrainment effect created by the high speed turning jets (Fig. 8). However, the ignition of the fresh mixture immediately as it enters the PDC raises back the pressure and stops again the admission. This effect is an artefact of the numerical simulation, in contradiction with the experimental observations [35]. Several reasons may be responsible for the numerical simulation not capturing the actual behavior of the flow inside the PDC. First, the used combustion model (EDM) is known to overpredict the flame thickness in reactive flow simulations [36]. As a result, the flame is less responsive to flow gradients, particular velocity gradients creating stresses and strains, and is much harder to quench [37]. Also, the boundary condition imposed on the PDC solid walls were specific to adiabatic walls, preventing the normal loss of heat through the wall to the environment and artificially supporting a high temperature. Finally, the computational domain is limited to the critical section of the SN, thus preventing pressure waves to travel upstream into the subsonic region of the SN, and to create full flow reversal through the SN. This way, the fresh mixture is always ready to enter the diverging part of the SN supporting combustion and not allowing the proper cooling of the flow inside the SN. To circumvent this shortcoming of the numerical simulation, the flow through the two SN was artificially stopped by closing the computational domain inlets placed in the critical sections of the SN.

3.3 The flow cooling phase: 0.600 - 0.900 ms

As mentioned before, the numerical simulation in this phase used a zero velocity boundary condition at the inlet. The results are presented in Figs. 11 – 13, showing, respectively, the scalar temperature field, the velocity vector field, and the scalar fields of pressure and water mass fractions. Figures also include the fields at 1.0 ms, in the readmission phase. Since the admission of fresh mixture in the computational domain is blocked, the Hydrogen mass fraction field is omitted. Also, the water mass fraction field closely follows the temperature field, and is omitted as well.

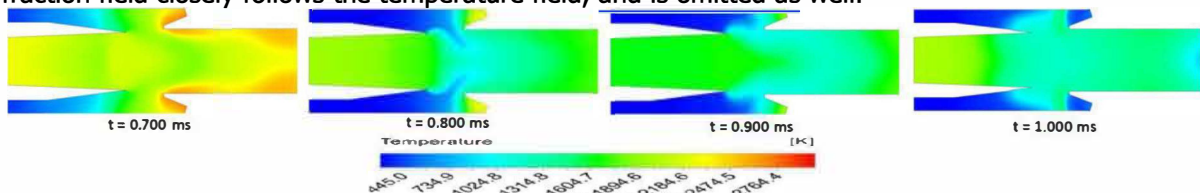


Figure 11 – Temperature scalar field evolution during the flow cooling phase

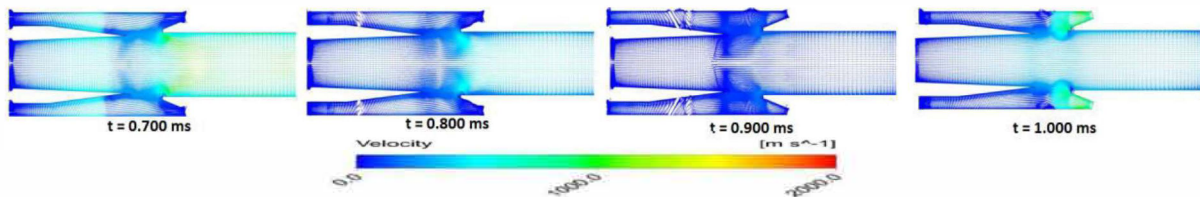


Figure 12 – Velocity vector field evolution during the flow cooling phase

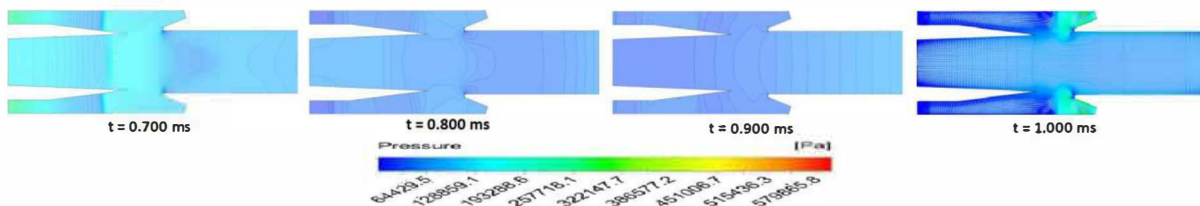


Figure 13 – Pressure scalar field evolution during the flow cooling phase

The effect of closing the inlet SN is immediately visible in the velocity field. The tangential velocity decreases suddenly (Fig. 12) once the incoming SJ disappear, and remain at very low values throughout the current phase. The axial velocity approaches zero almost immediately after the inlets

are closed, at $t = 0.700$ ms (Fig. 12). The central jet velocity decreases much slower, supersonic velocities being maintained up to 0.800 ms. The CDC velocity also decreases, at about the same pace. As the jets disappear, the flow angle in the central region decreases gradually (Fig. 12), the influence of the removed SJ being still felt at $t = 0.900$ ms, albeit weakly.

The temperature starts also decreasing throughout the PDC (Fig. 11), with high temperature regions being maintained towards the outlet, where the influence of the hot central jet core is still present, and near the walls, particularly in the CDC and in the divergent parts of the two SN. The LR cool much faster, since their temperature was much lower at the beginning of the phase anyway.

The water mass fraction field evolves in a pattern very similar to the temperature. Since, in the absence of combustion, no more water is produced, the water accumulated in the CDC and, partially, in the divergent section of the two SN is convected away, towards the exhaust of the PDC. It is noteworthy that the central detonation region remains filled by combustion products even at $t = 0.900$ ms. It is, therefore, very unlikely that this region will be washed during the next detonation cycle, and the combustion products replaced by fresh mixture. Hence, the participation of the CDC in the actual detonation process is reduced in this PDC design. This will have to be addressed, and the shape and size of the CDC represents an obvious target for further optimization studies. One possible approach is to increase the angle of the SJ to direct a larger part of the fresh mixture into the CDC.

The pressure starts decreasing first in the middle of the region between the central jet core and the back wall, both in the CDC and in the LR, as seen at $t = 0.700$ ms (Fig. 13). The pressure waves are reaching the back wall and are reflected back towards the outlet ($t = 0.800$ ms), while the general pressure level inside the PDC continues to decrease towards the atmospheric level, at $t = 0.900$ ms.

3.4 The flow cooling phase: 0.900 - 1.000 ms

Once the temperature downstream of the critical sections of the two SN dropped below the self-ignition point for Hydrogen, the initial simulation boundary conditions were reinstated, allowing fresh mixture to be admitted. The results are presented in the rightmost position in Figs. 11 – 13.

Obviously, fresh mixture enters the divergent region of the two SN and is convected into the PDC. The colder fresh mixture decreases the temperature in the SN below the ignition point of the fuel (Fig. 11), and no combustion products are formed in the SN. The pressure rises into the SN again (Fig. 13), and creates pressure waves that start propagating mainly into the two LR, restarting the detonation cycle. As before, the direction of the SJ exiting the SN is towards the LR (Fig. 12). From this point, the flow patterns inside the PDC are repeating the previous cycle, with a new ignition phase, followed by the detonation propagation phase, and the cooling phase.

4 FUTURE DEVELOPMENT DIRECTIONS

The numerical simulation of pulsed detonation flows is one of the most challenging problems in CFD and the results currently presented in the literature have only met with limited success (e.g. [38]. Significant numerical issues have been also encountered during the study presented herein. The reasons for the shortcomings are numerous, and they are directly resulting from the complex physics underlying the detonation process. To achieve reasonable accuracy, the intricate structure of the detonation wave needs to be captured. Generally, e.g. [39], a detonation wave is described as a shock wave that performs an adiabatic compression of the fuel mixture gas, followed by a thermally neutral induction zone, where the temperature and pressure remain close to their post-shock values while the reactants undergo chain initiation reactions producing free radicals. When a sufficient amount of free radicals is produced, a reaction zone develops downstream of the initiation zone, and the temperature increases substantially, due to the effect of highly exothermal chain branching reactions. The pressure decreases via expansion waves that create a forward thrust that supports the shock front. The discretization grid employed by the simulation must be fine enough to capture this wave, down to microns resolution [40], close to a Direct Numerical Simulation (DNS) size grid.

The resolution of the numerical grid employed in this study was harshly limited by the available computational resources, even though it is below 350η . The results show that this was not sufficient to accurately represent the near wall regions under the very high velocity conditions typical for detonation, possibly leading to the secondary ignition points in Fig. 2. A Large Eddy Simulation (LES) of the flow is necessary, and is planned for the near future.

Furthermore, the complexity of the chemical reaction mechanism used to model the Hydrogen oxidation needs to be sufficient to include realistic chemical reaction steps able to capture the key

dynamics of pulsed detonation [41]. Complex mechanisms for Hydrogen combustion are available, but the computational workload resulting from applying a them on a near-DNS computational grid renders the simulation almost unfeasible due to the huge computational resources required. To alleviate this, a combustion model able to model the effects of finite rate multi-step combustion at a sub-grid level, and thus permitting the use of a lower resolution needs to be developed.

5 CONCLUSIONS

The reactive numerical simulations presented in the paper confirm the self – ignition of the fuel inside the PDC and capture very well the ignition phase of the detonation process. The SJ entering the PDC through the two SN are first directed towards the two LR, where they trigger pressure waves that propagate towards the closed ends of the resonators, where they are reflected back towards the SN. When the reflected pressure waves meet the incoming jets, a couple of shock waves is formed. The temperature rise through these shock waves raises the temperature above the self – ignition point of Hydrogen and initiates combustion inside the PDC. The combustion wave propagates, as deflagration, through the LR and escapes into the central region of the PDC, igniting the fresh mixture convected here by jet entrainment created eddies. In the mean time, the pressure increases in the LR due to combustion, and the high pressure zone approaches the SN, forcing the two SJ to detach from the wall and turn towards the central region of the demonstrator, forming a central SJ core delimited by a shock wave. Here, the combustion wave accelerates and turns into a detonation wave formed by the coupling of the combustion wave with the shock wave delimiting the central jet core. The detonation wave subsequently propagates towards the PDC outlet. The numerical simulation fails to properly capture the next phase of the cycle due to combustion model limitations and wall boundary conditions issues. To simulate the cooling phase, the two inlets were artificially closed until the temperature immediately downstream of the two SJ dropped below the self – ignition value. After this, the initial boundary conditions were reinstated, and a new detonation cycle begun. Possible approaches to address the issue are presented. In the current design, the CDC does not play a significant role in the operation of the PDC, as it remains filled with burned products at the end of the detonation cycle and is never fully filled with fresh mixture. Further design optimization is required in the future.

ACKNOWLEDGEMENT

This work was funded by the European Commission, through the Framework Programme 7 European research project no. 335091 – TIDE

REFERENCES

1. D.L. Chapman, 1889, "On the Rate of Explosion in Gases," *Ph. Mag. S. 5*, **47** (284), pp. 90–104
2. E. Jouguet., 1905, "Sur la propagation des reactions chimiques dans les gaz", *Journal des Mathematiques Pures et Appliquees*, **1**, pp. 347–425
3. Y.B. Zeldovich, 1940, "K Teoriras prostranenia detonazi v gasoobrasnikh sistemakh", *Zhurnal Experimentalnoi Teoreticheskoi Fiziki*, **10**, pp. 543–568
4. J. von Neumann, 1963, "Theory of Detonation Waves", Progress Report to the National Defense Research Committee, Div. B, OSRD-549, (April 1, 1942. PB 31090), Ed. A. H. Taub in "*John von Neumann: Collected Works, 1903–1957*", **6**, Pergamon, New York
5. W.H. Heiser, D.T. Pratt, 2002, "Thermodynamic Cycle Analysis of Pulse Detonation Engine", *Journal of Propulsion and Power*, **18** (1), pp. 68–76
6. R. Bellini, F.K. Lu, 2010, "Exergy analysis of a pulse detonation power device", *Journal of Propulsion and Power*, **26** (4), pp. 875–878
7. K. Kailasanath, 2000, "Review of Propulsion Applications of Detonation Waves", *AIAA J.*, **38** (9)
8. N. Hoffmann, 1940, "*Reaction Propulsion by Intermittent Detonative Combustion*", German Ministry of Supply, AI152365, Volkenrode Translation, 1940
9. N. Shachtman, 2008, "*Explosive Engines Key to Hypersonic Plane*", Conde Nast Publications, San Francisco, CA, U.S.A
10. L.H. Back, W.L. Dowler, G. Varsi, 1983, "Detonation Propulsion Experiments and Theory", *AIAA Journal*, **21** (10), pp. 1418–1427
11. G.P. Menees, H.G. Adelman, J.L. Cambier, J.V. Bowles, 1992, "Wave Combustors for Trans-Atmospheric Vehicles", *Journal of Propulsion and Power*, **8**(3), pp. 709–713

12. L.H. Back, W.L. Dowler, G. Varsi, 1983, "Detonation Propulsion Experiments and Theory", *AIAA Journal*, **21** (10), pp. 1418–1427
13. L.H. Back, 1975, "Appl. of Blast Wave Theory to Explosive Propulsion", *A. Astr.*, **2**, pp. 391–407
14. R.J. Pegg, B.D. Couch, L.G. Hunter, 1996, "Pulse detonation engine air induction system analysis" *AIAA Paper 96-2918*, AIAA Meeting Papers on Disc
15. A.J. Dean, K.R. McManus, V.E. Tangirala, 2006, "Multiple detonation initiator for frequency multiplied pulsed detonation combustion", US Patent US7131260
16. S.Y. Lee, J. Watts, S. Saretto, S. Pal, C. Conrad, R. Woodward, R. Santoro, 2004, "Deflagration to Detonation Transition Processes by Turbulence-Generating Obstacles in Pulse Detonation Engines", *Journal of Propulsion and Power*, **20** (6)
17. N. Smirnov, 2007, "Pulse Detonation Engines: Advantages and Limitations", in "Advanced Combustion and Aerothermal Technologies, NATO Science for Peace and Security", Series C: Environmental Security, **6**, pp. 353-363
18. F. Ma, J.Y. Choi, V. Yang, 2008, "Internal Flow Dynamics in a Valveless Airbreathing Pulse Detonation Engine", *Journal of Propulsion and Power*, **24** (3)
19. V.L. Reingold, A. Quillevere, G. Delange, 1952, "Perfectionnements apportés aux foyers à circulation interne supersonique, notamment aux chambres de combustion pour moteurs à réaction d'aérodynes", French Patent FR1008660
20. V.M. Shmelev, S.M. Frolov, 2010, "Method and Device for Developing Thrust", Pat. RU2179254
21. J.H.S. Lee, 1984, "Dynamic param. of gas detonations", *Ann. Rev. Fl. Mech.*, **16**, pp. 311- 336
22. I.M. Bychkov, V.V. Vyshinsky, L.V. Nosachev, 2009, "Investigation of the flow pattern in a gas-jet Hartmann resonator", *Technical Physics*, **54** (8), pp. 1110-1115
23. M. Brouillette, J.S. Plante, 2008, "Rotary Ramjet Engine", US Patent US7337606
24. B.G. Kramer, 1918, "Rotary Explosion Engine" US Patent US1287049
25. G.D. Roy, S.M. Frolov, A.A. Borisov, D.W. Netzer, 2004, "Pulse Detonation Propulsion: Challenges, Current Status, and Future Perspective," *Prog. Enrg. Comb. Sci.*, **30** (6), pp. 545–672
26. C.F. Cuciumita, B.G. Gherman, I. Porumbel, 2013, "Novel Pulse Detonation Engine Concept", *CEAS 2013 Air and Space Conference – Innovative Europe*, Linköping, Sweden
27. T. Cuciuc, C.E. Hritcu, G.G. Ursescu, I. Porumbel, C.F. Cuciumita, 2017, "Valveless Pulsed Detonation Chamber Controlled by Hartmann Oscillators ", *CEAS 2017*, 16 - 20 Oct., Buch., Romania
28. B.F. Magnussen, B.H. Hjertager, 1976, "On mathematical models of turbulent combustion with special emphasis on soot formation and combustion", *16th Symp. (Intl.) Comb.*, Combustion Institute
29. A. Tyliczszak, A. Boguslawski, D. Nowak, 2016, "Numerical simulations of combustion process in a gas turbine with a single and multi-point fuel injection system "; *Applied Energy*, **174**, pp. 153-165
30. N.M. Marinov, C.K. Westbrook, W.J. Pitz, 1996, "Detailed and Global Chemical Kinetic Model for Hydrogen", *Transport Phenomena in Combustion*, **1**, Taylor and Francis
31. S.B. Pope, 2000, "Turbulent Flows", Cambridge University Press,
32. J.D. Anderson, 1990, "Modern Compressible Flows", McGraw-Hill, Second Edition
33. C. Lubert, 2009, "The Primary Noise Sources Associated with Turbulent Coanda Wall Jets", *The 16th International Congress on Sound and Vibration*, Krakow, 5 – 9 July
34. I. Porumbel, T. Cuciuc, C.F. Cuciumita, C.E. Hritcu, F.G. Florean, 2014, "Large Eddy Simulation of Non-Reactive Flow in a Pulse Detonation Chamber", *Advances in Applied and Pure Mathematics. Proc. 7th Intl. Conf. Finite Diff., Finite Elem., Finite Vol., Bound. Elem. (F-and-B '14)*, Gdansk, Poland
35. I. Porumbel, C.F. Cuciumita, C. Nechifor, R. Kuncser, T. Cuciuc, 2017, "Experimental Measurements in Hartmann Oscillators", *CEAS 2017*, 16 - 20 Oct., Bucharest, Romania
36. I. Porumbel, 2006, "Large Eddy Simulation of bluff body stabilized premixed and partially premixed combustion", *Ph.D. Thesis*, Georgia Institute of Technology, Atlanta, Georgia, USA
37. I. Porumbel, 2007, "Effect of inflow equivalence ratio variation on bluff body stabilized premixed flames", *Thermal Engines and Environmental Engineering METIME 2007*, Galați, Romania
38. F.J.S. Velasco, R.A. Oton-Martinez, J.R. Garcia-Cascales, S. Espin, N. Meynet, A. Bentaib, 2016, "Modelling detonation of H₂-O₂-N₂ mixtures in presence of solid particles in 3D scenarios", *International Journal of Hydrogen Energy*, **41**, pp. 17154 - 17168
39. W. Fickett, W.C. Davis, 1979, "Detonation", University of California Press
40. N. Tsuboi, 2007, "Numerical approach on hydrogen detonation: fundamentals and applications", *2nd European summer school on hydrogen safety*, Belfast, UK
41. M. Short, J.J. Quirk, 1997, "On the nonlinear stability and detonability limit of a detonation wave for a model three-step chain-branching reaction", *Journal of Fluid Mechanics*, **339**, pp. 89 - 119

Experimental Measurements in Hartmann Oscillators

Ionut Porumbel

Romanian Research and Development Institute for Gas Turbines COMOTI

Scientific researcher

220D, Iuliu Maniu Blvd., Bucharest, sector 6, 061126, Romania

ionut.porumbel@comoti.ro

Cleopatra F. Cuciumita

Romanian Research and Development Institute for Gas Turbines COMOTI

Scientific researcher

Cristian Nechifor

Romanian Research and Development Institute for Gas Turbines COMOTI

Scientific researcher

Radu Kuncser

Romanian Research and Development Institute for Gas Turbines COMOTI

Scientific researcher

Tudor Cucuic

Institute for Applied Physics

Scientific researcher

5, Academiei St., Chisinau, Republic of Moldova

cuciuctud@yahoo.com

ABSTRACT

The paper presents high frequency pointwise measurements of pressure and temperature carried out on a shock wave generator consisting of a couple of supersonic jets impinging on a Hartman oscillator system. The shock wave generator was developed as a means to achieve an aerodynamically controlled pulsed detonation chamber. The analysis allows the selection of the optimal geometry and inlet conditions for such an application. The effect of the inlet conditions and of the geometry of the experimental model on the frequency and amplitude of the pressure waves occurring in the system is analyzed. The paper also presents the effects of other geometrical parameters: the critical section of the jet nozzles, the volume ratio of the resonator geometry, and the inlet angles of the jets. Effects of inlet pressure and temperature are also included.

KEYWORDS: *detonation, supersonic propulsion, Hartmann oscillators, high frequency measurements*

APPLYING OF SIX-SIGMA METHODOLOGY FOR NOISE REDUCTION OF COMPLEX AEROSPACE ASSEMBLIES

Constantin Sandu^{1}, Dan Brasoveanu², Valentin Silivestru¹, Bogdan Filipescu³, Radu Constantin Sandu⁴*

¹*COMOTI, Bucharest, Romania*

²*Systems Engineering Group Inc. (SEG), MD, USA*

³*Teletrans. Craiova, Romania*

⁴*S.C. Structural Management Solutions S.R.L., Bucharest, Romania*

**Corresponding author: E-mail : constantin.sandu@comoti.ro*

ABSTRACT

This paper shows that Six-Sigma methodology used in aerospace industry for controlling products' quality can be extrapolated to reduction of noise generated by complex aerospace assemblies. In the last decades an important step forward was achieved in high-tech industries: the use of statistical methods for finding 'significant factors', which are responsible for low performances and quality of complex parts. Such a methodology is Six-Sigma. Using this methodology, the significant factors that affect the quality of a part are found and then appropriate solutions are applied for performance improving.

Noise emitted by a complex assembly can be considered a counter-performance of that assembly. Applying the Six-Sigma methodology the significant factors responsible for noise generating can be found. Then, appropriate solutions for noise level reduction are applied. Using of this methodology can generate surprising solutions for noise reduction which can complete the existing methods.

KEYWORDS: noise reduction, six sigma

The effects of multiple detonation waves in the RDE flow field

Bayindir H. Saracoglu

Department of Aeronautics and Aerospace, von Karman Institute for Fluid Dynamics

Senior Research Engineer

1640 Sint-Genesius-Rode, Belgium

bayindir@saracoglu.co.uk

Aysu Ozden

Department of Aeronautics and Aerospace, von Karman Institute for Fluid Dynamics

Graduate Student

1640 Sint-Genesius-Rode, Belgium

ABSTRACT

Rotating detonation engines (RDE) promise a highly efficient future combustion process due to elevated temperature and pressure attained at high frequencies. Variety of the studies in the literature are devoted to understand the physics of detonation in RDE with combustion across single wave. The current study investigates the effects of multiple detonation waves through numerical simulations performed with an open source unsteady Reynolds-averaged Navier-Stokes solver, OpenFoam. The solver used was able to capture deflagration-to-detonation transition of the hydrogen-air mixture with a devoted tool called ddtFoam. To observe the effects of multiple detonation waves, a flow field with two shocks was implemented. Different inlet total pressures were applied to observe the effect of the inlet pressure on downstream flow field. Comparison in terms of Mach number, outlet flow angle, thrust force, total pressure and temperature had done for one shock and two shocks cases at baseline conditions.

KEYWORDS : *rotating detonation engines, multiple shockwaves, OpenFoam, combustion*

Reconstruction of High-Frequency Lunar Digital Elevation Model using Shape from Shading

Min-Hyun Cho

*Department of Aerospace Engineering, Korea Advanced Institute of Science and Technology (KAIST)
Yuseong-gu, Daejeon, Korea (Republic of)
mhcho@fdcl.kaist.ac.kr*

Ji-Hoon Bai

*Department of Aerospace Engineering, Korea Advanced Institute of Science and Technology (KAIST)
jhbai@fdcl.kaist.ac.kr*

Min-Jea Tahk

*Department of Aerospace Engineering, Korea Advanced Institute of Science and Technology (KAIST)
mjtahk@kaist.ac.kr*

ABSTRACT

This paper deals with a procedure to reconstruct a lunar surface based on fusion of Shape from Shading with absolute depth information exploited from Lunar Orbiter Laser Altimeter data. The generation of accurate lunar digital elevation model which contains altitude and terrain shape of mission area is critical for lunar exploration mission design. The photoclinometric approach based on Shape from Shading yields dense, high-frequency information while range scanning data from Lunar Orbiter Laser Altimeter complements the photoclinometric reconstruction with low-frequency, large scale reliable depth information. The proposed Shape from Shading algorithm utilizes the laser altimetry data as initial guess and iteratively calculates the high-frequency altitude information from high resolution image. The high-frequency depth variation caused by small crater and boulder is recovered by applying Shape from Shading.

KEYWORDS : *High-Frequency Lunar Digital Elevation Model, Shape from Shading, Lunar Orbiter Laser Altimeter (LOLA) Data, Surface Reconstruction*

PASSENGERS' RESCUING IN CASE OF IMMINENT DISASTER OF LARGE AIRPLANES

Constantin Sandu^{1*}, Dan Brasoveanu², Valentin Silivestru¹, Bogdan Filipescu³, Radu Constantin Sandu⁴

¹COMOTI, Bucharest, Romania

²Systems Engineering Group Inc. (SEG), MD, USA

³Teletrans. Craiova, Romania

⁴S.C. Structural Management Solutions S.R.L., Bucharest, Romania

*Corresponding author: E-mail : constantin.sandu@comoti.ro

ABSTRACT

Air traffic is growing rapidly. Although current flight safety is extremely high, and the number of accidents with the number of flights decreases continuously, the risk of fatal crashes cannot be accepted indefinitely.

The problem of rescuing large aircraft passengers in case of imminent disaster is difficult and had no satisfactory solution yet. Using a parachute is a viable solution only for small airplanes with no more than 6 passengers. Large airliners cannot use this system because the parachute would be unsuitable large (hundreds of meters in size).

The authors of this article propose an original system for passenger's rescue, which involves rescue modules composed of groups of 2, 3 or 4 seats depending on the specific type of aircraft.

When disaster becomes imminent and forced landing is not a viable option, the rescuing modules slide onto the airplane sides in a precise sequence then parachutes open automatically. The rescuing modules are designed to protect the passengers from air stream during launching. It is demonstrated that due to the specific design, aircraft, strength, weight and manufacturing costs are insignificantly affected.

KEYWORDS: aircraft passengers saving, aircraft disaster, passengers' parachuting

1. INTRODUCTION

Due to continuous increasing of air traffic, passenger planes with very high capacity that can carry over 500 passengers have been built lately. Obviously, although at present the current flight safety is extremely high and is augmenting continuously. However, because the increased number of flights and flight hours the number of fatal accidents could become significant at global level. This could happen because regardless of technical safety, human factor remains a major cause of accident. Although at global level, the number of fatal accidents is and will be very small compared to the total number of flights, this risk cannot be accepted indefinitely.

The problem of rescuing large aircraft passengers in case of imminent disaster is one of the most difficult aviation problems and has no satisfactory solution yet.

Using a parachute is a viable solution only for small airplanes with no more than 6 passengers. The parachute is folded, compressed and stored in compressed state in a special location placed at on top of the small plane fuselage. In case of imminent disaster, the pilot can open the parachute to save the airplane and passengers. So far this system has saved dozens of small planes from crashes.

Large airliners cannot use this system because the parachute would be exceedingly large (hundreds of meters in size). Moreover, the parachute would have a very large volume, be difficult to fold and open. Also the parachute release and opening would require too much time. For these reasons, the pilot's ability to successfully manage a forced landing is the only hope of rescuing passengers today.

But the forced landing is not always an option: In numerous documented cases, pilots knew the crash is imminent and safe landing is impossible. For passenger aircraft an inoperative flight control system, a severely damaged lift surface such as a wing, impending collision, or inability to control flight, etc. means imminent disaster. Some solutions relying on airplane segmentation into several pieces equipped with separate parachutes have been proposed for rescuing passengers of large airplanes. These solutions cannot be applied for the same reasons discussed above.

The authors of this article propose here an original rescue system for passengers involving the use of modules for 2, 3 or 4 passenger seats. This system is presented in the next sections of this paper.

2. PRESENTATION OF SOLUTIONS PROPOSED BY NOW FOR AIRCRAFT PASSENGERS RESCUE

One of the most recent solutions for passengers' rescue was proposed by aviation engineer Vladimir Tatarenko (member of special investigation commission for aircraft accidents) [1] who worked for Antonov.

Tatarenko observed that statistics of aviation accidents prove that these accidents are caused by human errors in 80% of cases concluding that in future fatal accidents are unavoidable.

For saving aircraft passengers he proposed detaching the whole passenger cabin from the rest of aircraft (fig.1), free falling (fig.2), opening two large twin parachutes and reducing of falling speed (fig.3) and landing with the help of bottom inflatable dampers and solid rocket engines (fig.4).



Figure 1: Detaching of passengers' cabin



Figure 2: Free falling of passengers' cabin

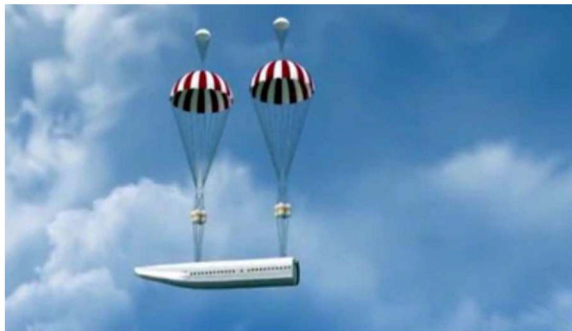


Figure 3: Braking of passengers' cabin falling with twin parachutes

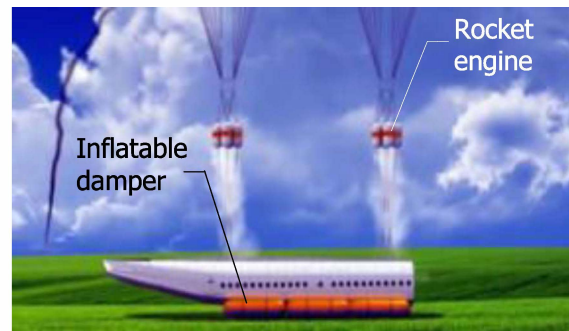


Figure 4: Landing of passengers' cabin using inflatable dampers and rocket engines

This solution cannot be applied for large passenger aircraft because the parachutes would be very large. Furthermore, it is difficult to fix the passenger cabin by an upper beam. That beam should be very strong for supporting the whole passenger cabin and the passenger cabin should be very strong for withstanding braking forces during parachutes opening. Additionally, this solution does not work when the wing is placed under or in the middle of fuselage.

There are some other solutions which involve separation of aircraft in several parts but their application requires an extensive redesign of the aircraft while the problem of the large areas of parachutes' surfaces is not yet solved.

3. PRESENTATION OF THE NEW SOLUTION FOR AIRCRAFT PASSENGERS RESCUE

The solution proposed in this paper considers the experience accumulated from small aircraft passengers such as Cessna and Cirrus. These small planes have a rescue parachute placed in a compartment over the cockpit in the center of the wing. The parachute is made of ultra-light composites material weighting 30 pounds and occupying a very small volume because after wrapping is compressed by an 11-ton press. The passengers are saved together with the entire aircraft when the pilot deploys the parachute. This solution already saved the lives of hundreds of people. [2]

Boris Popov from manufacturer of whole-plane parachutes Ballistic Recovery Systems (BRS), designed BRS parachutes for small aircraft carrying up to five people and tries now to design and install parachutes on planes accommodating up to 20 passengers in the next five years. He considers, too,

that the large commercial airliners will be equipped with a parachute recovery system, yet without recommending a solution for such large aircraft. It is really difficult to design a parachute system for carrying the weight of a passenger aircraft like Airbus A380 which can transport up to 853 people and is over 400 times heavier than a small personal aircraft. Such a parachute system would consist in multiple parachutes becoming too complex, bulky and heavy. It was evaluated that about 0.1sq m of parachute surface area is necessary to safely bring down a load of 0.5kg. Thus, in the case of Boeing 747 having about 500 people on board, 21 parachutes would be necessary, each of them being as large as a football field. [2]

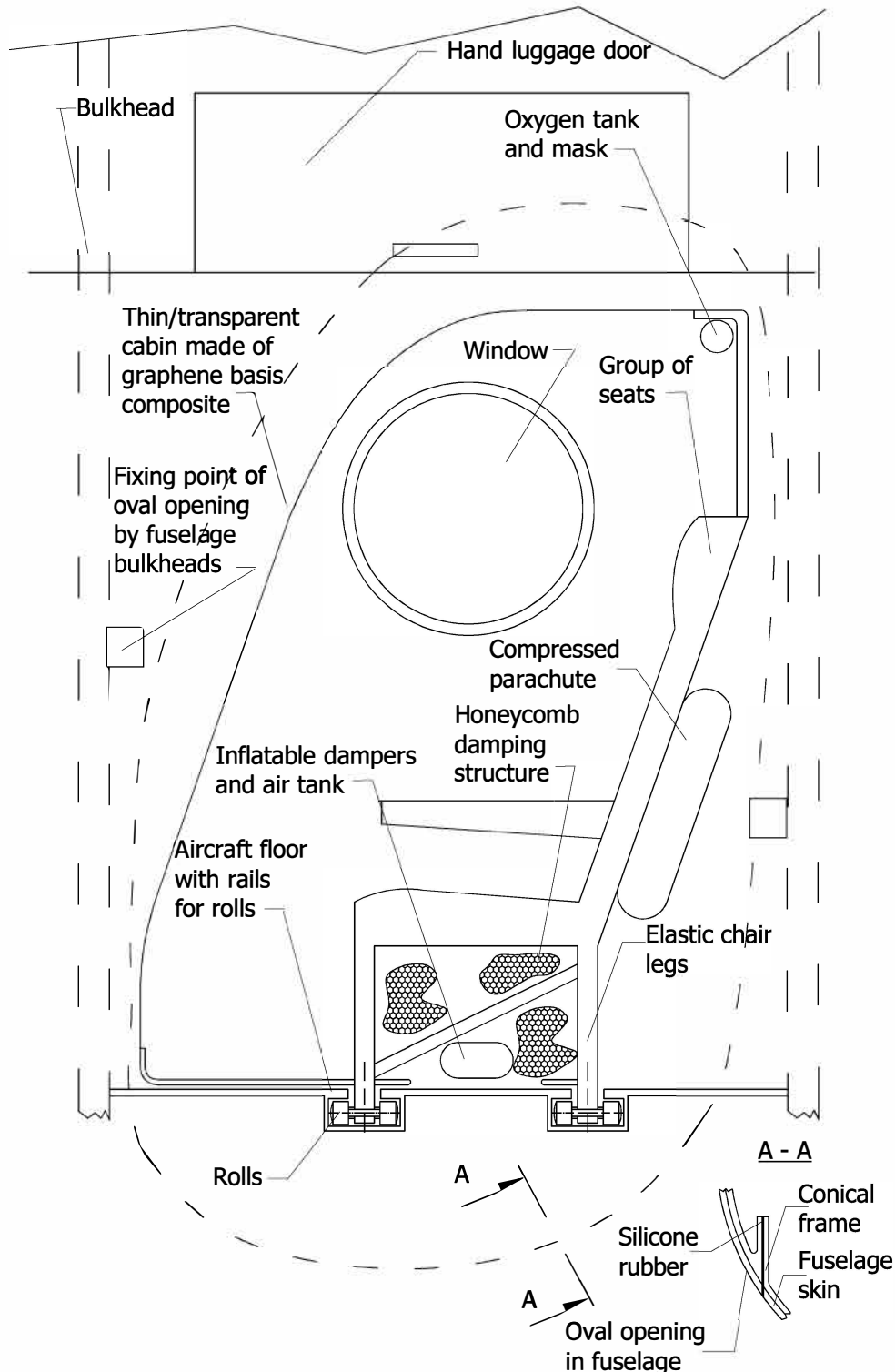


Figure 5: New solution proposed for rescuing of aircraft passengers

This diagram illustrates the water landing configuration of a spacecraft. The spacecraft is shown in a vertical orientation, with its nose pointing upwards. A deployed parachute is attached to the top of the spacecraft, with lines extending upwards. Inflated airbags for damping and floating are shown at the base of the spacecraft, surrounding the landing gear. The airbags are depicted as large, rounded shapes. The landing gear consists of two main wheels and a smaller nose wheel. The diagram is labeled with 'Deployed parachute' and 'Inflated airbags for damping and floating'.

Consequently, the groups of seats can slide along rails to the airplane sides together with a small oval portion of the fuselage fairing. The oval portion is located between the two adjacent ribs of fuselage. This oval portion has a conical frame for joining with the similar conical frame fixed by ribs and fuselage fairing. The oval portion is connected by each adjacent rib in one point and the sealing between the conical surfaces is done with silicone rubber. Behind each side of group of seats there are two compressed parachutes placed in two pockets. If disaster is imminent, at the pilot command, the groups of seats slide in a programmed sequence to both airplane sides. Each group of seats is actuated by a set of 3 cartridges which are ignited progressively. After ejection from aircraft, another set of 3 cartridges which are ignited progressively pushes each group of seats upwards. Finally the two parachutes of each seat are extracted automatically by two other cartridges. The launching sequence and timing of cartridge ignition is calculated to keep sidewise and vertical accelerations to acceptable levels and all the groups of seats are kept at a safe distance from aircraft and one another. Each group of seats is encapsulated in a compact transparent cabin made from several layers of graphene impregnated with a transparent epoxy resin. The capsules protect the occupants from the air stream after ejection from aircraft. In normal state, the units are fixed to the floor using two locks and the oval portion is secured to the two adjacent fuselage bulkheads by 2 other locks. After the pilot presses the ejection button, the sequence of ejection is controlled by an independent computer, which commands the unblocking of all the locks and the ignition of pyrotechnic cartridges that laterally push each unit. The launching sequence is: the groups of seats from the rear side of

fuselage are launched first, then launching continues to the front of fuselage, including pilots' group of seats and cabin crew group of seats. After a group of seats is ejected from aircraft, other two pyrotechnic cartridges extract the two parachutes for opening. After the parachutes open, an airbag made from several layers of graphene impregnated with silicone rubber inflates under each unit. The airbags dampen the landing shock and provides flotation for the group of seats in case of ditching (fig.6). In addition, the landing shock is dampened by a honeycomb structure placed under the seat and the elastic legs of chairs. The group of seats section contains an oxygen tank and masks for passengers during descent. In the case of spaceplanes the cabins should have side walls due to the very high flying speed and height.

An example of launching sequences is illustrated in fig.7 for Fokker 50.

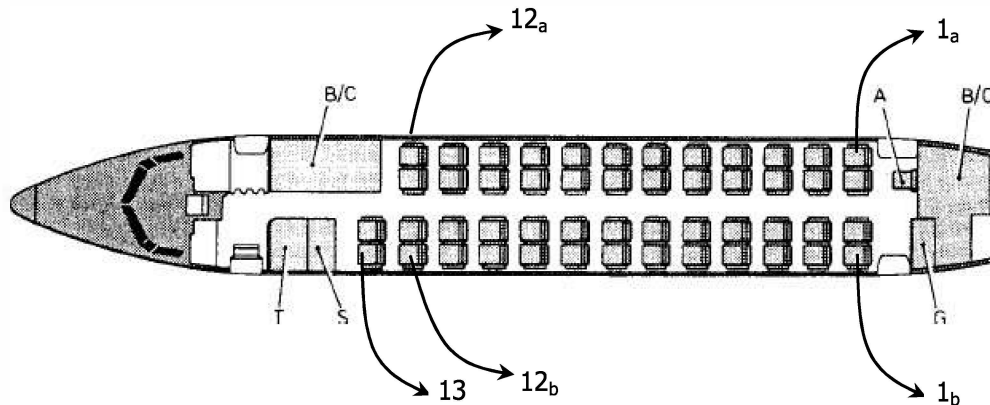


Figure 7: Evacuation of passengers at Fokker 50

The sequence of launching must maintain a horizontal distance between adjacent parachutes of at least five times the diameter of canopy. [3]

4. DISCUSSION ON DESIGN CHANGE FOR AIRCRAFT EQUIPPED WITH THE NEW PASSENGERS RESCUE SYSTEM

The present rescue system does not require major design changes for existing aircraft or additional expensive equipment for manufacturing.

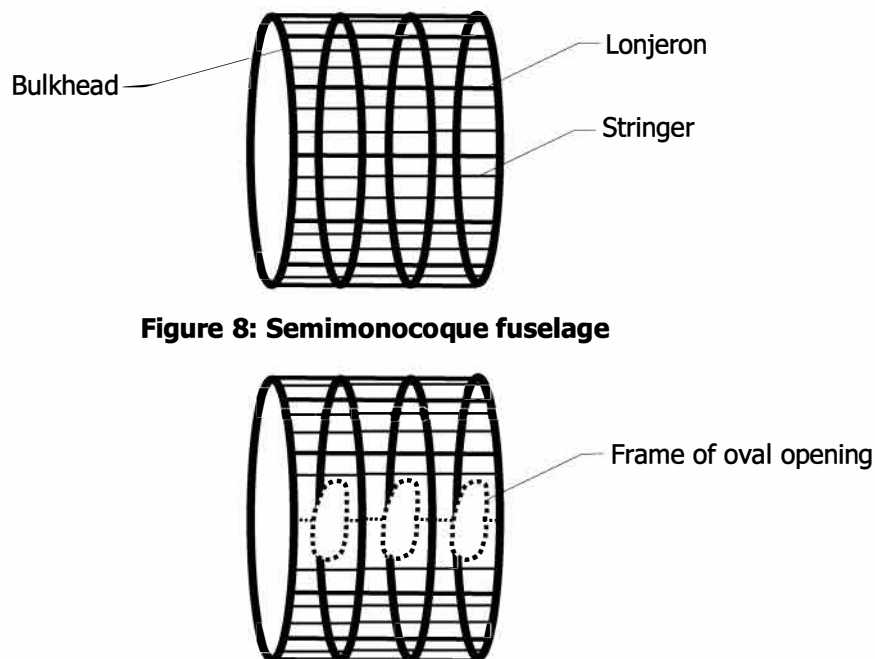


Figure 8: Semimonocoque fuselage

Figure 9: Semimonocoque fuselage transformed for the rescue system

For implementation of this rescue system, the seat pitch of aircraft must be increased from 34-36 in to 41-43 in. Additionally the seats must be placed exactly between fuselage bulkheads.

In figs 8 and 9, one can see the transformation of a monocoque fuselage for incorporating the rescue system. In fig. 8 it is presented a normal monocoque fuselage. In fig. 9 is presented the same fuselage with central lonjeron and upper and lower central stringers replaced by the frame of oval opening which is connected to the side of bulkheads.

This change is possible because the main bending stress of fuselage has minimum values in fuselage skin near the seats (fig.10).

Although the distance between bulkheads must be increased by about 20%, the frame of oval opening reduces the central bulking which appears when the distance between bulkheads is too large. [4]

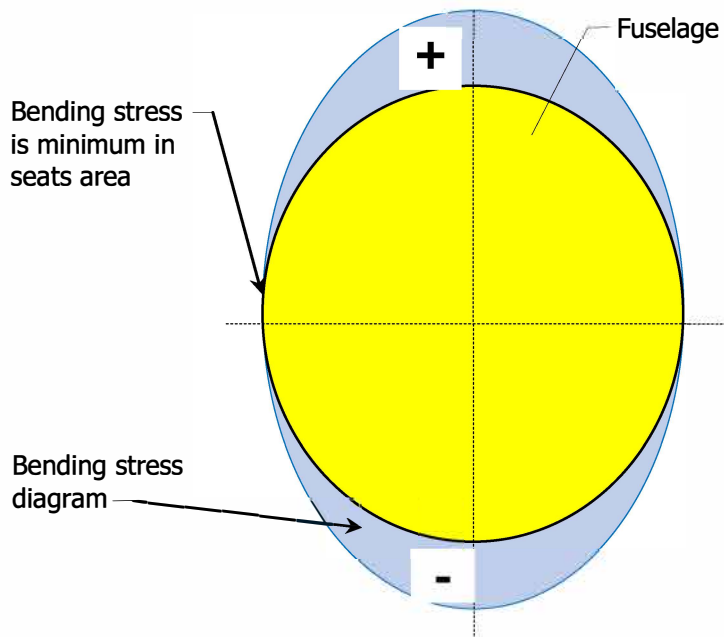


Figure 10: The bending stress in the fuselage skin and lonjerons/strings

In the case of a flying wing aircraft (fig.11), launching of groups of seats on a side is much more difficult because of the presence of leading edge of wing. Upward launching is difficult, too, because the passengers cannot tolerate the high accelerations involved in this type of launching. Downward launching is difficult, too, because of luggage space and landing gears.



Figure 11: Boeing 797 aircraft

5. CONCLUSIONS

- The passengers rescuing system for large aircraft presented in this paper proposes as rescue units composed of 2, 3 or 4 passengers to be ejected through fuselage sides in a controlled sequence.
- Experience from manufacturing small aircraft (up to 5 seats) shows that passengers can be rescued using parachutes if a light weight parachute is placed at the top of fuselage. The system for large aircraft presented here is similar except for application to rescue units composed of 2, 3, 4 seats each provided with two parachutes.
- This system can be applied with minor changes of present aircraft design.
- Analyzing this rescuing system, one can understand that there are not significant issues related to manufacturing aircraft with such system. The main issue is related to marketing. The market could require such aircraft in the near future.

REFERENCES

1. <http://www.independent.co.uk/travel/detachable-cabin-invented-to-save-lives-during-plane-crashes-a6814311.html>;
2. <http://www.bbc.com/future/story/20131223-should-planes-have-parachutes>;
3. Stein, K., Tezduyar, T., Kumar, V., Sather, S., Benney, R., Thornburg, E., Kyle, C., Nonoshita, T.; 2003; Aerodynamic Interactions between Parachute Canopies, ASME, Vol. 70, JANUARY 2003;
4. Arunkumar, K.N., Lohith, N., Ganesha, S.H.; 2012; Effect of Ribs and Stringer Spacings on the Weight of Aircraft Structure for Aluminum Material, Journal of Applied Sciences, 12: 1006-1012, 2012

A knowledge based engineering tool to support front-loading and multi-disciplinary design optimization of the fin-rudder interface

Akshay Raju Kulkarni
PhD candidate, Delft University of Technology
a.rajukulkarni@tudelft.nl

Gianfranco La Rocca
Assistant Professor, Delft University of Technology
g.larocca@tudelft.nl

Tobie van den Berg
Knowledge Based Engineering specialist, Fokker Aerostructures B.V.
tobie.vandenberg@fokker.com

Reinier van Dijk
CEO, ParaPy B.V. & PhD candidate, Delft university of Technology
reinier.vandijk@parapy.nl

ABSTRACT

Socio-economic challenges and global competition drive high-tech industries to combine their cutting-edge technology with improved time-to-market and cost efficiency. In order to meet these challenges, Tier 1 and Tier 2 companies need to organize and formalize their product development process and align their core competencies with the regulations, processes and tools of their customers i.e. Original Equipment Manufacturer (OEM). In order to reduce time-to-market, improvements in product development lead time are necessary, which, in turn requires a combination of a streamlined product development process and systematic design space exploration capabilities. A way forward to reduce lead time, improve cost efficiency and enhance competitiveness is to apply the so-called front-loading product development approach. Front-loading relies on the company's ability to develop (semi-) automated design systems and knowledge bases (KBs) that store their consolidated knowledge. These design systems and KBs are established before the actual start of a project, so as to enable their quick deployment for the preparation of proposals and to trigger new development processes to further reduce design lead time. Effective design space exploration needs to be carried out to generate better designs (even families of design variants) for the customer. This is made possible by performing MDO studies in advance and storing the results in the company's KBs. The research presented in this paper illustrates how the application of front-loading can help an airframe manufacturer, performing fin-rudder interface design, with the rapid generation of proposals for OEMs. It is demonstrated as to how the use of knowledge based engineering in combination with PIDO (Process Integration and Design Optimization) tools enables multi-stage front-loading process, thus supporting design studies ranging from basic "what-if" assessments to full blown single and multi-objective optimization. The presented technology demonstrator shows a potential lead time reduction of over 90% and an improvement in product performance of up to 30%.

KEYWORDS: *Front-loading, Knowledge Based Engineering, Multidisciplinary Design Optimization, Fin-rudder interface design*

Flight Software Development and Validation Workflow Management System

Dan Gultureanu

*Space Systems/Loral (SSL), Software Systems Engineering
Manager, Flight Software
3825 Fabian Way, Palo Alto, California 94303, USA
Dan.Gultureanu@sslmda.com*

Kevin Kerns

*Space Systems/Loral (SSL), Software Systems Engineering
Senior Software Engineer*

Tom Henthorn

*Space Systems/Loral (SSL), Software Systems Engineering
Manager, System Validation*

John Quach

*Space Systems/Loral (SSL), Software Systems Engineering
Senior System Validation Engineer*

Mitch Kleen

*Space Systems/Loral (SSL), Software Systems Engineering
Senior Software Engineer*

ABSTRACT

The aerospace industry is undergoing unprecedented transformation. New players, new ventures, and new technologies drive the established business towards a transition from traditional models and strategies to automated production and innovative methods. Software architecture for space systems needs to become more agile while preserving a high standard of quality. To that end, the rigorous verification and validation process that yields high quality software products should embrace automation and take full advantage of COTS hardware and software products. In line with the industry transformation, SSL's Flight Software Development and Validation Department uses a modular, layered architecture that has evolved over decades of orbital experience. This paper describes the SSL Flight Software Development and Validation Workflow Management System and the advantages of such a system/framework for development and verification of very complex spacecraft. This system/framework allows faster cyclical test-fix-test process and also provides a platform that can be extended for a multitude of applications.

KEYWORDS: *Software Development, Software validation, Testing architecture, Layered architecture, COTS hardware and software*

Initial Investigation of Aerodynamic Shape Design Optimisation for the Aegis UAV

Y. Azabi

School of Aerospace, Transport and Manufacturing, Cranfield University

PhD Researcher

MK43 0AL, UK

y.m.azabi@cranfield.ac.uk

A. Savvaris

Reader

a.savvaris@cranfield.ac.uk

T. Kipouros

Lecturer

t.kipouros@cranfield.ac.uk

ABSTRACT

This paper presents an aerodynamic design optimisation methodology used in further developing an already existing Unmanned Aerial Vehicle (UAV) platform called Aegis. This paper aims to deliver a medium altitude long endurance UAV for civilian purposes. The methodology used is also applicable to conceptual and preliminary design phases of any aerial vehicle platform. It combines a low fidelity aerodynamic analysis tool, Athena Vortex Lattice Code, with a design optimisation tool (Nimrod/O). The meta-heuristic algorithm, Multi-Objective Tabu Search-2 (MOTS2), is used to perform the optimisation process. This new methodological study optimises the UAV wing planform for level flight. It was used successfully to obtain a set of optimal wing shapes for the Aegis UAV flying at different speeds. Prior to the formulation of the design problem, a parametric study was performed to explore the design space, and provide an insight into how the objective functions behave with respect to the design variables. The methodology presented here is not finalized, it is a first step to constructing a general framework that can be used to optimise the design of a twin-boom UAV aerodynamic shape. The interfacing of the already successful packages Nimrod/O, MOTS2, and AVL software produces an initial result that shows the capability of the new methodology to provide correct support decisions making for a design optimisation process that will benefit the entire community of UAV researchers and designers when it is complete.

KEYWORDS: *multi-objective optimisation, nimrod/O tool, Tabu search, UAV conceptual design, parallel coordinates*

Convexification in Energy Optimization of a Hybrid Electric Propulsion System for Unmanned Aerial Vehicles

Ye Xie
Cranfield University
PhD Student
Bedford, UK, MK43 0AL
ye.xie@cranfield.ac.uk

Al Savvaris
Cranfield University
Reader

Antonios Tsourdos
Cranfield University
Professor

ABSTRACT

This paper presents the energy management of a hybrid electric propulsion system for unmanned aerial vehicles, using convex optimization. The primary energy optimization problem is formulated and then converted to a convex problem. The introduction of variable–battery internal energy is firstly proposed to convexify the state equality function. This convexification method can yield to a more straightforward and clear form of convex problem than previous studies. The relaxation of equality constraints is also employed without loss of equality. The numerical examples and forward simulations are carried out to validate the convexified problem. The result of flight scenario infers that the convex relaxation does not prejudice the optimality of the solution. By comparing with the benchmark optimization–dynamic programming, the convex optimization performs gentler optimal control and minimal optimal cost results, with much less optimization time. The most significant is that the convexification reduces the optimization computation to a level compatible with the practical application.

KEYWORDS: *UAV, Hybrid Electric Propulsion System, Fuel Optimization, Convex Optimization, Convexification, Lossless Relaxation*

NOMENCLATURE

x	- state variable of system	P	- power
u	- control variable of system	T	- torque
J	- cost function	ω	- rotational speed
\dot{m}_f	- fuel rate of engine	E	- battery internal energy
I	- current of battery	Subscripts	
Q_{max}	- the maximum capacity of battery	ICE	- engine
V_{oc}	- open circuit voltage of battery	EM	- electric motor
R_{int}	- internal resistance of battery	$loss$	- power loss
G	- gear ratio of gear box		

1 INTRODUCTION

Nowadays, a growing number of Unmanned Aerial Vehicles (UAVs) are powered by electric motors (EMs), because of lower emissions and noise, better overall efficiency, and lower maintenance requirements. However, the specific energy of electric energy storage sources, e.g. batteries, is much lower than that of fossil fuel [1]. As a result, the internal combustion engine (ICE) is preferred for relatively large or long-endurance UAVs, due to its high power and energy density [2]. The hybrid

electric propulsion system (HEPS) combines an electric powertrain with a conventional combustion engine to provide propulsion, in other words, being able to have the energy efficiency of an electric propulsion system with the extended range of an ICE. The aforementioned benefits make HEPS an attractive option to explore for powering UAVs.

The Air Force Institute of Technology (AFIT) has conducted several studies on aircraft hybrid electric technologies. Harmon et al. began the project with the theoretical design of neural network control for a parallel HEPS [3]. Continuing on from this work, Ausserer [4] implemented the physical integration and validation of a prototype. Queensland University of Technology (QUT) also conducted some studies [5]. Glasscock et al. successfully downsized the engine and improved the overall propulsive efficiency compared to the non-hybrid powered aircraft.

HEPS can provide better fuel economy and lower emissions without compromising performance. In addition, it can provide on-board electrical regeneration for powering different systems, but this flexibility and diversity comes at a cost of increase complexity in hybrid energy management.

The energy optimization is one of the most popular topics regarding hybrid energy management. Research work by scholars investigated various types of optimizations in order to achieve the best control trajectory for a given mission. The Dynamic Programming (DP) is one of the most studied theories because it can guarantee the global optimality of the solution [6]. However, large computational cost exists in DP due to nonconvex characteristics of the energy optimization problem. Consequently, the optimization result from DP is usually used as a benchmark for other strategies.

Convex optimization problem is widely favoured because it can be solved, very reliably and efficiently [7]. Using interior-point methods, the problem can be guaranteed convergence to the global optimum with a deterministic upper bound on the number of iterations, without requirement of pre-supplied initial guess. In other words, the global optimality, lower complexity and no request of use-specified initial value make the convex programming very promising for real application.

The convex optimization for energy management of hybrid ground vehicles was firstly proposed by researchers of Chalmers University of Technology [8], [9]. The studies are concentrated on convexifying the nonconvex primary problem. The model of energy buffer (capacitor or battery) was convexified by introducing the variable-pack energy [10]. Furthermore, a lossless relaxation and its detailed proof were also provided in [10], [11]. The works indicate that the global minimum of original problem can be obtained by solving the relaxed problem without the loss of equality. This paper proposes a new convexification method. It can retain the feature of lossless relaxation from previous studies, but also lead to a more straightforward and clear form of convex problem.

The results presented in this paper are part of the ongoing work performed as part of the AIRSTART project. AIRSTART is a £3.2 million collaborative Research and Development project developing key technologies to support long-endurance UAVs. Cranfield is working on the hybrid propulsion system, converting a Rotron UAV engine into a hybrid combustion-electric system. The platform for testing the hybrid propulsion system is a remotely piloted multi-purpose UAV—the Aegis. First, the primary energy management is formulated, in which the minimization of the total fuel use is selected as the objective function. Later, three various techniques are implemented to convexify the nonconvex original problem. The cost is fitted with the piecewise linear function, while the battery voltage and electric motor losses are approximated with quadratic and exponential equation, respectively. A new variable, called the battery internal power, is firstly introduced here to convexify transition equation of system state. The same techniques applied on [10] is then employed to relax the equality to inequality constraint. The last numerical examples and forward simulations are carried out to verify the optimal results of convex optimization.

2 ORIGINAL PROBLEM FORMULATION

Initially, the formulation of original problem has been presented. In this study, the objective of the energy optimization is to minimize the fuel consumption of engine during the complete flight mission. The cost function is expressed by:

$$J = \int \dot{m}_f(t) dt, \quad (1a)$$

where \dot{m}_f denotes the fuel consumption rate of engine, which is dependent on time t .

The control variable of formulated system is the engine output power P_{ICE} , i.e. $u(t) = P_{ICE}$; whereas the state variable is the battery's State-of-Charge (SoC), denoted by $x(t)$. According to the definition of SoC, the system state transition equation can be written as:

$$\dot{x}(t) = -\frac{I}{Q_{max}}, \quad (1b)$$

where I is the current flowing through the battery and Q_{max} is the battery maximum capacity. The battery model is commonly described by an ideal open-circuit voltage source in a series with an internal resistance [12] in hybrid vehicle analysis. It uses the open circuit voltage V_{oc} and internal resistance R_{int} to obtain the battery output power P_{batt} :

$$P_{batt} = I * V_{oc}(x) - I^2 R_{int}, \quad (1c)$$

in which the resistance R_{int} is assumed to be constant.

In addition to cost function and system dynamics, the optimization is also subject to limitations of each component and the powertrain capability. Put differently, the power demand P_{req} , in addition to the motor/generator losses $P_{EM,loss}$, appears as the sum of the engine and battery power contributions (see equation (1d)). Also, other constraints (power, state and current constraints) can be transformed and addressed by the equations (1e-1g).

$$P_{ICE} + P_{batt} = P_{req} + P_{EM,loss}, \quad (1d)$$

$$P_{ICE,min}(\omega_{ICE}) \leq P_{ICE} \leq P_{ICE,max}(\omega_{ICE}), \quad (1e)$$

$$x_{min} \leq x \leq x_{max}, \quad (1f)$$

$$I_{min} \leq I \leq I_{max}. \quad (1g)$$

3 CONVEXIFICATION

The original Problem (1) is not convex. The inequality constraints (1e-1g) are affine, but equality equations and cost function do not satisfy requirement of convex programming [7]. In the following text, three techniques—approximation, change of variables and relaxation are carried out to convert the Problem (1) into a convex Problem (10).

3.1 Approximation

The approximation is normally employed to reveal the inherent correlation between different variables with an algebraic expression, instead of the original numerical data from experiments. During the approximation, the convexity of original problem can also be investigated thoroughly.

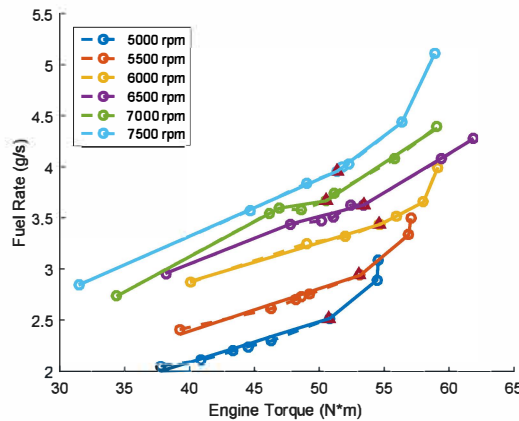


Figure 1. Piecewise linear approximation of the fuel rate at different speeds.

The best efficiency points are represented by triangle marks and fitted data are denoted by the solid curve.

In this case, the fuel rate (the integrand of objective function) is not a convex function of control variable, but it is piecewise linear (affine) dependent on engine torque at a given speed (see Figure 1). In other words, the fuel rate at each speed can be addressed by $\dot{m}_f = k(\omega_{ICE}) \frac{P_{ICE}}{\omega_{ICE}} + d(\omega_{ICE})$. The first turning point of different pieces indicates the best efficiency point for a given speed, if the fuel rate curve is piecewise convex [13]. This condition is not fulfilled at 6500 rpm and 7000 rpm, so their best efficiency points move to the second turning point due to the effect of nonconvex segment. To avoid large distortion and shift of the best efficiency region, the best efficiency points are needed to

be kept at its original value. The results of piecewise linear approximation is also revealed in Figure 1 with the solid curve.

In general, the curve of voltage as a function of SoC can be divided into three segments by two turning points: the end of the exponential zone and the end of the nominal zone (as shown in Figure 2). It is clear that the function V_{oc} is nonlinear and also not convex. Fortunately, the SoC is typically limited between (0.2, 0.8), i.e. the nominal zone, to extend the lifetime of battery. As a result, the V_{oc} can be fitted with a quadratic function: $V_{oc} = a_v x^2 + b_v x + c_v$. The convex approximation result is also drawn in Figure 2 and the coefficients (a_v, b_v, c_v) are (24.95, 9.319, 291).

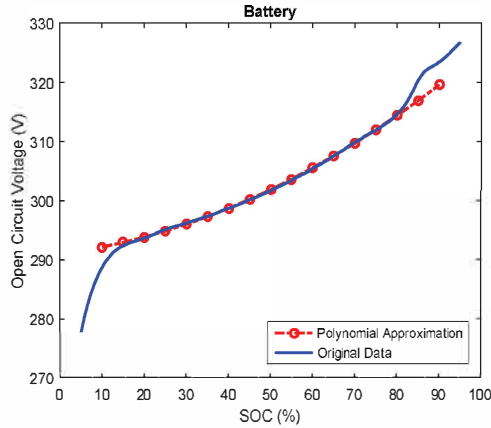


Figure 2. Approximation of open circuit voltage.

When a second order polynomial is applied on fitting, the coefficient of determination is 0.9993.

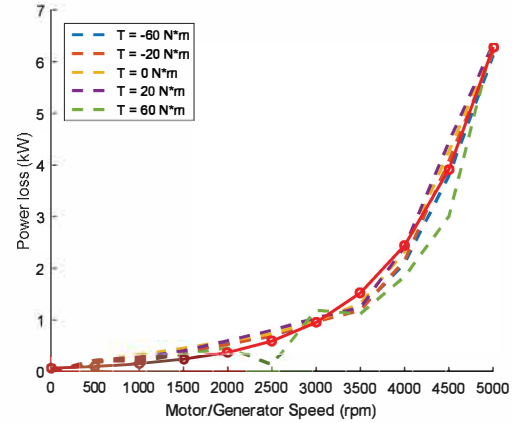


Figure 3. Approximation of the motor/generator power losses.

The fitted data are denoted by the solid curve marked with circles and its coefficient of determination is 0.9919.

The power loss of motor/generator is dependent on the output speed and torque. Figure 3 displays the relationship between power loss and speed under difference torques. The distance correlation between power loss and torque is 0.0541. This means that the power loss is weakly dependent on torque. As a result, the power loss is approximated as a formula only involving speed, using convex function $P_{EM,loss} = a_m * \exp(b_m \omega_{MG})$. The fitting results are also plotted in the Figure 3, with the red solid line marked by circles. The fitted coefficient is $a_m = 0.0563$, $b_m = 9.4248 * 10^{-4}$, when the unit of speed is revolutions per minute. It is notable that the original data is the expectation of power loss data at different torques.

3.2 Change of Variables

Afterwards, the change of variables is implemented to prepare for the formulation of new convex problem. Firstly, a battery internal power P_b which does not include battery loss is introduced, then equality constraints (1c-1d) are converted to:

$$P_b = I * V_{oc}(x), \quad (2)$$

$$P_{ICE} + P_b = P_{req} + P_{EM,loss} + P_{b,loss}. \quad (3)$$

The power loss of battery $P_{b,loss}$ defined here is mainly the dissipative power of resistance, which is dependent on the internal battery power and battery SoC (see Figure 4). Similar to $P_{EM,loss}$, the power loss is mainly correlated with battery power, rather than SoC. Meanwhile, it can be fitted with a convex quadratic function: $P_{b,loss} = a_l P_b^2$. The fitted coefficient is $a_l = 3.24 * 10^{-6}$. Likewise, the original data is the expectation of power loss data at difference charge-states.

Now, the inequality (1g) is substituted by:

$$I_{min} \leq \frac{P_b}{V_{oc}(x)} \leq I_{max}, \quad (4)$$

which is affine in the battery internal power P_b , but not guarantees convexity in the battery voltage $V_{oc}(x)$.

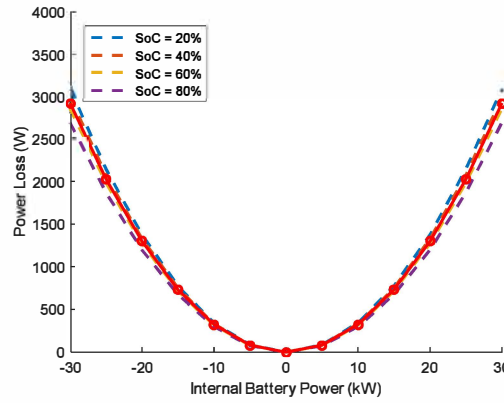


Figure 4. Approximation of the battery power losses.

The fitted data are denoted by the solid curve marked with circles and its coefficient of determination is 0.9998.

Consider approximating $V_{oc}(x)$ with two affine functions: $V_{lb}(x)$ and $V_{ub}(x)$. The $V_{lb}(x)$ is the Taylor expansion of $V_{oc}(x)$ around $x = 0.5$, while the curve defined by $V_{ub}(x)$ goes through two points at $x = 0.2$ and $x = 0.8$. Since $V_{oc}(x)$ is a convex function, the following constraints is satisfied:

$$I_{min}V_{oc}(x) \leq I_{min}V_{ub}(x) \leq P_b \leq I_{max}V_{lb}(x) \leq I_{max}V_{oc}(x). \quad (5)$$

Therefore, by solving problem with constraints (5), one never obtains solutions which violate constraints of the physical problem. The bounds on errors (e_{lb} , e_{ub}) introduced by the second approximation is computed and displayed in Figure 5. The figure clearly shows that the inequalities (4) are not compromised for all practical purposes when replaced by (5).

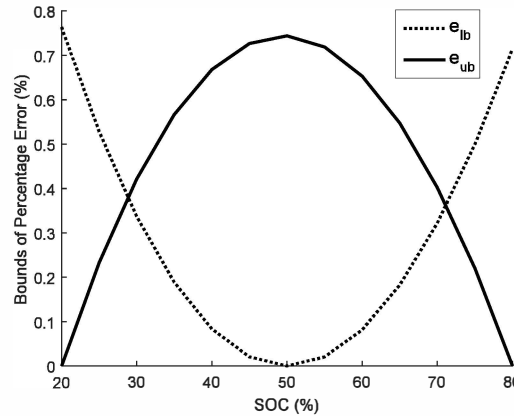


Figure 5. Error bounds of the second approximation.

The percents of errors of upper and lower bounds are both smaller than 1%.

From equation (1b) and (2), the state equality function can be deduced:

$$\dot{x}(t) = -\frac{P_b}{V_{oc}(x)Q_{max}}, \quad (6)$$

which still does not meet the requirement of convex programming. Therefore, a new variable called battery internal energy E is introduced to replace the original state variable (SoC). The new state transition equality is formulated:

$$\dot{E}(t) := Q_{max}V_{oc}(x)\dot{x}(t) = -P_b, \quad (7)$$

while x still denotes the battery SoC. Simple integration manipulation leads to:

$$E(x) = Q_{max} \int V_{oc}(x)dx = Q_{max} \left(\frac{1}{3}a_v x^3 + \frac{1}{2}b_v x^2 + c_v x + d_v \right), \quad (8)$$

where d_v is set to zero without loss of generality. Meanwhile, the inequality (1f) is transformed into:

$$E_{min} \leq E \leq E_{max}, \quad (9)$$

since the $E(x)$ is monotonically increased with x in the domain of definition. The E_{min} , E_{max} are calculated by $E(x_{min})$ and $E(x_{max})$, respectively.

3.3 Constraints Relaxation

With the substitution of variables, the equalities are converted to convex functions. Subsequently, the relaxation of equalities yields to a series of inequality constraints. As a result, the convex formulation of the original problem is constructed as follows:

$$J = \int_0^{t_n} \left(k(\omega_{ICE}) \frac{P_{ICE}}{\omega_{ICE}} + d(\omega_{ICE}) \right) dt, \quad (10a)$$

$$\dot{E}(t) = -P_b, \quad (10b)$$

$$P_{ICE} + P_b \geq P_{req} + P_{EM,loss} + P_{b,loss}, \quad (10d)$$

$$P_{ICE,min}(\omega_{ICE}) \leq P_{ICE} \leq P_{ICE,max}(\omega_{ICE}), \quad (10e)$$

$$E_{min} \leq E \leq E_{max}, \quad (10f)$$

$$I_{min} V_{ub}(x) \leq P_b \leq I_{max} V_{lb}(x). \quad (10g)$$

Note that the equality **(3)** is replaced by **(10d)**. As a consequence, the non-affine equality is successfully converted to a convex inequality. What is worth mentioning is that this relaxation does not prejudice the optimality of the solution. The claim has been logically reason in the [10]. Assume that the convex solver finds the optimal solution holding $P_{ICE} + P_b > P_{req} + P_{EM,loss} + P_{b,loss}$. This means that some energy supplied by the fuel and battery was wasted, thus a better solution can be found with **(10d)** holding with equality.

4 NUMERICAL EXAMPLE

The most commonly used hybrid powertrain configurations are series, parallel and series-parallel architecture. Compared with the series and series-parallel configuration, the parallel configuration is lighter and more reliable, whilst keeping the flexibility of hybrid. What's more, the parallel configuration is best suited for long-endurance UAVs, according to [14].

This paper applies the proposed convexification on the energy optimization of a parallel configured HEPS [15]. Hence, $P_{EM,loss}$ comes from the power loss of the single motor/generator. The power requirement is sum of power requested to drive the propeller and power demanded by the auxiliary devices of aircraft.

Two different hypothetical flight test scenarios are considered: the first test case is a complete mission that includes take-off, climbing, cruising and landing phases, where the battery charge-depleting and charge-sustaining strategy are both implemented on convex programming; second, the charge-sustaining based convex optimization is employed on a cruising flight mission and its performance is compared with the DP. Furthermore, the optimal control of second scenario is conducted and verified on a forward simulation model developed in the previous study [15].

4.1 Test Case 1

The test case used in this section simulates a complete 12 minutes flight mission that includes take-off, climbing, cruising and landing phases. The aircraft take-off run is in the first 1 minute and then continues to climb to the cruise height in the time interval 1-4.5 minute. Then, the aircraft will start its cruise phase at around 4.5 minute and finally the landing phase, after which the mission ends.

The power requirement of this flight mission is shown in Figure 6 with blue dotted line. The optimal control (ICE power) is also plotted with battery internal power. It is clear that the energy from two different sources combines together to power the aircraft during the climbing (between 1-4.5 minute). On the other hand, the battery is charged by the extra power from engine in take-off and landing phase.

Note that the power requirement is equal to the power consumption, which includes actual useful power and power losses. That means constraint **(10d)** holds with equality at the optimal trajectory. In other words, the relaxation presented in section 3.3 does not affect the results of optimization.

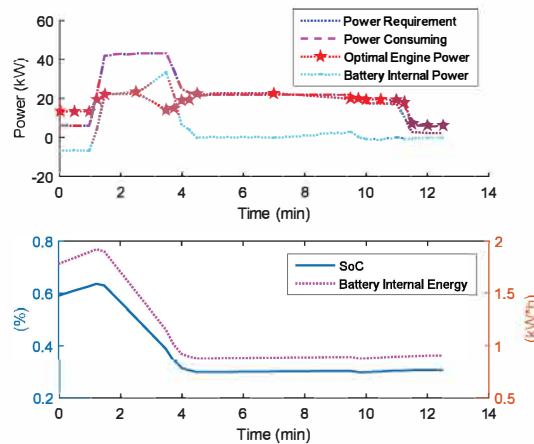


Figure 6. Optimization results of test case 1.

The initial value of SoC is set to 60%. The maximum and minimum value of SoC is 80% and 20%, respectively, considering the nominal operation range of battery. The SoC is allowed to be depleted to 30%, then the energy management is demanded to sustain the SoC around this value, to extend the lifetime of battery.

The Figure 6 also displays the virtual state variable E . The SoC and E both increase in the first 1 minute, due to battery charging during the take-off. Later, they drop by a large margin because the aircraft demands huge power for climbing. After reducing to 30%, the SoC is sustained around this value. The results demonstrate that the convex programming can achieve both depleting and sustaining strategies.

4.1 Test Case 2

The second instance exams the optimality of results from convex programming, by comparing with ones from global optimization–DP. Different from the test case 1, the forward simulation technique is applied on the optimization results to investigate their capabilities in practical application. The flight in this case considers cruising and excludes the take-off and landing phase. The power requirement of the flight mission is shown in Figure 7.

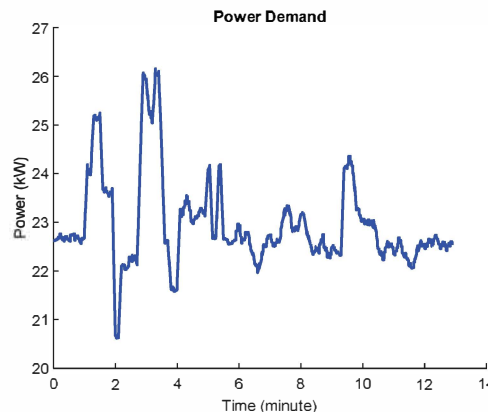


Figure 7. Power requirement of test case 2.

The Figure 8 compares the simulation results of battery SoC, engine power and fuel consumption between convex optimization and DP. The initial value of SoC is set to 50% and its value is supposed to be sustained in the 13-minute whole flight. The curves of SoC verify that two optimizations both can realize the charge-sustaining, but the DP obtains a more precise regulation of SoC. Moreover, the forward simulations demonstrate that optimal controls of two methods are both practical in real application. Yet the optimal control (engine power) derived from DP experiences more intense fluctuation than another one.

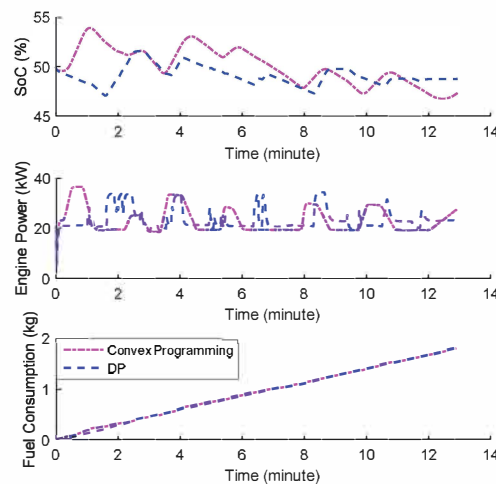


Figure 8. Comparison of convex optimization and DP in test case 2.

The most significant is that the convex programming can achieve better optimal cost (fuel use) than DP, as shown in Figure 8 and Table 1. To be fair, the final SoC of convex programming is lower than one of DP, which means the convex programming consumes more electric energy. In other words, the extra electric energy stored in the battery consumes the fuel spending in the DP. A real fuel consumption of two optimizations will be acquired by adjusting two final SoC values to the same one. Thus, the correction is introduced on the final of SoC.

Table 1: Comparison of consumptions between convex optimization and DP

	Convex Programming	DP
Final SoC (%)	47.37	48.80
Fuel Consumption (kg)	1.8235	1.8328
Corrected Final SoC (%)	50	50
Corrected Fuel Consumption (kg)	1.8304	1.8359
Energy Consumption (MJ)	84.85	85.13
Optimization Time (sec)	0.6708	7.9268

The corrected numbers are also displayed in the Table 1 and it shows that the convex optimization really has lower fuel usage compared with DP. Besides fuel using, another criterion—energy consumption also indicates that the convex optimization demands less energy to complete the flight mission.

Another significant advantage of convex optimization is the improved optimization time. It indicates that the convexification simplifies the original problem and reduces the computation to a level compatible with the practical application.

5 CONCLUSION

This paper presents the energy management of a hybrid electric propulsion system for unmanned aerial vehicles, using convex optimization. The primary energy management was formulated. The fuel minimization was selected as the cost and the battery SoC was chosen as the state variable.

Later, three techniques—approximation, variables and relaxation were implemented to convexify the nonconvex original problem. The nonconvex integrand of cost was fitted with the piecewise linear function. Under operation range, the battery voltage was able to be approximated with quadratic equation. The examination also shows that the power loss of motor is mainly dependent on motor speed with an exponential function. The convexification of state transition equality was successfully accomplished by proposed method, i.e. introducing battery internal voltage and energy. Subsequently, the lossless relaxation of equalities yielded to new inequality constraints.

The parallel hybrid configuration was nominated in the numerical test scenarios. The first test case verifies that the convex relaxation does not sacrifice the optimality of the solution. Also, the convex

programming can reach optimal results under both charge depleting and sustaining strategies. By comparing with the DP in the test case 2, the convex optimization performs gentler optimal control and better optimal cost results. It even demands less total energy to accomplish the flight mission. The most significant advantage of convex optimization is that it can converge to the optimal solution with the time much less than DP.

On account of benefits of the convex programming as mentioned above, a more rigorous proof of equivalence between original problem and its convexified formation will be conducted in future studies.

REFERENCES

1. C. C. Chan; Apr. 2007; "The State of the Art of Electric, Hybrid, and Fuel Cell Vehicles," *Proc. IEEE*, vol. 95, no. 4, pp. 704–718.
2. M. Dudek, P. Tomczyk, P. Wygonik, M. Korkosz, P. Bogusz, and B. Lis; 2013; "Hybrid fuel cell-battery system as a main power unit for small Unmanned Aerial Vehicles (UAV)," *Int. J. Electrochem. Sci.*, vol. 8, no. 6, pp. 8442–8463.
3. F. G. Harmon, A. A. Frank, and S. S. Joshi; Jul. 2005; "The control of a parallel hybrid-electric propulsion system for a small unmanned aerial vehicle using a CMAC neural network," *Neural Networks*, vol. 18, no. 5–6, pp. 772–780.
4. J. K. Ausserer; 2012; "Integration, Testing and Validation of a Small Hybrid-Electric Remotely-Piloted Aircraft," Air Force Institute of Technology.
5. J. Y. Hung, and L. F. Gonzalez; 2012 "On parallel hybrid-electric propulsion system for unmanned aerial vehicles," *Progress in Aerospace Sciences*, vol. 51, pp. 1–17.
6. P. Elbert, S. Ebbesen, and L. Guzzella; 2013; "Implementation of dynamic programming for n-dimensional optimal control problems with final state constraints," *IEEE Trans. Control Syst. Technol.*, vol. 21, no. 3, pp. 924–931.
7. S. Boyd, and L. Vandenberghe; 2010; *Convex Optimization*, vol. 25, no. 3. .
8. N. Murgovski, L. Johannesson, and J. Sjöberg; 2012; "Convex modeling of energy buffers in power control applications," *IFAC Proc. Vol.*, pp. 92–99.
9. X. Hu, N. Murgovski, L. Johannesson, and B. Egardt; 2013; "Energy efficiency analysis of a series plug-in hybrid electric bus with different energy management strategies and battery sizes," *Appl. Energy*, vol. 111, pp. 1001–1009.
10. P. Elbert, T. Nuesch, A. Ritter, N. Murgovski, and L. Guzzella; 2014; "Engine On/Off control for the energy management of a serial hybrid electric bus via convex optimization," *IEEE Trans. Veh. Technol.*, vol. 63, no. 8, pp. 3549–3559.
11. N. Murgovski, L. Johannesson, X. Hu, B. Egardt, and J. Sjöberg; 2015; "Convex relaxations in the optimal control of electrified vehicles," *Proc. Am. Control Conf.*, vol. 2015–July, no. 3, pp. 2292–2298.
12. O. Tremblay, L.-A. Dessaint, and A.-I. Dekkiche; 2007; "A Generic Battery Model for the Dynamic Simulation of Hybrid Electric Vehicles," in *2007 IEEE Vehicle Power and Propulsion Conference*, pp. 284–289.
13. C. Hou, M. Ouyang, L. Xu, and H. Wang; 2014; "Approximate Pontryagin's minimum principle applied to the energy management of plug-in hybrid electric vehicles," *Appl. Energy*, vol. 115, pp. 174–189.
14. R. M. Hiserote; 2010; "Analysis of hybrid-electric propulsion system designs for small unmanned aircraft systems," Air Force Institute of Technology.
15. Y. Xie, A. Savvaris, and A. Tsourdos; 2018; "Modelling and Control of a Hybrid Electric Propulsion System for Unmanned Aerial Vehicles," in *IEEE Aerospace Conference*.

Preliminary Design of Advanced Flight Control System Architectures for Commercial Transport Aircraft

Thomas Lampl

*Institute of Aircraft Design, Technical University of Munich
Research Associate
Boltzmannstraße 15, 85748 Garching, Germany
lampl@tum.de*

Timo Wolf

*Institute of Aircraft Design, Technical University of Munich
Graduate Student*

Mirko Hornung

*Institute of Aircraft Design, Technical University of Munich
Professor, Head of Institute*

ABSTRACT

The functional enhancement of Flight Control Systems (FCS) show potential benefits for commercial transport aircraft. Furthermore, the consideration of new technologies and more-electric concepts lead to a significant increase of the design space for FCS architectures. The objective of this contribution is to enable the preliminary design of advanced FCS architectures for a given FCS configuration. Based on a comprehensive literature research, the main subsystems are identified and simplified models of the architecture are developed. Additionally, technological constraints as well as design rules for actuator distribution, and power redundancy are defined. The design rules for advanced FCS architectures are derived from the basic design rules of existing FCS architectures of commercial transport aircraft. Finally, the presented method is implemented into a design tool. The resulting tool enables the preliminary design of multifunctional FCS architectures.

KEYWORDS: flight control system architecture, high-lift control system, flight control computer, actuator, power supply

Angular Momentum Analysis of Spacecraft with Control Moment Gyros

H. Leeghim

*Dept. of Aerospace Engineering, Chosun University
Gwangju 61452, Republic of Korea
h.leeghim@controla.re.kr*

ABSTRACT

In this paper, a fundamental approach to analyzing the maneuverability of spacecraft with mounted control moment gyros is addressed by searching feasible angular momentum. The geometrical array of control moment gyros considered is a roof array also known as a 2-SPEED system. Due to the simplicity of the singularity envelope of the array considered, it is reasonably practical to conduct rotational performance analysis of the spacecraft. This maneuverability analysis technique uses a unique chart developed in this work, which allows a guaranteed maximum torque output and angular momentum at any time without concern about the singularity problem of the control moment gyros. Therefore, the purpose of this paper is to provide a conservative method for maneuverability analysis of a spacecraft with installed control moment gyros by searching allowable maximum angular momentum. This method is demonstrated using an illustrative example.

KEYWORDS: *Angular Momentum Analysis, Roof Array, Two-Parallel Single-Gimbal Control Moment Gyros.*

Reference Trajectory Optimization Using the Particle Swarm Optimization

Alejandro Murrieta-Mendoza

Hugo Ruiz

SonyaKessaci

*Ecole de Technologie Supérieure / Université du Québec / LARCASE
1100 rue Notre-Dame Ouest, Montreal, Canada*

RuxandraMihaelaBotez

*Ecole de Technologie Supérieure / Université du Québec / LARCASE
Full Professor*

ABSTRACT

Aircraft requires fossil fuel to power engines. This fact brings as a consequence releasing polluting particles to the atmosphere. Among these particles, carbon dioxide has gained special importance due to its contribution to global warming. Aware of this problem, the aeronautical community has been improving over time to reduce fuel consumption. One way of reducing fuel requirements is by improving the aircraft's reference trajectory. Finding the altitudes and speeds that minimize the fuel consumption needed to fly a given mission brings as consequence reducing the pollution released to the atmosphere. There is also the advantage of reducing the flight cost. This paper proposes an algorithm able to find those speeds and altitudes while fulfilling the RTA constraint by using the particle swarm optimization algorithm. This paper has two main objectives. The first objective is to analyze if the algorithm is able to find more economical solutions than the shortest path trajectory by taking weather into consideration. The second objective is to observe if the algorithm provides trajectories respecting current flight constraints. Fuel consumption was computed by interpolating data obtained from a numerical performance database. Weather information was obtained from data provided by Weather Canada. Results showed that the algorithm was able to find economical trajectories respecting their current traffic constraints.

KEYWORDS: TRAJECTORY OPTIMIZATION, PARTICLE SWARM ALGORITHM, FUEL CONSUMPTION, OPERATIONS, AIRCRAFT.

GPU based Computational Simulation of Aircraft Evacuation: Temporal and Spatial Analysis

Minesh Poudel

*DUT, Durban, South Africa
 poudelminesh@gmail.com*

Bhaskar Chaudhury

*DA-IICT, Gandhinagar, India
 E-mail: bhaskar_chaudhury@daiict.ac.in*

Kshitij Sharma

DA-IICT, Gandhinagar, India

Pavel Yaroslavovich Tabakov

pashat@dut.ac.za DUT, Durban, South Africa

Félix Mora-Camino

ENAC, Toulouse, France

ABSTRACT

The effectiveness of Aircraft Emergency Evacuation plays a vital role in the safety of the passengers on board an Aircraft, in case of Emergency landing. In this paper, the implementation and development of a Cellular Automata (CA) based simulator which can be used to simulate the Aircraft Evacuation process is presented. Given the seat-map of the Aircraft, number of passengers, passenger feature distribution and number of functional exits, the simulator can calculate the approximate time of Evacuation. For computational implementation, a bi-dimensional as well as uni-dimensional grids which represents the 2D Aircraft seat-map and an agent which control the passenger movement during Evacuation of the Aircraft is used. Each agent represents a passenger and is characterized by the properties of a human being. An agent has properties like age, sex, walking speed, response time, position and status. The CUDA framework for the parallel implementation of our algorithm/code which can be executed on GPUs (graphics processing unit) has been used and thereby speeding up the simulation process. Several test cases are performed and the results on Aircraft Evacuation times have been compared with existing data collected by Aircraft manufacturers. Detailed investigations reveal useful information on the relationship between Evacuation time and important attributes such as passenger age and sex, number of gates open, passenger distribution etc. The simulator facilitates the investigation of spatial and temporal movement of the passengers, as well as the visualization of pattern formation and collective behavior.

KEYWORDS: Aviation Safety, Aircraft Evacuation, Cellular Automata, GPU Computing.

Bézier-curve Navigation Guidance for Impact Time and Angle Control*Gun-Hee Moon**Korea Advanced Institute of Science and Technology**Ph. D Candidate**Department of Aerospace Engineering, KAIST N7, Daehakro 291, Yuseong-gu,
Daejeon 34141, Rep. of. Korea
ghmoon@fdcl.kaist.ac.kr**Sang-Wook Shim**Korea Advanced Institute of Science and Technology**Ph. D Candidate**Min-Jea Tahk**Korea Advanced Institute of Science and Technology**Professor***ABSTRACT**

This paper addresses a novel impact time and angle control guidance law using a Bézier curve. The 2nd order Bézier curve consists of one control point and two boundary points; initial point P0, middle point P1 and end point P2. The curve is tangent to the line P0-P1 and the line P1-P2, respectively, and always exists in the convex hull of the control points. Proposed Bézier curve navigation guidance, makes the missile follow the Bézier curve with the feedback form of guidance command so that the missile hits the target on the desired time in the desired direction. We conducted numerical simulations on several terminal conditions to demonstrate the performance of proposed method.

KEYWORDS : *Bézier-curve navigation guidance, impact time, impact angle, anti-ship missiles*



The Effect of Sub-systems Design Parameters on Preliminary Aircraft Design in a Multidisciplinary Design Environment

Marco Fioriti
Politecnico di Torino
Researcher

C.so Duca degli Abruzzi n.24 – Turin, Italy
Marco.fioriti@polito.it

Luca Boggero
Politecnico di Torino
Ph.D. student

Sabrina Corpino
Politecnico di Torino
Researcher

Prajwal Shiva Prakasha
German Aerospace Center (DLR)
Researcher

Blohmstraße 20, 21079 Hamburg, Germany
Prajwal.Prakasha@dlr.de

Pier Davide Ciampa
German Aerospace Center (DLR)
Researcher

Björn Nagel
German Aerospace Center (DLR)
Head of Department

ABSTRACT

The remarkable complexity of the aircraft design is due to several reasons and one of these is certainly the high number of completely different design disciplines involved in the process. Many efforts are spent to harmonize and optimize the aircraft design trying to consider all disciplines together with the same level of detail. Within the ongoing H2020 AGILE research, an aircraft MDO (Multidisciplinary Design Optimization) process is setting up linking several design tools and, above all, competences together. This paper focuses on the evaluation of the effects of the main on-board systems design parameters on the other disciplines. Starting from a baseline aircraft (AGILE DC1 regional turbofan), the effect of each parameters have been quantified in terms of variation of aircraft weight, fuel consumption and engine performance. This analysis represents a useful starting point to better understand the importance and the influence of novel On-Board Systems configurations, such as More and All Electric, to the overall aircraft design.

KEYWORDS: *Multidisciplinary Design Optimization, Aircraft Sub-system Design, More Electric Aircraft, Design Space Parameters, Overall aircraft design.*

Configuration Design of Smart Structures with Array Antennas

Minsung Kim

The 7th (Aircraft Systems) R&D Institute, Agency for Defense Development

Principal Researcher

Youseong-gu, P.O. Box 35-7, Daejeon 305-600, Republic of Korea

castle@add.re.kr

Sangmin Baek

The 7th (Aircraft Systems) R&D Institute, Agency for Defense Development

Researcher

Myunggyun Ko

The 7th (Aircraft Systems) R&D Institute, Agency for Defense Development

Researcher

Jongwoo Seo

The 2nd (Command/Control/Information) R&D Institute, Agency for Defense Development

Senior Researcher

Youngsik Joo

The 7th (Aircraft Systems) R&D Institute, Agency for Defense Development

Principal Researcher

ABSTRACT

This study proposes a new configuration design of conformal load-bearing array antenna structures (CLAAS). The CLAAS, when deployed as the upper skin of an aircraft fuselage, can bear aerodynamic loads. The configuration design considers structural and antennal requirements. The maximum allowable deflection is one of these requirements. The simulation results show that the CLAAS deflects 0.5% of one edge length in the out-of-plane direction. The array antenna should perform within the maximum deflection range although the deflection shape differs depending on the structural load conditions. This study presents the antenna performance results for several deflection shapes. A Ku-band array antenna was embedded in the CLAAS. Tile antennas should operate without performance reduction under those deflected configurations. The deflected shape and deflection size were verified with structural tests. The antenna comprised 64 tile antennas in an 8×8 rectangle array configuration. Each tile has 64 radiating elements that act as a single antenna unit.

KEYWORDS: *Conformal Load-bearing Array Antenna Structure (CLAAS); Smart Skin; Array Antenna; Grid Structure*

Credibility of 21st Century numerical simulations in A/C crash and impact analysis

*E. Deletombe
ONERA, The French Aerospace Lab)
Senior Scientist
F-59045 Lille, France)
eric.deletombe@onera.fr*

*M. Mahé
AIRBUS Aircraft
Head of Numerical Simulation Department
F-31700 Blagnac, France
michel.mahe@airbus.com*

ABSTRACT

After a brief reminder of general specifications in commercial aircraft crash survivability regulation, the following paper addresses several issues related to the use of dynamic and crash tests as validation cases for numerical simulations, the current place of the modern numerical simulations in A/C crash analysis, and their main limitations today. A focus will be made on this last question, in order to review well known sources of error in these numerical simulations, recall now long established good practices in Crash FE modelling, and question the concept of a test-free verification and validation process (for virtual testing). Final conclusions and outlooks end the paper, with shorter term and more realistic objectives being optimistically claimed: make the actual crash simulation codes and good practices an acceptable mean to establish "robustness demonstrations" (by parametric/ sensitivity numerical analysis) of the crash performance of modern aircraft design.

KEYWORDS: *Safety, Aircraft, Numerical simulations, crashworthiness, good practices.*

The Influence of the Vaned Diffuser on the Turbo machinery

Gheorghe FETEA

National Research and Development Institute for Gas Turbines COMOTI

Technical Director

220 D Iuliu Maniu Bd., sector 6, cod 061126, OP 76, CP174, Bucharest, Romania

gheorghe.fetea@comoti.ro

Oana DUMITRESCU

Research Assistant

Bogdan GHERMAN

Head of CFD Department

Dan ROBESCU

POLITEHNICA University, Faculty of Power Engineering

Professor

313 Splaiul Independentei, sector 6, zip code 060042, Bucharest, EI 101

dan.robescu@upb.ro

ABSTRACT

This paper analyzes, through numerical methods, the influence of a vaneless diffuser on the performances of a centrifugal compressor with two stages, close to surge line, to see how this is affecting the stable operating range. Two cases were studied in this paper: a) both stages having a vaned diffuser, b) first stage with a vaned diffuser and the second with a vaneless diffuser. The results obtained showed that a vaned diffuser has overall performances better than a vaneless one. Also, in this case scroll played an important role in differentiating the two cases.

KEYWORDS: *CFD, centrifugal compressor, vaned diffuser, vaneless diffuser, stall*

NOMENCLATURE

Latin

CFD – Computational Fluid Dynamics

EV – Valve through which the compressed air leaves the discharge pipe

DV – Proportional discharge valve

VM – Manual valve

H – Total enthalpy

\dot{M}_a – Mass flow

n – Rotational speed

n_w – Working speed

$n_{protection}$ – Protection pressure ratio

p – Pressure

p_s – Selected pressure (required)

w – Molar mass

Greek

π_s – Selected pressure ratio

τ_{ij} – Viscosity tensor

ρ – Density

1 INTRODUCTION

In recent decades, the compressor design technique has been constantly improved, especially due to the development of CFD technology. Significant improvements in the performance of centrifugal compressors have been achieved by solving the three-dimensional Navier - Stokes equations by means of CFD. Experimental and numerical studies have shown that the diffuser has a significant importance on the stability limit of a centrifugal compressor, depending on the impeller design and on the interface between the impeller and the diffuser [2].

The mass flow, efficiency and pressure rise in a compressor are the three important parameters used in defining the performances of a compressor and in its selection. The efficiency and the pressure

ratio of centrifugal compressors depend on the design of the impeller and on the fluid flow inside the work channel, as well as on the losses in the diffuser [11].

Two-thirds of the total losses in a centrifugal compressor occur in the diffuser [2]. There are two types of diffusers, depending on their application. Vaneless diffusers have a wider operating range, lower efficiency and lower pressure recovery than vaned diffusers [1]. The space between the impeller tip and the diffuser vanes is critical to ensure an effective diffusion process and helps the uniformization of the impeller flow [2].

In the case of the vaneless diffuser the throat is absent; which is leading to a wide operating range. Performances of a vaneless diffuser are affected by the channel width and the radius ratio between the diffuser inlet and outlet [5].

In the case of the vaned diffuser, the positive incidence increases the likelihood of surge, while the negative incidence leads to blockage [6]. Surge can also occur in the vaneless diffuser [7]. Due to the influence of the negative pressure gradient, the boundary layers on the wall are deviated in a tangential direction rather than in the axial direction [8]. Generally, for vaneless diffusers, the pressure recovery is less than in the vaned diffuser case, up to 20%, and 10% less on a stage [17].

The vaned diffusers provides a better or similar discharge pressure compared to vaneless stators at a smaller diameter. A vaneless diffuser leads to a larger compressor dimension. A vaned stator allows the output angle of the diffuser to be controlled downstream of a volute [9, 16], which is important. There are 5 important design parameters that affect the overall performance of a diffuser: diffuser width, radius ratio, chord length, blades number and angle at diffuser inlet [10].

An increasing in fluid diffusion with decreasing of the flow rate will lead to compressor surge. Shaaban [12] showed that in a small turbocharger with vaneless radial diffuser the aerodynamic losses are 33-45% from the overall compressor aerodynamic losses at surge.

A numerical study regarding the rotating stall phenomena in a vaneless diffuser, using an incompressible viscous flow solver, was realized by Ljevar et al. [13]. It was found that the geometry design and the outlet and inlet flow conditions influence the stability limit.

In the case of vaned diffusers it was found that with the increasing of the number of vanes, the operating range narrows [14]. For a radial vaned diffuser, the most critical area, according to P. Delbert et al. [15], is the inlet triangle, or the "semi-vaneless" part, where the strongest backflow phenomena and the highest pressure gradients occur.

Vaned diffusers are used in many applications. Their impact on the operating range of a single stage compressor depends on parameters such as the Mach number at the inlet to the stator, the angle of inlet flow, the performance of the rotor and on the rotor - stator coupling [18].

In this paper, the influence of the vaned diffuser on the performances of a centrifugal two-staged compressor close to surge line is studied. The goal is to see how the range of stable operating regimes is affected. Two cases are studied: a) the centrifugal compressor with both stages having vaned diffusers, b) the centrifugal compressor with the first stage having a vaned diffuser, and the second one using a vaneless diffuser. Since the flow patterns on a diffuser are influenced by the velocity and flow angle distribution at the impeller outlet [15], those are the main characteristics to be surveyed.

2 PROBLEM FORMULATION

The novelty of the presented approach resides is the direct coupling between the two stages, allowing an assessment of the direct interaction between them. Also, the use of the vaneless contact section was taken into account in order to increase the range of stable regimes at which the compressor can work.

2.1 Mathematical Model

For this simulation, a compressible flow has been considered. The equations that govern the flow are the Reynolds-averaged Navies–Stokes equations, as presented below:

- Continuity equation:

$$\frac{\partial \rho}{\partial t} + \frac{\partial \rho u_j}{\partial x_j} = 0 \quad (1)$$

- Momentum equation:

$$\frac{\partial \rho u_i}{\partial t} + \sum \frac{\partial \rho (u_i u_j)}{\partial x_j} = - \frac{\partial p}{\partial x_i} + \frac{\partial}{\partial x_i} (\tau_{ij} - \rho u'_i u'_j) = 0 \quad (2)$$

where $\tau_{ij} = \mu \left(\frac{\partial u_i}{\partial x_j} + \frac{\partial u_j}{\partial x_i} \right)$.

- Energy equation:

$$\frac{\partial}{\partial t} (\rho H) + \sum \frac{\partial}{\partial x_j} \left(\rho u_j H + \rho u'_j H' - k \frac{\partial T}{\partial x_j} \right) = \frac{\partial p}{\partial t} + \sum \frac{\partial}{\partial x_j} (u_i \tau_{ij} + u'_i \tau'_{ij}) \quad (3)$$

- Equation of state:

$$\rho = \frac{wp}{R_0 T} \quad (4)$$

2.2 Geometry definition and spatial discretization

In this study, the analysis was performed using the commercial software ANSYS CFX. The computational domain consists of all the channels of the two stages of the analyzed centrifugal compressor, each stage with an shrouded impeller, vaned/vaneless diffuser and a volute, as shown in Fig. 1. The characteristics of the centrifugal compressor are presented in Table 1.

Table 1: Parameters of the compressor

Domain		No. of Blades	Angular velocity [rot/min]
First Stage	Impeller	11 (2 splitter blades)	37550
	Diffuser	18	
Second Stage	Impeller	15 (1 splitter blades)	41500
	Diffuser	20	

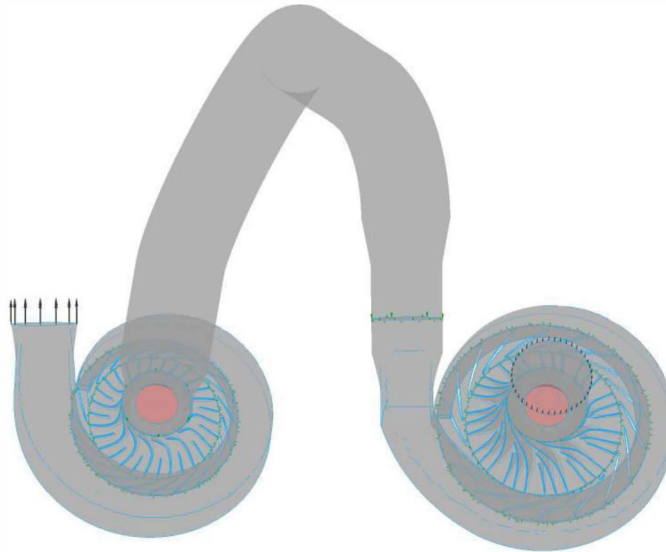


Figure 1: Geometry of the centrifugal compressor with vaned diffuser

The computational grid is structured for the impellers, diffusers and the contact section and unstructured for the volute. The structured grid for the impellers and diffusers was created using CFX – TurboGrid, while Ansys ICEM-CFD was used for the volute. The mesh obtained for the two cases has:

- Case with a vaned diffuser: 22.82 million nodes and 25.85 million elements;
- Case with a vanelles diffuser: 20.41 million nodes and 23.64 million elements;

The simulations are carried out for ideal air, stationary conditions, and the numerical scheme is of the second order in space.

At the interface between the rotational and the stationary parts, the *Frozen-Rotor* method has been used [19]. This type of interface is fixed; the relative orientation of the components is not changing, but depending on the motion defined by the domain the frame of reference is changing [19]. Between the stationary components a *None* setting is used, because there is no frame change or pitch change.

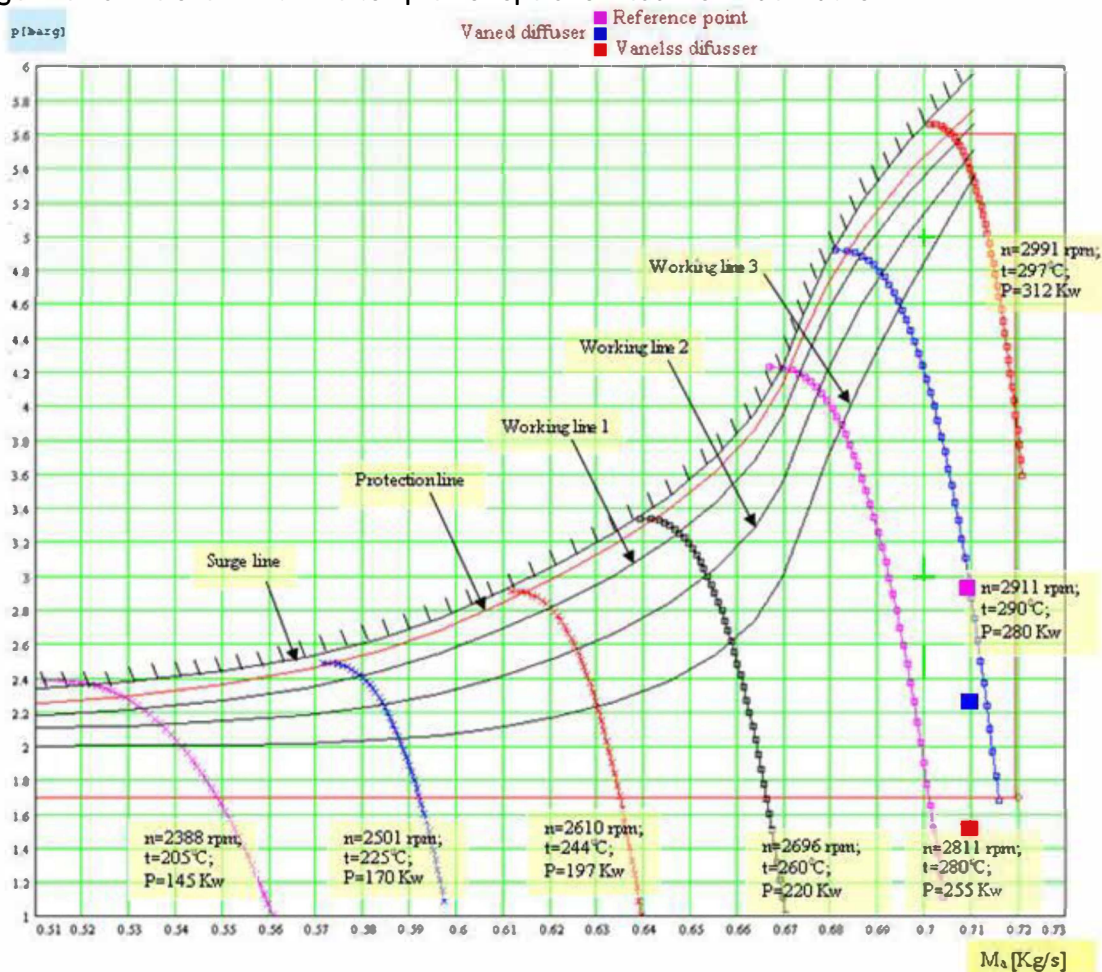
In defining the conditions of the domain, a reference pressure of 3 bar and a pressure ratio of 3.89 barg at the compressor exit have been used. In Table 2, the main boundary conditions of the computational domain are presented.

Table 2: Boundary conditions

Domain	Type of condition	Value	
First stage: entrance part	Inlet	Static Pressure	-2 [barg]
		Static Temperature	293 [K]
Second Stage: volute	Outlet	Mass Flow Rate	0.6 [kg/s]

The turbulence model used for this analysis is the k- ω SST (Shear Stress Transport) [3]. This model has been shown to yield accurate results, and is more suitable for such cases where it is important to capture both the phenomena occurring near the walls, and away from them [4].

Fig. 2 presents the work lines of centrifugal compressor (under standard conditions). In this case, the compressor characteristic was determined experimentally [18]. The surge line on which the machine protection line is set and the operating range of the machine were also established experimentally. The operating range of the compressor has been determined, resulting in a diagram illustrating the surge line - a line over which the compressor operation leads to its destruction.


Figure 2: Work lines of the compressor (in standard conditions) [18]

In order for the operation to be safe, the compressor working range must be defined. The first measure to be taken is related to compressor surge - protection, for avoiding reaching the surge line.

So, another line below the surge line is defined at a certain distance, called the surge protection line. This line is part of compressor automatics.

The surge protection line is defined as: [18]

$$n_{\text{protection}} = 3 + 3.35 \cdot \left(\left(\frac{n}{\sqrt{t_{\text{atm}} + 273}} - 134 \right) / 44 \right)^{1.7} \quad (5)$$

where: $n_{\text{protection}}$ – protection pressure ratio; n – speed [rot/min]

The compressor operating lines are [18]:

$$n1_w = (44 \cdot ((\pi_s - 2.8) / 3.9)^{0.625} + 134) \cdot \sqrt{t_{\text{atm}} + 273} \quad (6)$$

$$n2_w = (44 \cdot ((\pi_s - 2.7) / 3)^{0.67} + 134) \cdot \sqrt{t_{\text{atm}} + 273} \quad (7)$$

$$n3_w = (44 \cdot ((\pi_s - 2.6) / 2.3)^{0.71} + 134) \cdot \sqrt{t_{\text{atm}} + 273} \quad (8)$$

where:

π_s – selected pressure ratio

n_w – working speed [rot/min]

3 RESULTS

For the convergence of the solution, the residual history was monitored. A decrease of three orders of magnitude has been reached, obtaining a stable point where the fluid flow was in equilibrium. Also, the mass flow rate was monitored for both stages, at the first stage inlet and at the second stage outlet. For convergence, flow input must match the output within 5×10^{-3} .

To analyze the evolution of the fluid flow in the first compression stage, three planes were taken at 0.1, 0.5 and 0.8 of the impeller blade height, counting from the hub.

3.1 First stage:

Fig. 3 presents the total pressure variation in the impeller and diffuser of the first stage. As it can be seen, this variation is higher at the interface between these two components. This is due to boundary layer detachment from the blades and the consequent formation of recirculation zones. The pressure distribution is influenced by the rotor blade tip clearance. Differences between the two cases for the first stage, are minor, blade detachment and pressure losses appear in the same areas and between the two cases, the pressure difference is of nearly 0.12 bar.

In the diffuser, the appearance of shock waves leads to an increase in temperature, such that at the diffuser exit, the temperatures rises above 450 K. Shock waves are developing in the diffuser on the whole blade height and in each channel. Fig. 4 presents the velocity field in the rotating parts of the first stage. The appearance of shock waves limits the mass flow that can pass through flow channels of the rotating part. In the impeller, separation of the boundary layer occurs, but not as strong as in the case of diffuser.

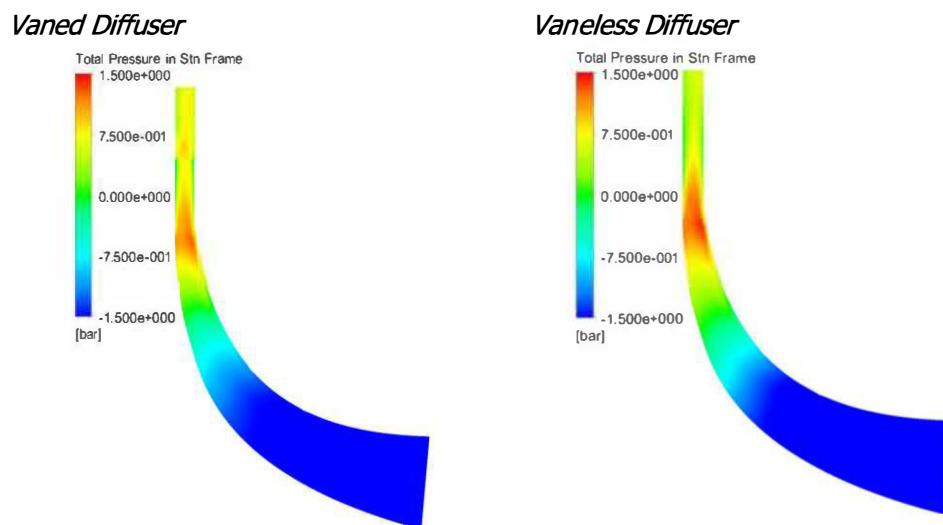


Figure 3: Total Pressure in Stn Frame

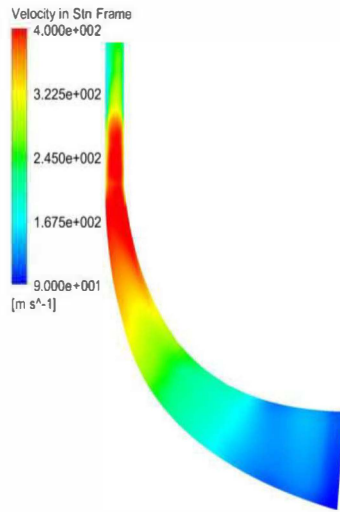
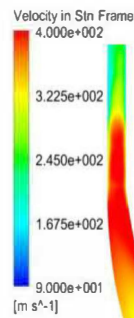
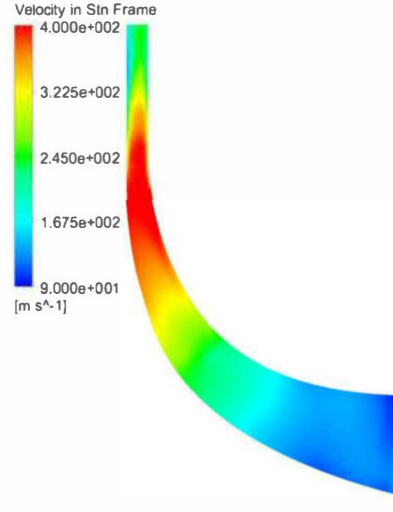
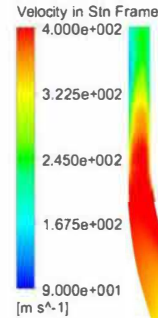
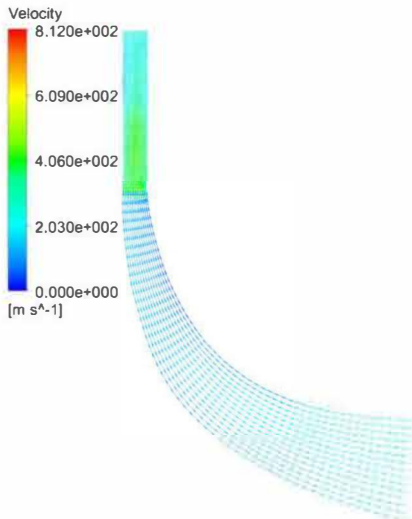
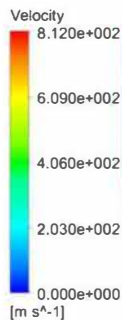
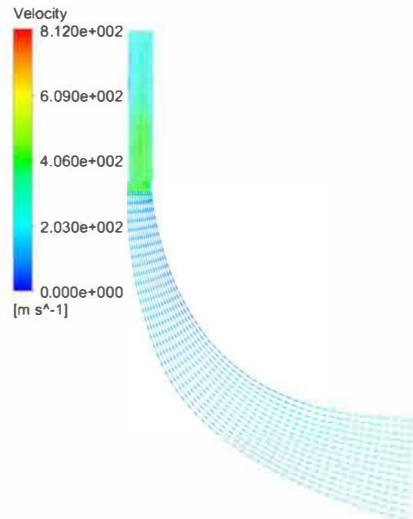
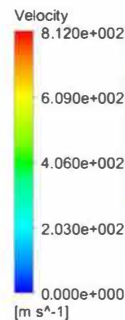
*Vaned Diffuser**Vaneless Diffuser***Figure 4: Velocity for the bladed parts of the first stage**

Fig. 5 presents the vector velocity fields for the first stage. Here, differences in velocity between the two cases are also minor.

3.2 Second stage results:

To determine the flow properties in both diffusers, six control points in every channel of the diffuser, both on the blade suction side and on the pressure side, have been chosen, at three different blade heights: 0.1, 0.5 and 0.9 of the blade span. In the radial direction, the points were situated near the diffuser outlet, as shown in Fig. 6, at a radius of 114 mm. For a better estimation of flow properties, the data in Fig. 8 is averaged across the blade height.

Vaned Diffuser*Vaneless Diffuser***Figure 5: Vector field on the rotating parts of the first stage**

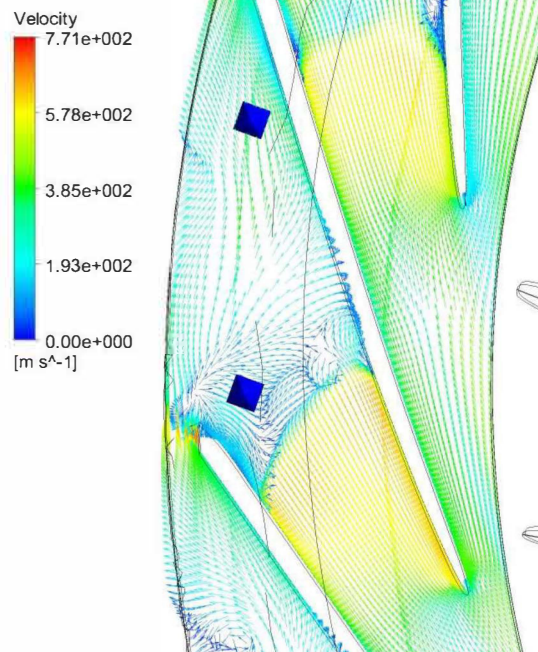


Figure 6: Vector field in vaned diffuser with two control points at 0.5 of the blade height

To determine the proper size of the first cell near the wall, Y^+ was calculated to be approximately 1 near blade wall as shown in Fig. 7.

Fig. 8 presents the averaged total pressure starting from the volute tongue. Because of the small area of the volute, near the tongue, the total pressure is much higher. With the increasing of the volute area, its influence on the diffuser is decreasing, leading to a better compression. In the case of the vaned diffuser a part-span stall is developing. The closer it gets on the blade tip, the area of the stall is increasing. The pressure variation is due to the position of the reference points, one near the pressure side of the blade and the other near the suction side of the blade, and also reflects the recirculation zones that form in each channel.

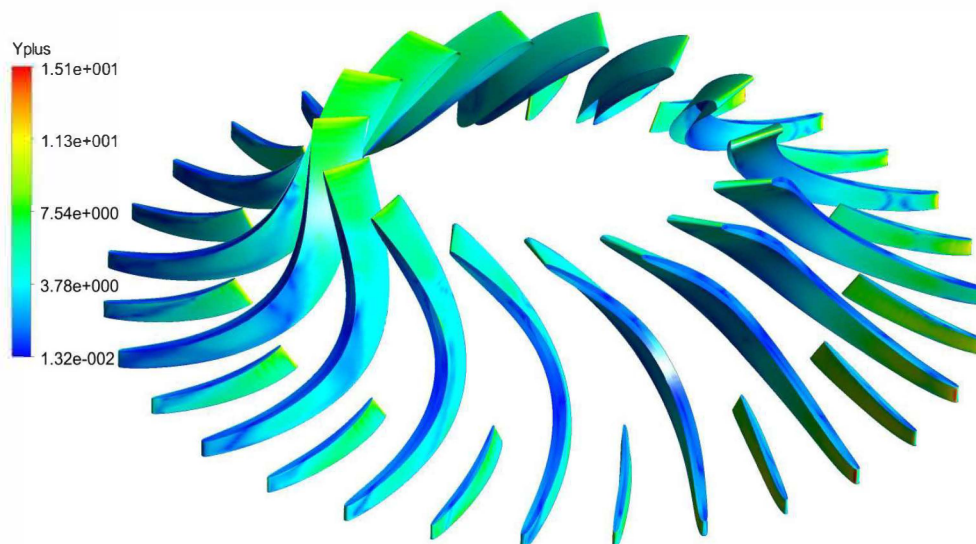


Figure 7: Distribution of dimensionless wall distance, Y^+ , on the surface of impeller blades, stage two

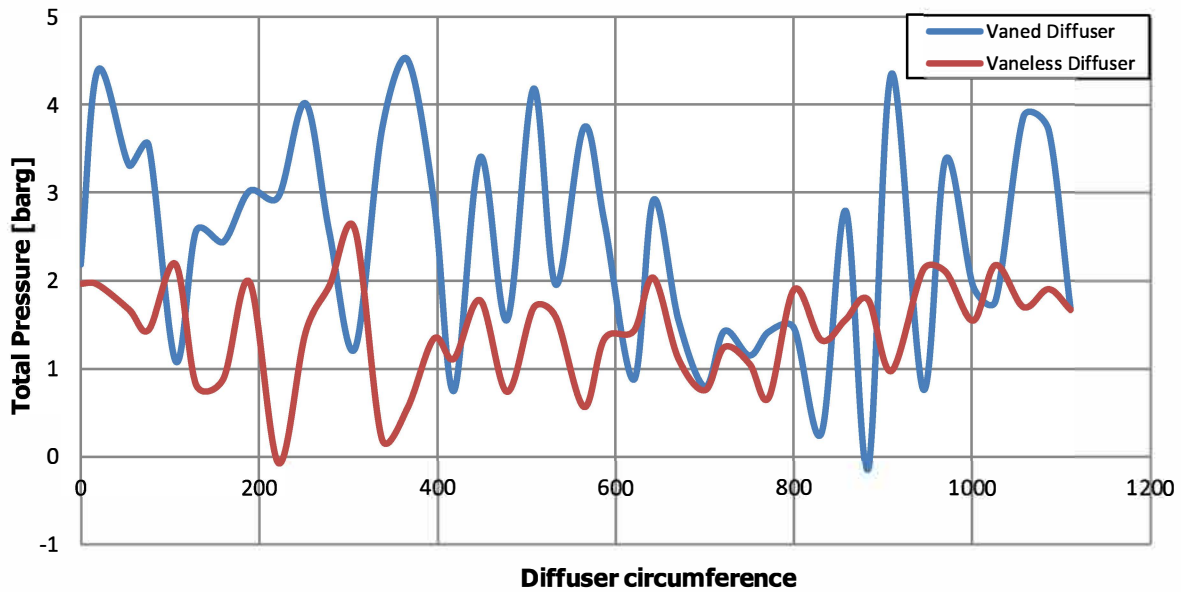


Figure 8: Average of Total Pressure on diffuser circumference

Velocity also represents an important factor in establishing compressor performances. In the case of vaneless diffuser, the velocity at compressor outlet was determined by the numerical simulation to be of 213 m/s; with 88 m/s higher than in the case of the vaned diffuser, leading to a decrease of performances.

Polytropic efficiency for the centrifugal components is presented in Fig. 9. Analyzing each component separately, it can be seen that the efficiency for the case of the vaned diffuser is much higher than for the vaneless one. But overall, the centrifugal compressor with vaneless diffuser has a polytropic efficiency higher by 0.11 %.

The evolution of the total pressure in the impeller of the second stage is presented in Fig. 10. Impeller inlet pressure is the same for both cases, but this is changing as we approach the volute outlet. In the vaneless diffuser, a decrease of total pressure up to 4.9 bar is observed, while in the case of the vaned diffuser, the pressure reaches a value of 6.43 bar. For the vaneless diffuser, the pressure loss in the diffuser is of almost 0.6 bar, which is lower compared with the vaned one, where the pressure loss is of 1.57 bar.

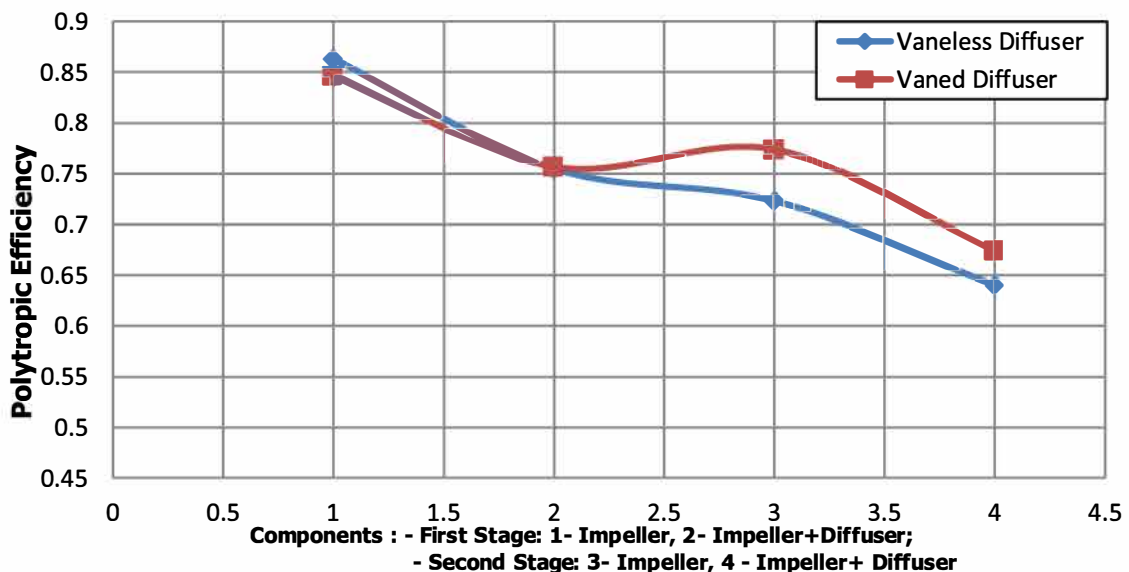


Figure 9: Polytropic efficiency for impellers and diffusers of both stages

For the studied compressor stage, the geometry of the scroll plays an important role, defining performances of the centrifugal compressor. In the case of the vaned diffuser, the pressure decreases at the exit to 4.26 bar, which is significant. For the vaneless diffuser, the pressure is decreasing to a value of 3.5 bar. It is noteworthy that in the experiments, the exit pressure was of 4.89 bar [18].

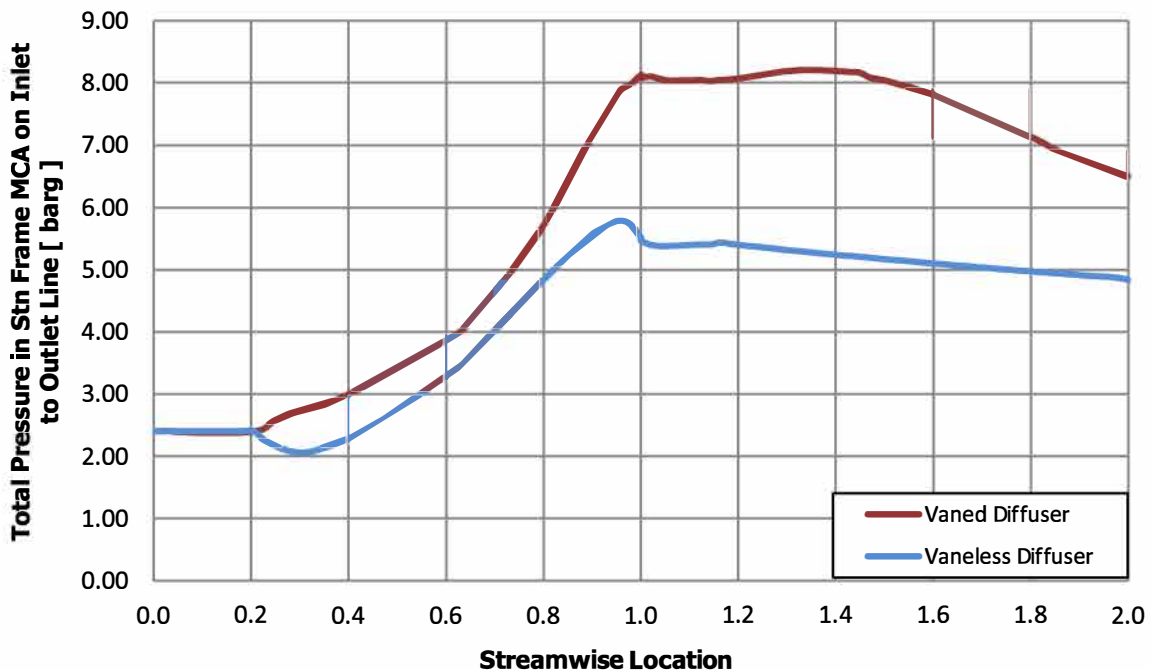


Figure 10: Total Pressure in Stn Frame for the impeller of the second stage

For streamwise locations above 1.4, the pressure drop is steeper for the vaned diffuser than for the vaneless diffuser probably due to shock waves.

4 CONCLUSION

In this paper, the influence of a vaneless diffuser on the performances of a centrifugal compressor with two stages close to surge line was studied. In order to see how the stable operating range is affected. Two cases were studied: a) both stages having a vaned diffuser, b) first stage with a vaned diffuser and the second stage with a vaneless one.

The numerical simulations carried out for the two stages of the centrifugal compressor were coupled, allowing a better comparison between the numerical and the experimental data. The vaneless diffuser not only influences the flow inside the scroll, but also the pressure ratio inside the second impeller. As proof, a difference of approximately 2 bar is observed in the simulations at the second stage stator. The agreement between the numerical and the experimental case is good, the difference in pressure between them being approximately 0.63 bar at the same location.

The scroll geometry plays an important role in establishing good performances for the compressor. This analysis shows that using vaneless diffuser this size will affect the overall pressure ratio of the compressor in a negative way. Also, the velocity in the vaneless diffuser was seen to be too large, 213 m/s, adversely affecting compressor performances. Probably a longer diffuser, with a different volute will result in improved performances, but this has to be verified as future work.

REFERENCES

1. A.Jaatin, "Performance Improvement of Centrifugal Compressor Stage with Pinched Geometry or Vaned Diffuser", Lappeenranta University of Technology, Lappeenranta, Finland, October, 2009
2. Waleed Al-Busaidi¹, Pericles Pilidis, "Techno-Economic Optimization of Diffuser Configuration Effect on Centrifugal Compressor Performance", *American Journal of Energy Research*, Vol. 3, No. 2, 37-48, 2015



3. P.E. Smirnov, F.R. Menter, "Sensitization of the SST turbulence model to rotation and curvature by applying the Spalart-Shur correction term", *ASME Paper* GT 2008-50480, Berlin, Germany, 2008.
4. N.J. Georgiadis, D.A. Yoder, "Evaluation of Modified Two-Equation Turbulence Models for Jet Flow Predictions", *44th AIAA Aerospace Sciences Meeting and Exhibit*, 9 - 12 January 2006, Reno, Nevada
5. A. Jaatinen, "Performance Improvement of Centrifugal Compressor Stage with Pinched Geometry or Vaned Diffuser", Lappeenranta University of Technology, 978-952-214-820-9
6. S. Shaab, "Design optimization of a centrifugal compressor vaneless diffuser", *ELSEVIER, International Journal of Refrigeration* 60 142-154, 2015
7. Senoo Y.&Kinoshiya Y., "Limits of rotating stall and stall in vaneless diffuser of centrifugal compressors", *ASME P* 78 GT 19.
8. P.Frigne, R. van den Braembussche, "One Dimensional Design of Centrifugal Compressors Taking Into Account Flow Separation in the Impeller", *Von Karman Institute for Fluid Dynamics*, Turbomachinery Department, June 1978
9. Kangsoo Im, "Development of a Design Method for Centrifugal Compressor", Dissertation, Michigan State University, Mechanical Engineering, 2012
10. David Japikse, "Centrifugal Compressor Design and Performance", Concepts ETI, Inc., ISBN 0-933283-03-2, 1996
11. Ernesto Benini, "Optimal Navier–Stokes Design of Compressor Impellers Using Evolutionary Computation", *International Journal of Computational Fluid Dynamics*, October 2003 Vol. 17(5), pp. 357–369
12. S.Shaaban, "Experimental investigation and extended simulation of turbocharger non-adiabatic performance", PhD Thesis, University of Hanover, Germany
13. S. Ljevar, H.C.de Lange, A.A. van Steenhoven, "Rotating stall characteristics in a wide vaneless diffuser", *Turbo Expo 2005*, vol.6, Nevada, USA, pp.1335-1342, June 6-9.
14. He, N. Tourlidakis, A., "Analysis of Diffusers with Different Number of Vanes in a Centrifugal Compressor Stage", *ASME TURBO EXPO*, 2001-GT-0321
15. P. Delbert, G. Gyarmathy, A. Sebestyen, "Flow Phenomena in a Vaned Diffuser of a Centrifugal Stage", *The American Society of Mechanical Engineers*, 93-GT-53, 1993
16. Sabri Deniz, "EFFECTS OF INLET CONDITIONS ON CENTRIFUGAL DIFFUSER PERFORMANCE", Gas Turbine Laboratory, Massachusetts Institute of Technology, GTL Report #225, Cambridge, March 1997
17. P. Dalbert, M. V. Casey, E. Schurter, "Development, Testing, and Performance Prediction of Radial Compressor Stages for Multistage Industrial Compressors", *J. Turbomach* 110(3), 283-292, Jul 01, 1988
18. Gheorghe Fetea, "Theoretical and experimental research on centrifugal air turbocompressors" (Cercetări teoretice si experimentale asupra turbocompresoarelor centrifugale de aer), - to be published
19. M.Ding, C.Groth, S.Kacker, D.Roberts, "CFD Analysis of Off-design Centrifugal Compressor Operation and Performances", Thesis (M.A.Sc.), University of Toronto, 2005



Development of a Software Tool for Comprehensive Flight Performance and Mission Analysis of Hybrid-Electric Aircraft

Gilbert Tay

*Technical University of Munich
Research Associate, Institute of Aircraft Design
85748 Garching, Germany
Gilbert.tay@tum.de*

Paul Keller

*Institute of Aircraft Design, Technical University of Munich
Graduate Student Researcher*

Mirko Hornung

*Institute of Aircraft Design, Technical University of Munich
Professor*

ABSTRACT

This paper presents a software tool developed to comprehensively evaluate flight performance and mission analysis of hybrid-electric aircraft. The modelling incorporates conventional propulsion systems as well as an alternative electric propulsion system for flight performance and mission analysis. As part of the overall technology assessment of the Bavarian research project "PowerLab", which aims to develop a hybrid-electric flying platform, this tool is incorporated to assess the reference missions of the project concept. Further analysis on the impact of energy density variation on the transport efficiency using the developed tool was also performed. Finally we present an outlook into the integration of the tool in an overall aircraft fleet system dynamics model to estimate future fleet development for various future scenarios.

KEYWORDS: *Flight performance analysis, mission analysis, hybrid-electric propulsion*

An improved method for transport aircraft for high lift aerodynamic prediction

Pierluigi Della Vecchia

Department of Industrial Engineering (DII) – University of Naples "Federico II"

Assistant Professor

Via Claudio 21, 80125 Napoli - ITALY

pierluigi.dellavecchia@unina.it

Fabrizio Nicolosi

Department of Industrial Engineering (DII) – University of Naples "Federico II"

Associate Professor

Manuela Ruocco

Department of Industrial Engineering (DII) – University of Naples "Federico II"

PhD Student

Luca Stingo

Department of Industrial Engineering (DII) – University of Naples "Federico II"

PhD Student

Agostino De Marco

Department of Industrial Engineering (DII) – University of Naples "Federico II"

Assistant Professor

ABSTRACT

The aim of this work is the development of a methodology to predict lift characteristics for transport aircraft in the whole flight envelope, useful in the preliminary aircraft design stage. The purpose is an attempt to improve the classical methodologies for wing load distribution and lift prediction, considering the airfoils aerodynamic characteristics until stall and post stall conditions during the process, and modifying 2D characteristics in case of high lift devices to take into account 3D effects introduced by the devices themselves. The method is a modification of Nasa Blackwell procedure, capable to predict wing stall aerodynamic characteristics for both clean and flapped configuration. As far the high lift devices effect is concerned, the improved method works substituting clean airfoil aerodynamic characteristics with the flapped aerodynamics ones, and introducing a correction to evaluate the 3D effects induced by high lift devices geometrical discontinuities. The results of the developed method have been compared with CFD and experimental data showing good agreement, making available a fast and reliable method, useful in preliminary aircraft design.

KEYWORDS: *Aircraft design, high lift aerodynamic, transport aircraft, span lift coefficient distribution, extended lifting-line theory.*

Automated Selection of Airliner Optimal On-board Systems Architecture within MDO Collaborative Environment

Riccardo Lombardi

Noesis Solutions N.V.

Gaston Geenslaan 11, B4, 3001 Leuven, Belgium

Marco Fioriti and Luca Boggero

Politecnico di Torino,

Turin, Italy

Luciana Lo Verde and Nicola Catino

Leonardo Aircraft,

Turin, Italy

Artur Mirzoyan

CIAM, Central Institute of Aviation Motors,

Moscow, Russia

And

Roberto d'Ippolito

Noesis Solutions N.V.

Gaston Geenslaan 11, B4, 3001 Leuven, Belgium

ABSTRACT

The test case described in the paper is a multidisciplinary, distributed, design optimization aimed at the identification of the best on-board system architecture for a regional airliner on the basis of its production and operative costs.

A key requirement was to integrate in a collaborative, multidisciplinary environment the analysis modules needed to investigate the effects of the chosen architecture on engine performance and actuator fairing design. The final objective is to determine if the higher installation and development costs of innovative architectures are paired by a lower operative cost due diminished fuel consumption (function of engine configuration and aerodynamic properties).

The collaborative MDO has been implemented using a commercial PIDO, Optimus by Noesis Solutions; this has been used to connect four different analysis tools (developed and operated by Politecnico di Torino, Leonardo Aircraft-Alenia and CIAM) adopting the communication protocols developed within the European Project AGILE. Only the integration platform, the connection protocols and the design tools are described in the paper; the complete distributed MDO is currently in the validation phase.

KEYWORDS: *Automated Design; Design Optimization Environment; MDO; On-Board Systems Design; Surrogate Model.*

NOMENCLATURE

AEA – All Electric Aircraft
 AGILE - (Aircraft 3rd Generation MDO for Innovative Collaboration of Heterogeneous Teams of Experts)
 CPACS - Common Parametric Aircraft Configuration Scheme
 DLR – German Aerospace Center
 DOE – Design of Experiment
 EM – Engine Module
 MEA – More Electric Aircraft
 MDA – Multidisciplinary Design Architecture
 MDO – Multidisciplinary Design Optimization
 OBS – On-Board System
 PIDO – Product Integration and Design Optimization
 SFC – Specific Fuel Consumption
 SM – Surrogate Model
 SOA – Service Oriented Architecture
 SOTA – State Of The Art

1 INTRODUCTION

Current aircraft designers have to address new competitiveness and environmental constraints aimed at the design of less noisy and expensive, as well as of more fuel-efficient, airplanes: these considerations have influenced not only engines, structures and aerodynamics, but also the on-board systems [1].

Thanks to the development of new technologies, innovative concepts like "More Electric Aircraft" (MEA) and "All Electric Aircraft" (AEA) have enriched the on-board systems design discipline. These new architectures potentially offer significant advantages over conventional ones [2], however evaluate their effectiveness is far from trivial due to the number of influenced global aircraft design elements [3] as engine performance, additional fuel weight, installation volume of the implants, aircraft reliability and safety, required electric, hydraulic and pneumatic power and their conversion, aerodynamic friction on engine nacelle, air-intakes and actuator fairings [4].

In order to be evaluated, all these aspects require different specialists with detailed competences and analysis tools. Parametric models and interaction schema commonly applied to the preliminary design phase [1] are typically tailored on convectional OBS architectures, thus they cannot fully describe the much more in-deep changes introduced by the switch from conventional to MEA or AEA.

Furthermore, only large companies and organizations have the financial resources required to maintain internal design teams able to cover all the engineering aspects associated to an airliner development; in most of the cases, sub-contractors or research institutes have to be involved to assess specific tasks [5].

This cooperation makes modern aircraft development a collaborative and multi-organizational design process that would benefit from the creation of standardized integration platforms and protocols; the development of these collaboration methodologies is one of the main objective of the AGILE project [6][7]. Once completed, the 3-years long project will enable the 3rd generation of multidisciplinary design and optimization through efficient collaboration among international, multi-site, aircraft design teams.

The interfaces and discipline-connection technologies assessed within the AGILE project by the end of its second year have been used to set up the current test case, specifically dedicated to investigate the OBS architecture fall-outs. To this end, 4 analysis tools dedicated to OBS, engine, external aerodynamic and costs have been improved and connected. Once validated, the constructed MDO will allow analysing the impact of the chosen on-board system architecture on the overall aircraft design with a higher fidelity than traditional conceptual design tools. It will also permit the identification of the most affordable solution considering the full extent of the airliner foreseen lifetime.

The test case relies on existing state of the art analysis tools and the focus has been put on their integration in a new, flexible, collaborative architecture, able to capture the significant aspects of the OBS-engine design influence since the conceptual stage of the aircraft development. The modularity of the implement approach will also allow for the future, independent development of the design tools to improve the accuracy and the validity of the performed analysis.

The paper has been organized as follows: section 2 describes collaborative MDO and existing problems, section 3 briefly reports how these challenges have been addressed in AGILE, section 4 introduces aircraft OBS and their effect on aircraft design, section 5 presents the implemented collaborative MDO test-case, section 6 illustrates the preliminary results achieved and section 7 anticipates the undergoing and future developments.

2 COLLABORATIVE MDO

The setup of a collaborative MDO is a key step in order to ensure the success of the design phase [7]. In the easiest scenario imaginable, all the design tools have been purposely build for the specific MDO problem, thus they are available within the same environment, have been developed by cooperating teams with well-defined competencies using the same architectures and methodologies, therefore there are limited issue related to communication between teams, or information exchange among tools. This scenario is also extremely unlikely: due to the time and effort required to develop and validate analysis tools and models, most MDO problems are addressed using a combination of general-purpose (often customized) and in-house developed software created for wider range of objectives by heterogeneous teams.

Two main cross-influencing communication issues emerge: between experts and between their tools. It is mandatory to efficiently bridge not only the product models and simulation capabilities but also to merge the competences of the different experts [7]. This include the arrangement of compliancy with regulations; the conclusion of contracts to define the costs and work distribution, hierarchies, responsibilities and communication lines; and agreements on the disclosure of information and knowledge, dissemination of the results. Then more human related aspects of collaboration have to be addressed, which include communication issues, differences in technical background and methodologies, variations in perceived priorities, naming conventions and unit of measurements, lack of awareness of each other's specific competences. All these aspects have to be acknowledged; pretend to solve all the listed issues would not be reasonable and often only mitigation strategies can be implemented [8].

Then the technical level of the multi-designer collaboration can be taken into care. Engineers will have to agree on set-up of joint models; connect possibly heterogeneous working environments and operating systems; coordinate the simulation campaigns; define data exchange formats, tools connection protocols. These challenges have been already investigated in other EU-funded projects, such as VIVACE [8], CESAR [9] and CRESCENDO [10] which had, among their objectives, the development of methods to support efficient multi-engineer collaboration.

A still existing obstacle is represented by the dynamic IT environments; organizations are constantly increasing their self-protection implementing layers over layers of security constraints as network restrictions, proxy servers, and firewalls that, in spite of agreements and contracts, make the set-up of a collaborating environment extremely difficult and resource-consuming [8].

3 AGILE FRAMEWORK

AGILE [6] (Aircraft 3rd Generation MDO for Innovative Collaboration of Heterogeneous Teams of Experts) is an EU funded project under the research schema Horizon 2020 and coordinated by the German Aerospace Center (DLR). AGILE is developing the next generation of aircraft Multidisciplinary Design and Optimization processes, which target significant reductions in aircraft development costs and time to market, leading to cheaper and greener aircraft solutions [6]. The aim of the project is to create a collection of methodologies and software to facilitate the communication among the design

teams and to integrate heterogeneous tools in a flexible, collaborative, multidisciplinary design environment.

The project is structured into three sequential, one year-long, phases, each targeting design campaigns with increasing levels of complexity while the framework is being built and upgraded. During Phase 1 and 2 the distributed MDAs for 2 regional turbojets have been developed and tested, while Phase 3 is dedicated to the application of the Paradigm to non-conventional configurations (as blended-body wing aircrafts, advanced turboprop, drones and Prandtl-wings).

The project is intended as a technology demonstrator; the objective is to develop methodologies to efficiently and reliably create executable multidisciplinary, distributed, design architectures. The operation of the MDA and the optimization of the aircraft design itself are not the main objectives. For the same reason, included analysis tools were already available and, although some of them have been improved during the project [11][12], this was not the main purpose.

3.1 Framework approach

The AGILE development framework is based on a system-wide approach of Service Oriented Architecture (SOA) in order to improve the integration of engineering services within development workflows. This implies that every specific activity, from the run of a simulation tool to the post-processing of the results, has to be wrapped to create a module with standardized interfaces and access protocols, thus making it possible to develop complex functionalities by connecting these simpler 'building blocks'.

In collaborative MDO several types of participants can be identified, according to their role, each operating within a specific step of the overall development. This arbitrary function-based separation within the AGILE project has led to the identification of the participative agents illustrated in Figure 1.

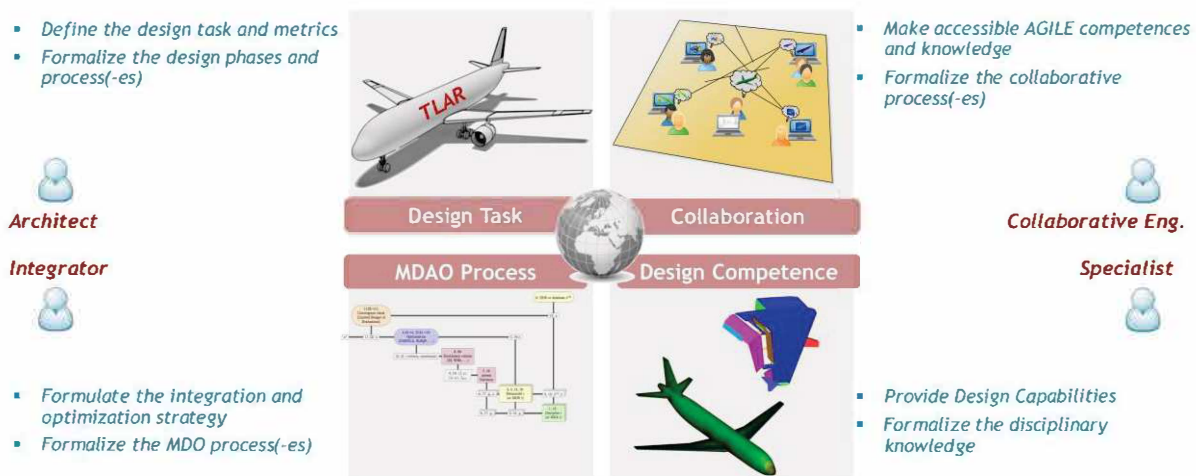


Figure 1: Participative agents identified within AGILE.

- **Architect.** Responsible for specification of the design case in the AGILE framework, such as collecting the required competences, defining the design phases and the dimensionality of the design space to be explored.
- **Integrator.** In charge for the deployment of the design and optimization (sub-) processes, and for the management of such processes within the AGILE framework. IP protection is also administrated.
- **Collaborative engineer.** Responsible for providing the integration within the framework, necessary to connect the various competences and making them accessible to the framework. It includes the secure integration of software apps in different networks.
- **Competence specialist.** Responsible for providing design competence within the framework, such as a simulation for a specific domain, or an optimization service. Specifications of the competences are managed in the AGILE development framework.

A fifth role, not included in Figure 1, is required in order to set-up and run the collaborative MDO: the *Customer* (and primary user of the framework), who is responsible for defining the design task, top-level requirements, and available development lead-time. It interacts during the operational phases, for instance to access the final or partial results, and to participate to the decision making process.

A mandatory precondition to enable the collaborative MDO is that every simulation capability is wrapped as an automatically executable engineering service. This provides the means to efficiently perform integrated design studies using distributed simulation workflows. The encapsulation procedure is aimed at avoiding the non-creative, repetitive, and error-prone manual data conversion steps, tool executions, and data exchange. The overall objective of the SOA implementation is to generate modular systems where every component can be interfaced, reused, upgraded and replaced independently.

3.2 Connection Protocol

In the AGILE Paradigm, procedures has been defined both to request a particular service execution (needed to integrate the service in the MDO) as well as to provide the service itself (by the design specialist). The two scenarios have been schematically depicted in Figure 2.

In this example, the process integrator (left) defines and deploys a design and optimization workflow in the *administrative domain 1*, characterised by 3 *local services* located within the same domain and 1 *remote service* (e.g. another organization network). The connections represented by means of arrows depict the data exchange between the services.

The *remote service*, indicated in green, represents an engineering capability within *administrative domain 2* (right). The input and output data needs to cross administrative domains when a remote design competence is included in the workflow. To allow for this data to be securely exchanged, a neutral domain is established, consisting of a central data server (that enforcing authentication and access-control mechanisms prevents the potentially confidential design information from being accessed by third-parties) for the instantaneous exchange of data.

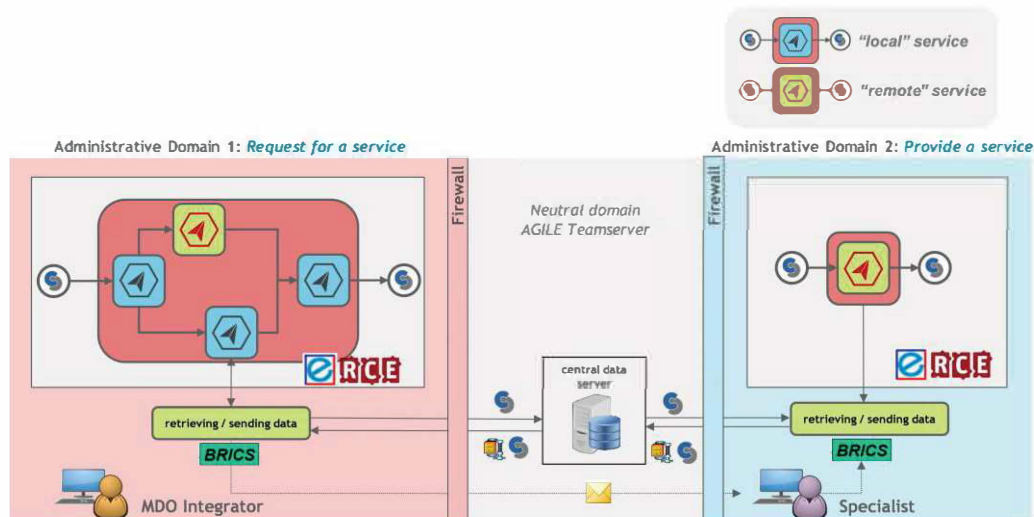


Figure 2: AGILE Collaborative Architecture. Service oriented scenario.

When the remote service is triggered, the required input data is uploaded to the central data server and the specialist receives a notification informing him/her that a single run/multiple runs of his/her tool is/are needed. The execution of the service is not automatically started as the control of the tool itself is always retained by the specialist. Only when the execution is started, data is automatically downloaded from the central data server and provided to the tool under consideration. After

execution, the enhanced results are automatically fed back to the central data server and automatically retrieved within *administrative domain 1*.

In AGILE this interconnection capability is provided by the NLR's software Brics [9][13]. It comprises protocols and middleware that facilitate remote execution of sub-processes from within a process, independent from the local PIDO environment being used.

3.1 Data exchange format

In order to minimize the number of interfaces between the services a common language has been selected to describe the MDO product. The AGILE project is aircraft dedicated, thus a non-completely neutral format has been selected, named Common Parametric Aircraft Configuration Scheme (CPACS)[14]. It has an xml-like structure which can be used to extract the input for the multiple design competences as well as to provide the output from the design competences. Although each design competence may provide additional data, in proprietary formats or other standards, the exchange between services is only via CPACS.

3.1 MDO implementation

The overall MDO structure could be implemented using almost any available scripting language; however such approach would result in cumbersome, time consuming, hard to debug and not easily understandable codes that could be adapted to different scenarios (as tools replacements or change in optimization strategy) only with a significant effort.

Process Integration and Design Optimization (PIDO) have been preferred to compose the MDO process. The exploitation of a common data format and a neutral communication protocol allow for implementations on different platforms to coexist in the same collaborative architecture as there are no direct links neither between different tools, not between design processes and MDO. Thanks to the dedicated PIDO interfaces it is possible to re-configure almost effortlessly existing design problems, adding, removing or exchanging tools. They also enable to analyse and explore the design space in order to gain the critical insights of the dynamics of the virtual design problem. Additional technologies, to enable the automatic construction of the MDA from tool input and output knowledge and architecture are under development [15].

4 AIRCRAFT ON-BOARD SYSTEMS DESIGN

The availability of more accurate, reliable and faster software and the progresses in IT infrastructures has made possible the execution in a reasonable time of complex analysis not just during the detailed design but also during conceptual and preliminary phases. This improved capacity has only partially influenced the definition of the OBS which, during conceptual design phase, are mainly considered for their weight using parameterized formulas based on literature data [1]; only from the subsequent preliminary design phase, architecture, required power and volume are taken into consideration.

However, in order to obtain a more integrated and optimized design since the conceptual phase, parameters and cross-influences traditionally considered only in later development phases are now at least partially [16] evaluated also during conceptual design. In the on-board systems case, these include (but are not limited to) supplementary fuel weight needed to supply them, installation volume, impact on aircraft reliability and safety, influence on performances.

In the last years, several technologies related to OBS have been developed, making new architectures a feasible alternative to traditional ones; the general trend is toward the electrification of the services, from actuators to air-conditioning. As shown on the left side of Figure 3, for SOTA architecture, the systems require hydraulic, electric and pneumatic power. The first two are derived directly from the mechanical power gathered from the engine (or the APU) by accessory drive gearbox whereas pneumatic power is generated using bleed air from engine compressor stages. Innovative architectures implement several variations of the concept presented on the right side of the same figure, characterised by a shift toward electric powered systems. The final users are still activated by the same power used in the SOTA architecture, but the mechanical power is the only one taken

directly from the engine and then converted into electric power. Electric motors are used to generate the non-electric power where needed. The rationale that justifies this approach is to minimize the impact on engine design (thus cycle efficiency [17]) with air bleed off-takes [18][19]. Additionally distribution systems for electricity are lighter and safer than for pressurised fluids.

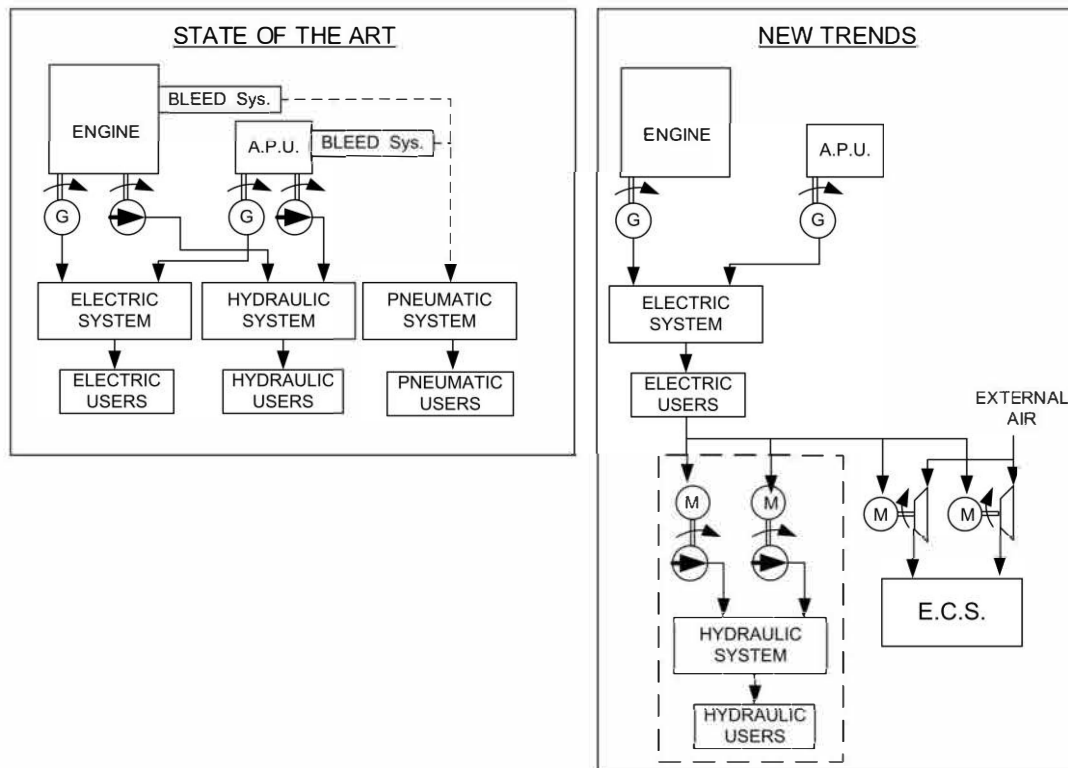


Figure 3: State-Of-The-Art and New trends On-Board systems architectures.

Regardless the power conversion strategy used, the starting point is always the engine, in the form of non-propulsive power that has to be extracted and converted. The specific architecture determines the magnitude of the following influences:

- Amount of additional fuel that has to be carried to ensure the engine capacity to operate as power source.
- Engine specific fuel consumption (affected by mechanical power off-takes and bleed air extraction [18] [19]).
- Engine configuration.
- Systems weight.
- Aircraft reliability and safety (due to the number of redundancy lines for electric, pneumatic and hydraulic power systems)
- Operative costs (logistic reliability).

In order to extract mechanical power from the shaft and pressurised air from the compressor stages, the engine has to be equipped with adequate interfaces; these have a direct impact on the engine efficiency. Consequently to maximize the performance, the engine designer has to consider the on-board system architecture; bleed-less configuration airliners like the Boeing 787 have purposely developed engines, based on conventional engines [19].

The balance between the three types of non-propulsive power, the sequence used to generate them, and the served utilities, determine the hardware configuration; e.g. an AEA is likely to be more fuel efficient and less maintenance intensive, but heavier due to the limitations of SOTA electrical actuators in force over weight ratio [19]. The total fuel consumption is affected too, due to variations in induced drag (related to systems weight) and in friction drag (affected by air intakes, nacelles and fairings size) [18]. In turn, fuel consumption and systems weight could lead to a cascade effect on structures, available volumes, lifting and control surfaces etc.

In force of the highlighted effects, depicted in Figure 4, it is essential to select (or at least to streamline) the candidate OBS architecture(s) as earlier as possible in the aircraft design process. The comprehensive evaluation of the afore-mentioned dependencies leads to a multidisciplinary design problem in order to be correctly assessed.

In this study, as the objective is to test and validate the collaborative MDO approach on a simplified, but still representative test case, only the direct influences on engines, aerodynamic and performances with respect to a nominal configuration have been included. This is not to be considered a limitation as, due to the modular nature of the approach adopted, additional elements could be added in the future.

The multidisciplinary design architecture (MDA) itself has been developed with the support of Leonardo Aircraft (formerly -Alenia Aermacchi) due to their expertise in aeronautical industrial design processes. A short description of each tool (dark grey blocks) is reported hereafter:

- ASTRID, in-house software conceived and realized by Politecnico di Torino, is a Matlab-based tool aimed at the preliminary design of the aircraft on-board systems. ASTRID inputs define the systems characteristic (like hydraulic pressure value, landing gear or control surfaces actuator technology, de-icing method) and estimates weight, mechanical shaft power off-takes and bleed off-takes. It includes methodologies to evaluate masses and secondary power requests both for conventional and innovative systems, such as MEAs and AEAs. Other details about ASTRID and the implemented design modules are reported in [20].
- The Engine Module (EM) developed by CIAM is based on the commercial software GasTurb v12 [21]. It is capable of running engine design and performances simulation with variable level of details. The preliminary design achieved using the EM includes constraints and aircraft generic information to perform engine cycle design, off-design simulation and engine overall geometry and mass assessment. The results of the EM feature the estimated engine deck properties (installation losses, flight envelope, intake pressure recovery description, thrust reverser ability, technical deliveries, performance for different operating conditions, dimensions description, sizing rules, automatic handling of air bleed). A comprehensive description of the engine model can be found in [22].
- Leonardo Aircraft developed an aerodynamic module, based on the reference aircraft, to evaluate the variations in viscous friction due to changes in actuator fairing surface and systems air intakes size. The CFD simulation is based on a reference aircraft and is adapted to match the different designs produced by the other tools. Due to the complexity and time required to update and re-mesh the model, the tool has not been integrated in the MDA as remote service. Instead, a fixed number of simulations for different combination of the input parameters have been performed off-the-loop and the results have been used to create a surrogate model.
- The cost module, a Matlab script, estimates the acquisition and operating costs of the proposed architecture considering on-board systems weight and additional fuel quantity for secondary power [23]. It has been developed by Politecnico di Torino.

As illustrated in Figure 4, the general inputs that characterize the reference aircraft are provided to ASTRID along with a specific set on data that defines the OBS architecture. Upon evaluation, the estimated systems volume, systems power/bleeded off-takes and systems mass are forwarded to the other modules. The drag variation module calculates the additional drag due to actuator fairings and systems air intakes. The drag data, combined with aircraft description and systems power/bleeded off-takes are used to investigate the engine performances; the engine module is able to assess both additional fuel required for power the systems and to produce the additional thrust required because of the drag increment. The engine parameters as geometry and total thrust are considered fixed inputs.

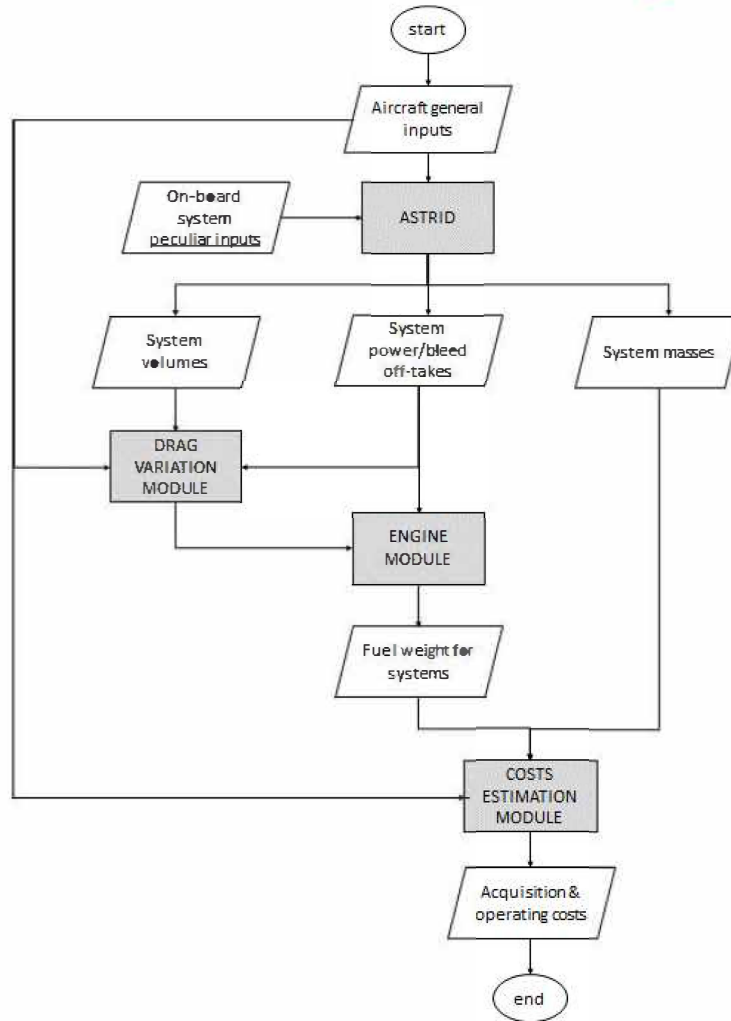


Figure 4: Interaction schema of the MDA components.

Finally, the total fuel required by aircraft systems, the engine fuel consumption and the systems weight are used by cost module to estimate the systems acquisition and operative costs.

5 COLLABORATIVE MDO IMPLEMENTATION

The MDA depicted in Figure 4 has been implemented into a functional workflow using the collaborative MDO methodology developed in AGILE; the objective was to convert the abstract connection schema into an actual collaborative workflow as in Figure 5. The identified agents involved were:

- *Architect*: Politecnico di Torino and Leonardo Aircraft
- *Integrator*: Noesis Solutions
- *Collaborative engineer*: Noesis Solutions
- *Competence specialist*: Politecnico di Torino, CIAM and Leonardo Aircraft

Politecnico di Torino also acted as main *Customer*.

The design starting point is a reference aircraft used in AGILE named DC-2 (from Design Campaign 2, a model that has been created to test the effectiveness and the reliability of collaborative MDO). In terms of size, configuration and performances is a regional airliner: range 3500 km, 90 passengers, design payload 9180 kg, cruise Mach .78, maximum take-off mass of 45046 kg, wing span 28.4 m [6].

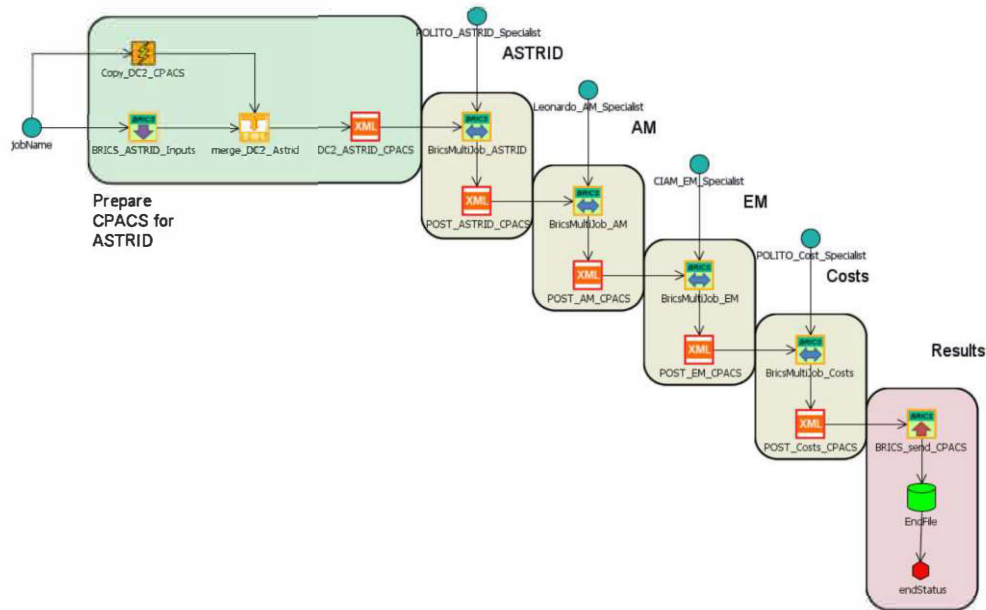


Figure 5: Implemented MDO workflow.

With their leading role of architects, Politecnico di Torino and Leonardo identified the relevant influences between the on-board systems choice and the other disciplines. The input/output relationships reported in Fig. 4 as connection lines, looks less articulated in the collaborative, Fig. 5. This is permitted by the common data format, CPACS, that collects the results and increases the stored knowledge: with this approach, ASTRID, although not connected explicitly with the cost module as in the conceptual MDA, is still able to provide information to it. The collaborative MDO has been built by the integrator (Noesis) that acted also as Collaborative Engineer. Politecnico di Torino created Optimus workflows to embed its tools whereas the two other involved disciplines (EM and Leonardo CFD) resulted to be computationally expensive and not easily automatable; in order to reduce the execution time, both have been replaced with functional models.

The entire MDO has been set up to be operated with Brics and CPACS not just to trigger the tools execution: the workflow exchanges information with the Customer using the collaborative protocol. Thus the complete MDO can be operated as a service and therefore integrated into a larger MDA.

5.1 MDO Disciplines

The disciplinary tools required minor adjustments to be executed as services: the information had to be retrieved from the CPACS file and mapped to the tool-specific input format and the Brics connection had to be established; to this end, template Optimus workflows have been used.

The en-capsulated ASTRID workflow has been reported in Fig. 6; the tool-specific components are those within the yellow box. The two Brics interfaces connected to it are required to perform the download and final upload of the enhanced CPACS file. The orange blocks map the data between Optimus and CPACS. Aircraft general inputs, such as Top Level Aircraft Requirements, airplane dimensions and geometries (e.g. fuselage length, wing area), design weights as maximum Take Off and Operative Empty are among the extracted data that are forwarded to the OBS design module. The values for engine power off-take, bled air and total estimated OBS mass are specified in the returned CPACS file.

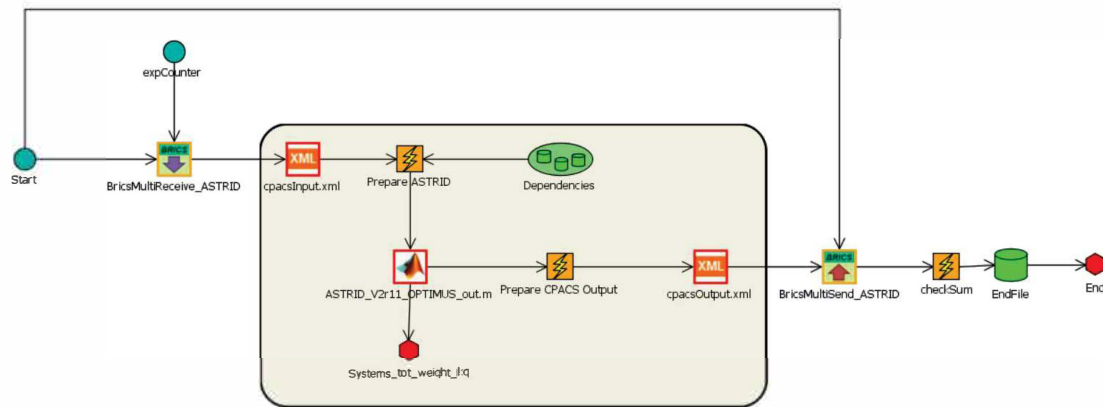


Figure 6: ASTRID tool wrapped using Brics interfaces.

The Aero Module is able to calculate the additional drag due to on-board systems. The two main contributions are due to wing actuator fairings and air intakes necessary to cool down the systems. The additional drag due to actuator fairings is related to the fairings dimensions hence, the actuators dimensions. The air intakes drag is calculated starting from OBS power off-takes. Statistically a certain part of the power produced by subsystems is lost in heat. Therefore, some external air is required and it is provided by means of several air intakes. Their dimensions and quantity (i.e. their additional drag) can be estimated starting from the systems power off-takes.

Due to the complexity of automatic mesh generation, the module was replaced by a surrogate model. A preliminary analysis using ASTRID was performed to determine the domain of the AM input variables; the information was used to build a DOE to extract the significant aspects of the AM. The evaluations performed were used to construct an interpolated SM that was wrapped using Brics to be executed upon call from the MDA.

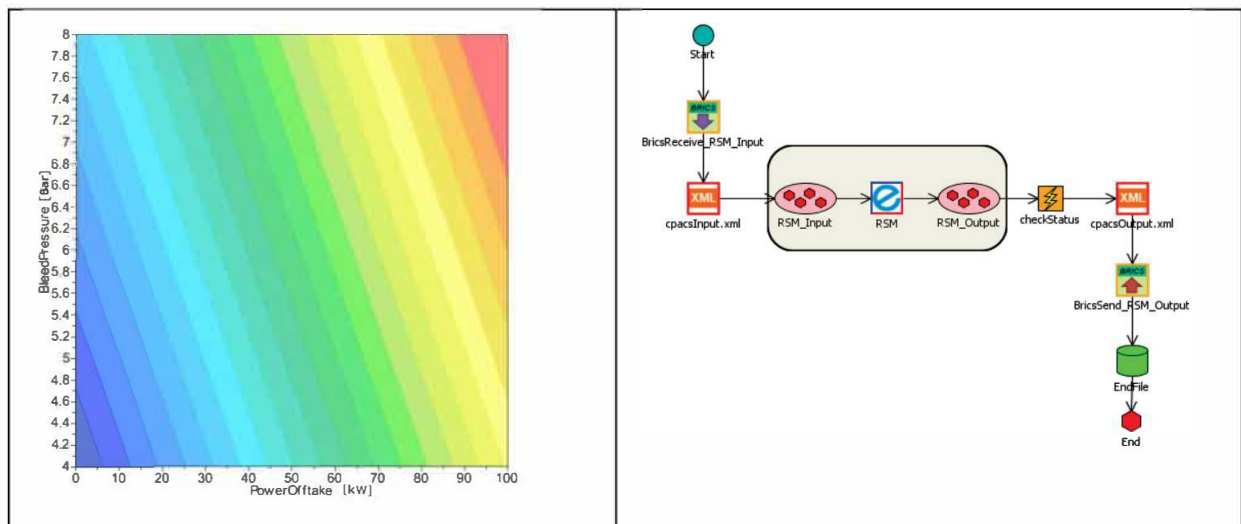


Figure 7: Engine Model, Specific fuel consumption variation (left) and implemented collaborative workflow (right).

Similarly to the Aero Module, also the Engine Module was replaced with a SM, Fig. 7. The engine surrogate model was modeled in Optimus by importing the DOE data and using one of the already available interpolation models [16]. The model was validated before its deployment using both cross-validation and comparison of predicted and off-point calculated values (from samples not included in the model construction). The EM surrogate was embedded into a workflow with Brics and CPACS compatibility. The inputs extracted from the CPACS are altitude and Mach number, power off-take,

bleeded-air pressure and flow. The specific fuel consumption and the fuel flow required to supply power to the systems are included in the output file.

The last module is the cost model, which, given the systems weight and the fuel quantity for secondary power, estimates the acquisition and operating costs of each system architecture. This model is based on the costs estimation methodology proposed in [15] modified and updated to consider the inflation and the acquisition cost of novel technologies. This depends on the technology level of the sub-system, their "quantity per aircraft" and the number of production units. Concerning the operating cost, the implemented module evaluates only the fuel cost overlooking the other items of the direct operating cost in this conceptual design phase. To balance the acquisition cost with the operating cost, the model is set to calculate the operating cost considering the entire life cycle (about 120000 flight hours).

In this test-case, the main design parameters used to define the on-board system architectures have been identified as:

- Power supply (electric or hydraulic) of Flight Control System, Landing gear (retraction, steering, braking).
- Hydraulic system pressure (207 or 344 bar).
- Braking system pressure, (207 or 344 bar).
- Electric voltage (115 VAC or 235 VAC).
- Primary electric machine (Integrated Drive Generator or Permanent Magnets Alternator + AC/DC converter).
- Pneumatic system architecture (bleed air off-take or bleedless configuration).

These parameters allow for a good characterization of the OBS; the total number of possible combinations is 512. It is not required to explore all of them as some are either equivalent or not relevant: if all the users have electric actuators, the pressure of the -not installed- hydraulic system is unimportant. The 16 unfeasible combinations have been identified and reject rules have been implemented in the Optimus workflow in order to rule them out.

6 COLLABORATIVE MDO EXECUTION

The collaborative MDO is currently under validation. Preliminary evaluations have been performed in order to test the validity of the approach and its real capability to investigate the impact of the different architectures. The results achieved are in line with those previously obtained using a non-collaborative workflow, without CPACS, Brics components and the Aero module [25][26]. The information exchange between ASTRID and the EM was performed using Optimus-native variables with the output knowledge stored in dedicated local files. This customized procedure, although easier to implement for MDA characterised by few tools, suffers from limited readability and when applied to complex problems could result in hidden bugs and inconsistencies. Additionally the lack of Brics interfaces, or other equivalent technologies, demanded that all the tools were on the operated workstation. The development of methodologies to address these limitations would not have been possible without a dedicated workgroup as the AGILE project.

In spite of the lack of definitive results about optimal on board system architecture, several lessons have been learned:

- The collaborative MDO methodology developed within AGILE allows for a significantly higher degree of flexibility. The exploitation of the CPACS as unique file grants both a compact data storage and a more understandable sequential information enrichment process. It also allows for easier replacement of a specific tool with no changes in the MDO.
- The collaborative MDO has faster construction and re-configuration times and grants connection with any matching tool; this largely outmatches the execution overhead caused by the Brics interfaces (a remote execution using the automated data upload and retrieval takes about 10 seconds more than the equivalent local one).
- Leonardo as industrial partner with experience in aircraft design highlighted the necessity to validate not just every step of the MDA construction procedure but also the analysis results.

In particular during the execution the specialists must have the possibility to inspect both provided inputs before analysis and results before CPACS upload. The rationale is that even when the communication protocols and integration methodologies are executed correctly, it is still possible that unforeseen interactions between the tools generate results that are either wrong or non-relevant. This is particularly true during DOE when the extremes of the design variable domains are explored. Design tools used in the industry have to pass a rigorous validation and certification procedure. The same philosophy has to be applied to the combination of tools, as the MDA. This is a considerable obstacle to the deployment of the framework into an industrial context.

- The neutral domain used to exchange file was not accessible by partners with particularly strict IT infrastructures or restrictions about information exchange without a clearance. To this end, the exploit of surrogate model allowed to (partially) overcome these limitations.
- Developed Surrogate Models required versioning and metadata association to keep track of the specific simulation parameters used to generate them.

7 FUTURE DEVELOPMENTS

The current test-case has to be considered as the starting point for more a comprehensive evaluation of the impact of the on-board system architecture on the aircraft performances. Previous analysis [25][26] have highlighted that estimated acquisition and operation cost for different configurations can be similar, thus efforts will be dedicated to investigate the accuracy of the cost tool and its sensibility to the specific components that define the architecture. In parallel the updated AGILE methodologies will be integrated in the current framework.

ACKNOWLEDGEMENTS

The research presented in this paper has been performed in the framework of the AGILE project (Aircraft 3rd Generation MDO for Innovative Collaboration of Heterogeneous Teams of Experts) and has received funding from the European Union Horizon 2020 Programme (H2020-MG-2014-2015) under grant agreement n° 636202. The authors are grateful to the partners of the AGILE Consortium for their contribution and feedback.

REFERENCES

1. I. Chakraborty, D. N. Mavris; 2016; "Integrated Assessment of Aircraft and Novel Subsystem Architectures in Early Design"; In *54th AIAA SciTech*; San Diego; CA; USA
2. M. J. Cronin; 1983; "All-Electric vs Conventional Aircraft: The Production/Operational Aspects"; *Journal of Aircraft*; vol. 20, no. 6, pp. 481-486
3. G. Norris, G. Thomas, M. Wagner; C. Forbes Smith; 2005; "Boeing 787 Dreamliner - Flying Redefined"; *Aerospace Technical Publications International*; ISBN 0-9752341-2-9
4. C. Schallert; 2007; "A Novel Tool for the Conceptual Design of Aircraft On-Board Power Systems"; *SAE Aerotech Congress*; Los Angeles; CA; USA
5. E. Kessler, M. Guenov; 2010; "Advances in Collaborative Civil Aeronautical, Multidisciplinary Design Optimization"; Reston: American Institute of Aeronautics and Astronautics
6. AGILE EU Project portal; "<http://www.agile-project.eu>"
7. P.D. Ciampa, B. Nagel; 2017; "The AGILE Paradigm: the next generation of collaborative MDO"; In *18th AIAA/ISSMO Multidisciplinary Analysis and Optimization Conference*; Denver; USA; June
8. E. Baalbergen, E. Moerland, W. Lammen, P.D. Ciampa; 2017; "Methods to Support Efficient Collaboration for Competitive Aircraft Design"; in *6th CEAS Aerospace Europe Conference*

9. E. Baalbergen, A. Kanakis, W. Vankan; 2009; "A practical approach for coordination of multi-partner engineering jobs in the design of small aircraft"; CESAR Special Issue of Journal Czech Aerospace Proceedings / Letecký zpravodaj; *Journal for Czech Aerospace Research*; vol. 3
10. P. Coleman, 2012; "Innovations in collaborative modelling and simulation to deliver the Behavioural Digital Aircraft. CRESCENDO Forum Participants Handbook"; Toulouse
11. A. A. Gastaldi; 2017; "Development of a Doublet-Lattice Method Program for Aero elastic Analysis in Conceptual Aircraft Design"; *Master Thesis*; Ecole Polytechnique Fédérale de Lausanne; Lausanne; CH
12. B. M. Verhagen; 2017; "Optimization of Non-Planar Wing Aircraft Configurations Accounting for Low Speed Mission Segments "; *Master Thesis*; Delft Technical University; Delft; The Netherlands
13. E. Baalbergen, J. Kos, C. Louriou, C. Campguilhem, J. Barron; 2016; "Streamlining cross-organisation product design in aeronautics"; in *6th EASN International Conference on Innovation in European Aeronautics Research*; Porto
14. B. Nagel, D. Böhnke, V. Gollnick, P. Schmollgruber, A. Rizzi, G. La Rocca, J. J. Alonso; 2012; "Communication in Aircraft Design: Can we establish a Common Language?"; in *28th International Conference of the Aeronautical Sciences*, Brisbane
15. I. van Gent, R. Lombardi, G. La Rocca, R. d'Ippolito; 2017; "A Fully Automated Chain from MDAO Problem Formulation to Workflow Execution"; in *International Conference on Evolutionary and Deterministic Methods for Design Optimization and Control with Applications to Industrial and Societal Problems*; Madrid; Spain; Sep 13-15
16. G. Xianguy, P. S. Prakasha, K. Anisimov, A. Savelyev; 2017; "Airframe – Propulsion System Integrated Optimization in Collaborative Aircraft Design framework: AGILE EU Project"; In *18th AIAA/ISSMO Multidisciplinary Analysis and Optimization Conference*; Denver; USA; June
17. National Academies of Sciences; 2016; "Commercial Aircraft Propulsion and Energy Systems Research: Reducing Global Carbon Emissions"; National Academies Press, ISBN 0309440998
18. P. Giannakakis, P. Laskaridis and P. Pilidis; 2011; "Effects of Offtakes for Aircraft Secondary-Power Systems on Jet Engine Efficiency"; *Journal of Propulsion and Power*; vol. 27; no. 5; pp. 1024-1031
19. M. Sinnet; 2007; "787 No-Bleed Systems: Saving Fuel and Enhancing Operational Efficiencies"; *Aero Quarterly*; vol 4; pp. 06-11
20. S. Chiesa, G. A. Di Meo, M. Fioriti, G. Medici, N. Viola; 2015; "ASTRID - Aircraft on board Systems sizing and TRade-off analysis in Initial Design"; in *5th SCAD - Symposium on Collaboration in Aircraft Design*; Naples; Italy
21. J. Kurzke; 2015; "GasTurb 12. Design and Off-Design Performance of Gas Turbines"; Germany: GasTurb GmbH
22. J. Kurzke, 2002; "Engine Modeling Methodology: Efficiency Definitions for Cooled Single and Multistage Turbines"; in *ASME 2002-GT-30497*
23. M. N. Beltramo, M. A. Morris, J. L. Anderson; 1979; "Application of Parametric Weight and Cost Estimating Relationships to Future Transport Aircraft"; in *38th Annual Conference of the Society of Allied Weight Engineers*; New York
24. Noesis Solutions; 2017; "Optimus Rev 10.19 - Users manual"
25. M. Fioriti, L. Boggero, S. Corpino, A. Isyanov, A. Mirzoyan, R. Lombardi, R. D'Ippolito; 2017; "Automated Selection of the Optimal On-board Systems Architecture within MDO Collaborative Environment"; *18th AIAA/ISSMO Multidisciplinary Analysis and Optimization Conference*; Denver; USA; June
26. M. Fioriti, L. Boggero, S. Corpino, A. Isyanov, R. Lombardi, M. Panzeri; 2016; "Aircraft System Architectures Selection for Aircraft Design Optimization in an Automated Process"; *6th EASN International Conference*; Porto; Portugal; October

Development of an End to End Maintenance Evaluation Strategy for new Technologies in the Context of IVHM

Hendrik Meyer
Deutsches Zentrum für Luft- und Raumfahrt
Researcher
Blohmstr. 20, 21079 Hamburg, Germany
hendrik.meyer@dlr.de

Nicolas Bontikous
M2P Consulting
Consultant
Bockenheimer Landstraße 94-96, 60323 Frankfurt/Main, Germany

Alexander Plagemann
Airbus
CS2 ADVANCE Project Coordinator
Airbus-Allee 1, 28199 Bremen, Germany

ABSTRACT

Abstract: In the Clean Sky II Platform 3 Large Passenger Aircraft (LPA) the work package 3.6 (WP3.6) "Maintenance" new technologies are developed for an integrated End to End (E2E) Maintenance Service Architecture. The technologies that will be developed are based on Integrated Vehicle Health Management Technologies supported by maintenance execution enhancement solutions. Inside WP3.6 three different projects are placed under the head of a leading partner consortium ADVANCE. The three Projects which are included in the WP3.6 are DEMETER, PACMAN and AIRMES. To evaluate the overall impact of the developed technologies, an E2E Evaluation Strategy for all technologies across the different projects is needed. The technologies in the different projects reach from structural health management, system health management, data analytics over virtual and augmented reality to mobile applications. Overall more than 20 improvements are identified that will be verified and validated through different scenarios, use cases and prototype demonstrations. To identify the global impact of the combination of these technologies on airline as well as European level an Evaluation strategy needs to be developed under the constraints of several partners in different projects and the influence of the scenarios and use cases. The paper describes the E2E Evaluation Strategy and shows the integration of different technologies and partner inputs. These include the impact identification process, the MRO (Maintenance, Repair and Overhaul) value chain analysis, the simulation on airline level and the global value chain impact. Also the participating process, the risk handling and the detailed processes for the different parts of the E2E Evaluation approach will be shown.

KEYWORDS: *Evaluation, Technology, Integrated Vehicle Health Management, E2E, IVHM*

NOMENCLATURE

IVHM - "Integrated Vehicle Health Management (IVHM) or Integrated System Health Management (ISHM) is the unified capability of systems to assess the current or future state of the member system health and integrate that picture of system health within a framework of available resources and operational demand." [1]

Stakeholder - The Stakeholder are according the DLR IVHM Stakeholder Model [1] defined. One party can reflect several stakeholders. As an example the airline can be the owner, operator and fleet manager at once. Based on [2], the main stakeholders of IVHM could be categorized from requirements perspective in the following manner:

- Owner (e.g. airline, lease company)

- Maintenance personnel and management (e.g. airline, MRO personnel)
- Original Equipment Manufacturer (OEM, e.g. Internal integrated engineering teams developing the product)
- Health Management (HM) system integrator (e.g. third party IVHM provider)
- Operator (e.g. airline)
- Fleet manager (e.g. mission commander)
- Regulatory authorities (e.g. airworthiness, certification)
- General public (e.g. employees)

It is necessary to mention that there are many other stakeholders with lower impact as shown in Figure 1:

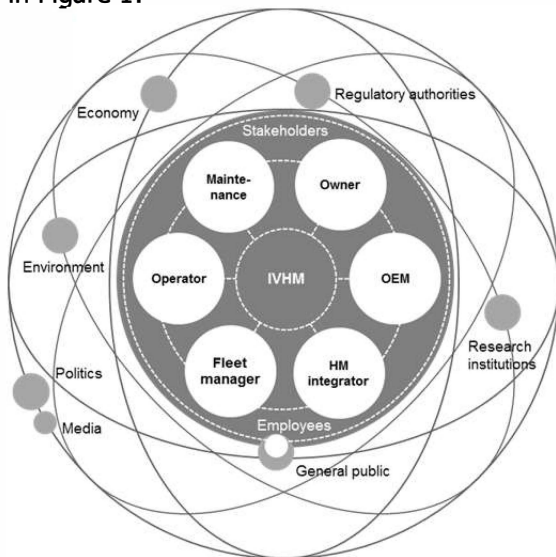


Figure 1: IVHM Stakeholder [1]

End-to-End (E2E) Maintenance - Extend terminology of the term maintenance to precise its application in an operational

1 PROJECT DESCRIPTION

Within WP3.6 ADVANCE (related to maintenance) of IADP Large Passenger Aircraft – Platform 3, the H2020 (Horizon 2020) challenges on seamless air mobility, industrial leadership and competitiveness will be addressed by enhanced reliability and affordability of the air transport system through less operational disruptions and higher maintenance economics efficiency. These challenges are addressed on the basis of a multidisciplinary integration of aircraft and ground based health monitoring and management and maintenance supporting technologies into a service-oriented, airline operational focused, collaborative environment.

In this context, validation for a global End-to-End maintenance service architecture and demonstration of the technical and operational maturity of the enabling technologies integrated at higher level into the global architecture will be provided to support the accomplishment of the following objectives:

- Reduction of operational disruption caused by unplanned maintenance for the European legacy fleet and short term derivatives

context and product life cycle context as shown in Figure 2:

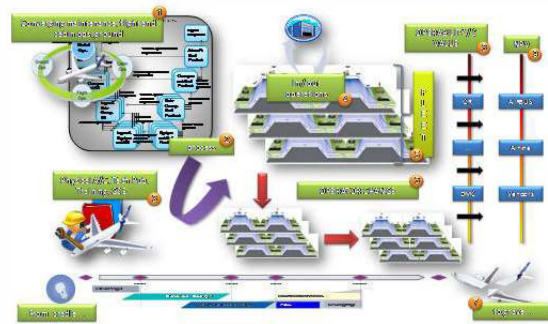


Figure 2: E2E Maintenance Context [3]

E2E Maintenance in the Operational Context - Holistic description of the operational maintenance processes, activities (incl. resources and actors) and product characteristics covering the operational flight cycle from flight preparation to flight closure and the full maintenance scope from scheduled to unscheduled events.

E2E Maintenance in the Product Life Cycle Context - Holistic description of maintenance performance enabling design and support activities along the product life cycle:

- From future projects to customer support
- From product conception to product disposal (Cradle to Grave)

SOA (State of the art) Technology – Includes all technologies, improvements and processes which are considered inside of the projects in WP3.6 and basis for further developments.

- Maximization of airline and maintenance asset utilization (aircrafts, maintenance resources and infrastructure)
- Improvement of the value chain through services for the main actors (Airlines, MROs, OEMs, Supplier)
- Exploration of the impact of new services on the way of working for maintenance actors
- Improvement of maintenance economics with focus on early opportunities for the legacy fleet and short term product derivatives

The demonstration of the achievements of the project objectives are based on further development and adaption of component level technologies with a minimum of TRL3 and their integration into a higher level architecture providing an increase from TRL3 to TRL6 on that level.

The multidisciplinary development of a service-oriented End-to-End (E2E) Architecture and the selection and integration of the enabling technologies requires an iterative approach to ensure the consistency between all elements. Furthermore the technical and project management dependencies of the different activities need to be fully understood and considered. Figure 3 illustrates key inputs and outputs between the architecture related WP's and the WPs providing the enabling technology bricks as well as the intermediate integration.

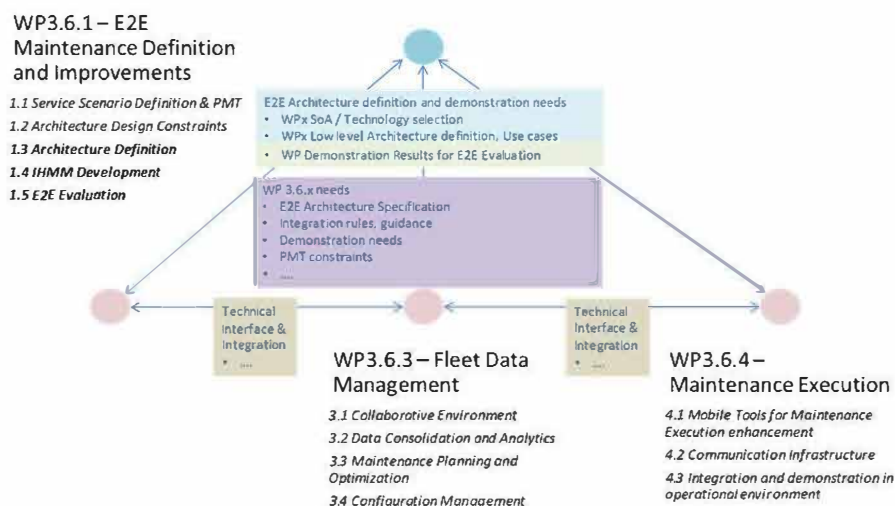


Figure 3: Relationship between CS2 WP

The overall architecture leading work packages is WP3.6.1. It will provide service scenarios, business and operational scenarios and the whole architecture including IHMM relevant technical, performance and integration requirements to the enabling WPs. Furthermore the overall process, methods, tools and KPIs will be provided. The development of the Architecture and its requirements will be based on state of the art analysis, technology feasibility studies and selections conducted by the enabling WP3.6.2 to WP3.6.4 and delivered as input to WP3.6.1. To ensure the overall demonstration of the End-to-End architecture WP3.6.1 will provides the global demonstration strategy and requirements taking into account the demonstration capabilities on lower and intermediate level as provided by the enabling WPs.

ADVANCE WP3.6 includes different projects: AIRMES (Airline Maintenance Operations implementation of an E2E Maintenance Service Architecture and its enablers), DEMETER (Development of E2E Maintenance architecture process and methods enabling a reliable and economic air transport system) and PACMAN (Prognostics And Computer Aided Maintenance). The three projects are independently from each other, but several deliverables contribute as an input for the other projects. Especially for the E2E Evaluation each partner, that delivers results of an improvement needs to interact with the other projects.

The involved Partners at the project AIRMES are Transportes Aereos Portugueses SA (TAP), Aerospace International Services Limited (AIS), Atos Origin Integration SAS (ATOS), Cranfield University (Cranfield), Instituto de Soldadura e Qualidade (ISQ), L-Up SAS (LUP), Meggitt SA (Meggitt), M2P Consulting GmbH (M2P), Office national d'etudes et de recherches aerospaciales (ONERA), Parametric Technology SA (PTC), Technische Universiteit Delft (TU Delft), Tecnologias de

Informacao SA (TEKEVER). The DEMETER Project includes the Deutsches Zentrum für Luft- und Raumfahrt E.V. (DLR) and Stichting Nationaal lucht- en Ruimtevaartlaboratorium (NLR). The PACMAN consortia is built by Honeywell International SRO and Vysoka Skola Banska – Technicka Univerzita Ostrava. [4]

Table 1 describes the E2E architecture relevant SOA-Technologies split for each project. Several of the technologies are already matured, but not in the context of an overall platform integration. That is one of the main goals of the projects.

Table 1 : Technologies list

	DEMETER	PACMAN	AIRMES
SOA-Technology	<ul style="list-style-type: none"> ▪ Indirect Structural Health Monitoring ▪ Direct Structural Health Monitoring 	<ul style="list-style-type: none"> ▪ APU Prognostic Solution ▪ Prognostic Architecture ▪ Augmented Reality Tools for Maintenance Execution enhancement 	<ul style="list-style-type: none"> ▪ Integrated Health Monitoring and Management (IHMM); ▪ Prognostic Solutions; ▪ Collaborative Environment and Data Analytics; ▪ Maintenance Planning and Performance Optimization Tool; ▪ Augmented Reality Prototype; ▪ Contextualized Documentation Tool ▪ Defects Reporting Tool ▪ Configuration Management Capturing ▪ Maintenance Elapse Time Control Tool ▪ Knowledge Database ▪ Dispatch Assessment Tool ▪ Workspace (Portable Service Tools) ▪ Software Infrastructure for Communication

2 E2E EVALUATION STRATEGY

Evaluation means proper and appropriate examination and assessment of a process or technology. [6] The complexity of the evaluation system for IVHM technologies is driven by two factors. On one side the connectivity that includes the type and number of connections in the system. On the other side the variety driven by the number and types of the involved system elements. [7] The goal is to integrate different demonstration results with different granularity into a global E2E Evaluation Simulation to determine the global impact on a virtual airline with different aircrafts (AC's), routes and business cases. Therefore, all developed SOA-Technologies need to be identified. Also the business scenarios and use cases are necessary inputs for the development of a comprehensive E2E Evaluation strategy. Figure 4 describes the workshare and deliverables (results) between the DEMETER and AIRMES project within the Evaluation. On DEMETER side the DLR is responsible for the E2E Evaluation. On the AIRMES side M2P is in charge of the Evaluation. This figure describes the interaction of M2P with DLR and the needed flow of results. The E2E evaluation is furthermore supported by TAP as the airline representative and Thales and Airbus as OEM representatives.

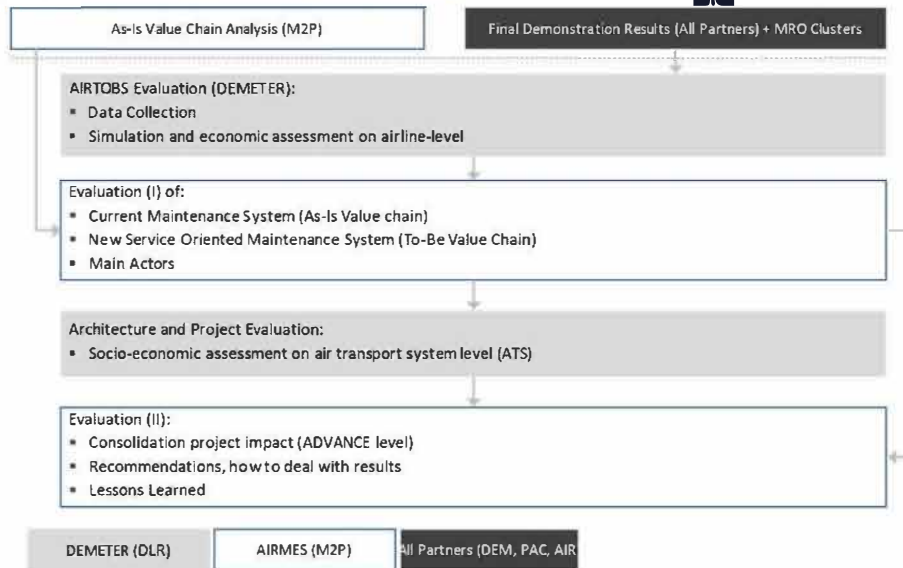


Figure 4: Approach for an E2E Evaluation (simplified)

Figure 5 delivers the IVV-structure from ADVANCE Level. As seen, the different prototype results will be integrated in the E2E Architecture and serve as a basis for the final E2E Evaluation. This includes further a virtual airline model. The virtual airline model deliver necessary input for the global value chain analysis. The figure describes further the dependencies between AIRMES, DEMETER and PACMAN. Therefore a participating evaluation strategy with transparent processes and responsibilities must be implemented.

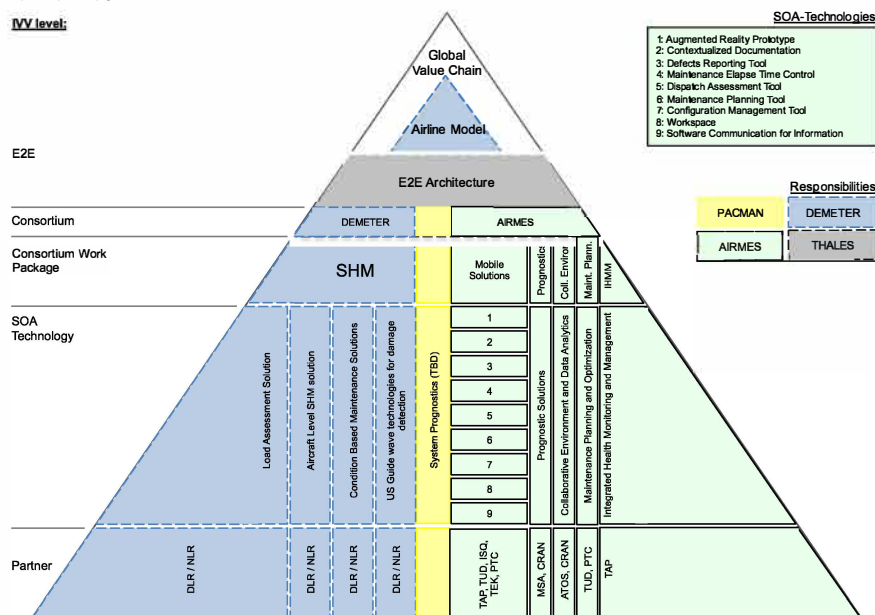


Figure 5: IVV-Structure from ADVANCE level, including relevant E2E aspects

3 EVALUATION PROCESS

The E2E Evaluation process is composed of four different steps:

1. The impact identification
2. The as-is Analysis
3. The tool development
4. The evaluation

The next paragraphs describe the four steps. Within WP3.6 step 1 and 2 are completed. Steps 3 is under progress by all involved partners. The evaluation itself will be performed by using the first demonstrator results at the second half of 2018.

3.1 Impact Identification

The Impact identification will be done by M2P and DLR. The value chain analysis of M2P includes already the estimated impacts of the different SOA-Technologies on the MRO processes. The DLR will add additional impacts based on expert knowledge inside of the DLR for the different technologies. The number of impacts per technology will be limited to ten, to limit the selection process to a reduced complexity. At the end of process a list with the indicator will be given to the next process step: the Indicator Selection. The overall selection and weighting process will be done by a participative multi-criteria synthesis and analysis process as described in Figure 6.

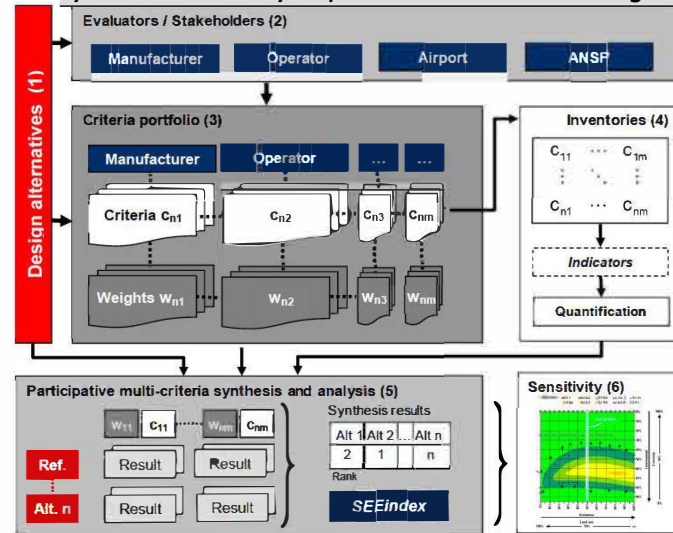


Figure 6: Participative Indicator Selection Process [4]

Each Stakeholder will be asked, for each technology he is involved, to rate the five most important indicators. The results of each stakeholder will be summarized in a list of the five most named indicators. The indicator weighting will be done for each technology and the relevant stakeholder. Each Indicator will be weighed against each other. The scale reaches from minus nine (-9) to nine (9). The result will be a weighted list of indicator. This list will be used to identify and measure the importance of the integration into the evaluation model. Inside these projects every partner will be asked to estimate the impact for all technologies regarding pre-developed scenarios and use cases. This will be used for a rectification of the importance of the integration of the single values. The results serve as a basis to estimate the impacts on ecologic and social level. This will be only integrated in a qualitative way in the overall E2E Evaluation. The Results for the economic impacts are the baseline for the evaluation tool development. The estimation should include the unit of estimated impact. E.g.: 5% or 3 minutes. Outside of the project it is planned to ask several aviation experts to give an estimation on the technology impacts in a specific context. This is planned by:

- Poster on Conferences
- Internal Questioner at the project partner at experts which are not involved into the project
- Dissemination activities
- Homepage.

It is planned to split the survey according to the DLR IVHM stakeholder model (ref. to Figure 1). This will enable later an analysis by the leading stakeholder for each technology. E.g. impact on maintenance estimated by an MRO, Impact on flight operation by airline. The Result will be used as a benchmark for the project results and a definition of a possible "to Be".

3.2 As-is Value Chain Analysis

In general, a value chain is described as a set of activities that a firm operating in a specific industry performs to deliver a valuable product or service for the market. Within the MRO-context, a value chain describes the sequence of necessary and involved process steps (planning, execution, reporting) to generate value and fulfills requirements (keep on airworthiness).

One major part of the tool development is the as-is analysis of the MRO market, existing services and MRO functions. To get detailed and all-embracing overview of the MRO demander, it is helpful to characterize airlines according to the following three models:

- Business Model
- Operational Model
- MRO Model

In general, a business model describes the ratio of how an organization creates, delivers, and captures value, in economic, social, and cultural and other contexts [7]. Further, the process of business model construction is part of the business strategy. Within the airline context, the business model can be described by analyzing the following factors:

1. Network Structure
2. Product type
3. Fleet size
4. Fleet structure
5. Fleet age
6. Leasing A/C split
7. Alliance membership
8. Fleet trends

Based on the business model analysis three different relevant airline clusters are identified. The large hub and spoke operator (L-H&S) describes an airline with more than 100 aircraft operating with hub and spoke concept. The small hub and spoke operator (S-H&S) has less than 100 aircraft. The point to point operator (P2P) has no dedicated home base for the whole fleet. In addition to the segmentation above, the three defined airline clusters specified with operational characteristics. For the maintenance aspect, relevant operational factors analyzed:

1. Average sector length
2. Average Turnaround Time (TAT)
3. On time performance (OTP)
4. Number of Hubs and Bases
5. Number of Destinations
6. Average Legs per day and A/C

The three defined and specified clusters (L-H&S, S-H&S and P2P) are furthermore detailed with relevant MRO characteristics. The relevant factors are:

1. Maintenance Regime
2. Number of Maintenance Bases

Table 2 lists the as-is analysis results. For presentation purpose the table is shorted on some relevant factors.

Table 2: As is analysis results

	L-H&S	S-H&S	P2P
Product Type [8]	Full Service	Full Service	Low Cost or Leisure
Avg. Fleet Size [10]	200	50	104
# Narrow-Body [10]	130	38	100
# Wide-body [10]	70	12	4
Avg. Fleet age [10]	11,3 years	12,4 years	8,9 years
Airline Alliance [10]	Member	Member	No Member
TAT (Short, middle)	50-90 minutes	45-80 minutes	30-60 minutes
TAT (Long)	200 minutes	180 minutes	150 minutes
# Legs (Short, Middle) [12]	5-6	6	7-8
# Legs (Long) [12]	2	2	2
MRO Regime [12]	In-House Airline 3 rd Party Provider	In-House Airline 3 rd Party Provider Independent 3 rd Party Provider	Airline 3 rd Party Provider Independent 3 rd Party Provider

3.3 Tool Development

For the E2E Evaluation two different tools will be used. For the Evaluation on Airline level the DLR AirTobs (Aircraft Technology & Operations Benchmark System) will be modified to integrate all improvements with transfer functions. The second tool will be E2E Evaluation System, developed by M2P. Each SOA-Technology will be integrated step-by-step into AirTobs. Therefore transfer functions will be developed. A transfer function can be a mathematical algorithm, a table manipulation, a single value manipulation or, a new program.

The main changes are estimated in the Maintenance Schedule Builder as shown in Figure 7. It is also estimated, that the improvements will have a large impact on the task data base and the cost data base. For the verification of the tool, the results will be analysed, for each implemented impact about the logical estimated result. For the validation, the results will be analysed according the expected results, estimated by experts outside of the project and literature values, by other projects or developments which are comparable.

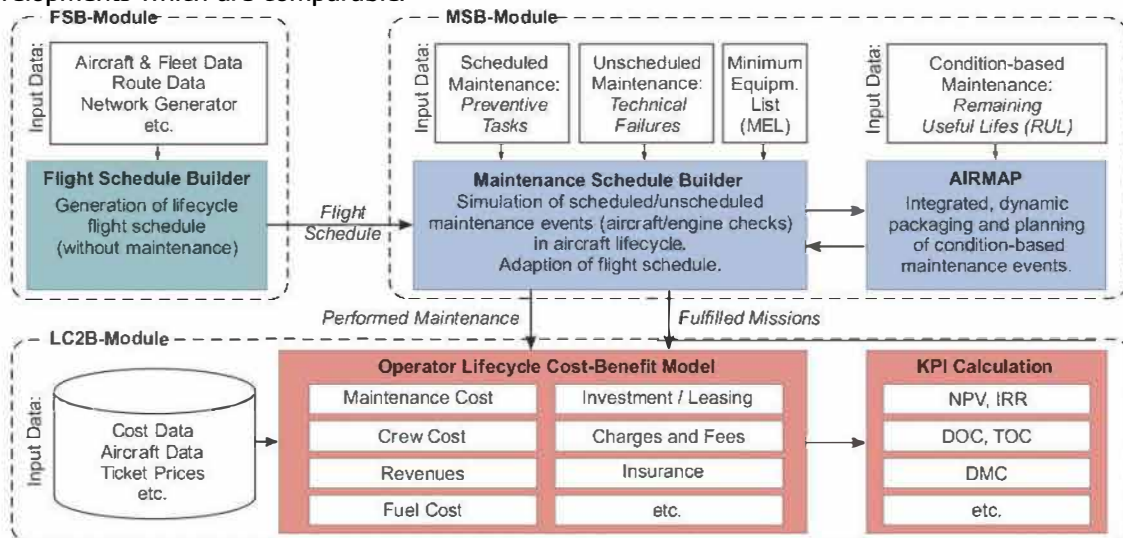


Figure 7: AirTobs Architecture [15]

For each technology and improvement DLR will start a single technology evaluation. The single technology evaluation will be based on first results of the technology owner. The result of the E2E Evaluation on single technology will be the baseline for adjustments and validation of the expectations for each single technology. With all technologies and improvements integrated into the DLR tool, the overall E2E Evaluation on airline level will be performed. It is planned to perform this analysis for three different airline clusters to reflect the complex airline structure within the European aviation network. The results will be the baseline for the E2E Evaluation on European Network Level. The results of the analysis on airline level will be extrapolated to the European Network Level to analyse the impact on the European Aviation Sector.

The E2E Evaluation System is the second tool which will be used. The AirTobs simulation results are necessary inputs to execute the E2E Evaluation System. Besides the AirTobs input, the as-is insights, especially the three defined airline clusters (L-H&S, S-H&S, P2P) flow into the E2E Evaluation System. Furthermore, necessary data and insights out of the MRO Business Analysis Report will be integrated. Therefore, the extrapolation for each airline cluster can be made with the number of airlines in that cluster. As a next step the scale effect for Europe is to be done by the sum of the different airline clusters. At this project stadium, it is planned to have the opportunity of retracing the impacts back to the single KPI's for each improvement.

3.4 Evaluation

The evaluation will follow the process described in Figure 8. It consists of six parts where different project partners are involved.

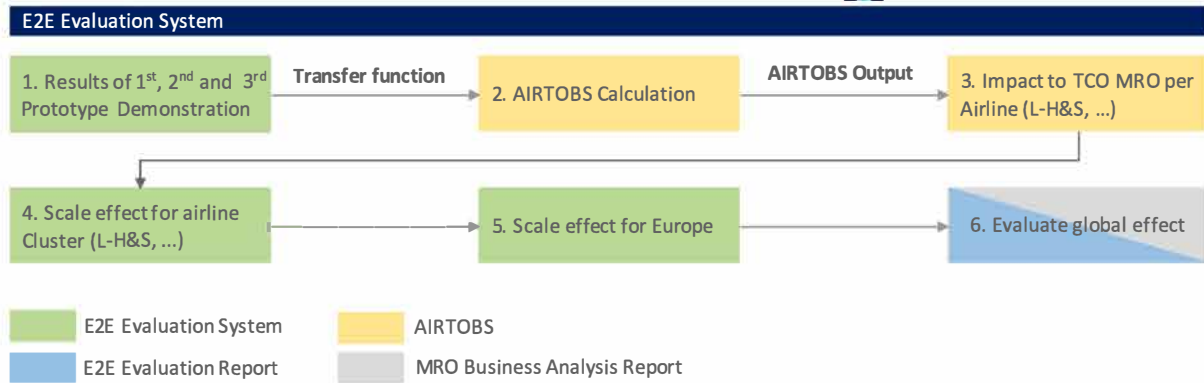


Figure 8: Simplified approach for an E2E Evaluation System [14]

The prototype demonstration will be performed by the technology and improvement owner accordingly to the validation and verification strategy of ADVANCE as well as the demonstration roadmap. The results of the demonstration activities will be transferred to the DLR. The demonstration team is responsible to assure that the results are valid and verified.

In the second step the AirTobs calculation will take place. The results of the demonstrations will be integrated via transfer functions into the E2E Evaluation System. The calculation will perform a life cycle cost benefit analysis of a fleet of aircraft in the context of three different airline clusters. As the fourth step the scale effect per airline cluster will be done. Therefore, the results of the single airlines will be integrated into the tool and multiplied by the number of airlines, considering the size of the different operators (number of bases, number of routes, maintenance regime) and regarding fleet size. These results will be integrated into the last step of the tool that calculates the scale effect for Europe about the impact of the different technologies on the main drivers in airline operations. The last step is a report about the E2E Evaluation concerning the impacts. Also, the MRO Business Analysis Report is derivate from that results, to show the business opportunities for the different stakeholder on the field of IVHM. The results of the evaluation will be compared with the as-is results from the business analysis, to show the benefits of the technology implementation. Additionally, the results will also be compared with the expectations.

4 CONCLUSION

This paper shows the principal approach for the E2E Evaluation inside the WP3.6 for the projects AIRMES, DEMETER and PACMAN within CleanSky II. The considered SOA-Technologies in the projects will be improved, changed or digitalized and contribute to an overall IVHM E2E architecture. To evaluate the impact of these SOA-Technologies on European level an E2E evaluation process needs to be developed. The complexity is given by the number and types of SOA-Technologies, partners, projects and connections between the different workpackages. To reduce this complexity a participating process for the impact factors has been performed. Additionally the as-is analysis delivers the inputs for suitable business and operational models and results into a scalable European aviation sector. Based on this preprocesses the tool development started. To ensure a comprehensive E2E evaluation process through the projects, a sufficient cooperation between the projects and the partners is established. Also the tools for the evaluation will be developed by different partners and end up in one E2E evaluation over all SOA-Technologies.



REFERENCES

- [1] I. K. Jennions, Integrated Vehicle Health Management - Perspectives on an Emerging Field, Warrendale: SAE International, 2011.
- [2] H. Meyer, „IVHM - Stakeholder,“ Deutsches Zentrum für Luft- und Raumfahrt, Hamburg, 2017.
- [3] R. Rajamani, A. Saxena und F. Kramer, Developing IVHM Requirements for Aerospace Systems, SAE International, 2013.
- [4] A. Plagemann, „Report on Terms and Definition,“ Airbus, Hamburg, 2016.
- [5] European Commision, „CORDIS - Community Research and Development Information Service,“ 29 September 2016. [Online]. Available: http://cordis.europa.eu/project/rcn/205837_en.html. [Accessed 27 July 2017].
- [6] Duden, „Duden Evaluation,“ [Online]. Available: <http://www.duden.de/rechtschreibung/Evaluation>. [Accessed 30 July 2017].
- [7] V. Gollnick, Air Transport System, Wien: Springer, 2016.
- [8] M. Weiss, N. Dzikus und X. Sun, „TECHNOLOGY ASSESSMENT OF FUTURE AIRCRAFT,“ in *ICAS*, Brisbane, 2012.
- [9] A. Osterwalder, Y. Pigneur und A. Smith, Business Model Generation, Hoboken: John Wiley & Sons, 2010.
- [10] Deutsches Zentrum für Luft- und Raumfahrt e.V., „Analysis of the European air transport market,“ 2008.
- [11] Airfleets.net, „Airfleets Aviation | Airline Fleets,“ [Online]. Available: www.airfleets.net. [Accessed 1 12 2016].
- [12] P. Goedeke, Networks in Aviation, Berlin: Springer-Verlag Berlin Heidelberg, 2010.
- [13] Flightradar24, „Aircraft by Airline,“ [Online]. Available: www.flightradar24.com. [Accessed 1 12 2016].
- [14] N. Bontikous und S. Billet, „Maintenance Business Analysis Report,“ M2P Consulting, Frankfurt, 2017.
- [15] N. B. Hölzel, T. Schilling und V. Gollnick, „An Aircraft Lifecycle Approach for the Cost-Benefit Analysis of Prognostics and Condition-based Maintenance based on Discrete-Event Simulation,“ Fort Worth, Texas, 2014, September 29 - October 02.
- [16] N. Bontikous und S. Billet, „E2E Evaluation System - Requirements,“ M2P Consulting, Frankfurt, 2017.
- [17] R. Ghosh, „THEORETICAL FRAMEWORK OF SYSTEMS DESIGN FOR THE AIR TRANSPORTATION SYSTEM INCLUDING AN INHERENTLY QUANTITATIVE PHILOSOPHY OF SCENARIO DEVELOPMENT,“ in *29th Congress of ICAS*, St. Petersburg, 2014.
- [18] European Commision, „CS2 Call for Proposal (CFP01),“ 2015. [Online]. Available: <http://www.cleansky.eu/>. [Accessed 15 03 2015].

Cost Efficiency Model for Civil Transport Aviation referring to Operations

M. A. Solazzo

CIRA S.C.p.A.

Reliability, Safety & Security of Critical Infrastructures, Senior Researcher

Via Maiorise, 81048 Capua (CE), Italy

m.solazzo@cira.it

L. Travascio

CIRA S.C.p.A.

Reliability, Safety & Security of Critical Infrastructures, Senior Researcher

l.travascio@cira.it

A. Vozella

CIRA S.C.p.A.

Reliability, Safety & Security of Critical Infrastructures, Head

a.vozella@cira.it

ABSTRACT

The air transport system is the global network of commercial aircraft operators, airports, air navigation service providers, manufacturers of aircrafts and their components, airline operators, ground and flight services, infrastructures. It is responsible for connecting the global economy, providing millions of jobs and making modern quality of life possible, thus strongly supporting the world's gross domestic product (GDP).

The costs of operating such a complex network are a major concern for all the identified stakeholders. Furthermore each of them has a specific paradigm and related control mechanisms to handle cost efficiency issues. They all concur to determine the performance of the overall transport system and improving cost efficiency (linked to competitiveness) requires a deep analysis along all the system life cycle from feasibility to disposal.

One of the highly ambitious goals identified and formalized by the European Commission in "The European Aviation Vision 2050" is the "cost effective transport chains" [44]. The adoption of a rigorous cost efficiency methodology based on analytic/statistical formulation is mandatory. Such approach is the only way suitable to assure the effectiveness of the generic technology innovation on the aviation sector as well as for any other industrial one.

Due to the experience matured within CAPPADOCIA, a coordination support action, funded by EC, devoted to identify gaps and bottlenecks affecting cost efficiency improvement in ATS towards Flightpath 2050 goals, an analytic model has been recognized as a useful tool. Such a framework supports the analytical evaluation of the benefits due to the adoption of new technologies, processes or methods in some specific domains of the ATS life cycle (e.g. airframe and avionics, ATM systems, ground systems, design, production, maintenance, etc).

This paper describes the framework, the assumptions and the considerations derived on a case study.

KEYWORDS: *Cost Efficiency, Civil Transport, Aviation, Operation, Global Network.*

NOMENCLATURE

A3	Aegean Airlines	CL	Lufthansa Cityline
AA	Australasia	DF	Degree of freedom
AC	Air Canada	EN	Air Dolomiti
AC	Aircraft	ET	Ethiopian Airlines
Adj	Adjusted	EU	Europe
ATS	Air Transport System	EW	Empty weight
A&ME	Africa and Middle East	FC	Fuel Capacity
CA	Air China	GDP	Gross Domestic Product

IATA International Air Transport Association
 ICAO International Civil Aviation
 Organization
 JP Adria Airways
 LH Lufthansa
 LX SWISS
 MTOW Max take-off weight
 MLW Max landing weight
 MRO Maintenance, Repair and Overhaul
 NA North America
 Nb Number
 NH All Nippon Airways

NZ Air New Zealand
 OEW Operating empty weight
 OU Croatia Airlines
 Ref. Reference
 SA South America
 SN Brussels Airlines
 SQ Singapore Airlines
 SS Sum of Squares
 TG Thai Airways International
 TP TAP Portugal
 UA United Airlines

THE APPROACHED PROBLEM AND PURPOSE OF THE PAPER

Being competitive in the global market is a "must" that every stakeholder in the aeronautics domain pursues. One of the mean to reach this goal is cost efficiency that has become a major issue for all the value chain actors: from airlines and airports to aircraft manufacturers passing through designers and supplier integrators and MRO stakeholders.

It is not by chance in fact that also ACARE (Advisory Council for Aeronautics Research in Europe) has addressed cost efficiency in its Strategic Research Agenda (SRA 2), that has become a guide for future public and private funding programmes. In its future views of the ATS, ACARE has identified five "High Level Target Concepts" (HLTC) addressing different aspects to create pools of technology for deployment to whichever future scenario actually develops. One of these HLTC is **"the highly cost efficient air transport system"** that focuses upon all of the costs that arise in the whole air system design and operation.

These considerations clarify that handling cost efficiency is an issue for which all the aeronautics stakeholders need solutions.

Over the last decades, civil aviation has deeply increased its service volumes due to rapid technological change resulting in a decrease in costs and prices, nevertheless airlines have experienced a low profit in general. The deregulation process of markets and growth of competition have increased capacity causing lower rates, even with its rising costs. Therefore, for airlines the approach to face with price decreasing is to start reducing costs.

Considering all the components of the total cost function, it is challenging to identify the influence of each component on total cost. So it is strategic to analyze such impact [47], though it is a complex matter. The effectiveness of reduction of each item that composes the total cost of airline can change over time, depending on both the business model as well as external factors.

The proposed framework is based on an empirical approach. Starting from public data and using statistical approaches, it identifies the analytic regression laws suitable to estimate the operative cost reduction due a change in the ATS system life cycle. Using specific functions, the proposed framework processes a large amount of data representing the typical aviation life cycle parameters related to costs. Table 1 resumes the input data grouped according to the highlighted categories:

Table 1: Input Data

Costs	Fleet	Traffic	A/C Model	A/C Perform.	Charact. Weights
Fuel consumption	Airlines	Number of flights	Airliner type	Cruise speed	MTOW
Raw material	Number of airliners	Operated airports	Wake class	Climb and descent ratio	MLW
Supplies	Airliner category	Passenger capacity	Seating capacity	Flight range	OEW
Purchased merchandise	Internal seat layout	Passenger load factor	Propulsion system	Specific fuel consumption	EW
Maintenance		Transport capacity	Installed power		Fuel Capac.

STATE OF THE ART

In literature there are few recent studies focused on efficiency analysis of European airlines as most of the related work use data collected before 2000. In general, a function cost is derived thorough the use of different estimation methods (parametric, nonparametric...) and input data. The optimum for this estimation is to have input prices of airlines, which are not usually available [48], [49]. The adopted approach in case of lack of prices data is to estimate technical efficiency based on input and output data, which are easier to access [50].

Another possible approach to derive the most important parameters influencing costs is described in [51]. In this method of decision support AHP (Analytic Hierarchy Process), the weights of the factors were determined through questionnaires sent to experts in the aviation field.

In [52] they measure efficiency and productivity decomposition in European airlines using panel data methods, building on time varying inefficiency specific to each airline and performing an econometric estimation of an airline total cost function. It is a function form for the long run cost function using panel data methods.

The proposed approach will use a mixture of factors, in terms of input data organized in different categories. They represent panel data synchronously ordered to determine co-variances among them and able to support cost reduction decisions.

CONTRIBUTION OF THE AUTHORS

Rational Assumptions

This paragraph describes the framework and the relative assumptions based on a case study. The characterization of the operating costs have been carried starting from the public info provided by LH describing their activities and the associated periodic financial results.

The proposed approach is devoted to build an empirical model able to evaluate the accomplishable benefits due to technological or operative innovations. It identifies the driver parameters affecting costs and derives the regression laws which in the most part of the cases are dimensionless. It does not analyze the financial aspects of the airlines from the economic stakeholder point of view.

In order to prepare the data for the statistical analysis, all the values relevant to the effects of interest vs adopted parameters have been collected, assuming the adopted parameters as "independent" in the early phase and relevant to the same conditions. In case of correlation between parameters, the data set is reduced. The adopted statistical tools belong to the toolbox "6 σ " methodologies. Obviously, different elements of the operating cost are linked between them. The sketch below (Figure 1) shows in an easy graphical way the operating cost structure.

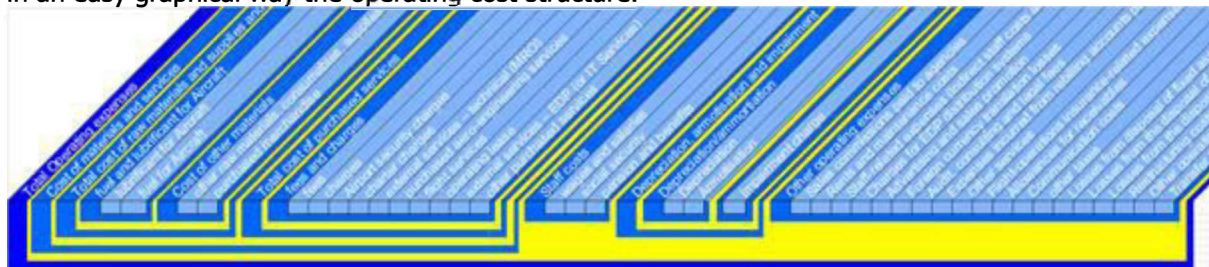


Figure 1: Graphic scheme of the operating cost structure

The reference values of the operating expenses have been retrieved from the periodic financial reports. These reports are yearly published and describe the status typically at December 31st. It is clear that the number of operating conditions is too low for statistical purposes, if compared to the large number of involved parameters. Consequently, it has been preferred a monthly time step with one observation period from December 31st, 1999 up to December 31st, 2016. In this way, the number of different events is equal to 204 at least for one single airlines. The monthly costs value has been calculated by means of linear regression laws starting from the yearly ones. The choice of the monthly time step is also due to the traffic description provided with such periodicity [2].

The framework target is to identify the strongest parameters able to affect the cost-efficiency w.r.t. target values, using the most suitable key performance indicators and specific statistical tools. This

model also allows to perform forecasts at a generic reference year and at a given confident level because it is strongly linked to public official data. The official data have been modified in dimensionless form adopting a common reference value (e.g. relevant to the start date: December 31st, 1999). The adopted time abscissa, which univocally describes the sequence of air traffic conditions, is:

$$\text{Time} = \text{Year} + \text{Month}/12 \quad (\text{Year} = 1999 - 2016 \text{ and Month} = 1, 2, \dots, 12)$$

The next sketch shows the total operating costs trend vs Year in dimensionless form setting the value 100[%] at year 2000. Analytically, the formulation is:

$$\text{Cost} [\%] = 100 * \text{Cost} (\text{Year}) / \text{Cost} (\text{Year}=2000)$$

Figure 2 shows the staff costs variation, as well as its contribution terms, assuming it is equal to 100, in percentage, at year 2000. Obviously, a similar description is available for the other costs and with the same detail.

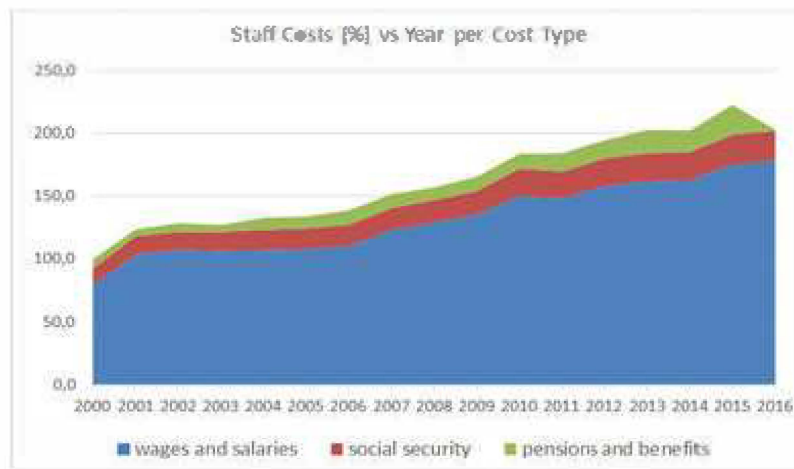


Figure 2: Staff Cost [%] vs Year per Cost Item

Another valuable info source is the monthly reporting of the performed flights. These reports describe in a very detailed way the airline monthly performance in terms of: passenger load factor [%], number of passengers [Kpeople], available seat*kilometre (in millions), revenue seat-kilometre (in millions) and the ration of the last two.

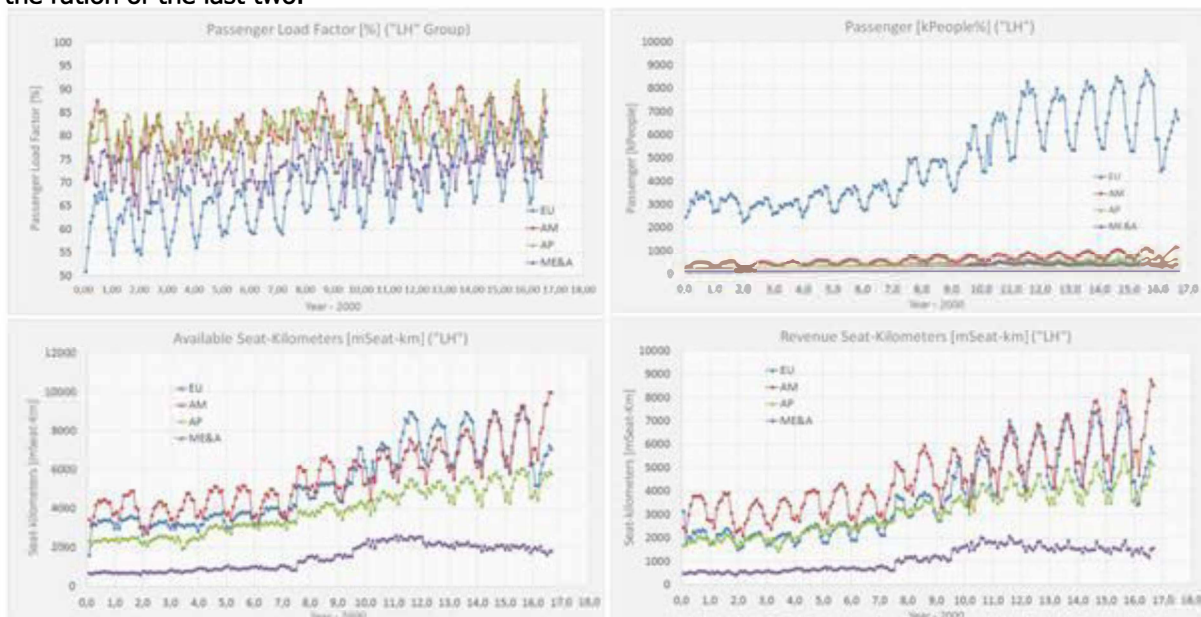


Figure 3: Monthly Operative State

The previous data show the fleet capacity and its effective utilization in the different world regions. Consequently, it is mandatory to include other source data to link the previous performance to the effective fleet composition (see Figure 4) and the performances of each airliner model.

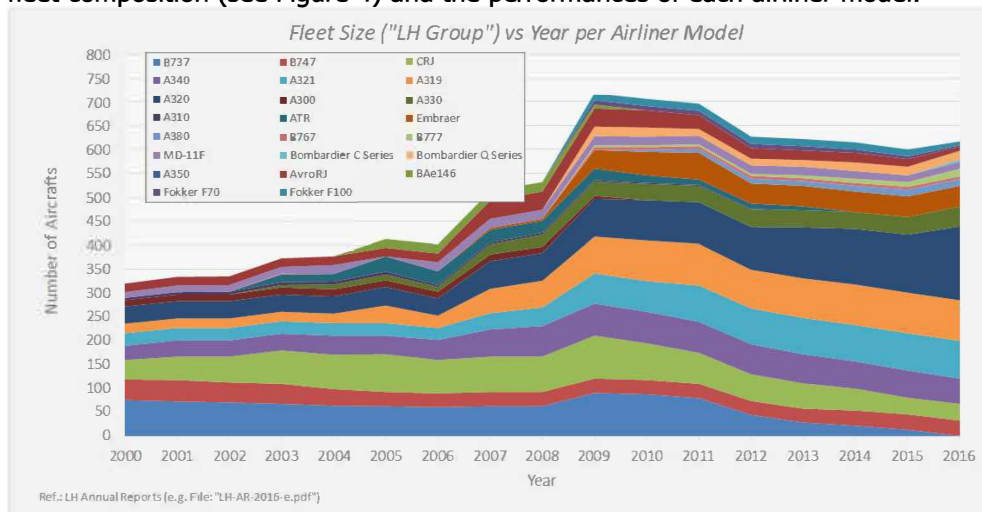


Figure 4: Fleet Size ("LH Group") vs Year per Airliner Model

The LH' timetable form provides for each planned flight an elementary data set including: the origin and destination cities, the associated UTC, departure and arrival airports with the associated code, the days of service, the departure and arrival times, flight number, airliner type and the involved partner carriers (#27). In particular, for each departure airport, the timetable provides a list of planned flights, identified by means of an assigned code. A detailed description may be retrieved from any LH' timetable (e.g. [01]) in its original version.

This database provides a detailed description of the air transport network, for a generic week during the timetable validity period. It is worth noting that the described airline traffic is the scheduled one, it does not see any delays or traffic variations due to force majeure.

The next pie chart shows the flight share vs carrier type (operator or partner). The values appear quite similar and close to fifty-fifty percent.



Figure 5: Weekly Scheduled LH and Partner Flights [%]

The total number of airports operated by LH and partners is equal to 252, in the referred period, and they are spread out through the world regions how show in Figure 6. The flight network connects the set of specified airports by means of 1044 distinct routes, labelled using the departure and arrive airport codes (e.g. FRA-MST is the label to identify the route from "Frankfurt" to "Amsterdam").

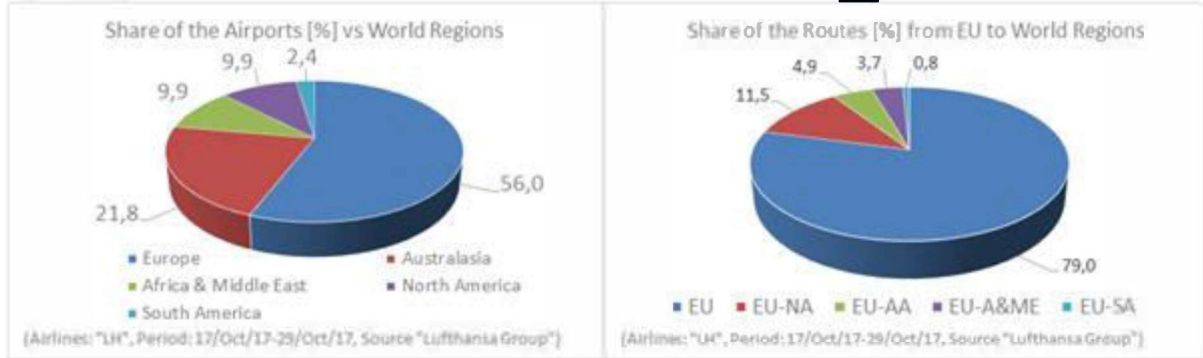


Figure 6: Operated Airports and Flight routes of the LH operator [%] vs World Area

The adopted distance is the minimum distance along the geodetic maximum circle joining the departure and destination airports. These distances have been calculated using an ellipsoidal formulation. So, the calculated distances show discrepancies w.r.t. the same measures made with the ruler in "Google Earth" tool also per intercontinental distances on any couple of latitude or longitude values.

The total number of flights (LH+Partners), from the European airports, is equal to 10821 and their destination airports are spread out through the world regions how showed below as well as for the flights from Australasia (#1137).

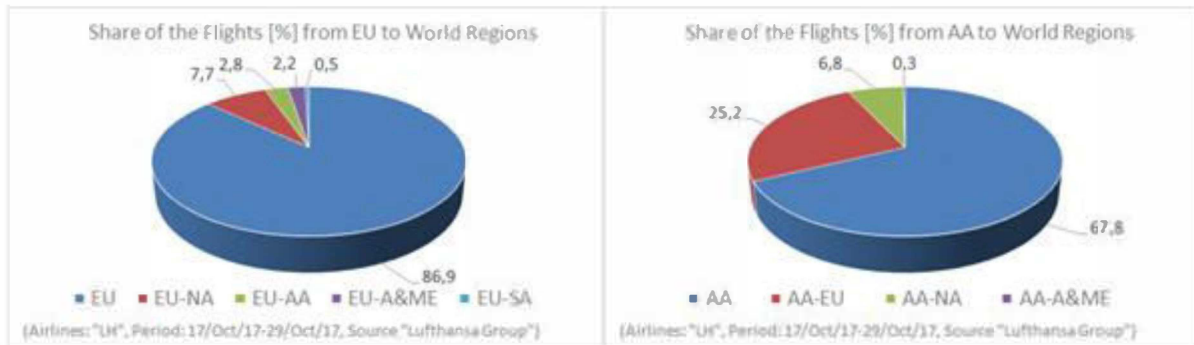


Figure 7: Operated Airports and Flight routes of the LH operators [%] vs World Area

Another aspect to consider is the local level of air traffic, on a specific airport or in given region (e.g. lander or arrondissement). A description of this kind of air traffic is mandatory to set up with adequate detail the daily operations and the associated ground service costs.

The next pie chart shows the movements (departures) vs European Countries.

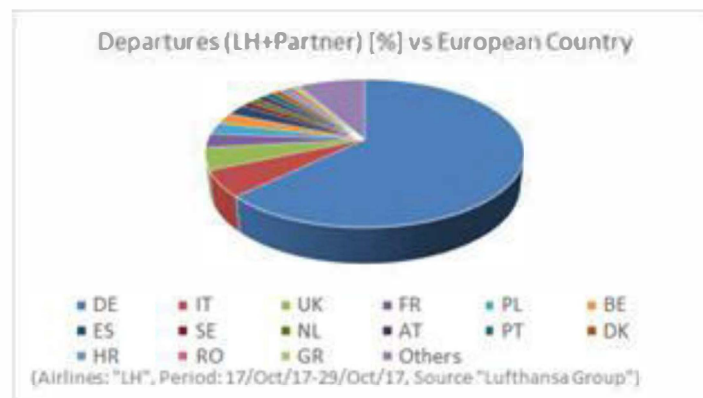


Figure 8: Departures (LH+Partners) [%] vs European Country

The previous data have been complemented with the information about the airliner models involved in the identified routes and the associated share per manufacturer. The sketch below shows, for instance, the flight rate per OEM in the reference period.



Figure 9: Share of the flights [%] per Manufacturer

By this way the LH's flight share w.r.t. its airliner models has also been characterised. The next two pie charts show the number of flights per model of the two major manufacturer providers: Airbus and Boeing.

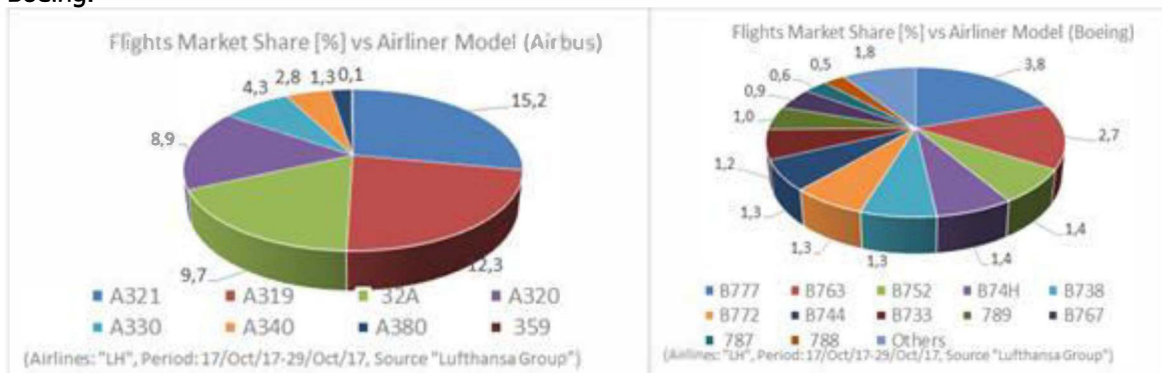


Figure 10: Flight Share [%] vs Airliner

This empirical description has allowed to derive the regression laws existing between the number of flights and the different independent parameters that are: operator, partners, operated airports, used routes, their geopolitical locations (NUTS, Country, World region), used airliners, manufacturers, etc. In other words, all air traffic components have been identified at any node of the transport network in aggregated or non-aggregated form with the identification of the main actors involved.

The same considerations are applicable to other traffic parameters: passenger capability (airliner configuration, number of seats), flown distances as well as "Seat*kilometers". It's worth noting that all the data retrieved from the timetables are related to a scheduled scenario, so they could not describe the real number of further transported passengers.

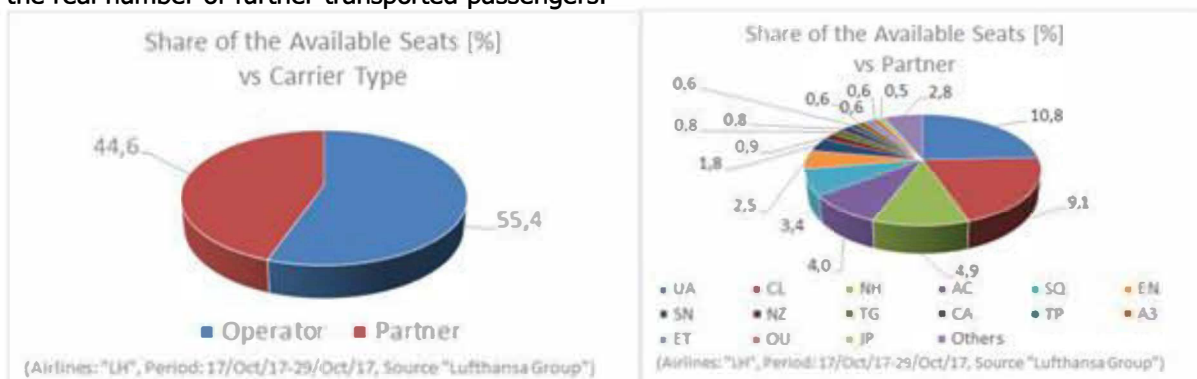


Figure 11: Weekly Available Seats [%] per Carrier Type and per each Partner

It is clear that the integrated set of data collecting the annual and monthly traffic results and the scheduled flights completes the full palette of colors suitable to paint the traffic panorama including its evolution vs time. The graph below shows the variation of the personnel composition vs month, while the pie chart shows the detail at year 2000.

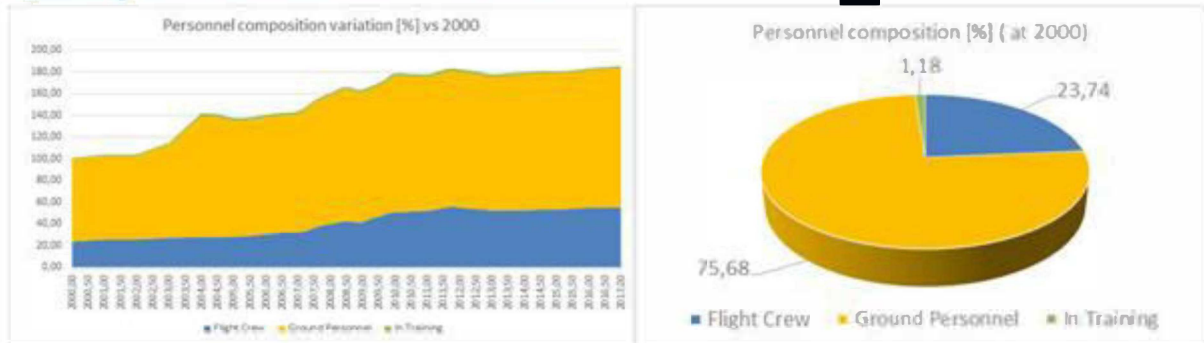


Figure 12: Personnel Composition [%] vs Month and detail at 2000

The geo-politic location of most of the airports have been performed by means of "Google Earth" as well as the route distances. The name of the departure city is linked to the associated airport code and time zone and provides the destination city and the scheduled flights by means of simple sub-roots. Obviously, the destination city includes the airport code and its relevant time zone.

The flights are listed according to the departure hour and a codified alphanumeric string, referring to the operated days. These data fully describe all the flights scheduled by the operator weekly.

Taken into account that one of the most relevant item associated to the flight activity is strictly related to the distance existing between the two airports, the route has been adopted as first driver parameter. The number of flights between the two airports has been calculated taken into account the listed flights and their week frequency. All flights between couples of airports of the same country, in Europe, are named "National", if one of the airport is located outside, the flight will be named "International" and all flight between airports internal to US will be defined "Domestic".

Statistical Analysis & Results

The aim of the proposed approach is to verify the existence of regression laws between the various parameters described by homogenized values and to weight the related parameter "relevance" by statistics. Time has been assumed as independent parameter because it is fundamental to describe the correspondence of the different values through the covariant parameters. In other words, it assures a common event reference frame for all parameters.

The preliminary actions have been devoted to identify the operative costs structure, which is homogeneously close to the stakeholder assumptions. All costs values have been modified in dimensionless values, using the associated total value at the year 2000.

For instance, in case of the "Staff costs", composed by "Wages and salaries", "Social security" and "Pension and benefits" ([1] - [17]), all values of the previous items have been modified in following way (e.g.): $\text{Var19 [\%]} = 100 * \text{"Wages and salaries cost"} / \text{"Staff costs"} (\text{Year}=2000)$, similarly for all addends including the totals. It is important to clarify that the monthly costs have been estimated by means of a linear interpolation starting from the yearly values. In other words, the cost rate has been assumed constant in each year.

The primary parameter adopted is the observed passenger request, in kilo-people, (var75) vs year (var69); this data has been considered as the starting one. The residual plots, referring to the best-fitted regression law, show an evident periodic variation of their values.

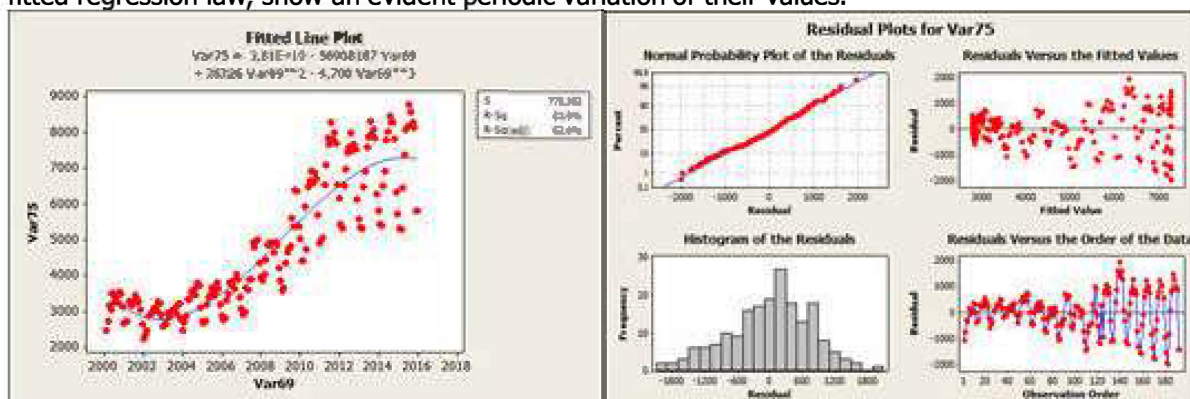


Figure 13: Fitted line plot of the Number of Passengers and related residuals.

Most of the observed residuals appear related to "month" (var68), consequently they are not only due to randomize effects but also to seasonal variation of the passengers request (see Figure 14).

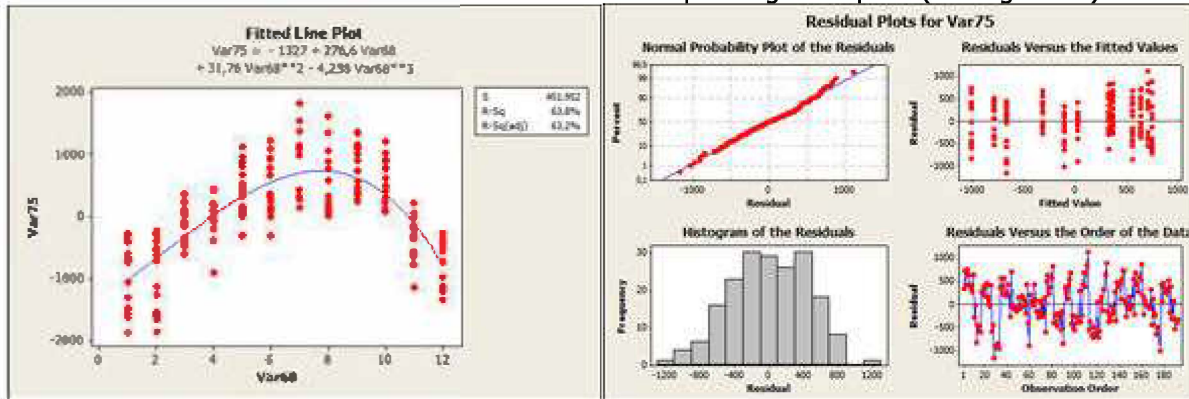


Figure 14: Variation of the Number of Passengers Discrepancies and related residuals.

The plot var75 vs var60 (Figure 15) shows that a polynomial fitted line of 3rd order, on all month range, is able to describe the observed trend, but it is better to make different best fits w.r.t. distinct portions of the month range.

The last residual plot, lower left, still shows the presence of variations. A capability analysis have been performed to verify and identify the possible covariance referring to other variables. Therefore, an analysis has been performed using ANOVA (**AN**alysis **OF** **V**ariance) method. A basic technical description of this methodology may be found in [45] and [46]. The commercial "Minitab" tool has been used to perform the identification of the driver parameters and to verify how these values vary w.r.t. their means.

The last residual variation vs its mean value has been compared to the similar variations observed referring to the parameters: Month, Number of Aircrafts and Time.

Analysis of Variance of the residual of "Var75", using Adjusted Square Sum for Tests, provides the following:

Source	Model	DF	Reduced DF	Seq. Sum of Squares
Var68		11	11	72025273
AC_Nb		139	135+	28274770
Var60		191	22+	3293282
Error		-150	23	2343758
Total		191	191	105937083
S = 319,222 R-Sq = 97,79% R-Sq(adj) = 81,63%				

Next figures show that the year 2008 is a watershed for the previous highlighted residual as well as for operated fleet. Consequently, it can be observed that the seasonal variations are strictly linked to the number of operated airliners.

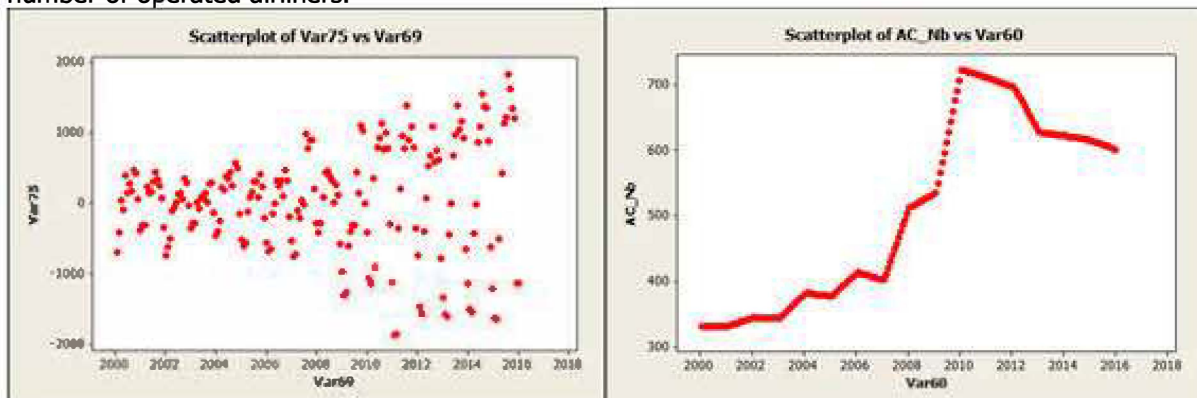


Figure 15: Residuals of the Number of Passengers and Fleet size vs Year.

Taking into account the identified covariant parameters, a reference passenger transport request model has been created for each world area: Europe, America, Asia and Pacific, Africa and Middle East and the overall one (worldwide).

A second step has been focused to identify the effective group of parameters in order to have a more limited number of case studies. The high number of involved parameters and interactions could cause a huge effort in the processing. In this situation, the matrix plot represents a useful tool able to show several scatter plots in a single image:

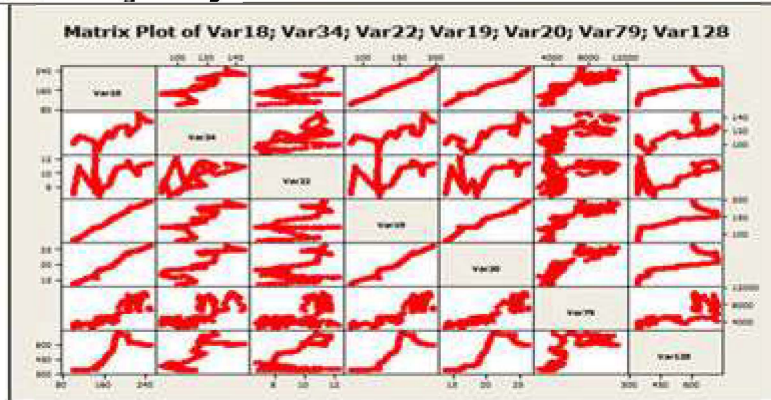


Figure 16: Matrix Plot of a set of possible involved parameters

The staff is a typical important pillar of a generic airline as well as for any commercial organization, it assures with its daily work the flight and support operations. Starting from the staff cost values, the Var08 expressed in percentage has been derived. This value has been assumed equal to 100 at year 2000.

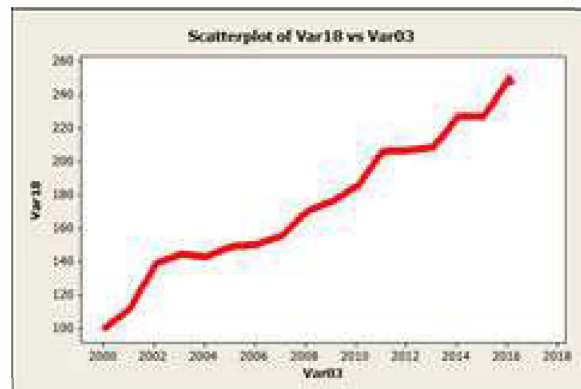


Figure 17: Staff Costs vs Year

A first analysis of variance of the residual of "Var18", using Adjusted Square Sum for Tests, w.r.t., provides:

Source	Model	DF	Reduced DF	Seq. Sum of Squares
Var19		161	161	261646,9
Var20		103	9+	92,4
Var21		95	4+	0,2
Error		-170	15	6,9
Total		189	189	261746,5

$S = 0,679043$ $R\text{-Sq} = 100,00\%$ $R\text{-Sq}(\text{adj}) = 99,97\%$

The previous variance result points out that most relevant covariance of the Staff costs (Var18) is associated to wages and salaries (Var19). Therefore, the analysis of variance of the "Var19", using Adjusted Square Sum for Tests, gives the following results:

Source	Model	DF	Reduced DF	Seq SS
Var61		179	179	261379,5

Var57	145	1+	96,1
Var34	170	1+	51,7
Var79	181	1+	16,4
Error	-486	7	202,8
Total	189	189	261746,5
S = 5,38304 R-Sq = 99,92% R-Sq(adj) = 97,91%			

The last variance shows that the most relevant covariance of the (Var19) appears associated to worldwide GDP (Var61), while other expected covariance vs the total personnel (Var57), other operating expenses (Var34) and total number of passenger transported (Var79) appear weak.

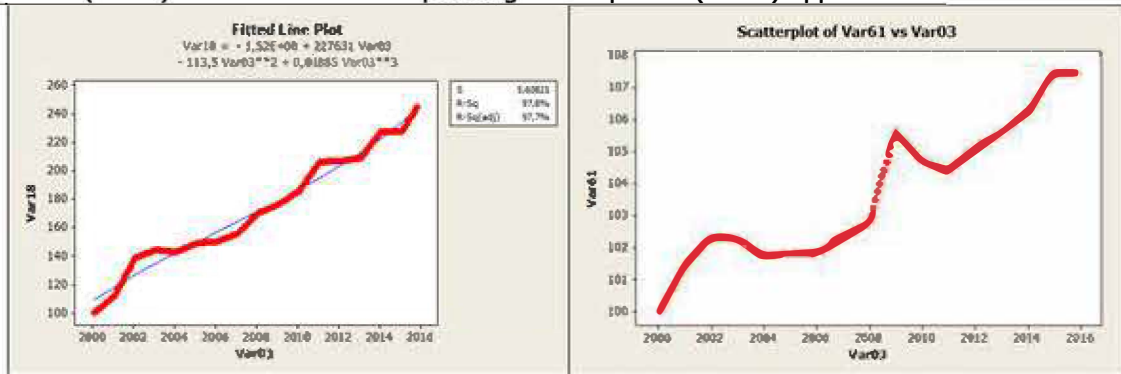


Figure 18: Fitted line plot of the Wages and .. [%] (=100 at 2000)

PREDICTION ANALYSIS CASE

To verify the added value of the approach, it is worth to perform estimation of unknown values relevant to the future. Consequently, we assume as working hypothesis, that the final date of available data is December 31, 2008. The repeated analysis of variance of the "Var19" in the time frame (January 1st, 2000 - January 1st, 2008) set of data, using Adjusted Square Sum for Tests, gives the following results:

Source Model	DF	Reduced DF	Seq SS
Var61%	57	57	8536,641
Var57%	36	11+	147,657
Var79%	93	14+	128,880
Var34%	95	5+	7,775
Error	-186	8	0,432
Total	95	95	8821,385
S = 0,232289 R-Sq = 100,00% R-Sq(adj) = 99,94%			

This confirms the previous covariance dependences and assures preliminarily good confidence to create a model with good level of accuracy. The regression line of Var19% vs year, working on the only selected data from January 1st, 2000 to January 1st, 2008), has been identified with associated residuals as shows below. The identified relationship has been used to perform the forecast for the next period (February 1st, 2008 – December 1st, 2016). The obtained results are compared to the real values for the same period.

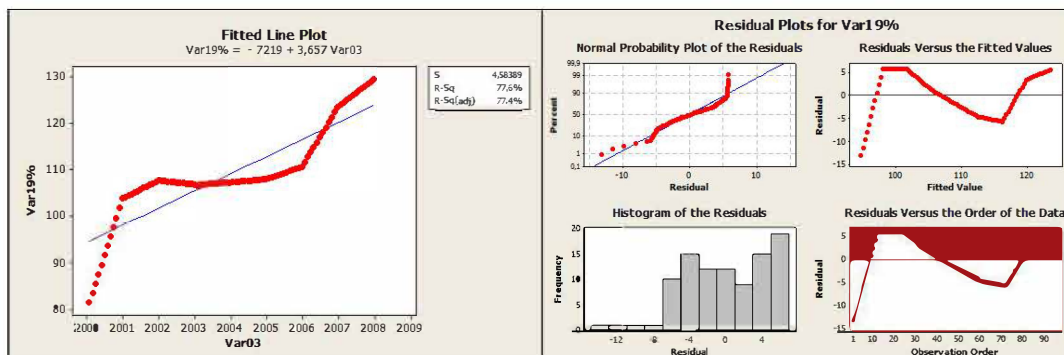
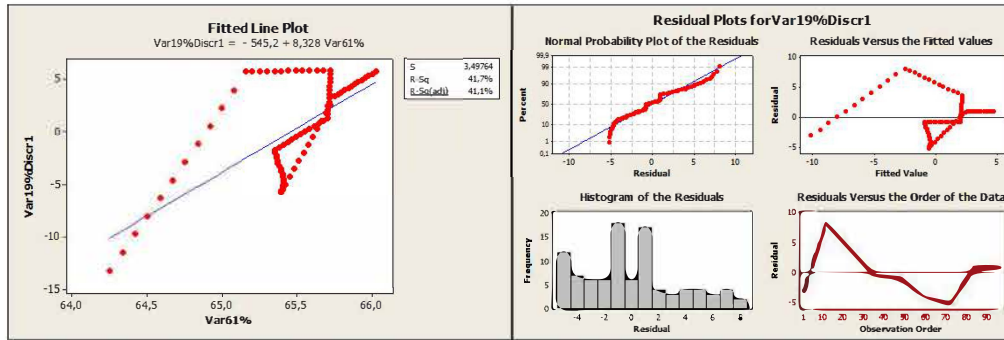
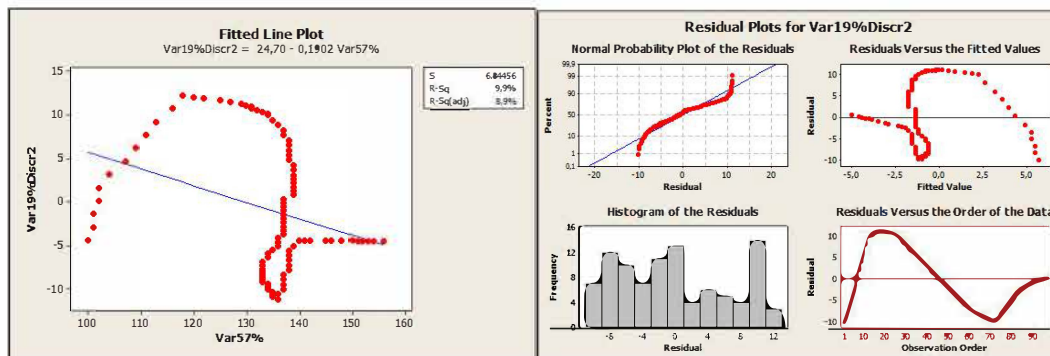


Figure 19: Fitted line plot of the Wages and .. [%] (Staff Cost =100 at 2000)

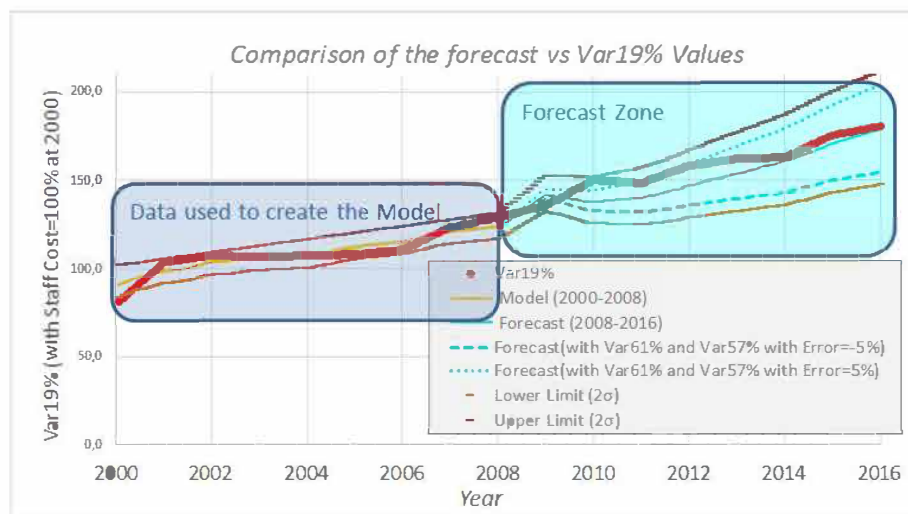
Similarly, the same analysis has been repeated about the discrepancies vs Var61% and then vs Var57%.


Figure 20: Fitted line plot of the VAR19%Discr1 vs Var61% [%] (Staff Cost=100at 2000)

Figure 21: Fitted line plot of the VAR19%Discr2 vs Var57% [%] (Staff Cost=100at 2000)

The combination of the previous three laws is suitable to provide the cumulated value of Var19% referring to the used variables (Var19, Var61 and Var57), so its law is:

$$\text{Var19\%} = 3,657 * \text{Var03} + 8,328 * \text{Var61\%} - 0,1902 * \text{VAR57\%} - 7739,5 \pm 3,69 (1\sigma)$$

The figure below shows the forecast from December 31st, 2008 up to December 1st 2016 performed with the model using the available information of this last period. The cyan solid line shows the forecasted values ascribing the known values to Var61% (GDP [%]) and Var57% (Total Staff [%]). While, the dashed curve and dot one, also cyan, shows the forecast in case the known Var61% and Var57% are affected by an error assumed equal to $\pm 5\%$ at December 1st, 2016 and 0% at January 1st, 2008 where the value is known.


Figure 22: Comparison forecast vs Var19% Values (Staff Cost=100 at 2000)

The previous calculation approach assumes that if eligible and reliable data sources exist, they may be taken into account or preferred to perform different independent estimations. In other words, it is possible to perform a sensitivity analysis vs data source.

Note: The lower limit (light brown) and the upper limit (brown) are respectively associated to dashed curve (-5%) and point curve (5%).

CONCLUSIONS

Aim of this paper is to support decisions on cost efficiency increase, using an analytical tool based on statistics, independent on the specific domain expertise, as the model driver is the covariance of parameters. The defined empirical model type has been adopted to preserve a strong link with the available public information. Such methodology provides estimated cost values in fast and slender way referring to any subset of elements in the operations framework.

The level of detail of the input data, in terms of granularity and quantity, is a necessary starting point to evaluate the impact associated to an implemented research innovation or a new technology.

It can also be an alternative and useful tool to perform forecasts with known accuracy.

It is possible to extend the model with further details and increase the robustness with upgraded database including different airlines and type of operators (e.g. Low cost airline).

The system will be verified in realistic conditions (taking into account change implementations, time dependency of choice consequences,..) with different input data, in terms of time reference and possibly by different airlines. Another future activity will be the validation of the framework. It will be performed by a twofold approach:

1. due to the interaction with an airline, who will be in charge of providing the most relevant parameters to work on to increase cost efficiency.
2. analyzing the measured cost values and identifying the covariance of the related parameters.

REFERENCES

- [1] Lufthansa Annual Report 2000; File "LH-AR-2000-e.pdf".
- [2] Lufthansa Annual Report 2001; File "LH-AR-2001-e.pdf".
- [3] Lufthansa Annual Report 2002; File "LH-AR-2002-e.pdf".
- [4] Lufthansa Annual Report 2003; File "LH-AR-2003-e.pdf".
- [5] Lufthansa Annual Report 2004; File "LH-AR-2004-e.pdf".
- [6] Lufthansa Annual Report 2005; File "LH-AR-2005-e.pdf".
- [7] Lufthansa Annual Report 2006; File "LH-AR-2006-e.pdf".
- [8] Lufthansa Annual Report 2007; File "LH-AR-2007-e.pdf".
- [9] Lufthansa Annual Report 2008; File "LH-AR-2008-e.pdf".
- [10] Lufthansa Annual Report 2009; File "LH-AR-2009-e.pdf".
- [11] Lufthansa Annual Report 2010; File "LH-AR-2010-e.pdf".
- [12] Lufthansa Annual Report 2011; File "LH-AR-2011-e.pdf".
- [13] Lufthansa Annual Report 2012; File "LH-AR-2012-e.pdf".
- [14] Lufthansa Annual Report 2013; File "LH-AR-2013-e.pdf".
- [15] Lufthansa Annual Report 2014; File "LH-AR-2014-e.pdf".
- [16] Lufthansa Annual Report 2015; File "LH-AR-2015-e.pdf".
- [17] Lufthansa Annual Report 2016; File "LH-AR-2016-e.pdf".
- [18] Lufthansa Monthly Report 01/2000; File "LH-Investor-Info-2000-01-e.pdf".
- [19] Lufthansa Monthly Report 02/2000; File "LH-Investor-Info-2000-02-e.pdf".
- [20] Lufthansa Monthly Report 03/2000; File "LH-Investor-Info-2000-03-e.pdf".
- [21] Lufthansa Monthly Report 04/2000; File "LH-Investor-Info-2000-04-e.pdf".
- [22] Lufthansa Monthly Report 05/2000; File "LH-Investor-Info-2000-05-e.pdf".
- [23] Lufthansa Monthly Report 06/2000; File "LH-Investor-Info-2000-06-e.pdf".
- [24] Lufthansa Monthly Report 07/2000; File "LH-Investor-Info-2000-07-e.pdf".
- [25] Lufthansa Monthly Report 08/2000; File "LH-Investor-Info-2000-08-e.pdf".
- [26] Lufthansa Monthly Report 09/2000; File "LH-Investor-Info-2000-09-e.pdf".
- [27] Lufthansa Monthly Report 10/2000; File "LH-Investor-Info-2000-10-e.pdf".
- [28] Lufthansa Monthly Report 11/2000; File "LH-Investor-Info-2000-11-e.pdf".

- [29] Lufthansa Monthly Report 12/2000; File "LH-Investor-Info-2000-12-e.pdf"
- [30] Lufthansa Monthly Report 01/2016; File "LH-Investor-Info-2016-01-e.pdf"
- [31] Lufthansa Monthly Report 02/2016; File "LH-Investor-Info-2016-02-e.pdf"
- [32] Lufthansa Monthly Report 03/2016; File "LH-Investor-Info-2016-03-e.pdf"
- [33] Lufthansa Monthly Report 04/2016; File "LH-Investor-Info-2016-04-e.pdf"
- [34] Lufthansa Monthly Report 05/2016; File "LH-Investor-Info-2016-05-e.pdf"
- [35] Lufthansa Monthly Report 06/2016; File "LH-Investor-Info-2016-06-e.pdf"
- [36] Lufthansa Monthly Report 07/2016; File "LH-Investor-Info-2016-07-e.pdf"
- [37] Lufthansa Monthly Report 08/2016; File "LH-Investor-Info-2016-08-e.pdf"
- [38] Lufthansa Monthly Report 09/2016; File "LH-Investor-Info-2016-09-e.pdf"
- [39] Lufthansa Monthly Report 10/2016; File "LH-Investor-Info-2016-10-e.pdf"
- [40] Lufthansa Monthly Report 11/2016; File "LH-Investor-Info-2016-11-e.pdf"
- [41] Lufthansa Monthly Report 12/2016; File "LH-Investor-Info-2016-12-e.pdf"
- [42] Lufthansa, "LH_Timetable_en_2017.pdf", Nonstop you Timetable, 26 Mar 17 – 28 Oct 7.
- [43] LH-Investor-Info-2016-03-e
- [44] European Commission, "Flightpath 2050 Europe's Vision for Aviation" - Report of the High Level Group EUR 098 EN, ISBN 978-92-79-19724-6, European Union, 2011
- [45] M.J. Kiemele, S.R. Schmidt, R.J. Berdine; 02/01/00;"6.6 Analysis of Variance (ANOVA)"; Editor AIR ACADEMY PRESS & ASSOCIATES, LLC; "BASIC STATISTICS Tools for continuous improvement"; *Fourth Edition; Colorado Springs CO 80920 USA; pp. 6.32 – 6.38.*
- [46] Minitab Support Web Site; 2017; "Understanding sums of squares"; <http://support.minitab.com/en-us/minitab/17/topic-library/modeling-statistics/anova/basics/what-is-a-general-linear-model/>.
- [47] R. Doganis; 2010; "Flying Off Course: Airline Economics and Marketing"; *Fourth Edition. Routledge, London*
- [48] G. Assaf, A. Josiassen; 2012; "European vs. US airlines: performance comparison in a dynamic market"; *Tourism Management. 33, 317-326*
- [49] C. Barbot, A. Costa, E. Sochirca; 2008; "Airlines performance in the new market context: A comparative productivity and efficiency analysis"; *Journal of Air Transport Management. 14, 270– 274*
- [50] A. Heshmati, J. Kim; 2016; "Efficiency and Competitiveness of International Airlines"; *DOI 10.1007/978-981-10-1017-0_2 © Springer Science+Business Media Singapore*
- [51] Rogéria de Arantes Gomes Eller, M. Moreira; 2016; "The main cost-related factors in airlines management"; *Journal of Transport Literature Vol.8, n.1, pp.8-23, Jan. 2014 Research Directory*
- [52] M. Duygun, D. Prior, M. Shaban, TA Emili; 2015; "Disentangling the European airlines efficiency puzzle: a network data envelopment analysis approach"; *Working paper Castellon, 2014/04*

Model-Based Fault Identification of Fighter Aircraft's Environmental Control System

Leo Mäkelä

*Tampere University of Technology
Laboratory of Mechanical Engineering and Industrial Systems
P.O.Box 589, FI-33101 Tampere, Finland
leo.makela@tut.fi*

Jussi Aaltonen

*Tampere University of Technology
Laboratory of Mechanical Engineering and Industrial Systems*

Kari T. Koskinen

*Tampere University of Technology
Laboratory of Mechanical Engineering and Industrial Systems*

Kari Mäentausta

The Finnish Defence Forces Logistics Command

ABSTRACT

The Environmental Control System (ECS) maintains conditions suitable for a crew inside aircrafts cabin. ECS controls temperature, pressurizes cabin, provides breathing air and removes excess air humidity. All ECS functionalities have great impact on pilots' safety, performance and comfort. Furthermore, aircrafts mission capability is largely dependent on ECS.

Since ECS working principle is relatively complex, fault detection or fault identification can be very challenging. Most common failures are relatively easy to identify and trace to a specific component. Challenges however arise from complex interactions inside ECS, where single valve or sensor can affect to a whole system and cause undesirable and unknown phenomena. To better understand these complex interactions, comprehensive calculations or simulations are needed. When considering the complexity of ECS, computer modeling turns out to more suitable option than conducting multiple complex calculations.

Objective of this project was to improve fault identification process with semi-empirical model of the specific military fighter jet. Moreover, aim was to acquire more profound knowledge of the system and its characteristics. Modeling provided new way of studying ECS system, its flaws and potential failures. Model was created to answer questions that could not be tested on a test bench or on ground-tests. Basically, modeling enabled possibility to virtually test multiple different scenarios and their probability. Project resulted partially verified AMESim model of the ECS, which can be considered valid in most of the common flight situations. ECS-model helped to narrow down possible causes of undesirable behaviour that was known to occur in specific flight situation. ECS-model basically clarified the underlying phenomena leading to these undesired events.

In future, model's reliability and accuracy will be enhanced with new comprehensive measurements. Model will also be transformed to simplified version which can be used to train new maintenance engineers.

KEYWORDS: *Environmental control system, ECS, fighter, jet*

1 INTRODUCTION

Fighter aircraft's environmental control system (ECS) have a major impact on pilot safety and aircraft mission capability. ECS maintains conditions suitable for crew inside aircrafts cabin by pressurizing cabin, regulating temperature and providing breathing air. ECS can also be used for: avionic cooling,

defog, anti-ice, muscle pressure, anti-G, reservoir pressurization and gun gas purge. Without fully functional and robust ECS, aircraft is unable to function properly and carry out missions safely. All of the ECS' functionalities are essential for aircraft's airworthiness, which addresses the importance of maintenance, fault isolation and fault identification.

Most of ECS' include only minimal amount of sensors monitoring it's operation during flight. Therefore aircraft ECS failure modes can usually be tested only on the ground. In most of the cases aircrafts failure modes can be identified and solved during ground testing. But, some of the problems only occur during flight, even if the aircraft has passed ground testing. In addition, ECS working characteristics change drastically during flight when compared to ground operation. Without additional tools such as computer modeling, troubleshooting of flight situations is beyond challenging. Simulations provide new information which otherwise could not be collected.

In this project, a semi-empirical simulation model was constructed in order to aid the fault identification process of fighter jet's ECS. Model was also designed for testing of multiple theories, regarding the causes of specific failure modes. Model is designed to work on both dynamic and steady-state simulations. Almost entire ECS needed to be modelled so that complicated interactions could be studied. Ultimately, the goals were to study ECS' dynamic response in multiple flight situations, estimate how well ECS performs in aircrafts flight envelope and how ECS reacts to different component failures.

2 ECS SYSTEM DESCRIPTION

Fig. 1 presents the simplified process diagram of the ECS. Hot air is bled from two jet engines and cooled down with reversed Brayton cycle. Some of the bleed air bypasses cooling cycle and is then utilized to control cabin supply air temperature as well as avionic cooling temperature. System uses air-to-air heat exchangers for cooling. Excessive humidity is extracted in high pressure water extractor and condensed water augments cooling in secondary heat exchanger.

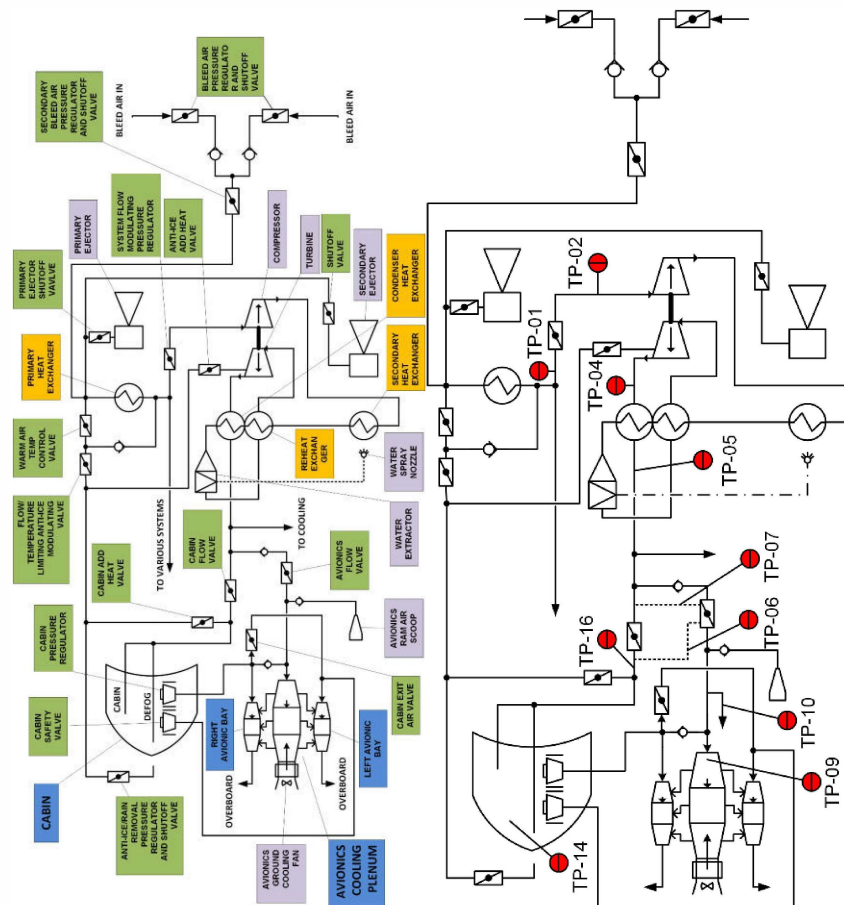


Figure 1: Simplified schematic of the complete ECS (left) and test port locations (right)
[1]

The ECS controls mass flow, temperature and pressure in both cabin and avionic bays. Supply air mass flow amount and temperature changes according to altitude and flight speed. One fully mechanical valve controls the cabin pressure by regulating the mass flow amount that flows overboard. Avionic bays are not pressurized hence pressure is near ambient.

3 STATE OF THE ART IN ENVIRONMENTAL CONTROL SYSTEM MODELLING

Modeling ECS and its complicated dynamic behavior is not unprecedented. Probably one of the first was Eichler (1975), who modelled whole ECS and studied its dynamic response [1]. Eichler already used multiple simplified models of controllers, sensors, valves and turbines. Since Eichler's study, computer modeling has evolved along with increasing computing power. Later studies have used modeling dynamic response from multiple slightly different standpoints. Tu and Lin (2010) modelled ECS using Flowmaster software and studied the thermal dynamic response of the ECS [2]. Tu and Lin (2011) further developed their simulation model and used it to improve ECS' control system [3]. Yin et al. (2016) used a simplified model of the ECS to study dynamic response, coupled with CFD based cabin thermal model [4]. Their study showed interaction between ECS operation and cabin thermal conditions.

Because of unpredictable and complicated behavior of ECS, many studies have gravitated more towards hardware-in-the-loop approach. If only computer based models are used, things like ice formation and two-phase flow are very hard to take into consideration and may ultimately lead to misleading results. To minimize the effect of unpredictable phenomena, Childs et al. (2015) used hardware-in-the-loop method and constructed full scale experimental and simulation tool for control system optimization and fault detection [5]. Childs et al. (2016) later used testing facility to investigate multiple failure modes and their effects [6]. Similar fashion Ashford (2004) utilized hardware-in-the-loop approach to study the f-22 raptors ECS responses and developed ECS' controlling software further [7].

Unlike Childs et al. (2016) and Ashford (2004), this study relies only on semi-empirical computer modeling. However, model validity is tested against multiple measurements conducted with physical aircraft. Hardware-in-the-loop method is simply troublesome to implement when flight at high altitude is one of the interests.

4 MODELLING THE ENVIRONMENTAL CONTROL SYSTEM

Semi-empirical model of ECS was established using LMS Imagine.Lab Amesim rev. 13. Amesim enables to model, simulate and analyze multi-domain systems. It has a wide range of component libraries that can be used to model ECS. Final model consists of Amesims standard library parts [9].

Parameters had to be resolved using real-life measurements. Component parameters were resolved by using a wide variety of measurements. Components' sizes and shapes were measured to match the Amesim submodel requirements. Some of the measurements were conducted by the manufacturer of the aircraft during its development e.g. ram air flow, heat exchangers' cooling effectiveness, compressor and turbine characteristic curves.

Model's validity in steady state situations, was tested by comparing simulation and ground test results. During a ground test, pressures inside ECS can be measured from 10 different test ports and temperatures from 4 points (cabin, avionics, louver and primary heat exchanger). Neither the pressure nor the temperature sensors can detect transient changes.

Model's accuracy in dynamic situations was studied against measurements. Aircraft was flown in many flight situations while data logger (MSR Electronics GmbH, model 145) recorded temperatures and pressures inside the cabin. Also, aircraft's flight recorder data was collected and then used as an input to the simulation model. Measurements in cabin were then compared to simulated results. Model of the ECS control system was altered in iterative process till results were comparable.

5 STEADY STATE SIMULATIONS AND RESULTS

In Table 1–4 model's steady state accuracy is presented. Both measurement and simulation data represent pressures during ground testing. Simulation results are compared to measurements in four different throttle settings (high throttle, medium throttle, idle and manual-mode). Test port locations are shown in Fig. 1.

Table 1: Comparison of simulation results with measurements in high throttle

<i>Test port</i>	<i>Measurement [barA]</i>	<i>Simulation result [barA]</i>	<i>Error [barA]</i>
TP-01	9.388	9.358	0.030
TP-02	2.631	2.658	0.026
TP-04	1.185	1.347	0.162
TP-05	1.177	1.147	0.030
TP-06	1.102	1.079	0.023
TP-07	1.165	1.142	0.023
TP-09	1.066	1.000	0.067
TP-10	1.001	1.013	0.012
TP-14	1.036	1.015	0.021
TP-16	1.104	1.079	0.025

Table 2: Comparison of simulation results with measurements in medium throttle

<i>Test port</i>	<i>Measurement [barA]</i>	<i>Simulation result [barA]</i>	<i>Error [barA]</i>
TP-01	6.356	6.317	0.040
TP-02	2.702	2.647	0.055
TP-04	1.149	1.359	0.210
TP-05	1.142	1.153	0.012
TP-06	1.049	1.085	0.036
TP-07	1.130	1.149	0.019
TP-09	1.045	1.001	0.044
TP-10	1.000	1.013	0.013
TP-14	1.041	1.020	0.020
TP-16	1.056	1.086	0.030

Table 3: Comparison of simulation results with measurements in idle

<i>Test port</i>	<i>Measurement [barA]</i>	<i>Simulation result [barA]</i>	<i>Error [barA]</i>
TP-01	2.013	2.029	0.016
TP-02	2.082	2.022	0.060
TP-04	1.140	1.258	0.118
TP-05	1.138	1.152	0.014
TP-06	1.076	1.088	0.012
TP-07	1.132	1.151	0.019
TP-09	1.066	1.001	0.065
TP-10	1.031	0.988	0.044
TP-14	0.993	1.022	0.030
TP-16	1.080	1.088	0.007

Table 4: Comparison of simulation results with measurements in manual-mode

<i>Test port</i>	<i>Measurement [barA]</i>	<i>Simulation result [barA]</i>	<i>Error [barA]</i>
TP-01	4.425	4.381	0.044
TP-02	4.494	4.331	0.163
TP-04	1.390	1.720	0.330
TP-05	1.383	1.329	0.054
TP-06	1.082	1.147	0.065
TP-07	1.342	1.315	0.028
TP-09	1.272	1.025	0.247
TP-10	1.032	1.059	0.027
TP-14	0.995	1.052	0.057
TP-16	1.100	1.147	0.047

Model is accurate in all ground test cases. The only notable problem occurs in TP-04 pressures which are greater than experimental results suggest. Two different things may cause pressure rise in simulated results. Either condenser heat exchanger gives too high flow resistance and causes pressure rise upstream, or simulated control system mixes too much warm air to the turbine downstream and causes pressure rise. Also, both sources of error may occur simultaneously. More measurements are needed to increase accuracy.

6 DYNAMIC SIMULATIONS AND RESULTS

Model's accuracy in dynamic simulation is shown in Fig. 2. The aircraft was flown at 45,000 feet altitude while throttle was altered rapidly to cause prominent pressure fluctuation. Simulation results represent measurements well. However, model only works at this specific altitude. If flight altitude changes more than 3,000 feet, measurements and simulation results start to differ. Control system's parameters must be tuned to different altitudes so that measurements and simulations are equivalent. Also, regardless of the flight altitude, computer model reacts to changing throttle position slower than the real system.

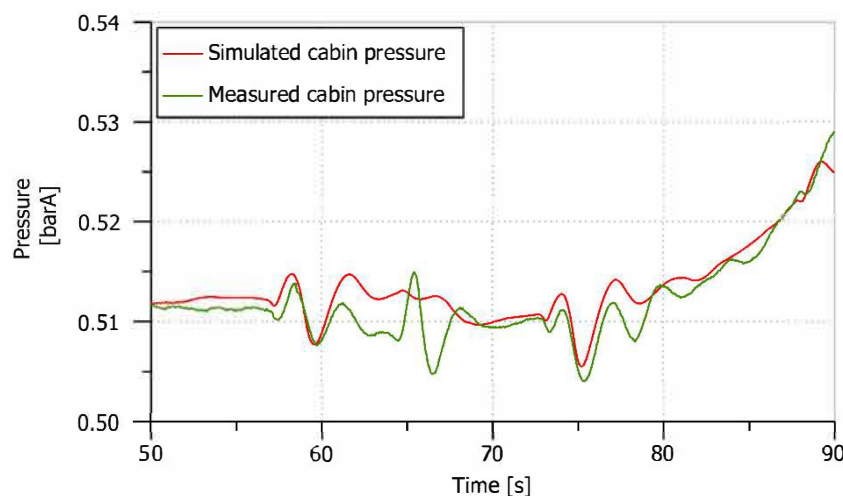


Figure 2: Cabin pressure at 45,000 feet altitude during rapid throttle alternation

In dynamic simulation shown in Fig. 2, simulated control system had to react on a distinctive way so that results matched with empirical measurements. In other words, valves must react in a specific order and speed. Otherwise, pressure curve will not form its characteristic shape. So, it can be concluded with high confidence that simulation represents reality very well. Therefore, highly tuned simulation model gave knowledge of how exactly control system reacts and how valves must be moving. Knowledge of the valve interactions may turn out to be important, especially if aircraft suffers from cabin pressure fluctuation.

As the dynamic simulations gave promising results, model was also used for predicting the outcome of a component failure. One concern was the effect of a cabin exit air valves (shown in Fig. 1) and its effect on cabin pressure at 45,000 feet altitude. Cabin exit air valve was controlled from closed position to fully open position and back to fully closed position. Then valve's effect to cabin pressure was studied (Fig. 3). Simulation results suggest that cabin exit air valve cannot solely cause severe failure, since pressure change is very small. Cabin exit air valve did not cause significant change to mass flows either.

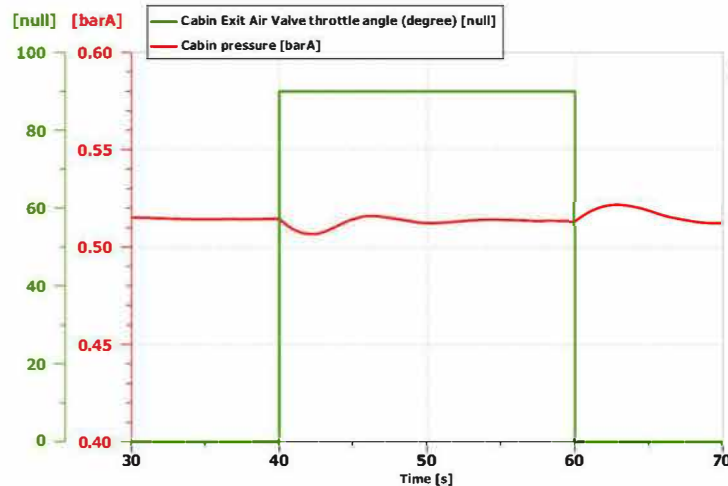


Figure 3: Cabin exit air valves effect to cabin pressure at 45,000 feet altitude.

Steady state accuracy during a flight is yet uncertain, since ground testing does not necessarily represent more complicated flight situations. Dynamic simulations gave promising results, though model had to be tuned to specific altitude and universally valid model could not be accomplished. Nonetheless, dynamic simulation accuracy enabled the ability to test and predict effect of a certain failures.

More empirical measurements are needed to further increase model credibility. Transient pressure and temperature changes must be measured inside the system during ground testing and flight. Only then the model's validity in multiple flight situations can be estimated with confidence. ECS valve interactions are simply too complicated to simulate with existing knowledge.

7 CONCLUSION

In this study model of an aircraft ECS was constructed using LMS Imagine.Lab Amesim rev. 13. Model's accuracy was verified against measurements of ground testing in steady state situation. Furthermore, model validity was tested in dynamic flight situation by comparing measured and simulated data. Finally, model's capability to predict outcomes of component failure was presented.

Steady state results were comparable with empirically measured data. The only significant difference occurred in test port TP-04. New measurements are needed to determine the clear cause of pressure difference in TP-04.

Results in dynamic flight situation were satisfactory and provided new knowledge of the ECS response characteristics. Simulation of dynamic response is valid only at one specific altitude at a time. More precise measurements inside the ECS are needed to increase model credibility.

Model ability to predict the outcome of cabin exit air valve failure was demonstrated in this study. It can be concluded that cabin exit air valve solely cannot cause severe pressure fluctuation or mass flow change in the cabin.

REFERENCES

1. J. Eichler; 1975; "Simulation Study of an Aircraft's Environmental Control System Dynamic Response"; *Journal of Aircraft* 12 (10): 757–58.
2. T. Yi, G.P. Lin; 2010; "Dynamic Simulation of Humid Air Environmental Control System"; 40th International Conference on Environmental Systems; 1–10. doi:10.2514/6.2010-6305.
3. T. Yi, G.P. Lin; 2011; "Dynamic Simulation of Aircraft Environmental Control System Based on Flowmaster"; *Journal of Aircraft* 48 (6): 2031–41.
4. H. Yin, X. Shen, Y. Huang, Z. Feng, Z. Long, R. Duan, C. H. Lin, D. Wei, B. Sasanapuri, Q. Chen; 2016; "Modeling Dynamic Responses of Aircraft Environmental Control Systems by Coupling with Cabin Thermal Environment Simulations"; *Building Simulation* 9 (4): 459–68; doi:10.1007/s12273-016-0278-3.



5. T. Childs, A. Jones, R. Chen; 2015; "Development of a Full Scale Experimental and Simulation Tool for Environmental Control System Optimisation and Fault Detection"; 53rd AIAA Aerospace Sciences Meeting; no. January: 1–11; doi:10.2514/6.2015-1196
6. T. Childs, A. Jones, R. Chen, A. Murray; 2016; "Evaluating Environmental Control System Thermal Response to Degraded Operating Conditions"; 54th AIAA Aerospace Sciences Meeting; no. January: 0–16. doi:10.2514/6.2016-1151.
7. R. Ashford; 2004; "Verification and Validation of the F/A-22 Raptor Environmental Control System/thermal Management System Software"; SAE Technical Papers; no. 724; doi:10.4271/2004-01-2573.
8. L. Makela; 2016; "Model-Based Fault Diagnosis of an Aircraft Environmental Control System"
9. LMS Amesim Libraries - <https://www.plm.automation.siemens.com/en/products/lms/imagine-lab/amesim/libraries/index.shtml>

Comparison Between Numerical Results and Operative Environment Data on Neural Network for Air Data Estimation

*Angelo Lerro
AeroSmart s.r.l.
Via Niccolini, 22-24 - Caserta (ITALY)
angelo.lerro@aerosmartsrl.it*

*Manuela Battipede ^a, Piero Gili ^b, Alberto Brandl ^c
Politecnico di Torino
Corso Duca degli Abruzzi, 24 – Torino (ITALY)
^a manuela.battipede@polito.it, ^b piero.gili@polito.it, ^c alberto.brandl@polito.it*

ABSTRACT

Several architectures exist to measure aerodynamic angles based on physical sensors. As far as Unmanned Aerial Vehicle (UAV) is concerned, traditional systems hardly comply with reliability and redundancy requirements due to size and weight limitations. A patented virtual sensor, based on Neural Network (NN) techniques, named Smart-ADAHRS (Smart-Air Data, Attitude and Heading Reference System) has been investigated as a good estimator for aerodynamic angles in simulated environment. This paper focuses on flight testing procedures in operative environment and data processing for the Smart-ADAHRS validation with real data. As many factors interfere during the generation of the NN training set, an accurate choice and integration of the FTI (Flight Test Instrumentation) system components becomes crucial. A comprehensive description has been included about the FTI equipment and its influence on the neural network performance. Differences between numerical simulation and operative environment data are detailed as final aim of this work. Finally, feasible solutions are suggested to solve the typical gap between virtual and real scenario, both in terms of data analysis and neural network architecture.

KEYWORDS: *aerodynamic angles, flight test, neural network, operative environment comparison, virtual sensor.*

Airframe - On Board System - Propulsion System Optimization for Civil Transport Aircraft: AGILE EU project

*Prajwal Shiva Prakasha, Pier Davide Ciampa
Research Scientist, German Aerospace Center
Blohmstrasse 20 21079 Hamburg
prajwal.prakasha@dlr.de*

*Luca Boggero, Marco Fioriti
Researcher, DIMEAS, Politecnico di Torino
C.so Duca degli Abruzzi 24, Torino 10129*

*Benedikt Aigner
Research Assistant, ILR, RWTH Aachen University
Wuellerstrasse 7, 52062 Aachen*

*Artur Mirzoyan, Alik Isyanov
Propulsion Department, CIAM
2, Aviamotornays Str., Moscow, 111116*

*Kirill Anisimov, Andrey Savelyev
Research Scientist, Propulsion Systems Aero Dept, TsAGI
1, Zhukovskiy, Moscow Oblast*

ABSTRACT

As part of H2020 EU project "AGILE", a Collaborative System of Systems Multidisciplinary Design Optimization research approach is presented in this paper. An approach to integrate airframe design analysis, as well as propulsion system, aircraft on-board systems, aerodynamics, structures and emission analysis in the early design process is presented. Moreover, the aim of this approach is to exploit the coupling parameters in an integrated analysis and optimization approach. Further, the disciplinary analysis modules from multiple organizations involved in the optimization are integrated within a distributed framework. The disciplinary analysis tools are not shared, but only the data is shared between partners through a secured network of framework. The collaborative design process is implemented by making use of XML based standard Common Parametric Aircraft Configuration Scheme (CPACS), which is the basis for communication within distributed framework to exchange model information between the multi-disciplinary analysis modules and between partner organizations involved in the research activity. The framework is validated with a regional jet passenger reference aircraft. The Sensitivity of varying Engine By Pass Ratio, On-Board System Architectures (Conventional/More Electric/All Electric) is performed through disciplinary modules, effects propagated and its impact on overall aircraft performance in terms of Fuel Burn, Emission and Life Cycle Cost is presented.

KEYWORDS: *Aircraft Design, Multi-Disciplinary, AGILE, CPACS, Optimization*

Uncertainty quantification and robust design optimization applied to aircraft propulsion systems

Marco Panzeri

Noesis Solutions

Research Engineer

Gaston Geenslaan, 11 Leuven - Belgium

marco.panzeri@noesisolutions.com

Andrey Savelyev

Central Aerohydrodynamic Institute (TsAGI)

Researcher

140180, Zhukovsky, Moscow Region, Russian Federation

Kirill Anisimov

Central Aerohydrodynamic Institute (TsAGI)

Researcher

Roberto d'Ippolito

Noesis Solutions

Research and Innovation Manager

Artur Mirzoyan

Central Institute of Aviation Motors (CIAM)

Head of Research Group and Project

Moscow, Russian Federation

ABSTRACT

The standard way of formulating optimization problems applied to aircraft design is based on the assumption that the underlying system is deterministic, i.e., that the knowledge associated with the design variables and with the system dynamic is not characterized by uncertainty. However, in real conditions randomness impacts the formulation of the design process in multiple ways and the system outputs (i.e., the key performance indicators and the design constraints) are also affected by uncertainty. A system designed under deterministic assumptions may therefore have an unreliable behavior due to the fluctuations associated with the input random variables. This problem can be tackled by adopting a probabilistic approach and re-formulating the design optimization problem with an additional set of constraints associated with the robustness / reliability of the target system. This work addresses the problem of optimizing the geometry of a turbofan engine nacelle subject on reliability constraints. An advanced, machine-learning based framework is adopted in order to (a) investigate the system behavior through an adaptive design of experiments technique and (b) build accurate surrogate models of the system dynamics. These surrogate models are then employed to run a set of probabilistic studies at an affordable computational cost. The results of these investigations include (a) an extensive suite of analyses aimed at characterizing the uncertainty associated with the output quantities of interest; (b) a robust optimization of the engine nacelle geometry and (c) an assessment of the reliability of the optimized design. The improved performance and reliability of the design, together with the limited number of overall system evaluations required to run the analyses, demonstrate the effectiveness and the engineering applicability of the proposed approach.



Low Speed Take-Off Aerodynamic Analysis

D. Charbonnier & J.B. Vos

CFS Engineering

EPFL Innovation Park, Batiment A, 1015 Lausanne, Switzerland

P.S. Prakasha

German Aerospace Center (DLR),

Institute of System Architectures in Aeronautics, Hein-Sassweg 22, 21129 Hamburg, Germany

A. Mirzoyan

Central Institute of Aviation Motors (CIAM), Aviamotornays Str. 2, 111116 Moscow, Russia

A. Savelyev

Propulsion Systems Aero Department, TsAGI, Zhukovskiy 1, 140180 Moscow Oblast, Russia

P. Della Vecchia

Dept. of Industrial Engineering, University of Naples "Federico II", Via Claudio 21, 80125 Napoli, Italy

ABSTRACT

In the frame of the EU funded H2020 project AGILE (Aircraft 3rd Generation MDO for Innovative Collaboration of Heterogeneous Teams of Experts) detailed CFD simulations were made to analyze the high lift system of an optimized regional aircraft. The paper presents shortly how the different components of the aircraft were obtained and integrated in a model suitable to perform the simulations. High-fidelity RANS (Reynolds-Averaged Navier-Stokes) CFD calculations were carried out, with a focus on take-off conditions, and aerodynamic coefficients as well as flow field distributions were extracted. The results are discussed, and point out in one hand the reliability of high-fidelity CFD simulations to highlight detailed flow phenomena like flow separations, and in another hand the importance to consider low speed flow regimes (take-off or landing) in an aircraft design and optimization process.

KEYWORDS: MDO, CFD, High-Lift

1. INTRODUCTION

Aircraft multidisciplinary optimization is a highly complex process requiring the involvement of a large number of specialists from a wide range of disciplines. Each of these specialist use their own tools, and these tools often have different levels of fidelity (= representation of the physics involved).

Traditionally the aircraft design process is divided into 3 phases, the Conceptual, the Preliminary and the Detailed Design. In the Conceptual Design phase many variants need to be studied and a fast turn around time of the tools being used is important. This means that mainly low fidelity tools are used in this phase, having the risk that this leads to flaws in the design requiring costly redesign at later stages in the design process. Since the middle of 1990's efforts are underway to increase the fidelity of the tools being used in the Conceptual Design phase through the so called 'Virtual Product' that was defined as a 'high-fidelity mathematical/numerical representation of the physical properties and the functions of a product' [1, 2]. Critical to the success of the 'Virtual Product' is the capability for rapid generation of high-fidelity information from all disciplines involved, and the implementation of new multidisciplinary simulation and optimization environments [3].

Aircraft development programs are today organized as collaborative and multi-organizational processes. A major challenge hampering a cost effective design is the integration of multidisciplinary competences in the so called 'Virtual Enterprise'. The challenge becomes even larger when the required competences are provided by heterogeneous teams of specialists distributed in different organizations and across nations. This requires new Multi-disciplinary Design Optimization (MDO) methodologies using a standard approach and interface for communication between disciplinary modules.

The AGILE (Aircraft 3rd Generation MDO for Innovative Collaboration of Heterogeneous Teams of Experts) Horizon 2020 funded project is developing and implementing the next generation of aircraft MDO processes

targeting a reduction of 20% in time to converge the design of an aircraft and a 40% reduction in time needed to setup and solve the MDO problem using a team of heterogeneous specialists.

The AGILE project involves a team of 19 industry, research and academia partners from Europe, Canada and Russia. The AGILE project has formulated the so called 'AGILE Paradigm' [4] accelerating the deployment of collaborative, large scale design and optimization frameworks, and in particular (as shown in Fig. 1):

- Accelerating the setup and deployment of distributed, cross-organizational MDO processes
- Supporting the collaborative operation of design systems: integrating people and tools
- Exploiting the potential offered by the latest technologies in collaborative design and optimization

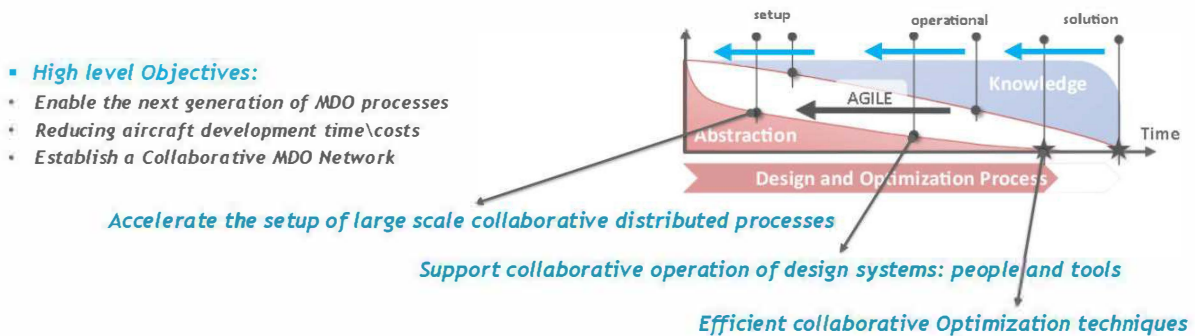


Figure 1: AGILE 3rd Generation Design and Optimization Processes.

The main elements of the AGILE Paradigm are the Knowledge Architecture (formalization of the product development process as a hierarchical structures process) and the Collaborative Architecture (enables cross-organizational and cross national integration of distributed design competences of the project partners) [4]. In AGILE the MDO activities are undertaken in 3 sequential work packages, targeting design cases with increasing level of complexity and addressing different aircraft configurations.

The work presented in this paper is concerned with the so-called Design Campaign-2 (DC-2) that was carried out in the 2nd year of the AGILE project [5]. The reference aircraft in this design campaign, coming from the DC-1 campaign, is a regional civil aircraft with the top level aircraft requirements summarized in Table 1 and the aircraft (before optimization) is shown in Fig. 2.

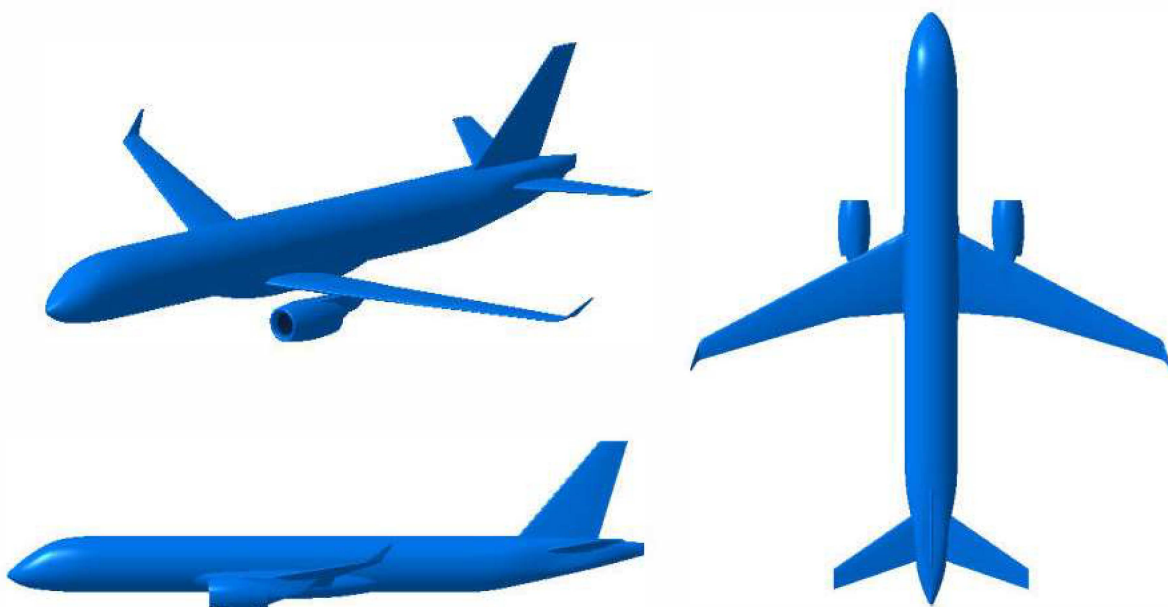


Figure 2: Starting point AGILE Design Campaign 2 aircraft.



Conventional Large Regional Jet Reference Aircraft (EIS: 2020)		
	<i>Metric</i>	<i>Imperial</i>
Range	3500 km	1890 nm
Design payload	9180 kg	20220 lbs
Max. payload	11500 kg	25330 lbs
PAX	90 pax @ 102 kg	90 pax @ 225 lbs
MLW (% MTOW)	90%	
Long Range Cruise Mach (LRC)	0.78	0.78
Initial Climb Altitude (ICA)	11000 m	36000 ft
Maximum Operating Altitude	12500 m	41000 ft
Residual climb rate	91 m/min	300 ft/min
TOFL (ISA, SL, MTOW)	1500 m	4921 ft
Vref (ISA, SL, MLW)	< 130 kts	
Max. operation speed (V_{mo} / M_{mo})	330 KCAS / 0.82	
Dive Mach number (M_d)	0.89	
Fuselage diameter	3 m	118 in
Fuselage length	34 m	111.5 ft
Service life	80,000 cycles	
Fuel reserves	5%	100 nm
A/C configuration	Low-wing, wing-mounted engines	
Engine	Provided (e.g.: PW1700G)	
Design objective	Minimize COC (alternatively, min. MTOW)	

Table 1: AGILE DC-2 Top Level Aircraft Requirements.

In DC-2 several different optimization studies were carried out by different teams. For example the Nacelle design was optimized using 18 different design variables [5]. The wing was optimized in DC-1 with preliminary high-lift device and medium fidelity aero-structure analysis helped to find the optimum configuration of the wing. This is the phase where a large design space is explored and reduced to one optimum which is DC2- aircraft [6]. The optimized wing and nacelle, together with the high-lift system were put together and a detailed high fidelity analysis was made studying the Take-off behaviour of the aircraft. The results of this study is presented in this paper. In section 2 the different components of the DC-2 aircraft used in this study are discussed. Section 3 discussed the grid generation and numerical set-up. Section 4 discussed the results obtained.

2. AGILE MULTI-DISCIPLINARY INTEGRATION

Figure 3 shows the Multi Disciplinary Optimization integration flow chart. The starting point are the Top Level Aircraft Requirements (TLAR) used in Design Campaign-2, see also Table 1, and further details can be found in [8].

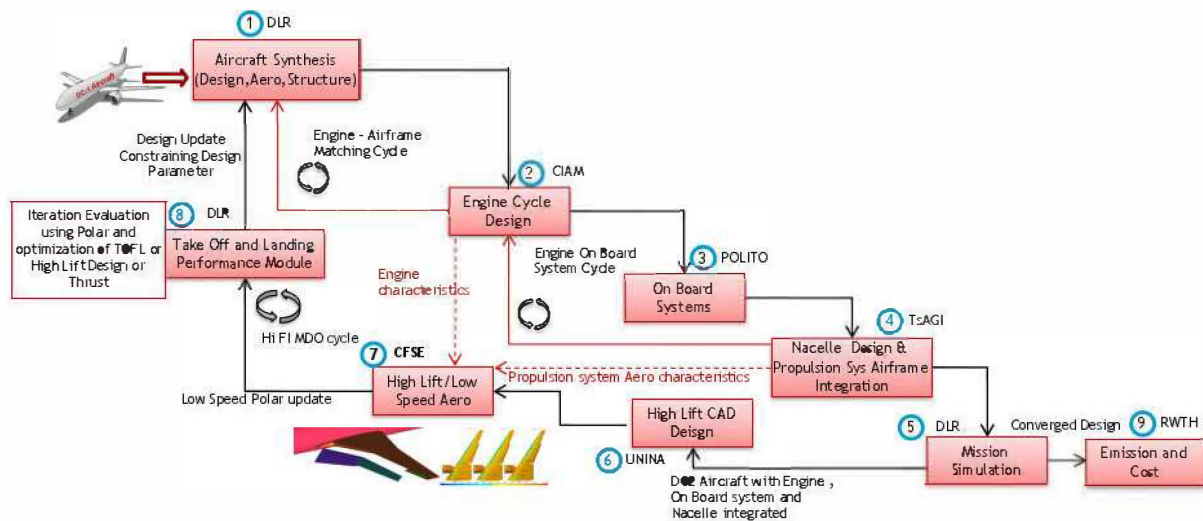


Figure 3: AGILE DC2 High Fidelity Multi-Disciplinary Optimization Integration Flowchart.

The MDO integration flowchart and AGILE partner involvement is as follows:

1. DLR : Initial synthesis based on requirements and Medium Fidelity Aero-Structure analysis is performed
2. CIAM: Based on Thrust requirements and Engine is designed through an iterative Engine-Airframe design matching cycle
3. POLITO: On Board System (OBS) is designed based on the TLAR, Cabin comfort and OBS architectural requirements (more electric or all electric or conventional) and weight and power offtakes are evaluated. Further OBS effect on Engine offtakes are considered in Engine-Onboard system cycle.
4. TsAGI: The Engine parameters are considered for nacelle design and integrated on the airframe. The propulsion system integration and aerodynamic optimization is performed at this point.
5. DLR: Mission simulation is performed with updated Weights, Aerodynamics and Engine performance, Fuel estimations are made. But these are based on High Fidelity cruise aerodynamic optimization. High fidelity low speed aerodynamics was desired for evaluating correct thrust and take off performance
6. UNINA: High Lift system design and CAD geometry generation to permit High Fidelity low speed aerodynamics evaluation
7. CFSE: Low speed aero performance was evaluated, and this is the focus of the current paper
8. DLR: Take Off and Landing Analysis will be performed using the updated Drag polars for the low speed regime and design optimization iteration with respect to High lift device, Engine Thrust (installed), Take off field length will be made. A tradeoff analysis.
DLR: Go back to step 1: and a second iteration for design optimization is started
9. RWTH: The converged design is evaluated for emission characteristics and life cycle cost. The fuel efficiency is the primary objective function, hence the cost and emission is not inside optimization loop.

Note : The focus of this paper is on Step 7. The results obtained from Step 7 will be used in steps 8,9 for optimization, as well as in steps 4 and 5 to re-investigate the nacelle position and the high-lift system design. Which will be updated and presented in a next publication.

3. MODEL SETUP

Several components of the DC2-aircraft (geometrical components or computational parameters) were taken from other sub-tasks of the AGILE project related to the creation of a 3D model suitable for high fidelity aerodynamic analysis, see also sections 3 and 4. These components are shortly discussed in the following subsections, namely:

- Nacelle design
- Engine deck
- High-lift devices

3.1. Nacelle design

TsAGI performed the aerodynamic optimization of the propulsion system of the DC-2 aircraft. This task included the optimization of the isolated nacelle, the nacelle positioning and the positioning of the pylon [9]. For the optimization, TsAGI used the engine deck provided by CIAM and the DC-2 airframe from DLR. The optimization was performed at cruise regime. As result TsAGI returned the geometry of nacelle and pylon, the drag and lift coefficients for the full configuration and for each of the elements separately.

The initial nacelle design used in the optimization was also provided by TsAGI. For the optimization all processes were integrated into one analysis workflow using the RCE environment [10], shown in Fig. 4a. The figure shows that the workflow consists of five tasks: CPACS [11] file reading, CPACS converting into internal formats, aerodynamic analysis, converting and writing a new CPACS file with the results. The aerodynamic analysis block includes geometry construction, meshing, CFD calculation and post-processing. For the CFD calculations, TsAGI uses the Electronic Wind Tunnel (EWT) in-house solver [12]. This aerodynamic analysis block is used for nacelle optimization procedure. When the isolated nacelle optimization is finished, the nacelle position optimization is started. During this part of the optimization the nacelle position is modified as shown in Fig. 4b. In a first phase, only the initial nacelle design and the installation angles are used for the wing optimization task.

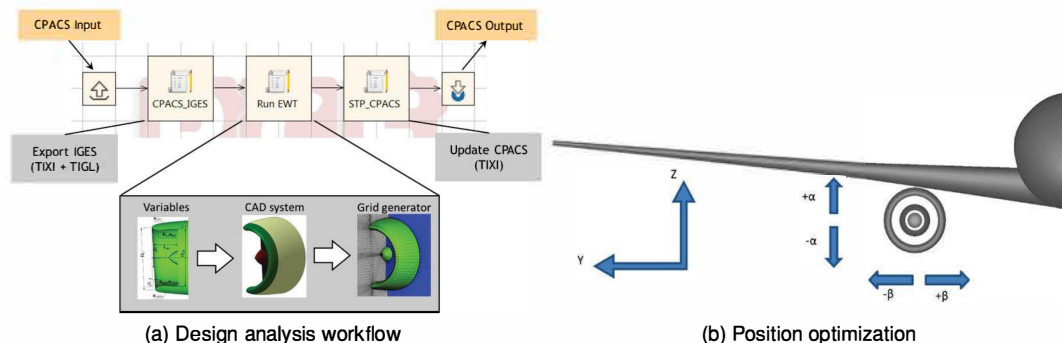


Figure 4: Nacelle design.

3.2. Engine deck

To generate the Engine Deck (ED), the commercial software tool GasTurb v12 for engine modeling was used by CIAM. This tool corresponds to an engine simulation using empirical methods of engine components (compressors, turbines, combustor, etc.), i.e. 'black boxes' without detailed (1D-3D) modeling. The GasTurb tool was used to evaluate the on-design and off-design engine parameters and the performance map. The engine component maps are presented in the engine tool using specific components maps. Engine model technology constraints and design rules are used in engine cycle design, off-design simulation and engine overall geometry and mass assessments. Technology constraints and design rules were applied to generate an ED consistent with the specified technology. More details about the engine simulation tool are given in [13, 14].

The following engine data were added to the CPACS file for their use in the Low speed aerodynamic CFD simulation: Engine installed thrust FN, fan inlet total pressure and temperature (station 2) Pt2 and Tt2, engine corrected mass flow rate (station 2) wDot2R, fan bypass exit total pressure and temperature (station 13)

Pt13 and Tt13, fan bypass exit mass flow rate (station 13) wDot13, core exit total pressure and temperature (station 5) Pt5 and Tt5, core exit mass flow rate (station 5) wDot5. The engine stations are shown in Fig. 5a.

All these engine data are calculated for Max TakeOff (MTO) flight conditions at Mach numbers M_{MTO} 0.20, 0.25 and 0.30. The M_{MTO} has a significant influence on the engine parameters as can be seen in Fig. 5b. For example, the Thrust FN is reduced by 25% when increasing M_{MTO} from 0 to 0.3, and the fan bypass exit massflow rate (wDot13) is increased by 11%.

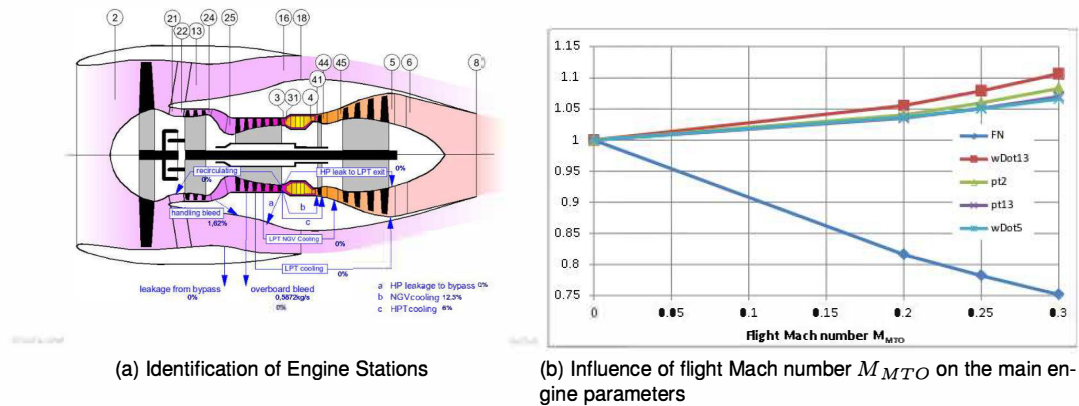


Figure 5: Engine deck.

3.3. High-Lift devices

The University of Naples (UNINA) has worked on the design of a high fidelity CAD model for the wing of the DC-2 aircraft including the high-lift movables. The flap design follows this procedure: starting from the optimized reference wing of the DC-2 aircraft, a semiempirical approach allows to choose the high-lift device type(slot, fowler, etc), the right chord extensions, span and deflections, to be compliant to top level aircraft requirements (see Table 1). Then an automated procedure allow to design the 3D geometry, cutting opportunely the wing, imposing the above computed parameters (see Fig. 6).

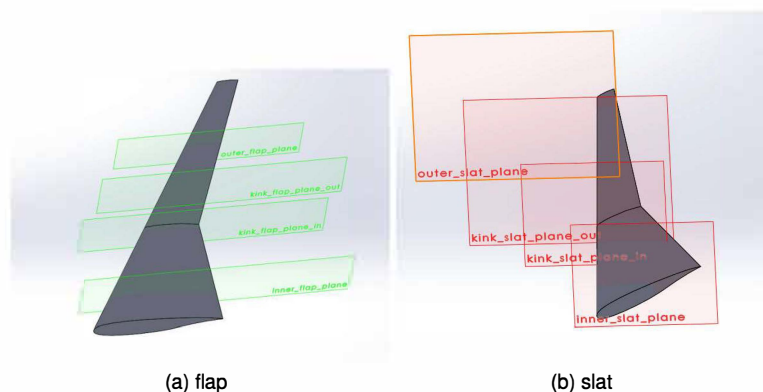


Figure 6: Cutting plane for high-lift device design on wing

A fowler flap and a leading edge slat have been chosen and designed at reference sections in a CAD environment, and then analysed and optimized one by one. A 2-dimensional aerodynamic analysis has been performed on two reference airfoils (one on the inner section and the other on the outer section), in order to define the better values for gap and overlap for both take-off and landing configurations. A genetic algorithm optimization procedure, performing on aerodynamic maps on both take-off and landing configurations (on an objective function which takes into account for C_{lmax} , $C_d@alpha=0$, C_{l0} and C_{lalpha}), leads to optimized multi-elements airfoil whose gap and overlap parameters have been employed to design the 3D CAD geometry. Based on 2D aerodynamic analyses and optimization, the 3D CAD (normal take-off, take-off and landind), including the optimized nacelle and pylon geometries provided by TsAGI, has been generated and provided

to partners.

In the present study, the high-lift components have been deflected for two flight configurations: landing and take-off, and exported in a CAD file suitable for mesh generation for CFD aerodynamic analysis. The design of the aircraft wing including the high-lift devices is shown in Fig. 7. For the landing configuration, the slat (both inner and outer) is deflected by 25° while the flap is deflected by 35° (Fig. 7b), and for the take-off configuration the slat and the flap are both deflected by 20° (Fig. 7c).

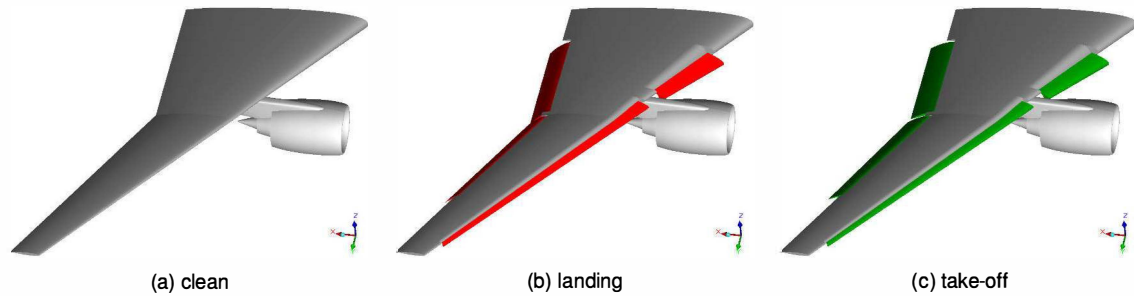


Figure 7: Wing configurations with or without deflected high-lift devices.

4. NUMERICAL SETUP

All the aircraft components from the different partners (DLR, UNINA, TsAGI, CIAM), described in section 3, were merged together in a 3D model suitable for the mesh generation process and high fidelity CFD aerodynamic simulations. The DC2-aircraft model is shown in Fig.8. The picture shows the input components with their formats (CPACS or CAD files) and the final 3D model after assembly. One can note that the pylon was removed on the final assembly. As a first approximation, in order to simplify the meshing process, it was decided to remove this part. However a small study was performed on a coarse grid, and the drag and lift coefficients were increased by 4% and 1% respectively for the case with the pylon.

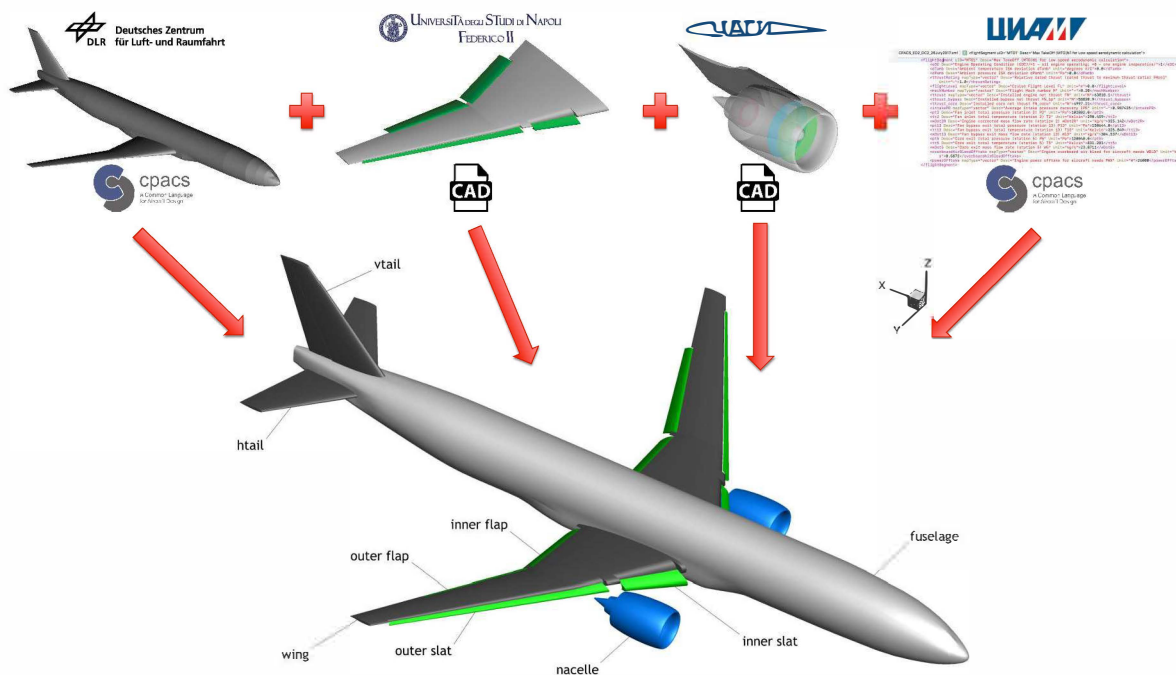


Figure 8: DC2-aircraft model for CFD aerodynamic analysis.

4.1. Grid generation

The ANSYS® ICEM CFD™ pre-processor tool was used to generate the multi-block structured grids needed by the Navier-Stokes Multi-Block flow solver NSMB. The grid topology was always generated for a half configuration, and a copy by mirror was applied for full configuration, if required for the case computed (rudder effect, one engine off effect,...) which was not the case in the analysis presented in this study, but in other tasks of the project. The grid was designed using the chimera method in order to simplify the mesh generation process and to generate quickly multiple configurations with different deflections of the control surfaces (high-lift devices on the wing as well as the rudder on the vertical tail), or to optimize the position of the nacelle. To resolve the viscous boundary layer an O-grid topology with a geometric cell distribution was used around the solid walls. The first cell height in the wall normal direction was set to obtain a y^+ value close to/below 1 to ensure the proper use of low-Reynolds turbulence modeling, and the growth ratio of the cells normal to the wall was typically close to 1.2.

The grid topology is made of 787 structured blocks, including 471 blocks for the main grid (fuselage, wing, horizontal tail and vertical tail), 229 blocks for the overlapping grid of the nacelle and finally 87 chimera blocks around the high-lift devices (inner slat, outer slat, inner flap and outer flap). In terms of number of cells, the grid for the half configuration comprises 23.3 Million cells, with respectively 17.9 Million, 3.3 Million and 2.1 Million for the airframe, the nacelle and the high-lift devices. Detailed views of the mesh are shown in Fig. 9. One can see the overlapping grids after blanking process on Fig. 9d and 9e, in blue for the nacelle and in green for the movable devices. Thanks to the chimera method, the displacement of the movables is straight-forward, without any remeshing process, as highlighted in Fig. 9e for two configurations at take-off conditions (fully or partially deployed).

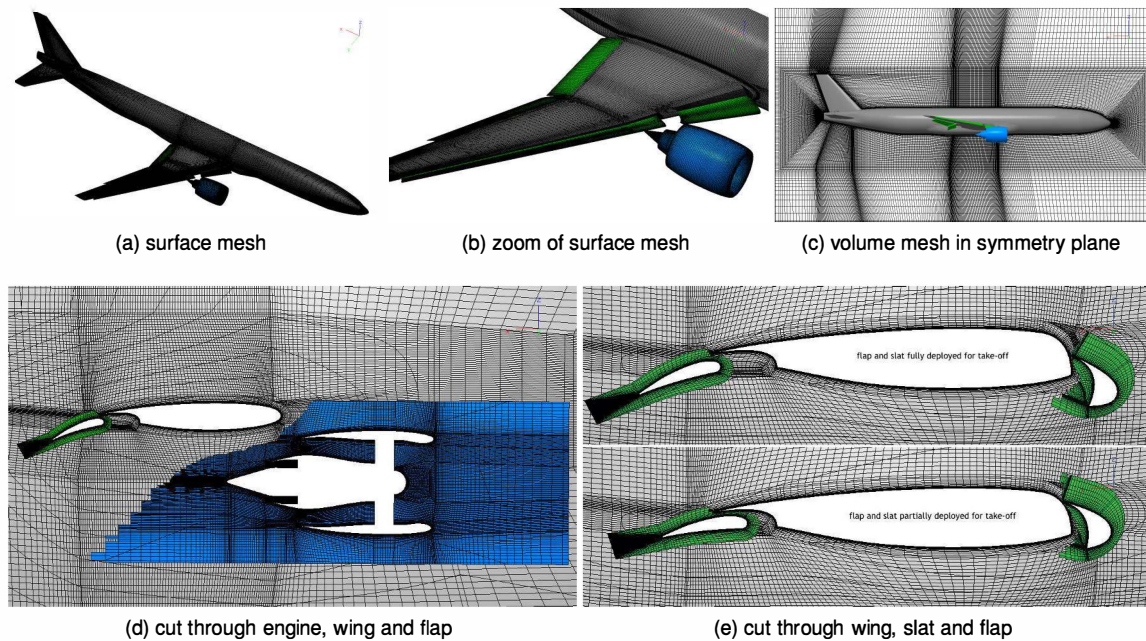


Figure 9: DC2-aircraft Chimera grid.

4.2. Computational setup

4.2.1. Computational code

All calculations were made using the NSMB solver. NSMB was initially developed in 1992 at the Swiss Federal Institute of Technology (EPFL) in Lausanne, and from 1993 onwards in the NSMB consortium composed of different universities, research establishments and industries. Today NSMB is developed by IMF-Toulouse (IMF Toulouse, France), ICUBE (Strasbourg, France), University of Munchen (TUM, Germany), University of the Army in Munchen (Germany), Airbus Safran (France), RUAG Aviation and CFS Engineering. A variety of papers have been published on NSMB, some examples are in [15–17]

NSMB is a CFD solver using the cell-centered finite volume method on multi block structured grids. To simplify the mesh generation for complex geometries NSMB uses the patch grid (also known as the sliding mesh) approach and the chimera method.

Space discretization schemes implemented in NSMB are the 2nd and 4th order central schemes with artificial dissipation and Roe and AUSM upwind schemes from 1st to 5th order. Time integration can be made using explicit Runge-Kutta schemes, or the semi-implicit LU-SGS scheme. Different methods have been implemented to accelerate the convergence to steady state, as for example local time stepping, multigrid and full multigrid, and low Mach number preconditioning. Unsteady simulations are made using the dual time stepping approach or using the 3rd order Runge Kutta scheme.

Turbulence is modelled using standard approaches as for example the algebraic Baldwin-Lomax model, the 1-equation Spalart model (and several of its variants) and the $k - \omega$ family of models (including the Wilcox and Menter Shear Stress models). Explicit Algebraic Reynolds Stress models and Reynolds Stress models have also been implemented, but are not used on a routine base. Transition to turbulence can be modelled by specifying transition lines or planes, or by solving the $\gamma - R_\theta$ transport equations [18]. For unsteady CFD simulations different Hybrid RANS-LES models are available.

4.2.2. Computational matrix

A first set of 15 calculations were made on the configuration with fully deployed high-lift devices (Fig. 9e top) varying the angle of attack and Mach number. Based on the results of these calculations, see Section 5 and additional 6 calculations were made on the configuration with partially deployed movables (Fig. 9e bottom). The entire computational matrix for these 21 calculations is given in Table 2. All the calculations were performed using the 2nd-order Roe upwind space discretization scheme and the LU-SGS time integration scheme. Local time stepping was employed to accelerate the convergence to steady state. A fully turbulent flow was assumed, and the turbulence was modelled using the $k - \omega$ Menter Shear Stress model. The engine

conditions, extracted from the Engine Deck (see section 3.2), were imposed at the boundary conditions of the nacelle, i.e. fan inlet, fan outlet and core outlet. The precise conditions are also given in Table 2.

Flight conditions		Flow conditions				Engine conditions						
configuration	high-lift devices	Mach	AoA	Alt	Re [m]	Turbulence model	Fan_in Pt	Fan_in Tt	Fan_out Pt	Fan_out Tt	Core_out Pt	Core_out Tt
take-off	fully deployed	0.2	5, 7, 9, 11, 13	0	4.66E+6	$k-\omega$ MSS	102882	290.46	150644	325.85	120040	831.28
		0.25			5.88E+6		104803	291.76	152941	326.92	120632	829.65
		0.3			6.99E+6		107120	293.34	155705	328.26	121157	827.68
	partially deployed	0.25	5, 9, 13	0	5.88E+6	$k-\omega$ MSS	104803	291.76	152941	326.92	120632	829.65
		0.3			6.99E+6		107120	293.34	155705	328.26	121157	827.68

Table 2: Computational matrix.

5. NUMERICAL RESULTS

Figure 10 shows the Mach number contours in a cutting plane through the engine. The case shown here is for the Mach number of 0.25 and the angle of attack 9° ; the behavior is similar for all other cases. The figure highlights the engine jet downstream of the nacelle and the good continuity of the flow through the chimera boundaries.

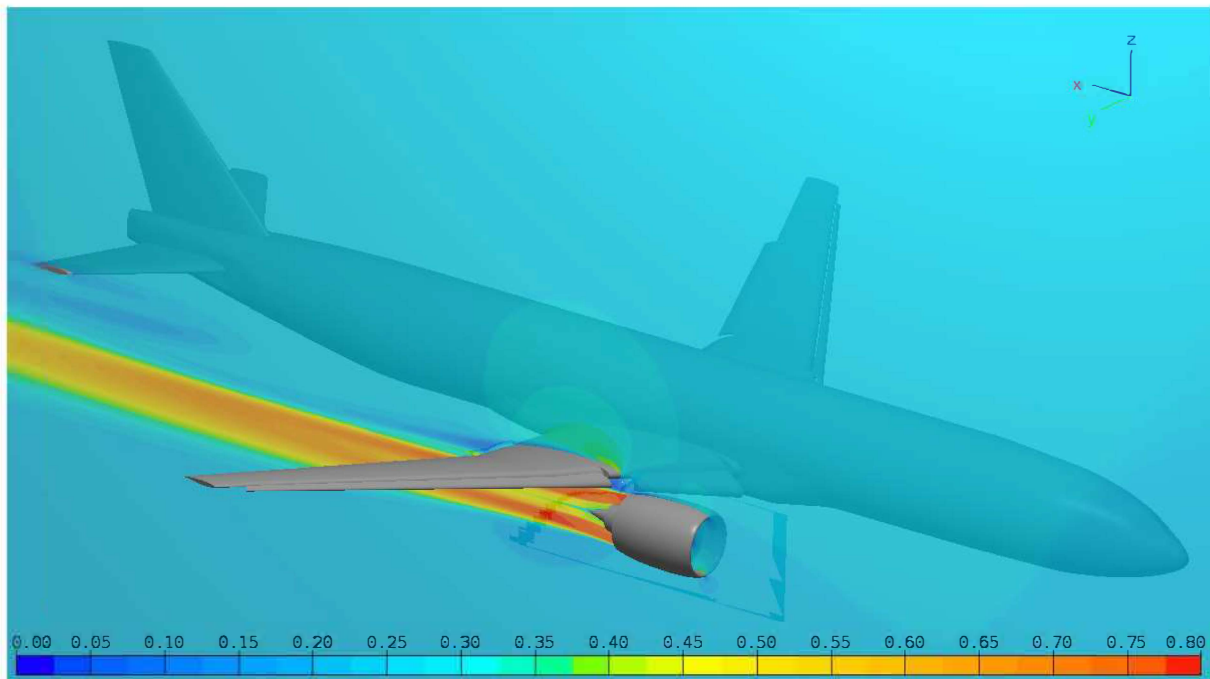


Figure 10: Mach number distribution in a cutting plane through the engine at Mach=0.25.

Table 3 summarizes the computed aerodynamic coefficients (drag coefficient C_D , lift coefficient C_L , pitching moment coefficient C_m), the aerodynamic forces (drag D , lift L) as well as the lift over drag ratio L/D of the 21 calculations. The aerodynamic coefficients were calculated using the reference length $C_{ref} = 3.541812$, the reference surface $S_{ref} = 75$ and the moment reduction centre $XYZ_{ref} = (15.6949, 0.0, 0.0)$ (with the origin at the nose of the aircraft). The results are for a half configuration aircraft, just as the thrust which concerns a single engine. These data are plotted on the curves in Fig. 11 as function of angle of attack, using different colors for different Mach numbers. The cases with fully deployed high-lift devices are depicted with solid lines, while the cases with the partially deployed movables are depicted with dashed lines. On Fig. 11e the engine thrust (depending on the Mach number considered) is also shown using dotted lines.

Figures 11a and 11b show what was to be expected, increasing the Mach number mostly influences the drag coefficient, leading to a lower C_D . This is mostly due to the fact that the dynamic pressure increases more rapidly with the Mach number than the drag force, see Fig. 11e. The lift coefficient shows that stall occurs between angles of attack between 11° and 13° for the fully deployed high lift system. No results at an angle of attack of 11° are available for the partially deployed high lift system. Deploying the high lift system only partially results in a considerable lower lift and drag force.

Figure 11e compares the computed drag force with the thrust provided by the engine. When using the fully



Case	Mach	AoA	Thrust [N]	CD [-]	CL [-]	Cm [-]	D [N]	L [N]	L/D [-]
Take-off fully deployed	0.2	5	63818	0.2029	1.3638	-0.7736	21583	145092	6.7227
		7		0.2322	1.5707	-0.8241	24708	167113	6.7634
		9		0.2639	1.7788	-0.8870	28077	189251	6.7405
		11		0.2997	1.9627	-0.9757	31886	208814	6.5489
		13		0.3499	1.8456	-0.9899	37224	196356	5.2750
	0.25	5	61169	0.1780	1.3733	-0.7706	29593	228299	7.7145
		7		0.2075	1.5809	-0.8165	34494	262796	7.6186
		9		0.2400	1.7947	-0.9096	39903	298351	7.4768
		11		0.2762	1.9464	-0.9454	45911	323556	7.0474
		13		0.3217	1.8010	-0.9781	53478	299398	5.5985
	0.3	5	58792	0.1643	1.3812	-0.7674	39325	330632	8.4076
		7		0.1943	1.5951	-0.8268	46516	381831	8.2085
		9		0.2259	1.7942	-0.8758	54066	429487	7.9437
		11		0.2641	1.9594	-0.9402	63216	469047	7.4198
		13		0.3049	1.7524	-0.9473	72992	419481	5.7470
Take-Off partially deployed	0.25	5	61169	0.1271	1.0090	-0.5426	21125	167729	7.9397
		9		0.1814	1.2238	-0.6020	30162	203433	6.7447
		13		0.2490	1.4431	-0.7254	41390	239889	5.7959
	0.3	5	58792	0.1146	1.0248	-0.5436	27443	245327	8.9396
		9		0.1626	1.3479	-0.6377	38914	322651	8.2915
		13		0.2379	1.4514	-0.7729	56958	347437	6.0999

Table 3: Aerodynamic coefficients and forces.

deployed high lift system one can see that for the Mach=0.3 case the thrust is lower than the drag at angles of attack of 11° and 13° . Partially deploying the high lift system solves this problem, but in this case the lift force is substantially lower, resulting in a lower climb rate. One should note that the typical take off speed of commercial aircraft are between Mach=0.20 and Mach=0.25, and that take-off in general takes place with an angle of attack between 7° and 11° [19].

Figure 12 shows the pressure distribution on the wing, the movables (inner slat, outer slat, inner flap and outer flap) and the nacelle, as well as the skin friction lines for the three highest angle of attack, for the selected Mach number of 0.25. The skin friction lines permits to highlight the separated flow area that occurs on the suction side of the wing downstream of the nacelle location at angle of attack 13° . This explains the behavior of the lift coefficient and lift force curves (Fig. 11b,11f) with a decrease of the lift when increasing the angle of attack over 11° . One can also observe that for these 3 angles of attack there is small flow separation on the wing tip.

The flow separation at the wing tip was further investigated, and Fig. 13 shows the calculated pressure contours and skin friction lines for the calculations with angles of attack of 5° and 7° and for the Mach numbers of 0.20 and 0.25. One can clearly observe that for the angle of attack of 5° there seems to be a small flow separation that seems to come from the gap between wing and slat. This flow separation has substantially grown for the angle of attack of 7° . The origin for this is that the tip twist angle is too low because the wing optimization process did not account for the load distribution.

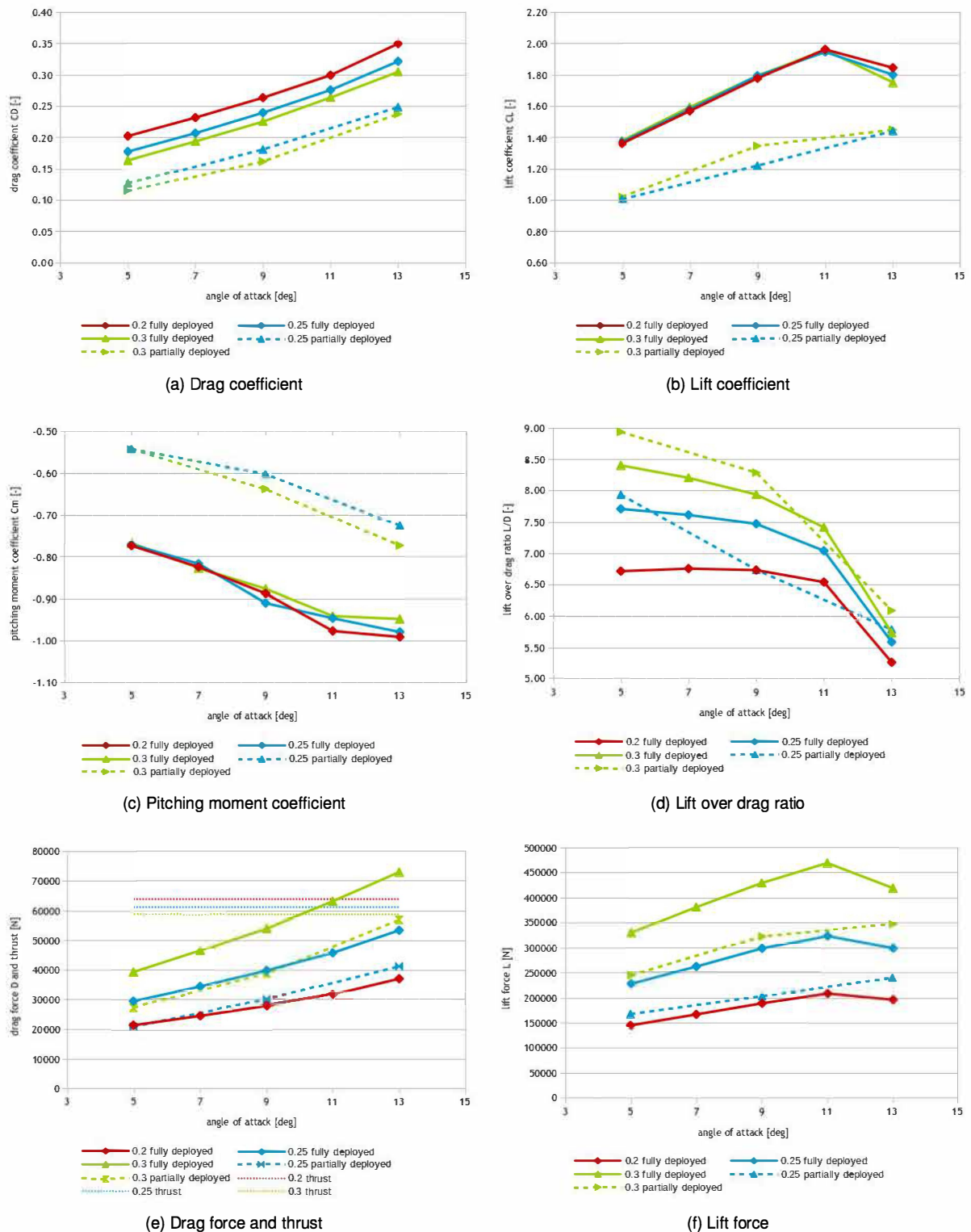


Figure 11: Aerodynamic coefficients and forces.

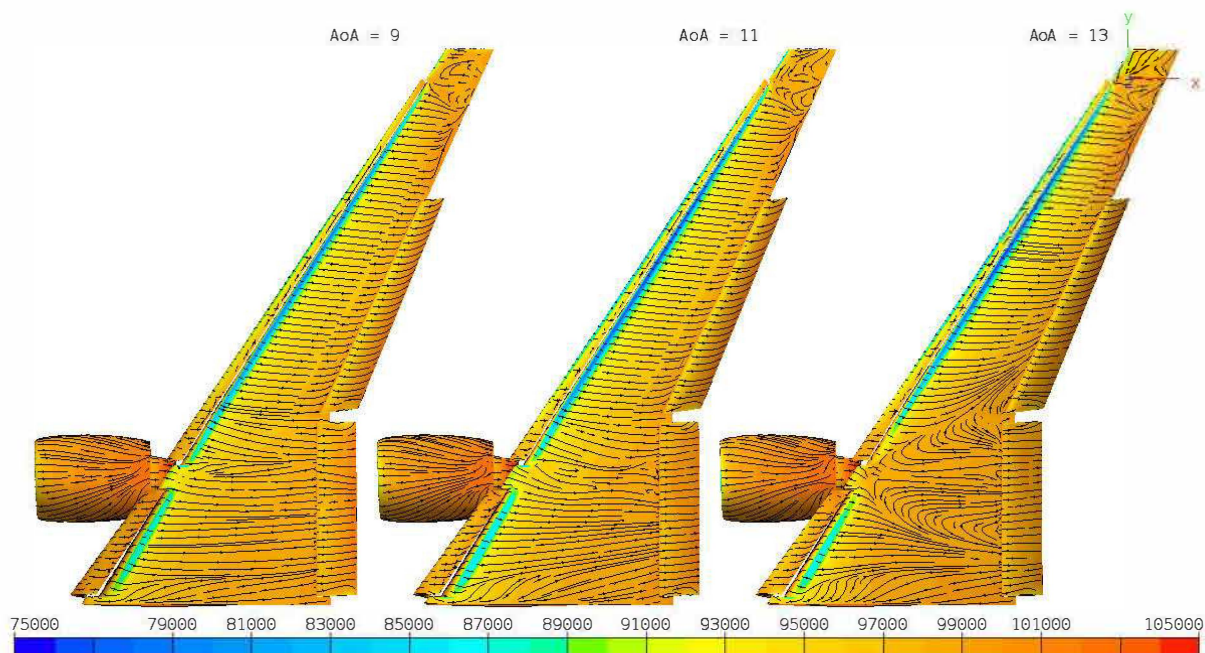


Figure 12: Pressure distribution and skin friction lines on the wing (fully deployed high-lift devices) at Mach=0.25.

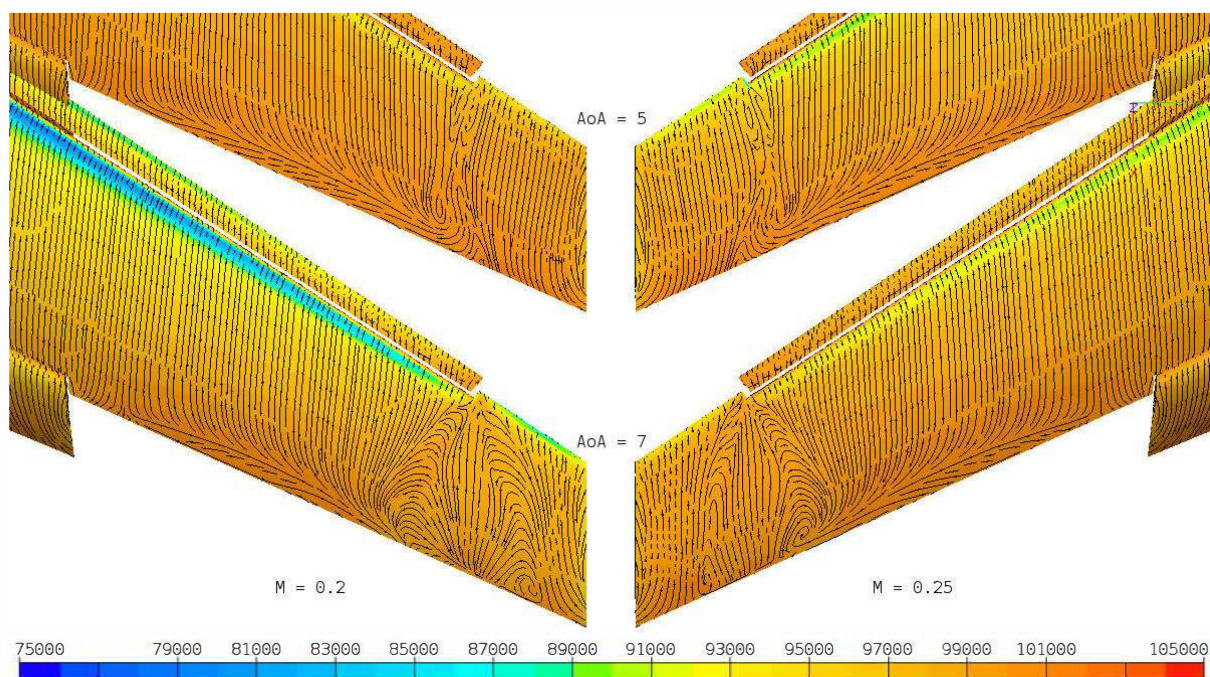


Figure 13: Pressure distribution and skin friction lines on the wing (fully deployed high-lift devices) at Mach=0.20 (left) and Mach=0.25 (right).



6. CONCLUSIONS & FUTURE WORK

Detailed CFD simulations were made for take-off conditions of the DC2 Aircraft designed in the EU funded H2020 AGILE project. The AGILE project is a collaborative project, and the different components of the aircraft (wing/fuselage, engine, pylon/nacelle, high lift system) were provided by different partners in the project. The different aircraft components were merged together to obtain a CAD model that could be used for CFD mesh generation. A multi block structured chimera grid was created to permit quick changes of the deflection angles of the high lift system.

The CFD simulations showed that stall occurs at relatively low angle of attack (between 11° and 13°) indicating that the design of the wing and its components (high-lift devices and nacelle/pylon) are not optimal for the take-off conditions. The pylon-wing interaction and the cutting of the slat at this region location can explain the stall anticipation. A flow separation at the wing tip was visible at even lower angles of attack, also a further optimization of the wing including the high-lift system should be made. In particular optimization of the twist distribution, taking into account the wing span loading and stall path behaviour is needed. This was not taken into account in the optimized wing coming from the DC-1 campaign due to the optimization of the clean wing only.

The simulations also showed that the installed thrust might be insufficient at high angle of attack, in particular for Mach numbers above 0.25.

The results of this study will be used to re-evaluate the design of the wing, high-lift system and installed thrust of the DC2 aircraft.

The study presented here shows that it is important to consider take-off conditions early in the aircraft design and optimization process.

ACKNOWLEDGMENTS

The research presented in this paper has been performed in the framework of the AGILE project (Aircraft 3rd Generation MDO for Innovative Collaboration of Heterogeneous Teams of Experts) and has received funding from the European Union Horizon 2020 Programme (H2020-MG-2014-2015) under grant agreement n° 636202. The Swiss participation in the AGILE project was supported by the Swiss State Secretariat for Education, Research and Innovation (SERI) under contract number 15.0162. The authors are grateful to the partners of the AGILE consortium for their contribution and feedback.

REFERENCES

1. Hirschel E.H. CFD - from Solitary Tools to Components of the Virtual Product. Proc. Basel World User CFD Conference in Applied Computational Fluid Dynamics, Freiburg, Germany, May 19 - 23, 1996, pp. 24.1 - 24.9.
2. Hirschel E.H. Towards the Virtual Product in Aircraft Design? Proc. NDF 2000 - Towards a New Fluid Dynamics with its Challenges in Aerospace Engineering. CNRS, Paris, November, 2000. In: Champion M, Periaux J, Pironneau O, Thomas P. (editors). NFD2000: Towards a New Fluid Dynamics. CIMNE Handbooks on Theory and Engineering Applications of Computational Methods, Barcelona 2000.
3. Vos J.B., Rizzi A., Darracq D. and Hirschel E.H. Navier-Stokes solvers in European aircraft design, Progress in Aerospace Sciences, No. 38, 2002.
4. Ciampa P.D. and Nagel B. The AGILE Paradigm: the next generation of collaborative MDO. AIAA 2017-4137, 2017.
5. Lefebvre T., Bartoli N., Dubreuil S., Manzeri M., Lombardi R., Della Vecchi P., Nicolosi F., Ciampa P.D., Anisimov K., Savelyev A. Methodological enhancements in MDO process investigated in the AGILE European Project. AIAA 2017-4140, 2017.
6. Bartoli N., Lefebvre T., Dubreuil S., Olivanti R., Bons N., Martins J.R.R.A., Bouhlel M.-A., Morlier J. An adaptive optimization strategy based on mixture of experts for wing aerodynamic design optimization. AIAA 2017-4433, 2017.
7. Della Vecchia P., Stingo L., Corcione S., Ciliberti D., Nicolosi F., De Marco A. Game Theory and Evolutionary Algorithms applied to MDO in the AGILE European Project. AIAA 2017-4330, 2017.
8. Prakasha P.S. and Ciampa P.D. Airframe-On Board System-Propulsion System Optimization for Regional Transport Aircraft: AGILE EU project CEAS Conference Paper ID-270, 2017.
9. Anisimov K.S. and Savelyev A.A. Aerodynamic Optimization of Airplane Propulsion System within the Framework of AGILE Project 30th ICAS Congress, Daejeon, 2016.



10. Seider D., Fischer P., Litz M., Schreiber A., Gerndt A. Open Source Software Framework for Applications in Aeronautics and Space, IEEE Aerospace Conference, March 2012.
11. DLR, Air Transportation Systems, CPACS Homepage [Online] <http://www.cpac.de>, 2017.
12. Neyland V.Y., Bosnyakov S.M., Glazkov S.A., Ivanov A.I., Matyash S.V., Mikhailov S.V. and Vlasenko V.V. Conception of electronic wind tunnel and first results of its implementation Progress in Aerospace Sciences, vol. 37, no. 12, pp. 121-145, 2001.
13. Kurzke J. Performance modeling methodology: Efficiency definitions for cooled single and multistage turbines. ASME 2002-GT-30497, 2002.
14. Kurzke J. Gas Turbine Cycle Design Methodology: A Comparison of Parameter Variation with Numerical Optimization. ASME 98-GT-343, 1998.
15. Vos J.B., Rizzi A.W., Corjon A., Chaput E., Soinne E., Recent Advances in Aerodynamics inside the NSMB (Navier-Stokes Multiblock) Consortium. AIAA paper 98-0225, 1998.
16. Hoarau Y., Pena D., Vos J.B., Charbonnier D., Gehri A., Braza M., Deloze T., Laurendeau E. Recent Developments of the Navier Stokes Multi Block (NSMB) CFD solver. AIAA Paper 2016-2056, 2016.
17. Vos J.B., Charbonnier D., Ludwig T., Merazzi S., Gehri A., Stephani P., Recent Developments on Fluid Structure Interaction in the Navier Stokes Multi Block (NSMB) CFD solver. AIAA Paper 2017-4458, 2017.
18. Langtry, R. and Menter, F. Correlation-based transition modeling for unstructured parallized computational fluid dynamic codes. AIAA Journal, Vol. 47, pp. 2894-2907, 2009.
19. Wakefield I. and Dubuque C. Exceeding Tire Speed Rating during Takeoff. Boeing Aeroquarterly, QTR_02, 2009.

The impact of flow features on formation of surface carbonaceous deposits under aero engine representative conditions

E. Alborzi

*The University of Sheffield
Aviation Fuel Research Fellow*

*Department of Mechanical Engineering, The University of Sheffield, Sheffield, S1 3JD, UK
e.alborzi@sheffield.ac.uk*

S. Blakey

*The University of Sheffield
Senior Lecturer*

Department of Mechanical Engineering, The University of Sheffield, Sheffield, S1 3JD, UK

P. Gadsby

*The University of Sheffield
Senior Lecturer*

Department of Mechanical Engineering, The University of Sheffield, Sheffield, S1 3JD, UK

ABSTRACT

The application of aviation fuel as a heat sink in advanced aircraft propulsion system is an attractive option for the integrated management of the cooling and heating requirements. The use of fuel as a heat sink is however limited by its thermal stability or its propensity to form surface carbonaceous deposits as it is heated. Improved understanding of the flow effects on deposit formation is significant for the staged combustion systems proposed in the next generation of engines particularly around the Reynolds number in transition region where the available literature seems to differ in its assessment of any affect. The impact of different flow features on surface carbonaceous deposit formation was investigated experimentally in an engine representative condition using "Aviation Fuel Thermal Stability test Unit (AFTSTU)" for two sets of simulated burner feed arms including cylindrical structure and contraction/expansion nozzle respectively. Transient CFD models with a two stage kinetic model of surface deposition were used to predict the growth of deposits layer at the inner surface of fuel wetted surface. The simulated results were in good agreement with the experiments.

KEYWORDS: *Aviation fuel thermal oxidative stability, Surface deposition, Aero engine*



Aircraft Optimization at the Early Stages of Design with a Hybrid Technique

Nesrin Cavus

German Aerospace Center (DLR), Air Transportation Systems

Scientific Assistant

Blohmstr. 20, 21079 Hamburg, Germany

Nesrin.Cavus@dlr.de

ABSTRACT

Aircraft design requires possessing huge amount of data analyses which are executed consecutively as well as parallel with different configurations. Throughout the design process many experts contribute to the design from different specializations not only with well-known handbook methods but also using engineering intuition like heuristic principles. These practical experiences which are aimed to be gained by a training algorithm are the main motivation of this research. In this study, a hybrid method is used to replace the random walk method of some optimization algorithms. The goal is to improve the steps for convergence and the results of a multidisciplinary optimization problem with changing number of design variables, which normally require over 1000 function evaluations to converge. An example aircraft design problem is used to determine if there are improvements in convergence steps while searching the whole design space. The results show that the applied technique increases the efficiency of the optimization for the early stages of aircraft design.

KEYWORDS: *artificial intelligence, probabilistic neural networks, aircraft design, multidisciplinary optimization*

Integrating Maintenance Work Progress Monitoring into Aircraft Maintenance Planning Decision Support

*Pieter Callewaert M.Sc.
Delft University of Technology
Kluyverweg 1, 2629 HS Delft, Netherlands*

*dr.ir. Wim J.C. Verhagen
Delft University of Technology
Assistant Professor
w.j.c.verhagen@tudelft.nl*

*prof. dr. Richard Curran
Delft University of Technology
Professor*

ABSTRACT

A decision support framework is proposed, allowing for the integration of aircraft maintenance work progress monitoring into the aircraft maintenance planning decision support process. The framework is able to monitor the progression of planned maintenance by analysing real-time data on work progress. This can be used to explore optimal task planning in case of delays or maintenance being ahead of schedule. Using a combination of reliability analysis, cost analysis, decision alternative generation and ranking yields a decision support tool which is able to deal with the stochastic nature of maintenance task execution. Case study results indicate that the framework is able to generate decision alternatives with a lower total cost than the reference alternative, while at the same time optimising the maintenance planning, resulting in a possible reduction of the maintenance costs of 45 to 90% (depending on parameter settings).

KEYWORDS: *Maintenance planning, work progress monitoring, decision framework*



Threshold identification and damage characterization of GF/CF composites under low-velocity impact

Amit Ramji

*Cranfield University - School of Aerospace, Transport and Manufacturing
 Cranfield, Bedfordshire MK43 0AL, UK
Amit.Ramji@cranfield.ac.uk*

Yigeng Xu

*Cranfield University - School of Aerospace, Transport and Manufacturing
Yigeng.Xu@cranfield.ac.uk*

Marzio Grasso (corresponding author)*

*University of Hertfordshire – School of Engineering and Technology
 College Lane Campus, Hatfield AL10 9AB, UK
m.grasso@herts.ac.uk*

James Watson

*Cranfield University - Cranfield Impact Centre Manager
j.w.watson@cranfield.ac.uk*

George Haritos

*University of Hertfordshire – School of Engineering and Technology
g.haritos@herts.ac.uk*

ABSTRACT

A significant factor affecting the widespread use of carbon fibre and glass fibre reinforced laminates is the detrimental effect of low-velocity impact damage during manufacture and while in service. Various damage mechanisms can be involved under low velocity impact of composite materials. For unidirectional composites the identification of the Delamination Threshold Load is performed considering the sudden drop in the force-time history curve under low velocity impact. For the woven composite the failure mechanisms seem to be different and the current literature is not providing any clear procedure regarding the identification of the delamination as well as the evolution of the failure mechanisms associated with it. In this paper, experimental data have been produced using glass and carbon fibres composites. The results have been analysed in terms of force-time and force-displacement history curves. Although delamination and other damages were clearly observed using C-scan, the analysis of the results is not showing any change in the trend of the curves that can be associated with the incipient nucleation of the delamination. A preliminary discussion regarding the nature of the mechanisms through which the delamination propagates in woven composite and a justification for the absence of a sudden variation of the stiffness is made.

KEYWORDS: *Low velocity impact, woven composite, delamination, Threshold identification,*

A Pedagogical Approach Based on Problem-Based Learning on Aeronautical Engineering Post-Graduation at Instituto Tecnológico de Aeronáutica (ITA)

Adson Agrico de Paula, Adjunct Professor, adson@ita.br

Roberto Gil Annes da Silva, Adjunct Professor, gil@ita.br

Instituto Tecnológico de Aeronáutica, Aircraft Design Departament

Praça Marechal Eduardo Gomes, 50 - Vila das Acácias, São José dos Campos - SP, 12228-900, Brazil

ABSTRACT

In the context of the Problem-based Learning, pedagogical interventions were introduced in the course Aerodynamic Applied to Aircraft Design (AA-234) of the post-graduation in aeronautics at Instituto Tecnológico de Aeronáutica (ITA). In this sense, the aim of this study is to describe the pedagogical process in the AA-234 course by using technical-scientific investigations in order to achieve a more efficient learning process. The characteristics of this pedagogical approach were developed in order to exercise the multiple skills and abilities related to technical, critical and teamwork capability. In addition, we intend to show that the characteristics of this pedagogical intervention is appropriate in an educational environment of aircraft design since the high technical ability, critical judgment and multidisciplinary characteristics required for this area becomes the project-based learning a tool extremely effective for aeronautical education.

KEYWORDS: *aircraft design, aerodynamics, aeronautical education, PBL, Active learning*

1 INTRODUCTION

Regarding innovative approaches for new engineering education, the Problem-Based Learning (PBL) appears as learning methodology efficient applied on American universities such as MIT (Massachusetts Institute of Technology). Project Based Learning according to [1] is a teaching and learning approach that causes transformations on education due to require more effort from students and teachers. PBL requires a critical approach when teachers develop their pedagogical activities. Teachers need to push students to an active learning process thus becoming the education more efficient. On the other hand, PBL methodology requires a student's understanding that it has the main role on its education. This understanding will bring a deeper learning process. In this active education environment, we can say that the main characteristics of the problem-based learning can be described from the following approaches: student at the center of the learning process, development of study groups and interdisciplinary environment.

In the context of the problem-based Learning, pedagogical interventions were introduced in the discipline Aerodynamic Applied to Aircraft Design (AA-234) on the postgraduate course belong to Instituto Tecnológico de Aeronáutica (ITA). The objective of this work is to describe the pedagogical process established in the discipline AA-234 through activities of the technical-scientific investigations that are based on PBL methodology. Additionally, it is intended to show that the learning process characteristics applied on the discipline are desirable to the aeronautical design environment, since the high technical skills, the critical judgment and the multidisciplinary characteristics required by the area make the problem-based learning to be an effective tool for teaching in aeronautics. The course Applied Aerodynamics to Aircraft Design belongs to the set of disciplines offered by the post-graduation of the Instituto Tecnológico de Aeronáutica (ITA). The course aims to bring for graduate students an understanding of aerodynamic phenomena related to aircraft design as well as the practice of solving aerodynamic problems in a real environment of design. In addition, the discipline also pursues to clarify the relationship among aerodynamics and other disciplines such as structures,

loads and flight dynamics facing with several requirements in an multidisciplinary environment of the aeronautical design.

The student profile is established by characteristics that involve the aeronautical technological park in São José dos Campos, Brazil (figure 1). Thus, master and doctoral full-time students in aeronautics attend the discipline. Also, there are students who conduct postgraduate activities at same time with their work activities in aeronautical companies. Most of these students are engineers of the EMBRAER. There are still students who attend the discipline in order to qualify for their activities in the aeronautical industry.



Figure 1: Engineers of the aeronautical industry (EMBRAER) and full-time postgraduate students at ITA.

2 TECHNICAL-SCIENTIFIC INVESTIGATIONS

The pedagogical activities are based on technical-scientific investigations related to the aeronautical design that are of interest of the industry or university. The educational intent is to motivate students through challenging technological problems presenting practical aspects, since they are related to the needs of the industry and the academy. In addition, an approach based on multidisciplinary view and teamwork activities brings to the student a real perception of the aeronautical design. The development of the activities followed two steps:

2.1 Choice of the study subject

The criterion of choice of the subjects for studies was based on current needs of the aeronautical industry and academic research topics in areas of the forefront of the knowledge (figure 2). Thus, the choice of the subjects is a key strategic to motivate students. In addition, some topics developed were related to master and doctoral subjects of students who attended the discipline. Summarizing, the criterion of choice of topics followed three characteristics:

- Research related to forefront of the knowledge
- Research of technological interest for the aeronautical industry.
- Investigations related to master and doctoral subjects of the students.

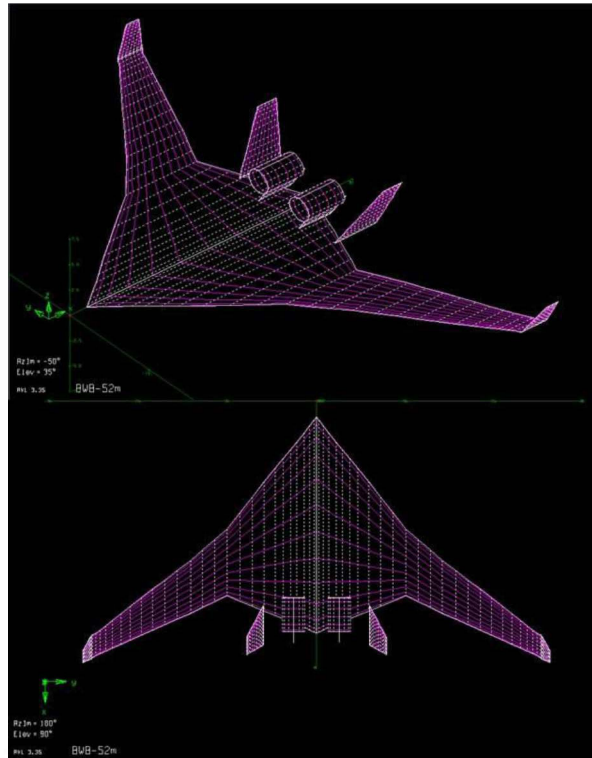


Figure 2: Aerodynamic numerical evaluation of a new concept in aircraft design (flying wing configuration).

Based on criteria previously mentioned, the following subject were established:

- Fuselage layout optimization
- Aerodynamic prediction tool for take-off and landing performance
- Aerodynamic evaluation for box-wing configuration
- Optimization tool for take-off and landing performance
- influence of the wing stiffness on drag and aerodynamic efficiency
- Multidisciplinary evaluation of the technological level of an airfoil
- A tool for excrescence prediction
- A review of innovative aircraft configurations
- Aeroelastic effects on wing aspect ratio

2.2 Pedagogical process

Students were arranged in groups of 4 or 5 members according to a personal affinity related to subjects. Researchers from ITA or engineers from EMBRAER conducted technical support of the studies. The tutors conducted the primarily orientations related to the specific aspects of the tasks, mathematical tools and bibliographic review. The work was divided into two parts: *Development of a*

CEAS 2017 paper no. 279

Page | 3

A Pedagogical Approach Based on Problem-Based Learning on Aeronautical Engineering Post-Graduation at Instituto Tecnológico de Aeronáutica (ITA)

Copyright © 2017 by author(s)

Scientific-Technical Research and a Scientific Article. After students conduct scientific-technical investigations and discussions of the results, a scientific paper was prepared by each student group in the format of the articles presented in the main Aeronautical Conference performed by The American Institute of Aeronautics and Astronautics (AIAA). After analyzing the articles, the tutors selected work that can potentially be pointed out for the AIAA conference. This indication guaranteed an award score on the final grade as a way to establish an environment of motivation and meritocracy. Figure 3 outlines the arrangement of the pedagogical activities carried out during the scientific-technical research for each student group.

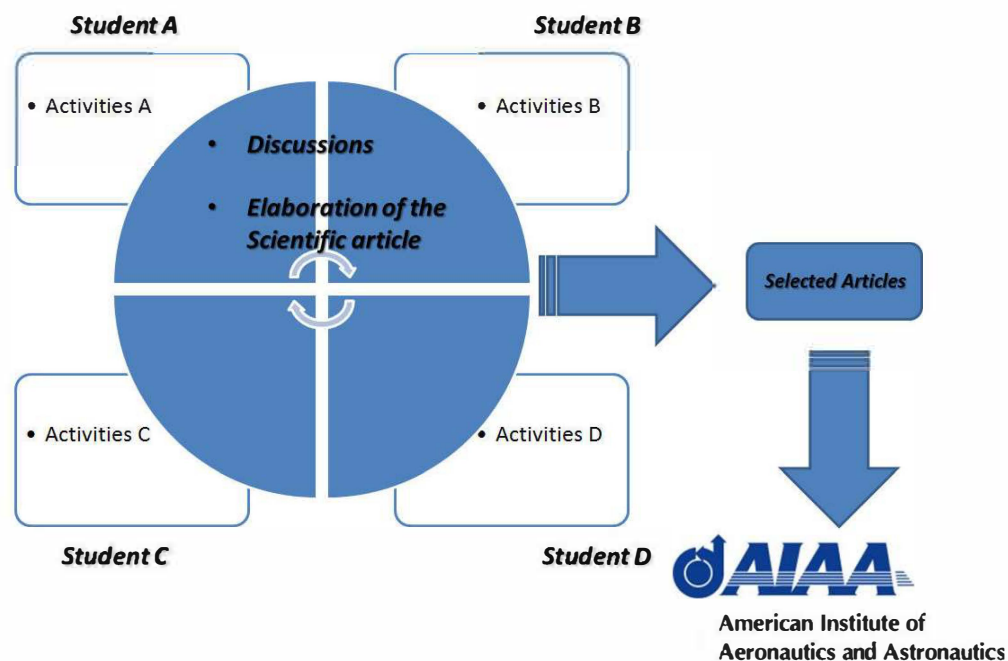


Figure 3: The pedagogical process during activities of the technical-scientific investigations

3 RESULTS

The student groups presented different result levels. Two work related optimization tool for take-off (figure 4) and landing performance and multidisciplinary evaluation of the technological level of an airfoil (figure 5) were chosen to be submitted to AIAA conference where the first one was accepted for presentation on 2017 Aviation AIAA conference . In addition, two more work, fuselage layout optimization and influence of the wing stiffness on drag and aerodynamic efficiency (figure 6 and 7), were accepted for 2017 EUCASS (European Conference for Aeronautics and for Space Science). In addition, the work regarding wing stiffness effect on drag and aerodynamic efficiency was selected during the conference to be a EUCASS journal.

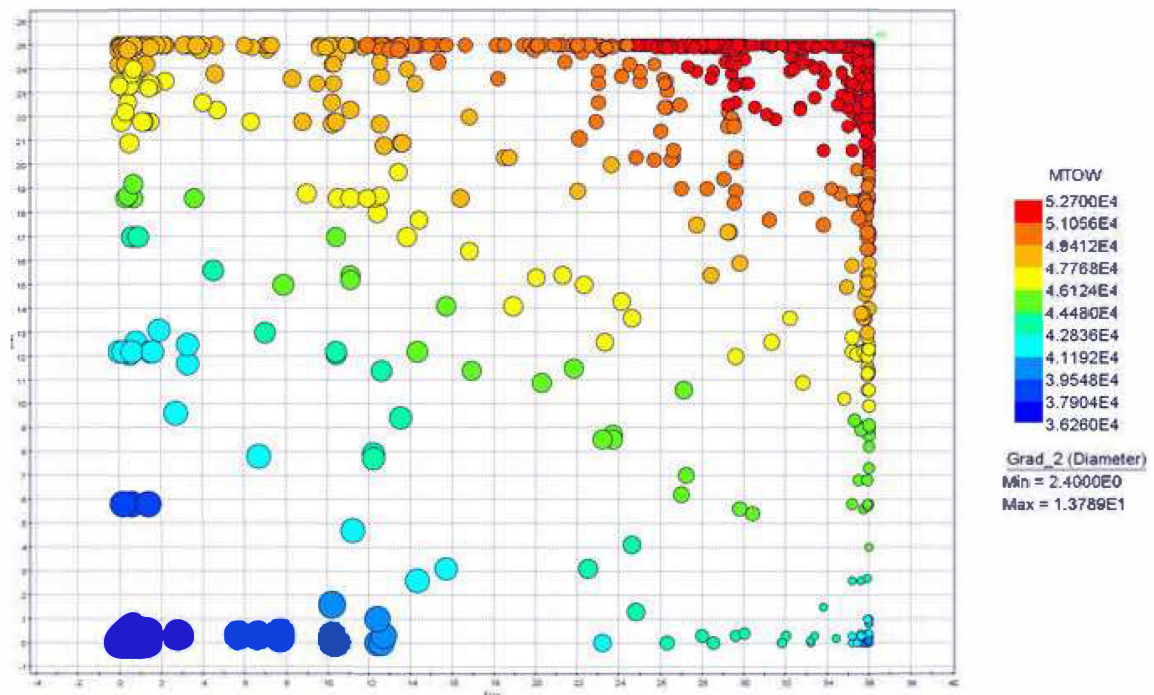


Figure 4: Optimization of the flap and slat position for take-off requirements.

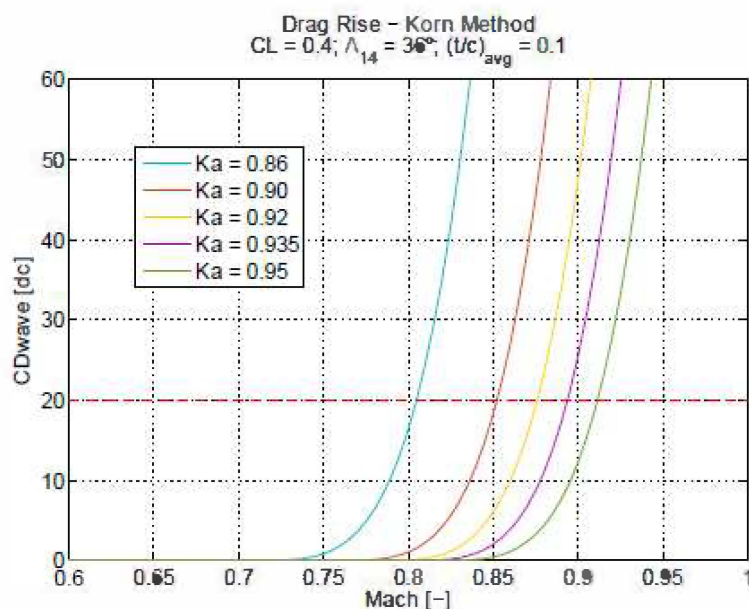


Figure 5: Airfoil technology factor effect on wing drag rise.

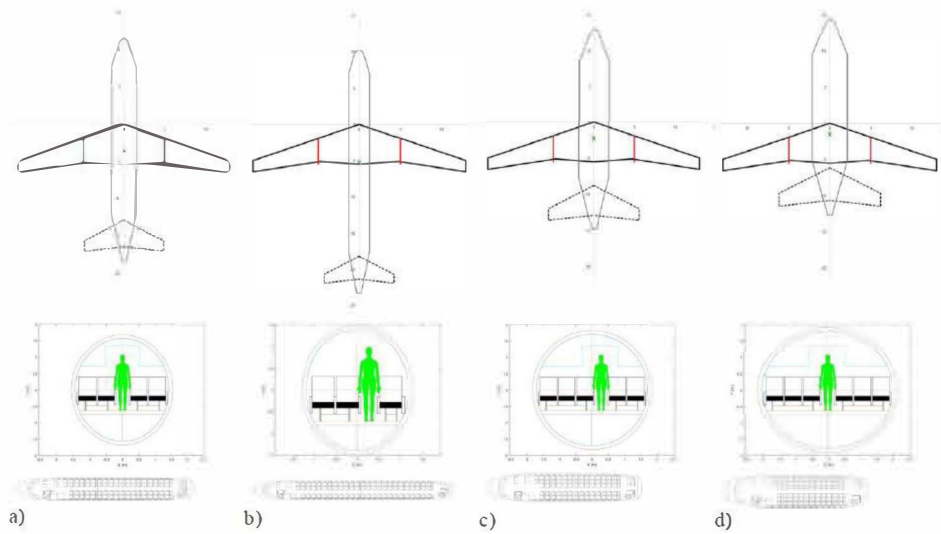


Figure 5: Fuselage layout optimization for EMBRAER 170

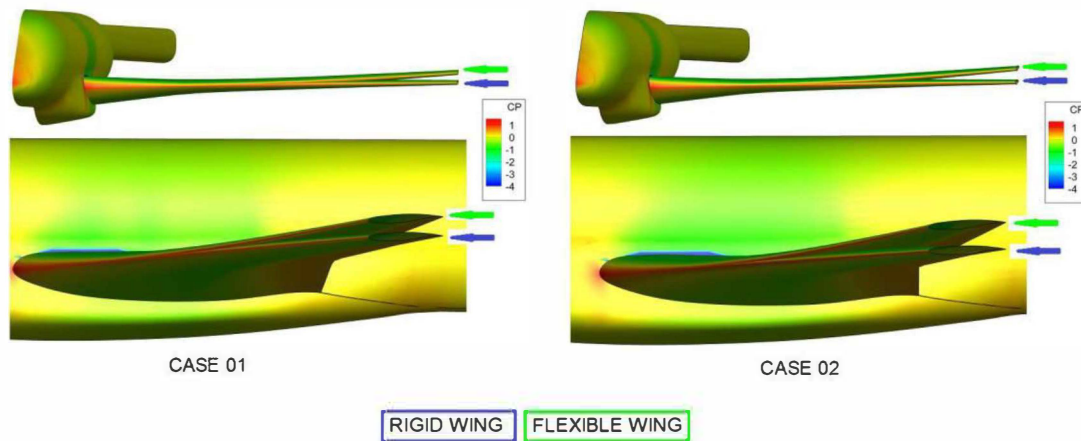


Figure 6: Wing stiffness effect on drag and aerodynamic efficiency.

Independently of the work level, all groups showed strong motivation and interest during the development of the whole task process. The students fill some formularies regarding the evaluation of the pedagogical process that they were submitted. In additional, in some informal talks, they made some comments related to learning process. Thus, follow some remarkable aspects that the students noticed as important learning process:

- Work in group: organization, planning, understanding of the member group skills.

- Academic work rigor: understanding of the several steps of the academic work
- Industrial interest: students working together with engineer from industry realized the specific interest of the industry in technologic problems
- Engineering tools: opportunity to detail with tools of the aeronautical industry environment (CFD software, semi-empirical methodologies, wind tunnel data)
- Active learning: students felt free to develop active learning regarding aerodynamic knowledge, and also they realize the importance of constructing this knowledge by themselves.

4 CONCLUSIONS

The course aerodynamics applied to aircraft design carried out in the post-graduate context of the Instituto Tecnológico de Aeronáutica presents objectives that bring great pedagogical challenges related to the multidisciplinary characteristics of the design, complex concepts of aerodynamics and practical experimentation. In this sense, the PBL methodology applied as pedagogical approaches on discipline AA-234 contributed to the success of the objectives of the discipline. The pedagogical process brought an additional motivation for the students due to develop activities related to the real aircraft design or to advanced research for future technological development. The possibility of developing subject of interest of industry considering issues of multidisciplinary kept a high level of motivation during the activities of the course. Thus, as consequence, a great number of extra-class hours spent for the activities were noticed. In addition, the students also spend many hours with the help of the tutors. The developed knowledge based on a scientific article exercised some aspects of the academic knowledge that must be considered in a postgraduate environment. Finally, some results of the activities in international conferences (AIAA and EUCASS) motivated students to keep their goal in the academic life, and also these results showed the desirable characteristics that scholars need to have to achieve good performance.

REFERENCES

1.MASSON, T.J; DE MIRANDA, L.F; MUNHOZ JR, A.H; CASTANHEIRA, A.M.P.;2012; "Metodologia de ensino: aprendizagem baseada em projetos (PBL)". O engenheiro professor e o desafio de educar; COBENGE.

Identification of Optimal Preventive Maintenance Decisions for Composite Components

*Paul Laks M.Sc.
Feldstraße 6, 90152, Erlangen, Germany
paul_laks@gmx.de*

*dr.ir. Wim J.C. Verhagen
Delft University of Technology
Assistant Professor
w.j.c.verhagen@tudelft.nl*

*prof. dr. Richard Curran
Delft University of Technology
Professor*

ABSTRACT

This research proposes a decision supporting tool which identifies cost-optimal maintenance decisions for a given planning period. Simultaneously, the reliability state of the component is kept at or below a given reliability threshold: a failure limit policy applies. The tool is developed to support repair-or-replacement decision making for composite components likely to suffer impact damage. As a core part of the tool, a cost minimization problem is defined and solved using a search tree algorithm with heuristic constraints. Application to a case study which utilizes historical damage data and subsequent simulation shows the potential of the tool to identify cost-minimal maintenance decisions. The decision support tool is capable of incorporating a wide range of parameters to study preventive maintenance decision making in depth.

An Investigation into All Electric and Hybrid Aircraft

Gareth England

Imperial College London

Aeronautical Engineering

Faculty of Engineering, South Kensington Campus, London, SW7 2AZ, UK

Gengland34@gmail.com

Errikos Levis

Imperial College London

Aeronautical Engineering

ABSTRACT

This study was an investigation into the feasibility of all-electric aircraft (AEA) and hybrid electric aircraft (HEA), including an analysis into the available technologies. AEA and HEA could dramatically reduce the aviation industry's contribution to global CO₂ emissions. There are several additional benefits of producing AEA/HEA aside from obvious environmental impacts. These include reduced thermal and acoustic signatures. Findings confirmed that due to the limitations of existing technologies, AEA with performance levels on par with current aircraft are not feasible in the short to medium term. HEA are feasible, with large potential gains found across a range of aircraft classes. A detailed analysis was carried out investigating the key factors affecting the relative performance of HEA when compared to existing conventionally powered aircraft.

KEYWORDS: *Electric, Hybrid, Aircraft*

Morphological Design and Analysis of Aircraft Wings

Jakub Drzewoszewski

*Brunel University, College of Engineering Design and Physical Sciences
 Mechanical, Aerospace and Civil Engineering Department
 Kingston Lane, Uxbridge, Middlesex, UB8 3PH, United Kingdom*

Cristinel Mares

*Brunel University, College of Engineering Design and Physical Sciences
 Mechanical, Aerospace and Civil Engineering Department
 Cristinel.Mares@brunel.ac.uk*

ABSTRACT

When developing the aircraft profile mission, one would want to achieve the most advantageous flight aerodynamic parameters for each specific segment. Nowadays traditional air vehicles and particularly their wings are not designed to satisfy the most optimal conditions for each segment but only designated to achieve sub-optimal performance of the entire flight envelope, putting the major focus on one or two crucial settings to achieve an overall consensus. A morphing wing is a concept that allows wing's transformation in flight so that the overall aircraft performance in terms of both mechanical behaviours and aeroelastic conditions is significantly enhanced. In this paper a thorough analysis of aircraft wings development in terms of existing morphing technologies was carried out using the Morphological Analysis Design method as initiated by Fritz Zwicky in 1930s, to get a comprehensive understanding of morphing technologies in aircraft wings development and to categorise the variable parameters of solutions. The Morphology is referred as a study of the simplicity, basic arrangements of all objects. Not only taking into account general structures such as aspects of geometry, geology or biology but also looking at more abstract interrelations between structures, ideas or any additions of substance. In this study, the analysis encompassed different mission segments to ensure the most crucial performance metrics and their variables were taken into account for fixed wings operation in subsonic region. An extended analysis using RQ-21A Blackjack selected as an aeroplane scope, highlighted performance improvements in both aerofoil and planform/out-of-plane morphing the Morphological Analysis starting with an initial set of 576 solutions. The discussion of possible as well as misjudged concepts is presented using comparative non-dimensional aerodynamic performance metrics.

KEYWORDS: Morphing, Morphological analysis, Wing Design

1 INTRODUCTION

Flight performance has been a matter of the utmost importance since the earliest development of any aircraft. Dependent on the aircraft's profile mission, one would want to achieve the most advantageous flight aerodynamic parameters for each of them. However, there are several constrains so that it can fulfil the mission with increased payload at faster speeds. Nowadays traditional air vehicles and particularly their wings are not designed to satisfy the most optimal conditions of each flight segment. They are only designated to achieve sub-optimal performance of the entire flight envelope, putting the major focus on one or two crucial settings to achieve an overall consensus [1]. As the demand for commercial and military air transport capabilities increase, the investigation into cost-effective solutions that enhance aircraft performance becomes more and more vital. The estimates give the image of as little as 1% decrease in aerofoil drag could give the total saving of \$140 millions per year when analysing US transport fuel with the cost of fuel of \$0.70 per gallon [2]. The nature has been immensely inspirational for aircraft designers for years. Not only the simplicity but mainly the aerodynamic efficiency, that is the most significant characteristic of all flying species, became the major background for aircraft designers to resemble the nature creations [2]. A simple bird can provide an ideal state

conditions for an aircraft wing as it can drastically reshape itself to satisfy the most optimal geometrical requirements for all flight conditions [1]. Falcons are one of the most important examples as they have the ability for long endurance loitering with the aid of e.g. air currents and for swift morphing of their body to strike their detected prey [2]. The challenge of transforming the geometry of an aircraft wing has been investigated as early as at the beginning of 20th century with the Wright brothers' development of the heavier-than-air The Wright Flyer aircraft. It was claimed as one of the firsts attempt at controlling the structural flexibility by using manpower to twist the wing to influence roll properties [3]. This can be treated as one of the first usages of morphing technologies in aircraft wing development. A morphing wing is a concept that allows wing's transformation in flight so that the overall aircraft performance in terms of both mechanical behaviours and aeroelastic conditions is significantly enhanced [4]. The shape and structural flexibility were found during aircraft design optimisation to be the two key elements influencing the performance, hence changing the geometry in flight is the major focus of reference when one speaks about aircraft morphing [3],[5]. Within the literature there are proposed several classifications of techniques to obtain a morphing wing that could focus on the level of morphing classifying transformations as large, medium or small [1] or group all morphing capabilities in aerofoil, planform or out-of-plane alterations [2],[6]. The classification represented in Table 1 will be here object of study expanding on the meaning of each morphing idea and explaining the aerodynamic effects as referred to actuation and skin coverage methods.

Table 1: Classification of geometrical wing morphing aspects [6]

Shape Morphing Wing	Aerofoil Adjustment	Camber Variation
		Thickness Variation
	Planform Alteration	Span Variation
		Chord Length Variation
		Sweep Angle Variation
	Out-of-plane Transformation	Twist Variation
		Dihedral / Gull Variation
		Spanwise bending

Some historical aspects regarding the morphing technology evolution are discussed in Section 2, followed by a presentation of the Morphology Analysis Design Method [7] in Section 3. The application of this method for the development of morphing wings is presented in Section 4, followed by conclusions and possible future work ideas. Extended analysis and results are presented in [8], which formed the basis of the present work.

2 MORPHING TECHNOLOGIES

For the most vital comprehension of morphing developments, the existing constrains and limits of various designs should be reviewed. One of the most famous examples developed in 1970s is the Grumman F-14 Tomcat, widely known just as F-14. Its specific construction allowed the wings sweep angle to vary between 20° to 68° degrees, which provides the most optimal lift-to-drag ratio in flight configuration [1]. The idea of planform alteration that succeeds in the variable sweep angle comes from the need for both the most optimal low-speed operation during take-off and landing as well as high-speed for fast cruise, even at supersonic conditions. Particularly for the second flight operation there is an advantage of delaying the drag rise at Mach numbers approaching 1.0 due to the alteration of wing sweep. To contrast these great performance advantages that would be highly favourable especially for military application one must consider what are the drawbacks of running an aircraft with such applications in place. In the Grumman F14 Tomcat case, the biggest penalty was the additional weight and the complexity of an aircraft, what not only lowers the fuel efficiency but in longer term, increases the cost of running the aircraft. All the F-14's became retired by US Navy in 2006 due to high maintenances required that were not only complex but also not cost-effective. Unfortunately, even its replacement F/A-18E did not exceed the specification due to reduced payload by smaller fixed wings [1]. Despite having represented The Wright Flyer from the beginning of 20th century many could find other examples of even earlier advancements of not only the technological advancements in aeroplane technology but also the history of the world. Starting with Icarus that comes from Greek mythology, attempts at both flying and resembling the nature were mentioned such as those represented by

primitive feathers glued with wax to create bird-like wings [9]. The early aviation also brings a history of Otto Lilienthal from 1881 whose systematic bird studies succeeded in a series of simple but elegant gliders. He discovered the curved shape of bird's wings was the key element to the secret of flight. Having applied it to aircraft shape would harness the success for a flying machine, Lilienthal is claimed to be the first to underpin the principles of the force of lift as there was very first realisation of how the shape of wing affects the flow surrounding the wing [10]. As early as in 1914, Gallaudet D-1 has been a subject to variable wing tips study what was further studied by North American XB-70 Valkyrie in 1964 [11]. The span extension could be observed from 1931 when Makhonine MAK-10 was implemented with telescopic wing allowing up to 62% in retraction and the variable sweep was used 20 years before Grumman F14 Tomcat for Bell X-5 operated exclusively by NACA High-Speed Flight Station between 1952-1955 [12]. More complex and unusual configurations which can be mentioned are the Goodyear Inflatable, the concept of an inflatable aeroplane produced from 1952 and sponsored by United States Army, or the NASA AD-1, the concept of an asymmetric-oblique sweep that works like a pair of scissors to enhance low-to-high speed performance, both with potential usage in other vehicle configurations [13]. The current state of the art in aircraft design presents many interesting solutions which are under investigation and development. In this paper the main focus is the subsonic wing design and possibilities to use morphing techniques to create concept solutions with enhanced performances during the flight envelope, starting from existing configurations and varying their design characteristics within the framework of a powerful design methodology.

3 MORPHOLOGICAL DESIGN ANALYSIS

The modelling tool to assess the constraints of morphing wing technologies will be Morphological Analysis as initiated by Fritz Zwicky in 1930s, a Swiss astronomer and a professor of Astronomy at California Institute of Technology [7], and further studied by different several institutions such as California Polytechnic State University San Luis Obispo [14] and Swedish Morphological Society [15]. Morphology is referred as a study of the simplicity, basic arrangements of all objects. Not only by taking into the account general structures such as the aspects of geometry, geology or biology but also looking at more abstract interrelations between ideas or any additions of substance. General Morphological Analysis has been established as a method for describing, structuring and investigating the finite set of possible relationships within often non-quantifiable problem with high complexity factors [7]. The approach the Fritz Zwicky undertook comprised of five iterative steps:

- (1) Clear and concise formulation of a problem to be investigated,
- (2) Analysis of all Morphological Analysis Field descriptive parameters that could possibly be of an importance for providing the solution to the problem,
- (3) Construction of a Morphological Box, a multidimensional matrix that describes all of the solutions to the problem as based on pre-defined parameters,
- (4) Examination of every solution within the Morphological Box to determine their performance with respect to each other,
- (5) Evaluation of the most viable solutions to the investigated problem as based on the performance between each solution for pre-defined descriptive parameters within Morphological Analysis Field.

To clarify the process, an example of one of the most significant investigations carried out as a preparatory step towards defining a new propulsive system [15] is presented. The Morphological Analysis Field variables were set as *Initial Energy Form*, *Transmission* and *Final Storage Form* that simplified provides 5 equal solutions for each of the variables such as *Kinetic*, *Electrical*, *Chemical*, *Thermal* and *Nuclear*. The simplified Morphological Box, called in other words as a Morphological Analysis Field for the exemplar problem is represented in Table 2. As indicated, the top row contains *Variables* and each row underneath represents singular *Solutions*.

Table 2, A simplified Morphological Analysis Field used for defining a new propulsive power in 1960s [15].

Descriptive Parameters ↓	Variations →				
d1	d1.1	d1.2	d1.3	d1.4	d1.5
Initial Energy Form	Kinetic	Electrical	Chemical	Thermal	Nuclear
d2	d2.1	d2.2	d2.3	d2.4	d2.5
Transmission Energy Form	Kinetic	Electrical	Chemical	Thermal	Nuclear
d3	d3.1	d3.2	d3.3	d3.4	d3.5
Final Energy Storage Form	Kinetic	Electrical	Chemical	Thermal	Nuclear

The example of an overall solution d1.1, d2.2, d3.3 that is highlighted in cells above provides a configuration of *Initial Energy Form* as *Kinetic*, *Transmission Form* as *Electrical* and lastly *Final Storage Form* as *Chemical*. Nowadays such a configuration is widely known as a hydroelectric energy generation stored in a battery. Another instances to spot within the solutions space could be an internal combustion energy stored in a flywheel (*Chemical – Thermal – Kinetic*) or a simple refrigerator (*Electrical – Chemical – Thermal*). The maximum amount of arrangements depends on the size of a matrix, that in given case could provide 125 (5x5x5) possible configurations. The exploration of given results enables the assessment of not only currently existing solutions to stated problems but it also may allow the discovery of undeveloped paths that were not taken into consideration before. The introduced form of Morphological Analysis is used for the investigation of morphing technologies existence in aircraft wings development. In order to follow the *5 Iterative Steps* as described by Fritz Zwicky, there is a need for an additional tool to reduce the number of final possible configurations and overcome the practical limits of the original method. For this reason, Cross-Consistency Assessment (CCA) has been put in place to study whether the combinations of all provided solutions are actually plausible and are not contradictory. Obtaining of the CCA eliminates any inconsistencies between particular configurations and ensures the remaining ones are logically consistent [16]. By performing the CCA, the analysis of a solution space with the established Morphological Box may allow easier designation of any undeveloped results and a possible room for improvement to overcome existing challenges and derive vital performance analysis.

In the present study, following the Morphological Analysis methodology, a comprehensive study of the morphing technologies was carried out: classifying the variable parameters of solutions within geometrical shape morphing for aerofoil, planform and out-of-plane majoring alterations (Table 1), evaluating the goals of different technologies, underlining the relationships between identified solutions' categories to eliminate any inconsistencies, and establishing a benchmark of flight mission aerodynamic performance metrics that will be further used to assess viable solutions. A solution space of morphing ideas was created identifying any undeveloped technologies or areas that could be applied differently based on configuration simulation, and performing a comparison of performance against the set benchmark using mathematical formulations referred to the aerodynamic effects and computational study in Xfoil [17] and XFLR5 [18] programmes, with a goal to underline the principles of applicable actuation systems and material capabilities for the favourable solutions and forecast of future state-of-art technologies that could enhance flight capabilities.

4 RESULTS

As described in [14] the construction of analysis field consists of descriptive parameters or variables that are abstract enough to cover a wide variety of objects, but specific enough to be applicable. The problem has been formulated and thoroughly studied outlining the challenges and limitations in Section 3 and on that basis there was created a Morphological Analysis Field or as referred by others a Morphological Box. In order to get the best understanding of the possible concepts to be generated using Morphological Analysis there were not included the methods of actuation and possible skin types. The variety of morphing alternations may not be possible to achieve with the same actuation method and including them for every parameter studied would create high-level of complexity of the analysis. For the reason, only 'what' – aerodynamic performance is discussed within Morphological Analysis and 'how' – is summarised for selected configurations. The classification of morphing technologies introduced the most important parameters for the purpose of benchmark analysis described in Section

1. There were identified four descriptive parameters directly referring to wing morphing capabilities, d2-d5 and one parameter that puts the wing into the context of the type of aircraft it could be used for referred to as d1. The Morphological Box is outlined in Table 3 with full specification of all possible solutions for all descriptive parameters as listed. The reference aeroplane, d1 that would be the subject of wing's application is deemed to have one, two or zero fuselages, so called 'flying wing'. Aerofoil morphing, d2 is concerned with changes applied to leading edge, trailing edge or a full camber transformation. Planform morphing concerns two parameters such as span, d3 and sweep d4. For span morphing there are concerned two generic ideas of uniform extension such as in [19] or [20] and non-uniform that relates mainly to separate winglets represented in [21]. Sweep angle morphing represents a summary of ideas within forward, backward and asymmetric also called oblique transformation. Lastly, out-of-plane morphing d5, has been combined for both dihedral and gull degrees, representing straight dihedral for an entire wing alteration, tip dihedral and gull morphing as represented in [22].

Table 3: Morphological Analysis Field for studied morphing technologies.

Descriptive Parameters ↓	Variations →				Variations Count
d1 Aeroplane	d1.1	d1.2	d1.3		k1 = 3
Number of Fuselages	None – Flying Wing	One	Two		
d2 Aerofoil	d2.1	d2.2	d2.3	d2.4	k2 = 4
Morphing Camber	None	Leading Edge	Trailing Edge	Entire Camber	
d3 Planform	d3.1	d3.2	d3.3		k3 = 3
Morphing Span	None	Uniform	Non-Uniform		
d4 Planform	d4.1	d4.2	d4.3	d4.4	k4 = 4
Morphing Sweep	None	Forward	Backward	Asymmetric 'Oblique'	
d5 Out-of-plane	d5.1	d5.2	d5.3	d5.4	k5 = 4
Morphing Dihedral/Gull	None	Straight Dihedral	Tip Dihedral	Gull	
					Total k = 576

Having established the complete Morphological Analysis Field, the spectrum of all solutions have been summarised providing the total of 576 solutions that can be achieved within the analysis, what gives 192 configurations for each type of the fuselages. Additionally, as described in [14] focused mainly on architectural projects, in order to provide the highest accuracy of multi-dimensional design analysis there were added variants that allow the lack of certain type of morphologies. It increases the dimensionality of different non-quantifiable configurations that could be analysed either by random selection, constraint imposition or preference ordering in order to remove bias and prejudice from design. As introduced by Zwicky and further studied by Swedish Morphological Society, there is an inevitable need to minimise the number of all possible solutions through cross-consistency analysis of solution's feasibility what overcomes the practical limits of the original Morphological Analysis developed in 1930s [16]. Additionally, as presented in the Phase 1, SUGAR – Subsonic Ultra Green Aircraft Research, a similar approach was used not only to study the compatibility of proposed solutions but also the enhancement that favourable configurations could impose on dynamic decision making [23]. The report carried out in-depth analysis of airline current market outline to design a new aeroplane concept, also covering variable camber and planform wing morphing. It depicted that medium size airliners will be almost 50% off all air vehicles entering service from 2030. It enforced additional efforts on a right identification of relations between solutions to start their evaluations.

Having listed the all descriptive parameters and variants in the matrix represented in Table 3, the incompatible configurations were decided to be the following:



1. d1.1 Aeroplane Fuselage, None – Flying Wing
 - a. d1.1 x d2.4 – Aerofoil Morphing, Entire Camber
 - b. d1.1 x d3.3 – Planform Morphing, Non-uniform Span
 - c. d1.1 x d4.2 – Planform Morphing, Forward Sweep
 - d. d1.1 x d4.3 – Planform Morphing, Backward Sweep
 - e. d1.1 x d5.2 – Out-of-plane Morphing, Straight Dihedral
 - f. d1.1 x d5.3 – Out-of-plane Morphing, Tip Dihedral
 - g. d1.1 x d5.4 – Out-of-plane Morphing, Gull
2. d5.4 Out-of-plane Morphing, Gull
 - a. d5.4 x d1.1 – Aeroplane Type, No Fuselage – Flying Wing
 - b. d5.4 x d1.1 – Aeroplane Type, Two Fuselages
 - c. d5.4 x d4.2 – Planform Morphing, Forward Sweep
 - d. d5.4 x d4.3 – Planform Morphing, Backward Sweep
 - e. d5.4 x d4.4 – Planform Morphing, Oblique Sweep

Further, the overall number of conflicting solutions gave the total of 264, what by taking out all of them from the available solution of morphological box, left 312 feasible solutions out of initial 576. There will be also performed an additional analysis to confirm the CCA task was performed correctly by confronting the performance of removed configurations. Out of remaining 312 solutions, 156 were compatible for d1.2 an aeroplane type with one fuselage. Moreover, for the purpose of maximisation the performance analysis in order to satisfy benchmark criterion, there were further eliminated all non-morphing solutions from the morphological space, such as d2.1 – Zero Aerofoil Camber Morphing, d3.1 – Zero Planform Span Morphing, d4.1 – Zero Planform Sweep Morphing and d5.1 – Zero Out-of-plane Dihedral/Gull Morphing. Having done that, the final 36 solutions were obtained for one fuselage aeroplane, extended to 72 solutions. To give some more details, the following 6 solutions were decided for further consideration as an initiation point of morphological space analysis:

- 1) d1.2 x d2.4 x d3.2 x d4.2 x d5.2: Wing with entire camber morphing aerofoil that can uniformly expand span and transform to forward swept position at straight dihedral angle.
- 2) d1.2 x d2.4 x d3.2 x d4.2 x d5.3: Wing with entire camber morphing aerofoil that can uniformly expand span and transform to forward swept position at wing tips dihedral angle.
- 3) d1.2 x d2.4 x d3.2 x d4.3 x d5.2: Wing with entire camber morphing aerofoil that can uniformly expand span and transform to backward swept position at straight dihedral angle.
- 4) d1.2 x d2.4 x d3.2 x d4.3 x d5.3: Wing with entire camber morphing aerofoil that can uniformly expand span and transform to backward swept position with wing tips at dihedral angle.
- 5) d1.2 x d2.4 x d3.3 x d4.3 x d5.3: Wing with entire camber morphing aerofoil that can non-uniformly expand span and transform to backward swept position with wing tips at dihedral angle.
- 6) d1.2 x d2.2 x d3.2 x d4.3 x d5.3: Wing with leading edge camber morphing aerofoil that can uniformly expand span and transform to backward swept position with wing tips at dihedral angle.

Table 4: Cross-Consistency Assessment for the developed Morphological Analysis Field

1 Compatible Solution 0 Incompatible Solution				d1 Aeroplane – Number of Fuselages			d2 Aerofoil – Morphing Camber			d3 Planform – Morphing Span			d4 Planform – Morphing				d5 Out-of-plane – Morphing Dihedral/Gull																				
		None - Flying Wing		One		Two		None		Leading Edge		Trailing Edge		Entire Camber		None		Uniform		Non-Uniform		None		Forward		Backward		Oblique		None		Straight Dihedral		Tip Dihedral		Gull	
d1	d1.1	d1.2	d1.3	d2.1	d2.2	d2.3	d2.4	d3.1	d3.2	d3.3	d4.1	d4.2	d4.3	d4.4	d5.1	d5.2	d5.3	d5.4																			
	d1.1	1																																			
	d1.2	0	1																																		
	d1.3	0	0	1																																	
d2	d2.1	1	1	1	1																																
	d2.2	1	1	1	0	1																															
	d2.3	1	1	1	0	0	1																														
	d2.4	0	1	1	0	0	0	1																													
d3	d3.1	1	1	1	1	1	1	1	1																												
	d3.2	1	1	1	1	1	1	1	0	1																											
	d3.3	0	1	1	1	1	1	1	0	0	1																										
d4	d4.1	1	1	1	1	1	1	1	1	1	1	1																									
	d4.2	0	1	1	1	1	1	1	1	1	1	0	1																								
	d4.3	0	1	1	1	1	1	1	1	1	1	0	0	1																							
	d4.4	1	1	1	1	1	1	1	1	1	1	0	0	0	1																						
d5	d5.1	1	1	1	1	1	1	1	1	1	1	1	1	1	1																						
	d5.2	0	1	1	1	1	1	1	1	1	1	1	1	1	0	1																					
	d5.3	0	1	1	1	1	1	1	1	1	1	1	1	1	0	0	1																				
	d5.4	0	1	0	1	1	1	1	1	1	1	1	0	0	0	0	0	1																			

- 7) d1.2 x d2.4 x d3.2 x d4.2 x d5.2: Wing with entire camber morphing aerofoil that can uniformly expand span and transform to forward swept position at straight dihedral angle.
- 8) d1.2 x d2.4 x d3.2 x d4.2 x d5.3: Wing with entire camber morphing aerofoil that can uniformly expand span and transform to forward swept position at wing tips dihedral angle.
- 9) d1.2 x d2.4 x d3.2 x d4.3 x d5.2: Wing with entire camber morphing aerofoil that can uniformly expand span and transform to backward swept position at straight dihedral angle.

- 10) d1.2 x d2.4 x d3.2 x d4.3 x d5.3: Wing with entire camber morphing aerofoil that can uniformly expand span and transform to backward swept position with wing tips at dihedral angle.
- 11) d1.2 x d2.4 x d3.3 x d4.3 x d5.3: Wing with entire camber morphing aerofoil that can non-uniformly expand span and transform to backward swept position with wing tips at dihedral angle.
- 12) d1.2 x d2.2 x d3.2 x d4.3 x d5.3: Wing with leading edge camber morphing aerofoil that can uniformly expand span and transform to backward swept position with wing tips at dihedral angle.

The computational performance evaluation was split across all described morphing segments to get an understanding of how different solutions generated contribute towards the performance improvement. The benchmark study was selected to be RQ-21A Blackjack UAS introduced in 2014, an unmanned aerial surveillance vehicle produced by Boeing Insitu, with the capabilities of the maximum endurance of 16h with operating up to ceiling of 20,000ft [24]. RQ-21A creates an ideal benchmark plane to understand how wing morphing could improve its overall performance as its fuselage design allow the wing to be easily replaced if further wind tunnel analysis was required, as represented in Figure 1. For the study the aerofoil shape was assumed to be NACA 0012 and the specifications of wing with removed winglets were increased by factor 1.6 for chord and 1.531 for wing span to simplify the computational analysis.

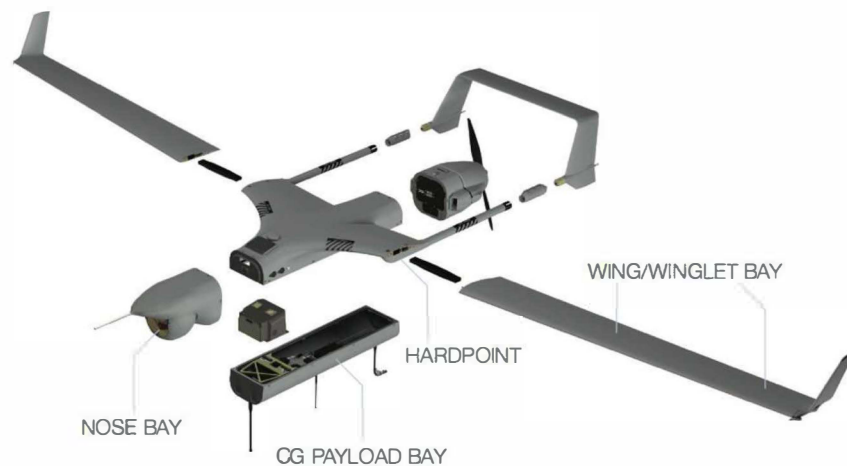


Figure 1: RQ-21A [24].

Table 5: RQ-21A [24] wing parameters used for the optimisation process.

Wing Span	4.9	m	7.5	m	+53.1%
Chord	0.3125	m	0.5	m	+60%
Aspect Ratio	15.68		15.0		-4.3%
Taper Ratio	1		1		
Total Length	2.5	m	4	m	+60%
OEW	36.7	kg	58.7	kg	+60%
MTOW	61	kg	97.6	kg	+60%
Max Payload	17.7	kg	28.3	kg	+60%

A similar investigation has been conducted in [25] taking BQM-34 Firebee UAV as the study scope. In order to learn and compare the results, similar settings for Mach numbers were used at the selected mission profile segments presented in Table 6. An extended set of simulations were carried out using

XFLR with the initial configuration allowing a comparison of the different design solutions discussed in Tables 3,4.

Table 6: Testing conditions for selected benchmark mission profiles.

Mission Segment	Unit	Take-off	Range			Endurance	
Altitude	ft	0	0	29520	59040	29520	59040
	m	0	0	9000	18000	9000	18000
Mach No.		0.2	0.3	0.6	0.7	0.7	0.7
Speed at SL	m/s	340.3	340.3	303.8	295.1	303.8	295.1
Speed at altitude	m/s	68.06	102.09	182.28	206.57	212.66	206.57
Reynold No.	$\times 10^6$	2.33	3.49	2.85	0.88	3.33	0.88
Test Reynolds No.	$\times 10^6$	2.50	3.50	3.00	1.00	3.50	1.00

A number of airfoils were analysed the best performance being achieved for NACA6412 and FX74-CL5-140 aerofoils, having 6% and 10% effective camber respectively. The greatest improvement has been observed across 4 and 6% camber for high-altitude endurance and high-altitude range achieving between 40-100% improvements giving superior results, with NACA6412 having better performance than FX74-CL5-140 in all range related missions. From previous evaluations the cases selected were "d3.2, d4.2, d5.2"; (2) "d3.2, d4.2, d5.3"; (3) "d3.2, d4.3, d5.2" and (4)/(6) "d3.2, d4.3, d5.3". The testing constraints were set at Reynolds No. 3×10^6 to resemble flight conditions of Mach No. 0.25 at sea-level altitude or Mach No. 0.6 at MA, medium altitude 9000m as introduced within aerofoil optimisation. The benchmark aerofoil has been selected as NACA6412 to provide the most optimal effective camber performance without the need of achieving 10% effective camber. The results have been constrained for 1/3 AR, aspect ratio increase up to 20 from initial AR 15, and 2/3 increase of AR up to 25. The taper ratio has been set as 1, chord length at constant 0.5m and the inertia of the wing has been selected at one-quarter chord length with corresponding 1/3 and 2/3 OEW weight increase for AR 20 and AR 25 from initial OEW.

The results were obtained for tip to root sweep angle Λ varied from -15° forward sweep angle, d4.2 up to 30° backward sweep angle, d4.3 and dihedral angle Γ that was varied for straight alteration, d5.2 up to 10° and 45° wing tip, d5.3. The 1/3 increase of AR from 15 to 20 has shown the increase in both range and performance factors of +36% and +40% respectively. The computational analysis in Xfoil for aerofoil morphing in Reynold No. between 1.00×10^6 - 3.50×10^6 showed a great advantage of an effective camber transformation from 0% to up to 6% for range and 10% for endurance improvement. Further use of flow control such as AHLE MOLEC could enhance lift improvement by at least 95% when compared to traditional Kruger flaps in take-off segment. XFLR5 was used to perform a comparison of different planform for Reynold No. 3.0×10^6 that has shown up to 140-180% improvement across all mission segments when allowing 2/3 aspect ratio expansion, root to sweep angle variation between -15° and 15° , straight dihedral of $0-10^\circ$ and tip dihedral of up to 45° .

5 CONCLUSIONS

An initial study for performance improvement using airfoil, planform and out-of-plane shape morphing has been carried out using the Morphological Analysis giving a set of 576 possible solutions based on the aerodynamic performance calculations, the mass constraints and actuators capability not being considered. A reduced set of configurations allowed the analysis of performance obtained through different morphing options in combinations as derived using the Morphological Analysis.

REFERENCES

1. J. Sun, Q. Guan, Y. Liu, 2016, "Morphing Aircraft Based on Smart Materials and Structures: A State-of-the-Art Review", *Journal of Intelligent Material Systems and Structures*, **27**(17), pp. 2289-2312
2. S. Barbarino, O. Bilgen, R.M. Ajaj, M.I.Friswell, D.J. Inman, 2011, "A Review of Morphing Aircraft", *Journal of Intelligent Material Systems and Structures*, **22**(9), pp. 823-877

3. S. Slesongsom, S. Bureerat, K. Tai (2013), "Aircraft morphing wing design by using partial topology optimization", *Structural and Multidisciplinary Optimization*, **48**(6), pp. 1109-1128
4. S. Vasista, L. Tong, K.C. Wong, 2012, "Realization of Morphing Wings: A Multidisciplinary Challenge", *Journal of Aircraft*, **49**(1), pp. 11-28
5. C. Bill, K. Massey, E. J. Abdullah, 2013, "Wing Morphing Control with Shape Memory Alloy Actuators", *Journal of Intelligent Material Systems and Structures*, **24**(7), pp. 879-898
6. A.Y.N. Sofla, S.A. Meguid, K.T. Tan, W.K. Yeo, 2010, "Shape Morphing of Aircraft Wing: Status and Challenges", *Materials and Design*, **31**(3), pp. 1284-1292
7. F. Zwicky, 1969, "Discovery, Invention, Research Through the Morphological Approach", MacMillan
8. J. Drzewoszewski, 2017, "Morphological Design Analysis and Development of Aircraft Wings", BSc Aerospace Engineering Dissertation, Supervisor C. Mares, Brunel University London, College of Engineering, Design and Physical Sciences, Mechanical, Aerospace and Civil Engineering
9. P.Y. Chen, J. McKittrick, M.A. Meyers, 2012, "Biological Materials: Functional Adaptations and Bioinspired Designs", *Progress in Materials Science*, **57**(8), pp. 1492-1704
10. R.J. Shaw, 2014, "History of Flight". Available at: <https://www.grc.nasa.gov/www/k-12/UEET/StudentSite/historyofflight.html>. (Accessed: 17/04 2017)
11. L.M. Nicolai, G. Carichner, 2001, "Fundamentals of Aircraft and Airship Design", *American Institute of Aeronautics and Astronautics*
12. Y. Gibbs, 2015, "NASA Armstrong Fact Sheet: X-5 Research Aircraft", Available at: <https://www.nasa.gov/centers/armstrong/news/FactSheets/FS-081-DFRC.html>. (Accessed: 03/15 2017)
13. B.I. Larrimer, 2013, "Thinking Obliquely: Robert T. Jones, the Oblique Wing, NASA's AD-1 Demonstrator, and Its Legacy". *National Aeronautics and Space Administration*
14. D.P. Grant, 1975, "How to Construct a Morphological Box", *Design Methods and Theories*, **11**(3)
15. T. Ritchey, 1998, "General Morphological Analysis, A General Method for Non-Quantified Modelling", *16th Euro Conference on Operational Analysis*, Brussels
16. T. Ritchey, 2015, "Principles of Cross-Consistency Assessment in General Morphological Modelling", *Acta Morphologica Generalis*, **4**
17. Xfoil, Available at <http://rafael.mit.edu/xfoil>. (Accessed 03/15/2017)
18. XFLR, Available at <http://www.xflr5.com>. (Accessed 03/15/2017)
19. D. Neal, J. Farmer, D. Inman, 2006, "Development of a morphing aircraft model for wind tunnel experimentation", *47th AIAA/ASME/ASCE/AHS/ASC Structures, Structural Dynamics, and Materials Conference 14th AIAA/ASME/AHS Adaptive Structures Conference 7th.*, 2141
20. R.M. Ajaj, E.I. Saavedra Flores, M.I., Friswell, G., Allegri, B.K.S. Woods, A. T. Isikveren, W.G. Dettmer, 2012, "The Zigzag wingbox for a span morphing wing", *Aerospace Science and Technology*, **28**(1), pp. 364-375
21. R.A. Shelton, A. Tomar, J. Prasad, M. Smith, N. Komerath, N., 2006, "Active multiple winglets for improved unmanned-aerial-vehicle performance", *Journal of Aircraft*, **43**(1), pp. 110-116
22. M. Abdulrahim, R. Lind, 2004, "Flight testing and response characteristics of a variable gull-wing morphing aircraft", *AIAA Guidance, Navigation, and Control Conference and Exhibit*
23. M.K. Bradley, C.K. Droney, 2011, "Subsonic Ultra Green Aircraft Research: Phase I Final Report", Hampton, Virginia: National Aeronautics and Space Administration Langley Research Center
24. InsituInc, 2016, *RQ-21ABlackjack*,
https://insitu.com/images/uploads/pdfs/RQ21ABlackjack_SubFolder_Digital_DU100616.pdf: (Accessed 03/15/2017)
25. S.P. Joshi, Z. Tidwell, W.A. Crossley, S. Ramakrishnan, 2004, "Comparison of morphing wing strategies based upon aircraft performance impacts", *45th AIAA/ASM/ASCE/AHS/ASC/Structures, Structural Dynamics and Materials Conference*, Palm Spring, California, pp. 2348-2354.

The flow separation development analysis in subsonic and transonic flow regime of the laminar airfoil

R. Placek and P. Ruchala
Institute of Aviation
Specialist, Assistant
Al. Krakowska 110/114, 02-256 Warsaw, Poland
robert.placek@ilot.edu.pl
pawel.ruchala@ilot.edu.pl

ABSTRACT

Wind tunnel tests of a laminar airfoil have been performed at the Institute of Aviation in Warsaw. The main goal of the investigation was to study the separation process development in subsonic and early transonic flow regime. The airfoil chord was 0.2 m. During wind tunnel test the natural laminar-turbulent transition was applied. The Mach numbers were 0.3 and 0.7. Reynolds number were approximately equal to $1.22 \cdot 10^6$ and $2.85 \cdot 10^6$ respectively. The angle of incidence was increased up until the flow was fully separated. During the experimental research, chosen test methods such as pressure measurements and Schlieren visualization were applied. Wind tunnel results were analyzed in terms of aerodynamic coefficients and flow separation type identification. The wind tunnel investigation revealed that separation phenomena at subsonic and transonic flow regime affected in a different manner on the airfoil aerodynamic performance. This was mainly because of the change of the flow pattern influencing on the separation process.

KEYWORDS: *laminar airfoil, separation, experiment, subsonic, transonic*

Investigation of viscosity influence on transonic flutter

S. Kuzmina

*Leading research scientist, Central Aerohydrodynamic Institute n.a. Prof. N.E. Zhukovsky (TsAGI)
Aeroelasticity Department
Zhukovsky, Russia
Email: kuzmina@tsagi.ru*

F. Ishmuratov

*Head of Division, Central Aerohydrodynamic Institute n.a. Prof. N.E. Zhukovsky (TsAGI)
Email: stataer@tsagi.ru*

A. Chizhov

*Junior research scientist, Central Aerohydrodynamic Institute n.a. Prof. N.E. Zhukovsky (TsAGI)
Email: stataer@tsagi.ru*

O. Karas

*Senior research scientist, Central Aerohydrodynamic Institute n.a. Prof. N.E. Zhukovsky (TsAGI)
Email: stataer@tsagi.ru*

ABSTRACT

The paper is devoted to computational study of transonic flutter when the viscosity can influence significantly on dynamic aeroelasticity characteristics of aircraft. The work has been done in the direction of development of methodology and software, which are used in ARGON (TsAGI) system for multidisciplinary analysis and optimization in airplane design. Considerable attention is paid to the validation of the proposed software. Experimental results of the NASA Common Research Model in the European Transonic Wind Tunnel (ETW) are used for comparison with computations. The results of flutter analysis are presented for the passenger middle range airplane with the high aspect ratio wing and the engine under the wing. Comparisons of aeroelasticity characteristics in transonic flow are carried out for cases of a set of Mach and Reynolds numbers. The computational results presented in the paper show the essential influence of transonic features on flutter characteristics.

KEYWORDS: *flutter, aeroelasticity, viscosity, Reynolds number*

Flight Test Design for Remotely-Piloted Aircraft in Confined Airspace

Alejandro Sobron, David Lundström, Petter Krus
Department of Management and Engineering
Linköping University
SE-58183, Linköping, Sweden
alejandro.sobron@liu.se

Christopher Jouannet
SAAB Aeronautics
SE-58254, Linköping, Sweden

Luiz C.S. Góes
Instituto Tecnológico de Aeronáutica
12228-900, São José dos Campos (SP), Brazil

ABSTRACT

This paper presents various techniques and procedures that aim to simplify flight testing of fixed-wing, remotely-piloted aircraft with the purposes of performance evaluation and system identification. These methods have been specifically developed for flight within visual line-of-sight, a type of operation that limits the available airspace severely but offers major cost advantages considering the current regulations for unmanned flight in most Western countries.

KEYWORDS: *flight testing, visual line-of-sight, UAS, data acquisition, flight dynamics*

1 INTRODUCTION

According to the current regulatory frameworks for unmanned aircraft systems (UAS) in most European countries, there is in most cases a considerable economic and logistical step between certified operations within visual line-of-sight (VLOS) and beyond visual line-of-sight (BVLOS). Low-cost equipment for BVLOS operations is nowadays available in the market and it is often used even by hobbyists for recreational purposes according to model flying regulations. However, for certified commercial or research operations of remotely-piloted aircraft (RPA), most aviation authorities still require the use of a segregated airspace. The cost of such airspace plus the eventual certification of the relevant aircraft systems often motivates the choice of a much more affordable VLOS certification.

Flight testing fixed-wing RPA in general, and under VLOS rules in particular, requires different approaches than those traditionally followed by manned aircraft. The reduced testing time, the need for constant manoeuvring and the difficulty of executing precise excitation manoeuvres are just some of the factors that complicate the process severely.

1.1 Typical Regulatory Scenario

At this time there is no international or European standard regulating the operations of civil UAS, although work in this direction is progressing quickly [1]. According to the European Aviation Safety Agency (EASA), the regulation of UAS with a maximum take-off mass (MTOM) of less than 150 kg currently falls within the competence of each state. However, for the kind of operations and limitations that concern this paper, there seems to be a comparable framework within most Western countries. In this case, the current Swedish regulation of civil UAS [2] is taken as reference.

Conforming to this regulation, any civil UAS operation that is not carried out solely for recreational purposes needs a platform-specific authorization and a different set of safety elements in consonance with the corresponding category. There are currently four different categories which take into account both the proximity of operation (VLOS or BVLOS) and system characteristics such as mass and maximum kinetic energy. Fig. 1 shows qualitatively the tremendous operating cost increase associated with BVLOS operations, mainly caused by two safety factors: the requirement of some sort of type certification, and the necessity of booking a segregated airspace. The significant cost difference often motivates the choice of VLOS operation, at least during the phases of development and flight testing.

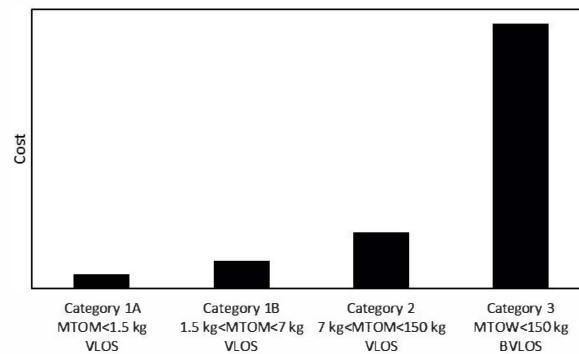


Figure 1: Qualitative comparison of operating cost between the four civil UAS categories according to the current Swedish regulation. The description of the categories has been simplified and the cost figures are based on estimations.

1.2 Purposes of Flight Testing RPA

As usual in manned aircraft, flight testing is an unavoidable stage of UAS development. Besides a qualitative assessment of the flying qualities, quantitative measurements are possible by means of sensor data acquisition and processing. Flight tests can be designed to evaluate the performance of the platform and its systems, but also to obtain its flight-mechanical characteristics through system identification. This information is critical to validate or to improve simulation models and flight control systems. Testing autonomous navigation and communication systems is in many cases only relevant during flight BVLOS. Autonomous flight is therefore disregarded here since no real advantage can be expected from testing these within VLOS.

There is also an increasing use of remotely-piloted subscale demonstrators for research and development; see reference [3] for a good overview. This method, often referred to as *subscale flight testing*, is based on studying the performance and dynamics of a scaled model in order to increase the knowledge and confidence over an eventual full-scale design. The final purpose of the platform is, therefore, the flight testing itself. As a complementary design tool, the short development time and cost savings associated with VLOS operation become even more relevant. However, flight testing in a very confined airspace can become challenging when the test objects are heavy and large dynamically-scaled models such as in [4], [5] and [6]. The latter, shown in Fig. 2, is with 20 kg of MTOM one of the heaviest fixed-wing platforms used for research at Linköping University. Its high flying speed makes it a challenging case for flight testing within VLOS, and therefore it is used as an application example throughout this paper.



Figure 2: The *GFF* demonstrator: a 2-meter, jet-powered platform used for research at Linköping University [6].

2 METHODOLOGY

The ideas, techniques or procedures proposed here do not originate from a particular methodology. Some of them have been adapted from existing "full-scale" industry practices and more traditional techniques found in the literature. Others are based on the authors' experience in UAS operation or inspired by radio-controlled model flying techniques. However, the ideas presented here have proven, in the authors' opinion, to be of practical use for this kind of flight testing using different platforms. All these techniques have been either systematically evaluated through experimentation, or are currently being tested and refined.

3 FINDINGS

For the sake of clarity, the results are grouped and discussed into separated topics.

3.1 Essential Flight Test Instrumentation

In the case that the test object is a platform designed for autonomous or semi-autonomous flight, measurements can be acquired directly from the installed sensors and/or existing flight controller. If the platform is not aimed towards autonomous flight, it has to be equipped with an additional data acquisition system. Low-cost data acquisition systems are nowadays able to provide reliable flight data thanks to relatively advanced sensor-fusion and flight path reconstruction algorithms, some of which are included even in open-source distributions such as [7]. In fact, algorithms used in open-source autopilot projects can be sometimes useful for data acquisition during tests within VLOS since they are already well tuned for small platforms with very fast dynamics and turbulent environments. See reference [8] for a previous development at Linköping University.

An accurate GPS (or equivalent) positioning system is strongly recommended for flight tests within VLOS. This kind of flight involves constant manoeuvring and quick changes of trajectory and speed. Precise position measurements at a rate of at least 5 Hz facilitate considerably flight path reconstruction. GPS augmentation methods such as Real Time Kinematic (RTK) systems are ideal for this purpose.

In addition, the authors recommend to include flow angle transducers in the data acquisition system. Although there are relatively accurate flow-angle estimation techniques such as [9], it has been observed that direct measurements of the flow properties ease and improve considerably the data analysis, especially in the case of the highly-dynamic flight testing within VLOS. The *Instituto Tecnológico de Aeronáutica* has experience with 5-hole pressure probes, while Linköping University typically uses custom-made flow angle vanes such as in [6], Fig. 3.

Another consideration is to provide means to increase the awareness of the actual aircraft airspeed to the pilot. Initial (or entrance) airspeed is often an important parameter that has to be set appropriately before each manoeuvre execution. This can be sometimes difficult to assess by a remote pilot due to the lack of visual clues and the energy losses during the tight turns. To avoid loss

of visual contact with the platform, the most straightforward solution is to read out loud the incoming airspeed values from the ground station. The authors are also testing a new system that transforms airspeed values received via telemetry into beeping sounds of variable pitch, in a similar way to the electronic variometers typically found in gliders.

Regarding communication links between air and ground, these can be kept uncomplicated since the platform is continuously within VLOS: high-power transmitters or tracking antennas are usually not needed. Again, this is a significant advantage in terms of cost and simplicity.



Figure 3: Direct measurement of the flow conditions improves significantly the flight reconstruction. Image shows a custom-made airdata nose-boom with alpha and beta transducers installed on the *GFF* platform.

3.2 Flight Test Crew

In some cases, the minimum personnel and roles to be covered are specified by the respective regulation. Besides this, the minimum crew required is often determined by the platform characteristics and specific logistical needs. However, even with the smallest and simplest of the platforms, the authors have identified that to carry out a flight test in VLOS it is needed an absolute minimum of three people: test conductor, pilot, and safety manager. An additional ground station operator must be added in the case that this exists. Although the chain of persons carrying out the test should be kept as straightforward and direct as possible, additional crew members can facilitate significantly tasks like test documentation and surveillance of the test area.

3.3 Facilities

Since no segregated airspace is required, flight testing within VLOS can take place in a much broader range of airfields and suitable areas. Model-flying clubs are often a convenient and affordable choice. Ultimately, the characteristics of the platform and team logistics will determine the most appropriate option. However, the local regulation might set specific guidelines or eventual restrictions, as it will be discussed later in 3.5.

3.4 Flight Test Planning

Although for organizations used to operating larger platforms or familiarised with aircraft certification this point could seem obvious, the authors would like to mention the importance of defining a precise flight test plan with specific step-by-step instructions. This practice is often forgotten to some extent during test campaigns with small platforms mainly due to the very low cost-per-flight-hour. However, it remains as one of the easiest and most effective ways of improving the efficacy, safety, and documentation of flight tests, especially with hard constraints in airspace and time frame.

In a nutshell, the authors recommend the following procedure: according to the project's general flight test programme (if this exists) or logistical considerations, it usually possible to define a feasible number of flights per session. Once the available test-time per flight is known or estimated, the

intended manoeuvres have to be translated into individual test points or "positions". For each flight, it is convenient to write down the sequence of test points in a one-page document, together with other relevant information such as aircraft configuration and desired flight conditions. The order of the test points must be chosen carefully to balance the flight, save time, and account for eventual variable factors such as fuel weight. Finally, a flight test card containing all the relevant information has to be prepared for each one of the test points, as the example shown in Fig. 4. Experience has shown that it is convenient to prepare also alternative "b" test sequences in case that necessary parts of a previous sequence cannot be completed.

Standardised flight test cards streamline considerably the communication between the pilot and the test conductor. During the flight, the test conductor reads out the respective test card to the pilot, mentioning clearly the desired initial conditions at the beginning of the manoeuvre. In this way, mistakes are minimised and the pilot does not lose visual contact with the aircraft at any time. In addition, the test conductor can write down on the test card any eventual observation that needs to be documented.

These procedures are nevertheless very similar to traditional practices used in "full-scale" flight testing. See for example references [10] and [11] for more ideas and further information.

Position	Altitude	Speed	Header	Config.	Fuel	Test type
1	100 m	40 m/s	50 %	Sys. Identification
Manoeuvre description Relevant configuration ...				Notes ...		

Figure 4: Example of a generic flight test card.

3.5 Management of the Available Airspace

The airspace available in flight within VLOS is extremely limited. While the maximum allowed distance between the aircraft and the pilot is ultimately determined by the definition of VLOS, the most common presumption is 500 meters. The maximum allowed flight altitude is usually 120 meters above ground level (AGL), although this might vary according to local airspace rules or eventual temporary clearances by the air traffic control services. These results in a cylindrical airspace of very limited dimensions, in which is often difficult to deal with fast-flying platforms with high wing-loadings such as the mentioned GFF demonstrator. Another important disadvantage is that the flight takes place close to the ground, i.e. in the most turbulent atmospheric layer. Hence, flight within VLOS often requires calm wind conditions for successful test results.

According to the regulations, this airspace cannot cover any populated area at the time of the test. Consequently, the ground covered by this airspace – plus a defined safety margin – must be kept free of any persons outside the test crew. The responsibility of keeping this area clear lies on the safety manager. Since it could be difficult to monitor the entire area, the authors recommend using only half of the cylindrical airspace, as it is usually done in model flying clubs. This decision should be agreed during the pre-flight planning according to practical criteria such as visibility, sun position, and wind direction.

Once the testing team location and active runway have been decided, it is important to agree on visual references for external the safety area, the intended manoeuvring area, and the test window. For the latter, the runway itself is often a convenient reference. Fig. 5 shows these areas over the trajectory of a flight test in VLOS performed with the *GFF* demonstrator.

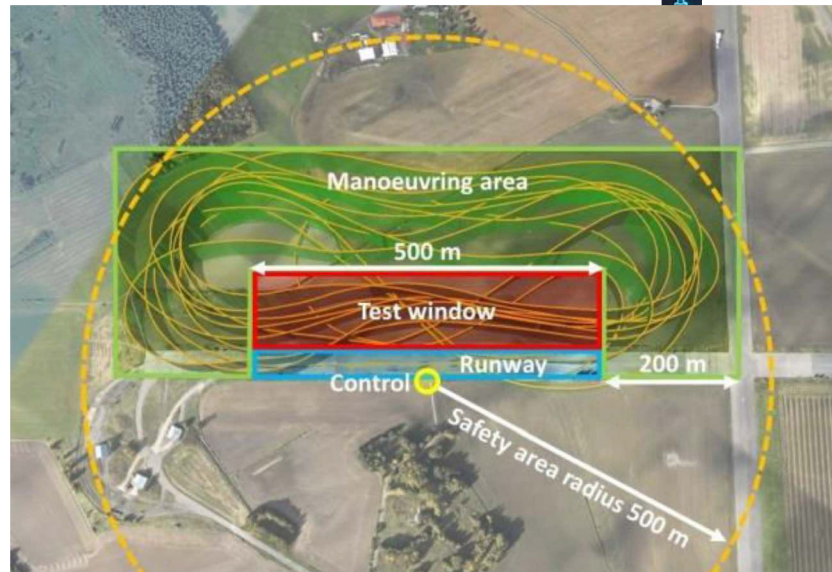


Figure 5: Trajectory followed during a real flight test under VLOS rules carried out with the *GFF* platform. The coloured polygons help to visualize the precise management of the very limited airspace.

3.6 Automation of the Excitation Manoeuvres

Probably the most significant contribution of this work is a novel method for commanding pre-programmed excitation manoeuvres automatically, without the need of any closed-loop flight controller or any ground station. This means that only a minimum equipment – a radio control system and a data logger – is needed to take full advantage of precisely-executed input signals on any of the control surfaces. On one hand, this benefits the smallest, low-cost platforms by saving further costs and simplifying their development. On the other, it allows more complex platforms to perform automated flight test manoeuvres even before the automatic flight control system is correctly tuned.

In fact, it is possible to program full sequences of test points covering the entire flight test plan. As a result, the pilot can focus on the challenging task of flying the aircraft through the manoeuvring area and entering the test window at the required speed, altitude and attitude.

This "magic" is possible thanks to the latest software developments in computerized radio-control transmitters: motivated by the hobby market demands, some manufacturers have equipped their transmitters with the possibility of interpreting and executing custom scripts written in *Lua* programming language [12]. Although these scripts are mainly used by the public to visualize in sophisticated ways information from the sensors on board the model aircraft, the authors explored the possibilities of using them to actuate the controls following complex signals.

The result is a *Lua* application that allows the testing team to assemble easily an entire sequence of testing points, both using a computer or directly on the transmitter screen. The application uses an external library of input signals that can be updated independently at any moment. Both analytically-described functions and discrete point-defined signals can be loaded. During the flight, the pilot selects the corresponding test point and triggers the manoeuvre by flipping a switch. The corresponding signals will be then executed on the intended control surfaces according to the specified timing and recurrence. An information window can also be displayed on the transmitter's main screen, showing the test point status and any eventual errors, Fig. 6. In addition, audible signals and commands are played out through the transmitter's speakers so the pilot does not need to lose visual contact with the aircraft.

Several safety measures have been incorporated during the development of the application in order to avoid any sort of malfunction to affect the platform. Ultimately, the pilot can always regain manual control of the aircraft at any time by releasing the trigger switch.

Due to hardware limitations, the signals can be transmitted at a maximum frequency of 50 Hz at the moment. However, this is the same order of magnitude than the typical refresh rate of the radio-control link (from 50 Hz to 100 Hz) and the servo-actuators (about 50 Hz).

This application is still under continuous development at Linköping University, but so far it has been tested on real flight tests with excellent results. Ideally, the authors would recommend configuring the application settings during the development of the flight test plan. This specific copy of the code can be kept as part of the electronic documentation of each flight.



Figure 6: Information window of the custom *Lua* application for flight test, displaying the automatic execution of a test point. The screenshots are extracted from the main screen of the pilot's transmitter, in this case a *Jeti Model DC-24* [13].

3.7 Use of Highly Efficient Input Signals

The following Fig. 7 shows the maximum time that an aircraft remains in a 500 m test window in straight flight. Manoeuvres with very long exposure time, such as the measure of the phugoid motion, are usually not possible under VLOS rules. On the contrary, given the reduced dimensions of the test window, the manoeuvres need to produce as much information as possible in a very short time.

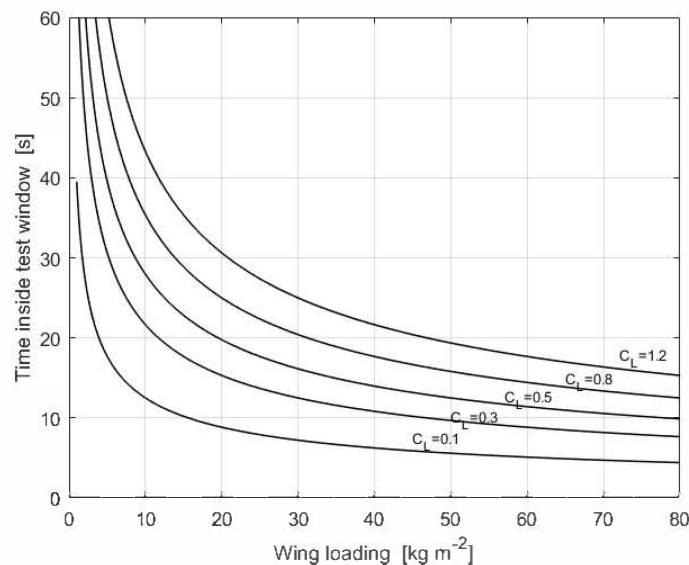


Figure 7: Estimated time to cross a 500 m test window in straight flight.

Focusing on flight testing for system identification, it is beneficial to optimize the excitation inputs from the beginning. An estimation of the expected responses should be obtained from previous flights or from analytical analysis as in [14]. It is also important to further optimize the excitation inputs as soon as new estimations are available.

In fact, there are many different theories on efficient inputs for system identification in the literature. Although these are usually designed for manned aircraft, in most cases it is possible to adapt the techniques to smaller RPA by scaling the dynamic responses accordingly. So far the authors have obtained successful results in the time domain using somewhat-conventional manoeuvres such as pulses, doublets, and "3211" [14]. In the frequency domain, promising experiments are being performed following literature like [15] and [16]. These include inputs such as frequency sweeps along a wide frequency band.

The authors have also started to experiment with novel techniques for optimal input design, multi-sine signals, and simultaneous excitations. As an example, reference [17] describes the procedure to generate orthogonal optimised multi-sine inputs that combine the time efficiency of multi-axis excitation with optimised (minimum) input amplitudes, wideband frequency content, and multiple-input orthogonality in both the time domain and the frequency domain. Even though these techniques are mainly aimed towards shortening the costly flight-test of manned platforms, they could also become a good solution for highly-condensed flight testing within VLOS. However, at the time of writing this paper, it is still too early to offer solid results.

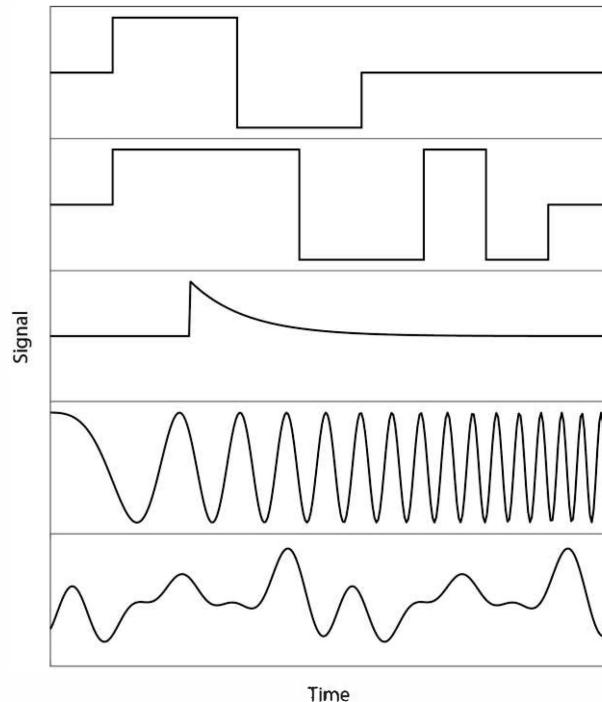


Figure 8: Various input signals generated directly by the radio transmitter using the *Lua* flight test application. From top to bottom: doublet, 3211, pulse with exponential decay, sinusoidal frequency sweep, and random-phase multi-sine.

3.8 Immediate Data Analysis and Feedback

Although this point is shared with any other kind of flight testing, increasing the awareness of the measurements' quality is a key factor for successful results. Ideally, the assessment of the incoming flight data quality and even the estimated aircraft parameters should be done in real time. This would allow, for example, taking corrective measures during flight and saving a significant amount of testing time [18]. Due to the usually-short duration of flights within VLOS and their relatively low cost-per-flight-hour, this does not seem a critical factor here. However, in the author's opinion, it is extremely useful to have the necessary resources to be able to download and analyse the logged data briefly at least between each flight. This provision has proven very useful preventing hardware failures, configuration mistakes, and unnecessary repetitions.

In the case of Linköping University, relevant parameters and system health are usually monitored in real time from a simple ground station: a light laptop running a modified version of the open-source software Mission Planner [19], linked with the platform through a variable-rate telemetry connection. In addition, a set of MATLAB scripts denominated ALAN have been developed in order to analyse, display, and export the flight data within seconds after the platform is shut-down. Nevertheless, both methods continue under constant development and evaluation.

4 CONCLUSIONS

The paper presents some of the most relevant "lessons learnt" from the authors' experience flight testing multiple platforms under the challenging VLOS rules.

Ideas for an efficient planning and execution are given. Specific equipment and procedures are recommended in order to improve the test efficacy and data collection. The authors also present a novel method for commanding automatically complex excitation manoeuvres directly from the radio-control transmitter, i.e. without the need of a closed-loop flight controller. The benefits of platform-specific, optimized excitation manoeuvres are briefly discussed.

In general, these recommendations are useful for economical flight testing of subscale demonstrators for research purposes, as well as for the evaluation and development of UAS under safe conditions. Some of the proposed methods, such as the remote manoeuvre automation, are also suitable for other types of flight testing BVLOS.

In conclusion, flight testing RPA within VLOS entails additional complications over conventional operations. The need for constant manoeuvring and the reduced testing time can become challenging limitations, especially with heavier platforms. However, there is a clear economic benefit that can motivate this choice. The authors continue working towards improving these and other techniques aiming to simplify this process.

ACKNOWLEDGEMENTS

The authors would like to express their gratitude to Roger Larsson from *SAAB Aeronautics*; his experience from the industry have brought very good ideas regarding flight-test planning and execution. Additionally, his expertise in input-manoevre optimization and multi-sine signals has opened a new and exciting path for further collaboration.

REFERENCES

1. European Aviation Safety Agency; 2017; "Introduction of a regulatory framework for the operation of drones, Notice of Proposed Amendment 2017-05 (A)"; https://www.easa.europa.eu/system/files/dfu/NPA2017-05{%28A{%29}_{_}0.pdf2
2. Transport Styrelsen (Swedish Transport Agency); 2017; "Obemannade Luftfartyg UAS: TSFS 2009:88, TSFS 2013:27 and TSFS 2014:45"; <https://www.transportstyrelsen.se/sv/luftfart/Luftfartyg-och-luftvardighet/Obemannade-luftfartyg-UAS/>
3. J. R. Chambers; 2009; "Modeling Flight: The Role of Dynamically Scaled Free-Flight Models in Support of NASA's Aerospace Programs"; NASA, Washington DC, USA.
4. T.L. Jordan and R.M. Bailey; 2008; "NASA Langley's AirSTAR Testbed: A Subscale Flight Test Capability for Flight Dynamics and Control System Experiments"; *AIAA Guidance, Navigation and Control Conference and Exhibit*; Honolulu, USA; August
5. Z. Goraj, K. Kitmann, R. Voit-Nitschmann and M. Szender; 2010; "Design and integration of flexi bird – a low cost sub-scale research aircraft for safety and environmental issues"; *27th Congress of International Council of the Aeronautical Sciences*; Nice, France
6. D. Lundström, A. Sobron, P. Krus, C. Jouannet and R.G.A. da Silva; 2016; "Subscale Flight Testing of a Generic Fighter Aircraft"; *30th Congress of the International Council of the Aeronautical Sciences*; Daejeon, South Korea
7. ArduPilot Dev Team; 2017; "ArduPilot open-source autopilot suite: Plane"; <http://ardupilot.org/plane/>
8. A. Sobron, D. Lundström, I. Staack and P. Krus; 2016; "Design and Testing of a Low-Cost Flight Control and Data Acquisition System for Unstable Subscale Aircraft"; *30th Congress of the International Council of the Aeronautical Sciences*; Daejeon, South Korea
9. E.A. Morelli; 2012; "Real-Time Aerodynamic Parameter Estimation Without Air Flow Angle Measurements"; *Journal of Aircraft*, vol. 49, no. 4; pp. 1064–1074
10. Various authors; 2005; "Introduction to Flight Test Engineering"; *AGARDograph*, Research and Technology Organisation (RTO) of NATO



11. R.D. Kimberlin; 2003; "Flight Testing of Fixed-Wing Aircraft"; *AIAA Education Series*, Reston, USA
12. Lua Dev community; 2017; "Official web site of the Lua programming language"; <http://www.lua.org/>
13. Jeti Model; 2017; "DC-24 Computerized Radio Control System" <http://www.jetimodel.com/en/katalog/Transmitters/@produkt/DC-24/>
14. R.V. Jategaonkar; 2006; "Flight Vehicle System Identification: A Time Domain Methodology"; *Progress in Astronautics and Aeronautics*, Volume 216; AIAA, Reston, USA
15. M.B. Tischler and R.K. Remple; 2006; "Aircraft and Rotorcraft System Identification"; AIAA, Reston, USA
16. V. Klein and E.A. Morelli; 2006; "Aircraft System Identification: Theory and Practice"; AIAA, Reston, USA
17. E.A. Morelli; 2012; "Flight Test Maneuvers for Efficient Aerodynamic Modeling"; *Journal of Aircraft*; vol. 49, no. 6; pp. 1857–1867
18. R. Larsson; 2013; "System Identification of Flight Mechanical Characteristics"; *Licentiate thesis*, Linköping University; Linköping, Sweden
19. M. Osborne and Dronecode Project Inc.; 2017; "Mission Planner open-source ground station software"; <http://ardupilot.org/planner/>



Helicopter Roll-Axis Instabilities induced by Pilot Cyclic Control: A Physical Explanation

Marilena D. Pavel

*Delft University of Technology, Faculty of Aerospace Engineering
Kluyverweg 1, 2629HS Delft, The Netherlands
m.d.pavel@tudelft.nl*

Achim Ionitã

*National Institute for Aerospace Research Elie Carafoli (INCAS)
Bulevardul Iuliu Maniu 220, Bucharest, Romania*

ABSTRACT

The main objective of this paper is to give a basic understanding of the mechanisms through which pilot cyclic inputs in lateral cyclic interacts with high-order rotor dynamics destabilizing the helicopter roll motion. The paper will use a "Newtonian formulation" representing the main forces acting on the airframe body-rotor system as the pilot applies his/her control. It will be demonstrated that pilot lateral controls applied through his/her arm (which may involve also pilot biodynamics, i.e. the dynamics of pilot neuromuscular inputs and contraction dynamics of his/her muscles) may excite much higher-order frequency rotor dynamics than thought at the present.

KEYWORDS

Helicopter, Pilot Assisted Oscillations, Rotorcraft Pilot Couplings, Lead-lag mode, Rotor dynamics



The studies on low-noise laminar wing aircraft for regional and short range routes

A.L.Bolsunovsky

Head of aerodynamic department

Central AeroHydroDynamic institute (TsAGI)

Zhukovsky 1, Zhukovsky, Moscow reg., Russia 140180, skomorohov@tsagi.ru

N.N.Bragin

Head of aerodynamic group

N.P.Buzoverya

Leading research scientist

I.L.Chernyshev

Head of perspective layouts department

ABSTRACT

Presented are recent studies conducted in TsAGI on regional and short range low-noise aircraft with natural laminar flow (NLF) transonic wings. At designing of such wings a distinct trade-off between laminar and turbulent mode of a flow, between viscous and wave drag amount and also between NLF and high lift characteristics has to be considered. A description of the special multicriterion optimization procedure for aerodynamic design of laminar wings developed by the authors is given. Several aerodynamic models were designed and manufactured for transonic wind tunnels testing including configurations with over-wing-trailing-edge engine arrangement which can reduce community noise and open the road to fuel-efficient ultra-high-bypass-ratio turbofans with large fan diameter on short range planes. Selected experimental results are also presented.

KEYWORDS: NATURAL LAMINAR FLOW, OVER-WING-TRAILING-EDGE ENGINE ARRANGEMENT, AERODYNAMIC DESIGN, MULTICRITERIAN OPTIMIZATION PROCEDURE, WIND TUNNEL TESTS

Numerical investigation of a new LH2 centrifugal pump concept used in space propulsion*Ion Mălăel**National Research and Development Institute for Gas Turbines COMOTI**Senior researcher**220 D Iuliu Maniu Bd., sector 6, cod 061126, OP 76, CP174, Bucharest, Romania**ion.malael@comoti.ro**Bogdan George Gherman**National Research and Development Institute for Gas Turbines COMOTI**Senior researcher**Ionuț Porumbel**National Research and Development Institute for Gas Turbines COMOTI**Senior researcher***ABSTRACT**

The present study deals with efficiency increase of a centrifugal pump for liquid rocket propulsion by using an innovative concept. With this new pump design the axial length will be reduced by 60% and 20% mass weight towards a classic two stage centrifugal pump. To estimate the performances, the CFD methods was used. The CFD analysis will be performed on 3D domains with the CFD commercial code ANSYS CFX. The numerical solvers used are pressure based with the SIMPLE method for RANS. The domain discretization was done by using dedicated grid generators like TurboGrid and Icem CFD. The results were compared with a classic configuration with two stages in series. Centrifugal pump characteristics, such as pressure inlet-outlet variation, velocity and streamline patterns are presented in the paper.

KEYWORDS: centrifugal pump, innovative design, liquid hydrogen, CFD.

Subsonic Jet Pump Comparative Analysis

George Bogdan GHERMAN

Scientific Researcher

*National Research and Development Institute for Gas Turbines COMOTI
220 D Iuliu Maniu Bd., sector 6, cod 061126, OP 76, CP174, Bucharest, Romania
bogdan.gherman@comoti.ro*

Florin FLOREAN

Scientific Researcher

Ionut PORUMBEL

Scientific Researcher

ABSTRACT

The paper presents the numerical and experimental studies carried out to optimize, from an aerodynamic point of view, a subsonic jet pump used on aircraft. The optimization of the subsonic jet pump will be done from the aerodynamic, aiming to re-design it such as to reduce as much as possible the emitted noise levels. For this, in a first stage, a parametric set of Reynolds Averaged Navier - Stokes numerical simulation was used on several possible designs, starting from an existing baseline, and including it. The goal was to identify the trends in the flow behavior when key baseline design parameters were varied. During the second stage, aerodynamic measurements were carried out on the two selected configurations and on the baseline configuration for the determination of the instantaneous flow velocity field. The measurements were carried out using cutting edge experimental measure techniques, namely Particle Image Velocimetry. The paper presents a comparison of the numerical and the experimental results and the conclusions of the analysis of the results.

KEYWORDS: *jet pump, subsonic, experimental test rig, RANS, efficiency calculation*

Experimental Approach Regarding the Ignition of H_2/O_2 Mixtures in Vacuum Environment

Jeni A. Popescu

Romanian Research and Development Institute for Gas Turbines COMOTI

Senior Researcher

220D Iuliu Maniu Bd., 061126, Bucharest 6

jeni.popescu@comoti.ro

Valeriu A. Vilag

Romanian Research and Development Institute for Gas Turbines COMOTI

Senior Researcher

Ionuț Porumbel

Romanian Research and Development Institute for Gas Turbines COMOTI

Senior Researcher

Cleopatra F. Cuciumita

Romanian Research and Development Institute for Gas Turbines COMOTI

Senior Researcher

Nicolae Macrișoiu

Romanian Research and Development Institute for Gas Turbines COMOTI

Senior Researcher

ABSTRACT

The paper, elaborated in the framework of the ESA activity "Green thruster for attitude control and orbital manoeuvres of small satellites (GREENTH)", focuses on the preliminary stages of an experimental program aiming to evaluate the feasibility and to increase the maturity level of a H_2/O_2 pulsed technology for small scale space propulsion applications. For demonstrating the capability of the H_2/O_2 mixture to be pulsed and ignited in a vacuum environment, the paper presents the main technical requirements, some addressing the thruster itself, related to system dimensioning, such as the nature of manoeuvres, the thrust level, the minimum impulse bit, the operating conditions, and some addressing the experimental campaign to be performed. The design of the experimental installation has taken into account the demands coming for the challenges and limitations raised by the small-scale satellites (telecommunications satellites or even CubeSats) applications, including vacuum system dimensioning, injection and ignition systems dimensioning and equipment and instrumentation specifications. The testing program covers the selected ranges of operational parameters and the operating sequences, for pulse mode and steady state tests, in order to determine the performance level and to evaluate the pulse repeatability, respectively to demonstrate the process stability.

KEYWORDS: *clean propulsion, vacuum, experimental setup*

Experimental studies on injection nozzle flame stability for gas turbines using in-situ combustion applications

Cleopatra Cuciumita

Romanian Research and Development Institute for Gas Turbines COMOTI

Senior Researcher

220 D Iuliu Maniu Bd., sector 6, 061126, Bucharest, Romania

cleopatra.cuciumita@comoti.ro

Daniel Olaru

Romanian Research and Development Institute for Gas Turbines COMOTI

Researcher

Marius Enache

Romanian Research and Development Institute for Gas Turbines COMOTI

Researcher

Florin Florean

Romanian Research and Development Institute for Gas Turbines COMOTI

Senior Researcher

ABSTRACT

This paper presents the experimental results of the test conducted on 3 different geometries for injection nozzles. The objective of these experimental studies was to determine the optimal configuration with respect to flame stability in high velocity flows and aiming for an increase in temperature small enough to be comparable with the decrease in temperature due a subsequent expansion. These conditions are a consequence of the intended application, gas turbines using in-situ combustion. This uses a supplementary combustion in the turbine, intended to best approximate an isothermal expansion that would ensure a better efficiency for the gas turbine. Taking into account the drop in temperature is of approximately 100 degrees after a turbine stage, and the flow velocity is about 100 m/s at the exit of the turbine stage, a suitable solution was sought. The experimental results shown that none of the tested configurations matched the desired conditions, but one of the three geometries had a significantly better behaviour. At the same time, it was concluded that the number and dimension of the injection holes do not play a major role in flame stability in high velocity flows, but rather their shape. The injection nozzles with divergent holes proved to be the most stable and to provide the smallest increase in temperature for high velocity flows.

KEYWORDS: *experimental, flame stability, gas turbine, in-situ combustion*

Numerical Calculation of 3D Low Speed Delta Wing Fighters Jet Aircraft

Haci Sogukpinar

*Department of Electric and Energy,
 Vocational School, University of Adiyaman,
 Adiyaman 02040, Turkey, hsogukpinar@adiyaman.edu.tr*

ABSTRACT

In this study, numerical calculations are conducted to investigate aerodynamic characteristics of the delta wing 3D fighter jet aircraft at low speed. Since the NACA 64A204 and 63A203 airfoil data are not available in the literature therefore 64A210 airfoil data are taken as a reference for estimation. The fuselage of the aircraft is created with 64A204 airfoil, and for the wings 64A204 and 64A203 airfoils are used. Numerical calculations are performed for estimated 2D airfoils and lift coefficient are calculated and compared with other numerical study. Numerical simulations are then conducted for 3D model by varying angle of attack to investigate wing tip vortexes by using SST turbulence model. 3D model aircraft are simulated for cruise flight, climb and descent at the angle of attack $+10^\circ$ and -10° respectively. The simulation results are interpreted in terms of fluid dynamics. A huge vortex covering the entire plane is simulated during the climb and descent. Numerical calculation results show that vortexes direction changed in climb and descent. The vortex rolls up and continues to curl inward at the angle of attack $+10^\circ$ and roll down during negative angle of attack.

KEYWORDS : *3D simulation, Aircraft, vortex, airfoil, Aerodynamic Analysis, lift, drag*

NOMENCLATURE

c_p	Pressure coefficient	μ	Dynamic viscosity
c_L	Lift coefficient	S	magnitude of the vorticity,
f_{w1}	Damping fuction	\tilde{S}	Modified vorticity
P	Static pressure	S_{ij}	Mean strain rate
P_∞	Free stream pressure	Ω_{ij}	Mean rotation rate
U_r	Relative velocity	μ_{eff}	Effective dynamic viscosity
U_∞	Free stream velocity (wind velocity)	α	Angle of attack
ν	Kinematic viscosity	ϕ	Scalar quantity of the flow
c	Airfoil chord	CFD	Computational fluid dynamics
t	Percentage of the maximum thickness	DES	Detached-Eddy Simulation
k	Turbulence kinetic energy	NACA	National Advisory Committee for Aeronautics
κ	Von Kármán constant,	NASA	National Aeronautics and Space Administration
l_{ref}	Reference length scale	RANS	Reynolds Averaged Navier Stokes equations
L	Length scale of flow	SST	Shear Stress Transport
ε	Turbulence dissipation rate		
ω	Specific dissipation rate		
ω_t	Wall vorticity at the trip		
ρ	Density		
ρ_∞	Freestream density		

1 PAPER CONTENT

1.1. Introduction

Today with the development of high-quality computer, computational fluid dynamics (CFD) has taken the complementary position to wind tunnel and flight test. In this way, the CFD methods shorten preliminary design times and provide economic advantages as well. Thirty to forty years ago only the analytical methods were used before the flight and wind tunnel tests, but nowadays, computational fluid dynamics have taken the first stage in design process.

In order to complete the design of an aircraft at Boeing Commercial Airplanes Company, more than 20,000 CFD cases were run before completion [1]. For instance, examples which is part of the design that it is not possible to test in the wind tunnel or it may be dangerous to carry out the flight test; on these drums only the CFD method is used to investigate aerodynamic behaviors [2]. Prior to the application of such CFD methods, they should be evaluated against wind tunnel and test flight. Another issue that effect accuracy of simulation is proper choice of the physical model used. Employing too simple or too complex physical model affects computational results. Mathematical definition of the flow physics is provided by Navier-Stokes equations. Different models were developed like SST (Shear Stress Transport), k- ω , Spalart-Allmaras to simulate the turbulence flow depending on the Reynolds Average Navier-Stokes (RANS) equations. CFD calculations along the X-31 aircraft were conducted at the high angle of attack by using k- ω turbulence model and obtained data were compared with wind tunnel test. Results provide an excellent data set for verification and evaluation [2]. Comparison of measured and Block Structured Simulation were performed for F-16XL aircraft by using three RANS model of k- ϵ , k- ω and Algebraic Stress turbulence model for the feature of vertical flow [3]. The agreement between numerical approaches and the flight test data is very good. Detached-Eddy Simulation (DES) was conducted for the F-15E at the angle of attack 65° with Reynold numbers of 13.6×10^6 and Mach number of 0.3. [4] DES method simulates based on modification of Spalart-Allmaras model and reduces RANS formulation near solid surfaces and away from wall to a sub-grid model [5, 6]. The lift, drag and pitching moments predicted from both RANS and DES shows good agreement with the Boeing database but DES shows slightly better predictions. 3D flow calculation over a realistic aircraft was conducted to validate simulation integrity of the Computational Fluid Dynamics using an unstructured mesh method [7]. High-lift configuration with a nacelle-pylon was simulated by Spalart-Allmaras turbulence model without trip term and compared with experimental data. CFD calculation result indicates that there is a good agreement including the local flow. Numerical simulation was performed to investigate Wing-Body Stage flow separation by using Navier-Stokes and Cartesian grid Euler equation at the Mach numbers of 2 to 6 [8]. A good agreement was observed between Navier-Stokes, Euler and wind tunnel results in steady state. CFD is now accepted to provide significant value and has created a paradigm shift in vehicle design, analysis and support processes [1] and has joined the wind tunnel and flight test as primary tools of the trade [9].

It is rarely seen that a whole plane is simulated and a three-dimensional velocity graph around airplane is plotted. However, three dimensional turbulence flow image in real flight tests are available. Therefore in this study, to see the harmony between the theoretical calculation and the experiment, a fighter jet is designed and modeled in computer environment and numerical calculation is carried out by using SST turbulence model at the airflow velocity of 10 m/s, and obtained results compared with real flight test. The resulting waves, vortices are interpreted and visually presented in figures.

1.2. SST Turbulence Model Methodology

A Reynolds-Averaged Navier-Stokes (RANS) equation with Menter's Shear Stress Transport (SST) turbulence model is a widely used as robust two-equation eddy-viscosity turbulence model in Computational Fluid Dynamics (CFD). SST turbulence model combines the superior behavior of the k- ω model in the near-wall region with the robustness of the k- ϵ model [10]. To achieve this, the k- ϵ model is converted into a k- ω formulation but it contains some improvements [11]. The model equations are represented in terms k and ω with the Eq.1 and Eq.2.

$$\rho \frac{\partial k}{\partial t} + \rho u \cdot \nabla k = P - \rho \beta_0^* k \omega + \nabla \cdot ((\mu + \sigma_k \mu_T) \nabla k) \quad (1)$$

$$\rho \frac{\partial \omega}{\partial t} + \rho u \cdot \nabla \omega = \frac{\rho \gamma}{\mu_T} P - \rho \beta \omega^2 + \nabla \cdot ((\mu + \sigma_\omega \mu_T) \nabla \omega) + 2(1 - f_{v1}) \frac{\rho \sigma_\omega \omega^2}{\omega} \nabla \omega \cdot \nabla k \quad (2)$$

Where, ρ is density, u is velocity field of wind, k is turbulent kinetic energy, μ is dynamic viscosity of air, ω is specific dissipation rate, β_0^* , σ_k , β , σ_ω are turbulence model parameters.

A production limiter is used in the SST model to prevent turbulence formation in stagnation zones.

$$\tilde{P} = \min(P_k, 10\rho\beta_0^*k\omega) \quad (3)$$

Where, P_k is production term and expressed by Eq.4:

$$P_k = \mu_T \left(\nabla u : (\nabla u + (\nabla u)^T) - \frac{2}{3} (\nabla \cdot u)^2 \right) - \frac{2}{3} \rho k \nabla \cdot u \quad (4)$$

Where, μ_T is turbulence eddy viscosity and expressed by Eq.5:

$$\mu_T = \frac{\rho a_1 k}{\max(a_1 \omega, S f_{v2})} \quad (5)$$

Where, S is the constant measure of the strain rate, f_{v1} and f_{v2} are first and second blending functions [12] respectively, and are defined by Eq.6 and Eq.7.

$$f_{v1} = \tanh \left(\min \left[\max \left(\frac{\sqrt{k}}{\beta_0^* \omega l_\omega}, \frac{500 \mu}{\rho \omega l_\omega^2} \right), \frac{4 \rho \sigma_\omega^2 k}{\max(\frac{2 \rho \sigma_\omega^2}{\omega} \nabla \omega \cdot \nabla k, 10^{-10}) l_\omega^2} \right] \right) \quad (6)$$

$$f_{v2} = \tanh \left(\max \left(\frac{\sqrt{k}}{\beta_0^* \omega l_\omega}, \frac{500 \mu}{\rho \omega l_\omega^2} \right)^2 \right) \quad (7)$$

According to the k- ϵ model, f_{v1} is equal to zero away from the surface but in k- ω model that switches over to the inside of the boundary layer. l_ω is the distance to the closest wall and these blending functions include an explicit measurement of the wall distance. The default constants for this model are given by:

$\beta_1 = 0.075, \gamma_1 = \frac{5}{9}, \sigma_{k1} = 0.85, \sigma_{\omega1} = 0.5, \beta_2 = 0.0828, \gamma_2 = 0.44, \sigma_{k2} = 1.0, \sigma_{\omega2} = 0.856, \beta_0^* = 0.09, \sigma_1 = 0.31$. Reynolds Average Navier-Stokes (RANS) equations are solved for conservation of momentum and continuity equation for conservation of mass. Turbulence effects are modeled using two of Shear Stress Transport (SST) Eq.1 and Eq.2. The SST model is also called the Low Reynolds Number Model and flows are solved all the way to the wall by using wall distance equation. The inlet port is set to velocity inlet and outlet port is set to pressure outlet with zero atmospheric pressure. Inlet velocity is decided as normal inflow velocity of 10 m/s. No slip boundary condition is applied for the model surface. The commercial software COMSOL, based on finite volume method is applied. An airfoil with max thickness 4% at 40% chord and max camber 1% at 40% chord which is similar to the real NACA 64A204 is created by using the 64A210 airfoil data as reference. Closed-up of the newly created airfoil is given in Fig. 1.



Figure 1. Close up of airfoil section.

The full designed model aircraft is given in Fig. 2.

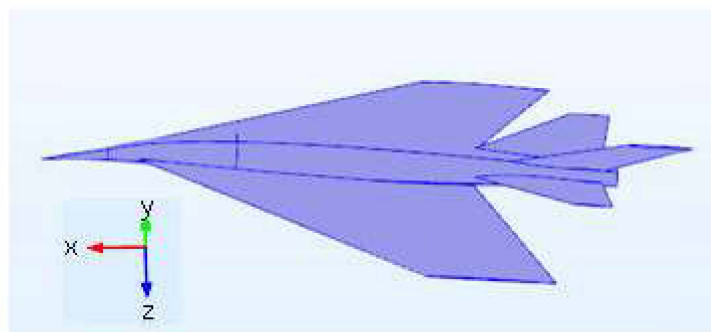


Figure 2. Model aircraft

Model consists of 16 domain and tetrahedral mesh type is applied. Model plane is splitted into 718356 mesh elements. An intense mesh distribution is applied to the outer surface portion of the model and mesh distribution is given in Fig.3.

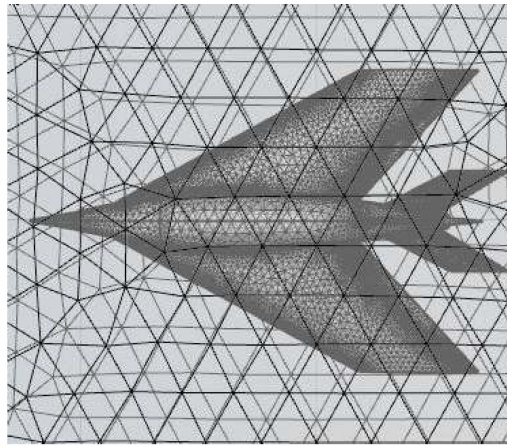


Figure 3. Mesh distribution around the model

1.3. Results and Discussions

Since NACA 64A204 and 64A203 airfoil data are not found in the literature, so these two airfoil data are estimated by using NACA 64A210 data, which is thought to be the most similar to these airfoils. Previously, numerical calculation is performed for NACA 64A210 airfoil using SST turbulence model and the obtained data are compared with those obtained other calculation in Ref. [13] to validate simulation accuracy of this calculation. Lift coefficient with respect to angle of attack for NACA 64A210 is shown in Fig.4. The comparison between this calculation and previous one show good agreement and results are found to be very well matched for NACA 64A210. Therefore, numerical approaches are reliable to investigate aerodynamic performance of other airfoil in this study. 64A204 and 64A203 are simulated by using SST turbulence model and lift coefficient are calculated and presented in the same Fig.4 together with NACA 64A210 airfoil data. The maximum lift coefficient is calculated at around 6° to 7° for both airfoils, and lift coefficient began to decrease with the increasing angle of attack further than 7° . Geometric and computer analysis of the F-35A Lightning II airfoil of 64A206 was reported at the Ref. [14] and maximum lift coefficient calculated as 0.62 at the angle of attack around 9° . Although airfoils used in this study are slender, the maximum lift coefficient is calculated as 0.6 at the angle of attack around 7° . The maximum lift coefficient angle is lower than NACA 64A206 because 64A210 airfoil is thinner.

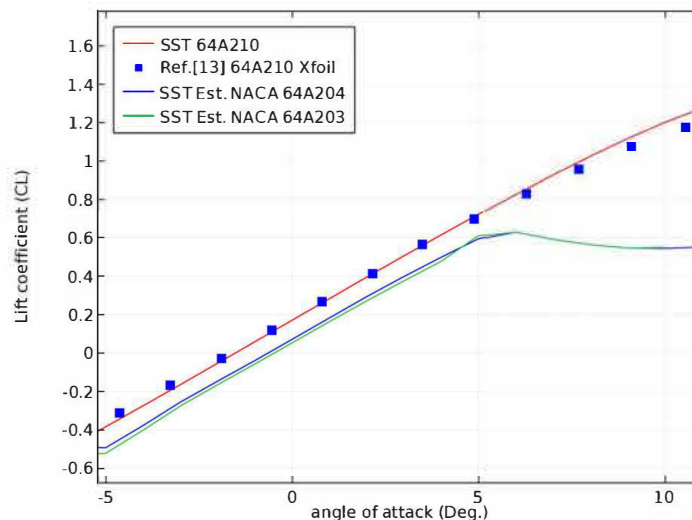


Figure 4. 2D computational results for the lift coefficient vs. angle of attack.

The model aircraft's fuselage is designed with NACA 64A204, and for the other part 64A204 and 64A203 airfoils are used. 10° anhedral angle is set to wing so wing tip is lower than x-y plane. Angle between the fuselage center line and wing chord line is set to zero degree. Numerical calculation is conducted at the Reynolds numbers of 1×10^6 and inlet wind speed set to 10 m/s. In all calculations, the fluid is sent from the front to the back side (+x to -x) of the airplane. The distance between the streamlines is taken quite short to prevent mixing streamlines and also for the clear view of the vortex directions. The bottom and top views of streamline simulation result of the plane for the cruise flight are given in Fig.5(a) and Fig.5(b). Streamlines goes from left to right and figure shows that the airflow velocity on the surface of the body is reduced due to the no slip condition. There is also a wake zone in the back of the aircraft where the shedding effect dominates, and low speed region extended further more.

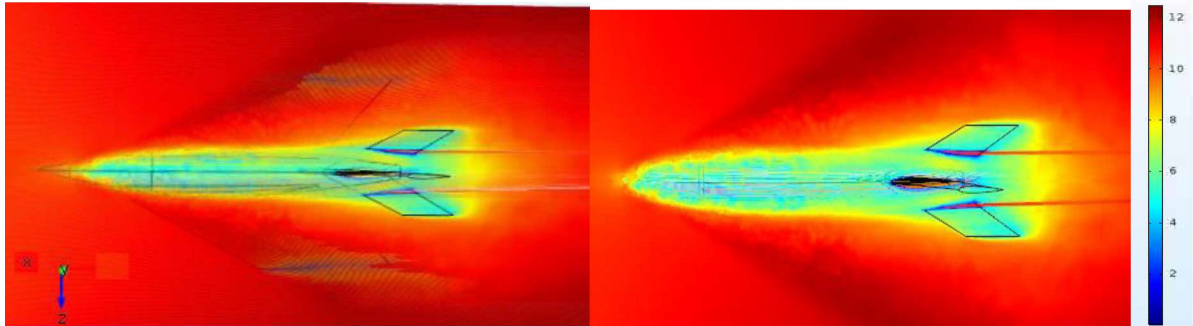


Figure 5. Velocity (m/s) streamlines of bottom (a) and top view (b) of the plane during a straight flight

For the numerical calculation, airflow is sent over x-y plane along the fuselage center line at cruise flight and calculation data for velocity streamline for upper rear side view of model aircraft is given in Fig.6. Vortex is observed in places where the fluid interacts with the wing then wave rolls up and then continue to curl inward. Negative dihedral angle appears to increase vortex formation as seen in the Fig.6. A lower dihedral angle can be set to increase the lift or to reduce the drag coefficient but for spiral stability negative dihedral angle is necessary for fighter jet. Positive dihedral angle also acts in the direction of increasing vortex formation but positive dihedral angle is set to transport aircraft to adjust lateral stability. Depending on the operational requirement, a positive or negative dihedral angle may be set, but it should be noted that the more laterally stable aircraft means less rolling controllable.

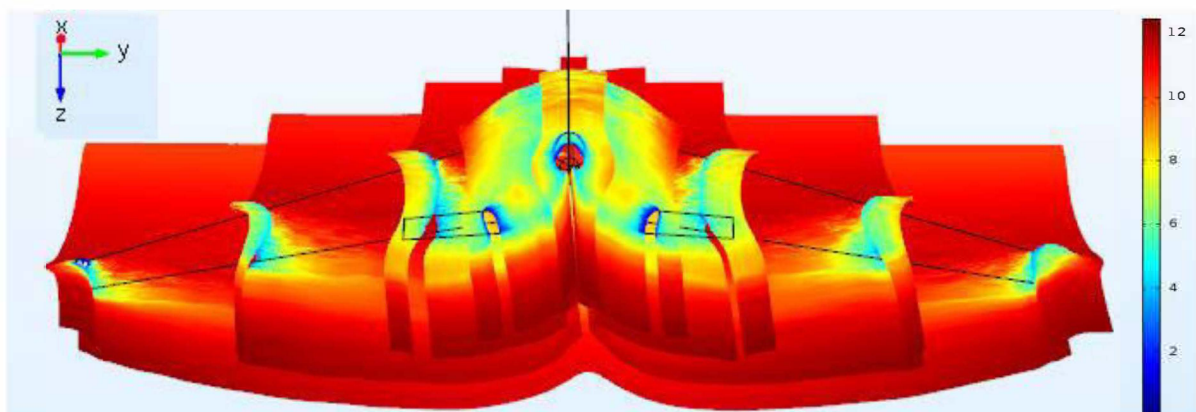


Figure 6. Velocity (m/s) streamlines of upper rear side view of cruise flight

The upper rear views of the wing tip vortex, covering the entire surface of the aircraft ascending with the angle of attack 10° , is given in Fig.7. For this part, fluid is sent over the x-y plane along the fuselage centerline (+x to -x direction) as two layers, first one is passing over the top and second one is along the bottom surface. In rectangular or trapezoid wings, it is known that the vortex occurs only at the wing tip, but it appears that the vortex formation covers the entire aircraft in delta wings as shown in Fig. 7. NASA conducted experimental test to investigate wing vortices for C-5A wings at NASA Langley Research Center [15]. The test was carried out using colored gases spraying at different heights over the mast from ground during low level flight. Experimental test shows that the

vortex waves were observed to roll up the whole body bilaterally. A video was recorded during take-off by Alessandra Otondo, a large spiral vortex covers half of the plane and it is available in Ref. [16]. The numerical results obtained in this study are consistent with the experimental data given in the Ref. [15] and Ref. [16].

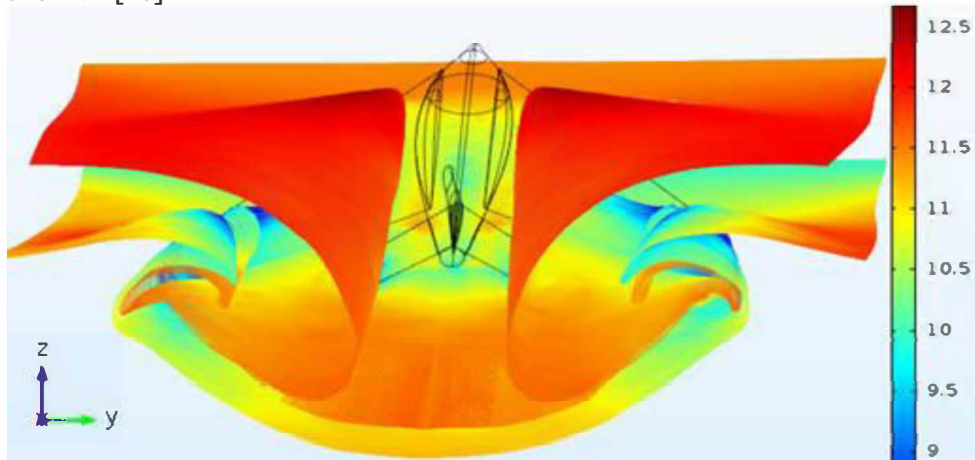


Figure 7. The rear upper side view of velocity (m/s) streamline of plane, ascending at 10° angle of attack.

Upper rear view of streamline velocity of the wing tip vortex, covering the entire surface of the aircraft descending with the angle of attack -10°, is given in Fig.8. During positive angle of attack, wave rolls up and continue to curl inward behind the plane but when the plane is inclined downward with the angle of attack -10°, the vortex is formed in the reverse direction as shown in Fig.8. This is due to the low pressure happening in the rear upper or rear lower part of the aircraft. When the plane is inclined upwards, low pressure occurs at the rear upper part of the aircraft and the fluid is curled and moved to this part. However when the plane is inclined downward, low pressure occurs at the rear lower part of the aircraft and the fluid is curled toward this side.

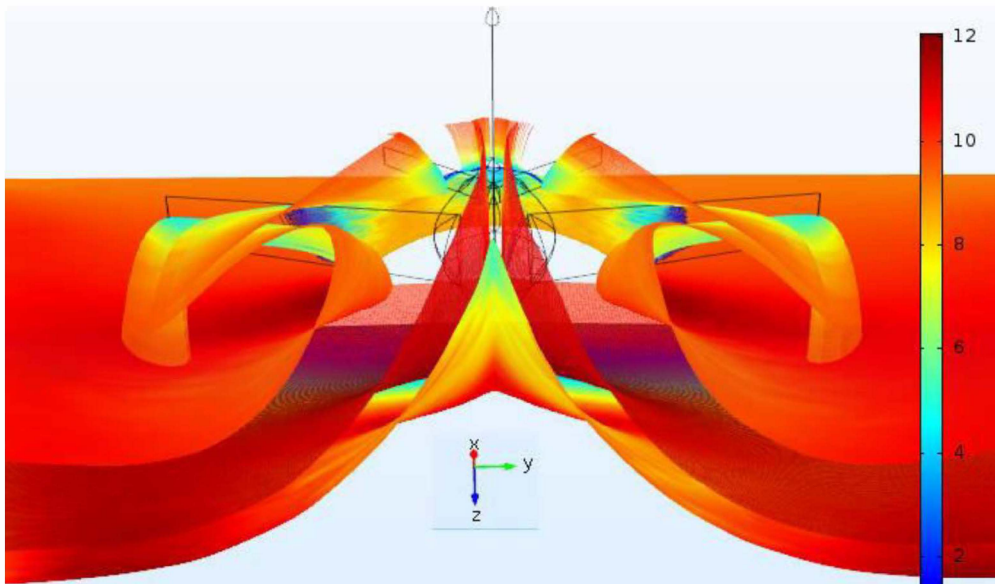


Figure 8. The upper rear view of velocity (m/s) streamline of plane descending at -10° angle of attack

Side views of velocity (m/s) streamline of the aircraft ascending and descending at the angle of attack 10° are given in Fig.9(a) and Fig.9(b) respectively. In Fig.9(a), the airplane is tilted upward by +10 degrees and the airflow is sent on x-y plane over the tip of the aircraft's nose from +x to -x direction. Calculation results show that the fluid bends down to the plane surface as it goes to the back side. This is because a low pressure region is formed on the rear upper surface of the aircraft. As shown in Fig.9(b), airflow is sent beneath the tip of the nose from +x to -x direction on the x-y plane. In this

case fluid bends upper side as it goes to the back. This is because a low pressure region is formed on the rear lower surface of the aircraft.

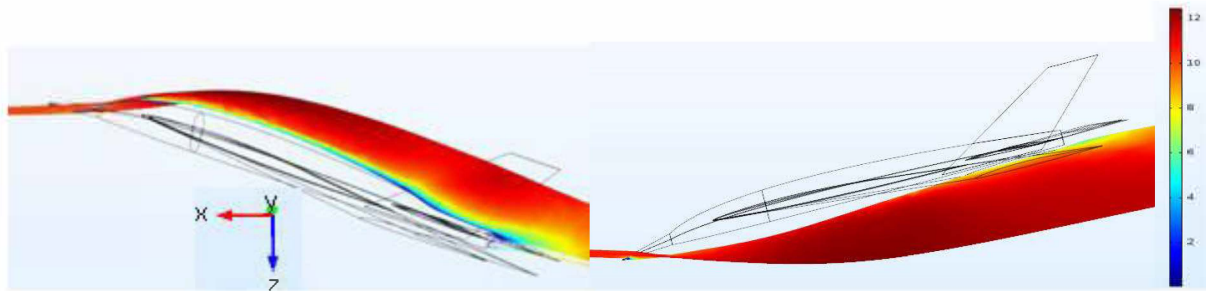


Figure 9. Side view of velocity (m/s) streamline of the plane ascending (a) and descending (b) at 10 degree angle of attack.

1.4. Conclusion

In this study, the interaction of the fluid with the whole aircraft is numerically investigated by using SST turbulence model. Initially, numerical calculations are performed for NACA 64A210 airfoil and obtained data are compared with other numerical data to validate simulation accuracy of this calculation. The comparison shows good agreement for numerical approaches. Then, 64A203 and 64A204 airfoils are estimated by using 64A210 airfoil's data as reference. 64A203 and 64A204 airfoils are simulated and compared with those obtained from other numerical study conducted for NACA 64A210 airfoil. The comparison shows good agreement for the lift coefficient at the angle of attack from -5° to $+6^\circ$. With the increasing angle of attack, the lift coefficient increases in parallel with the reference airfoil but it starts to decrease starting from 6° . The fuselage of jet aircraft is created from 64A204 airfoil, and for the wings, both 64A203 and 64A204 airfoils are used. Next, the whole aircraft is simulated and aerodynamic performance is investigated for cruise flight, climb and descent at the angle of attack $+10^\circ$ and -10° respectively by using SST turbulence model. As the plane tilted up or down, wingtip vortex is observed to covers the whole aircraft. While the plane is ascending at the positive angle of attack ($+10^\circ$), it rolls up and continues to curl inward along the lateral wing surface, and when the plane is descending at negative angle of attack (-10°), circular wave rolls down outward from the lateral surface. Numerical calculation shows that this is caused by the pressure difference between the front and rear side of the airplane. When the plane is inclined upwards, low pressure is created at the top back of the airplane; while the plane was inclined downward, low pressure is created at the lower back side of the airplane.

ACKNOWLEDGMENT

Many thanks to Middle East Technical University and Adiyaman University for technical support.

REFERENCES

1. T. J. Forrester, E. N. Tinoco, N. J. Yu; 2005; "Thirty years of development and application of CFD at Boeing Commercial Airplanes"; *Computers & Fluids*; 34; pp. 1115–1151.
2. O.J. Boelens; 2012; "CFD analysis of the flow around the X-31 aircraft at high angle of attack"; *Aerospace Science and Technology*; 20; pp. 38–51.
3. O. J. Boelens; 2009; "Comparison of measured and block structured simulation results for the F-16XL aircraft." *Journal of Aircraft*; 46(2); pp. 377–384.
4. J. R. Forsythe, K. D. Squires, K. E. Wurtzler, and P. R. Spalart; 2004; "Detached-Eddy Simulation of the F-15E at High Alpha"; *Journal of Aircraft*; Vol. 41; No. 2; pp. 193–200.
5. P. R. Spalart, S. R. Allmaras; 1994; "A One-Equation Turbulence Model for Aerodynamic Flows" *La Recherche Aerospatiale*; No. 1; pp. 5–21.



6. P. R. Spalart; 2000; "Strategies for Turbulence Modeling and Simulations"; International Journal of Heat and Fluid Flow; Vol. 21; pp. 252–263.
7. M. Murayama, Y. Yokokawa, K. Yamamoto, and Y. Ueda; 2007; "CFD Validation Study for a High-Lift Configuration of a Civil Aircraft Model"; 25th AIAA Applied Aerodynamics Conference; June 25 - 28, Miami, FL; pp. 1-20.
8. P.G. Buning, R. J. Gomez, and W. I. Scallion; 2004; "CFD approaches for simulation of wing-body stage separation"; 22nd Applied Aerodynamics Conference and Exhibit; August 16 - 19, Providence, Rhode Island; pp.1-11.
9. E.N Tinoco; 1998; "The changing role of computational fluid dynamics in aircraft development"; 16th AIAA Applied Aerodynamics Conference, Fluid Dynamics and Co-located Conferences; Albuquerque, NM; June 15-18; pp.161-174.
10. F.R. Menter; 1994; "Two-Equation Eddy-Viscosity Turbulence Models for Engineering Applications," AIAA Journal; vol. 32; no. 8;
11. D. C. Eleni, I. T. Athanasios and M. P. Dionissios; 2012; "Evaluation of the turbulence models for the simulation of the flow over a National Advisory Committee for Aeronautics (NACA) 0012 airfoil" Journal of Mechanical Engineering Research; Vol. 4(3); pp. 100-111.
12. F. R. Menter, M. Kuntz, and R. Langtry; 2003; "Ten years of industrial experience with the SST turbulence model"; Turbulence, heat and mass transfer 4; 4(1); pp.625-632.
13. "Airfoil database search"; 2017; <http://airfoiltools.com/>.
14. A.Bhatt, M. Harvey, R. Hofmeister; 2017; "Computer and Geometrical Analysis of the F-35A Lightning II"; www.dept.aoe.vt.edu.
15. M.Curry; 2017;"C-5A Wing Vortice tests at NASA Langley Research Center"; <https://www.dfrc.nasa.gov>
16. T. Cookers; 2017; "Wingtip Vortices"; <http://www.f1technical.net>

Interaction of supercooled droplets and nonspherical ice crystals with a solid body in a mixed cloud

Ivan A. Amelyushkin

*Affiliation Central Aerohydrodynamic Institute, Moscow Institute of Physics and Technology
 Function Senior researcher, lecturer
 Address Russia, Moscow region, Zhukovsky, Zhukovskogo street, 1, Gagarina street 16
 E-mail Amelyushkin_Ivan@mail.ru*

Albert L. Stasenko

*Affiliation Central Aerohydrodynamic Institute, Moscow Institute of Physics and Technology
 Function Principal researcher, professor
 Address Russia, Moscow region, Zhukovsky, Zhukovskogo street, 1, Gagarina street 16
 E-mail Stasenko@serpantin.ru*

ABSTRACT

Mathematical models of nonspherical particles' motion in nonuniform flow were proposed for continuous flow approach as well as for single particles' motion simulation. Lagrangian approach was used to simulate aerosol flow with nonspherical particles around transversal cylinder. Peculiarities of supercooled water crystallization were investigated via cryostat, infrared spectroscopy and original devices for supercooled droplets' impact simulation. The results of the experimental study of the supercooled water crystallization are presented. The relationship between the parameters of intermolecular interaction with the parameters of macroscopic phenomena accompanying the crystallization of supercooled water was determined. Mathematical models of the supercooled liquid crystallization and the expression for the minimum rate for the beginning of the supercooled droplets crystallization on impact with the surface of the aircraft were developed. The numerical and experimental evaluations of physical parameters characterizing the supercooled liquid crystallization in the icing problem are performed. Two-phase boundary layer formation near nanostructured surface was investigated via molecular dynamics method.

KEYWORDS: *nonspherical particles, supercooled droplets, aerosol flow, interaction of two-phase flow with a solid body.*



Numerical Calculation of Wind Tip Vortex Formation for Different Wingtip devices

Haci Sogukpinar

*Department of Electric and Energy,
Vocational School, University of Adiyaman,
Adiyaman 02040, Turkey, hsogukpinar@adiyaman.edu.tr*

ABSTRACT

In this study numerical calculations are conducted to understand implementation of different wingtip device for wingtip vortexes formation. Numerical methods are performed over NACA 0012 winglet at the varying Reynolds numbers from 0.5×10^6 to 1×10^6 with the angle of attack 10° and compared with other study. Implementations of winglet are divided into four categories and these are one winglet up or down sloping, split winglet up and down sloping, and single winglet with two-step inclined. First, up and down sloping winglet are designed and simulated then split winglet are investigated numerically with the varying angle. Finally, winglets with two step inclined angles are investigated. For the up sloping winglet, wingtip vortexes formation is reduced considerably as the angle with wing surface approaches 90 degrees. But vortexes formation is clearly happening at the angle starting less than 90° and beyond 135 degree. For the down sloping, while there is a visible vortex formation below 90 degrees but more uniform flow is observed compared to conventional wing tips at around 90 degrees. For the split winglet configurations, less vortex formation is observed generally compared to other. As a result, single or split winglet up or down sloping perpendicular or wider angle with lateral surface decreases wingtip vortex formations.

KEYWORDS : *wingtip device, wingtip, vortexes, fuel efficiency, vortices,*

Formation Flight Mechanics and its Integrated Logistics

Tomas Melin

The Swedish Aeronautical Institute

Director of research

Westmansgatan 37, Linköping, SE-581 83, Sweden

melin@sftiab.se

Diane Uyoga

Moi University, Kenya

Head of Department, Aerospace Security and Logistics

P. O. Box 7256-30100, Eldoret

ABSTRACT

This paper presents an investigation of the fuel cost reduction effects of formation flight when applied to two different type aircraft. The first case is a general aviation case with a Cessna 152 and a Cessna 182 in staggered formation. The second case is a commercial transport with two Bombardier Dash-8 in staggered formation. The method used to analyze the induced drag is a vortex lattice method which keeps both aircraft in trim throughout the simulation. The total drag reduction for the trailing aircraft was found to be 4.4% and 8 % for the two cases respectively – this would reflect in fuel consumption and CO₂ emissions. In order to assess the effects of the cost of setting up the formation, a trade study in operational logistics was made for a sample route where flights between Stockholm/London and Linköping/Amsterdam joined up mid-flight for a fractional formation flight. Formation flying with its integrated logistics can be optimized and sustained since fuel represents 50% of the total expenses of air cargo freight transportation.

KEYWORDS

Formation flight, operational logistics, integrated logistics, fuel saving, air cargo.

Detached Eddy-Simulations of Delta-Wing Post-Stall Flow Control

Buzica Andrei

Technical University of Munich, Department of Mechanical Engineering

Research Engineer

Boltzmannstr. 15, 85748-Garching b. München, Germany

andrei.buzica@yahoo.com

Biswanger Manuel

Technical University of Munich, Department of Mechanical Engineering

Graduate Student

Breitsamter Christian

Technical University of Munich, Department of Mechanical Engineering

Chief Scientist

ABSTRACT

Flow control can significantly improve the aerodynamic performances of delta wings. Yet, despite numerous studies of vortex control by leading-edge blowing still little research is focused on the post-stall regime and further consideration of the shear-layer reattachment through flow control is needed. This paper reports on the effects of unsteady jets on the global flow field at a very high angle of attack, $\alpha = 45^\circ$. For this, Detached-Eddy Simulations are conducted and validated with wind tunnel test results. The vortex shedding of the unperturbed delta-wing flow is investigated and compared to the perturbed case. It concludes that unsteady blowing energizes the shear layer and reorders at the same time the shedding mechanism eventually forming a big burst vortex structure that increases the lift significantly.

KEYWORDS: *Delta Wings, Flow Control, Post-Stall, DES*

A method for calculus of Internal Forces

Thien Van NGUYEN ⁽¹⁾, I. Stroe ⁽¹⁾, A. Craifaleanu ⁽¹⁾, Roxana Alexandra Petre ⁽¹⁾, Dan Dumitriu ^{(1), (2)}

¹ "POLITEHNICA" University of Bucharest

313 Splaiul Independenței, Bucharest 060042, Romania

bangden33468@gmail.com, ion.stroe@gmail.com

² Institute of Solid Mechanics of the Romanian Academy

Str. Constantin Mille 15, Bucharest 010141, Romania

dumitri04@yahoo.com, dumitriu@imsar.bu.edu.ro

ABSTRACT

A new method to compute internal forces in a multi-bodies system is presented in the paper. Lagrange equations are used to study the motion of a system under the action of known external forces. If an internal force has to be found, a supplementary mobility is considered in the system and the corresponding internal force for the new mobility is found for null value of the mobility, as well as its first and second orders of derivatives. The method is a general one, but a particular case of mechanism used in the dynamics of the airplane elevator is analyzed to verify the validity of the proposed method.

KEYWORDS: *airplane, multi-bodies system, constraint, dynamics.*

Flutter Uncertainty Analysis of an Aircraft Wing Subjected to a Thrust Force Using Fuzzy Method

M. Rezaei

Ph.D Candidate

School of Mechanical Engineering, Shiraz University, Shiraz, Iran

S.A. Fazelzadeh

Professor

fazelzad@shirazu.ac.ir

School of Mechanical Engineering, Shiraz University, Shiraz, Iran

A. Mazidi

Assistant Professor

amazidi@yazd.ac.ir

School of Mechanical Engineering, Yazd University, Yazd, Iran

ABSTRACT

Flutter uncertainty analysis of an aircraft wing subjected to a thrust force using fuzzy method is investigated. The wing model contains bending and torsional flexibility and the aeroelastic governing equations are derived based on Hamilton's Principle. The aerodynamic loading is simulated based on finite state unsteady thin airfoil theory. Partial differential equations of motion are converted to a set of ordinary differential equations using Galerkin method. The wing bending and torsional rigidity, aerodynamic lift curve slope and air density are modeled as fuzzy uncertain parameters with triangle membership function. The eigenvalue problem with fuzzy input parameters is solved using fuzzy Taylor expansion method and a sensitivity analysis is performed. Flutter boundary is extracted as a membership function. Furthermore the upper and lower bounds of Flutter region in different α -cuts are extracted. Results show that this method is a low-cost method with reasonable accuracy to estimate the flutter speed and frequency.

KEYWORDS: *Uncertainty; Flutter; Aircraft wing; Thrust Force; Fuzzy Method*

Hybrid Optimization of Star Grain Performance Prediction Tool

Anwer E. A. Hashish

MSc. Student

Anwar.hashish@mtc.edu.eg

Mahmoud Y.M. Ahmed

Associate Professor in Aerospace Engineering

Hamed M. Abdallah

Associate Professor in Aerospace Engineering

Mohamed A. Alsenbawy

Associate Professor in Aerospace Engineering

Aerospace Department – Military Technical College

ABSTRACT

In solid propellant rocket propulsion, the design of the propellant grain is a decisive aspect. The grain design governs the entire motor performance and, hence, the whole rocket mission. The ability to decide, during design phase, the proper grain design that satisfies the predefined rocket mission with minimum losses is the ultimate goal of solid propulsion experts. This study enables to predict the pressure time curve of rocket motor with star grain configuration and also to optimize the performance prediction tool through optimization methods to maximize its prediction efficiency. A hybrid optimization technique is used. Genetic Algorithm (GA) is first implemented to find the global optimum followed by Simulated Annealing (SA) optimization method to find the accurate local optimum. A program for predicting the pressure time curve of the rocket motor is created on MATLAB and then linked to GA - SA optimizers as an application on a case study. The purposed approach is validated against satisfying data. It is found that the developed optimized program is capable of predicting rocket motor performance (including the effect of erosive burning) with acceptable accuracy for preliminary design purposes.

KEYWORDS: *solid propellant propulsion, star grain, hybrid evolutionary optimization.*

NOMENCLATURE

Uppercase letters

A_p - Port area of star grain at each burning step
 A^* - Critical section area of the nozzle,
 A_b - burning area of the grain at each step
 C^* - Propellant characteristic velocity
 L_g - Length of star grain
 M_n - Gas Mach number at the nozzle end of the grain
 N - No of star points
 P_{on} - Stagnation pressure of flowing gases
 P_n - Pressure at nozzle end
 P_h - Gas pressure at head end of the grain
 R_{in} - Grain inner radius
 $RMSE$ - Root mean square error
 P_D - discharge pressure
 V_{cf} - Final chamber volume
 V_n - flow velocity of gases at the nozzle end
 V_{ci} - Initial volume of combustion chamber

Lowercase letters

a - Burning rate coefficient
 d_{cr} - Initial critical diameter of nozzle
 er_{rate} - Erosion rate of nozzle critical section
 f - Fillet radius
 j - Burning step
 \dot{m}_D - Rate of discharge of gases
 \dot{m}_G - Rate of generation of gases
 n - Pressure exponent
 r_h - Burning rate at the head end of the grain
 r_n - Total burning rate at the nozzle end due to applying the erosive burning rate
 r_{av} - Average burning rate of the grain
 Δt - Time increment
 t_{delay} - Delay time until begin of erosion
 w - Web thickness
 Δy - Distance burnt
 Greek symbols



α - Step regression factor	Subscripts
β - Head end regression factor	b – Burning
γ - Specific heat ratio of the combustion gases	n – Nozzle
ε - Angle fraction	h – Head
ρ - Density of the burning propellant	i – Initial
θ - Star point angle	f – Final
Γ - Specific gas constant	cr - Critical

1 INTRODUCTION

The solid propellant grain design involves numerous parameters that are commonly referred to as the grain ballistic parameters. These parameters can be classified into distinct categories as follows [1]:

- Properties of solid propellant, this category includes the following parameters: Total impulse, specific heat ratio, Propellant material, burning rate, characteristic velocity and propellant density.
- Mission requirements which include both thrust and thrust coefficient.
- Grain geometry: that includes web fraction, propellant geometric configuration, volumetric loading coefficient and slenderness ratio.
- Nozzle geometry, this category includes: exit area, throat area, nozzle shape, convergence and divergence angles and expansion ratio, erosion pattern of nozzle throat.
- Other ballistic parameters includes: combustion chamber material, weight and pressure, exit pressure, combustion temperature, burning time and motor diameter.

Clearly, the proper design of solid propellant rocket motors (SPRMs) involves multi-disciplinary algorithms to develop efficiently and accurately the designs related to the required performance parameters. Over the years, researchers developed tools for the preliminary design of SPRMs that can be optimized to the required performance criteria. Generally, these tools comprise three steps: geometric modeling, burn back analysis and optimization.

Many optimization objectives have been acquire through numerous optimization techniques.

One objective was to minimize the propellant mass. Nisar [2] used a hyprid optimization technique (genetic algorithm and sequential quadratic programming) on 3D finocyl grain involving 18 parameters. Similarly, Fredy [3] used GA on different grain geometries (end burning, tubular, star, etc.) which had up to 8 parameters. In contrast, Kamran[4] investigated different optimization objectives such as maximum volumetric loading fraction, minimum sliver fraction and maximum total impulse using GA on convex star grain with 6 parameters. In another study, Kamran [5] also used GA to find the maximum average thrust of 3D grain configuration with radial slots having 24 different parameters.

The research group of Raza et. al. conducted a series of studies on optimizing the dual thrust rocket motors (DTRMs). In these studies [6-9], the focus was to maximize the average boost-to-sustain thrust ratio and total impulse of DTRMs. They used different hybrid optimization techniques on different types of 3D grains. In [6], they used hybrid evolutionary GA and SA on 3D wagon wheel with 10 parameters. Similarly, in [7, 9] Raza et. al. used the same hybrid optimization technique on 3D finocyl grains (convex star tapered hollow cylinder grain geometry with 8 different design parameters and fin tapered hollow tubular with 8 design parameters). In contrast, in [8] they used a different hybrid optimization technique (SA and pattern search) on 3D finocyl grain with 8 parameters.

In all cases, researchers rely on theoretical techniques to predict the performance of SPRMs. The accuracy of such tools is a crucial aspect as far as credibility of these tools is concerned. This motivated many researchers to improve the accuracy of the tool they use via, in many cases, optimization. In this respect, the optimization technique is used to minimize the root mean square error (RMSE) between the desired and computed performance merit. In [10-13], different optimization methods were used such as complex method, pattern search and genetic algorithm. Sforzini [12] used pattern search for optimizing the computed thrust-time profile of a 3D finocyl grain with 10 parameters. Both Acik [11] and Yücel [10] used complex method to find the minimum RMSE but on different cases. Acik [11] optimized different grain geometries (end burning, internal burning tube, slot, slot-tube, star and star-tube) with parameters up to 9. Yücel [10] optimized a 3-D finocyl grain with 8 axial slots at the fore end and a radial slot at the aft end with 11 parameters. He also used genetic algorithm on his case study. Recently, Gawad [13] used genetic algorithm to find the minimum RMSE but on DTRM with tubular grain with two different diameters and sloped grain near its head end with 10 parameters.

It is clear that many studies implemented GA as the optimization method. This may be justified by its ability to define the global optimum inside the domain of study. For more accurate results, researchers refine optimization results via a hybrid optimization technique with a method for global search followed by a method using local search superiority.

The focus of the present study is to develop an optimized tool to predict the pressure time profile of a star grain. Acik [11] conducted a similar study, but using complex as the optimizer method. In this study, a different approach is adopted in which a hybrid GA-SA optimization is implemented.

The remainder of this paper is organized as follows. The next section presents the case study and the methodology of calculating pressure-time history followed by the optimization technique. The following section includes the results of this study. Conclusion and future work wrap up the paper.

2 CASE STUDY AND METHODOLOGY

2.1 Internal ballistics prediction model

A mathematical model for the internal ballistics of the solid propellant grain is developed based on the mass balance of the gas products [14, 15]. The developed model adopts the following assumptions:

- The flow of gases is adiabatic. The flow along the combustion chamber is isentropic.
- The gas products are ideal gases.
- Regression of surface along the grain length is linear.

The computations are performed in two sections; at the head and nozzle end of the grain and the grain erosive burning is accounted for. The typical pressure time profile can be divided into three phases; the initial pressure rise, the quasi-steady state phase, and the exhaust phase. These phases are illustrated schematically in Figure 1.

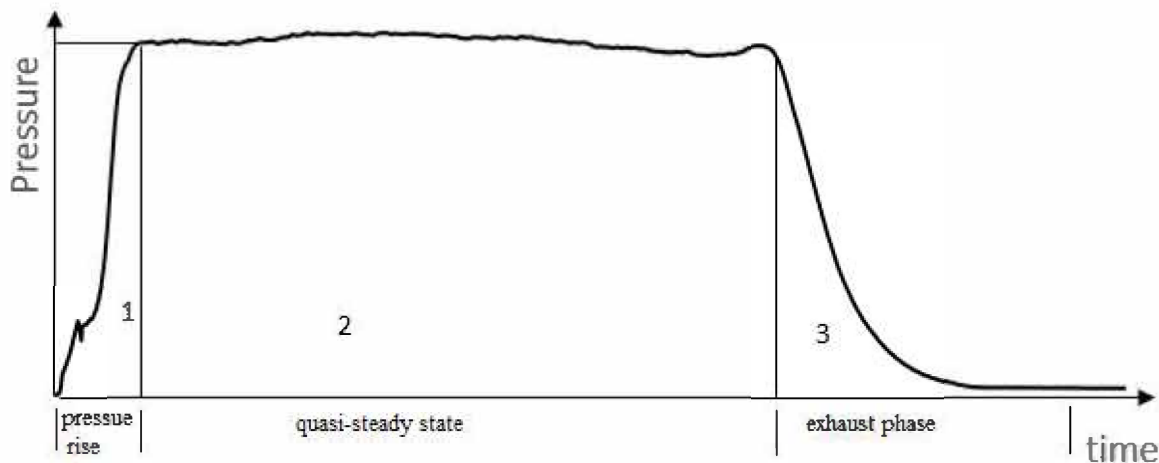


Figure 1: Pressure time profile phases

In the initial pressure rise (ignition) phase, the igniter is activated to bring the chamber pressure to a level sufficient to ignite the propellant grain surface. The initial pressure rise is dependent on the igniter charge rather than the main propellant grain. It is thus overlooked in the model. The Quasi steady state operation phase generally occupies the longest time in the motor operation. In the present analysis, this phase starts directly after ignition. The phase ends at the moment when the burning gases reach the inner wall of the combustion chamber for star perforated grains, this phase is divided into two regimes. The first regime is till the star leg is ended while the second ends when the web is finished. The prediction of pressure history is performed according to the following procedures.

A grain burn-back analysis is performed through analytical method to calculate the burning and port areas of star grain configuration. The gas Mach number at the nozzle end of the grain is evaluated (iteratively) by the following equation;

$$M_n = \frac{A^*}{A_p} \left[\frac{2}{\gamma+1} \left(1 + \frac{\gamma-1}{2} M_n^2 \right) \right]^{\frac{\gamma+1}{2(\gamma-1)}} \quad (1)$$

where γ , A_p , A^* are Specific heat ratio of the combustion gases, port area of star grain at each burning step and critical section area of the nozzle, respectively. The flow velocity of gases at the nozzle end is then estimated as follows:

$$V_n = \sqrt{\gamma C^* \Gamma M_n} \left(1 + \frac{\gamma-1}{2} M_n^2\right)^{-\frac{1}{2}} \quad (2)$$

where Γ , C^* are specific gas constant and characteristic velocity of the propellant, respectively. The stagnation pressure of flowing gases is estimated from the relation:

$$P_{on} = [a \rho_p C^* A_b / A^*]^{\frac{1}{1-n}} \quad (3)$$

where ρ_p , A_b , n are propellant density, burning area of the grain at each step and the pressure exponent of the propellant, respectively. Hence, the pressure at nozzle end is:

$$P_n = P_{on} \left(1 + \frac{\gamma-1}{2} M_n^2\right)^{-\frac{\gamma}{\gamma-1}} \quad (4)$$

Now, the rate of discharge of gases is calculated as:

$$\dot{m}_D = \frac{A^* P_{on}}{C^*} \quad (5)$$

Hence the gas pressure at head end of the grain is:

$$P_h = P_n + \frac{\dot{m}_D V_n}{A_p} \quad (6)$$

The burning rate at the head end of the grain can be obtained by:

$$r_h = a P_h^n \quad (7)$$

where a is the burning rate coefficient. The total burning rate at the nozzle end due to applying the erosive burning rate is:

$$r_n = a P_h^n + \alpha (\dot{m}_D / A_p)^{0.8} L^{-0.2} e^{(-\beta r_p A_p / \dot{m}_D)} \quad (8)$$

where α , L , β are step regression factor, grain length and head end regression factor. The rate of generation of gases is estimated using the following equation:

$$\dot{m}_G = A_b \rho_p r_{av} \quad (9)$$

$$\text{where } r_{av} = \frac{r_h + r_n}{2}$$

The discharge mass flow rate is obtained more accurately (iteratively) through the following equations:

$$\dot{m}_D = \dot{m}_G - \frac{\bar{r}_{av}}{r^{2.5} c^{0.2}} (\bar{P}_{av} \bar{A}_b + V_c \frac{dP}{dy}) \quad (10)$$

$$\text{where: } V_c = V_{ci} + \sum_j \Delta y_i \bar{A}_{bj}$$

V_{ci} and j are the initial volume of combustion chamber and the burning step, respectively. The rate of change of chamber pressure (dP/dy) is computed as follows:

$$\frac{dP}{dy} = \frac{\bar{P}_{av} \Delta r_{av}}{\bar{r}_{av} \Delta y} + \frac{\bar{P}_{av} \Delta A_b}{\bar{A}_b \Delta y} \quad (11)$$

During the quasi-steady state phase, the chamber pressure varies due to the change in the grain surface. The computation of the pressure time curve requires iteration because the burning surface is a function of the distance burnt Δy during a time increment Δt . The grain web is divided into equal distances Δy . Hence the time increment for the calculations is:

$$\Delta t = \frac{\Delta y}{r_{av}} \quad (12)$$

Finally, during tail off, the burning surface decreases sharply in two distinct regimes. In the first regime, the mass of gases produced by combustion still represents a fraction of flow discharge through the nozzle. In the second regime, after the burning is completed, the remainder of combustion gases is simply exhausting out of the nozzle. The first regime characterized by high port area in the nozzle end section together with a reduced mass flow rate in consequence of reduced burning surface. The

conditions of reduced gas velocity and absence of erosive burning (hence, absence of pressure gradient along the chamber) are thus assumed. This can be formatted as follows:

$$P_h = P_n = P_{on} \quad (13)$$

Hence: $r_h = r_n$. The rate of change of chamber pressure is obtained from:

$$\frac{dP}{dy} = \frac{P_{on}}{(1-n)\bar{A}_b} \frac{\Delta A_b}{\Delta y} \quad (14)$$

The second regime is characterized by: (1) zero burning surface and (2) the rate at which the chamber pressure decreases with time is relatively high. The pressure is computed from the relation:

$$P_{on} = P_D \exp[-r^2 c^* A^* (t - t_D) / V_{cf}] \quad (15)$$

where V_{cf} , P_D are the final free volume of the combustion chamber and the discharge pressure, respectively. The discharge mass flow rate can be obtained from:

$$\dot{m}_D = \frac{P_c A_{cr}}{c^*} = \dot{m}_G - \frac{d}{dt} \rho V = \frac{-V}{RT} \frac{dP}{dt} \quad (16)$$

Nozzle critical section erosion is typical in many cases and can significantly impact the value of chamber pressure. The developed model account for nozzle erosion in critical section where the critical diameter expands with time due to erosion expressed by factor (E_r) according to the relation [13]:

$$d_{cr} = d_{cri} + (2 * er_{rate}(t - t_{delay})) \quad (17)$$

where d_{cr} and d_{cri} are instantaneous and initial critical diameters, respectively. er_{rate} is the erosion rate, and t_{delay} is the time lag between motor ignition and nozzle throat erosion onset.

2.2 Internal ballistics prediction model

A grain with star perforation geometry used designed and tested by Maklad [16] in a standard test motor. Results of this static test are adopted here to validate the performance prediction program. Figure 2 shows the star grain geometry. Table 1 lists the parameters of the grain and the test motor whereas Figure 3 illustrates the measured pressure-time profile of the test case.

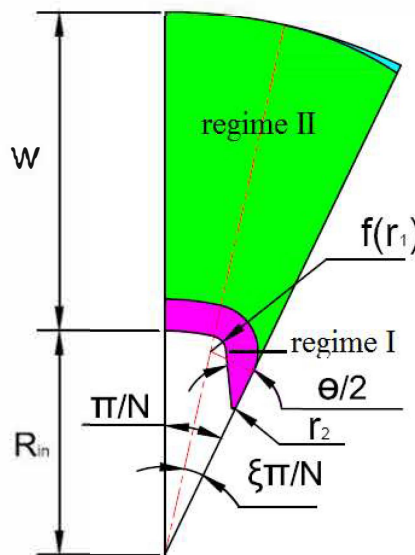
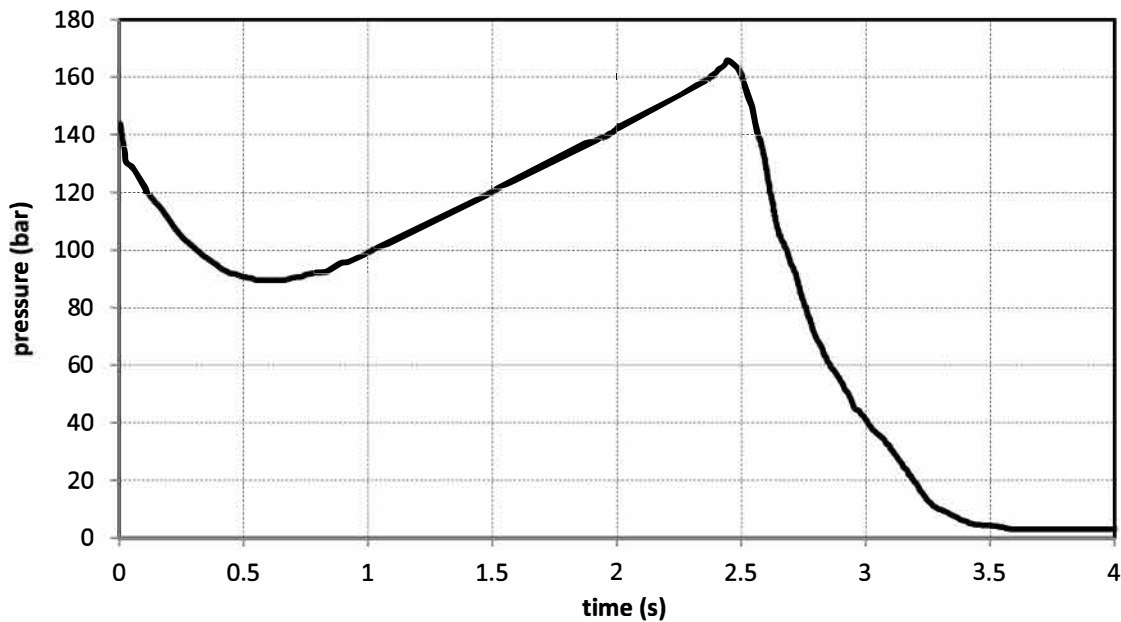


Figure 2: star grain parameters

Table 1 Case study parameters

Propellant characteristics	symbol	value	unit
Propellant characteristic velocity	C^*	1560	m/s
Pressure exponent	n	0.42	---
Burning rate coefficient	a	0.0000113	---
Density of the burning propellant	ρ	1680	Kg/m ³
Specific heat ratio of the combustion gases	γ	1.24	---
Motor characteristics			
Initial critical diameter of nozzle	d_{cr}	0.036	m
Initial free volume of the combustion chamber	V_{ci}	0.004286	m ³
Final chamber volume	V_{cf}	0.017356	m ³
Star grain parameters			
No of star points	N	7	---
Star point angle	θ	74	degree
Angle fraction	ε	0.5058	---
Grain inner radius	R_{in}	0.0235	m
Fillet radius	f	0.0016	m
Web thickness	w	0.0335	m
Length of star grain	L_g	1.6041	m

**Figure 3: Measured pressure-time profile [14]**

2.3 Optimization methods

The developed prediction model involves uncertainties in the given ballistic parameters of the propellant. Six parameters are considered hence namely; burning rate coefficient, a , pressure exponent, n , step regression factor, α , head end regression factor, β , erosion rate of nozzle critical section, er_{rate} , and delay time for the onset of erosion, t_{delay} . The prediction accuracy of the model is thus dependent on the values of these parameters. The set of values of these parameters that maximize the model accuracy are attained by optimization. The six parameters in concern are allowed to vary within their respectable ranges according to the table below. The values for a and n are arbitrarily chosen to engulf the baseline values provided by the experimental work [16]. Values of other parameters are specified based on previous experience of the authors [13].

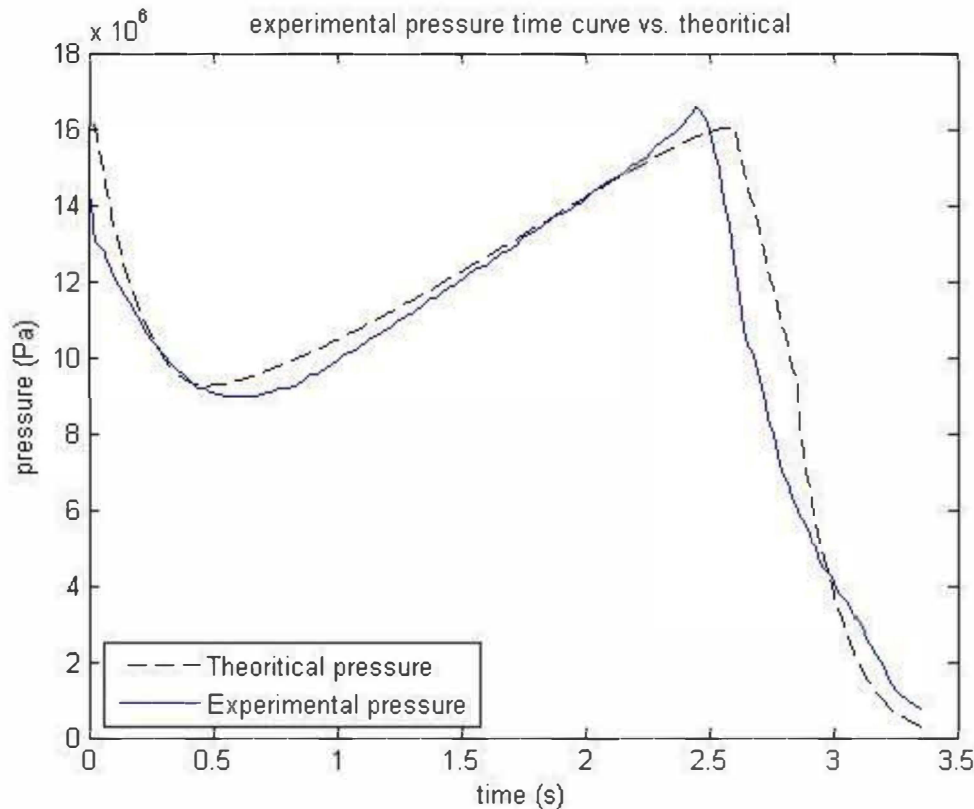
Table 1 Ranges of variation of grain and motor parameters in concern

Design parameters	Symbols	Lower Bound	Upper Bound
Burning rate coefficient	a	100e-07	120 e-07
Pressure exponent	n	0.41	0.43
Step regression factor	α	295e-07	315 e-07
Head end regression factor	β	140	160
Erosion rate of nozzle critical section	er_{rate}	1e-04	3 e-04
Delay time until begin of erosion	t_{delay}	0.01	0.9

A hybrid optimization technique is used to get the minimum RMSE between the theoretical and experimental pressure time profile using Genetic algorithm [17] globally and simulated annealing [18] locally. Genetic Algorithms, GAs, [17] are based on the principle of genetics and natural selection. Here, a "population" is chosen randomly, the fitness of each individual is determined. The operations of selection, crossover, and mutation are used to create the next generation. Simulated Annealing (SA) [18] method simulates the natural process of very slow cooling of heated solids in which the crystalline structures seek the minimum energy path towards solidification. The RMSE is calculated during the quasi-steady state phase only. The optimization is conducted using MATLAB toolbox [19].

3 RESULTS AND DISCUSSION

Figure holds a comparison between the experimental and predicted pressure time profiles of the star perforated grain in concern.

**Figure 4: Theoretical and experimental pressure-time profiles**

Generally, prediction tool manages to predict the trend of pressure-time profile. However, the theoretical model overestimates the starting pressure value and the pressure drop rate during the starting regressive burning phase. This may indicate an overestimation of the initial burning surface area of the star perforation. The model also overestimates the steady-state phase duration. The overall root mean square of prediction during the steady-state phase only (enduring for about 2.5 seconds) is 6.5%.

Next, the optimization algorithm is applied. Figure show the convergence history of genetic algorithm optimizer. The solution was found to converge after 200 iterations. The RMSE of prediction during the steady-state phase is improved to 2.38 %. Optimization is then continued using Simulated Annealing. Figure shows the function value convergence during the simulated annealing optimization. The solution is found to converge after 3245 iterations and the RMSE is improved during the steady-state phase to 2.36 %. The slight improvement in the SA optimization phase indicates that GA has reached the global optimum solution is a high accuracy.

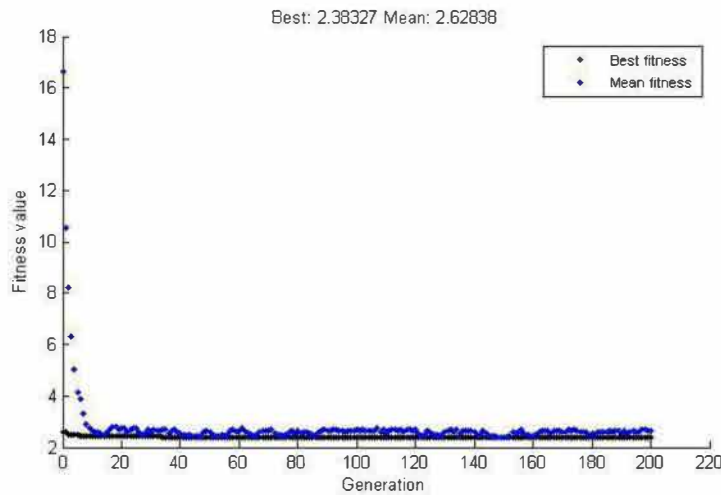


Figure 5: Convergence history of GA optimization

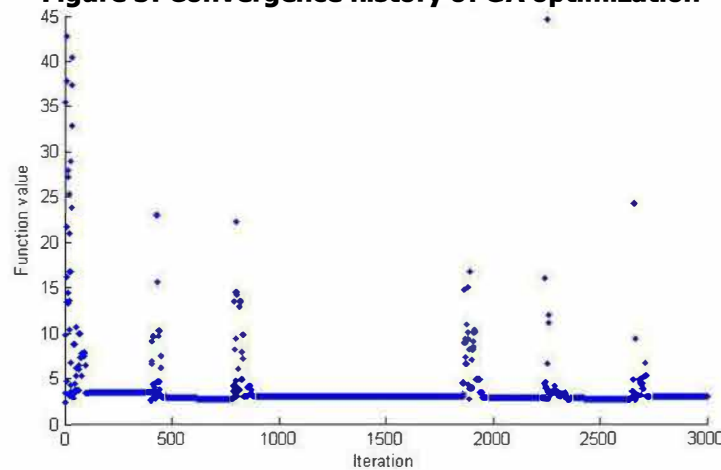


Figure 6: Convergence history of SA optimization

Figure 7 shows the optimized pressure-time profile. The improvement in prediction accuracy is evident especially in the starting regressive burning phase.

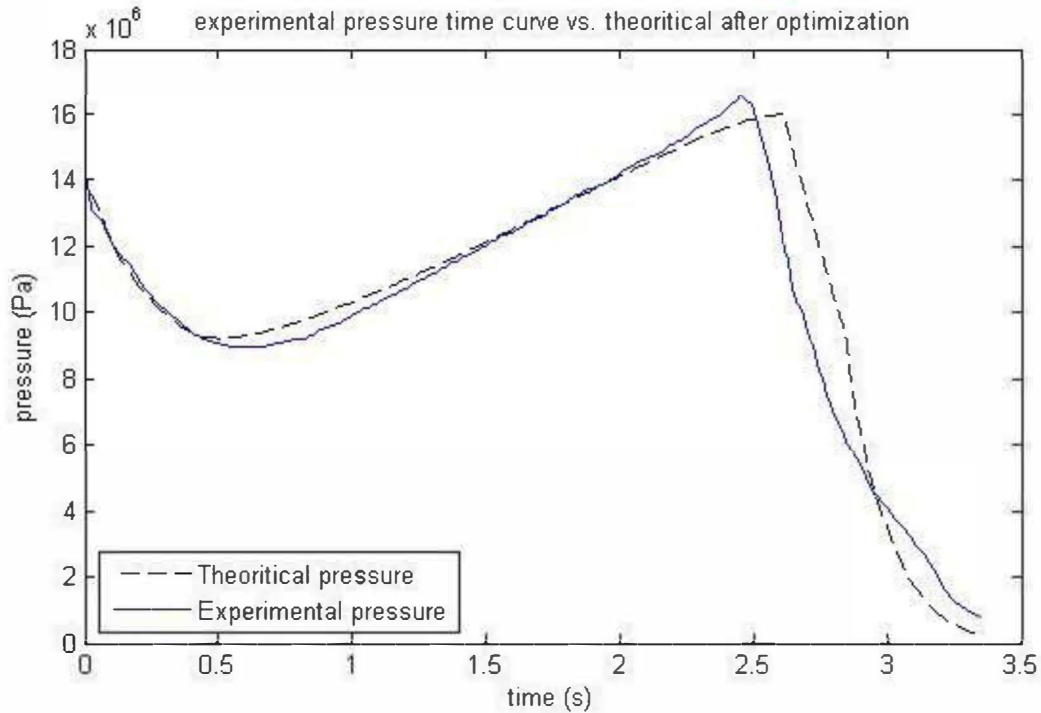


Figure 7: Pressure time curve after optimization

Table 2 below lists the optimized values of the parameters in concern in this study. For the sake of comparison, the corresponding baseline values, lower and upper bounds of variation are also listed.

Table 2 Design parameters at all design phases and lower and upper bounds.

Design parameters	Symbols	Lower Bound	Upper Bound	Base line values	Optimized solution GA	Optimized solution SA
Burning rate coefficient	a	100e-07	120 e-07	113e-07	110.13 e-07	110.12 e-07
Pressure exponent	n	0.41	0.43	0.42	0.422	0.421
Step regression factor	α	295e-07	315 e-07	308e-07	304.91 e-07	304.81 e-07
Head end regression factor	β	140	160	150	154.909	154.859
Erosion rate of nozzle critical section	er_{rate}	1e-04	3 e-04	2e-04	1.053 e-04	1.049 e-04
Delay time until begin of erosion	t_{delay}	0.01	0.9	0.7	0.0256	0.0254
Root mean square error of prediction	RMSE	-	-	6.5 %	2.38 %	2.36 %

4 CONCLUSIONS AND FUTURE WORK

A mathematical model is developed to predict the pressure-time profile of a star-perforated solid propellant grain. The developed tool is capable of predicting the performance of a test case that was experimentally tested with a reasonable accuracy. The prediction accuracy of the model is enhanced by tuning the grain ballistic and geometric parameters using a hybrid GA/SA. Upon performing the hybrid optimization technique, the prediction model tool becomes more accurate. Further work should focus on improving the prediction accuracy of the model during the exhaust phase. The developed

technique can be also utilized in predicting of grain geometry to satisfy a predefined performance. The model can be enhanced by incorporating different grain geometries.

REFERENCES

1. G. Puskulcu; 2004; "Analysis of 3-D Grain Burnback of Solid Propellant Rocket Motors and Verification with Rocket Motor Tests"; *MS. Thesis*, Dept. of Mechanical Engineering; METU.
2. K. Nisar, L. Guozhu, and Q. Zeeshan; 2008; "A hybrid optimization approach for SRM finocyl grain design"; *Chinese Journal of Aeronautics*; **21**; pp. 481-487.
3. F. M. Villanueva, L. S. He, and D. J. Xu; 2014; "Solid Rocket Motor Design Optimization Using Genetic Algorithm"; *Advanced Materials Research*; **509**; pp. 502-506.
4. A. Kamran, L. Guozhu, A. F. Rafique, S. Naz, and Q. Zeeshan; 2010; "Star Grain Optimization using Genetic Algorithm"; in *51st AIAA/ASME/ASCE/AHS/ASC Structures, Structural Dynamics, and Materials Conference 18th AIAA/ASME/AHS Adaptive Structures Conference 12th*; pp. 3084.
5. A. Kamran and L. Guozhu; 2010; "Design and optimization of 3D radial slot grain configuration"; *Chinese Journal of Aeronautics*; **23**; pp. 409-414.
6. M. A. Raza and W. Liang; 2013; "Design and Optimization of 3D Wagon Wheel Grain for Dual Thrust Solid Rocket Motors"; *Propellants, Explosives, Pyrotechnics*; **38**; pp. 67-74.
7. M. A. Raza and W. Liang; 2012; "Robust performance optimization of dual thrust rocket motor"; *Aircraft Engineering and Aerospace Technology*; **84**; pp. 244-251.
8. M. A. Raza and W. Liang; 2011; "Robust Design Optimization of an Aerospace Vehicle Prolusion System"; *Mathematical Problems in Engineering*; **2011**.
9. M. Aamir Raza and W. Liang; 2012; "Robust Design Optimization of Dual Thrust Solid Propellant Motors due to Burning Rate Uncertainties"; *Propellants, Explosives, Pyrotechnics*; **37**; pp. 476-488.
10. O. Yucel, S. Acik, K. A. Toker, Z. Dursunkaya, and M. H. Aksel; 2015; "Three-dimensional grain design optimization of solid rocket motors"; in *Recent Advances in Space Technologies (RAST), 7th International Conference on*; pp. 471-476.
11. S. Acik; 2010; "Internal Ballistic Design Optimization of a Solid Rocket Motor"; *Master Thesis*, Mechanical Engineering; Middle East Technical University; Turkey.
12. R. H. Sforzini; 1980; "An automated approach to design of solid rockets utilizing a special internal ballistics model"; *AIAA*.
13. A. R. A. Gawad, M. Y. Ahmed, H. M. Abdalla, and M. A. El-Senbawy; 2016; "Pressure Profile Prediction of Dual-Thrust Rocket Motors under Uncertainties"; *Propellants, Explosives, Pyrotechnics*; **41**; pp. 965-971.
14. M. Barrere; 1960; *"Rocket Propulsion"*.
15. G. P. Sutton and O. Biblarz; 2010; *"Rocket Propulsion Elements"*.
16. A. Maklad; 1994; "Design Optimization of Solid Rocket Motors"; *Master Thesis*; MTC.
17. D. E. Goldberg; 1989; "Genetic Algorithms in Search, Optimization, and Machine Learning, 1st ed "; Addison-Wesley, Reading, MA.
18. S. Kirkpatrick, C. D. Gelatt, M. P. Vecchi; 1983; "Optimization by Simulated Annealing"; *Science*; **220** (4598), pp: 671-680.
19. M. Abramson; 2004; "Genetic Algorithm and Direct Search Toolbox User's Guide For Use with MATLAB"; *The MathWorks*.

Optimization of noise abatement aircraft terminal routes using a multi-objective evolutionary algorithm based on decomposition

V. Ho-Huu¹, S. Hartjes², L. H. Geijselaers³, H. G. Visser⁴, R. Curran⁵

Faculty of Aerospace Engineering, Delft University of Technology, Delft, The Netherlands

¹PhD candidate, ²Assistant professor, ³Master student, ⁴Associate professor, ⁵Professor

Address: P.O. Box 5058, 2600 GB Delft, The Netherlands

E-mails: v.hohuu@tudelft.nl (V. Ho-Huu), s.hartjes@tudelft.nl (S. Hartjes),

lisset.geijselaers@gmail.com (L. H. Geijselaers) h.g.visser@tudelft.nl (H. G. Visser), r.curran@tudelft.nl (R. Curran)

ABSTRACT

Recently, a multi-objective evolutionary algorithm based on decomposition (MOEA/D) has emerged as a potential method for solving multi-objective optimization problems (MOPs) and attracted much attention from researchers. In MOEA/D, the MOPs are decomposed into a number of scalar optimization sub-problems, and these sub-problems are optimized concurrently by only utilizing the information from their neighboring sub-problems. Thanks to these advantages, MOEA/D has demonstrated to be more efficient than the non-dominated sorting genetic algorithm II (NSGA-II) and other methods. However, its applications to practical problems are still limited, especially in the domain of aerospace engineering. Therefore, this paper aims to present a new application of MOEA/D for the optimal design of noise abatement aircraft terminal routes. First, in order to optimize aircraft noise for aircraft terminal routes while taking into account the interests of various stakeholders, bi-objective optimization problems including noise and fuel consumption are formulated, in which both the ground track and vertical profile of a terminal route are optimized simultaneously. Then, MOEA/D is applied to solve these problems. Furthermore, to ensure the design space of vertical profiles is always feasible during the optimization process, a trajectory parameterization technique recently proposed is also used. This technique aims at reducing the number of model evaluations of MOEA/D and hence the computational cost will decrease significantly. The efficiency and reliability of the developed method are evaluated through case studies for departure and arrival routes at Rotterdam The Hague Airport in the Netherlands.

KEYWORDS: *terminal routes, trajectory optimization, noise abatement, fuel consumption, MOEA/D.*

THE RELATIVE MOTION OF A SPACECRAFT NEAR A GEOSTATIONARY POSITION

Roxana Alexandra Petre

University "Politehnica" of Bucharest

PhD student

313 Splaiul Independenței, Bucharest 060042, Romania

petre.roxana.alexandra@gmail.com

Ion Stroe

University "Politehnica" of Bucharest

Professor

ion.stroe@gmail.com

Andrei Craifaleanu

University "Politehnica" of Bucharest

Professor

ycraif@yahoo.com

Thien Van Nguyen

University "Politehnica" of Bucharest

PhD student

bangden33468@gmail.com

ABSTRACT

In this paper the relative motion of a vehicle in the neighborhood of a geostationary orbit is studied. The vehicle is a satellite equipped with a propulsion system capable of providing the necessary force for pulse orbital transfer, so that the satellite remains in the desired region. Different numbers of necessary maneuvers applied to the satellite were considered and compared, in order to determine the most advantageous situation. Also considering that the fuel consumption is directly proportional to the developed pulse, it results that a lower number of maneuvers is more advantageous for the fuel consumption.

KEYWORDS: *relative motion, satellite, latitude, longitude, pulse.*

NOMENCLATURE

A - fixed point in space

B - point on the equatorial line above which the satellite is at a certain moment of time

i - inclination of orbit

M_0 - satellite

n - number of maneuvers

R - radius of the Earth

θ - position angle of the satellite on the inclined orbit

γ - longitude difference between the satellite and the station

φ - latitude of the satellite

λ - longitude

α - angle between the velocity direction and the local parallel

v - total speed

Δp - pulse

Δp_i - total pulse

m - mass of satellite

n - number of maneuvers

1 INTRODUCTION

Numerous technical applications, such as radio communications and TV programs broadcasting, are facilitated by the use of geostationary satellites, since such bodies orbiting in the equatorial plane are in apparent rest with respect to the ground. But the increasing use of this type of space objects has led to the congestion of the circumterrestrial zone in which the geostationary motion is possible.

A solution to this problem is the flight in geostationary orbits parallel to the equatorial plane. However, a satellite in free motion in a non-equatorial plane is moving with respect to the Earth [1]. As a result, maintaining the geostationary motion at non-zero latitudes requires the application of a continuous traction in meridian plane [2], which involves continuous fuel consumption. In reference [5] the possibility of using space sails in order to produce this traction is considered.

In this paper another strategy is proposed, which consists in maintaining a satellite near a small latitude geostationary orbit by following a path composed of arcs on which the motion takes place freely, the transition from one arc to the other being carried out with pulse traction [2], [3] (Fig. 1). The study is performed for a number n of maneuvers. By pulse orbital transfer, the shape and orientation of the satellite orbit is changed.

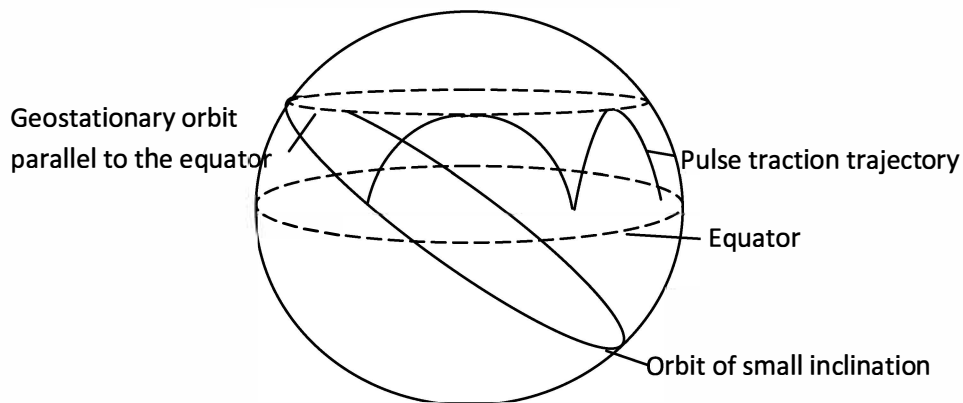


Figure 1: The pulse traction trajectory of the satellite

2 APPARENT MOTION OF THE SYNCHRONOUS SATELLITE ON AN INCLINED ORBIT

It is considered that the satellite orbit is synchronous and inclined with a certain angle. The motion takes place in a central gravitational field, with the assumption that the satellite is a material point upon which there are no influences from aerodynamic forces. The radiation pressure is neglected. The trajectory of the satellite is described in Fig. 2.

By studying triangle ABM_0 in Fig. 2, the following relations can be obtained [1]:

$$\begin{cases} \sin \theta = \frac{\sin \varphi}{\sin i} \\ \cos \theta = \cos \varphi \cos (\theta - \gamma) \end{cases} \quad (1)$$

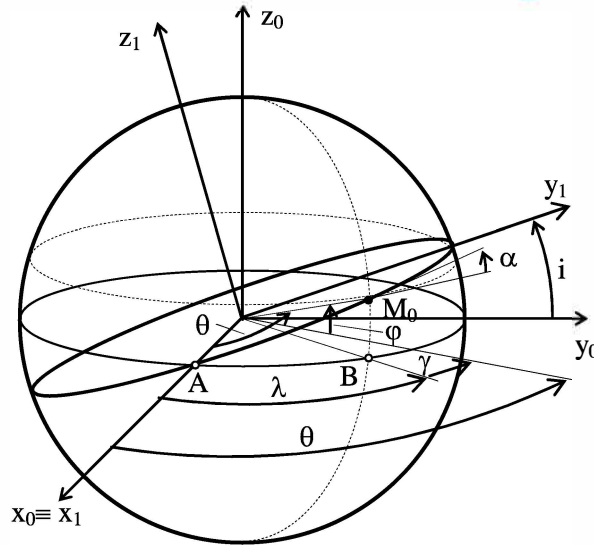


Figure 2: Apparent motion of satellite

The necessary calculations can be performed by studying only the first quadrant represented in Fig. 2, due to symmetry reasons. Thus, by eliminating θ from Eq.1, γ is obtained:

$$\gamma = \theta - \arccos \frac{\cos \theta}{\cos \varphi} = \theta - \arccos \frac{\sqrt{1 - \frac{\sin^2 \varphi}{\sin^2 i}}}{\cos \varphi} \quad (2)$$

or

$$\gamma = \arccos \sqrt{1 - \frac{\sin^2 \varphi}{\sin^2 i}} - \arccos \frac{\sqrt{1 - \frac{\sin^2 \varphi}{\sin^2 i}}}{\cos \varphi} \quad (3)$$

The above equation can be rewritten as

$$\gamma = \arccos \frac{1}{\cos \varphi} \left(1 - \frac{1 - \cos i}{\sin^2 i} \sin^2 \varphi \right) \quad (4)$$

and noting

$$K = \frac{1 - \cos i}{\sin^2 i} = \frac{1}{2 \cos^2 \frac{i}{2}} \quad (5)$$

the following relation is obtained [1]:

$$\cos \gamma = \frac{1 - K \sin^2 \varphi}{\cos \varphi} \quad (6)$$

The above relation describes the dependency between φ and γ .

3 PULSE ORBITAL TRANSFER

In order to apply a number n of pulse orbital transfer maneuvers, so that the satellite remains in the geostationary region, the angle α must be calculated (Fig. 2). This angle determines the orientation of

the pulse that has to be applied to the satellite.

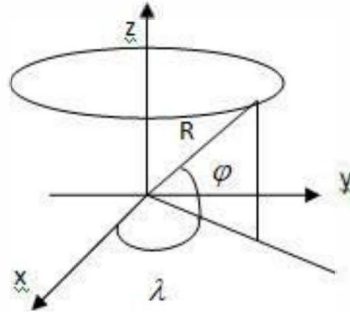


Figure 3: Coordinates of the satellite

The following relations were determined using the notations in Fig. 2 and Fig. 3:

$$\begin{cases} x = R \cos \varphi \cos \lambda \\ y = R \cos \varphi \sin \lambda \\ z = R \sin \varphi \end{cases}, \quad (7)$$

where $\varphi = \text{const}$.

The tangent vector to the local parallel and its components with respect to reference system $x_0y_0z_0$ are:

$$\vec{U} : \begin{cases} \dot{x} = -R\dot{\lambda} \cos \varphi \sin \lambda \\ \dot{y} = R\dot{\lambda} \cos \varphi \cos \lambda \\ \dot{z} = 0 \end{cases}. \quad (8)$$

The parametric equations of the inclined orbit with respect to reference system $x_1y_1z_1$ are:

$$\begin{cases} x_1 = R \cos \theta \\ y_1 = R \sin \theta \\ z_1 = 0 \end{cases}. \quad (9)$$

The tangent vector to the inclined orbit and its components with respect to reference system $x_1y_1z_1$ are:

$$\vec{V} : \begin{cases} \dot{x}_1 = -R\dot{\theta} \sin \theta \\ \dot{y}_1 = R\dot{\theta} \cos \theta \\ \dot{z}_1 = 0 \end{cases}. \quad (10)$$

The transformation formula of the components of an arbitrary vector \vec{x} with respect to the reference system $x_1y_1z_1$ to reference system $x_0y_0z_0$ is:

$$\begin{Bmatrix} x \\ y \\ z \end{Bmatrix}_0 = \begin{Bmatrix} 1 & 0 & 0 \\ 0 & \cos i & \sin i \\ 0 & -\sin i & \cos i \end{Bmatrix} \begin{Bmatrix} x \\ y \\ z \end{Bmatrix}_1. \quad (11)$$

By combining Eq.10 and Eq.11, the following expression is obtained for the components of vector \vec{V} with respect to reference system $x_0y_0z_0$:

$$\vec{v} : \begin{Bmatrix} \dot{x}_1 \\ \dot{y}_1 \\ \dot{z}_1 \end{Bmatrix}_0 = \begin{Bmatrix} -R\dot{\theta} \sin \theta \\ R\dot{\theta} \cos \theta \cos i \\ -R\dot{\theta} \cos \theta \sin i \end{Bmatrix} \quad (12)$$

The angle α is obtained:

$$\cos \alpha = \frac{\vec{u} \cdot \vec{v}}{|\vec{u}| |\vec{v}|} = \sin \theta \sin \lambda + \cos \theta \cos \lambda \cos i \quad (13)$$

By replacing Eq.1 in Eq.13, the following form is obtained

$$\cos \alpha = \frac{\sin(\theta - \gamma) \sin \varphi}{\sin i} + \cos^2(\theta - \gamma) \cos \gamma \cos i \quad (14)$$

The unitary pulse, i.e. the pulse divided by the mass of the satellite, is

$$\frac{\Delta p_t}{m} = 2v \sin \alpha \quad (15)$$

The total pulse is

$$\Delta p_t = n \Delta p \quad (16)$$

4 NUMERICAL APPLICATION

A Matlab program was used in order to obtain the needed numerical results, and the dependency of one date upon the other, in order to deduce the optimum solution.

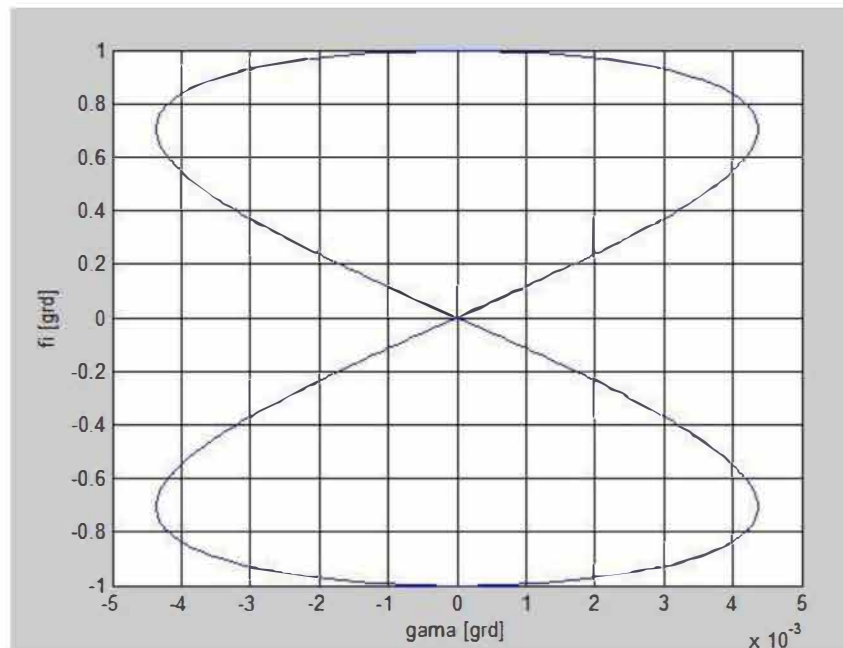


Figure 4: The apparent motion of the satellite at incidence 1°

Fig. 4 shows the dependence between φ and γ when the orbit has a small inclination of 1°. Since the

distances covered by the satellite are proportional with φ and γ , the satellite performs an 8-shaped apparent motion on the celestial sphere.

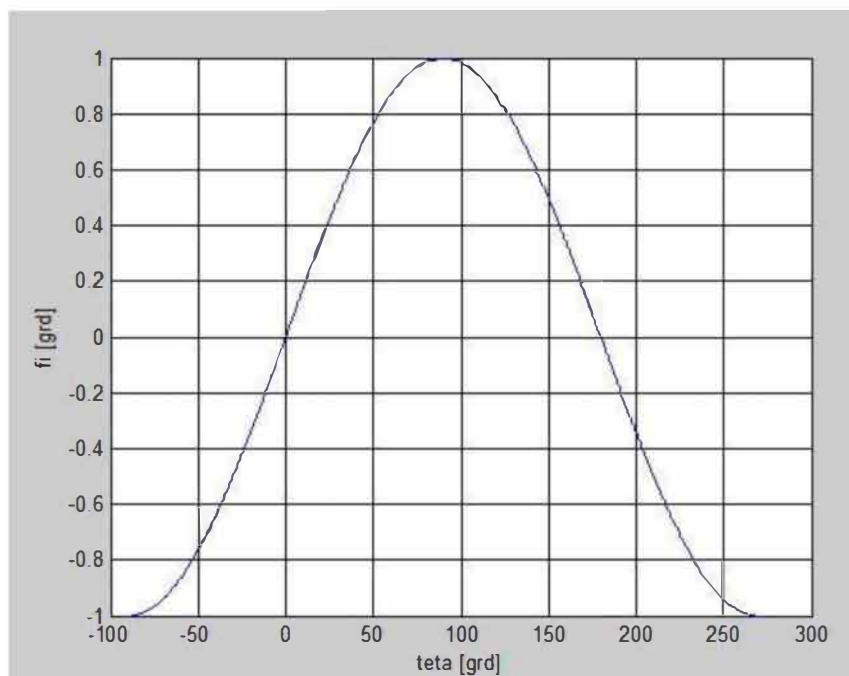


Figure 5: The variation of φ with respect to θ

Fig. 5 describes the variation of φ with respect to θ , i.e. the variation of the angular coordinates of the satellite with respect to the ground.

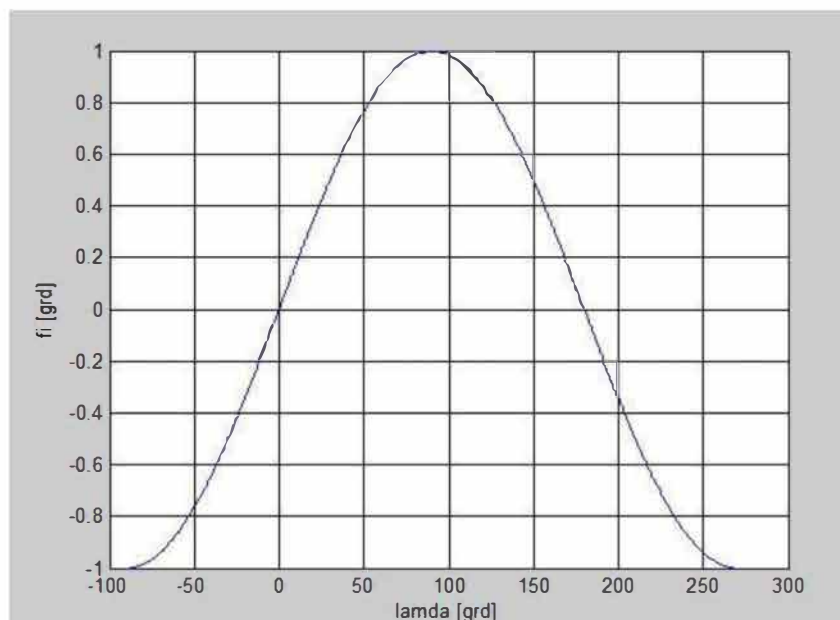


Figure 6: The variation of φ with respect to λ

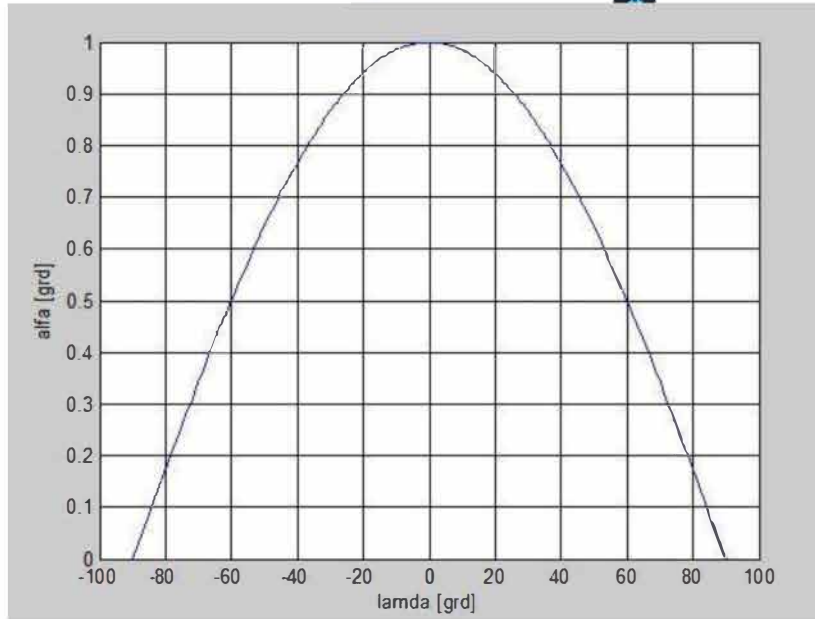


Figure 7: The variation of angle α with respect to λ

The numerical values obtained for various parameters defining the motion of the satellite are shown in Table 1.

Table 1: numerical values obtained in Matlab

n	φ (degree)	θ (degree)	λ (degree)	α (degree)	v (m/s)	$\frac{\Delta p_t}{m}$ (m/s)
3	-0.5	-29.9962	120	0.8660	92.8611	278.5833
4	0	0	90	1	107.2227	428.8907
6	0.5	30.0038	60	0.8660	92.8576	557.1453
12	0.8660	60.0038	30	0.5	53.6113	643.34
24	0.9659	75.002	15	0.2588	27.7513	666.03

The analyzed cases show that the total pulse necessary to maintain the satellite on the orbit increases with the number n of pulse traction maneuvers. It follows that among the analyzed cases the optimal situation is obtained when $n=3$ maneuvers, which means that the satellite will need to execute only three maneuvers during a whole rotation about the Earth. The fuel consumption is also optimal at $n=3$, since the fuel consumption is directly proportional to the pulse needed for the satellite to execute the maneuvers.

3 CONCLUSIONS

The paper deals with the relative motion of a satellite on an orbit of 1° inclination. The apparent free motion of the satellite is studied and, afterwards, a pulse is applied to the satellite so that it will move to the desired geostationary orbit. Various values were obtained, depending on the number of maneuvers applied to the satellite in order to bring it back to the orbit. The optimal value was obtained for only 3 maneuvers. This is also optimal from the point of view of fuel consumption, due to the fact that the fuel consumption is proportional to the value of the pulse needed to be applied.



REFERENCES

1. Mugur Savescu; 1976; "Intiere in radiocomunicatii prin sateliti"; Ed.Tehnica.
2. M.M. Niță; 1973; "Teoria zborului spațial"; Ed. Academiei.
3. I. Stroe; "Attitude control of the satellite for elliptic orbits"; IAF-96-A.5.07.
4. M.M. Niță, I. Stroe, P. Pârvu, S. Cioc; 1998; "Rotația relativă a corpurilor în raport cu stații orbitale de mari dimensiuni"; *Studii și Cercetări de Mecanica Aplicată*, 57; (1);pp.18-28.
5. Jeannette Heiligers; 2010; "Displaced Geostationary orbits using Hybrid Low-Thrust Propulsion", *Advanced Space Concepts Laboratory*; University of Strathclyde; Glasgow, United Kingdom.

System and method for flight envelope expansion via piezoelectric actuation

Ioan Ursu

INCAS – National Institute for Aerospace Research "Elie Carafoli"

Senior Researcher

Iuliu Maniu 220, Bucharest 061126, Romania

Dragos Daniel Ion Guta

INCAS – National Institute for Aerospace Research "Elie Carafoli"

Senior Researcher

George Tecuceanu

INCAS – National Institute for Aerospace Research "Elie Carafoli"

Senior Researcher

Alexandru-Gabriel Persinaru

INCAS – National Institute for Aerospace Research "Elie Carafoli"

Aerospace Engineer

Daniela Enciu

INCAS – National Institute for Aerospace Research "Elie Carafoli"

Research Scientist

Corresponding author: enciu.daniela@incas.ro

Ionel Popescu

STRAERO – Institute for Theoretical and Experimental Analysis

of Aeronautical-Astronautics Structures

Aerospace Engineer

Cornel Stoica

INCAS – National Institute for Aerospace Research "Elie Carafoli"

Senior Researcher

ABSTRACT

The paper presents the design and the complex tests of a laboratory demonstrator which aims to show that it is possible to increase the flutter speed and thus to widen the aircraft flight envelope. The demonstrator was developed within the national UEFISCDI Project "Antiflutter demonstrator with piezoelectric actuation" (AFDPA) and is in fact an intelligent model of wing, which is itself a control system, with sensors, piezo actuator and an implemented control law. Research and tests in the subsonic wind tunnel are underway and will be completed until September this year. The piezoelectric actuator was manufactured and tested. The working of the control law based on the method of receptance was studied by numerical simulations and was verified on a laboratory scale model. The main advantage of the piezo actuator, the bandwidth (about 30 Hz, versus the measured about 5 Hz flutter frequency), is exploited. The main advantage of the receptance method of eigenvalues assignment is that the control law is obtained based on measurements rather than on the conventional matrix theory, which is typically for state space methods. It is important to mention that the receptance method requires the online measurement of frequency response functions so that there is no requirement to know or to evaluate the structural mass, damping and stiffness matrices, or the



aerodynamic matrices. Also, the difficult operations of model order reduction and observer building to estimate the unmeasured state variables are avoided.

The content of the paper refers in detail to technical solutions for wing model design, for amplification of the actuator output displacement, simultaneously with the optimization of useful force, and to preliminary experimental results in subsonic wind tunnel.

KEYWORDS: *active control, flutter frequency, flutter speed, flight envelope, receptance method*

Sealing technologies trade-off for a Phobos Sample Return Mission

Radu MIHALACHE

Romanian Research and Development Institute for Gas Turbines COMOTI

Scientific Researcher

220 D Iuliu Maniu Bd., sector 6, cod 061126, OP 76, CP174, Bucharest, Romania

radu.mihalache@comoti.ro

Dragos MIHAI

Romanian Research and Development Institute for Gas Turbines COMOTI

Scientific Researcher

220 D Iuliu Maniu Bd., sector 6, cod 061126, OP 76, CP174, Bucharest, Romania

dragos.mihai@comoti.ro

Gheorghe MEGHERELU

Romanian Research and Development Institute for Gas Turbines COMOTI

Scientific Researcher

220 D Iuliu Maniu Bd., sector 6, cod 061126, OP 76, CP174, Bucharest, Romania

gheorghe.megherelu@comoti.ro

Ionut Florian POPA

Romanian Research and Development Institute for Gas Turbines COMOTI

Assistant Researcher

220 D Iuliu Maniu Bd., sector 6, cod 061126, OP 76, CP174, Bucharest, Romania

ionut.popa@comoti.ro

Daniel OLARU

Romanian Research and Development Institute for Gas Turbines COMOTI

Assistant Researcher

220 D Iuliu Maniu Bd., sector 6, cod 061126, OP 76, CP174, Bucharest, Romania

daniel.olaru@comoti.ro

Dan IFRIM

Romanian Research and Development Institute for Gas Turbines COMOTI

Technical Development Engineer

220 D Iuliu Maniu Bd., sector 6, cod 061126, OP 76, CP174, Bucharest, Romania

dan.ifrim@comoti.ro

ABSTRACT

The Phobos Sample Return Mission (PhSR) is a phase of the Mars Robotic Exploration Preparation program, with the main objective to acquire and return 100 grams of Phobos soil (regolith) on Earth. First, a complete surface map with topographic and mineralogic information will be obtained by the spacecraft. After a successful sampling, an ERV containing the ERC with the regolith sample will head back to the Earth. Following touch-down, the ERC will be retrieved and opened in a dedicated environment. Given the importance and value of such return sample, it must be well protected between the moment when the ERC is closed on Phobos after the sampling operation until landing on Earth surface. Thus, a special containment system is necessary, capable of withstanding the harsh space environment and the mechanical stress occurred during the mission, while preserving the integrity of the regolith sample. Following previous sampling missions (Hayabusa, Stardust) and the problems raised by the contamination, one can say that the sealing system is probably the most important part of a sample containment system, as it shall protect the sample from Earth contaminants, but also to protect the Earth against possible micro-organisms or other hazardous substances found in space. This paper aims to analyse a variety of sealing technologies with importance in space applications like a sample return mission, measuring qualitatively and quantitatively the performance of a sealing



technology when it comes to fulfilling a series of requirements imposed by the sample return mission profile. Using these requirements and mission data as inputs, a trade-off analysis was made, to identify the most suitable sealing technology for a PhSR Mission. It was concluded that sealing technologies such as O-rings and Gaskets can be successfully used in these kind of missions, paying also attention to a proper design of the containment system.

KEYWORDS: *sealing system trade-off, sample return, exploration.*

Development of a Methodology for Assessing and Exploiting Innovative Aircraft Concepts and Technologies

Dr.-Ing. Yaolong Liu

*Institute of Aircraft Design and Lightweight Structures, TU Braunschweig
and Aeronautics Research Centre Niedersachsen (NFL)*

*Postdoctoral research fellow
38108 Braunschweig, Germany
yaolong.liu@tu-braunschweig.de*

Prof. Dr.-Ing. Peter Horst

*Institute of Aircraft Design and Lightweight Structures, TU Braunschweig
Head and Professor*

Prof. Dr.-Ing. Jens Friedrichs

*Institute of Jet propulsion and Turbomachinery, TU Braunschweig
Head and Professor*

ABSTRACT

Aiming to reduce the CO₂ and NO_x emissions or even to achieve emission-free air transport, aeronautic researchers and engineers have made effort to pursue green and efficient on-board energy storage and conversion systems with advanced aircraft technologies. In the framework of Energy Transition in Aviation Project (EWL), the perspectives concerning aircraft design are studied. The challenges and requirements of aircraft design for integrating new airframe and energy system technologies are discussed at first. Then, the modelling approaches including parameterization and disciplinary simulation methods are illustrated in detail. After that, some preliminary results regarding the overall aircraft level impacts (takeoff weight, operating weight empty and fuel burn) of technology progress are presented and discussed.

KEYWORDS: Aircraft conceptual design, modeling and simulation, alternative fuel, sustainable aviation

Scaling of Airborne Ad-hoc Network Metrics with Link Range and Satellite Connectivity

Kai-Daniel F. Büchter

Bauhaus Luftfahrt e.V.

Future Technologies and Ecology of Aviation

Willy-Messerschmitt-Str. 1, 82024 Taufkirchen, Germany

kai-daniel.buechter@bauhaus-luftfahrt.net

Oleg Milshtein

Bauhaus Luftfahrt e.V.

Student Researcher Future Technologies and Ecology of Aviation

ABSTRACT

In this contribution, performance metrics for commercial aeronautical ad-hoc networks are presented and evaluated. The investigation is based on a simulation environment which uses input from 2016 flight schedule and aircraft performance databases for flight movement modeling, along with a defined infrastructure of ground gateways and communication satellites. A cluster-based algorithm is used to build the communication network topology between aircraft. Cloud top pressure data can be considered to estimate cloud height and evaluate the impact of link obscuration on network availability, assuming a free-space optics-based communication network.

The effects of communication range, satellite availability, fleet equipage ratio and clouds are discussed. It is shown how network reach and performance can be enhanced by adding taps to the network in the form of high-speed satellite links. The effect of adding these is two-fold: firstly, network reach can be increased by connecting remote aircraft clusters. Secondly, larger clusters can effectively be split into smaller ones in order to increase performance especially with regard to hop count and available overall capacity. In a realistic scenario concerning communication range and with moderate numbers of high-speed satellite terminals, on average, 78% of all widebody aircraft can be reached. With clouds considered (assuming laser links), this number reduces by 10%.

KEYWORDS: *Aeronautical Ad-hoc Networks, Aeronautical Telecommunications, Laser Communication*

ESTIMATION OF MISSION FUEL SAVINGS POTENTIAL USING THERMOELECTRIC RECUPERATION IN AERO-ENGINES

*Kai-Daniel F. Büchter
 Bauhaus Luftfahrt e.V.
 Future Technologies and Ecology of Aviation
 Willy-Messerschmitt-Str. 1, 82024 Taufkirchen, Germany
 kai-daniel.buechter@bauhaus-luftfahrt.net*

*Ulrich Kling
 Bauhaus Luftfahrt e.V.
 Researcher Visionary Aircraft Concepts*

*Christoph Bode and Jens Friedrichs
 Institute of Jet Propulsion and Turbomachinery
 University of Braunschweig
 Hermann-Blenk-Str. 37, 83108 Braunschweig, Germany*

ABSTRACT

The reduction of fuel consumption represents a major challenge on the way to an environmentally friendly air transport system. Thermoelectric generators (TEG) can offer a robust solution for direct conversion of lost heat from an aero-engine to electricity, reducing the fuel burn fraction of engine offtake and thereby required mission fuel. The overarching goal of the TERA-project (Thermoelectric Energy Recuperation for Aviation) within Germany's fifth Aeronautical Research Program (LuFo-V) is thus to evaluate the potentials of TEG on engine and aircraft level. To that effect, integration between the hot section of the engine and the cooler bypass flow is considered to quantify achievable output power.

Fundamentally, two aspects determine the success of the concept: Firstly, the gravimetric power density of the TEG, which depends on thermoelectric material properties and thermal conditions, determines whether a break-even performance can be reached. Beyond break-even, mission fuel is saved. Secondly, the total generated power, limited by the TEG size and available area, determines the overall fuel savings potential.

In this contribution, a trade-study approach is presented. In order to evaluate the fuel savings potentials, an aircraft with entry-into-service in 2035 was defined and sized for future requirements as a baseline. Mission fuel is calculated as function of TEG power and weight of the TEG system. Two models are used: a simple model based on the Breguet range equation considering cruise phase only, and a more elaborate mission-based model, in which the aircraft is sized according to engine offtake and weight modifications. Results are presented for design and off-design missions and collated to expected TEG performance. From the trade studies, break-even power density is determined, and the fuel savings potential evaluated. Preliminary studies, based on a TEG integrated into the engine nozzle, indicate a fuel savings potential of one tenth of a percent.

KEYWORDS: *Aero-engine, Energy Recuperation, Fuel Savings, Thermoelectric Generator, Waste Heat Recovery*



Parametric Study on Taper-ended Internal-burning Solid Propellant Grains

Mahmoud Y. M. Ahmed

Aerospace Department, Military Technical College, Cairo, Egypt Mahmoud.yehia@mtc.edu.eg

ABSTRACT

The design of the solid propellant grain is a decisive aspect of the solid propellant rocket motor performance. Tubular grain design is a favorable design since it produces a high neutral thrust profile. However, neutrality of tubular grains deteriorates as the aspect ratio of the grain deviates from an optimum value that is dependent on the web thickness. In some cases, the undesirable phenomenon of erosive grain burning may take place. One simple solution to restore neutrality is to add taper to the ends of the grain. Loss of motor filling comes as penalty for adding these tapered ends. The grain should thus be tailored to simultaneously satisfy both desired design objectives namely, neutrality and filling. The present paper aims to address the dependence of these two design objectives on the design of a taper-ended tubular grain. The designs that are likely to yield erosive burning are also addressed. A parametric study is conducted involving the aspect ratio of the grain, its web thickness, and the taper angles on both ends.

KEYWORDS: *Solid propellant rocket propulsion, grain design, neutrality, filling coefficient, erosive burning.*

Control of cavity acoustics by surface waviness in landing configurations

Mr. BELKALLOUCHE Abderrahmane, Prof. REZOUG Tahar
Laboratoire des Sciences Aeronautiques, I.A.E.S (Universite Saad Dahlab-Blida1). Algeria
aerotechiab@hotmail.fr

Prof. DALA Laurent
Mechanical and Construction Engineering Department
Northumbria University Newcastle, NE1 8ST, UK

ABSTRACT

Aircraft noise is dominant for residents near airports when planes fly at low altitudes such as during departure and landing. Flaps, wings, landing gear contribute significantly to the total sound emission. This paper investigates the use of a sinusoidal surface modification application upstream of a cavity as a passive acoustics control device in approach conditions. Optimum sinusoidal amplitude and frequency were previously determined by the means of a two-dimensional computational fluid dynamics analysis for a cavity with a length to depth ratio of 4. The overall sound pressure level was reduced with the surface modification at the majority of the points investigated.

KEYWORDS : *Aeroacoustics, Landing Configurations, Cavity Noise, Surface waviness, OpenFOAM.*

NOMENCLATURE

D - Cavity Depth	$P_{ref} - P_{ref} = 2 \times 10^{-5}$ Pa, The value adopted as the minimum audible sound pressure variation
L - Cavity Length	SPL - Sound Pressure Level
δ - Boundary layer thickness	PSD - Power Spectral Density
f - Acoustic frequency of disturbance	OASPL - Overall Sound Pressure Level
f_m - Frequency of the m^{th} mode	$\hat{f}f\hat{t}$ - Fast Fourier Transform
p' - Pressure perturbations	OpenFOAM - Open Field Operation And Manipulation
p_{rms} - Root mean square pressure	
Re - Reynolds number	
St - Strouhal number	

1 INTRODUCTION

Airframe noise refers to the noise generated by all components of the aircraft except the propulsion system. With the implementation of quieter jet propulsion systems, airframe noise becomes especially significant for larger, modern commercial aircraft. Moreover, the environmental regulations are concerned with the noise levels at and around airports during the take-off and landing situations. The international civil aviation organization (ICAO) annex 16 is the one involved with setting the standards of noise levels for aircraft and engine manufacturers. Thus, the radiation of airframe noise will be a necessary component of the development of future commercial aircraft, particularly in the subsonic fleet. Earlier investigations indicated that there are many sources that contribute to airframe noise. One such component is cavity noise. Flow over cavities on solid surfaces became a topic of interest in the late 1950s and early 1960s with the introduction of high speed combat aircraft. The primary concerns at that time were the buffeting of the cockpits and the drag induced by flow over bomb bays and landing gear compartments, Fig. 1. In many experimental studies, it has been observed that cavity flow produces intense acoustic tones.

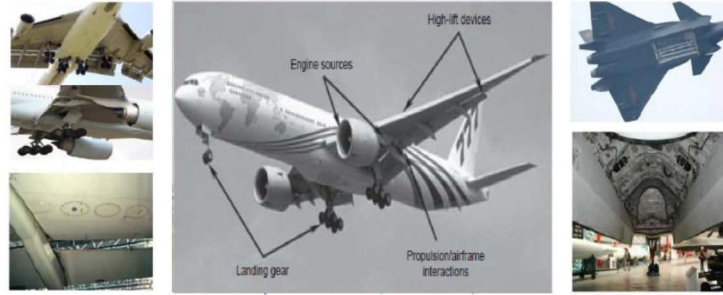


Figure 1: Bomb bays and landing gear.

2 CONTROL OF CAVITY NOISE

Many control techniques have been tested in order to reduce the cavity acoustic tones with variable results. Both active and passive control systems have been used. Passive control devices are the easiest to implement and a wide variety of systems were tested, in particular: spoilers, mass injection and modification of the cavity leading and/or trailing edge. These concepts sometimes proved to be very effective in reducing energetic tones but, in general, they did not succeed in suppressing multiple acoustic modes simultaneously.

The effect of a waviness surface in incompressible cross flow parallel to the leading edge of the cavity is another passive device that proved to be very efficient, as shown first by GARRY Hughes and Laurent DALA [1].

3 INVESTIGATION OF FLOW PHENOMENA FOR CAVITY FLOW

3.1 Cavity geometry

Fig. 2-(a) illustrates the length L , depth D and width W with the stream wise flow direction and the Fig. 2-(b) carries details showing the incoming boundary layer at the leading edge of the cavity, shear layer over the cavity and the pressure perturbation from the trailing edge of the cavity due to the impingement of the shear layer on the corner of the downstream of the cavity. Cavities can be classified based on the geometrical ratios of the length to depth (L/D).

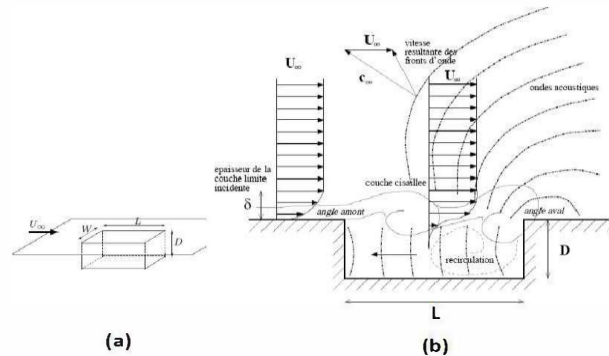


Figure 2: Cavity dimensions and flow characteristics

3.2 Ratio of Length over Depth L/D

Cavity flows exhibit a wide variety of phenomena whose precise nature depends sensitively on a number of parameters including the value of L/D . In the literature, vastly different values of L/D have been quoted to define the flow types. For instance: $L/D < 7$ for open and $L/D > 13$ for closed cavity flow is reported by Stallings and Wilcox [2] whereas $L/D < 10$ for open and $L/D > 13$ for closed cavity flow is reported in the work of Plentovich [3]. Similarly, Dix and Bauer [4] quote $L/D < 9$ for open and $L/D > 13$ for closed cavity flow whereas Srinivisan and Baysal [5] quote $L/D < 3$ for open and $L/D > 10$ for closed cavity flow fields. Tracy and Plentovich [6] investigated the variations in the values of L/D and concluded that the vast disagreements in the literature were due to the dependence of the cavity flow type on Mach number as well as L/D . Fig. 3-(b) shows separation point at the upstream of the cavity and stagnation point at the downstream of the cavity with dividing streamline for the open

cavity at subsonic velocity. For the closed cavity at the subsonic speed Fig. 3-(c), a separation point occurs at the leading edge of the cavity, impingement point and second separation point are at the bottom of the cavity with a stagnation point at the trailing edge of the cavity. In the closed cavity configuration, the profile of the dividing streamline starts from the bottom of the cavity.

Open cavities refer to flow over cavities where the boundary layer separates at the upstream corner and reattaches near the downstream corner. Open cavities may further be divided into shallow and deep cavities. The cavities with aspect ratio $L/D > 1$ may be considered as shallow and $L/D < 1$ for the cavities may be considered deep Fig. 3-(a). Cavities are closed when the separated layer reattaches at the bottom of the cavity and again separates ahead of the downstream wall of the cavity.

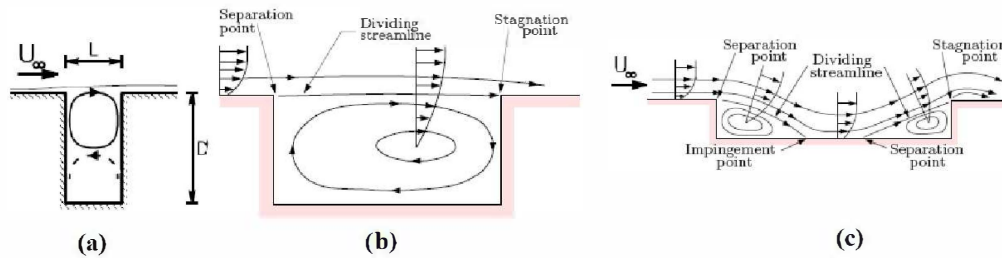


Figure 3: Schematic of deep (a), and shallow cavities: open (b), and closed (c)

3.3 Incoming flow

The influence of the free stream flow velocity has been investigated in the majority of the experimental studies. The cavity flow physics and its resonance depend on several flow parameters.

3.3.1 Mach number

The effects of Mach number on non-dimensional frequency fb/U_e have been studied by many investigations for both laminar and turbulent boundary layers. On the basis of high speed shadow-graphs of cavity oscillation, Rossiter [9] speculated that periodic vortices are shed at the upstream corner in sympathy with the pressure oscillation produced by interaction of the vortices with the downstream corner. Based on this idea Rossiter derived a formula for the oscillation frequency. Heller [10] and Covert studied shallow cavities over a wide range of Mach numbers and correlated a great many experimental results with Rossiter's formulation of cavity oscillation frequency, the vortices shed from the upstream cavity corner are assumed to convect at a constant phase velocity through the shear layer, resulting in a linear phase distribution. The variation in the resonant frequencies with Mach number is consistent with the Rossiter Eq. 1.

3.3.2 Boundary layer thickness

The boundary layer thickness at the cavity lip is also an important parameter [7]. Colonius [11] states that the momentum thickness θ_0 at the leading edge of the cavity plays a vital role in the selection of the modes and in governing the growth of the shear layer. They also found L/θ for lower limit for the cavity resonance to be approximately $L/\theta \approx 80$. When the ratio of the cavity length to the momentum thickness of the incoming boundary layer (L/θ) is in the range $80 < L/\theta < 120$, the self-sustained oscillations take place in the shear layer mode. When L/θ exceeds 120, another mode of cavity oscillation has been observed, but has received much less attention, and is relatively poorly understood. In incompressible experiments for an axisymmetric cavity, Gharib and Roshko [12] observed a wake mode, where the oscillating flow over the cavity resembles the wake behind a bluff body, rather than a free shear layer. Flow features in this wake mode were qualitatively very different from those in the shear-layer mode described by Rossiter, and wake mode was accompanied by a large increase in drag. Similar dramatic increases in drag had been previously observed by Fox [13] as the cavity length was increased, in flows with thin laminar upstream boundary layers, and Roshko [14] observed an intermittency analogous to the large fluctuations of drag which occur on a bluff cylinder in the critical range of

Reynolds number, where the flow may be switching between shear-layer mode and a type of wake mode.

Sarohia [8] stated that the parameters cavity depth D and initial momentum thickness θ_0 at the leading edge also are as important as the cavity length L , for a fixed value of the edge velocity U_e , depth D and Width W , there exists a maximum value of shear thickness above which the cavity does not oscillate. As the shear layer thickness δ_0 is decreased ($\delta_0 < \delta_{0_{max}}$), the frequency of cavity oscillations increases.

3.4 Flow Models

Rossiter In 1964 [9], proposed a semi-empirical formula for predicting the discrete tones detected in the experiments. The vortices which are shed from the cavity leading edge are convected downstream until they interact with the aft cavity wall, generating acoustic pulses. These acoustic pulses propagate upstream in the cavity eventually reaching the front cavity wall. At this time they induce separation of the shear layer which results in the shedding of another vortex, completing the feedback loop. Based on this description a formula was proposed to predict the frequencies, given by Eq. 1:

$$f_m = \frac{U_\infty}{L} \frac{m - \gamma}{M_\infty + \frac{1}{\kappa}} \quad (1)$$

Where m is an integer index for the frequency of interest ($m=1, 2, 3, \dots$), is constant for a fixed L/D and κ represents the ratio of the speed of the vortices to the free-stream speed.

The Fig.4 illustrate typical spectra for cavity with open flow as well as a section of the resonant range classification presented in [15] corresponding to the cavity dimensions of interest for this study.

Where κ is empirical constant, $\kappa = 0.57$ yields a fairly good collapse with the experimental data.

For shallower cavities (L/D from 4 to 10), Rossiter adjusted the constant, by using the values of Table.1.

Table 1: Values of γ as a function of the length-to-depth ratio L/D , from Rossiter [9]

L/D	γ
4	0.25
6	0.38
8	0.54
10	0.58

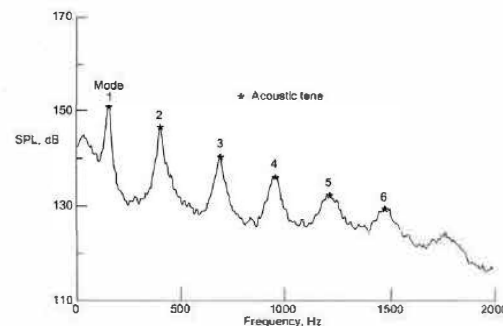


Figure 4: Typical Spectral View of Rossiter Modes [15]

Bilanin and Covert's In 1973 [16], this analysis consists of three parts: the analysis of the shear layer stability: the calculation of the interior acoustics of a rectangular cavity; and the prediction of the cavity oscillation frequency. In the first part of the calculation, the shear layer is modeled as a vortex sheet that is only dependent upon the depth of the cavity. With this assumption, the effect of shear layer impingement at the downstream edge of the cavity is eliminated, and the separation of upstream and downstream edge effects and the pressure field from the upstream edge have little effect on the vortex sheet except near the upstream edge.

Therefore, the only boundary conditions required in the stability analysis are the rigid wall boundary condition at the floor of the cavity, the kinematic and dynamic boundary conditions at the shear layer interface, and the outgoing radiation boundary condition above the shear layer. According to the photographs taken by Krishnamurty [17], the shear layer impingement generates an acoustic source at the downstream edge of the cavity. Hence, in the second part of the analysis, Bilanin and Covert [16] assumed a mass addition and removal at the downstream edge of the cavity as the cause of the acoustic source. The following expression is derived:

$$St = \frac{n - \frac{3}{8} - \frac{\phi}{2\pi}}{\frac{\alpha_r U_\infty}{\omega} + M \frac{c_+}{c_-}} \quad (2)$$

Where ϕ and $2\pi \times 3/8$ correspond to the phase lags, respectively due to the upstream and downstream edges, ω and α_r are the radian frequency and the real part of the complex wavenumber of the unstable vortex sheet solution respectively and U_∞ is the velocity outside the cavity. This formula takes the compressibility factor into account through the ratio c_+/c_- between the exterior and interior sound speeds.

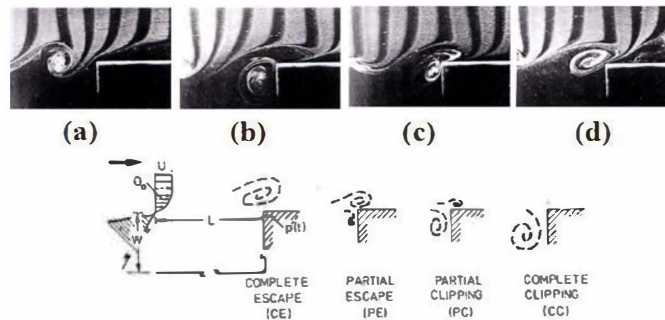


Figure 5: Classes of possible of vortex-corner interactions.
From Rockwell and Knisely [18]

In the study by Bilanin and Covert [16], the internal cavity wave structure is uncoupled from the shear layer motion in order to simplify the analysis. It is assumed that the cavity internal pressure modes force the shear layer only at the upstream edge and, therefore, only the downstream wave motion of the shear layer is considered. To eliminate this assumption, Heller and Bliss [10, 19] introduced the concept of the pseudopiston effect Fig. 5 [18]. This is similar to the replacement of the downstream cavity wall with an oscillating piston. The mass addition and removal creates pressure fluctuations that travel upstream in the cavity, and further amplifies the vortices shed at the upstream edge. In this manner, the internal cavity acoustic wave is coupled with the shear layer motion, and the feedback loop is complete.

4 COMPUTATIONAL AERO-ACOUSTICS

Aeroacoustics is a study of flow-induced noise, concerned with the sound generated by turbulent and/or unsteady vortical flows including the effects of any solid boundaries in the flow. With the increases in performance of computers, the numerical simulation of aeroacoustics, or computational aeroacoustic (CAA), has become more popular. Computational Aeroacoustics combines the classical approaches of flow field computation with acoustics. Computational methods for flow-generated sound can be divided into two kinds: direct computation and indirect, or hybrid computation.

- The direct approach computes the sound together with its fluid dynamic source field by solving the governing equations without modeling;
- In the hybrid approach, the computation of flow is decoupled from the computation of sound, which can be performed during a post-processing stage based on aeroacoustic analogy.

5 ACOUSTIC ANALOGIES

Modern aeroacoustic science was pioneered in the 1950's by Sir James Lighthill [20] who derived an 'acoustic analogy' for the estimation of the intensity of sound radiated by a turbulent flow. Lighthill transformed the Navier-Stokes and continuity equations to form an exact, inhomogeneous wave equation whose source terms are important only within the turbulent region.

5.1 Lighthill's acoustic analogy

Lighthill gives a reformulation of the fluid dynamics equations in such a way that he obtains a wave equation for the acoustic density fluctuations with a source term on the right hand side. The following equation is obtained:

$$\frac{\partial^2 \rho}{\partial t^2} - C_0^2 \Delta \rho = - \frac{\partial^2 T_{ij}}{\partial X_i \partial X_j} \quad (3)$$

Where ρ is the density, C_0 is the ambient sound speed and $T_{ij} = \rho u_i u_j + (P - c_0^2 \rho) \delta_{ij} - \tau_{ij}$ is known as the Lighthill stress tensor, u_i , p , τ_{ij} being the velocity components, the pressure and the viscous stresses respectively.

5.2 Curle's Analogy: the influence of solid boundaries

As an extension to Lighthill's acoustic analogy, Curle [21] proposed a formal solution to Lighthill's analogy in 1955 to include the influence of the solid static boundaries. The presence of surfaces strongly modify the sound production:

- Changes in the radiated acoustic field in comparison with the previous case of free turbulent flows;
- Extension of the integral formulation to the case of wall-bounded turbulent flows;

We assume a solid body, placed normally to a mean flow: The volume V is the entire space occupied by the fluid, and V is delimited by a surface S enclosing the body. \vec{n} is the outer normal to the volume V at the surface S , directed towards the body.

$$\rho(\vec{x}, t) = \frac{x_i x_j}{4\pi c_0^4 |\vec{x}|^3} \frac{\partial^2}{\partial t^2} \iiint_V [T_{ij}] d\vec{y} - \iint_S \frac{1}{4\pi c_0^2 |\vec{x}|} \frac{\partial}{\partial t} [\rho u_i] n_i dS - \frac{x_j}{4\pi c_0^3 |\vec{x}|^2} \frac{\partial}{\partial t} \iint_S [\rho u_i u_j + p \delta_{ij} - \tau_{ij}] n_i dS \quad (4)$$

- The first integral (volumic integral) represents the noise due to the turbulence in the source volume, similarly to the case of a free turbulent flow;
- The second integral (surfacic integral) results from a volume injection through the surface S enclosing the body, which can be due to a flow through a porous surface or to pulsations of the body;
- The third integral (surfacic integral) results from the momentum flux through the surface S and from the surface stresses on S (pressure and viscosity forces);

6 DOMAIN GENERATION METHODOLOGY

The geometrical parameters of the cavity model in paper are displayed in Fig. 6 (a- baseline Cavity geometry and b- wavy cavity geometry). The computational domain and boundary conditions shown in Fig. 7 are taken from the computational domain of Garry Hughes and Laurent Dala [1], the sound signals are received on receiver-A. Different surface modifications were simulated by varying the amplitude and frequency of surface waviness was constructed using **OpenFOAM** program.

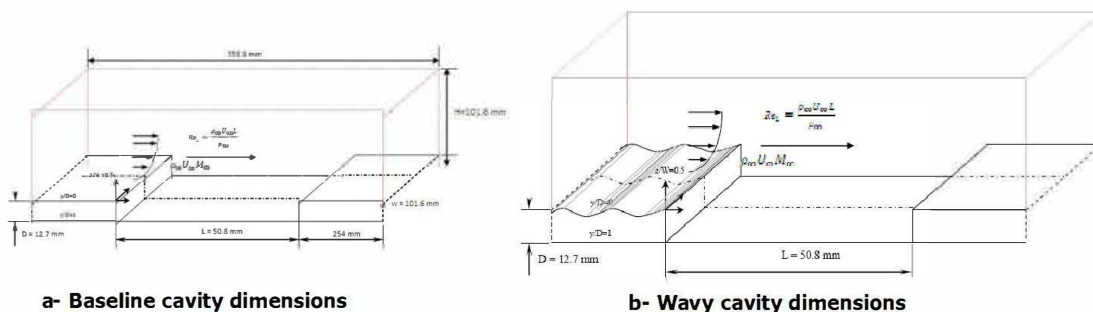


Figure 6: Cavity geometry

All simulations were performed on the cavity of aspect ratio $L/D = 4$. Through out the work, the length of the cavity is maintained as 50.8 mm and depth of the cavity as 12.7 mm. Fig. 7 illustrates

the schematic diagram of two dimensional domain adopted to simulate cavity flows. The flow is from left to right hand side. The domain extends between $0 \leq x/D \leq 45$ and $-1 \leq y/D \leq 8$.

The computational domain extends to 20D and 20D upstream and downstream of the cavity leading and trailing edges, respectively.

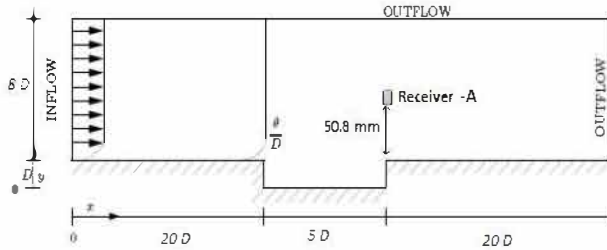


Table 2: Details of the Geometry

Total length of the domain	558.8 mm
Height of the domain	101.6 mm
Cavity length L	50.8 mm
Cavity depth D	12.7 mm
Aspect ratio of the cavity $\frac{L}{D}$	4

Figure 7: Schematic diagram of the computational domain

The Table 2 summarizes the details related to the geometry of the two dimensional cavity. Fig. 8 shows the density of mesh resolution near the walls and in the cavity region. The boxed region which is highlighted at the upper left corner represents the high mesh density. It is the region where the shear layer and other important mechanisms begin for hydrodynamics and aeroacoustics.

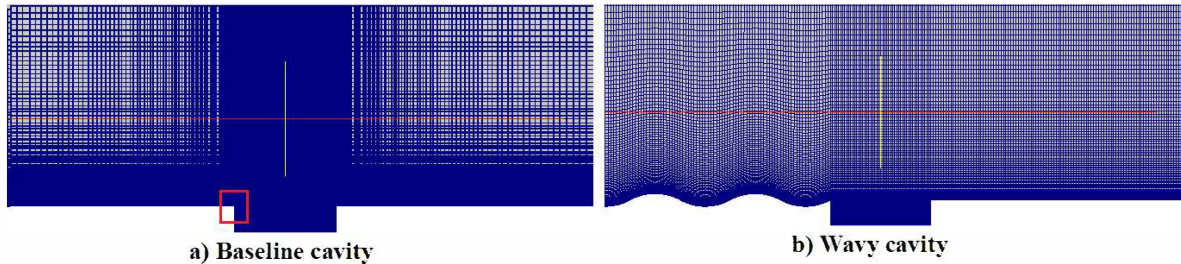


Figure 8: Mesh density: a) Baseline cavity b) Wavy cavity

7 RESULTS

7.1 Aerodynamics

When a shear layer passes a cavity, it mainly keeps flowing downstream but the rest comes into the cavity and forms a recirculating flows. The predictions of instantaneous velocity flow field from **LES** simulations are shown in Fig. 9.

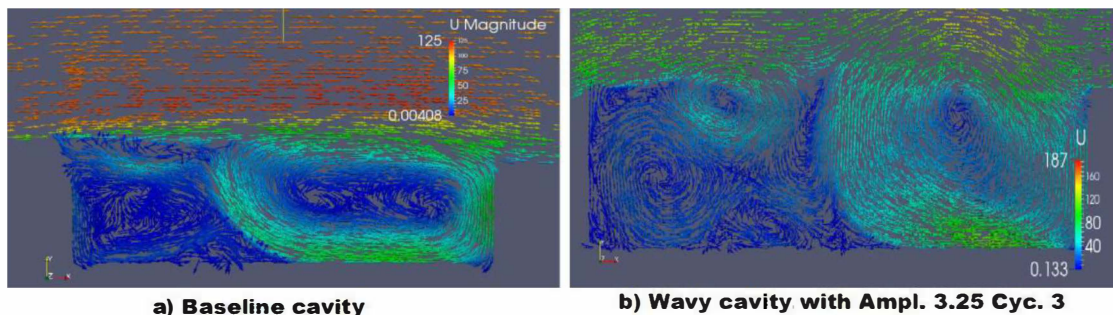


Figure 9: Instantaneous flow field from LES simulations

7.2 Shear mode

The test case (Ampl. 0 Cyc. 0) oscillates in shear mode. Fig.10 illustrates instantaneous vorticity contours in the cavity flow-field at different flow time after 60 computational periods.

The turbulent boundary layer which separates from the leading edge of cavity forms an oscillating shear layer. Fig. 10-(a) shows the shear layer stretching from the upstream of the cavity and is parallel to the bottom of the cavity. Over the right upper corner of the cavity, shear layer with a tongue like structure extends to the downstream of the cavity from the vortex near to the vertical

wall of the cavity. Fig. 10-(b) describes the complex interaction between the shear layer and the vortex at the downstream wall of the cavity. The incoming shear layer extends until the middle of the cavity region and the lip of the shear layer swipes on the vertical wall at the trailing edge of the cavity. (The swiping action cuts the tongue like shear layer to travel downstream of the cavity.)

The shear layer which extends due to the oscillation, impinges on the upper right corner of cavity and breaks into two (see Fig. 10-(c)) and at time period $3T/4$ i.e in the Fig. 10-(d), one part of the lip of the broken shear layer enters the cavity creating a eddy close to the downstream wall with the size of cavity depth, while the other part of the shear layer moves downstream of the cavity with less energetic eddies.

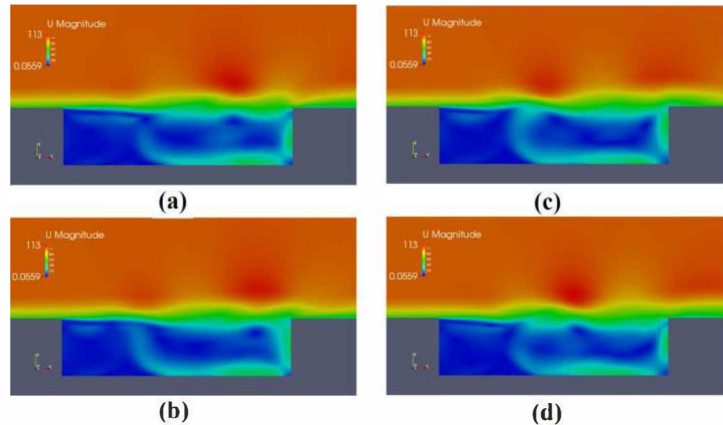


Figure 10: Instantaneous vorticity contours in the baseline cavity.
(a) 60.25T; (b) 60.5T; (c) 60.75T (d) 70T

7.3 Wake mode

Fig. 11 shows the instantaneous vorticity fields U over a period. A vortex is formed from the trailing edge and fills the cavity region is shown in Fig. 11-(a). In Fig. 11-(b), the vortex detaches and impinges on the downstream corner of the cavity. Due to the impingement, it ruptures and moves out of the cavity, while another eddy enters the cavity from the leading edge of the cavity (see Fig. 11-(c)). The eddy which is broken at this point of time moves downstream of the cavity, while another new eddy grows to fill the cavity is shown in the Fig. 11-(d). The flow above the cavity region is affected by the flow from the cavity.

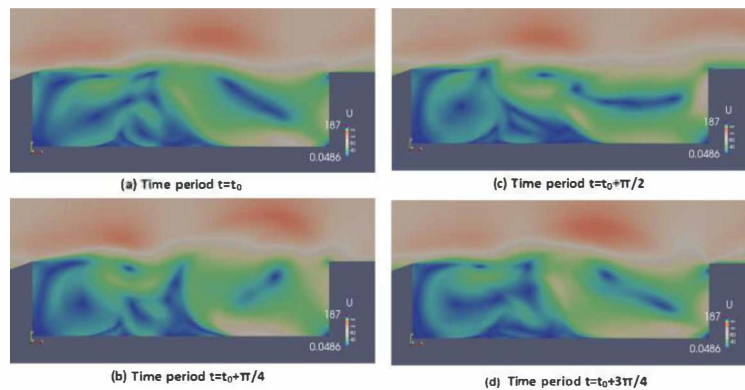


Figure 11: Instantaneous vorticity fields U for wake mode at four different times (a-d) corresponding to approximately a quarter of a period of oscillations. Only a small portion of the computational domain near the cavity is shown

8 AEROACOUSTIC

Acoustic Parameters: The pressure perturbations $p'(p' = p - p_0)$ which propagate as waves and which can be detected by the human ear. For harmonic pressure fluctuations the audio range is $20\text{Hz} \leq f \leq 20\text{kHz}$. The Sound Pressure Level (SPL) is a logarithmic scale measure of the pressure

unsteadiness in which the minimum pressure fluctuation detected by the human ear $p_{ref} = 2 \times 10^{-5} Pa$ is taken as the reference. For continuous pressure signals, the SPL is defined by:

$$SPL = 10 \log \left(\frac{PSD}{p_{ref}} \right) \quad (5)$$

The PSD describes how the power of a signal or time series, in our case the time dependent pressure, is distributed with frequency. The PSD spectrum is determined by means of a Fast Fourier Transform (FFT) utilizing windowing as to smoothen the PSD estimate, in our case the Hanning window. The

FFT of a signal $P(t)$ is defined as $FFT(t, f) = \int_{-\infty}^{\infty} P(\tau) w(\tau - t) e^{-j2\pi f \tau} d\tau$ where $w(t)$ is the Hanning

window function, applied to obtain a clear definition of the fundamental frequencies. Time averaging

the pressure fluctuations one would obtain the mean pressure $\bar{P} = \frac{1}{N - N_0} \sum_{k=N_0}^N P_k(t)$ where N is the

total number of samples taken and N_0 is the first sample number at which the time averaging starts. The root mean square pressure is therefore calculated via the equation

$$P_{rms} = \sqrt{\frac{1}{N - N_0} \sum_{k=N_0}^N (P_k(t) - \bar{P})^2}$$

Using the acoustic spectrum results, an overall sound pressure level (OASPL) can be obtained by adding all noise amplitudes of the spectrum, the OASPL can be obtained applying the following

$$expression: OASPL = 20 \log \sqrt{\sum_i (10^{SPL_i/20})^2}$$

Sound pressure levels (SPL) for the acoustic field above the cavity predicted by Rowley, et al [22] and paper are shown in Fig. 12, peak radiation to the far field occurs at an angle of about 135° from the downstream axis.

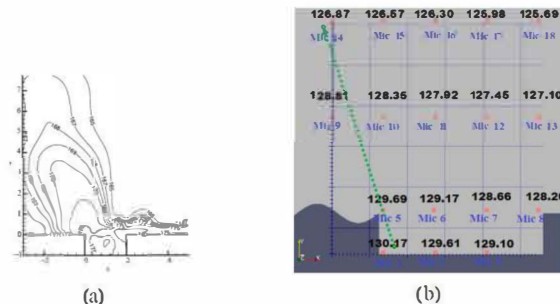


Figure 12: SPL distributions. (a) 2D-DNS predicted by Rowley, et al. [22]; (b) 2D-LES with surface wavy

Fig. 13 shows the sound pressure level of the computed acoustic signal at Mach 0.3 (flow velocity 99.44 m/s). The spectral resolution of these results is 6.97 Hz. over the whole frequency range [0-10000] Hz. From the acoustic analysis it can be seen that the significant peak of the sound pressure level is at the frequency 2000 Hz correspond to the 2nd Rossiter mode.

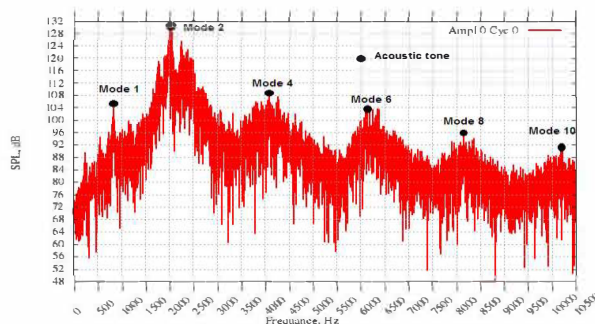


Figure 13: SPL at one receiver for baseline cavity

Table 3: Rossiter modal frequencies Wth associated Strouhal Numbers [9]

m	St	f(Hz)
1	0.412	807.60
2	0.962	1884.39
3	1.512	2961.19
4	2.068	4037.98
5	2.612	5114.78
6	3.163	6191.57
7	3.713	7268.37
8	4.263	8345.16
9	4.813	9421.96
10	5.363	10498.75

The highest sound pressure level at this frequency is 129 dB (for receiver A, Fig. 7). the peaks at 840 Hz, 2000 Hz, 4080 Hz, 6122 Hz, 80150 Hz and 10300 Hz correspond very well to the results predicted by Rossiter, Eq. 1. (see Table 3)

It is seen that in Fig. 14-(a) the cavity for an applied surface waviness with frequency of 19.7×10^{-3} and 11.8×10^{-3} cycles per mm increase the resonance peak by 9 dB compared to the baseline case and also the peak of the sound pressure level is at the frequency 1000 Hz correspond to the 1st Rossiter mode for wake mode.

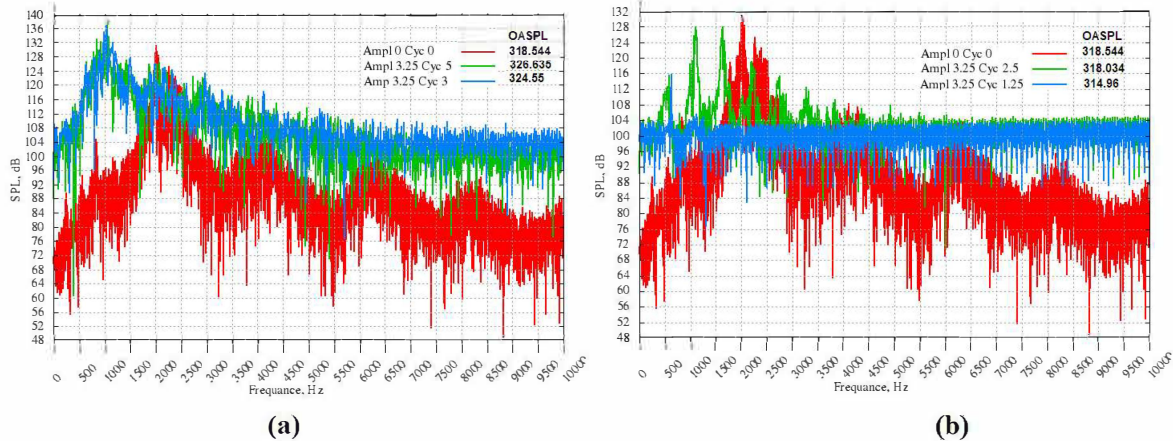


Figure 14: Sound pressure level with and without surface waviness

Fig. 15 shows frequencies of the two most energetic peaks in the spectra for the series of run with $L/D = 4$, compared to experimental data and predictions from Eq. 1, the transition to wake mode oscillations for $M > 0.3$.

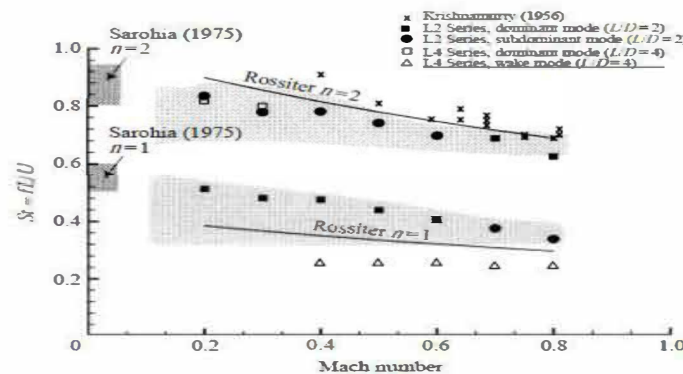


Figure 15: Strouhal numbers for peaks in spectra for the shear-layer mode and wake modes

The results for surface wavy control, Fig. 14-(b), show a considerable attenuation of the dominant Rossiter peak, it was clarified that the tonal sound reduced for frequency of 4.92×10^{-3} , 9.84×10^{-3} cycles per mm. The maximum noise level of 116 dB was observed at $f = 625$ Hz for frequency 4.92×10^{-3} cycles per mm and the maximum noise level of 127.8 dB was observed at $f = 1095$ Hz for frequency 9.84×10^{-3} cycles per mm. It was observed that the attenuation achieved using this configuration was of the highest value, giving an overall reduction in SPL of 14 dB. The comparison of the numerical simulation with the experimental measurements for acoustic part has not been carried out yet. But this study proves the influence of the surface wavy in the attenuation or amplification of sound and its intensity.

9 CONCLUSION

A complete two-dimensional analysis of both the baseline and the modified configuration were carried out. Additionally the flow regime was demonstrated with success by the use of CFD flow visualisation. The results of different geometry modifications applied to the leading edge of a cavity with length to depth ratio of 4, in order to reduce the resonance of flow at Mach 0.3 have been presented. The

amplitude of 3.25 mm and the frequency of 4.92×10^{-3} cycles per mm was observed as achieving the best reduction in cavity resonance.

To fully understand the wavy surface impact on the cavity flow control, the following further work is required:

- Applying the used control mechanism on a range of Mach numbers is needed to further verify the effectiveness of the control system;
- Increasing the mesh density and study the influence on accuracy of the results;
- Wind Tunnel testing of an optimum 2D model.

Acknowledgments The Computations were performed on the Al-Farabi Cluster computer of the Ecole Nationale Polytechnique Oran - MAURICE AUDIN

REFERENCES

1. G. Hughes, Mamo T., and Dala L. "Use of active surface waviness for control of cavity acoustics in subsonic flows". 15 th AIAA/CEAS Aeroacoustics Conference (30th AIAA Aeroacoustics Conference), Miami ,Florida, AIAA-2009-3202, May 2009.
2. R. Stallings and F. Wilcox. "Experimental cavity pressure distributions at supersonic speeds". NASA-TP-2683, June 1987.
3. E. Plentovich. "Three-dimensional cavity flow fields at subsonic and transonic speeds". Fluid Mech, TP-3358, 1992.
4. R. E. Dix and R. C. Bauer. "Experimental and predicted acoustic amplitudes in a rectangular cavity". AIAA, 2002-0472, 2000.
5. S. Srinivisan and O. Baysal. "Navier-stokes calculations of transonic flow past cavities". Fluid Engineering, 113:369–376, September 1991.
6. M. B. Tracy and E. Plentovich. "Measurements of fluctuating pressure in a rectangular cavity in transonic flow at high Reynolds number". NASA TM 4363, TP-3358, 1992.
7. K.K. Ahuja and J. Mendoza. "Effects of cavity dimensions, boundary layer, and temperature on cavity noise with emphasis on benchmark data to validate computational aeroacoustic codes". 1995.
8. Sarohia. "Experimental and analytical investigation of oscillations in flows over cavities". PhD thesis, 1975.
9. J.E. Rossiter. "Wind-tunnel experiments on the flow over rectangular cavities at subsonic and transonic speeds". Aeronautical Research Council Reports and Memoranda, Technical Report 3438, 1964.
10. H.H. HELLER and D.B BLISS. "The physical mechanism of flow induced pressure fluctuation in cavities and concepts for their suppression". AIAA, pages 75–491, 1975.
11. T. Colonius and S. K. Lele. "Computational aeroacoustics: progress on nonlinear problems of sound generation". Progress in Aerospace Sciences 40,6:345 416, August 2004.
12. M. GHARIB and A. ROSHKO. "The effect of flow oscillations on cavity drag". Fluid Mech, 177:501–530, 1987.
13. J. Fox. "A criterion for the transition between flow regimes in turbulent cavity flow". 4:364–365, 1968.
14. A. ROSHKO. "Some measurements of flow in a rectangular cutout". 3488, 1955.
15. E. B. Plentovich, R. L. Stallings, Jr., and M. B. Tracy. "Experimental cavity pressure measurements at subsonic and transonic speedsstatic-pressure results". TP-3358, 1993.
16. A.J. Bilanin and E.E. Covert. "Estimation of possible excitation frequencies for shallow rectangular cavities". AIAA, 11:347 351, 1973.
17. K. Krishnamurty. "Acoustic radiation from two-dimensional flow in rectangular cutouts in aerodynamic surfaces". Naca Technical, TN 3487, 1955.
18. D. Rockwell and C. Knisely. "Vortex-edge interaction: Mechanisms for generating low frequency components". Phys. Fluids, 23(2):239/240, 1980.
19. H.H. HELLER, DG. HOLMES, and E.E. COVERT. "Flow-induced pressure oscillations in shallow cavities". Sound Vib., 18:545–553, 1971.
20. M.J Lighthill. "On sound generated aerodynamically the royal society of london". 1952.
21. N. Curle. "The influence of solid boundaries upon aerodynamic sound".
22. Rowley,C.W. and Colonius, T. "On self-sustained oscillations in two-dimensional compressible flow over rectangular cavities". Journal of Fluid Mechanics., 315:346, 455, 2002.

Proposal for a EU quality label for aerospace education

Franco Bernelli-Zazzera

*Politecnico di Milano – Dept. of Aerospace Science and Technology
 Via La Masa 34, 20156 Milano, Italy
 franco.bernelli@polimi.it*

Maria Angeles Martin Prats

*Universidad de Sevilla – Dept. of Electronics Engineering
 Avda. Camino de los Descubrimientos s/n, 41092 Seville, Spain*

Francesco Marulo

*Università degli Studi di Napoli "Federico II" – Dept. of Industrial Engineering
 Via Claudio 21, 80125 Napoli, Italy*

Daniel Hanus

*Czech Technical University in Prague – Dept. of Air Transport
 Konviktska 20, 11000, Praha 1, Czech Republic*

Joris Melkert

*TU Delft - Faculty of Aerospace Engineering
 Kluyverweg 1, 2629 HS, Delft, Netherlands*

Giorgio Guglieri

*Politecnico di Torino – Dept. of Mechanical and Aerospace Engineering
 Corso Duca degli Abruzzi 24, 10129 Torino, Italy*

Pascal Bauer

*ISAE-ENSMA - Institut Pprime - Dept "Fluides, Thermique, Combustion"
 Téléport 2 - 1 avenue Clément Ader, 86961 Futuroscope Chasseneuil CEDEX, France*

Irene Pantelaki

EASN TIS

Patras Science Park, Stadiou str., Rio 26504, Patras, Greece

Iring Wasser

ASIIN e.V.

Robert-Stolz Str. 5, 40470 Dusseldorf, Germany

Herman Deconinck

*von Karman Institute for Fluid Dynamics– Aeronautics and Aerospace Dept.
 Chaussee de Waterloo 72, 1640 Rhode Saint Genese, Belgium*

Ruxandra Bosilca

INCAS - International Cooperation Unit

Iuliu Maniu 220 Sector 6, 061121 Bucuresti, Romania

Hanna-Kaisa Saari

Aerospace Valley

118 route de Narbonne, 31432 Toulouse, France

ABSTRACT

The paper presents a possible roadmap for the definition of a European quality label for aerospace related higher education degrees. The proposal is the result of a two-years long Horizon 2020 project that has involved a great portion of the European stakeholders in aerospace: Universities, research centres, industries (both small and large) networks, associations and accreditation agencies. The core concept established is that it is possible to establish a sector-specific, content based, quality system, that can complement the existing national or European accreditation systems, providing added value to the internal and/or external quality assurance processes that are in place in most EU countries. The



tools and processes proposed are sufficiently simple to be manageable by Universities in addition to their national accreditation processes or as stand-alone assessment. The main goal of the proposed process is the evaluation of the quality of the aerospace curricula in the European context, whereas the accreditation of the programme can be seen as an optional extension of the process, subject to further national regulations. The process is proposed in view of the awarding of a sector-specific, content based, quality label, to be issued by an appropriate legally recognized and qualified institution. 8 field tests with volunteering universities throughout Europe have been performed. They experienced the method as very practical and to the point.

KEYWORDS: *aerospace higher education, quality in education, learning outcomes*

Award-Winning Innovative Aircraft Design Projects at Politecnico di Milano

Lorenzo Trainelli

Department of Aerospace Science and Technology, Politecnico di Milano

Associate Professor

Via G. La Masa 34 – 20156 Milano, Italy

lorenzo.trainelli@polimi.it

Carlo E. D. Riboldi

Department of Aerospace Science and Technology, Politecnico di Milano

Assistant Professor

ABSTRACT

In the "Aircraft Design" course at Politecnico di Milano, M.Sc. Aeronautical Engineering, students are called to team up and carry out a complete conceptual and preliminary design for a new aerial vehicle. Often, during this process, bright, innovative ideas emerge in an effort to improve on preceding realizations and find new, more sustainable solutions. Some of these projects have been submitted to various international design competitions. Four highly successful projects, namely Flybrid, a hybrid-electric regional liner, finalist in Fly Your Ideas 2013; Nibbio, a dual-propulsion morphing tilt-rotor, second place in AHS 2014; Flynk, an all-electric air taxi, winner of AIAA 2015; and Hybris, a structural-battery enabled hybrid-electric 4-seater, winner of RAeS 2016, are illustrated, together with the main characteristics and educational outcomes of the "Aircraft Design" course.

KEYWORDS: *aircraft design, electric aircraft, morphing tilt-rotor, air-taxi, structural batteries*

1 INTRODUCTION

Among the subjects traditionally taught in the M.Sc. in Aeronautical Engineering at the Politecnico di Milano, the "Aircraft Design" course offers the students an opportunity to develop the original conceptual and preliminary design of an aircraft. Several projects among those developed in recent years have been submitted to various international design competitions, achieving a remarkable success rate. The present paper introduces four recent design proposals that earned a place in the upper three rankings of four different contests. These are project "Flybrid" (Fig. 1, left), awarded in the Airbus-sponsored Fly Your Ideas 2013 challenge; project "Nibbio" (Fig. 1, right), awarded in the AHS International Graduate Student Design Competition in 2014; project "Flynk" (Fig. 2, left), awarded in the AIAA Graduate Student Design Competition in 2015; and project "Hybris" (Fig. 2, right), awarded in the Royal Aeronautical Society General Aviation Design Challenge in 2016.

In the following, after a presentation of the "Aircraft Design" graduate course and some of its peculiar characteristics, the main features of these projects are briefly addressed. As pointed out in the discussion, the interested reader may refer to more detailed illustrations in the literature [1-5].



Figure 1: Artist's impressions of the "Flybrid" hybrid-electric regional liner (left) and the "Nibbio" morphing tilt rotor (right).



Figure 2: Artist's impressions of the "Flynk" all-electric air taxi (left) and the "Hybris" hybrid-electric 4-seater (right).

2 THE AIRCRAFT DESIGN GRADUATE COURSE

2.1 General characteristics

The "Aircraft Design" graduate course is a long-standing characteristic of the MSc educational program in Aeronautical Engineering at the Politecnico di Milano. Following a revision of the program, it was changed from a mandatory course into an elective in the year 2011 and is now typically attended by graduate students belonging to the "Flight mechanics and systems" track, one of the five recommended tracks in Aeronautical Engineering (in the Italian system, a student may also compose a personalized track himself, subjected to a mandatory approval by the school officials).

The focus of the course is the conceptual and preliminary design of manned or unmanned aircraft, mainly in the fixed-wing category. The course consists of lectures and exercises, concentrated in the first half, and design laboratories, mostly held in the second half. Between two and four seminars lectured by experts invited from the industry are held every year. They mainly come from aircraft manufacturing companies, such as Leonardo Aircraft, Piaggio Aerospace, Pipistrel, Blackshape Aircraft, and Solar Impulse. The course is not based on a specific textbook, but a range of suggested references is provided and referred to whenever appropriate [6-11].

The students are required to conceive and design an aircraft, starting from a relatively loosely defined theme bestowed by the teacher. As this leaves them a wide amount of freedom of interpretation, they first perform a thorough market study, before defining appropriate mission requirements. Design specifications are drafted on this basis and the conceptual design is approached with the preliminary sizing and the choice of the configuration, engines, and onboard systems. Subsequently, disciplinary in-depth analysis and design is carried out to complete the preliminary design of the integrated vehicle. This includes: the aerodynamic design, with special emphasis on lifting surfaces, control surfaces and high-lift devices; the structural design; the design of the propulsion system, possibly including the propeller design; the design of other on-board systems, such as landing gear, hydraulic system electric system, etc.; the weight and balance characteristics; performance and flying qualities; the definition of operational usage and possibly of ground support systems. Finally, an estimation of costs and project economics is derived. The fundamental idea is thus to learn how to perform a conceptual and preliminary design of an aircraft by actually doing it.

Therefore, while theory lectures introduce the design framework, present the methodologies and discuss typical problems, and exercises give examples of applications of the above methods, the laboratory hours are available for developing a project.

2.2 Project development

As anticipated, a fundamental requirement in the course is the development of an original conceptual and preliminary design of aircraft. This is carried out within a team of maximum eight students, with a recommended size of four to six students. This size is motivated by the experience collected in the past, as a lower number would imply too high a workload, and a higher number may end up in excessive project complexity and difficulties related to task segregation and mutual interaction. Indeed, while student teams are encouraged to form on their own initiative, trying to obtain the most favorable 'mix' of capabilities, with at least one student responsible for each discipline (aerodynamics, structures, flight mechanics, systems, propulsion, etc.), a fundamental aim of the course is to provide the opportunity for all students to be involved in all project phases and to obtain intimate knowledge of the whole work performed, instead of only one's own specific disciplinary work package. This would clearly be hindered by too large a team.

Once a team is formed, a Team Leader is designated. Teammates are encouraged to burden their Team Leader with actual coordinating tasks, not only as a point of contact or spokesperson. In fact, teams are pushed to get the best from their group activity by setting up an appropriate project management plan. This includes setting clear deadlines for the various tasks, monitoring the design process throughout its full duration, planning periodic revisions and assessing the project state in relation to what was planned, continuously identifying problems and risks, and providing appropriate solutions and mitigating actions. Often, *ad-hoc* methods are developed, to cope with specific design needs, from initial sizing to various disciplinary design optimizations.

Given the special character of the student assignments, the course teacher and assistants are continuously available for tutoring, helping in reviewing the project status and providing technical support if needed. In addition, every year, current students attend a lecture presented by a team of students of the previous year, chosen among the most successful. The past students illustrate their experience, with the aim of getting inspiration, profiting from lessons learned and other elements that can be useful to the current students' ongoing activity.

Often, among the themes available, one or more are fit for the participation in an international design competition. This opportunity is clearly declared and recommended, as normally it is not difficult to match the requirements for participation with those that apply for the course project. In all cases to date, the difference between contest and course requirements did not compel to redo parts of the work. The typical situation is that course requirements include contest ones as a subset, so that teams need to perform some work in addition to that strictly needed for contest participation.

2.3 Project evaluation

In the "Aircraft Design" course, the final evaluation consists in the project assessment and an oral examination. The project is assessed through the evaluation of a written technical report and of an oral presentation that is typically carried out in two hours (120-150 slides). All members of the team must participate actively in the project presentation. When the presentation is carried out, the oral examination is also held, by questioning the students on specific elements of their project, as well as various course topics.

The project design report is required to fully detail the work done and the tools produced by the team, using either Italian or English. The contents must include the items detailed in Table 1.

Table 1: Project design report content

Report items
1. Theme description
2. Work organization within the group
3. Analysis of the theme, market study, state of the art, certification framework
4. Emission of requirements, design specifications, mission profiles, technological and economic constraints, etc.
5. Initial sizing of weight, thrust-to-weight/power-to-weight ratio and wind loading
6. Comparative analysis of possible candidate configurations
7. Selection and motivation of a configuration
8. Design of the fuselage
9. Design of the wing (including high-lift devices), tail, control surfaces, trim, etc.
10. Selection and integration of propulsion (including propeller, if applicable) and on-board systems
11. Structural sizing
12. Analysis of weight performance, center-of-gravity travel
13. Performance analysis (including trimmed polars, flight envelope, point and integral performance)
14. Static stability and control in level and maneuvering flight
15. Dynamic stability and flying qualities
16. Cost analysis
17. Drawings (3-view, internal arrangements, etc.)
18. Conclusions, comparison of results with existing products, critical evaluation in reference to initial goals
19. Bibliography & sitography

The final evaluation criteria are: completeness, accuracy and depth of the analysis of the proposed design solutions; detail and in-depth analysis of specific critical topics; evaluation of sensitivity/robustness and criticalities of the proposed design solutions; possible use of refined analysis tools (such as in the estimation of aerodynamic characteristics); possible use of optimization techniques and parametric studies; approach to work planning and level of interaction within the group; style, completeness and clarity in the oral exposition, the written presentation, and the written report; ability to answer questions posed by the teaching staff.

2.4 Educational outcomes

In the "Aircraft Design" course, the students are involved in the whole conceptual and preliminary design process, starting from the preliminary studies that motivate the determination of mission requirements and other design specifications. A strong emphasis is given to the selection process of a design solution among multiple candidates at all levels, when a reasonable choice is required to be firmly grounded and motivated, often with respect to the results of the preliminary studies.

Of course, designing an original flying machine from scratch is an exciting experience, and is perceived by the students as one of the most fruitful activities in their last year of studies. Their work is often characterized by a very effective blend of creativity and inspiration, mixed with solid technical skills and convincing results.

The educational results of the course may be summarized as follows:

- the students apply technical competence and out-of-the-box thinking to the solution of a problem that is initially only summarily sketched, finding the related real-life implications and then determining quantitative requirements that will drive the design process;
- the students develop the notion of an aircraft as a complex system of several interacting subsystems and experience the impact of this interaction in the design process;
- the students apply in an integrated, multidisciplinary fashion a large set of notions, methods and experiences matured in previous disciplinary studies;
- the students develop important qualitative elements in learning, such as initiative and self-criticism, use of technical language and English language, written and oral communication abilities (reporting and final presentation);
- the students enjoy a long-term, intense, goal-oriented teamwork, developing abilities that have not necessarily been acquired in previous activities, such as project planning and monitoring, exploiting of diversity and effective sharing of choices, results, insight within the team.

In addition, in some cases, students are involved in the preparation of a scientific paper, as in [1-5], and in the subsequent presentation of these works at international conferences or other public events. As anticipated, in the recent past, a remarkable series of awards was bestowed to teams formed in the "Aircraft Design" course in some of the most prestigious international student design competitions. Also, a number of projects displayed a degree of maturity and timely approach to current market needs that led to the interest of several companies for possible industrial developments. Another proof of this substantial quality is the submission of a patent [12] directly issued from the latest of the award-winning projects, the Hybris.

3 PROJECT FLYBRID

3.1 The "Fly Your Ideas 2013" competition

The 2013 edition of the "Fly Your Ideas" international student competition sponsored by Airbus and supported by the United Nations Educational, Scientific and Cultural Organization (UNESCO) was a challenge for students worldwide to develop new ideas promoting a greener aviation industry (not necessarily new aircraft designs). This was the third edition of this biennial contest from its start in 2008-2009, and the first time a student team from Politecnico di Milano was involved.

Teams were invited to participate in a three-round process. In Round 1, a concise proposal had to be submitted through an online questionnaire. After assessment by committees composed of Airbus staff and industry experts, a selection was carried out. Surviving teams competed in Round 2, where a substantial written report and a three minute-long video were submitted. Again, the material was assessed and a final selection was accomplished, ending with five finalists. These teams were

requested to give a final presentation to a jury composed of top-level Airbus staff and industry experts. The winning team and the runner-up team received substantial prize money.

The number of teams participating in Round 1 totaled 618, with over 2,500 students from 82 countries. Only 102 teams were chosen to compete in Round 2, with 32 of them from Europe. Among the five finalists, the only European team selected was Team Flybrid. Team Flybrid formed during the Academic Year 2012-2013 as one of the design groups within the Aircraft Design graduate course at Politecnico di Milano. They resolved to participate with a proposal focused on a highly innovative aircraft for future regional aviation, and its related operational strategy and infrastructure.

3.2 The Flybrid concept

The Flybrid project is essentially based on novel regional airliner concept for the 2030s scenario. The market study led to size a 90-passenger aircraft for a 700 km design mission, intended to be effective in missions with a block range between 250 and 1,000 km. These range figures emerged from the thorough analysis of the companies which operate the ATR and Q400 turboprops worldwide, considering 959 routes. In order to deliver a cost-efficient airplane with a highly reduced environmental impact, a hybrid-electric solution was investigated. In particular, given the considerable amount of batteries necessary and the drawbacks of battery in-flight recharge due to duration and low energy-efficiency, a parallel hybrid solution with pre-charged battery packs was devised.

In this parallel architecture, a turboshaft engine is mechanically coupled with an electric motor (EM) to provide shaft power to the propeller, and the battery pack feeding the EM is not recharged in flight (Figure 3). This, compared to a serial hybrid architecture, allows to discard the need for an additional electric generator driven by the turboshaft and all the connected mechanical and electric components, saving weight and reducing complexity. Indeed, a careful sizing of the airplane in both serial and parallel variants showed a reduction in cost by 5% and emissions by 10% in favour of the latter.

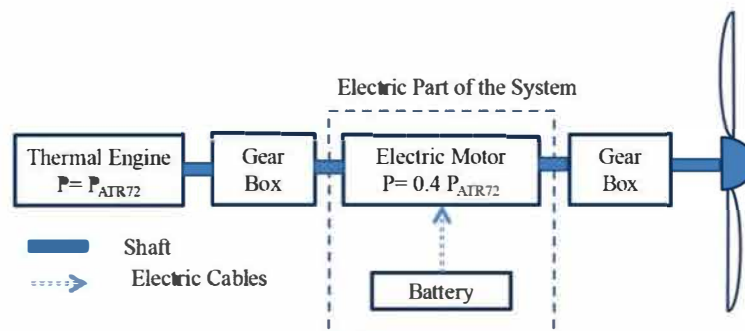


Figure 3: Flybrid's parallel hybrid-electric powertrain schematics.

An apparent penalization is the sizing of the turboshaft according to conventional procedures, so that the aircraft would be able to perform the mission even without batteries onboard. This choice entails a number of advantages in terms of airworthiness, operational flexibility and safety. Indeed, it is assumed that such an airplane would sustain lower certification burdens compared to a more optimized design involving an undersized internal combustion engine (ICE), given that in this case electrical power is not crucial to insure performance and safety. As an example of operational flexibility, such an aircraft would be able to operate without any restrictions from airports not endowed with a battery management service. In addition, the proposed solution naturally improves safety margins in all phases of flight in case One-Engine-Inoperative (OEI) emergency conditions, when operating the live propulsive unit in hybrid mode would boost the power available above 50% nominal maximum power required.

A characteristic element in the project integration is the design of the pre-charged battery packs. These are conceived to be hosted in specially modified Unit Load Devices (ULDs), i.e. standard-sized containers that are routinely handled in airports, to be carried in the aircraft cargo bay (Figure 4). Battery units are sized to store 400 kWh, giving a good trade-off between the contrasting needs to embark large energy amounts and to limit the time necessary for battery loading/unloading on ground. In the Flybrid design, up to nine modified ULD-shaped battery packs can be boarded. Only

the required number of batteries are loaded at each mission, depending on mileage, thus optimizing the airplane's weight. Battery operations would be integrated with normal ground operations, with exhausted batteries unloaded together with normal baggage containers and replaced with pre-charged ones. A dedicated area of the airport is envisaged for battery collection, repository and recharge. As this may imply very large amount of batteries involved in the continuous on-airport recharge process, a remarkable opportunity may be seized in implementing such areas as storage nodes within the land-based electric grid, opening up promising scenarios within the "smart grid" policy being implemented in many countries worldwide [13,14].



Figure 4: Flybrid's modified ULD-shaped battery pack for cargo bay loading.

Table 2 provides the main Flybrid specifications in terms of weight and predicted performance. In a typical short-haul flight, savings compared to conventional solutions may be substantial. For example, with a 550 km route and 70 passengers on board, CO₂ emissions are reduced by more than 40% and total mission cost by more than 30%. A detailed illustration of the preliminary studies, design methodology and main outcomes of the Flybrid project can be found in [1].

Table 2: Main Flybrid specifications

Maximum take-off weight	32,500 kg _f
Maximum payload weight	9,600 kg _f
Maximum fuel weight	5,000 kg _f
Maximum battery weight	3,600 kg _f
Cruising speed	560 km/h
Maximum range (90 pax)	750 km
Ceiling	7,000 m

4 PROJECT NIBBIO

4.1 The 31st Annual AHS International Student Design Competition

The American Helicopter Society (AHS) International announced the 31st edition of its Student Design Competition in 2014, sponsored by AgustaWestland (now Leonardo Helicopters). The sponsorship rotates between some of the major VTOL (Vertical Take-off and Landing) world-class manufacturers plus the U.S. Army. The contest challenges students to design a vertical lift aircraft that meets specified requirements. Two categories are available: undergraduate and graduate. Each of the winning teams is awarded a cash stipend, plus other benefits such as an invitation to the AHS International Annual Forum and Technology Display to present their projects. It was the first time a student team from Politecnico di Milano was involved.

The 2014 competition challenged students to respond to a Request for Proposal (RFP) for an experimental VTOL aircraft intended to achieve exceptional performance, including sustained hover with efficiency not lower than 75%, high useful load capability, long-range cruise with a lift-to-drag ratio of at least ten, and sustained flight at airspeeds between 300 and 400 kn (or 550 and 740 km/h), which is about three times the maximum speed of today's helicopters.

The only Italian team participating was Team Caurus, which scored the second place and "best new entrant" awards. Team Caurus formed during the Academic Year 2013-2014 as one of the design groups within the Aircraft Design graduate course at Politecnico di Milano. They chose to participate with a proposal focused on a high-performance tilt-rotor aircraft, the "Nibbio" (Italian for the kite bird of prey, *Milvus Milvus*), which is characterized by two peculiar design choices.

4.2 The Nibbio concept

The Nibbio is a novel morphing VTOL concept aimed at solving the drawbacks inherent to the tradeoff between the requirements for efficiency in both vertical flight and high-speed cruise. The severe and mutually contrasting requirements of the RFP called for the development of radically new design solutions. After an in-depth study of the potential market for such a vehicle, additional requirements have been set by Team Caurus, in order to define, more than a mere demonstrator, a possible platform for tasks such as corporate business and air-taxi, off-shore transportation, Search and Rescue (SAR), Emergency Medical Service (EMS), and law enforcement.

The choice of the configuration was of paramount importance to the subsequent design. In fact, since a conventional tilt-rotor cannot fully satisfy the demanding RFP performance requirements, due to the impossibility to optimize its prop-rotor simultaneously for hover and cruise conditions, a novel solution was devised to overcome this inherent limitation. The key element is represented by the design of a unique dual-propulsion system. This involves the use of two separate optimized devices for hover and cruise, with the former being a morphing system: two large, tractor, foldable rotors are employed in vertical and low speed flight, while two pusher propellers empower high speed flight (Figure 5, left).

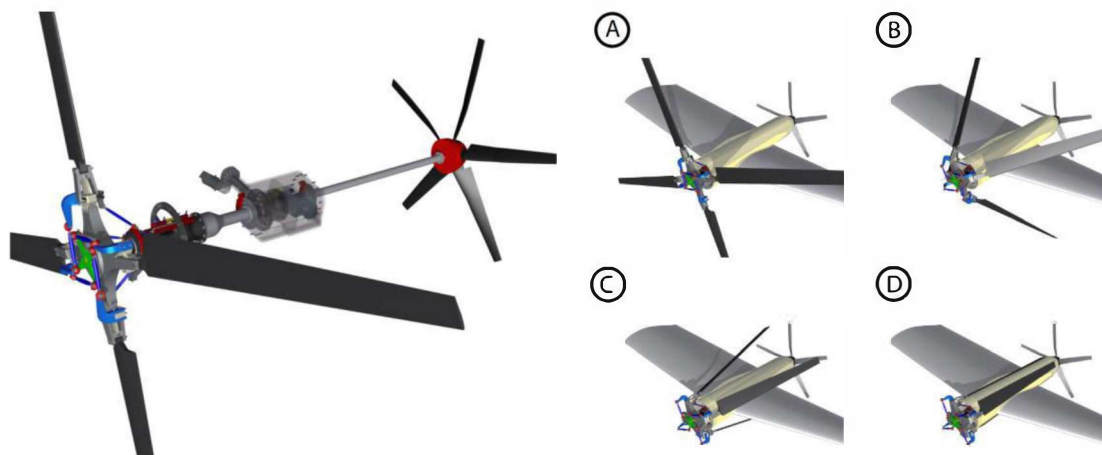


Figure 5: Nibbio's propulsive arrangement with front rotor, rear propeller and nacelle transmission system (left), and blade folding sequence (right).

The conversion maneuver from low to high speed flight is performed as follows: after vertical take-off and climb in "helicopter mode", low-speed forward flight is initiated; then nacelles are tilted and rear propellers are activated, before stopping and folding the rotors; at this point, high-speed flight in "airplane mode" can be achieved.

The gimbaled hingeless rotor is designed to be slowed down until full stop during the transition from low to high speed flight. Once stopped, the blades are appropriately feathered, then folded and stowed within dedicated slots on the nacelle to minimize their impact on vehicle drag (Figure 5, right). The structure of the rotor hub was specifically designed to perform blade folding in flight. When the folding system is activated, a dedicated electric motor generates a torque that is amplified and transmitted by the elliptical gearbox to a folding wheel or "spider", which forwards the motion onto the folding arms using ball joint links.

The resulting design is a complex, but exceptionally performing, compound tilt-rotor with a partially tilting wing, endowed with slender nacelles supporting each a front foldable rotor and a rear propeller, able to carry six to nine passengers with a very promising cost-effectiveness. In fact, the maximum specific range achieves 0.56 NM per pound (4.08 km per kg) of fuel, about 16% lower than that of turboprops of the same class, while being nearly 15% higher than that of typical business jets. Figure 6 shows Nibbio's remarkable payload-range performance, derived by the high cruise efficiency in "airplane mode", which radically improves on current VTOL vehicles, including the Bell Boeing V-22 and AgustaWestland AW609 tilt-rotors and the Airbus Helicopters X3 compound helicopter.

The main Nibbio specifications are provided in Table 3. A detailed illustration of the preliminary studies, design methodology and main outcomes of the Caurus Nibbio project can be found in [2,3].

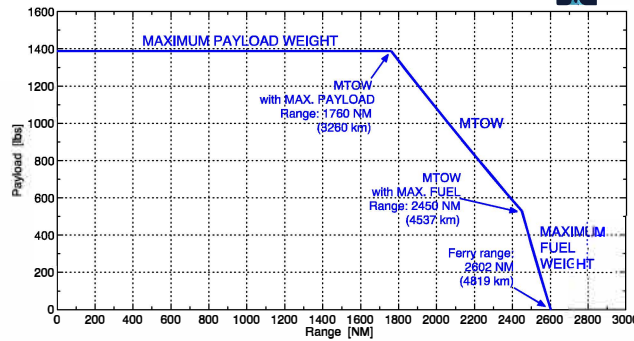


Figure 6: Nibbio's payload-range diagram.

Table 3: Main Nibbio specifications

Engine power	2 x 1,342 kW
Wingspan	16.0 m
Length	11.5 m
Height	3.0 m
Rotor diameter	6.5 m
Max gross weight	5,000 kg _f
Range	3,370 km
Service ceiling	13,800 m
Maximum airspeed	740 km/h

5 PROJECT FLYNK

5.1 The AIAA Graduate Student Design Competition 2014-2015

The American Institute of Aeronautics and Astronautics (AIAA) Foundation announced the 2014-2015 edition of its annual Student Design Competition in 2014. The contest calls students to provide a solution to a RFP, preparing a design report in which they describe such solution, testing the hypothesis, evaluating its effectiveness, and possibly doing some cost analysis. Two categories are available: undergraduate and graduate. Each of the winning teams is awarded a cash stipend, plus other benefits such as invitation to the AIAA Aviation Forum and Exposition to present their projects. It was the first time a student team from Politecnico di Milano was involved.

The 2015 competition RFP focused on the design of an air taxi system that must operate in large metropolitan areas such as New York or San Francisco, with either VTOL or STOL (Short Take-off and Landing) capability. In addition to the design of the aircraft, an operations model of the air taxi corporation was requested, as well as adequate cost and revenue models demonstrating the viability of the proposed system. The proposed solution, framed in the year 2020, had to be of better value than future solutions of automobiles, rail and airline service – which is a fairly severe requirement.

The only Italian team participating was Team Flynk (a contraction of "flying link"), which scored the first place. Team Flynk formed during the Academic Year 2014-2015 as one of the design groups within the Aircraft Design graduate course at Politecnico di Milano. They resolved to participate with a proposal focused on a novel very-short haul passenger aircraft powered by electric propulsion.

5.2 The Flynk concept

The Flynk is an innovative all-electric, 9-passenger STOL airplane designed for low-fare air taxi missions used for mass commuter transportation, in an attempt to contribute to the improvement of the quality of life in large metropolitan areas. The challenging RFP inspired a thorough preliminary study to investigate the actual needs of a metropolitan community. New York City was chosen as the area to be serviced, as its residents face the longest commuting times among workers in the thirty largest cities in the U.S.A., spending an average of 6 h 18 m per week on the road. In order to better outline their needs, an online survey was posted on a social network, gathering over 200 replies.

Based on this survey, five primary requirements have been identified for a competitive air transportation system: affordable fares, low noise emission levels, reliability, passenger comfort, and faster connection than its competitors.

These include elements already present in the RFP, while other elements emerged that contributed to the definition of the Flynk air taxi system design specifications. Among these, it was found that the location of take-off/landing spots is of strategic importance, in order to minimize the need for additional, unwelcome ground transportation means. Also, unmanned solutions were discarded in favor of piloted aircraft, given the importance of “perceived” safety for interviewed potential customers.

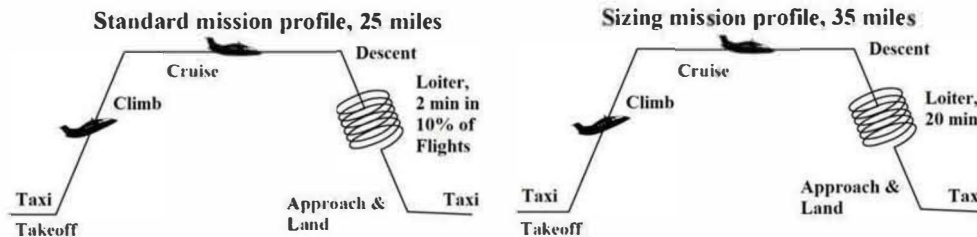


Figure 7: Flynk's mission profiles.

Based on the market study, a “Standard Mission” profile was determined, composed by taxi to runway threshold, take-off, climb to cruise altitude, cruise for 25 mi (or 40 km), descent, loiter for two minutes, approach, landing, taxi to apron (Figure 7, left). Candidate configurations were sized in order to achieve the best performance for the Standard Mission, while retaining the capability to complete a more demanding task, the “Sizing Mission” profile, where the cruise leg amounts to 35 mi (or 56 km) and loiter lasts for 20 minutes (Figure 7, right). Cruise speed was required to be not lower than 290 km/h, in order to guarantee an average block speed over 180 km/h, while cruise altitude was set at 500 ft (or 150 m) AGL (Above Ground Level). Given the atypical mission, the widest possible array of manned air vehicle types potentially applicable was considered in the choice of the configuration, including traditional and compound helicopters, gyroplanes, tilt-rotors, and fixed-wing airplanes. Based on the scores attributed to each configuration with respect to economic performance, noise impact, average speed, robustness, and VTOL capability, a decision-making process was carried out and the fixed-wing STOL emerged as the best configuration. Also, an all-electric configuration was preferred, because it was found that, for the peculiar missions addressed, it outperforms conventional and hybrid-electric types not only with regard to environmental impact (both chemical and noise emissions), but even concerning economic performance. Four engine-propeller groups power the aircraft, with nacelles partially buried in the wing thickness. The 6-blade propeller was designed to meet severe noise requirements. Given the very short missions and the need for quick ground operations between flights, non-replaceable batteries were chosen, to be subjected to high-voltage fast recharge.

High STOL performance are achieved by a careful design of the lifting surfaces, which include a slightly oversized wing, with largely oversized trailing edge double-slotted flaps, compared to traditional designs (Figure 8). This solution increases the actual wing surface by 21% and, together with the blown-wing effect from propellers, allows reaching lift coefficient values in excess of 4.0. A further contribution to exceptional field performance comes from the partially-tilting wing-tip nacelles.



Figure 8: Flynk's fully-extended flap configuration.

The envisaged operations model features a network of sixteen airfields in the New York Metropolitan Area, five of which inside Manhattan. Routes have been designed in compliance with Air Traffic Management (ATM) rules, paying attention to avoid flying over Manhattan and other heavily populated areas, with two main airways located over the Hudson River and the East River. The Flynk

service was then simulated in full working condition, to calculate separations between traffic in the two main routes. The number of vehicles required for the service was estimated as 72, including backup aircraft.

The main Flynk specifications are provided in Table 4. A detailed illustration of the preliminary studies, design methodology and main outcomes of the Flynk project can be found in [4].

Table 4: Main Flynk specifications

Engine power	4 x 110 kW
Wing surface	20 m ²
Aspect ratio	9.4
Max payload weight	915 kg _f
Max gross weight	2,870 kg _f
Runway length	150 m
Cruising speed	370 km/h

6 PROJECT HYBRIS

6.1 The 1st RAeS First Annual General Aviation Design Competition

The Royal Aeronautical Society (RAeS) announced the first edition of its Annual General Aviation Design Competition – E-conditions Fixed-Wing Aircraft Design Challenge in 2015. This international competition was not reserved to students, but open to any interested design team, and saw the participation of groups of professionals, in additions to university teams. The winning team was awarded a cash stipend, plus an invitation to the RAeS General Aviation Conference “Advanced Design of Light Aircraft” to present their project. It was the first time a student team from Politecnico di Milano was involved in a RAeS-sponsored contest.

The contest aimed at promoting innovative designs, in an attempt to encourage a drastic renovation of light aviation in the UK. E-conditions represent a new means to operate an aircraft without a Certificate of Airworthiness or a Permit to Fly established by the RAeS and the British Civil Aviation Authority. The competition called for fixed-wing aircraft using any form of power source.

The only Italian team participating was Team Hybris (from “hybrid” and the Greek topos ὑβρις), which scored the first place. Team Hybris formed during the Academic Year 2015-2016 as one of the design groups within the Aircraft Design graduate course at Politecnico di Milano. They resolved to participate with a proposal focused on a highly innovative 4-seat airplane with a promising potential in reducing the environmental impact of General Aviation (GA) operations, as well as operating costs.

6.2 The Hybris concept

The Hybris is a groundbreaking concept for an airplane with a promising potential in reducing the environmental impact of GA, as well as operating costs. A thorough market study, including a survey aimed at UK Aero Clubs and pilots, was carried out to identify needs, desiderata, competitors and other useful preliminary information. As a result, high operational cost stood up as the main problem, followed by internal and external noise. Desiderata include traditional aft-tail, low-wing, tricycle landing gear configuration; range between 300 and 500 NM (or 550 and 920 km); cruising speed between 115 and 155 kn (or 210 and 290 km/h), at an altitude ranging among 2,000 and 5,000 ft (or 600 and 1,500 m); maximum altitude of 10,000 ft (or 3,000 m); between two and four passengers. On this basis, current (Piper PA28, Cessna 172, Cirrus SR22) and near-future (Pipistrel Panthera) competitors have been analysed and mission requirements have been drafted to improve on them.

In view of the lightest possible environmental impact, pure electric propulsion was considered, but soon abandoned because of the limitations in range. These apply, although much less severely, also to a serial hybrid-electric configuration, where an ICE is employed to produce electric energy through a generator, without mechanical connections to the propellers, which are driven by EMs. In order to enhance on-board energy storage, structural batteries (SB) were considered. These are innovative multi-functional materials, similar to structural composites, but capable of storing electrical energy. Therefore, SB may be employed in the airframe, contributing to structural strength, while at the same time allowing additional electric energy to be stored, replacing structurally-useless, heavy classic batteries.

The outcome is a radically innovative design for an aft-tail, low wing, single propeller, tricycle retractable landing gear, 4-seat airplane, in which a great part of the airframe is made by SB, with

only the upper wing surface and the movables using classic Carbon-Fiber Reinforced Polymer (CFRP) composites. This configuration is depicted in Figure 9. The concept of an integrated SB airframe is the subject of a pending patent [12].

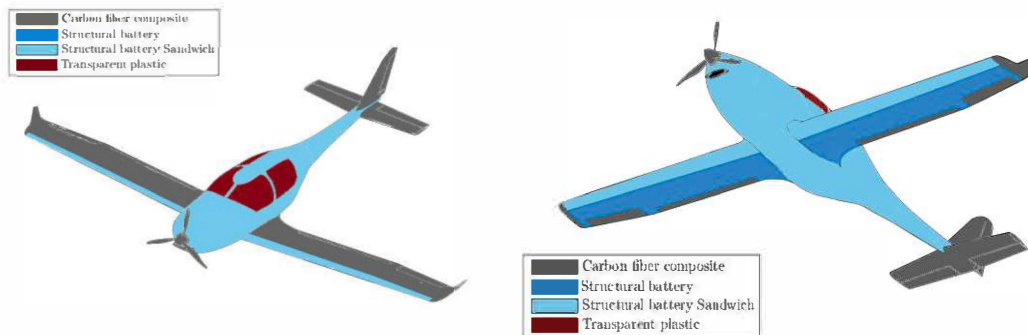


Figure 9: Hybris' airframe materials.

The coupled sizing of propulsion and airframe was carried out to allow to take-off and complete the first climb segment in pure-electric mode, up to 3,000 ft (or 900 m) AGL. Then the ICE is turned on to power the climb to cruise altitude. When this is reached, ICE power provides the required shaft power and a surplus recharge the batteries. When descending below 3,000 ft AGL, the ICE is turned off and the aircraft lands in pure-electric mode. Therefore, ICE emissions vanish in the most environmentally-critical flight phases, i.e. terminal maneuvers. Moreover, given the possibility to recharge batteries during flight, this configuration does not require any special recharging facility on the airfields.

Based on a fairly pessimistic performance level for SB, degraded by 40% with respect to the values expected in the year 2020, the final design features 45% of the structural weight made by SB. On the other hand, SB form 73% of the total mass of batteries. This entails a modest MTOW saving, but at the same time the predicted range performance (Figure 10) make Hybris fully comparable with its most modern competitors, at operational costs that, under reasonable assumptions, may be 22% and 17% lower compared to the Cirrus SR22 and Pipistrel Panthera, respectively.

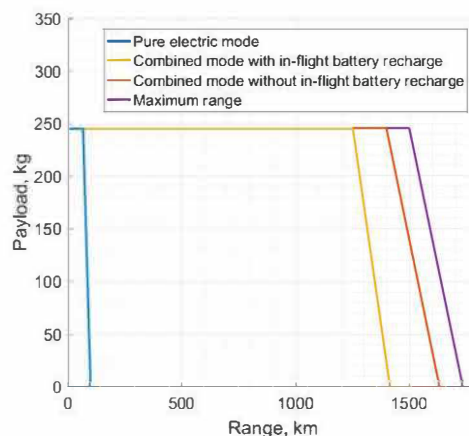


Figure 10: Hybris' payload-range diagram.

Table 5: Main Hybris specifications

EM max power (continuous/transient)	60/150 kW
Wingspan	10.5 m
Length	11.5 m
Max gross weight	1,275 kg _f
Range	>2,200 km
Cruising speed	280 km/h
Cruise altitude	2,400 m

Table 5 provides the Hybris main specifications. A detailed illustration of the preliminary studies, design methodology and main outcomes of the Hybris project can be found in [5].

7 CONCLUDING REMARKS

In the "Aircraft Design" course at Politecnico di Milano, remarkable projects involving the conceptual and preliminary design for innovative aerial vehicles have been presented over the years. Recently, at least one of these projects was submitted to an international design competition each year. In particular, four projects, participating in four different contests, were ranked between third and first place: Flybrid (2013), Nibbio (2014), Flynk (2015), and Hybris (2016). The paper discussed the approach adopted in the "Aircraft Design" course and its educational results at large. The four award-winning projects were introduced very concisely, due to the limited amount of space, discussing the most original design choices and the key elements that contributed to their success. The interest aroused around these four concepts, at a research level and within the industry as well, is a strong motivation to pursue the "Aircraft Design" course approach further on, in an effort to provide a highly formative and thrilling experience to young engineers engaged in their M.Sc. studies, while eliciting new ideas for the progress of aviation at large.

REFERENCES

1. G.E. Bona, M. Bucari, A. Castagnoli, L. Trainelli; 2014; "Flybrid: Envisaging the Future Hybrid-Powered Regional Aviation"; AIAA paper no. 2014-2733; *AIAA/3AF Aircraft Noise and Emissions Reduction Symposium, AIAA Aviation and Aeronautics Forum and Exposition 2014*; Atlanta, USA; June 16 - 20, pp. 1 - 15
2. L. Sala, G. Alitta, D. Berbenni, C. Capocchiano, A. Fugazza, S. Rojas, S. Sangalli, A. Scaringello, P. Waffo, L. Trainelli; 2015; "Project Caurus "Nibbio" – A Novel Tilt Rotor Concept for Very High Speed Applications"; *American Helicopter Society International 71st Annual Forum*; Virginia Beach, USA; May 5 - 7, pp. 1 - 10
3. L. Sala, G. Alitta, D. Berbenni, C. Capocchiano, A. Fugazza, S. Rojas, S. Sangalli, A. Scaringello, P. Waffo, L. Trainelli; 2015; "The 'Nibbio' High-Speed Tilt Rotor Concept"; *XXIII Congresso Nazionale AIDAA*; Torino, Italy; November, 17 - 19; pp. 1 - 19
4. A. Broglia, L. Clozza, M. Russo, C. Spada, L. Vendemini, A.G. Zuanetti, C.E.D. Riboldi, L. Trainelli; 2017; "Flynk – The future all-electric commuter concept for metropolitan areas", *XXIV Congresso Nazionale AIDAA*; Palermo-Enna, Italy; September 18-22; pp. 1 - 8
5. A. Bernasconi, F. Biondani, L. Capoferri, A. Favier, C. Velarde Lopez de Ayala, C.E.D. Riboldi, L. Trainelli; 2017; "Conceptual Design of a Structural-Battery Hybrid-Electric Aircraft"; *XXIV Congresso Nazionale AIDAA*; Palermo-Enna, Italy; September 18-22; pp. 1 - 8
6. D.P. Raymer; 2006; *Aircraft Design: a Conceptual Approach*; AIAA Education Series
7. J. Roskam; 1997; *Airplane Design: Parts I through VIII*; DAR Corporation
8. E. Torenbeek; 2013; *Advanced aircraft design : conceptual design, analysis, and optimization of subsonic civil airplanes*; Wiley
9. E. Torenbeek; 1982; *Synthesis of Subsonic Airplane Design*; Delft University Press, Kluwer Academic Publishers
10. P.M. Sforza; 2014; *Commercial airplane design principles*; Oxford, Butterworth-Heinemann.
11. S. Gudmundsson; 2014; *General Aviation Aircraft Design: Applied Methods and Procedures*; Oxford, Butterworth-Heinemann
12. A. Bernasconi, F. Biondani, L. Capoferri, A. Favier, C. Velarde Lopez de Ayala, F. Gualdoni, C.E.D. Riboldi, L. Trainelli; 2016; "Velivolo con Batterie Elettriche, in Particolare Velivolo Ibrido (Aircraft with Electric Battery, in Particular Hybrid Aircraft)"; Italian Patent Application No. 102016000114808
13. Anon.; 2010; "Understanding the Benefits of the Smart Grid"; National Energy Technology Laboratory; U.S. Department of Energy, DOE/NETL-2010/1413
14. K.M. Valsamma; 2012; "Smart Grid as a desideratum in the energy landscape: Key aspects and challenges"; 2012 IEEE International Conference on Engineering Education: Innovative Practices and Future Trends (AICERA); Kottayam, India; 19-21 July; pp. 1 - 6

The design of an annular combustion chamber

Marius Enache

Junior Researcher

*National Research and Development Institute for Gas Turbines COMOTI
 220 D Iuliu Maniu Bd., sector 6, cod 061126, OP 76, CP174, Bucharest, Romania
marius.enache@comoti.ro*

Andreea Mangra

Scientific Researcher

Razvan Carlanescu

Scientific Researcher

Florin Florean

Scientific Researcher

ABSTRACT

The design of an annular combustion chamber for a micro gas turbine engine is presented in this paper. The combustion chamber is designed for using biogas as fuel. It is designed based on the constant pressure, enthalpy addition process. The present methodology deals with the computation of the initial design parameters and arriving at optimized values. Then the dimensions of the combustor are calculated based on different empirical formulas. The air mass flow is then distributed across the zones of the combustor. The cooling requirement is met using cooling holes. The whole combustion chamber is modeled using Catia V5. The model is then analyzed using various parameters at various stages and levels to determine the optimized design. The aerodynamic flow characteristics are numerically simulated by means of the ANSYS CFX software. The air-fuel mixture, combustion-turbulence, the thermal and cooling analysis is carried out. The results are then presented in image outputs and graphs.

KEYWORDS: Aerodynamic design; annular combustion chamber; CFD (computational fluid dynamics) analysis.

NOMENCLATURE

LATIN

S-section area [mm^2];
 T-temperature [K];
 \dot{m} -mass flow [kg/s];
 v-velocity [m/s];
 r-radius [mm];

GREEK

α -excess air;
 ρ -density [$\frac{kg}{m^3}$];
 ϕ -hole diameter [mm];

1. INTRODUCTION

The scope of this article is to present a design methodology for a combustor which will be part of a micro gas turbine for a 350 kW cogeneration power plant which works after a Brayton recovery cycle. The compressor and the turbine are the single-stage centrifugal type. The combustion chamber is of annular type. The micro gas turbine is designed to function using biogas as fuel.

The combustion chamber, or combustor, of a gas turbine, is the device that receives the pressurized air from the compressor mixes it with fuel, and burns this mixture to release the heat energy through a combustion reaction. Gas turbines work with a high excess of air, usually out of the flammability limits, and so a flame tube, or liner, is used to improve the distribution of air through the reactor.

Basically, the liner divides the combustion chamber into three zones: the primary zone, the secondary or intermediate zone and the dilution zone. In the primary zone, a recirculation zone is created to ensure the stability of the flame. The main function of the primary zone is to anchor the flame and provide sufficient time, temperature, and turbulence to achieve essentially complete combustion of the incoming fuel-air mixture. In the primary-zone a portion of the hot combustion gases are entrained and recirculated in order to provide continuous ignition to the incoming air and fuel. If the primary-zone temperature is higher than around 2000 K, dissociation reactions will result in the appearance of significant concentrations of nitrogen oxides. On the other hand, incomplete combustion will lead to the formation of carbon monoxide (CO) and unburned hydrocarbons (UHC) in the efflux gases. Should these gases pass directly to the dilution zone and be rapidly cooled by the addition of massive amounts of air, the gas composition would be "frozen," and CO, which is both a pollutant and a source of combustion inefficiency, would be discharged from the combustor unburned. Thus, in the secondary zone, the temperature is dropped to an intermediate level by the addition of small amounts of air encourages the burnout of soot and allows the combustion of CO and any other unburned hydrocarbons (UHC) to proceed to completion. The role of the dilution zone is to admit the air remaining after the combustion and wall-cooling requirements have been met and to provide an outlet stream with a temperature distribution that is acceptable to the turbine.

Combustion chamber design methodologies have been proposed by Lefebvre [1] and Melconian & Modak [2]. However, these methodologies have been developed for the design of aeronautical and large industrial gas turbine combustors. These methods have been successfully used to design combustion chambers [3, 5, 6] and there has even been developed software in which these methods have been implemented [4].

Mohammad and Jeng [7] have developed a computer code for annular combustor design. The design algorithm employs empirical and semi-empirical models which include diffuser section design, air distribution computations, combustor sizing, fuel nozzle design, axial swirler design, heat transfer calculations (with/without cooling, thermal barrier coating) and dilution holes design.

Conrado et al. [8] present a methodology for gas turbine combustor basic design. Criteria for selecting a suitable combustor configuration are examined followed by design calculations for the dimensions of the casing, the liner, the diffuser, and the swirler. Calculations of gas temperature in the various zones of the combustor and liner wall temperatures in the presence of film cooling are performed along with design calculations for the dimensions of the air admission holes. A computational program was developed based on the sequence of equations discussed in the paper.

In [9] is presented a combustion chamber design methodology using a software developed for this purpose. The software developed calculates the dimension for a straight through tubular combustion chamber that operates with gaseous fuel. This software allows visualizing the main aerodynamics parameters that are involved in the project of a simple combustor. The equations involved on the calculus of the program are based on the methodology developed by Lefebvre.

2. DESIGN METHODOLOGY

The first step in designing the combustor was the determination of the excess air and fuel mass flow starting from the input data presented in Table 1 and Table 2.

Table 1: Parameters of the gas turbine cycle

Parameter	Value	Units
Compression ratio	5:1	
Intake temperature of Turbine (T_3)	1173	K
Output temperature of Compressor (T_2)	750	K
Air Mass flow	2.6	kg/s
Efficiency of air compressor	80	%
Efficiency of turbine	85	%

Table 2: Chemical composition of the fuel

	Volume percent (%)	Density (kg/Nm ³)
CH ₄	50	0,656
CO ₂	45	1.842
N ₂	3	1.165
O ₂	0.8	1.331
NH ₄	0.6	0.73
H ₂	0.2	0.089
CO	0.2	1.14
H ₂ S	0.2	1.434

The density of the biogas, according to the chemical composition in Table 2 is 1.21 kg/Nm³.

The low calorific power of the biogas was determined using Eq. 1:

$$H_i = 12720 \cdot (CO) + 10800 \cdot (H_2) + 35910 \cdot (CH_4) + 23400 \cdot (H_2S), kJ/Nm^3 \quad (1)$$

where (CO), (H₂), (CH₄) and (H₂S) represent the volume percent for each component of the biogas [10]. Thus a low calorific power of 18048 kJ/Nm³ was obtained. Or taking into account the biogas density, a low calorific power of 14889 kJ/kg.

Eq. 2 was used for determining the theoretical quantity of oxygen necessary for complete combustion [10]:

$$O_{min} = 0,5 \cdot [(CO) + (H_2)] + \sum(m + \frac{n}{4}) \cdot (CmHn) + 1,5 \cdot (H_2S) - (O_2) \left[\frac{m_N^3}{m_N^3} \right] \quad (2)$$

where (CO), (H₂), (C_mH_n), (H₂S) and (O₂) represent the volumetric participations for each component of the biogas [10]. Using Eq. 2, for m=1 and n=4, the following value was obtained: $O_{min}=0.997$. The theoretical quantity of air necessary for complete combustion was determined using Eq. 3:

$$L_{min} = \frac{O_{min}}{0,21} \quad (3)$$

obtaining the value: 4.74.

The excess of air was determined using Eq. 4:

$$\alpha = \frac{H_i - c_{pg} \cdot T_3}{c_{pg} \cdot T_3 \cdot L_{min} - c_{pa} \cdot T_2 \cdot L_{min}} \quad (4)$$

where c_{pa} represents the specific heat of air and c_{pg} represents the specific heat of exhaust gases [9]. For $T_2=750\text{ K}$ and $T_3 = 1173\text{ K}$ an air excess of 5.37 was obtained.

For an air mass flow of 2.6 kg/s and using Eq. 5:

$$m_c = \frac{m_a}{\alpha \cdot L_{min}} \left[\frac{kg}{s} \right] \quad (5)$$

a fuel mass flow of 0.092453 kg/s was obtained.

The next step in designing the combustor was to determine the excess of air and the temperature alongside the liner.

For this purpose the combustor was divided into three regions:

1. The fuel injectors region;
2. The primary zone;
3. The dilution zone;

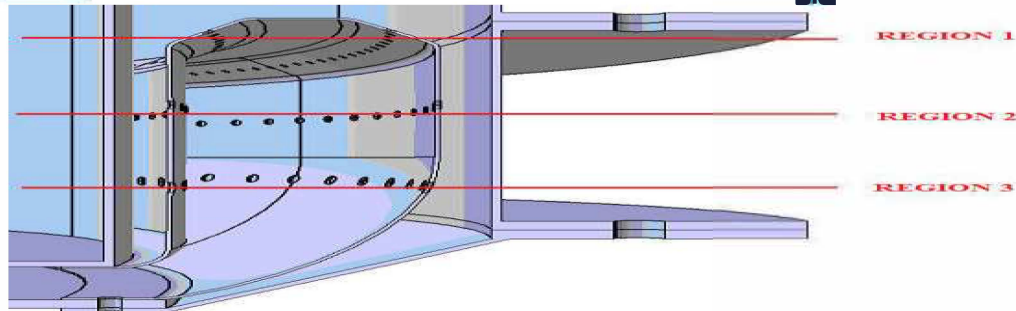


Figure 1: The three regions of the combustion chamber

Taking into consideration the information presented in the specialty literature [1], it was considered that 10% of the total air mass flow enters the fuel in the injectors region, 18% of the total air mass flow enters in the primary zone and the rest of 72% enters the dilution zone.

Table 3: Parameters resulted for the three regions of the combustion chamber

Regions	1	2	3
$m_a(\text{kg/s})$	0.260	0.468	1.872
α (excess air)	0.593	1.661	5.932

The temperature along the combustion chamber was determined using Eq. 6:

$$T = \frac{efic \cdot H_i + \alpha \cdot L_{\min} \cdot T_2 \cdot H_i}{(1 + \alpha \cdot L_{\min}) \cdot c_{p-g}} [\text{K}] \quad (6)$$

where *efic* represents the combustion efficiency. Its values were taken according to [11]. As expected the temperature maximum value is obtained in the primary zone.

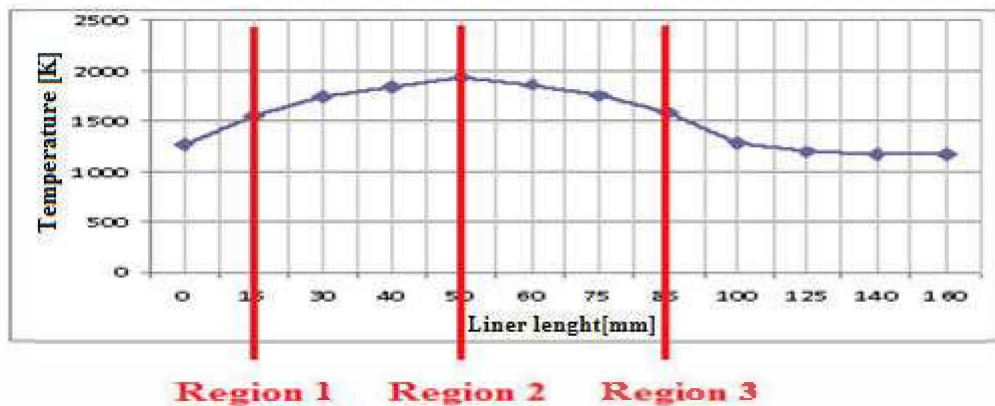


Figure 2: Temperature distribution

The final step in the design process was to determine the velocities outside and inside the fire tube and the liner holes diameters based on the jet penetration.

The pressure at the compressor's exit is 500000 Pa (p_2). Since the distance from the compressor exit to the combustor entrance is considerable due to the micro gas turbine constructive solution, it was considered that the air pressure at the combustor entrance is 475000 Pa.

The velocities outside and inside the fire tube have been calculated using Eq. 7:

$$v = \frac{\dot{m}}{\rho \cdot S} \left[\frac{\text{m}}{\text{s}} \right] \quad (7)$$

where S represents the section area.

Table 4: Repartition of velocity exterior of the fire tube

Exterior air annular section			
r_{ext} (mm)	r_{int} (mm)	m_c (kg/s)	m_a (kg/s)
322	311	0.092453	2.6
$S=21863.82 \text{ mm}^2$			
Interior air annular section			
r_{ext} (mm)	r_{int} (mm)	m_c (kg/s)	m_a (kg/s)
261	250	0.092453	2.6
$S=17649.94 \text{ mm}^2$			
Region	1	2	3
Pressure loss (dp%)	1	2	3
Pressure (Pa)	467775	463050	458325
Air density (ρ_a)	2.1797	2.1577	2.1357
Mass flow (kg/s)	2.6	2.34	1.872
v (m/s)	30.1862	27.4448	22.1822

Table 5: Repartition of velocity interior of the fire tube

r_{ext} (mm)	r_{int} (mm)	m_c (kg/s)	m_a (kg/s)
311	261	0.092453	2.6
$S=89804 \text{ mm}^2$			
Region	1	2	3
Pressure loss (dp%)	1.25	2.25	3.25
Pressure (Pa)	466593.75	461868.8	457143.8
Fuel density (ρ_g)	0.9359	0.8344	1.3338
Mass flow (kg/s)	0.3524	0.8204	2.6924
v (m/s)	4.1934	10.9490	22.4776

The jet penetration was calculated using Eq. 8 [11]:

$$H_{ji} = 3.1 \cdot \phi \cdot \left(0.3 + 0.415 \cdot \frac{V_a}{V_g} \right) \quad (8)$$

Table 6: Jet penetration

Region	1	2	3
Air Velocity(V_a)	30.18	27.44	22.18
Fuel Velocity(V_g)	4.19	10.94	22.47
Hole diameter ϕ (mm)	2.5	5	6.5
Jet penetration (H_{ji})	25.49	20.78	14.29

Based on the calculations presented above a first version of the combustor geometry, presented in Fig. 3, has resulted.

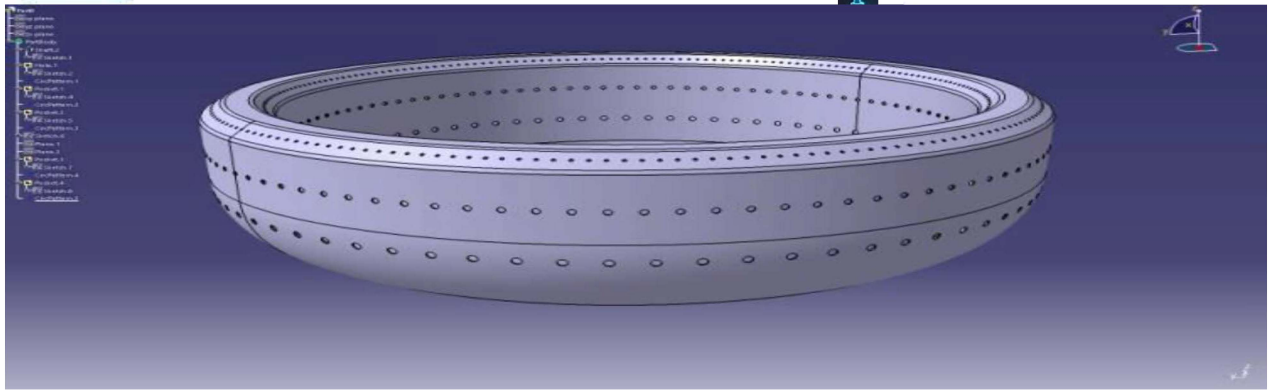


Figure 3: Fire tube

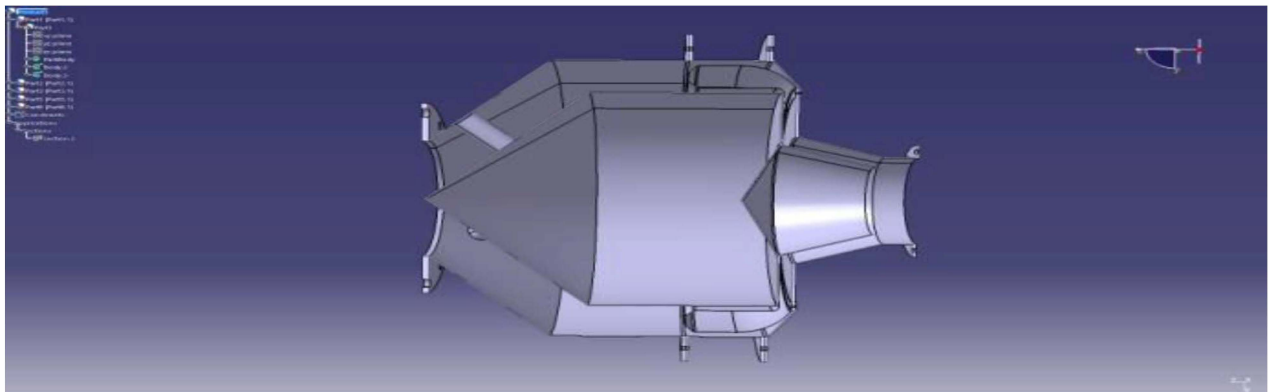


Figure 4: Combustion chamber assembly

3. Three-dimensional numerical simulation results

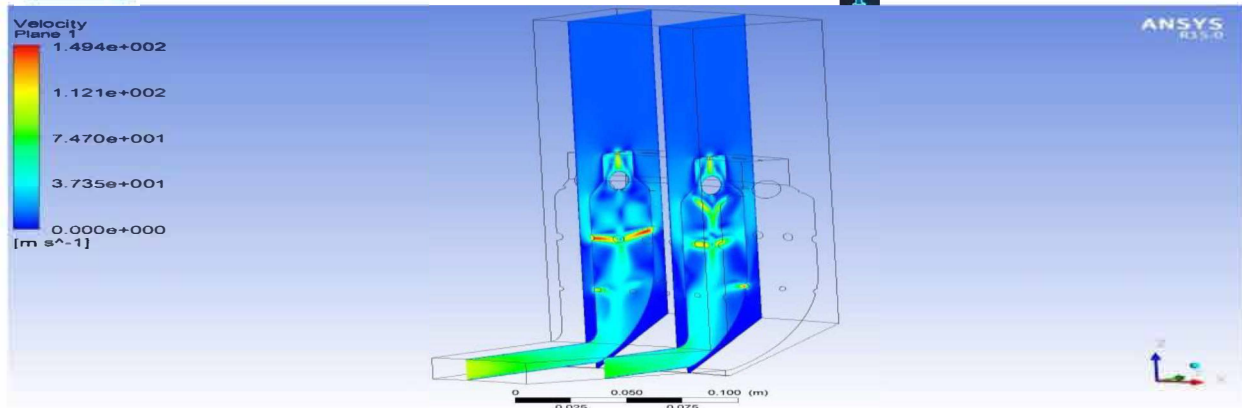
In order to obtain quicker results due computing limitation, the model was simplified into a 22.5-degree cut section for the combustor. The computational aerodynamic analysis is carried out to validate theoretical results and to obtain a detailed preview of the outcome design.

The numerical simulations were carried out using ANSYS CFX software. The RANS approach was used with an unstructured type mesh has been generated for the computational domain and with the Domain Motion Stationary. The total number of Tetrahedral Elements is 8231719.

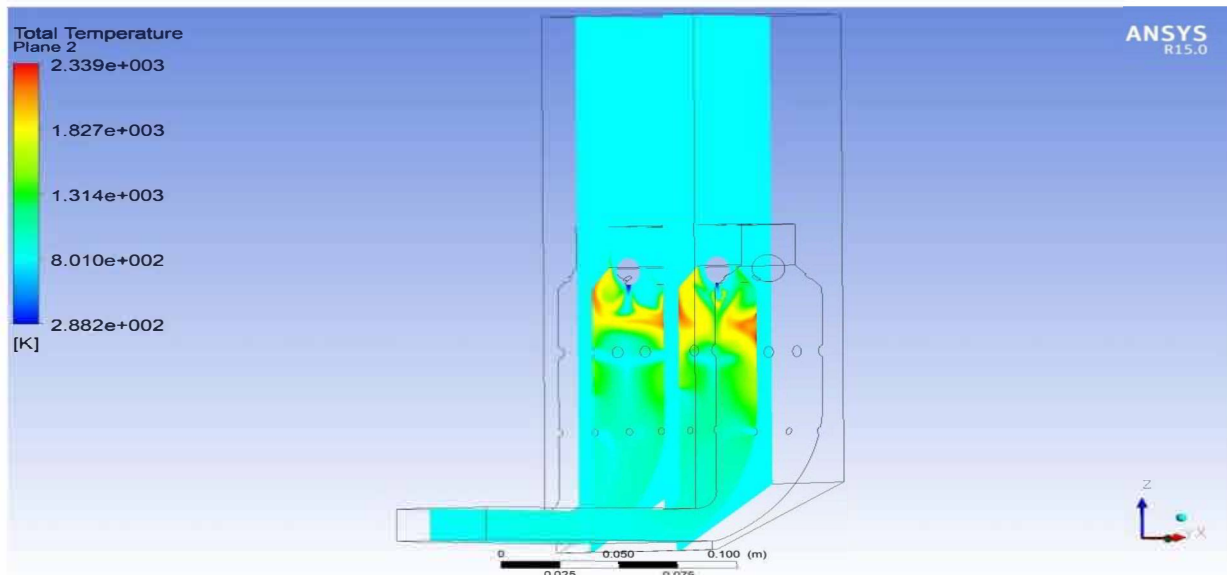
The following boundary conditions were used. At air inlet, there were imposed the air mass flow and temperature, at fuel inlet there were imposed the fuel mass flow and temperature and at the outlet, the pressure was imposed.

The Eddy Dissipation combustion model was used, in combination with the K-epsilon turbulence model. This model was chosen because it allows accurate simulation of the heat release and the distribution of the main chemical species. Reaction mechanism used in the simulation was Methane-Air WD2 in two steps where mass fraction for CO₂ and CH₄. The other elements from the chemical composition of the fuel are neglected due to their the small volume percentage.

The velocity distribution presented in Fig. 5 shows high velocity in the central region. Jet penetration is very strong, thus the created turbulence will affect combustion process.

**Figure 5: Velocity distribution**

From Fig. 6 it can be observed that the flame temperature presents high values mainly near the combustor's walls. This is in good correlation with the velocity profile presented in Fig. 5. The high-velocity values from the central region of the fire tube make difficult the mixing of the air and fuel in the primary region.

**Figure 6: Total temperature distribution**

In Fig. 7 are presented 4 temperature iso-surfaces inside the fire tube (red=2200 K, orange=2000 K, yellow=1800 K, green 1500 K). As it was observed before, the high flame temperatures are developing near the walls. This is not a good sign. It can lead to serious damage to the fire tube. It also can be seen that the flame has a very irregular structure.

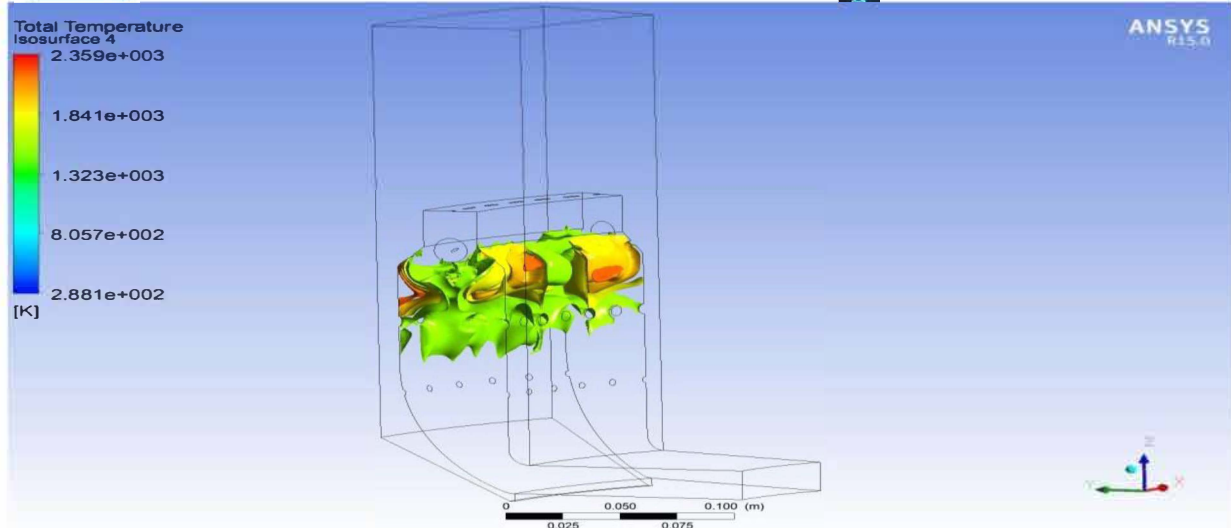


Figure 7: Total temperature Isosurface distribution

The average temperature at the exit of the combustor was 1150K. Even though this temperature value is very close to the one imposed in Table 1, based on the results obtained so far it was concluded that same changes have to be done to the combustor geometry.

A deflector was added to the original geometry in order to concentrate the flow in the central region of the fire tube and to prevent flame adhesion to the walls of the combustor. The improvement can be observed in Fig. 8 and Fig. 9. The flow velocity has diminished and the flame is concentrated in the center of the fire tube.

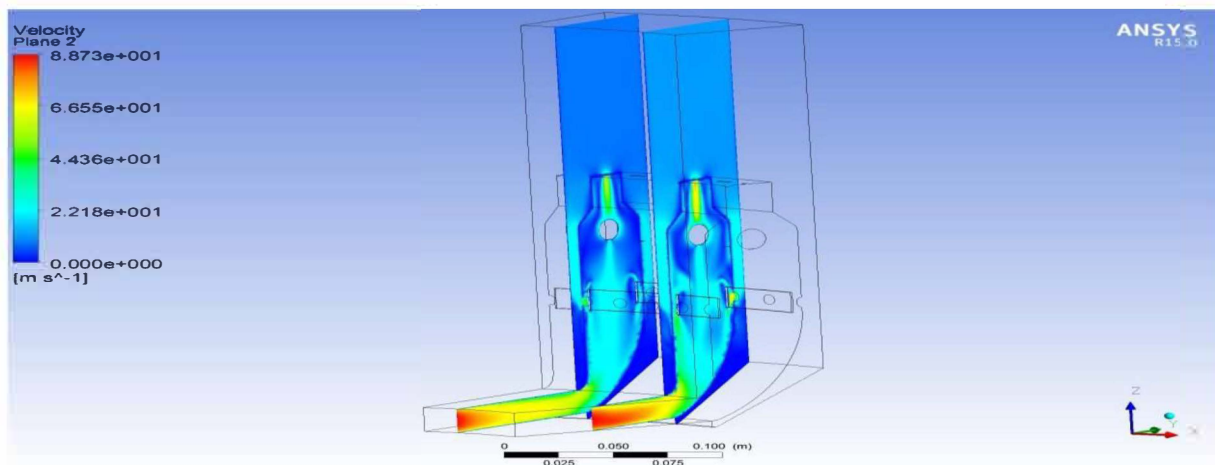


Figure 8: Velocity distribution

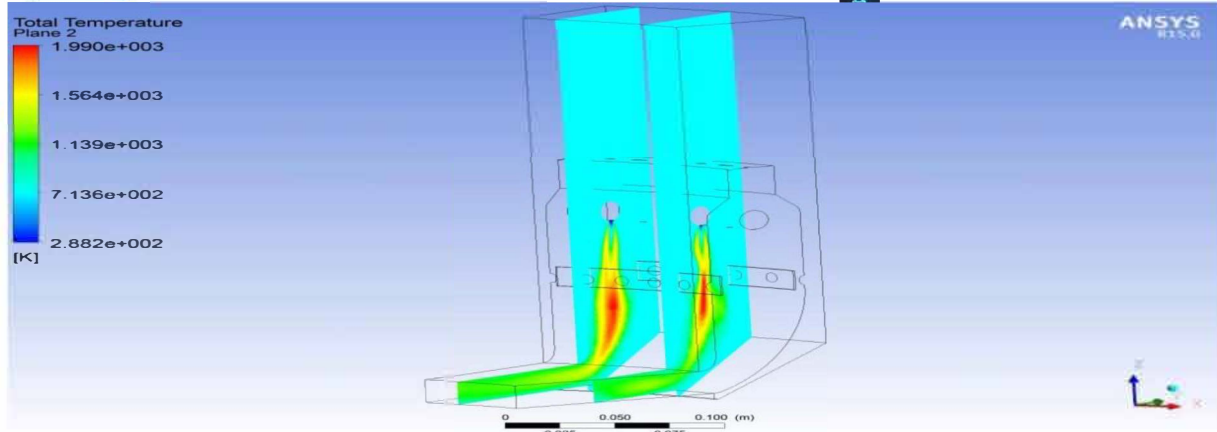


Figure 9: Total temperature distribution

In Fig. 10 the temperature distribution along the fire tube is presented. As it can be seen, the temperature rise up to 1400 K in the region of the injectors, afterward reaching a maximum of 2100 K in the primary zone. After that, the addition of air leads to a decrease of the flame temperature.

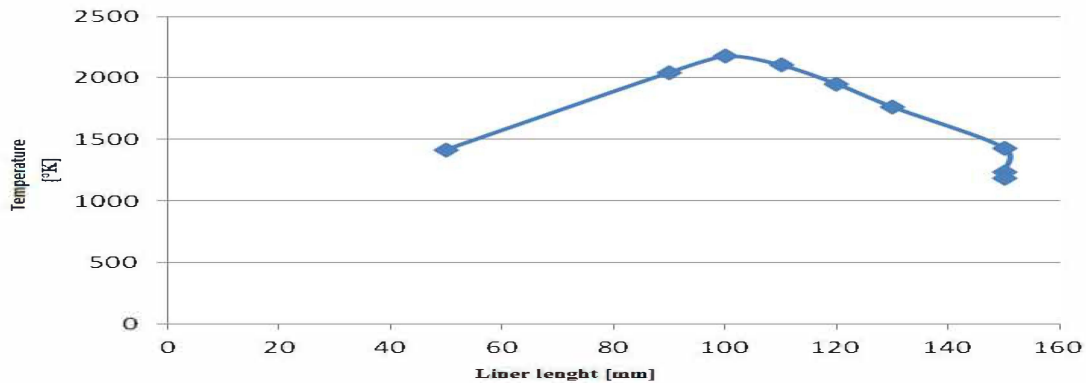


Figure 10: Total temperature distribution

Form Fig. 11 it can be seen that the flame has a uniform structure and the flame does not exceed the fire tube length. Thus it won't affect the turbine.

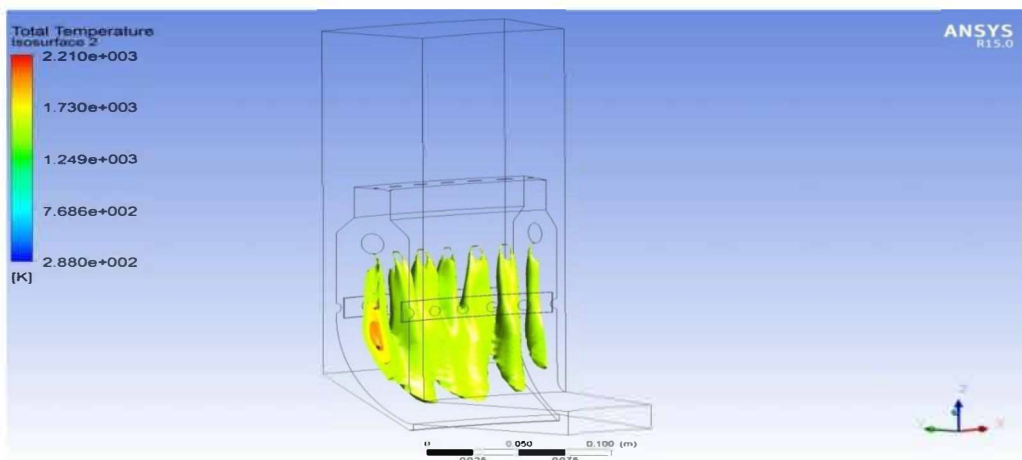


Figure 11: Total temperature Isosurface distribution

The average outlet temperature is 1180 K, being close to the required value.

4. Conclusions

The complete annular combustor design using just the initial design parameters has been discussed in this paper. This is a design methodology which can be used for the preliminary design. The transparent and detailed approach is focused on reducing design time and complexity. This gives an overall advantage in total design time and prototype building. Using the methodology, a practical design is presented. The obtained values are used for modeling and further simplified for analysis. The analysis was also carried out with higher accuracy using the combustion-turbulence interaction model and the results show that the optimum gas exit temperature was obtained for the present design. The design was successfully calculated and modeled.

REFERENCES

1. A.H. Lefebvre, D.R. Ballal, 2010; Gas Turbine Combustion 3rd edition, CRC Press Taylor & Francis Group
2. Melconian, J.W. Modak; 1985; Combustors Design, Sawyer's Gas Turbine Engineering Handbook: Theory & Design, Vol. 1, Turbomachinery International Publications, Connecticut.
3. C. P. Mark, A. Selwyn; 2016; Design and analysis of annular combustion chamber of a low bypass turbofan engine in a jet trainer aircraft, Propulsion, and power research; vol 5 (2); pp 97-107
4. R.E.P. Silva, P.T. Lacava; 2013; Preliminary design of a combustion chamber for micro turbine based in automotive turbocharger, Proceedings of the 22nd COBEM; pp. 412–422,
5. S.A. Hashim; 2013 Design and fabrication of an annular combustion chamber for the micro gas turbine engine applications, IJERT, vol 2
6. N. Pegemanyfar, M. Pfitzner; 2006; Development of a combustion chamber design methodology and automation of the design process, 25th International Congress of the Aeronautical Sciences, Hamburg, Germany
7. B.S. Mohammad, S.M. Jeng; 2009; Design procedures and a developed computer code for preliminary single annular combustor design, 45th AIAA Joint Propulsion Conference & Exhibit, Denver, Colorado
8. A.C. Conrado, P.T. Lacava, A.C.P. Filho, M.D.S. Sanches; 2004; Basic design principles for gas turbine combustor, in: Proceedings of the 10th ENCIT, paper no.0316.
9. L.J. Mendes Neto, A. Paramonov, E.E. Silva Lora, M.A. Rosa do Nascimento, Preliminary design of micro gas turbine combustion chamber for biomass gas;
<http://seeds.usp.br/pir/arquivos/congressos/CLAGTEE2003/Papers/RNCSEP%20B-103.pdf>
10. B. Popa, C. Vintila, 1973; Termotehnica, masini si instalatii termice, Ed. Didactica si pedagogica, Bucuresti
11. V. Pimsner, C.A. Vasilescu, G.A. Radulescu, 1964; Energetica turbomotoarelor cu ardere interna, Editura Academiei Republicii Populare România, București

A New Framework for Rotorcraft In-flight Noise Monitoring

Lorenzo Trainelli

Department of Aerospace Science and Technology, Politecnico di Milano

Associate Professor

Via G. La Masa 34 – 20156 Milano, Italy

lorenzo.trainelli@polimi.it

ABSTRACT

An original approach to the in-flight noise monitoring of maneuvering rotorcraft was recently pursued, developing the fundamental ingredients that allow estimating the acoustic emission in real time and presenting a convenient information of such emission to the pilot. This is obtained through a new cockpit instrument, the Pilot Acoustic Indicator, which is supported by a noise estimation algorithm that exploits offline, accurate acoustic predictions, runtime available parameters from the avionic bus, and an observation method that provides the values of non-directly-measurable parameters, such as the main rotor angle of attack. The observer uses the measurements of the main rotor blade angles, which are achieved by a new contactless measurement system based on stereo vision. These technologies and tools have been fully developed and tested in either highly representative, or real operating conditions. The paper describes the complete framework, its main components and the related results, and sketches possible activities towards a complete implementation on board current or future production rotorcraft.

KEYWORDS: *rotorcraft noise, noise abatement, noise monitoring, low-noise procedures, blade attitude sensor*

1 INTRODUCTION

The present paper offers a comprehensive review of the work performed while setting up a methodology and the habilitating technologies and tools for a novel approach to rotorcraft in-flight monitoring of emitted noise, and sketches a few ideas for future steps.

Radiated noise stands as one of the biggest hindrances in performing rotorcraft operations, as these are typically carried out at low altitudes and impact significantly on the overflown human and natural environment. On the other hand, the peculiarity of some of the mission tasks performed by helicopters and tiltrotors is such that, even considering the rapid pace of the diffusion of unmanned rotary-wing vehicles for aerial work applications, it makes their usage inevitable and therefore inspires continuous development and optimization. Therefore, an important research topic in recent years is represented by noise reduction strategies. Basically, four approaches are investigated:

1. Vehicle design for low noise (e.g., blade aerodynamic design).
2. Active control for emitted noise abatement (e.g. higher harmonic pitch control).
3. Flight procedure design for low noise (e.g. steep descent profiles).
4. In-flight monitoring to allow noise-alleviating actions by the pilot.

The last approach is of interest here, being the main focus of the MANOEUVRES (Manoeuvring Noise Evaluation Using Validated Rotor State Estimation Systems) project, carried out in response to the Clean Sky GRC5 Call for Proposal SP1-JTI-CS-2013-01 "Innovative measurement and monitoring system for accurate on-board acoustic predictions during rotorcraft approaches and departures". The project was developed by a consortium composed by Politecnico di Milano, Università Roma Tre, Vicoter (a small engineering company skilled in structural dynamics and testing) and Logic (a leading avionics company), in close cooperation with Leonardo Helicopters (LH).

Within the Clean Sky Joint Technology Initiative, the Green Rotorcraft (GRC) Integrated Technology Demonstrator was concerned with multiple applied research actions for sustainability and environmental friendliness of rotorcraft. In particular, the GRC5 "Environment friendly flight paths" sub-project was strongly concerned in the achievement of one of the ACARE environmental objectives for 2020, i.e. the reduction of the noise perceived on ground by 10 EPNdB or halving the noise footprint area by 50%.

2 THE MANOEUVRES FRAMEWORK

Therefore, in the MANOEUVRES project, a feasible noise-abatement approach based on in-flight monitoring of the emitted acoustic radiation was conceived, for possible integration on current and future production helicopters [1–3]. This approach is intended to deliver methodologies and practical tools that concur to provide a synthetic, intuitive noise information to the pilot in real-time, allowing him the possibility to adopt suitable actions to maintain or reduce the vehicle's acoustic impact while following a given trajectory. Special attention has been given to terminal operations, and therefore to maneuvers such as decelerations and descents performed in the approach to landing. In this approach, actual vehicle characteristics (weight, configuration) and operating conditions are taken into account through their combined effects on some direct measurements, including elements of the kinematic state of the rotorcraft and its main rotor (MR). Based on this, a complex algorithm invoking relatively simple numerical modelling – fit for real-time computation needs – allows to estimate the noise emission and to relate it to specified thresholds.

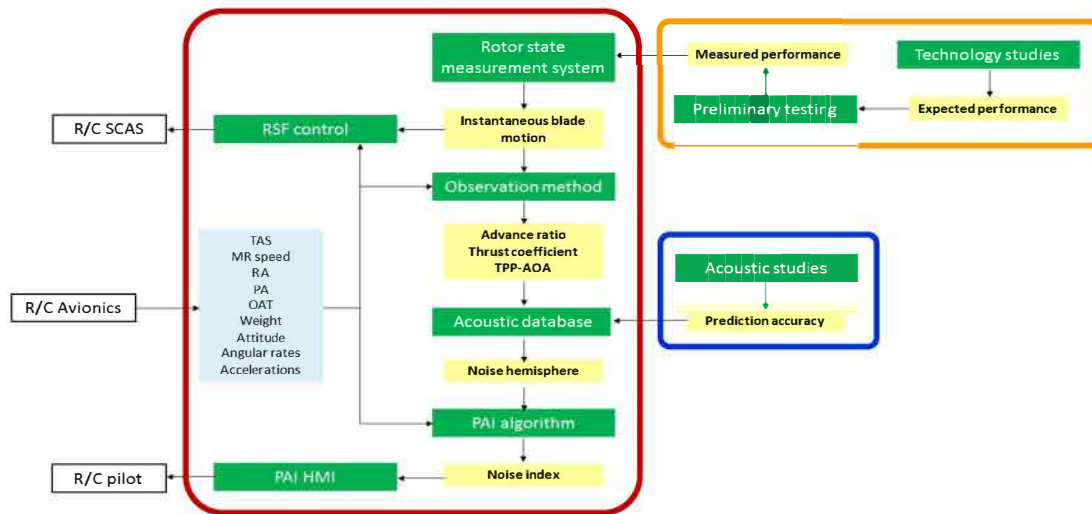


Figure 1: MANOEUVRES integrated concept

The functional scheme of the MANOEUVRES integrated concept is shown in Figure 1. Within the red contour, the components of the noise estimation and indication system are shown: green boxes identify original elements developed within the MANOEUVRES project, i.e. methods or equipment providing as output the parameters addressed in the yellow boxes. Starting from below, the pilot receives emitted noise information through a new cockpit instrument, the Pilot Acoustic Indicator (PAI), through a dedicated HMI (Human-Machine Interface) [4,5]. The PAI HMI conveniently displays the value of a noise index, which is computed by the PAI algorithm based on of an estimation of the present acoustic emission of the vehicle. This emission is described by a SPL (Sound Pressure Level) distribution over a suitable portion of a spherical surface rigidly connected with the aircraft, retrieved from a pre-calculated database covering the flight envelope of interest (Figure 2).

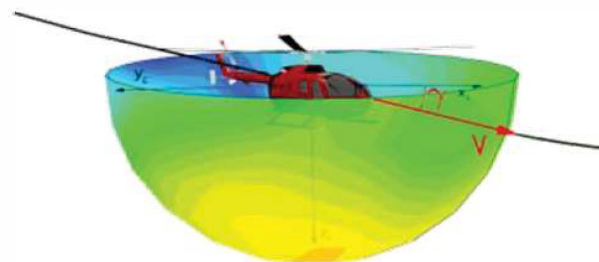


Figure 2: Acoustic (hemi)spherical SPL distribution connected with the vehicle

The database is interrogated by entering the values of three quantities that conveniently parameterize the acoustic phenomenon: the advance ratio, the thrust coefficient, and the angle of attack (AOA) of the tip-path plane (TPP), or TPP-AOA. The first represents the ratio of vehicle translation airspeed on MR rotational speed, the second the MR disk loading, and the third the relative orientation of the MR disk with respect to the vehicle airspeed vector [6].

While the advance ratio is estimated from airspeed and MR speed, effortlessly retrieved from the avionic data bus, the thrust coefficient and even more the TPP-AOA may not be estimated as easily, since a direct measurement of the thrust and of the rotor disc attitude are not normally available on typical production helicopters. In particular, the TPP-AOA can be seen as the result of two relative rotations, one being the orientation of the vehicle with respect to the airspeed vector and the other the orientation of the TPP with respect to the vehicle.

The former may be measured in principle by angle of attack and sideslip vanes placed on an air data boom, but this is not a common equipment on rotorcraft, and may suffer from significant inaccuracy due to the complex aerodynamic field generated by the MR wake and its interaction with the fuselage. For the latter, a measurement of the MR cyclic flapping is needed. Experimental devices are sometimes used by helicopter manufacturer to collect a direct measurement of the blade motion, typically expressed by the three angles of lead-lag, flap and pitch (an example is LH's Movpal system [7]). Although these sensing devices are available, their exploitation is not sufficient for the TPP-AOA estimation, as they only can support the estimation of the TPP angle of incidence with respect to the fuselage. Therefore, an observation method has been developed to take advantage of cyclic flapping measurements to derive an estimation of the thrust coefficient and TPP-AOA, based on an procedure that identifies the coefficient of a linear, airspeed-scheduled model [8,9].

The real-time blade motion parameters can be retrieved through a blade motion sensor such as those cited above. However, these contact-based sensors are prone to significant mechanical fatigue and may be integrated on board production helicopters with some difficulty. Hence, a brand-new rotor state measurement system based on contactless technology was designed and implemented [10,11].

In addition to noise estimation, the availability on board of a direct measurement of the MR blade motion can be beneficial to further applications, including FCS (Flight Control System) augmentation. For this reason, within the MANOEUVRES project, a study was conducted in which measured values of the blade angles are also feeding a Rotor State Feedback control system, to be integrated within the Stability and Control Augmentation System (SCAS), in order to enhance overall rotorcraft handling qualities [12,13].

The white boxes represent rotorcraft system components, i.e. the SCAS and the pilot, both receiving information from the MANOEUVRES noise estimation and indication system, and the avionic bus, which provides the input data contained in the cyan box. Within the orange contour, the preparatory activities carried out to develop the new rotor state measurement system are indicated, while the acoustic studies that led to the production and assessment of the noise emission database appear within the blue contour [14,15].

In the following sections, the main outcomes of the MANOEUVRES project are concisely presented, before drawing concluding remarks and indications for future work.

3 NOISE INDICATIONS TO THE PILOT

The PAI has been designed in order to derive emitted noise information and convey it to the rotorcraft pilot in a convenient fashion. It has been conceived as a practical tool, to monitor acoustic performance and help the steering of the vehicle, for example when tracking a low-noise procedure, such a steep approach, or in the case of flying at low altitude close to noise-sensitive areas.

For this reason, the value of a suitable noise index is displayed on a MFD (Multi-Function Display) according to different operational modes, resulting from the combination of two alternative computations and two alternative visualizations. In fact, the computation of the noise index can be performed in "Emitted mode" or in "Ground mode". The "Emitted mode" computation is based on the processing the SPL values distributed on the noise hemisphere (SPLH) of interest, while the "Ground mode" computation relies on processing the SPL values radiated from the hemisphere to the terrain below the rotorcraft. In the latter case, a simplified radiation model is employed to determine the acoustic footprint on the ideal flat ground, by retrieving additional information from the avionic bus, such as vehicle attitude angles and radar altitude. Figure 3 illustrates the conceptual PAI flowchart.

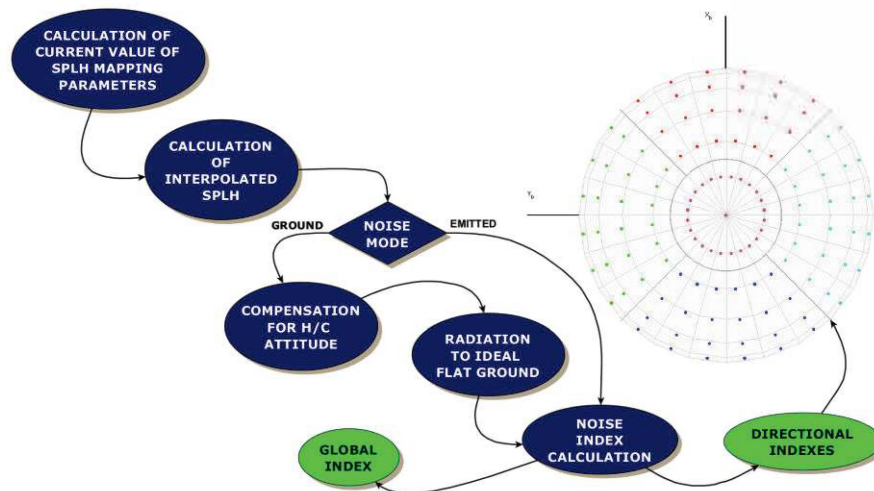


Figure 3: PAI algorithm flowchart

The noise index is then presented through the “Global indicator” or the “Directional indicator”. The “Global indicator” shows the value of the current noise index and the predicted value within a near-future time window (a few seconds, adjustable by the pilot), computed by taking into account the whole SPL distribution, either on the hemisphere or on the ground, depending on the active mode. The noise index values are arranged within an articulated, but intuitive visualization in which applicable noise thresholds can be seen, as well as predetermined suggestions to steer the vehicle in order to avoid increasing the noise impact. The “Directional indicator” displays five values at a time, corresponding to the noise index, each one calculated from the SPL distribution within one of the four coordinate sectors (front, left, rear, right), plus the bottom spherical cap (lower sector). Figure 4 shows the appearance of the two presentations, with an explanations of the symbology employed.

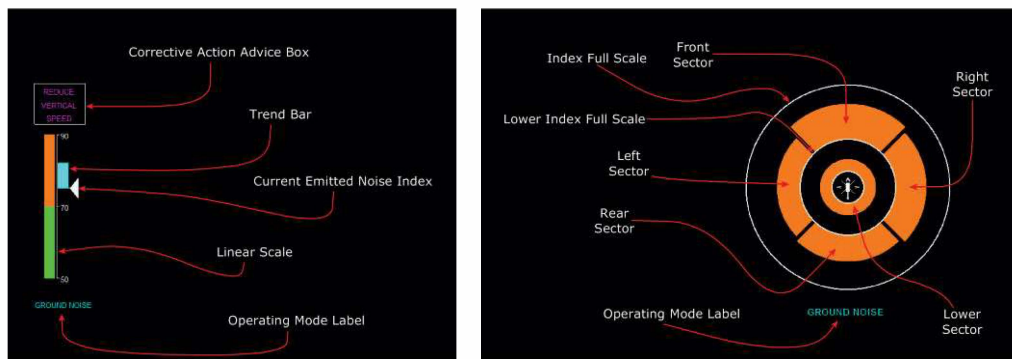


Figure 4: Global (left) and Directional (right) PAI presentations

The noise index is computed as the absolute maximum value of OASLP (Overall SPL) found in the region of interest. This means that first the current noise hemisphere is interpolated based on the current values of advance ratio, thrust coefficient, and TPP-AOA. Then, for “Emitted mode” operations, the maximum value within the full hemisphere (for the “Global Indicator” display) or the maxima within each of the five sub-regions of the hemisphere (for the “Directional Indicator” display) are considered. In the case of “Ground mode” operations, the noise distribution on the hemisphere is radiated to the ideal flat ground, taking into account the vehicle current attitude and altitude, and then the maximum value within the full footprint (for the “Global Indicator” display) or the maxima within each of the five sub-regions of the footprint (for the “Directional Indicator” display) are considered. The reader is referred to [3,4] for a detailed discussion of PAI design and implementation.

The database of OASPL hemispherical distributions is computed offline for a given helicopter with a sophisticated aeroacoustic steady-state prediction tool. As the database is queried through the instantaneous values of advance ratio, thrust coefficient, and TPP-AOA, a quasi-steady estimation is obtained, fit for real-time computations. The accuracy of this method has been assessed by

comparison with the application of a computationally cost-intensive fully-unsteady aeroacoustic prediction tool [14,15]. Results showed the good agreement between the two approaches and the advantage of the method using the measured instantaneous values of the three parameters with respect to a completely steady approximation.

The PAI was implemented as a stand-alone equipment, laboratory tested and then integrated within a LH research flight simulator. Simulated flights carried out by test pilots were performed, assessing the functionality and adequacy of the noise indication, collecting lessons learned and suggestions for further development and optimization. PAI final testing is discussed in [5].

4 OBSERVING THE TPP-AOA

The fundamental ingredient for the PAI noise estimation algorithm is the triad of values assumed by the database parameterizing quantities: advance ratio, thrust coefficient, and TPP-AOA. Once the former is given, from the avionic data bus, the two latter quantities are retrieved through an observation method. This allows to overcome the difficulties related to the unavailability of direct measurements for these two parameters. The method has been proposed in [8] and further refined and extended in [9].

The basic idea is to derive a linear model in which the observed quantities are computed as functions of an array of measurements. These are basic flight condition parameters (weight, air density) and MR blade attitude components (collective and cyclic flappings), complemented in [9] by the tail rotor (TR) control position, or TR collective pitch. The strongly nonlinear, inherent dependence on airspeed, or advance ratio, is taken into account by scheduling the models with respect to this variable. For the observer synthesis, the model coefficients are determined by an identification process, computing a number of maneuvers in such a way that the envelope of interest is well represented, spanning all relevant variables: weight, air density, airspeed, flight path angle, angle of sideslip. Figure 5 shows on the left the observation accuracy for the TPP-AOA obtained when using the method at 35 kn (black) and 45 kn (blue) airspeed, based on the identification performed at 30, 40 and 50 kn, ranging from 68% to 100% in weight and from 3 to 7 deg in descent angle. As seen, the errors are very limited, amounting to an average value of 1.91%. The corresponding performance for the thrust coefficient is even better, with an average error below 0.06%.

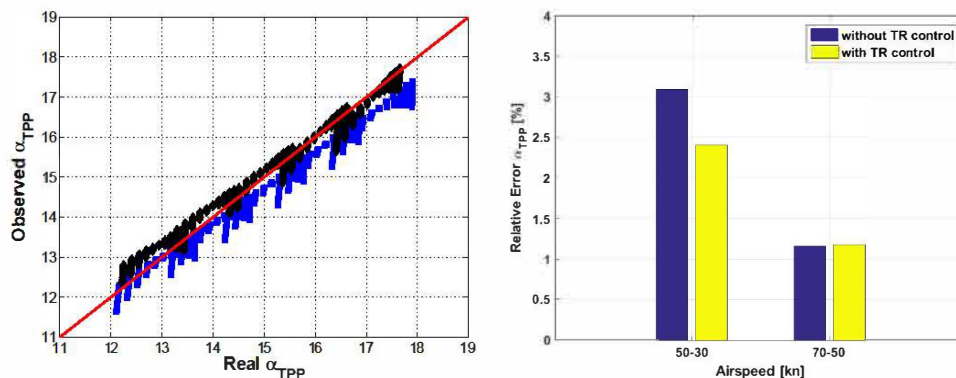


Figure 5: Observation accuracy for TPP-AOA

This approach has proven effective when applied to constant-speed descents in symmetric flight, in both design and off-design conditions, the latter involving non-symmetric flight and decelerations [8]. Further developments, recently published in [9], showed that the inclusion of the TR collective pitch allows to expand significantly the applicability of the approach to decelerated and non-symmetric flight conditions. Figure 5 shows on the right the average errors found when considering two off-design decelerated descents at a given weight, one between 50 and 30 kn, and the other between 70 and 50 kn. Comparing the initial model of [8] and the extended model of [9], the beneficial effect of including the TR pitch control among the measurements is apparent.

The extended model also allows retrieving also the angles of attack and sideslip of the fuselage among the observed set of variables. The knowledge of these quantities may be beneficial to other applications, beyond noise estimation, such as FCS-related functions.

5 CONTACTLESS ROTOR BLADE MEASUREMENTS

From the preceding discussion, it appears that a fundamental ingredient for the in-flight monitoring of emitted noise targeted in the MANOEUVRES project is the availability of real-time measurements of the MR blade angles, in particular the collective and cyclic flappings. Therefore, a highly-structured development path was conceived to design and implement a new vision-based rotor state measurement system capable of supporting the needs of the MANOEUVRES integrated system. This path started with a technology survey, passing through a preliminary selection that provided three candidate sensor systems, all based on the main rotor and pointing to a target placed on the top surface of the blade root: one based on a 2D laser, and two based on camera systems [16]. The latter were different in their measuring principle, as one featured a single camera and used a pose-estimation algorithm, while the other employed two cameras in a stereo arrangement. These candidate sensor systems were actually implemented in full scale, laboratory tested and assessed on the basis of measured performance. Figure 6 shows the mean errors obtained in a specific test case for the three systems, replicating in-flight measured time histories of the blade angles: on the left, the errors on the static components appear and, on the right, those on the cyclic components.

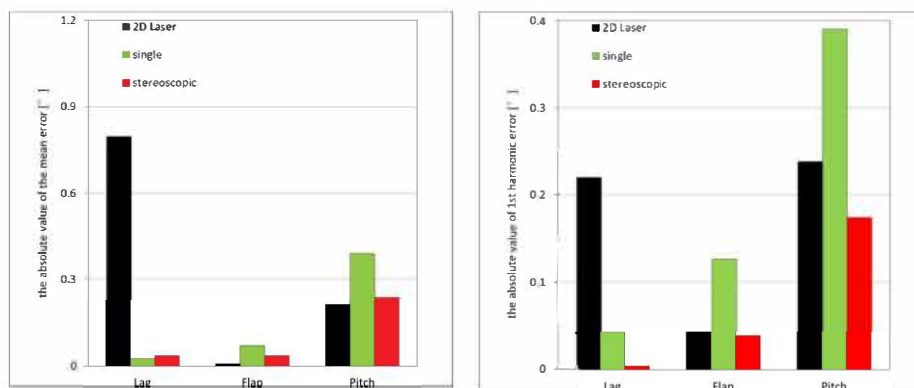


Figure 6: Measurement errors for the three candidate systems

Although all three fulfilled the design requirements, eventually, the stereo system achieved the best accuracy. The sensor part of this system is composed of a pair of smart cameras and a lighting device using LEDs, with an optical target glued to the blade root (Figure 7, left). Its performance is listed in Table 1 and is to be compared with the required accuracy considered in the MANOEUVRES project for the flapping measurement, 0.5 deg (mandatory) and 0.1 deg (desired). Furthermore, these figures show a significant improvement on a recent device based on an array of Anisotropic Magnetoresistive (AMR) presented in [17], which showed an accuracy of 1.0 deg in lag, 0.3 deg in flap, and over 1.0 deg in pitch during laboratory tests in much simplified conditions.

Table 1: Accuracy of the three candidate systems

Measurement system	Mean value error [deg]	Cyclic value error [deg]
2D laser	0.72	0.89
Single camera	0.15	0.35
Stereoscopic	0.15	0.09

The stereo system was chosen for the final phase of development [10,11]. This involved two main tasks. The first was the optimization of the system and the integration on the main rotor head of a AW139 helicopter. The system was installed on the MR experimental beanie provided by LH and thoroughly tested in order to fulfill the following requirements:

1. Optimize the system parameters and support subsystems (such as signal processing and transmission devices, synchronization, lighting, etc.).
2. Assess the installed system functionality and metrological performance.
3. Assess the structural performance and the overall safety of the installation.

The latter is clearly a fundamental prerequisite for the achievement of the permit to fly.

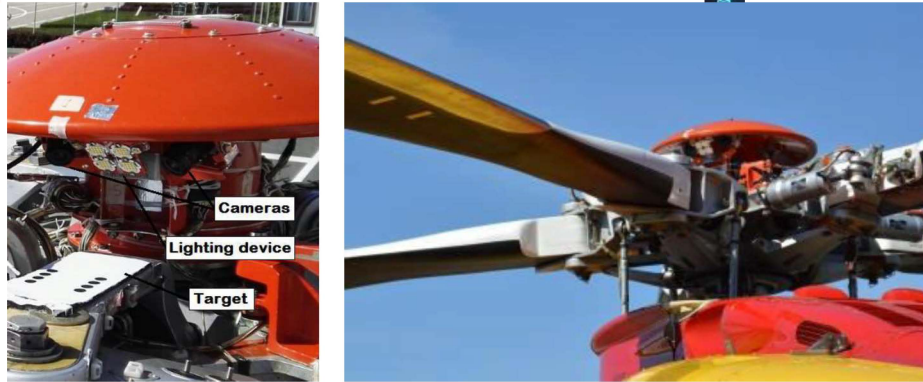


Figure 7: Measurement system installed on board a AW139

Indeed, the second task called for testing the rotor state measurement system on board a AW139 helicopter (Figure 7, right), involving overall more severe conditions with respect to rig testing. Initially, the project was intended to end with a ground demonstration only (TRL5), but given that the system performance exceeded expectations under many respects, an additional effort was made to perform a comprehensive flight test campaign, with 4 flights and over 3 hours of continuous system operations without any failure (TRL6). This was the first ever stereo camera system for blade attitude measurement to be flight tested to date.

The acquired data were processed and compared with those gathered through an independent, contact-based sensor system used for experimental activities at LH, the Movpal [7]. The analysis showed a very good agreement, except for an offset that may be attributed to the combination of a number of factors, including the on-board calibration procedure of both systems and modelling assumptions employed in the data processing of the contact-based system. The mean discrepancy between the two measuring systems was found to be 0.15 deg, 0.97 deg and 0.59 deg for lag, flap and pitch angles, respectively. The values of the 1/rev amplitudes (cyclic components) showed a maximum discrepancy of 0.55 deg.

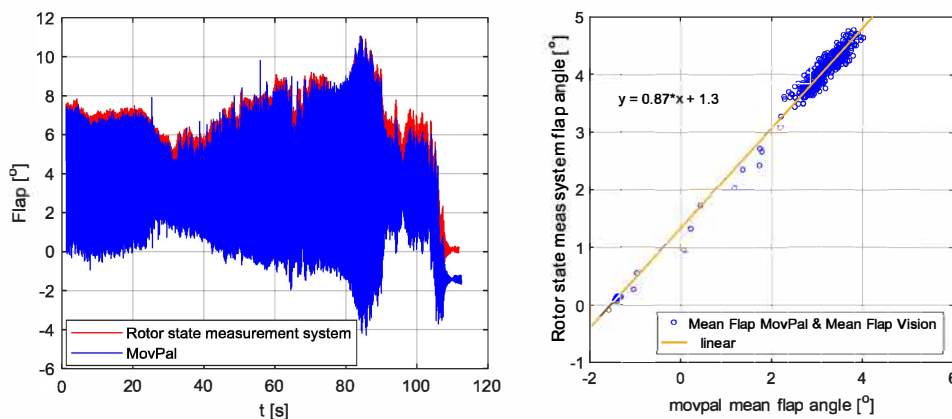


Figure 8: Flap angle in-flight measurements

Figure 8, on the left, depicts the time histories for the flap angle during one of the test flights: the contact-based system data are shown in blue, while the MANOEUVRES system data in red. The same figure, on the right, shows the correlation between the running averages of both data series. The test flight preparation and outcomes are discussed in detail in [18].

6 CONCLUSIONS AND FUTURE WORK

A significant effort has been made in developing and validating habilitating technologies and tools necessary to an integrated system aimed at providing a rotorcraft pilot with an accurate, reliable, real-time information of the external acoustic impact. The system conceived aims at a possible integration on board current and future production rotorcraft, going beyond a mere concept demonstration. The paper introduced the complex framework established within the MANOEUVRES project, which involves: noise index definition, computation and cockpit presentation; accurate offline

acoustic predictions; in-flight estimation of non-measurable quantities; and rotor blade motion measurements. The Pilot Acoustic Indicator, a new flight instrument providing noise information on a dedicated HMI in the cockpit, has been implemented and tested in a simulated environment. The new vision-based rotor state measurement system was implemented and tested, first in a laboratory setting, and then in flight on board a helicopter. The general results of this activities are considered very successful and worth further developments.

Indeed, many lessons have been learnt in the process and further ideas emerged, in an attempt to achieve the maximum effectiveness of the proposed framework. A first possible activity exploiting the PAI may focus on pilot training on acoustic impact. This aims to make the pilot aware of the noise emission, in relation to the specific flight conditions and maneuver strategies. The PAI may be used in its current state of development, or enhanced by integrating a presentation of the ground acoustic footprint on a map of the overflown terrain, completed with noise-sensitive area markings. This would allow the pilot familiarization on the acoustic effects of its actions in a simulated flight environment, and may lead to the drafting of a training protocol to drill pilots in low-noise steering.

The same outfit may be used for the assessment of low-noise procedures through simulated flight test campaigns. This would contribute to the design and optimization of these highly-desired procedures, shrinking the costs of validation to a minimal fraction of what is currently needed, which involves flying the aircraft on an ground area instrumented with a number of microphones.

Concerning the rotor state measurement system, the equipment developed within the MANOEUVRES project is characterized by a high degree of reliability and portability on different rotor systems. An industrialized version for experimental activities (relying on an experimental MR slipring) may be easily obtained through limited interventions on the target, the lighting device, and/or the signal electronics. Furthermore, a stand-alone solution (not relying on an experimental MR slipring or other FTI items) fit for standard production helicopters may be derived by powering the system with suitable batteries placed on the rotor head and storing acquired data on a local mass memory, so that the whole measurement system would stay on the rotating subsystem and would not interact with the fuselage in any way. This solution would allow, in addition to noise-related applications, the gathering of a very significant amount of data for health and usage monitoring activities, with possible impacts on flight safety, as well as on operating costs.

An enhanced version of the rotor state measurement system may also make use of strain gauges placed along the monitored blade, in an arrangement that may provide shape sensing [19] along with blade rigid motion, for a full characterization of the blade dynamic response.

Finally, further optimization and validation of the TPP-AOA observation methodology may constitute a promising first step towards the design and implementation of a specific equipment, conceived to be integrated within the on-board avionics. The observation system may then be assessed through simulated flight tests and, upon reach of an adequate maturity, installed on board and thoroughly flight tested. This would allow to reach the complete goals of the MANOEUVRES project by completing the integration with the rotor state measurement system and the PAI, allowing the final flight testing of the integrated noise monitoring equipment. Also, the observer may be used in new FCS-related applications, exploiting its ability to estimate the TPP-AOA and also the fuselage angles of attack and sideslip with remarkable accuracy.

REFERENCES

1. Trainelli L., Cordisco P., Gennaretti M., Grassetti R., Lovera M., Redaelli M., Rolando A., Zappa E.; 2016; "Innovative Rotor-State Measurements Enabling Helicopter In-Flight Noise Monitoring and Enhanced Attitude Control"; *American Helicopter Society International 72nd Annual Forum*; West Palm Beach, USA; May 17-19; 1-7.
2. Trainelli L., Gennaretti M., Zappa E., Lovera M., Rolando A., Cordisco P., Grassetti R., Redaelli M.; 2016; "Development and Testing of Innovative Solutions for Helicopter In-flight Noise Monitoring and Enhanced Control Based on Rotor State Measurements"; *42nd European Rotorcraft Forum (ERF 2016)*; Lille, France; September 5-8; 1-10.
3. Trainelli L., Gennaretti M., Bernardini G., Rolando A., Riboldi C. E. D., Redaelli M., Riviello L.; 2016; "Innovative Helicopter In-Flight Noise Monitoring Enabled by Rotor State Measurements"; *Noise Mapping*, **3**; (1); 190-215.

4. Rolando A., Rossi F., Riboldi C. E. D., Trainelli L., Grassetti R., Leonello D., Redaelli M.; 2015; "The Pilot Acoustic Indicator: A Novel Cockpit Instrument for the Greener Helicopter Pilot"; *41st European Rotorcraft Forum (ERF 2015)*; Munich, Germany; September 1-4; 1-14.
5. Rolando A., Rossi F., Trainelli L., Leonello D., Maisano G., Redaelli M.; 2016; "Demonstration and Testing of the Pilot Acoustic Indicator on a Helicopter Flight Simulator"; *42nd European Rotorcraft Forum (ERF 2016)*; Lille, France; September 5-8; 1-8.
6. Gennaretti M., Serafini J., Bernardini G., Castorrini A., De Matteis G., Avanzini G.; 2016; "Numerical Characterization of Helicopter Noise Hemispheres"; *Aerospace Science and Technology*, **52**; 18–28.
7. Colombo A., Locatelli A.; 2004; "Measuring blade angular motions: A kinematical approach"; *30th European Rotorcraft Forum (ERF 2004)*; Marseilles, France; September 14-16; 1-10.
8. Trainelli L., Riboldi C. E. D., Bucari M.; 2015; "Observing the Angle of Attack of the Tip Path Plane from Rotor Blade Measurements"; *41st European Rotorcraft Forum (ERF 2015)*; Munich, Germany; September 1-4; 1-14.
9. Trainelli L., Riboldi C. E. D., Salucci F.; 2017; "Developing an Observation Methodology for Non-Measurable Rotorcraft States"; *43rd European Rotorcraft Forum (ERF 2017)*; Milano, Italy; September 12-15; 1-10.
10. Cigada A., Colombo A., Cordisco P., Ferrario A., Grassetti R., Manzoni S., Redaelli M., Rolando A., Terraneo M., Trainelli L., Vigoni E., Zappa E.; "Contactless Rotor Flapping Sensor Design, Implementation and Testing"; *American Helicopter Society International 72nd Annual Forum*; West Palm Beach, USA; May 17-19; 1-11.
11. Zappa E., Trainelli L., Cordisco P., Vigoni E., Rolando A., Redaelli M., Rossi F., Liu R.; 2016; "A Novel Contactless Sensor for Helicopter Blade Motion In-flight Measurements"; *42nd European Rotorcraft Forum (ERF 2016)*; Lille, France; September 5-8; 1-14.
12. Panza S., Lovera M.; 2015; "Rotor state feedback in the design of rotorcraft attitude control laws"; Bordeneuve-Guibé J., Drouin A., Roos C.; *Advances in Aerospace Guidance, Navigation and Control*; Springer; Berlin.
13. Panza S., Lovera M., Bergamasco M., Viganò L.; 2015; "Rotor State Feedback in Rotorcraft Attitude Control"; *41st European Rotorcraft Forum (ERF 2015)*; Munich, Germany; September 1-4; 1-14.
14. Gennaretti M., Bernardini G., Serafini J., Trainelli L., Rolando A., Scandroglio A., Riviello L., Paolone E.; 2015; "Acoustic Prediction of Helicopter Unsteady Manoeuvres"; *41st European Rotorcraft Forum (ERF 2015)*; Munich, Germany; September 1-4; 1-12.
15. Gennaretti M., Bernardini G., Hartjes S., Scandroglio A., Riviello L., Paolone E.; 2016; "Experimental/Numerical Acoustic Correlation of Helicopter Unsteady Manoeuvres"; *42nd European Rotorcraft Forum (ERF 2016)*; Lille, France; September 5-8; 1-12.
16. Zappa E., Liu R., Trainelli L., Ferrario A., Cordisco P., Terraneo M., Grassetti R., Redaelli M.; currently under review; "Laser and vision-based measurements of helicopter blade angles".
17. Schank T. C., Schulte K. J.; 2015; "A Smart Position Sensor for Articulated Rotors"; *American Helicopter Society International 71st Annual Forum*; Virginia Beach, USA; May 5-7; 1-10.
18. Redaelli M., Zappa E., Liu R., Trainelli L., Rolando A., Rossi F., Cordisco P.; 2017; "In-Flight Demonstration of a Novel Contactless Sensor for Helicopter Blade Motion Measurement"; *28th Annual Society of Flight Test Engineers European Chapter Symposium*; Milano, Italy; September 13-15; 1-13.
19. Bernardini G., Porcelli R., Serafini J., Masarati P.; 2017; "Shape Sensing and Structural Health Monitoring of Rotor Blades from Strain Analysis"; *American Helicopter Society International 73rd Annual Forum*; Fort Worth, USA; May 9-11; 1-10.

Preliminary Weight Sizing of Light Pure-Electric and Hybrid-Electric Aircraft

Carlo E.D. Riboldi

*Department of Aerospace Science and Technology, Politecnico di Milano
Assistant Professor
Via G. La Masa 34 – 20156 Milano, Italy
carlo.riboldi@polimi.it*

Federico Gualdoni

*Department of Aerospace Science and Technology, Politecnico di Milano
Research Assistant*

Lorenzo Trainelli

*Department of Aerospace Science and Technology, Politecnico di Milano
Associate Professor*

ABSTRACT

The lack of consolidated preliminary design techniques coping with the characteristics of most recent electric and hybrid-electric power plants is often an obstacle for aircraft manufacturers and for owners and operators as well, making the design process less straightforward and hampering comparisons with respect to more traditional designs. In this paper, a technique for the preliminary weight sizing of electric aircraft in the General Aviation category is explained. This is based on existing procedures typical to conventionally-powered aircraft, integrated in a common framework to suitably tackle the issues raised by the peculiar features of electrically-powered aircraft. Then, an expansion of the design method to the case of a series hybrid propulsion system is investigated. Results in virtual environment on a realistic design are also presented.

KEYWORDS: *electric propulsion; hybrid propulsion; aircraft design procedure; preliminary weight sizing*

On the Theoretical and Experimental Activities Performed by Professor Hermann Oberth in Romania

Nicolae Florin ZĂGĂNESCU
Prof. Dr. IAA Member
Romania
zaganescurf@upcmail.ro

Constantin Marcian GHEORGHE
M. Sc. aircraft & propulsion systems
Romania
costinmarcian2@yahoo.co.uk

ABSTRACT

Finishing studies at Heidelberg University, Hermann Oberth (b. June 25th, 1894 at Sibiu, Romania) returned in Romania and successfully sustained in 1923, at the Cluj University, his thesis: "The Rocket to the Interplanetary Spaces" (published in Munich, also in 1923). Until 1938, Oberth was mathematics and physics professor at a high school in Mediaş, Romania. In this period he developed his first book into the much larger "Ways to Spaceflight" (published in 1929, also in Munich); building and testing solid and liquid fuelled rocket engines, and designing an original launching system. On June 23rd 1930, Oberth tested his first liquid fuelled (gasoline and liquid oxygen) rocket engine in Germany, achieving 70 N thrust and 756 m/s jet speed. After this test, Oberth returned to Mediaş where he tested the principle of electrostatic rocket engine, using the high school's electrical workshop. Also in Mediaş, in the workshops of Romanian Air Force Superior Military School, he built and tested fuel pumps, combustion chambers and nozzles. Oberth received the Romanian Patent No.19516 of March 6th 1931, for „Process and Apparatus for quick combustion”. In the same period, he discovered the phenomenon that scientist Esnault-Pelterie will later call: „The Oberth Effect”. In 1935, Hermann Oberth performed in Mediaş a real liquid fuelled rocket launching: in a letter to Willy Ley in December 24th 1948, Oberth wrote: "...I really raised my first liquid fuelled rocket in 1935..." Many of his achievements were conceived during the years when he lived and worked in Romania. As he said in an interview: "[...] during that time I was able not only to elaborate the space technique theory, but also made the most significant discoveries and experiments which confirmed that I was on the right way"[1].

KEYWORDS: *spaceflight, theory, liquid, fuel, rocket*

1 FROM DREAMS TO SCIENTIFIC, GROUND-BREAKING THEORY

As a child in Sibiu and also in Sighişoara, Hermann Oberth was always interested in flight and especially in space flight: at the age of fifteen he sketched a spacecraft model propelled by successive explosions of powder, while at sixteen he imagined a rocket model, using as liquid propellants a combination of an alcohol and liquefied oxygen [1]. During his high school studies, Oberth imagined a centrifugal device with a 35m long arm, very much resembling to the centrifuges used today for astronauts training. After 1919, Oberth designed one of his first models of a multistage spacecraft. In February 1919 he started his studies at the University of Cluj-Napoca, the department of mathematics-physics of the Second Faculty of Philosophy. After the first six months, he continued his studies in München, Göttingen and Heidelberg. In order to obtain his Ph.D. from Heidelberg University, Oberth presented in 1922 a scientific work with the title: "Die Rakete zu den Planetenräumen (The Rocket to the Interplanetary Spaces)" in which he detailed the spaceflight theory: the optimal speed value allowing precise computation of the fuel burning time; the weights ratio; the accelerations and the climbing time; the equation connecting the reactive nozzle and the discharge speed of the jet; the analysis of the free extra-atmospheric flight equations; some selection criteria for optimal fuel in various space missions. In order to assure the spaceship stability and

precise direction control in flight, Oberth imagined the application of a gyroscope; for speed control and regulation of the active part of the trajectory, he elaborated electrical and remotely operated devices. Also he calculated and designed in detail two types of liquid fuelled rockets: the first designed for high-atmospheric research (Model B) and the second for space flight. The paper was rejected with the motivation to have a technical and not astronomical character.

Finally, the paper was printed in 1923 by Oldenbourg Verlag P.H. in München, with the same title (*Die Rakete zu den Planetenräumen*). In this book (issued again in 1925, 1960 and 1964) Oberth scientifically proves the foundations of modern astronautics, as follows [2], [3]:

- the rocket theory mathematical bases;
- using ethylic alcohol and hydrocarbons with liquid oxygen as liquid fuels for rockets;
- the staged rocket functional principles;
- the fundamentals for some optimal ascent trajectories and for six synergetic curves;
- the use of an orbiting station for spacecraft refuelling;
- the future manned space stations with artificial gravity;
- an astronaut training program and some radiation protection systems;
- the mathematical study of rocket behaviour, both in the atmosphere and in the outer space;
- the Earth artificial satellites and research rockets utilization fields.

Finishing his studies and preparations, Oberth returned home in Romania and, in order to be appointed school master, presented to the Special Commission for School Masters Examination the paper rejected at Heidelberg. The Chairman of the Commission, Professor Augustin Maior (inventor of a multiplex telephone communications system) appreciated the paper, accepted it and conferred him the title of "Profesor Secundar" (School Master). Thus Oberth was employed at the High School and at the "Bergschule" (The "Hill School") in Sighişoara, until 1924 when he leaved for Mediaş. From 1924 to 1938, Oberth was employed in Mediaş as School Master for Mathematics and Physics at the "Stephen Ludwig Roth" high school. From Sighişoara he wrote letters to K.E. Tziolkovski, Max Valier, Frantz von Hoefft, Walter Hohmann, G.A. Crocco, Guido von Pirquet, Johannes Winkler, Robert Esnault-Pelterie and others.

In 1923, Oberth received from Robert Hutchins Goddard his report "A Method of Reaching Extreme Altitudes" published by Smithsonian Institute and starts a brief correspondence with K.E. Tziolkovski, who will send him his book "Research of Outer Space with Reactive Devices" ('*Issledovanie mirovih prostranstvy reaktivnimi priborami*' - 1903).

2 EXPERIMENTAL CONFIRMATION OF LIQUID FUEL ROCKET PROJECT

Since 1925 Hermann Oberth looked his paper over and prepared a new one, which will be printed in 1929 by Oldenbourg P.H. with the title "*Wege zur Raumschiffahrt (Ways to Spaceflight)*" [4]. Oberth presented in this paper some rocket engines he imagined and studied, showing their functioning with the theoretical and practical explanations of reaction principles and thrust generation by the rocket-engines. The publication of calculations and projects for two-stage rockets was very important: a rocket-engine using as fuel liquefied hydrogen was the second stage and an alcohol rocket-engine was the first stage. Figure No.1 shows a drawing from the up mentioned book, illustrating this concept which became classic for modern rockets. Figure No.2 shows the "Model B" rocket, from the same book [5]. The red coloured lines (or gray, in a black/white printing) of the two figures represent elements of the hydrogen-fuelled rocket; the black lines are elements of the alcohol-fuelled rocket.

Both figures use the following notations: **a** – ogive-shaped head of hydrogen (or alcohol) fuelled rocket; **f** – parachute; **I** – equipment compartment; **T** – access to **I**; **e** – hydrogen (or alcohol) tanks; **S** – oxygen tanks; **p** – periscopes; **m**, **n** – pumps for heating gases; **p₁**, **p₂** – pumping chambers for fuel; **p₃**, **p₄** – pumping chambers for oxygen; **z** – atomizer; **o** – burners; **l** – adjusting pins; **t** – nozzles wall; **v** – flow on the nozzles wall and the flow control equipment; **w** – tail planes.

The drawings show original technical ideas, such as the following:

- The ogive-shaped segments, protecting the upper part of the rocket, were equipped (for recovery) with inside air tanks;
- The pressure in the alcohol-water mixture tank (c) was kept constant with pumps assistance;
- The alternation of the (y) valves opening and closing, ensures an uninterrupted flow from the tank (e) to the (p1) and (p2) chambers, while the other chamber pump is introducing the mixture in the (z) atomizer;

- The thermal protection of the rocket skin and combustion chamber is realised by fuel's vaporisation between the thin wall (t) and the skin;
- The rocket was provided with automatic controlled tail planes ensuring flight stability, as well the spacecraft deceleration in the descending flight period;
- The alcohol rocket was to be equipped with electric power source, supersonic stabilisation equipment, accelerometers, pressure gauges, temperature sensors etc;
- The stabilisation and flight control tail planes were operating by deflection of reactive jet, this principle being also used in modern missiles design [5];
- For the Model B, the project provided the use of an alcohol engine booster rocket, having a total weight of 20 kg.

Oberth was not only a visionary; he always was a scientist, researcher and experimenter. He stated once in a conference: "Sure, to build a great rocket will put tremendous technical difficulties. But I'm dealing with these problems since 17 years ago and I never found anything that would make them impossible or, at least, to put the problem in such a way" [6].

As a scientific counsellor at UFA German film Company for the movie "A woman on the Moon", Oberth succeeded on June 23rd 1930 to test his liquid fuelled combustion chamber: in 1.5 minutes the rocket burned 1 kg of gasoline with 6.6 kg of liquid oxygen, achieving a 70 Newton continuous thrust and reaching a jet speed of 756 m/s. By this achievement, his scientific calculus and technical project on the liquid fuelled rocket engine got a brilliant confirmation.

After performing this successful test in front of the specialists from the "Chemisch Technische Reichsanstalt" (Chemical-Technical Institute of the Reich) in Berlin, Oberth returned to his job in Mediaş, the nice and quiet town on the Târnava River, in Romania.

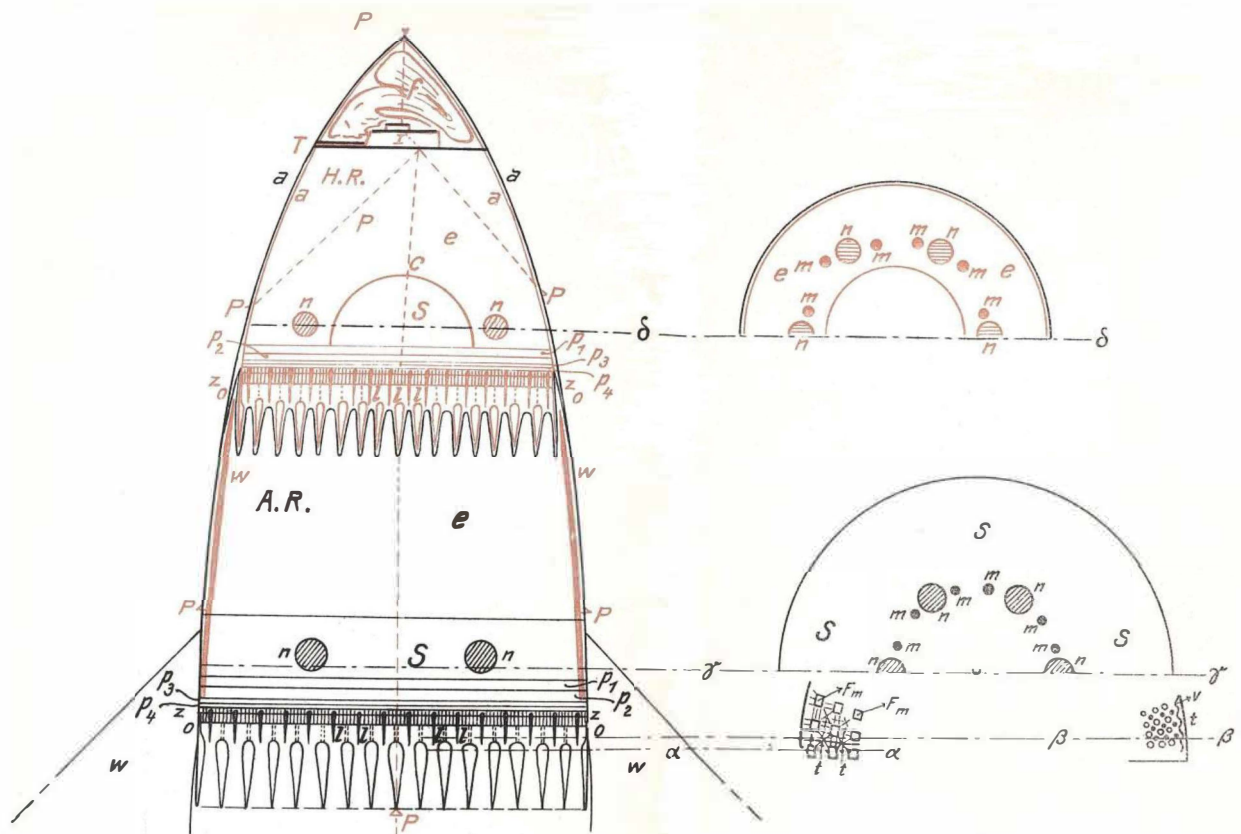


Figure 1: Hydrogen/oxygen (2nd stage) and alcohol/oxygen (1st stage) rockets

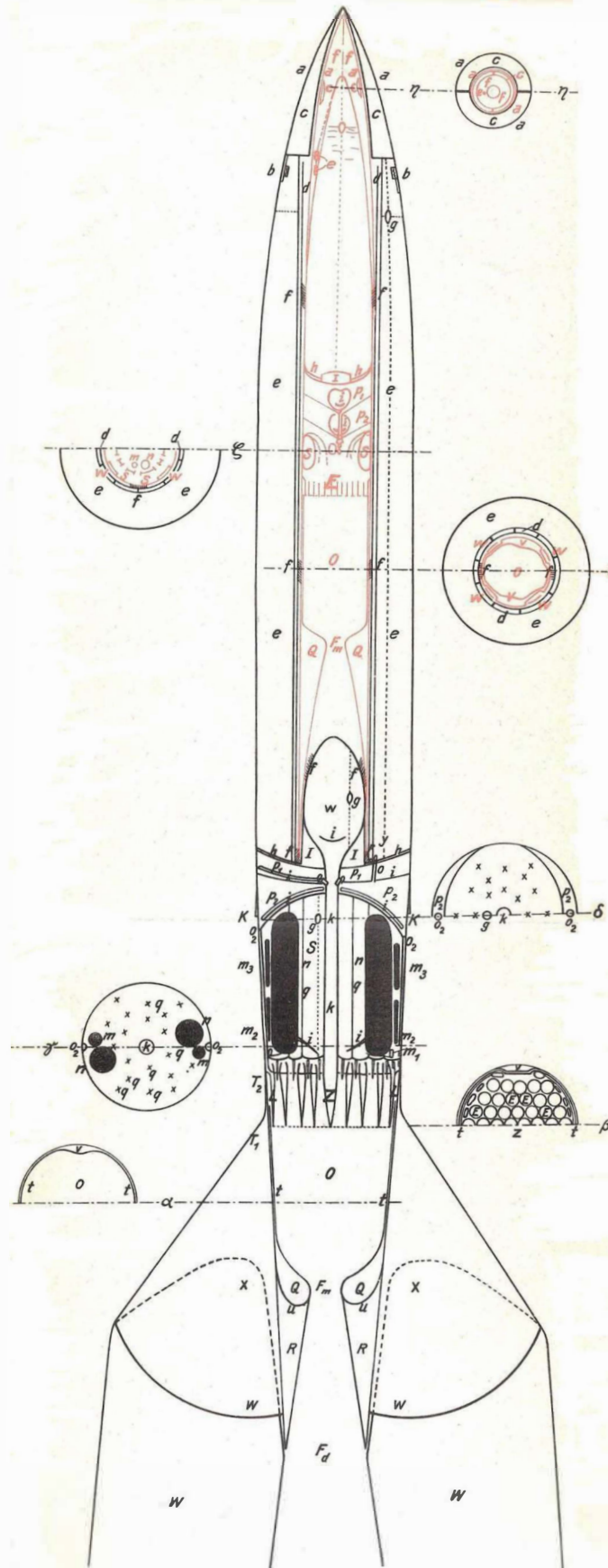


Figure 2: "Model B" rocket design



3 EXPERIMENTS IN MEDIAS – ROMANIA

Following a paper presented on a meeting at the Polytechnic School in Bucharest, Oberth returned to his studies on the combustion chamber of the rocket-engine with liquid propergols. For the first stage of the rocket, Oberth observed the necessity to use fuels with high specific weight and low ejection jet speed, different from the case of superior stages. The lack of high temperature resisting materials (as today's super-alloys or Titan alloys) put him very difficult problems in choosing the propergols and the combustion time too. As a device for controlling and regulating the reactive jet's speed, he proposed and tested the employment of a combustible mixture including a substance which doesn't participate in the burning process but through its evaporation absorbs heat. That is the basis of the phenomenon called by Robert Esnault Pelterie "The Oberth Effect".

Concerning the problem of propergols, at 9th March, 1931 Oberth presented and obtained from the Romanian Patent Office, the Patent No. 19510, entitled: "Process and Apparatus for quick Combustion"; here he claimed priority for a fast burning of fuels not containing oxygen (as do the explosive materials) a process characterized by injection of fuel in liquid oxygen or, vice versa, by injection of oxygen in liquid fuel [7], [8].

It is interesting to look at some of the great scientist's ideas, written in the patent request: "In different situations, especially in generating propulsion gases for rockets, it's important to realize the quick burning of big quantities of fuel in a restricted space. If the combustion is requested to be as fast as an explosion, then the explosive materials have great disadvantages, because they are dangerous and the speed of their combustion might not be calculated. It's more favourable to use fuels for which the necessary oxygen is delivered in the moment of combustion. This idea is already known, but it was not applied in such a way that a high combustion speed could be achieved or even to reach the nature of an explosion. This is realized by the present invention..." Further, Oberth is writing: "...That regards essentially the fact that the two materials involved in combustion, the oxygen and the fuel are mixed by spraying in such a way that the liquid oxygen particles are penetrating in liquid fuel, or fuel particles are penetrating in oxygen. The author established by experiment that the combustion taking place in these conditions has the speed of an explosion; he also established that in these conditions a preliminary chemical combination of oxygen and fuel is no more necessary, as it happens with a common explosive material. Also, it is not even necessary a reciprocal absorption capacity through dissolution or similar" [7].

In an article published in the Romanian scientific review *Natura* on the 15th December 1932, under the title "Zborul rachetelor și zborul în vid (Rocket flight and flight in vacuum)" Professor Oberth stated: "We are not willing to accept the limits of the Earth atmosphere as the limits of our existence!" In this article Oberth wrote:

"...My researches show that the rocket capacity could be larger by employing liquid fuels such gasoline, alcohol or cryogenic liquefied gases. Liquefied air has the power to increase enormously the combustion. If, for instance, for the combustion in my rocket, gasoline and liquefied air are mixed in an established proportion, it results a fire powerful enough to lift by reaction at considerable altitudes a sufficiently big rocket. [...] The speed of such rockets might grow to 1 km/s or even more than the bullet speed; the rocket might be equipped with sensitive instruments, because that velocity would not be reached suddenly. Such a rocket might land by parachute and will never fail. Usual rockets are climbing vertically, but this might be so arranged that the rocket should not climb too high and instead would fly on some determined curves, for flying over established zones... These rockets could be equipped with photographic cameras; in comparison with a reconnaissance plane, they would have the advantage of an easier and cheaper construction. For example, all the raw materials for my little test rocket which I'm building in Medias, are now produced in the country. My targets are some rockets flying very high and extremely far [...] These rockets may be automatically controlled [...] Such a device for controlling meteorological rockets is ready. It was tested on the stand for some time (in Medias, a.n.) and if it will resist, we may rely on a precision of 1/10,000 of the trajectory [...] If such a vehicle will reach the velocity of 8 – 10 km/s, it will happen something amazing, it will... never land after the consumption of the fuel, it will continue to fly on an elliptical trajectory which would remove it from the Earth [...] Landing of the rocket transformed in a spaceship, could take place only tangential to the planets owing an atmosphere; in that case, the spaceship will cover a long way in the atmosphere and it would be braked, avoiding burning like a meteorite, by flying the suitable trajectory [...] and landing tangential to the Earth..." [5].



Professor Oberth designed in Romania, in Medias, two of the rockets he described in the article from *Natura* review and in the speech at Radio Bucharest. The first rocket was designed as a liquid propergol rocket carrying 3.5 tons over a distance of 1,000 km and having a weight of 100 tons and a length of 24 m at launch. The second rocket, also with liquid propergols, was radio guided and designed as a ballistic missile or an AA missile. The start of this rocket would be assisted by solid fuel rockets. Concerning this solid fuel, it probably resembled to the "black powder" including ammonium nitrate, potassium nitrate, charcoal and water. Oberth will try to re-evaluate this project in 1943 at the Research Center in Wittenberg on Elbe. But he really finished this study in the period 1950-1955, when he worked for the Italian Navy in the La Spezia Laboratories. The Diesel Medal, which was awarded to Oberth in 1954, was also related to the construction of the ammonium nitrate rocket. This idea germinated in the brain of this great scientist when he was still in Medias, in the period 1930-1935. During that period, professor Oberth was also in charge of students' workshop training at "Stephan Ludwig Roth" High School. This way, he got the possibility to realise mechanical and electrical parts, necessary for his experiments, during the locksmith and electro-technology training – including testing the electrostatic rocket engine principle in the electro-technology workshop.

In 1932 Hermann Oberth sustained several conferences at the Polytechnic Society in Bucharest; as a result he got the Government's approval to work in the workshops of the Air Force Superior Technical School in Medias.

Between the experiments made at the Air Force Superior Technical School, we notice the test of several liquid fuel pumps for rocket engines; the pumps were drive by a gas turbine and introduced the fuel in the combustion chamber. Oberth suggested that the turbine might be driven by the same fuel in order to avoid building supplementary fuel tanks in the rocket; he assembled his combustion chamber under the microscope. For his combustion experiments with the new assembly – combustion chamber and nozzle – Oberth transported liquefied air from Braşov City [9].

In 1935, in Medias - Romania, Oberth tested a liquid fuelled rocket, test regarded by different sources and by himself as a real launching.

A clear proof that one of professor Oberth liquid fuelled engine was built and tested in Medias, is the letter written from Feucht to Willy Ley, on December 24th 1948: "...After our separation (1930) I started to deeply learn the job of a locksmith, to get those dexterities which I missed; because I think that Ford was right when he said that nobody should invent something he isn't able to build himself. It seems that I was talented for this profession because since 1933, I took the responsibility of leading a didactic mechanical workshop, complementary to my job of School Master of mathematics and physics, which I practice again since 1931. Nearby I made experiments with rockets and in 1935 I really raised my first liquid fuelled rocket..." [9, vol.1, pg.151] This success is also mentioned in professor Oberth's technical report edited in Switzerland, 1948. Knowing that Oberth launched also several solid fuel rockets in Medias, this town in Romania can be regarded as one of the first places in the world which were witness of rocket launching, after Roswell (New Mexico, USA) Dessau and Berlin (Germany), Moscow (USSR).

Interesting technical details about the construction of the liquid fuelled rocket can be found in a previous letter, dated April 16th 1933, which Oberth sent from Medias to dipl.eng. Otto Wiemer in Essen [9]: "...Presently, I have at my disposal an experimental model, half finished, 1,400 mm long and with a maximum diameter of 142 mm. For liquefied air removal from the tank to the combustion chamber, I used gasoline and at least (one – a.n.) liquefied carbon dioxide capsule. This (the capsule, a.n.) has an ignition fuse protected with Cellon varnish against gasoline action. At starting the ignition was electrical, the fuse was burning and the access of gasoline to the oxygen tank was free. Gasoline was sprayed over a piece of calcium oxide (quicklime), soaked with liquefied air and burned, combustion being ignited electrically with an electric device... This rocket combustion chamber is brass canned and plated inside with Stamak kit; because of that, the combustion chamber is extremely heavy, though the stock left was totally rasp down. It has to be searched a company able to can the chamber with a light alloy..." In the same letter, Oberth informed about his new intentions: "Following this model, a 14-15 m long and 250 mm diameter rocket will be built; before the construction of the 15 m rocket, it's necessary to answer the following questions:

- Obtaining the pressure in the pumps; the experimental models worked without pumps;
- At the 15 m long rocket the fuel tank will be placed in the superior part and the oxygen tank, 10-12 m long, in the lower part; the oxygen pumps are also in the lower part. Because finally it will attain 10g, they must reach 10 atm in order to lift the oxygen at least in the ascent pipes;



- In order to preserve the gasoline pressure, I used the burning of ammonium nitrate powder in the tank; that's not a nice solution because of the impurity generation, but for the gasoline pump I would be pleased to introduce something else, let's say liquefied air, which I would spray in the burning fuel;
- Not circular, but spherical pumps will be necessary; I don't know if there will be any problems; in two-three months I may be able to send you projects for the pumps;
- I don't have any satisfactory metallic thermometer, but I would be interested to know how hot the combustion gases are, before exhausting from the engine;
- I would need some accessories very difficult to obtain here, as for instance, ignition conductors: I need insulators with a maximum external diameter of 1 mm. At the tested model I introduced (don't laugh) the wire through dried straw... I would need also a good material for welding of "Elektrometall", and so on;
- Definitive construction and testing of acceleration sensors and control devices." [9]

The letters he wrote to his scientist friends [6], [10] are relevant for Professor Oberth's prolific activity developed in Romania, and also for his well-known modesty. On February 21st 1933, Oberth wrote from Mediaș, also to Wiemer: "...Answering your letter of 15th current month, I let you know that I am continuing my experiments here, although (because of) the natural facilities absence, they are very much delayed... I will not work anymore in Germany. If you are going to realize in Essen an experiment facility, I am pleased to be at your disposal with my experiments already performed. It is easier to realize that because, in fact, I'm working only for the interest of the problem; the income interests me only for higher efficiency. Generally the building of a liquid fuel rocket must be easier the bigger the rocket is. For the moment, I'm not interested in a too big publicity. Maybe, at the end of this year, I will publish some of my experimental results. The early publicity doesn't help, it's more detrimental. The Spaceflight Association will not send my apparatus to the exhibition. I don't like to present after four years some devices built in the first half year of my practical activity". [9]

Oberth's essential contribution to the first rocket gliders development is clearly shown in a letter he sent to Guido von Pirquet: "...I let (Max) Valier to assume alone the inventor position of the rocket airplane, although we worked together at the development of this idea... Because he was not a specialist, I elaborated at his request the rocket-plane theory and showed him a calculation example..." [9] In spite of his modesty, these words clearly indicate that Professor Oberth anticipated the modern technologies of rockets and missiles.

4 A PRECIOUS LEGACY

Wernher Von Braun, who was a young (18 years) student when he begun experimental works with the professor, said about him:

"Hermann Oberth was the first, who when thinking about the possibility of spaceships grabbed a slide-rule and presented mathematically analysed concepts and designs [...] I, myself, owe to him not only the guiding-star of my life, but also my first contact with the theoretical and practical aspects of rocketry and space travel. A place of honour should be reserved in the history of science and technology for his ground-breaking contributions in the field of astronautics." [11]

Many of these contributions were conceived by Hermann Oberth during the years when he lived and worked in Romania. He was well aware of this fact and, during a 1982 Symposium, confirmed the remarks on this subject, made by Romanian astronaut Dumitru Prunariu [12].

Professor Hermann Oberth was kindly available to meet Romanian scientists and researchers, encouraging them to persevere in their work, as shown in a photo taken at the 34th International Astronautical Federation Congress in Budapest, in 1983, together with Romanian astronaut Dumitru Prunariu and the first author of this paper.



Figure 3: Prof. Hermann Oberth (3rd from left) with Romanian astronaut Dumitru Prunariu (4th from left) and prof. Florin Zăgănescu (1st from left)

One of the best certifications of Professor Hermann Oberth's activity in Romania was his own opinion, expressed in an interview offered to the Romanian Television (in 1977, for a biographical film):

"My friend and biographer Hans Barth declared that during the years spent here I realized already most of that what brought me a later celebrity. I have to admit that's just so; it's true that during that time I was able not only to elaborate the space technique theory, but also made the most significant discoveries and experiments which confirmed that I was on the right way" [1].

REFERENCES

1. Barth, H.; 1974; *Hermann Oberth – Titan der Weltraumfahrt (H. Oberth, Titan of Space Navigation)*, Kriterion P.H.; Bucharest.
2. Buedeler, W.; 1975; *Geschichte der Raumfahrt (History of Astronautics)*; Sigloch P.H., Salzburg.
3. Iacovachi, I.; 1967; "Hermann Oberth – Creatorul astronauticii (H. Oberth – Creator of Astronautics)"; *Revista transporturilor (Review of transports)*; **14**; (5).
4. Oberth, H.; 1929; *Wege zur Raumschiffahrt (Ways to Spaceflight)*; First edition; Oldenburg P.H., München.
5. Oberth, H.; 1932; "Zborul rachetelor și zborul în vid (Rockets flight and Flight in Vacuum)"; *Natura* review; No.10; December 15th 1932; Bucharest.
6. Oberth, H.; 1972; "Din opțiunile mele pentru navigația spațială (From my Options concerning Space Navigation)"; *lecture*; Romanian Academy; Bucharest.
7. Oberth, H.; 1931; "Procedeu și dispozitiv de combustie rapidă (Process and Apparatus for Quick Combustion)"; Romania; Patent No. 19,516 /March 6th 1931.
8. Zăgănescu, F.N.; 1984; "Some important aspects in the three hundred years old history of the Romanian aerospace techniques"; *The 18th Symposium on the History of Astronautics, XXV IAF Congress*; Lausanne; 08-13 October, 1984.
9. Barth, H.; 1979, 1984; *Hermann Oberth – Briefwechsel (H. Oberth - Correspondence)*; **1, 2**; Kriterion P.H.; Bucharest.
10. Gartman, H.; 1965; *L'Aventure Astronautique (The Adventure of Astronautics)*; France Empire P.H., Paris.
11. Von Braun, W.; "Foreword" to Oberth, H.; 1964; *The Rocket to the Interplanetary Spaces*; Fourth Edition; UNI-VERLAG Dr. E. Markstaller P.H., Nürnberg.
12. Prunariu, D.; 1994; „Cuvânt înainte (Foreword)” to Oberth, H.; 1994; *Racheta spre spațiile interplanetare (The Rocket to the Interplanetary Spaces)*; Romanian Edition; Translation in Romanian by prof.dr.ing. Hans Helmut Rehner; Hanns Seidel Foundation; Romania.

On the Contributions of Dr. Irene Sänger-Bredt in the Field of Astronautics

Constantin Marcian GHEORGHE
M. Sc. aircraft & propulsion systems
Romania
costinmarcian2@yahoo.co.uk

Nicolae Florin ZĂGĂNESCU
Prof. Dr. IAA Member
Romania
zaganescurf@upcmail.ro

ABSTRACT

Irene Sänger-Bredt (born in 1911 at Bonn) had remarkable contributions in space science and technology. In 1937, after obtaining a Doctorate in Physics, she became scientific researcher at the German Research Center for Rockets in Trauen, led by Prof. Dr. Eugen Sänger. She became the first assistant of Dr. Sänger, who married her after the war, in 1951. There are three main periods in the development of her career: The first one was as researcher at Trauen (1937–1942) where she was mainly in charge of thermodynamic problems of liquid-fuelled rocket engines and of friction problems related to the rocket-powered launching-sled. The second one was as senior researcher at Aining (1942–1945) where she was in charge of ramjet performances flight testing and also co-author of the cornerstone technical report "A Rocket Engine for a Long-Range Bomber". The third one was after the war, when she was scientific advisor or director in various civil and military research institutes and universities. Dr. Irene Sänger-Bredt worked together with Prof. Dr. Eugen Sänger to develop important theories, like ramjet thermodynamic theory and photon rocket theory, and also in establishing the International Astronautical Federation (IAF) and the International Academy of Astronautics (IAA). She worked with Prof. Dr. Eugen Sänger so efficiently integrated, that tracing a clear limit between their individual contributions to the ground-breaking achievements they made together remains a difficult endeavour. To this day, many important achievements of space science and technology, like the space plane and its regenerative cooling engine design, are still referred to as "Sänger-Bredt design".

KEYWORDS: *hypersonic, plane, ramjet, photonic, rocket*

1 A SCIENTIFIC EDUCATION

At the beginning of the 20th Century, many books and magazines continued the science fiction visions of Jules Verne regarding space travel. On the other hand, women performances were becoming more and more remarkable in all domains of activity, especially after the First World War, when they made impressive and substantial contributions, in all nations involved.

Irene Reinhild Agnes Elisabeth BREDT, born on April 12th 1911 in Renania, was one of these brilliant women who demonstrated that they can perform in sciences at least as high as men do. She graduated from high school in Köln and studied at the Universities of Köln, Freiburg and Bonn.

Köln was also the place where she could see a piece of real-life rocketry: one of the experimental cars of Fritz von Opel, „Opel-Rak 1“ equipped with 12 rockets, which reached a record speed of 100km/h in 8 seconds on April 12th 1928. She looked for a book on this subject, and she only found one about rockets for fireworks, but that was nevertheless a trigger to study rocketry. Another trigger was watching the movie „A woman on the Moon“, for which Prof. Hermann OBERTH contributed as scientific adviser of Berlin UFA Studios [1]. However, during studies at the Universities of Köln, Freiburg and Bonn, Irene was focused on another domain: "The Roentgen Spectra of Rare Earths", which will be the subject of her PhD thesis, sustained in 1937. The same year, rocketry came back into her attention when she received a job from the Research Center for Aviation in Trauen, which conducted rocket propulsion researches, although not recognising it officially. Before going there, she had been warned that: "...Possibly, it would be a matter of rockets" but that was, in fact, good news

for her. She was determined to obtain the job and even told the interview commission: "...but I know what you are doing here - rockets!" After examination, she got the job and soon became the best assistant of Dr. Eugen Sänger - the head of the Center [2].



Figure 1: Dr. Irene Bredt and Dr. Eugen Sänger

Her knowledge and skills were more than welcomed in the complex, interdisciplinary domain of rockets, and the way she worked with Dr. Sänger was so efficiently integrated, that tracing a clear limit between their individual contributions to the ground-breaking achievements they made together remains a difficult endeavour, to this day.

2 "SILVER BIRD" - THE GRANDFATHER OF SPACE SHUTTLE

In a 1951 speech, Prof. Dr. Eugen Sänger pointed out the difficulties awaiting space exploration development in the future, if mankind would "stubbornly" use only solutions based on rockets and capsules [3]. Thirty years later, the Space Shuttle brilliantly proved his point and – in spite of two tragic events that marked the programme – led the way to other projects, like "Buran", "Sanger", "Hermes", "HOTOL", all aiming to develop the space planes flotilla of the future.

A contract signed in February 1st 1936 with „Deutsche Versuchsanstalt für Luftfahrt – DVL (German Organisation for Aviation Researches)" requested Dr. Sänger to perform two difficult tasks: to design a Research Institute for Rockets Technology, and to elaborate a Research Program for liquid-fuel rocket engines [4]. As a result, a new Research Center for Rockets was built at Trauen, disguised under the public name „Flugzeugprüfstelle" (Aircraft Test Center) and subordinated to „Luftfahrtforschungs Anstalt H.G. – LFA" („H.G." Aviation Research Institute). In 1937, Dr. Sänger was very much in need of the best assistants he could get, as the main task of his Research Center at Trauen was tremendous: to design and build a suborbital space plane able to reach the antipodes and also the rocket engine needed for that! He was happy to receive two very capable contributors: Dr. Irene Bredt and Helmut von Zborowski, an experienced engineer coming from Bayerische Motorenwerke Munich. Von Zborowski undertook the responsibility of the Test Rig for big rockets engines with 1,000 kN thrust. [5]

As of Dr. Irene Bredt, she begun by deeply studying Dr. Sänger's work: „Gaskinetik sehr grosser Fluggeschwindigkeiten" (Gas kinetics at very high flight speeds) which had been demanded under a contract with the Central Office for Scientific Reports (ZWB). Working together, Dr. E. Sänger and Dr. Irene Bredt delivered in May 1938 this technical report, which showed for the first time the formulae and numeric values of aerodynamic forces acting on a space-plane at altitudes where the atmosphere can no longer be considered a continuous medium. This ground-breaking study was published in English by Dr. H.S. Tsien (May 1950) as NACA Technical Memorandum No 1270: „Super-aerodynamics – Mechanics of Rarefied Gases" [4].

The second task of Dr. Bredt was to solve the theoretic problems of gases thermodynamics associated with building and testing various liquid-fuel rockets, including the one with 1,000 kN thrust

needed for the construction of the semi-ballistic rocket plane. Dr. Bredt's work relayed also on another Dr. Sänger's paper: "On the Construction Principles and Performances of Rocket Planes", published in February 1933 at Deutsch-Österreichische Tages-Zeitung Publishing House. This concept would be later detailed by Dr. Sänger in his book: „Raketenflugtechnik (Rockets Technology)" published in 1933, at R. Oldenbourg Publishing House [6].

Dr. Irene Bredt also received the responsibility of thermodynamic calculus of combustion processes in liquid fuel rocket engines, including the case of weightlessness. Especially, she had to solve the problems of alcohol combustion in liquid oxygen (primed with Zn-diethyl) in various rocket configurations. In October 1938, the Trauen Center already made a steel scale model (1:20) of a supersonic glider. Because of the dome-shaped body and flat bottom of that model, Dr. Sänger assistants (including Dr. Bredt) nicknamed it „the flat-iron". [5].

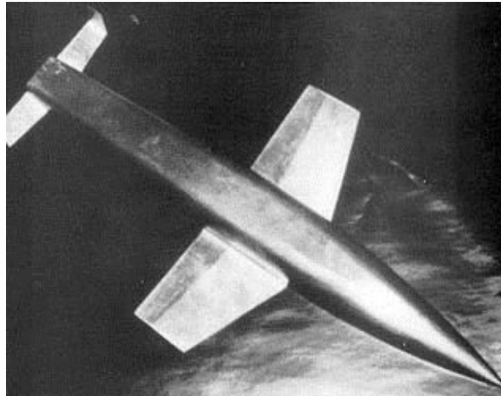


Figure 2: "Silver Bird" steel model at 1:20 scale

Dr. Sänger's concept about this space-plane (named "Silver Bird") was to accelerate it up to a speed of 500m/s before take-off, by means of a rocket-powered launching-sled sliding on a straight horizontal rail, several kilometres long. Such a solution required a careful analysis of the dynamic processes generated by the friction between the sled and the rail, including the large amount of heat to be controlled. Dr. Irene Bredt undertook this task and she understood that, at very high sliding speeds and high negative accelerations during the breaking after launch, it was necessary to ensure the dynamic floating of the sliding surfaces by adequately designing the geometry of the lubrication gap and choosing an adequate lubricant. But for such extreme operating conditions there were no reference data in the scientific literature of that time, and some people even pointed out that it would be impossible to control frictional heat and therefore, the whole concept of the rail catapult was doubtful. [5]

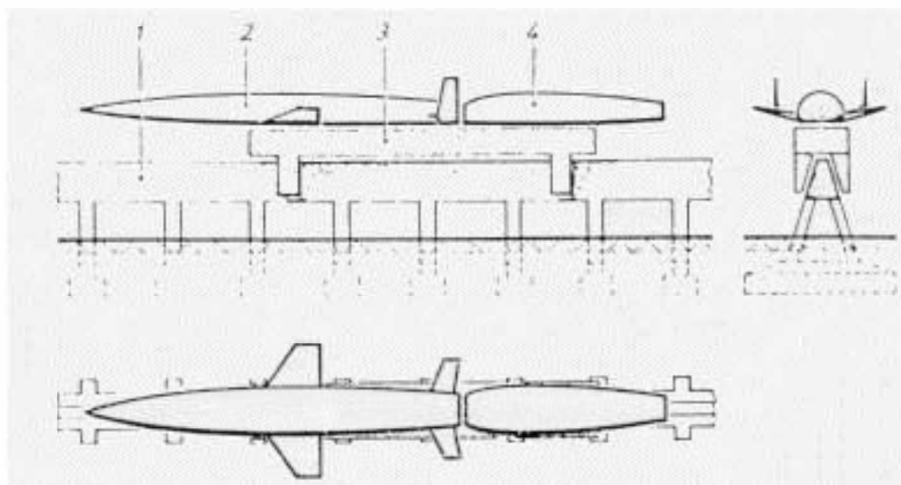


Figure 3: The „Silver Bird" on the launching rail

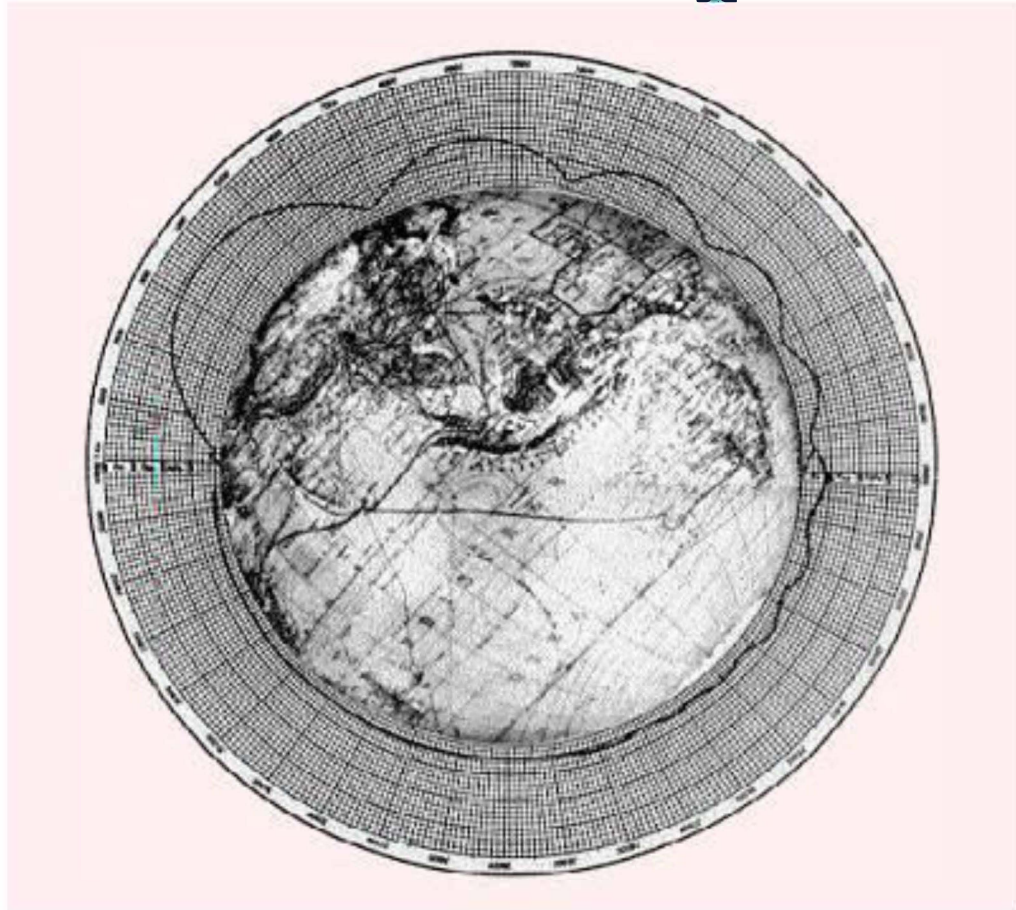


Figure 4: „Silver Bird” multiple ricochets flight path

Initially, Dr. Bredt intended to obtain test data about friction and lubrication processes from the specialists of „Institute für Technische Strömungsforschung” (Institute for Technical Research of Flow Processes) in Berlin; however, the maximum sliding speed obtainable in their test rig was only a fraction of the speed needed at Trauen. Consequently, Dr. Sänger and Dr. Bredt designed a new, spiral-shaped test rig, using as test model a stainless steel bullet fired with initial velocity of 800 m/s. The experiments carried out in 1939 demonstrated the feasibility of the horizontal launching rail allowing a slide speed of 500m/s, provided the rail is carefully finished and well lubricated [5].

By the end of 1939, the Deutsche Luftwaffe had issued a formal order that the entire activity of the Center shall be focused on objectives which could be used in the ongoing war [2]. In this context, the opportunity of working on the complex and futuristic “antipodal bomber” became doubtful. The “Silver Bird” rocket plane study, including analysis and calculus of bombs trajectories, impact ballistics and other combat capabilities, became a Top Secret Technical Report: „Über einen Raketenantriebe für Fernbomber (A Rocket Engine for a Long Range Bomber)” [7]. In 1941, Dr. Sänger and Dr. Bredt submitted this report for approval to the Aviation Ministry, which answered by the autumn of 1942 with an order to stop working on the 1,000 kN thrust rocket engine development. The war requested solutions quickly usable in operations, and the rocket plane, although extremely advanced, was far from becoming operational.

With a 100 tons take-off weight and 100 atm pressure in the combustion chamber, „Silver Bird” was the first project in the class of space vehicles later to be called „Single Stage To Orbit (SSTO)” – a technology which is a huge challenge even today. However, the „Silver Bird” rocket plane delivered important and lasting legacy solutions, like the “regenerative cooling engine” design, in which fuel or oxidizer is circulated around the engines, cooling the engines and pressurizing the fluid. This solution, used today in modern rocket engines, is referred to as the “Sänger-Bredt design” [8]. Another legacy is the sled-launching concept, still envisaged today by some SSTO projects, like “Maglifter” [9].

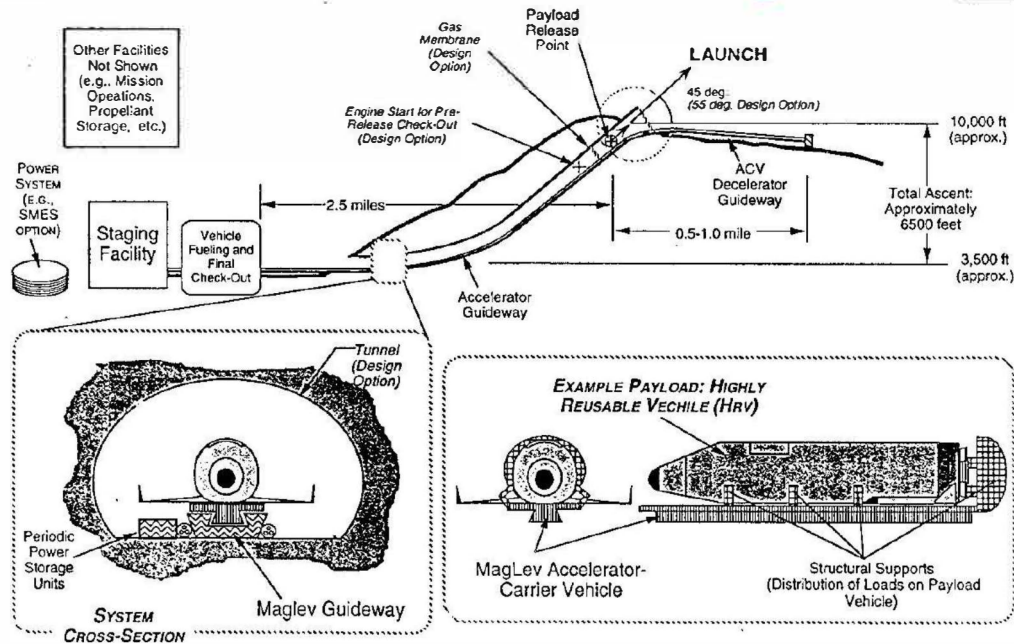


Figure 5: „Maglifter” sled-launching concept

As for Dr. Sänger and his team, they were allowed to continue their scientific work only in the field of ramjet propulsion, under the leadership of the German Research Institute for Gliding Flight (Deutsche Forschungsanstalt für Segelflug – DFS) of Ainring, in the Upper Bavaria.

3 RAMJET PROPULSION PROJECTS AND FIRST FLIGHT TESTS

Looking back to the visit made by Wehrmacht General Staff at Trauen in 1940, they obviously wanted to define ways to achieve superiority for Germany in the ongoing air war. At that time, Dr. Sänger proposed to equip German fighters with ramjet engines. This suggestion being accepted, Dr. Sänger began very fast the Ramjet Project, built a prototype and installed it on a flying test bed – an old Do-17 bomber, obtained by pilot Capt. Paul Sprenberg. Weighing 12 tons, having installed on its back the ramjet tube (6m length and 1,5m diameter) the old Do-17 took off with Capt. Sprenberg and Dr. Sänger at the controls, becoming the first aircraft to fly with a ramjet engine. This half-hour first flight was reported to Berlin and rewarded with a...punishment, because the Research Office of the Aviation Ministry had not approved such a flight. [5]



Figure 6: Ramjet test flight on Do-17

Dr. Sänger and Dr. Bredt as his first assistant were transferred at Ainring to continue their work under the direct supervision of Prof. Walter Georgli, director of DFS. Dr. Irene Bredt was promoted Senior Researcher at the Special Propulsion Center of the Ainring Institute, being in charge with the development of ramjet engine performances. However, Dr. Bredt will later uncover the real motivation of the punishment order which referred only at Dr. Sänger and herself: "... the difference of opinions between Dr. Sänger and his chief in LFA, obliged him to stop his work on the 100 tons rocket engine for the antipodal bomber" [4].

At the Ainring Institute, Dr. Sänger and Dr. Bredt convinced Prof. Georgli to print, in September 22nd 1944, a very short variant – a secret excerpt – of their technical report, under the title „Raketenantriebe für Fernbomber" (A Rocket Engine for a Long Range Bomber). Their tenacious preoccupation for this report was motivated by the scientific value of setting the foundation principles

of the new aerodynamics of rarefied gases, where the forces acting on a space plane are entirely different, and also their priority in conceiving a new method of de-orbiting a space plane, using a semi-ballistic flight path later to be known as "Rikoschettier flight (ricochet flight)" when the space plane is ricocheting on the denser layers of air, like a flat stone thrown at small angle on water surface. In this way, the flight path will be much longer than what can be obtained by using a simple aerodynamic descent [5]. In her memories [4] Dr. Bredt writes that "approximately 70 copies of that secret report had fallen into the hands of the Allies". These have certainly been useful for the researches developed in USA, which ultimately led to the Space Shuttle. The Russians were also interested in the space-plane concept, and even planned to bring Sänger and Bredt to the Soviet Union. That didn't happen, but Russian scientist Mstislav Keldysh developed a project in 1947 for a version of the Sänger-Bredt antipodal bomber, without the launch sled and the ricochet trajectory, and using two big ramjets. [10]. Even if that variant of space-plane was not built, this line of research was useful for the development of other Russian space projects [11].

Dr. Bredt helped Dr. Sänger to develop the correct and complete thermodynamic theory of ramjet engine. She was permanently in charge with flights schedule and the performances obtained with the flying test bed aircraft (initially Do-17, later an improved variant Do-217) equipped with a functional ramjet, with which the pilot Paul Sprenberg performed the flights from Hörsching Airfield. Taking advantage of the ramjet operation time of 10 to 30 min, the daring pilot performed rapid climbing to 7,000m altitude and reached 720 km/h in a dive from 4,000m to 1,500m (performances obtained not with a fighter plane, but with an old bomber!). The pilot Fritz Stammer (who was the first man to ever fly a rocket powered aircraft) representing Prof. Georgli at the test flights, was completely astonished [5].

In 1944, a Technical Report sent by Dr. Sänger and Dr. Bredt to the Aviation Ministry in Berlin stated that the ramjet tests results have demonstrated the possibility of supersonic flight. Some official high-ranking person from Berlin was so surprised, that he wrote a resolution on this report: „What kind of imbeciles! At such speed it will not be possible to fly or to aim a target [2].“ It was not for the first time in the history of science and technology, that this type of reactions appeared; and if one thinks of the difficulties experienced in controlling the fighter planes of that time (like the Focke-Wulf 190 or the P-38 Lightning) in fast dive manoeuvres, that reaction becomes more understandable. However, solutions were not so far away, if we think at the swept wing fighter designs like Willy Messerschmitt's "Me-262" and "Škoda-Kauba Sk P.14" project [12] equipped with Dr. Eugen Sänger's ramjet or if we consider the widely spread use of hydraulic controls today.



Figure 7: "Škoda-Kauba Sk P.14" fighter project [13] with Dr. Eugen Sänger's ramjet

4 THE CONCEPTS OF SCRAMJET AND PHOTONIC ROCKETS

After the war, as residents of the part of Germany administrated by France, Dr. Sänger and Dr. Bredt were selected and invited in 1946 by the French Aviation Ministry to work as scientific researchers at the Aeronautical Arsenal of France, at Paris-Chatillon, which became later SFECMAS under the leadership of Société Nationale des Constructions Aéronautiques (SNCA) du Nord. Until 1954, Dr. Irene Sänger-Bredt (she had married Dr. Eugen Sänger in 1951) was also consulting engineer at the French Rocket Company MATRA in Paris-Billancourt division. [5]

Together with her husband, Dr. Irene Sänger-Bredt proposed the rocket combustion chambers with cooling channels; they also imagined pressurized mixer systems for combustion gases, and a system for precise measurement of speed and temperature of combustion gases, based on the Doppler

Effect. They also developed the theory of corrugated propelling nozzles, the theory of luminescence in burning processes, the theory of solid bodies' explosion, and they studied the reactions of burning nuclei.

Dr. Irene Sänger-Bredt helped her husband to develop the concept of Aerospace Transporter „SCRAMJET“ (Supersonic Combustion RAMJET) which they considered to represent the future of air transport. Dr. Eugen Sänger vision on future of air transport was that it will be integrating the technologies of aviation and astronautics, and he also demonstrated that this solution could only be achieved by international cooperation. With the help of his wife, he also discovered the principles which allow the gradual increase of aircraft speeds, up to those of future spacecraft [14]. Working together, they wrote many studies and scientific papers, like [5]:

- Gemischtauf bereitung on Stationären Feuerungen (Mixer for Stationary Combustion Chambers), Paris, 1948;
- Ionisation und Lumineszenz in Flammen (Ionization and Luminescence of Flames), Paris, 1949;
- Thermodynamik der Überschall-Gerät stoss diffusors (Thermodynamic of Supersonic Nozzles with Right Shockwaves), Berlin, 1954;
- Stationäre kernverbrennung in Raketen (Stationary Nuclei in Combustion Processes inside Rocket Engines), Viena, 1955.

As Dr. Eugen Sänger was tasked to lead the new German Institute for Physics and Jet Propulsion in Stuttgart-Pfaffenwald, the Sänger family returned to Germany in 1952. From 1954 to 1962, Dr. Irene Sänger-Bredt was Scientific Director of the Pfaffenwald Institute, contributed to its reconstruction and elaborated its Research Program. From 1963 to 1972, she was external consultant engineer at the Junkers Inc. Company (later integrated into MBB). From 1951 to 1958, she was also professor examiner at the Faculty of Aerodynamics of the Chromepoy-Madras Institute of Technology, in India. In all these periods, she wrote and published numerous scientific books and papers [14], [15], [16].

The common work of Dr. Eugen Sänger and Dr. Irene Sänger-Bredt stands also the foundations of the photonic rocket engine concept. Following the essay „Zur Strahlungs Physik der Photonenstrahlantriebe (On the Physics of Radiations of Photons Emission Propulsion Systems)“ which they published together in Munchen in 1957, Dr. Eugen Sänger published in 1959 his fundamental work „Zur Richtprobleme der Photonenstrahlantriebe (On the Principle of Propulsion by Photons Emission)“ [5]. Their vision was that mankind should make the effort to build and use the photonic rocket engine – the ultimate version of space propulsion system.

5 CONCLUSIONS

Dr. Irene Sänger-Bredt has many important contributions to space science and technology, most of them achieved working together (as they always did) with her husband Dr. Eugen Sänger:

- Creating the bases of the new aerodynamics of very high altitudes, where the distances between air molecules are comparable with the dimensions of the space planes;
- Concept and design of the stratospheric jet bomber and pioneering the technology known today as „Single Stage To Orbit (SSTO)“ [17];
- Concept of the new method of de-orbiting a space plane by ricochets on the denser layers of the upper atmosphere [18];
- The „Sänger-Bredt design“ of regenerative cooling liquid fuel rocket engine [15];
- Development of corrugated propelling nozzles theory;
- Creation of the ramjet engine theory;
- Demonstration of the possibility to build SCRAMJET (Supersonic Combustion RAMJET) propulsion systems;
- Creation of the photonic rocket engine theory.

Dr. Irene Sänger-Bredt was a founding member of the International Academy of Astronautics, and she constantly promoted the ideal of international cooperation in space exploration. By a series of letters kindly sent to Prof. Dr. Nicolae Florin ZĂGĂNESCU between 1973 and 1978, she helped him presenting to Romanian readers the ground-breaking space science developments achieved by Dr. Eugen Sänger and herself.



REFERENCES

1. Zăgănescu, N.F.; 1975; *De la Icar la cuceritorii Lunii (From Icarus to the Conquerors of Moon)*; First edition; Albatros P.H.; Bucharest.
2. Gartmann, H.; 1955; *L'Aventure Astronautique*; Editions France-Empire, Paris.
3. Zăgănescu, N.F.; 1978; "Preface" to Gheorghiu, C.C.; 1980; *Zborul spre infinit (Flight towards Infinity)*; First edition; Dacia P.H.; Cluj-Napoca, Romania.
4. Sănger-Bredt, I.; 1977; "The Silver Bird Story: A Memoir"; Ed. R. Cargill Hall; *Essays on the Hist. of Rocket & Astro. Proc. Of the 3rd to 6th Hist. Symposia of the IAA*; Washington DC.
5. Zăgănescu, F.N., Zăgănescu, R., Popa, G., Popa, L.; 1999; "Dr. Irene Sănger-Bredt, A Life For Astronautics"; *Acta Astronautica*; **55**; (11); 2004; pp. 889–894.
6. Sănger-Bredt, I.; 1974; *Lebenlauf der Prof.dr.ing. Eugen Sănger (Biography of Prof.dr.ing. Eugen Sănger)*; First edition; Hermann Freitag P.H.; Stuttgart.
7. Sănger E., Sănger-Bredt, I.; 1944; *Über einen Raketenantriebe für Fernbomber (A Rocket Engine for a Long Range Bomber)*; Deutsche Luftfahrtforschung UM 03538; Ainring, Germany.
8. "Silbervogel"; [<https://en.wikipedia.org/wiki/Silbervogel>]; [31st July 2017].
9. "Rocket sled launch"; [https://en.wikipedia.org/wiki/Rocket_sled_launch]; [31st July 2017].
10. Westman, J.; 2017; „Global Bounce”; <https://web.archive.org/web/20071009055651/http://www.pp.htv.fi/jwestman/space/sang-e.html>.
11. Ordway, F.I., Sharpe, M.R.; 1979; *The Rocket Team*; T.Y. Crowell Publ.; NY.
12. Zazvonil, Z.T.J.; 2017; "Skoda-Kauba Flugzeugbau"; <http://www.histaviation.com/Skoda-Kauba.html>;
13. Hildwine, J.; 2017; "Luft '46 images"; <http://www.luft46.com/jhart/lufartjh.html>.
14. Sănger-Bredt, I.; 1964; *Entwicklungsgesetze der Raumfahrt (Fundamentals of Spaceflight Development)*; First edition; Krausskopf Flugwelt Verlag P.H.; Mainz.
15. Sănger-Bredt, I., Engel, R.; 1969; "The Development of the Regenerative Cooled Liquid Rocket Engines in Austria and Germany, 1926-1942"; *Smithsonian Annals of Flight*; **10**; 21; USA.
16. Sănger-Bredt, I., Reiniger, K.; 1974; *Requiem für Eugen Sănger (In memoriam Eugen Sănger)*; L. Bölkow P.H., Germany.
17. Zăgănescu, F.N.; 1977; *Dicționar de astronomie și astronautică (Dictionary of Astronomy and Astronautics)*; Ed. Științifică și Enciclopedică, București.
18. Hallein, P.R.; 1990; *The Antecedents of the Space Shuttle*; A.I. Skolog Univelt P.H., Cal., USA.

Importance of a Second Entrance in a Test Cell

Oana DUMITRESCU

National Research and Development Institute for Gas Turbines COMOTI

Research Assistant

220 D Iuliu Maniu Bd., sector 6, cod 061126, OP 76, CP174, Bucharest, Romania

oana.dumitrescu@comoti.ro

Bogdan GHERMAN

Head of CFD Department

Ionut PORUMBEL

Scientific Researcher II

ABSTRACT

The present paper studies the influence of a secondary intake and its effect on the jet stability. Three configurations have been analyzed: one with the secondary intake closed, the second having a convergent nozzle after the augmentor tube and the third case using a perforated augmentor tube. The secondary intake is used to supply air for cooling the exhaust system. Numerical simulation was realised using the k- ϵ model, which is the most used CFD turbulence model, especially for turbulent flow conditions. The results obtained showed that secondary intake influences the jet stability, because of the pressure differences from the two zones. To resolve this closing the secondary intake is the best option available.

KEYWORDS: CFD, *secondary intake, test cell*

SOUNDING ROCKETS

Analysis, simulation and optimization of a solid propellant motor

Laura Navarrete Martín
Polytechnic University of Madrid
Graduated Student
Plaza del Cardenal Cisneros 3, 28040 Madrid
l.navarrete@alumnos.upm.es

Petter Krus
University of Linköping
Professor and head of the Division of Fluid and Mechatronic Systems
SE-581 83 Linköping, Sweden
Petter.krus@liu.se

ABSTRACT

The aim of the present paper is to expose the performance simulation of a small sounding rocket that operates with a solid propellant motor. In order to contribute in the understanding of solid propellant rocket engines, this work analyses the basic functioning of this type of motor and simulates its performance in the experimental rocketry field.

In a solid propellant rocket, the combustion is clearly determined by the grain shape, which establishes the burning surface as a function of time. It affects directly the chamber pressure and, along with burn rate, it determines thrust. So, as well as propellant characteristics, the burning surface is an essential parameter and the engineer can modify it in order to obtain the desired performance. The simplicity of the solid motor and the large number of possible grain burning shapes make solid propellants an interesting option for a rocket engine design.

Therefore, the focus of this study is to build a complete model of solid combustion, with a specific burning shape, that simulates the rocket performance. The motor dimensions have been based on an *Aerotech* engine used in experimental rocketry. It has served as a model for the first calculations and its real performance has proved to be a good comparison tool for the results obtained. The simulation has been carried out in *Hopsan*, a multi-domain software developed at the Linköping University.

Once the simulation is completely built, an optimization of the engine has been done in order to improve the performance and to increase the altitude reached by the rocket.

Finally, the results obtained with the current burning shape are compared to the ones that would have been gathered with another grain pattern. Hence, the comparison of different burning shapes gives an idea of how performance parameters such as thrust, chamber pressure or burn rate change when varying the way of combustion.

KEYWORDS: *solid propellant, grain shape, sounding rocket*

Application of Hamilton Principle in the control of Tethered Satellite System Pendular Motion

P. Tirop

Beijing Institute of Technology

PhD Student

No. 5 ZhongGuancun Street, Haidian District, Beijing, China Zip Code: 100081

paultirop@yahoo.com

J. Zhang

Beijing Institute of Technology

Professor

ABSTRACT

The control of a tethered satellite system pendular motion is done by application of Hamiltonian equation of motion on a control design method known as planar H tracking. In this case, the reference motion is considered a natural planar motion. The control of the TSS is accomplished by using the inside plane control inputs as well as the outside plane control inputs. The designed control laws are able to drive the pendular motion to a natural planar trajectory with the required characteristics. The control inputs are analyzed using their magnitude ability. The numerical simulation results for each control inputs show that the inside of plane input not only has strong magnitude, but also effectively controls the pendular motion of the tethered satellite system.

KEYWORDS: *Tethered Satellite System, Hamiltonian equation, Control laws, Pendular motion*

Failure analysis of a high-speed offset bearing

Daniela M.BUZESCU

INCDT COMOTI

Senior researcher

Bucharest ROMANIA

daniela.buzescu@comoti.ro

Sorin Gabriel TOMESCU

INCDT COMOTI

Senior researcher

ABSTRACT

There are presented the consequences of the events during the operation of two variants of sliding bearings (offset type) within two gearboxes of similar construction and way of loading. Both assemblies have suffered serious damages of the gear transmission (gear teeth breaking, active flanks scoring, etc.), accidents that occurred after a longer or shorter period of use. During operation, each gearbox was monitored and the parameters values were recorded: gas turbine speed, driving power, important temperatures (oil input, bearing surface, etc.), vibrations (proximity sensor on the input shaft, accelerometer on the gearbox housing). For each type of bearing, the geometric characteristics are presented, the antifriction material is described by its mechanical properties, and the dynamic characteristics of the bearing surface are used to estimate the critical mass which establishes the boundary between stable and unstable operation. Relying on the operating parameters, the behaviours of two HS bearings (HS Sun pinion bearings), which have been analysed are compared mainly during instability occurrences and especially in the last period before their removal from service. The conclusion is that the stability of the undamaged fluid film bearing is proved both from the computational model and by the dynamic response of bearing to external loading.

KEYWORDS: offset-halves bearing, high speed, low load, vibration, cavitation erosion,

Time-domain aeroelastic model for compound helicopter propeller-wing configuration

Zi Wang

*PhD Student at the University of Nottingham
Department of Mechanical, Materials and Manufacturing Engineering,
University of Nottingham, University Park, Nottingham, UK, NG7 2RD
Zi.Wang@nottingham.ac.uk*

Alessandro Anobile

Research Fellow at the University of Nottingham

Atanas A. Popov

Professor at the University of Nottingham

ABSTRACT

A simplified numerical model for time-domain aeroelastic analysis of a wing structure in a propeller-wing configuration is described in the paper. A linear beam model with deformable elastic axis under torsional deformation and out-of-plane bending is considered to simulate a wing structure with tip mounted propeller, relying on efficient, analytical formulations. The complete aeroelastic system of equations is solved using Galerkin's approach, and numerically integrated by the Newmark-beta method. The computational tool developed is able to predict the wing aeroelastic transient behaviour and the wing-propeller interaction effects in the time domain. The purpose of such a tool is to provide accurate enough predictions of the system aeroelastic response to be included in structural optimisation and control synthesis procedures. A complete analysis on the solver used and an aeroelastic analysis of a Eurocopter X3-like compound helicopter wing/propeller configuration are demonstrated.

KEYWORDS: *Aeroelasticity, Rotorcraft, Compound helicopter, Wing-propeller interaction*

Methods Supporting the Efficient Collaborative Design of Future Aircraft

Erik Baalbergen

NLR - Netherlands Aerospace Centre

Senior scientist Collaborative Engineering

Anthony Fokkerweg 2, 1059 CM, Amsterdam, the Netherlands

Erik.Baalbergen@nlr.nl

Erwin Moerland

German Aerospace Center (DLR)

Research associate & Team lead Collaborative Engineering group,

Hein-Saß-Weg 22, 21129, Hamburg, Germany

Erwin.Moerland@dlr.de

Wim Lammen

NLR - Netherlands Aerospace Centre

R&D engineer Modeling and Simulation

Anthony Fokkerweg 2, 1059 CM, Amsterdam, the Netherlands

Wim.Lammen@nlr.nl

Pier Davide Ciampa

German Aerospace Center (DLR)

Research associate & Team lead Multidisciplinary Design and Optimization group,

Hein-Saß-Weg 22, 21129, Hamburg, Germany

Pier.Ciampa@dlr.de

ABSTRACT

The paper describes the need for and advantages of efficient and effective collaboration within the aircraft development supply chain. It discusses the barriers on the organisational, human and technical levels that hamper efficient collaboration. One of the focal points of the European Horizon2020 project AGILE is the creation of technical solutions for resolving the challenges that come with collaboration. In this light, the paper focuses on two methods being investigated and developed for supporting multidisciplinary teams from different organisations in collaborative aircraft design. The first method concerns the realisation of cross-organisational workflows for multidisciplinary design of aircraft. The workflows support the definition and smooth application of multiorganisation collaborative product development analyses. The second method concerns the deployment and management of surrogate models, which support efficient collaborative multidisciplinary aircraft design while dealing with intellectual property issues and computational speed limitations. After the introduction of the methods, two representative use cases which are successfully supported by the methods are highlighted. An important observation is that efficient collaboration is not straightforward when engineers from different and usually geographically dispersed organisations attempt to achieve a common design target. Once the collaboration methods are in place however, investigation of novel aircraft configurations is enabled by optimally leveraging the dedicated disciplinary knowledge of all involved experts.

KEYWORDS: *collaborative engineering, design of more competitive aircraft, cross-organisation workflows, surrogate model repository*



Pitch Stabilization with Tailored Canard Compliance

Petter Krus

*Department of Management and Engineering
Linköping University
E-mail: petter.krus@liu.se*

Birgitta Lantto
Saab AB

ABSTRACT

The aircraft design problem is an example of a highly integrated design, which calls for a multidisciplinary approach from the very beginning. With every generation of aircraft, it gets more difficult to make substantial improvements since so much already have been done to produce as efficient aircraft as possible. Next generation civil aircraft needs to take every possibility to increase efficiency. One potential area of improvement is to reduce drag due to the requirement of positive stability. The stability requirement is a result of safety regulations, and with the present state of the art, it is difficult to get a system certified that can artificially stabilize an aircraft. If this can be overcome, there are potential gains in drag, since all horizontal surfaces can be used for lift, and hence total planform area, and hence parasitic drag, can be reduced. Another advantage is that a wider cg range can be allowed.

In this paper we propose a configuration with dynamic load canards, suitable for business aircraft (biz jet and biz prop), as well as large next generation transport aircraft, with prop fans that have to be located in an aft position.

The approach used here is to look at control surface actuators and different means to utilize force control, possibly together with position control, to introduce compliance in proper positions of the system. As a side effect, excessive loads on control surfaces can also be avoided, which can translate into weight reduction. There is also scope to reduce gust sensitivity, for e.g. passenger comfort.

KEYWORDS: *Aircraft design, flight control, canard, force control*

Preliminary Investigation on the Impact of Missile Design on its Aerodynamic Features

Mahmoud M. Abdel-Fattah

Undergraduate student

Ahmed E. Hassan

Undergraduate student

Mahmoud Y. M. Ahmed

Department of Aerospace Engineering, Military Technical College, Cairo, Egypt

Email: Mahmoud.yehia@mtc.edu.eg

ABSTRACT

The dependence of aerodynamic features of a conventional missile on its configuration is examined. The features in concern are the zero-lift drag coefficient, the lift-curve slope and the center of pressure location. These coefficients are estimated using a commercial reliable tool that is used for conceptual design and preliminary sizing of rockets of simple shapes.

KEYWORDS: *Aerodynamic coefficients, Missile aerodynamics, Surrogate models.*

NOMENCLATURE

B	nose roundness	L	normalized conical nose section length
b	wing semispan [m]	L_N	total nose length [m]
C_r	normalized wing root chord	R	missile radius [m]
C_t	normalized wing tip chord	r	nose tip roundness radius [m]
C_{Do}	zero-lift drag coefficient	S_F	wing planform area [m ²]
C_L^α	lift curve slope [rad ⁻¹]	x_{cp}	normalized center of pressure location
D	missile caliber [m]	δ_c	conical nose semi-apex angle
l_c	length of conical nose section [m]		
l	overall missile length [m]		

1 INTRODUCTION

Predicting the aerodynamic characteristics of a missile is a crucial step in the procedure of missile system design. These values are fundamental inputs to the subsequent calculations of flight trajectory, accuracy, and lethality. In addition, the processes of developing new missiles or upgrading existing ones involve the estimation of aerodynamic coefficients.

For given flight conditions, the aerodynamic characteristics of a missile are solely dependent on its airframe configuration. Understanding this dependence is important for any missile airframe designer. This dependence is obvious and needs no proof. The objective of this paper however, is to quantize the dependence of main aerodynamic features on the missile airframe design. The aerodynamic features are estimated using a simplified engineering tool of an acceptable accuracy as far as preliminary design is concerned.

2 CASE STUDY

The missile examined in this study is the conventional fin-stabilized unguided ground-launched short-range tactical missile Luna-M [1]. The configuration of the missile is a spherically-blunted cone-cylinder of caliber $D = 544 \text{ mm}$ with four right-trapezoidal stabilizing fins at the end of the body. The figure below illustrates the missile configuration, dimensions are in mm .

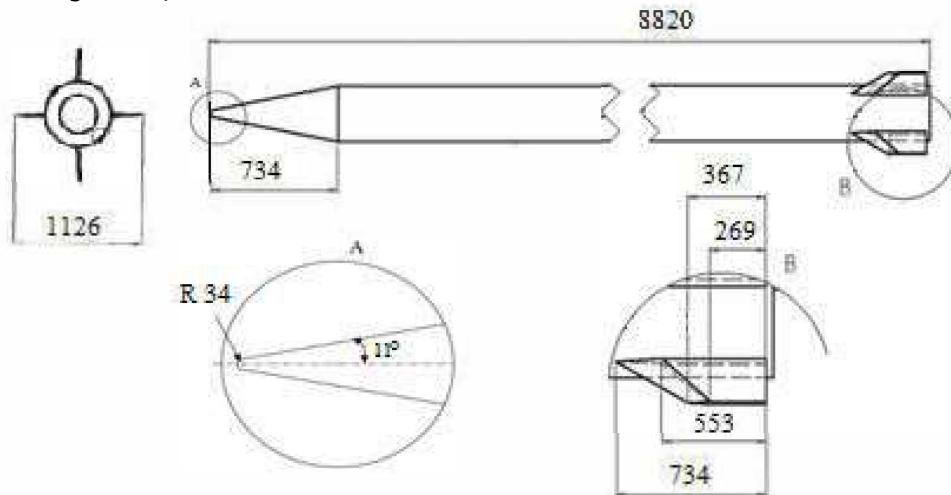


Figure 1: Configuration of the case study missile, dimensions are in mm

The operating conditions are selected corresponding to flight Mach number of 1.5 at sea level conditions in a standard atmosphere.

3 METHODOLOGY

3.1 Definition of the design parameters

The objective is to explore the impact of varying the missile configuration on its aerodynamic coefficients. The missile overall length, l , caliber, D , and fin area, S_F are kept unchanged as the baseline configuration (Fig. 1) whereas other dimensions of other geometric elements of the missile are varied. In addition, the distance from missile base to fin trailing edge at root is assumed to be unchanged as the baseline configuration. For the un-winged body, the varying dimensions are:

- radius of nose hemispherical tip,
- nose cone semi-apex angle,
- nose length, and
- cylindrical body length.

For the fin, the dimensions are:

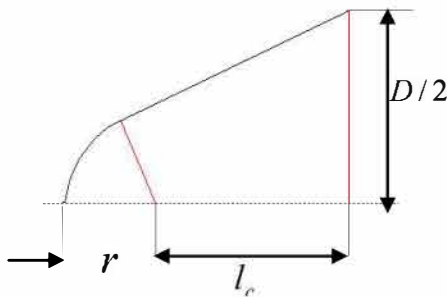
- root chord,
- tip chord,
- span,
- leading edge sweep angle, and
- distance from nose tip to fin leading edge at root.

Among the nine geometric dimensions above, only five are adopted to be the independent parameters and are allowed to vary within reasonable arbitrarily-defined ranges. The remaining four geometric elements

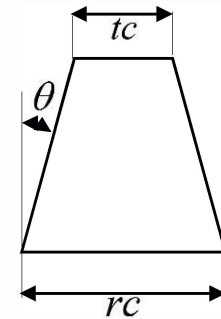
can be calculated based on geometric constraints. For a more generic representation, the independent parameters representing linear dimensions are normalized with respect to the missile caliber. The normalized independent parameters and the corresponding ranges of variation are listed in the table below.

Table 1. Missile independent geometric parameters and their corresponding ranges of variation

Geometric parameter	Range of variation	
	Lower limit	Upper limit
Nose tip roundness, $B = r/(0.5D)$, Fig. 2.a	0	1
Length of conical part of the nose, $L = l_c/D$, Fig. 2.a	0	5
Fin tip chord, $c_t = tc/D$, Fig. 2.b	0	4
Fin root chord, $c_r = rc/D$, Fig. 2.b	0.2	4
Fin leading edge sweep angle, θ , Fig. 2.b	-70° (forward sweep)	$+70^\circ$ (backward sweep)



(a) spherically-blunted nose



(b) trapezoidal fin

Figure 2: Geometric parameters of the missile

The remaining dependent geometric elements are calculated based on geometric constraints using the following relations:

1- nose cone semi-apex angle:

$$\delta_c = \cos^{-1} \left[\frac{Rr + l_c \sqrt{l_c^2 - r^2 + R^2}}{l_c^2 + R^2} \right]$$

2- nose length:

$$L_N = l_c + r$$

3- cylindrical body length:

$$L_c = l - L_N$$

4- fin span:

$$b = 2S_F / (tc + rc)$$

5- distance from nose tip to fin leading edge at root:

$$x_F = l - rc$$

3.2 Sample selection

By independently varying the geometric parameters listed in Table 1, distinct missile configurations are attained. The proper combinations of these parameters is important in selecting the designs in this 5D design space. The selected designs (locations in the design space) should be uniformly distributed as well

as space-filling. Various sampling techniques are available however, the Latin Hypercube Sampling [2] is adopted in this study. Using DoE toolbox in Matlab [3], 500 samples are generated. For each of the 500 designs, the aerodynamic coefficient in concern namely, zero-lift drag coefficient, C_{D0} , lift curve slope, C_L^α , and location of center of pressure, x_{cp} , are estimated. The flight conditions are selected to be corresponding to sea-level standard atmospheric conditions with a speed of Mach 1.5 (which is the nominal Mach value experienced by the missile during powered trajectory [1]).

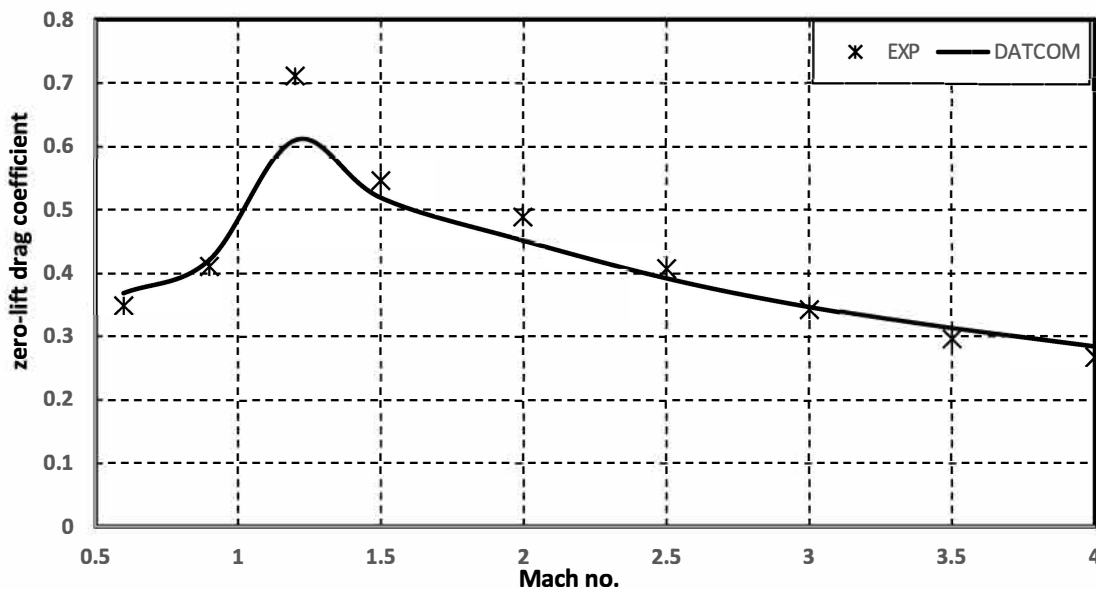
3.3 Aerodynamic prediction tool

Missile Datcom [4] is a reliable preliminary aerodynamic design tool that has been used in a huge body of studies over the decades and until recently (e.g. [5, 6]). In this work, the commercial version of the tool with GUI that is available on the web [7] is implemented.

4 RESULTS AND DISCUSSION

4.1 Validation of aerodynamic calculation tool

The studies focusing on the aerodynamic characteristics of the baseline design of the missile in concern have been studied by many researchers, e.g., [8-10]. In this study, the experimentally measured values of the missile available in [8] are utilized to assess the validity of the used aerodynamic prediction tool. Figure 3 below compares the zero-lift drag coefficient (at different Mach values) and the lift coefficient (at Mach 1.5) of the baseline missile as predicted by Missile Datcom and measure experimentally [8]. The comparison shows the satisfactory accuracy of the used tool especially in the supersonic regime of freestream Mach number even at high incidence angles.



(a) Zero-lift drag coefficient vs. Mach number

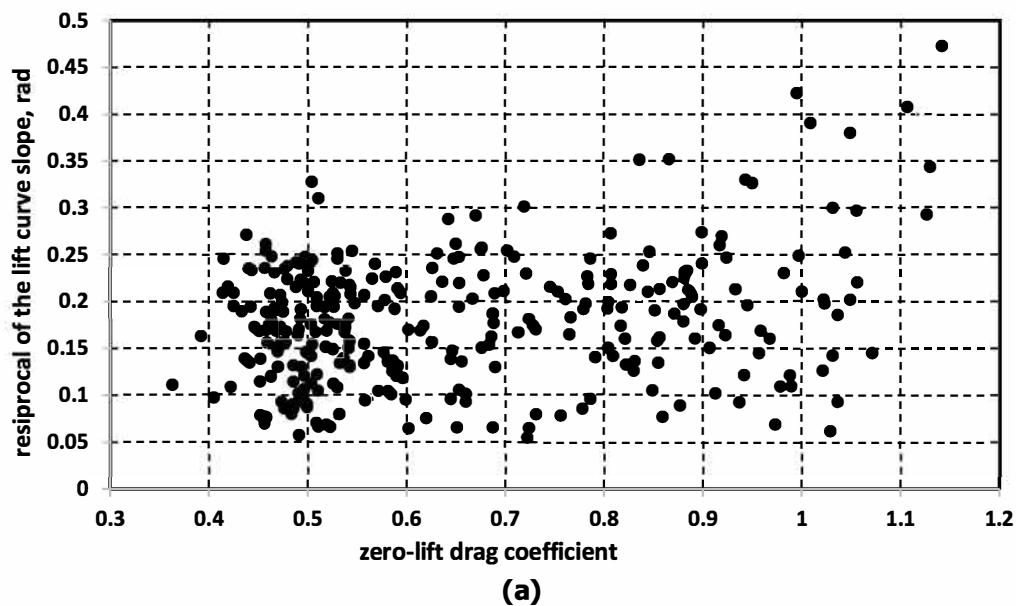


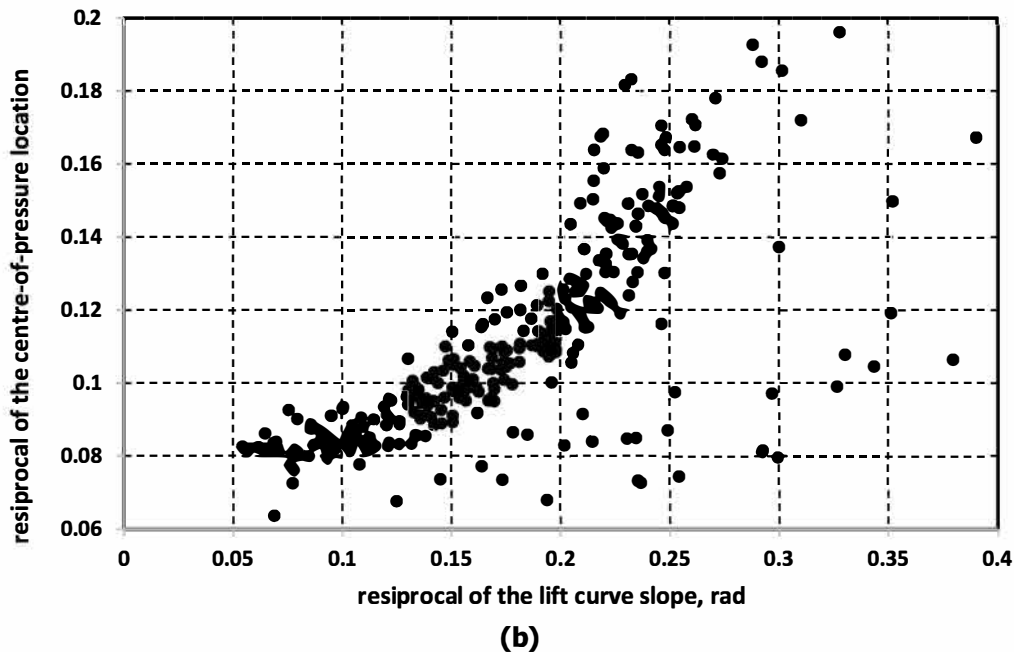
(b) Lift coefficient vs. incidence angle at Mach 1.5 freestream

Figure 3: Validation results for the aerodynamic prediction tool

4.2 Realization of the objective space

The figures below show the loci of all 500 sample designs in the objectives space. Since three objectives are in concern, each pair of objectives is displayed separately. Figure 4a shows preliminary realization of the objective space with zero-lift drag coefficient and reciprocal of lift slope as the coordinates. A state of competition is clear between the two objectives. This implies that a single design that satisfies both minimum drag and maximum lift is unattainable and a tradeoff between the two design objectives is necessary. In Fig. 4b, the lift curve slope and the center of pressure location objectives are illustrated. The figure shows that these two objectives are less competing and a single design may satisfy both objectives.




Figure 4: Preliminary objective space of the case study

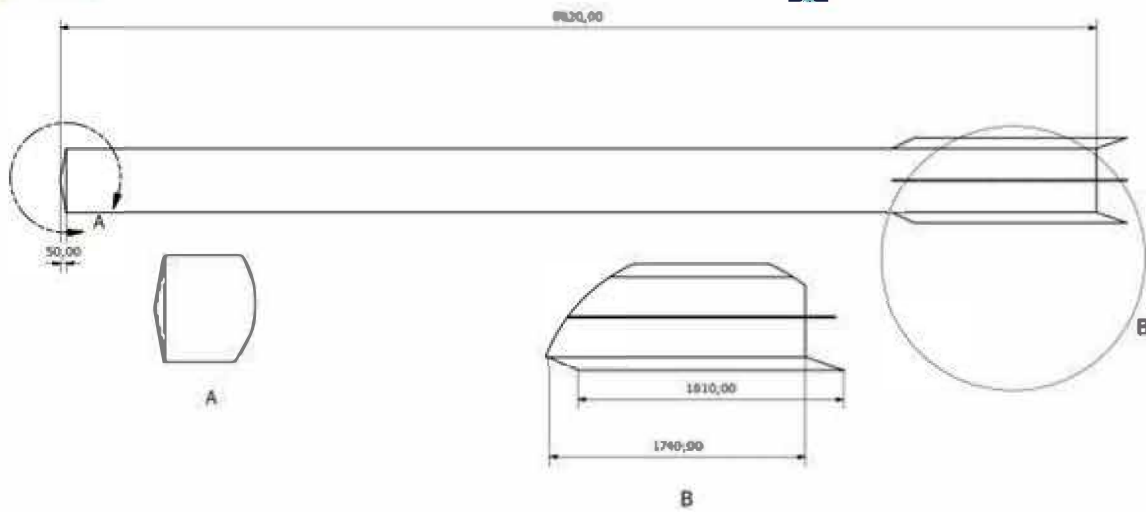
4.3 Designs of extreme aerodynamic performance

The table below lists the features of the designs with extreme aerodynamic performance among the set of samples involved in the study. Clearly, the design that yields the maximum drag coefficient is highly blunt. The length nose cone is only 0.5% of the overall missile length with a sharp pointed tip corresponding to nose slenderness ratio of 0.09. It is in fact the sample with the shortest nose cone. In contrast, the design that generates the minimum drag has a nearly pointed nose cone which length is 29% of the overall missile length; a nose slenderness ratio of 4.7.

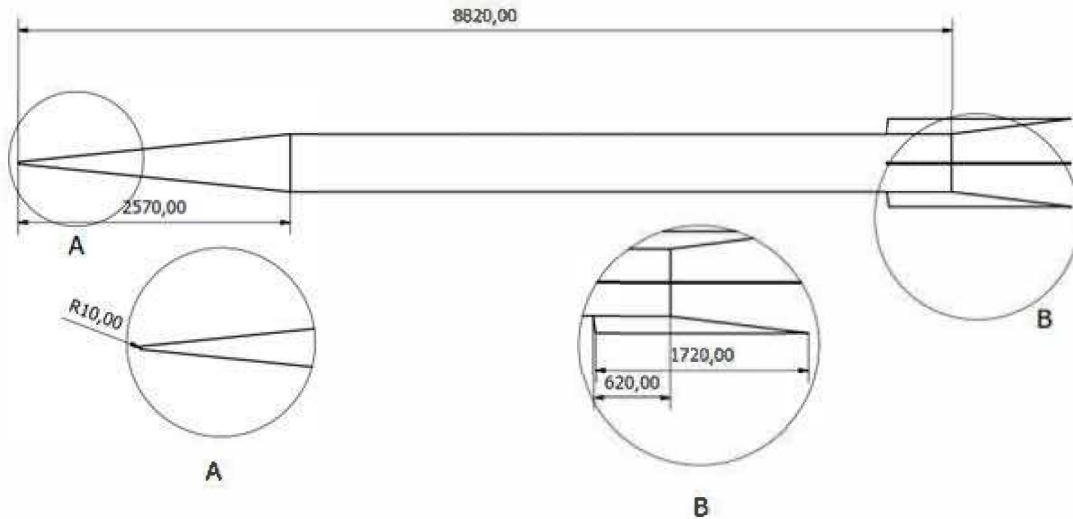
Table 2. Features of designs of extreme aerodynamic performance

Geometric parameter	Units	Aerodynamic performance criteria					
		C_{D0}		C_L^α		x_{cp}	
		Max. =1.888	Min. =0.363	Max. =13.386	Min. =0.8457	Max. =23.467	Min. =2.696
Nose tip roundness	[cm]	0	1	6	15	15	26
	normalized	0.0	0.04	0.22	0.55	0.55	0.96
Length of conical part of the nose	[cm]	5	257	64	268	268	31
	normalized	0.09	4.72	1.18	4.93	4.93	0.57
Fin root chord	[cm]	174	62	192	15	15	34
	normalized	3.20	1.14	3.53	0.28	0.28	0.63
Fin tip chord	[cm]	181	172	165	86	86	204
	normalized	3.33	3.16	3.03	1.58	1.58	3.75
Fin leading edge sweep angle		+65°	+9°	+1°	+66°	+66°	+3°

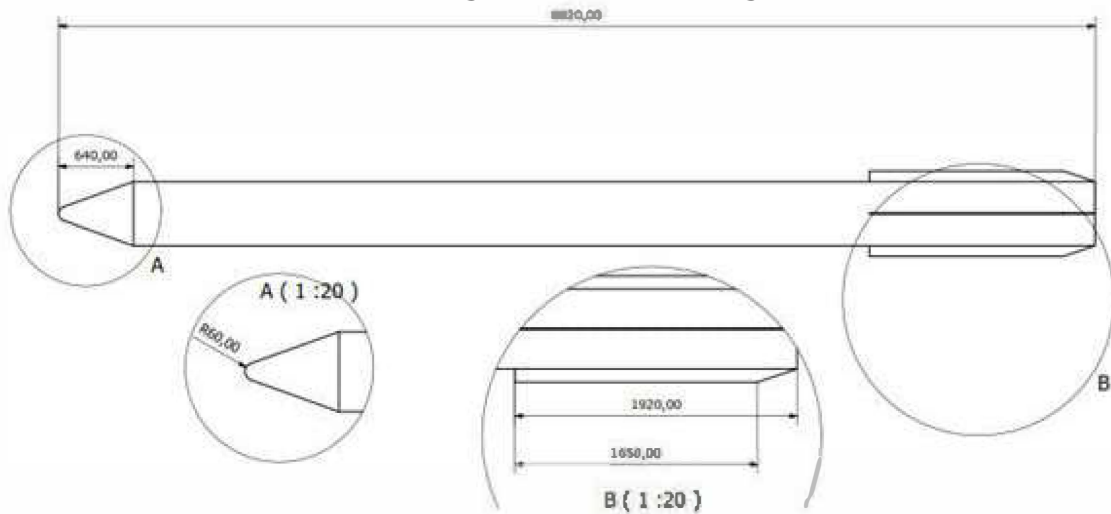
The set of figures below illustrate the airframe configurations of designs with extreme aerodynamic characteristics.



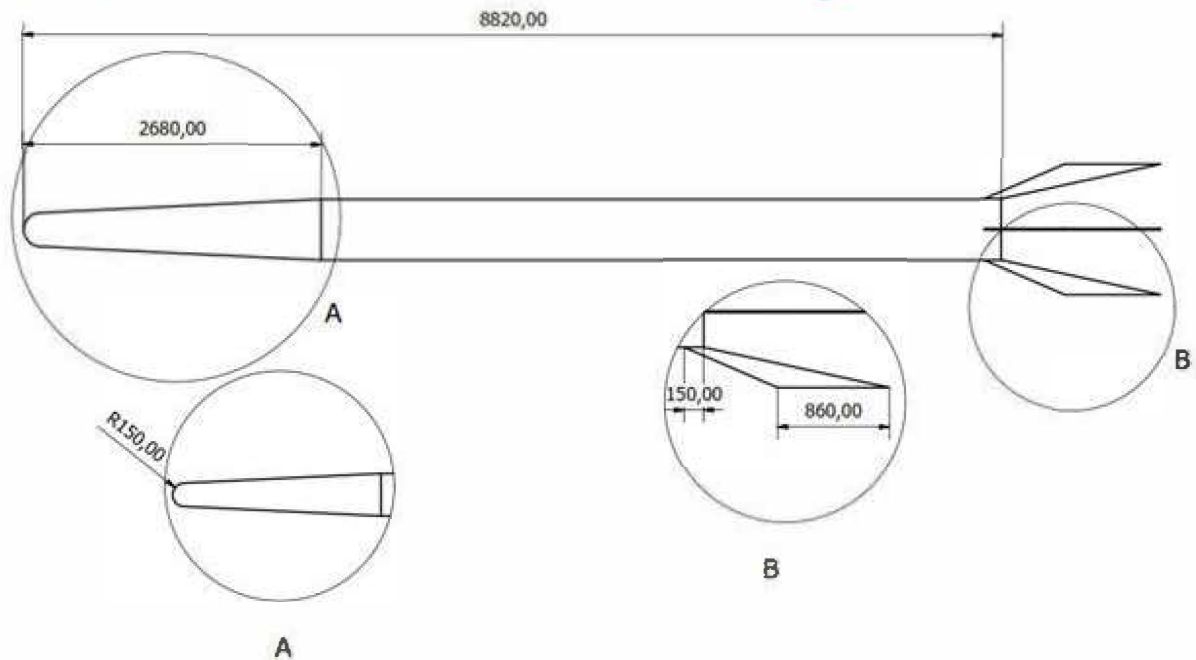
(a) design with maximum drag



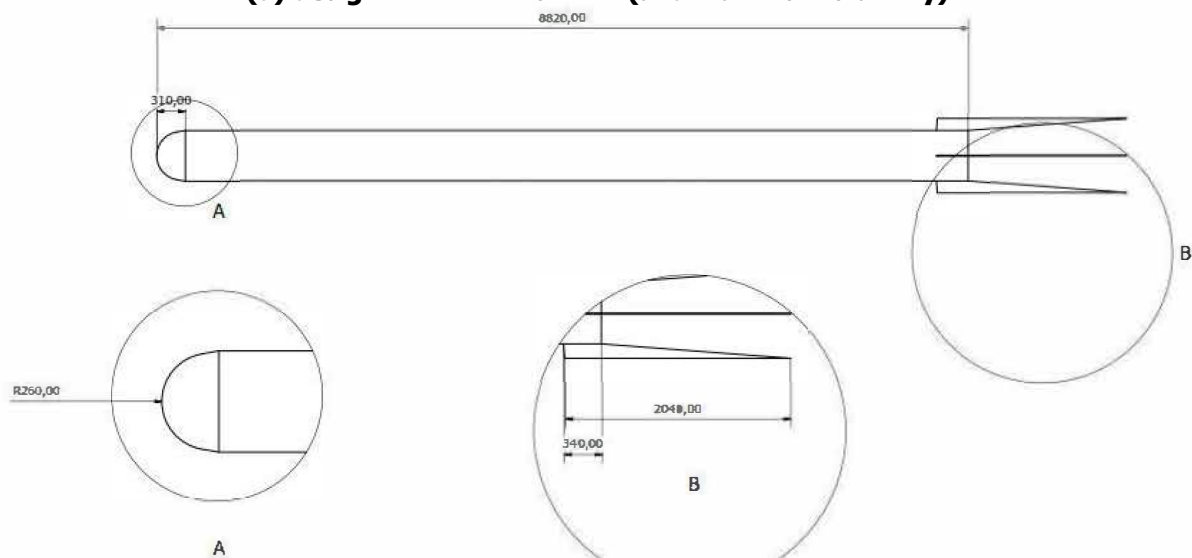
(b) design with minimum drag



(c) design with maximum lift



(d) design with minimum lift (and maximum stability)



(e) design with minimum stability

Figure 5: Illustration of designs with extreme aerodynamic characteristics

Clearly, the design that produces the maximum drag is extremely blunt. It has the shortest nose length with no nose roundness. In contrast, the design with a very long nose and a slight tip roundness produces the minimum drag. This indicates that the missile drag is mainly driven by the forebody configuration. The design that yields the maximum lift curve slope is characterized by very long chord and, hence, a very narrow span. Such design would maximize the wing-body interference and hence, increase the lift capability of the wing. In addition, the nose that has a relatively high semiapex angle adds to the overall missile lift. The design that provides minimum lift curve slope has an unrealistic wing design that experiences almost no interference with the body. The nose is also very long such its contribution to lift is minimized. This

design is the one that provides the highest stability criteria (expressed as the distance to the missile pressure center location).

4.4 Surrogate representation of the missile aerodynamic features

It is interesting to attempt visualizing the relations between the missile aerodynamic features and its design parameters based on data extracted from the prediction tool. This simplest way to do this is to construct metamodels (surrogates) for each of the missile aerodynamic features. In this study, the first-order regression polynomial response surface metamodel is implemented. The tool developed by Viana [11] is utilized. Based on the data obtained for the 500 sample designs, the zero-lift drag coefficient is expressed in terms of the normalized geometric parameters as:

$$C_{D0} = 0.7728 - 0.0056(C_r) - 0.0087(C_t) - 0.00055(\theta) + 0.5531(B) - 0.0891(L)$$

By comparing the coefficients of all terms of the above expression, it can be inferred that nose tip roundness and length are the most dominant parameters. These two parameters have the highest coefficients. In contrast, the geometric parameters of the missile wing are the least dominant. As indicated by the signs, the drag increases as the nose length decreases and nose roundness increases. However, it should be noted that both nose length and tip roundness contribute to the nose bluntness; the key design feature that dictates the drag. Similarly, the lift curve slope of the missile can be expressed as:

$$C_L^\alpha = 7.2587 - 0.2133(C_r) - 0.2945(C_t) - 0.0093(\theta) - 0.1062(B) + 0.1936(L)$$

From the above expression, it can be inferred that wing geometric parameters dominate the lift curve slope value. Other parameters are of a less importance. As inferred by the signs, the lift curve slope varies directly with nose length and inversely with other parameters. Finally, the location of center of pressure can be expressed in terms of the design parameters according to the following expression:

$$x_{cp} = 10.779 - 0.453(C_r) - 0.063(C_t) + 0.0023(\theta) - 0.3105(B) - 0.0444(L)$$

Similar to lift curve slope, the nose roundness and wing root chords are the dominant design parameters as far as center of pressure location is concerned.

5 CONCLUSIONS

The objective of the present study was to understand the impact of the missile design on its aerodynamic characteristics. Five design parameters fully describing the design a simple fin-stabilized tactical missile were investigated. These design parameters were varied and the impact of their variation of the aerodynamic characteristics of the missile was explored. Focus was made on zero-lift drag, lift slope, and location of missile center of pressure. 500 different designs were developed and their aerodynamic characteristics were estimated using a reliable empirical prediction tool. The three-dimensional space of the sample designs was realized and the designs with extreme behavior were illustrated. Simplified expressions were developed using polynomial regression surrogate. The study was intended to shed more light on the impact of missile airframe design on its aerodynamic characteristics. The study can be extended by optimizing the missile airframe design taking into consideration the compromise among different aerodynamic characteristics. Other design considerations that aerodynamics such as fuselage inner volume should also be taken into account.

6 References:



1. Wikipedia; "LUNA Missile"; https://en.wikipedia.org/wiki/9K52_Luna-M, cited Feb, 2017.
2. M. D. McKay, R. J. Beckman, W. J. Conover; 1979; "A Comparison of Three Methods for Selecting Values of Input Variables in the Analysis of Output from a Computer Code"; *Technometrics*; **21**(2); pp: 239-245.
3. Matlab R2014, *MathWorks*, MS, USA.
4. C. Rosema, J. Doyle, W. Black; 2017; "AFRL-RQ-WP-TR-2014-0281 Missile Data Compendium (DATCOM) User Manual"; AFRL, USA.
5. T. J. Sooy, R. Z. Schmidt; 2005; "Aerodynamic Predictions, Comparisons, and Validations Using Missile DATCOM (97) and Aeroprediction 98 (AP98)"; *Journal of Spacecraft and Rockets*; **42**(2); pp: 257- 265.
6. J. T. White; 1995; "An Assessment of Missile DATCOM Prediction Accuracy Relative to Generic Body+Wing+Tail Missile Pitch Aerodynamics"; [13th Applied Aerodynamics Conference](#); San Diego, CA, U.S.A; June, 19 - 22
7. "Missile DATCOM GUI"; <http://jblaox.persianguig.com/>; cited Feb. 2017.
8. L. A. El-Mahdy; 2015; "Computational Prediction of Aerodynamic Coefficients"; MSc Thesis; Aerospace Engineering Department, Military Technical College; Cairo, Egypt
9. L. A. El-Mahdy, M. Y. M. Ahmed, O. K. Mohamed, O. E. Abdel-Hameed; 2017; "A Comparative Study of Prediction Techniques for Supersonic Missile Aerodynamic Coefficients"; *Journal of Mechanical Engineering*; **14**(1); pp: 33-55.
10. E. M. E Khalil; 2009; "Prediction of Aerodynamic Coefficients for Slender Bodies"; MSc Thesis; Aerospace Engineering Department, Military Technical College; Cairo, Egypt.
11. F. A. C. Viana; "SURROGATES Toolbox User's Guide," <http://fchegury.googlepages.com>, Cited, Dec. 2009.

Losses and blade tip clearance for a centrifugal compressor

Oana DUMITRESCU

National Research and Development Institute for Gas Turbines COMOTI

Research Assistant

220 D IuliuManiu Bd., sector 6, cod 061126, OP 76, CP174, Bucharest, Romania

oana.dumitrescu@comoti.ro

Ramona STANCIUC

Research Assistant

Bogdan GHERMAN

Head of CFD Department

Valeriu DRĂGAN

KTH Royal Institute of Technology

Post-doctoral Researcher

Kungl Tekniska Högskolan, SE-100 44 STOCKHOLM

valeriu@kth.se

ABSTRACT

The present paper presents the numerical analysis for a transonic centrifugal compressor using steady state CFD. The blade tip clearance effect over the position of shock waves, tip losses and the performances of the impeller are studied. Numerical simulations have been performed using RANS modelling, with the k-omega SST turbulence model (Shear Stress Transport). Eight cases were taken into consideration for the impeller with the following blade tip clearances values: 0 mm, 0.1 mm, 0.3 mm, 0.4 mm, 0.5mm, 0.7 mm, 1 mm, 2 mm, at the same operating conditions. For the entire stage only seven cases were studied, without the value for 0.1 mm because of its abnormal behaviour, as can be seen in the case of the impeller simulations. Results showed that the position of the shock wave does not change with the increase of the tip clearance. Aerodynamic losses due to shock wave, secondary flow and turbulence can be seen in the polytropic efficiency of the centrifugal impeller and the difference between the two extreme cases is about 3.2 %.

KEYWORDS: *CFD, centrifugal compressor, tip clearance, losses*

Conceptual Design of a Stratospheric Hybrid Platform for Earth Observation and Telecommunications

Vincenzo R. Baraniello

*CIRA Italian Aerospace Research Center
Land, Environment & Cultural Heritage, Researcher
Via Maiorise, Capua (CE) Italy
v.baraniello@cira.it*

Giuseppe Persechino

*CIRA Italian Aerospace Research Center
Remote Sensing & Cultural Heritage, Deputy*

ABSTRACT

The interest in long endurance unmanned stratospheric platforms for Earth observation and telecommunications (also known as HAPS: high altitude pseudo satellites) has increased in the last years, because they represent a complementary solution to satellites and RPAS.

In this paper, we have focused our interest on a stratospheric platform for Earth observation and telecommunications having a maximum takeoff mass less than 1000 kg and a design airspeed equal to 16 m/sec.

We will compare the results obtained by our conceptual design loops concerning the following platforms: a flying wing, an airship and two hybrid platforms having a different configuration. The conclusion of our analysis is that hybrid platform represents the best configuration, in terms of power consumption, size, weight and safety.

KEYWORDS: *Stratospheric Platform, HAPS, HAA, Hybrid Airship, Long Endurance Flight*

NOMENCLATURE

AR - Aspect Ratio

AoA - Angle of Attack

BR - Buoyancy Ratio

FR - Fineness Ratio

GaAs – Gallium Arsenide

HAA – High Altitude Airship

HAPS - High-Altitude Pseudo Satellite

HTA - Heavier-than-Air

LTA - Lighter-than-Air

RPAS - Remotely piloted air systems

UAV - Unmanned Air Vehicle

1 INTRODUCTION

1.1 Stratospheric Platforms

The lower part of the stratosphere (around 20 km of altitude) is an interesting environment for Earth observation and telecommunications because weather is quite calm and the temperature is approximately constant, consequently, convective phenomena have low magnitude and the intensity of winds is lower than at different altitudes.

This region of the space is generally named Near Space Environment.

The interest in long endurance unmanned stratospheric platforms (also known as HAPS: high altitude pseudo satellites) has increased in the last years. Some applications are proposed in [2], [3], [4], [5], [6] and [7].

These applications concern essentially Earth observation and telecommunications. At this altitude, the platform will be able to view a 1000 km diameter footprint of the ground [1]. HAPS represent a complementary solution to satellites and RPAS. In comparison to satellites, they allow observation of a less extended area (local scale) but with greater resolution and greater revisit time than satellites. Moreover, they are able to maintain station (station-keeping) on a predefined area (at a significantly

lower altitude than geostationary satellites). Maintenance and updating of their equipment and payload is also possible because platforms can land and take-off again.

A fleet of RPAS could also guarantee local scale coverage, but in this case, the complexity of the system, in terms of management and maintenance, is greater in comparison to single HAPS.

Stratospheric platforms do not interact with commercial aircrafts during the operative phase of their missions. Obviously, during climb and descent phases, operators could agree some preventive measures with aviation authorities.

Different HAPS configurations have been developed in the last years. For example, Airbus Zephyr family and Facebook Aquila project fall within the flying wing configuration, HiSentinel80 is an airship, while Google Loon project is based on balloons. In the flying wing configuration, the weight is completely balanced by aerodynamic forces generated thanks to the relative speed of the air respect to the wing. In airships and balloons, the weight is balanced by the buoyancy due to the difference of density between the air and gas mixture inside the hull. A more exhaustive description of the different projects is available in [8].

Hybrid airships represent another interesting configuration, exploiting at the same time aerodynamic and aerostatic forces to balance the weight.

Considering that air density at 20 km is the 7% of the sea level air density, platforms may benefit of a reduced drag than at sea level (for equal volume/surface and speed), with enormous advantages in terms of power consumption; but, on the opposite, to generate sufficient aerodynamic or aerostatic forces, the required volume or speed can get larger (increasing again the drag) than at lower altitudes. A large platform can be difficult to manage during climb and descent phases due to the higher loads, which are a consequence of the higher density and wind at intermediate altitudes.

Moreover, stratospheric platforms are typically designed with low power-to-weight ratios. This condition could lead to low controllability at lower altitudes, where higher intensity winds could move the platform from the predefined trajectory and the thrust generated by the power system could not be sufficient to control the platform.

The design of a stratospheric platform consists in a trade-off between the need of surfaces or volumes able to generate the required aerodynamic/aerostatic forces to balance the weight; but which, at the same time, are not too much large in order to do feasible operations on ground and during the flight phases in troposphere (climb and descent). At the same time, the shape of the platform shall minimize the drag at the different altitudes.

The purpose of this paper is the definition of different conceptual design processes for different configurations (flying wing, airship and two configurations for the hybrid platforms) in order to have a preliminary assessment of the main parameters: power consumption, size and mass, mass budget. We will compare the proposed configurations in order to show that the best one in terms of power consumption, volume and final mass, is the hybrid platform.

1.2 State of the art

Concerning hybrid platforms, several works analyzed the optimal buoyancy ratio. The buoyancy ratio is the buoyancy-to-weight ratio. In [9] the optimal buoyancy ratio for a hybrid platform is analyzed. The flight altitude is 20 km while the payload mass is set equal to 10000 kg. Moreover, the platform is powered by fuel. The optimal buoyancy ratio has been computed under the hypothesis of invariant zero-lift drag coefficient, independently from the size of the platform, because of the similarity in the shape. This hypothesis should be better investigated, because the zero-lift drag coefficient depends on the Reynolds number, which depends on the characteristic dimension of the platform and not only on the shape.

In [10] the authors propose a configuration for a solar powered hybrid high-altitude platform. A wing, to generate the lift, and two bodies, to generate the buoyancy, compose the platform (in addition to the tail, used to guarantee stability and control). The weight is balanced for the 55% by the buoyancy. The platform has been designed for a flight altitude of 20 km and a speed of 31.5 m/sec. The wing has a length of 66.3 m and a surface of 293.4 m². The two bodies have a length of 42.4 m and a maximum diameter of 4.71 m.

Other works take into account the conceptual design of hybrid airships for regional transport. In [11] the authors propose a multi-lobed shape, while in [12] the proposed configuration is a winged hybrid airship.

In [13] the conceptual design of a solar powered stratospheric airship is presented. The authors estimate the size and the mass budget for a stratospheric airship flying at an altitude of 20 km at two locations: Taipei and Beijing. The latitude at whom the mission is performed, together with the day of the year, influences the size/mass of the power generation system. Effectively, the wind speed and the solar irradiance magnitude depend on "where" and "when" the mission is performed, consequently the size/mass of the solar panel array and the required power depend on them.

The authors also investigate the technology trends in the fields of interest (for example solar-cell mass, battery efficiency, etc...) in order to determine which could be the improvements in the design of the airship.

In [14] the available methodologies for conceptual design of a solar powered stratospheric airship are analyzed. The authors propose a new methodology based on the coupling of the different available methodology.

In [15] the conceptual design of a HAPS, having a fixed wing configuration, is developed by analyzing energy balance and developing mass estimation model.

In [16] the authors compare performances and costs of several HAPS configurations for two missions: hurricane science and communications relay. HTA and LTA, powered by a consumable fuel or solar regenerative (SR) propulsion system are analyzed. A hybrid configuration (with 10% of lift generated by aerodynamic), powered by solar regenerative fuel cell, is examined.

The authors conclude their work asserting that the best configuration is an LTA powered primarily by consumable fuel associated with solar energy, because LTA have greater endurance but solar energy, as only power source, could not provide sufficient energy even in the most favorable day-night cycle of the required mission period.

This work is ten years old, nowadays technology innovations in the field of solar cells and battery have enabled longer endurance flights powered only by solar energy (in 2010 Zephyr HALE UAV obtained the duration record in stratosphere [17]).

2 METHODOLOGY

As stated, the aim of this work is to carry on a conceptual design of stratospheric long endurance platforms having different configurations in order to show that the best solution in terms of minimum mass, required power and volume and safety is represented by the hybrid platform.

Specifically, we have investigated the following configurations:

- Solar Powered Airship ("Fig. 1")
- Solar Powered Flying Wing ("Fig. 2")
- Solar Powered Hybrid platform with AR=10 ("Fig. 3")
- Solar Powered Three-lobed hybrid airship (FR=3) ("Fig. 4")

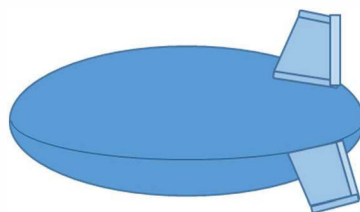


Figure 1: Airship

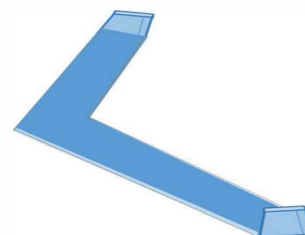


Figure 2: Flying Wing

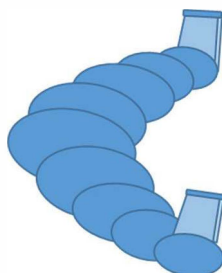


Figure 3: Hybrid Platform with AR=10

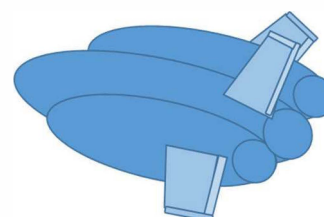


Figure 4 Three-lobed hybrid airship

A hybrid platform balances its weight by lift (aerodynamically generated) and buoyancy. In this paper, we have considered the helium as lifting gas for hybrid platforms and the airship. Concerning hybrid platforms, we have analyzed two configurations. The first one, identified by the aspect ratio equal to ten, has a shape more similar to a flying wing, while the second one has an airship-like shape; in fact, we have used the fineness ratio to describe proportions between in-plane dimensions. For each one of this configuration we have defined a design process.

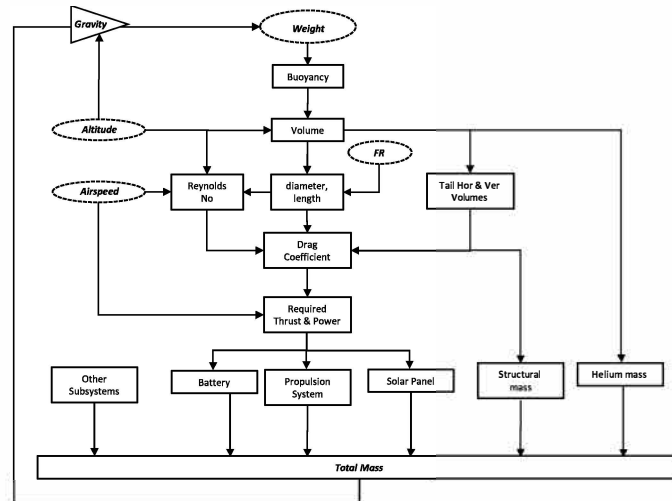


Figure 5: Conceptual design process for a solar powered airship

In "Fig. 5", we reported the process followed for the conceptual design of the airship. The input parameters are the initial guess weight, the flight altitude, the airspeed and the fineness ratio.

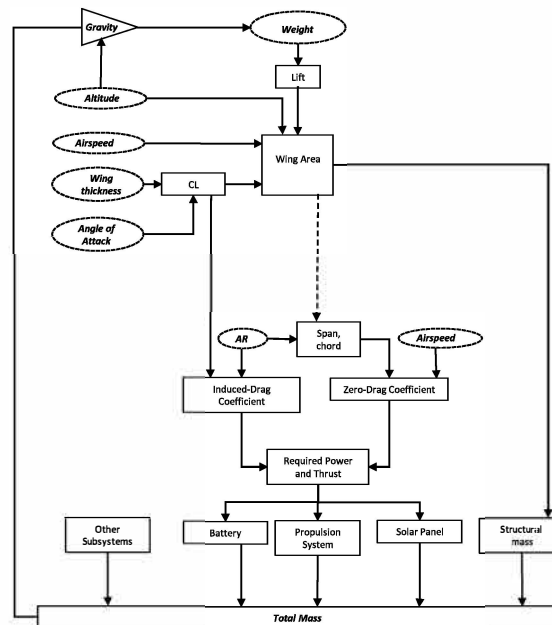


Figure 6: Conceptual design process for a solar powered flying wing

In the case of the flying wing conceptual design, the process is reported in "Fig. 6". In this case, the input parameters are the initial guess weight, the cruise altitude, the airspeed, the aspect ratio and chord thickness. In a more detailed design, the chord thickness can be set depending on both: the required storage area for batteries, avionic, other equipment and the required structural stiffness.

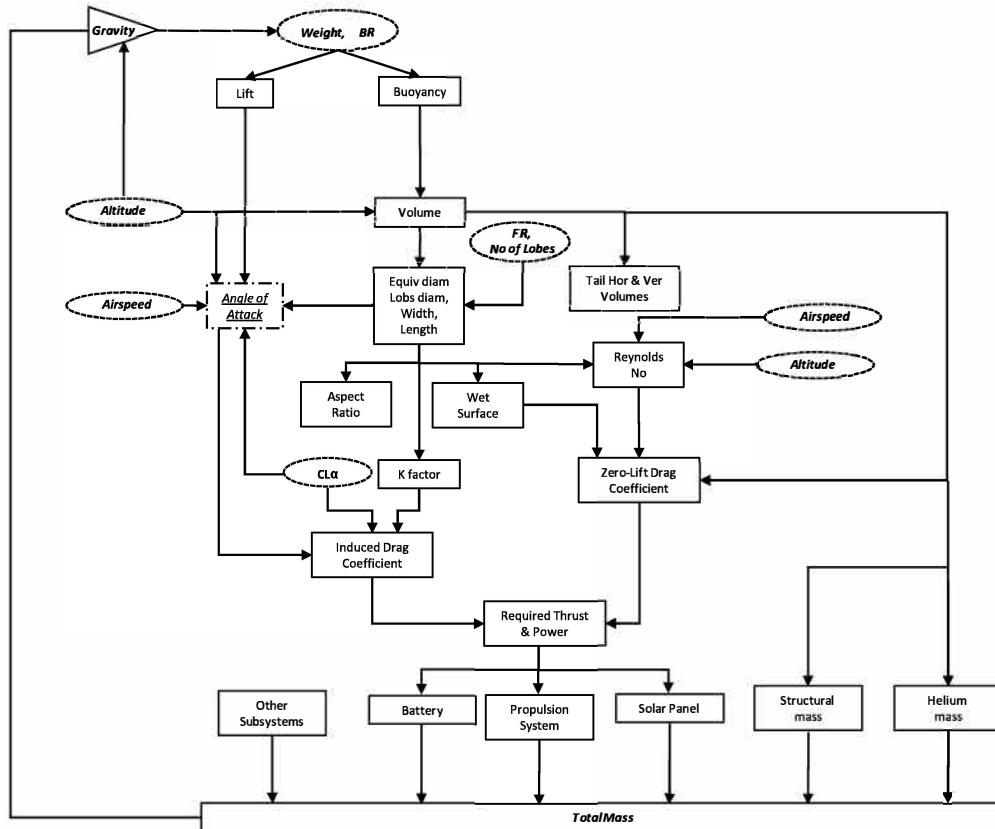


Figure 7: Conceptual design process of a solar powered hybrid three-lobed airship

In the case of a hybrid three-lobed airship, the conceptual design process, reported in "Fig. 7", is more complex because of the presence of the aerodynamic and aerostatic modules, which have different requirements. In this case, the input parameters are always the initial guess weight, the altitude and the airspeed, the fineness ratio as for the airship and some specific parameters as the buoyancy ratio, the number of lobes (three lobes for this study) and the lift coefficient curve slope. The required buoyancy, calculated as product between the weight and the buoyancy ratio, determines the volume and consequently the other geometric parameters. We have not directly used the required lift to size the platform, but it is considered a constraint. The geometry (particularly, the available reference area useful to generate lift), associated with the lift curve slope and the desired airspeed, determines the angle of attack to generate the required lift. The angle of attack shall be less than a predefined threshold in order to make flight feasible. This choice influences the conceptual design optimization in terms of the optimal buoyancy ratio, because we discard buoyancy ratios corresponding to an angle of attack greater than this threshold. The hybrid airship has a wide in-plane area but, compared to a wing which typically has a span several times greater than its chord, its ability to generate aerodynamic lift is limited because its greater dimension is in the direction of the airstream (the length is greater than the width). Using typical wing's parameters, an airship is characterized by a low aspect ratio (less than unity). If the required lift was used to design the surface, the hybrid airship should have a greater volume, more than is required to generate the required buoyancy, thus a certain volume should be occupied by ballonets with the negative consequence of a greater final weight.

Unlike the simple airship configuration, in the case of a hybrid airship the induced drag shall be also taken into account.

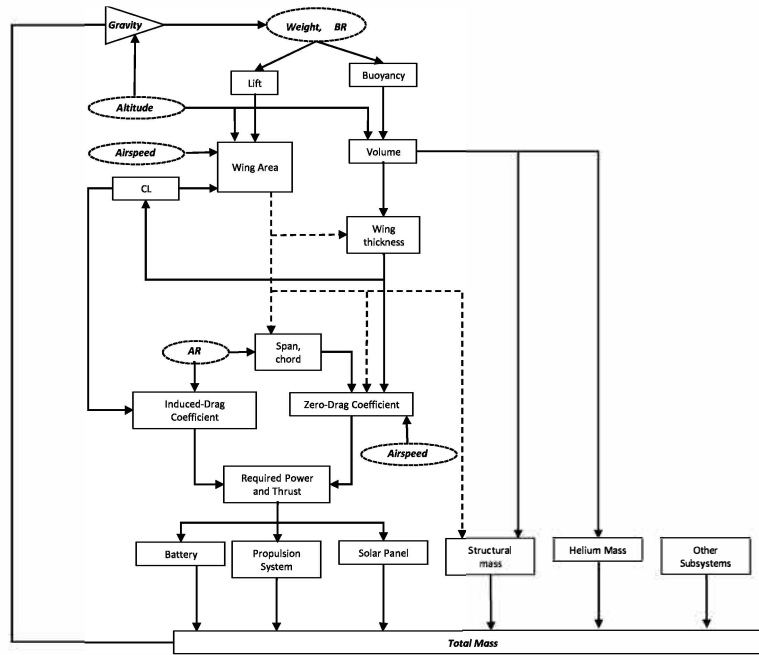


Figure 8: Conceptual design process of a solar powered hybrid platform with AR=10

In "Fig. 8", we reported the workflow for a hybrid platform having higher aspect ratio. This configuration is more similar, for example, to a hybrid flying wing which balances the gross weight (due to its structure, equipment and payload) using aerostatic (buoyancy) and aerodynamic lift. In this case, the required lift is a key parameter in the sizing process because it determines the in-plane area while the buoyancy determines the volume and consequently the profile thickness. We have included a first iterative loop to determine the platform in-plane area and volume, because the profile thickness influences the lift curve slope and thus the wing in-plane area.

3 RESULTS AND DISCUSSION

In order to select the best configuration, we have investigated the following case study: stratospheric platform flying in the skies over southern Italy, carrying a payload of 100 kg. The mission of this platform consists in maintaining station over a predefined area.

The geographical position of the platform determines statistics for wind intensity and the solar radiation, which are important factor in the platform's sizing process. Main parameters used in our calculations are summarized in "Table 1".

Table 1: Mission Parameters

Payload	100 Kg
Location	Southern Italy
Altitude	20000 m
Energy System	Rechargeable Batteries with Solar Energy
Power	Electric Engines
Airspeed	16 m/sec
Night Duration	15 h
Mass category	less than 1000 Kg

The desired airspeed has been set on the basis of wind statistics around the year at the selected altitude in Southern Italy. The mass category has been set equal to less than 1000 kg, which is considered achievable based on current prototypes and commercial platforms.

In the case of the three-lobed hybrid airship and pure airship, we have determined the aerodynamic coefficients, as well as, mass predictions for various subsystems, by semi-empirical formulation as suggested in [18], while, for the flying wing configuration and for the hybrid platform with higher aspect ratio, using semi-empirical formulation described in [19], [20] and [21]. We have updated the mass prediction models reported in [21], to take into account progress in aerospace structures and materials, battery capacity and solar panel density.

For this analysis, we have taken into account the properties and characteristics GaAs-based solar cells, while concerning the energy storage system, we have considered the properties of lithium-sulfur batteries as reference value, because they have a higher energy density. Batteries based on this technology have also powered the Airbus Zephyr high altitude pseudo-satellite.

We have firstly investigated the airship configuration. We have reported the results in "Table 2".

Table 2: Final results for the airship configuration

Mass [kg]	Volume [m ³]	Power [kW]
615	6910	3.6

In the case of the flying wing, the constraint on the final mass, limits the minimum airspeed. In fact, the desired airspeed (equal to 16 m/sec) is unfeasible with a platform having a mass less than 1000 kg. Thus, we have not further investigated the flying wing configuration.

In the "Fig. 9" and "Fig. 10" we have reported the mass, the required power and the volume for a hybrid three-lobed airship carrying 100 kg of payload. It is interesting to note that increasing the buoyancy ratio, the total mass and required power decrease as a monotonic function because lift induced drag decreases, but the volume has a minimum at BR equal to 0.8. The optimal buoyancy ratio is a compromise between the need to reduce the mass and the required power, avoiding an excessive increase of the volume.

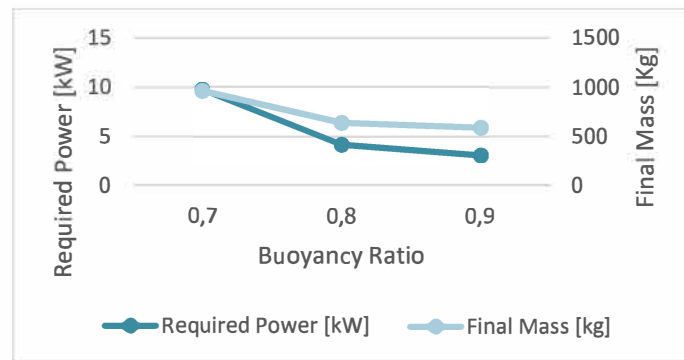


Figure 9: Final Mass and Required Power for the three-lobed hybrid airship

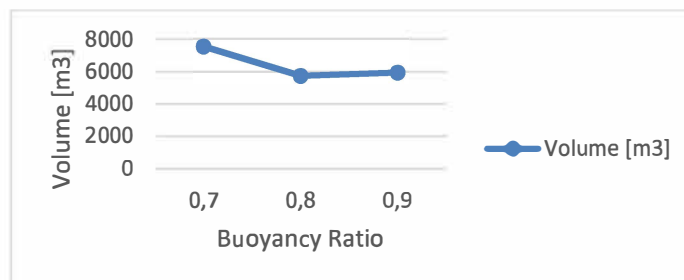


Figure 10: Volume for the three-lobed hybrid airship

The final mass, the required power and the volume of the hybrid three-lobed airship tend to the values of the pure airship when the BR approximates to the unity.

Table 3: Final results for the three-lobed hybrid airship

BR	Mass [kg]	Volume [m ³]	Power [kW]
0.8	640	5750	4.3

In the case of the stratospheric hybrid platform having $AR=10$, the optimal BR ("Fig. 11" and "Fig. 12"), in terms of required power and final mass, is equal to 0.2. The volume also remain limited for this buoyancy ratio.

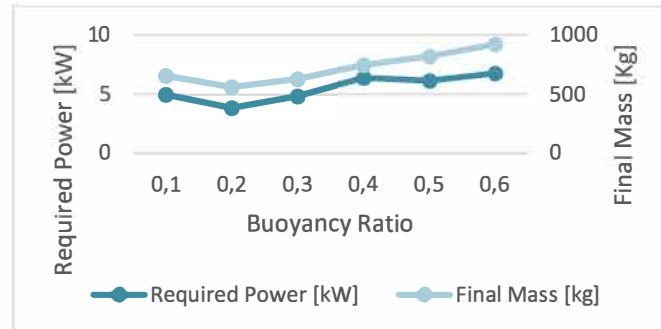


Figure 11: Final Mass and Required Power for the $AR=10$ stratospheric hybrid platform

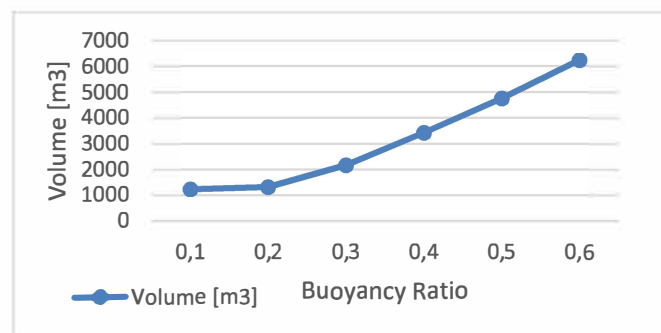


Figure 12: Volume for the $AR=10$ stratospheric hybrid platform

Comparing the optimal buoyancy ratios of the two hybrid platform configurations (three-lobed airship and $AR=10$ platform), two different behaviors emerge. Indeed, the optimal BR is strictly related to the chosen shape. This is an important result, because in previous works, the shape of the platform has never been considered a determining factor in the optimization process of the buoyancy ratio. The three-lobed hybrid airship has a limited capability to generate lift in spite of its wide in-plane area. This is due to its geometry, because the length, (which is in the direction of the airspeed), is longer than the width (which is in the direction orthogonal to the airspeed). Using the airplane wings terminology, it is like the three-lobed hybrid airship had a chord longer than its wingspan. A request of more lift means longer width and consequently longer length, greater mass and required power. Therefore, in the case of three-lobed airships the optimal BR has a high value (which means low percentage of lift) in order to limit the final mass, volume and required power.

In the case of the $AR=10$ platform, we have, on the contrary, the optimal BR is considerably lower than in the previous case. This is due to the higher capability to generate lift of a platform with a sufficiently high aspect ratio.

Table 4: Final results for the $AR=10$ stratospheric hybrid platform

BR	Mass [kg]	Volume [m³]	Power [kW]
0.2	580	1700	4.3

Concerning safety aspects, the flying-wing platform, in case of a catastrophic failure could fall without control. In case of airship catastrophic failure, the fall could get slower than in the previous case (consequently, the kinetic energy would be lower too) because of the remaining buoyancy and the greater aerodynamic drag. In fact, the helium contained in the envelope, is not instantaneously expelled. Moreover, this configuration has a bigger external area, which would be subject to a greater aerodynamic drag during a hypothetical fall.

Thus, hybrid platforms have the advantages of the airship because they have greater external area and buoyancy; moreover, they could be aerodynamically controlled in case of helium losses (because the shape could be not instantaneously lost).

We have not included the design of ballonets for the platforms including buoyancy. This choice is motivated by the expected operation mode, because the platform will be operated at a quasi-constant altitude and internal pressure changes will be absorbed by structural elements.

4 CONCLUSIONS

In this paper we have presented four processes for the conceptual design of a stratospheric platform based on four different configurations. Specifically, we have analyzed the following configurations: flying-wing, airship, two hybrid configurations (the term "hybrid" is here used to indicate that the weight is balanced by aerodynamic and aerostatic forces). We have used the proposed processes in order to estimate mass, volume and required power for each one of the configurations under some specified hypotheses. The flying wing configuration is not suitable to be used with an airspeed equal to 16 m/sec at an altitude of 20 km, because it has a mass excessively beyond the desired mass limit (1000 kg). The airship configuration offers the minimum required power, because power is required only for in-plane movements of the platform while the buoyancy balances the weight. The drawback of the airship configuration lies in the big volume, which makes difficult ground operation. The two examined hybrid configurations have two different optimal BR. The first one, having a three-lobed configuration, has an optimal BR equal to 0.8; while the second one, having the $AR=10$, has an optimal $BR = 0.2$. At the optimal BR, these two configurations have similar required power (about 4.3 kW) and comparable mass (about 600 kg). The main difference in the two configurations lies in the volume. In fact, the volume of the hybrid platform with $AR=10$ is one third of the volume requested by the other hybrid configuration and by the airship.

This is a great advantage, which, even though the little handicap in terms of required power, makes this configuration more suitable to the stratospheric flight within our hypotheses.

Moreover, a hybrid platform has a greater safety because of less kinetic energy during a hypothetical fall and a residual possibility to control using aerodynamic or aerostatic forces.

Future works will concern a more detailed assessment of the geometry, mass and power budget for the analyzed configurations and the definition of operational aspects.

REFERENCES

1. Modica, G.D, T. Nehrkorn, T. Meyers; An investigation of stratospheric winds support of the High Altitude Airship; Preprints, 13th Conf. on Aviation Range and Aerospace Meteorology; AMS; New Orleans; LA; 2007
2. F Lega, M., Ferrara, C., Persechino, & G., Bishop, P.; Remote sensing in environmental police investigations: aerial platforms and an innovative application of thermography to detect several illegal activities; Environmental Monitoring and Assessment journal; Volume 186; Issue 12; pp 8291–8301; 2014; <http://dx.doi.org/10.1007/s10661-014-4003-3>
3. Lega, M., Kosmatka, J., Ferrara, C., Russo, F., Napoli, R. & Persechino, G.; Using advanced aerial platforms and infrared thermography to track environmental contamination; Environmental Forensics; 13(4); pp. 332–338, 2012; <http://dx.doi.org/10.1080/15275922.2012.729002>
4. Quaranta, V., Ameduri, S., Tomassetti, G., Persechino, G., Lega, M.; Acoustic Antenna on Aerial Platforms: the Advanced Hybrid Airship, a Proof of Concept; proceedings of the 2012 Euronoise conference, Prague, 2012
5. D. S. Ilcev and S. S. Sibiya; Weather observation via stratospheric platform stations; *2015 IST-Africa Conference*, Lilongwe; 2015; pp. 1-12; doi: 10.1109/ISTAFRICA.2015.7190585
6. O. García-Crespillo, E. Nossek, A. Winterstein, B. Belabbas and M. Meurer; Use of High Altitude Platform Systems to augment ground based APNT systems; *2015 IEEE/AIAA 34th Digital Avionics Systems Conference (DASC)*; Prague; 2015; pp. 2A3-1-2A3-9; doi: 10.1109/DASC.2015.7311358
7. Z. Michael, K. Vitaliy, I. Michael, N. Teodor, K. Serhii and C. Leonid; Prospects of using of aerial stratospheric telecommunication systems"; *2016 International Conference Radio Electronics & Info Communications (UkrMiCo)*; Kiev; 2016; pp. 1-4; doi: 10.1109/UkrMiCo.2016.7739636
8. Flavio Araripe d'Oliveira, Francisco Cristovão Lourenço de Melo, Tessaleno Campos Devezas; 2016; "High-Altitude Platforms — Present Situation and Technology Trends"; J. Aerosp. Technol. Manag.; São José dos Campos; Vol.8; No 3; pp.249-262; DOI: 10.5028/jatm.v8i3.699



9. Aman Raj Verma, K. Kiran Sagar, and Pankaj Priyadarshi; 2014; "Optimum Buoyant and Aerodynamic Lift for a Lifting-Body Hybrid Airship"; Journal of Aircraft; Vol. 51; No. 5; pp. 1345-1350; DOI: 10.2514/1.C032038
10. Guangqiang Chen, Bingyan Chen, Pengfei Li, Peng Bai, Chunqun Ji; 2014; "Study of Aerodynamic Configuration Design and wind tunnel test for Solar powered Buoyancy-lifting Vehicle in the Near-space"; Proceedings of the "APISAT2014"; Asia-Pacific International Symposium on Aerospace Technology; DOI: 10.1016/j.proeng.2014.12.509
11. Jeremy Agte, Thomas Gan, Fabrice Kunzi, Andrew March, Sho Sato, Brandon Suarez and Brian Yutko; 2010; "Conceptual Design of a Hybrid Lift Airship for Intra-regional Flexible Access Transport"; proceedings of the 48th AIAA Aerospace Sciences Meeting Including the New Horizons Forum and Aerospace Exposition; 4 - 7 January 2010; Orlando; Florida; doi.org/10.2514/6.2010-1391
12. Anwar U. Haque, Waqar Asrar, Ashraf A. Omar, Erwin Sulaeman, and Jaffar M. Ali; 2014; "Conceptual Design of a Winged Hybrid Airship"; 21st AIAA Lighter-Than-Air Systems Technology Conference; AIAA AVIATION Forum; (AIAA 2014-2710); doi.org/10.2514/6.2014-2710
13. Qi Chen, Ming Zhu, Kang-wen Sun; 2011; "Analysis to Effects on Conceptual Parameters of Stratospheric Airship with Specified Factors"; Journal of Computers; Vol. 6; No. 5; May 2011; DOI: 10.4304/jcp.6.5.1055-1062
14. Mohammad Irfan Alam and Rajkumar S. Pant; 2013; "A Methodology for Conceptual Design and Optimization of a High Altitude Airship"; Proceedings of the AIAA Lighter-Than-Air Systems Technology (LTA) Conference 25-28 March 2013; Daytona Beach; Florida; DOI: 10.2514/6.2013-1363
15. Gao Xian-Zhong, Hou Zhong-Xi, Guo Zheng, Zhu Xiong-Feng, Liu Jian-Xia, Chen Xiao-Qian; 2013; "Parameters determination for concept design of solar-powered, high-altitude long-endurance UAV"; Aircraft Engineering and Aerospace Technology; Vol. 85; Iss 4; pp. 293 – 303; doi.org/10.1108/AEAT-Jan-2012-0011
16. Craig Nickol, Mark Guynn, Lisa Kohout, and Tom Ozoroski; 2007; "High Altitude Long Endurance Air Vehicle Analysis of Alternatives and Technology Requirements Development"; Proceedings of the 45th AIAA Aerospace Sciences Meeting and Exhibit; Reno; 8-11 January 2007; doi.org/10.2514/6.2007-1050
17. [http://www.guinnessworldrecords.com/world-records/longest-flight-by-solar-powered-spyplane-\(uav\)](http://www.guinnessworldrecords.com/world-records/longest-flight-by-solar-powered-spyplane-(uav))
18. Grant E. Carichner, Leland M. Nicolai; 2013; "Fundamentals of Aircraft and Airship Design"; AIAA Education Series; 2013
19. S.F. Hoerner ;1965;"Fluid-Dynamic Drag".
20. Raymond F. Anderson, "Determination of the characteristics of tapered wings"; NACA Report No. 572
21. André Noth; "Design of Solar Powered Airplane for Continuous Flight", DISS.ETH No. 18010; September 2008; http://www.sky-sailor.ethz.ch/docs/Thesis_No_2008.pdf



MDO Architectures Comparison on Analytical Test Case and Aerostructural Aircraft System Design Problem

Francesco Torrigiani

*DLR, German Aerospace Center, Systems Architectures in Aeronautics
Research Engineer
Hein-Saß-Weg 22, 21129 Hamburg
Francesco.Torrighiani@dlr.de*

Pier Davide Ciampa

*DLR, German Aerospace Center, Systems Architectures in Aeronautics
Group Leader
Pier.Ciampa@dlr.de*

ABSTRACT

An aircraft system design problem is intrinsically a multidisciplinary problem. If the design configuration is unconventional, sound low-fidelity analysis methods are not available. Complex high-fidelity tools are often the only solution to obtain reliable results, and for these reasons designers are deeply interested in the interactions and organization of these tools. Inside a Multidisciplinary Design Optimization (MDO) process, different architectures are possible. Analysis and comparison of six MDO architectures is the aim of this paper. The considered architectures are All-At-Once (AAO), Simultaneous Analysis and Design (SAND), Individual Discipline Feasible (IDF), Multidisciplinary Feasible (MDF), Collaborative Optimization (CO), Bi-Level Integrated System Synthesis (BLISS). The comparison is conducted on mathematical benchmark cases and on a simplified aerostructural aircraft design problem. Results expressed in a unified nomenclature are available as open source. Further, the CMDOWS (Common MDO Workflow Schema) developed in the AGILE project is used to translate the neutral description of the MDO problem into an executable implementation and it will be released as open source too. The aim is to promote the discussion on MDO architectures within the MDO research community.

KEYWORDS: *Multidisciplinary Design Optimization (MDO), MDF, IDF, CO, CMDOWS, AGILE, BLISS, SAND, AAO*



Knowledge-based automatic Airframe Design using CPACS

J.-N. Walther

German Aerospace Center (DLR), Air Transportation Systems (LY)

Research Associate

Blohmstraße 20, 21079 Hamburg, Germany

jan-niclas.walther@dlr.de

P. D. Ciampa

German Aerospace Center (DLR), Air Transportation Systems (LY)

Research Associate and Team Lead MDO Group

ABSTRACT

The CPACS data format [1, 2] has long been established as the primary means of data exchange in preliminary aircraft design projects within DLR. As described by Scherer et al. [3], it contains a wide range of options for describing the structural layout of a design including frames and stringers, floors, bulkheads, etc. Based on these descriptions, several finite element model generators comparable to the one described by Walther et al. [4] have been implemented, which can provide detailed computational structural models of a given design. However, all model generators require the information on the structural layout to be available in CPACS upfront.

Within a larger aircraft design context, this necessitates the augmentation of the description of the structure to a given plain aircraft geometry. So far, this has been accomplished through a manual process, which not only results in an increased risk of errors, but also prohibits the exposure of parameters to a larger multidisciplinary optimization.

In the presented paper, a newly developed knowledge-based airframe augmentation module will be introduced. Implemented in Python, it provides methods to automatically initialize a full structural layout on a given CPACS geometry, based on a manageable number of control parameters. In addition to an outline of the governing design rules, several application cases will also be given.

KEYWORDS: CPACS; preliminary aircraft design; fuselage structures; knowledge based design

Enhanced Kinematics Calculation for an Online Trajectory Generation Module

Patrick Piprek, Volker Schneider, Vincent Fafard, Simon P. Schatz, Christoph Dörhöfer, Patrick J. Lauffs, Lars Peter, and Florian Holzapfel

*Institute of Flight System Dynamics
Technische Universität München
Boltzmannstraße 15, 85748 Garching bei München
{patrick.piprek, volker.schneider, simon.p.schatz, florian.holzapfel}@tum.de
fafardv@in.tum.de*

ABSTRACT

This paper presents an extension to a previously published method by the authors, which implemented clothoids within an integrated flight guidance and control system with independent speed control. This method was then used in real flight tests of a highly-automated CS-23 aircraft. The method provided a steady entry and exit manoeuvre to a turn. Now, the aim of this paper is to show an enhancement of the previously published algorithm in the context of the trajectory reference point kinematics calculation for the clothoid manoeuvre. Nonetheless, the proposed methodology remains applicable for a variety of other trajectory curves (e.g. splines). The improved reference point calculation yields a smoother command for the trajectory controller, which uses 2nd order error dynamics. To illustrate the enhancements by the proposed algorithm, exhibits from a high-fidelity simulation framework of the CS-23 aircraft are depicted. Additionally, results of a flight test with the CS-23 aircraft are shown, discussed, and related to the previously published results. Furthermore, a worst-case approximation, in a Monte-Carlo like approach, of the maximal projection error for the proposed method is presented.

KEYWORDS: *trajectory generation, flight path following, clothoids, orthogonal projection, waypoint flying*

Detecting Future Potentials for Step-change Innovation in Aeronautics – Progress and Challenges

L. Koops, A. Sizmann

Bauhaus Luftfahrt e.V

Future Technologies and Ecology of Aviation

Willy-Messerschmitt-Str. 1, 82024 Taufkirchen, Germany

lily.koops@bauhaus-luftfahrt.net

ABSTRACT

Prospective overall concepts for aeronautics require a fundamental understanding of future technology options, their physical boundaries and technical challenges. For this reason, Bauhaus Luftfahrt (BHL) has established the “technology radar” based on future technology analysis in the domains of energy, materials, photonics, sensors and information. It acts as an antenna for the early detection of innovation potentials and brings design-driving and disruptive developments from all disciplines into the focus of aviation. In this contribution, we present progress and challenges of future technology analysis in general and in particular of the proprietary processes at BHL. Using example cases, such as substitution of fossil by renewable electric energy, and relevance and mitigation potentials of cosmic radiation exposure in future aviation, we demonstrate the value of the four cornerstones of the above-mentioned “future technology analysis” methodology and comment on derived application potentials for aeronautics.

KEYWORDS: *electric aircraft, electro-fuel, radiation shielding, hydrogen, hypersonic flight*

NOMENCLATURE

AIRCAT - Assessment of the Impact of Radically
Climate-Friendly Aviation Technologies

bpd - barrels per day

FTA - future technology analysis

GHG - greenhouse gas

GtL - Gas-to-Liquid

ICRP - International Commission on
Radiological Protection

LAPCAT - Long-Term Advanced Propulsion
Concepts and Technologies (EU project)

LH₂ - liquid (cryogenic) hydrogen

NCRP - National Council on Radiation Protection
and Measurements

PtL - Power-to-Liquid

StL - Sunlight-to-Liquid

Φ – geographic latitude

1 INTRODUCTION

1.1 The need for future technology analysis

“More than anything else, technology creates our world” writes W. B. Arthur in his book on “The Nature of Technology” and adds that “it creates our wealth, our economy, our very way of being” [1]. In fact, F. P. Boer says in his book on risk-adjusted “Valuation of Technology” that the “creation of wealth through technological innovation is one of the most important economic phenomena of the modern world”, yet “technological innovation is a notoriously risky and competitive business” [2]. Obviously, innovation leaders with very long product life-cycles require long-term foresight capabilities to successfully navigate this risky territory. It is our mission at Bauhaus Luftfahrt to research long-term future mobility solutions in order to provide best-possible future-proof guidance in the “fog” of the unknown world of 2035 and beyond. Innovation leaders, policy makers and the public in general require this foresight in order to make informed decisions within the constraints of the inherent uncertainty in the nature of science, innovation and futurist foresight.

A high priority therefore is future technology scouting, analysis and monitoring. How can we identify future technologies, determine their future innovation potentials, and do this holistically for a long-term time scale? Here we present an approach that works for a wide scope of technologies from component

level to integrated system level. This paper presents progress and challenges of future technology analysis in general and in particular of the gained knowledge of continuous conducted proprietary processes.

1.2 Structure and outline

The paper is organized as follows:

Section 2 presents the challenges and context in which the methodology for future technology analysis (FTA) is developed. The challenge is to practice a scientific futurist approach instead of prediction, in the same sense that e.g. past history is subject to high-standard of scientific research. The challenge is also to understand the relevance of scientific and technological advancements, and their combinatorial possibilities outside the classical aviation disciplines. The context of FTA is also defined by the two forces of "push" and "pull". Breakthrough achievements in science, in technology development and in combinatorial innovation ("push") as well as ambitious long-term targets for aviation ("pull") require future technology analysis.

Section 3 outlines the four cornerstones of Bauhaus Luftfahrt's approach to FTA. Section 4 illustrates selected aspects of FTA using two example cases, the long-term perspectives of introducing renewable electric energy into the aviation system, and relevance and mitigation potentials of cosmic radiation exposure in future aviation. We demonstrate the value of the four cornerstones of BHL's "future technology analysis" methodology and comment on derived application potentials for aeronautics. The final Section 5 concludes the paper with a summary.

2 CHALLENGE AND CONTEXT OF FUTURE TECHNOLOGY ANALYSIS

2.1 Future performance potentials versus future performance prediction

Anticipating the future is a key element of strategic decision-making, of securing competitive advantage and of circum-navigating potential threats. However, the notion of correctly anticipating the future, especially step-change innovation or long-term perspectives, from present knowledge is an illusion. Before presenting progress and challenges of future technology analysis in aeronautics, we accept two seemingly contrasting notions, firstly, that of fundamental unpredictability of the future and secondly, that of sufficiently robust insights into the long-term future resulting from in-depth analysis instead of prediction, forecast or trend extrapolation.

The first notion of unpredictability accepts that there exist no "hidden indicators" that accurately predict step-change and/or long-term forecasts. The illusion of predictability may have several roots. For example, Moore's Law of 1959 was based on Gordon Moore's observation at that time [3] and had no proof of long-term future technology potentials when formulated. It was an educated guess based on technology history and extrapolation rather than the result of a technology analysis of the long-term future. Still it is viewed by some as a reliable method of predicting future trends and is used for the semiconductor industry's strategic roadmap [3], thus having attributes of a self-fulfilling prophecy. However, mechanisms of indeterminism in complex or in strongly coupled systems such as modelled by W. B. Arthur showed that technological development and returns in the economy including random events, amplified by positive feedback through increasing economic returns, leads to a probabilistic selection of the outcome over time [1]. There is abundant proof of the impossibility and failure to predict the future.

The second notion says that there are scientifically sound approaches that produce useful cognition about the long-term future, that provide guidance in strategic decision-making. Leaving aside impossible prediction, there are indeed several other types of possible and useful approaches to "future management", e.g. by researching future possibilities and potentials [4]. Rather than asking which solution comes at what time in the future, which tries to elicit predictions, we must ask, what is the (physical, technical, operational, economic etc.) potential or performance limit of a set of solutions incorporating the selected technology in a distant future. Although combinatorial innovation brings about radical discontinuities that nobody could have anticipated [1], we believe that possibilities and potentials for such discontinuities can be assessed: this type of insight about the future can be derived on a scientifically sound basis [5,6]. This type of approach is presented in this paper.

Future performance potentials and/or innovation potentials represent the quantitative limits of performance by which a set of technology solutions is bound and give valuable insight. The next step is to identify the driving technology factors that exploit this performance potential. These driving factors provide guidance in the resource allocation to find promising solutions. In short, resource allocation decisions need first the knowledge of ultimate performance potentials before any particular solution involving a novel technology is developed. The “envelope” function of how far a technology solution can improve things -when fully developed- provides guidance in setting priorities for further research and development. Experience in future technology analysis shows that in the process sometimes unanticipated innovation perspectives emerge, as application case 2 in this paper presents (see .4.2)

2.2 Prerequisite for detecting future potentials for step-change innovation

There are several prerequisites to identifying significant developments that have the potential for step-change innovation [6], which are an

1. interdisciplinary team of experts who understand the relevance (for aviation) of breakthrough results in both basic science as well as in technological innovation outside the field of aviation,
2. combinatorial creativity and
3. intelligent analysis capability with a “future technology analysis” methodology.

Novel technologies may be the product of breakthrough results in “use-inspired basic science” [7] but there are other complementary origins of innovation as well. Looking deeper into the history of technological evolution, we find examples of radical innovation by a novel combination of existing technologies, or by transferring existing technologies into a new context. This is obviously true for electric Tesla cars initially being powered by laptop (mobile computing) batteries. Recent examples are electric personal air vehicles still showing the phenotype inherited from electric multi-copter drones. The first-ever production of Sunlight-to-Liquid aviation fuel [8] points at a future radical innovation potential drawing from both breakthrough science (redox reactant material and reactor design) [9,10] and a combinatorial innovation in system technology (heliostat concentrators originally used for power plants, redox reactor for syngas production and Fischer-Tropsch reactor for fuel production) [11].

In order to detect future potentials for step-change innovation in aviation, we have to look outside the classical aviation disciplines. “The change in vision” proposed by W. Brian Arthur is to shift “from seeing technologies as stand-alone objects each with a fixed purpose, to seeing them as objects that can be formed into endless new combinations” [1]. Such combinatorial vision of step-change innovation is definitely true for the fast-evolving and mere endless combinatorial possibilities in the digital age.

2.3 Technology push-pull context

Future technologies are analyzed from a push and pull perspective. The technology push originates e.g. from advances in science and technology that may have innovation potential in aviation. Technology pull is caused by “drivers of change”, opportunities and threats, such as climate change, urbanization, and digital transformation. Examples of both technology push and pull in aviation are listed in Table 1.

Technology pull arises e.g. from ambitious long-term targets for aviation that are formulated in Flightpath 2050 [12] and the roadmap documented in the Strategic Research and Innovation Agenda [13] and IATA [17]. Furthermore, there are global, European or national strategies in the domains of energy, materials, transportation, environment, information and communication technologies etc. In its early years, Bauhaus Luftfahrt identified and quantified technology pull in the topics of travel time reduction, airport capacity, electric and hybrid-electric flight, alternative energies and fuels, efficient propulsion, aerodynamic efficiency by in-flight morphing, and process and data management for aircraft design, later followed by e.g. cosmic radiation shielding, high-temperature materials, structural health monitoring, airborne broadband communication, data analytics and Artificial Intelligence (AI) support for aircraft design, manufacturing and operations. At the same time, the FTA approach has been used to identify promising technologies that push into the solution space.

Technology push arises e.g. from significant advancements in technologies such as future high-C-rate batteries, non-biogenic fuel production via Sun-to-Liquid (StL), Power-to-Liquid (PtL), graphene and nanotechnology in lightweight composite materials, additive manufacturing, broadband free-space

laser communication technology, Nobel-award-winning optical comb frequency-stabilization and blue laser diodes, quantum technologies, and cyber-physical systems, to name a few. A selection is listed in Table 1 below.

Table 1: Push/pull representation: The push created from a selection of potentially disruptive technologies, and the pull originating from ambitious targets that call for radical rather than evolutionary innovation

Energy and fuel technologies	
Push	Power-to-Liquid [14] and Sunlight-to-Liquid [15] aviation fuel technologies
	High-C-rate (charge/discharge) electrical energy storage >5 kW/kg [16]
Pull	Global fleet 50% Green House Gas (GHG) emission reduction in 2050 relative to 2005 [17]
	New aircraft 75% CO ₂ emission reduction in 2050 relative to 2000 [12,13]
	High-capacity electrical energy storage towards 1 kWh/kg [18]
Material and structure technologies	
Push	Boron-nitride nanotube composites [19-21] (see also Section 4.2)
	Graphene (R&I funded with 1 billion € by the EU Graphene Flagship Project [22])
Pull	Multifunctional lightweight materials, radiation shielding materials
	Adaptive (morphing) lightweight materials
Information, communication and sensor technologies	
Push	Cyber-physical systems (e.g. Internet of Things, ubiquitous sensors)
	European high-performance IT infrastructure (EU Cloud Initiative, ~ 2 billion € [23])
Pull	Integration of air transport and data networks and services
	Autonomous, intelligent & evolving systems

3 THE BAUHAUS LUFTFAHRT APPROACH TO FUTURE TECHNOLOGY ANALYSIS

The in-house approach to future technology analysis relies on an analytical methodology especially developed to guarantee a quantitative, reproducible and transparent assessment of innovation potentials. Its four cornerstones are:

1. Derivation of (universal) **metrics** (performance indicators, criteria, technology functions) and figures of merit to identify step-change improvements and enable the comparison of fundamentally different technologies.
2. **Benchmarking**, i.e. the derivation of performance reference values such as physical limits (e.g. Carnot efficiency) or technical targets, expressed in terms of the developed metrics to gain knowledge on what the potential performance benefit of a novel technology is.
3. Analysis of the **scaling** behavior to quantify the adaptability of an emerging technology, e.g. to the volume, size, or power requirements of the potential application. This gives insight into whether the technology may be implemented on a large scale with the same degree of efficiency or performance as on the laboratory scale.
4. **Disruptive potential** analysis, i.e. a quantification of a technology's potential to radically improve the economic or technical performance of a product, service or business model and to thereby lead to a discontinuous change.

Metrics or performance indicators and their reference values (benchmarks) need to be carefully chosen to be useful. It is common practice to take the state of the art as reference, and the results show a potential for improvement over the state of the art. We find it in most situations more useful to take the best-possible performance under idealized conditions as a benchmark for reference. This creates an envelope function in the sense of an innovation potential. If this is sufficiently promising, then particular technologies are evaluated and compared against this potential as a frame of reference.

These choices need expert knowledge because of a dilemma in achieving either objectivity and "future-proofness" or system-level decision support by (economic, utilitarian, ecological) "valuation" of technology. Physical indicators such as conversion efficiencies, energy and power densities yield rather future-proof results but need to be interpreted at system level. System-level figures of merit on the

other hand, such as direct operating cost or cost-competitiveness, life-cycle GHG emission or socio-economic impact are very useful for decision support but include assumptions on many unknown quantities and are therefore less future-proof. It is therefore important that the derivation of performance is traceable to these assumptions. Traceability allows to perform parametric studies that show the Pareto envelope, the robustness of results and the dominating "driving" performance parameters.

The in-house approach to future technology analysis was applied to determine performance potentials in the aeronautical context at various levels of complexity, from components, devices, to integrated systems, covering "physical" technologies as well as "cyber-physical" and information technologies for digital transformation. This approach led, for instance, to the early detection of future potential for step-change innovation in de-carbonization of aviation: prime examples are the BHL analyses for electric flying [18,24,25] and for non-biogenic solar fuels [26]. The methodology led to the detection of novel technical synergy potentials for sustainable flying at low cosmic radiation levels emerging for nanocomposites as new structural material [19,20] and for hydrogen as a fuel [19,27,28]

4 APPLICATION CASES

To illustrate elements of the FTA approach, we selected two key drivers, firstly, climate change mitigation and secondly, travel time reduction, and match them with selected aspects of technology analyses for decarbonizing aviation and for cross-polar as well as high-altitude hypersonic flight.

4.1 Application case 1: Decarbonizing aviation with renewable electric energy

The transformation of the energy base from fossil to renewable energy is one of the most important challenges for the aviation industry's long-term future [26]. This creates a pull for alternative fuel technologies and for electrification of aviation [25].

In the long-term future, the largest resource and the largest part of harvested renewable energy will be in the form of electrical energy [29], either from direct solar-to-electrical conversion, wind or water energy resources (although with regionally varying characteristics of sustainable scalability, supply stability and cost). Therefore, various ways of decarbonizing aviation with renewable electric energy are of particular interest.

4.1.1 Fully electric aircraft

Battery-electric flight came into the focus of future technology analysis at Bauhaus Luftfahrt in 2008, triggered by news of several scientific breakthroughs pushing the limits of battery performance. One such breakthrough was the development of nanowire silicon anodes that could reversibly expand and absorb large amounts of lithium ions with a step-change improvement in battery anode capacity [30]. At the same time, nano-coatings on certain electrode materials enhanced ion mobility and enabled extremely high power densities. The progress of electro-mobility at a macroscopic level seemed to be partly determined by progress of ion and electron mobility in the nano-world. This observation brought nanotechnology into the focus of detecting future step-change improvements in electrifying aviation.

On component level, two key performance indicators for FTA are the specific energy (energy-mass ratio) and specific power (power-mass ratio). For a useful comparison of batteries with kerosene and hydrogen, we must take the specific "useful energy" (i.e. "exergy") as a metric, not the (total) specific energy, and the relevant component or sub-system mass. This appreciates the fact that a fuel heating value has less exergy than energy content (Second Law of Thermodynamics and technical limitations) and that a battery is an integrated energy storage and electric power delivery device, corresponding to the system boundaries of a package of kerosene with turbo engine and generator or, e.g., the combination of hydrogen with a fuel cell. Alternatively, one may compare shaft power, taking the system boundaries of a battery with electric engine for comparison to kerosene with turbo-engine.

The specific energy of kerosene is 50-60 times higher than for batteries but the more appropriate specific exergy is only approximately a factor of 25 apart. This is an important insight if we take kerosene as a reference (benchmark) value. Future technology analysis takes results from single

electrode and cell research to determine the specific exergy values of a standard cell and its future potential [25], which is to achieve specific exergies beyond 500 to up to 800 Wh/kg. The rapid increase of specific energies for lithium batteries by an average rate of 7 % year-over-year between 1994 and 2010 is an interesting observation but extrapolation of this trend in the sense of a Moore's law for specific energy of batteries has no scientific basis, in contrast to our performance potential analysis.

At an integrated system level the evaluation of the performance indicators such as propulsive power, mass, block energy and aircraft efficiency, and their benchmarking with conventional turbo-engine systems requires modelling of optimized electric transmission cable and propulsor, design and sizing of the structural weight (growth factors), aerodynamics of integration etc. Therefore, the choice of metrics and benchmarks at higher integrated level requires cross-disciplinary competence. Significant disruptive potential in battery-operated 190-PAX transport aircraft over a 900-nm range was determined to require batteries on the order of 1.5 to 2 kWh/kg, while specific power of 1.2 kW/kg for take-off is within the performance envelope of batteries today. [18]

At an integrated global air transport system level, a key performance metric is the "CO₂ savings potential on global fleet level in 2050", with the expected fuel consumption by aviation in 2050 or in 2005 as a reference [31]. The Bauhaus Luftfahrt Ce-Liner study [18] of a fully electric aircraft with entry into service in 2035 and conservative production ramp-up assumptions showed a 3-4% CO₂ savings potential on global fleet emissions in 2050 [32,34]. The study was presented in the context of the recent "Assessment of the Impact of Radically Climate-Friendly Aviation Technologies" (AIRCAT) Workshop where an evaluation by another group based on rather optimistic assumptions of production ramp-up yielded a 12-15% CO₂ savings potential [33]. These results show that, compared to the radical progress a single fully electric aircraft represents with potentially more than 80% CO₂ savings compared to conventional aircraft, the global impact on CO₂ savings is severely limited to few percent. The reason is limited production capability, fleet growth and renewal, i.e. the relatively small number of such novel aircraft entering into operation compared to the number of conventional aircraft remaining in service. The same is true for any radical aircraft innovation, be it the introduction of fuel-cell powered aircraft using renewable hydrogen or other technology using non-drop-in fuels that cannot be retrofitted. However, if we evaluate direct operating cost in the global fleet, the performance metrics must capture aspects such as cost of electric energy and battery life, impact on local emissions (NO_x, particulate matter and noise) and corresponding airport fees, which could also enter a future analysis on CO₂ abatement cost.

In conclusion, even with step-change reduction of emissions by such radical aircraft innovation, the climate mitigation impact towards 2050 is very limited [34]. The battery is a more than adequate source of power but a very limited source energy to go the distance [35]. Therefore, today we experience two developments, firstly a strong "push" for short missions down to 30 min, driving the development of all-electric ultra-short reach personal air vehicles, and intensive research towards hybrid-electric architectures which offer a combinatorial variety of new solutions, typical for combinatorial innovation. For operating the air transport system on renewable electricity, technologies other than fully or hybrid electric motive power systems need to be considered as well.

4.1.2 Electro-fuels

An alternative path is the introduction of electrical energy in aviation via "drop-in" or "non-drop-in" electro-fuels for internal combustion engines or for fuel cells: the production of "electro-fuels" such as Power-to-Liquid (PtL) synthetic paraffinic kerosene, methane, alcohols or hydrogen. These technology options come with widely differing characteristics, to be investigated along the four cornerstones of FTA. Key performance indicators are energy conversion efficiency, land use or area-specific yield, water demand, production potential, production cost and competitiveness, specific life-cycle (well-to-wake) GHG emissions, and potential impact on global GHG emission reduction. Their definition is well developed along with their benchmark values which also have been used in multiple-criteria assessment frameworks for evaluating different paths to drop-in fuels [14,36].

There is an obvious "physical" disadvantage to overall efficiency of using electro-fuels for mobility in general. Converting electricity, which is 100% exergy, to a fuel, the heating value of which is then used to create "useful" motive power is a chain of inefficient processes – but technically speaking, for aviation

this efficiency penalty is over-compensated by the benefit of the high on-board specific energy (and exergy) of liquid hydrocarbon fuel. The extent to which these fuels will enter the aviation system strongly depends on the economic viability. This metric needs to assume a fixed spot price of fossil kerosene as a practical reference value, with the disadvantage of price volatility now and in the future.

The third cornerstone of FTA, the scaling property, is of particular interest: key performance indicators such as fuel production cost may scale favorably with plant size and cumulative production capability, due to economy-of-scale effects and learning curve effects, respectively. However, the sustainability and production potential of feedstocks, and associated cost of procurement are possible limiting effects in the net GHG emission reduction potential. This metric is linked to the specific carbon intensity of the fuel and to the scale of the production volume to satisfy the future demand of the global fleet.

At an integrated global air transport system level, the performance metrics are the CO₂ savings potential on global fleet level in 2050. Drop-in capable electro-fuels (PtL) in form of paraffinic kerosene can be introduced to the entire fleet, and can decarbonize the entire fleet with no modifications to airport infrastructure or aircraft fuel systems. Therefore, the limitations of introducing this innovation by fleet renewal and growth do not apply. Yet, the ramp-up of production capability still applies, firstly, to the feedstock renewable CO₂ from air capture (in the long term at large scale), secondly, to the provision of renewable electricity, and thirdly to the fuel production plant.

The scaling problem arises from the estimated 450-500% increase in fuel demand in 2050 compared to 2005 [31,33,34]. To reach the IATA target of 50% reduction of GHG emission in 2050 compared to 2005 approximately 90% of the CO₂ emissions (compared to conventional Jet A) need to be removed. Most renewable fuel technologies do not satisfy this condition. Power-to-Liquid (PtL) and Sunlight-to-Liquid (StL) fuels have the potential for such low values if precaution is taken to use purely renewable CO₂ and renewable primary energy [14,15], and are technically scalable to the growing demand. Even with an extremely low carbon intensity of 10%, i.e. 90% less than fossil kerosene, a 100% substitution of the estimated 570 Mt/a of fossil kerosene in 2050 would be required in order to reach the IATA target of 50% reduction relative to 2005.

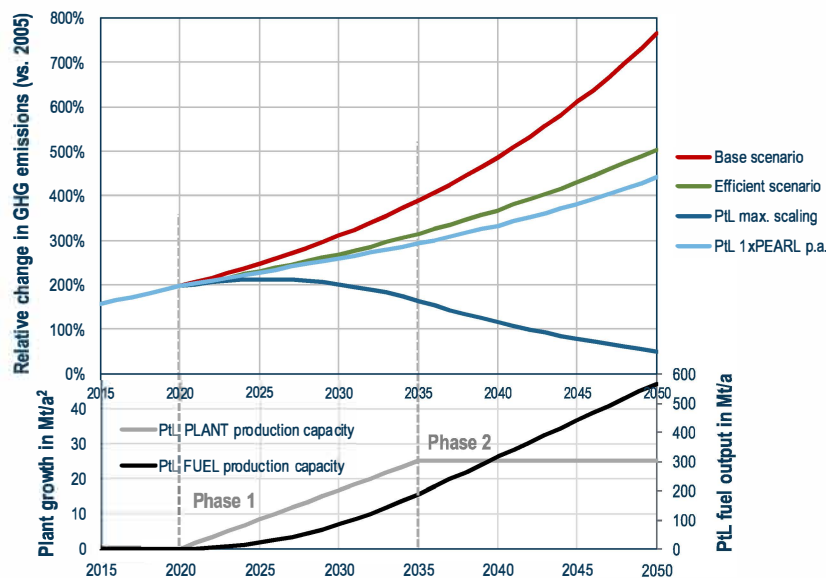


Figure 1: PtL fuel production volume and its impact on the global fleet GHG emission; in phase 1 production capacity for PtL plants is developed from zero in 2020 to a maximum value in 2035. In phase 2, PtL plants are produced at maximum rate. If that maximum rate corresponds to one PEARL-size plant deployed per year, then only 12.5% GHG emission savings are achieved in 2050. The extreme case of maximum scaling to 25.2 Mt/a² for 100% substitution of Jet A (570 Mt/a fuel output in 2050) yields a 50% emission reduction in 2050 relative to 2005.

In order to calculate the CO₂ savings potential on global fleet level we assume for simplicity that scaling solely depends on the ramp-up function of fuel production with 10% carbon intensity (90% reduction for substituted fossil kerosene). We assume that the production capability for PtL plants develops in two phases:

- In phase 1, the short- and medium-term 2020-2035 time frame, linear growth of PtL plant production capability
- In phase 2, the long-term 2035-2050 time frame, constant maximum PtL plant production capability

The linear ramp-up of production capacity for PtL plants (measured in Mt/a²), by integration over time, leads to quadratic increase in cumulative fuel production capacity (measured in Mt/a). This ramp-up-phase is assumed to start in 2020 and to reach its full PtL plant production capacity in 2035. In phase 2 from 2035 to 2050 the constant production capacity for PtL plants at this maximum value leads to a linear growth of PtL fuel production capacity.

We consider two cases: (a) the necessary scaling of production capability to reach the IATA goal in 2050 with PtL fuel alone, and (b) the CO₂ savings potential on global fleet level in 2050 if the maximum production capability for PtL plants is equivalent to the deployment of one PEARL-size Gas-to-Liquid (GtL) plant (see below) per year, including the plants for CO₂ air capture and the required renewable electricity production.

a) Scaling of PtL production capability for 100% substitution of Jet A by 2050

In order to reach a 100% substitution of 570 Mt/a Jet A by 2050, the annual production of PtL plants needs to rise from zero in 2020 to 25.2 Mt/a² in 2035, and to remain at this level to 2050. This leads to a quadratic growth of PtL fuel production capability from zero in 2020 to 190 Mt/a in 2035, followed by a linear growth to 570 Mt/a in 2050, assuming all plants are kept in operation until 2050 (no retirement of plants). The deployment rate of PtL fuel production capability of 25.2 Mt/a² translates into adding each year a PtL kerosene production capability of 538 000 bpd.

For comparison, the large GtL plant "PEARL" in Qatar (development cost around 20 billion Euro) has a production capability of 140 000 bpd liquid hydrocarbon fuel (gas-to-liquids products containing kerosene). If we assume that future Fischer-Tropsch plants produce with one liter jet fuel also 0.87 liter naphta, then a PEARL-size plant would deliver 74 900 bpd (3.50 Mt/a) jet fuel. The required deployment rate of PtL plant capacity is then equivalent to 7.2 times the PEARL plant per year. The investment cost would be far higher than 7.2 times the PEARL reference, because the production capacity for renewable CO₂ and renewable electricity has to be installed as well.

b) Scaling of PtL production capability equivalent to one PEARL-size plant per year

Assuming a maximum deployment rate of PtL plant capacity equivalent to one PEARL plant per year (in phase 2, 2035-2050), the annual production of PtL plants rises in from zero in 2020 to 3.50 Mt/a² in 2035 (in phase 1), and remains at this level to 2050 (in phase 2). This leads to a quadratic growth of PtL fuel production capability to 26.4 Mt/a in 2035, then to a linear growth to 79.2 Mt/a in 2050, an approximate PtL fuel production capability equivalent to 22.6 PEARL-size plants. With this capacity, 14% of conventional fuel can be substituted. Assuming a carbon intensity of 10% relative to conventional jet fuel, this fraction leads to a CO₂ savings potential of 12.5% on global fleet level in the long-term perspective of 2050, equivalent to a factor of 4.4 emission increase compared to 2005.

This result shows the "size" of the challenge the IATA goals present and how important a scaling assessment is for the evaluation of these novel fuel technologies in the global fleet context.

In summary, the future technology analysis of introducing renewable electric energy into the air transport system covers the entire scope from nanotechnology to emission impact at the global fleet level. Although electro-fuels are technically capable of decarbonizing air transport by 90% by 2050 (equivalent to the IATA goal of reducing to a 50% level in 2050 compared to 2005), the practical issues such as economic viability and market mechanisms as well as scaling limitations due to cost and availability of capital are likely to limit the impact. It will be interesting to compare the effort for the three strategies (PtL, hydrogen and (hybrid-) electric aircraft) of reaching a reduction target sin 2050, i.e., to include hydrogen-operated aircraft as a third alternative. For quantification of the effort one should evaluate indicators such as the overall required investments (infrastructure, supply, aircraft development, manufacturing and operations), direct operating cost (including airport fees for local

emissions) as well as a "CO₂ abatement cost" function in aviation, which is beyond the scope of this paper.

4.2 Application case 2: Cosmic radiation shielding – relevance and technical synergy potentials

Since 2011, BHL confronts future trends in air traffic with the associated increase in cosmic radiation exposure and analyzes technical synergy potentials for its mitigation [19,20,27,28]. In the following, the identified associated aviation drivers of change, their implications in terms of radiation exposure as well as significant co-benefits of future technologies for radiation shielding will be presented based on the BHL approach to future technology analysis (cf. Section 3).

4.2.1 Technology pull in response to future trends in cruising altitudes and polar route frequencies

Travel time reduction is a key driver for air traffic development. As an example, it has led to the ever-increasing number of cross-polar flights from a couple of hundreds at the turn of the millennium to more than 15,000 today. Compared to conventional routes requiring gas stops, besides flight time reduction and direct intercontinental connections, cross-polar routes allow for benefits with regards to fuel burn, associated environmental emissions and climate impact due to contrail formation [37].

Useful metrics for measuring the relevance of cross-polar flights rely on the associated Revenue Passenger Kilometers (RPK) and include in particular their growth rate and their relation to the corresponding ones for all intercontinental flights. While by now the average RPK of cross-polar flights makes up a couple of percent of that of all intercontinental flights, we find the associated average RPK growth rate to be with impressive 26% per year almost 6 times larger than for intercontinental flights. This continuing trend mirrors the rapid growth of Asian markets (with economic growth rate of 4.1% per year, outpacing the global average by 2.9 % [38]), which drives economic bonding with North America and boosts the demand for polar routes in comparison to other segments of air traffic. Furthermore, driven by a significant potential for travel-time reduction, future high-altitude, high speed air transportation concepts are being explored with cruise speeds (substantially) exceeding that of the supersonic airliner Concorde operating until 2003. For instance, by means of hypersonic flight, direct connections over the largest intercontinental distances could be realized within a few hours of travel time (cf. Figure 2) [39].



Figure 2: Representative flight trajectories for the baseline mission Brussels to Sydney of the EU-funded LAPCAT study [39] for a route with A) hypersonic cruise (at Mach 5) and B) the conventional subsonic reference.

From the confrontation of the above-mentioned on-going trends in polar route frequencies and flight altitudes with the associated risks due to cosmic radiation for aircrews, frequent flyers and avionics, Bauhaus Luftfahrt has derived a technology pull with regards to the mitigation of potential radiation exposure in future air traffic.

It stems from the fact that owing to the composition of the Earth's atmosphere and its magnetic field, up to 20-25 kilometres above ground, radiation intensities strongly grow and are maximal at the poles

[27,28,40]. Accordingly, compared with trajectories at lower latitudes, transpolar flights are generally subject to a higher effective dose rate, which serve as a metric for the biological response to ionizing radiation.

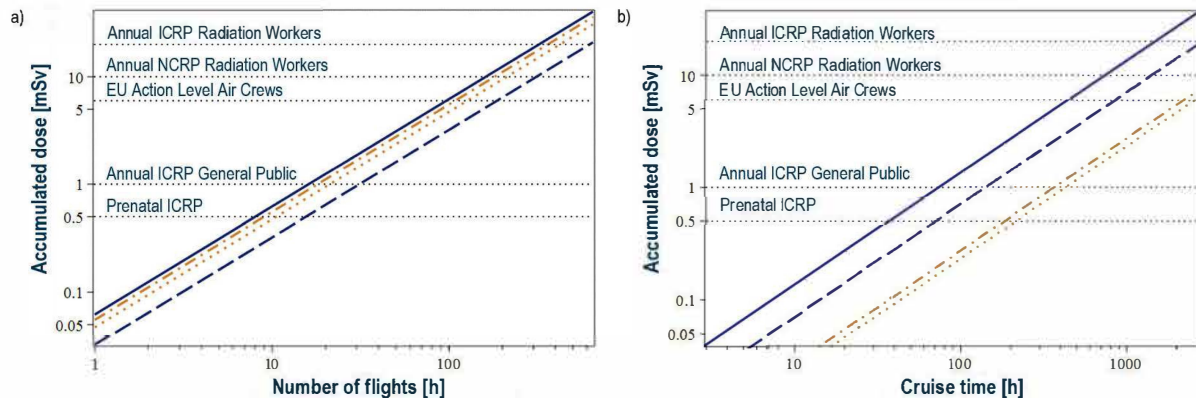


Figure 3: Accumulated dose on the trajectories A) and B) (cf. Figure 2) during solar minimum (solid and dot-dashed) and solar maximum (dashed and dotted) for a) increasing flight number and b) increasing flight hours together with the recommended annual radiation limits.

As an instructive means to evaluate the relevance of cosmic radiation in air traffic, we have calculated the dependence of the annual effective dose on the number of flights as well as on cruise time for representative subsonic and hypersonic missions for solar maximum and minimum, respectively corresponding to the two periods with respectively lowest/highest time-averaged radiation intensities in the sun's 11-year activity cycle. Selected results are plotted in Figure 3 together with various recommended annual dose limits for aircrews (classified as radiation workers) as well as for the general public [41-43]. For instance, for the general public as well as radiation workers these annual limits correspond to the equivalent of respectively about 10 and up to 200 chest-x-rays [40].

While elevated cruise speeds go along with higher flight altitudes and typically with transpolar routes, at least for passengers, the resulting higher dose rates may (partially) be traded by shorter flight and hence irradiation times, which is in particular the case during solar maximum (cf. Figure 3a)). One furthermore observes that in periods of solar minimum on the hypersonic and subsonic trajectories A) and B), allowable limits for the general public would already be surpassed by about one return-flight every 1.5 months (or correspondingly respectively 8 and 9 return-flights per year). Triggering of EU action levels for aircrews as well as excess of the recommended NCRP annual limits for radiation workers would respectively happen for about 48 and 80 return-flights per year. Yet, during solar minimum, this only corresponds to respectively 500 and 700 flight hours on trajectory A), after which the exposures on trajectory B) would still be a factor of 3 and 5 lower (cf. Figure 3b)) and thus would not be considered as critical¹. Hence, in general, for aircrews with fixed block hours, flying at higher altitudes implies an increase in annual dose, where the maximal exposure results for cruising speeds of about Mach 5 [28].

As concerns route-planning and aviation decision-making, economical penalties may in particular be caused by solar storms, when the associated solar particle events, i.e. sizeable fluxes of energetic charged particles, hit the Earth's atmosphere. While they occur at random, the frequency of aviation-relevant events varies between one every two months to one every two years with durations between a few hours up to maximum ten days with order of magnitude increased dose rates [45]. During these periods, hypersonic routes may not be served. The reason is that as opposed to subsonic airliners, re-routing to lower latitudes and altitudes in response to temporarily increased radiation levels tends to be difficult [27,28].

¹ Note that the subsonic trajectory B) proceeds at moderate latitudes and hence is subject to dose rates up to a factor of four lower than on a subsonic polar route, e.g. from Brussels to Beijing, for which recommended annual limits would be exceeded for a lower number of flight hours.

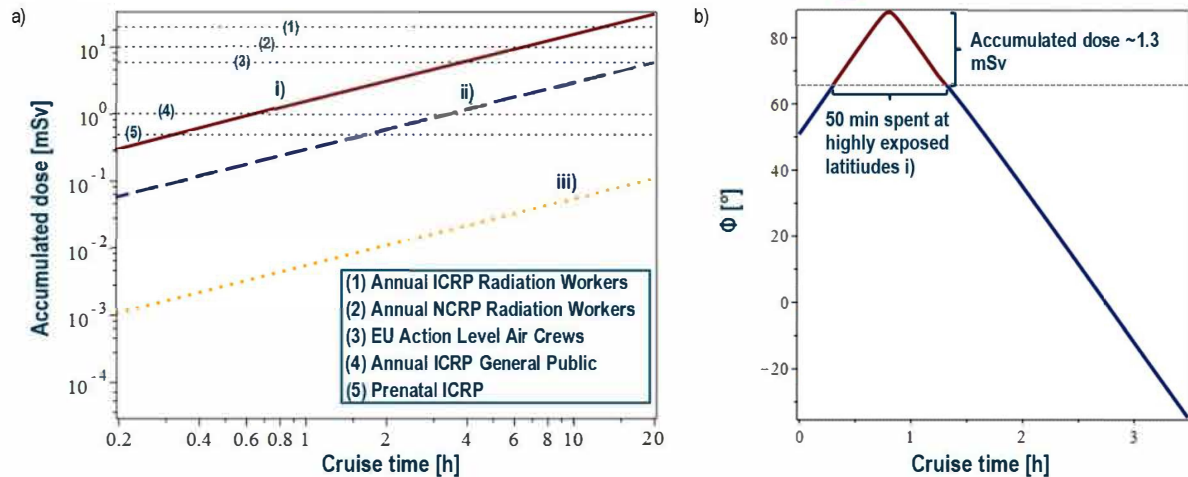


Figure 4: a) Accumulated effective dose as a function of flight time during a severe solar storm (based on event-averaged radiation rates from NASA data [40,44] for the solar particle event 3 from October 29th-October 31st 2003) calculated at 25 km altitude at different latitudes respectively for western/eastern hemisphere i) $\Phi \geq (55^\circ-65^\circ)^2 / (65^\circ-75^\circ)^1$ (solid) ii) $\Phi \approx (40^\circ-50^\circ)^1 / (50^\circ-60^\circ)^1$ (dashed) and iii) $\Phi \approx (30^\circ-40^\circ)^1 / (40^\circ-50^\circ)^1$ (dotted) compared with various radiation limits; b) geographic latitude as a function of cruise time for the baseline hypersonic mission Brussels to Sydney on route a) (cf. Figure 2) at cruise altitude and speed of respectively 25 km and Mach 5. As indicated, already the contribution of the 50-min-route segment with latitudes $\Phi \geq 65^\circ$ would lead to an accumulated effective dose of 1.3 mSv, which exceeds the allowable annual limit for the general public by 30%.

As demonstrated by Figure 4a), during a solar storm, the effective radiation dose strongly grows with geographic latitude and allowable annual limits for the general public may easily be surpassed after less than an hour of flight in the polar region (cf. also Figure 4b)).

Current research goes into the exploration of space weather indicators or precursors that may be used for reliable and timely prediction of solar storm events and their extends e.g. for real-time immediacy warning of airlines and for aviation decision-making [40,44,46,47].

In summary, fostered by future trends in polar route frequencies and cruising altitudes, synergy potentials for flying economically above and beyond Earth's natural radiation protection are in demand.

4.2.2 Technology push: identifying technical synergy potentials for radiation shielding

Effective shielding of crew or radiation workers and electronic equipment from directly and indirectly ionizing radiation provides an important challenge in various domains, including aerospace and aeronautics, medicine, nuclear power installations and accelerator facilities. The conceptual design of protection supplies against cosmic radiation for airborne applications is particularly demanding. While in this case radiation spectra extend up to very high energies, yet, lightweight material solutions with high shielding effectiveness are required. In particular, at current aircraft altitudes and up to about 25 km above ground the dominant hazard to humans and aircraft electronics emerges from cosmic neutrons [48].

² Depending on longitude and on period within solar storm event

Highly energetic, very fast neutrons could be efficiently attenuated by radiation shielding concepts involving material components that firstly guarantee an efficient slow-down and energy loss of the incident neutrons and secondly exhibit high performance in low-energy-neutron absorption – both at minimal weight penalty [19].

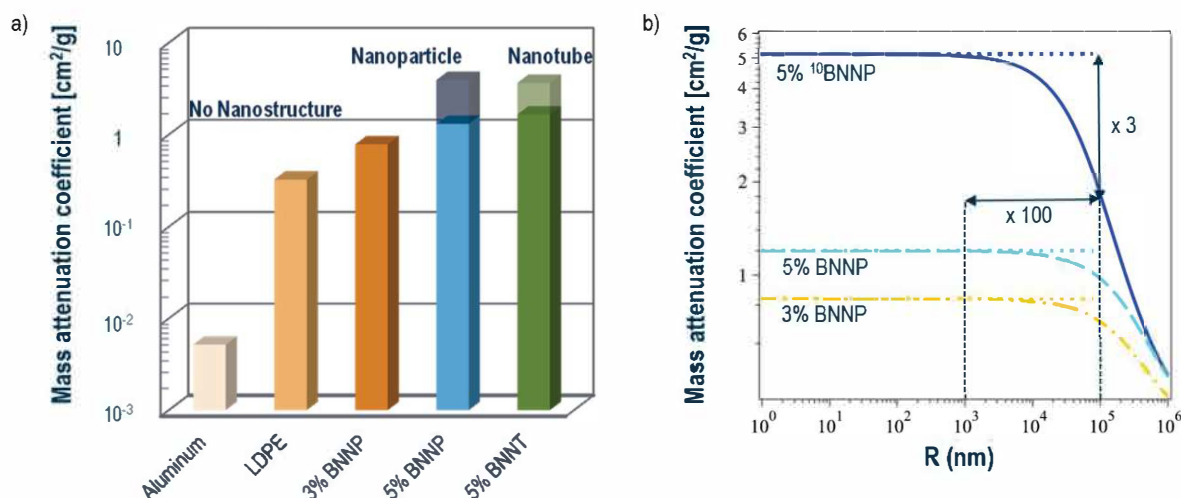


Figure 5: a) Mass attenuation coefficient as a metric for the effectiveness of low-energy-neutron shielding in relation to the mass penalty a) for Low-Density Polyethylene (LDPE), low-loading Boron Nitride Nanoparticle (BNNP) and Boron Nitride Nanotube (BNNT)/polyimide composites as well as aluminium as a benchmark; b) for polyimide composites as a function of filler particle size with varying loadings and elemental compositions (including boron nitride with isotopically enriched boron (^{10}BN) (solid)).

Key identified science and technology developments (“push”) allowing for significant improvement in radiation shielding technology possibly in combination with enhanced structural integrity result from a) novel, specifically tailored, lightweight polymeric nanocomposite materials [19,20]. Moreover, b) valuable synergy potentials for radiation shielding were found to naturally emerge from alternative propellant options for future aviation and particularly for hypersonic systems [19]. Both options may be considered separately or be combined in order to optimize shielding performance. Insights and application potentials derived from future technology analysis are presented in the following.

a) Nanocomposites – step-change improvements in radiation shielding efficiency

Nanocomposite materials, e.g. composed of a lightweight polymeric matrix and nanoscale inclusions such as particles, nanotubes or platlets, are under intense research, since a variety of exceptional physical or chemical properties emerges as soon as at least one of the characteristic dimensions of the fillers (length/width/thickness) falls in the range of 1 to 100 billionth of a meter. This may have a geometric origin (e.g. exceptionally large surface-to-volume ratio of nanostructures or large aspect ratio e.g. of nanotubes) or be due to wave-mechanical effects gaining in importance at scales close to the quantum realm ([20] and references therein). By this means, step-change improvements for instance in mechanical properties, but also in the radiation shielding ability or both (in the sense of multi-purpose material design) may be achieved compared with conventional engineering materials. For example, nanocomposites comprising boron-containing nanostructures enable efficient neutron shielding (particularly for low neutron energies) with much less volume and weight than other benchmark materials ([20] and references therein). For instance, compared with aluminum, they exhibit a two orders-of-magnitude higher mass attenuation coefficient, which can be defined as a metric for shielding performance in relation to the mass penalty (cf. Figure 5a)). As was demonstrated by one of the authors in Ref.[20], polymer composites with neutron absorbing inclusions essentially reach the physical benchmark for optimized shielding at minimal weight penalty as soon as the filler size drops within the nanometer range (cf. Figure 5b)). This complies with the physical intuition that a uniform distribution of neutron absorbing atoms throughout the composite material (best case for shielding) is achieved more efficiently by dispersing neutron absorbing nanostructures in the composite instead of e.g. larger

microstructures conventionally used. As indicated in Figure 5b), for instance, the shielding of a 5% ^{10}BN / polymer composite increases by a factor of 3, when the radius of the fillers is reduced from $100\text{ }\mu\text{m}$ ($= 10^5\text{ nm}$) by at least a factor 100 to nanometer-scale $< 1\text{ }\mu\text{m}$ ($< 10^3\text{ nm}$).

While such nanomaterials are currently investigated for applications in industries other than aviation (e.g. in aerospace or for terrestrial applications), in principle, boron-containing nanocomposites could easily be applied for instance to (parts of) the ceiling of the aircraft cabin or the cockpit in the form of a thin film, paste or foam. We verified that order-of-millimeters thin layers would lead to efficient (low-energy-)neutron absorption [19].

In order to effectively reduce the weight penalty of such a shielding solution, multifunctional application besides radiation protection – including the use for structural integrity – is conceivable. For instance, boron-nitride nanotubes embedded in a polymer matrix were shown to exhibit excellent neutron and UV shielding ability, transparency, and extremely high strength at minimal weight penalty [21].

b) Significant co-benefits of alternative fuel technologies for cosmic radiation shielding

Driven by emission as well as travel time reduction targets, alternative propellants for future aviation and for hypersonic systems are under investigation, such as for instance liquid hydrogen (LH_2) (cf. [39,49,50] and references therein). Associated challenges emerge amongst others from the required storage volume (four times larger than kerosene for the same energy content), which tends to increase the wetted area of the aircraft. Yet, the attenuation efficiency of highly energetic cosmic neutrons increases with both the dimensions and hydrogen content of the shielding assembly. Accordingly, comparing for instance conventional jet fuel with the same energy content as liquid hydrogen, a four times higher shielding volume with about 34% higher hydrogen content is at disposal for effectively reducing the energy/slowing-down highly energetic neutrons by means of elastic collisions with hydrogen nuclei (protons) [19].

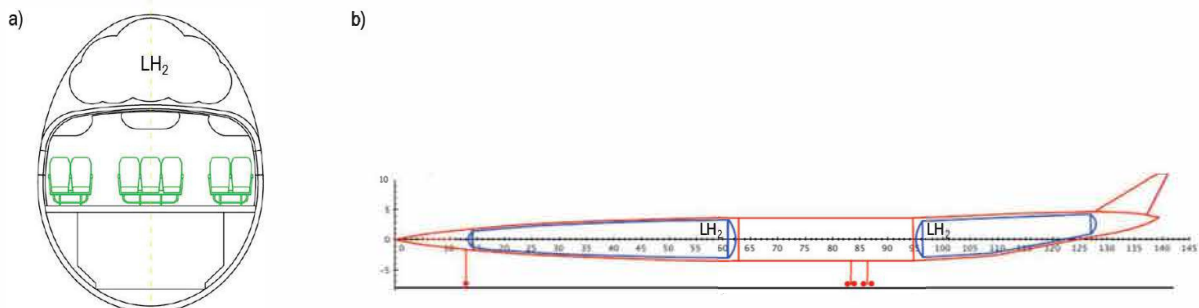


Figure 6: Considered configurations for the storage of LH_2 a) cross-sectional view of the cabin with tanks on top of the passenger cabin [49] and b) in front and behind of the passenger cabin [50].

For the determination of the dose reduction potential by means of liquid hydrogen stored in tanks, the following models/simulations are required:

- 1) Tank layout and position (e.g. on top or left and right of the passenger cabin, cf. Figure 6)
- 2) Atmospheric neutron fluence depending on neutron energy and angle as well as on altitude/latitude and on solar conditions
- 3) Energy loss in tanks as a function of neutron energy and incident angle that may be converted to effective neutron dose reduction as a function of position in the aircraft
- 4) Fractional contribution of the neutron dose to the total cosmic radiation dose at the desired altitude/latitude in dependence on solar conditions

In Table 2, we have summarized our results assuming simplified representations as well as realistic dimensions of tank layouts considered in the literature (cf. Refs. [49,50] and references therein) (a) cryoplane technology with tanks on top of a substantial fraction of the fuselage and (b) LAPCAT A2 hypersonic technology with extended tanks left and right of the passenger cabin (cf. Figure 6) for various solar conditions.

Table 2: Case-study-based reduction of the effective dose resulting from the propagation of neutrons through the LH₂ tanks (for details of the analysis cf. [19,51])

Aircraft configuration	Altitude/Latitude	Solar conditions	Maximal neutron dose reduction	Neutron contribution to total dose	Best-shielded position
a) Cryoplane	10 km/ high northern latitudes	Solar maximum	48%	~50-60%	Center of aircraft (passenger cabin)
		Solar storm	63%	~80-90%	
b) LAPCAT A2	25 km/ high northern latitudes	Solar minimum	40%	~50-60%	Next to the tanks (passenger cabin/cockpit)
		Solar storm	49%	At most few tens of percent	

Main insights of the analysis (cf. Table 2) that may give valuable support for future design considerations and for the analysis of e.g. wetted area/shielding trade-offs are

- Due to the variation of the angular distribution of neutrons with energy (roughly isotropic up to energies around tens of MeV, mostly downwards directed for higher energies [52]), the best shielding efficiency emerges for tank layouts on top of the fuselage.
- Exceptions arise during solar storms, since here the neutron spectra do not extend up to the very highest energies such that both tank configurations achieve about equally good neutron attenuation. However, the fractional contribution of the neutron effective dose to the total one decreases with increasing altitude such that case a) would allow for the highest, impressive overall dose reduction with (at most) 58%³.
- For tank layouts left and right of the passenger cabin the radiation exposure of pilots and crew is minimized, if the cockpit as well as the main residence area of the crew is as close as technically possible to the tanks.

Like in any other aircraft configuration inside of the aircraft a sizable, position dependent additional dose reduction would result from scattering processes of neutrons with other hydrogen containing material (e.g. baggage, cargo, humans) [53]. Liquid hydrogen is further expected to induce a decrease in the effective dose contribution stemming from cosmic protons. For the considered altitudes, the latter dominates that of neutrons during solar storms and falls second under any other solar condition [40]. A detailed analysis will follow in subsequent work [51].

In summary, clearly, the shielding ability diminishes with fuel-consumption and varies with position. Yet, in particular, the combination of liquid hydrogen as new propellant and neutron absorbing nanocomposites as novel structural material bears a significant potential for economic radiation protection in air traffic, while at the same time allowing for a sustainable growth of aviation with an extremely low impact on the environment.

5 CONCLUSION

We presented progress and challenges of future technology analysis in general and in particular of the proprietary processes at BHL. Using example cases, we demonstrated the value of the four cornerstones of BHL's "future technology analysis" methodology and elaborated on derived application potentials for aeronautics.

The first application case was concerned with introducing renewable electric energy for decarbonizing the air transport system. Fully electric aircraft and drop-in PtL fuels are potentially disruptive innovations. We presented selected aspects of key metrics, benchmarks and discussed the scaling properties and their impact on global GHG emission reduction by 2050. In contrast to fully-electric aircraft, electro-fuels are technically capable of decarbonizing air transport by 90% by 2050 (equivalent

³ For the cosmic neutrons generated during the solar particle event, the result assumes a similar angular distribution as that presented in Ref. [53].

to the IATA goal of reducing to a 50% level in 2050 compared to 2005). The practical scaling issues limit the impact of fully-electric aircraft to around 4% GHG reduction (up to the year 2050) and the build-out of production capability for electro-fuels seems challenging as well – adding PtL fuel production capability of 3.50 Mt/a² equivalent to one PEARL-size PtL plant every year after 2035, after a linear ramp-up of PtL plant production capability, the total impact remains at 12.5% GHG reduction in 2050. In order to exploit functioning market mechanisms, FTA has to identify those technologies that make electro-fuel production techno-economically viable in the long-term future.

The second application case, concerned with the relevance and mitigation potentials of cosmic radiation exposure in future aviation, provided an example for future technology analysis at the intersection of technology push and pull. Main drivers found that may cause increasing radiation-induced safety concerns in aviation involve the reduction of emissions and travel time, leading to strongly growing polar route exploitation (with very high average RPK-growth rate of 26%) and to the exploration of higher flight altitudes. As key science and technology development ("push"), specifically tailored, lightweight nanocomposites were identified as possible high-performance structural materials with orders-of magnitude increased radiation shielding ability compared to e.g. aluminum. Amongst polymer composites, these nanocomposites were demonstrated to essentially reach the physical benchmark of optimized shielding performance at minimal weight penalty.

Further significant synergy potentials for radiation shielding were shown to naturally emerge from liquid hydrogen as novel propellant option for future aviation and particularly for hypersonic systems. Key insights from the analysis involve that for instance for future hydrogen powered hypersonic aircraft with tanks left and right of the passenger cabin, the radiation exposure of pilots and crew can be minimized by design. Namely, from a radiation shielding perspective, the cockpit as well as the main residence area of the crew should be as close as technically possible to the LH₂ tanks. The identification of such trade-offs may provide valuable support for future design considerations and may help to economically fly above and beyond Earth's natural radiation protection.

REFERENCES

1. W.B. Arthur; 2009; *The Nature of Technology*; Penguin; London, England
2. F.P. Boer; 2004; *Technology Valuation Solutions*; Wiley; Hoboken, NJ, USA
3. R.R. Schaller; 1997; "Moore's Law: past, present and future"; *IEEE Spectrum*; June; pp. 53 – 59
4. P. Micic; 2007; *Die fünf ZukunftsBrillen: Chancen früher erkennen durch praktisches Zukunftsmanagement*; Gabal; Offenbach, Germany
5. L. Koops; 2012; "Future Technology Perspectives"; *Bauhaus Luftfahrt Expert Symposium*; March, Munich
6. A. Sizmann; 2013; "A multidisciplinary think-tank approach"; *Workshop on Aeronautics Research Looking for "The Origins of Innovation"*; Brussels; April, 19
7. D.E. Stokes; 1997; *Pasteur's Quadrant: Basic Science and Technological Innovation*; Brookings; Washington, DC, USA
8. D.A. Marxer, P. Furler, J.R. Scheffe, H. Geerlings, C. Falter, V. Batteiger, A. Sizmann, A. Steinfeld; 2015; "Demonstration of the entire production chain to renewable kerosene via solar-thermochemical splitting of H₂O and CO₂"; *Energy & Fuels*; **29**(5), pp. 3241-3250
9. W.C. Chueh, C. Falter, M. Abbott, D. Scipio, P. Furler, S.M. Haile, A. Steinfeld; 2010; "High-Flux Solar-Driven Thermochemical Dissociation of CO₂ and H₂O Using Nonstoichiometric Ceria"; *Science*; **330**(6012); pp. 1797-1801
10. P. Furler, J. Scheffe, D. Marxer, M. Gorbar, A. Bonk, U. Vogt, A. Steinfeld; 2014; "Thermochemical CO₂ splitting via redox cycling of ceria reticulated foam structures with dual-scale porosities"; *Phys. Chem. Chem. Phys.*; **16**(22); pp. 10503-105011
11. SUN-to-LIQUID; 2016; "SUNlight-to-LIQUID: Integrated solar-thermochemical synthesis of liquid hydrocarbon fuels"; EU Horizon 2020 grant agreement No 654408; <http://www.sun-to-liquid.eu/>
12. European Commission; 2011; "Flightpath 2050: Europe's Vision for Aviation"; Report of the High Level Group on Aviation Research; Publications Office of the European Union, Luxembourg
13. Advisory Council for Aviation Research and Innovation in Europe (ACARE); 2017; "Delivering Europe's Vision for Aviation: Strategic Research and Innovation Agenda"; Update; **1**; pp. 1-100



14. P. Schmidt, W. Weindorf, A. Roth, V. Batteiger, F. Riegel; 2016; "Power-to-Liquids: Potentials and Perspectives for the Future Supply of Renewable Aviation Fuel"; German Environment Agency; pp. 1-32
15. C. Falter, V. Batteiger, A. Sizmann; 2016; "Climate Impact and Economic Feasibility of Solar Thermochemical Jet Fuel Production"; *Environmental Science and Technology*; **50**(1); pp. 470-477
16. Y. Kato, S. Hori, T. Saito, K. Suzuki, M. Hirayama, A. Mitsui, M. Yonemura, H. Iba, R. Kanno; 2016; "High-power all-solid-state batteries using sulfide superionic conductors"; *Nature Energy*; **1**; pp. 1-7
17. International Air Transport Association (IATA); 2009; "A Global Approach to Reducing Aviation Emissions"
18. M. Hornung, A.T. Isikveren, M. Cole, A. Sizmann; 2013; "Ce-Liner – Case Study for eMobility in Air Transportation"; 2013 Aviation Technology, Integration, and Operations Conference; Los Angeles, CA, USA; August 12-14; pp. 2-11
19. L. Schrempp (Koops); A. Sizmann; 2012; "Shielding Cosmic Radiation in Air Traffic"; *28th Congress of the International Council of the Aeronautical Sciences*; September; 23 - 28; Brisbane; Australia
20. L. Koops; 2013; "Size Effects on the Efficiency of Neutron Shielding in Nanocomposites – a Full-Range Analysis"; *Int. J. Nanosci.*; **12** (3); pp. 1350015-22
21. S.A. Thibeault et al.; 2012; "Radiation Shielding Materials Containing Hydrogen; Boron; and Nitrogen: Systematic Computational and Experimental Study -Phase I"; *NIAC Final Report*; pp. 1 – 31
22. A.C. Ferrari, et al.; 2015; "Science and technology roadmap for graphene, related two-dimensional crystals, and hybrid systems"; *Nanoscale*; **7**(11); pp. 4598-4810
23. EU Communication; 2016; "European Cloud Initiative – Building a competitive data and knowledge economy in Europe"; <https://ec.europa.eu/digital-single-market/en/%20european-cloud-initiative>
24. A. Sizmann; 2009; "Physical Science and Technological Innovation"; *Bauhaus Luftfahrt Expert Symposium*; February, Garching
25. H. Kuhn, A. Sizmann; 2012; "Fundamental Prerequisites of Electric Flying", *German Aerospace Congress*; Berlin; September, 10 – 12; pp. 1 – 8
26. H. Kuhn, C. Falter, A. Sizmann; 2011; "Renewable Energy Perspectives for Aviation"; *3rd CEAS Air&Space Conference and 21st AIDAA Congress*; Venice, Italy; pp. 1249-1259
27. L. Koops; A. Sizmann; "Relevance of Cosmic Radiation Exposure for Hypersonic Flight"; German Aerospace Congress 2014; September; 17. – 18.; Augsburg; Germany
28. L. Koops; 2017; "Cosmic Radiation Exposure on Future Hypersonic Missions"; *Rad. Prot. Dosimetry*, **175** (2), pp. 267–278
29. U. Bossel; 2014; *Energiewende zuende gedacht*; Bossel, Oberrohrdorf, Switzerland
30. C.K. Chan, H. Peng, G. Liu, K. McIlwrath, X.F. Zhang, R.A. Huggins, Y. Cui; 2008; "High-performance lithium battery anodes using silicon nanowires"; *Nature Nanotechnology*; **3**(1); pp. 31-35
31. G.C. Fleming, U. Ziegler; 2016; "Environmental Trends in Aviation 2050"; *ICAO Environmental Report - On Board a Sustainable Future*; ICAO Environment; Montreal, ON, Canada; pp. 16-22
32. K. Plötner; 2015; "A case study of the Ce-Liner: Operational Implications of eAviation"; *AIRCAT Workshop*; Geneva, Switzerland; March, 29 – 30
33. T. Schilling, T. Rötger, K. Wicke; 2016; "Assessment of the Impact of Radically Climate-Friendly Aviation Technologies"; *Greener Aviation*; Brussels, Belgium; October, 11 - 13; pp. 1 – 12
34. K.O. Ploetner, R. Rothfeld, M. Urban, M. Hornung, G. Tay, O. Oguntona; "Technological and Operational Scenarios on Aircraft Fleet-Level towards ATAG and IATA 2050 Emission Targets", *17th AIAA Aviation Technology, Integration, and Operations Conference, AIAA AVIATION Forum*; (AIAA 2017-3771); pp. 1-13
35. A. Sizmann, H. Kuhn; 2015; "Advanced Batteries for Future Aviation: Problems, Progress and Perspectives"; *Europe-Japan Symposium "Electrical Technologies for the Aviation of the Future", Delegation of the EU to Japan*; Tokyo, Japan; March 26-27
36. A. Roth, A. Sizmann; 2015; "Deliverable 4.4: Report on compilation, mapping and evaluation of R&D activities in the field of conversion technologies of biogenic feedstock and biomass-independent pathways (Final report)"; *CORE-JetFuel: Coordinating research and innovation in the field of sustainable alternative fuels for aviation*; pp. 1-89; <http://www.core-jetfuel.eu>



37. H.K. Ng; B. Sridhar; S. Grabbe; N. Chen; 2011; "Cross-polar aircraft trajectory optimization and the potential climate impact"; *IEEE/AIAA 30th Digital Avionics Systems Conference*; October; 16. – 20; Seattle; WA; USA
38. Boeing; 2016; "Current Market outlook 2016-2035";
http://www.boeing.com/resources/boeingdotcom/commercial/about-our-market/assets/downloads/cmo_print_2016_final_v5.pdf
39. J. Steelant et al.; 2008; "Long-Term Advanced Propulsion Concepts and Technologies (LAPCAT)"; European Commission; 6th Framework; Final Activity Report; AST4-CT-2005-012282
40. C. J. Mertens; B. T. Kress; M. Wiltberger; W. K. Tobiska; B. Grajewski; X. Xu; 2012; "Atmospheric Ionizing Radiation from Galactic and Solar Cosmic Rays"; *Current Topics in Ionizing Radiation Research*; Editors; M. Nenoj; InTech Publisher; Rijeka; Croatia; pp. 683-738
41. National Council on Radiation Protection and Measurements (NCRP); 1993; "National Council on Radiation Protection and Measurements: Limitations of exposure to ionizing radiation"; **116**
42. C. Dyer; F. Lei; 2001; "Monte carlo calculations of the influence on aircraft radiation environments of structures and solar particle events"; *IEEE Trans. Nucl. Sci.*; **48** (6); pp. 1987–1995;
43. International Commission on Radiological Protection (ICRP); 2008; "ICRP Publication 103: 2007 Recommendations of the International Commission on Radiological Protection"; *Elsevier*, **103**; ISBN 0-7020-3048-1
44. C. J. Mertens; B. T. Kress; M. Wiltberger; S. R. Blattnig; T. S. Slaba; S. C. Solomon; M. Engel; 2010; "Geomagnetic influence on aircraft radiation exposure during a solar energetic particle event in October 2003"; *Space Weather*, **8** (3)
45. D. F. Smart; M. A. Shea; 1985; *Handbook of Geophysics and the Space Environment*; Editors A. S. Jursa; Air Force Geophysics Laboratory; Bedford; MA; USA
46. C. J. Mertens; M. M. Meier; S. Brown; R. B. Norman; X. Xu; 2013; "NAIRAS aircraft radiation model development; dose climatology; and initial validation"; *Space Weather*, **11** (10); pp. 603–635
47. W. K. Tobiska; 2015; "Advances in Atmospheric Radiation Measurements and Modeling Needed to Improve Air Safety"; *Space Weather*, **13** (4)
48. J. R. Davis; R. Johnson; 2012; "Cosmic Radiation"; Editors J. R. Davis; R. Johnson; J. Stepanek; J. A. Fogarty; *Fundamentals of Aerospace Medicine*; Fourth edition; **4**; Wolters Kluwer; Philadelphia; PA; USA; pp. 221-235
49. F. Donus, D. Kirchner, M. Myrczik, H. Schubert, M. Schwarze; 2007; Group 7, "Highliner HL170"; *Aircraft design seminar*, IFB, University of Stuttgart
50. Ch. Beauthier; A. Mahajan; P. Hendrick; S. Sharifzadeh; D. Verstraete; 2015; "Hypersonic cryogenic tank design using mixed-variable surrogate-based optimization"; *Engineering Optimization 2014*; Editors H. Rodrigues; J. Herskovits; Ch. Mota Soares; J. Miranda Guedes; A. Araujo; J. Folgado; F. Moleiro; J. Aguilar Madeira, First edition, **1**, CRC Press, Taylor & Francis Group, London, UK;
51. L. Koops; 2017; work in progress
52. G. Battistoni; A. Ferrari; M. Pelliccioni; R. Villari; 2004; "Monte Carlo calculation of the angular distribution of cosmic rays at flight altitudes"; *Radiation Protection Dosimetry*, **112** (3); pp. 331–343
53. A. Ferrari; M. Pelliccioni; R. Villari; 2004; "Evaluation of the influence of aircraft shielding on the aircrew exposure through an aircraft mathematical model"; *Radiation Protection Dosimetry*, **108** (2); pp. 91 – 10

Spacecraft bracket design using additive manufacturing

Alexandru-Mihai CISMILIANU

INCAS - National Institute for Aerospace Research "Elie Carafoli"

Aerospace Design Engineer

Bd. Iuliu Maniu 220, Bucharest 061126, Romania

cismilianu.alexandru@incas.ro

Camelia Elena MUNTEANU

INCAS - National Institute for Aerospace Research "Elie Carafoli"

Aerospace Stress Engineer

Ionut-Cosmin ONCESCU

INCAS - National Institute for Aerospace Research "Elie Carafoli"

Aerospace Stress Engineer

Mihaela NASTASE

INCAS - National Institute for Aerospace Research "Elie Carafoli"

Aerospace Stress Engineer

Radu-Petru BIBIRE

INCAS - National Institute for Aerospace Research "Elie Carafoli"

Aerospace Design Engineer

Ion DIMA

INCAS - National Institute for Aerospace Research "Elie Carafoli"

Head of Structures and Materials Department

Mihai Victor PRICOP

INCAS - National Institute for Aerospace Research "Elie Carafoli"

Head of Flow Physics

ABSTRACT

The major efforts in the space industry have the aim of finding ways to reduce the overall costs of building and launching a spacecraft (S/C). A combination of structural optimization and additive layer manufacturing (ALM) can be the answer for respecting the most decisive elements like mass reduction and minimum lead time, which translates into cost saving. This paper presents two different concepts of design and structural optimization for thruster support brackets. One approach was to use an in-house tool of optimization which resulted into a stiff and reliable structure. The second design was obtained using commercial of the shelf (COTS) tools of structural optimization. Both approaches significantly decreased the number of design iterations and the time needed to obtain the final solution. In order to take full advantage of the design flexibility given by ALM and reduce the mass furthermore, internal cavities were considered in both design concepts. This raised a contamination problem of the S/C's components which was avoided by designing closely with the manufacturer, a powder removal procedure. The combination of ALM, structural optimization and joint effort with the manufacturer, lead the team to high-quality and efficient structures with fewer points of potential failure and a lower production cost.

KEYWORDS: spacecraft design, structural optimization, additive manufacturing, internal cavities, powder removal.

Finite Element Modelling and Performance Optimization of an Ion Thruster depending on the nature of the propellant

Ionuț-Florian POPA

Romanian Research and Development Institute for Gas Turbines COMOTI

Assistant Researcher

220 D Iuliu Maniu Bd., sector 6, cod 061126, OP 76, CP174, Bucharest, Romania

ionut.popa@comoti.ro

Anna-Maria Theodora ANDREESCU

Romanian Research and Development Institute for Gas Turbines COMOTI

Assistant Researcher

theodora.andreescu@comoti.ro

Dan IFRIM

Romanian Research and Development Institute for Gas Turbines COMOTI

Technical Development Engineer

dan.ifrim@comoti.ro

Radu MIHALACHE

Romanian Research and Development Institute for Gas Turbines COMOTI

Scientific Researcher

radu.mihalache@comoti.ro

Dragoș MIHAI

Romanian Research and Development Institute for Gas Turbines COMOTI

Scientific Researcher

dragos.mihai@comoti.ro

Grigore CICAN

"POLITEHNICA" University of Bucharest, Faculty of Aerospace Engineering

Lecturer PhD Eng.

Gh. Polizu Street 1-5, 011061, Bucharest, Romania

grigore.cican@upb.ro

ABSTRACT

The electrostatic propulsion is a class of space propulsion which make use of electrical power and this kind of systems are characterized by high exhaust velocities and specific impulse, enhancing the propulsive performances of thrusters compared to conventional chemical thrusters. Since the ionized particles exhaust velocity is a function of the ration between the electrical charge and their molecular mass, the obvious solution is to use ions with low electrical charge-molecular mass ratio. Currently, the most used propellant for the space propulsion is the Xenon gas, as it has a series of important advantages, but is quite expensive when compared to other propellants. This paper aims to make an optimization of the ideal ion propulsion systems depending on the nature of the propellant, like common used substances in the space propulsion, but also other substances which are potential candidates for this application. A variety of ion thruster performances will be analyzed, such as: force, specific impulse, efficiency for the same power available onboard, the same accelerating voltage, and the same ion current. Also, for the Xenon case a numerical simulation was performed to highlight the behavior and trajectory of the ionized particles and their velocity. The conclusion obtained following the study is that a reasonable ion thruster regarding the dimensions should use an accelerating potential of at least 4000 V and 2 A of ion current.

KEYWORDS: *ion thruster, propellant, optimization, exhaust velocity, numerical simulation*

Gust Alleviation of Aeroelastic Aircraft Using CFD Simulation

Aleš Prachař

*VZLU – Czech Aerospace Research Centre
Research Scientist
Beranových 130, 199 05 Prague, Czech Republic
prachar@vzlu.cz*

Pavel Hospodář

*VZLU – Czech Aerospace Research Centre
Research Engineer*

Petr Vrchota

*VZLU – Czech Aerospace Research Centre
Research Engineer*

ABSTRACT

A CFD study of a gust alleviation technique based on the use of aircraft's control surfaces on the main wing and on the horizontal tail plane is presented. The NASA Common Research model of an airliner is used as the reference configuration. The gust model is based on adding artificial gust velocities into the governing equations, so-called Disturbance Velocity Approach. The gust is identified as a change in the Angle of Attack upstream of the aircraft nose. A series of gusts is used to measure response of the aircraft and to establish the dynamic gust model. The elasticity of the aircraft model is taken into account employing modal analysis and the response of the aircraft structure is studied. The movable control surfaces are defined and characterized by CFD using the mesh deformation technique in the unsteady RANS simulations. Finally, the dynamic model based on both the gust data on one hand and on the control surfaces on the other is exploited to define the controller with the aim to alleviate the gust. The required time response of the movable control surfaces is studied to clarify limits of this alleviation technique.

KEYWORDS: *CFD, gust response, moving control surfaces, NASA Common Research Model*

Evaluation of Piston Engine Modes and Configurations in Composite Cycle Engine Architectures

Markus Nickl

Bauhaus Luftfahrt e.V.

Junior Researcher

Willy-Messerschmitt-Str. 1, 82024 Taufkirchen, Germany

Markus.Nickl@bauhaus-luftfahrt.net

Sascha Kaiser

Bauhaus Luftfahrt e.V.

Junior Researcher

ABSTRACT

Radical aircraft propulsion concepts based on a Composite Cycle Engine architecture are presented to improve significantly the core efficiency of aero engines. Therefore, three different piston engine modes and configurations (a two-stroke and a four-stroke reciprocating piston configuration, as well as a Wankel-type rotary engine) are evaluated in order to identify the most promising piston engine concept in a Composite Cycle Engine application. The qualitative and quantitative assessment of the piston systems consider thermodynamic performance, weight and NO_x emissions, as well as cooling, lubrication and integration aspects.

To compare the performance of the different piston systems, models for the non-stationary thermodynamic cycle of the piston engines are presented and integrated in a turbo engine performance simulation framework. A turboshaft platform with 22 MW shaft power at typical Take-Off conditions and unified state of art turbo component characteristics are used for the evaluation of the piston configurations. Further, approaches for the prediction of piston engine weights, cooling fin design and NO_x emissions are introduced.

The four-stroke reciprocation piston engine configuration is identified as most promising option due to thermal material requirements, NO_x-emissions and specific fuel consumption. It is found that the high scavenging efficiency and the lower temperature level compared to the two-stroke engine compensate the additional scavenging cycle. A preliminary geometric design of the four-stroke piston engines is illustrated for the investigated application case.

KEYWORDS: Composite Cycle, Piston Engine

Twin-jet and trijet aircraft: a study for an optimal design of regional aircraft

Edgar Coelho Inouye
 EMBRAER

Product Development Engineering
 EMBRAER, São José dos Campos, SP, 12227-900, Brazil
 edgar.tdk@gmail.com

Adson Agrico de Paula
 Department of Aircraft design, ITA
 Adjunct Professor

Instituto Tecnológico de Aeronáutica, Department of aircraft design, São José dos Campos, SP, 12228-900, Brazil
 adson@ita.br

Patrice London Guedes,
 EMBRAER

Product Development Engineering
 EMBRAER, São José dos Campos, SP, 12227-900, Brazil
 patrice.london@embraer.com.br

William Martins Alves
 EMBRAER

Product Development Engineering
 EMBRAER, São José dos Campos, SP, 12227-900, Brazil
 wma.mecatronica@gmail.com

ABSTRACT

Aircraft with three engines, as known as trijet, became a standard design among manufacturers after 1964 when the FAA's 60-minute rule was established for these aircraft. This regulation restricted the flight path to 60 minutes' flying time to a suitable airport, therefore affecting the operation costs and limiting the range of twin-jet aircraft. However, improvements to the engine's reliability in the following decades allowed ETOPS certification for twin-jet aircraft. The traditional trijet designs were slowly retired, the last commercial trijet flight was in 2014. The industry abandoned the trijet design as solution for commercial aviation; however, executive jets such as the Falcon 7x and Falcon 8x, certified in 2016, show that this configuration might still be advantageous for specific markets. The certification at one engine inoperative condition presents advantage for trijet aircraft reducing take-off thrust, since when one engine is inoperative, 75% of the installed thrust is available for the trijet aircraft, while this value is only 50% for a twin-jet aircraft. An initial study conducted showed a trend of lower thrust to weight ratio for trijet aircraft when compared to twin-jet aircraft, being particularly evident for MTOW (maximum take-off weight) lower than 75,000 lb. The aim of this work is to study the viability of a trijet aircraft configuration and potential advantages for a regional aviation scenario. The trijet configuration performance was evaluated and compared to twin-jet configuration in a multidisciplinary design environment considering disciplines such as aerodynamics, noise, performance, flight mechanic, weight, and structure. An aircraft with MTOW of 48,500 lb was studied and the results show that a reduction up to 9.4% of installed thrust might be achieved with the trijet design compared to twin-jet aircraft when the balanced field length is the critical constraint. However, flyover noise and structural weight might increase slightly in trijet design.

KEYWORDS: trijet; balanced field length; multidisciplinary design; installed thrust reduction

A modelling framework to support power architecture trade-off studies for More-Electric Aircraft

Ana Garcia Garriga

*United Technologies Research Centre Ireland
 Research Scientist
 Cork, Ireland
 Garciaga@utrc.utc.com*

Parithi Govindaraju

*United Technologies Research Centre Ireland
 Senior Research Scientist
 Govindp@utrc.utc.com*

Sangeeth Saagar Ponnusamy

*United Technologies Research Centre Ireland
 Senior Research Scientist
 ponnuss@utrc.utc.com*

Nicola Cimmino

*Università degli Studi di Napoli "Federico II"
 MSc. Candidate
 Napoli, Italy
 ni.cimmino@studenti.unina.it*

Laura Mainini

*United Technologies Research Centre Ireland
 Senior Research Scientist
 maininl@utrc.utc.com*

ABSTRACT

This work presents a modelling framework to enable comparison and trade-off study of different aircraft system architectures. The framework integrates a computational module to select feasible architectures with a modelling platform that simulates the power generation, distribution and fuel consumption of the aircraft as well as system-level models for the system being evaluated. Its capabilities are demonstrated for the case of the electrification of the primary flight control system (PFCS) using different electric technologies (EHA, EMA) and different levels of electrification ranging from the conventional hydraulic to the all-electric. The performances of different architectures are analysed with respect to the change in the mechanical power extracted from the engine, the weight and the fuel burn of the aircraft. The framework demonstrates the capability of evaluating multiple, different, system architectures in a way that is scalable for different systems or different aircraft. It supports a designer evaluating the aircraft-level impact of their design choice at system-level, and it can aid in assessing technology options early in the design process.

KEYWORDS: *More-Electric Aircraft, Architecture Evaluation, Trade-off Analysis, Modelling and Simulation*

Synthesizing a massive training dataset based on real lunar data for image-based navigation and crater recognition

Hoonhee Lee

*Korea Aerospace Research Institute (KARI)
 169-84 Gwahak-ro, Yuseong-gu, Daejeon 34133, South Korea
 lhh@kari.re.kr*

Dawoon Jung

Korea Aerospace Research Institute (KARI)

Seunghee Son

Korea Aerospace Research Institute (KARI)

Han-Lim Choi

Korea Advanced Institute of Science and Technology (KAIST)

ABSTRACT

Image-based navigation is a key technology for landing on the Moon and other planetary bodies. Image-based navigation requires real-time crater detection/recognition for position determination during descent and touchdown. In this research, we present an algorithm that uses lunar images to assist in navigation and/or landing. In particular, this algorithm is able to robustly recognize craters in sub-optimal illumination conditions such as near the lunar South Pole where permanently shadowed regions exist. Until now, image-based crater recognition and counting algorithms required well-lit, clearly-defined features. The proposed algorithm utilizes a machine-learning technique known as a convolutional neural network (CNN). This approach requires an extensive training set to successfully classify and recognize images. We propose generating CNN training data using synthetic lunar images based on digital elevation models (DEMs). Since the Moon has no atmosphere, its surface does not substantially change over time ensuring that computer-generated images will closely resemble ground truth. Several tens of thousands of images are rendered with differing camera parameters and Sun positions. The algorithm was tested by training the CNN on generated images of the Shackleton, de Gerlache and Shoemaker craters. The trained CNN is confirmed to recognize these craters in real lunar images with a high degree of accuracy. In summary, this research presents a novel method of generating and using synthetic lunar images for assisting in the navigation of spacecraft or landers. The method was tested by generating images of craters near the South Pole under varying viewing and illumination conditions, training a CNN with the generated images, and verifying that the CNN recognizes the trained craters accurately. This technique is robust under challenging illumination conditions and is suitable for navigation near the lunar South Pole.

KEYWORDS : *CNN, ConvNets, Convolutional Neural Network, Image based Navigation*

NOMENCLATURE

Θ_1 - Elevation angle from centre of crater to the Sun
 ϕ_1 - Azimuth angle from the North to the Sun, clockwise around crater horizon
 Θ_2 - Elevation angle from center of crater to camera
 Φ_2 - Azimuth angle from the North to the camera, clockwise around crater horizon
 σ - Ratio of width of square to a crater diameter
 α - Diameter of crater

• INTRODUCTION

The Korean lunar exploration program started in January 2016 and is currently in the preliminary design phase of a lunar orbiter that will carry a variety of scientific payloads including optical cameras. Research and development of key technologies for a future lander and surface rover is also taking place. Candidate landing sites might include maria or rugged highlands. In particular, the lunar poles, which have a high probability of harbouring reserves of water, are particularly interesting yet challenging destinations for lander missions.

In this study, we propose a machine learning method for lunar navigation in polar regions that is capable of high performance even with very limited training data.

At the Moon and Mars, where satellite-based accurate position information cannot be obtained, the current position, attitude, or velocity is calculated by referencing topography or other surrounding features. Previous studies have focused on flat landing sites with clearly-discernible terrain such as lunar maria at equatorial latitudes. For example, algorithm [1] finds the centre and size of a circular or elliptical crater on flat terrain, and matches it with an existing database of craters or generates navigation parameters relative to surrounding craters. This method is difficult to use in high-latitude regions however because of low Sun elevation angles that cause elongation and truncation of apparent crater outlines due to shadowing.

Instead of considering shadows as obstacles to successful pattern matching, Shadow-Based Matching [2] uses shadows themselves as feature points or indicators for self-localization of a lunar lander. However, this method is unsuitable at polar latitudes where the majority of terrain is covered with overlapping shadows.

Support Vector Machine (SVM) [3] was used to classify image features as non-craters and craters [4]. However, only a small number of real images were used for training the network and results depend heavily on the preprocessing method used as opposed to Convolutional Neural Networks (CNN) [5]. In order to improve the performance of classical SVM, there is a recent case [6] in which CNN is applied to automatically search Mars topography. However this research did not try to recognize and identify single feature points or indicators, but to determine the distribution of features in a large area. CNN has also been applied in the case of the Moon [7], [8], but none of these address how to detect and classify irregular features, or to increase the amount of useful training data along trajectories that a lander might travel but no orbiter has taken.

The lack of training data is a common problem in machine learning algorithms, especially when the number of neural networks increases. A simple method to increase the volume of training data is to duplicate the original image and apply rotation, cropping, jittering, and mirroring [9]. However, the quantitative increase is limited and may not be applicable depending on the problem domain.

Instead of altering existing data, synthetic, labelled training data can be generated and has been applied to human gaze estimation [10]. However, this method concentrated on refining synthetic imagery and was applied in an environment where real images can be obtained sufficiently and has not been tested on terrain imagery.

DEM-based synthetic images combined with PCA and a polynomial classifier were used to recognize lunar craters [11]. However, the method was not tested on heavily-shadowed terrain. We expect that it is not suitable for polar navigation because of the high-dimensionality of complex, shadowed crater features.

In this paper, we present a CNN design and novel learning method that can perform effectively in dark, shadowed terrain such as the lunar poles. Section 2 presents background and motivation. Section 3 describes our method. Section 4 compares the performance of our LunarNet CNN with its feature based SVM according to parameter's changes. Finally, Section 5 discusses the results and directions for further research.

• MOTIVATION

DEM data acquired using the laser altimeters on board previous and current orbital missions forms the basis for constructing synthetic training images in this study. In the case of the Moon, the cost of producing each synthetic image is low because the surface remains fairly constant due to lack of weathering and so DEMs do not need to be updated frequently. Additionally, it is only necessary to

generate training images of the regions that will be visible along the mission trajectory which may be quite narrow for a lander.

As DEM data is acquired through active laser imaging, it provides accurate base geometry even in heavily-shadowed regions. However, we still need images that appear as they might be taken by a navigation camera; that is, correctly lit by sunlight. This can be achieved by generating, or rendering, scenes in simulation software taking as input the DEM, Sun position, camera trajectory and attitude, and field-of-view (FOV), and a surface reflectance model.

Fig. 1 shows a test rendering using LRO LROC LOLA [12] data compared with the corresponding real image taken by the Selenological and Engineering Explorer (SELENE [13]) High-Definition Television (HDTV) camera. A simplified Hapke reflectance model with five parameters was used. Shadows are approximated with shadow mapping [14] instead of more accurate ray tracing techniques. Differences from the real image such as the sharpness of shadow edges are due to use of these simplified light transport models. However, overall the synthetic image closely approximates the real image. This is because the Moon has no atmosphere and the topography of the pictured area is relatively smooth.

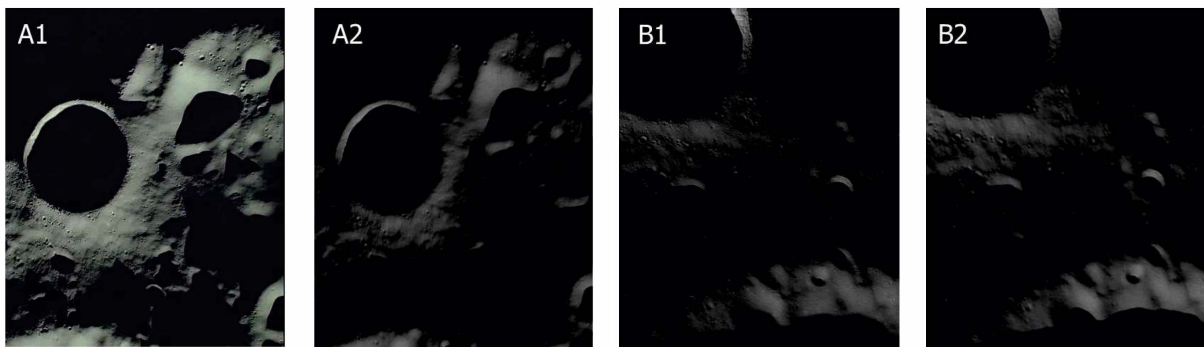


Figure 1: Comparison between real images A1, B1 and synthetic images A2, B2 respectively (A1: a snapshot from SELENE HDTV, B1: DTMTCO_03_04806S893E0519PS from SELENE Terrain Camera)

Additional training images can also be produced by photographing a physical scale model using a setup such as Fig. 2. These can be used in edge cases where purely-synthetic computer-renderings do not produce the desired result.



Figure 2: Illuminated Hybrid Hardware-Software Simulation Bench at KARI [15]

This paper makes the following contributions:

- We show that by changing the parameters for generating the synthetic image, the machine learning performance can be improved.
- We solve the data augmentation problem in machine learning by using a combination of real imagery, synthetic imagery, and DEM data in a feedback loop until performance is satisfied.
- We avoid overfitting and reduce the difference between the actual images and the model because we do not include actual images in the training data.

• METHOD

• Machine-Learning System Overview

Fig. 3 illustrates the novel machine learning system constructed for this paper. It is a closed-loop crater classifier that provides image-based navigation information suitable for dark polar regions characterised by heavy shadowing and lack of reliable training images.

The main features are described below.

1. In order to train the crater classifier to recognize craters (one feature of the terrain), the training set and validation set are generated from DEM-based synthetic rendered images only.
2. Real images obtained from actual lunar missions are used only to evaluate the performance of the crater classifier.
3. If the performance result does not meet the desired criteria, the system repeatedly changes image generation parameters to generate additional training and validation sets, and repeats the learning process. In general machine learning systems, the validation set is used to determine when to terminate learning but in this study, closed-loop learning can be performed indefinitely based on the threshold set by the user. However, since there will always be a small difference between model and reality, this threshold is assumed to be a trade-off target and the performance is assumed to converge at a certain value.

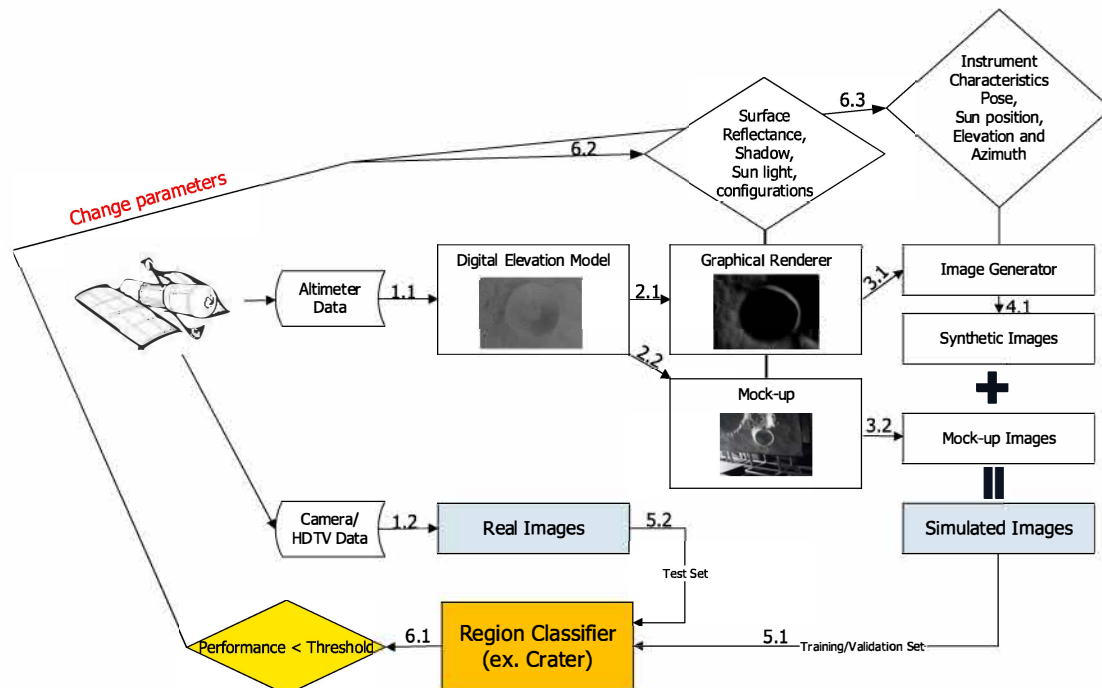


Figure 3: Overall Training System basing Synthetic Images

The purpose of (1) and (2) is to utilize synthetic images only for the training and validation sets, not the test set to avoid overfitting, assuming that the DEM-based synthetic images are similar to image obtained from actual cameras. (3) aims to optimize the learning process.

The mock-up in Fig. 3 was previously shown in Fig. 2. It is a test bench for simulating lander movement in three axes with the ability to photograph a lunar surface model under realistic illumination conditions. In this study, only synthetic images were used.

For this training system, we collected actual images of three craters, de Gerlache, Shackleton, and Shoemaker near the lunar South Pole and performed labelling to express the truth of each image. In addition, a high-resolution LOLA DEM was imported as a surface model using the method described in [16]. The synthetic image generation system takes as input the camera position, attitude, Sun position, and camera characteristics.

• Test Configuration

The DEM was based on data from the LRO Lunar Orbiter Laser Altimeter (LOLA) payload, currently the most accurate available at the lunar poles. Crater images were extracted from SELENE Terrain Camera (TC) and HDTV video frames, and LRO LROC images were also used. 3D images were created using the graphical renderer, PANGU [17], and the composite image was generated by changing the camera posture, position, and sun position of the lunar lander. The Sun was assumed to be monochromatic (white) and the lunar surface reflectance model was set to Hapke (a simplified version using five parameters and single wavelength). The crater classifier uses a high performance SVM as a non-neural network and a CNN with a shallow network for comparison. In the case of the SVM, the preprocessing performance of the feature is a very important factor. Therefore, we compare the results of the CNN and the optimal SVM by using feature that was created using the CNN.

Table 1: Training Preparation

Synthetic Images		Real Images		Crater Classifier	
Based DEM:	de Gerlache (22,500 pics)	Image sources: 1. SELENE TC 2. HDTV, 3. LRO LROC	de Gerlache (300 pics)	Non-CNN : a multiclass SVM (CNN [LunarNet_ex] FC feature)	LunarSvm_ex
LRO LOLA	Shackleton (22,500 pics)		Shackleton (300 pics)		
Graphical Renderer: PANGU	Shoemaker (22,500 pics)		Shoemaker (300 pics)	a shallow CNN	LunarNet_ex

From a camera and lunar surface perspective, both the sun and the camera have elevations and azimuth angles of 360 degrees. At the lunar South Pole, the elevation of the sun is actually within 1.6 degrees, and the image information taken below 1 degree is very small, so the range between 0.6 and 1.6 degrees is chosen. The elevation of the camera ranged from 54 to 90 degrees because it was insignificant in the testing phase because there was almost no lunar South Pole imagery taken at low elevation.

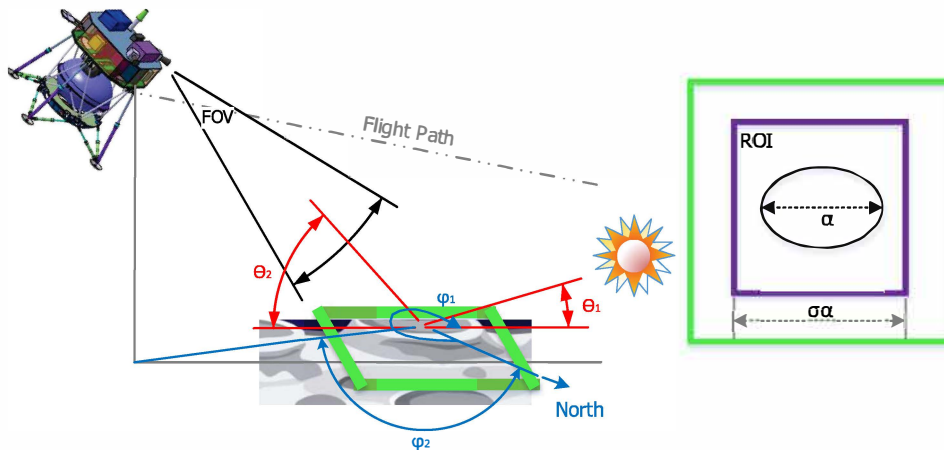


Figure 4: Camera Pose Parameters

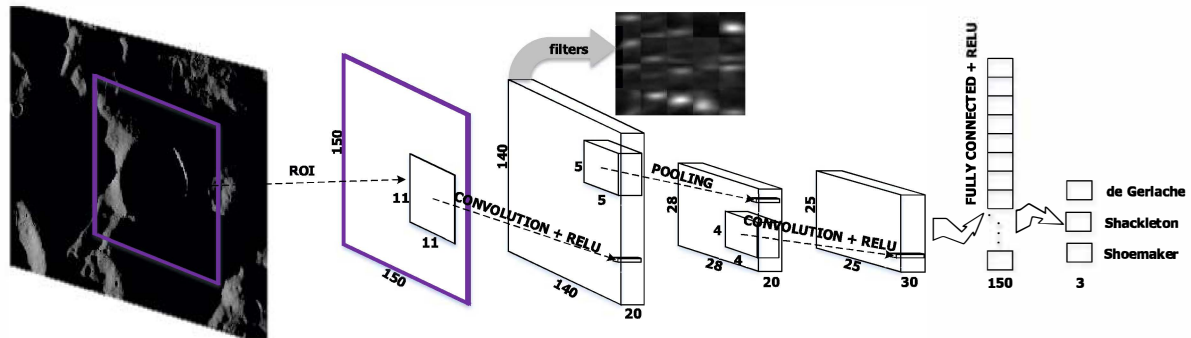
The parameters for the generation of composite images are defined in detail. The position of the sun in Fig. 4 defines the angle azimuth ϕ_1 between the axis of the sun toward the north of the Moon and the azimuth of the sun on the horizontal plane from the origin of the crater, and the elevation Θ_1 from the surface. The field of view (FOV) for the camera, the angle between the vertical axis and the focal axis of the camera at the centre of the crater Θ_2 , and azimuth ϕ_2 are defined. The Purple box is the Region of Interest (ROI) that you want to use for learning in a wide 2D image (Green box) shot at 90 degrees FOV. In other words, the size of the ROI representing this learning range was considered as one parameter in this study. The ROI is a square and the ratio σ to the diameter α of the crater's major axis is used to select the length of one side. For example, if σ is 1, the ROI becomes a square with the length of the major axis of the crater. The larger the ratio σ , the more pixel information around the crater is included.

Table 2: Parameters for Synthesis

Class	Parameter	Range	Sampling Frequency	Sampling Location
Sun	Elevation, Θ_1	$0.16 \sim 1.6^\circ$	2, 4, 6, 8, 10	increased by 0.16
	Azimuth, ϕ_1	$0 \sim 360^\circ$	3, 6, 9, 12, 15	increased by $360^\circ/\text{Sample Count}$
Camera	Elevation, Θ_2	$54 \sim 90^\circ$	2, 4, 6, 8, 10	increased by 0.16
	Azimuth, ϕ_2	$0 \sim 360^\circ$	3, 6, 9, 12, 15	increased by $360^\circ/\text{Sample Count}$
	FOV	90° (fixed)	-	-
ROI	ROI ratio, σ	$1.0 \sim 1.4$	1, 2, 3	increased by 0.2

• Crater Classifiers

A multiclass SVM classifier, LunarSVM_ex, was trained using supervised learning and a stochastic gradient solver. Unlike CNN, SVM cannot automatically acquire image features through learning. Therefore, it is necessary to select an appropriate feature and convert it to a pre-prepared composite image. HOG [18] is a typical feature detector that is suitable for images such as craters. However, the prior results showed that the performance of HOG is less than 30%. Therefore we exploit the activation feature of CNNs [19] for LunarSVM_ex and rely on the fully connected layer of LunarNet_ex to generate suitable features.

**Figure 5: LunarNet_ex Architecture**

LunarNet_ex consists of 9 layers as shown in Fig. 5 with a relatively shallow CNN as CONVOLUTION (CONV1), Rectified Linear Unit (ReLU1), POOLING, CONV2, ReLU2, FULLY CONNECTED (FC1), ReLU3, FC2 and Softmax. The performance can be improved with a deeper design, but the validation accuracy as a stop condition was set to 90% on average when learning the synthetic data used in this experiment. Rather than designing optimal CNNs, the feasibility of the synthetic data and the closed-loop learning system using it was examined.

In Fig. 5, the input image of 150 x 150 is determined by considering the average size of the ROI, and the stride of the filter of CONV1 is set to 1 to use as much information as possible. It is designed to remove the following POOLING layer after CONV2 and preserve as much information as possible. The final number of classes are three, corresponding to the three craters via a loss function.

• RESULT

The performance of LunarSVM_ex using the activation feature of a specific layer of LunarSVM_ex did not seem to be better in all cases, but it is generally high. The mean difference in accuracy was not significantly different from LunarNet_ex.

Intuitively, the performance can be expected to be improved by increasing the sampling frequency of parameters. The test results as shown in Fig. 6 clearly show that performance increases with higher Sun elevation angles (Sun elevation sampling frequency is increased proportionally with elevation angle). It can be guessed that as the Sun elevation increases, more area is illuminated, increasing the information available to classify craters. However, in the case of ROI of 1.4, accuracy decreases as sampling frequency increases as shown in Fig. 6 on top left. We presume that this is due to increasing ROI while the input image resolution remains fixed at 150 by 150. Also, ROI 1.0 sized test data such as shown in Fig. 7 accounted for the largest portion of the total.

Performance does not increase proportionately with increasing sample frequency for Sun azimuth. We observe this because azimuth sampling is done uniformly between 0-360 degrees, and the test data do not contain enough useful information (i.e., were almost completely black) at certain azimuth angles.

Varying the camera elevation sampling frequency does not result in a marked improvement in performance. An average improvement of 5% by increasing the number of training samples from 2,250 to 20,250. LRO, and SELENE cameras were mainly pointed at the nadir direction, which may explain why training lower elevations does not increase accuracy.

Varying camera azimuth generally results in better performance, but the signal is not monotonically increasing and appears to be correlated to camera elevation. The interpretation of this result requires further research. Nevertheless, in the algorithm of Fig. 3, only the Sun Elevation is changed in the machine learning process through the closed loop, which means that the user can set the desired threshold to about 85% as a test accuracy.

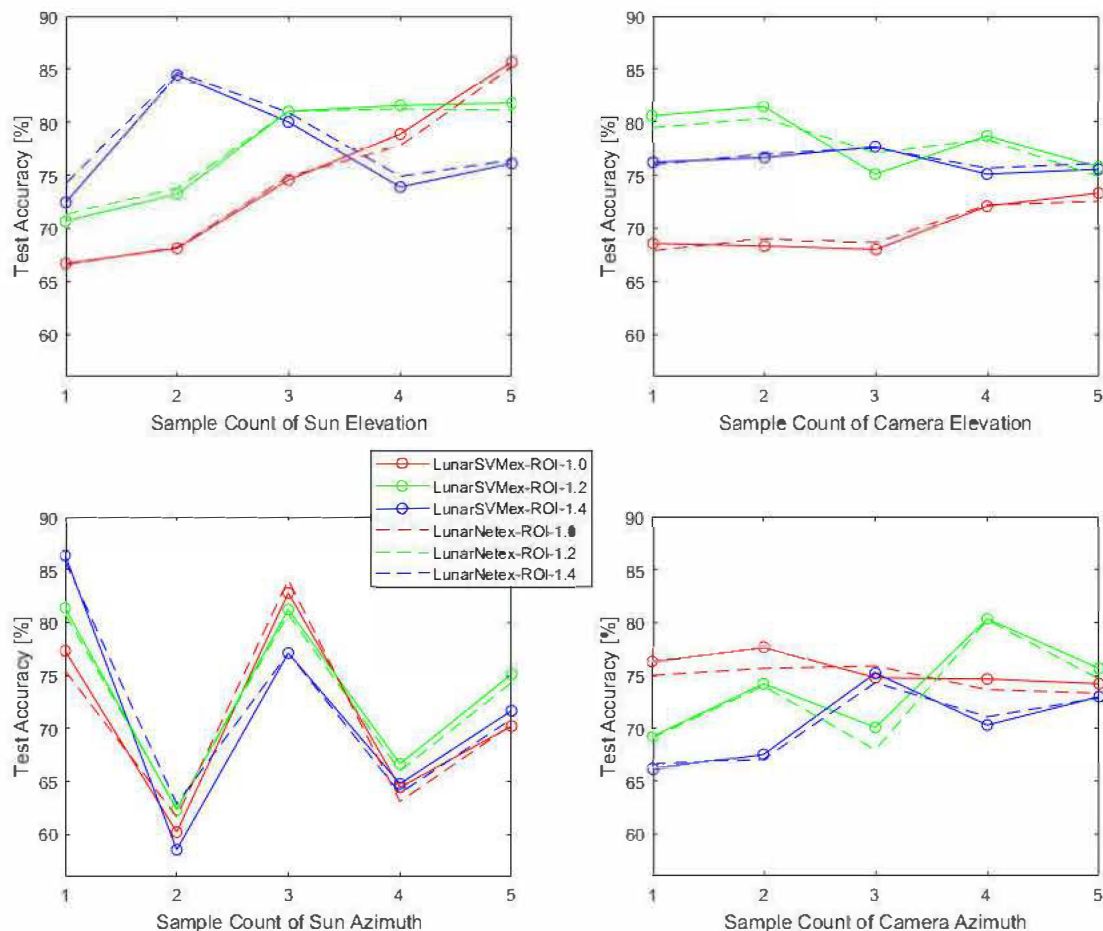


Figure 6: Test Accuracy by Test Conditions



Figure 7: Test Data with ROI 1.0 and Slewing: A (de Gerlache from TC1W2B0_01_00582S883E2719), B (Shackleton from M101457600MC_pyr), C (Shoemaker from M139810920MC_py) and D (Shackleton from SELENE HDTV)

• DISCUSSION

The validity of the parameters was examined without finding their optimal values. The possibility of training a dark region classifier was demonstrated using synthetic images infinitely obtained by finely manipulating the parameters in the closed loop algorithm. However, increasing the number of the synthetic data could result in unnecessary time consuming rather than improving performance. We have confirmed that there are still many limitations in evaluating its performance using small amounts of real images with respect to their multiformity. Finally, there is a need to look further at the unexpected result by the parameter, Camera azimuth.

REFERENCES

1. M. Yu, H. Cui, Y. Tian; 2014; "A new approach based on crater detection and matching for visual navigation in planetary landing", *Advances in Space Research*; **53**; pp. 1810 - 1821
2. H. Kaufmann, M. Lingenauber, T. Bodenmueller, M. Suppa; 2015; "Shadow-Based Matching for Precise and Robust Absolute Self-Localization during Lunar Landings"; *IEEE Aerospace Conference*; Big Sky, MT, USA; 7-14 March 2015
3. D. Meng, C. Yunfeng, W. Qingxizn, 2013, "Novel approach of crater detection by crater candidate region selection and matrix-pattern-oriented least squares support vector machine", *Chinese Journal of Aeronautics*; **26**; (2); pp. 385 – 393
4. C. Cortes and V. Vapnik, 1995, "Support-Vector Networks", *Machine Learning*, **20**; (3); pp. 273-297
5. Y. LeCun, Y. Bengio, G. Hinton, 2015, "Deep learning". *Nature*, **521**; (7553), pp. 436-444
6. L.F. Palafox, C.W. Hamilton, S.P. Scheidta, A.M. Alvarez; 2017; "Automated detection of geological landforms on Mars using Convolutional Neural Networks"; *Computers & Geosciences*; **101**; pp. 48 - 56
7. J.P. Cohen, H.Z. Lo, T. Lu, W. Ding; 2016; "Crater Detection via Convolutional Neural Networks"; *47th LPSC, Lunar and Planetary Science Conference*; Texas, USA; 21-25 March 2016
8. E. Emami, G. Bebis, A. Nefian, T. Fong; 2015; "Automatic Crater Detection Using Convex Grouping and Convolutional Neural Networks"; *International Symposium on Visual Computing Conference*; Nevada, USA; 14-16 December 2015
9. S.C. Wong, A. Gatt, V. Stamatescu, D. McDonnell; 2016; "Understanding data augmentation for classification: when to warp?"; *DICTA, Digital Image Computing: Techniques and Applications Conference*; Queensland, Australia; 30 November-2 December 2016
10. A. Shrivastava, T. Pfister, O. Tuzel, J. Susskind, W. Wang, R. Webb; 2016; "Learning from Simulated and Unsupervised Images through Adversarial Training"; arXiv:1612.07828
11. A. Boukercha, A. Al-Tameemi, A. Grumpe, C. Wohler; 2014; "Automatic Crater Recognition Using Machine Learning with Different Features and their Combination", *45th LPSC, Lunar and Planetary Science Conference*; Texas, USA; 17-21 March 2014
12. NASA; 2017; "PDS Geosciences Node – LOLA Data Node"; <http://pds-geosciences.wustl.edu/missions/lro/lola.htm>
13. M. Kato, S. Sasaki, Y. Takizawa, Kaguya Project Team, 2010, "The Kaguya Mission Overview", *Space Sci Rev*, **154**; (3); pp. 3-19
14. L. Williams, 1978, "Casting Curved Shadows on Curved Surfaces", *Computer Graphics (Proceedings of ACM SIGGRAPH 78)*, pp. 270-274
15. H.H. Lee, D.W. Jung; 2017; "Construction of Validation Bench for Testing of Vision-Based Navigation Methods in the Korean Lunar Exploration Program"; *SESP (Simulation and EGSE for Space Programmes)*; **1**; Noordwijk, Netherlands; 28-30 Mar;
16. H.H. Lee, G. H. Ju; 2014; "A Study on Real Measurement Data based Lunar Virtual Surface Generation"; *KSAS Autumn Conference*; **1**; Jeju, Korea; 19-21 Nov;
17. STAR-Dundee; "PANGU – Planet and Asteroid Natural scene Generation Utility"; <https://www.star-dundee.com>
18. N. Dalal, B. Triggs; 2005; "Histograms of Oriented Gradients for Human Detection"; *IEEE Computer Vision and Pattern Recognition Conference*; **1**; pp. 886-893
19. J. Donahue, Y. Jia, O. Vinyals, J. Hoffman, N. Zhang, E. Tzeng, T. Darrell; 2013; "Decaf: A deep convolutional activation feature for generic visual recognition"; arXiv:1310.1531

UNSTEADY FULL ANNULUS MULTI-STAGE COMPRESSOR CALCULATIONS – DETAILS ON CFD-EXPERIMENT COMPARISON

Oliver Reutter

*DLR, German Aerospace Center
 Institute of Propulsion Technology
 Researcher in Dept. Fan and Compressor
 Linder Höhe
 51147 Köln, Germany
 oliver.reutter@dlr.de*

Graham Ashcroft

*DLR, Institute of Propulsion Technology
 Group leader in Dept. Numerical Methods*

Eberhard Nicke

*DLR, Institute of Propulsion Technology
 Head of Dept. Fan and Compressor*

Edmund Kügeler

*DLR, Institute of Propulsion Technology
 Head of Dept. Numerical Methods*

ABSTRACT

The unsteady flow in a multi-stage compressor has been simulated using time-domain methods to gain a better insight into the complex flow physics and address the computational bottlenecks associated with large scale numerical simulations in the time domain. For these investigations the time-periodic flow in the DLR research compressor Rig250 has been simulated. Rig250 is a 4.5 stage axial flow compressor with a swan neck that includes struts for support. In the time-domain simulation the struts, IGVs and first two stages are computed time-accurately using a full annulus mesh to fully capture the blade row interactions. The remaining two stages are included in the simulation by solving, with single passages, for the time-mean flow. In total, the low Reynolds full annulus mesh comprises nearly 1×10^9 nodes distributed over 6000 blocks.

For an operating point close to maximum efficiency, comparisons are made between the time-accurate full annulus calculation and experimental test data to see how Kiel probe stagnation pressure measurements can be resolved. It is shown, that with larger efforts in simulations also the comparison between numerical and experimental data has to be conducted with greater care. The numerical and experimental results are in good agreement.

KEYWORDS: *Full annulus, CFD, validation, Kiel probe, virtual twin*



Thermal shock, tribological and mechanical properties of micro and nano structured zirconia partially stabilized with yttria and ceria

Dragomirescu Alina¹, Botan Mihail¹, Manoliu Victor¹, Ionescu Gheorghe¹, Stefan Adriana¹, Mihailescu Alexandru¹

¹National Institute for Aerospace Research "Elie Carafoli" Bucharest, Materials Unit, 220 Iuliu Maniu Blvd, 061126 Bucharest, Romania

botan.mihail@incas.ro

ABSTRACT

Plasma sprayed micro and nano-structural zirconia coatings were investigated under thermal shock and evaluation of tribological and mechanical properties. Tribological performances of coatings were investigated by stainless steel ball against coated disk testing procedure under dry friction conditions. Better wear performance of the nano-structured zirconia stabilized with yttria (7.5YSZ) is due to the microstructure and mechanical properties enhancements compared with micro structured coating stabilized with ceria (CSZ). Advantages of nano-structured zirconia (7.5YSZ) coating were observed under thermal shock compared with ceria stabilized (CSZ) coating. Thermal shock was performed under quick heating and cooling of Nimonic-90 based alloy coated samples with a heat and cooling maximum gradient about of 100C°/s using a dedicated installation from INCAS. The SEM structural investigation showed a complex microstructure. SEM images of plasma sprayed micro (CSZ) and nano (7.5YSZ) structured zirconia present well and partially melted splats and areas. A higher thermal shock resistance, tribological and mechanical properties were found on nano-structured zirconia coatings stabilized with yttria, this effect was correlated by nano structured areas in coating microstructure and the presence of melted splats.

KEYWORDS: ZIRCONIA, CERIA, TBC, THERMAL SHOCK, TRIBOLOGY

NOMENCLATURE

A – Contact area, mm²
C_p - heat capacity, (Jg⁻¹K⁻¹)
d - Arithmetic mean of the two diagonals, d1 and d2 in mm
D_{th} - thermal diffusivity, (m²s⁻¹)x10⁻⁶
E - Young's modulus, elastic modulus, GPa
F – Load in kgf
F(N) - normal applied force, N,
H - nano, micro, macrohardness, kg/mm², GPa
H_V - Vickers hardness number, kg/mm², GPa
L - sliding distance, m
T_m - melting point, (K)
W - Wear
W_m – Massic wear

Greek Symbols

α - thermal expansion coefficient, (K⁻¹)x10⁻⁶
Δ_m - mass loss at the end of the test, mg
λ - thermal conductivity, Wm⁻¹ K⁻¹
ν - Poisson's number,

Subscripts

m – mass, melting
th. - thermal
V - Vickers

1 Introduction

Thermal Barrier Coating (TBC) materials are widely used as thermal protection systems. There are many application of (TBC) from aerospace, turbine engine to nuclear [1]–[5]. Modern Aircraft industry aimed in using of gas turbine engines to get higher temperatures for improving the efficiency and reduction of CO₂ emission. In this respect, researchers focused on developing more efficient Thermal Barriers Coatings (TBCs) and associated technics of deposition to protect metallic alloys components. Depending on application of TBC's and regarding the technology readiness level, there were developed several techniques of deposition, such as Atmospheric Plasma Spraying (APS), High Velocity Oxy-Fuel (HVOF), Electron Beam-Physical Vapor Deposition (EB-PVD) and Plasma Spray-Physical Vapor Deposition (PS-PVD). The last two seemed the most performant due to the special columnar structure of the resulted coating [3], [5], [6]. Given the TBC's applications, numerous factors for achieving a good protection system such as: powder morphology, pre-treatment of the metal substrate, bond coat solutions, type of coating method, were taken into account.[3], [4], [7].

Currently, most of TBCs are based on Yttria Stabilized Zirconia (YSZ) and are commonly applied using the Atmospheric Plasma Spraying (APS) and Electron Beam Physical Vapor Deposition (EB-PVD) techniques [5], [8], [9]. Several authors reported that the addition of CeO₂ into YSZ coating is supposed to be effective for the improvement of thermal cycling life regarding its higher thermal expansion coefficient and a lower thermal conductivity than YSZ [1], [3], [5], [10], [11].

In literature some other rare earth oxides as stabilizers of ZrO₂ besides Y₂O₃ and CeO₂ have been reported, such as Dy₂O₃, Nd₂O₃, Er₂O₃, Sm₂O₃, Yb₂O₃, Sc₂O₃, Gd₂O₃, Ta₂O₅, Nd₂O₅[3], [11]. Stabilizers used for TBC coatings are characterized by different level of stabilizing ability and stabilizing mechanisms which are correlated with the ability at high temperature of cation migration [3], [11]. Furthermore, new promising TBC material based on zirconia are doped by different rare-earth cations. These additions lead to the formation of dopant systems such as in the ZrO₂–Y₂O₃–Nd₂O₃(Gd₂O₃, Sm₂O₃)–Yb₂O₃(Sc₂O₃) system which lead in reduction of the thermal conductivity [5]. In Table 1 are represented some TBC solutions and their properties.

Table 1: Some properties for TBC solutions [3]–[6], [11], [12]

Materials	T _m (K)	D _{th} (m ² s ⁻¹)x10 ⁻⁶	λ (Wm ⁻¹ K ⁻¹)	α (K ⁻¹)x10 ⁻⁶	E (GPa)	C _p (Jg ⁻¹ K ⁻¹)	ν
ZrO ₂	2953	0.43	2.17	15.3	21		0.25
8YSZ (APS)	2680	-	2.20-2.50	10.3-11	40	0.64	0.22
CeO ₂	2873	0.86	2.77	13	172	-	0.27-0.31
La ₂ Zr ₂ O ₇	2573	0.54	1.58	9.1	175	0.49	-
La ₂ Ce ₂ O ₇		0.19	0.6	12.3		0.43	-
CaZrO ₃	2550		2	8.4-8.9	149.3		0.28
BaZrO ₃	2963	1.25	3.42	8.1	181	0.45	-
SrZrO ₃	2883	1.4	2.08	10.9	170	0.46	0.25
Mullite	2123	-	3.3	5.3	30	-	0.25

D_{th}, thermal diffusivity; E, Young's modulus; α, thermal expansion coefficient; λ, thermal conductivity; C_p, heat capacity; ν, Poisson's number; T_m, melting point.

In the current research, the thermal shock, tribological and mechanical behavior of ZrO₂7.5%Y₂O₃ and ZrO₂24%CeO₂2.5%Y₂O₃ coatings made by APS technique, were tested and compared in the as-sprayed state. Tribological tests were performed using CETR UMT-universal tribometer, utilizing the module ball on ring under dry regime. Thermal shock tests were performed on a dedicated installation conceived by INCAS namely QTS-2-(Quick Thermal Shock) and hardness testing were performed using Vikers indentation method.

2 Samples and powder description.

Coatings were carried out onto Nimonic 90 substrates with zirconia based ceramic, stabilized with nano yttria and ceria powders over a bond coat MeCrAlY commercially named AMDRY 997.

The samples were coated by High Velocity Oxy-Fuel (HVOF) technique for bond coat (BC) and for top coat (TC) Air Plasma Spraying (APS) technique was used. Corresponding spraying conditions are described in Table 3. Two types of zirconia doped powders were used, hereinafter namely: INFRAMAT ($\text{ZrO}_2 7.5\% \text{Y}_2\text{O}_3$ - nanostructured powder = 7.5YSZ) and M205NS ($\text{ZrO}_2 25\% \text{CeO}_2 2.5\% \text{Y}_2\text{O}_3$ – ceria stabilized zirconium oxide powder = CSZ) with powder characteristics presented in Table 2. Ceria stabilized zirconium oxide M205NS ($\text{ZrO}_2 25\% \text{CeO}_2 2.5\% \text{Y}_2\text{O}_3$) have a 2,5% of Y_2O_3 , this coating solution surpasses the cyclic and thermal fatigue resistance of common 8% yttria stabilized zirconia ($8 \text{Y}_2\text{O}_3 \text{ZrO}_2$) [13]–[15].

Table 2: Nominal powder characteristics[13]–[15].

Materials	Particle size	Chemical formula	Density	Service temperature	Trade name
INFRAMAT (7.5YSZ)	30-60 nm	$\text{ZrO}_2 7.5\% \text{Y}_2\text{O}_3$	6.10 g/cm ³	1345°C (2450°F)	4039ON-8601
M205NS (CSZ)	+11-125 µm	$\text{ZrO}_2 25\% \text{CeO}_2 2.5\% \text{Y}_2\text{O}_3$	5.3 – 5.5 g/cm ³	1250 °C (2280 °F)	Metco 205NS

In table 3, powders and associated parameters for coatings using METCO 7M installation (Plasmajet s.r.l, Bucharest, Romania) are presented.

Table 3: Spraying parameters used to perform top coat structures by APS.

Nr.crt	Powder type	Gun	Thickness [mm]	Debit Ar/H ₂	I[A]	U[V]	Injector	Nozzle	Distance [mm]
1	$\text{ZrO}_2 25\% \text{CeO}_2 2.5\% \text{Y}_2\text{O}_3$	7MB	0.1-0.2	120/12	600	65	#2	SM6mm	100
2	$\text{ZrO}_2 7.5\% \text{Y}_2\text{O}_3$	7MB	0.1-0.2	120/12	600	65	#2	SM6mm	120

For bond coat (BC), HVOF deposition technique was used. The parameters for HVOF coating are: distance 230 mm, Substrate cooling was ensured by compressed air, oxy-fuel: oxygen and propylene, with flow rate for $\text{O}_2 = 3410 \text{ mm}^3/\text{sec}$ and for propylene $\text{O}_2 = 1488 \text{ mm}^3/\text{sec}$, feed rate for bond coat powder 0.315g/sec.

The sample geometry dimensions are 30x50x2 mm for Nimonic90 substrate. The thickness of the bond coat (BC) deposition was about 45-70 µm and 270-310 µm for the top coat (TC).

3 Testing methods and results

3.1 Tribological testing

In order to investigate the tribological behavior of investigated coatings, testing was performed by using of the CETR UMT-universal tribometer (Figure 1). Tests were performed with the ball on ring module under dry regime. The reason of this testing type selection was to investigate the mechanism of wear using as a counterpart a steel ball, the ball composition is according to- STAS 1456 11250 CS 200, Rul 1 DIN 100Cr6.

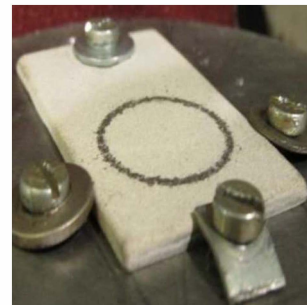
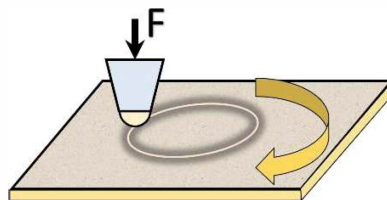


Figure 1 Arrangement of the sample and principles of ball on disk testing method.

Testing conditions are: Normal Force=10N, sliding speed=0.25m/s, sliding distance =100 m. (sliding radius =10mm, ball diameter =4.9 mm, $w=238.735\text{rot/min}$. The test was performed under controlled ambient temperature which was about 25°C all the time during testing performance.

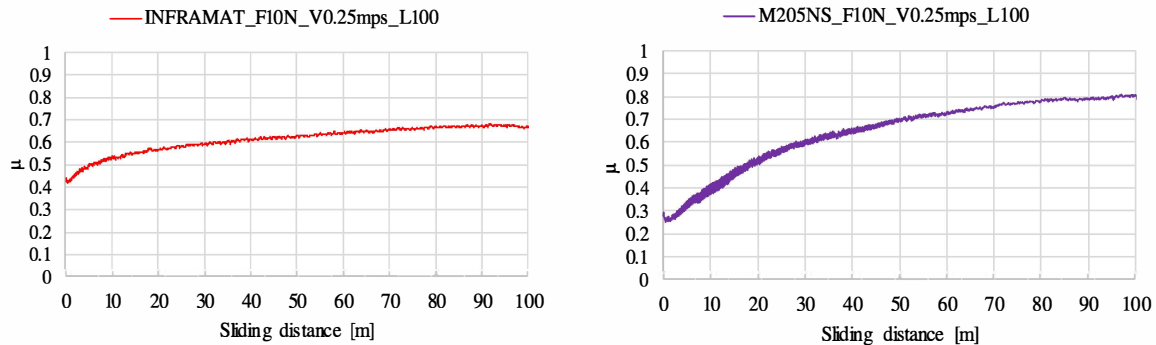


Figure 2: Friction curves during the ball on disc test.

For calculation of wear rate W_m was used formula Eq.1:

$$W_m = \frac{\Delta m(mg)}{F(N) \cdot L(m)} \quad (1)$$

where $\Delta m(mg)$ is mass loss at the end of the test, $F(N)$ is normal applied force, $L(m)$ is sliding distance. The results of wear rate are presented in Figure 2 and Figure 3. In this study was used the correlation of wear rate in order to underline the performances between coatings against steel ball.

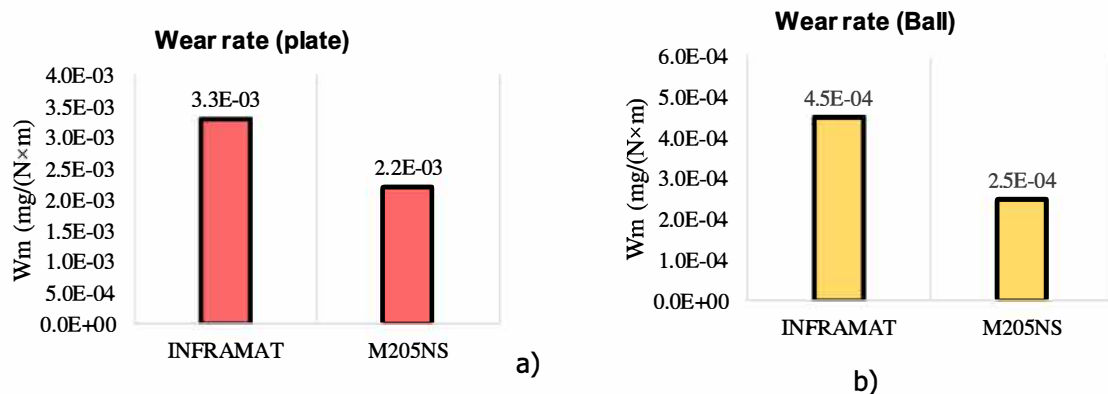


Figure 3: Wear rate for a) coated plate b) steel ball.

The average friction coefficients at the end of the test seems to be approximately the same for the investigated samples namely 0.60 for 7.5YSZ and 0.65 for CSZ. The differences can be seen in the shapes and the slope of the friction curves. The 7.5YSZ (INFRAMAT $\text{ZrO}_2 7.5\% \text{Y}_2\text{O}_3$) present a smooth shape with small scattering values along the curve. It can be easily observed that 7.5YSZ friction curve starts almost from 0.4 friction coefficient value, leading to the conclusion that it has a strong abrasive surface. After 50 m of sliding distance, it was observed a stabilization of the friction coefficient around 0.62 and a maximum value of 0.69 at the end. Friction coefficient evolution along the test for M205NS ($\text{ZrO}_2 25\% \text{CeO}_2 2.5\% \text{Y}_2\text{O}_3$ –CSZ), have an almost linear grow trend starting from 0.25 at the beginning, after 50 m of sliding the friction coefficient was ~ 0.70 , the highest values for friction coefficient being around 0.82 at the end of the test (Figure 2). The tribological investigation present a lower massic wear rate of CSZ compared with YSZ.

3.2 Hardness testing

The Vickers hardness test method consists of indenting the test material with a diamond indenter, in the form of a right pyramid with a square base and an angle of 136 degrees between opposite faces subjected to a load. In this paper Vicker's micro-hardness (H_v) was performed on the polished cross-section of the samples, with an indentation load of 1971N for 15 seconds by selecting 5 locations

randomly. The Vickers hardness is the quotient obtained by dividing the kgf load by the A, the surface area of the resulting indentation in square millimeter Eq.2.

$$H_V = \frac{F}{A} = \frac{2 \cdot F \cdot \sin\left(\frac{136^\circ}{2}\right)}{d^2} \quad [\text{kgf/mm}^2, \text{GPa}] \quad (2)$$

where F is load in kgf, A is the surface area of the resulting indentation in mm², d is arithmetic mean of the two diagonals, d1 and d2 in mm. The Vicker's micro-hardness (Hv) was performed on top coat, bond coat and Nimonic90 substrate. The results are presented in Table 4 and Table 5.

Table 4: Vicker's micro-hardness for samples with 7.5YSZ.

TC-(7.5YSZ) (Hv 0.2)	BC- Amdry997 (Hv 0.2)	Nimonic90 (Hv 0.2)
244.4	189.6	169.6

Table 5: Vicker's micro-hardness for samples with (CSZ).

TC (CSZ) (Hv 0.2)	BC-Amdry997 (Hv 0.2)	Nimonic90 (Hv 0.2)
218.8	173	165.4

Vicker's micro-hardness (Hv) of CSZ is 229.8 (Hv 0.2), smaller compared to YSZ 244.4 (Hv 0.2). denoting and proving the poor behavior during the tribological tests of CSZ.

3.3 Thermal shock testing

Thermal shock tests were done on a research equipment designed and conceived by INCAS called QTS-2-(Quick Thermal Shock) [1], [2]. The purpose of the installation is to perform thermal shock tests, allowing a fast and economical method of quick ranking of the multilayered ceramic coating. Developed testing system and constantly upgraded equipment, ensures the reproducibility of the testing conditions by operating in semi-automatic regime. Functional parameters of the QTS-2 equipment are: maximum testing temperature – 1500°C, variable heating speed and quick cooling speed of tested specimen with an average up to 70°C/sec by compressed air and higher values achieved by new cryogenic cooling system. The installation is equipped with continuous temperature measurement pyrometers for specimen and oven during all thermal cycles steps. Temperatures variations are recorded and stored automatically by data acquisition under LabVIEW software. Coatings for thermal cycling test in this work are listed in Figure 4.

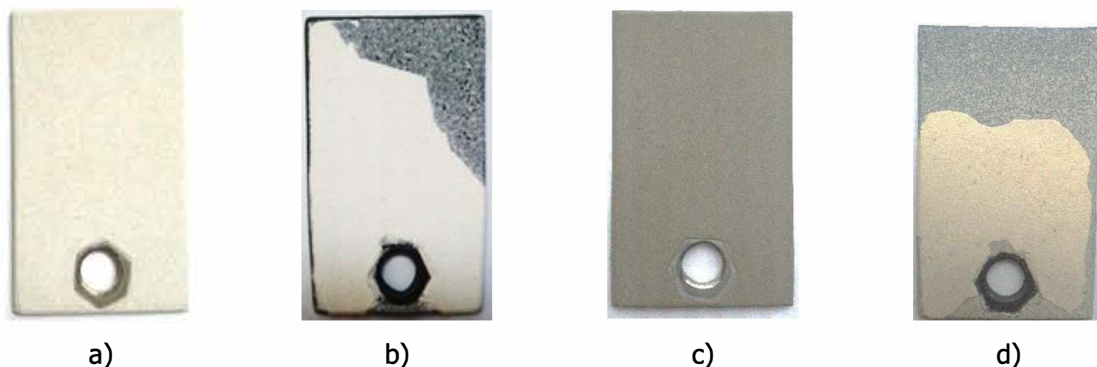


Figure 4: a) YSZ sample before thermal shock, b) YSZ sample after 90 cycles, c) CSZ sample before thermal shock, d) CSZ sample after 75 cycles

In this study, thermal shock cycles were done by exposing for 5 minutes to 1200°C and then cooled down by 8-9 bars compressed air for 1 minute using a 4mm nozzle at 35 mm distance from sample. Testing procedure for thermal shock is that the testing is terminated if a spallation of more than 20% of coated surface occurred. For the thermally tested samples coated with 7.5YSZ and CSZ, spallation for 7.5 YSZ occurred after 90 cycles and for CSZ after 75 thermal cycles.

3.4 Microstructure

Two different structural microstructures were observed in this study Figure 5 and Figure 6. They are mainly different for as coated morphostrucral surfaces.

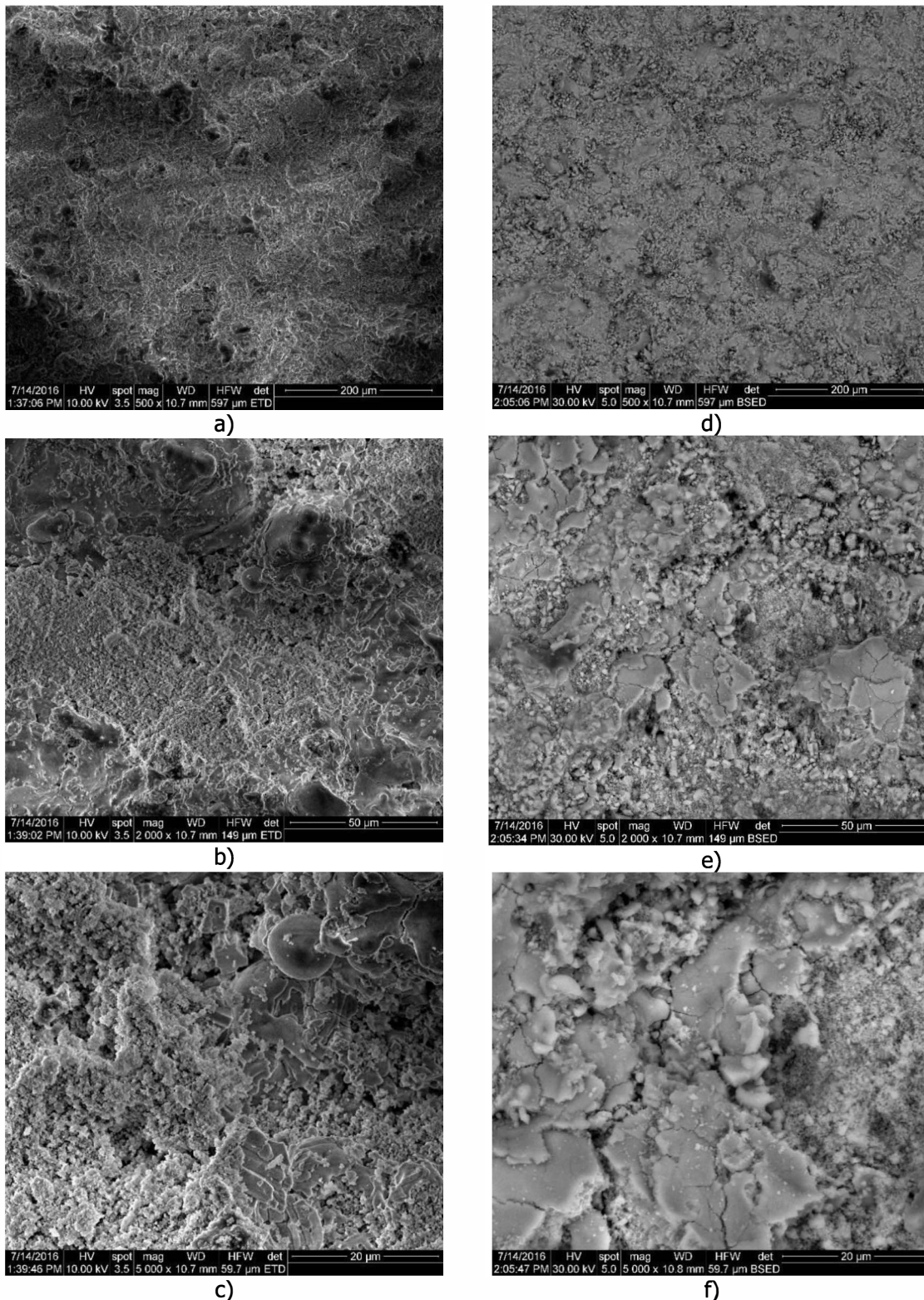


Figure 5: SEM images of the surface for 7.5YSZ coating, a,b,c-before tribological testing, d,e,f-after tribological testing

A prominent grainy surface for 7.5YSZ and with small splats on surface, leading to the formation of a melted stretched surface with nano recrystallized droplets on top, given the supersonic velocity of particles during coating process deposition Figure 5 a, b, c.

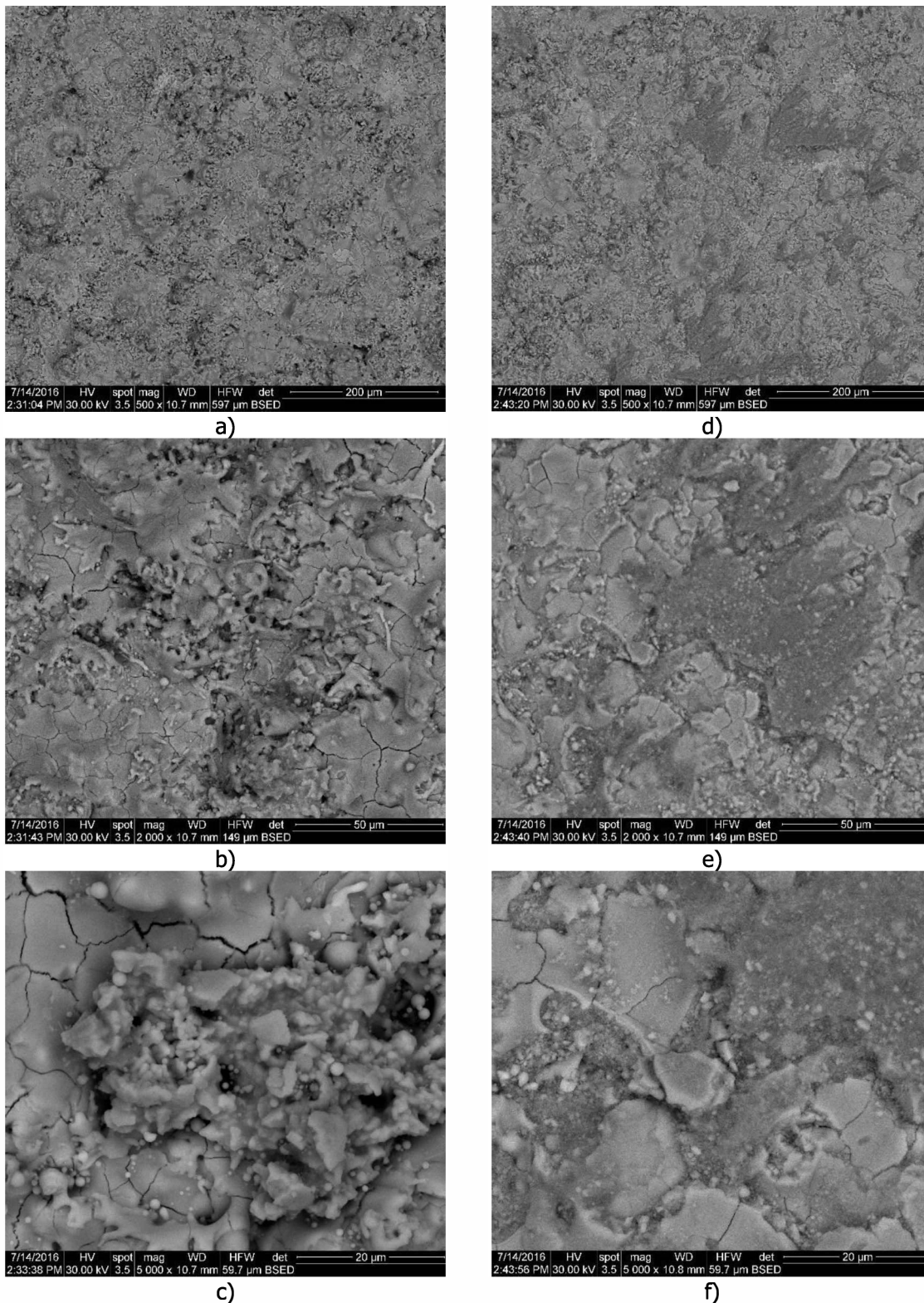


Figure 6: SEM images of the surface for CSZ coating, a) before tribological testing, b) after tribological testing

The SEM morphostrucral images for CSZ represent a cover with well melted particles, with large stretched droplets. The different from it others are observed in SEM images for CSZ coating Figure 6 a,

b, c, with represent a network of developed nano cracks on the surface, mostly on well melted stretched droplets. SEM images for 7.5 YSZ and CSZ after tribological testing are represented in Figure 5 d, e, f and Figure 6 d, e, f. The main conclusion on tribological evolution and microstructural consideration of coatings are that, a lower coefficient of friction was obtained for 7.5YSZ regarding the presence of nano grainy surface and removed during the test, living in contact with the steel ball the harder surface of melted droplets, conducting to a stabilization of the coefficient of friction YSZ (Figure 2).

In the case of CSZ, which was described with a well meted surface of the droplets but with a wide network of nano cracks, the contact of steel ball with the surface led to the segmentation of the surface created by nano cracks and then fragmentation. As the result of fragmentation, delamination of sharp splinters was leading to a higher coefficient of friction for CSZ and constantly growing of it during the test.

4 Summary and conclusions

Plasma sprayed micro and nano-structural zirconia coatings were investigated under thermal shock and an evaluation of tribological and mechanical properties was performed. Tribological performances of coatings were investigated against stainless steel with a ball on disk testing procedure under dry friction conditions. Better wear performance of the nano-structured zirconia stabilized with yttria (7.5YSZ) is due the microstructure and mechanical properties enhancements compared with micro structured coating stabilized with ceria (CSZ). Advantages of nano-structured zirconia (7.5YSZ) coating were observed under thermal shock compared with ceria stabilized (CSZ) coating. The SEM structural investigation showed a complex microstructure. SEM images of plasma sprayed micro (CSZ) and nano (7.5YSZ) structured zirconia present well and partially melted splats and areas. A higher thermal shock resistance, tribological and mechanical properties was found on nano-structured zirconia coatings stabilized with yttria, this effect was correlated by nano structured areas in coating microstructure and the presence of melted splats. The main conclusion on tribological evolution and microstructural consideration of coatings are that the use of nano structured powders for coatings can bring improvements in the coefficient of friction and less nano cracks on the as coated surface. For the CSZ coating one shows a well meted surface but with a wide network of nano cracks resulting in segmentation and fragile fragmentation and splinters occurrence. This result reveals that the CSZ coating has a higher coefficient of friction and lower wear rate compared to 7.5YSZ.

Acknowledgement

The paper was prepared thanks to the Nucleus Program, contract no. PN 16 38 05 02 powered by UEFISCDI - Romanian Executive Agency for Higher Education, Research, Development and Innovation.

REFERENCES:

- [1] V. Manoliu, A. Mihailescu, G. Ionescu, and A. Stefan, "The behaviour of turbo engine associated thermal barrier coating structures from a tribological perspective.," *J. Int. Sci. Publ.*, vol. 9, pp. 269–278, 2015.
- [2] S. Dimitriu, V. Manoliu, G. Ionescu, and A. Stefan, "Multilayer Ceramic Materials Testing under the Terms of High Heating-Cooling Gradients.," in *Advanced Materials Research*, 2015, vol. 1114, pp. 190–195.
- [3] X. Cao, "Development of New Thermal Barrier Coating Materials for Gas Turbines," Doctoral dissertation, Forschungszentrum Jülich in der Helmholtz-Gemeinschaft, 2004.
- [4] T. CUI, J. WANG, R. GUAN, L. Chen, and G. QIU, "Microstructures and Properties of Thermal Barrier Coatings Plasma-Sprayed by Nanostructured Zirconia.," *J. Iron Steel Res. Int.*, vol. 14, no. 5, Supplement 1, pp. 116–120, 2007.
- [5] R. Vaßen, M. O. Jarlago, T. Steinke, D. E. Mack, and D. Stöver, "Overview on advanced thermal barrier coatings," *Surf. Coatings Technol.*, vol. 205, no. 4, pp. 938–942, 2010.
- [6] L. Pawlowski, *The Science and Engineering of Thermal Spray Coatings*. 2008.
- [7] B. Bernard *et al.*, "Thermal insulation properties of YSZ coatings: Suspension Plasma Spraying (SPS) versus Electron Beam Physical Vapor Deposition (EB-PVD) and Atmospheric Plasma Spraying (APS).," *Surf. Coatings Technol.*, vol. 318, pp. 122–128, 2017.
- [8] K. K. Szkaradek, "Thermal barrier ZrO₂ -Y₂O₃ obtained by plasma spraying method and laser melting," *Manuf. Eng.*, vol. 17, no. 1, pp. 77–80, 2006.



- [9] S. Sodeoka, M. Suzuki, K. Ueno, H. Sakuramoto, T. Shibata, and M. Ando, "Thermal and Mechanical Properties of ZrO₂-CeO₂ Plasma-Sprayed Coatings," *J. Therm. Spray Technol.*, vol. 6, no. September, pp. 361–367, 1997.
- [10] Y. Wang *et al.*, "Microstructural evolution of plasma sprayed submicron-/nano-zirconia-based thermal barrier coatings," *Appl. Surf. Sci.*, vol. 363, pp. 101–112, 2016.
- [11] H. Xu and H. Guo, *Thermal barrier coatings*, vol. 90, no. 8. Woodhead Publishing Limited, 2011.
- [12] Y. Zhang *et al.*, "Mechanical properties of zirconia composite ceramics," *Ceram. Int.*, vol. 39, no. 7, pp. 7595–7603, 2013.
- [13] "***Material Product Data Sheet Ceria-Yttria Stabilized Zirconium Oxide."
- [14] "***Material Product Data Sheet 8 % Yttria Stabilized Zirconia."
- [15] "***<http://www.advancedmaterials.us/4039ON-8601.htm>."

Near Optimal Explicit Guidance Law with Impact Angle Constraints for a Hypersonic Reentry Vehicle

Karthikeyan Kalirajan
Research Scholar,
Department of Aerospace Engineering,
Indian Institute of Technology, Bombay, India 400076.
karthik@aero.iitb.ac.in

Ashok Joshi
Professor,
Department of Aerospace Engineering,
Indian Institute of Technology, Bombay, India 400076.
ashokj@aero.iitb.ac.in

ABSTRACT

Two guidance laws are discussed in this paper. The first one is the Vector guidance law. This guidance law when equipped with the appropriate gains has the capability to hit a target at the desired impact angle. A parametric method to find the optimal gains of this guidance law which will maximize the impact velocity and keep the miss distance and impact angle errors within bounds is developed in this research. Further, it is seen that the separation in the upper and lower bounds increases with increase in one of the gain values. Also, it is found that, only one of the gain values is independent and that the other dependent gain value is related through a simple straight-line expression. Next guidance law to be discussed is the Diveline guidance law. This law uses multiple divelines to hit a target at the desired impact angle. In the present research, the capability of this Diveline guidance law using a single diveline is analyzed. A method to derive the Diveline guidance law from the Vector guidance law is given in this study. The miss distance and impact angle errors evolving because of reducing the maximum acceleration limit is studied using simulations. Finally, three methods to increase the capture region (i.e. bounds on the set of initial states to achieve zero errors) of a guidance law is discussed.

KEYWORDS: *Diveline guidance, Explicit Guidance, Impact angle constrained Guidance, Reentry guidance.*

Assessment of chemical time scale for a turbine burner

Dragoș ISVORANU

Dept. of Aerospace Sciences, Fac. of Aerospace Engineering, Univ. Politehnica of Bucharest

Professor

1-7, Gheorghe Polizu street, 011061, Bucharest, ROMANIA

dragos.isvoranu@upb.ro

Sterian DĂNĂILĂ

Dept. of Aerospace Sciences, Fac. of Aerospace Engineering, Univ. Politehnica of Bucharest

Professor

Alina BOGOI

Dept. of Aerospace Sciences, Fac. of Aerospace Engineering, Univ. Politehnica of Bucharest

Assoc. Professor

Constantin LEVENȚIU

Dept. of Aerospace Sciences, Fac. of Aerospace Engineering, Univ. Politehnica of Bucharest

PhD., Lecturer

ABSTRACT. Understanding the relationship between chemical kinetics and turbulent mixing characteristic time scales provides the necessary knowledge to establish the type of combustion regime, which, furthermore, helps grasping the main characteristics of the flame physics. One of the most convenient tools for evaluating the turbulence/chemistry interaction is provided by the analysis of the Damköhler number field distribution. Literature survey provides several examples of Damköhler number computation, mostly regarding single global chemical reaction. The present work aims at applying this procedure for the calculation of the chemical time-scale (and thus of the Damköhler number) for the two-step kinetic mechanism of Westbrook and Dryer used in the simulation of gas reheat inside a turbine stage. Based on this methodology, we may be able to establish which chemistry-turbulence interaction model is more appropriate for a specific simulation (finite-rate eddy dissipation concept, flamelet approach, etc.). The research has set forth important variations of the Damköhler number (in the order of hundreds of units) throughout the flow domain. In the wake of the injector where the turbulent intensity is high and the incipient incomplete mixing prohibits fuel ignition, the flow is completely controlled by turbulence and Damköhler number is low. Hence, the appropriate turbulence/chemistry model could very well be an eddy dissipation concept type. Similar approach should be chosen for the rotor-stator passage, also. Conversely, in the rotor passage, due to the blocking effect of the walls and the strong interactions between fluid tensions and pressure, the turbulence intensity is diminished and the appropriate fuel oxidizer mixing triggers ignition and flame sustainability.

KEYWORDS: turbine burner, Damköhler number, chemical time scale



Design and aerodynamic analysis of a regional turboprop innovative configuration

Fabrizio Nicolosi

Associate Professor

Department of Industrial Engineering (DII)- University of Naples "Federico II"

Via Claudio 21, 80125 Napoli – ITALY

fabrnico@unina.it

Salvatore Corcione

Post Doc

Pierluigi Della Vecchia

Assistant Professor

Vittorio Trifari

PhD student

Manuela Ruocco

PhD student

Agostino De Marco

Assistant Professor

ABSTRACT

This paper deals with the fundamental results of the first loop of design and aerodynamic analysis of a new regional turboprop concept.

The aircraft has a low wing and two innovative architecture of turboprop engine installed at the horizontal tail tips. It can seat up to 130 passengers with a design range of about 3000km. It is designed to fly at Mach number of about 0.62 at a cruise altitude of 9000m with an efficiency about 18. The required maximum lift coefficients in clean, take-off and landing conditions are 1.6, 2.4 and 3.0 respectively.

Wing sections have been specifically designed to comply with the very challenging requirements in terms of minimum drag (natural laminar flow), maximum clean lift coefficients and compressibility effects. The high lift devices have been designed too. A single fowler flap layout has been considered. To augment the aircraft maximum lift capabilities in landing condition, preserving the wing laminar flow, the effects of a simple droop nose have been investigated. To improve climb performance a specific winglet design has been assessed, results show that a reduction of about 10% of the induced drag during both climb and cruise phase could be achieved.

All the criticalities emerged during the first loop will feed a second design loop to well asses this innovative concept.

KEYWORDS: *Aircraft Design, Aerodynamic analysis, Aircraft performance, Innovative Turboprop*

NOMENCLATURE

ADAS - Aircraft Design and Analysis Software
 CFD - Computational Fluid Dynamic
 CIRA - Italian Aerospace Research Center
 DAF - Design of Aircraft and Flight Technologies research group
 DATCOM - USAF Stability and Control (Data Compendium)

FL - Flight Level
 FusDes - Fuselage Design Methods
 IRON - Innovative turbopROP configuration
 ISA - International Standard Atmosphere
 JPAD - Java-Based Framework for Aircraft Preliminary Design and Optimization
 MLW - Aircraft Maximum Landing Weight



MTOW - Aircraft Maximum Take Off Weight
 MZF - Aircraft Zero Fuel Weight
 NACA - National Advisory Committee for Aeronautics
 OEW - Aircraft Operative Empty Weight
 RANS - Raynolds Average Navier Stokes
 SFC - Specific Fuel Consumption
 TLAR - Top Level Aircraft Requirements
 TRL - Technology Readiness Level
 UNINA - University of Naples
 b_w - Wing span
 C - wing section chord
 C_d - Airfoil drag coefficient
 C_D - Aircraft drag coefficient
 C_{D0} - Aircraft parasite drag coefficient
 C_{DW} - Isolated wing drag coefficient
 C_L - Aircraft lift coefficient
 C_l - airfoil lift coefficient
 C_{Leq} - Aircraft lift coefficient in trimmed condition
 C_{Lmax} - Aircraft maximum lift coefficient
 C_{lmax} - airfoil maximum lift coefficient
 C_{LW} - Isolated wing lift coefficient

C_m - Airfoil pitching moment coefficient
 C_r - Wing root chord
 C_t - Wing tip chord
 E - Aircraft aerodynamic efficiency
 ϵ - local wing section twist angle
 e_w - Wing induced drag factor
 M - Mach number
 Re - Reynolds Number
 S_w - Wing area
 t/c - local wing section non-dimensional thickness
 X_{cg} - Centre of gravity longitudinal position
 X_{le} - local wing section leading edge longitudinal position
 α^* - local wing section angle of attack at the end of lift curve linear segment
 α_{zi} - local wing section zero lift angle of attack
 η - non-dimensional wing span
 λ - Wing taper ratio
 $\Lambda_{c/4}$ - Wing sweep angle at the quarter chord line

1 INTRODUCTION

The Innovative turboprop configuration (IRON) project complies with the European Union topic JTI-CS2-2015-CPW02-REG-01-03 (Green and cost efficient Conceptual Aircraft Design including Innovative Turbo-Propeller Power-plant) as part of the Clean Sky 2 program for Horizon 2020.

The topic leader is Leonardo and several core-partners are involved into the project. CIRA (Italian Aerospace Research Center) is coordinator of IRON project.

The project is focused on the feasibility study of an innovative turboprop regional configuration. The research, addressed to the analysis and design of this innovative regional aircraft will be developed through 3 different loops with increasing level of complexity and fidelity. The project aims to complete the design through numerical simulations and experimental validations will be performed so that at the end of the project a Technology Readiness Level (TRL) 4 will be reached.

The loop 1 analysis started in July 2016 from a baseline configuration provided by Leonardo Company. It is an innovative layout with low wing and engines mounted on the horizontal tail tips. Top Level Aircraft Requirements (TLAR) have been issued by Leonardo Company, which also provided the aircraft maximum takeoff weight and wing area. TLAR are very challenging, requiring a cruise speed of 0.62 Mach number at 9144m (30000 feet), with a moderately high lift coefficient and low drag coefficient to achieve a value of 18 in cruise aerodynamic efficiency, a maximum lift coefficient of 1.6 in clean conditions and 3.0 in landing conditions. Moreover, it is expected that the wing inner airfoils have an 18% relative thickness to allow landing gear to be stored within. Most of the design and analysis tools used in this phase are semi-empirical methods and panel codes, with the possibility to perform few CFD RANS analyses to check the obtained results.

In this paper, a summary of the most significant results obtained during the loop 1 of design is presented. The second section of this paper deals with a brief description of the aircraft layout and TLAR requirements provided by Leonardo Company. The third section is focused on the design and the aerodynamic analysis of the wing sections, highlighting all the efforts encountered during the airfoil design phase to comply with the challenging tasks deriving from the TLAR. The fourth section complies with the two-dimensional design of the high lift system and the prediction of the three-dimensional high lift capabilities of the wing. The fifth section illustrates the method used to build up per aircraft components the complete aircraft drag polar in several conditions. These drag polar have been used to perform both stability and control analysis and performance evaluations. Finally, in section 6 some conclusions are drawn highlighting all the criticalities emerged from the loop 1 activities about this innovative aircraft configuration that will feed the input for the loop 2 of design process.



2 I RON REFERENCE AI RCRAFT AND REQUI REMENTS

The reference aircraft, design requirements and Top-Level Aircraft Requirements (TLAR) were provided by Leonardo Company at the beginning of the loop 1. In section 2.1 mission specification and aerodynamic requirements are summarized, and in section 2.2 the baseline geometric layout and its most significant characteristics are illustrated.

2.1 Mission specification and requirements

Design requirements issued by Leonardo on 15 November 2016 are summarized in Table 3, the aerodynamic target and the aircraft baseline assumptions are summarized in Table 2, while some main external geometric characteristics are summarized in Table 1. A sketch of the aircraft layout is presented in Fig. 1.

Table 1: Aircraft baseline input geometric data

Fuselage	Height/width	3.55 m
	Length	38.04 m
Wing	Planform area	100-110 m ²
	Aspect ratio	12
	Leading edge sweep angle	5°-10°

Table 2: Aerodynamic requirements and preliminary weight calculation

Aerodynamic targets	
Cruise efficiency	18
C_{Lmax} landing	3.0
C_{Lmax} T.O. and approach	2.4
C_{Lmax} clean	1.6
Aircraft baseline assumptions	
OEW	33550 Kg
MTOW	53610 Kg
MZFW	49345 Kg
MLW = 97% MTOW	52000 Kg
Payload	13585 Kg
Fuel (Design range)	6475 Kg
Max Str. Payload	15795 Kg
Climb phase	190 KCAS

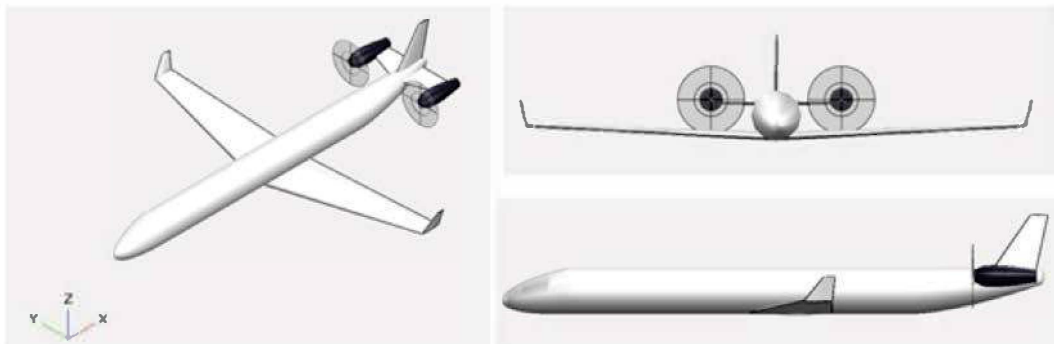


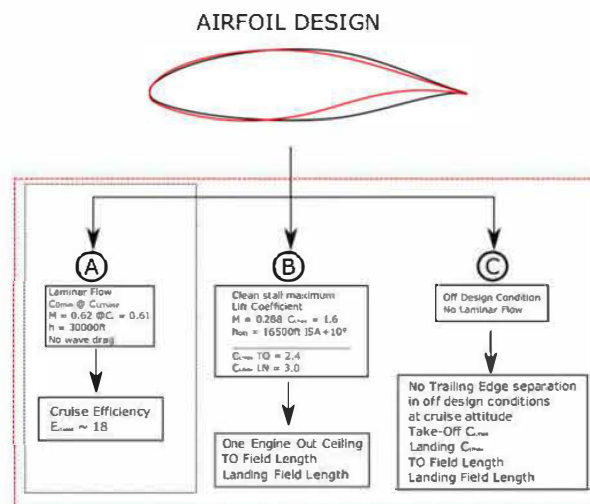
Figure 1: Innovative turboprop aircraft baseline

**Table 3: Top Level Aircraft Requirements provided by Leonardo Company**

1	Passenger capacity	130 pax at 32" seat pitch	
2	Range with Standard Passenger Payload	Max payload @ 1600 nm (104.5 Kg x pax); Reserve: a) 30' holding @ 1500 ft b) 100 nm alternate c) 5% of trip fuel	
3	Cruise Speed	@ FL300 - ISA - 97% MTOW $M_{CR} = 0.62$	
4	Time to climb	@ MTOW - ISA - from 1500 ft to FL250 $\leq 13'$	
5	Weight Definition		
	A	Pax + Baggage	103 Kg @ pax
	B	Catering	1.5 Kg @ pax
	C	OEW	33580 kg
6	Field Performance		
	A	Take off field length	ISA - SL -MTOW BFL < 4600 ft (1400m)
	B	Take off from Denver	@ 5400 ft Alt. - ISA+30 - TOW for 400 NM: AC Take-Off with full Pax
	C	Landing field length	@ ISA SL - MLW - Dry runways: LFL < 4260 ft (1300 m)
	D	Steep Approach	Descent approach = 5.5 deg.
7	CEILING		
	A	OEI (One Eng. In.)	@ ISA +10° - 97% MTOW - AC ON One Engine Net > 16500 ft (5029 m)

3 AIRFOIL DESIGN AND WING ANALYSIS

To comply with the aerodynamic requirements of the IRON project, a specific airfoil has been designed. The design of the airfoil moved around three main points (see Fig. 2).

**Figure 2: Scheme of the airfoil targets for its design**



To match the required cruise efficiency a laminar airfoil (wing) was required, avoiding any drag increase deriving from strong shock waves (Target A of Fig. 2). To reach the prescribed maximum lift coefficients, the airfoil must have a good enough maximum clean lift coefficient (Target B of Fig. 2). Finally, to avoid a large decay of the aerodynamic performance, the off-design conditions must be checked (Target C of Fig. 2). Moreover, Leonardo's requirements provide for a fixed thickness distribution along the wing span: the root and kink sections must have a thickness of 18% of the local chord while the tip section must have a thickness of 14% of the local chord.

To perform the airfoil design, a preliminary wing analysis was required to better understand the most significant aerodynamic conditions at which the airfoil should work. To accomplish this a reference set of airfoil has been assumed. According to the Target A of Fig. 2, a laminar airfoil is needed, thus as good starting points the NACA 66(3)-418 airfoil has been chosen for both root and kink section (having the same percentage thickness), while for the tip airfoil a NACA 63-415, scaled to 14% of thickness, has been considered. These airfoils have been investigated by means of MSES software [1]. The main data to accomplish a preliminary wing analysis are illustrated in Table 4.

The approach used to assess the preliminary wing analysis in terms of lift 3-D lift curve and wing span loading is described in [3]. The wing span loading calculation has been coupled with a classical stall path approach in order to derive the maximum clean lift coefficient of the wing under investigation.

Results of the preliminary wing analysis are shown in Fig. 3, where the wing span loading distribution at a wing lift coefficient of 0.6 is illustrated. The summary of this results is shown in Table 5. This preliminary 3-D analysis allowed to define the aerodynamic conditions for the airfoil design. According to results of Table 5, the wing section should have a minimum drag in the range of lift coefficient of about 0.5 and 0.7 for both root and kink sections, while for the tip the minimum drag should be placed in the range of C_l of about 0.2 and 0.4.

Table 4: main aerodynamic and geometric characteristics of reference set of airfoil and relative aerodynamic conditions

Section	Y(m)	H	C(m)	$X_{le}(m)$	$\epsilon_{ps}(deg.)$	$\alpha_{stl}(deg.)$	t/c	$\alpha^*(deg.)$	C_{lmax}	CRUISE		STALL	
										Re	M	Re	M
Root	0.00	0.00	4.48	19.09	0.00	-3.21	0.18	12	1.83*	25.8e ⁶	0.620	17.6e ⁶	0.288
Kink	5.32	0.30	3.47	20.00	0.00	-3.14	0.18	12	1.81*	20.0e ⁶	0.620	13.6e ⁶	0.288
Tip	17.75	1.00	1.65	22.22	-2.00	-2.99	0.14	12	1.74*	9.5e ⁶	0.620	6.5e ⁶	0.288

*Estimated with MSES, available experimental data about these airfoil are lower than the numerical estimations [2].

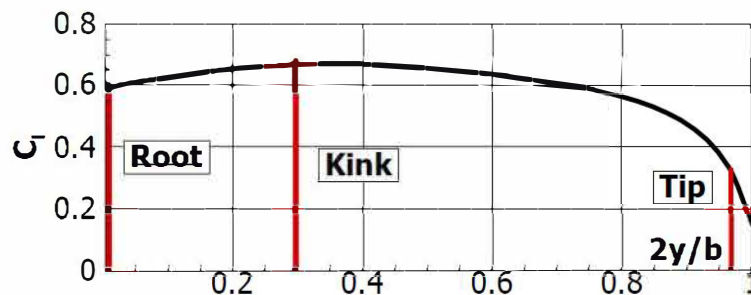


Figure 3: Preliminary 3-D wing span loading at cruise condition (NACA airfoil)

Table 5: Wing sections lift coefficients required to reach a wing $C_L = 0.60$
Required airfoil lift coefficient for the cruise (wing twist -2°)

Section	Y(m)	η	C(m)	$X_{le}(m)$	$\epsilon_{ps}(deg.)$	t/c	C_l cruise
Root	0.00	0.00	4.48	19.09	0.00	0.18	0.60
Kink	5.325	0.30	3.47	20.00	0.00	0.18	0.68
Tip	17.75	1.00	1.65	22.22	-2.00	0.14	0.25



The design of the airfoil has been accomplished by means of the inverse design routine of MSES software, by modifying the pressure coefficient distribution on the airfoil until the desired aerodynamic characteristics have been reached. The inverse design started from the NACA 66(3)-418 reference airfoil and was focused on the kink airfoil because this is the most significant wing section. The designed airfoil for the kink section is illustrated in Fig. 4, where there is also shown the comparison with the reference NACA airfoil. The main tool used to investigate the aerodynamic characteristics of this airfoil is MSES. Fig. 5 shows the kink airfoil drag polar in cruise condition in both design and off-design (loss of laminar flow, fully turbulent conditions). The minimum drag is spread over a wide range of lift coefficient, the airfoil shows a minimum drag coefficient of about 40 drag counts at the cruise lift coefficient (about 0.6-0.7). This characteristic allows the tip airfoil design can be derived by simply scaling the kink section thickness. Fig. 6 shows the lift curve of the kink airfoil in stall condition. The high lift characteristics have been also assessed by means of numerical analysis performed through a high-fidelity tool like a RANS (Raynolds Average Navier Stokes) solver, as illustrated in Fig. 6 where the comparison between MSES and RANS results is shown. Fig. 7 illustrates the pitching moment coefficient of the kink airfoil in cruise and stall conditions (MSES calculations). Fig. 8 shows the non-dimensional abscissa of the flow transition on the upper and lower surface of the kink airfoil in cruise condition by means of MSES, at cruise condition (Cl around 0.6-0.7 the airfoil exhibits a laminar flow extension of about 50% of the chord). The same numerical analyses have been accomplished also for the root and the tip sections to have a complete airfoil aerodynamic database to be used for the wing analysis.

This airfoil design was not an easy task because of the very challenging aerodynamic requirements and the thickness constraints. This design was a good comprise among the various aspects involved into the design campaign.

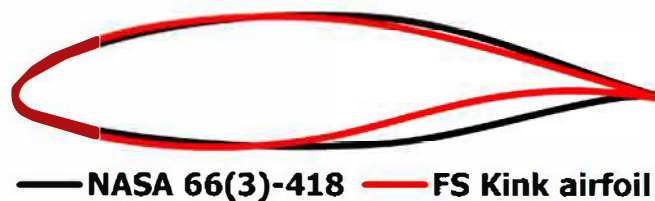


Figure 4: Kink airfoil, comparison with the reference NACA 66(3)-418

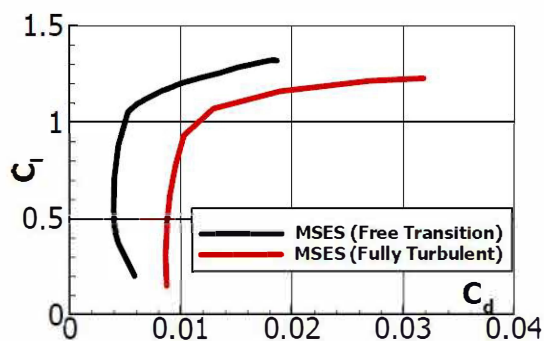


Figure 5: Kink airfoil, drag polar in cruise condition, free transition vs. fully turbulent

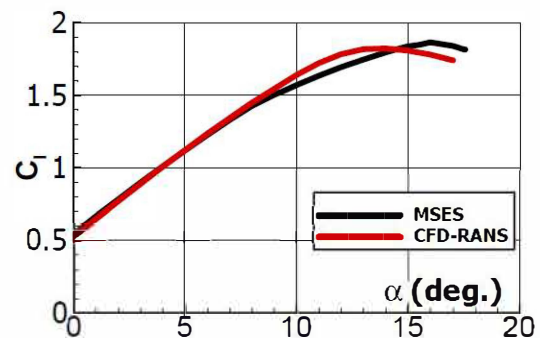


Figure 6: Kink airfoil, lift curve in stall condition, MSES vs. CFD

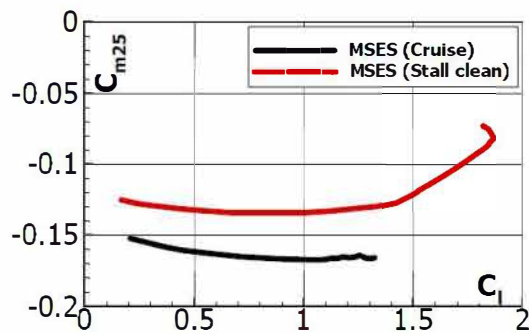


Figure 7: Kink airfoil, pitching moment coefficient in cruise and stall conditions

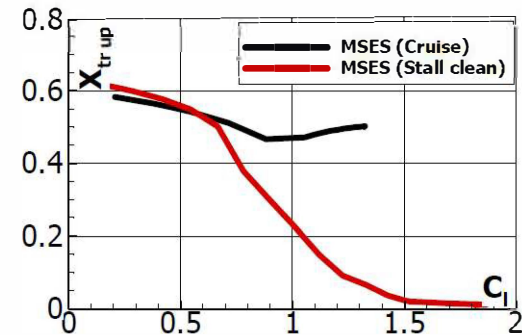


Figure 8: Kink airfoil, non-dimensional transition abscissa

4 2-D HIGH LIFT DEVICES DESIGN AND 3-D WING HIGH LIFT PREDICTION

Once the design of the wing sections has been assessed, the high lift devices design has been accomplished. To meet the requirements provided by Leonardo in terms of maximum lift coefficients for the take-off and landing, a single slot fowler flap has been considered as suitable trailing edge high-lift device. The design of the fowler flap has been assessed for three wing sections: inner flap, kink section and outer flap section. This has been necessary because those three sections have three different flap chord ratios as illustrated in Table 6 and sketched in Fig. 9. Suggestions about the flap chord and wing span extension have been derived from a preliminary design and sizing phase performed at the beginning of the loop 1 of design.

Table 6: Flap geometry and aerodynamic conditions

Sec.	η	c_f/c	Take-Off		Landing	
			M	Re	M	Re
Inner	0.11	0.27	0.171	$16.2e^6$	0.154	$14.5e^6$
Kink	0.30	0.32	0.171	$17.7e^6$	0.154	$16.0e^6$
Outer	0.78	0.32	0.171	$8.8e^6$	0.154	$7.8e^6$

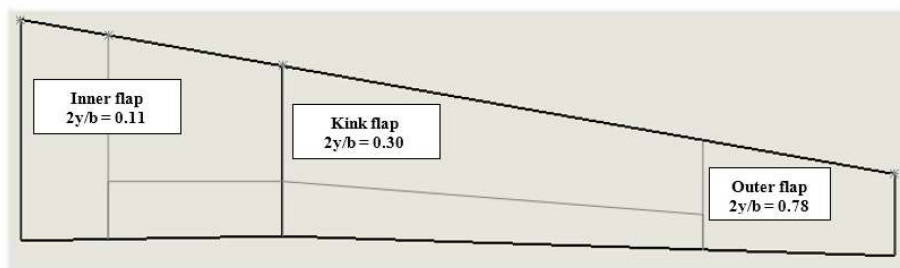


Figure 9: High-lift devices wingspan location sketch

The design of the fowler flap has been performed following the suggestions that can be found in the NASA report CR 2443 [4]. This paper is a report of a two-dimensional wind-tunnel evaluation of two fowler flap configurations on GA(W)-1 airfoil. Two fowler flap configurations are investigated, one configuration has a fowler flap chord of 29% chord and the second one has a flap chord length of 30% of chord. Optimum flap deflection, slot gap and overlap are reported as function of C_l , the maximum achieved C_{lmax} is 3.8 for a deflection of 40° .

Following the suggestions presented in this report the slot and the flap geometry have been designed on the IRON wing.



Based on the preliminary flap sizing accomplished during the preliminary design phase, where the baseline configuration layout has been assessed by means of two software developed at UNINA called

ADAS (Aircraft Design and Analysis Software) and JPAD (Java-Based Framework for Aircraft Preliminary Design and Optimization) [5][6][7], the high lift systems extends from the 11% to 78% of the wing span and the mean value of the flap chord length is 32% of chord.

The flap design has been performed on the kink section which is the most significant wing section (the 3D wing will exhibit aerodynamic characteristics close to this section), the same flap design parameters derived for the kink have been applied to both inner and outer flap.

The positioning of the fowler flap is achieved by a combined translational and rotational movement that drives the pivot point (see Fig. 10) to be placed in such position that guarantees the best values of both slot gap and slot overlap (these two parameters are defined according to [4]). The pivot point is the centre of the circumference which is tangent to the leading edge of the flap. The deflection angle of the flap is referred to a rigid body rotation around the pivot point.

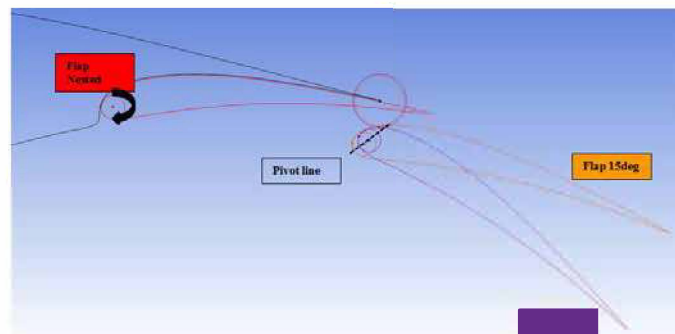


Figure 10: Fowler flap design: flap positioning

To choose the right gap and overlap values different positions of the flap have been analysed by means of MSES tool. The right positioning of the flap has been accomplished by the “airset” routine of MSES software, this routine allows the user to define a reference point (the blue circle in Fig. 11 left) with respect to the flap can be moved and rotated. The right positioning of the flap for a specific deflection has been chosen to place the expansion peak of the pressure coefficient almost at the exit of the flap slot, in order to have the maximum flow acceleration avoiding the flow separation on the flap (see Fig. 11 right). Once the right positioning of the flap has been fixed the flap geometry has been exported in terms of cartesian coordinates and has been analysed by means of both MSES and CFD RANS solver.

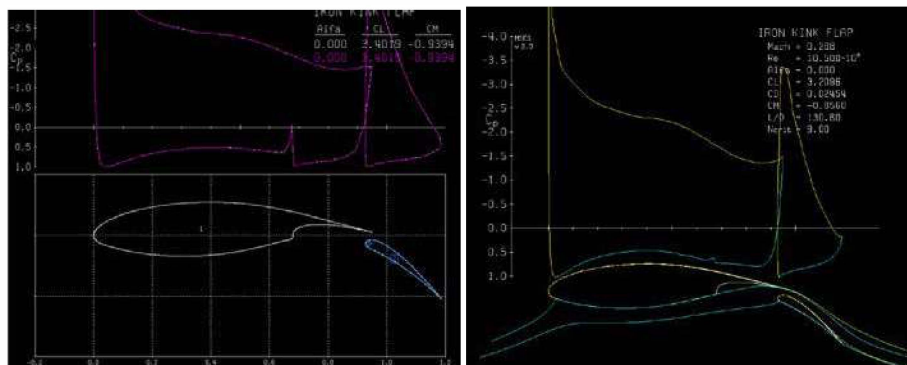


Figure 11: Fowler flap design: flap positioning with “airset” tool of MSES software

Fig. 12 shows the final positions of the kink flap at the three considered flap deflections (15-20° for the take-off conditions and 35° for the landing). Fig. 13 shows the comparison between the numerical results of MSES and CFD-RANS calculations in terms of lift curve for the kink section with a flap



deflection of 15° , while Fig. 14 shows the pressure contour calculated by means of CFD-RANS simulation at the take-off conditions for the kink flap section at angle of attack of 15° .

Same results are shown in Fig. 15 and Fig. 16 where the kink flap section has been analysed at the landing condition with a flap deflection of 35° .

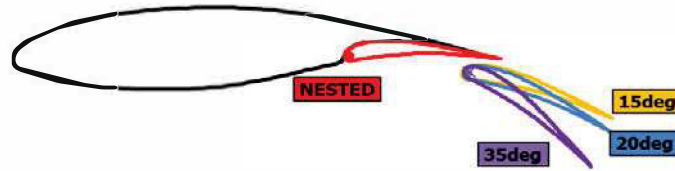


Figure 12: Fowler flap design for the kink section, flap chord length is 0.32% of chord.

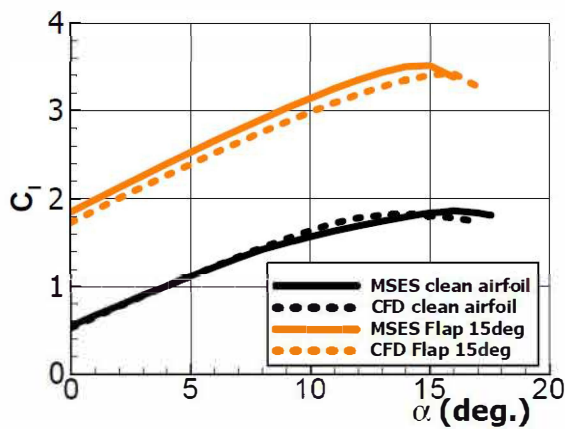


Figure 13: Fowler flap design: flap 15 deg. MSES vs. CFD, $M = 0.17$ $Re = 13.7e6$

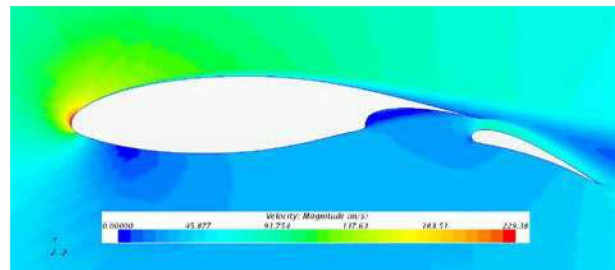


Figure 14: Fowler flap design: flap 15 deg. CFD velocity magnitude contour, $M = 0.17$ $Re = 13.7e6$ $\alpha = 15^\circ$

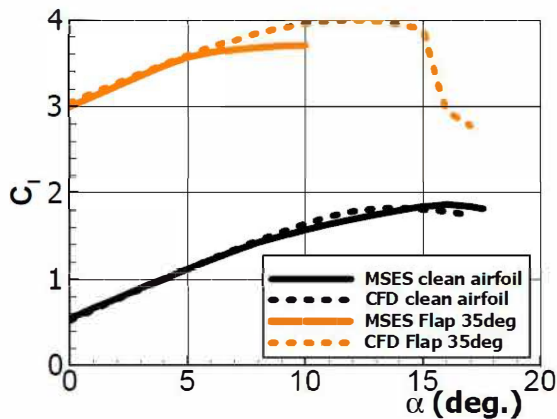


Figure 15: Fowler flap design: flap 35 deg. MSES vs. CFD, $M = 0.15$ $Re = 12.3e6$

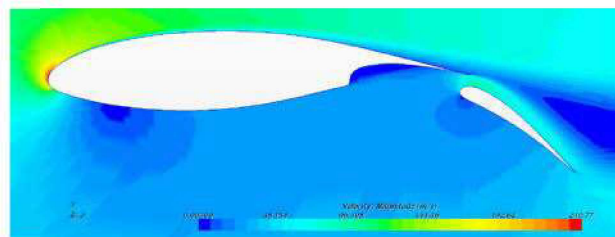


Figure 16: Fowler flap design: flap 35 deg. CFD velocity magnitude contour, $M = 0.154$ $Re = 12.3e6$ $\alpha = 15^\circ$

From Fig. 18 to Fig. 20 the lift curve, the drag polar and the pitching moment variation are illustrated for the kink flap sections at several flap deflections (solid lines).

Table 7 shows the summary of the 2-D results in terms of maximum achievable lift coefficient, $\Delta C_{l_{max}}$ and ΔC_{D0} for the take-off conditions. Same results concerning the landing flap deflection are summarized in Table 8.



Because the prescribed maximum lift coefficients for the landing requirements could be hardly achieved with a single fowler flap, a possible design of leading edge high lift device has been also evaluated. Because the wing laminar flow is mandatory to achieve the target efficiency and the conventional leading edge high lift devices (i.e. slats) disturbs the flow and could cause transition to turbulent flow

immediately after the slat gap, smart seamless and gapless high lift devices at the wing leading edge are mandatory for a laminar wing of significantly increased aerodynamic efficiency.

A possible design of a droop nose here is presented. Authors have investigated the effects of morphing in previous articles [8]. In this case the benefit of the smart droop nose comes from a smooth surface without gaps and steps. Following some suggestions that can be found in the literature [9], a simplified droop nose geometry is here derived and analysed by means of CFD RANS solver, to derive some useful information about the effects of a possible droop nose on the high lift characteristics of the IRON wing.

Table 7: IRON kink flap main results Take Off Conditions Flap= 15°, CFD results

Flap 15deg.	C_{lmax}	ΔC_{lmax}	$\Delta C_l @ \alpha_B = 13^\circ$	$\Delta C_d @ \alpha_B = 13^\circ$	$\Delta C_m @ \alpha_B = 13^\circ$
Clean airfoil	1.76	---	---	---	---
Inner section	3.24	1.48	1.24	0.0161	-0.332
Kink section	3.42	1.66	1.45	0.0241	-0.425
Outer section	3.36	1.60	1.31	0.0264	-0.425

Table 8: IRON kink flap main results Landing Conditions Flap= 35°, CFD results

Flap 35deg.	C_{lmax}	ΔC_{lmax}	$\Delta C_l @ \alpha_B = 10^\circ$	$\Delta C_d @ \alpha_B = 10^\circ$	$\Delta C_m @ \alpha_B = 10^\circ$
Clean airfoil	1.76	---	---	---	---
Inner section	3.74	2.03	2.16	0.0405	-0.553
Kink section	4.00	2.28	2.46	0.0524	-0.656
Outer section	3.75	2.04	2.26	0.0631	-0.615

The simplest droop nose geometry, here investigated, is obtained by rotating the 15% of the local chord with respect to a point located on the lower airfoil surface at the specified $x/c=0.15$. This design is a simplification of the droop nose geometry that can be found in [9], where both numerical CFD and experimental wind tunnel tests have been performed to evaluate the effects of droop nose on the high lift characteristics on the airfoil of high efficiency laminar wing. In this preliminary design and analysis of the droop nose, the effects of a deflection of 15 degrees has been considered for all flap conditions. However, in landing conditions the droop nose deflection could be higher than 15°, as suggested in [9], where the best combination was 25 degrees of droop nose with 35-40 degrees of flap. In this work, only the combination of flap 35 degrees and droop nose of 25 degrees has been analysed, useful in landing condition. Fig. 17 shows the simple droop nose geometry used in this analysis.

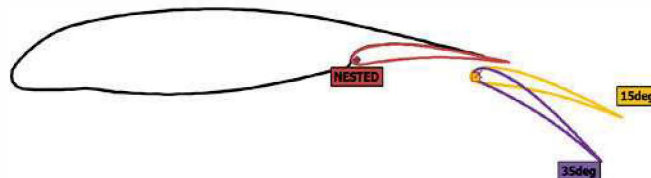


Figure 17: Kink flap section with 15% c and 15° and 35° of droop nose geometry.

From Fig. 18 to Fig. 20 the effects of the droop nose on the lift, drag and pitching moment coefficient respectively are illustrated concerning the kink section (dotted lines), the same analyses have been performed also on the inner and outer flap sections. The droop nose delays the stall and increases the maximum lift coefficient. In Table 9 and Table 10 the variations in terms of stall angle and maximum achievable lift coefficients are summarized for the take-off and landing conditions



respectively. A droop nose deflection of 15 degrees meanly increases the maximum achievable lift coefficient around 0.1 for each wing section, while a 25 degrees droop nose deflection on 35 degrees of flap increases the C_{lmax} around 0.2. This droop nose design, having an extension of 15% of the chord and a deflection of 15 degrees or 25 degrees, does not affect in a significantly way the pitching moment coefficient.

At high lift coefficients, the droop nose reduces the drag. Comparable results in terms of drag variation can be found in [9]. The drag reduction due to the droop nose can be found at high lift coefficients typical of flap down configurations.

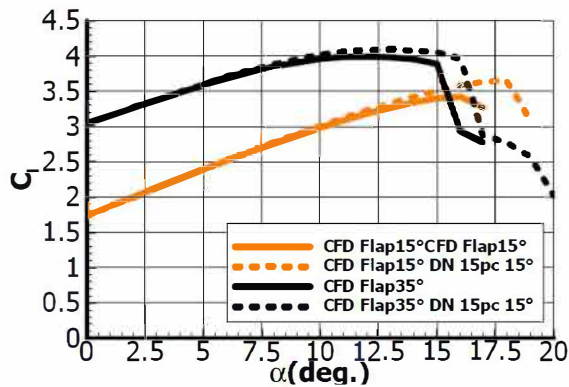


Figure 18: Kink flap section, effect of droop nose on lift coefficient, CFD results

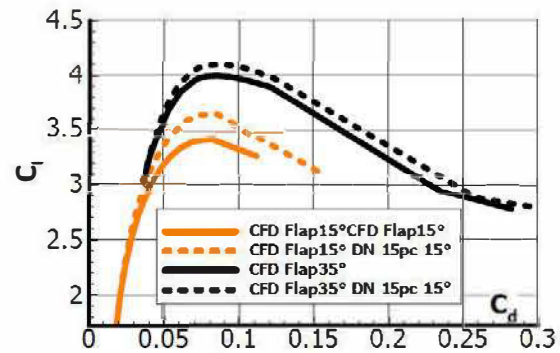


Figure 19: Kink flap section, effect of droop nose on the drag polar, CFD results

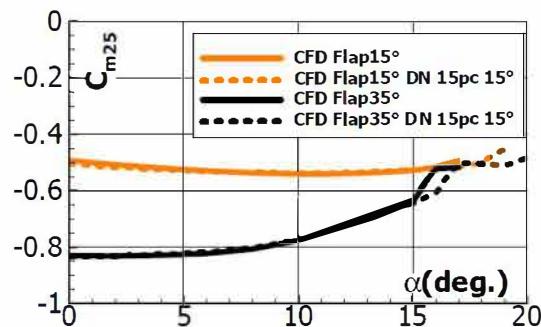


Figure 20: Kink flap section, effect of droop nose on the pitching moment coefficient, CFD results

Table 9: IRON droop nose CFD results Take Off Conditions Flap= 15° and Droop-Nose defl. = 15°

	C_{lmax}		ΔC_{lmax} (Droop-Clean)	$\Delta C_l @$ $\alpha_B = 13^\circ$ (Droop-Clean)	$\Delta C_d @ \alpha_B = 13^\circ$ (Droop-Clean)	$\Delta C_m @ \alpha_B = 13^\circ$ (Droop-Clean)
Clean airfoil	1.76		---	---	---	---
Flap 15deg.	Flap Only	Flap& Droop				
Inner section	3.24	3.40	1.64	1.35	0.0118	-0.324
Kink section	3.42	3.65	1.89	1.58	0.0181	-0.422
Outer section	3.36	3.57	1.81	1.57	0.0183	-0.400

Table 10: IRON droop nose CFD results Landing Conditions Flap= 35°, Droop-Nose defl. = 25°

	C_{lmax}		ΔC_{lmax} (Droop-Clean)	$\Delta C_l @$ $\alpha_B = 10^\circ$ (Droop-Clean)	$\Delta C_d @ \alpha_B = 10^\circ$ (Droop-Clean)	$\Delta C_m @ \alpha_B = 10^\circ$ (Droop-Clean)
Clean airfoil	1.76		---	---	---	---
Flap 35deg.	Flap	Flap&				



	Only	Droop				
Inner section	3.74	3.99	2.23	2.23	0.0341	-0.557
Kink section	4.00	4.21	2.44	2.56	0.0452	-0.662
Outer section	3.75	4.08	2.32	2.47	0.0452	-0.662

Once the 2-D aerodynamic effects of flap and droop nose have been evaluated, the 3D high lift prediction has been accomplished through semi-empirical approach.

The method here used is a combination of numerical results concerning the 2-D data of the flap sections and a classical semi-empirical approach for the prediction of the 3-D wing high lift characteristics.

Concerning trailing edge devices, the DATCOM method has been used to compute the increment in maximum lift coefficient for the wing [10]. The two-dimensional $\Delta C_{l_{max}}$ have been assumed from the CFD calculations shown in Table 9 and Table 10. According with the 2D $C_{l_{max}}$ estimation from the CFD calculations, the maximum achievable 3D $C_{L_{max}}$ (in untrimmed conditions) are summarized in Table 11. The maximum achievable untrimmed $C_{L_{max}}$ is about 2.7 at take-off flap at 15° without droop nose and about 2.8 at flap deflection of 20° without droop nose. In landing configuration with a flap deflected at 40° the $C_{L_{max}}$ is about 3.0 without the droop nose and about 3.1 with a droop nose deflected at 25° . To assess the prediction of the maximum lift coefficient of the wing, some CFD-RANS calculations of the isolated wing with flap deflected (without droop nose deflection) have been performed. Results are shown in Fig. 21 and Fig. 22 in terms of lift curve, where the comparison between the semi-empirical 3-D prediction (orange circles) and CFD results (blue circles) is made, some pressure contours and streamlines are shown in Fig. 22 and Fig. 24. The CFD predictions lead to a $C_{L_{max}}$ at take-off (flap 15° no droop nose) of about 2.7 at a higher angle of attack than the semi-empirical predictions. At landing the CFD numerical prediction show a $C_{L_{max}}$ of about 3.4 larger than the predicted one by means of semi-empirical estimation.

Table 11: High lift devices: aerodynamic coefficient increments in take-off and landing conditions

Flap	$\Delta C_{l_{max}}$				ΔC_D				ΔC_M		
	Flap Only	Flap Droop 15°	Flap Droop 25°		Flap Only	Flap Droop 15°	Flap Droop 25°		Flap Only	Flap Droop 15°	Flap Droop 25°
15°	1.04	1.18	---		0.0164	0.0120	---		-0.288	-0.285	---
20°	1.18	1.30	---		0.0219	0.0171	---		-0.341	-0.331	---
35°	1.38	1.45	1.53		0.0373	0.0325	0.0304		-0.443	-0.450	-0.454

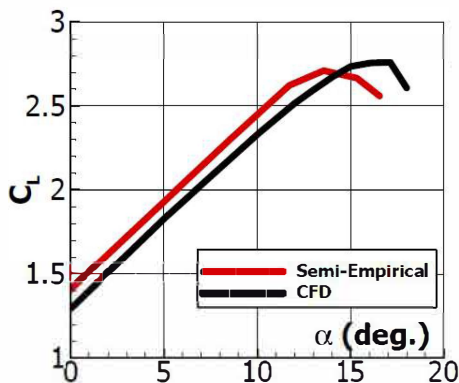


Figure 21: Isolated Wing flap at 15° , CFD vs. Semi-empirical prediction

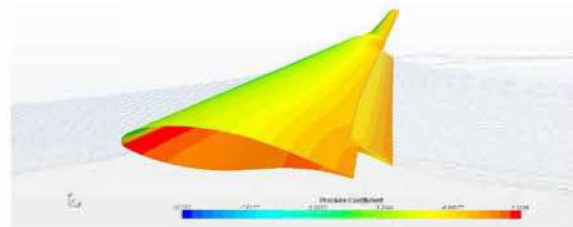


Figure 22: Isolated Wing at take-off conditions with flap at 15° , $\alpha = 10^\circ$

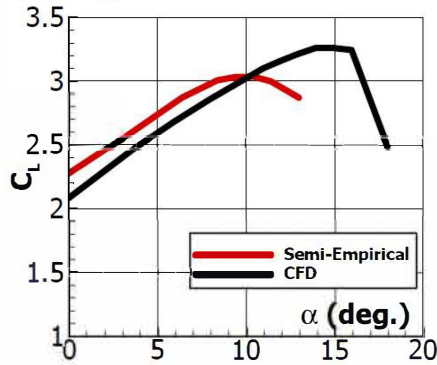


Figure 23: Isolated Wing flap at 35°, CFD vs. Semi-empirical prediction

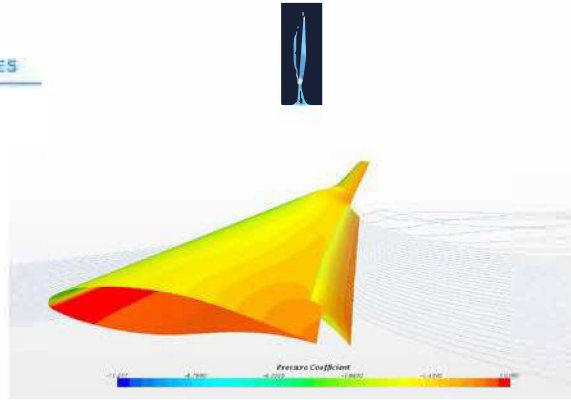


Figure 24: Isolated Wing at landing conditions with flap at 35°, alpha = 10°

5 DRAG POLAR ESTIMATION

Once the aerodynamic design and analysis phase has been accomplished the complete aircraft drag polar has been calculated in several aircraft configurations and conditions (according to the distinct phases of the aircraft mission profile). The fuselage aerodynamic contributions, also in terms of pitching moment instability (which influences the trim drag) has been carefully considered. Several calculations (CFD analysis) have been also performed on the fuselage and classical semi-empirical methods have been applied (see [9-11]). The fuselage results obtained through a dedicated methodology proposed by the authors has been also considered [12].

Several articles, also produced by the authors in the last years, have been used in order to assess the aircraft design and sizing (see [15-17]) and the aircraft drag polar and the aerodynamic contribution of different aircraft components (see [18][19]).

Methods to predict some drag contributions (like fuselage windshield drag) from classical sources (see [20][21]) have been also used. The aircraft drag polar is sum of several contributions calculated as follows:

- **WING:** integration of airfoils drag coefficient (coming from MSES aerodynamic calculations) along the wing span to estimate the parasite contribution. For take-off and landing conditions, the effect of high lift devices has been considered.
- **FUSELAGE:** CFD Navier-Stokes calculations have been used as function of fuselage angle of attack [$C_D = f(\alpha_B)$].
- **HORIZONTAL:** this contribution has been computed in the same manner of wing (integration of airfoil parasite drag along tail span); the drag dependent from horizontal tail lift has also been considered according parabolic formulation with $e_H = 0.9$; the drag contribution to trim the aircraft has been calculated as sum of 2 terms: i) $\Delta C_{DTRIM} = f(\Delta C_{LH})$; ii) parasite drag variation due to tail attitude and elevator deflection
- **OTHER COMPONENTS:** Vertical tail, nacelles, wing-fuselage interference, horizontal-nacelles interference, excrescences and miscellaneous items have been considered as a constant parasite drag source (see [20] [21]).
- **TAKE-OFF AND LANDING:** landing gear contribution has been considered according to [20]. In these conditions, only the flap deflections effects have been considered (no droop nose effects have been considered).

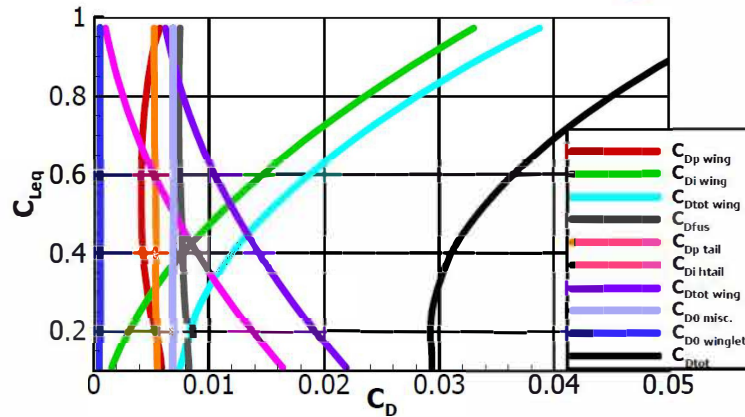


Figure 25: Drag breakdown, Cruise condition at $X_{cg} = 0.25\%$ MAC

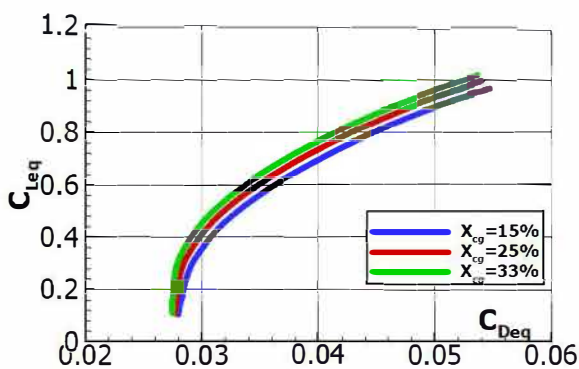


Figure 26: Aircraft trimmed drag polar, Cruise condition at several X_{cg} position

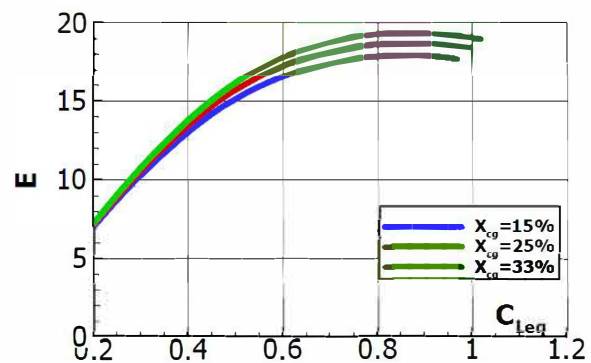


Figure 27: Aircraft efficiency in Cruise, trimmed conditions at several X_{cg} position

Fig. 25 shows the drag breakdown of complete aircraft vs. the trimmed lift coefficient in cruise conditions with a centre of gravity located at 25% of the mean aerodynamic chord of the wing. Fig. 26 shows the trimmed drag polar at several aircraft centre of gravity locations, Fig. 27 shows instead the complete aircraft efficiency. The cruise efficiency is strongly affected by the centre of gravity location and the target of 18 can be achieved only in the most backward position (33% of mean aerodynamic chord). This is due to the high trim drag required for this configuration with rear engine installation.

Fig. 28 shows the comparison between the aircraft efficiency in cruise with and without the winglet with a centre of gravity placed at 25% of MAC. To account for the additional wetted area of the winglet, a ΔC_{D0} about 5 drag counts has been considered. As it can be appreciated the aircraft efficiency in winglet off configuration is always lower than 18. The winglet has been specifically designed for this aircraft giving a reduction of about 10% of the induced drag, especially in the climb condition, but also in cruise, the designed winglet gives a benefit in terms of induced drag reduction since the aircraft will fly at moderately high cruise lift coefficient (about 0.6).

Fig. 29 shows the complete aircraft trimmed drag polar in several conditions with the centre of gravity placed at 25% of the mean aerodynamic chord. Fig. 30 shows the complete aircraft efficiency in clean stall conditions (take-off and first segment climb) at several positions of the centre of gravity.

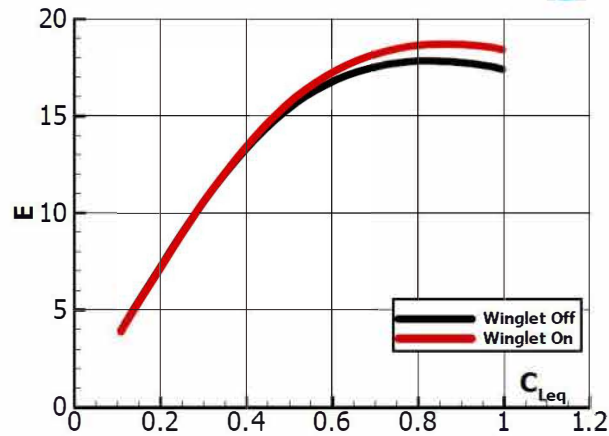


Figure 28: Aircraft efficiency with and without winglet, cruise conditions, at $X_{cg} = 0.25\%$ MAC

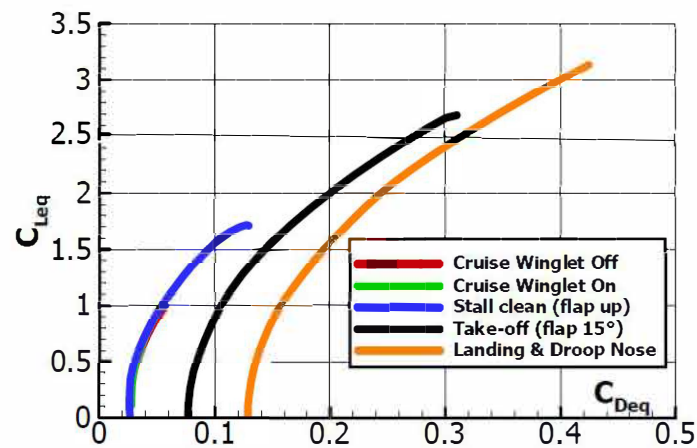


Figure 29: Aircraft trimmed drag polar, for several configurations, $X_{cg} = 25\%$ MAC

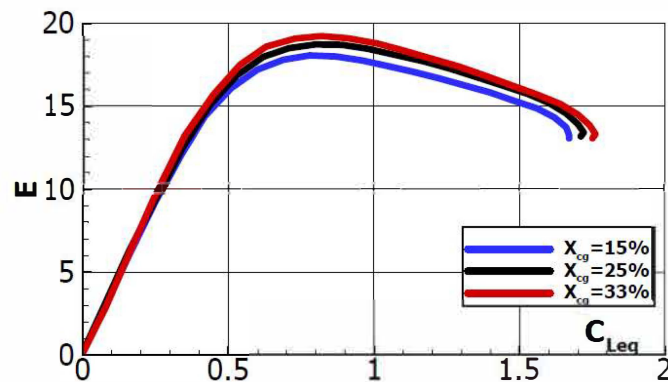


Figure 30: Aircraft aerodynamic efficiency, take-off and first segment climb (flap up) at several X_{cg} positions



6 CONCLUSIONS

The paper presents a synthesis of the main aerodynamic results of the first loop of design of an innovative turboprop aircraft configuration with rear engine installation. A set of wing sections has been specifically designed to comply with the requirements of this project. To reach the prescribed ground performance the high lift devices have been also designed and the effects of a possible morphed droop nose high lift device have been also investigated to augment the maximum lift capability of the aircraft in take-off and landing conditions.

The complete drag polar breakdown has been performed and the aircraft trimmed drag polar curves have been calculated to produce a complete aerodynamic data set that could feed the evaluation of the aircraft performance (not shown in this paper). Almost all the aerodynamic and performance requirements have been met, some criticalities dealing with this innovative configuration have emerged. The aircraft efficiency, trim and stability is strongly affected by the center of gravity position. All the criticalities emerged from the first loop of design and analysis will feed a refined assessment of the aircraft layout for a second loop.

ACKNOWLEDGEMENTS

The project leading to these results (IRON project) has received funding from the Clean Sky 2 Joint Undertaking under the European Union's Horizon 2020 research and innovation program under *Grant Agreement* n° 699715. The authors are grateful to the partners of the IRON consortium for their contributions and feedback.

REFERENCES

1. M. Drela; 1996; "Two-Dimensional Transonic Aerodynamic Design and Analysis Using the Euler Equations"; *Ph. D. Thesis, MIT*.
2. I.H. Abbott and A.E. Doenhoff; 1949; *Theory of Wing Sections: Including a Summary of Airfoil Data*; Dover Publications, INC; New York.
3. J.A. Jr. Blackwell; 1969; "A finite step method for calculation of theoretical load distribution for arbitrary lifting surface arrangements at subsonic speeds"; *NASA Langley Research Center, NASA-TN-D-5335*; Washington, United States; 1st July 1969.
4. W. Seetharam and H.J. Wentz; 1974; "Development of a fowler flap system for high performance general aviation airfoil"; *Center for Research, INC. University of Kansas, Kansas for Langley Research Center, NASA CR-2443*; Washington, D.C.; 1st Dec. 1974.
5. F. Nicolosi and G. Paduano; 2011; "Development of A software for Aircraft Preliminary Design and Analysis"; *3rd CEAS Air & Space Conference*; Venezia (IT); 702-714.
6. F. Nicolosi, A. De Marco, L. Attanasio and P. Della Vecchia; 2016; "Development of a Java-Based Framework for Aircraft Preliminary Design and Optimization"; *Journal of Aerospace Information System*; **13**; 234-242.
7. V. Trifari, M. Ruocco, V. Cusati, F. Nicolosi, A. De Marco; 2017; "Java framework for parametric aircraft design – ground performance"; *Aircraft Engineering and Aerospace Technology (EMERALD)*; Volume **89**, Issue **4**; DOI 10.1108/AEAT-11-2016-0209.
8. P. Della Vecchia, S. Corcione, R. Pecora, F. Nicolosi, I. Dimino, A. Concilio; 2017; "Design and integration sensitivity of a morphing trailing edge on a reference airfoil: The effect on high-altitude long-endurance aircraft performance"; *Journal of Intelligent material system and structures (JIMS)*; ISSN: 1045-389X; DOI: 10.1177/1045389X17704521
9. M. Kintscher, M. Wiedemann and H. Monner; 2011; "Design of a smart leading edge"; *International Journal of Structural Integrity*; **2(4)**; 383-405.
10. P. Sforza; 2014; *Commercial Airplane Design Principles*; Elsevier Science.
11. C. Perkins and R. Hage; 1949; *Airplane Performance Stability and Control*; John Wiley & Sons Inc.
12. F. Nicolosi, P. Della Vecchia, D. Ciliberti and V. Cusati; 2016; "Fuselage aerodynamic prediction methods"; *Aerospace Science and Technology*; 323-343.



13. F. Nicolosi, P. Della Vecchia, D. Ciliberti; 2013; "An investigation on vertical tailplane contribution to aircraft sideforce, "; *Aerospace Science and Technology (Elsevier) AESCTE* 2873, Volume **28**, Issue **1**, Pages 401–416; ISSN 1270-9638; DOI: 10.1016/j.ast.2012.12.006.
14. P. Della Vecchia, F. Nicolosi; 2013; "Aerodynamic guidelines in the design and optimization of new regional turboprop aircraft"; *Aerospace Science and Technology (Elsevier) AESCTE*, Volume **38**; Pages 88-104; ISSN 1270-9638; DOI: 10.1016/j.ast.2014.07.018.
15. F. Nicolosi, S. Corcione and P. Della Vecchia; 2016; "Commuter Aircraft Aerodynamic Characteristics through Wind Tunnel Tests"; *Aircraft Engineering and Aerospace Technology (EMERALD)*; Volume **88**; Issue **4**; 4 July 2016; Pages 523-534.
16. F. Nicolosi, P. Della Vecchia and D. Ciliberti; 2015; "Aerodynamic interference issues in aircraft directional control"; *ASCE's Journal of Aerospace Engineering*, Vol. **28**; N. **1**; January 2015, ISSN 0893-1321.
17. F. Nicolosi, P. Della Vecchia and S. Corcione; 2015; "Design and Aerodynamic Analysis of a Twin-engine Commuter Aircraft"; *Aerospace Science and Technology (Elsevier) AESCTE*, Vol. **40**; Jan. 2015; pp. 1-16, ISSN 1270-9638; DOI 10.1016/j.ast.2014.10.008.
18. H. Multopp; 1942; "Aerodynamic of the Fuselage"; National Advisory Committee for Aeronautics; Technical Memorandum 1036.
19. M. Munk; 1924; "The Aerodynamic Forces on Airship Hulls"; National Advisory Committee for Aeronautics; Technical Report 184.
20. J. Roskam; 2000; *Airplane Design – Part VI: Preliminary Calculation of Aerodynamic, Thrust and Power Characteristics*. DAR Corporation; Lawrence (KS).
21. D.P. Raymer; 1999; *Aircraft Design: A conceptual Approach*; 3rd edition; AIAA Education Series.

The effect of heat treatment on the homogenization of CMSX-4 Single-Crystal Ni-Based Superalloy

A. Paraschiv

*Romanian Research and Development Institute for Gas Turbines COMOTI
Scientific researcher
220D Iuliu Maniu Ave., Bucharest 6, Romania
alexandru.paraschiv@comoti.ro*

G. Matache

*Romanian Research and Development Institute for Gas Turbines COMOTI
Scientific Director*

C. Puscasu

*Romanian Research and Development Institute for Gas Turbines COMOTI
Head of the Department of Special components for gas turbines*

ABSTRACT

Two solution heat treatments were used for the homogenization of as-cast CMSX-4 single crystal Ni-based superalloy and their effects were investigated. The heat treatment temperatures were established using thermodynamic calculations based on the CALPHAD method. The effect of heat treatment on the homogenization degree was evaluated quantitatively using the local chemical composition and partition coefficients, and qualitatively using element distribution maps and backscattered electron images after each cycle of heat treatments. The evolution of porosity and dissolution of the γ/γ' eutectic pools and coarse γ' fractions were investigated using the quantitative image analysis. The experimental results showed that the strongly segregated microstructure of the as-cast superalloy homogenize with different rates as a function of temperature. In both cases a low residual level of microsegregation still maintain even after long term exposure at high temperatures. Long holding time at both temperatures generates a notable increase of porosity levels being more accentuated with the increase in temperature.

KEYWORDS: *superalloy, homogenization, heat treatment, porosity*

Collaborative Design of Aircraft Systems - Multi-Level Optimization of an Aircraft Rudder

Wim Lammen

*NLR - Netherlands Aerospace Centre
 R&D Engineer Modelling and Simulation
 P.O.Box 90502, 1006 BM Amsterdam, The Netherlands
 Wim.Lammen@nlr.nl*

Bert de Wit

*NLR - Netherlands Aerospace Centre
 R&D Engineer Multidisciplinary Design and Optimization*

Jos Vankan

*NLR - Netherlands Aerospace Centre
 Senior Scientist Multidisciplinary Design and Optimization*

Huib Timmermans

*NLR - Netherlands Aerospace Centre
 R&D Engineer Aeroelasticity and Loads*

Ton van der Laan

*GKN Fokker Aerostructures
 Knowledge Based Engineering Specialist
 PO Box 1, 3350 AA Papendrecht, The Netherlands*

Pier Davide Ciampa

*DLR - German Aerospace Center
 Research associate & Team lead Multidisciplinary Design and Optimization group
 Hein-Saß-Weg 22, 21129, Hamburg, Germany*

ABSTRACT

The design and development of modern aircraft is a complex process involving many actors from different companies, e.g. the aircraft Original Equipment Manufacturer (OEM) and suppliers of (sub)systems and parts. The suppliers are responsible for their own system or part design, while the OEM is responsible for the overall aircraft design and the interfaces between the aircraft systems and parts. A system design that is optimal from system or part perspective may not be optimal from the global aircraft perspective. In order to avoid costly redesign iterations there is a need to optimize both the design of the overall aircraft and of its systems in an integrated way. This paper describes two methods for applying Multi-Level Optimization (MLO), in order to integrate the local system/part design optimization within the global aircraft design optimization. The design of an aircraft rudder is applied as use case. The use case addresses the coupling of a specific aircraft design analysis with a specific rudder design analysis and the global and local optimizations. First the MLO method Analytical Target Cascading (ATC) is applied to a theoretical example of fictive rudder design. Second a surrogate-based MLO approach is applied to a collaborative aircraft rudder design study involving multi-partner analysis tools. Both methods illustrate that applying MLO provides insight into the coupled design problem both for the OEM and for the supplier and reduces development time.

KEYWORDS: *multi-level optimization, collaborative design, aircraft rudder, surrogate models.*

Vibration Energy Harvesting Potential for Turbomachinery Applications

Adrian Stoicescu

COMOTI National Research and Development Institute for Gas Turbines

Scientific Researcher

Bd. Iuliu Maniu 220D, Bucharest, Romania

contact@comoti.ro

Marius Deaconu

COMOTI National Research and Development Institute for Gas Turbines

Scientific Researcher

Romeo Dorin Hrițcu

COMOTI National Research and Development Institute for Gas Turbines

Engineer

Cristian Valentin Nechifor

COMOTI National Research and Development Institute for Gas Turbines

Research Assistant

Cristinel-Ioan Hărăguță

COMOTI National Research and Development Institute for Gas Turbines

Engineer

Valeriu Alexandru Vilag

COMOTI National Research and Development Institute for Gas Turbines

Scientific Researcher

ABSTRACT

The vibration energy harvesting process represents one of the research directions for increasing power efficiency of electric systems, increasing instrumentation nodes autonomy in hard to reach locations and decreasing total system mass by eliminating cables and higher-power adapters. Research based on the possibility of converting vibration energy into useful electric energy is used to evaluate the potential of its use on turbomachinery applications. Aspects such as the structure and characteristics of piezoelectric generators, harvesting networks, their setup and optimization, are considered. Finally, performance test results are shown using piezoelectric systems on a turbine engine.

KEYWORDS: *turbomachinery, vibration, piezoelectric, energy harvesting*

Assessment of Electric Taxiing Considering Aircraft Utilization and Maintenance Cost

Ulrich Kling

Bauhaus Luftfahrt e.V.

Researcher Visionary Aircraft Concepts

Willy-Messerschmitt-Straße 1, 82024 Taufkirchen, Germany

ulrich.kling@bauhaus-luftfahrt.net

Clemens Steger

Bauhaus Luftfahrt e.V.

Student Researcher Visionary Aircraft Concepts

Fabian N. Peter

Bauhaus Luftfahrt e.V.

Lead Systems and Aircraft Technologies

Michael Schmidt

Bauhaus Luftfahrt e.V.

Researcher Visionary Aircraft Concepts

ABSTRACT

Electric taxiing is one of the technologies which could help to fulfill the goals of the European Commission's Flightpath 2050. An electric taxiing system propels aircraft on the ground without using its engines and therefore, reduces the emissions on ground. The application of such a system affects the operating cost of an aircraft in several ways, especially fuel consumption but also direct maintenance cost as engine operation time is reduced. Several parameters determine the influence of an electric taxiing system on the operational cost of an aircraft. In this paper the considered parameters are: Aircraft type, aircraft utilization, fuel price, taxiing time, weight and maintenance effort of the electric taxiing system itself. Studies are presented to show the influence of these parameters on the operational cost of a narrow-body and a wide-body aircraft. The results show that especially the type of maintenance schedule of the main engines has a large impact on the operational cost when using an electric taxiing system.

REVLANSYS: MISSION AND GNC DESIGN OF TERMINAL ENTRY AND LANDING MISSIONS FOR ADVANCED RE-ENTRY VEHICLES

*Antonio Russo, Alina Ionița, Fernando Pina Caballero
DEIMOS Space S.R.L.
Bucharest, Romania
antonio.russo@deimos.com.ro*

*Giovanni Medici, Cristina Recupero, Gabriele De Zaiacomo, Murray Kerr
DEIMOS Space S.L.U.
Tres Cantos, Spain*

*Celia Yabar Valles
ESA - ESTEC
Noordwijk, Netherlands*

ABSTRACT

The ESA REVLANSYS study aims to develop key technologies in the field of Mission Engineering and GNC for autonomous re-entry vehicles, and to derive coherent mission, system and GNC requirements for the specific terminal entry and landing phases. As such, REVLANSYS will provide support to European activities towards an autonomous end-to-end mission for a reusable re-entry system, as the SPACE RIDER, with the objective of performing an end-to-end design of the Terminal Area Energy Management (TAEM), Descent, and landing phases. A preliminary design activity was carried out to evaluate different solutions, including winged vehicles landing on a runway and lifting bodies performing a soft landing with a parafoil. A Multidisciplinary-Design Analysis and Optimization process (MDA-MDO) has been implemented as the instrument to evaluate the performance of the different concepts as a function of key design parameters, and produce optimized solutions that have been traded-off to identify the best option for a detailed Mission and GNC design. A Guidance method has been developed to provide trajectory generation capability from TAEM until landing, and a hybrid Navigation system has been tailored. Mission and GNC performance have therefore been assessed in terms of flying qualities, trajectory, Guidance and Navigation, considering a high fidelity simulation environment adapted to the TAEM and landing scenario. This study resulted in the design of a Mission and GNC solution for the terminal entry and landing phases of a return mission, consistent with the overall mission needs. Also, it allowed identifying the capabilities of the detailed design solution, and the possible limitations and improvements that are necessary to achieve a complete and robust mission and GNC design. Thanks to the knowledge gained during the project, DEIMOS Space Romania (DMR) is now capable of offering Mission Engineering and autonomous GNC solutions for future European re-entry missions.

This paper presents the activities carried out and the results obtained in the study, focusing on the detailed design phase.

KEYWORDS: *Air Transport Systems, Avionics, Flight Physics, Guidance Navigation and Control, Mission Design, Space Systems.*



Sizing Considerations of an Electric Ducted Fan for Hybrid Energy Aircraft

Patrick C. Vratny
Bauhaus Luftfahrt e.V.
Researcher Visionary Aircraft Concepts
Willy-Messerschmitt-Str. 1, 82024 Taufkirchen, Germany
patrick.vratny@bauhaus-luftfahrt.net

Mirko Hornung
Bauhaus Luftfahrt e.V.
Executive Director Research and Technology

ABSTRACT

Hybrid and universally-electric aircraft are promising configurations to potentially handle the ambitious emission reduction targets set for example by the Advisory Council of Aviation Research in Europe with the Strategic Research and Innovation Agenda. Those concepts are confronted usually with high mass impacts caused by the electric system architecture design. In this paper a closer look is taken on the sizing of the electric power train components and sizing options of the electric motor powering a ducted fan for a discrete parallel hybrid-electric aircraft concept. In such a configuration, the electric system is used as an assistance system to enable a downsizing of the gas turbine and to increase the overall power train efficiency. The studies include considerations concerning geared versus direct drive systems and its implications on overall aircraft level. Furthermore, using the electric system as assistance system different motorization options are discussed to identify the sizing point offering the best utilization of the electric system during the entire mission. As baseline an A320 class aircraft is used for an entry into service year of 2035+ and a 1300nm design range. Finally, for this aircraft concept trade-factors will be provided to cover the impact of a changed electric system mass and efficiency on the overall aircraft mass.

KEYWORDS: electric ducted fan, electric architecture, hybrid-electric aircraft, thrust envelope

Experimental Investigations on Aerodynamic Response of Panel Structures at High Subsonic and Low Supersonic Mach Numbers.

Jannis Lübker

*DLR, German Aerospace Center
PHD Student, Institut of Aeroelasticity
Bunsenstrasse 10, 37073, Göttingen, Germany
Jannis.Luebker@dlr.de*

Marko Alder

*DLR, German Aerospace Center
PHD Student, Institut of Aerodynamics and Flow Technology
36108, Braunschweig, Germany*

ABSTRACT

The phenomenon panel flutter is known since the mid 1940's. Intense investigations in experiment and theory followed in the 60's and 70's. The developed theories are capable of describing panel flutter in the subsonic and high supersonic Mach number domain but are insufficient in the transonic domain. In the recent years new Fluid-Structure-Interaction (FSI) methods by means of coupled CFD and FE calculations have shown more accurate results in that Mach number domain. Within a common project of the Airbus Company and the German Aerospace Center (DLR) the described computational approach is used on the theoretical side. Experiments were performed in 2015 and 2017 to gain data for validation. The wind tunnel experiments were conducted by means of a forced motion experiment in a Mach number range of $0.7 < M < 1.2$. The objective is to obtain the aerodynamic response to the panel's deformation. In order to simulate its first bending mode shape the all edge clamped panel is deflected by a hydraulic actuator. The structure is deflected sinusoidal over a wide range of amplitudes and frequencies. The wind tunnel's flow conditions are varied by means of the Mach number and the total pressure (Reynolds Number). Beside the measurement of the panel deformation by a stereo camera marker tracking system, the flow response is measured by high sensitive miniature pressure transducers.

KEYWORDS: *Forced Motion, Wind Tunnel Experiment, Transonic Domain, Aerodynamic Response, Aeroelastic stability*

Considerations regarding optimization of low speed balancing of high speed flexible rotors

*Eng. Alexandru Tudorache
INCD Turbomotoare COMOTI
Scientific Research Assistant
Iuliu Maniu Blvd., No. 220D, Bucharest, Romania
alexandru.tudorache@comoti.ro*

*Prof. Dr. Eng. Ion Fuiorea
INCD Turbomotoare COMOTI
Senior Scientific Researcher
Iuliu Maniu Blvd., No. 220D, Bucharest, Romania
ifuiorea@yahoo.com*

ABSTRACT

The research conducted revealed some particularities of the rotors manufactured and/or assembled at INCD Turbomotoare COMOTI. Different phenomena were encountered, named, and described, using data recorded while dynamically balancing the rotors, like the phenomenon where a rotor spins with progressively lower amplitude of vibration when increasing the rotation speed (named self-centering phenomenon), to a point where the rotor stabilises, and the phenomenon where the heavy point of a specific correction plane appears to move angularly while balancing at progressively increased speeds (phenomenon usually encountered in the case of flexible rotors). The recorded data was used to create six graphs that give a clear image of a rotors' behaviour on a specific range of speeds. After gathering a lot of experimental data, certain patterns emerged that helped formulate a balancing procedure based on these graphs. The procedure was tested successfully and it noticeably reduced the time required for dynamic balancing with better results while operating in normal conditions, at the designed nominal speed.

KEYWORDS: *dynamic balancing, high speed rotors*

NOMENCLATURE

- a The distance between the left bearing and the left correction plane
- b The distance between the two correction planes
- c The distance between the right correction plane and the right bearing
- d Distance between bearings, $a + b + c$
- gmm Unit of measurement for unbalance (mass multiplied by the radius where the correction is made)

1 INTRODUCTION

In all the work related to this field it has been concluded that the dynamic balancing of the rotors is a fundamental necessity for the correct operation of any machine and that the residual unbalance of a rotor is one of the major factors leading to incorrect operation or even the destruction of a machine.^{[1][3]}

This has prompted specialists in the field to work continuously to improve both the dynamic balancing process and the balancing machines, which has led to a high degree of competitiveness.

During this project, materials related to the rotor dynamics, dynamic balancing and documents on the operation and use of dynamic balancing machines were studied in order to design and carry out dynamic low-speed balancing experiments of high speed flexible rotors.^[1-5] As an introduction to rotor dynamics and dynamic balancing, the two best references are [1] and [2]. They both give a detailed description of the phenomena, math and methodology behind rotor dynamic balancing.

The methodology used in the experimentation and the results are briefly described in this paper.

2. EXPERIMENTATION PLANNING

The experiments were designed to be performed on the main types of rotor configurations most commonly used in COMOTI: centrifugal compressor rotors and bladed rotors, pinions, gears and helical screw compressor rotors.

Main parameters to be varied:

- a. **Speed** - we attempt to measure the unbalance of each rotor at various speed intervals to see how important data acquisition resolution is and whether a broader range is acceptable or not.

Planned measuring intervals are 100 RPM, 200 RPM, 300 RPM, 400 RPM, and 500 RPM, starting from a speed of 500 RPM, to the maximum speed possible of the balancing machine.

In general, balancing speed is chosen in terms of several aspects:

- Must be far enough away from critical or harmonic speeds;
- If the balancing machine has "soft" bearings, it must not be too large so the vibration amplitude will not damage the bearings or the transducers of the machine;
- Must be high enough so that the self-centering phenomenon (explained in section 3.1) occurs.

An optimum in choosing the balancing speed can be found by studying the evolution curve of the residual unbalance in relation to the speed resulting from the unbalance measurement (see section 3.3).

- b. **Correction Planes**

- For **long** and **symmetrical** / **asymmetrical** rotor configuration (Figure 1)
 - $b > a, c$;
 - Will vary a and c , keeping a fixed distance between the bearings, if and as long as each rotor permits;
 - Will vary $d (= a + b + c)$, as long as each rotor permits.

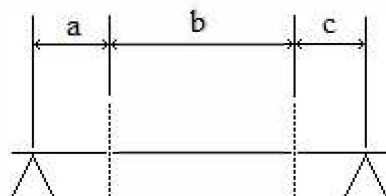


Figure 1 Long symmetrical/asymmetrical rotor configuration schematic

- For **narrow** rotor configuration (Figure 2)
 - $b < a, c$;
 - Will vary b , keeping a fixed distance between the bearings, if and as much as each rotor permits;
 - Will vary d ($a + b + c$), if and as long as each rotor permits.

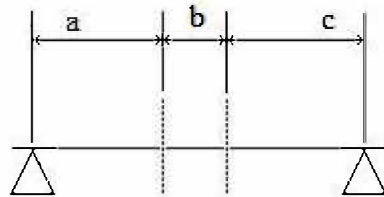


Figure 2 Narrow rotor configuration schematic

- For **console** rotor configuration (Figure 3)
 - will vary the position of the entire rotor on the bearings (provided that the centre of gravity is maintained between them in order not to overturn), if and as long as each rotor permits;
 - d will be varied if and as much as each rotor permits.

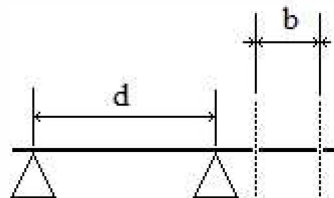


Figure 3 Console rotor configuration schematic

- For **dual console** rotor configuration (Figure 4)
 - the position of the entire rotor on the bearings will be varied;
 - d will vary, if and as much as each rotor permits.

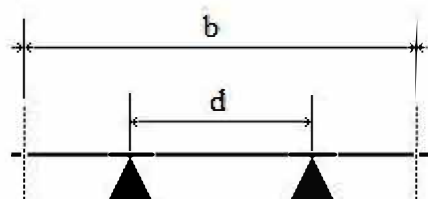


Figure 4 Dual console rotor configuration

c. **Balancing technique**^{[7][8][9]}

- **"left-right"** - involves the elimination of residual imbalance in the left or right plane, either one at a time or simultaneously.
- **"Static-couple"** - means eliminating usually static residual unbalance first, then the couple unbalance, but it is also possible vice versa.

The approach to balancing a rotor depends on its configuration. For example, a helical rotor from a CU90G screw compressor falls into the category of long and symmetrical rotors. In the way it is seated on the balancing machine bearings, the correction planes are far from the opposite bearings, so the interference of the correction planes is minimal, and the best approach to balancing is the "left-right" technique. In the case of balancing the gear in the multiplier of the same compressor, which falls within the narrow rotor category, the two correction planes are very close to each other and a balancing approach using „static-couple“ technique is recommended in order to bypass the correction plane interference effect.

Computerized data acquisition was decided to be made in intervals of 100 RPM, with plans to try 50 RPM intervals for even better resolution. We cannot use a shorter speed interval because the accuracy of the speed measurement does not allow this (the sensor measures from 60 RPM to 300 RPM with a ± 1 RPM error, from 300 RPM to 6000 RPM with a ± 10 RPM, and from 6000 RPM to 60000 RPM, the maximum speed of the IRD 246 balancing device, with an error of ± 100 RPM).^[3]

Connecting the IRD 246 balancing device to a computer was done with an RS232 communication cable.

Fig. 5 shows the schematic of the existing IRD 246 balancing machine and in the dashed line the added equipment for automated data acquisition.

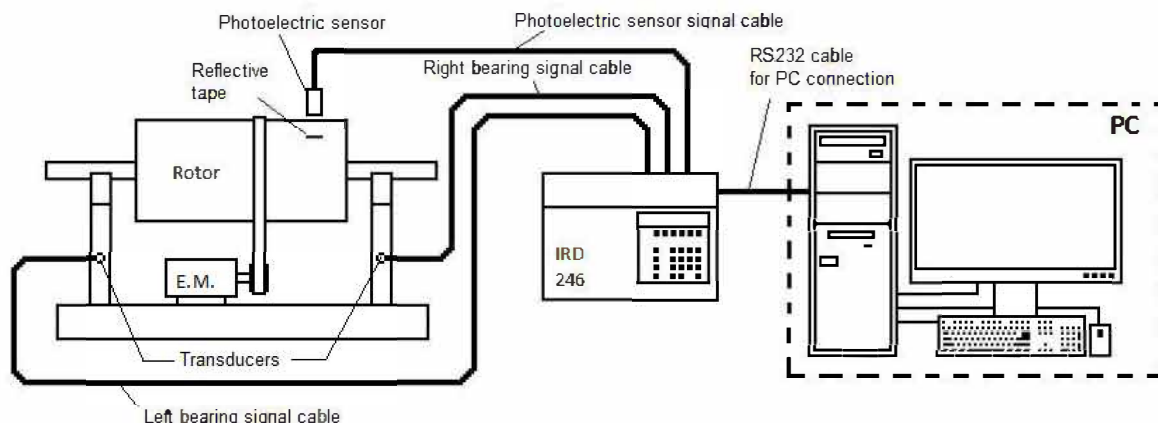


Figure 5 IRD balancing machine with IRD246 balancing device schematic

3. DATA ANALYSIS

Experimental data has been accumulated to identify common elements that appear in rotor behaviour (depending on their type) have been analysed and some phenomena that have occurred frequently in each type of investigated rotor have been identified, which helped taking decisions to balance the rotors.

With these data, graphs have been developed that show the rotor behaviour over the entire speed range at which it can be tested. Thus, these graphs provide a fairly clear picture of the phenomena taking place and ease the decision-making process on the rotor balancing approach.

3.1. THE SELF-CENTERING PHENOMENON

We call "self-centering phenomenon" the phenomenon that occurs when gradually raising the speed from a very low one. From the graphs (Fig. 6), where we represent the residual unbalance and the vibration amplitude measured according to the speed at which the measurement is made, it is observed how the effect of the vibration decreases, the vibration amplitude of the rotor becoming less and less.

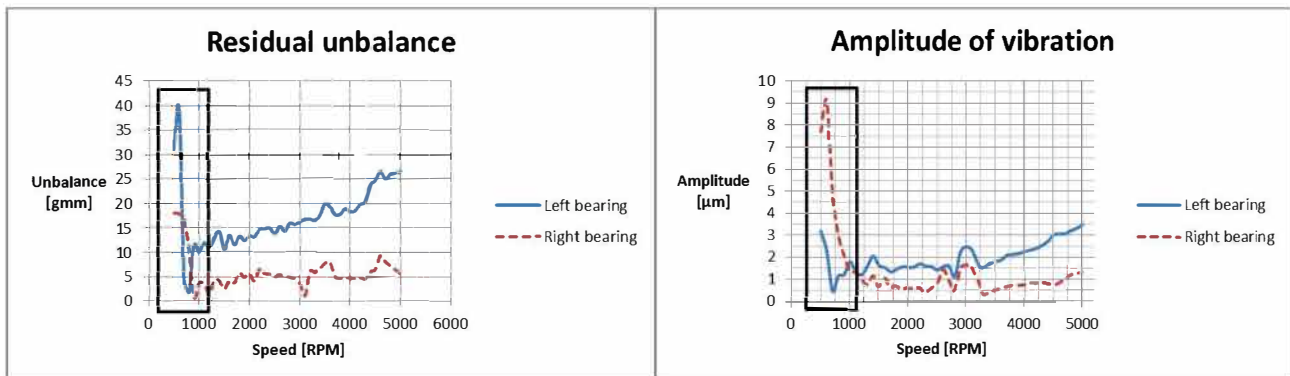


Figure 6 Example for self-centering phenomenon

3.2. HEAVY POINT „MIGRATION” PHENOMENON

The heavy point is the place where the mass of material is causing the imbalance.

At each data recording made by the balancing machine, it specifies the angular position of the heavy point in the correction plane chosen, as well as the amount of mass to be removed. In the graphs (Fig. 7), we represented the angular position of the heavy point in polar coordinates, the radius representing the residual imbalance value (left), and the angular position relative to the speed (right).

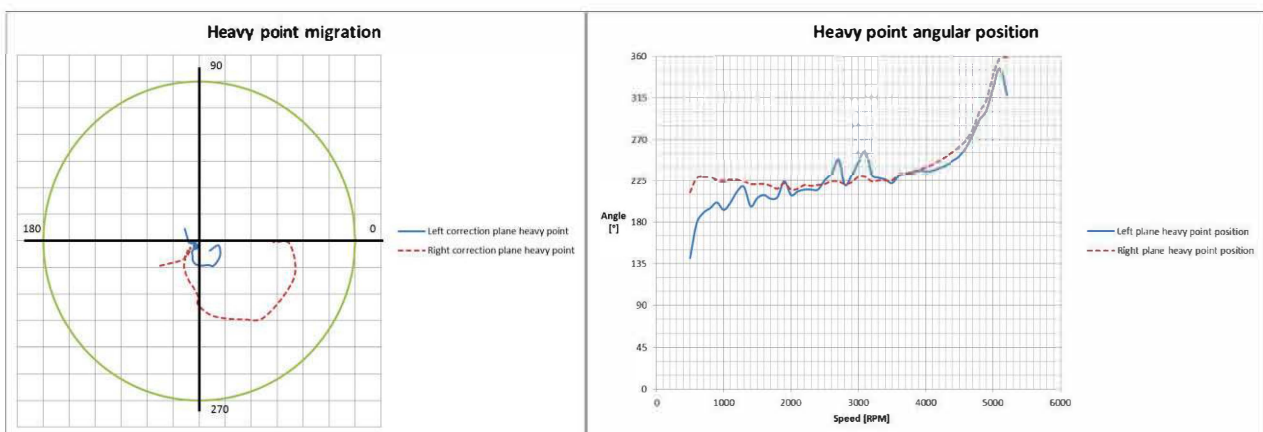


Figure 7 Example for the heavy point migration phenomena

It is noted that, most of the time, with increasing speed, the angular position of the heavy point changes. We call this change of position "heavy point migration".

3.3. SELECTION OF BALANCE SPEED

In the balancing standard, a certain value or a way of choosing the balancing speed is not specified. Several sets of recommendations are defined depending on the rotor configuration, the number of components, or whether it is an assembly, in which case the individual balancing of each component is recommended. The balancing speed must be large enough for the self-centering phenomenon to manifest itself completely, but below the speed at which the heavy point begins to migrate strongly (the two above-mentioned phenomena).

For example, the measured values for a test rotor assembly (Figures 8a / 8b).

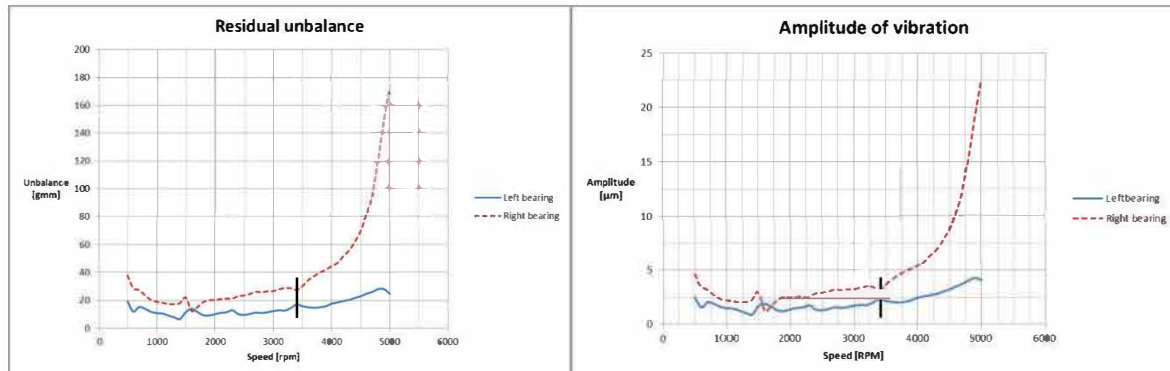


Figure 8a Example for choosing the balancing speed, test rotor assembly

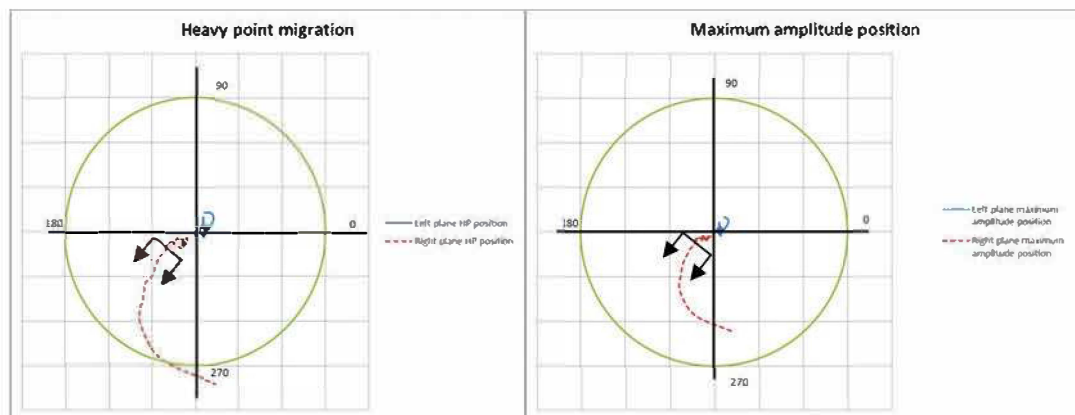


Figure 8b Example for choosing the balancing speed, test rotor assembly

In this case, we notice that we find the two above-mentioned phenomena, so we have to choose the speed taking these into account. Thus, the balancing speed must be large enough for the self-centering phenomena to manifest completely (at approximately 1000 RPM), but below the speed at which the heavy point begins to migrate strongly.

After analysing the values obtained, it was observed that from the speed of 3300-3400 RPM the heavy point strongly changes its position as the speed increases, and the amplitude and the unbalance grow directly proportional.

If we choose the balancing speed above this value, the mass the balancing machine indicates will be larger than the real one, because although the imbalance increases, the mass does not change, but only the effect of the mass on the flexible rotor, which introduces an error in the machine. It is not completely wrong to balance at a higher speed, but it should be taken into account that the mass needed to be removed is much smaller than indicated, the amplitude values must be measured again after the removal, and the process should be repeated several times as necessary, especially if too much mass is removed and the values indicated are opposite to the previous ones. Experience has shown that it saves time and you intervene as little as possible if this is true: the

balancing speed is above the speed of the full manifestation of the self-centering phenomena and below the speed of migration of the heavy point.

3.4. LEFT-RIGHT OR STATIC-COUPLE

Also from the graphs previously elaborated, one can see whether a certain type of unbalance is dominant. For example, in the first graphs (Figure 9) it is observed that the two imbalances remain approximately on the same side through the entire speed range after the self-centering phenomenon manifests. Thus, it can be concluded that there is a predominantly static unbalance and that it is a priority to be eliminated first.

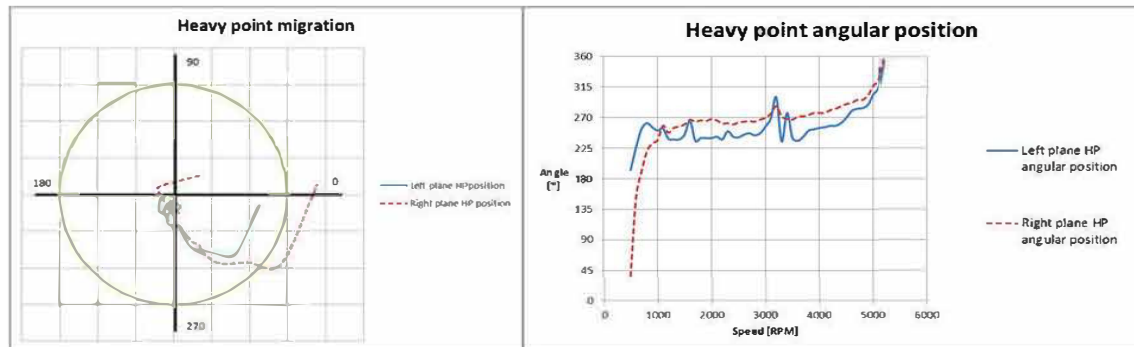


Figure 9 Example of static unbalance

In this other example (Figure 10), it is observed that the two unbalances remain on opposite sides and we can conclude that the predominant is the couple type of unbalance, which is a priority to be eliminated first.

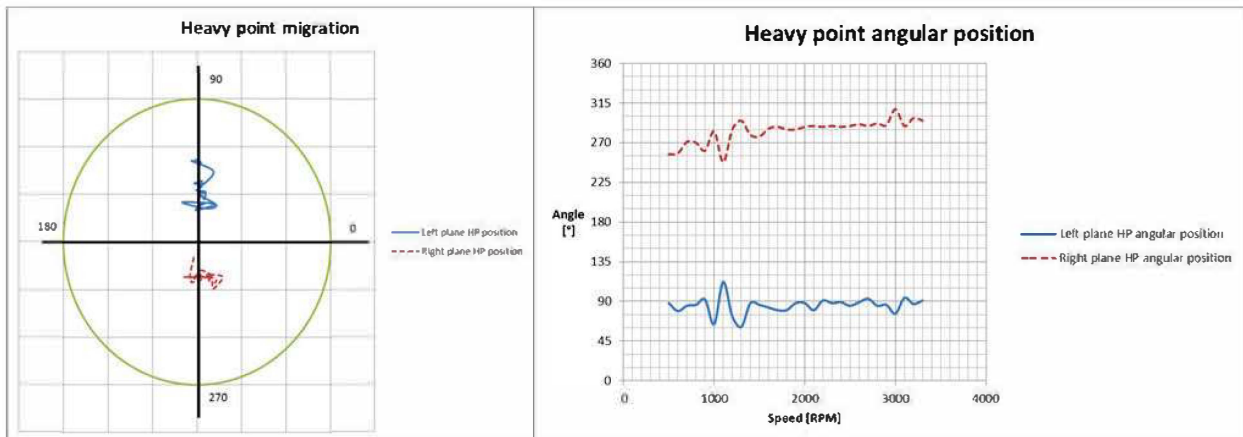


Figure 10 Example of couple unbalance

4.2.5. OTHER OBSERVATIONS

During dynamic balancing, it has been found that in the case of very long and thin rotors, the drive belt may introduce errors in measurements if an arc is formed by tightening it. The best example for this situation is a coupling shaft (Figure 11), about 380 mm long, with a diameter of 24 mm.

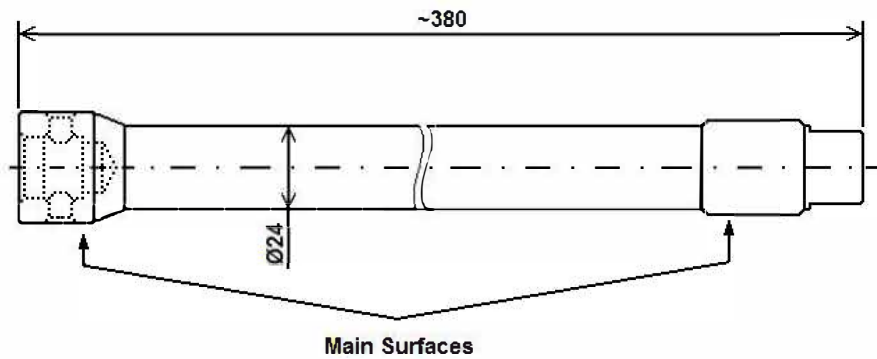


Figure 11 Coupling shaft schematic

Another notable case is that of a jet micro-engine rotor, equipped with a centrifugal compressor stage and an axial flow turbine stage, with a total weight of 1100 grams (Figure 12). The rotor is of small size, too short to be placed on the cylindrical portion of the shaft, 97 mm long, and initially we tried placing it on the inner ring of the bearing near the compressor (left) and on the conical surface near the turbine (right), but the amplitudes were much higher than in the final configuration (and the correct one): setting on both inner bearing rings, clearly indicating that the laying surface is very important, even though the surface is of high quality and within tolerances, small shape deviations significantly affect the measured values, especially for very small rotors.

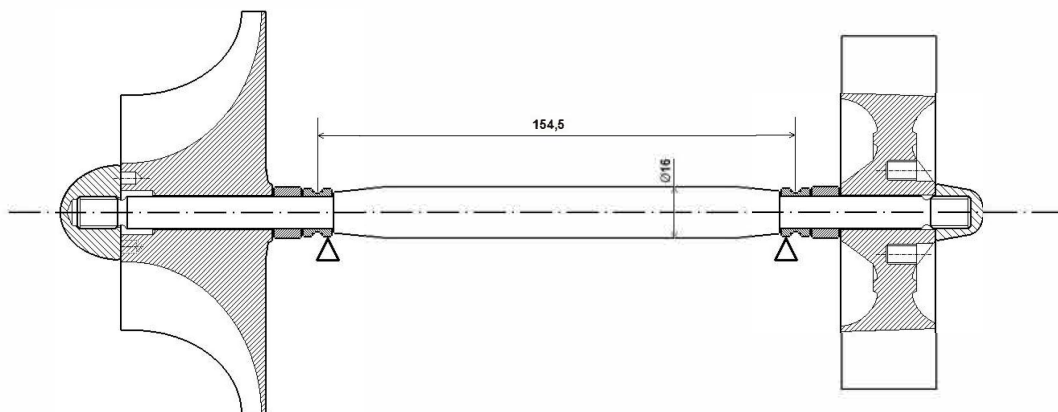


Figure 12 Jet micro-engine rotor schematic

5. CONCLUSIONS

All these observations and experiments were used to create a dynamic balancing procedure, with recommendations and indications, for balancing high speed flexible rotors, but it can be easily applied to all types of rotors, with the purpose of reducing the time required for balancing without sacrificing the quality or reaching higher qualities of balancing in a shorter time than usual.

All rotors balanced using this procedure were monitored while in use for their intended purpose and the feedback received indicated lower levels of machinery vibration than the rotors balanced with normal procedures.

This procedure has been validated for all types of rotors used in INCD Turbomotoare COMOTI, having better results than the previous methods, and will remain as a standard to be used for all future dynamic balancing of any rotor.

REFERENCES

1. M. Radeş, "Dinamica maşinilor", Ed. Printech 2008;
2. E. J. Gunter, Ph.D., ASME, "Introduction To Rotor Dynamics - Critical Speed and Unbalance Response Analysis", RODYN Vibration Analysis, Inc. 1932 Arlington Boulevard, Suite 223 Charlottesville, VA 22903-1560, October 2001.
3. "Static and Dynamic Balancing of Rigid Rotors", Macdara MacCamhaoil, Brüel & Kjær;
4. "Dynamic Balancing Handbook Form #2049", IRD Mechanalysis Inc., Oct 1990;
5. "Dynamic balancing of rotors", Dr. Rajiv Tiwari, Department of Mechanical Engineering, Indian Institute of Technology, Guwahati 781039;
6. "Control of surge in centrifugal compressors by active magnetic bearings – Theory and implementation"; Chapter 2 – Introduction to rotor dynamics; Yoon, S.Y.; Lin, Z.; Allaire, P.E.; Springer 2013;
7. "Ref. doc. MI 104 - NOTA TEHNICA – Consideratii privind echilibrarea rotoarelor rigide", Mobil Industrial AG, 2009;
8. "Ref. doc. MI 105 - NOTA TEHNICA – Echilibrarea dinamica a rotoarelor flexibile", Mobil Industrial AG, 2009;
9. Standards: ISO 1940-1:2003, ISO 11342:1998 and ISO 19499:1998;
10. Documentation for dynamic balancing machines IRD 246 and IRD 290.

Unified Longitudinal Flight-dynamic and Aeroelastic Analysis of a PrandtlPlane Configuration

Rocco Bombardieri
University Carlos III of Madrid
PhD student
Av. de la Universidad 30, 28911 Leganés , MA

Francesco Auricchio
University Federico II of Naples
Visiting graduate student

Rauno Cavallaro
University Carlos III of Madrid
Assistant Professor
rauno.cavallaro@uc3m.es

ABSTRACT

Longitudinal flight-dynamic behavior of a *flexible* joined-wing PrandtlPlane configuration is here investigated. The baseline model was previously designed by partner universities through several optimizations and ad-hoc studies in the field of aeroelasticity and flight mechanics.

First, longitudinal stability analyses are performed on the rigid configuration. The possibility to rely on a frequency-domain panel method for the evaluation of aerodynamic forces requires particular care in the rational function approximation method used to interpolate forces at low reduced frequencies. Moreover, short-period poles are stable for the considered speed range but differences in their characteristics have been found, compared to solvers relying on steady panel methods, which was considered as due to the contribution of unsteady aerodynamic derivatives that are only present in the first approach.

As a second step, unified analysis considering the flexibility of the vehicle are carried out. Given the presence of the short-period mode, flutter speed increases if compared to the cantilever wing system. Reciprocally, the short-period mode is influenced by the vehicle's flexibility and its frequency and damping ratio change above the considered speed interval. Values of the damping ratio, however, always fulfill the flying quality level requirements.

Another load condition of the same configuration is studied, characterized by different inertial properties and margin of stability. Short period is stable and similar to what seen for the previous configuration. Unified analyses highlight flutter of the third elastic mode in the considered speed range. Cause is associated to the different modal properties of the layout caused by different load distribution on the two wings. Again, elasticity is found to influence the short-period response but values of the damping comply with flying quality requirements.

CFD analysis for an improved concept of ventilation system for the Crew Quarters on board of the International Space Station

Florin Bode^{a,b}, Ilinca Năstase^{a,}, Matei-Răzvan Georgescu^a, Ioan Ursu^f, Dragoș Guță^c*

^a *CAMBI, Technical University of Civil Engineering in Bucharest, Building Services Department, 66 Avenue Pache Protopopescu; 020396, Bucharest, Romania; * correspondent author*
ilina.nastase@utcb.ro

^b *UTCN – Technical University of Cluj-Napoca, Faculty of Mechanics, Mechanical Engineering Department, Cluj-Napoca, Romania*

^c *INCAS - National Institute for Aerospace Research "Elie Carafoli" B-dul Iuliu Maniu 220, Bucharest 061136, Romania*

ABSTRACT

The current concept of Crew Quarters (CQ) on board of the International Space Station (ISS) demonstrated the possibility of a private place with reduced noise levels compared to the relatively acoustically noisy ISS aisle way. However, several issues were recorded by NASA and ESA, the most important ones pertaining to the noise levels and the accumulation of CO₂ and dust. Currently, 13% and 6%, respectively of the total mass and volume of a CQ are allocated to acoustic reductions. Interplanetary missions, unlike the low orbit ISS, would likely not allow this level of mass and volume penalty. It is believed the CQ has good air flow but high CO₂ levels are attained inside the station when the Carbon Dioxide Removal Assembly (CDRA) is not functioning to its capacity. Our project QUEST is intended to propose a new concept of improved CQ design for better acoustical performance, increased the space dedicated to the crew member, reduced the total weight, improved efficiency of the air distribution and a supplementary personalized strategy of air diffusion for eliminating CO₂ from the breathing zone. This paper presents a CFD study in which a numerical model of the air flow inside this enclosure. The numerical model was developed as a preliminary approach by our team as one of our goals is to understand the flows occurring in the actual design of air diffusion system of the existing CQ on the ISS. The results are showing that for all three air flow rates at which the present system is designed to function, the resulting flow patterns and velocity distributions are likely to produce draught discomfort. In this case, it appears that lower velocity values at the inlet diffuser, distributed over a larger surface, as well as diffusers with improved induction would be a better choice.

KEYWORDS: *International Space Station, Crew Quarters Ventilation, Air distribution and comfort, Computational Fluid Dynamics*

Data-driven Optimisation of Closure Coefficients of a Turbulence Model

Andrea Da Ronch
University of Southampton
Lecturer
Southampton, SO17 1BJ, UK
a.da-ronch@soton.ac.uk

Marco Panzeri
Noesis Solutions N.V.
Research Engineer
3001 Leuven, Belgium

Jernej Drofelnik
University of Southampton
Research Associate
Southampton, SO17 1BJ, UK

Roberto d'Ippolito
Noesis Solutions N.V.
Research and Innovation Manager
3001 Leuven, Belgium

ABSTRACT

The solution of the Reynolds-averaged Navier-Stokes equations employs an appropriate set of equations for the turbulence modelling. The closure coefficients of the turbulence model were calibrated using empiricism and arguments of dimensional analysis. These coefficients are considered universal, but there is no guarantee this property applies to test cases other than those used in the calibration process. This work aims at revisiting the universality of the closure coefficients of the original Spalart-Allmaras turbulence model using machine learning, adaptive design of experiments and accessing a high-performance computing facility. The automated calibration procedure is carried out once for a transonic, wall-bounded flow around the RAE 2822 aerofoil. It was found that: a) an optimal set of closure coefficients exists that minimises numerical deviations from experimental data; b) the improved prediction accuracy of the calibrated turbulence model is consistent across different flow solvers; and c) the calibrated turbulence model outperforms slightly the standard model in analysing complex flow features around the ONERA M6 wing. A by-product of this study is a fully calibrated turbulence model that leverages on current state-of-the-art computational techniques, overcoming inherent limitations of the manual fine-tuning process.

A Review of Recent Personal Air Vehicle Concepts

*Michael Shamiyeh
Bauhaus Luftfahrt e.V.
Research Associate, Visionary Aircraft Concepts
82024 Taufkirchen
michael.shamiyeh@bauhaus-luftfahrt.net*

*Julian Bijewitz
Bauhaus Luftfahrt e.V.
Research Associate, Visionary Aircraft Concepts*

*Mirko Hornung
Bauhaus Luftfahrt e.V.
Executive Director of Research and Technology*

ABSTRACT

Recent activities on the field of urban air mobility have brought up a broad range of personal air vehicle configurations. This review paper provides an overview of these configurations with emphasis on operational capabilities, design focus and system complexity. Initially, a classification scheme is proposed, to identify clusters containing concepts with comparable performance characteristics. Further, a comprehensive overview of the current vehicle programs is given. Technical aspects and design characteristics are discussed regarding urban air transportation. Performance data available from the public domain is presented and compared. Finally, two metrics for system complexity analysis of personal air vehicles are described. The obtained complexity of representative configurations is evaluated and compared to a common reference.

KEYWORDS: *personal air vehicle, VTOL, urban air mobility, performance, system complexity*

Discrete Gust Response of a Box-wing Configuration

Rauno Cavallaro
University Carlos III of Madrid
Assistant Professor
Av. de la Universidad 30, 28911 Leganés, MA
Rauno.cavallaro@uc3m.es

Juan Palacios Santos
University Carlos III of Madrid
Undergraduate student

Rocco Bombardieri
University Carlos III of Madrid
PhD Candidate

ABSTRACT

This paper investigates the discrete symmetric gust response of an unconventional aircraft layout called Box Wing, also known as PrandtlPlane, and gives a very introductory perspective on the gust-induced stress states, and thus, insight into the structural design of such configuration. The typical box-wing aircraft features a closed-wing system that, seen frontally, reminds of a box shape. Its aerodynamics is characterized by mutual wing down/upwash interference and, from the structural point of view, it is an overconstrained system; these properties, as underlined by different studies, strongly complicate the design promoting counterintuitive behaviours. Regulations regarding symmetric gust response for the specific class of the aircraft are followed to set the gust parameters. With the aid of DYNRESP code, a robust tool for determining dynamic loads, the dynamic response of the flexible free-free aircraft is obtained for several gust parameters and two points in the envelope. The time-response is then critically analyzed, and also, based on the deformed shapes, few conditions are selected for a deeper investigation. Stress analyses performed on the chosen response instants showed that only marginal areas of the structure undergo higher stresses than those observed on the reference limit load (load factor 2.5) condition.

KEYWORDS: Box Wing, *Discrete Gust Response, PrandtlPlane, Aeroelasticity, Dynamic loads.*

Parameter Estimation of a Mini Aerial Vehicle using Multiple Trim Flight Data

Pranavkumar V. Patel
Indian Institute of Technology Bombay
Research Scholar
Powai, Mumbai, India - 400076
pranavkumar@aero.iitb.ac.in

Hemendra Arya
Indian Institute of Technology Bombay
Associate Professor

ABSTRACT

In this work, a novel flight test approach for accurate aerodynamic parameter estimation is designed. As low aspect ratio mini aerial vehicles have highly nonlinear aerodynamics, 3-2-1-1 doublets are used for elevator deflection to perturb aircraft at two different trim conditions, at low angle-of-attack (high velocity) and high angle-of-attack (low velocity). A combination of these two flight data is used to estimate the parameters. Realistic flight data is generated using complete nonlinear aircraft model. Equation-error estimation technique is used for parameter estimation. Parameter estimates using multiple trim flight data are compared with parameter estimates using different trim flight data. This comparison shows that multiple trim flight data is effective to get accurate estimates for a nonlinear aircraft model, even by using simple least square estimation technique.

KEYWORDS: *Parameter Estimation, Mini Aerial Vehicle, Maneuvers*

Progress of Subscale Winged Rocket Development and Its Application to Future Fully Reusable Space Transportation System

Koichi YONEMOTO

Kyushu Institute of Technology

Professor, Department of Mechanical and Control Engineering

1-1 Sensui, Tobata, Kitakyushu, Fukuoka, Japan 8048550

yonemoto.koichi873@mail.kyutech.jp

Takahiro FUJIKAWA

Kyushu Institute of Technology

Assistant Professor, Department of Mechanical and Control Engineering

Toshiki MORITO

Japan Aerospace Exploration Agency

Manager, Research Unit IV, Research and Development Directorate

Tsukuba Space Center, 2-1-1 Sengen, Tsukuba, Ibaragi, Japan 305850

Joseph WANG

University of Southern California

Associate Professor, Department of Astronautical Engineering

854 Downey Way, Los Angeles, California, USA 90089

Ahsan R. CHOUDHURI

University of Texas at El Paso

Professor and Chair, Department of Mechanical Engineering

500W University Ave., Eng. Annex Suite A126, El Paso, Texas, USA 79968

ABSTRACT

Kyushu Institute of Technology has been studying unmanned suborbital winged rocket called WIRES (WInged REusable Sounding rocket) and its research subjects concerning aerodynamics, NGC (Navigation, Guidance and Control), cryogenic composite tanks etc., and conducting flight demonstration of small winged rocket since 2005. WIRES employs the original aerodynamic shape of HIMES (HHighly Maneuverable Experimental Sounding rocket) studied by ISAS (Institute of Space and Astronautical Science) of JAXA (Japan Aerospace Exploration Agency) in 1980s. This paper presents the preliminary design of subscale non-winged and winged rockets called WIRES#013 and WIRES#015, respectively, that are developed in collaboration with JAXA, USC (University of Southern California), UTEP (University of Texas at El Paso) and Japanese industries. WIRES#013 is a conventional pre-test rocket propelled by two IPA-LOX (Isopropyl Alcohol and Liquid Oxygen) engines under development by USC. It has the total length of 4.6m, and the weight of 1000kg to reach the altitude of about 6km. The flight objective is validation of the telemetry and ground communication system, recovery parachute system, and launch operation of liquid engine. WIRES#015, which has the same length of WIRES#013 and the weight of 1000kg, is a NGC technology demonstrator propelled by a fully expander-cycle LOX-Methane engine designed and developed by JAXA to reach the altitude more than 6km. The flight tests of both WIRES#013 and WIRES#015 will be conducted at the launch facility of FAR (Friends of Amateur Rocketry, Inc.), which is located at Mojave Desert of California in United States of America, in May 2018 and March 2019 respectively. After completion of WIRES#015 flight tests, the suborbital demonstrator called WIRES-X will be developed and its first flight test will be performed in 2020. Its application to future fully reusable space transportation systems, such as suborbital space tour vehicles and two-stage-to-orbit launch vehicle, is discussed.

KEYWORDS: *reusable space transportation, unmanned winged rocket*



Different Fidelity Computational Models in Aeroelastic Design of Aircraft and WT Models

V.V. Chedrik

Central Aero-Hydrodynamic Institute (TsAGI)

Head of Division

Zhukovsky, Moscow region, Russia, 140180

chedrik@tsagi.ru

F.Z. Ishmuratov

Central Aero-Hydrodynamic Institute (TsAGI)

Head of Division

ABSTRACT

Using of different fidelity computational models and relations between them in the multidisciplinary design system is considered. A structural design procedure and optimization methods for aeroelastic design of aircraft and wind tunnel models are discussed. An application of the topology-based optimization together with the two-level structural sizing method is considered. Main stages of the approach to synthesis of structural layouts of aircraft components are described. Some numerical examples of analysis and aero-structural optimization of aircraft wings are considered to demonstrate the proposed methods and algorithms. The accuracy, reliability and efficiency of using of the considered structural models at design studies are discussed.

KEYWORDS: *aircraft structure, computational model, aeroelasticity, strength, optimization*



A Preliminary Heat Transfer Analysis of Pulse Detonation Engines

Berke Olcucuoglu

Von Karman Institute for Fluid Dynamics

Graduate Student

Chaussee de Waterloo 72, B-1640, Rhode-Saint-Genese, Belgium

berke.olc@gmail.com

Bayindir H. Saracoglu

Von Karman Institute for Fluid Dynamics

Senior Research Engineer

bayindir@saracoglu.co.uk

ABSTRACT

Detonation engines offer higher theoretical thermal efficiencies as compared to their deflagration-based counterparts. Simultaneous pressure gain during heat addition through the detonation wave provides the superiority to the Zeldovich-von Neumann-Döring (ZND) cycle which is used to define the thermodynamic process of detonation engines. Combustion temperatures can rise as high as 3000 K across the detonation wave. The continuous exposure to such elevated temperature may risk the integrity of the structural components of the engines. Consequently, heat management of the detonation engines highlights an important parameter on the construction of a demonstrator. In order to be able to design an appropriate cooling system, both for pulse detonation and rotating detonation engines (PDE & RDE), an accurate estimation of the heat load stands as an essential prerequisite. Hence, a preliminary numerical study of the heat transfer on a pulse detonation engine model was conducted to quantify the heat load. Conservation equations for deflagration-to-detonation transition (DDT) in detonation engines were solved through open source fluid dynamics solver OpenFOAM equipped with ddtFoam module. Reactive flow field of premixed mixtures (Hydrogen-air) was modeled with a URANS second-order approximate Riemann solver equipped with Weller combustion model, and Arrhenius equations of O'Connaire reaction scheme for Hydrogen-air detonation. Multiple boundary conditions were tested to achieve the most appropriate model. Natural convection over the lateral combustor peripheries found to be the most realistic boundary condition for the problem. In order to observe cooling process better, PDE tubes in different length were also simulated. Finally, the transient heat transfer phenomenon across the pulse detonation tube is documented for various conditions investigated.

KEYWORDS: *detonation engine, heat transfer, pulse detonation, OpenFOAM, combustion*

DEFINITION AND DISCUSSION OF THE INTRINSIC EFFICIENCY OF WINGLETS

Dieter Scholz

Aircraft Design and Systems Group (AERO), Hamburg University of Applied Sciences

Professor

Berliner Tor 9, 20099 Hamburg, Germany

info@ProfScholz.de

ABSTRACT

Three simple equations are derived to define the "intrinsic aerodynamic efficiency of winglets" independent of the horizontal extension of the winglet and independent of the winglet's (relative) height. This "intrinsic aerodynamic efficiency" allows a quick comparison of purely the aerodynamic shape of winglets independent of the selected size chosen for a certain aircraft installation. The intrinsic aerodynamic efficiency is calculated in 3 steps: STEP 1: The relative total drag reduction due to the winglet is converted into an assumed contribution of the winglet only on the span efficiency factor. STEP 2: If the winglet also increases span, its performance is converted into one without the effect of span increase. STEP 3: The winglet's reduction in induced drag is compared to a horizontal wing extension. If the winglet needs e.g. to be three times longer than the horizontal extension to achieve the same induced drag reduction, its "intrinsic aerodynamic efficiency" is the inverse or $1/3$. Winglet metrics as defined are calculated from literature inputs. In order to evaluate winglets further, the mass increase due to winglets is estimated in addition to the reduction of drag on aircraft level and fuel burn.

KEYWORDS: *wingtip, winglet, induced drag, wing mass, aircraft design*



SUBSCALE FLIGHT TEST MODEL DEVELOPMENT AND TESTING AS A TOOL FOR UNCONVENTIONAL AIRCRAFT DESIGN

Diego de Matos Monteiro
Instituto Tecnológico de Aeronáutica
Doctorate student
Praça Marechal Eduardo Gomes, 50, São José dos Campos, Brazil
Monteirodiego86@gmail.com

Leonardo Murilo Nepomuceno
Instituto Tecnológico de Aeronáutica
Master student

Roberto Gil Annes da Silva
Instituto Tecnológico de Aeronáutica
Professor
gil@ita.br

Marcos da Silva e Souza
Instituto de Aeronáutica e Espaço
Research Engineer
marcosmss@iae.cta.br

Flávio José Silvestre
Instituto Tecnológico de Aeronáutica
Professor
flaviojs@ita.br

Petter Kruss
Linköping University
581 83 Linköping, Sweden
Professor
petter.krus@liu.se

Alejandro Sobrón Rueda
Linköping University
PhD student
Alejandro.sobron@liu.se

ABSTRACT

This work has the objective to show development of a non-conventional subscale aircraft tests and compare a preliminary numerical analysis with wind tunnel tests. The subscale flight tests can be used as a low cost tool and that can improve the learning curve, considering the future aircrafts are characterized by the use of new technologies and radical configurations. For this validation was built the ITA-BWB aircraft, a single engine and tailless concept. This project demonstrates all steps of preliminary analysis with VLM software, preliminary flight tests and wind tunnel tests, where these data were used for simulations of specific maneuvers used in parameter identification. Finally, the simulations demonstrated consistency between the static derivatives acquired by VLM software and wind tunnel tests, which were used to estimate dynamic derivatives that allowed the simulation of specific maneuvers for subscale flight tests.



KEYWORDS: *Wind Tunnel, Subscale Flight Test, Stability and Control, Flight Mechanics, VLM*

Investigation of the Flow Around an Aircraft Wing of Section NACA 2412 Utilising ANSYS Fluent

Rob Ives,

*School of Science & Engineering, Teesside University
Middlesbrough, TS1 3BA, UK
M2084041@live.tees.ac.uk*

(Andrew) Stewart Keir

*School of Science & Engineering, Teesside University
Middlesbrough, TS1 3BA, UK*

Edet Bassey

*School of Science & Engineering, Teesside University
Middlesbrough, TS1 3BA, UK*

F A Hamad

*School of Science & Engineering, Teesside University
Middlesbrough, TS1 3BA, UK*

ABSTRACT

The aim of this paper is to produce and validate a simulated model of the external flow around the NACA 2412 using ANSYS Fluent; utilising experimental data for a low velocity case (20.73 m/s) from literature. This model will be subsequently used to produce data for a high velocity case (272.1 m/s, Mach = 0.8) which is the practical velocity for commercial aircraft. Both an infinite aspect ratio wing (2D) and a finite aspect ratio wing (3D) will be the subjects of this investigation. Experimental data on which the simulated models will be compared and hence validated is taken from Jacobs et al. (1935). This experimental data contains both a finite aspect ratio wing and an infinite aspect ratio wing. An accurate simulation model of the external flow around a wing will be beneficial in the visualisation of the flow; particularly in the investigation of the onset of a stall and the aerodynamic characteristic differences between the wing root and wing tip. The model will also provide simulated data of an external flow condition of which no experimental data currently exists. Finally, value will be gained in the investigation between the differences of an external flow around a 2-dimensional (2D) wing versus a 3-dimensional (3D) wing.

All simulations exhibited flow physics consistent with those seen in experimental data; further validating the results. A detailed methodology has been provided with a view that new data becomes available for this aerofoil and wing geometry. Considering the aerofoil simulation, incredible accuracy has been achieved. However, with regards to the wing simulation, further work is required to identify the issue which resulted in a lower lift curve slope when compared to the experimental data.

KEYWORDS: CFD SIMULATION, FINITE WING, LIFT COEFFICIENT, DRAG COEFFICIENT, PRESSURE COEFFICIENT

CFD Analysis of C-D Nozzle compared with Theoretical & Experimental Data

(Andrew) Stewart Keir

*School of Science & Engineering, Teesside University
Middlesbrough, TS1 3BA, UK
N3085595@live.tees.ac.uk*

Rob Ives

*School of Science & Engineering, Teesside University
Middlesbrough, TS1 3BA, UK*

F A Hamad

*School of Science & Engineering, Teesside University
Middlesbrough, TS1 3BA, UK*

ABSTRACT

In modern Computational Fluid Dynamic (CFD) Analysis of Convergent-Divergent (C-D) Nozzles, current research has shown that, it is common practice to use either experimental or analytical results to predict the accuracy of the CFD models by comparison of the results. It is also commonly agreed, amongst the literature reviewed, that the CFD modelling software packages available do not accurately model turbulence for applications such as transonic C-D nozzles.

This study aims to develop a theoretical approach for calculation of flow properties along the axis of the C-D nozzle based on the fundamental gas dynamic equations. The theoretical analyses is validated by experimental data. Then, the CFD model is used to simulate the experimental cases which are compared with the data from both theoretical analysis and experimental measurements. Then, the validated CFD model can be used for more complex analyses, representing more elaborate flow phenomena such as internal shockwaves and boundary layers.

The geometry used in the analytical study and CFD simulation is constructed to model the experimental rig. The [1, 2] analytical study is undertaken using isentropic and adiabatic relationships and the output of the analytical study, the 'shockwave location tool', is created. The results from the analytical study are then used to optimize the redesign an experimental rig to for more favorable placement of pressure taps and gain a much better representation of the shockwaves occurring in the divergent section of the nozzle.

The results from the CFD model can then be directly compared other results in order to gauge the accuracy of each method of analysis. The validated model can then be used in order to create several, novel nozzle designs which may offer better performance and ease of manufacture and may present feasible improvements to existing high-speed flow applications.

KEYWORDS: *Convergent-Divergent Nozzle, CFD Simulation, Shockwave-Boundary Layer Interaction, Experimental Study*



Disciplinary Data Fusion For Multi-Fidelity Aerodynamic Application

*Mengmeng Zhang
Airinnova AB (AIRI)
Research Scientist
Stockholm, Sweden*

*Aidan Jungo
CFS Engineering (CFSE)
Research Scientist
Lausanne, Switzerland*

*Nathalie Bartoli
ONERA, The French Aerospace Lab, Information Processing and Systems Department
Research Engineer
Toulouse, France*

ABSTRACT

This paper presents some multi-fidelity activities in the field of aerodynamic in the ongoing EU-funded research project AGILE. Different computational tools corresponding to different levels of fidelity are used in the project and the idea is to combine all the data in a global surrogate model to reduce the computational time in an optimization process for instance. The paper focuses on the data fusion tool embedded in the AGILE framework with the choice of the surrogate models, the choice of the tool's fidelity and the choice of the sampling points via an iterative process. The paper details the different steps of the proposed approach to set up and operate the data fusion service proposed to the AGILE partners.

KEYWORDS: Data fusion, surrogate models, multi-fidelity, AGILE, aerodynamics



Overview Of MDO Enhancement In The AGILE Project: A Clustered And Surrogate-Based MDA Use Case

Thierry Lefebvre

*ONERA, The French Aerospace Lab, Information Processing and Systems Department
Research Engineer
Toulouse, France*

Nathalie Bartoli

*ONERA, The French Aerospace Lab, Information Processing and Systems Department
Research Engineer
Toulouse, France*

Sylvain Dubreuil

*ONERA, The French Aerospace Lab, Information Processing and Systems Department
Research Engineer
Toulouse, France*

Riccardo Lombardi

*NOESIS Solutions
Research Engineer
Leuven, Belgium*

Marco Panzeri

*NOESIS Solutions
Research Engineer
Leuven, Belgium*

Wim Lammen

*NLR - Netherlands Aerospace Centre
R&D Engineer Modeling and Simulation
Amsterdam, the Netherlands*

Mengmeng Zhang

*AIRINNOVA AB
Research Scientist
Stockholm, Sweden*

Imco van Gent

*Faculty of Aerospace Engineering, Delft University of Technology
Ph.D. Student
Delft, The Netherlands*

Pier Davide Ciampa

*German Aerospace Center (DLR)
Research associate & Team lead Multidisciplinary Design and Optimization group
Hamburg, Germany*

ABSTRACT

This paper presents innovative methodological investigations performed as research activities in the field of MDO for conceptual aircraft design in the ongoing EU-funded research project AGILE. The next generation of aircraft Multidisciplinary Design and Optimization processes is developed in AGILE, which targets significant reductions in aircraft development costs and time to market, leading to cheaper and greener aircraft solutions. The paper introduces the AGILE project structure and recalls the achievements of the 1st year (Design Campaign 1 or DC-1) leading to a reference distributed MDO system. Design Campaign 2 (DC-2) is briefly described, investigating the ease of the optimization of complex workflows, characterized by a high degree



of discipline interdependencies, high number of design variables in the context of multilevel processes and multipartner collaborative engineering projects. The paper focuses on an innovative approach where a complex aircraft design workflow has been simplified and implemented by using surrogate models for clusters of disciplines to reduce the computational time. The paper will detail the different steps of the retained approach to set up and operate this test case, involving a team of surrogate specialists, and taking advantage of the AGILE distributed MDO framework.

KEYWORDS: AGILE, MDO, surrogate models, optimization, collaborative framework, knowledge framework

NOMENCLATURE

AGILE	H2020 EU Project: Aircraft 3rd Generation MDO for Innovative Collaboration of Heterogeneous Teams of Experts
CMDOWS	Common MDO Workflow Schema
CPACS	Common Parametric Aircraft Configuration Schema
DACE	Design and Analysis of Computer Experiments
DC	Design Campaign
DOE	Design Of Experiments
DP	Design Process
FPG	Fundamental Problem Graph
IT	Information Technology
KADMOS	Knowledge- and graph-based Agile Design for Multidisciplinary Optimization System
LHS	Latin Hypercube Sampling
MDA	Multi-Disciplinary Analysis
MDAO	Multidisciplinary Design Analysis and Optimization
MDO	Multidisciplinary Design Optimization
MDPG	MDAO Data and Process Graph
MOE	Mixture Of Experts
MTOM	Maximum Take-Off Mass
OAD	Overall Aircraft Design
OBS	On Board Systems
OEM	Operating Empty Mass
PIDO	Process Integration and Design Optimization
POD	Proper Orthogonal Decomposition
RCE	Remote Component Environment
RCG	Repository Connectivity Graph
RSM	Response Surface Method
SEGOMOE	Super Efficient Global Optimization based on Mixture Of Experts
SM	Surrogate Model
VISTOMS	VISualization TOOl for MDO Systems
XDSM	eXtended Design Structure Matrix

1. INTRODUCTION

Over the past century, the aircraft design and development process has evolved from pioneering - one or few people building a simple and small aircraft in a shed - into a highly complex but well-established engineering process. Today, aircraft are highly advanced technological and competitive products that are developed by multidisciplinary expert teams. To keep up with the growing demand for more complex and innovative products in shorter time and in higher volumes, the industry digitizes rapidly. The highly advanced aircraft industry increasingly applies innovative design approaches based on digital modelling, simulation and optimization technology to take design decisions as early as possible and hence develop state-of-the-art aircraft more timely and cost efficiently. Still, with the large computational power that is available nowadays, there remains the challenge to master the complexity of the multidisciplinary design workflow and all corresponding variables. High-dimensional data sets resulting from various design competences need to be handled in an efficient way.

In the last three decades, there has been a growing interest in improving the efficiency of vehicle design processes through the use of multidisciplinary design optimization (MDO) numerical tools and techniques.

Nevertheless, the exploitation of the full MDO potentials for the development of a complete aircraft is still an open challenge mainly due to the technical and management issues encountered during the set up and the operations of such a complex architecture. Even though many of the MDO algorithms have been applied into industrial applications, the necessity of novel methodology to encapsulate knowledge and skills has been identified [1, 2] in order to be able to manage the increasing design complexities. In that aim, since 2015, EU funded Horizon2020 AGILE project is developing the next generation of aircraft Multidisciplinary Design and Optimization processes, focusing on the reduction of the aircraft development time at the early stages of the design process in the context of multi-level and multi-partner collaborative engineering projects. This paper presents an innovative approach investigated in the context of the project aiming at simplifying a complex workflow through the combination of clusters of design competences and the extensive use of surrogate models (SM).

The paper is organized as follows. Section 2 provides an overview of the EU H2020 AGILE project structure and the main achievements of Design Campaign (DC) 1 an 2 are exposed. Section 3 details the different scenarios to build associated multidisciplinary process based on surrogate models in order to compare several MDO strategies. In addition, improvements brought by AGILE framework, both by knowledge based technologies and IT solutions, to support the surrogate models scenarios are also presented. Section 4 describes the overall process to be apply to DC-1 MDA in order to obtain an equivalent workflow only involving surrogate models of the associated design competences. Section 5 presents the results obtained at the main steps of the process with a focus on the building of the surrogate models. Section 6 summarizes the work performed and identifies the future steps.

2. AGILE PROJECT OVERVIEW

AGILE [3] (Aircraft 3rd Generation MDO for Innovative Collaboration of Heterogeneous Teams of Experts) is an EU funded project under the research schema Horizon 2020 and coordinated by the German Aerospace Center (DLR). AGILE is developing the next generation of aircraft Multidisciplinary Design and Optimization processes, which target significant reductions in aircraft development costs and time to market, leading to cheaper and greener aircraft solutions [4]. The developed AGILE Paradigm [5] will enable the 3rd generation of multidisciplinary design and optimization through efficient collaboration among international multi-site aircraft design teams. The AGILE project is structured into three sequential phases, targeting design campaigns with increasing levels of complexity, addressing different aircraft configurations and dedicated MDO techniques. The overall structure is shown in Fig. 1. In the 1st phase (Initialization), a reference aircraft

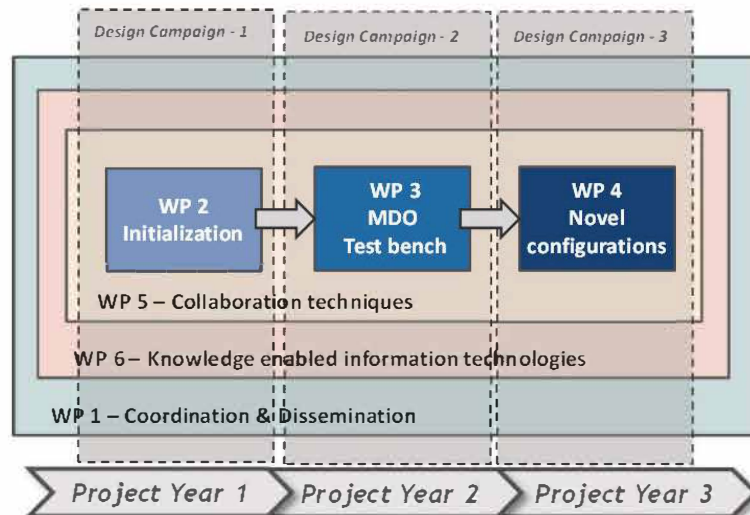


Figure 1. AGILE project structure

configuration is optimized using state-of-the-art techniques. The reference MDO problem is then used to investigate and benchmark novel optimization techniques individually and later in smart combinations (MDO test bench). Finally, the most successful MDO strategies are applied to significantly different aircraft configurations (Novel Configurations). The three sequential work packages are embedded within two enabling layers. The 1st enabling layer (Collaboration techniques) targets the development of the technologies enabling distributed collaboration, comprising the process of collaboration between involved specialists, collaborative

pre- and post-processing, visualization and the enhancement of existing framework. The second enabling layer (Knowledge enabled technologies) develops the information technologies, which support the management and the formalization of knowledge within an MDO process. The parallel activities are clustered in three phases (or periods), Design Campaigns (DC), each one lasting one year. Each of the sequential design campaigns focus on the solution of the use cases, which are setup to develop specific collaborative and knowledge based technologies. Design Campaigns, address an increasing complexity from use case perspective (progressing from conventional aircraft to novel configurations), and from MDO environment perspective (from the state-of-the-art MDO system to the 3rd generation system).

2.1. Design campaign 1

The DC-1 is the first use case in the project that has been formulated and collaboratively solved by the AGILE team. This case consists of the design and optimization task for a large regional jet, with Entry Into Service 2020. Starting from the specification of the Top Level Aircraft Requirements provided by the aircraft manufacturer partner (Bombardier), an Overall Aircraft Design (OAD) task targeting conceptual and preliminary development stages was implemented in DC-1. Fig. 2 shows a representation of the DC-1 distributed OAD process. The figure indicates the domains of the specialists' competences which have been integrated into

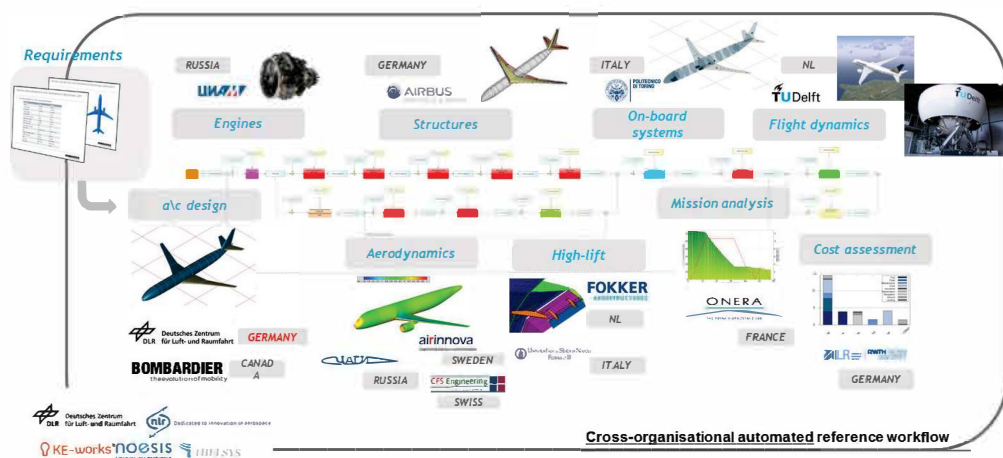


Figure 2. AGILE Collaborative design process: individual competences are distributed multi-site, and hosted at the different partners' networks

the process, the location where such simulation competences are hosted, and the specific partners providing such a competence within their IT networks. The corresponding deployed collaborative MDO workflow is represented in Fig. 3. A design exploration method is "calling" the OAD process (here labelled as MDA) as

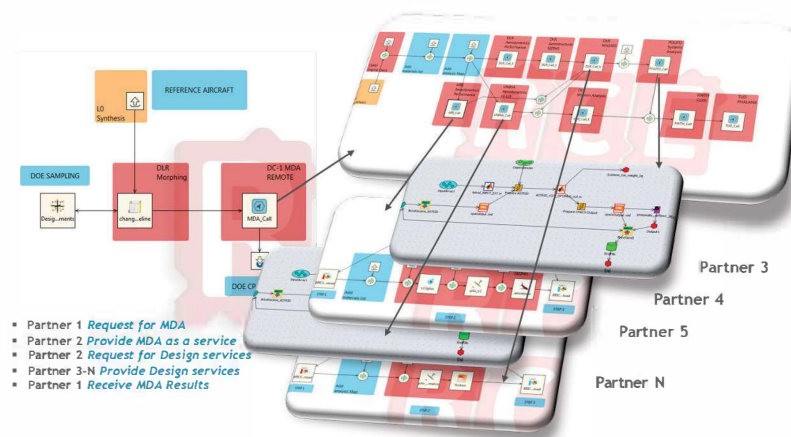


Figure 3. AGILE DC-1 workflow. Partner 1 deploys a Design Of Experiment requesting as remote service the cross-organizational MDA workflow, deployed at Partner 2. The MDA is composed by disciplinary competences provided as remote services to Partner 2 by Partners 4 to N

a remote service, which integrates all the distributed disciplinary competences, which are in turn called as

remote services (deployed as disciplinary workflows) within the MDA process. All competences communicate via a CPACS model [6] corresponding to the AGILE aircraft product model. They are deployed as disciplinary workflows and provided as remote services. Furthermore, the deployed “workflow of workflows” has been provided as “service of services” and coupled to an optimization strategy, named SEGOMOE, developed by ONERA [7]. An MDO problem was therefore formulated for the optimization of the reference aircraft using a MDF formulation resulting in an improved design.

2.2. Design campaign 2

The DC-2 activities are based on the DC-1 work, and were implemented during the second year of the project. In addition, the number of use cases is expanded to five parallel ones. For each use case, a novel MDO strategy (addressing a specific collaborative scenario) was investigated and assessed for the resolution of the design of the reference aircraft. Depending on the test cases, classical MDO formulations (such as MDF, IDF [8] or Analytical Target Cascading [9]) or more adapted ones have been proposed.

- First use case focused on the improvement of MDO strategies with the development and integration of new design competences in terms of optimization algorithms and surrogates modelling. These investigations are presented in [10, 11].
- The implementation of Uncertainty Quantification (UQ) methods and robust based design optimization in complex, variable fidelity optimization was the objective of second use case [10].
- The development of mixed-fidelity MDO strategy was tackled with the integration of high-fidelity design competences and its combination with Overall Aircraft Design (OAD) level. The process is presented in [12] and illustrated on Fig. 4-a.
- A multi-scale application is described in [13] aiming at investigating the improvement of involving an aircraft component supplier (aircraft rudder) in the overall aircraft optimization process while keeping its specific framework. The coupled optimization problem is illustrated on Fig. 4-b.
- A large-scale system-of-systems application was also studied, coupling Aircraft - Engine - On-Board-Systems (OBS) - Emissions in a distributed framework approach with the involvement of disciplinary services from the other partners [14].

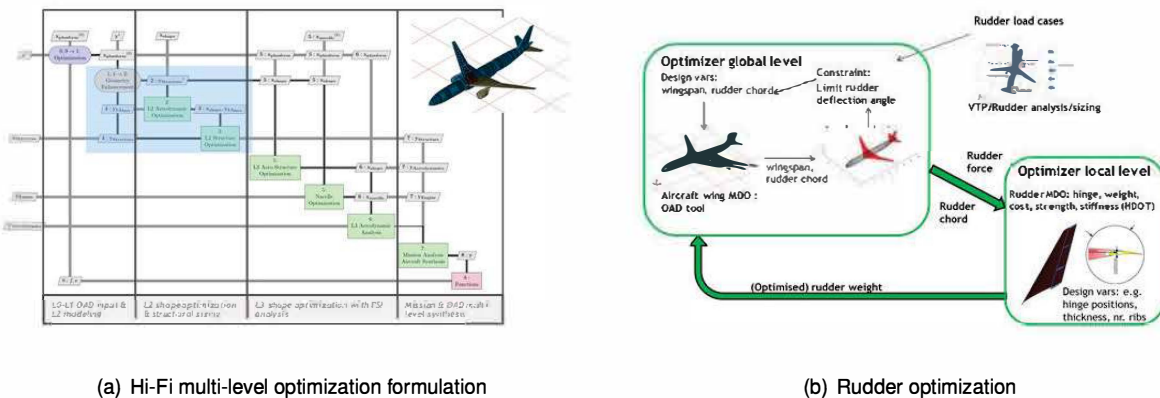


Figure 4. DC-2 investigation examples

Furthermore, based on the best practice developed during the DC-1, during the DC-2 the overall AGILE framework was enhanced by knowledge based technologies [15] and IT solutions [16], which contribute to accelerate the deployment of the complex MDO processes addressed by the DC-2 use cases.

This paper will present DC-2 investigations performed on first use case and focusing on enhanced MDO strategies which took advantage of surrogate models aiming at converging the process more rapidly to the best solutions.

3. MDO THROUGH SURROGATES

All the methods developed during DC-2 have the common goal of enhancing the optimization of complex workflows, which are characterized by a high degree of discipline interdependencies, high number of design

variables in the context of multilevel and multi-partner collaborative engineering projects. One of the most straightforward solutions is the use of surrogate models. A surrogate model (SM) is an analytical formula that replaces a complex model, or even a design analysis workflow, by means of data fitting. Consequently a surrogate model requires only little computation time, which is particularly useful for capturing complex analysis methods and applying them multiple times as part of a global optimization. In collaborative design studies during the early aircraft design phases, surrogate models are valuable to support the collaborative analysis of as many design alternatives as possible in a short time and at low cost, preferably with as much knowledge of the systems under consideration as possible.

3.1. Objectives

In the context of DC-2, two main scenarios were considered for the use of surrogate models to enhance MDO strategies:

- The 1st scenario (see Fig. 5) is related to the investigations of MDO formulations on complex workflows. The objective is to benchmark various MDO formulations such as MultiDisciplinary Feasible (MDF), Individual Discipline Feasible (IDF), Collaborative Optimization (CO). All of these different formulations are described in [8]. In order to compare these formulations in terms of number of function evaluations and/or accuracy of the optimal solution, the idea is to take advantage of surrogate models to reduce the computational costs. The key point here is to use surrogate models, instead of real tools while keeping the disciplinary results accurate. The accuracy of the surrogate models (computed for instance with the Root Mean Square Error criterion on a validation set of points) can be reduced with the use of a large database or with an iterative process to enrich the database as described in [17].

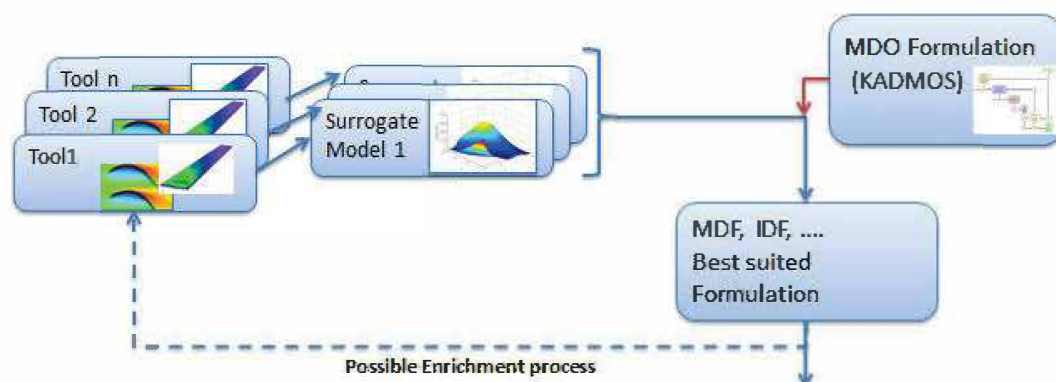


Figure 5. Scenario for automatic MDO process

- The 2nd scenario (see Fig. 6) concerns the optimization process using surrogate models and the propagation of uncertainty associated to each surrogate. By using surrogate models in an MDO instead of the real tools, some approximation errors are done and they are propagated within the process. The first objective is to quantify these uncertainties in the MDA in order to have the probability distribution of the objective function (dispersion of the objective function due to the use of surrogates) [18]. The second objective concerns the enrichment process to choose the next promising point and improve the surrogate models. This step is under investigation and implies some theoretical aspects linked to the probability distribution of the objective function and its discretization to determine its extreme values.

3.2. Enhanced framework

During DC-2 activities, the overall AGILE framework was enhanced both by knowledge based technologies and IT solutions enabling a quicker and more efficient understanding and deployment of the complex MDO processes. Next paragraphs will provide a brief description of two improvements brought by those enabling layers to support the surrogate models scenarios.

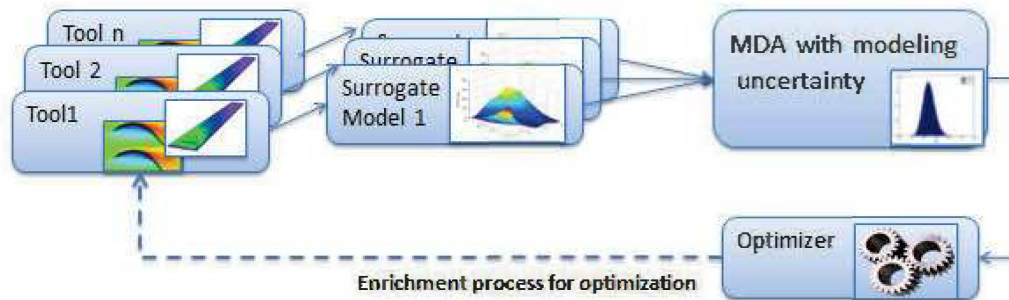


Figure 6. Scenario relative to propagation of the modeling uncertainty in the process

3.2.1. Collaborative architecture

In AGILE, the MDA/MDO workflows are configured, deployed and executed by making use of PIDO (Process Integration and Design Optimization) environments available at the different process integration sites. Multiple PIDO environments are available in AGILE. One integration environment used in AGILE is the “Remote Component Environment” (RCE) [19], developed by DLR. NOESIS provides an alternative/complementary collaborative framework by means of Optimus [20]. Both are deployed in AGILE to compose the main processes, as well as disciplinary sub-processes. The cross-organizational mechanism available in AGILE is Brics [21], developed by NLR. Brics provides technology for interconnecting PIDO environments. It comprises a protocol and supporting middleware for creating cross-organisation workflows as federations of native and legacy local workflows, tools and scripts, complying with the prevailing security constraints. Therefore, nested complex collaborative MDO workflows, connecting multiple organizations, can be deployed. Thanks to the standardized interface by means of CPACS [6], processes implemented using different PIDO platforms can be integrated in the same MDO. A schematic of workflows in different administrative domains is illustrated in Fig. 7. More information on all the developments of collaborative architecture is available in [15] and [22].

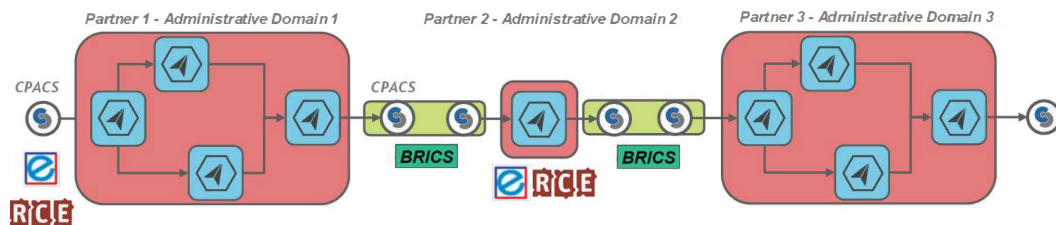


Figure 7. Connection of PIDO workflows hosted at multiple administrative domains

3.2.2. Knowledge architecture

The knowledge architecture under development in AGILE integrates different applications to enhance the MDO development process. The full AGILE knowledge architecture is discussed in [16]. Here, two elements of the architecture have been used to support the creation of the different surrogate models: the graph-based MDO formulation system KADMOS (Knowledge- and graph-based Agile Design for Multidisciplinary Optimization System) [23] and the visualization tool for MDO systems VISTOMS (VISualization TOol for MDO Systems) [24].

The five main stages of the AGILE development framework are shown in Fig. 8. KADMOS and VISTOMS support the development process in the first three steps of the framework and enable the design team to formulate MDO systems of any size and complexity. This support is provided by KADMOS using a graph-theoretic approach for the set-up and manipulation of multidisciplinary systems. In this approach, different graphs are created to represent the three different formulation stages shown in Fig. 8.

Repository Connectivity Graph (RCG): The RCG is a graph that represents the repository of (CPACS-compatible) tools that are available to the design team. CPACS-compatible tools all operate on a CPACS input file and create a CPACS output file. KADMOS interprets these different files and establishes the interdisciplinary dependencies (couplings), system inputs and system outputs.

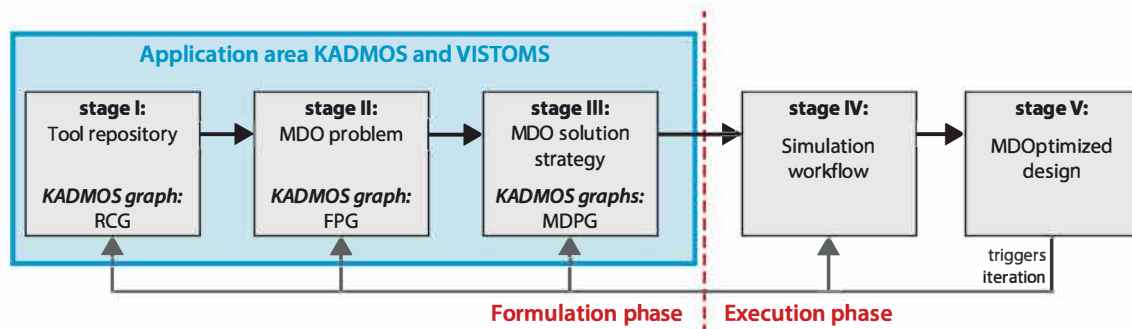


Figure 8. The five stages of a multidisciplinary system in the AGILE development framework

Fundamental Problem Graph (FPG): Based on the RCG an FPG can be created by the design team. This FPG is an enriched subgraph of the RCG, hence only a selection of the RCG tools which are necessary to solve a certain problem are still in the graph. Furthermore, key variables are indicated in the FPG, such as design variables and quantities of interest, which are necessary to define a Multidisciplinary Design Analysis and Optimization (MDAO) strategy. In this paper, the FPG is used to define different clusters for which Designs of Experiments (DOE) are executed to be able to create the surrogate models of a subset of disciplinary tools.

MDAO Data and Process Graph (MDPG): The MDPGs are automatically created by KADMOS based on the FPG. If the FPG contains a definition of a DOE strategy for a cluster of tools, then the MDPG will contain the description of the data and process flow required to execute this DOE. The MDPG itself is still just a combination of two graphs in KADMOS and cannot be executed.

Note that the link to the execution of the solution strategy is also enabled by KADMOS through the CMDOWS (Common MDO Workflow Schema) format [25], however, this development is not discussed in this paper and all workflows have been built manually based on the formulation provided by the KADMOS graphs.

As the graphs grow in size very quickly, their visualization becomes a challenge, while at the same time this would help the design team to inspect and debug the multidisciplinary system in each stage of the process. In AGILE, VISTOMS has been developed for this purpose and it is used in this paper to visualize the different KADMOS graphs. Throughout this paper the dynamic eXtended Design Structure Matrix (XDSM) [26] view from VISTOMS is used to represent the different KADMOS graphs.

4. APPLICATION TO DC-1 MDA

The scenarios described in Section 3.1 should demonstrate the improvements brought by the use of surrogate models on the optimization of complex workflows in the context of multilevel and multi-partner collaborative projects. A typical application of these investigations is the former MDA workflow defined and implemented during DC-1 activities with a realistic complexity of the problem w.r.t. industrial aircraft design (in terms of number of design competences, amount of coupling ...). Fig. 9 provides an overview of DC-1 MDA in XDSM format [26].

The objective was therefore the preparation of the workflows for the envisaged scenarios, using the DC-1 MDA as use case. Fig. 10 describes the different steps required to build the "MDA through surrogates" process:

- Identify the disciplinary tools and their associated domain of variation for each of the inputs.
- Create the associated DOEs and build the associated surrogate models.
- Build the associated workflow within any PIDO framework.
- Run the scenarios.

Next paragraphs will expose the pre-processing modifications applied to DC-1 MDA taking advantage of KADMOS and VISTOMS capabilities.

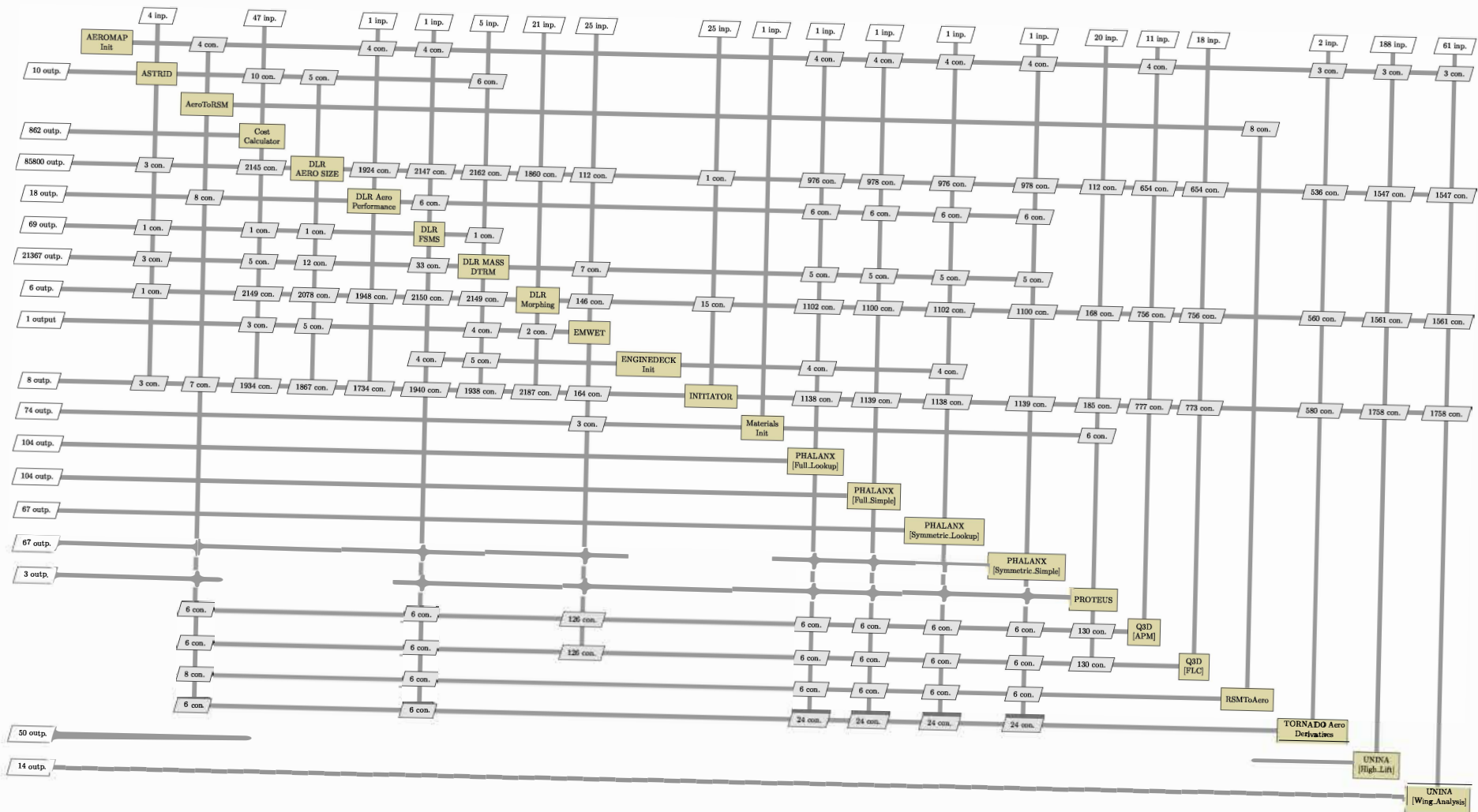


Figure 9. Overview of the DC-1 disciplinary tool repository (RCG visualized with XDSM data flow view)

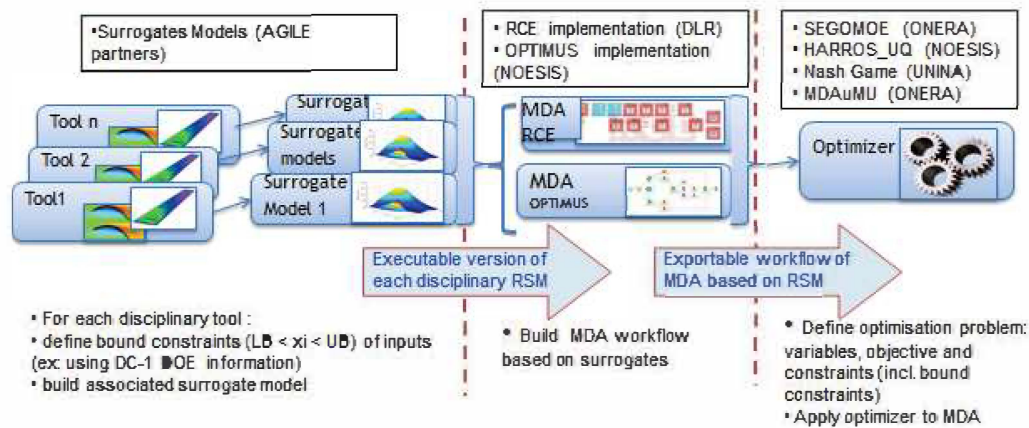


Figure 10. Description of the approach to optimize the MDA using surrogate models

4.1. DC-1 simplification

Fig. 9 presents the RCG of the full DC-1 MDA process. A first analysis indicated that more than 2000 connections can exist between design competences and that some design competences have more than one hundred inputs and outputs. In order to reduce the complexity of the problem while keeping as much as possible its similarity w.r.t aircraft design process, several adaptations were performed:

- Reduction of the number of design competences to be considered, mainly removing the Flight Dynamics assessment part and the Cost assessment part, both used as post processing tools in the DC-1 workflow. In addition, the engine characteristics are fixed. The retained design competences from DC-1 MDA, mainly made of low to medium fidelity tools, are the following:
 - Aerodynamics performance provided by DLR (German Aerospace Center)
 - High Lift Performance provided by UNINA (University of Naples "Federico II")
 - Propulsion system performance provided by CIAM (Central Institute of Aviation Motors)
 - Loads and structural sizing provided by DLR
 - On-board systems design provided by POLITO (Politecnico di Torino)
 - Mission performance provided by DLR
- Slight reduction of the complexity of the optimization problem to be considered compared to DC-1. Here, only seven inputs, linked to the wing design are selected as global variables (wing area, wing sweep, aspect ratio, thickness at tip and at kink, twist at tip and at kink) and outputs will be linked to the aircraft performances, such as weights (fuel weight, MTOM (Maximum Take-Off Mass), OEM (Operating Empty Mass) ...) or low speed characteristics (CLmax).

All these modifications were not sufficient to reduce the dimensions of the coupling variables (ie connections between the design competences) that would prevent the use of surrogates' capabilities. Indeed the main difficulty to build a SM is driven by the input characteristics: their number and their location. Two main sources of high number of coupling variables can be identified as follows:

1. The coupling between the Geometry and most of the other design competences, such as Aerodynamic performance one, need as inputs, the whole geometry of the aircraft, stored in multiple CPACS branches.
2. The coupling between the Aerodynamic performances and the Mission performance as the Mission performance tools need, as inputs, the whole aerodynamic performance map, stored in a CPACS branch. This lookup table of aerodynamic coefficients is given as function of the mission dependent parameters Mach, Reynolds Number (Re), Angle of Yaw (AoY) and Angle of Attack (AoA).

In order to reduce drastically the 1st source of coupling, a design competence was introduced in the workflow: the Aircraft Morphing design competence (provided by DLR) that enables the modification of wing geometry from a set of design parameters which are not explicitly defined/directly accessible in CPACS. Therefore the

full wing geometry, representing hundreds of variables can be controlled by less than a dozen parameters. This design competence was already used for the MDO application of DC-1 as a pre-processing tool and is now introduced inside the workflow.

For the 2nd source of coupling, another approach was retained through the use of a specific surrogate model that should embed the Aerodynamic look up table and that is described more in detail in the next paragraph.

4.2. Clustering of design competences

Adding new tools, such as Aircraft Morphing Tool in the workflow, will only lead to reduce the coupling if it is clustered with the other design competences. For instance, making a cluster of the Morphing tool and a Structural sizing tool will expose a limited set of inputs, here the wing design parameters, of the cluster and a limited set of outputs, here the wing weight, as outputs, while keeping the full geometry description as an internal coupling variables between the clustered tools. As an extension of this approach, it was decided to make clusters of design competences of the MDA exposing the following characteristics:

- These clusters should exhibit low dimensions of inputs (less than 20) in order to be accurately represented by a surrogate model.
- These clusters should not have internal feedback coupling between design competences (to prevent the use of convergence process inside the cluster).
- These clusters should be representative of an aircraft design process.

In order to fulfill those requirements, four clusters were built using the retained design competences.

Aerodynamic Cluster This cluster gathers Morphing tool and aerodynamic performance computations including the low- speed configurations. It takes as input the wing design parameters and provides the lookup tables for aerodynamic coefficients, related to the specified wing design.

On-board systems Cluster This cluster aims at providing the On Board systems performance, in terms of weights and power, using the wing design parameters and other inputs such as the Fuel Weight and other operational weights such as MTOM (Maximum Take-Off Mass).

Structural sizing and Weight Cluster This cluster provides the weight breakdown of the whole aircraft, using as inputs the wing design parameters, the fuel weight and the systems weight. It also contains the Load and structural sizing competence that sizes the wing structure and computes its weight.

Mission performance Cluster This cluster contains the Mission performance tool and uses as inputs, the wing design parameters, the operational weights and the Aerodynamic look up tables to run the full mission and provides the fuel weight.

Fig. 11 provides the FPG of the four clusters. One can notice that, each cluster can contain design competences of various partners that will be called through AGILE framework.

At this step, two approaches have been identified in order to derive a surrogate model of the Aero Cluster and link it to the Mission Cluster.

- A two-step approach: In this case the AeroClusterSM predicts - as a function of wing design parameters - a representation of the aero lookup tables, e.g. by predicting polynomial coefficients that will be transferred to the MissionClusterSM.
- An "all-in-one" approach: In this case the AeroCluster SM directly predicts the aerodynamic coefficients as a function of wing design parameters and mission parameters (Mach, Re, AoY and AoA). As such the AeroClusterSM becomes an integrated part of the MissionCluster (and therefore also of the MissionCluster SM which is to be derived).

Eventually, Fig. 12 summarizes the MDA workflows obtained with the clusters defined above for the two possible approaches. In agreement with the clusters' requirements, both MDA are representative of an aircraft design problem with different disciplines (Aerodynamic, Structure, Performance) coupled together. A surrogate model of each cluster now needs to be created in order to build the MDA workflow.

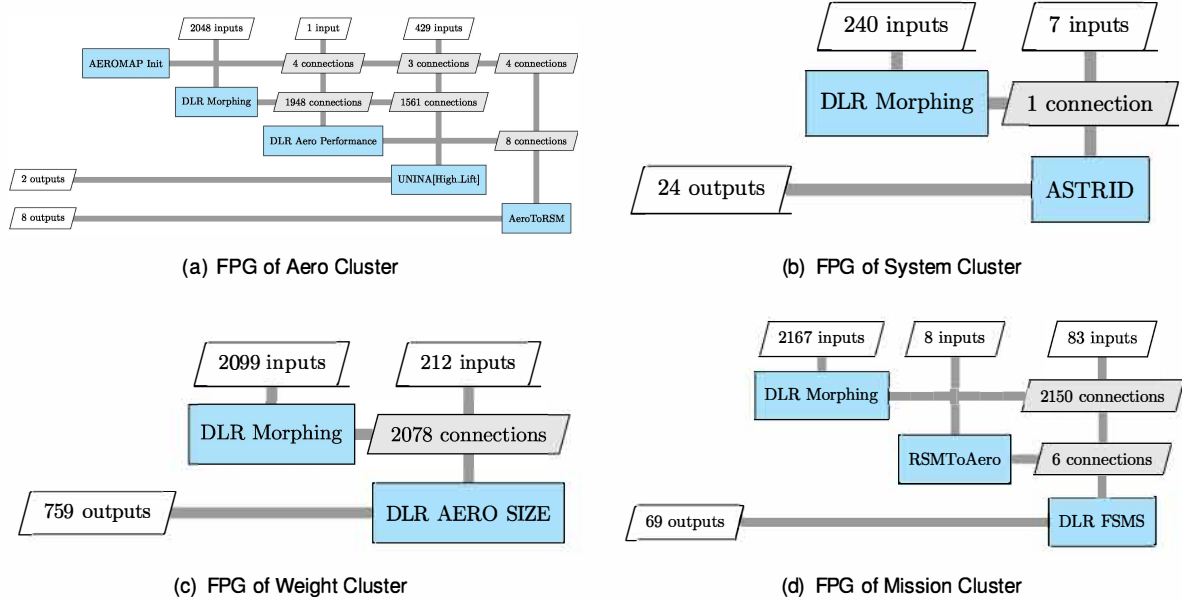


Figure 11. FPG of the 4 retained clusters (2-steps approach)

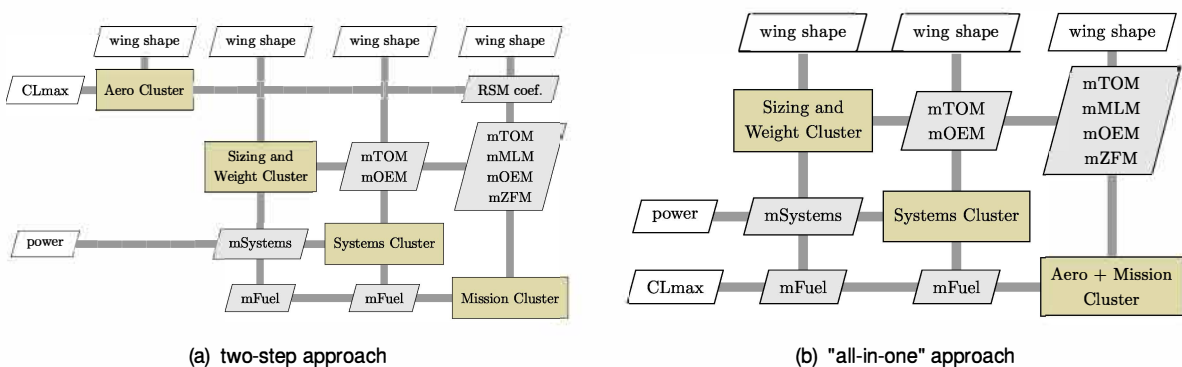


Figure 12. Workflow(s) of MDA through surrogates with the two different approaches

5. RESULTS

5.1. DOE

After the formulation of design competence clusters, these have been implemented as collaborative service oriented workflows, and executed within DOE studies in order to generate the databases for the clusters' surrogate models. An XDSM view of the clusters DOEs, automatically created by KADMOS (i.e. MDPG), for the two-step approach are provided in Fig. 13. Each DOE study only exposes from 7 to 11 independent variables, including wing design parameters (7) and aircraft masses (e.g. Operating Empty Mass (OEM)) as coupling variables (0 to 4) that will be provided by the other clusters. In order to generate the individual clusters database, the first challenge is the selection of the range of variation of the coupling variables. The adopted approach was to make use of the results from DOEs performed during the DC-1 optimization activity. Since in the clusters DOEs, the range of variation for the wing shape parameters has been kept similar to the DOEs performed during the DC-1, the 15 configurations in the DC-1 database have been used to estimate the range of variation of the coupling variables between the clusters (i.e. inputs of DOE of the clusters).

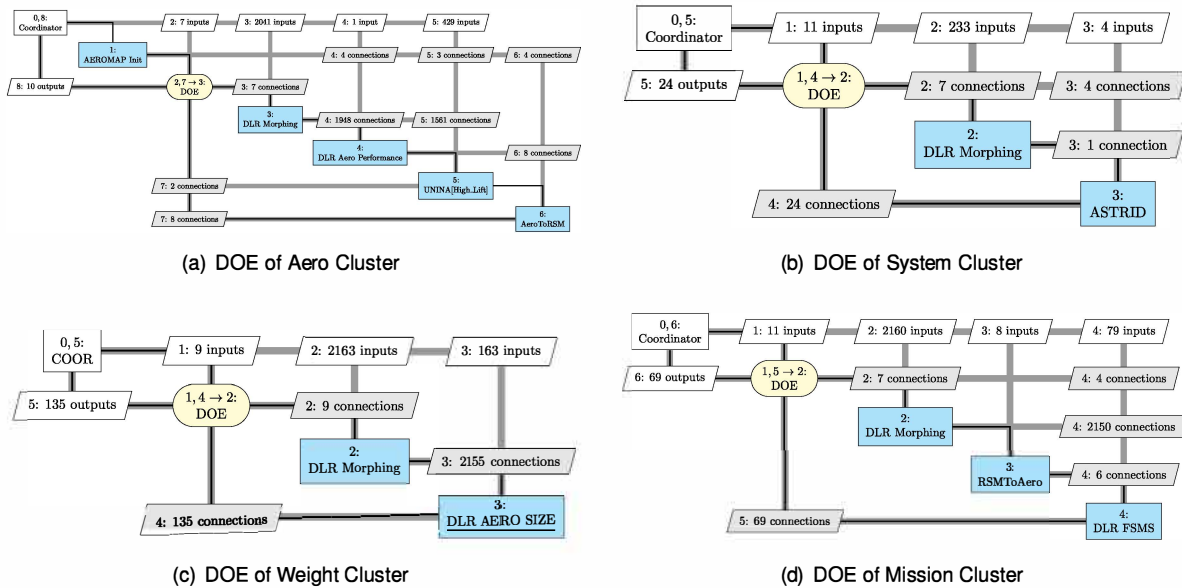


Figure 13. XDSM view of the DOE architectures for 4 competence clusters (two-step approach). The XDSMs are a visualization by VISTOMS package of the MDPG created by KADMOS.

Once the range of each design variable has been determined, the DOE sampling plans have been generated for each cluster, by using a LHS (Latin Hypercube Sampling) sampling method. The number of DOE samples was selected to minimize the numbers of calls to the cluster while providing a sufficient accuracy. Thereafter, the 4 clusters have been integrated and executed as collaborative workflows. The characteristics of the DOE sampling plan are given in Table 1.

	Initial DOE samples	Number of design variables
Aero Cluster	40	7
System Cluster	60	10
Weight Cluster	60	10
Mission Cluster	70	11

Table 1. Characteristics of cluster DOE studies database

A collaborative DOE study service approach, has been developed within the DC-2 by DLR with the objective to facilitate the execution of collaborative DOE studies, whose different steps are performed at different organization. The nested steps are illustrated in Fig. 14 and briefly addressed in the following.

- Step 1: A DOE sampling plan is generated by a specialized Partner, stored in a dedicated CPACS study branch, and provided to the Partner which is responsible for the integration and the execution of the DOE samples via the so-called DOE Study service.

- Step 2: The Partner responsible for the DOE Study service receives the complete sampling plan, and the contained input and output quantities are mapped to the parameters which need to be varied within the specific clusters' workflows. For the described DOE clusters, the sampling plan quantities have been mapped to the DLR aircraft geometry morphing tool, which provides the input (a CPACS aircraft) to the specific cluster's workflow to be executed for each DOE point. Note that such a cluster workflow is also hosted at a different Partner, which is responsible for the specific cluster's workflow integration, and offered as a remote service to the Partner initializing the DOE sampling plan in the previous step.
- Step 3: The specific cluster's workflow receives the DOE sample point as input, it is executed as a remote service requested in step 2. The specific cluster's workflow is also composed by multiple competences, which are CPACS compatible and hosted at different Partners' sites and provided as remote services. The list of the design competences used in the 4 clusters is provided in Section 4.1.

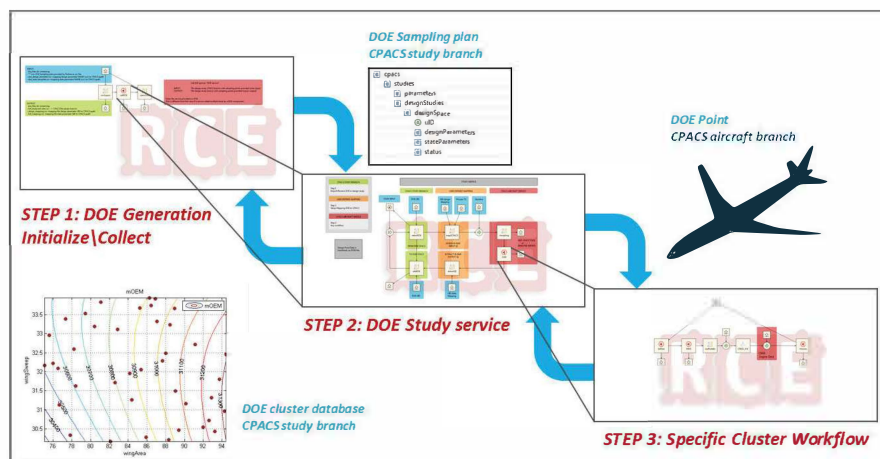
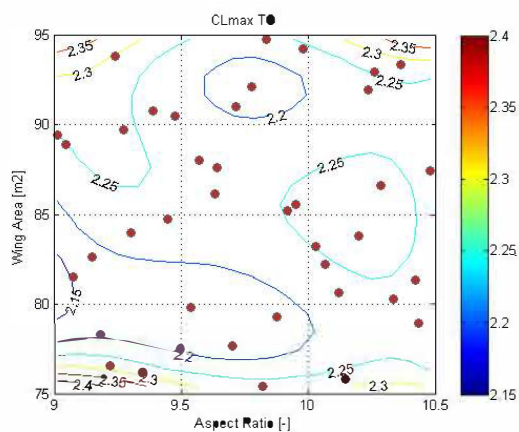


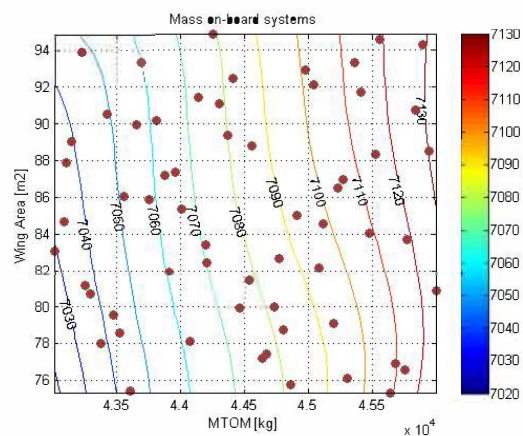
Figure 14. Collaborative DOE study: nested steps approach

The results obtained within the cluster's workflows (in step 3) are collected by the DOE Study service workflow (in step 2) and mapped back as DOE output for each sampling point, and the complete DOE database is provided back to the Partner initializing the DOE (in step 1). Afterwards, the DOE database stored as CPACS study branch is forwarded to the Partners responsible for the generation of the cluster surrogate models, or for the further enhancement of the DOE sampling plan. For all the 4 DOE clusters shown in Fig. 13, the described three steps have been implemented as individual RCE workflows hosted at different Partners' sites. The deployed approach makes use of the AGILE Collaborative Architecture's elements for requesting and providing the remote services. The complete process for the DOE sampling generation-execution-enhancement is fully automated. As described in Section 4.2 each of the DOE has a specific set of input parameters, and output parameters provided by the distributed design competences which are selected for the cluster. Therefore, for each of the DOE 4 clusters illustrated by the XDSM in Fig. 13, a selection of output parameters is shown in Fig. 15, and briefly summarized in the following.

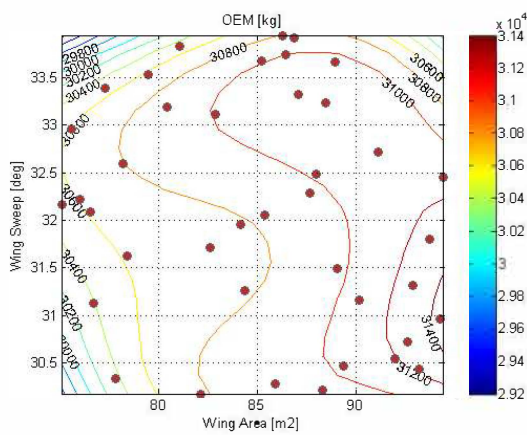
- Aero Cluster: wing planform parameters (aspect ratio and wing area displayed) are provided as DOE input to the cluster's workflow composed by the aerodynamics analysis modules provided by DLR and UNINA (maximum lift coefficient at take-off displayed).
- System Cluster: wing planform (wing area displayed) and design masses (Maximum Take-Off Mass displayed) are provided as DOE input to the cluster's workflow composed by the on-board systems design competence provided by POLITO (mass of the sized on-board systems displayed).
- Weight Cluster: wing planform parameters (wing sweep angle and wing area displayed) are provided as DOE input to the cluster's workflow composed by the loads analysis and structural sizing design competence provided by DLR (operating Empty Mass displayed).
- Mission Cluster: wing planform (wing area displayed) and design masses (Operating Empty Mass displayed) are provided as DOE input to the cluster's workflow composed by the mission performance analysis module provided by DLR (mass of the mission fuel displayed).



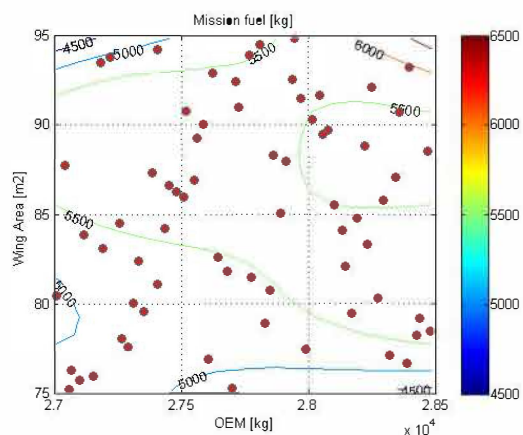
(a) DOE output of Aero Cluster: CLmax at take-off



(b) DOE output of System Cluster: Mass on-board systems



(c) DOE output of Weight Cluster: Operating Empty Mass (OEM)



(d) DOE output of Mission Cluster: Mass mission fuel

Figure 15. DOE clusters sample points results



5.2. Surrogate models

5.2.1. Available methods

Thanks to AGILE consortium, multiple methods are available regarding surrogate models (SM) competence. During DC-2, one of the objective was to make these methods accessible to the partners through their integration as remote services in one of the PIDO framework, like any other design competence. Multiple SM competences were investigated in the frame of this use case.

- NLR's toolbox, called MultiFit [27] which provides a MATLAB based integration of multiple data fitting methods (e.g. polynomial, kriging, spline, neural network). The toolbox guides the user through the steps of deriving and delivering an optimal surrogate model. This includes data analysis and selection, fit method assessment, and deployment of the surrogate model. MultiFit has been used in AGILE to derive surrogate models of wing MDA, loads analysis, engine behaviour and rudder design. Developed surrogate models are made available to partners through the Surrogate Model Repository (SMR), which has also been developed in AGILE [22].
- ONERA's tool, MOE, a Mixture of Experts technique which combines local surrogate models [28]. Mixture of Experts method [29, 30] for surrogate modeling provided uses a clustering of the training basis into regions where the function to be approximated is expected to be continuous or at least more simple. It strongly relies on the Expectation-Maximization (EM) algorithm for Gaussian mixture models (GMM). With an aim of regression, the inputs are clustered together with their output values by means of parameter estimation of the joint distribution. A local expert is then built (linear, quadratic, cubic, radial basis functions, or different forms of kriging) on each cluster and all the local experts are finally combined using the Gaussian mixture model parameters found by the EM algorithm to get a global model. MOE has been made available to AGILE partners for different applications [17].
- NOESIS Optimus kernel which provides a set of surrogate models and accuracy evaluation tools. Three main classes of surrogate models are available:
 - Least squares fit for Taylor polynomial (linear, quadratic, cubic order) or user defined model. The definition of the model terms can be changed by the user or performed automatically to identify an optimal set of terms.
 - Interpolating, either Kriging or radial basis function (linear, thin-plate, quadratic, cubic).
 - User: Optimus offers the possibility to calculate a User-defined RSM. This type of models uses shared libraries and is configured in XML-files.

Generated models can be evaluated from Optimus or exported and integrated in other application as executable or Functional Mockup Units.

- Surrogate model built by AIRINNOVA is Kriging & co-Kriging [31] based on Matlab DACE toolbox [32]. This process is built initially to provide a "data fusion" technique in AGILE, where a great quantity of low-fidelity data is coupled with a small amount of high-fidelity data to enhance the accuracy of a surrogate model. Using DACE toolbox the surrogate model can be built by choosing the proper regression model (polynomials of order $N = 0$ (constant), 1 (linear) or 2 (quadratic)) and correlation function.

AIRINNOVA provides an alternative (Matlab-license independent) to DACE co-Kriging, Python's built-in persistence *model* (*scikit-learn*), containing the co-Kriging model parameters corresponding to the co-Kriging surrogate trained with incoming training data. The co-Kriging (Kriging) predictor is inherently strongly coupled with its Hessian computation, which will be examined and the suggested new training data can be provided according to maximum Hessian [17].

5.2.2. Modeling of the Aero Cluster

This subsection analyses multiple methods for creating a surrogate model (SM) of the Aerodynamic analysis cluster (AeroCluster) and describes the results obtained with the MultiFit toolbox. The AeroCluster takes as input the wing design parameters. As a result of the performed analysis the AeroCluster provides lookup tables for aerodynamic coefficients, related to the specified wing design. The lookup tables are given as function of the mission dependent parameters Mach, Reynolds Number (Re), Angle of Yaw (AoY) and Angle of Attack (AoA). The lookup tables will be used later on in the Mission performance Cluster, in order to calculate the actual values of the aerodynamic coefficients and from there contribute to the overall design objectives, e.g. fuel mass.

As already mentioned in Section 4.2, two approaches have been identified in order to derive a surrogate model of the AeroCluster (AeroClusterSM) and relate it to the MissionCluster:

- A two-step approach. In this case the AeroClusterSM predicts - as a function of wing design parameters - a (representation of) the aero lookup tables, e.g. by predicting polynomial coefficients. This approach is illustrated in Fig. 16.
- A "all-in-one" (AI1) approach. In this case the AeroClusterSM directly predicts the aerodynamic coefficients as a function of wing design parameters and mission parameters. As such the AeroClusterSM becomes an integrated part of the MissionClusterSM. This approach is depicted in Fig. 17.

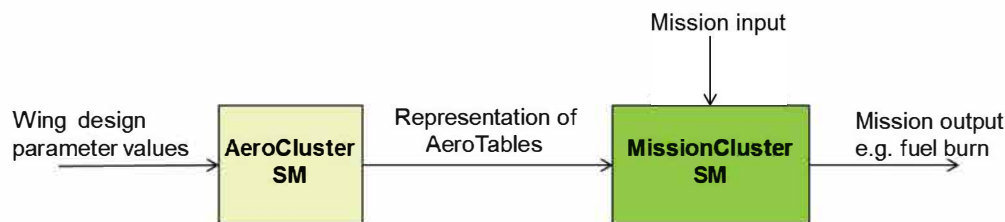


Figure 16. Depiction of the "two-step" approach. For simplicity the other clusters have been left out here.

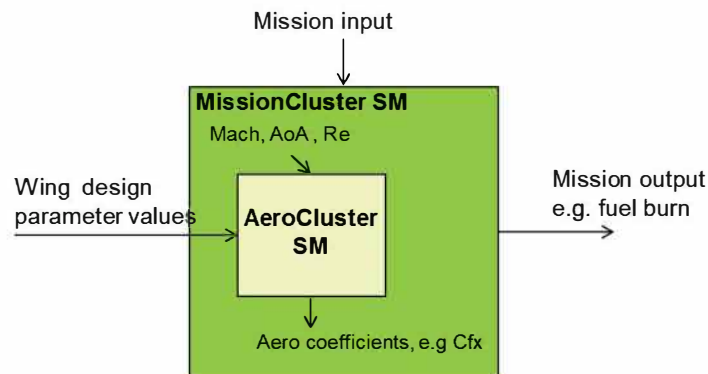


Figure 17. Depiction of the "all-in-one" (AI1) approach. For simplicity the other clusters have been left out here.

As indicated in Section 5.1, a database of 40 aircraft configurations (with varying wing design parameter values) have been processed by the AeroCluster. The aero table parameter AoY was not varied and is therefore ignored. Below surrogate model derivations are described both for the two-step and the AI1 approach. In each case the surrogate model is created using a training set based on the first 39 configurations. The 40th configuration is used for validation of the surrogate models. Only the first aerodynamic output Cfx is considered here, for simplification. The other aerodynamic coefficients (e.g. Cfy, Cfz) could be predicted in a similar fashion.

Two-step approach With this approach two methods for creating the AeroClusterSM have been applied.

- Method1: Approximation of the aero lookup tables using polynomials and prediction of these polynomial coefficients (as function of wing design) again using polynomials.
 - Method2: Prediction of the aero lookup tables using Proper Orthogonal Decomposition (POD) [33] and polynomial prediction of the POD coefficients (as function of wing design).
1. Method1: For all configurations the stepwise fit resulted in a 2nd order polynomial (as a function of Mach, Re and AoA) with 7 coefficients: using the constant term, three linear terms, the cross term $\text{Mach} \times \text{AoA}$ and the quadratic terms Mach^2 and AoA^2 . Fig. 18 shows that all 40 sets of polynomial coefficients have a piecewise similar order of magnitude. Therefore they could be fitted as well as function of the design configuration. The sets of polynomial coefficients have again been stepwise fitted by a 2nd order polynomial, leaving the 40th polynomial out for validation. This last stepwise fit represents the AeroClusterSM. The 40th polynomial (consisting of 7 coefficients) has been predicted with the AeroClusterSM and has been applied in order to predict the aero lookup

table values of the 40th configuration. The results are depicted in Fig. 19. A maximum absolute Cfx prediction error of less than 0.02 has been achieved. Fig. 19 shows that this corresponds to a relative error of about 10 percent. Other methods (e.g. kriging) for fitting the set of polynomial coefficients have been tried as well, but they gave worse prediction results on the 40th configuration than the stepwise fit AeroClusterSM. Concluding, the AeroClusterSM derived with this method predicts 7 polynomial coefficients that can be passed on to the mission cluster for prediction of the aerodynamic coefficients later on.

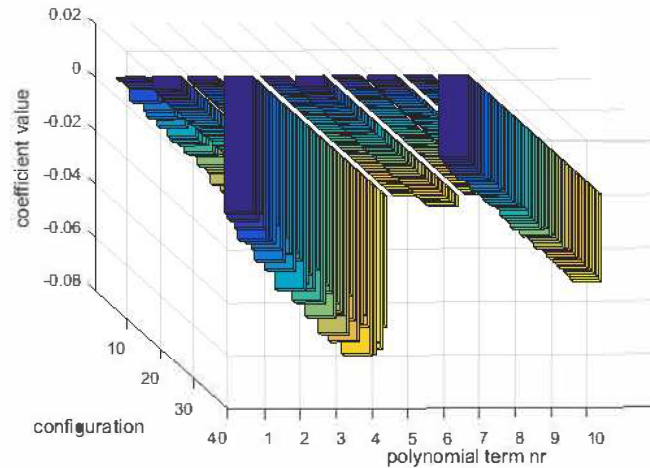


Figure 18. Coefficient values of a 2nd degree polynomial (derived with stepwise fit of the aero lookup tables), for all 40 aircraft configurations

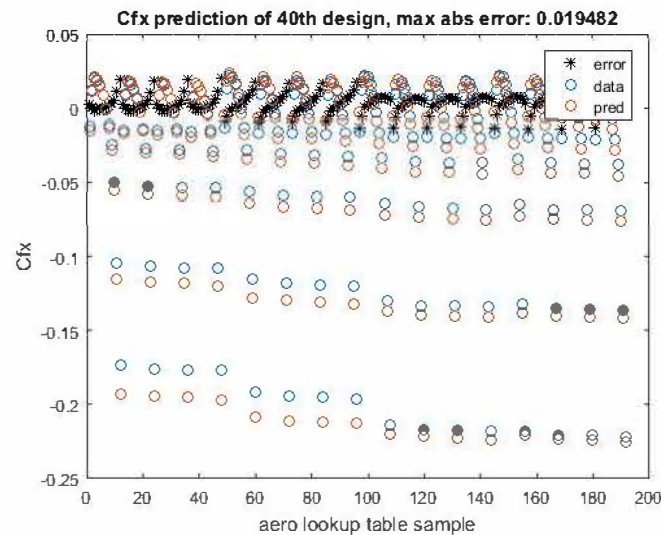


Figure 19. Prediction of the Cfx aero table values on the 40th configuration : Method1 with Nested stepwise polynomial fits

2. Method2: Alternatively, when the lookup table values of Cfx are ordered into one long row (of 192 samples) they can be considered as a "snapshot" of the i^{th} aircraft configuration. This results in a "snapshot-matrix" A of 40 x 192. A can be reduced using POD. A singular value decomposition

$$A = U \times S \times V^T$$

is derived. From S the dominant singular values are selected, in this case the first three. The matrix $U \times S$ contains the POD vectors (row-wise). The first three columns of this matrix are to be fitted, as a function of aircraft configuration. The 40th row of $U \times S$ is left out and the remaining 39 rows are fitted, again using stepwise fit of a 2nd order polynomial. The 40th POD vector is

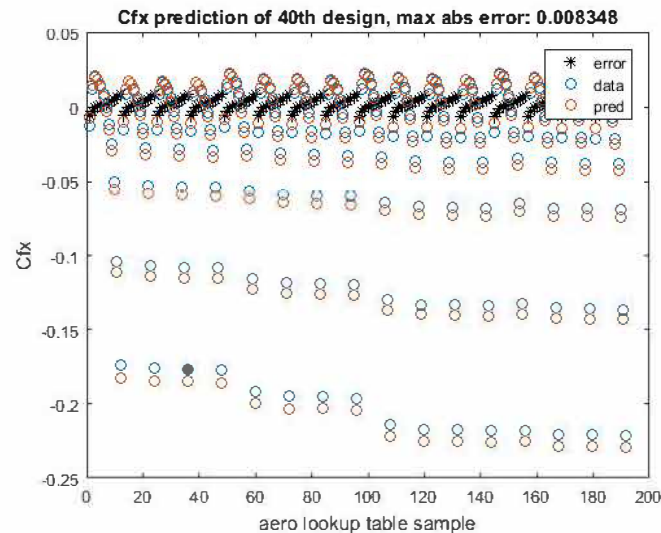


Figure 20. Prediction of the C_{fx} aero table values on the 40th configuration: Method2 with Stepwise polynomial fit of POD vectors.

predicted using this polynomial and back transformed to a prediction of the 40th row of A (40th aero table "snapshot"). The results are depicted in Fig. 20. This result is a maximum prediction error of less than 0.01, which is better than the validation result with Method1.

Concluding, the AeroClusterSM derived with this method is composed by a stepwise polynomial fit and POD transformation functions. The AeroClusterSM predicts the full aero lookup table (as function of wing design parameters) which can be passed on to the mission cluster for prediction of the aerodynamic coefficients later on.

All-in-one approach With the AI1 approach the 7 wing design parameters and the 3 mission parameters have been combined, resulting in a dataset of $40 \times 192 = 7680$ points, with 10 inputs and 1 output (C_{fx}). An Artificial Neural Network (ANN) has been fitted on to the first 7488 points, which correspond with the 39 configurations. One hidden layer with 10 neurons has been used. The aero lookup table values of the 40th configuration are predicted as validation of the method. The results are depicted in Fig. 21. This result is a maximum prediction error of less than 0.01, which is comparable to the validation result with Method2 of the previous approach.

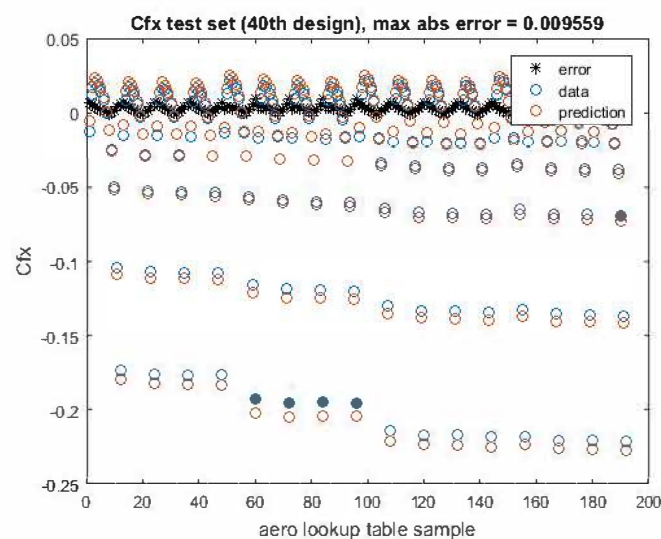


Figure 21. ANN Prediction of the C_{fx} aero table values on the 40th configuration based on the AI1 approach

Concluding, the AeroClusterSM derived with this approach consists of an ANN that must be integrated with the MissionClusterSM, as illustrated Fig. 17.



Similar investigations were performed by other partners on the AeroCluster and similar approach was also applied to the other clusters once the database was made available. One should note that the objective, here, was not to benchmark the various SMs of the partners but to make accessible multiple surrogate Design Competences through the AGILE framework to build the surrogate-based MDA workflow.

5.3. MDA clusters workflow

This paragraph presents the next step of the approach: the building of the MDA workflow of surrogate models in a PIDO framework. The results shown here were obtained using the Optimus framework and the surrogate models were provided by NOESIS but, thanks to AGILE framework, this workflow could also be established using the RCE PIDO framework and surrogate models provided by other partners could be applied (as a remote competence or as an executable version).

To illustrate the approach, the four clusters have been embedded in a single Optimus MDA workflow depicted on Fig. 22 that reproduces the simplified connection schema depicted in the XDMS (see Fig. 9). As the SMs were already available on the same platform, a non-collaborative implementation of the MDA has been preferred. The MDA does not exploit neither the potentiality offered by Brics to connect remote tools nor the unified file CPACS to enrich the information space. It has been implemented using a single PIDO platform and the surrogate models have been deployed on the same workstation used for the simulations. This direct implementation has been made possible by the clusters created using the knowledge-based part of the AGILE framework, that minimized the number of variables and connections from the complexity represented in Fig. 9 to something manageable by hand. The information exchange between the cluster has been managed using the Optimus native variables. The SMs, exported as binary models, have been prepared for execution via an external evaluator (thus their analysis is triggered from within the workflow, but run independently). The highlighted blocks in the Fig. 22 are:

Yellow color: Aero Cluster	Green color: Structural sizing and Weight Cluster
Red color: On-board systems Cluster	Azure color: Mission Cluster

The structure of the workflow can be adapted with minimal efforts to match the collaborative framework methodology; each colored block can be replaced with a 3-components assembly that performs the CPACS mapping, Brics task creation and extraction of the output values from the enriched CPACS. The operations with the surrogate models operated as remote discipline have been successfully tested using the Multi-task feature of Brics.

There are 2 nested convergence loops (represented by the circular icons on Fig. 22). They are required as the connections among the tools, which have been severed for the DOEs, have to be re-established to ensure the MDA functionality; in some cases this implies that a cluster may receive the input before the corresponding output has been generated by another cluster. To this end, a nominal initialization value, subsequently refined in the following iterations, has been used. Each loop has been addressed using a fixed point iteration until the assigned tolerance is reached (difference between 2 successive iterations lesser than 0.1%). The inner loop connects weight and system clusters and is required to ensure the consistency of the systems weight value (mSystem coupling variable). The outer also includes the Mission cluster and is mandatory to achieve convergence on the fuel weight (mFuel coupling variable) information. On average to achieve convergence on both loops, 45 evaluations have to be performed (9 runs of the outer loop, each requiring 5 runs of the inner). Input values have been gathered on the top of the workflow; the two main array are InputWingGeometry (top left, which include all the AeroCluster inputs) and the InputMission (top right). The design variables for Structural sizing and Weight and On-board systems Clusters are either inherited or generated as output. System and fuel mass are not to be considered independent design variables.

A single run of the non-collaborative MDA takes about 10 seconds; 4 iterations of the internal loop and 5 of the outer one are required to achieve the convergence requirements. The total number of calls to the SM evaluator is 46 (Aero 1, Weight 20, Systems 20, Mission 5). The equivalent collaborative workflow requires around 300 seconds, due to the overhead introduced by data upload and download on the sharedpoint server. The overhead is particularly relevant using SM because of the significantly reduced execution time of the modeled discipline, from seconds/minutes to less than a second. The non-collaborative version of the MDA has been used for the following analysis.

Thanks to the reduced execution time it has been possible to perform a DOE to explore the design space and investigate the impact of the design variables. A 100 experiments Latin Hypercube Sampling has been used. The analysis of the Pearson (measure of the linear correlation) coefficients has been reported in Fig. 23. Values can vary between +1 (total positive linear correlation) and -1 (total negative linear correlation). Colors are proportional to the absolute value of the coefficient and emphasize outputs that are significantly affected

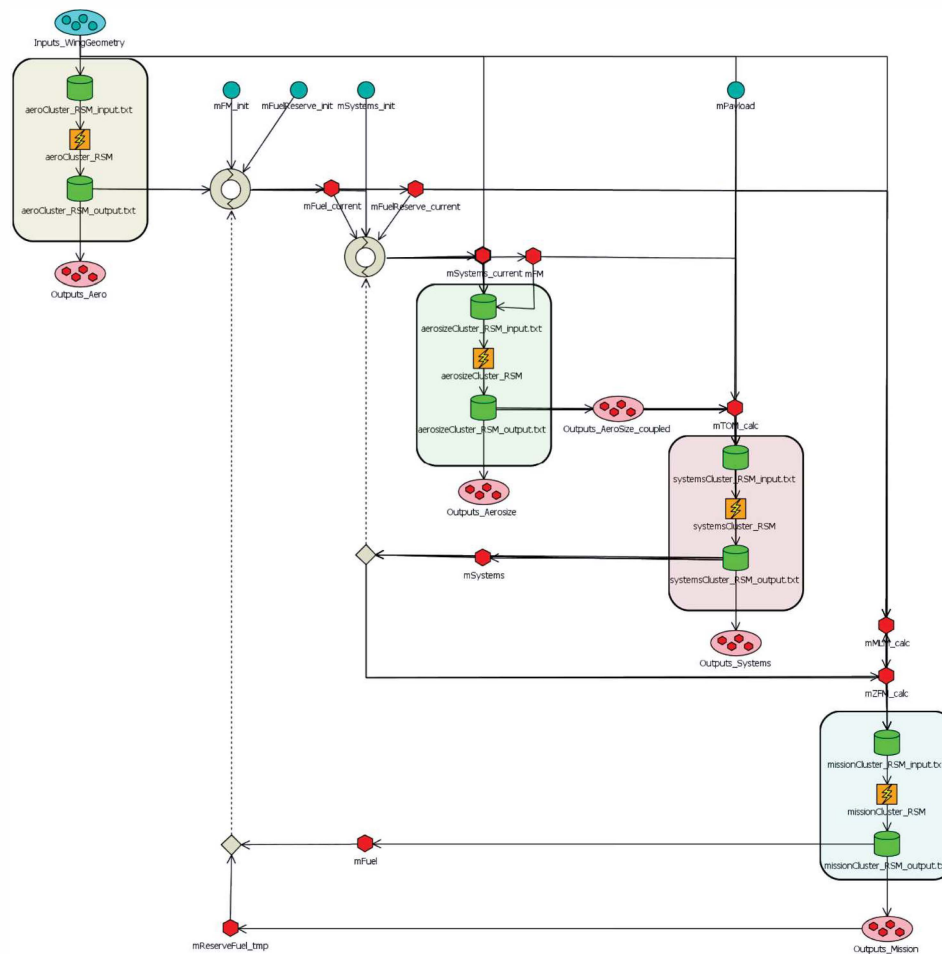


Figure 22. MDA through surrogates with 4 clusters

Pearson	aspectRatio	tcKink	tcTip	twistKink	twistTip	wingArea	wingSweep	CLmaxL	CLmaxTO	mFuel	mOEM	mSystems	mTOM	mWing
aspectRatio	1.000	-0.010	-0.018	-0.035	-0.007	-0.029	0.005	0.034	0.068	-0.564	0.450	-0.051	-0.474	0.457
tcKink	-0.010	1.000	-0.037	-0.018	0.001	0.022	-0.035	0.311	0.192	-0.190	-0.007	-0.324	-0.299	0.004
tcTip	-0.018	-0.037	1.000	0.012	-0.017	0.036	0.046	0.132	0.135	0.033	0.036	0.113	0.099	0.032
twistKink	-0.035	-0.018	0.012	1.000	0.018	0.021	0.016	0.145	0.201	-0.151	0.093	-0.159	-0.132	0.099
twistTip	-0.007	0.001	-0.017	0.018	1.000	-0.046	0.045	-0.860	-0.887	0.149	0.229	0.451	0.441	0.216
wingArea	-0.029	0.022	0.036	0.021	-0.046	1.000	-0.011	0.180	0.155	-0.665	0.832	0.257	-0.252	0.832
wingSweep	0.005	-0.035	0.046	0.016	0.045	-0.011	1.000	-0.290	-0.262	0.150	0.033	-0.367	-0.225	0.046

Figure 23. MDA through surrogates, design variable influence on evaluated outputs - Pearson coefficient

by a specific design variable (i.e. wing mass and wing area). As an example in Fig. 23, are highlighted the (almost linear) influence that the wing area has on Wing Total Mass, Operative Empty Weight and Systems Weight and the negative effect on both the evaluated lift coefficients due to wing tip twist.

The MDA has been used to test an optimization aimed at minimize the maximum Take Off Mass with a constraint on the minimum range. A global search method, the Self Adaptive Evolution [20] has been selected as optimization algorithm. The method performs an expensive initial exploration of the entire design space but is robust against local minima. The evolution of design variables, outputs and objective has been reported in Fig. 24. The colors represent the iteration number; a convergence pattern is clearly visible. The final configuration has been reported in Table 2. The optimization algorithm selected a thinner, larger wing in order to minimize the drag and consequently fuel consumption; the range improvement has been accompanied by an estimated reduction of total fuel mass. This has a negative effect on the (unconstrained) lift coefficients.

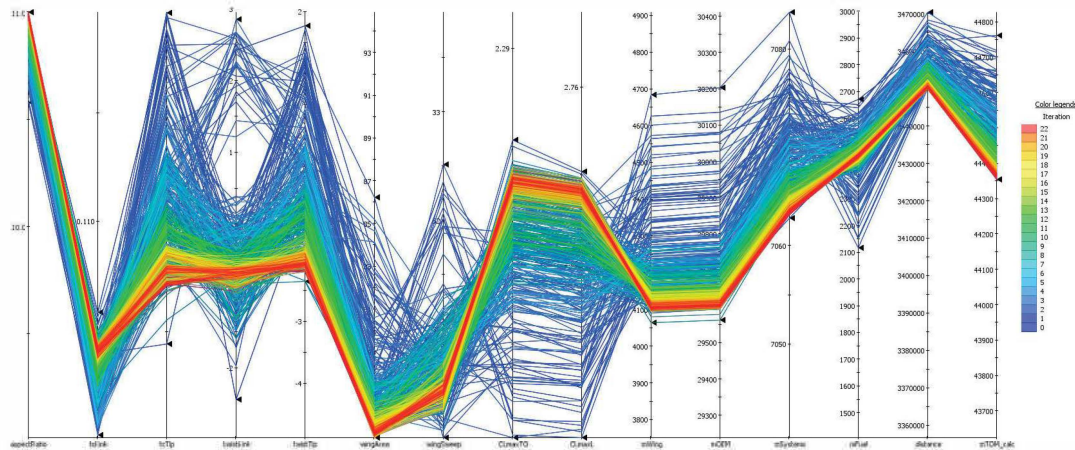


Figure 24. MDA through surrogates, parallel coordinates

	Start	End (983)	Low	High
Inputs				
aspectRatio	10	10.99915	9	11
tcKink	0.11	0.1042	0.1	0.12
tcTip	0.1	0.0971	0.09	0.11
twistKink	0	-0.6882	-3	3
twistTip	-1.5	-2.075	-5	2
wingArea [m^2]	85	75.2221	75	95
wingSweep	32	30.4007	30	34
Outputs				
CLmaxTO	2.2584	2.2234		
CLmaxL	2.7255	2.7021		
mWing [kg]	4330.23	4108.19		
mOEM [kg]	29824.72	29606.31		
mSystems [kg]	7059.62	7063.26		
mFuel [kg]	2956.61	2452.57		
distance [m]	3396172.04	3450220	3450000	
reserveFuelMass [kg]	754.65	796.75		
mTOM [kg]	44281	44355.64		

Table 2. Optimization, initial and final configurations

The optimization has been performed only to test the MDA through surrogates functionality and the achieved results are for demonstration purposes only. Next step will be to evaluate the optimal configuration with the real MDA in order to quantify the error induced by the simplified process. Nevertheless, the target workflow, representative of the DC-1 MDA through the use of surrogate models, was successfully implemented in a PIDO framework, enabling the explorations of new MDO strategies.



6. CONCLUSIONS AND FUTURE DEVELOPMENTS

This paper has presented an innovative approach where a complex workflow, representative of a conventional aircraft MDA, has been successfully simplified and implemented using surrogate models for clusters of disciplines to reduce the computational time. Taking advantage of the improvements brought by the knowledge based architecture, the set-up phase of the process was strongly eased and the clustering of design competences was investigated in a collaborative way involving all tools' specialists. A field of improvement concerns the clustering process which could be partially automated as it is currently an expert-based and manual process.

During the operational phase, the features implemented in the collaborative architectures, such as DOE service workflow, enabled a quick execution of all the DOEs for all the clusters, each one being a distributed workflow of partners' design competences. In addition, multiple methods regarding surrogate models (SM) competence were investigated and SM were made available to the partners in different formats, such as executable or remote access through a PIDO framework. Eventually, the target workflow, coupling the surrogate models of the clusters, was successfully implemented in Optimus and provided encouraging preliminary results, thus demonstrating the success of the proposed approach.

The next step will be to use the MDA workflow in the two identified scenarios to investigate classical and innovative MDO formulations, potentially with an increase of complexity (adding local variables in some clusters for instance). In addition, this use case will also be used as a mock-up for testing the automation of the execution phase of an MDO system, mainly the execution of the DOE strategy, enabled by KADMOS, through the CMDOWS (Common MDO Workflow Schema) [25] format. Last but not least, the use of surrogate models for clusters of design competences has proven to be a feasible and effective approach and will also be applied to novel configurations in the frame of Design Campaign 3 of AGILE.

Another main consideration concerns the propagation of modeling uncertainties induced by the errors associated to the use of surrogate models. Surrogate model must provide mean value of the output of the discipline as well as an uncertainty on this mean value. Solving the MDA only based on surrogate models implies that the quantity of interest is computed approximately (due to the uncertainty associated to each surrogate). Taking into account the uncertainty associated to each surrogate in the resolution of the MDA implies the resolution of a stochastic non linear system. In order to solve this system an approach based on semi-intrusive polynomial chaos expansion has been proposed in [18] and will be applied in this MDA workflow in order to enrich the surrogate models in area of interest for the objective function.

Significant reduction in aircraft development costs and time to market is essential to achieve cheaper and greener aircraft solutions. The AGILE project is developing the next generation of aircraft Multidisciplinary Design and Optimization processes, focusing on the reduction of the aircraft development time at the early stages of the design process. Many challenges have been identified to ease the optimization of complex workflows in the context of multi-level and multi-partner collaborative engineering projects that characterize aircraft design. However, it can be concluded that the technical solutions developed by AGILE, by smart combination of knowledge based technologies, IT solutions, and MDO strategies provide a fruitful approach for handling those challenges and therefore contribute to a shorter aircraft development time.

ACKNOWLEDGMENTS

The research presented in this paper has been performed in the framework of the AGILE project (Aircraft 3rd Generation MDO for Innovative Collaboration of Heterogeneous Teams of Experts) and has received funding from the European Union Horizon 2020 Programme (H2020-MG-2014-2015) under grant agreement n° 636202. The authors are grateful to the partners of the AGILE consortium for their contribution and feedback.

OPEN-SOURCE REFERENCES

KADMOS	https://bitbucket.org/imcovangent/kadmoss
RCE	http://rcenvironment.de
CPACS	http://cpacs.de/
CMDOWS repository	http://cmdows-repo.agile-project.eu
CMDOWS visualization interface	http://cmdows.agile-project.eu



REFERENCES

1. "Report from ICAS workshop on complex systems integration in aeronautics," *30th ICAS Congress*, Daejeon, Korea, September 2016.
2. "Co-Evolution of Aeronautical Complex System & Complex System Engineering," *ICAS Workshop - Complex Systems Integration in Aeronautics*, Krakow, 2015.
3. "AGILE EU Project portal," <http://www.agile-project.eu>.
4. Ciampa, P. D. and Nagel, B., "Towards the 3rd generation MDO collaboration Environment," *30th ICAS Congress*, Daejeon, Korea, September 2016.
5. Ciampa, P. D. and Nagel, B., "The AGILE Paradigm: the next generation of collaborative MDO," *18th AIAA/ISSMO Multidisciplinary Analysis and Optimization Conference*, Denver, USA, June 2017.
6. "CPACS – A Common Language for Aircraft Design," <http://www.cpacs.de>, accessed 28 August 2017.
7. Bartoli, N., Lefebvre, T., Dubreuil, S., Olivanti, R., Bons, N., Martins, J. R. R. A., Bouhlel, M.-A., and Morlier, J., "An adaptive optimization strategy based on mixture of experts for wing aerodynamic design optimization," *18th AIAA/ISSMO Multidisciplinary Analysis and Optimization Conference*, Denver, USA, June 2017.
8. Martins, J. R. R. A. and Lambe, A. B., "Multidisciplinary design optimization: A survey of architectures," *AIAA Journal*, Vol. 59, No. 9, 2013, pp. 2049–2075.
9. Tosserams, S. and Etman, L., Papalambors, P., and Rooda, J., "An augmented lagrangian relaxation for analytical target cascading," *Structural and Multidisciplinary Optimization*, Vol. 31, No. 3, 2006, pp. 113–122.
10. Lefebvre, T., Bartoli, N., Dubreuil, S., Panzeri, M., Lombardi, R., Vecchia, P. D., Nicolosi, F., Ciampa, P. D., Anisimov, K., and Savelyev, A., "Methodological enhancements in MDO process investigated in the AGILE European project," *18th AIAA/ISSMO Multidisciplinary Analysis and Optimization Conference*, Denver, USA, June 2017.
11. Della Vecchia, P., Stingo, L., Corcione, S., Ciliberti, D., Nicolosi, F., and De Marco, A., "Game theory and evolutionary algorithms applied to MDO in the AGILE European project," *AIAA AVIATION*, Denver, USA, June 2017.
12. Daoud, F., Maierl, R., Ciampa, P. D., and Gu, X., "Aeroelastic Shape and Sizing Optimization of Aircraft Products supported by AGILE Design Paradigm," *18th AIAA/ISSMO Multidisciplinary Analysis and Optimization Conference*, Denver, USA, June 2017.
13. Lammen, W., de Wit, B., Vankan, J., Timmermans, H., van der Laan, T., and Ciampa, P. D., "Collaborative Design of Aircraft Systems - Multi-Level Optimization of an Aircraft Rudder," *6th CEAS Aerospace Europe Conference*, October 2017.
14. Prakasha, P. S., Mirzoyana, A., and Ciampa, P. D., "Collaborative System of Systems Multidisciplinary Design Optimization for Civil Aircraft: AGILE EU project," *18th AIAA/ISSMO Multidisciplinary Analysis and Optimization Conference*, Denver, USA, June 2017.
15. Ciampa, P. D., Moerland, E., Seider, D., Baalbergen, E., Lombardi, R., and D'Ippolito, R., "A Collaborative Architecture supporting AGILE Design of Complex Aeronautics Products," *18th AIAA/ISSMO Multidisciplinary Analysis and Optimization Conference*, Denver, USA, June 2017.
16. van Gent, I., Ciampa, P. D., Aigner, B., Jepsen, J., Rocca, G. L., and Schut, J., "Knowledge architecture supporting collaborative MDO in the AGILE paradigm," *18th AIAA/ISSMO Multidisciplinary Analysis and Optimization Conference*, Denver, USA, June 2017.
17. Zhang, M., Jungo, A., and Bartoli, N., "Disciplinary Data Fusion for Multi-Fidelity Aerodynamic Application," *6th CEAS Aerospace Europe Conference*, paper no.953, Bucharest, Romania, October 2017.
18. Dubreuil, S., Bartoli, N., Gogu, C., and Lefebvre, T., "Propagation of modeling uncertainty by polynomial chaos expansion in multidisciplinary analysis," *Journal of Mechanical Design*, Vol. 138, No. 11, 2016, pp. 111411.
19. "DLR, German Aerospace Center," <https://rcenvironment.de/>.
20. "Noesis Solutions, Optimus Rev 10.19 - Users Manual," 2017.
21. Baalbergen, E., Kos, J., Louriou, C., Campguilhem, C., and Barron, J., "Streamlining cross-organisation product design in aeronautics," *Proceedings of the Institution of Mechanical Engineers, Part G: Journal of Aerospace Engineering*, 2016, pp. 0954410017716480.
22. Baalbergen, E., Moerland, E., Lammen, W., and Ciampa, P. D., "Methods to Support Efficient Collaboration for Competitive Aircraft Design," *6th CEAS Aerospace Europe Conference*, October 2017.
23. van Gent, I., La Rocca, G., and Veldhuis, L. L. M., "Composing MDAO symphonies: graph-based generation and manipulation of large multidisciplinary systems," *18th AIAA/ISSMO Multidisciplinary Analysis and Optimization Conference*, Denver, USA, June 2017.



24. Aigner, B., van Gent, I., La Rocca, G., Stumpf, E., and Veldhuis, L. L. M., "Graph-based algorithms and data-driven documents for formulation and visualization of large MDO systems," *6th CEAS Air and Space Conference*, 2017.
25. van Gent, I., La Rocca, G., and Hoogreef, M. F. M., "CMDOWS: A Proposed New Standard to Store and Exchange MDO Systems," *6th CEAS Air and Space Conference*, 2017.
26. Lambe, A. B. and Martins, J. R., "Extensions to the design structure matrix for the description of multidisciplinary design, analysis, and optimization processes," *Structural and Multidisciplinary Optimization*, Vol. 46, No. 2, 2012, pp. 273–284.
27. Vankan, J. and Lammen W.F. and Maas, R., "Meta-modeling and multi-objective optimization in aircraft Design," *Advances in collaborative civil aeronautical multidisciplinary design optimization. Progress in Astronautics and Aeronautics*, pp. 155–192.
28. Bartoli, N., Kurek, I., Lafage, R., Lefebvre, T., Priem, R., Bouhrel, M.-A., Morlier, J., Stilz, V., and Regis, R., "Improvement of efficient global optimization with mixture of experts: methodology developments and preliminary results in aircraft wing design," *17th AIAA/ISSMO Multidisciplinary Analysis and Optimization Conference*, Washington D.C., USA, June 2016.
29. Bettebghor, D., Bartoli, N., Grihon, S., Morlier, J., and Samuelides, M., "Surrogate modeling approximation using a mixture of experts based on EM joint estimation," *Structural and Multidisciplinary Optimization*, Vol. 43, No. 2, 2011, pp. 243–259, 10.1007/s00158-010-0554-2.
30. Liem, R. P., Mader, C. A., and Martins, J. R. R. A., "Surrogate Models and Mixtures of Experts in Aerodynamic Performance Prediction for Mission Analysis," *Aerospace Science and Technology*, Vol. 43, 2015, pp. 126–151.
31. Forrester, A., Keane, A., et al., *Engineering design via surrogate modelling: a practical guide*, John Wiley & Sons, 2008.
32. Lophaven, N., Nielsen, H., and Sondergaard, J., "DACE: A Matlab Kriging Toolbox, Version 2.0, August 1, 2002," *Technical University of Denmark*, 2000.
33. Volkwein, S., "Model reduction using proper orthogonal decomposition," *Lecture Notes, Institute of Mathematics and Scientific Computing, University of Graz*. see <http://www.uni-graz.at/imawww/volkwein/POD.pdf>, 2011.

Robust optimization of a rudder hinge system taking into account uncertainty in Airframe parameters

*Ton van der Laan,
GKN Fokker Aerostructures
Knowledge based engineering specialist
Industrieweg 4, 3351 LB Papendrecht, The Netherlands
Ton.vanderlaan@fokker.com*

*Luc Hootsmans
GKN Fokker Aerostructures
Senior design specialist*

*Marco Panzeri
Noesis Solutions N.V.
Gaston Geenslaan 11, 3001 Leuven, Belgium*

*Roberto d'Ippolito
NOESIS Solutions N.V.*

ABSTRACT

For a tier 1 supplier of aircraft components it is essential to develop components that can absorb changes in its requirements without having a negative influence on the supplier's profit margin. In order to achieve this, the effect of design changes needs to be investigated early in the design process. To realize this vision the design process must be highly automated and incorporate solution finding techniques such as Design Of Experiments (DOE's) and optimizations.

In this paper a framework is presented that estimates the weight and cost of an aircraft rudder hinge system. This framework has been researched and developed within the context of the H2020 AGILE project to support 3rd generation multidisciplinary design optimization teams. The process is fully automated and packaged in the Process Integration and Design Optimization (PIDO) tool Optimus. This packaging allows the generation of DOE data with which robustness analyses can be performed. The robustness analysis presented in this paper is the response of the rudder hinge system to a change in design loads. It is shown that the best design found in a deterministic approach, so looking at one design point only, is not the best design available from a robustness point of view. In this way the value of robustness analysis in the design process of aircraft components is demonstrated.

KEYWORDS *Multi-Level Optimization, Collaborative Design, Aircraft Rudder, Knowledge Based Engineering, Uncertainty Quantification*

Aircraft Normal Modes...Friend or Foe? An Airbus Answer

Mercedes Oliver Herrero

Airbus Defence and Space / TEAGD Aeroelasticity and Structural Dynamics

John Lennon s/n, 28906 Getafe, Spain

mercedes.oliver-herrero@airbus.com

Félix Arévalo Lozano

Airbus Defence and Space / TEAGD Aeroelasticity and Structural Dynamics

Héctor Climent Máñez

Airbus Defence and Space / TEAGD Aeroelasticity and Structural Dynamics

ABSTRACT

Dynamic loads and Aeroelasticity have played a relevant role in the history of aviation and continue being two of the most important aspects in the aircrafts design and certification process. Dynamic Loads (Gust/Turbulence, Dynamic Landing, Taxiing, etc.) are often amongst the sizing critical load cases in many aircraft components, while Aeroelasticity determines not only the lifting and control surfaces design but also the maintainability requirements after the aircraft entry into service. The classical approach to solve response-type (Loads) or instability (Aeroelasticity) problems relies on considering that the aircraft structure flexible deformation can be written as a combination of the zero-damped structure normal modes. This paper aims to show the normal modes relevance in the solution of Structural Dynamics and Aeroelastic problems in general and the Airbus civil and military aircrafts specificities when analysed from a normal modes point of view.

KEYWORDS: *Structural Dynamics, Aeroelasticity, Normal modes, Dynamic Loads, Flutter*

NOMENCLATURE

A/C	Aircraft	M&L	Medium & Light
CPU	Central Processing Unit	MLG	Main Landing Gear
DTG	Discrete Tuned Gust	MRTT	Multi Role Tanker Transport
EMS	Engine Mounting System	MTOW	Maximum Take-off Weight
FCL	Flight Control Laws	NLG	Nose Landing Gear
FEM	Finite Element Method	OWE	Operational Weight Empty
FVT	Flight Vibration Test	PSD	Power Spectral Density
GVT	Ground Vibration Test	R/H	Right-hand
HTP	Horizontal Tailplane	RMS	Root mean square
L/H	Left-hand	SD&A	Structural Dynamics and Aeroelasticity
LG	Landing Gear	VTP	Vertical Tailplane

1 INTRODUCTION

The dynamic loads and aeroelasticity analyses performed for the aircraft feasibility, design, checkstress and certification phases are based on aircraft structure dynamic equations. The dynamic equations of a system can be stated in direct form, using all the degrees of freedom of the system, or in modal approach, which is based on using information of the system response in a free vibration condition. The free vibration condition assumes that the structure is not subjected to any external excitation, the structural damping is negligible, and therefore its motion occurs only from the initial conditions of displacement and velocity. This condition is relevant because the analysis of the structure response in free motion provides substantive information regarding the dynamic properties of the structure. These properties are the natural frequencies and the corresponding vibration mode shapes, what we call the structure normal modes.

The use of normal modes base for the structure displacement linear decomposition shows to be the most accurate (compared with other approximate methods such as Rayleigh-Ritz).

On the other hand, the nature of structures normal modes make them more than a mathematical stratagem used in dynamic loads and aeroelasticity analyses: The structure displacement when harmonically excited in one of its natural resonances (a normal mode frequency), other than damp, tends to amplify. Therefore the structure deformation shape will mainly be determined by the excitation normal modes contribution.

Understanding the aircraft normal modes is, therefore, fundamental to identify the root causes of a certain dynamic response or stability phenomenon. The normal modes frequency and shape are determined by the stiffness and inertia distributions, which, in turn, are directly correlated with the aircraft configuration (e.g. low, mid, or high wing), size, design weights, and payload/fuel distribution, or the control surfaces actuators' stiffness.

2 STRUCTURAL DYNAMICS AND AEROELASTICITY IN THE A/C DESIGN AND CERTIFICATION PROCESS

2.1 Structural Dynamics and Aeroelasticity History

Throughout the history of aviation and from its very beginning, Structural Dynamics and Aeroelasticity have dramatically fostered its progress and conditioned the aircrafts conception and design. The following list shows the earliest and the most relevant events, which may be considered milestones of the SD&A history:

- Divergence, *structure collapse because of high external aerodynamic loading*:
 8/12/1903 Samuel P. Langley's *Aerodrome*
 24/01/1917 Albatross DIII
 19/08/1918 Fokker D.VIII
- Control reversal, *the control surface rotation (e.g. aileron) effect is nullified by the torsion of the fixed part (wing)*:
 1940 Mitsubishi A6M "Zero"
- Flutter, *dynamic instability caused by the coalescence of normal modes*:
 1916 Handley Page 0-400 Bomber
 1917 De Havilland DH-9
 1920 Van Berkel W.B. Monoplane
 1931 Gee Bee racer
 1939 Heinkel He 177
 1943 Gloster Meteor
 1961 Convair 990
 1970's-1980's Beech Bonanza Model 35 (likely)
 1997 F117 Stealth
- Whirl Flutter, *propeller instability*:
 1959-1960 Lockheed Electra
- Aeroservoelasticity: *coupling of flexible modes with control surfaces rotation commanded by FCL*:
 A3J-1 "Vigilante"
- Dynamic response of the flexible system under external forces:
 Dynamic Landing: 1940 Consolidated B-24 Liberator
 Taxi: 1989 Fokker 100
 Gust & Turbulence:
 1963 B-52 Stratofortress
 1966 Boeing 707 at Mount Fuji
 1982/1990 de Havilland Canada DH-6 Twin-Otter
- Buffet, *dynamic response under external wake excitation*:
 1930 Junkers F.13
 1980's F18
- Ditching, *aircraft forces in a controlled landing in water*:
 1909. Antoinette IV monoplane

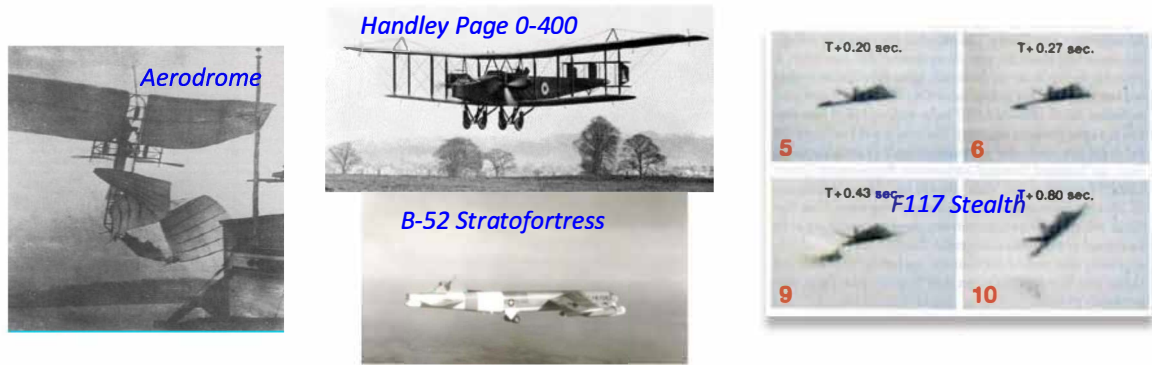


Figure 1: Examples of relevant aeroelastic and dynamic loads events

Some authors point that Aeroelasticity-related effects are responsible for delaying the first controlled and sustained flight, which could have been reached by Langley on December 8, 1903 if the Divergence instability had not appeared. It is somehow exaggerated, but the real fact is that the Wright brothers had success some days later (December 17, 1903) by avoiding any aeroelastic instability (basically Divergence and Flutter) and controlling the aircraft using the torsion flexibility of the wing, both aspects related to the Aeroelasticity.

Aeroelasticity plays therefore a crucial role for the successful design of any aircraft and nowadays the state of the art has allowed not only to mitigate the negative effects of the flexibility but also to take advantage of it: aeroservoelastic active control methodology ([1]), aeroelastic tailoring, usage of the wing torsion to control the aircraft (like Wright brothers!), etc.

2.2 Structural Dynamics and Aeroelasticity today

After more than one-hundred years learning from aviation operation and understanding the root causes of accidents, the airworthiness regulations have progressively evolved in order to guarantee aircrafts safety by requesting suitable analyses and tests. In this framework, SD&A plays a fundamental role during all the aircraft life, from the design phase to the entry into service and afterwards.

For current military and civil aircrafts, dynamic loads conditions are among the sizing critical load cases. Figure 2 shows Heavy Military Transport Aircraft components dimensioned by dynamic loads or flutter.

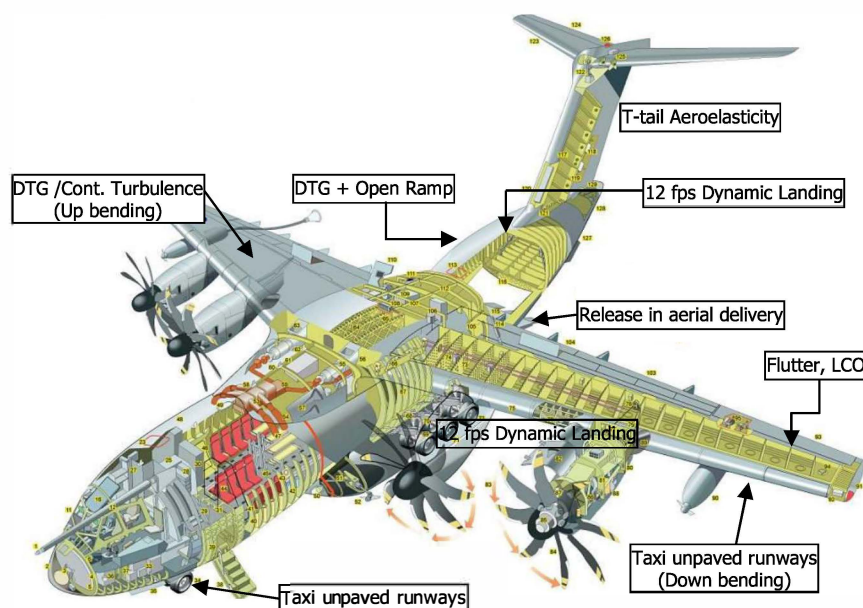


Figure 2: Military transport A/C components dimensioned by dynamic loads or flutter

On the other hand, apart from the implications of aeroelasticity in the structure or control laws design, which may impact directly in the aircraft weight or manoeuvrability, certain requirements to in-service actions, such as maintenance, repairs or painting, have the "Aeroelasticity" stamp.

In the SD&A dartboard shown in Figure 3, when looking at the multiple disciplines involved, the **normal modes** are a common denominator in most of them.

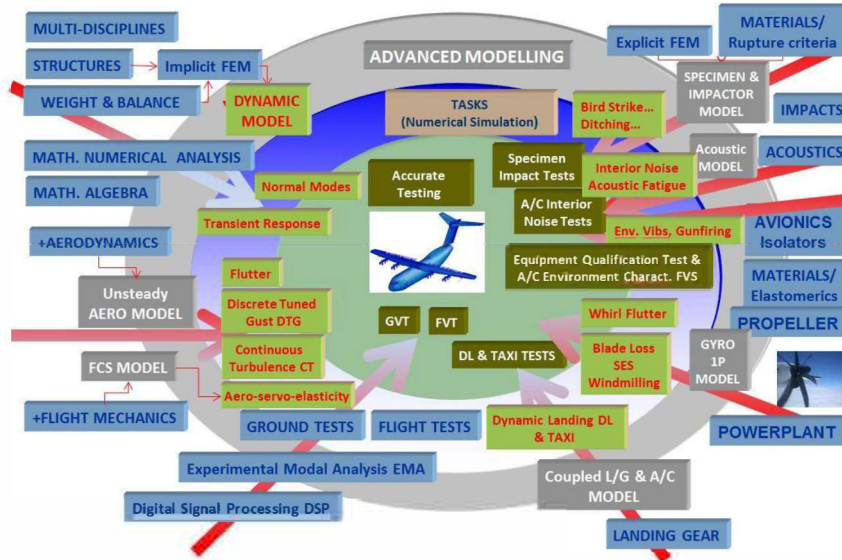


Figure 3: Structural Dynamics and Aeroelasticity dartboard

3 USE OF EIGENVALUES AND EIGENVECTORS TECHNIQUE IN SD&A PROBLEMS SOLUTION

The dynamic equations of a system are detailed into many classical books and, in particular, in aeroelastic-related references as [2] and [3]. These are written as:

$$[M] \cdot \{\ddot{x}\} + [D] \cdot \{\dot{x}\} + [K] \cdot \{x\} = \{P(t)\} \quad (2)$$

where:

[M]: mass matrix
 [D]: damping matrix
 [K]: stiffness matrix
 x: displacement vector
 \dot{x} : velocity vector
 \ddot{x} : acceleration vector
 $\{P(t)\}$: applied load as a function of time

For a free and undamped system, where $[P(t)] = [D] = [0]$, and assuming a harmonic solution,

$$[M] \cdot \{\ddot{x}\} + [K] \cdot \{x\} = \{0\} \rightarrow ([K] - \omega^2[M]) \cdot \{\phi\} = \{0\} \quad (3)$$

where:

ω : eigenfrequency or natural frequency of a free vibrating system
 $\{\phi\}$: eigenvector or modal shape of a free vibrating system

Equation (3), analogue to the eigenvalue equation in linear algebra, has the non-trivial solution ($\{\phi\} \neq \{0\}$):

$$\det([A] - \lambda[I]) = 0 \quad (4)$$

where

$[A] = [K] \cdot [M]^{-1}$: real square matrix
 $\lambda = \omega^2$: eigenvalue
 $\{x\} = \{\phi\}$: eigenvector

The size of equation (2) matrices and vectors when expressed in physical coordinates is the number of all structural degrees of freedom or, in MSC-NASTRAN terms, the g-set size G . For the current structural models size, the degrees of freedom are of the order of magnitude of 10^6 , and equation (2) results to be a 10^6 size coupled equation. In spite of the High Performance Computers availability, this becomes a very costly problem, from the CPU time point of view, especially when facing hundreds of thousands calculations.

By introducing the modal transformation depicted in next equation (5), the G physical coordinates $\{x_G\}$ are substituted by the modal coordinates $\{\xi\}$ with the eigenvectors being the columns of the change of basis matrix $[\phi]$. The matrix $[\phi]$ size is G rows by N columns, being G the number of structural degrees of freedom and N the number of modes.

$$\{x_G\} = [\phi] \cdot \{\xi\} \quad (5)$$

Equation (2), then, becomes:

$$[M_G] \cdot [\phi] \cdot \{\ddot{\xi}\} + [D_G] \cdot [\phi] \cdot \{\dot{\xi}\} + [K_G] \cdot [\phi] \cdot \{\xi\} = [P(t)] \quad (6)$$

Pre-multiplying by $[\phi]^T$ and making additional assumptions regarding the damping matrix (i.e. modal damping, $[D_G]$ is substituted by $[C_G]$),

$$[m] \cdot \{\ddot{\xi}\} + [b] \cdot \{\dot{\xi}\} + [k] \cdot \{\xi\} = [p(t)] \quad (7)$$

where

$$\begin{aligned} [m] &= [\phi]^T \cdot [M_G] \cdot [\phi]; \text{ N x N real square diagonal matrix} \\ [b] &= [\phi]^T \cdot [C_G] \cdot [\phi]; \text{ N x N real square diagonal matrix} \\ [k] &= [\phi]^T \cdot [K_G] \cdot [\phi]; \text{ N x N real square diagonal matrix} \end{aligned}$$

Modal formulation has two advantages: equation (7) is uncoupled and its size is the number of modes, typically of the order of magnitude of 10^2 . Its solution, $\{\xi(t)\}$, can be reverted to the physical coordinates $\{x_G\}$ through (5).

Examples shown in Figure 4 illustrate that few normal modes are enough to compute the aircraft response to transient excitation. It shows a Heavy Military Transport dynamic response to a discrete tuned gust, DTG. Two relevant magnitudes, wing root bending moment for a vertical DTG and VTP root bending moment for a lateral DTG are shown.

Top graphs show the two magnitudes transient response versus time. Mid and bottom graphs show the PSD and Accumulated PSD versus frequency, where it can be observed that all the response is produced at low frequency.

The peak in PSD graphs corresponds to the normal mode which is contributing the most to the response, 1st wing bending (symmetric) for the wing root bending moment and HTP yaw + Fuselage bending (antisymmetric) for the VTP root bending moment. These mode shapes are shown in Figure 5.

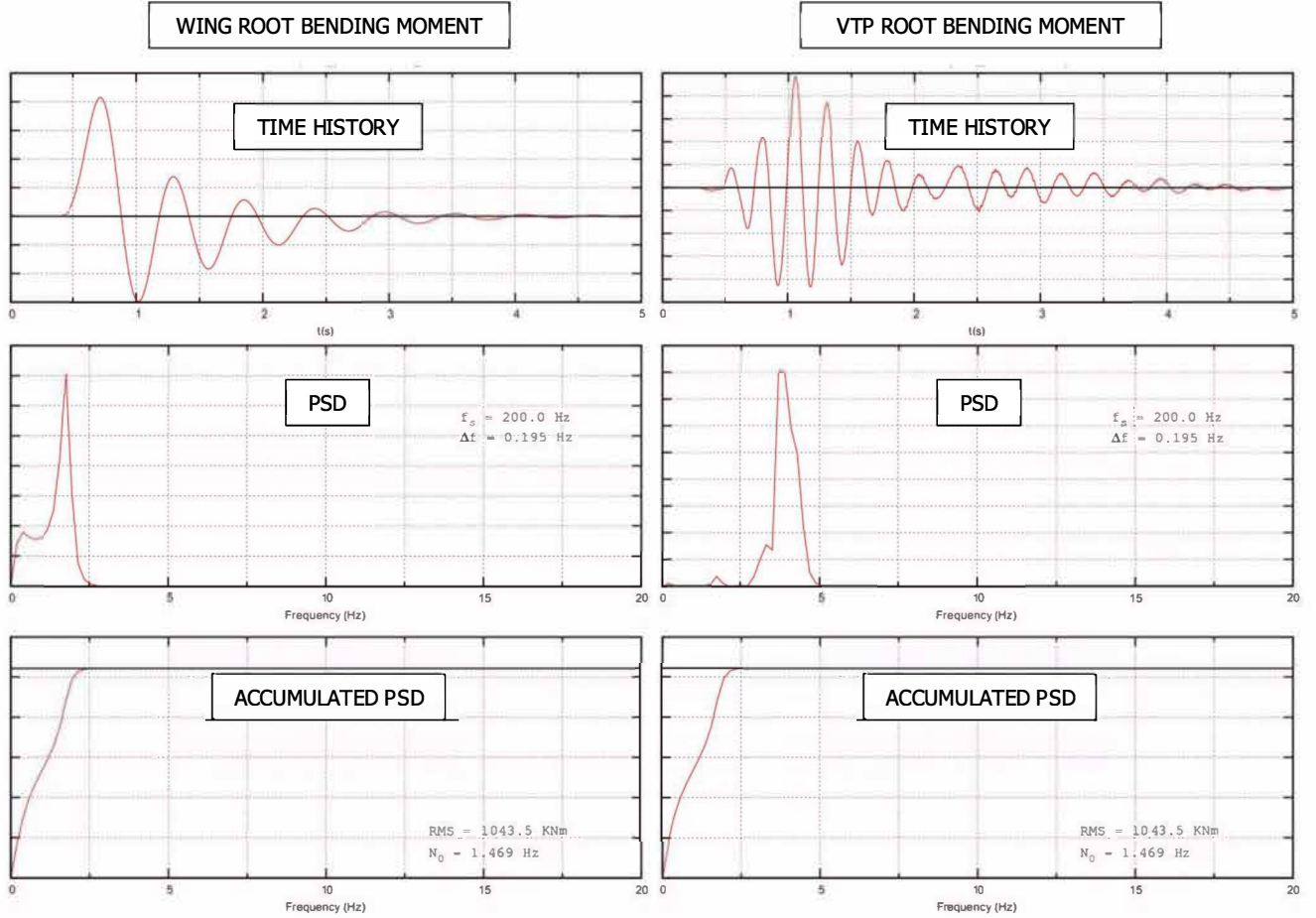


Figure 4: Heavy Military Transport A/C response to a DTG. Time history and PSD

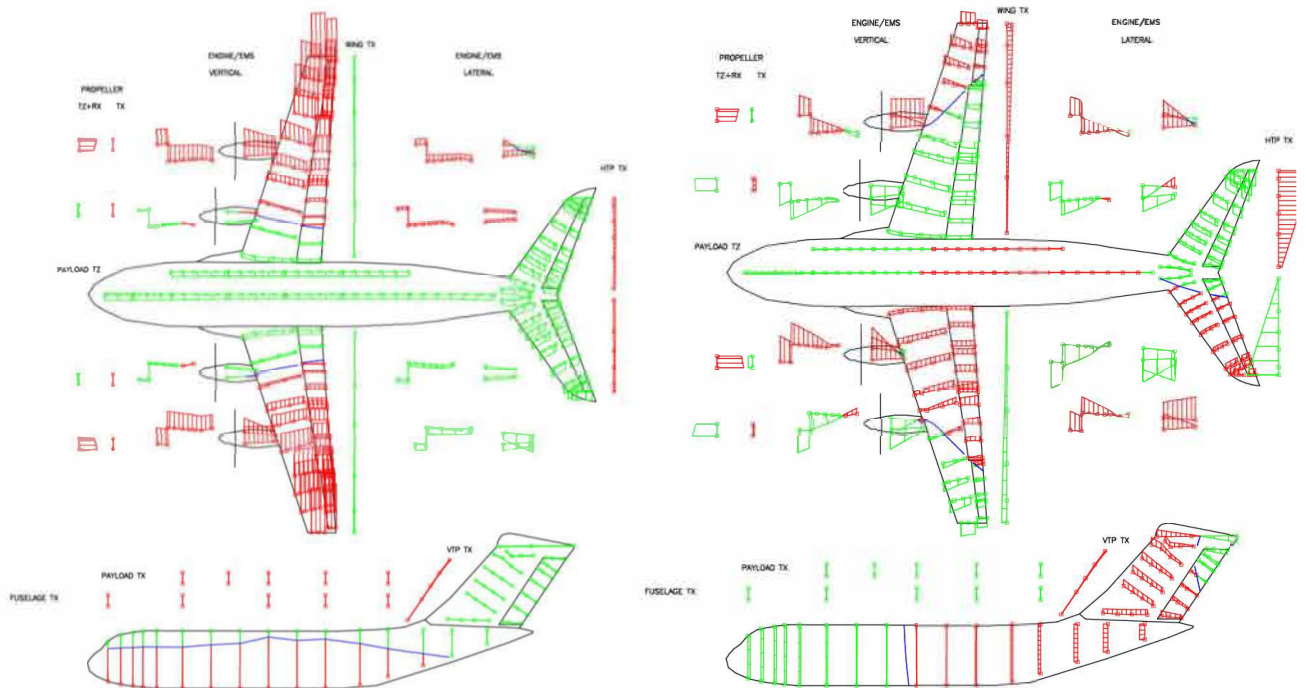


Figure 5: Heavy Military Transport A/C normal mode shape
Left: 1st wing (S) bending (2 nodal lines) – Right: HTP yaw + Fuselage lateral bending

4 AIRCRAFTS NORMAL MODES AND THEIR RELEVANCE

4.1 Aircrafts normal modes shapes and frequencies

The mesh, geometry, connectivities and properties embodied in classical aircraft FEM models make them suitable to represent the dynamic behaviour of the structure at least up to 50. Hz. Nevertheless, commercial and military aircrafts dynamic loads and aeroelasticity events are typically driven only by a reduced set of low-frequency modes, usually with frequencies lower than 20. Hz. Table 1 shows the tanker MRTT first 50 modes identification and, amongst them, the 22 modes which are responsible for most of the dynamic or aeroelastic phenomena.

no.	MODE SHAPE DESCRIPTIONS	S/A
1-6	Rigid body modes	S/A
7	2N Wing Bending	S
8	3N Wing Bending	A
9	Ant. Engine Lateral	A
10	Sym. Engine Lateral	S
11	Rear Fuselage Lateral Bending	A
12	Sym. Engine Vertical	S
13	Ant. Engine Vertical	A
14	2N Fuselage Vertical Bending	S
15	HTP Roll	A
16	4N Wing Bending	S
17	2N Fuselage Lateral Bending	A
18	2N Wing Fore & Aft	S
19	Ant. Engine Roll & Yaw	A
20	Sym. Engine Roll & Yaw	S
21	5N Wing Bending	A
22	2N HTP Bending	S
23	1N VTP Bending	A
24	HTP Yaw (out of phase with fuselage)	A
25	HTP Yaw (in phase with fuselage)	A
26	6N Wing Bending	S
27	Fuselage Torsion	A
28	3N Fuselage Vertical Bending	S
29	Ant. Wing torsion	A
30	Sym. Wing torsion	S
31	2N VTP Bending	A
32	7N Wing Bending	A
33	Sym. Winglet Bending	S
34	8N Wing Bending	S
35	FRU Lateral	A
36	VTP Fore & Aft	S
37	Sym. HTP Fore & Aft	S
38	Ant. Pod Lateral	A
39	Rudder rotation	A
40	Sym. Pod Lateral	S
41	HTP torsion	A
42	Ant. Winglet Bending	A
43	Sym. Elevator rotation	S
44	Ant. Elevator rotation	A
45	Sym. Winglet Bending	S
46	VTP and Rudder Tip Bending	A
47	Ant. Pod Yaw	A
48	Sym. Pod Yaw	S
49	Ant. Aileron rotation	A
50	Sym. Aileron rotation	S

relevant



no.	MODE SHAPE DESCRIPTIONS	S/A
7	2N Wing Bending	S
8	3N Wing Bending	A
11	Rear Fuselage Lateral Bending	A
14	2N Fuselage Vertical Bending	S
16	4N Wing Bending	S
17	2N Fuselage Lateral Bending	A
18	2N Wing Fore & Aft	S
21	5N Wing Bending	A
22	2N HTP Bending	S
23	1N VTP Bending	A
26	6N Wing Bending	S
28	3N Fuselage Vertical Bending	S
29	Ant. Wing torsion	A
30	Sym. Wing torsion	S
32	7N Wing Bending	A
37	Sym. HTP Fore & Aft	S
39	Rudder rotation	A
41	HTP torsion	A
43	Sym. Elevator rotation	S
44	Ant. Elevator rotation	A
49	Ant. Aileron rotation	A
50	Sym. Aileron rotation	S

< 20Hz

Table 1 Tanker A/C first fifty normal modes and relevant modes selection

The typical normal modes shapes representations are 2D views, showing the nodal lines and projecting the relevant components displacements outside of the A/C shape, or 3D views, more intuitive and easy to understand but with the drawback that some details may be missed.

Figure 6 shows the MRTT 1st wing symmetric bending and Figure 7 shows the MRTT Aileron antisymmetric rotation. The first is, probably, the most important mode for dynamic loads, contributing to the response to Dynamic Landing, Taxi and Turbulence, which are often dimensioning the wing. The second mode is one of those involved in the Aeroelastic dynamic instabilities as lifting and control surfaces flutter mechanisms.

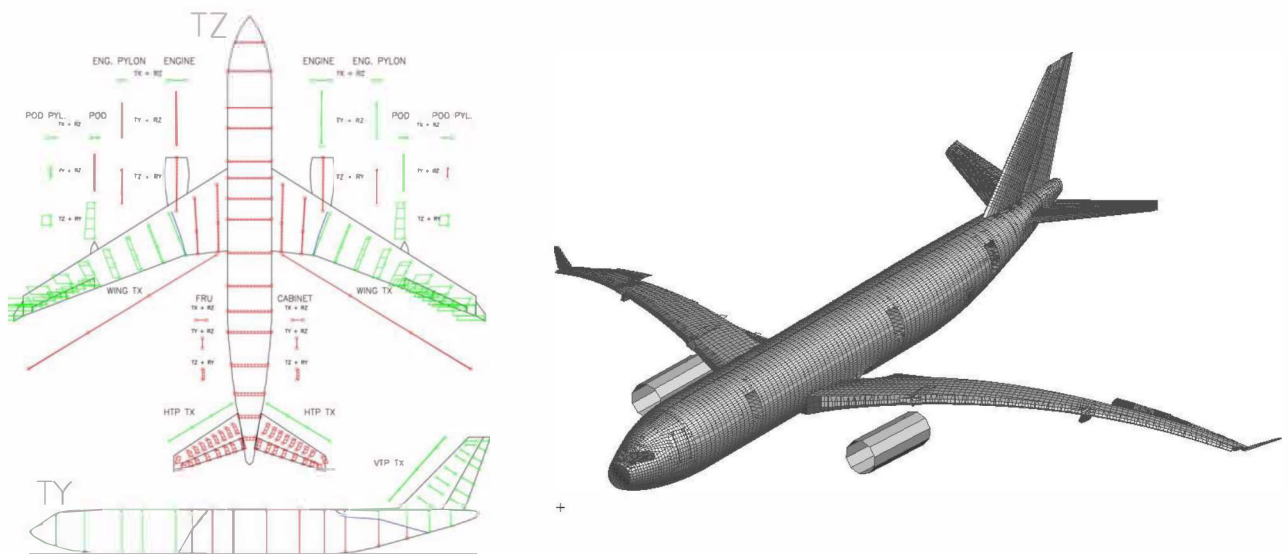


Figure 6: Tanker A/C normal modes. 1st wing (S) bending (2 nodal lines)

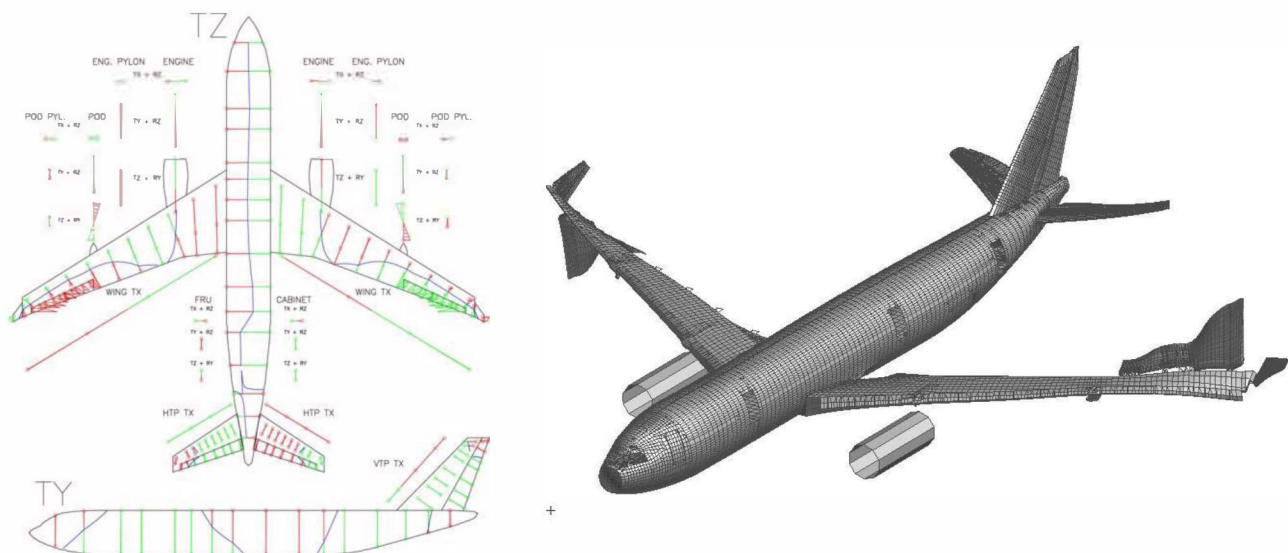


Figure 7: Tanker A/C normal modes. Aileron (A) rotation

4.2 Aircraft normal modes relevant for Dynamic Loads

Some aircraft scenarios provoke transient excitations:

- On ground: dynamic landing, taxi, nose wheel imbalance, etc.
- In flight: discrete tuned gust, continuous turbulence, buffet, etc.

With the exception of buffet, which may exhibit mid-high frequency contents, the rest of dynamic loads scenarios excitations have a frequency contents that rarely exceeds 10-15 Hz. Therefore, only the aircraft lower frequency modes will be excited by these transient loads. Amongst the low frequency modes, those contributing the most to the dynamic loads are:

- 1st wing bending
- 1st wing torsion
- 1st Horizontal Tailplane bending
- 1st Vertical Tailplane bending
- 1st fuselage bending

How are these modes? Where are their natural frequencies?

As a general principle it can be stated that the heavier and the more flexible aircrafts are, the lower normal modes frequencies they have. But there are other characteristics, such as wing sweep, span, engine location or tail position which affect the normal modes frequencies.

This section is a compilation of the typical aircrafts families' most relevant normal modes frequencies, emphasizing differences and similarities of the different aircrafts types: Commercial narrow body and wide body, Military Transport Light to Heavy, Fighter or Trainer. In all the figures, the frequency in Hz is represented versus the Maximum Take-off Weight (MTOW) in tonnes. For each aircraft type or family, the vertical bars representing the frequency copes with the different mass status (payload/fuel distribution), from OWE to MTOW.

Figure 8 shows the 1st wing bending modes for the different aircrafts families. In general, the lighter the aircraft, the higher the frequency; Fighter delta wings (top graph) have higher bending frequencies than M&L aircrafts with similar MTOW (centre graph), and straight wing frequencies (centre graph), are higher than rearward-swept wings ones (bottom graph). The fuel contents in the wing or the fighter underwing stores make the frequencies to decrease.

The wing torsion is less affected by the wing fuel contents, as it can be seen in Figure 9. Low-weight and straight-wings aircrafts are usually stiffer in torsion, thus having higher frequencies. The Fighter (top graph) is a particular case in which wing torsion frequency has a big variation due to its delta wing and wide variety of underwing external stores.

Horizontal and vertical tails bending modes behaviour are similar to the wing ones: the heavier the aircraft, the large and more flexible the tails and therefore, the lower the frequencies. Figure 10 and Figure 11 show two particularities:

- For commercial aircrafts (Figure 10 bottom graph) trimmed with HTP fuel tanks, the HTP bending frequency shows a range of variation. This variation is associated to the different fuel contents.
- The Heavy Transport with T-tail has much lower VTP bending frequency than the similar size aircrafts with standard tail (Figure 11 mid and bottom graphs).

As shown in Figure 12, behaviour of all aircrafts in terms of fuselage vertical bending is similar to the one observed in wing and HTP components: small aircrafts are stiffer, with higher frequencies, while large commercial ones are more flexible, with lower frequencies. Contrary to what could be expected, bottom graph heaviest wide body aircraft has higher frequency than the trend shown by the rest of wide body aircrafts, due to its relatively shorter length and larger cross-section for its double deck.

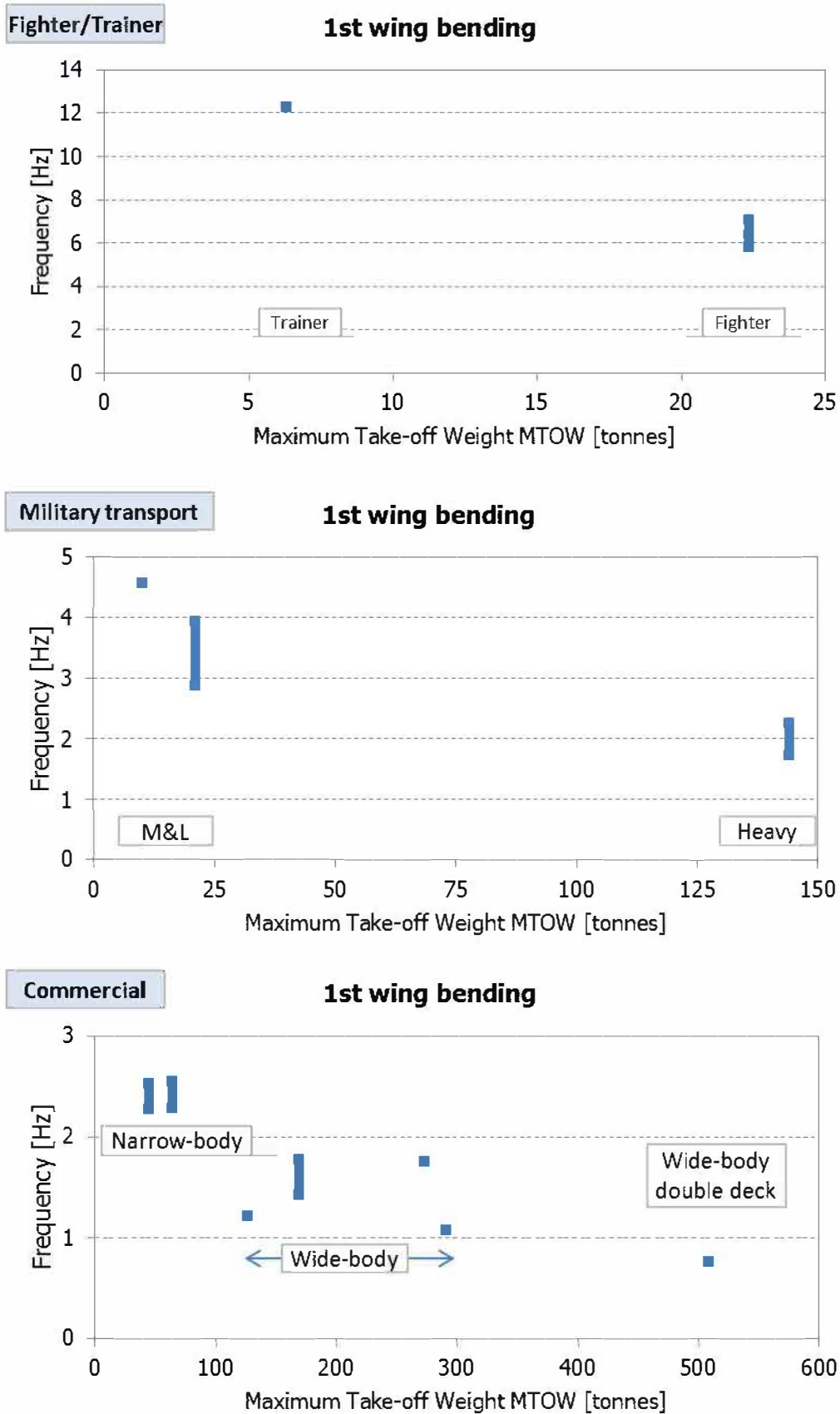


Figure 8: 1st wing bending normal mode frequency vs MTOW

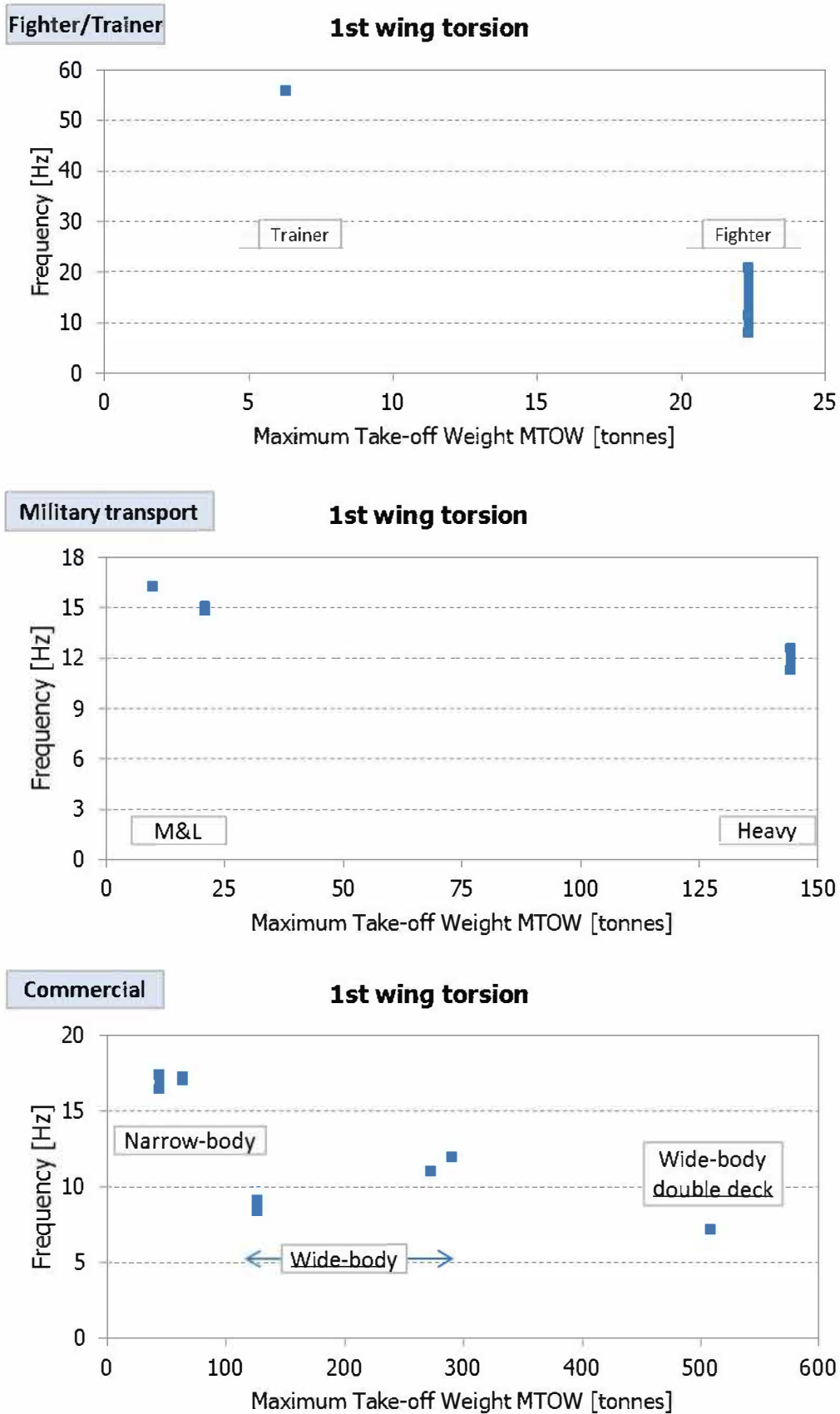


Figure 9: 1st wing torsion normal mode frequency vs MTOW

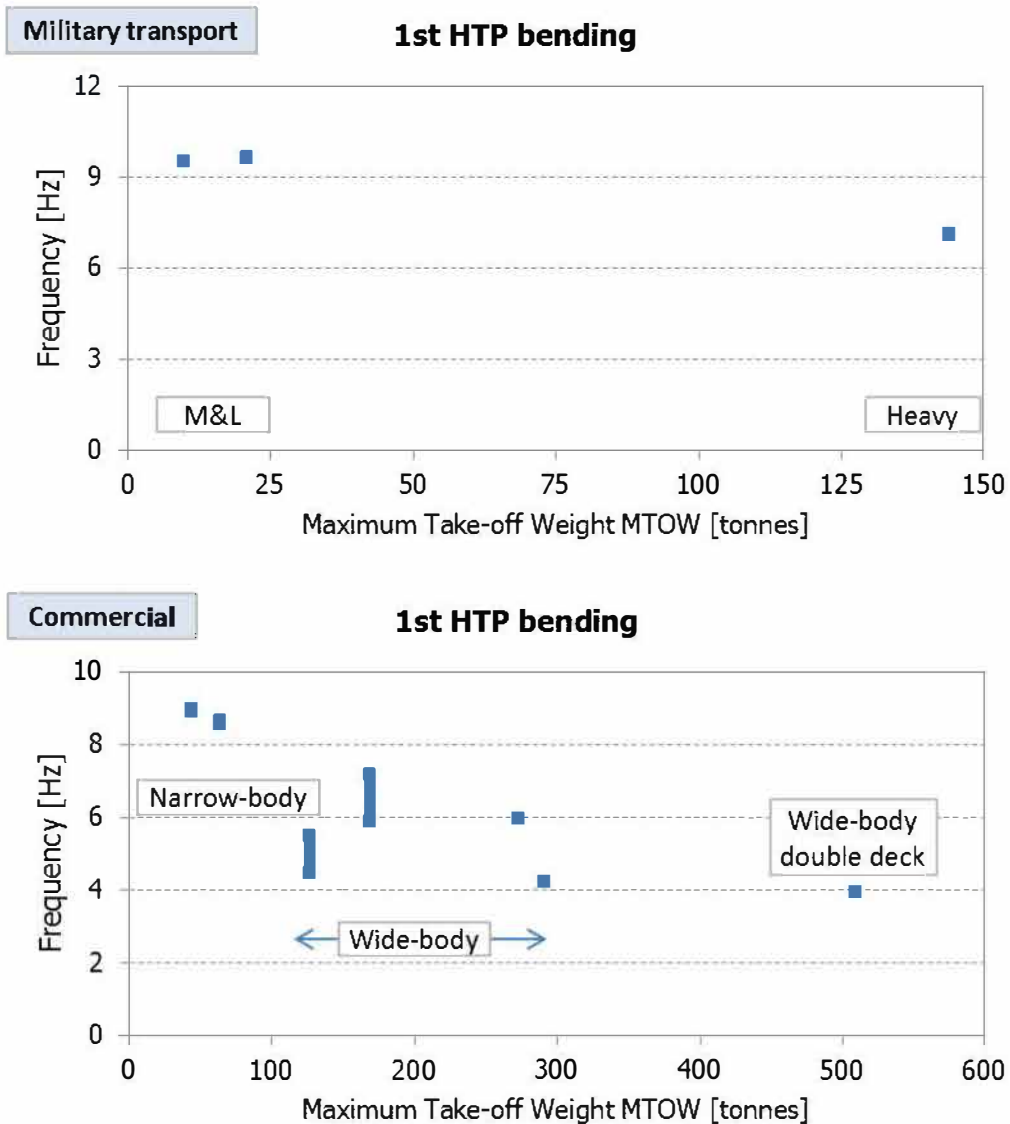


Figure 10: 1st HTP bending normal mode frequency vs MTOW

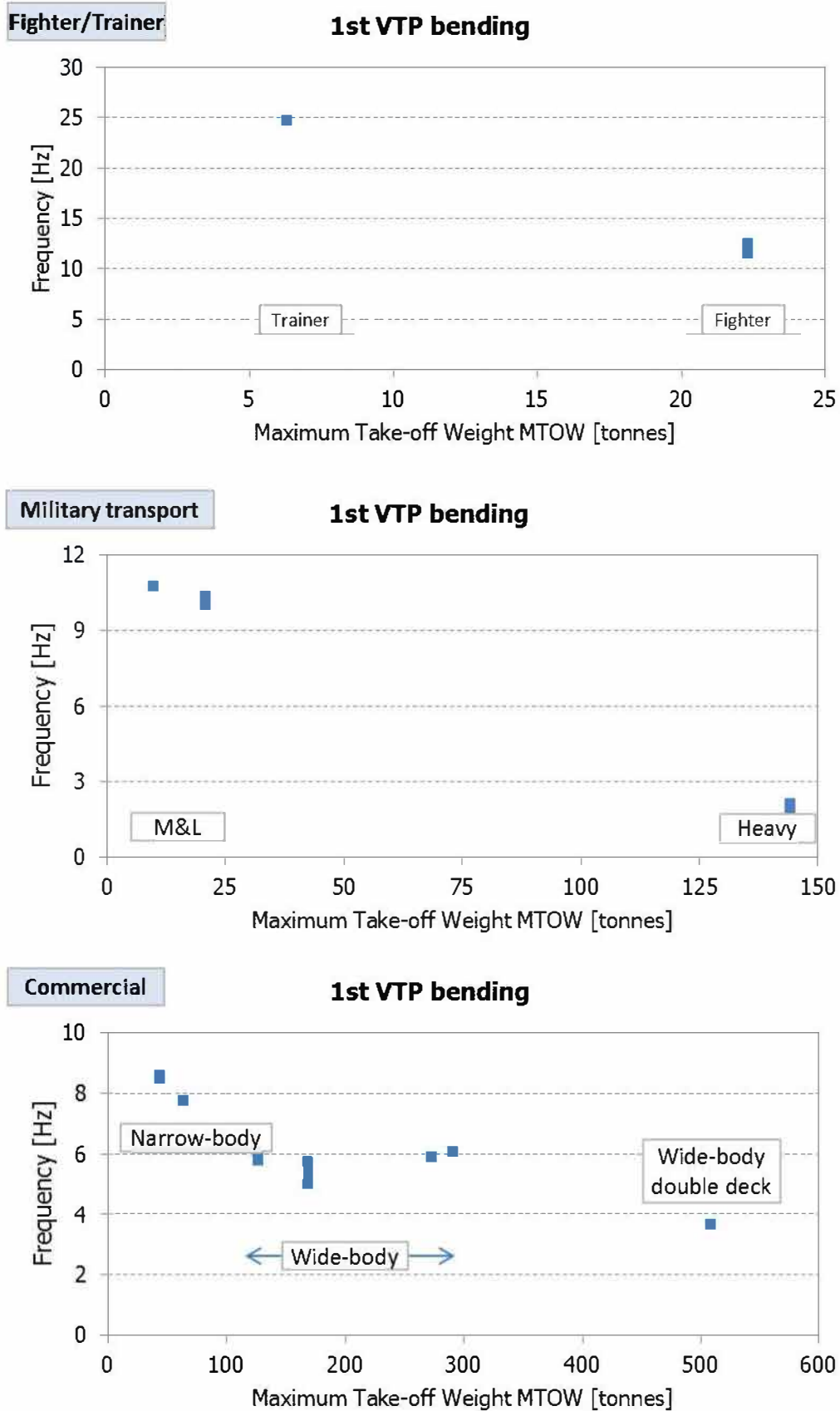


Figure 11: 1st VTP bending normal mode frequency vs MTOW

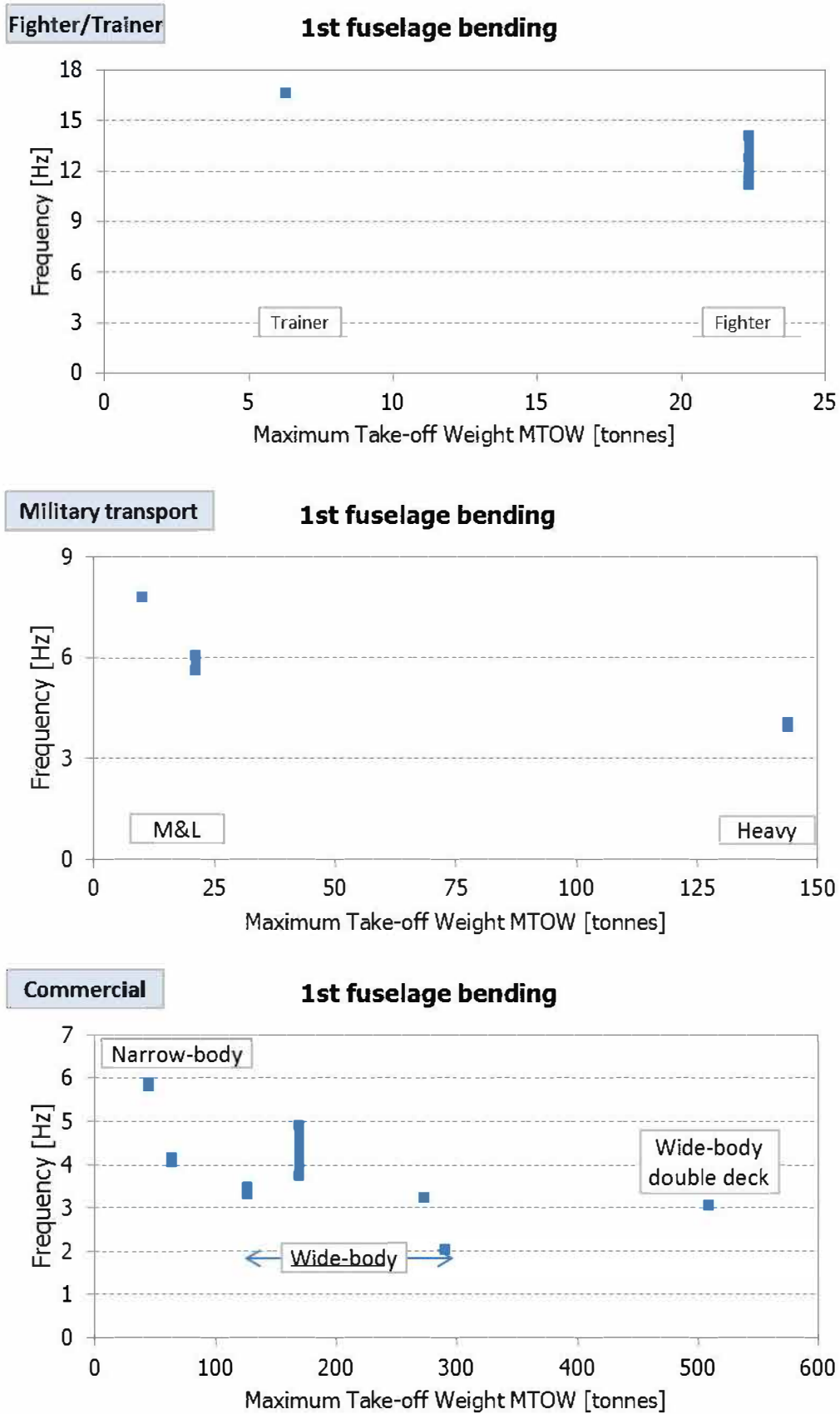


Figure 12: 1st fuselage bending normal mode frequency vs MTOW

4.3 Additional aircrafts normal modes relevant for Aeroelasticity

In addition to the low frequency modes shown in previous section, there is a group of modes also relevant for aeroelasticity: the control surface rotation modes.

Basically, control surfaces may be actuated in two ways:

1. Manual controls, i.e., direct wires between the control column in the cockpit and the control surface.
2. Controls with actuators.

For manual controls, the control surface rotation mode frequency is roughly zero Hz; friction makes this frequency to be slightly above zero.

For controls with actuators, the control surface rotation mode frequency lies in the range 10 to 20 Hz, depending mainly on the control surface size.

Figure 13 shows the effect of the aircraft controls type on the control surfaces rotation frequency for a wide variety of military and commercial aircrafts.

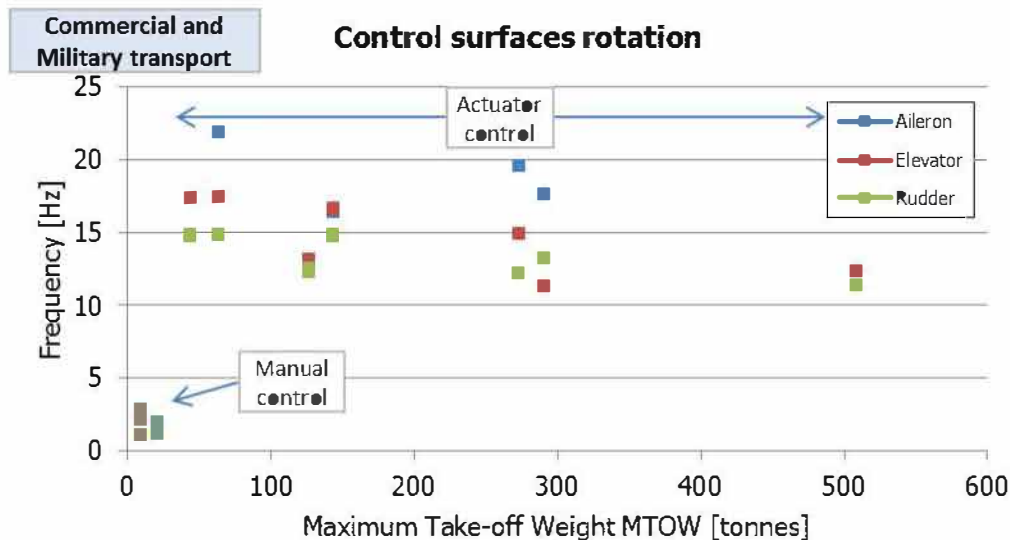


Figure 13: Control surfaces rotation vs MTOW

Control surface flutter mechanism is typically consequence of the lifting surface bending and the control surface rotation modes coupling. The control surfaces actuators stiffness is a driving parameter for those modes, affecting not only to its rotation mode frequency but also to its mode shape.

In order to better understand the flutter mechanism, sensitivity analyses to this stiffness are performed during the design phase. The flutter behaviour in an actuator failure case and the actuator tolerances have also to be assessed in the certification phase.

Figure 14 shows a commercial aircraft normal modes frequencies evolution when reducing its L/H actuator nominal stiffness to a value close to its disconnection in five steps:

1. Both aileron actuators nominal stiffness ($K_{R/H} = K_{L/H} = K_{NOM}$).
 - Pink curve: Ailerons symmetric rotation. Nominal frequency, same as antisymmetric.
 - Dark blue curve: Ailerons antisymmetric rotation. Nominal frequency, same as symmetric.
 - Green curve: 1st wing symmetric bending. Nominal frequency.

Mode shapes: Ailerons modes show certain torsion along their span. Wing mode is a pure uncoupled bending mode. See also Figure 15.
2. L/H aileron actuator stiffness reduced one order of magnitude and R/H aileron actuator stiffness remains unchanged ($K_{L/H} \downarrow, K_{R/H} = K_{NOM}$).
 - Pink curve: L/H Aileron rotation at a frequency lower than the nominal one.

- Dark blue curve: R/H Aileron rotation at the nominal frequency.
 - Green curve: 1st wing symmetric bending. Nominal frequency.
- Mode shapes:** Two uncoupled R/H and L/H ailerons rotation modes instead both sides symmetric and antisymmetric. Both modes show certain torsion along their span. Wing mode is a pure uncoupled bending mode.
3. L/H aileron actuator stiffness reduced two more orders of magnitude and R/H aileron actuator stiffness remains unchanged ($K_{L/H} \downarrow \downarrow$, $K_{R/H} = K_{NOM}$).
 - Pink curve: L/H Aileron rotation at a frequency close to the than the 1st wing symmetric bending one.
 - Dark blue curve: R/H Aileron rotation at the nominal frequency.
 - Green curve: 1st wing symmetric bending. Nominal frequency.

Mode shapes: R/H aileron mode shows certain torsion along its span. L/H aileron rotation mode is a pure rotation mode. Wing mode is coupled with the aileron rotation.
 4. L/H aileron actuator stiffness reduced one more order of magnitude and R/H aileron actuator stiffness remains unchanged ($K_{L/H} \downarrow \downarrow \downarrow$, $K_{R/H} = K_{NOM}$).
 - Pink curve: L/H Aileron rotation at a frequency between flexible modes and rigid body modes.
 - Dark blue curve: R/H Aileron rotation at the nominal frequency.
 - Green curve: 1st wing symmetric bending. Nominal frequency.

Mode shapes: Same as step 3.
 5. L/H aileron actuator stiffness reduced to a value close to zero and R/H aileron actuator stiffness remains unchanged ($K_{L/H} \approx 0$, $K_{R/H} = K_{NOM}$).
 - Pink curve: L/H Aileron rotation at a frequency close to zero (rigid body mode).
 - Dark blue curve: R/H Aileron rotation at the nominal frequency.
 - Green curve: 1st wing symmetric bending. Nominal frequency.

Mode shapes: Same as step 3. See also Figure 15.

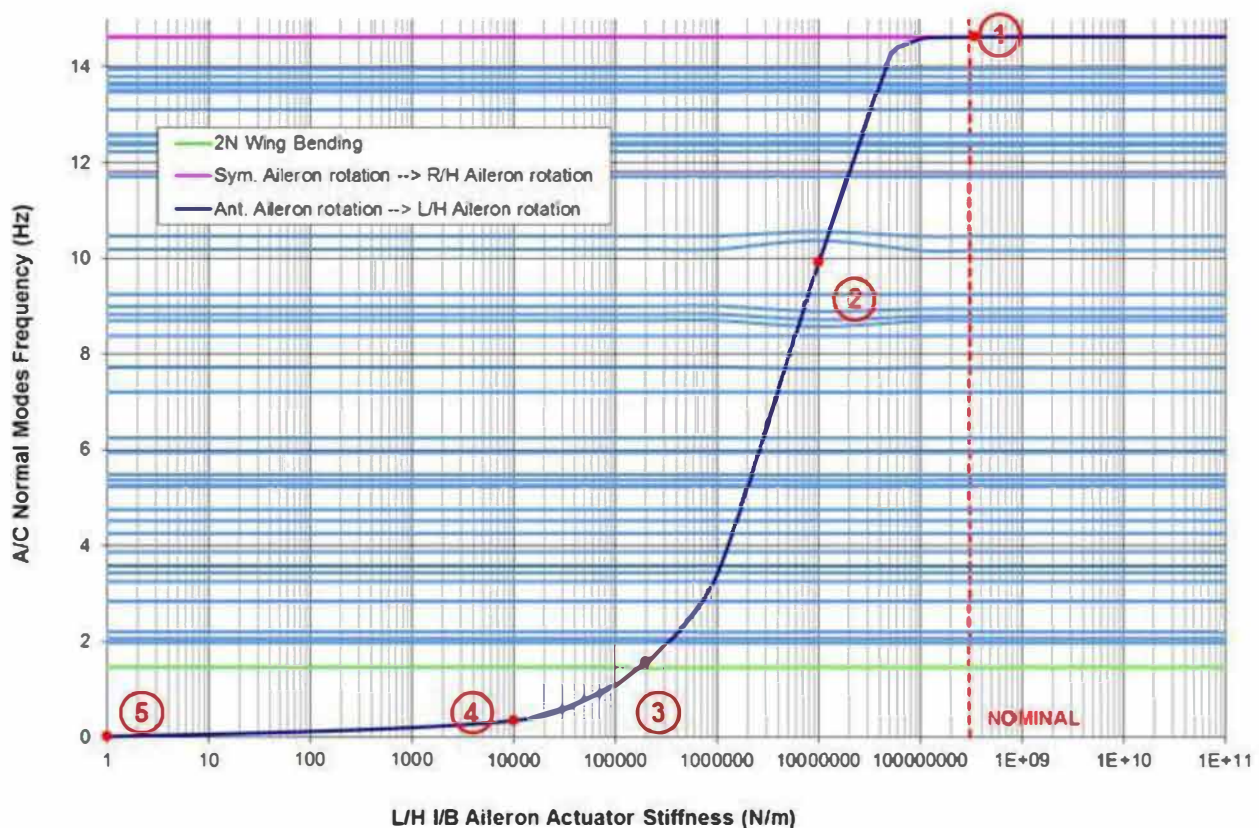


Figure 14: Commercial A/C - Normal modes frequency sensitivity to one-side aileron actuator stiffness

Figure 15 shows the change in the aileron and wing bending normal modes: With the actuator nominal stiffness (left hand plots) the wing bending is an uncoupled mode and the ailerons rotation shows a degree of torsion along its span. When reducing the actuator stiffness to a value close to disconnection (right hand plots), the wing bending mode is coupled with the L/H aileron rotation, which on its part is a rotation rigid body mode.

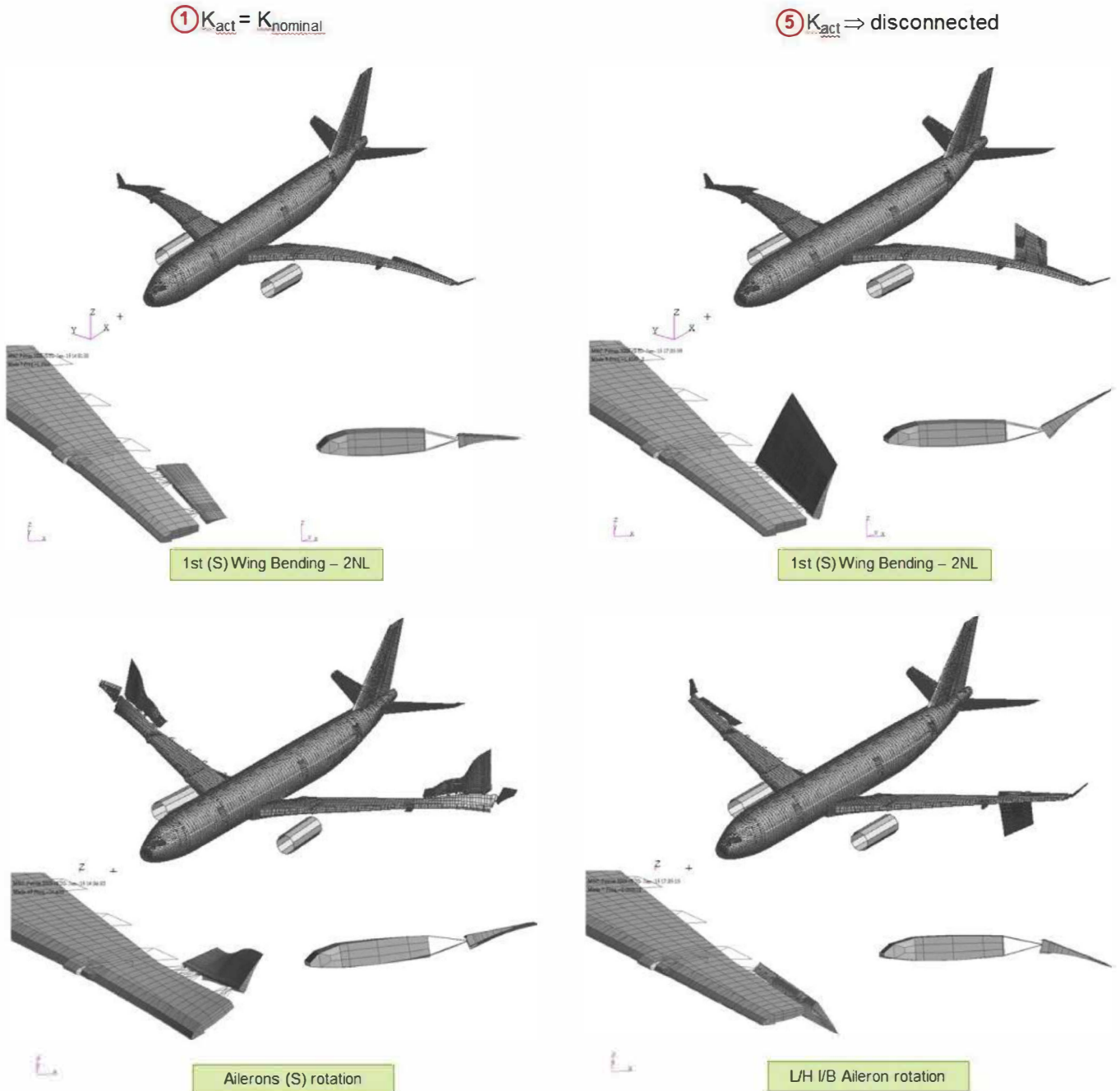


Figure 15: Commercial A/C - Normal modes shapes sensitivity to one-side aileron actuator stiffness

4.4 How to alter the bending – control rotation coupling through mass balance

Mass balance is often used to prevent the lifting and control surface flutter. For this purpose, high density material weights (e.g. lead, tungsten, etc.) are added either to the control surface or to the torsion box, depending on the nature of the control system and on the modes coupling to be avoided:

- In **manual control** by wires, the mass is added to the control surface in order to move its centre of gravity ahead the hinge line. When the wing bends up the control surface rotates up leading to a negative aerodynamic force that reduces the wing bending. The mass is added to the torsion box in order to change the phase between the control surface rotation and the wing bending motion
- In **controls with actuators**, the mass balances is to change the mode shapes and frequencies, thus de-coupling the potential flutter modes.

Figure 16 shows the effect of balance mass added in a classical flutter of control surface with actuators coupling with lifting surface bending.

Left hand graph shows the structure normal modes damping and frequency evolution with the A/C speed. Mode 1, lifting surface bending, couples with mode 2, control surface rotation, as their frequencies approach with the speed increase. Mode 1 damping drops thus becoming unstable when crossing the zero damping line.

Right hand graph shows the effect of the balance mass added to the torsion box tip: the frequencies split and separate and the lifting surface bending damping increases. For a certain amount of mass, the mode does not cross the zero damping line and no flutter appears at any speed. The blue arrows show the sense of increasing balance mass.

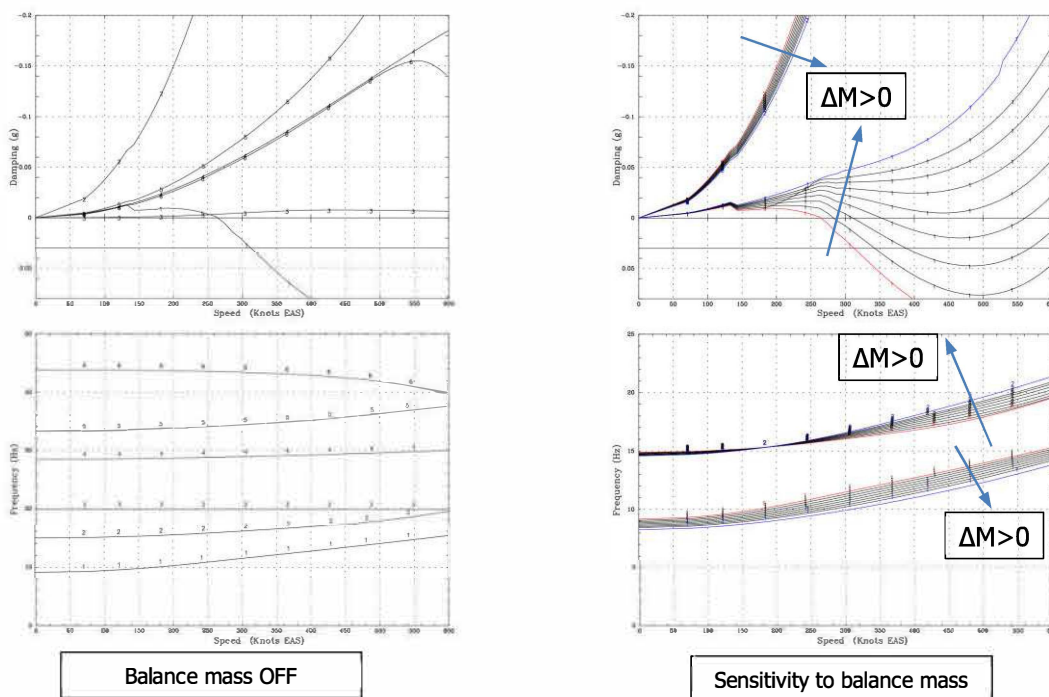


Figure 16: Classical flutter prevention by adding mass balance

5 STRUCTURAL DYNAMIC MODELS VALIDATION

5.1 General

Airworthiness regulations proof of compliance require the analytical results to be supported by ground and flight tests, [4]. This section briefly shows the most relevant aspects of the structural Finite Element dynamic models validation by Ground Vibration and Flight Tests, and the influence of non-linearities in the A/C normal modes and, consequently, in this validation.

5.2 Ground Vibration Tests

The Ground Vibration Tests objective is to obtain experimentally the normal modes of the complete aircraft and in particular:

- Frequencies & mode shapes.
- Damping & modal mass.
- Non-linearities (if any).

In turn, results are used to validate or update (if needed) the structure FEM model. Figure 17 shows a typical structural dynamic model validation flow chart.

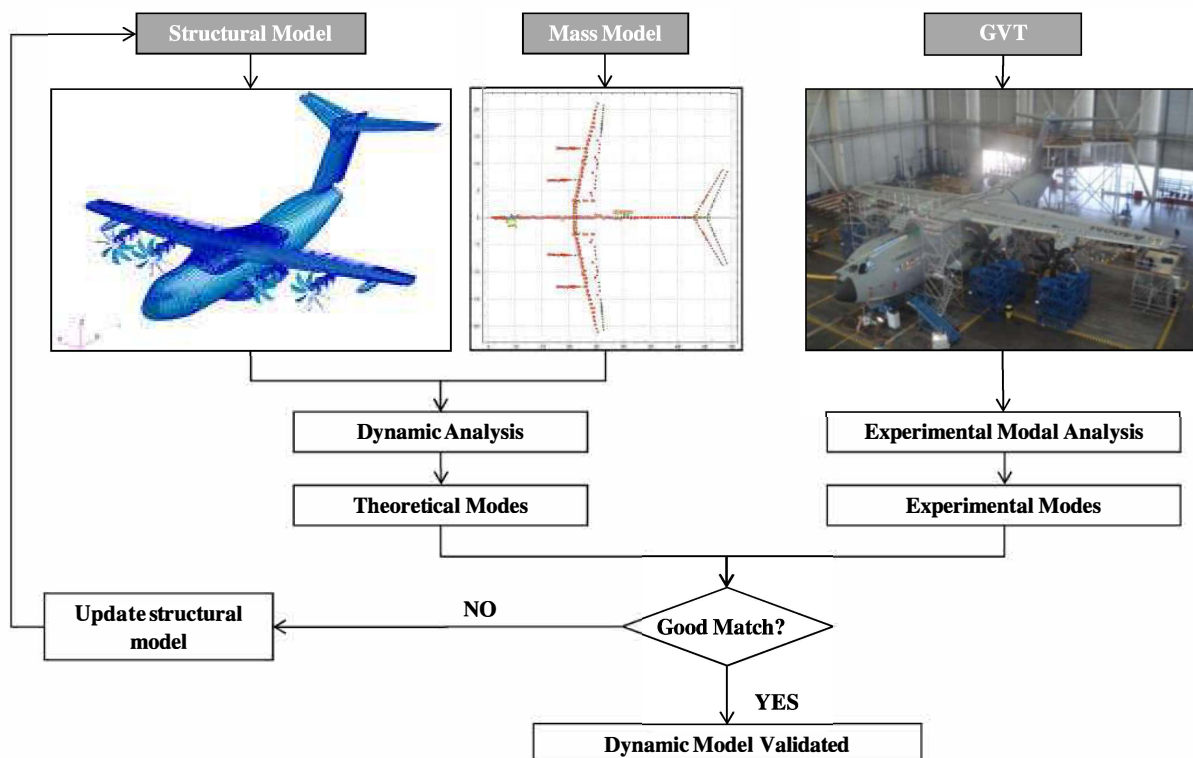


Figure 17: Commercial A/C flutter prevention by mass balance

GVT results are typically represented in a graph that compares theoretical modal frequencies (obtained from a FEM model, for instance) with experimental data. Ideally, test results should be aligned with the 45° division line (continuous red line of Figure 18). The closer these data are to that line, the better the model is behaving and fewer changes will be needed.

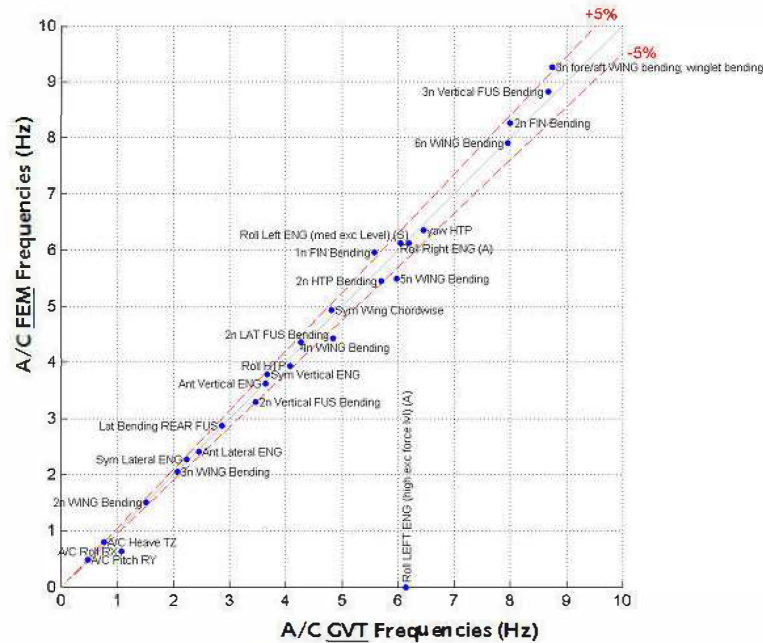


Figure 18: Typical GVT results plot

More information on the test instrumentation and execution, as well as the model validation and adjustment can be found in [5] and [6].

5.3 Flight Tests

During every aircraft Flight Test campaign, loads and accelerations are monitored and they are used not only to assess their peak values but also to extract from them the modal information which can be used to validate the aircraft models.

Figure 19 shows a typical dynamic ground loads model validation flow chart. After the landing gear validated by the drop and free extension tests and the structural dynamic model validated by the GVT, the landing gear coupling to the A/C structural model is validated by means of dedicated firm landing and taxi tests. In both cases the flow chart is similar: Flight test data are compared with the analytical results obtained with the integrated A/C-L/G model. The coupling model is adjusted if necessary and finally validated.

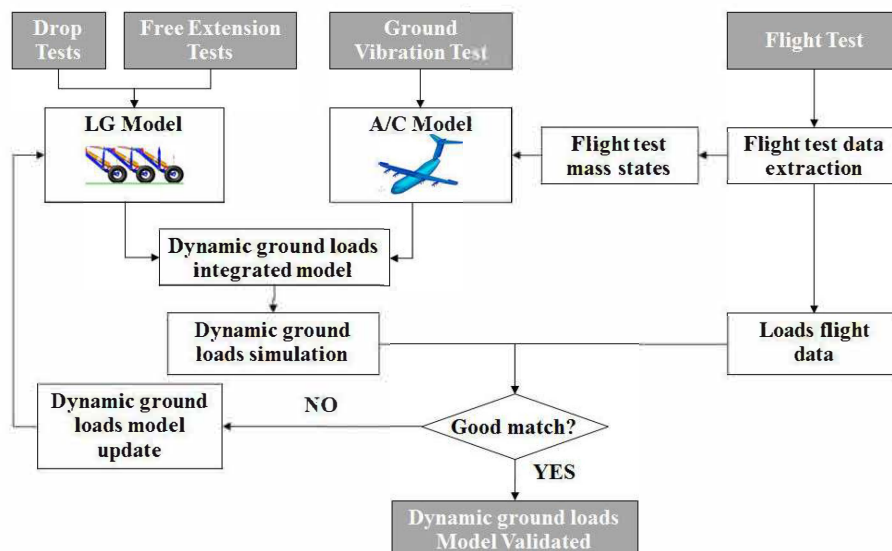


Figure 19: Dynamic ground loads model validation flow chart

Flight Flutter Tests are used to clear the A/C flight envelope and also check the modes frequency and damping evolution with speed, thus providing means to validate the flight dynamic loads and aeroelastic model. Figure 20 shows the model validation flow chart.

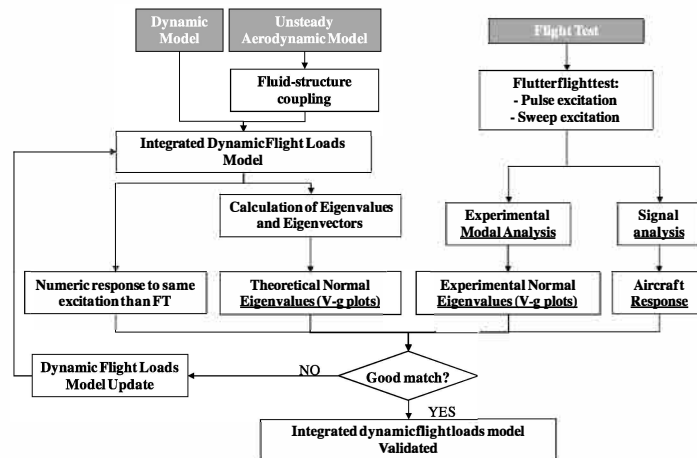
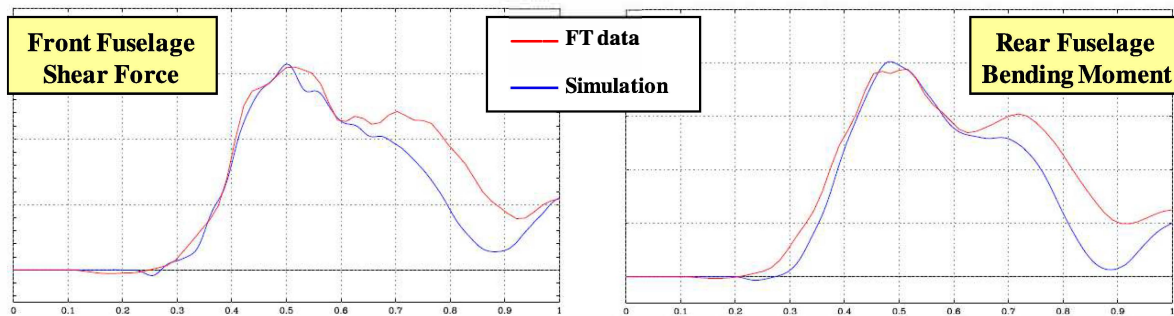
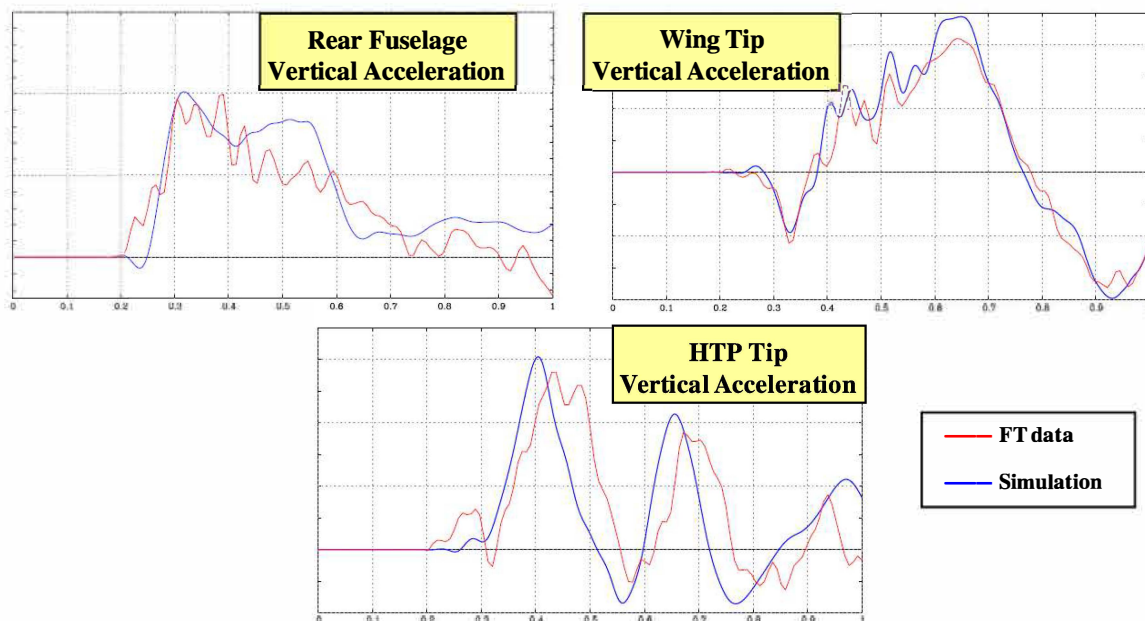


Figure 20: Heavy transport aircraft flight loads model validation flow chart

Figure 21 to Figure 25 show the comparison between the heavy transport aircraft flight tests and analytical results for a set of loads and accelerations. Results obtained in hard landing and taxi tests show good agreement. For a deeper discussion and more results, see [5].



**Figure 21: Heavy transport aircraft test-simulation loads comparison.
10.9 ft/s landing**



**Figure 22: Heavy transport aircraft test-simulation accelerations comparison.
10.9 ft/s landing**

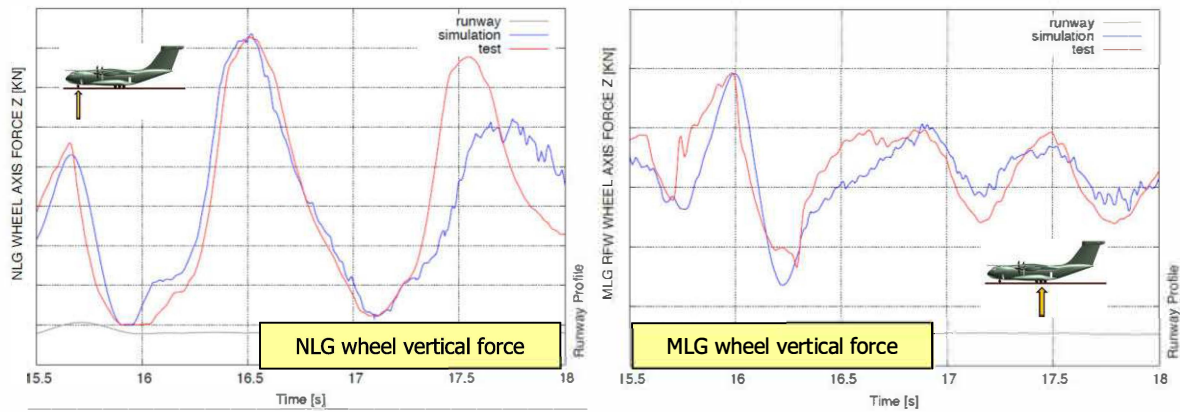


Figure 23: Heavy transport aircraft test-simulation LG loads comparison. Taxi over (1-cos) bump

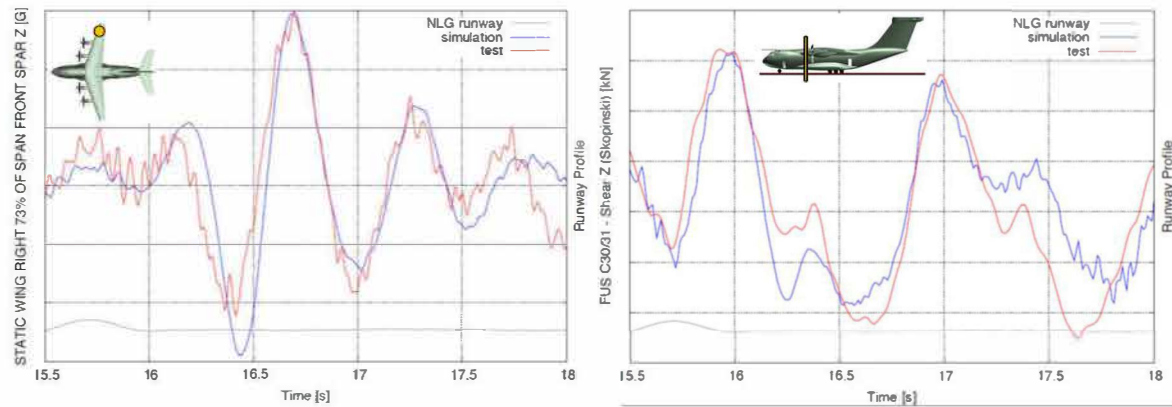


Figure 24: Heavy transport aircraft test-simulation comparison. A/C loads. Taxi over (1-cos) bump

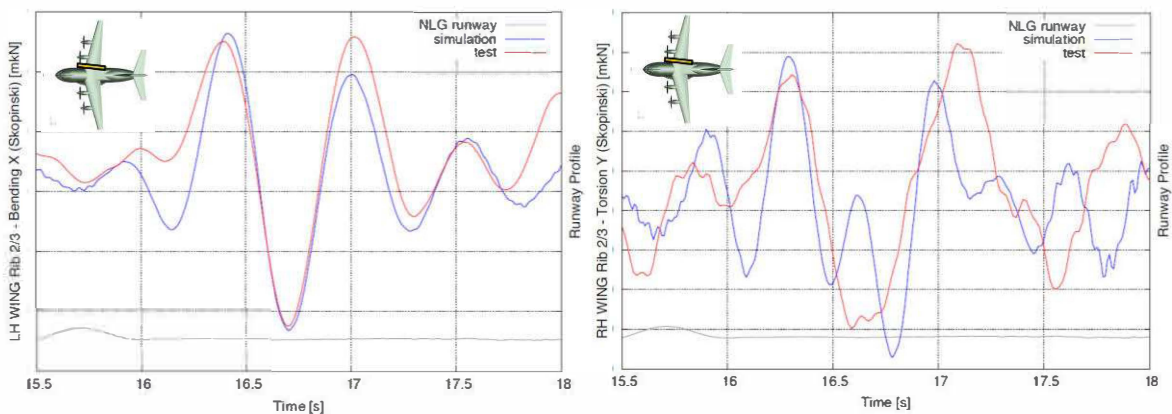


Figure 25: Heavy transport aircraft test-simulation comparison. A/C accelerations. Taxi over (1-cos) bump

Figure 26 and Figure 27 show the Flight Vibration Tests Results represented in form of the classical flutter V-g and V-f plots for the wing bending modes. Both, frequency and damping test results show good agreement with the theoretical analyses. The adjustment made to the theoretical damping at zero frequency is based on the GVT results, obtained for small displacements. Due to some A/C non-linearities, this is a conservative assumption.

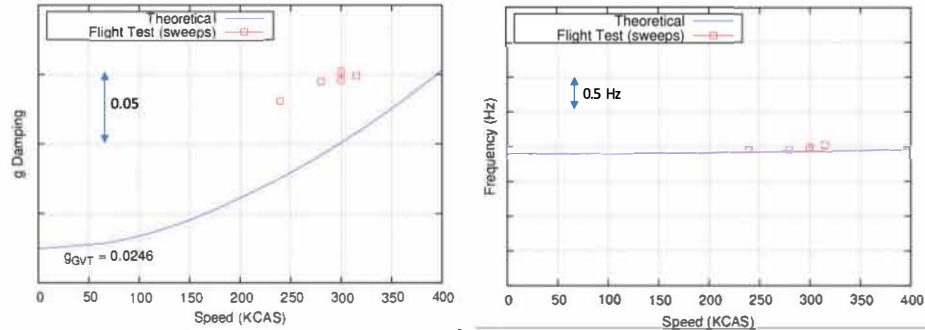


Figure 26: V-g plots for 1st symmetric wing bending mode

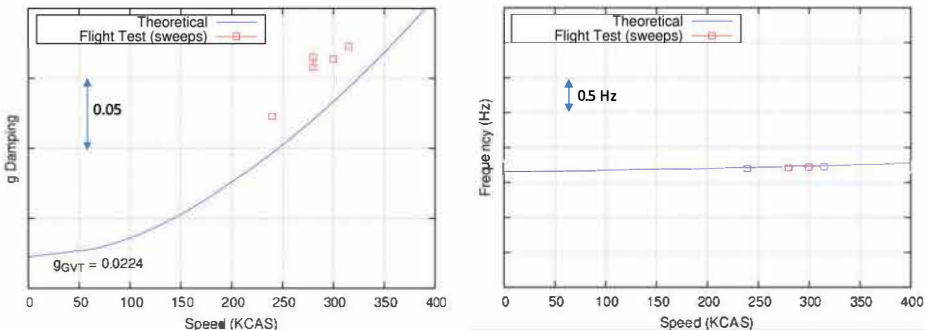


Figure 27: V-g plots for 1st antisymmetric wing bending mode

5.4 Effect of A/C non-linearities in normal modes

One of the eigenvalue technique basic assumptions is the system linearity. In some cases this assumption is valid close to the nominal conditions for which the dynamic model has been defined.

All real structures present some non-linear behaviour up to some extent. Significant sources of non-linearity in aerospace structures include riveted metallic construction, nacelle latches, hydraulic actuators of control surfaces (freeplay, hysteresis, or non-linear spring-type force) and elastomeric engine mounts.

As described in [6], the main footprint of non-linear effects affecting a vibrating structure is the variation of frequency peaks in the response to different levels of energy introduced into the structure. In many vibration tests, the increase of excitation force levels in order to corroborate the changes in those peaks is very common. Figure 28 shows an example of frequency peak variation with excitation force level and normal mode frequency and damping evolution with excitation force level.

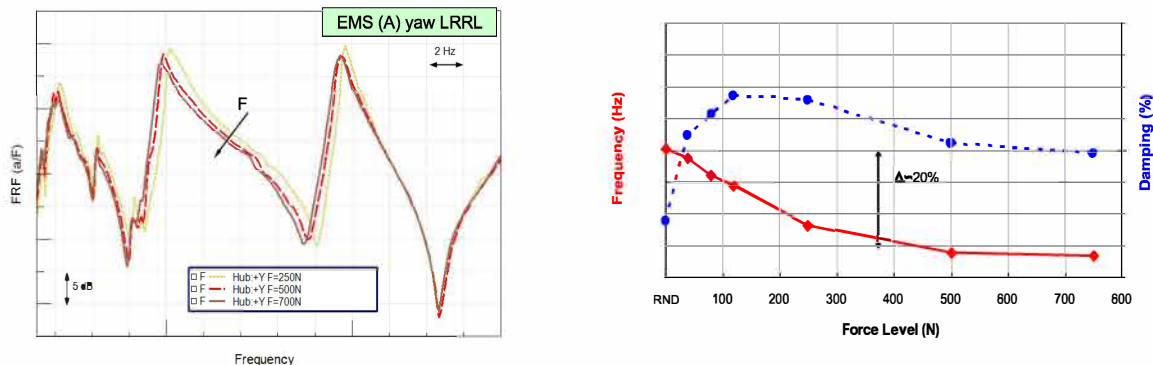


Figure 28: Driving point FRF's (left) and normal mode frequency and damping (right) for increasing excitation force level.

Secondary structures (fairings, some non-structural aircraft doors, etc.) are often conservatively excluded from checkstress models, which are usually the basis for structural dynamic models definition. These secondary structures may also contribute to a non-linear behaviour of the normal modes in a Ground Vibration Test. In the heavy transport aircraft GVT described in [6], the engine composite cowlings were identified as a possible source of non-linearity on the EMS modes. Engine cowls were removed and EMS normal modes measured for different excitation force levels in order to compare with COWLS-ON cases. Measured results for EMS Roll mode (Figure 29) confirmed this statement. It could be appreciated a stabilization of EMS roll mode from medium excitation levels, whereas COWLS-ON case had not shown normal mode stabilization at the highest excitation forces reached on GVT.

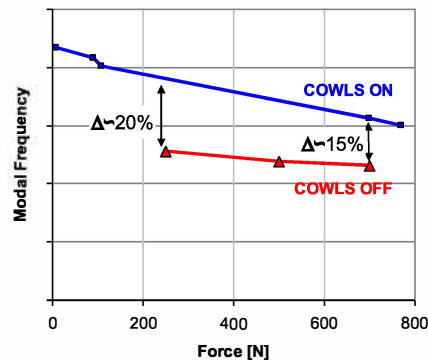


Figure 29: Cowling removal effect on EMS Roll mode.

Other non-linear effect is the structure high-flexibility, which affects its normal modes frequencies in a similar way as the violin string tuning.

By performing non-linear normal modes calculation for a highly flexible aircraft it can be predicted this behaviour. Figure 30 shows the effect of the applied load (from -1g gravity on ground to +2.5g manoeuvre in flight) on a very flexible aircraft normal modes. The origin of abscissa axis corresponds to the un-deformed or "jig" shape, which is the basis for the A/C design and structure model definition. Broadly speaking, in-flight loads produce a decrease of the normal modes frequency. On the other hand, the on-ground gravity produces a similar effect in some of the modes frequency, but the opposite in others. In other words, the model adjustment to match GVT results might be in the opposite sense to that intended for its applicability to flight.

More information can be found in [7], where it is also shown that the effect of applied loads in a less flexible aircraft is negligible.

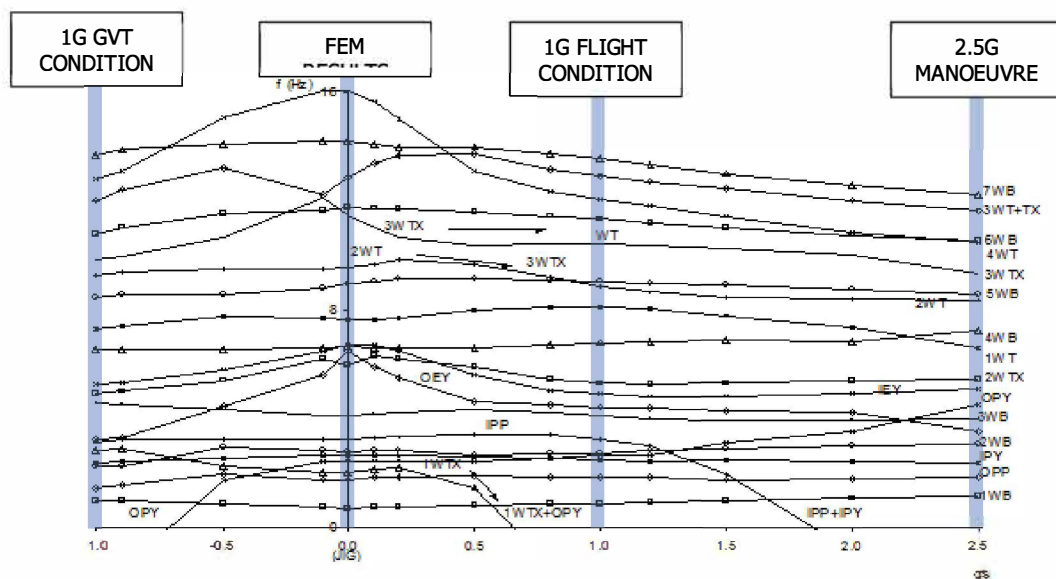


Figure 30: Non-linear effects of applied loads and large deformations on aircraft normal modes



6 CONCLUSIONS

Are normal modes Friends or Foes? ... Both?

FOES

- When exciting an aircraft in one of its mode shapes and at the corresponding natural frequency, the amplitudes obtained may be very large with very low level of input excitation. This, in turn, may jeopardize the aircraft structural integrity.
- In presence of unsteady aerodynamics, two or more modes may couple and extract energy from the flow, thus creating the catastrophic instability of **flutter**.
- Modes may be "dangerous companions"; it is the duty of the engineer working in structural dynamics and aeroelasticity to know where they are (frequency) and how they are (mode shape).

FRIENDS

- The dynamic equations expression in the normal modes base allows to reduce the problem size by 3-4 orders of magnitude with almost no lack of accuracy.
- The normal modes of an aircraft may accurately be measured in a Ground Vibration Test, a non-destructive test that can be performed in few weeks producing a fabulous outcome of precious results for the aeroelastician.
- The apparently weird aircraft response to a transient excitation can be better interpreted when illuminated with the light of the aircraft normal modes.

Modes, maybe the aeroelastician best friends...

REFERENCES

- [1] A. Tewari; 2015, "Aeroservoelasticity: Modeling and Control"; Birkhäuser.
- [2] R.L. Bisplinghoff, H. Ashley, and R.L. Halfmann; 1996; "Aeroelasticity"; Dover.
- [3] D.H. Hodges and G.A. Pierce; 2011; "Introduction to Structural Dynamics and Aeroelasticity"; Cambridge University Press.
- [4] EASA CS-25; 2007; "Certification Specifications for Large Aeroplanes"; Airworthiness certification; Amendment 3; https://www.easa.europa.eu/system/files/dfu/CS-25_Amdt%203_19.09.07_Consolidated%20version.pdf.
- [5] M. Oliver, G. Pastor, M.A. Torralba, S. Claverías, J. Cerezo and H. Climent; 2013; "A400M Aeroelastics and Dynamic Tests". *CEAS 2013 Air and Space Conference*; Linköping, Sweden; 16-20 September.
- [6] M. Oliver, J. Rodríguez, J. Martinez, H. Climent, R. de Diego, J. de Alba; 2009; "A400M GVT: The Challenge of Nonlinear Modes in Very Large GVT's". *International Forum of Aeroelasticity and Structural Dynamics IFASD2009*, Seattle, USA; 22-24 June.
- [7] M. Oliver, H. Climent and F. Rosich; 1999; "Non-linear Effects of Applied Loads and Large Deformations on Aircraft Normal Modes". *Specialists' Meeting of the RTO Applied Vehicle Technology Panel (AVT)*; Ottawa, Canada; 18-20 October. RTO Meeting Proceedings 36, Chapter 21.

Preliminary transonic CFD analyses of a PrandtlPlane transport aircraft

Cipolla Vittorio

SkyBox Engineering, Via G. Caruso 8 56122 Pisa (Italy), v.cipolla@skyboxeng.com

Frediani Aldo

University of Pisa, Department of Civil and Industrial Engineering, Via Caruso 8 56122 Pisa (Italy)

Abu Salem Karim

University of Pisa, Department of Civil and Industrial Engineering, Via Caruso 8 56122 Pisa (Italy)

Binante Vincenzo

SkyBox Engineering, Via G. Caruso 8 56122 Pisa (Italy)

Maganzi Marco

University of Pisa, Department of Civil and Industrial Engineering, Via Caruso 8 56122 Pisa (Italy)

Rizzo Emanuele

SkyBox Engineering, Via G. Caruso 8 56122 Pisa (Italy)

ABSTRACT

In the framework of the PARSIFAL research project, funded by the European Community in the Horizon 2020 program, the PrandtlPlane (PrP) configuration has been proposed as an innovative alternative to the current commercial aircraft of conventional architecture; the PrP configuration development is presented in order to satisfy the future air traffic growing requirements with better performances than conventional one, in terms of fuel efficiency, safety, pollution and noise emissions. In this paper a preliminary aerodynamic investigation of the transonic behavior of the PrP wing system is presented; this study has been carried out by means of CFD analyses, with the aim to collect relevant information and to detect the proper design and operative space, fundamental for the following aerodynamic design activity of the aircraft. Investigations have been made on macro parameters (like wing loading or cruise Mach number) and also on local critical issues. The results obtained allows to design some initial reference configurations with satisfactory cruise performance in this very initial stage of the design process.

KEYWORDS: *PrandtlPlane, PARSIFAL, CFD, Transonic, Aerodynamics*

Concurrent engineering and fast-mapping/crowd-mapping using IoT, Big Data and Cloud Computing

George Suci
BEIA Consult International
R&D and Innovation Manager
Str. Peroni 16, Bucharest, Romania
george@beia.ro

Adrian Pasat
BEIA Consult International
R&D Department

Laurentiu Bezdedeanu
BEIA Consult International
R&D Department

Iulian Iordache
INCDIE ICPE-CA
Scientific Researcher, Advanced Materials Department
Splaiul Unirii 313, Romania, Bucharest

Gabriela Iosif
INCDIE ICPE-CA
Project Manager, Knowledge and Information Management Office
Splaiul Unirii 313, Romania, Bucharest

Emil Costea
INCAS
Head of Technical Department
Iuliu Maniu 220, Romania, Bucharest

ABSTRACT

Information sciences and technologies are clustering, heading towards a mixture of computer platforms, operating systems, data containers, communication technologies, and delivery methodologies. So, knowing that for technology to be successfully deployed and embraced, we need computing professionals who can assess and select appropriate technologies, and design integrated solutions. This paper presents the approach of the E-STAR project, which aims to increase the capacity of Romanian research and industry entities, facilitating their participation in programs of science and technology integration, through applications that have specific objectives in mind, namely: creating a framework for developing partnerships between industry and research areas such as space, air, soil, subsoil, water; developing an IT platform for concurrent engineering, ensuring the integration of relevant data from ESA; advance and promote applications based on satellite telecommunications and Earth observation (satellite data); creating a database containing information pulled from different research areas. As mentioned, the key factor within the E-STAR platform will be the synthesis of concurrent engineering basic tools and principles with significant data from relevant sources, including IoT (Internet of Things) and fast-mapping/crowd-mapping. We envision advancing an innovative tool focused on optimizing the engineering design processes, substituting the traditionally sequential flow by integrating multidisciplinary teams working

collectively, in parallel, at the same place with the objective of making a design in the most efficient and consistent way possible, right from the start.

The E-STAR platform will implement adequate search engines like EXALEAD OnePart and EXALEAD CloudView solutions, that would offer the possibility to search within the platform files and also connect to relevant big data sources (ESA, ROSA, etc.).

Also, the platform will allow the design of new parts by using software solutions like Solidworks and CATIA in the cloud. Beside 3D Experience platform from Dassault Systèmes, we analyzed and compared two other PLM (Product Lifecycle Management) architectures: Team Center from Siemens and Windchill from PTC.

The platform would be accessible to the companies and institutions which are interested to work in areas related to space datasets. Future work must take into consideration the issues related to licenses, security, technical problems, competition and access to resources.

KEYWORDS: *Concurrent engineering, fast-mapping, crowd-mapping, IoT, Big Data, Cloud Computing*

1 INTRODUCTION

The first time the term concurrent engineering (CE) appeared was in 1989 and can be called as well Simultaneous Engineering, implying a systematic approach which includes a concurrent design of products and other processes that are related and have in their build the manufacture and support [1].

Traditionally, CE was used the sequential engineering method where people from various departments worked one after the other on successive phases of development, method which has a linear format. After a task is completed it is left alone and then everything is concentrated on the next one, being a lengthy process. It often led to a lot of design changes when the prototype testing began, due to production problems, delays or design flaws. Then, concurrent engineering was implemented in industry, and not only, as an approach directed to engineering cycles and optimization, as shown in Fig. 1.

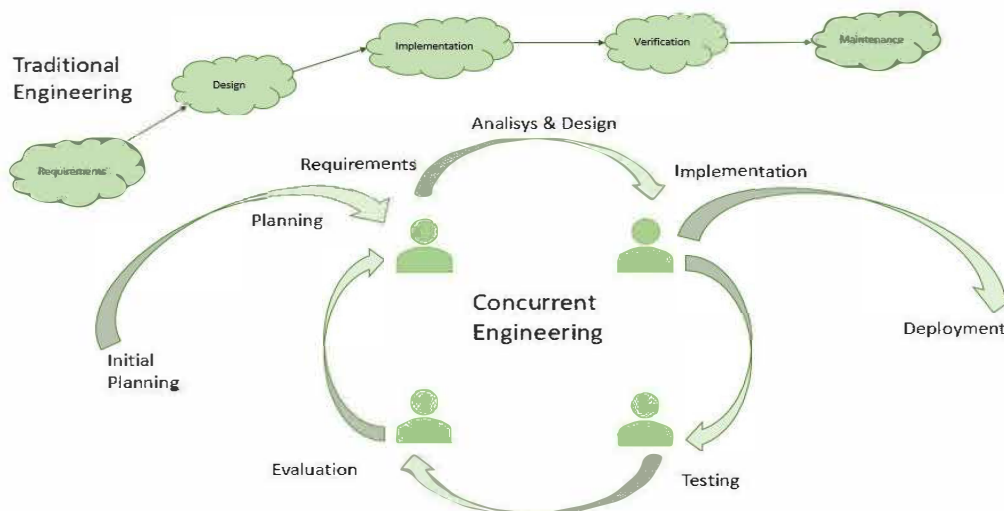


Figure 1: The difference between concurrent engineering and traditional engineering

Although, initially, concurrent engineering was adopted in the industry for product design, subsequent, it was adopted also in information and content automation field. Essentially, concurrent engineering provides a collaborative, co-operative and simultaneous engineering working environment [2].

The concurrent engineering approach is based on five key elements:

- a process



- a multidisciplinary team
- an integrated design model
- a facility
- a software infrastructure

Fast mapping is used in the context of data acquisition, through Earth Observation service, and it is related to ongoing crisis and post crisis situations [3]. There are several projects, which aim to increase automation of disaster mapping chains by fast production and monitoring cycles, and Big Data. This can be done by optical and radar data from French, German, Romanian Space Agency (ROSA), European Space Agency (ESA) Sentinel, and Copernicus Emergency Management Service rapid mapping activation sources [4].

Another concurrent engineering approach is crowd-mapping, which is a form of collaborative work that empowers users to share geographic knowledge [5]. One good example of crowd-mapping would be OpenStreetMap which is a crowd-sourced geographical map dataset. The system behind crowd-mapping is crowd-sourcing which introduces the concept of knowledge gathering whereas people are put to gather and keep a lot of information, such as Wikipedia. Crowd-mapping can make very detailed real-time data, which any other kind of map would not be possible to copy it. This concept appeared in a global disaster relief movement, because online maps were not enough to keep track of some medical supplies in the disaster of Haiti and Chile, these kind of maps being created through text messages and social media [6].

Furthermore, concurrent engineering is closely related to Product Lifecycle Management (PLM) [7] which defines a solution for the improvement of development processes for a product and of bringing to the market faster, through a better management of information and collaboration during the entire lifecycle of the product, from the idea until the withdrawal of this.

Such PLM platforms, which consider the simulation of the lifecycle of the product and the impact on the environment, can be used as a decision system in early phases of design [8]. Moreover, the product-service systems are business models, which can be considered smart products [9].

Also, for a modular product-service system, there are designed collaborative integrated platforms, which can gather valuable information for the decision process with the help of smart sensors networks [10].

Hence, in the rest of the paper, we will present in Section 2 an overview of the PLM architectures implemented in industry and other CE systems. In Section 3 we present the experimentations with Big Data tools, while in Section 4 we will describe the CE platform architecture and its functionality. Also, we realize a SWOT analysis of PLM solutions for concurrent engineering. In section 5 we draw the conclusions.

2 RELATED WORK

Product development companies have an interesting way of providing customers the best of their services, as they reuse old quality assured designs while introducing them to new products [6]. The reuse of parts it's not profitable because sometimes customers' wishes or requirements can hectically change. Though to avoid the development lead-time, another type of reuse is needed. Studies shown in this thesis demonstrate that literature based on information searched through platforms do not provide the need to support holistic platform development over a lifecycle. To solve this issue configurable system elements are created through model platforms. In addition, some platforms for development can be backed by a Product Lifecycle Management architecture for engineering-to-order configuration.

Satellite systems are becoming more complex day by day so that the conceptual design key is even more expensive to have [11]. A solution is to establish a collaborative systems engineering environment and to adopt a model-driven engineering approach (MDE). This introduces a new application of a novel knowledge-based software tool, called SatBudgets, which is based on satellite SysML (Systems Modelling Language).

Scientists and public institutions face a lot of problems when it comes to geospatial data that has a lot of heterogeneous data [12], using automatic metadata extraction approach which generates



distinctive optical data from different kind of satellite missions (i.e. MODIS, LANDSAT, RapidEye, Suomi-NPP VIIRS, Sentinel-1A, Sentinel-2A), Geonetwork Open Source stores all important metadata information regarding satellite data and all of this is put in an online catalog. The EURAC research group institute for Applied Remote Sensing works in real time to manage all data for Earth observation, meaning data processing, metadata extraction and so on, such as the TESSA [13] project is an interoperable data platform solution and it allows fast navigation and entry to data from a data archive. It is for scientists mainly and situational sea awareness high-level services which is the decision support system (DSS). It can be accessed through three parts: the Data Access Service (DAS), the Metadata Service and the Complex Data Analysis Module (CDAM). In paper [14] the open platform amePLM is described, which is made on a semantic data model. It enables an integrated view of data and information available software system and the linking of the solution to existing engineering software systems.

With the diversity of IT infrastructure, it is difficult to think of a fusion between the production system and information technology, such as big data fusion and analysis platform using cloud computing [15].

The Internet of Things field (IoT) produces data that maps the surroundings of sensing objects and send notifications to a data processing platform for supplementary investigation. The notion of background attentiveness of applications is done by merging this observed data, or by altering the linked data. The article [16] presents MASSIF, an information driven stage for the semantic explanation and thinking on IoT information. It permits the joining of various measured thinking administrations that can work together in an adaptable way to encourage complex basic leadership forms.

In [17], an object-oriented manner to deal with the advancement of item stages is proposed to expand effectiveness through reuse and adaptability of outlines among a group of items. Two methods of the stage improvement handle are tended to: stage planning and stage execution. Stage planning endorses the techniques expected to show stage objects, utilizing upgraded work that implies models and set-based concurrent engineering techniques. All along the stage execution procedure, sets of outline options can be designed simultaneously all through the theoretical, structure, and point by point periods of the stage advancement.

In paper [18], the authors present how item stage arranging can enormously bolster item variation plan, which is of extraordinary help to the usage of mass customization (MC). Most of the item stage arranging strategies, item modules and item families have been generally preplanned before items are planned. In this paper, we propose a strategy for item stage arranging utilizing the current item information in product lifecycle management (PLM) database. The proposed technique presents two key innovations, i.e., pruning investigation and property coordinating. The pruning investigation is utilized to discover the sharing parts of various item families, which constitutes the fundamental structure of item stage. The adequacy of the proposed technique is confirmed by the item information in the PLM database for valves. The proposed technique enormously enhances the reuse rate of existing item assets, giving a successful and quick path for ventures to execute the MC procedure.

Nowadays, fabricating is heading towards client driven and learning is based on dedicated development, as presented in [19]. Shorter product life cycles prompt to expanded elaboration in fields like item and process outline, industrial facility organization and generation operations. To deal with this unpredictability, new information based techniques and advancements are expected to demonstrate, trigger, advance and screen fabricating frameworks. Learning based and collaborative process administration include a blend of organized and non-organized procedures. Organized procedures administration can be diminished to an arrangement of completely characterized rules prompting high productivity and additionally, low adaptability, whereas the administration of non-organized procedures is not inclined to a full formalization. A mix of both organized and unstructured administration approaches is required with a specific end goal to accomplish a fruitful compromise between effectiveness, adaptability and controllability. Huge undertaking data frameworks, force organized and unsurprising work processes, while learning based community oriented procedures are erratic to some degree, including high extents of

human-choice. Moreover, the article [19] presents an arrangement of ideas, strategies and instruments of an imaginative Hybrid Process Management approach approved by a genuine business case in the car business.

Necessity administration speaks to one of the key procedure in the perplexing product life cycle since it is included toward the start, as well as in the further stages where the meaning of the specialized details at times involves prerequisites tradeoff because of discordances [20]. Hence, the part of RM instruments and strategies, that regularly depicts a solitary arrangement, needs to change and to be more incorporated in the Product Lifecycle Management stage. Presently, a genuine shared incorporated RM arrangement does not exist and hence it is important to equip a system for supporting the customization of the accessible RM answers. Furthermore, [21] presents a systematic approach that combines client focused plan standards into the customization procedure of the mechanism. The proposed philosophy puts the client, as opposed to the framework, at the focal point of the procedure on account of that the RM arrangement could be viewed efficiently just if it is capable of sparing time and cash in the information administration, by clients. In addition, this device evaluation technique can help associations productively establish applicant utensils.

3 TOOLS EXPERIMENTATION

In this section we will present the development and experimentation of the following Big Data tools for concurrent engineering: Exalead OnePart, Exalead CloudView, and Exalead Onecall [22]. To test the CE and PLM applications, we deployed on our private cloud computing platform several Virtual Machines (VMs), with the specifications presented in Table 1.

Table 1: System's specifications

OS Name	Microsoft Windows Server 2012 R2 Standard
Version	6.3.9600 Build 9600
System Name	VM-WIN2012R2-EX
System Type	x64-based PC
Processor	Intel(R) Xeon(R) CPU E5-2620 0 @ 2.00GHz, 1995 Mhz, 4 Core(s), 4 Logical Processor(s)
BIOS Version/Date	VMware, Inc. VMW71.00V.0.B64.1607292324, 29.07.2016
BIOS Mode	UEFI
System Directory	C:\Windows\system32
Boot Device	\Device\HarddiskVolume2
Locale	Romania
Hardware Abstraction Layer	Version = "6.3.9600.17196"
Time Zone	GTB Daylight Time
Installed Physical Memory (RAM)	16,0 GB
Total Physical Memory	16,0 GB
Available Physical Memory	15,0 GB
Total Virtual Memory	18,4 GB
Available Virtual Memory	17,4 GB
Page File Space	2,38 GB

3.1 Exalead OnePart

Exalead OnePart is a set of applications that help order company assets, find master parts which reuse old information, this happens while the company is monitoring over time the execution of company police. It was installed on the VM and has a user friendly interface as seen in Fig. 2.

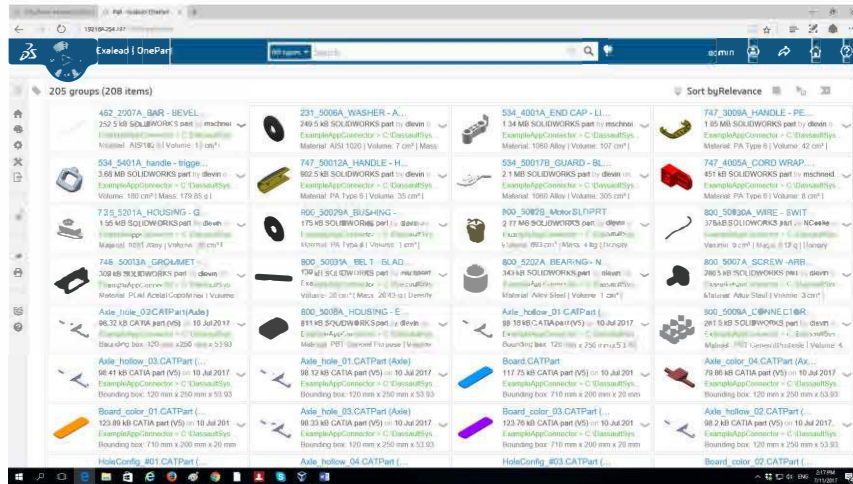


Figure 2: Exalead OnePart dashboard

Exalead OnePart main characteristics are: access and reutilize parts, drawings, specifications, test results and connected data in the entire enterprise.

During the experimentation, OnePart suggests many elements that match according to the author, material, etc. Then the number of elements that fit the research appears. The results of the research are shown under listed form in the panel on the right side and in the one on the left there are the facets. These can be used for refining the research and for filtering. OnePart can even found miswritten parts and detect the number of holes in the geometry of each searched part. After selecting the part from the list, on the left side there is the preview and on the right are shown:

- The components' attributes; extracted from a binary file;
- The OnePart attributes; calculated by OnePart;
- The containers' attributes; supplied by the source

Also, OnePart shows the connected documents with parts and we developed a page where the selected elements can be compared to the reference element on the first column. The attributes that differ from the reference element are highlighted with red. In the case of sets, it is possible to browse the product structure.

Furthermore, EXALEAD OnePart provides a full set of applications to organize company assets, find master parts for reuse, and assure engineers select the preferred part, while tracking over time the accomplishment of company policy. Even more, Sourcing and Procurement will influence these applications to optimize ordering by grouping orders or choosing the right price of technically feasible alternative solutions.

The key capabilities experimented included search for parts, sets, drawings, documents, patents, images in more than 200 formats, access to many sources with different data: files systems, SOLIDWORKS PDM Professional, ENOVIA SmartTeam, ENOVIA Designer Central, and many other PDMs, ERPs and data bases. Moreover, we performed searches for complete text with automated fill of the users' interrogations, advanced search with dynamically and disjunctive faceted search, including searches with 3D mechanically characteristic (locating parts based on holes, supports, channels and other characteristics), which discover part through 3D lookalike. We configured real-time analysis charts that enables better data understanding, automated arrangement of the identical files, labeling the parts and the documents by the users, for easy finding and workflow.

Finally, declarative, audited security mechanisms guarantee the users to see only the content to which they have permission

3.2 Exalead CloudView

Exalead CloudView is a search engine that collects unstructured and structured data from any kind of source and it makes it into a single structured information source, which is the basis of Exalead OnePart. Exalead CloudView uses the best web technologies to create enterprise information systems that exploit all your business data resulting in the most reactive, intelligent systems on the market. Modern search engines like Exalead CloudView provide database connectors that allow a user to search databases without learning database query syntax.

Furthermore, Exalead Cloudview features database connectors which give the possibility to the user to search a database without having to know database query syntax. Worth mentioning is that Exalead CloudView is based on semantic search and we developed the search mash-up using the following structure:

- CloudView semantic platform
- Natural language processing
- Semantic for content and classification
- Semantics for search presentation

The platform architecture is composed out of 4 services, as presented in Fig. 3:

- COLLECT: Gathers unstructured and structured data from any kind of sources
- PROCESS: The collected data is transformed into one single structured resource
- ACCESS: The enhanced data, the processor user and application queries are updated
- INTERACT: The interaction via a customizable Web interface



Figure 3: Cloud interface

3.3 Exalead OneCall

The Exalead OneCall solution, is capable of addressing the Big Data challenge for communication tasks in concurrent engineering. OneCall is a unique search engine that connects all data sources. The tool makes comprehensive use of data to provide a multi-channel vision that centralizes all the information about the customer experience, delivering a consistent 360° vision of the relationship between the customer and the company, an example being shown in Fig. 4.

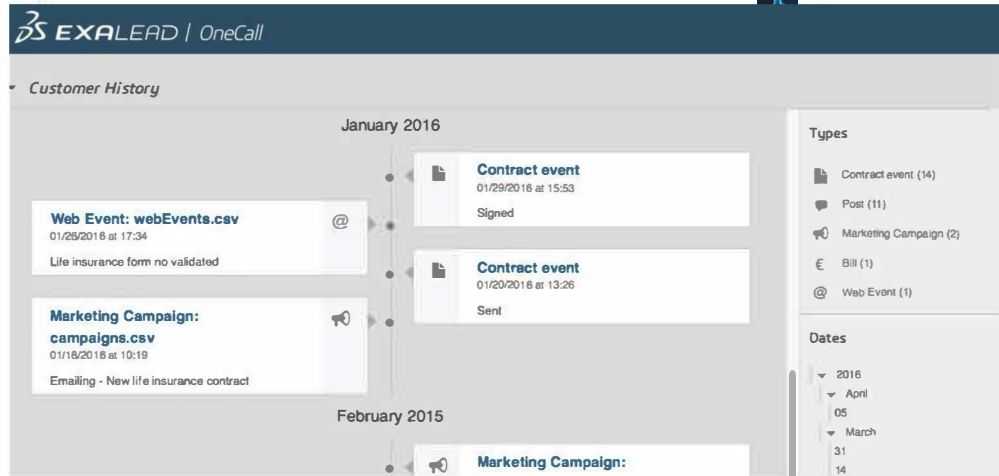


Figure 4: History of multi-channel events

OneCall requires at least 25 GB of available disk space, so we needed to increase the storage space of the VM. To maximize the I/O performances when indexing, it is recommended to use the SCIS, SAS, SAN over FC or SSD disks (unlike SATA disks), for storing files with data. For reasons of performance and reliability, the data directory cannot be on a network file system such as NFS, CIFS and so on. Also, we increased the memory to 8 GB RAM. OneCall comes with a SQLite server for the backend storing services, for client profiles. It is recommended, however, a data base already prepared, like MySQL or Oracle.

4 PLATFORM ARCHITECTURE

In the project E-STAR [23], the coordinator ICPE and partners INCAS and BEIA developed a concurrent engineering platform architecture, integrating the Exalead tools into the PLM collaborative platform as presented in Fig. 5. Basically, we use Exalead OnePart functionalities to search through various documents (emails, PDF documents, CAD designs, etc.) and we will use Exalead CloudView to collect data from external links (ROSA database, ESA, telemetry platforms), while managing communications with Exalead OneCall.

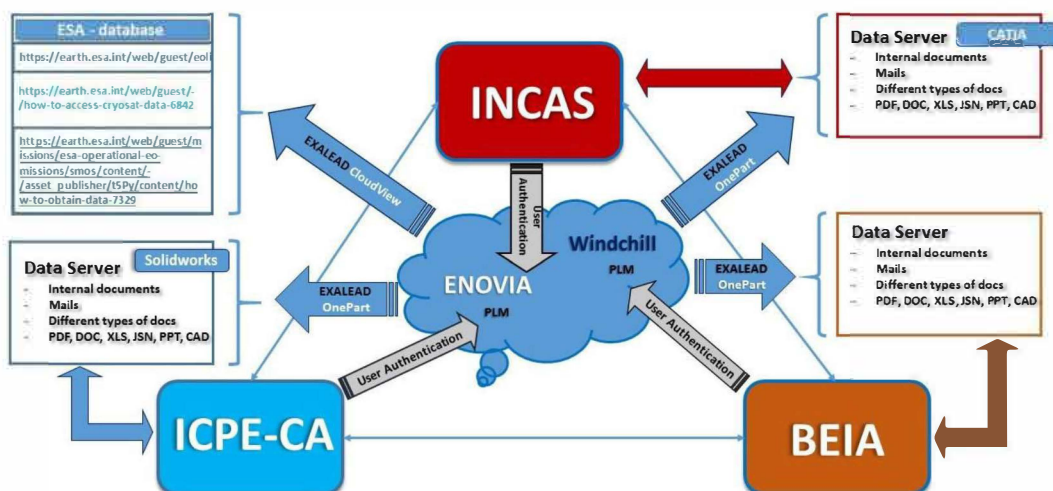


Figure 5: E-STAR Platform Architecture



The Exalead tools provide fast crowd-mapping functionality and allow easy integration through Java connectors into the PLM solutions. We present a comparative analysis of the PLM architectures and functionalities in Table 1.

Table 2: PLM feature comparison

Name			
SWOT analysis	Teamcenter Siemens	Enovia 3DS	Windchill PTC
Strong points	<ul style="list-style-type: none"> - designed for Industry 4.0 projects - Digital Factory Planning and Optimization 	<ul style="list-style-type: none"> - direct compatibility with CAD solutions (used by project partners) - direct compatibility with Exalead solutions - open API 	<ul style="list-style-type: none"> - unlimited number of web users: viewers - permanently monitoring of the database - facilitates the release of managed products documentation with the mentioned solution
Weak points	<ul style="list-style-type: none"> - no maintenance - no connectors - does not offer many CAD solutions 	<ul style="list-style-type: none"> - not fully extended towards manufacturing process management and product publishing 	<ul style="list-style-type: none"> - there are no CAD connectors - supplementary costs for updating the licenses

Consequently, Teamcenter is suitable for smart manufacturing in Industry 4.0 projects, such as Product Lifecycle Management and Digital Factory Planning and Optimization. On the other side, Windchill PLM can manage the content of a product from conception to service, while IoT solutions from PTC allow safety connection of Smart Things, management and analysis of data and the creation of applications. However, Enovia solution from Dassault Systemes (3DS) was the solution

5 CONCLUSIONS

In this paper we presented a concurrent engineering platform for processing big data on cloud platforms from three partners in E-STAR project: ICPE-CA, INCAS and BEIA. The platform is based on the search EXALEAD CloudView search engine which will connect data from ESA, ROSA and other relevant sources. This paper presents related work and proposes a CE platform for the Romanian research community and industry. This system will integrate other PLM software from Dassault Systemes, such as Solidworks and CATIA.

Future work will focus on performance evaluation and comparison with similar PLM platforms that use concurrent engineering and focus on problems which the current platform will not be able to solve. These are related to the reuse of old parts models in the product lifecycle, access to heterogeneous satellite data, and strategies for item stage arranging. Also issues related to IoT data and their aggregation will be added into the proposed E-STAR platform.

REFERENCES

1. S.N Dwivedi, A. K. Verma, J. E. Schneckenberger; 1991 "CAD/CAM Robotics and Factories of the Future '90"; Vol 1; Springer Verlag ; Berlin Heidelberg; pp 1-30
2. ESA; 2017; "What is concurrent engineering"
http://www.esa.int/Our_Activities/Space_Engineering_Technology/CDF/What_is_concurrent_engineering
3. C. Witharana et al.; 2013; "Evaluation of pansharpening algorithms in support of earth observation based rapid-mapping workflows"; Applied Geography; Volume 37; pp 63-87.



4. C. Huber et al.; 2016; "Improving the extraction of crisis information in the context of flood, landslide, and fire rapid mapping using SAR and optical remote sensing data"; 2016 IEEE International Geoscience and Remote Sensing Symposium (IGARSS); pp. 5781-5784.
5. G. Quattrone, M. Dittus, L. Capra; 2017; "Work Always in Progress: Analysing Maintenance Practices in Spatial Crowd-sourced Datasets"; 20th ACM Conference on Computer-Supported Cooperative Work and Social Computing (CSCW 2017); pp. 1876-1889
6. NESTA; 2017; "Crowdmapping. A single map is worth a thousand words" <http://www.nesta.org.uk/digital-social-innovation/crowdmapping>
7. X. Lu, S. Menzel, K. Tang, X. Yao; 2017; "Cooperative Co-evolution based Design Optimisation: A Concurrent Engineering Perspective" IEEE Transactions on Evolutionary Computation; pp. 1-8
8. D. Penciu et al.; 2016; "Product life cycle management approach for integration of engineering design and life cycle engineering"; Cambridge University Press; vol. 30; issue 4; pp. 379-389
9. A. Elgammal, M. Papazoglou, B. Krämer, C. Constantinescu; 2017; "Design for Customization: A New Paradigm for Product-Service System Development"; Procedia CIRP; vol 64; pp. 345-350
10. M. Matsas et al.; "An Integrated Collaborative Platform for managing Product-service Across their Life Cycle"; Procedia CIRP; 2017; vol. 59; pp. 220-226
11. C. E. Levandowski; 2014; "Platform Lifecycle Support using Set-Based Concurrent Engineering"; Ph. D. Thesis; Chalmers University of Technology; Gothenburg
12. W. A. Dos Santos, A. Hardwick A, B.B. Leonor, S. Stephany; 2010; "Enabling Collaborative Conceptual Design for Space Systems Projects"; IDMME – Virtual Concept; pp. 1-4
13. M. Innerebner, A. Costa, E. Chuprikova, R. Monsorno, B. Ventura; 2017; "Organizing earth observation data inside a spatial data infrastructure"; Earth Science Informatics; vol. 10; issue 1; pp. 55-68
14. A. D'Anca, L. Conte, P. Nassisi, C. Palazzo, R. Lecci, S. Cretì, M. Mancini, A. Nuzzo, M. Mirto, G. Mannarini, G. Coppini; 2017; "A multi-service data management platform for scientific oceanographic products"; Natural Hazards and Earth System Sciences; vol. 17; no. 2; pp. 171-184
15. J. Lentès, N. Zimmermann; 2017; "amePLM: a platform providing information provision in engineering"; International Journal of Production Research; vol. 55; issue 13; pp. 3832-3841
16. C. Kühnert, I. M. Arango; 2016; "A Generic Data Fusion and Analysis Platform for Cyber-Physical Systems"; Machine Learning for Cyber Physical Systems; pp. 45-54
17. P. Bonte et al.; 2017; "The MASSIF platform: a modular and semantic platform for the development of flexible IoT services"; Knowledge and Information Systems; vol. 51; issue 1; pp. 89-126
18. H. Johannesson, J. Landahl, C. Levandowski, D. Raudberget; 2017; "Development of product platforms: Theory and methodology"; Concurrent Engineering; pp. 1063293X17709866
19. Q. Zhang et al.; 2017; "A method for product platform planning based on pruning analysis and attribute matching"; Journal of Intelligent Manufacturing; pp. 1-15
20. F. Ferreira et al.; 2017; "Product lifecycle management in knowledge intensive collaborative environments: An application to automotive industry"; International Journal of Information Management; vol. 37; issue 1; part A; pp. 1474-1487
21. M. G. Violante et al.; 2017; "An integrated approach to support the Requirements Management (RM) tool customization for a collaborative scenario"; International Journal on Interactive Design and Manufacturing; vol. 11; issue 2; pp. 191-204
22. A. Ochian, G. Suci, O. Fratu, V. Suci; 2014; "Big data search for environmental telemetry", IEEE International Black Sea Conference on Communications and Networking (BlackSeaCom); pp. 182-184
23. E-STAR; 2017; "STAR for everyone in ESA frame program"; <http://www.beiario.eu/e-star>



CMDOWS: A Proposed New Standard To Store And Exchange MDO Systems

Imco van Gent

Faculty of Aerospace Engineering, Delft University of Technology

Ph.D. Student

Kluyverweg 1, 2629 HS, Delft, The Netherlands

Gianfranco La Rocca

Faculty of Aerospace Engineering, Delft University of Technology

Assistant Professor

Maurice F. M. Hoogreef

Faculty of Aerospace Engineering, Delft University of Technology

Postdoc Researcher

ABSTRACT

This paper proposes a new format to store and exchange multidisciplinary design optimization (MDO) systems. Here, the generic term MDO system refers to the organized set of disciplinary tools, and their exchanged data and the process connections that, all together, define an MDO computational setup. In the process leading to the formal specification of such a computational system, i.e. starting from a repository of disciplinary tools, down to the specification of the actual optimization problem and finally to the implementation of a specific MDO architecture, the aforementioned set of tools, data and connections evolves, until the complete MDO system formulation (thus not yet executable) is reached. The proposed new standard, called CMDOWS (Common MDO Workflow Schema), has been developed to enable this process by providing a means to store and exchange any MDO system and its associated information in a neutral format. Furthermore, CMDOWS provides the starting point to translate any MDO system formulation into an executable computational workflow, by means of a Process Integration and Design Optimization (PIDO) tool of choice. To the authors' knowledge, such an exchange format does currently not exist, notwithstanding the enormous potential it would have for the exploitation of large-scale MDO in industry. CMDOWS is one of the outcomes of the EU project AGILE, where one of the main goals is to reduce the development time of distributed MDO workflows created by large and heterogeneous teams of experts. CMDOWS is an XML schema (XSD) that, in its set-up and structure, shows similarities with the Common Parametric Aircraft Configuration Schema (CPACS) developed by the German Aerospace Center (DLR), which is becoming a de-facto standard to store and exchange aircraft design and performance data. Whereas CPACS allows the user to store aircraft data in a standard format, CMDOWS enables the storing the specification of a full system of multidisciplinary tools, including the data and process links between its various operating blocks (e.g. disciplinary tools, objective and constraint functions, optimizers, convergers, etc.). The key aspect of this proposed format for MDO systems is its neutral XML-based data representation, which is both human-readable and machine-interpretable, making any stored MDO system exchangeable between the design team members and the applications developed to support the team in setting up the MDO system. The latter form of exchangeability is a key enabler for the creation of a versatile MDO framework that includes applications such as tool repositories, MDO system formulation platforms, visualization packages, and collaborative workflow execution platforms. The CMDOWS definition is available, including examples, through a publicly available software repository. Although the schema is under continuous development within the AGILE project, a case study demonstrating the use of CMDOWS version 0.7 in the AGILE MDO framework is presented in this paper. Based on this case study, it can be concluded that the current version of CMDOWS already provides a robust standard to exchange MDO systems between MDO framework applications. The schema will be extended to meet future developments and promote its adoption as a recognized standard in the broader MDO community.

KEYWORDS: MDO, CMDOWS, standard format, workflow schema, XML, MDO framework

Improved NEO data processing Capabilities for the ESA SSA-NEO software system

Teodorescu Claudiu

DEIMOS SPACE S.R.L.

Software Developer

75-77 Buzesti Street 8th Floor Office 25 Sector 1 Bucharest Romania

claudiu.teodorescu@deimos-space.com

Teodorescu Ana-Maria

DEIMOS SPACE S.R.L.

Software Developer

Koschny Detlef

ESA/ESTEC, Noordwijk, The Netherlands

Head NEO Segment, SSA Programme Office

ABSTRACT

"ESA SSA-NEO software system" is defined as the overall system composed by the ESA-NEOCC (Near-Earth Object Coordination Centre) system in ESRIN, Frascati (Italy), together with the NEODYs (Near-Earth Object Dynamic Site) and AstDyS (Asteroids Dynamic Site) systems, located at the University of Pisa and managed for ESA by the University Spin-off SpaceDyS. The ESA Space Situational Awareness (SSA) Programme foresees that both NEODYs and AstDyS systems will migrate to the NEOCC during the next two years through an activity that includes a full software rewriting of the orbit determination software (OrbFit). In the meantime, the SSA programme has built the precursor services in ESRIN and has funded several projects aimed to provide new and unique services to the scientific community and the general ESA customers. One of these projects, called P2-NEO II, foresaw an enhancement of OrbFit and the implementation of a visualization tool for the display of impact corridors and of the fly-by area based on the calculations produced by OrbFit. DEIMOS SPACE Romania was in charge of developing this tool which consisted in two separate visualizations, ICV (Impact Corridor Visualizer) and FAV (Fly-By Area Visualizer), depending on the close encounter scenario. First, if the object is on a collision course with our planet, it shows the impact corridor (i.e. the possible locations where it could hit the Earth surface consistent with the uncertainties of the trajectory determination) and provides essential information for mitigation purposes. Secondly, when the object performs a deep fly-by to our planet and a collision can be safely excluded, it shows the nominal trajectory and the associated uncertainty region and it provides an important graphical support for understanding the underlying dynamics. In this paper we will present in detail the functionalities of the ICV and FAV tools.

KEYWORDS: NEO, ICV, FAV, ILD

NOMENCLATURE

API – Application Programming Interface

ESA – European Space Agency

FAV – Fly-By Area Visualizer

ICV – Impact Corridor Visualizer

ILD – Impact Location Displayer

NEO – Near Earth Object

SSA – Space Situational Awareness

1 ICV TOOL

The ICV (Impact Corridor Visualizer) software is responsible for displaying in a user-friendly way the impact corridor area using the Google Map/Google Earth APIs and its main function is to plot the contour lines of the impact corridor on the Earth surface. It is available on the ESA NEO web portal but only to registered users having the necessary privileges.

1.1 Functionalities

The ICV tool already incorporates the following functionalities:

- Produces a high-quality 2D and 3D graphical visualization of the impact corridor on the ground for identified potential impactors with Earth, the Moon and other planets.
- Draws the boundaries of the region where an impact is possible.
- Allows the user to show information of the underlying data such as the time corresponding to impact locations and the corresponding geographical coordinates.
- Is able to produce an additional output suitable for printing on A4 paper.
- Is using Google Maps and Google Earth to represent the 2D Earth surface and the 3D Earth globe respectively.
- Uses the contour lines for displaying the impact corridor on the ground at different sigma levels (1, 3, and 5).
- Draws the contour lines corresponding to atmospheric entry, e.g. the contour lines at 100 km altitude.
- Uses a green colour to represent the impact corridor in the atmosphere and a red colour for the impact corridors on the Earth surface.
- Allows to exchange the standard topographic representation of the Earth surface with freely available thematic maps (e.g. population density).
- Runs on any browser adopting HTML 5 web technologies with no significant overhead time during the loading of the data.
- Accepts as input JS and KML formatted files in order to use existing software assets such as Google Earth/Maps.
- Produces graphical outputs downloadable in jpg format.
- Produces 2D interactive outputs using Google Maps.
- Allows displaying coordinates and time of impact using cursor-tips.
- Produces a downloadable file with instructions for displaying it on the user computer using Google Earth.
- Reports the total impact probability in the plot.

The ICV tool was implemented using JavaScript and Google APIs.

1.2 Snapshots of the functionalities

After authentication, the link to the ICV is made available on the web portal. By clicking the ICV link, a web page with the list of asteroids is made available. The last two columns in the provided table (see **Figure 1**) redirect to the visualizer corresponding to the selected object.

Past impactors list				
Object Name	Date/Time [UTC]	Impact Probability	2D map	3D visualization
2014AA	2014-01-02 01:33:55	1.0000		
2008TC3	2008-10-07 02:50:16	1.0000		

[Download as CSV file](#)
[Download as Excel file](#)

Figure 1: Past impactors list for ICV

The following figures present the functionalities using 2008TC3 asteroid:

- First view when 2D visualization window is opened and "Location region" functionality (**Figure 2**)
- View of 2D ICV for 2008TC3 at 100 km altitude over the terrain (**Figure 3**)
- View of 2D ICV for 2008TC3 at 0 km altitude over the terrain (**Figure 4**)
- View of 3D ICV for 2008TC3 at 100 km altitude over the terrain using .kml file and Google Earth (**Figure 5**)
- View of 3D ICV for 2008TC3 at 0 km altitude over the terrain using .kml file and Google Earth (**Figure 6**)



Figure 2: 2008TC3 ICV 2D view with Locate region enabled

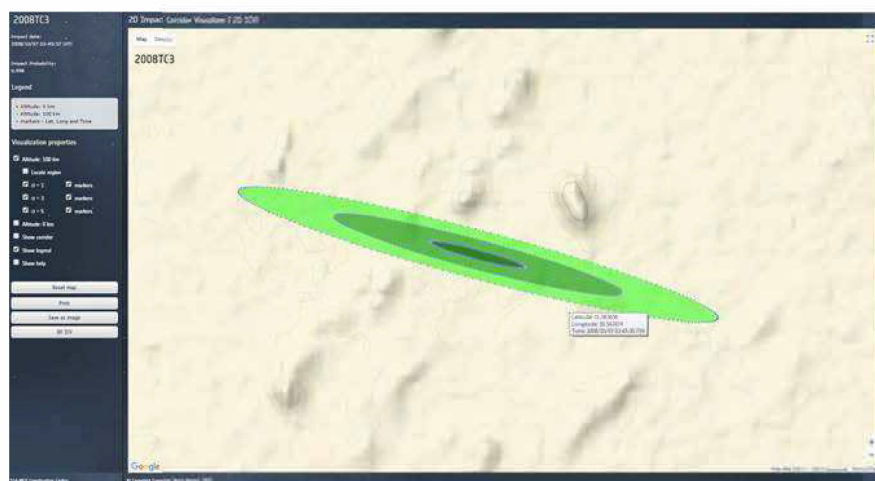


Figure 3: 2008TC3 ICV 2D view 100 km altitude over the terrain

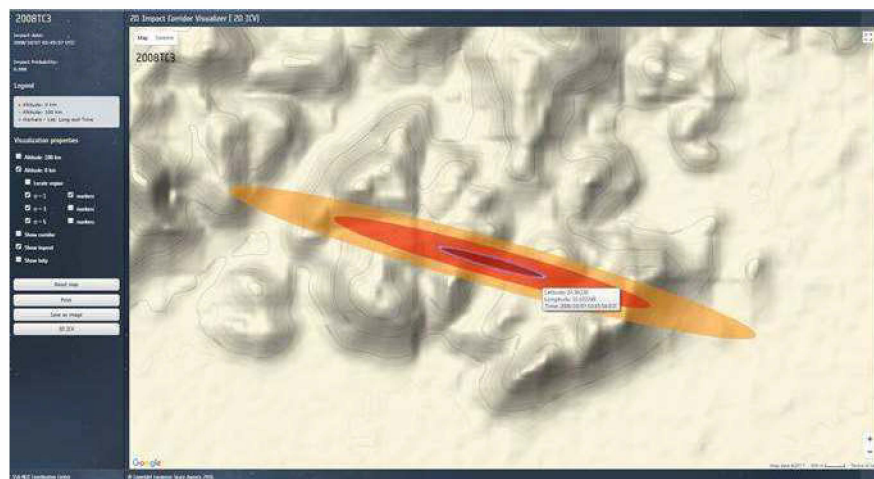


Figure 4: 2008TC3 ICV 2D view 0 km altitude over the terrain

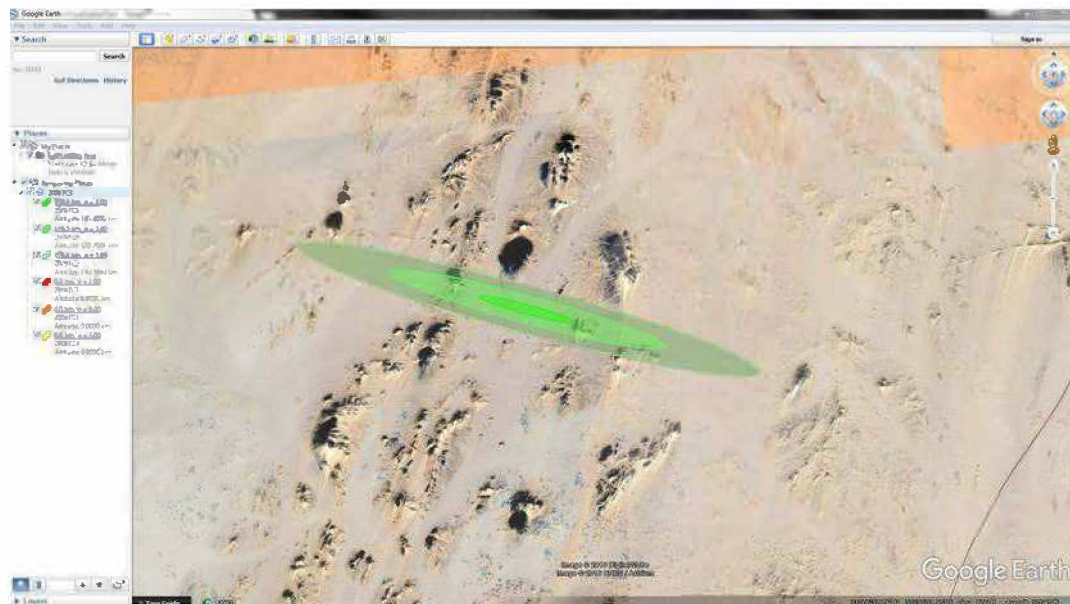


Figure 5: 2008TC3 ICV 3D view 100 km altitude over the terrain using .kml file and Google Earth

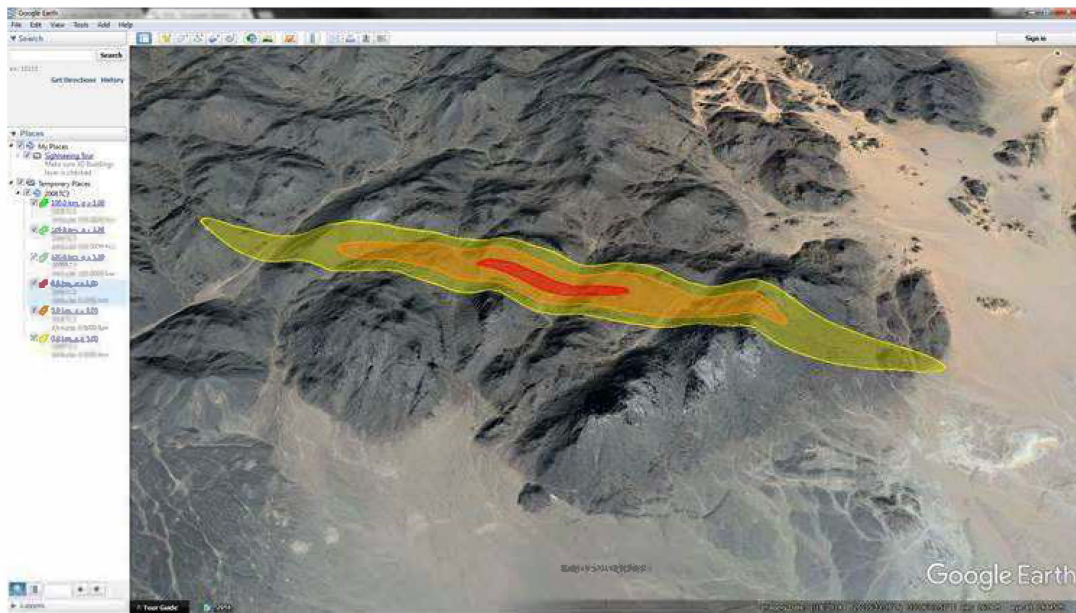


Figure 6: 2008TC3 ICV 3D view 0 km altitude over the terrain using .kml file and Google Earth

2 FAV TOOL

The FAV (Fly-By Area Visualizer) software is responsible for displaying in a user-friendly way the flyby area, which includes the nominal trajectory and the error ellipse contour lines at the time of closest approach. It plots on a 3D representation of the near-Earth space the nominal trajectory and the associated error ellipse. It is available on the ESA SSA-NEO web portal but only to registered users having the necessary privileges.

2.1 Functionalities

The FAV tool already incorporates the following functionalities:

- Produces a high-quality 3D graphical visualization of the flyby area near-Earth space for identified potential impactors with Earth, the Moon and other planets.
- Draws the nominal trajectory of the asteroid and the uncertainty area around it using contour lines.
- Is able to produce an additional output suitable for printing on A4 paper (e.g. using white background).
- Displays Earth fly-bys occurring at distances less than 3 lunar distances. If the fly-by occurs outside the threshold, it will be always possible to run the program on a single object on demand.
- Runs on any browser adopting HTML 5 web technologies with no significant overhead time during the loading of the data.
- Accepts as input JS files in order to use existing software.
- Shows on 3D visualization: the minimum distance during the close approach (i.e. the object distance at closest approach), the time of the closest approach, the position of the object at closest approach, a sampling of the confidence region boundary at closest approach, nominal trajectory, Sun direction with respect to the Earth at the time of the closest approach, position of the Moon at the time of the closest approach, Moon trajectory computed for the same time interval of the asteroid's flyby, Moon direction, axes, country borders, asteroid direction.
- Produces graphical outputs downloadable in jpg format.
- Draws a static 3D representation of the fly-by area.

- Allows the user to interactively change the point of view and the zooming factor.

The FAV tool was implemented using JavaScript API WebGL.

2.2 Snapshots of the functionalities

After authentication, the link to the FAV is made available on the web portal. By clicking the FAV link, a web page (**Figure 7**) with the list of asteroids is made available. The last column in the table redirects to the visualizer corresponding to the selected object.





Upcoming flyby list					
Object Name	Date/Time (UTC)	Min. Distance from Earth (AU)	Min. Distance from Earth (LD)	Min. Distance from Moon (LD)	Fly-by visualizer
2006SR131	2017-09-23 18:06:29	0.001079	0.421411	1.010026	
2012TC4	2017-10-12 08:03:03	0.00069	0.269349	1.192374	
2016HP6	2018-05-12 09:02:47	0.005476	2.295174	3.006379	
2014US7	2018-10-17 14:00:22	0.007333	2.864299	3.289565	
2014AK51	2019-01-06 19:18:11	0.001947	0.768736	1.74558	
2019QG	2019-03-04 20:42:28	0.003058	1.194635	1.629391	
2015WN1	2020-11-11 12:41:33	0.00078	0.282789	1.189985	
2015FP36	2021-05-19 00:29:51	0.00282	0.984315	1.542756	
2013ED68	2022-03-16 23:42:34	0.00171	0.667987	1.14131	
2016FZ11	2022-02-19 12:12:15	0.005454	2.130464	2.451464	

Figure 7: FlyBy table on NEOCC portal

Next figures will present the functionalities using different asteroids:

- 3D flyby visualization window for 2017OM1 asteroid at closest approach, the small confidence ellipse which means the position is very well determined, Earth-Sun direction, Moon position and trajectory functionality (**Figure 8**)
- 3D flyby visualization window for 2014US7 asteroid at closest approach, confidence ellipse is more visible (**Figure 9**)
- 3D flyby visualization window for 2015WN1 asteroid at closest approach, white background for printing, zoom, save as image and print functionality (**Figure 10**)

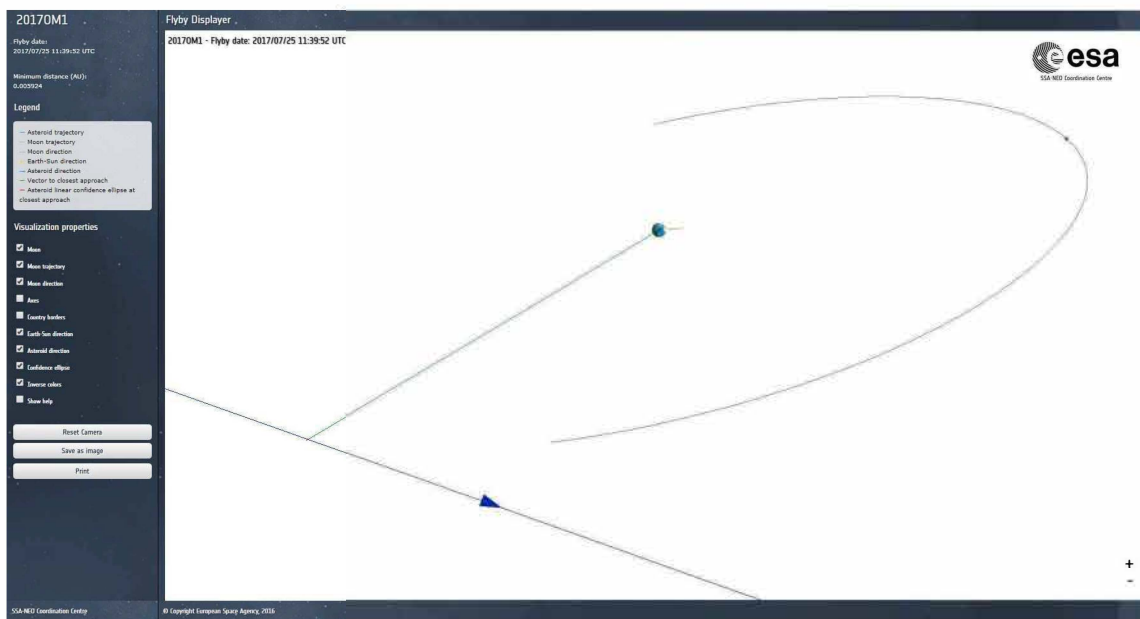


Figure 8: 3D flyby visualization window for 2017OM1 asteroid at closest approach

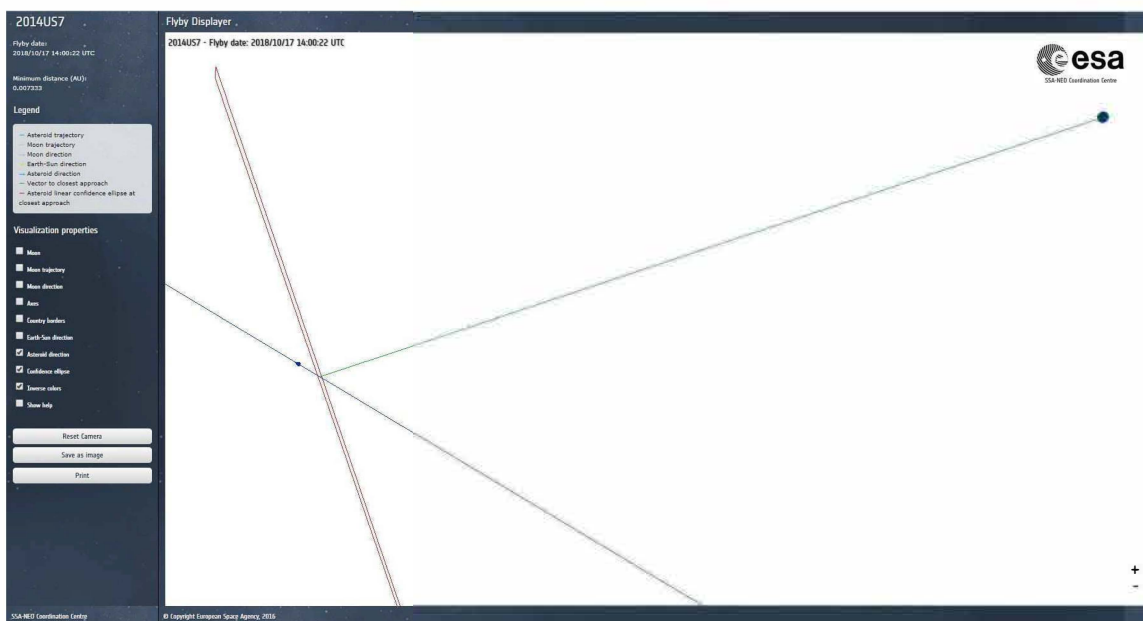


Figure 9: 3D flyby visualization window for 2014US7 asteroid at closest approach

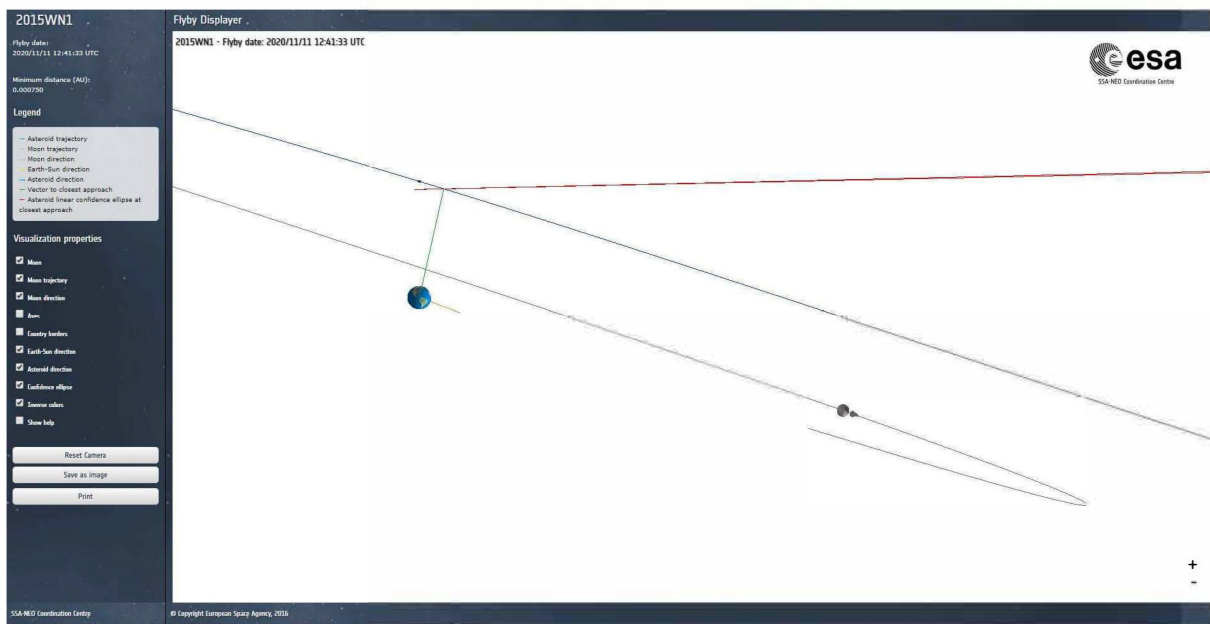


Figure 10: 3D flyby visualization window for 2015WN1 asteroid at closest approach

CONCLUSIONS:

In this paper we presented the main functionalities of the ICV tool that shows the impact corridor on Earth and of the FAV tool that shows the fly-by area during a close approach.

ACKNOWLEDGMENTS

This research was conducted under ESA contract No. 4000113555/15/D/MRP.
 Thanks to SpaceDyS S.R.L for computing the data used by the two graphical tools.

REFERENCES

- [1] Milani A.; 1999; *Icarus*, **137**; pp. 269-292
- [2] Milani A., Gronchi G. F.; 2010; Theory of Orbit Determination; Cambridge University Press
- [3] Milani A. et al.; 2005; *Icarus*, **173**; pp. 362-384

A new vision - Eco-friendly launching propulsion – The Future

Ene Călinescu Alexandru

Engineer

B-dul Callatis

Enealex90@gmail.com

ABSTRACT

The project contains a low pressure plastic with many powerful solenoids placed along the tube (from 10 to 10 m). This plastic tube is placed in a vertical position and it serves for launching satellites/remote controlled space-crafts. At the bottom, the satellite/remote controlled spacecraft will be positioned on a ferromagnetic material (a half-sphere for example) which will take the satellite/remote controlled spacecraft into space. During the lifting, some oil/air cushion will be placed inside the tube from place to place (around 2m) to keep the ferromagnetic material in the middle of the tube during the launching. The height of the prototype low pressure plastic tube will be 1km and the width of the tube will be 2m and will be placed at 1000m altitude. I've used a step by step method calculating all the values for velocity from the bottom of the tube until the ferromagnetic material leaves the low pressure tube to see, after some distance travelled into space, if it can beat the Earth's escape velocity of 11,186 km/s and reach the geostationary Earth orbit or even far.

KEYWORDS: *future, vision, space launcher, levitation*

NOMENCLATURE

1. LOW PRESSURE TUBE DESCRIPTION:

In the figure below it is presented the low pressure tube with all of its components:

- Anchoring devices (placed half outside the ground and the other side buried in the ground);
- Flexible supports available for supporting the tube against high pressure winds etc.
- The low pressure tube is made of solid plastic;
- The circles placed around the tube from place to place (around 10m) represent the solenoids
- The brown box represents the transformer station;
- The blue box represents the capacitor banks station;
- The green box represents the laboratory;
- The red vertical tube which is placed on the side of the low pressure tube represents the cable tray for the wires;
- The bearings from the upper part of the tube, attached to the flexible supports, are supposed to keep the parts all together;
- The flexible support from the bottom of the station which has a circle form has the purpose to keep the side flexible supports together;

Symbols and notations:

A – area of solenoid = 3,79 m²

I – solenoid current intensity = 1458 A

N – number of turns of the solenoid = 3000 turns

a – acceleration of the ferromagnetic material

d – distance that the ferromagnetic material has passed through the plastic tube

m – mass of the ferromagnetic material = 7000 kg

ρ – density of the air = 1,27 kg/m³

μ – magnetic permeability of the ferromagnetic material – Carbon steel $\approx 1,26 \cdot 10^{-4}$ H/m

F_S – force of the solenoid transferred to the ferromagnetic material

F_G – force of the ferromagnetic material represented by its weight

F_M – force transferred by the solenoid to the ferromagnetic material from which we decreased F_G

C_d – drag coefficient (for a half-sphere = 0,42)
 F_D – drag force
 A_S – area of the half-sphere = 2,54 m²
 v_i – initial velocity
 v_f – final velocity at different altitudes
 v_e – escape velocity in our case
 g_1 – Earth's standard gravitational acceleration = 9.81 m/s²
 g_2 – Earth's specific gravitational acceleration at relative height
 r_1 – Earth's radius = 6371km
 r_2 – radius at relative height (in our case 6372km, at the exit of the tube) beside Earth's center
 d_e – distance which the ferromagnetic material has travelled after it exits the plastic tube
 E_C – initial kinetic energy

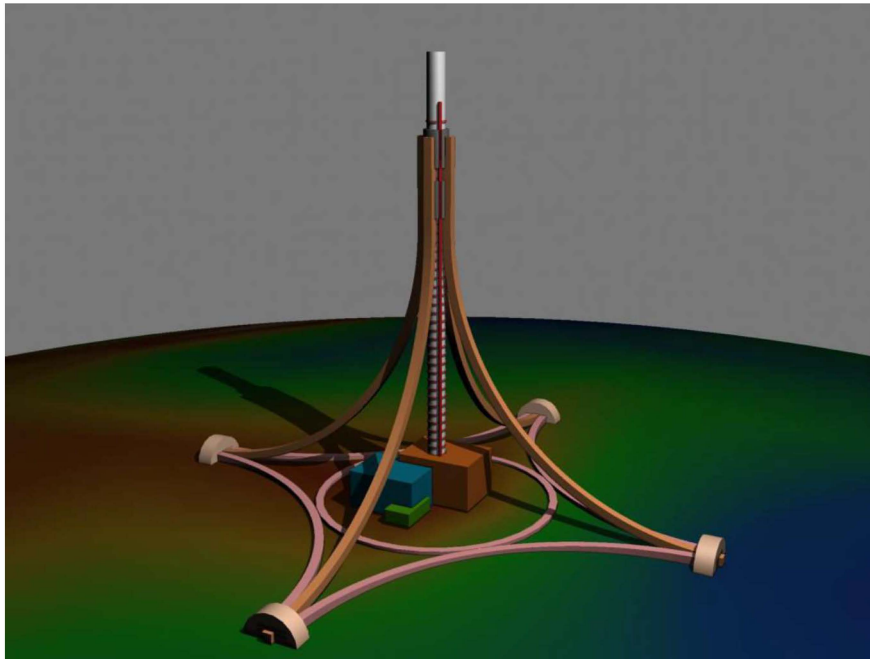


Figure 1: Low pressure tube launching station

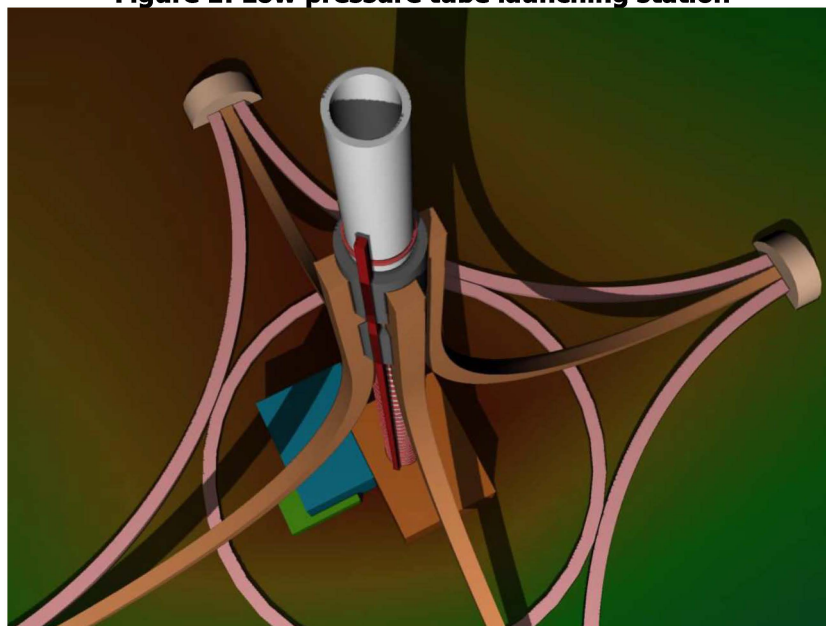


Figure 2: Low pressure tube launching station (top view)

2. LAUNCHING PRINCIPLES:

The propulsion force is created using solenoids powered by capacitor banks. The principle is the same as in reluctance coil-guns, by cutting off the current through a particular coil when the ferromagnetic material (on which the satellite/remote controlled spacecraft is positioned) reaches its center. After some distance, the next coil is activated (using sensors that detect when the ferromagnetic material reaches the optimum distance from the center of the coil).

3. CALCULATIONS:

The main problems that must be taken care of are the escape velocity, the velocity of the ferromagnetic material at the exit of the tube and of course the current intensity, number of turns, drag force, acceleration, etc.

To calculate the gravity at the exit of the plastic tube we need to apply the following formula:

$$\frac{g_1}{g_2} = \left(\frac{r_2}{r_1}\right)^2 \Rightarrow g_2 = \frac{g_1 \cdot r_1^2}{r_2^2} = \frac{9.81 \cdot 6371^2}{6372^2} = \frac{397778481,8}{40602384} = 9,79 \text{ m/s}^2 \quad (1)$$

The force created by the solenoid and transferred to the ferromagnetic material is calculated with the following formula:

$$F_s = (N \cdot I)^2 \cdot \frac{\mu \cdot A}{2g^2} = (3000 \cdot 1458)^2 \cdot \frac{1,26 \cdot 10^{-4} \cdot 3,79}{2 \cdot 9,80^2} = 47447052.48 \text{ N} \quad (2)$$

The force offered by the solenoid to ferromagnetic material (Newton's second law) from which we will decrease the force of the ferromagnetic material represented by its weight is found in the following equation:

$$F_M = F_s - F_G = F_s - m \cdot g_1 = 47447052.48 \text{ N} - 7000 \text{ kg} \cdot 9,81 \text{ m/s}^2 = 47378382.48 \text{ N}$$

$$F_M = m \cdot a \Rightarrow a = \frac{F_M}{m} = \frac{47378382.48 \text{ N}}{7000 \text{ kg}} = 6867,34 \text{ N} \quad (3)$$

The velocity of the ferromagnetic material offered by the solenoid (kinematics formula Eq.4):

- The velocity after the first solenoid ($\cong 10\text{m}$):

$$v_f^2 = v_i^2 + 2ad \quad (4)$$

$$v_f^2 = v_i^2 + 2ad = 0 \text{ m/s} + 2 \cdot 6867,34 \text{ m/s}^2 \cdot 10 \text{ m} \Rightarrow v_f = \sqrt{137346.8 \text{ m/s}^2} = 370.6 \text{ m/s}$$

**Table 1: Variation of V_f with altitude**

V_f (m/s)	V_i (m/s)	a (m/s ²)	Altitude (m)	Constant
370.6033	0	6867.34	10	2
641.9018	370.6	6867.34	20	2
907.7863	641.9	6867.34	30	2
1171.944	907.78	6867.34	40	2
1435.332	1171.94	6867.34	50	2
1698.311	1435.332	6867.34	60	2
1961.043	1698.311	6867.34	70	2
2223.615	1961.043	6867.34	80	2
2486.078	2223.615	6867.34	90	2
2748.464	2486.078	6867.34	100	2
3010.792	2748.464	6867.34	110	2
3273.077	3010.792	6867.34	120	2
3535.328	3273.077	6867.34	130	2
3797.552	3535.328	6867.34	140	2
4059.754	3797.552	6867.34	150	2
4321.938	4059.754	6867.34	160	2
4584.108	4321.938	6867.34	170	2
4846.265	4584.108	6867.34	180	2
5108.412	4846.265	6867.34	190	2
5370.55	5108.412	6867.34	200	2
5632.681	5370.55	6867.34	210	2
5894.804	5632.68	6867.34	220	2
6156.922	5894.804	6867.34	230	2
6419.035	6156.922	6867.34	240	2
6681.144	6419.035	6867.34	250	2
6943.249	6681.144	6867.34	260	2
7205.35	6943.249	6867.34	270	2
7467.448	7205.35	6867.34	280	2
7729.535	7467.44	6867.34	290	2
7991.628	7729.535	6867.34	300	2
8253.718	7991.628	6867.34	310	2
8515.806	8253.718	6867.34	320	2
8777.892	8515.806	6867.34	330	2
9039.907	8777.82	6867.34	340	2
9301.992	9039.907	6867.34	350	2
9564.075	9301.992	6867.34	360	2
9826.157	9564.075	6867.34	370	2
10088.24	9826.157	6867.34	380	2
10350.32	10088.24	6867.34	390	2
10612.4	10350.32	6867.34	400	2
10874.48	10612.4	6867.34	410	2
11136.56	10874.48	6867.34	420	2



11398.64	11136.56	6867.34	430	2
3476.567	2458.304	6867.34	440	2
4274.006	3476.567	6867.34	450	2
4958.329	4274	6867.34	460	2
5571.377	4958.32	6867.34	470	2
6134.559	5571.37	6867.34	480	2
6660.533	6134.55	6867.34	490	2
7157.514	6660.53	6867.34	500	2
7631.162	7157.51	6867.34	510	2
8085.582	7631.16	6867.34	520	2
8523.848	8085.58	6867.34	530	2
8948.328	8523.84	6867.34	540	2
9360.903	8948.32	6867.34	550	2
9763.09	9360.903	6867.34	560	2
10156.12	9763.09	6867.34	570	2
10541.01	10156.12	6867.34	580	2
10918.62	10541.01	6867.34	590	2
11289.69	10918.62	6867.34	600	2
11654.66	11289.5	6867.34	610	2
12014.43	11654.66	6867.34	620	2
12369.29	12014.43	6867.34	630	2
12719.65	12369.29	6867.34	640	2
13065.87	12719.65	6867.34	650	2
13408.28	13065.87	6867.34	660	2
13747.15	13408.28	6867.34	670	2
14082.75	13747.15	6867.34	680	2
14415.3	14082.75	6867.34	690	2
14745	14415.3	6867.34	700	2
15072.05	14745	6867.34	710	2
15396.61	15072.05	6867.34	720	2
15718.84	15396.61	6867.34	730	2
16038.88	15718.84	6867.34	740	2
16356.85	16038.88	6867.34	750	2
16672.88	16356.85	6867.34	760	2
16987.07	16672.88	6867.34	770	2
17299.53	16987.07	6867.34	780	2
17610.34	17299.53	6867.34	790	2
17949.08	17610.34	6867.34	800	2
18256.36	17949.08	6867.34	810	2
18562.25	18256.36	6867.34	820	2
18866.82	18562.25	6867.34	830	2
19170.13	18866.82	6867.34	840	2
19472.25	19170.13	6867.34	850	2
19773.22	19472.25	6867.34	860	2



20073.1	19773.22	6867.34	870	2
20371.94	20073.1	6867.34	880	2
20669.78	20371.94	6867.34	890	2
20966.66	20669.78	6867.34	900	2
21262.63	20966.66	6867.34	910	2
21557.72	21262.63	6867.34	920	2
21851.97	21557.72	6867.34	930	2
22145.41	21851.97	6867.34	940	2
22438.07	22145.41	6867.34	950	2
22729.99	22438.07	6867.34	960	2
23021.19	22729.99	6867.34	970	2
23311.7	23021.19	6867.34	980	2
23601.54	23311.7	6867.34	990	2
23896.67	23607.54	6867.34	1000	2

$V_f = 23896.67$ m/s represents the final velocity of the ferromagnetic material at the exit at the tube.

Drag force will be calculated with the following formula:

$$F_D = \frac{1}{2} \cdot \rho \cdot v_f^2 \cdot C_d \cdot A_s \quad (5)$$

$$F_D = \frac{1}{2} \cdot \rho \cdot v_f^2 \cdot C_d \cdot A_s = \frac{1}{2} \cdot 1,27 \frac{\text{kg}}{\text{m}^3} \cdot (23896.67 \text{ m/s})^2 \cdot 0,42 \cdot 2,54 = 16188.03 \text{ N}$$

Initial kinetic energy at the exit of the tube will be calculated with the following formula:

$$E_{C_i} = \frac{m \cdot v_i^2}{2} \quad (6)$$

$$E_{C_i} = \frac{m \cdot v_i^2}{2} = \frac{7000 \text{ kg} \cdot (23896.67 \text{ m/s})^2}{2} = 199,86 \cdot 10^{10} \text{ J}$$

The escape velocity after the ferromagnetic material has got out the low pressure tube at 35863 km above Earth will be calculated with the following equation:

$$V_e = \sqrt{\frac{E_{C_i} - F_D \cdot d_e}{m}} \quad (7)$$

$$V_e = \sqrt{\frac{E_{C_i} - F_D \cdot d_e}{m}} = \sqrt{\frac{199,86 \cdot 10^{10} \text{ J} - 16188.03 \text{ N} \cdot 35863 \text{ km}}{7000 \text{ kg}}} = 16894,73 \text{ m/s} = 60821,028 \text{ km/h}$$

As you can observe we can easily beat Earth's escape velocity of 11,186 km/h and going even far using these values for number of windings, current, the mass of the ferromagnetic material etc.

We must consider that in this example we used only the mass of the ferromagnetic material on which the satellite/remote controlled spacecraft is positioned for launching so we also need to add the weight of the satellite/remote controlled spacecraft to consider a real launching. Also air density, gravity and velocity will be modified as we increase the altitude.

This is just an example to show that it's possible and it can be done.



4. REFERENCES:

1. Prof. dr. ing. AL. Fransua, Asist. Univ. Ing. S. Canescu; 1969; "Electronică și electrotehnică" ("Electronics & Electrotehnics")
2. www.physicsforums.com
3. www.wikipedia.com
4. www.google.com

Launch Vehicle - MDO in the development of a Microlauncher

Tudorel-Petronel AFILIPOAE

INCAS - National Institute for Aerospace Research "Elie Carafoli"

Research Scientist

B-dul Iuliu Maniu 220, 061126, Bucharest, Romania

afilipoae.tudorel@incas.ro

Ana-Maria NECULĂESCU

INCAS - National Institute for Aerospace Research "Elie Carafoli"

Research Scientist

neculaescu.ana@incas.ro

Alexandru-Iulian ONEL

INCAS - National Institute for Aerospace Research "Elie Carafoli"

Research Scientist

onel.alexandru@incas.ro

Mihai-Victor PRICOP

INCAS - National Institute for Aerospace Research "Elie Carafoli"

Head of INCAS Flow Physics Department

pricop.victor@incas.ro

Alexandru MARIN

INCAS - National Institute for Aerospace Research "Elie Carafoli"

Assistant manager

marin.alexandru@incas.ro

Alexandru-Gabriel PERȘINARU

INCAS - National Institute for Aerospace Research "Elie Carafoli"

Aerospace engineer

persinaru.alexandru@incas.ro

Alexandru-Mihai CIȘMILIANU

INCAS - National Institute for Aerospace Research "Elie Carafoli"

Research Scientist

cismilianu.alexandru@incas.ro

Ionuț-Cosmin ONCESCU

INCAS - National Institute for Aerospace Research "Elie Carafoli"

Research Scientist

oncescu.ionut@incas.ro

Adrian TOADER

INCAS - National Institute for Aerospace Research "Elie Carafoli"

Research Scientist

toader.adrian@incas.ro

Adriana SIRBI

ESA - European Space Agency

FLPP Technologies Project Manager

Rue Jacques Hillairet 52, 75012, Paris, France

adriana.sirbi@esa.int



Samir BENNANI
ESA - European Space Agency
GNC Systems Engineer
Keplerlaan 1, 2201 AZ Noordwijk, Netherlands
samir.bennani@esa.int

Teodor-Viorel CHELARU
Research Center for Aeronautics and Space, University POLITEHNICA of Bucharest,
Professor
Str. Ghe. Polizu, no. 1, Bucharest, Romania
teodor.chelaru@upb.ro

ABSTRACT

In the Frame of Romanian Incentive Scheme Programme under European Space Agency, a feasibility study of a Small Orbital Launcher was performed by "Politehnica" University of Bucharest. Building on the results obtained in the project, European Space Agency's Space Transportation Directorate through the Future Launchers Preparatory Programme awarded INCAS a Phase 0/A contract for a microlauncher concept. The targeted market is the micro-satellites sector developed by universities, but also by small companies for research purpose and validation of applications/products before commercialization, with a mass lower than 150 kg. This paper presents a conceptual design for a microlauncher having a target mission to deliver a small satellite of 150 kg into a 600 km circular polar orbit with the launching site located in Europe. The microlauncher concept is obtained using an in-house multi-disciplinary optimization tool, which contains four modules: weights and sizing, aerodynamics performance assessment, propulsion, trajectory computation and optimization.

KEYWORDS: small launcher, multi-disciplinary optimization, small satellites, polar orbit

Aviation Regulations of Russia: a Transition from One Type to Another

Oleksiy Chernykh

Nanjing University of Aeronautics and Astronautics, College of Civil Aviation

Assistant Professor

29 Jiangjun Avenue, Nanjing, 211106, Jiangsu province, China

alex@nuaa.edu.cn

Mambet Bakiiev

Antonov Company, Department of Fuselage Airframe Computer Projects

Design Engineer

1 Tupolev Street, Kyiv, 03062, Ukraine

mambet12@gmail.com

ABSTRACT

Chinese Aerospace Engineering has lately initiated a wide-body airplane project which has been planned to be designed and built in close cooperation with Russia. This aim has raised the necessity of studying Russian airworthiness management system. The presented paper highlights a transition period in work of Russian aviation authorities, which is conditioned by two types of aviation regulations being in use in the Russian Airworthiness and Operations management system, and continuous reformations of aviation agencies. The two types of aviation regulations used in Russia have been: the Aviation Regulations and the Federal Aviation Regulations. The transition is accompanied with a number of challenges to be dealt with, such as: a non-unified structure of regulations on Aircraft Operation management, various independent agencies responsible for regulation issuance and control instead of one national aviation authority, confusions in naming and referencing. Additionally, the paper offers a list of currently effective Russian regulations of both types as of November 2016.

KEYWORDS: *Russian Aviation Regulations, Russian Federal Aviation Regulations, Aircraft Airworthiness management, Aircraft Operation management*

1 INTRODUCTION

For a long time, China has been an operator of foreign-built aircraft purchased overseas. In recent years, the development trend has been directed towards advancing the works of designing and manufacturing own Chinese aircraft. Namely, the efforts of Chinese COMAC Aircraft Company (中国商用飞机有限责任公司) have been extended to a new long range wide-body commercial airplane (C929/C939) which has been planned in collaboration with Russia. In 2017, it has been announced that a new joint venture named the China-Russia Aircraft International Corporation (CRAIC) involving COMAC Aircraft Company and Russia's United Aircraft Corporation (UAC) has been founded to be in charge of the planned cooperation [1].

A new airplane cannot enter into a serial production and commercial flight operation until a manufacturer has demonstrated the compliance of an airplane with aviation airworthiness regulations under guidance and supervision of a national aviation authority. Aircraft airworthiness substantiation closes the entire aircraft development process. Since the established China-Russia joint cooperation has involved a foreign country as the "second party", Russian aviation regulations have become a challenge for Chinese professionals in Aerospace industry to be additionally taken into consideration during the whole process of aircraft development. This fact has also been put on the basis of further improvement of educational trends in Chinese Aerospace-related universities [2].

The above-mentioned challenge of working with Russian regulations is caused by their principal differences (in structure and content arrangement) from Chinese Civil Aviation Regulations (CCAR) and worldwide known Federal Aviation Regulations (FAR or 14 CFR, being part of Title 14 of the Code of Federal Regulations) of the Federal Aviation Administration (FAA) of the U.S.A. or Certification Specifications (CS) of the European Aviation Safety Agency (EASA) of the European Union.



The Russian aviation regulations consist of two principal types:

- (1) the Aviation Regulations and
- (2) the Federal Aviation Regulations.

The full list of Russian aviation regulations covering documents of both types, to the authors' knowledge, hasn't been found in open English-language sources and hasn't even been provided in Russian-language informative space. However, the regulations themselves can be collected on a number of official websites of Russian authorities.

The Interstate Aviation Committee (IAC), being responsible for issuance of the 1st type of regulations, the Aviation Regulations, lists them on the official website [3]. The 2nd type of regulations, the Russian Federal Aviation Regulations have been issued and handled by separate agencies that manage aviation industry in Russia: the Government of the Russian Federation [4], the Ministry of Transport [5], the Ministry of Defence [6], the Federal Air Transport Agency [7], the State Corporation for Space Activities [8], and the Ministry of Industry and Trade [9]. As a result, the Federal Aviation Regulations have been spread on the websites of those ministries and agencies, unfortunately, in an uncoordinated manner. Each ministry or an agency only offers documents of its own issuance, direct influence and control [2, 4-9]. This is, on the one hand, reasonable, but, on the other hand, it brings extra difficulties when regularly attempting to keep database of currently effective documents updated.

Surprisingly, even though the early Russian Federal Aviation Regulations have started to be issued since 1998 [10], they haven't even been mentioned in the book on certification of Russian aviation products [11] published by Krasotkin, the IAC Aviation Register chairman Advisor, 9 years later in 2007. The book of Krasotkin contains only a short list of the 1st type, the Aviation Regulations, not covering all of them, and no any mentioning of documents of the 2nd type, the Federal Aviation Regulations.

The Federal Aviation Regulations have been in use for almost 20 years. But there has not been composed any fully unified list of the regulations so far. However, it is worth noting, the first attempt to compose such a unified list of all Russian aviation regulations has been made by the Federal State Unitary Enterprise Scientific Research Institute of Standardization and Unification in 2014 resulting in establishment of the Unified System of Aviation Standards [12], but its website hasn't been properly updated since 2014, so it has been found providing regulations which are no more effective.

This paper attempts to bridge the gap offering the full list of Russian aviation regulations (of both types) collected by the authors as of November 2016.

2 AVIATION REGULATIONS (AP)

The Aviation Regulations (AP) [13] have been issued by the Interstate Aviation Committee (IAC) and are effective in all member countries of the interstate Civil Aviation and Airspace Use Treaty [14]. Russia, being a member of the IAC, also adopted this set of regulations since it had signed the Treaty in 1991.

The Aviation Regulations (AP) contents have been published in Russian language exceptionally [13]. The regulations are commonly shortened to a confusing abbreviation "AP" (instead of "AR") which has come from a transliteration "Aviatsionnye Pravila" of their Russian name "Авиационные Правила". The content has been arranged in Parts with a serial number "AP-XXX". The list and titles of the AP regulations can be found on the official website of the IAC [3] and are given below with explanations (the IAC website's original translation into English):

1. AP-21. Certification procedures for Aeronautical Products, Design Organisations and Manufacturers.
2. AP-23. Airworthiness standards for Light Airplanes. *(invalid in Russia)*
3. AP-25. Airworthiness standards for Transport category Airplanes. *(invalid in Russia)*
4. AP-OLS. Airworthiness standards for Very Light Airplanes. *(AP-VLA – literally)*
5. AP-27. Airworthiness standards for Normal category Rotorcraft. *(invalid in Russia)*
6. AP-29. Airworthiness standards for Transport category Rotorcraft.
7. AP-31. Airworthiness standards for Manned Free Balloons.
8. AP-33. Airworthiness standards for Engines.
9. AP-34. Emission Requirements.
10. AP-VD. Airworthiness standards for Auxiliary Power Units. *(AP-APU – literally)*
11. AP-35. Airworthiness standards for Propellers.



12. AP-36. Noise Certification. (invalid in Russia)
13. AP-39. Airworthiness Directives.
14. AP-139. Certification of Aerodromes. (invalid in Russia)
 - Volume I – Procedures for Certification of Aerodromes.
 - Volume II – Certification Requirements to Aerodromes.
15. AP-145. Repair Stations.
16. AP-170. Certification of Aerodrome and En-Route Equipment.
 - Volume I – Procedures for Certification of Aerodrome and En-Route Equipment. (invalid in Russia)
 - Volume II – Certification Requirements to Aerodrome and En-Route Equipment. (invalid in Russia)
17. AP-183. Aviation Register Representatives. (invalid in Russia)

One more example of a transliterated abbreviation found in the list needs to be explained:

- AP-OLS stands for "*Ochen Legkie Samolety*" (Russian: *Очень Легкие Самолеты*) and means "*Very Light Airplanes*".
- AP-VD stands for "*Vspomogatelnyi Dvigatel*" (Russian: *Вспомогательный Двигатель*) and means "*Auxiliary Power Unit*".

In general, the Parts of the Aviation Regulations (AP) follow the typical content structure and serial numbers of worldwide commonly accepted structure of regulations (such as, of the American FAR regulations). This has been an outcome of a continuous harmonization process started in 1990s by the Interstate Aviation Committee (IAC) [11]. But it's worth noting that the AP regulations do not have as many parts and do not cover as large scope of topics as the American FAR regulations or European CS rules do. The issued Parts primarily contain Initial Airworthiness matters and are all listed above.

However, it has recently been announced that the seven AP Parts (AP-23, AP-25, AP-27, AP-36, AP-139, AP-170 Volume I, and AP-183) have become ineffective in Russia and the relevant governmental orders have been signed [15,16]. Although, Russia hasn't left the Treaty, still keeping its membership. And the Parts themselves continue to remain effective in all other member countries as the Parts of the AP regulations managed by the Interstate Aviation Committee (IAC).

3 FEDERAL AVIATION REGULATIONS (FAP)

The Federal Aviation Regulations (FAP) [10] have been issued as Orders of various Russian agencies [2, 4-9] working in Aviation field. The abbreviation is shortened as "*FAP*" which has also come from a transliteration "*Federal'nye Aviatsionnye Pravila*" of the Russian name "*Федеральные Авиационные Правила*". It's worth highlighting, the FAP regulations are considered Russian national regulations being effective in Russia exceptionally.

It has been largely surprised that the name of the Russian regulations sounds completely identical to the American Federal Aviation Regulations (FAR). Such confusion has been due to the fact that the full name of Russia as a country has been "*the Russian Federation*". This is why all Russian governmental organizations hold the Federal status, and the word "*Federal*" has also come into the name of Russian national regulations. To reduce misunderstanding, the above-mentioned abbreviation "*FAP*" has been established.

The FAP regulations contents have also been published in Russian language only [10], being distributed among numerous separate documents named "*Orders*". Their numbering has been with a serial number and a year of issuance, such as "*Order XXX (Year)*". It has been noted above that the full list of the FAP regulations hasn't been found in open sources. Having been collected by the authors, they are listed below according to responsible authorities (the authors' translation into English):

- *Orders of the Government of the Russian Federation*
1. *Order 360 (1998)*. About Federal Regulations of airspace use and Federal Aviation Regulations.
 2. *Order 138 (2010)*. Federal Regulations of Russian Federation airspace use.
 3. *Order 530 (2008)*. Federal Aviation Regulations of search and rescue in the Russian Federation.
 4. *Order 303 (2000)*. Rules of aircraft accident and incident investigation for Experimental Aircraft.
 5. *Order 1329 (1999)*. Rules of aircraft accident and incident investigation for Public Aircraft.
 6. *Order 609 (1998)*. Rules of aircraft accident and incident investigation for Civil Aircraft.



----- *Orders of the Ministry of Transport*

7. *Order 262 (2015)*. Requirements to aerodromes intended for take-off, landing, taxiing, and parking of Civil aircraft.
8. *Order 251 (2015)*. Procedure of state registration of Civil Aviation aerodromes and heliports.
9. *Order 250 (2015)*. Procedure of landing ground owner's notification on commencement, suspension, or termination of landing ground operation for Civil aircraft flights, and registration in Civil Aviation authority.
10. *Order 216 (2015)*. Requirements to juridical persons who implement aeronautical service for aircraft of Russian Federation airspace users.
11. *Order 297 (2014)*. Radio communication support of aircraft flights and aircraft electrical communication in Civil Aviation.
12. *Order 60 (2014)*. Meteorological information support for aircraft flight management.
13. *Order 32 (2014)*. Requirements to Civil Aviation personnel license formatting.
14. *Order 362 (2012)*. Implementation of radio communication in Russian Federation airspace.
15. *Order 6 (2012)*. Russian Federation airspace use planning and management.
16. *Order 293 (2011)*. Air transport management in the Russian Federation.
17. *Order 69 (2011)*. Requirements to landing grounds located on land and water.
18. *Order 249 (2009)*. Requirements to mandatory certification of natural and juridical persons performing aviation works. Certification procedure.
19. *Order 216 (2009)*. Requirements to air traffic dispatchers and parachute instructors.
20. *Order 128 (2009)*. Flight preparation and implementation in Civil Aviation.
21. *Order 147 (2008)*. Requirements to air crew men, aircraft maintenance engineers, and flight support crew / flight dispatchers in Civil Aviation.
22. *Order 141 (2008)*. Rules of dangerous cargo transportation by civil aircraft.
23. *Order 82 (2007)*. General Regulations of passenger, baggage, cargo air transportation and requirements to passenger, consignor, consignee service.
24. *Order 142 (2005)*. Aviation safety requirements to airports.
25. *Order 31 (2005)*. Joint facilities of air traffic implementation.
26. *Order 1 (2005)*. Flight checks of ground radio communication equipment, aircraft electrical communication, and light signalling equipment of Civil Aviation aerodromes.
27. *Order 202 (2003)*. Technical means for Aviation work implementation. Requirements and certification procedures.
28. *Order 150 (2003)*. Certification requirements to juridical persons engaged in airport works in passenger, baggage, cargo and mail service.
29. *Order 149 (2003)*. Certification requirements to juridical persons engaged in airport works in electrical light support of flights.
30. *Order 147 (2003)*. General Aviation operators. Requirements to General Aviation operators, procedures of registration and inspection of General Aviation operator service.
31. *Order 132 (2003)*. Aircraft Example. Requirements and certification procedures.
32. *Order 118 (2003)*. Rules of putting single aircraft examples into General Aviation service.
33. *Order 29 (2003)*. Aviation safety requirements to General Aviation operators.
34. *Order 19 (2003)*. Certification of ground aviation equipment.
35. *Order 126 (2002)*. Certification requirements to organizations implementing quality check for aircraft fuel, oils, lubricants and special liquids.

----- *Orders of the Ministry of Defence*

36. *Order 265 (2009)*. Medical support of Public Aviation flights.
37. *Order 60 (2009)*. Unification of Public aviation personnel work conditions.
38. *Order 150 (2007)*. Federal Aviation Regulations of Public Aviation Navigation.
39. *Order 275 (2004)*. Federal Aviation Regulations of Public Aviation flight implementation.
40. *Order 460 (2002)*. State registration of Public aircraft.
41. *Order 440 (2002)*. State registration of Public Aviation aerodromes.
42. *Order 431 (2001)*. Federal Aviation Regulations of ground service organization in Public Aviation.
43. *Order 420 (2001)*. Organization of objective supervision in Public Aviation.
44. *Order 412 (2001)*. Organization of training centre in Public Aviation.

----- *Orders of the Russian Air Navigation Agency (abolished in 2009)*

45. *Order 119 (2007)*. Placement of marking facilities on buildings, constructions, communication lines, electricity lines, radio equipment and other units installed for aircraft flight safety protection.
46. *Order 116 (2007)*. Certification Regulations for joint facilities of air traffic implementation.



- *Orders of the Russian Aerospace Agency (present name – State Corporation for Space Activities)*
47. *Order 165 (2003)*. Organization of works of experimental aviation medical staff.
48. *Order 164 (2003)*. Organization of flight medical centre works for examination of experimental aviation.
49. *Order 80 (2003)*. Flight medical examination of experimental aviation flight staff.
- *Orders of the Federal Air Transport Service (present name – Federal Air Transport Agency)*
50. *Order 121 (2000)*. Certification requirements to juridical persons who implement airport work in aerodrome support of aircraft flights.
51. *Order 89 (2000)*. Certification requirements to organizations of aviation fuel supply for air transportation.
52. *Order 115 (1999)*. Certification of juridical persons who implement medical examination of aviation staff.
53. *Order 10 (1999)*. Mandatory certification of organizations engaged in supply of onboard food for passengers and air crew.
- *Collective Order of Russian Ministries*
54. *Order 136/42/51 (2002) of the Ministry of Defence, Ministry of Transport, Russian Aerospace Agency*. Federal Aviation Regulations of flights in airspace of the Russian Federation.
- *Orders commonly referred to as "FAP-XXX" with a serial number*
55. "FAP-16". *Order 397 (2007) of the Government*. About the improvement of state regulation of air carriers in air transportation.
56. "FAP-67". *Order 50 (2002) of the Ministry of Transport*. Medical examination of air crew, dispatchers, flight attendants, pilot students, and entrants to schools of Civil Aviation.
57. "FAP-119". *Order 246 (2015) of the Ministry of Transport*. Requirements to juridical persons, private entrepreneurs, who implement commercial air transportation.
58. "FAP-142". *Order 289 (2015) of the Ministry of Transport*. Requirements to educational institutions and organizations preparing aviation specialists of proper level.
59. "FAP-145". *Order 285 (2015) of the Ministry of Transport*. Requirements to juridical persons, private entrepreneurs, who implement maintenance of Civil Aviation aircraft.
60. "FAP-151". *Order 286 (2015) of the Ministry of Transport*. Requirements to operators of Civil Aviation aerodromes.
61. "FAP-173". *Order 270 (1998) of the Federal Aviation Service*. Radio communication support of aircraft flights and aircraft electrical communication. Certification requirements.

It can be found in the list (e.g. positions 55-61) that some of the Orders, in addition to their serial number and a year, have commonly been referred to as "FAP-XXX" with a separate serial number [17-21]. But it's worth noting that neither of above-mentioned serial numbers "FAP-XXX" can be seen in body of a relevant Order, for example [22]. It means that these references "FAP-XXX" can just be treated as a professional slang intended to simplify work with the FAP regulations just indicating the corresponding American FAR regulations but **NOT** having any legal power.

In general, the Russian Federal Aviation Regulations (FAP) are mainly used for Aircraft Operation and Continued Airworthiness management. But the content structure significantly differs from relevant American or European regulations. The FAP regulations display their own content structure [10,22,23] not following typical Aircraft Operation regulations, such as in the American FAR parts [24], or the European CS parts [25], and being very different from the International Civil Aviation Organization (ICAO) regulatory documents [26].

The absolutely non-unified structure of the Russian Federal Aviation Regulations (FAP) is supposed to be a consequence of the distribution of Airworthiness management tasks and responsibilities among a number of independent agencies [2, 4-9] instead of establishing one main national aviation authority that has been a common way in other countries.

4 CONCLUSION

The collaboration between Chinese Aerospace industry and Russia has been found to have certain difficulties in regulation management system. The main reason is that the Russian regulations content is arranged into parts differently from Chinese regulations, not being fully harmonized with unified American or European Union regulations either. The Russian Aerospace industry is currently utilizing two different types of regulations: (1) the Aviation Regulations (AP) and (2) the Federal Aviation Regulations (FAP).

The both types of regulations are still in use within their particular appliance. The 1st type, the Aviation Regulations (AP), contains Initial Airworthiness requirements providing a corresponding



to the worldwide regulations commonly adopted structure of contents. The 2nd type, the Federal Aviation Regulations (FAP), concentrates on Aircraft Operation and Continued Airworthiness requirements. And it has indeed legally been treated as national Russian regulations. The main concern is that the FAP regulations follow unusual arrangement of contents being distributed among numerous Orders which have been managed by a wide range of independent Russian authorities.

Other confusing key issues have also been addressed to be shared among international Aerospace industry professionals in order to minimize risks of misunderstanding the Russian regulations, such as shortening to "AP" and "FAP" abbreviations which has been caused by transliteration of their Russian names; referring to Orders with an indicating reference of "FAP-XXX" that has been advised to avoid such cases keeping to a reference of "Order XXX (Year)" exceptionally.

To conclude with, the lists of the Russian regulations of the two types clearly display that the Aviation Regulations (AP) are on the way to become completely ineffective having more and more Parts invalidated. Meanwhile, there are more and more Orders of the Federal Aviation Regulations (FAP) having been issued in recent 5-10 years. However, for instance, there haven't been found any FAP regulations focused on Initial Airworthiness aspects, while appropriate AP regulations Parts have already become ineffective resulting in a fact of confusion caused to interested parties of the Russian Aerospace industry. The Russian Airworthiness and Operations management system is currently going through a difficult transition phase full of reformations from one type of regulations to another.

REFERENCES

1. 2017; "China, Russia Join Hands to Develop Wide-body Jumbo"; <http://www.airshow.com.cn>
2. O. Chernykh, M. Bakiiev; 2016; "Learning of Russian Aviation regulations by Chinese and international students"; *Asian Workshop on Aircraft Design Education*, Nanjing; October, 8 - 11; pp. 130 - 134
3. 2016; "Interstate Aviation Committee"; <http://www.mak-iac.org>
4. 2016; "Government of the Russian Federation"; <http://government.ru>
5. 2016; "Ministry of Transport of the Russian Federation"; <http://www.mintrans.ru>
6. 2016; "Ministry of Defense of the Russian Federation"; <http://mil.ru>
7. 2016; "Federal Air Transport Agency of the Russian Federation"; <http://www.favt.ru>
8. 2016; "State Corporation for Space Activities of the Russian Federation"; <http://www.roscosmos.ru>
9. 2016; "Ministry of Industry and Trade of the Russian Federation"; <http://www.minpromtorg.gov.ru>
10. №360; 27.03.1998 (ред. от 18.02.2016); "О федеральных правилах использования воздушного пространства и федеральных авиационных правилах"; *Постановление*, Правительство Российской Федерации (No.360; 27.03.1998 (ed 18.02.2016); "About Federal Regulations of airspace use and Federal Aviation Regulations"; *Order*, Government of the Russian Federation) (in Russian)
11. A.A. Красоткин; 2007; *Сертификация Авиационной Техники*, Московский Авиационный Институт; Москва (A.A. Krasotkin; 2007; *Certification of Aircraft*, Moscow Aviation Institute; Moscow) (in Russian)
12. 2016; "Unified System of Aviation Standards"; <http://esas.niisu.ru>
13. АП Часть 21; 2013; "Сертификация Авиационной Техники, Организаций Разработчиков и Изготовителей"; *Авиационные Правила*, Межгосударственный Авиационный Комитет (AP Part 21; 2013; "Certification Procedures for Aeronautical Products, Design Organizations and Manufacturers"; *Aviation Regulations*, Interstate Aviation Committee) (in Russian)
14. 25.12.1991; "О гражданской авиации и об использовании воздушного пространства"; *Соглашение*, Минск (25.12.1991; "Civil Aviation and Airspace use"; *Treaty*, Minsk) (in Russian)
15. №11; 25.01.2016; "Об отмене приказов Министерства Транспорта Российской Федерации"; *Приказ*, Министерство Транспорта Российской Федерации (No.11; 25.01.2016; "About invalidation of Orders of the Ministry of Transport of the Russian Federation"; *Order*, Ministry of Transport of the Russian Federation) (in Russian)
16. №316; 26.10.2015; "Об отмене приказа Министерства Транспорта Российской Федерации от 06.11.2014 №308"; *Приказ*, Министерство Транспорта Российской Федерации (No.316; 26.10.2015; "About invalidation of the Order of the Ministry of Transport of the Russian Federation from 06.11.2014 No.308"; *Order*, Ministry of Transport of the Russian Federation) (in Russian)



17. К.Э. Акопян, А.Н. Арепьев, В.С. Шапкин; 2011; "Совершенствование нормативно-правовой и методической базы эксплуатации воздушных судов иностранного производства в авиапредприятиях Российской Федерации"; *Научный Вестник Московского Государственного Технического Университета Гражданской Авиации*, **163**; с. 7 - 13
 (K.E. Akopyan, A.N. Arepjev, V.S. Shapkin; 2011; "Perfection of normative-legal and methodical documents of operation of foreign manufacture airplanes in the air enterprises of Russian Federation"; *Scientific Bulletin of Moscow State Technical University of Civil Aviation*, **163**; pp. 7 - 13) (in Russian)
18. М.С. Громов, С.В. Диогенов, В.С. Шапкин; 2009; "Проблемы государственного контроля и регулирования процессов поддержания летной годности и обеспечения безопасности полетов воздушных судов гражданской авиации на современном этапе и пути их решения"; *Научный Вестник Московского Государственного Технического Университета Гражданской Авиации*, **141**(серия Аэромеханика, прочность, поддержание летной годности ВС); с. 14 - 22
 (M.S. Gromov, S.V. Diogenov, V.S. Shapkin; 2009; "Problems of state's control and regulating of airworthiness continuing and providing of flight safety of civil aircraft at modern stage and ways of its solution"; *Scientific Bulletin of Moscow State Technical University of Civil Aviation*, **141**(series Aeromechanics, strength, aircraft airworthiness); pp. 14 - 22) (in Russian)
19. А.А. Кулешов; 2009; "Концептуальные аспекты развития и функционирования системы послепродажного обеспечения отечественной авиационной техники на современном этапе"; *Научный Вестник Московского Государственного Технического Университета Гражданской Авиации*, **141**(серия Аэромеханика, прочность, поддержание летной годности ВС); с. 23 - 29
 (A.A. Kuleshov; 2009; "Conceptual aspects of development and functioning of system of maintenance of domestic air engineering after sale at the present stage"; *Scientific Bulletin of Moscow State Technical University of Civil Aviation*, **141**(series Aeromechanics, strength, aircraft airworthiness); pp. 23 - 29) (in Russian)
20. И.Г. Кирпичев, А.Ю. Коньков, А.Н. Шарыпов; 2010; "Анализ и перспективы развития системы сертификации организаций-поставщиков АТИ в рамках закона о техническом регулировании"; *Научный Вестник Московского Государственного Технического Университета Гражданской Авиации*, **153**(серия Аэромеханика, прочность, поддержание летной годности); с. 106 - 112
 (I.G. Kirpichev, A.U. Konkov, A.N. Sharyпов; 2010; "Analysis and perspectives of development the system of procedures of the suppliers of aviation products and parts under the law technical regulation"; *Scientific Bulletin of Moscow State Technical University of Civil Aviation*, **153**(series Aeromechanics, strength, aircraft airworthiness); pp. 106 - 112) (in Russian)
21. М.С. Громов, В.С. Шапкин; 2006; "Особенности поддержания летной годности экземпляра ВС в условиях безремонтной эксплуатации"; *Научный Вестник Московского Государственного Технического Университета Гражданской Авиации*, **103**(серия Аэромеханика и прочность, поддержание летной годности ВС); с. 7 - 13
 (M.S. Gromov, V.S. Shapkin; 2006; "Features of maintenance by the validity of an airplane in conditions of operation without repair"; *Scientific Bulletin of Moscow State Technical University of Civil Aviation*, **103**(series Aeromechanics, strength, aircraft airworthiness); pp. 7 - 13) (in Russian)
22. №289; 29.09.2015; "Об утверждении Федеральных авиационных правил "Требования к образовательным организациям и организациям, осуществляющим обучение специалистов соответствующего уровня согласно перечням специалистов авиационного персонала"; *Приказ*; Министерство Транспорта Российской Федерации
 (No.289; 29.09.2015; "About ratification of Federal Aviation Regulations "Requirements to educational institutions and organizations preparing aviation specialists of proper level"; *Order*; Ministry of Transport of the Russian Federation) (in Russian)
23. №147; 12.09.2008 (ред. от 16.09.2015); "Об утверждении Федеральных авиационных правил "Требования к членам экипажа воздушных судов, специалистам по техническому обслуживанию воздушных судов и сотрудникам по обеспечению полетов (полетным диспетчерам) гражданской авиации"; *Приказ*; Министерство Транспорта Российской Федерации
 (No.147; 12.09.2008 (ed 16.09.2015); "About ratification of Federal Aviation Regulations "Requirements to air crew men, aircraft maintenance engineers, and flight support crew / flight dispatchers in Civil Aviation"; *Order*; Ministry of Transport of the Russian Federation) (in Russian)
24. 2016; "Federal Aviation Administration"; <http://www.faa.gov>
25. 2016; "European Aviation Safety Agency"; <https://www.easa.europa.eu>
26. 2016; "International Civil Aviation Organization"; <http://www.icao.int>

Turboprop Engine Nacelle Optimization for Flight Increased Safety and Pollution Reduction

Cristian DOROBĂȚ^{1,a}, Gheorghe MOCA^{1,b}, Elena PRESURĂ^{1,c}

¹ *COMOTI Romanian Research and Development Institute for Gas Turbines
220D Iuliu Maniu Ave. 061126 Bucharest ROMANIA*

^a*cristian.dorobat@comoti.ro*, ^b*gheorghe.moca@comoti.ro*, ^c*elena.presura@comoti.ro*

ABSTRACT

Commuter airplanes defined in CS-23 as being propeller driven, twin-engine, nineteen seats and maximum certified take-off weight of 8618 Kg had lately a special development due to advantages of turboprop engine compared with piston or jet engines. Nacelle optimization implies a sound and vibrations proof engine frame, engine fuel consumption reduction (through smaller nacelle drag and weight, better lift, better pressure recovery in air induction system, smaller drag of exhaust nozzles, engine cooling and nacelle ventilation more efficient, composite nacelle fairings with noise reduction properties, etc.). Nacelle aerodynamic experimental model, air induction experimental model and other nacelle experimental systems tested independently allow construction efficiency due to minimizing modifications on nacelle assembly and more safety in operation [1].

KEYWORDS: *nacelle, optimization, commuter, experimental model.*

Stepper motors for space applications-ICPE Activities

Mircea Modreanu

ICPE

Senior Scientific Researcher

313 Splaiul Unirii, Bucuresti, Romania

mircea.messico@icpe.ro

Ioana Ionica

ICPE

Scientific Researcher

Cristian Boboc

ICPE

Scientific Researcher

ABSTRACT

The paper presents the development of stepper motors for space applications in ICPE. The approach of these motors has beginning within first ESA contract - Electric Motor Technology Spin Into Space – EMSIS and continued in the second ESA contract, named Stepper Motor for Multimedia Antenna Deployment & Pointing Mechanism of 2nd generation - SM MADPM MKII. The main objective of the first contract is the evaluation of the suitability of ICPE electric motors for the space sector. For the second contract, the main objective is the development of a new version of steppers to address TAS needs for the Multimedia Antenna Pointing Mechanism of 2nd generation (MADPM MKII). The main activities from the projects stages, including design, numerical modeling, manufacturing results from breadboarding stages and experimental results from EM test campaign will be detailed. ICPE, a well-established manufacturer of electric motors at an international level, is in an entering position on this new market through harmonization of the existing electric motor technology with the standard required for the space applications.

KEYWORDS: stepper motor, space applications, numerical modeling, FEM analysis



Mission Planning Approach for an Exoplanet Characterization Satellite

Javier Fernández-Villacañas Cabezas

DEIMOS Space S.R.L.

Project Engineer

javier.fernandez-villacanas@deimos-space.com / jfvillacanas@outlook.com

Paulo J. S. Gil

CCTAE, IDMEC, Instituto Superior Técnico, Universidade de Lisboa

Assistant Professor

Antonio Gutiérrez Peña

DEIMOS Space S.L.

Head of Ground Segment BU

ABSTRACT

As space observation techniques evolve, more and more astronomical objects and events are discovered. This large number of observable objects need to be precisely characterized by observation satellites; therefore a good planning of the observations is required. In addition, observation satellites are orbiting a planet, typically the Earth. Consequently, the target visibility will be affected by several constraints which will produce interruptions in the observation because of either the occultation of the targets or the possibility of damage in the sensor. In this work, we will optimize the observations of an exoplanet characterization satellite, considering key parameters. To proceed with the optimization, we first have to calculate the visibility of the targets by determining its constraints, such as the occultation produced when the Earth is between the satellite and the target. This work shows that the major driver of the visibility problem is the Sun's exclusion angle constraint, which allows to reduce the spectrum of solutions of the optimization problem. The optimization is performed maximizing the effective visibility time and the number of observations with Local Search and Monte Carlo methods.

KEYWORDS: *targets visibility, exoplanet characterization satellite, observations planning, observations optimization, visibility and optimization constraints.*

Table of content

1. Validation of the SmartBasing Aircraft Rotation and Retirement Strategy , Jeffrey M. Newcamp, Wim J.C. Verhagen, Richard Curran.....	3
2. Towards automation of aerial refuelling manoeuvres with the probe-and drogue system: Modelling and simulation , Nicolas Fezans, Thomas Jann.....	4
3. Composite wind turbine blade using prepreg technology , Ionut S. Vintilă, Mihaela R. Condruz, Ion Fuiorea, Ion Mălăel, Mihail Sima.....	5
4. Composite material designs for lightweight space packaging structures , Mihaela R. Condruz, Raluca L. Voicu, Cristian Puscasu, Ionut S. Vintilă, Mihail Sima, Marius Deaconu, Luminita Drăgăsanu.....	15
5. More electrical non-propulsive architectures integration , Nawal Jaljal, Jean-Philippe Salanne, René Meunier, Bruno Thoraval, Clélia Level.....	27
6. Testing of experimental and numerical methods for investigation of the unsteady flow induced by rotor influence on heliport , Wit Stryczniewicz, Paweł Ruchała, Grzegorz Krysztofia, Wiesław Zalewski, Adam Dziubiński, Małgorzata Wojtas, Kazimierz Szumański.....	28
7. Graph-based algorithms and data-driven documents for formulation and visualization of large MDO systems , Benedikt Aigner, Imco van Gent, Gianfranco La Rocca, Eike Stumpf, Leo L.M. Veldhuis.....	29
8. Application of a visualization environment for the mission performance evaluation of civilian UAS , Ekaterina Fokina, Jens Feger, Mirko Hornung	30
9. Automated handling and positioning of large dry carbon fibre cut-pieces with cooperating robots in rear pressure bulkhead production , Lars Brandt, Mona Eckardt.....	31
10. A thermal-solar system for de-orbiting of space debris , Constantin Sandu, Dan Brasoveanu, Valentin Silivestru, Bogdan Filipescu, Radu C. Sandu	40
11. Solar-gravitational spacecraft used for traveling in the solar system , Constantin Sandu, Dan Brasoveanu, Valentin Silivestru, Bogdan Filipescu, Radu C. Sandu.....	41
12. Aircraft ground operations: steps towards automation , Diego Alonso Tabares, Felix Mora-Camino.....	53
13. External wireless system for ultimate flight control in contingency situations , Filip Niculescu, Andrei Mitru, Constantin Sandu, Constantin Vilcu	54
14. Space technology for reduction of desert areas on Earth and weather control , Constantin Sandu, Dan Brasoveanu, Valentin Silivestru, Bogdan Filipescu, Radu C. Sandu.....	55
15. An Object-Oriented Approach to a Scenario-Based System Dynamics Fleet Model , Gilbert Tay, Raoul L. Rothfeld.....	56
16. Considerations of direct solar thermal power generation systems for space propulsion , Alexandru Onea, Nerea Diez de los Rios Ramos, Wolfgang Hering, Robert Stieglitz.....	57
17. Analysis of aircraft rolling over potholes and ruts , Jose E. Gómez Viñas, Jose M. Chorro Martínez, Angel Martínez Pérez, Silvia Parra Adan, Alvaro Ros Contreras.....	58
18. Technology for terraformation of mars, other planets and natural satellites , Constantin Sandu, Dan Brasoveanu, Valentin Silivestru, Bogdan Filipescu, Radu C. Sandu.....	60
19. Passenger spaceplanes and airplanes that have variable configuration for sonic boom reduction , Constantin Sandu, Dan Brasoveanu, Valentin Silivestru, Bogdan Filipescu, Radu Constantin Sandu.....	68
20. A new design of space equipment for rapid disintegration in atmosphere after reentry , Constantin Sandu, Dan Brasoveanu, Valentin Silivestru, Bogdan Filipescu, Radu Constantin Sandu...69	

21. Resistance of composite laminates to the initiation and propagation of delamination under low velocity impact , Yigeng Xu, Zeng Shen, William Tiu, Yizhong Xu, Amit Ramji, Marzio Grasso.....	76
22. Onboard Functional Requirements for Specific Category UAS and Safe Operation Monitoring , Christoph Torens, Florian Nikodem, Johann C. Dauer, Joerg S. Dittrich.....	77
23. Wind tunnel testing of the control system for a new morphing wing application with a full-scaled portion of a real wing , M.J. Tchatchueng Kammegne, R.M. Botez, L.T. Grigorie, M. Mamou, Y. Mebarki	78
24. Solar-gravitational system for deorbiting space debris and reentry in Earth's atmosphere and accelerating active satellites for orbit reestablishment , Constantin Sandu, Dan Brasoveanu, Valentin Silivestru, Bogdan Filipescu, Radu Constantin Sandu.....	79
25. A Java Toolchain of Programs for Aircraft Design , Agostino De Marco, Vincenzo Cusati, Vittorio Trifari, Manuela Ruocco, Fabrizio Nicolosi, Pierluigi Della Vecchia.....	88
26. Effects of MR Damper on Flutter of a Wing/Store Configuration , A.Mazidi, H. Pourshamsi, S. A Fazelzade.....	105
27. A Study on the Micro Gravity Sloshing Modeling of Propellant Quantity Variation , Dongyeon Lee, Min-hyun Cho, Han-lim Choi, Min-jea Tahk.....	106
28. Numerical analysis of propeller effects on wing aerodynamic: tip mounted and distributed propulsion , P. Della Vecchia, D. Malgieri, F. Nicolosi, A. De Marco.....	107
29. Valveless Pulsed Detonation Chamber Controlled by Hartmann Oscillators , Tudor Cuciuc, Constantin E. Hritcu, Gabriel G. Ursescu, Ionut Porumbel, Cleopatra F. Cuciumita.....	108
30. Numerical Simulation of Detonation in a Valveless Pulsed Detonation Chamber , Ionut Porumbel, Bogdan G. Gherman, Ion Malael, Valeriu Dragan.....	119
31. Experimental Measurements in Hartmann Oscillators , Ionut Porumbel, Cleopatra F. Cuciumita, Cristian Nechifor, Radu Kuncser, Tudor Cuciuc.....	129
32. Applying of Six-Sigma Methodology for Noise Reduction of Complex Aerospace Assemblies , Constantin Sandu, Dan Brasoveanu, Valentin Silivestru, Bogdan Filipescu, Radu Constantin Sandu	130
33. The effects of multiple detonation waves in the RDE flow field , Bayindir H. Saracoglu, Aysu Ozden.....	131
34. Reconstruct ion of High-Frequency Lunar Digital Elevat ion Model using Shape from Shading , Min-Hyun Cho, Ji-Hoon Bai, Min-Jea Tahk.....	132
35. Passengers Rescuing in case of Imminent Disaster of Large Airplaines , Constantin Sandu, Dan Brasoveanu, Valentin Silivestru, Bogdan Filipescu, Radu Constantin Sandu.....	133
36. A knowledge based engineering tool to support front-loading and multidisciplinary design optimization of the fin-rudder interface , Akshay Raju Kulkarni, Gianfranco La Rocca, Tobie van den Berg, Reinier van Dijk	140
37. Flight Software Development and Validation Workflow Management System , Dan Gultureanu, Kevin Kerns, Tom Henthorn, John Quach, Mitch Kleen	141
38. Initial Investigation of Aerodynamic Shape Design Optimisation for the Aegis UAV , Y. Azabi, A. Savvari, T. Kipouros.....	142
39. Convexification in Energy Optimization of a Hybrid Electric Propulsion System for Unmanned Aerial Vehicles , Ye Xie, Al Savvaris, Antonios Tsourdos.....	143
40. Preliminary Design of Advanced Flight Control System Architectures for Commercial Transport Aircraft , Thomas Lampl, Timo Wolf, Mirko Hornun.....	152
41. Angular Momentum Analysis of Spacecraft with Control Moment Gyros , H. Leeghim...153	

42. Reference Trajectory Optimization Using the Particle Swarm Optimization , Alejandro Murrieta-Mendoza, Ruxandra Mihaela Botez.....	154
43. GPU based Computational Simulation of Aircraft Evacuation: Temporal and Spatial Analysis , Minesh Poudel, Bhaskar Chaudhury, Kshitij Sharma, Pavel Yaroslavovich Tabakov, Félix Mora-Camino.....	155
44. Bézier-curve Navigation Guidance for Impact Time and Angle Control , Gun-Hee Moon, Sang-Wook Shim, Min-Jea Tahk.....	156
45. The Effect of Sub-systems Design Parameters on Preliminary Aircraft Design in a Multidisciplinary Design Environment , Marco Fioriti, Luca Boggero, Sabrina Corpino, Prajwal Shiva Prakasha, Pier Davide Ciampa, Björn Nagel.....	157
46. Configuration Design of Smart Structures with Array Antennas , Minsung Kim, Sangmin Baek, Myunggyun Ko, Jongwoo Seo, Youngsik Joo.....	158
47. Credibility of 21st Century numerical simulations in A/C crash and impact analysis , E. Deletombe, M. Mahé.....	159
48. The Influence of the Vaned Diffuser on the Turbo machinery , Gheorghe Fetea, Oana Dumitrescu, Bogdan Gherman, Dan Robescu.....	160
49. Development of a Software Tool for Comprehensive Flight Performance and Mission Analysis of Hybrid-Electric Aircraft , Gilbert Tay, Paul Keller, Mirko Hornung.....	170
50. An improved method for transport aircraft for high lift aerodynamic prediction , Pierluigi Della Vecchia, Fabrizio Nicolosi, Manuela Ruocco, Luca Stingo, Agostino De Marco.....	171
51. Automated Selection of Airliner Optimal On-board Systems Architecture within MDO Collaborative Environment , Riccardo Lombardi, Marco Fioriti and Luca Boggero, Luciana Lo Verde and Nicola Catino, Artur Mirzoyan, Roberto d'Ippolito.....	172
52. Development of an End to End Maintenance Evaluation Strategy for new Technologies in the Context of I VHM , Hendrik Meyer, Nicolas Bontikous, Alexander Plagemann.....	186
53. Cost Efficiency Model for Civil Transport Aviation referring to Operations , M. A. Solazzo, L. Travascio, A. Vozella.....	196
54. Model-Based Fault Identification of Fighter Aircraft's Environmental Control System , Leo Mäkelä, Jussi Aaltonen, Kari T. Koskinen, Kari Mäentausta.....	210
55. Comparison Between Numerical Results and Operative Environment Data on Neural Network for Air Data Estimation , Angelo Lerro, Manuela Battipede, Piero Gili, Alberto Brandi.....	218
56. Uncertainty quantification and robust design optimization applied to aircraft propulsion systems , Marco Panzeri, Andrey Savelyev, Kirill Anisimov, Roberto d'Ippolito, Artur Mirzoyan.....	219
57. Low Speed Take-Off Aerodynamic Analysis , D. Charbonnier & J.B. Vos, P.S. Prakasha, A. Mirzoyan, A. Savelyev, P. Della Vecchia.....	220
58. The Impact of flow features on formation of surface carbonaceous deposits under aero engine representative conditions , E. Alborzi, S. Blakey, P Gadsby.....	235
59. Aircraft Optimization at the Early Stages of Design with a Hybrid Technique , Nesrin Cavus.....	236
60. Integrating Maintenance Work Progress Monitoring into Aircraft Maintenance Planning Decision Support , Pieter Callewaert, Wim J.C. Verhagen, Richard Curran.....	237
61. Threshold identification and damage characterization of GF/CF composites under low-velocity impact , Amit Ramji, Yigeng Xu, Marzio Grasso, James Watson, George Haritos.....	238
62. A Pedagogical Approach Based on Problem-Based Learning on Aeronautical Engineering Post-Graduation at Instituto Tecnológico de Aeronáutica (ITA) , Adson Agrico de Paula, Roberto Gil Annes da Silva.....	239

63.	Identification of Optimal Preventive Maintenance Decisions for Composite Components, Paul Laks, Wim J.C. Verhagen, Richard Curran.....	246
64.	An Investigation into All Electric and Hybrid Aircraft, Gareth England, Errikos Levis.....	247
65.	Morphological Design and Analysis of Aircraft Wings, Jakub Drzewoszewski, Cristinel Mares.....	248
66.	The flow separation development analysis in subsonic and transonic flow regime of the laminar airfoil, R. Placek, P. Ruchała.....	258
67.	Investigation of viscosity influence on transonic flutter, S. Kuzmina, F. Ishmuratov, A.Chizhov, O. Karas.....	259
68.	Flight Test Design for Remotely-Piloted Aircraft in Confined Airspace, Alejandro Sobron, David Lundström, Petter Krus, Christopher Jouannet, Luiz C.S. Góes.....	260
69.	Helicopter Roll – Axis Instabilities induced by Pilot Cyclic Control: A Physical Explanation, Marilena D. Pavel, Achim Ionita.....	270
70.	The studies on low-noise laminar wing aircraft for regional and short range routes, A.L.Bolsunovsky, N.N.Bragin, N.P.Buzoverya, I.L.Chernyshev.....	271
71.	Numerical investigation of a new LH2 centrifugal pump concept used in space propulsion, Ion Mălăeș, Bogdan George Gherman, Ionuț Porumbel.....	272
72.	Subsonic Jet Pump Comparative Analysis, George Bogdan Gherman, Florin Florean, Ionut Porumbel.....	273
73.	Experimental Approach Regarding the Ignition of H₂/O₂ Mixtures in Vacuum Environment, Jeni A. Popescu, Valeriu A. Vilag, Ionuț Porumbel, Cleopatra F. Cuciumita, Nicolae Macrisoiu.....	274
74.	Experimental studies on injection nozzle flame stability for gas turbines using in-situ combustion applications, Cleopatra Cuciumita, Daniel Olaru, Marius Enache, Florin Florean.....	275
75.	Numerical Calculation of 3D Low Speed Delta Wing Fighters Jet Aircraft, Hacı Sogukpinar.....	276
76.	Interaction of supercooled droplets and nonspherical ice crystals with a solid body in a mixed cloud, Ivan A. Amelyushkin, Albert L. Stasenko.....	284
77.	Numerical Calculation of Wind Tip Vortex Formation for Different Wingtip devices, Hacı Sogukpinar.....	285
78.	Formation Flight Mechanics and its Integrated Logistics, Tomas Melin, Diane Uyoga.....	286
79.	Detached Eddy-Simulations of Delta-Wing Post-Stall Flow Control, Andrei Buzica, Manuel Biswanger, Christian Breitsamter.....	287
80.	A method for calculus of Internal Forces, Thien Van Nguyen, I. Stroe, A. Craifaleanu, Roxana Alexandra Petre, Dan Dumitriu.....	288
81.	Flutter Uncertainty Analysis of an Aircraft Wing Subjected to a Thrust Force Using Fuzzy Method, M. Rezaei, S.A. Fazelzadeh, A. Mazidi.....	289
82.	Hybrid Optimization of Star Grain Performance Prediction Tool, Anwer E. A. Hashish, Mahmoud Y.M. Ahmed, Hamed M. Abdallah, Mohamed A. Alsenbawy.....	290
83.	Optimization of noise abatement aircraft terminal routes using a multiobjective evolutionary algorithm based on decomposition, V. Ho-Huu, S. Hartjes, L. H. Geijselaers, H. G. Visser, R. Curran.....	300
84.	The relative Motion of a SpaceCraft Near a Geostationary Position, Roxana Alexandra Petre, Ion Stroe, Andrei Craifaleanu, Thien Van Nguyen.....	301

85. System and method for flight envelope expansion via piezoelectric actuation , Ioan Ursu, Dragos Daniel Ion Guta, George Tecuceanu, Alexandru-Gabriel Persinaru, Daniela Enciu, Ionel Popescu, Cornel Stoica.....	309
86. Sealing technologies trade-off for a Phobos Sample Return Mission , Radu Mihalache, Dragos Mihai, Gheorghe Megherelu, Ionut Florian Popa, Daniel Olaru, Dan Ifrim.....	311
87. Development of a Methodology for Assessing and Exploiting Innovative Aircraft Concepts and Technologies , Yaolong Liu, Peter Horst, Jens Friedrichs.....	313
88. Scaling of Airborne Ad-hoc Network Metrics with Link Range and Satellite Connectivity , Kai-Daniel F. Büchter, Oleg Milshtein.....	314
89. Estimation of Mission Fuel Savings Potential using Thermoelectric Recuperation in Aero-Engines , Kai-Daniel F. Büchter, Ulrich Kling, Christoph Bode, Jens Friedrichs.....	315
90. Parametric Study on Taper-ended Internal-burning Solid Propellant Grains , Mahmoud Y. M. Ahmed.....	316
91. Control of cavity acoustics by surface waviness in landing configurations , Abderrahmane Belkallouche, Laurent Dala.....	317
92. Proposal for a EU quality label for aerospace education , Franco Bernelli-Zazzera, Maria Angeles Martin Prats, Francesco Marulo, Daniel Hanus, Joris Melkert, Giorgio Guglieri, Pascal Bauer, Irene Pantelaki, Iring Wasser, Herman Deconinck, Ruxandra Bosilca, Hanna-Kaisa Saari.....	328
93. Award-Winning Innovative Aircraft Design Projects at Politecnico di Milano , Lorenzo Trainelli, Carlo E. D. Riboldi.....	330
94. The design of an annular combustion chamber , Marius Enache, Andreea Mangra, Razvan Carlanescu, Florin Florean.....	342
95. A New Framework for Rotorcraft In-flight Noise Monitoring , Lorenzo Trainelli.....	352
96. Preliminary Weight Sizing of Light Pure-Electric and Hybrid-Electric Aircraft , Carlo E.D. Riboldi, Federico Gualdoni, Lorenzo Trainelli.....	361
97. On the Theoretical and Experimental Activities Performed by Professor Hermann Oberth in Romania , Nicolae Florin Zaganescu, Constantin Marcian Gheorghe.....	362
98. On the Contributions of Dr. Irene Sänger-Bredt in the Field of Astronautics , Constantin Marcian Gheorghe, Nicolae Florin Zaganescu.....	370
99. Importance of a Second Entrance in a Test Cell , Oana Dumitrescu, Bogdan Gherman, Ionut Porumbel.....	378
100. SOUNDING ROCKETS Analysis, simulation and optimization of a solid propellant motor , Laura Navarrete Martín, Petter Krus.....	379
101. Application of Hamilton Principle in the control of Tethered Satellite System Pendular Motion , P. Tirop, J. Zhang.....	380
102. Failure analysis of a high-speed offset bearing , Daniela M. Buzescu, Sorin Gabriel Tomescu.....	381
103. Time-domain aeroelastic model for compound helicopter propeller-wing configuration , Zi Wang, Alessandro Anobile, Atanas A. Popov.....	382
104. Methods Supporting the Efficient Collaborative Design of Future Aircraft , Erik Baalbergen, Erwin Moerland, Wim Lammen, Pier Davide Ciampa.....	383
105. Pitch Stabilization with Tailored Canard Compliance , Petter Krus, Birgitta Lantto.....	384
106. Preliminary Investigation on the Impact of Missile Design on its Aerodynamic Features , Mahmoud M. Abdel-Fattah.....	385
107. Losses and blade tip clearance for a centrifugal compressor , Oana Dumitrescu, Ramona Stanciuc, Bogdan Gherman, Valeriu Drăgan.....	395

108. Conceptual Design of a Stratospheric Hybrid Platform for Earth Observation and Telecommunication , Vincenzo R. Baraniello, Giuseppe Persechino.....	396
109. MDO Architectures Comparison on Analytical Test Case and Aerostructural Aircraft System Design Problem , Francesco Torrigiani, Pier Davide Ciampa.....	406
110. Knowledge-based automatic Airframe Design using CPACS , J.-N. Walther, P. D. Ciampa.....	407
111. Enhanced Kinematics Calculation for an Online Trajectory Generation Module , Patrick Piprek, Volker Schneider, Vincent Fafard, Simon P. Schatz, Christoph Dörhöfer, Patrick J. Lauffs, Lars Peter, Florian Holzapfel.....	408
112. Detecting Future Potentials for Step-change Innovation in Aeronautics – Progress and Challenges , L. Koops, A. Sizmann.....	409
113. Spacecraft bracket design using additive manufacturing , Alexandru-Mihai Cismilianu, Camelia Elena Munteanu, Ionut-Cosmin Oncescu, Mihaela Nastase, Radu-Petru Bibire, Ion Dima, Mihai Victor Pricop	426
114. Finite Element Modelling and Performance Optimization of an Ion Thruster depending on the nature of the propellant , Ionut-Florian Popa, Anna-Maria Theodora Andreescu, Dan Ifrim, Radu Mihalache, Dragos Mihai, Grigore Cican.....	427
115. Gust Alleviation of Aeroelastic Aircraft Using CFD Simulation , Aleš Prachař, Pavel Hospodář, Petr Vrchota.....	428
116. Evaluation of Piston Engine Modes and Configurations in Composite Cycle Engine Architectures , Markus Nickl, Sascha Kaiser.....	429
117. Twin-jet and trijet aircraft: a study for an optimal design of regional aircraft , Edgar Coelho Inouye, Adson Agrico de Paula, Patrice London Guedes, William Martins Alves.....	430
118. A modelling framework to support power architecture trade-off studies for More-Electric Aircraft , Ana Garcia Garriga, Parithi Govindaraju, Sangeeth Saagar Ponnusamy, Nicola Cimmin, Laura Mainini.....	431
119. Synthesizing a massive training dataset based on real lunar data for image-based navigation and crater recognition , Hoonhee Lee, Dawoon Jung, Seunghee Son, Han-Lim Choi.....	432
120. Unsteady Full Annulus Multi -Stage Compressor Calculations - Details on CFD-Experiment Comparison , Oliver Reutter, Graham Ashcroft, Edmund Kügeler.....	440
121. Thermal shock, tribological and mechanical properties of micro and nanostructured zirconia partially stabilized with yttria and ceria , Dragomirescu Alina, Botan Mihail, Manoliu Victor, Ionescu Gheorghe, Stefan Adriana, Mihailescu.....	441
122. Near Optimal Explicit Guidance Law with Impact Angle Constraints for a Hypersonic Reentry Vehicle , Karthikeyan Kalirajan, Ashok Joshi.....	450
123. Assessment of chemical time scale for a turbine burner , Dragos Isvoranu, Sterian Dănilă, Alina Bogoi, Constantin Leventiu.....	451
124. Design and aerodynamic analysis of a regional turboprop innovative configuration , Fabrizio Nicolosi, Salvatore Corcione, Pierluigi Della Vecchia, Vittorio Trifari, Manuela Ruocco, Agostino De Marco.....	452
125. The effect of heat treatment on the homogenization of CMSX-4 Single-Crystal Ni-Based Superalloy , A. Paraschiv, G. Matache, C. Puscasu.....	469
126. Collaborative Design of Aircraft Systems - Multi-Level Optimization of an Aircraft Rudder , Wim Lammen, Bert de Wit, Jos Vankan, Huub Timmermans, Ton van der Laan, Pier Davide Ciampa.....	470

127. Vibration Energy Harvesting Potential for Turbomachinery Applications , Adrian Stoicescu, Marius Deaconu, Romeo Dorin Hrițcu, Cristian Valentin Nechifor, Cristinel-Ioan Hărăguță, Valeriu Alexandru Vilag.....	471
128. Assessment of Electric Taxiing Considering Aircraft Utilization and Maintenance Cost , Ulrich Kling, Clemens Steger, Fabian N. Peter, Michael Schmidt.....	472
129. REVLANSYS: Mission and GNC Design of Terminal Entry and Landing Missions for Advanced Re-entry Vehicles , Antonio Russo, Alina Ionita, Fernando Pina Caballero, Giovanni Medici, Cristina Recupero, Gabriele De Zaiacomo, Murray Kerr.....	473
130. Sizing Considerations of an Electric Ducted Fan for Hybrid Energy Aircraft , Patrick C. Vratny, Mirko Hornung.....	474
131. Experimental Investigations on Aerodynamic Response of Panel Structures at High Subsonic and Low Supersonic Mach Numbers , Jannis Lübker, Marko Alder.....	475
132. Considerations regarding optimization of low speed balancing of high speed flexible rotors , Alexandru Tudorache, Ion Fuiorea.....	476
133. Unified Longitudinal Flight-dynamic and Aeroelastic Analysis of a PrandtlPlane Configuration , Rocco Bombardieri, Francesco Auricchio, Rauno Cavallaro.....	485
134. CFD analysis for an improved concept of ventilation system for the Crew Quarters on board of the International Space Station , Florin Bode, Ilinca Năstase, Matei-Răzvan Georgescu, Ioan Ursuc, Dragos Guță.....	486
135. Data-driven Optimisation of Closure Coefficients of a Turbulence Model , Andrea Da Ronch, Marco Panzeri, Jernej Drofelnik, Roberto d'Ippolito.....	487
136. A Review of Recent Personal Air Vehicle Concepts , Michael Shamiyeh, Julian Bijewitz, Mirko Hornung.....	488
137. Discrete Gust Response of a Box-wing Configuration , Rauno Cavallaro, Juan Palacios Santos, Rocco Bombardieri.....	489
138. Parameter Estimation of a Mini Aerial Vehicle using Multiple Trim Flight Data , Pranavkumar V. Patel, Hemendra Arya.....	490
139. Progress of Subscale Winged Rocket Development and Its Application to Future Fully Reusable Space Transportation System , Koichi Yonemoto, Takahiro Fujikawa, Toshiki Morito, Joseph Wang, Ahsan R. Choudhuri.....	491
140. Different Fidelity Computational Models in Aeroelastic Design of Aircraft and WT Models , V.V. Chedrik, F.Z. Ishmuratov.....	492
141. A Preliminary Heat Transfer Analysis of Pulse Detonation Engines , Berke Olcucuoglu, Bayindir H. Saracoglu.....	493
142. Definition and Discussion of the Intrinsic Efficiency of Winglets , Dieter Scholz.....	494
143. Subscale Flight Test Model Development and Testing as a Tool for Unconventional Aircraft Design , Diego de Matos Monteiro, Leonardo Murilo Nepomuceno, Roberto Gil Annes da Silva, Marcos da Silva e Souza, Flávio José Silvestre, Petter Kruss, Alejandro Sobrón Rueda.....	495
144. Investigation of the Flow Around an Aircraft Wing of Section NACA 2412 Utilising ANSYS Fluent , Rob Ives, (Andrew) Stewart Keir, Edet Bassey, F A Hamad.....	497
145. CFD Analysis of C-D Nozzle compared with Theoretical & Experimental Data , (Andrew) Stewart Keir, Rob Ives, F A Hamad.....	498
146. Disciplinary Data Fusion For Multi-Fidelity Aerodynamic Application , Mengmeng Zhang, Aidan Jungo, Nathalie Bartoli.....	499

147. Overview Of MDO Enhancement In The AGILE Project: A Clustered And Surrogate-Based MDA Use Case , Thierry Lefebvre, Nathalie Bartoli, Sylvain Dubreuil, Riccardo Lombardi, Marco Panzeri, Wim Lammen, Mengmeng Zhang, Imco van Gent, Pier Davide Ciampa.....	500
148. Robust optimization of a rudder hinge system taking into account uncertainty in Airframe parameters , Ton van der Laan, Luc Hootsmans, Marco Panzeri, Roberto d'Ippolito.....	525
149. Aircraft Normal Modes...Friend or Foer An Airbus Answer , Mercedes Oliver Herrero, Félix Arévalo Lozano, Héctor Climent Máñez.....	526
150. Preliminary transonic CFD analyses of a PrandtlPlane transport aircraft , Vittorio Cipolla, Aldo Frediani, Karim Abu Salem, Vincenzo Binante, Marco Maganzi, Emanuele Rizzo.....	551
151. Concurrent engineering and fast-mapping/crowd-mapping using IoT, Big Data and Cloud Computing , George Suci, Adrian Pasat, Laurentiu Bezdedeanu, Iulian Iordache, Gabriela Iosif, Emil Costea.....	552
152. CMDOWS: A Proposed New Standard To Store And Exchange MDO Systems , Imco van Gent, Gianfranco La Rocca, Maurice F. M. Hoogreef.....	562
153. Improved NEO data processing Capabilities for the ESA SSA-NEO software system , Teodorescu Claudiu, Teodorescu Ana-Maria, Koschny Detlef.....	563
154. A new vision - Eco-friendly launching propulsion – The Future , Ene Călinescu Alexandru.....	571
155. Launch Vehicle - MDO in the development of a Microlauncher , Tudorel-Petronel Afilipoae, Ana-Maria Neculăescu, Alexandru-Iulian Onel, Mihai-Victor Pricop, Alexandru Marin, Alexandru-Gabriel Persinar, Alexandru-Mihai Cismilianu, Ionut-Cosmin Oncescu, Adrian Toader, Adriana Sirbi , Samir Bennani, Teodor-Viorel Chelaru.....	578
156. Aviation Regulations of Russia: a Transition from One Type to Another , Oleksiy Chernykh, Mambet Bakiiev.....	580
157. Turboprop Engine Nacelle Optimization for Flight Increased Safety and Pollution Reduction , Cristian Dorobăt, Gheorghe Moca, Elena Presură.....	587
158. Stepper motors for space applications-ICPE Activities , Mircea Modreanu, Ioana Ionica, Cristian Boboc.....	588
159. Mission Planning Approach for an Exoplanet Characterization Satellite , Javier Fernández-Villacañas Cabezas, Paulo J. S. Gil, Antonio Gutiérrez Peña.....	589

ISBN: 978-973-0-25597-3

Edited by the Romanian Research and Development Institute for Gas Turbines COMOTI